Focus on Neutrino Physics

Francis Halzen *et al* 2004 *New J. Phys.* **6** doi:10.1088/1367-2630/6/1/E02

2004 will see the publication in *New Journal of Physics* of a Focus Issue on the topic of Neutrino Physics. Its objective is to form an extensive, open-access resource that provides a collective representation of the latest research conducted in the field. The articles below represent the first contributions and further additions from leading groups within the astrophysical, experimental and theoretical neutrino communities will appear later in the year.

Searching for dark matter with neutrino telescopes
Dan Hooper and Joseph Silk

Solar models and solar neutrino oscillations
John N Bahcall and Carlos Peña-Garay

Supersymmetric origin of neutrino mass
M Hirsch and J W F Valle

The role of neutrinos, rotations and magnetic fields in collapse-driven supernovae
Shoichi Yamada, Kei Kotake and Tatsuya Yamasaki

Physics of the neutrino mass
R N Mohapatra

New plots and parameter degeneracies in neutrino oscillations
Osamu Yasuda

Non-Abelian discrete symmetries and neutrino masses: two examples
Ernest Ma

Some aspects of thermal leptogenesis
W Buchmüller, P Di Bari and M Plümacher

Models of neutrino masses and mixings
Guido Altarelli1 and Ferruccio Feruglio

Neutrinos in cosmology
Steen Hannestad

Neutrino masses, mixing, Majorana CP-violating phases and $(\beta\,\beta)_{0\nu}$ decay
S T Petcov

Sequential dominance

Stefan Antusch and S F King

Neutrino telescopes in the Mediterranean Sea
J Carr and G Hallewell

SNEWS: the SuperNova Early Warning System
Pietro Antonioli, Richard Tresch Fienberg, Fabrice Fleurot, Yoshiyuki Fukuda, Walter Fulgione, Alec Habig, Jaret Heise, Arthur B McDonald, Corrinne Mills, Toshio Namba, Leif J Robinson, Kate Scholberg, Michael Schwendener, Roger W Sinnott, Blake Stacey, Yoichiro Suzuki, Réda Tafirout, Carlo Vigorito, Brett Viren, Clarence Virtue and Antonino Zichichi

BBN for pedestrians
James P Kneller and Gary Steigman

Solar neutrinos
A B McDonald

Status of global fits to neutrino oscillations
Michele Maltoni, Thomas Schwetz, Mariam Tórtola and José W F Valle

Unity of CP and T violation in neutrino oscillations
Martin Blom and Hisakazu Minakata

Neutral currents and tests of three-neutrino unitarity in long-baseline experiments
V Barger, S Geer and K Whisnant

Evidence for the MSW effect
Gianluigi Fogli and Eligio Lisi

Extra-galactic sources of high-energy neutrinos
Eli Waxman

Reactor neutrino oscillation studies with KamLAND
K Inoue

The particle physics reach of high-energy neutrino astronomy
Tao Han and Dan Hooper

Relic neutrino background from cosmological supernovae
Shin'ichiro Ando and Katsuhiko Sato

Atmospheric neutrinos
Takaaki Kajita

Massive neutrinos and flavour violation

Antonio Masiero, Sudhir K Vempati and Oscar Vives

Next generation double-beta decay experiments: metrics for their evaluation
F T Avignone III, G S King III and Yu G Zdesenko

Neutrino mixing and nucleosynthesis in core-collapse supernovae
A B Balantekin and H Yüksel

Neutrino masses from cosmological probes
Øystein Elgarøy and Ofer Lahav

Leptonic CP violation and neutrino mass models
Gustavo C Branco and M N Rebelo

Neutrino detection with inclined air showers
Enrique Zas

New Journal of Physics
An Institute of Physics and Deutsche Physikalische Gesellschaft Journal

Searching for dark matter with neutrino telescopes

Dan Hooper[1] **and Joseph Silk**[1,2]

[1] Denys Wilkinson Laboratory, Astrophysics Department,
OX1 3RH Oxford, UK
[2] Institut d'Astrophysique de Paris, Paris, France
E-mail: hooper@astro.ox.ac.uk, silk@astro.ox.ac.uk

New Journal of Physics **6** (2004) 23
Received 1 December 2003
Published 13 February 2004
Online at http://www.njp.org/ (DOI: 10.1088/1367-2630/6/1/023)

Abstract. One of the most interesting mysteries of astrophysics is the puzzle of dark matter. Although numerous techniques have been explored and developed to detect this elusive substance, its nature remains unknown. One such method uses large high-energy neutrino telescopes to look for the annihilation products of dark matter annihilations. In this paper, we briefly review this technique. We describe the calculations used to find the rate of capture of WIMPs in the Sun or Earth and the spectrum of neutrinos produced in the resulting dark matter annihilations. We will discuss these calculations within the context of supersymmetry and models with universal extra dimensions, the lightest supersymmetric particle and lightest Kaluza–Klein particle providing the WIMP candidate in these cases, respectively. We will also discuss the status of some of the experiments relevant to these searches: AMANDA, IceCube and ANTARES.

Contents

1. Introduction **2**
2. Particle dark matter candidates **2**
2.1. Supersymmetry 2
2.2. Universal extra dimensions 3
3. Capture and annihilation in the Sun **3**
4. Neutrinos and their detection **5**
5. Prospects **7**
Acknowledgments **9**
References **9**

PII: S1367-2630(04)72739-1
© IOP Publishing Ltd and Deutsche Physikalische Gesellschaft

1. Introduction

There exists an enormous body of evidence in favour of cold dark matter. This evidence includes observations of galactic clusters and large-scale structure [1], supernovae [2] and the cosmic microwave background (CMB) anisotropies [3, 4]. Recently, WMAP has provided the most detailed information on the CMB to date, quoting a total matter density of $\Omega_{\rm m}h^2 = 0.135^{+0.008}_{-0.009}$ [4]. Furthermore, data from WMAP and other earlier experiments indicate a considerably smaller quantity of baryonic matter [4, 5]. At the 2σ confidence level, the density of non-baryonic and cold dark matter is now known to be $\Omega_{\rm CDM}h^2 = 0.113^{+0.016}_{-0.018}$ [4].

Many methods have been proposed to search for evidence of particle dark matter. In addition to accelerator searches, direct and indirect dark matter detection experiments have been performed. Direct dark matter searches attempt to measure the recoil of dark matter particles scattering elastically off the detector material [6]. Indirect dark matter searches have been proposed [7] to observe the products of dark matter annihilation including γ-rays [8, 9], positrons [10], anti-protons [11] and neutrinos [12].

Each of these methods has its advantages and disadvantages. Direct detection is most suited for WIMPs with relatively large elastic scattering cross-sections with nucleons. Indirect detection using γ-rays is often studied in the context of observing annihilations in the galactic centre region, which depends significantly on the dark matter profile used. Alternatively, dark matter substructure could be studied with this method. However, this would still depend on poorly known dark matter distributions [9]. Measurements of the local anti-proton or positron cosmic-ray spectrum depend critically on the location of, and amount of, dark matter substructure within tens of kiloparsecs and a few kiloparsecs, respectively. Also, positrons and anti-protons do not point towards their sources making an unambiguous separation from backgrounds very difficult.

WIMPs which scatter elastically in the Sun or Earth may become gravitationally bound in these gravitational wells. Over the age of the solar system, they may accumulate in substantial numbers in these objects, greatly enhancing their annihilation rate. Although γ-rays, positrons and anti-protons produced in these annihilations do not escape the Sun or Earth, neutrinos often can. Also, unlike other indirect dark matter searches this method does not depend strongly on our galaxy's dark matter halo profile or on the distribution of dark matter substructure. In this paper, we review this method of indirect dark matter detection, and discuss the prospects for such observations in existing and planned experiments.

2. Particle dark matter candidates

Numerous particles have been discussed in the literature as dark matter candidates. It would be impossible and undesirable for us to attempt to review all of them here. Instead, we will focus on two examples which arise in popular particle physics scenarios: supersymmetry and models with universal extra dimensions.

2.1. Supersymmetry

In models with supersymmetry, each fermion has a bosonic partner (and vice versa), which exactly cancels all quadratic divergences to the Higgs mass, thus naturally solving one of the major problems associated with the standard model. Furthermore, the lightest supersymmetric

particle (LSP) is stable in most viable models due to the conservation of R-parity [13]. In many supersymmetric models, the LSP is the lightest neutralino, a mixture of the superpartners of the photon, Z and neutral higgs bosons, and is electrically neutral, colourless and a viable dark matter candidate [14].

If such a particle were in equilibrium with photons in the early universe, as the temperature decreased, a freeze-out would occur, leaving a thermal relic density. The temperature at which this occurs and the density which remains depends on the annihilation cross-section and mass of the lightest neutralino. It is natural for supersymmetry to provide a dark matter candidate with a present abundance similar to those favoured by the WMAP experiment.

The details of any SUSY model are subject to the way supersymmetry is broken (i.e. how masses are given to the superpartners). Most often, the LSP is predominantly gaugino, although it is possible to have a substantial higgsino fraction in some cases.

2.2. Universal extra dimensions

Models with extra dimensions appearing at or near the TeV scale have become very popular in recent years. One class of these models are those in which all of the fields of the standard model propagate in 'universal' extra dimensions [15, 16]. In these models, Kaluza–Klein (KK) excitations appear as particles with masses of the scale of the extra dimension. Due to conservation of momentum in the higher dimensions, a symmetry called KK parity can arise which can, in some cases, make the lightest KK particle (LKP) stable [17]. KK-parity functions in a way which is analagous to R-parity in supersymmetric models, making it possible for the LKP to be a viable dark matter candidate [18].

The identity of the LKP depends on the mass spectrum of the first KK level. The LKP is, most naturally, the first KK excitation of the B^1. The KK spectrum to one-loop level is given in [19]. Using this spectrum, the relic density of the LKP can be calculated as a function of its mass. It has been found that the appropriate density is predicted when the mass is moderately heavy, between 600 and 1200 GeV [18], somewhat heavier than the range favoured for supersymmetry. This range of the LKP mass depends on the details of the co-annihilations of LKPs with heavier KK particles.

Another difference between dark matter particles in universal extra dimensions and supersymmetry is that unlike for a neutralino LSP, the bosonic nature of the LKP means there is no chirality suppression of the annihilation signal in fermions. The annihilation rate of the LKP is therefore roughly proportional to the hypercharge of the final state, leading to a large rate in leptons, including neutrinos. The annihilation and co-annihilation cross-sections are determined by standard model couplings and the mass spectrum of the first KK level.

3. Capture and annihilation in the Sun

To provide an observable flux of neutrinos, dark matter particles must be gathered in high concentrations. Deep gravitational wells such as the Sun, Earth or galactic centre are examples of regions where such concentrations may be present. In the following calculation, we will focus on the Sun, as its prospects are the most promising.

The rate at which WIMPs are captured in the Sun depends on the nature of the interaction the WIMP undergoes with nucleons in the Sun. For spin-dependent interactions, the capture rate

is given by [20]

$$C_{\rm SD}^{\odot} \simeq 3.35 \times 10^{20}\,{\rm s}^{-1}\left(\frac{\rho_{\rm local}}{0.3\,{\rm GeV\,cm}^{-3}}\right)\left(\frac{270\,{\rm km\,s}^{-1}}{\bar{v}_{\rm local}}\right)^{3}\left(\frac{\sigma_{\rm H,SD}}{10^{-6}\,{\rm pb}}\right)\left(\frac{100\,{\rm GeV}}{m_{\rm DM}}\right)^{2}, \tag{1}$$

where $\rho_{\rm local}$ is the local dark matter density, $\sigma_{\rm H,SD}$ the spin-dependent WIMP-on-proton (hydrogen) elastic scattering cross-section, $\bar{v}_{\rm local}$ the local rms velocity of halo dark matter particles and $m_{\rm DM}$ is our dark matter candidate. The analogous formula for the capture rate from spin-independent (scalar) scattering is [20]

$$C_{\rm SI}^{\odot} \simeq 1.24 \times 10^{20}\,{\rm s}^{-1}\left(\frac{\rho_{\rm local}}{0.3\,{\rm GeV\,cm}^{-3}}\right)\left(\frac{270\,{\rm km\,s}^{-1}}{\bar{v}_{\rm local}}\right)^{3}\left(\frac{2.6\sigma_{\rm H,SI}+0.175\sigma_{\rm He,SI}}{10^{-6}\,{\rm pb}}\right)\left(\frac{100\,{\rm GeV}}{m_{\rm DM}}\right)^{2}. \tag{2}$$

Here, $\sigma_{\rm H,SI}$ is the spin-independent WIMP-on-proton elastic scattering cross-section and $\sigma_{\rm He,SI}$ the spin-independent WIMP-on-helium elastic scattering cross-section. Typically, $\sigma_{\rm He,SI} \simeq 16.0\sigma_{\rm H,SI}$. Factors of 2.6 and 0.175 include information on the solar abundances of elements, dynamical factors and form factor suppression.

Although these two rates appear to be comparable in magnitude, the spin-dependent and spin-independent cross-sections can differ radically. For example, with KK dark matter, the spin-dependent cross-section is typically 3–4 orders of magnitude larger than the spin-independent cross-section [18], and solar accretion by spin-dependent scattering dominates.

If the capture rates and annihilation cross-sections are sufficiently high, the Sun will reach equilibrium between these processes. For N (number of) WIMPs in the Sun, the rate of change of this number is given by

$$\dot{N} = C^{\odot} - A^{\odot}N^{2}, \tag{3}$$

where $C^{\odot}$ is the capture rate and $A^{\odot}$ the annihilation cross-section times the relative WIMP velocity per volume. $C^{\odot}$ is as defined in (1), whereas $A^{\odot}$ is

$$A^{\odot} = \frac{\langle \sigma v \rangle}{V_{\rm eff}}, \tag{4}$$

with $V_{\rm eff}$ being the effective volume of the core of the Sun determined roughly by matching the core temperature with the gravitational potential energy of a single WIMP at the core radius. This was found in [21] to be

$$V_{\rm eff} = 5.7 \times 10^{27}\,{\rm cm}^{3}\left(\frac{100\,{\rm GeV}}{m_{\rm DM}}\right)^{3/2}. \tag{5}$$

The present WIMP annihilation rate is

$$\Gamma = \tfrac{1}{2}A^{\odot}N^{2} = \tfrac{1}{2}C^{\odot}\tanh^{2}\left(\sqrt{C^{\odot}A^{\odot}}\,t_{\odot}\right), \tag{6}$$

where $t_\odot \simeq 4.5$ billion years is the age of the solar system. The annihilation rate is maximized when it reaches equilibrium with the capture rate. This occurs when

$$\sqrt{C^\odot A^\odot}\, t_\odot \gg 1. \tag{7}$$

For the majority of particle physics models which are most often considered (e.g., most supersymmetry or KK models), the WIMP capture and annihilation rates reach or nearly reach equilibrium in the Sun. This is often not the case for the Earth. This is true for two reasons. First, the Earth is less massive than the Sun and, therefore, provides fewer targets for WIMP scattering and a less deep gravitational well for capture. Secondly, the Earth accretes WIMPs only by scalar (spin-independent) interactions. For these reasons, it is unlikely that the Earth will provide any observable neutrino signals from WIMP annihilations in any planned experiments.

If very high densities of dark matter are present in the galactic centre, such as expected for very cuspy halo profiles [22] or density spikes [23], sizable neutrino fluxes could be produced. For most particle dark matter candidates, however, very large fluxes of γ-rays would accompany such neutrinos and it would be unlikely that neutrinos would be observed in the absence of a γ-ray signal. However neutrino experiments could help confirm that a γ-ray signal was the result of dark matter annihilations rather than a more traditional astrophysical source.

4. Neutrinos and their detection

The rate of neutrinos produced in WIMP annihilations is highly model-dependent as the annihilation fractions to various products can vary largely from model to model. We will attempt to be as general in our discussion as possible while still considering some specific cases.

In supersymmetry, there are no tree level diagrams for direct neutralino annihilation to neutrinos. However, many indirect channels exist. These include neutrinos from heavy quarks, gauge bosons, tau leptons and higgs bosons. These processes result in a broad spectrum of neutrinos, but with typical energies of 1/2 to 1/3 of the neutralino mass. For experimental energy thresholds of 10–100 GeV, lighter WIMPs can be very difficult or impossible to detect for this reason.

For neutralinos lighter than the $W^\pm$ mass (80.4 GeV), annihilation to $b\bar{b}$ typically dominates, with a small admixture of $\tau^+\tau^-$ as well. In these cases, neutrinos with less than about 30 GeV energy are produced and detection is difficult. For heavier neutralinos, annihilation into gauge bosons, top quarks and higgs bosons are important in addition to $b\bar{b}$ and $\tau^+\tau^-$. In particular, gauge bosons can undergo two-body decay ($Z \to \nu\nu$ or $W^\pm \to l^\pm\nu$) producing neutrinos with an energy of about half of the WIMP mass. Neutralinos with substantial higgsino components often annihilate mostly into gauge bosons.

For KK dark matter, the picture is somewhat different. The LKP annihilates directly to a pair of neutrinos about 3–4% of the time [18, 24]. Although this fraction is small, the neutrinos are of higher energy and are, therefore, easier to detect. The more frequent annihilation channels for KK dark matter are charged leptons (60–70%) and up-type quarks (20–30%). Of these, the $\tau^+\tau^-$ mode contributes the most to the neutrino flux. Unlike in supersymmetry, a large fraction of LKPs annihilate into long-lived particles, such as up-quarks, electrons and muons, which lose their energy in the Sun long before decaying. Bottom and charm quarks lose some energy before decaying, but not significantly.

Neutrinos which are produced lose energy as they travel through the Sun [25]–[27]. The probability of a neutrino escaping the Sun without interaction is given by [27]

$$P = \mathrm{e}^{-E_\nu/E_k}, \tag{8}$$

where E_k is $\simeq$130 GeV for ν_μ, $\simeq$160 GeV for ν_τ, $\simeq$200 GeV for $\bar{\nu}_\mu$ and $\simeq$230 GeV for $\bar{\nu}_\tau$. Thus we see that neutrinos above a couple of hundred GeV are especially depleted, although those which escape are also more easily detected. For a useful parametrization of solar effects, see [25]. Note that neutrino oscillations can also play an important role in calculating the flux of muon neutrinos in a detector [27].

A small fraction of the muon neutrinos which reach the detector are converted into muons through charged current interactions [28]. These muons then propagate through the Cerenkov medium of the detector, where they are detected by photomultiplier tubes distributed through the effective volume. For a review of high-energy neutrino astronomy, see [29].

As a muon propagates, it loses energy at the rate

$$\frac{\mathrm{d}E}{\mathrm{d}X} = -\alpha - \beta E, \tag{9}$$

where $\alpha = 2.0\,\mathrm{MeV\,cm^2\,g^{-1}}$ and $\beta = 4.2 \times 10^{-6}\,\mathrm{cm^2\,g^{-1}}$. The distance a muon travels before dropping below the threshold energy, called the muon range, is then given by [30]

$$R_\mu \simeq \frac{1}{\rho\beta} \ln\left[\frac{\alpha + \beta E_\mu}{\alpha + \beta E_{\mathrm{thr}}}\right], \tag{10}$$

where ρ is the density of the detector medium, $\alpha \simeq 2.0\,\mathrm{MeV\,cm^2\,g^{-1}}$ and $\beta \simeq 4.2 \times 10^{-6}\,\mathrm{cm^2\,g^{-1}}$. E_μ^{thr} is the energy threshold of the detector, typically 10–100 GeV for deep ice or water detectors. The effective volume in which a muon producing interaction can occur and be observed is simply the muon range times the effective area of the detector.

Currently, the AMANDA experiment is taking data at the South Pole [31]. With an effective area of 50 000 m^2 and a muon energy threshold of about 30 GeV, AMANDA is currently the largest volume high-energy neutrino telescope. Due to its 'soda can' geometry, however, it is not very sensitive in the direction of the Sun (the horizon), and thus only places useful limits from the centre of the Earth. As we said before, the rate of dark matter annihilations in the Earth is much smaller than in the Sun, making detections unlikely.

ANTARES [32], now under construction in the Mediterranean, will not have this problem. With a lower energy threshold (10 GeV) and larger effective area (100 000 m^2), ANTARES will be significantly more sensitive to dark matter annihilations compared with AMANDA. Unlike neutrino telescopes at the south pole, ANTARES will also be sensitive to neutrinos coming from the galactic centre.

IceCube [33], under construction at the South Pole, will have a full square kilometre of effective area, but with a somewhat higher energy threshold (50–100 GeV). Unlike its predecessor, AMANDA, IceCube will be sensitive to neutrinos in the direction of the Sun.

The background for this class of experiments consists of atmospheric neutrinos [34] and neutrinos generated in cosmic ray interactions in the Sun's corona [35]. In the direction of the Sun (up to the angular resolution of a neutrino telescope), tens of events >100 GeV and of the order of 1 event per year >1 TeV km^{-2} are expected from the atmospheric neutrino flux. Fortunately,

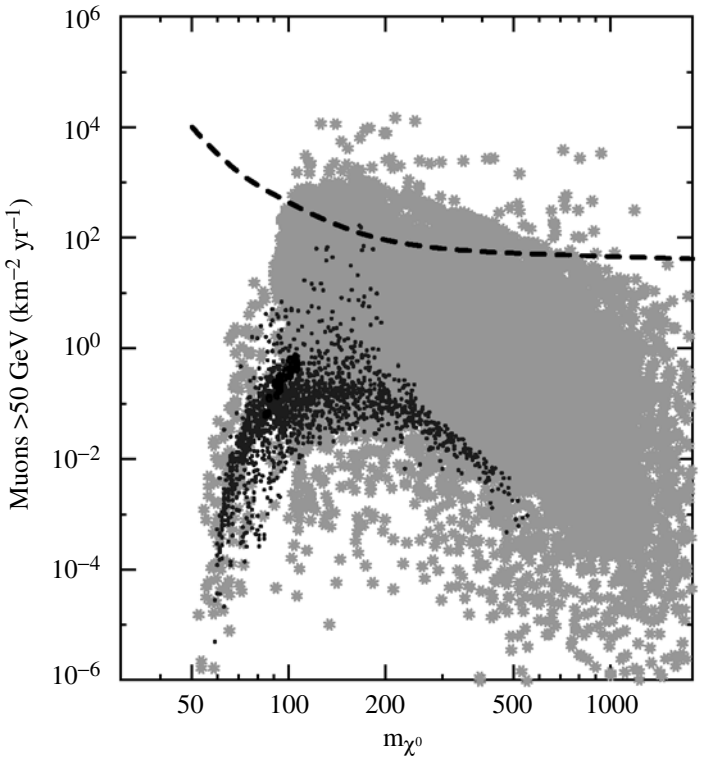

Figure 1. The number of events from neutralino annihilation in the Sun per year in a detector with effective area equal to 1 km^2 and a 50 GeV muon threshold [36]. The lightly shaded region represents the general minimal supersymmetric standard model (MSSM), the darker region corresponds to mSUGRA models, a subset of the MSSM. For each point shown, the relic density is below the maximum value allowed by the WMAP data ($\Omega_\chi h^2 \leqslant 0.129$). The sensitivity projected for IceCube is shown as a broken line [37].

for a very large-volume detector with sufficient statistics, this background is expected to be significantly reduced and possibly eliminated. Furthermore, this rate could be estimated based on the rate from atmospheric neutrinos, a level of about a few events per year. The final background is then further reduced by selecting on judiciously chosen angular and/or energy bins. Neutrinos generated by cosmic ray interactions in the Sun's corona, however, cannot be reduced in this way. This irreducible background is predicted to be less than a few events per year per square kilometre >100 GeV.

5. Prospects

The current limits on dark matter annihilation from AMANDA and other similar experiments are not very strong. Experiments with lower energy thresholds (ANTARES), larger effective areas (IceCube) and which can observe in the direction of the Sun (ANTARES and IceCube) will greatly enhance this sensitivity in coming years.

The sensitivity of a square-kilometre neutrino detector with a moderate muon energy threshold (50 GeV) to supersymmetric dark matter is shown in figure 1. From this figure,

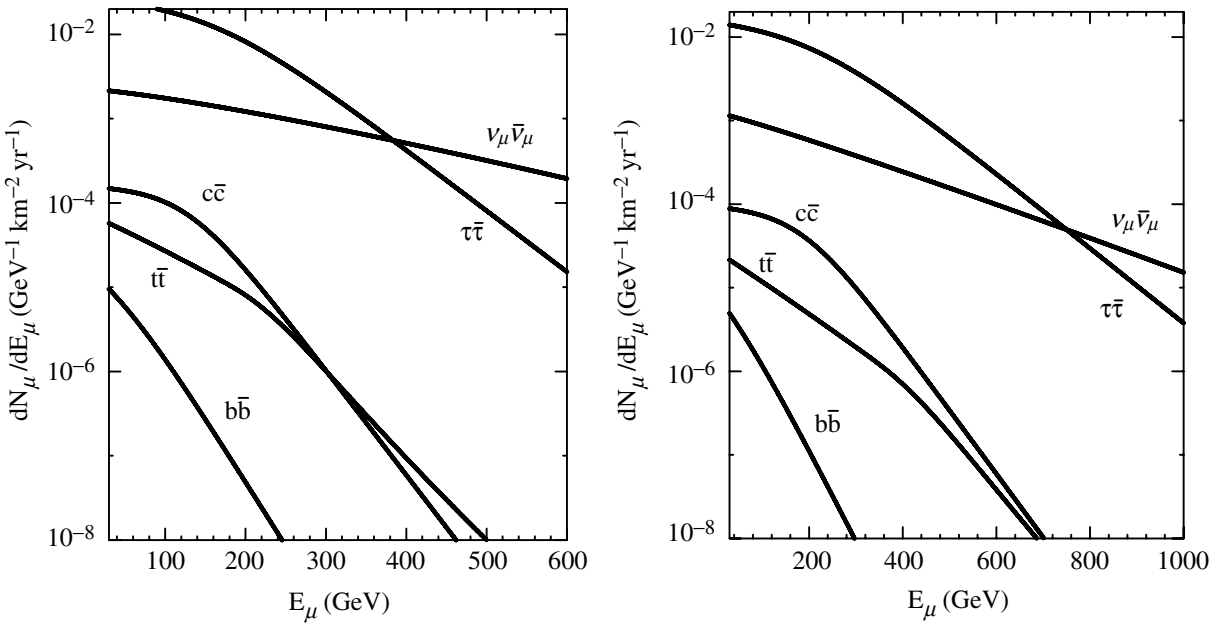

Figure 2. The spectrum of muons at the Earth generated in charged-current interactions of muon neutrinos generated in the annihilation of 600 GeV (left side) and 1000 GeV (right side) KK dark matter particles in the Sun [24]. The elastic scattering cross-section used for capture in the Sun was fixed at 10^{-6} pb for both graphs and the rates are proportional to the cross-section.

it is clear that high-energy neutrinos will be an observable signature in only a small fraction of possible supersymmetry models, although such experiments are still certainly an important probe.

For KK dark matter, the prospects for detection via high-energy neutrinos are substantially better. This is largely due to which annihilation modes dominate. The spectrum of muons in a detector on Earth due to LKP annihilations in the Sun is shown in figure 2 for various annihilation channels and for two choices of LKP mass. Unlike for supersymmetry, annihilation to neutrinos and taus dominate the neutrino spectrum. In supersymmetry, b quarks and gauge bosons dominate, producing fewer observable neutrinos.

In figure 3, the event rates in a square-kilometre detector are shown (using a threshold of 50 GeV). Each of the three lines corresponds to a different value of the next-to-lightest KK particle's mass. The expected size of the one-loop radiative corrections predicts $0.1 \lesssim r_{q_R^1} \lesssim 0.2$, where $r_{q_R^1}$ is the mass splitting of the LKP and the next-to-LKP over the LKP mass. For this range, a kilometre-scale neutrino telescope would be sensitive to a LKP with mass up to about 1 TeV. The relic density of the LKP varies from low to high values from left to right in the figure. The range of mass of the LKP that gives the appropriate relic density was estimated from [18] and is shown in the figure by the solid sections of the lines. Combining the expected size of the one-loop radiative corrections with a relic density appropriate for dark matter, we see that IceCube should see a few to tens of events per year.

For detectors with smaller effective areas one simply has to scale the curves down by a factor $A/(1\ \mathrm{km}^2)$ to obtain the event rate. In particular, for the first-generation neutrino telescopes

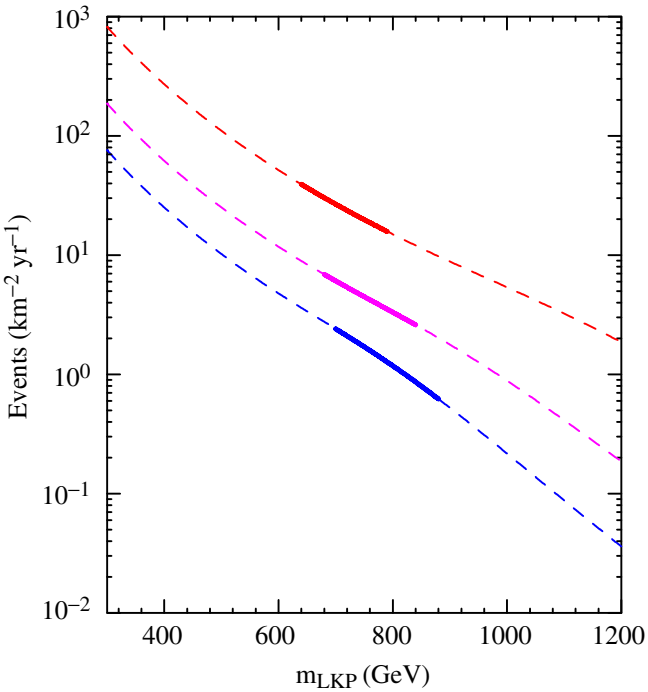

Figure 3. The number of events per year from KK dark matter annihilation in the Sun in a detector with an effective area equal to 1 km^2 and a muon energy threshold of 50 GeV [24]. Contours are shown, from bottom to top, for $r_{q_R^1} = 0.1$, 0.2 and 0.3, where $r_{q_R^1}$ is the mass splitting of the LKP and the next-to-LKP over the LKP mass. The expected size of the one-loop radiative corrections predict $0.1 \lesssim r_{q_R^1} \lesssim 0.2$; therefore, the $r_{q_R^1} = 0.3$ contour is shown merely for comparison. The relic density of the LKPs lies within the range $\Omega_{B^1} h^2 = 0.16 \pm 0.04$ for the solid sections of each line. The relic density is smaller (larger) for smaller (larger) LKP masses.

including AMANDA, ANTARES and NESTOR, with effective areas of order 0.1 km^2, the event rate could be as high as a few events per year for a LKP mass at the lower end of the solid line region.

Acknowledgments

DH is supported by the Leverhulme trust.

References

[1] Abazajian K *et al* (SDSS Collaboration) 2003 *Preprint* astro-ph/0305492
Begeman K G, Broeils A H and Sanders R H 1991 *Mon. Not. R. Astron. Soc.* **249** 523
Davis M, Efstathiou G, Frenk C S and White S D 1985 *Astrophys. J.* **292** 371
[2] Perlmutter S *et al* (Supernova Cosmology Project Collaboration) 1999 *Astrophys. J.* **517** 565
[3] de Bernardis P *et al* 2000 *Nature* **404** 955
Netterfield C B *et al* (Boomerang Collaboration) 2002 *Astrophys. J.* **571** 604
[4] Bennett C L *et al* 2003 *Preprint* astro-ph/0302207

[5] Burles S, Nollett K M, Truran J N and Turner M S 1999 *Phys. Rev. Lett.* **82** 4176
Fukugita M, Hogan C J and Peebles P J 1998 *Astrophys. J.* **503** 518
[6] Drukier A and Stodolsky L 1984 *Phys. Rev.* D **30** 2295
Goodman M W and Witten E 1985 *Phys. Rev.* D **31** 3059
Bottino A, de Alfaro V, Fornengo N, Mignola S and Scopel S 1994 *Astropart. Phys.* **2** 77
Baer H and Brhlik M 1998 *Phys. Rev.* D **57** 567
[7] Silk J and Srednicki M 1984 *Phys. Rev. Lett.* **53** 624
[8] Bergstrom L, Edsjo J and Ullio P 2001 *Phys. Rev. Lett.* **87** 251301
Bergstrom L, Edsjo J and Gunnarsson C 2001 *Phys. Rev.* D **63** 083515
Bengtsson H U, Salati P and Silk J 1990 *Nucl. Phys.* B **346** 129
Berezinsky V, Bottino A and Mignola G 1994 *Phys. Lett.* B **325** 136
Hooper D and Dingus B L 2002 *Preprint* astro-ph/0210617
Bergstrom L, Ullio P and Buckley J H 1998 *Astropart. Phys.* **9** 137
[9] Koushiappas S M, Zentner A R and Walker T P 2003 *Preprint* astro-ph/0309516
Evans N W, Ferrer F and Sarkar S 2003 *Preprint* astro-ph/0311145
[10] Kane G L, Wang L T and Wells J D 2002 *Phys. Rev.* D **65** 057701
Kamionkowski M and Turner M S 1991 *Phys. Rev.* D **43** 1774
Baltz E A, Edsjo J, Freese K and Gondolo P 2002 *Preprint* astro-ph/0211239
Kane G L, Wang L T and Wang T T 2002 *Phys. Lett.* B **536** 263
Baltz E A and Edsjo J 1999 *Phys. Rev.* D **59** 023511
[11] Bergstrom L, Edsjo J and Ullio P 1999 *Preprint* astro-ph/9906034
Bottino A, Donato F, Fornengo N and Salati P 1998 *Phys. Rev.* D **58** 123503
Donato F, Fornengo N, Maurin D, Salati P and Taillet R 2003 *Preprint* astro-ph/0306207
[12] Silk J, Olive K and Srednicki M 1985 *Phys. Rev. Lett.* **55** 257
Hagelin J S, Ng K W and Olive K A 1986 *Phys. Lett.* B **180** 375
Halzen F, Stelzer T and Kamionkowski M 1992 *Phys. Rev.* D **45** 4439
Feng J L, Matchev K T and Wilczek F 2001 *Phys. Rev.* D **63** 045024
Barger V D, Halzen F, Hooper D and Kao C 2002 *Phys. Rev.* D **65** 075022
Berezinsky V, Bottino A, Ellis J, Fornengo N, Mignola G and Scopel S 1996 *Astropart. Phys.* **5** 333
Bergstrom L, Edsjo J and Gondolo P 1997 *Phys. Rev.* D **55** 1765
Bergstrom L, Edsjo J and Gondolo P 1998 *Phys. Rev.* D **58** 103519
Bergstrom L, Edsjo J and Kamionkowski M 1997 *Astropart. Phys.* **7** 147
Corsetti A and Nath P 2000 *Int. J. Mod. Phys.* A **15** 905
Faraggi A E, Olive K A and Pospelov M 2000 *Astropart. Phys.* **13** 31
Freese K 1986 *Phys. Lett.* B **167** 295
Krauss L M, Srednicki M and Wilczek F 1986 *Phys. Rev.* D **33** 2079
Gaisser T K, Steigman G and Tilav S 1986 *Phys. Rev.* D **34** 2206
[13] Weinberg S 1982 *Phys. Rev.* D **26** 287
Hall L J and Suzuki M 1984 *Nucl. Phys.* B **231** 419
Allanach B C, Dedes A and Dreiner H K 1999 *Phys. Rev.* D **60** 075014
[14] Goldberg H 1983 *Phys. Rev. Lett.* **50** 1419
Ellis J, Hagelin J S, Nanopoulos D V, Olive K and Srednicki M 1984 *Nucl. Phys.* B **238** 453
[15] Antoniadis I 1990 *Phys. Lett.* B **246** 377
Antoniadis I, Benakli K and Quiros M 1994 *Phys. Lett.* B **331** 313
[16] Appelquist T, Cheng H C and Dobrescu B A 2001 *Phys. Rev.* D **64** 035002
[17] Kolb E W and Slansky R 1984 *Phys. Lett.* B **135** 378
Dienes K R, Dudas E and Gherghetta T 1999 *Nucl. Phys.* B **537** 47
[18] Servant G and Tait T M 2002 *Preprint* hep-ph/0206071
Cheng H C, Feng J L and Matchev K T 2002 *Preprint* hep-ph/0207125

[19] Cheng H C, Matchev K T and Schmaltz M 2002 *Preprint* hep-ph/0204342
Cheng H C, Matchev K T and Schmaltz M 2002 *Preprint* hep-ph/0205314
[20] Gould A 1991 *Astrophys. J.* **388** 338
Jungman G, Kamionkowski M and Griest K 1996 *Phys. Rep.* **267** 195
[21] Griest K and Seckel D 1987 *Nucl. Phys.* B **283** 681
Griest K and Seckel D 1988 *Nucl. Phys.* B **296** 1034 (erratum)
Gould A 1987 *Astrophys. J.* **321** 571
[22] Navarro J F, Frenk C S and White S D 1996 *Astrophys. J.* **462** 563
Navarro J F, Frenk C S and White S D 1997 *Astrophys. J.* **490** 493
Moore B, Ghigna S, Governato F, Lake G, Quinn T, Stadel J and Tozzi P 1999 *Astrophys. J.* **524** L19
[23] Bertone G, Sigl G and Silk J 2002 *Preprint* astro-ph/0203488
Ullio P, Zhao H and Kamionkowski M 2001 *Phys. Rev.* D **64** 043504
Gondolo P and Silk J 1999 *Phys. Rev. Lett.* **83** 1719
[24] Hooper D and Kribs G D 2003 *Phys. Rev.* D **67** 055003
[25] Edsjo J 1995 *Nucl. Phys. Proc. (Suppl.)* **43** 265
[26] Jungman G and Kamionkowski M 1995 *Phys. Rev.* D **51** 328
[27] Crotty P 2002 *Preprint* hep-ph/0205116
[28] Gandhi R, Quigg C, Reno M H and Sarcevic I 1996 *Astropart. Phys.* **5** 81
[29] Halzen F and Hooper D 2002 *Rep. Prog. Phys.* **65** 1025
Learned J G and Mannheim K 2000 *Ann. Rev. Nucl. Part. Sci.* **50** 679
[30] Dutta S I, Reno M H, Sarcevic I and Seckel D 2001 *Phys. Rev.* D **63** 094020
[31] Andres E *et al* 2001 *Nature* **410** 441
[32] Blanc F *et al* (ANTARES Collaboration) 2003 *Proc. 28th Int. Cosmic Ray Conf. (ICRC 2003) (Tsukuba, Japan, 31 July–7 August 2003)* to appear
Katz U F (The ANTARES Collaboration) 2003 *Preprint* astro-ph/0310736
[33] Ahrens J *et al* (The IceCube Collaboration) 2003 *Nucl. Phys. Proc. (Suppl.)* **118** 388
Ahrens J (IceCube Collaboration) 2003 *Preprint* astro-ph/0305196
[34] Gaisser T K, Halzen F and Stanev T 1995 *Phys. Rep.* **258** 173
Gaisser T K, Halzen F and Stanev T 1996 *Phys. Rep.* **271** 355 (erratum)
[35] Bergstrom L, Edsjo J and Gondolo P 1997 *Phys. Rev.* D **55** 1765
Bergstrom L, Edsjo J and Gondolo P 1998 *Phys. Rev.* D **58** 103519
[36] Hooper D and Wang L T 2003 *Preprint* hep-ph/0309036
[37] Edsjo J 2002 *Preprint* astro-ph/0211354

New Journal of Physics
An Institute of Physics and Deutsche Physikalische Gesellschaft Journal

Solar models and solar neutrino oscillations

John N Bahcall and Carlos Peña-Garay
Institute for Advanced Study, School of Natural Sciences, Princeton, NJ 08540, USA
E-mail: jnb@ias.edu and penya@ias.edu

New Journal of Physics **6** (2004) 63
Received 5 April 2004
Published 16 June 2004
Online at http://www.njp.org/
doi:10.1088/1367-2630/6/1/063

Abstract. We provide a summary of the current knowledge, theoretical and experimental, of solar neutrino fluxes and of the masses and mixing angles that characterize solar neutrino oscillations. We also summarize the principal reasons for performing new solar neutrino experiments and what we anticipate from future studies.

Contents

1. Introduction **2**
2. Solar model fluxes **2**
2.1. Fluxes from different solar models 2
2.2. Flux uncertainties 5
3. Experimentally determined solar neutrino parameters **6**
3.1. Solar neutrino oscillations 6
3.2. The vacuum–matter transition 8
3.3. Experimentally determined solar neutrino parameters 9
4. Neutrinos as dark matter **11**
5. Test of CPT conservation with reactor and solar neutrino experiments **12**
6. What can be learnt from new solar neutrino experiments? **14**
6.1. Why low-energy solar neutrino experiments? 14
6.2. A ^{7}Be experiment 15
6.3. A p–p experiment 15
6.4. A pep experiment 16
6.5. Proton decay experiments and solar neutrino measurements 17
Acknowledgments **17**
References **17**

PII: S1367-2630(04)79061-8
© IOP Publishing Ltd and Deutsche Physikalische Gesellschaft

1. Introduction

In this paper, we present a snapshot (taken on 1 March 2004) of the present status of solar neutrino theoretical research. We do not attempt to review the literature on this subject. For details of the extensive literature, the reader is referred to earlier, more comprehensive studies [1]–[19].

The related subject of solar neutrino experiments will be reviewed in this volume by McDonald [20]. We therefore do not discuss the experimental aspects of solar neutrino research in this paper, although we do emphasize the relation between theoretical ideas and predictions and solar neutrino measurements.

We begin in section 2 by summarizing our current theoretical knowledge of the solar neutrino fluxes. We then discuss in section 3 the numerical results regarding solar neutrino parameters and neutrino fluxes that have been inferred from solar neutrino and reactor experiments. Neutrinos are the first cosmological dark matter to be discovered. We describe in section 4 what solar and atmospheric neutrino experiments have taught us about the cosmological mass density of neutrinos. We summarize in section 5 the constraints on CPT in the neutrino sector that result from comparing solar neutrino experiments with reactor anti-neutrino experiments. Finally, in section 6 we discuss the reasons for undertaking future solar neutrino experiments and the scientific results that may be obtained from the proposed new experiments.

To establish the appropriate context for our discussion, we note that measurements of the speed of sound inside the Sun (via a technique called helioseismology, which is similar to terrestrial seismology) agree with solar model predictions to an rms accuracy of better than 0.1%. This excellent agreement between the measured and predicted sound speeds established, as early as 1996, that the solution of the 'solar neutrino problem' lay in new particle physics, not in new astrophysics [21].

2. Solar model fluxes

In this section, the discussion is based on the results reported in the recent paper [22]. Full numerical details of the solar models, BP04 and BP00 discussed below are available together with earlier solar models in this series, at the web site http://www.sns.ias.edu/∼jnb . In particular, the primordial hydrogen and helium mass fractions for the BP04 model discussed below are $X_0 = 0.7078$ and $Y_0 = 0.2734$, respectively, whereas the current surface abundances are $X_S = 0.7397$ and $Y_S = 0.2434$.

2.1. Fluxes from different solar models

Table 1, taken from [22], gives the calculated solar neutrino fluxes for a series of solar models calculated with different plausible assumptions about the input parameters. The range of fluxes shown for these models illustrates the systematic uncertainties in calculating solar neutrino fluxes. The second (third) column, labelled BP04 (BP04+), of table 1 presents the currently available best solar model calculations for the neutrino fluxes. The uncertainties are given in column 2.

Figure 1 presents the neutrino energy spectrum predicted by the BP04 solar model for the most important solar neutrino sources.

The model BP04+ was calculated with the use of new input data for the equation of state, nuclear physics and solar composition. The currently preferred model BP04, is similar to BP04+ except that BP04 does not include the most recent analyses of the solar surface composition [24],

Table 1. Predicted solar neutrino fluxes from solar models. The table presents the predicted fluxes, in units of 10^{10}(pp), 10^{9}(^{7}Be), 10^{8}(pep, ^{13}N, ^{15}O), 10^{6}(^{8}B, ^{17}F) and 10^{3}(hep) cm^{-2} s^{-1}. Columns 2–4 show BP04, BP04+ and the previous best model BP00 [4]. Columns 5–7 present the calculated fluxes for solar models that differ from BP00 by an improvement in one set of input data: nuclear fusion cross-sections (column 5), equation of state for the solar interior (column 6) and surface chemical composition for the Sun (column 7). Column 8 uses the same input data as for BP04 except for a recent report of the ^{14}N + p fusion cross-section. References to the improved input data are given in the text. The last two rows ignore neutrino oscillations and present the capture rates in SNU (1 SNU = 10^{-36} events (target atom)$^{-1}$ s^{-1}) for the chlorine and gallium solar neutrino experiments. Owing to oscillations, the measured rates are smaller: 2.6 ± 0.2 and 69 ± 4, respectively. The neutrino absorption cross-sections and their uncertainties are given in [23].

Source	BP04	BP04+	BP00	Nucl.	EOS	Comp.	^{14}N
pp	5.94 (1 ± 0.01)	5.99	5.95	5.94	5.95	6.00	5.98
pep	1.40 (1 ± 0.02)	1.42	1.40	1.40	1.40	1.42	1.42
hep	7.88 (1 ± 0.16)	8.04	9.24	7.88	9.23	9.44	7.93
^{7}Be	4.86 (1 ± 0.12)	4.65	4.77	4.84	4.79	4.56	4.86
^{8}B	5.82 (1 ± 0.23)	5.28	5.05	5.79	5.08	4.62	5.77
^{13}N	5.71 ($1^{+0.37}_{-0.35}$)	4.06	5.48	5.69	5.51	3.88	3.23
^{15}O	5.03 ($1^{+0.43}_{-0.39}$)	3.54	4.80	5.01	4.82	3.36	2.54
^{17}F	5.91 ($1^{+0.44}_{-0.44}$)	3.97	5.63	5.88	5.66	3.77	5.85
Cl	$8.5^{+1.8}_{-1.8}$	7.7	7.6	8.5	7.6	6.9	8.2
Ga	131^{+12}_{-10}	126	128	130	129	123	127

which conflict with helioseismological measurements. We prefer the model BP04 over the model BP04+ because the abundance of the lower heavy element used in calculating BP04+ causes the calculated depth of the solar convective zone to conflict with helioseismological measurements.

The error estimates, which are the same for the three models labelled BP04, BP04+ and ^{14}N in table 1 include the recent composition analyses.

Column 4 of table 1 presents the fluxes calculated using the preferred solar model, BP00 [4], which was posted on the archives in October 2000. The BP04 best-estimate neutrino fluxes and their uncertainties have not changed markedly from their BP00 values despite refinements in input parameters. The only exception is the CNO flux uncertainties, which have almost doubled due to the larger systematic uncertainty in the surface chemical composition as estimated in the present paper.

We describe improvements in the input data relative to BP00. Quantities that are not discussed here are the same as for BP00. Each class of improvement is represented by a separate column, columns 5–7, in table 1. The magnitude of the changes between the fluxes listed in the different columns of table 1 are one measure of the sensitivity of the calculated fluxes to the input data.

Column 5 contains the fluxes computed for a solar model that is identical with BP00 except that improved values for direct measurements of the ^{7}Be(p, γ)^{8}B cross-section [25, 26], and the calculated p–p and hep cross-sections [26]. The reactions that produce the ^{8}B and hep neutrinos

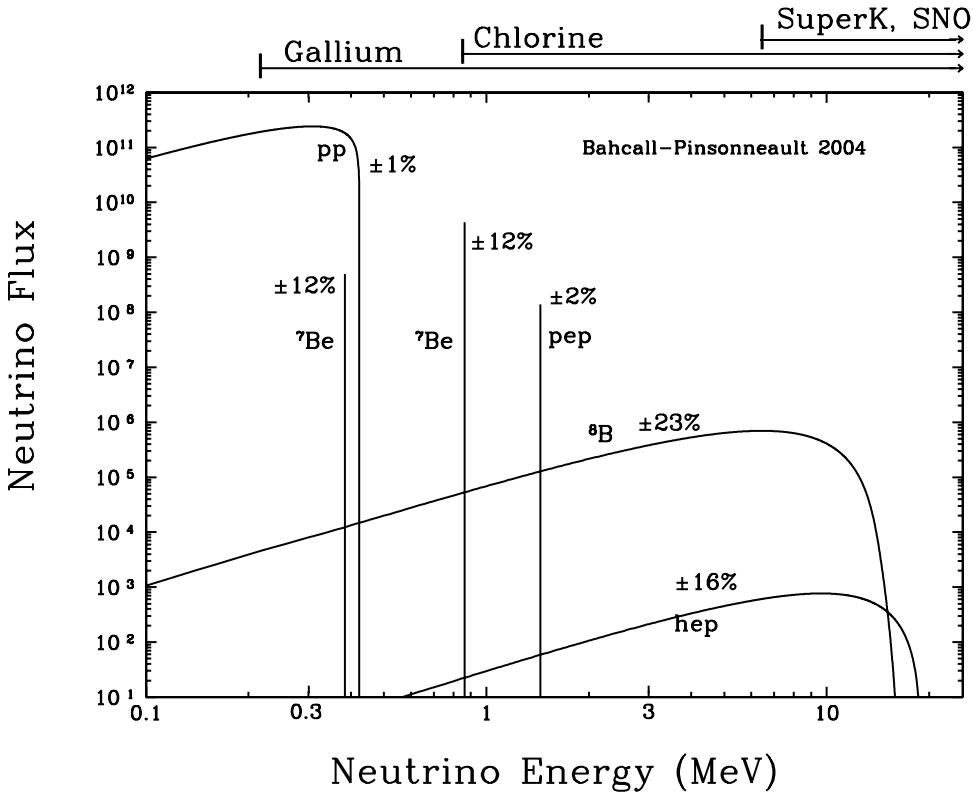

Figure 1. The predicted solar neutrino energy spectrum. The figure shows the energy spectrum of solar neutrinos predicted by the BP04 solar model [22]. For continuum sources, the neutrino fluxes are given in number of neutrinos $cm^{-2}\,s^{-1}\,MeV^{-1}$ at the Earth's surface. For line sources, the units are number of neutrinos $cm^{-2}\,s^{-1}$. Total theoretical uncertainties taken from column 2 of table 1 are shown for each source. To avoid complication in the figure, we have omitted the difficult-to-detect CNO neutrino fluxes (see table 1).

are rare; changes in their production cross-sections affect only the ^{8}B and hep fluxes respectively. The 15% increase in the calculated ^{8}B neutrino flux, which is primarily due to a more accurate cross-section for ^{7}Be(p, γ)^{8}B, is the only significant change in the best-estimate fluxes.

The fluxes in column 6 were calculated using a refined equation of state, which includes relativistic corrections and a more accurate treatment of molecules [27]. The equation of state improvements between 1996 and 2001, although significant in some regions of parameter space, change all the solar neutrino fluxes by $<1\%$. Solar neutrino calculations are insensitive to the present level of uncertainties in the equation of state.

The most important changes in the astronomical data from BP00 result from the new analyses of the surface chemical composition of the Sun. The input chemical composition affects the radiative opacity and hence the physical characteristics of the solar model, and to a lesser extent the nuclear reaction rates. New values for C, N, O, Ne and Ar have been derived [24] using three-dimensional rather than one-dimensional atmospheric models, including hydrodynamical effects, and paying particular attention to uncertainties in atomic data and observational spectra. New estimates of the abundance, together with the previous best estimates for other solar surface abundances [28], imply a ratio of heavy elements to hydrogen by mass of $Z/X = 0.0176$, much

Table 2. Principal sources of uncertainties in calculating solar neutrino fluxes. Columns 2–5 present the fractional uncertainties in the neutrino fluxes from laboratory measurements of the ^{3}He–^{3}He, ^{3}He–^{4}He, p–^{7}Be and p–^{14}N nuclear fusion reactions, respectively. The last four columns, 6–9, give the fractional uncertainties due to the calculated radiative opacity, the calculated rate of element diffusion, the measured solar luminosity and the measured heavy element to hydrogen ratio, respectively.

Source	3–3	3–4	1–7	1–14	Opacity	Diffusion	$L_\odot$	Z/X
pp	0.002	0.005	0.000	0.002	0.003	0.003	0.003	0.010
pep	0.003	0.007	0.000	0.002	0.005	0.004	0.003	0.020
hep	0.024	0.007	0.000	0.001	0.011	0.007	0.000	0.026
^{7}Be	0.023	0.080	0.000	0.000	0.028	0.018	0.014	0.080
^{8}B	0.021	0.075	0.038	0.001	0.052	0.040	0.028	0.200
^{13}N	0.001	0.004	0.000	0.118	0.033	0.051	0.021	0.332
^{15}O	0.001	0.004	0.000	0.143	0.041	0.055	0.024	0.375
^{17}F	0.001	0.004	0.000	0.001	0.043	0.057	0.026	0.391

less than the previous value of $Z/X = 0.0229$ [28]. Column 7 gives the fluxes calculated for this new composition mixture. The largest change in the neutrino flux for the p–p chain is the 9% decrease in the predicted ^{8}B neutrino flux. The N and O fluxes are decreased by much more, ~35%, because they reflect directly the inferred C and O abundances.

The CNO nuclear reaction rates are less accurately determined than the rates for the more important (in the Sun) p–p reactions [29]. The rate for ^{14}N(p, γ)^{15}O is poorly known, but is important for calculating CNO neutrino fluxes. Extrapolating to the low energies relevant for solar fusion introduces a large uncertainty. Column 8 gives the neutrino fluxes calculated with an input data identical with BP04 except for the cross-section factor $S_0(^{14}\mathrm{N} + \mathrm{p}) = 1.77 \pm 0.2$ keV b that is about half the current best estimate; this value assumes a particular R-matrix fit to the experimental data [30]. The p–p cycle fluxes are changed by only ~1%, but the ^{13}N and ^{15}O neutrino fluxes are reduced by 40–50% relative to the BP04 predictions. CNO nuclear reactions contribute 1.6% of the solar luminosity in the BP04 model and only 0.8% to the model with a reduced $S_0(^{14}\mathrm{N} + \mathrm{p})$.

2.2. *Flux uncertainties*

Table 2, also taken from [22], shows the individual contributions to the flux uncertainties. These uncertainties are useful in deciding how accurately we need to determine a given input parameter. Moreover, the theoretical flux uncertainties continue to play a significant role in some determinations of neutrino parameters from solar neutrino experiments (see e.g. [31]).

Columns 2–5 present the fractional uncertainties from the nuclear reactions whose measurement errors are most important for calculating neutrino fluxes. Unless stated otherwise, the uncertainties in the nuclear fusion cross-sections are taken from [29].

The measured rate of the ^{3}He–^{3}He reaction, which changed by a factor of 4 after the first solar model calculation of the solar neutrino flux [32], and the measured rate of the ^{7}Be + p reaction, which for most of this series has been the dominant uncertainty in predicting the ^{8}B neutrino flux, are now very well determined. If the current published systematic uncertainties

for the ^{3}He–^{3}He and ^{7}Be + p reactions are correct, then the uncertainties in these reactions no longer contribute in a crucial way to the calculated theoretical uncertainties (see columns 2 and 4 of table 2). This felicitous situation is the result of an enormous effort extending over four decades, and represents a great collective triumph for the nuclear physics community.

At present, the most important nuclear physics uncertainty in calculating solar neutrino fluxes is the rate of the ^{3}He–^{4}He reaction (see column 3 of table 2). The systematic uncertainty in the rate of ^{3}He(^{4}He, γ)^{7}Be reaction (see [29]) causes an 8% uncertainty in the prediction of both the ^{7}Be and the ^{8}B solar neutrino fluxes. It is scandalous that there has not been any progress in the last 15 years in measuring this rate more accurately.

For ^{14}N(p, γ)^{15}O, we have continued to use in table 2 the uncertainty given in [29], although the recent re-evaluation in [30] suggests that the uncertainty could be somewhat larger (see column 7 of table 1).

The uncertainties due to the calculated radiative opacity and element diffusion, as well as the measured solar luminosity (columns 6–8 of table 2), are all moderate, non-negligible but not dominant. For the ^{8}B and CNO neutrino fluxes, the uncertainties that are due to the radiative opacity, diffusion coefficient and solar luminosity are all in the range 2–6%.

The surface composition of the Sun is the most problematic and important source of uncertainties. Systematic errors dominate the effects of line blending, departures from local thermodynamic equilibrium and details of the model of the solar atmosphere. In the absence of detailed information to the contrary, it is assumed that the uncertainty in all important element abundances is approximately the same. The 3σ range of Z/X is defined as the spread over all modern determinations (see [3, 4, 32]), which implies that at present $\Delta(Z/X)/(Z/X) = 0.15$ (1σ), 2.5 times larger than the uncertainty adopted in discussing the predictions of the model BP00 [4]. The recent uncertainty quoted for oxygen, the most abundant heavy element in the Sun, is similar: 12% [24].

Heavier elements such as Fe affect the radiative opacity and hence the neutrino fluxes more strongly than the relatively lighter elements [4]. This is the reason for the difference between the fluxes calculated with BP04 and BP04+ (or between BP00 and Comp., see table 1) being less than that expected for the 26% decrease in Z/X. The abundances that have changed significantly since BP00 (C, N, O, Ne and Ar) are all for lighter species for which meteoritic data are not available.

The dominant uncertainty listed in table 2 for the ^{8}B and CNO neutrinos is the chemical composition, represented by Z/X (see column 9). The uncertainty ranges from 20% for the ^{8}B neutrino flux to ~35% for the CNO neutrino fluxes. Since the publication of BP00, the best published estimate for Z/X decreased by 4.3σ (BP00 uncertainty) and the estimated uncertainty due to Z/X increased for ^{8}B(^{15}O) neutrinos by a factor of 2.5 (2.8). Over the past three decades, the changes have almost always been towards a smaller Z/X. The monotonicity is surprising since different sources of improvements have caused successive changes. Nevertheless, since the changes are monotonic, the uncertainty estimated from the historical record is large.

3. Experimentally determined solar neutrino parameters

3.1. Solar neutrino oscillations

Solar neutrino experiments have demonstrated that solar neutrinos undergo flavour conversion. Recently, the mechanism of conversion has been identified as neutrino oscillations, i.e. flavour

conversion induced by neutrino masses and mixing angles. The confirmation of the predicted neutrino oscillation deficit provided by the measurements from the Japanese reactor (anti)neutrino detector KamLAND [33] represents a triumph of several decades of research on solar neutrinos.

The Standard Model of particle physics has to be extended to include neutrino masses and mixing angles. Oscillation experiments are sensitive to mixing angles, defined by the non-trivial relation between flavour and mass neutrino fields. Oscillation experiments are not sensitive to absolute masses but to the differences of squared masses, i.e. global phases are not observable but relative phases are observable. A detailed discussion of the space of oscillation parameters can be found in [34].

Solar neutrino oscillations are characterized by just one function, the survival probability of electron neutrinos. Neutrino production, evolution and detection are the same for muon and tau neutrinos. For any solar neutrino observable, the conversion probability to μ neutrinos ($P_{e,\mu}$) or to τ neutrinos ($P_{e,\tau}$) appears only in the combination $P_{e,\mu} + P_{e,\tau}$.

The survival probability of electron neutrinos, P_{ee}, can be related to the survival probability, $P_{ee}^{2\nu}$, for effective two neutrino oscillations by the equation [35, 36]

$$P_{ee} = \cos^4\theta_{13} P_{ee}^{2\nu}(\Delta m^2, \theta_{12}; \cos^2\theta_{13} n_e) + \sin^4\theta_{13}, \tag{1}$$

where Δm^2 and θ_{1i} are differences in the squares of the masses $m_2^2 - m_1^2$ and the vacuum mixing angles, respectively. The effective two-neutrino problem is solved with a rescaled electron density, $\cos^2\theta_{13} n_e$. The effect of ΔM^2, the mass difference squared characteristic of atmospheric neutrinos $\left(m_3^2 - m_2^2 \cong m_3^2 - m_1^2\right)$, averages out in equation (1) for the energies and distances characteristic of solar neutrino propagation. Results from the CHOOZ reactor experiment [37, 38] places a strong upper bound on $\sin^2 2\theta_{13}$, implying that θ_{13} is close to 0 or $\pi/2$. Atmospheric and solar data select the first option ($\sin^2\theta_{13} < 0.052$ at 3σ [39]). Thus the main effect of a small allowed θ_{13} on the survival probability is the introduction of the factor $\cos^4\theta_{13}$ in equation (1).

The effective Hamiltonian for two-neutrino propagation in matter can be written conveniently in the familiar form [2, 3, 7, 35], [40]–[42]

$$H = \begin{pmatrix} \dfrac{\Delta m^2 \cos 2\theta_{12}}{4E} - \dfrac{\sqrt{2} G_F \cos^2\theta_{13} n_e}{2} & \dfrac{\Delta m^2 \sin 2\theta_{12}}{2E} \\ \dfrac{\Delta m^2 \sin 2\theta_{12}}{2E} & -\dfrac{\Delta m^2 \cos 2\theta_{12}}{4E} + \dfrac{\sqrt{2} G_F \cos^2\theta_{13} n_e}{2} \end{pmatrix}, \tag{2}$$

where E is the energy of the neutrino and G_F the Fermi coupling constant. The relative importance of the MSW matter term and the kinematic vacuum oscillation term in the Hamiltonian can be parametrized by the quantity, β, which represents the ratio of matter to vacuum effects. From equation (2), we see that the appropriate ratio is

$$\beta = \frac{2\sqrt{2} G_F \cos^2\theta_{13} n_e E_\nu}{\Delta m^2}. \tag{3}$$

The quantity β is the ratio of the oscillation length in matter to the oscillation length in vacuum. In convenient units, β can be written as

$$\beta = 0.22 \cos^2\theta_{13} \left[\frac{E_\nu}{1\,\mathrm{MeV}}\right] \left[\frac{\mu_e \rho}{100\,\mathrm{g\,cm^{-3}}}\right] \left[\frac{7 \times 10^{-5}\,\mathrm{eV}^2}{\Delta m^2}\right], \tag{4}$$

where μ_e is the electron mean molecular weight ($\mu_e \approx 0.5(1+X)$, X is the mass fraction of hydrogen) and ρ is the total density. For the electron density at the centre of the standard solar model, $\beta = 0.22$ for $E = 1\,\mathrm{MeV}$, $\theta_{13} = 0$, and $\Delta m^2 = 7 \times 10^{-5}\,\mathrm{eV}^2$.

3.2. The vacuum–matter transition

For the large mixing angle (LMA) region ($\Delta m^2 > 10^{-5}\,\mathrm{eV}^2$), the daytime survival probability can be written to a good approximation in the following simple form [2, 3, 7, 36], [40]–[42]:

$$P_{ee} = \cos^4\theta_{13}(\tfrac{1}{2} + \tfrac{1}{2}\cos 2\theta_{12}^M \cos 2\theta_{12}), \tag{5}$$

where the mixing angle in matter is

$$\cos 2\theta_{12}^M = \frac{\cos 2\theta_{12} - \beta}{\sqrt{(\cos 2\theta_{12} - \beta)^2 + \sin^2 2\theta_{12}}}. \tag{6}$$

In equation (6), β is calculated at the location where the neutrino is produced. The evolution is adiabatic, i.e. the parameters in the Hamiltonian vary slowly enough to allow the created neutrino to follow the changing Hamiltonian eigenstate. Thus the survival probability depends on the initial and final density but not on the details of the density profile.

Figure 2 illustrates the energy dependence of the LMA survival probability, P_{ee}. If $\beta < \cos 2\theta_{12} \sim 0.4$ (for solar neutrino oscillations), the survival probability corresponds to vacuum averaged oscillations,

$$P_{ee} = \cos^4\theta_{13}(1 - \tfrac{1}{2}\sin^2 2\theta_{12}) \quad (\beta < \cos 2\theta_{12}, \text{vacuum}). \tag{7}$$

If $\beta > 1$, the survival probability corresponds to matter-dominated oscillations,

$$P_{ee} = \cos^4\theta_{13}\sin^2\theta_{12} \quad (\beta > 1, \text{MSW}). \tag{8}$$

The survival probability is approximately constant in either of the two limiting regimes, $\beta < \cos 2\theta_{12}$ and $\beta > 1$. The LMA solution exhibits a strong energy dependence only in the transition region between the limiting regimes. The quantity β is defined by equations (3) and (4).

At what neutrino energy does the transition take place between vacuum oscillations and matter oscillations? The answer to this question depends on which neutrino source is studied, since the fraction of the neutrino flux that is produced at a given radius (i.e. density and μ_e) differs from one neutrino source to another. The ^{8}B neutrinos are produced at much smaller radii (higher densities) than the p–p neutrinos; the ^{7}Be production profile is intermediate between the ^{8}Be and p–p neutrinos. According to the BP00 solar model, the critical energy at which $\beta = \cos 2\theta_{12}$ is, for $\tan^2\theta_{12} = 0.41$,

$$E(\text{crit}) \simeq \begin{cases} 1.8\,\text{MeV}\ (^8\text{B}); \\ 2.2\,\text{MeV}\ (^7\text{Be}); \\ 3.3\,\text{MeV}\ (\text{p–p}). \end{cases} \tag{9}$$

The actual energies for p–p and ^{7}Be neutrinos are below the critical energy where they are produced. To a very good approximation, ^{8}B neutrinos are always in the MSW regime (equation (8)), while p–p and ^{7}Be neutrinos are in the vacuum-averaged regime (equation (7)).

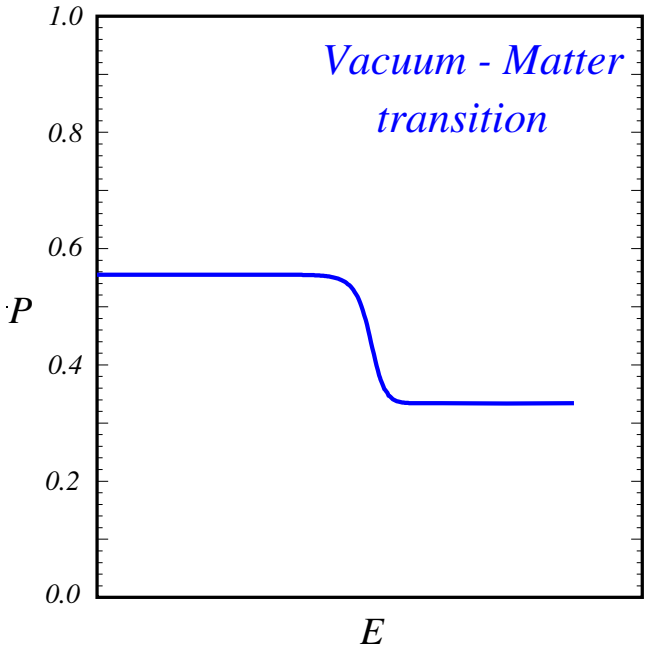

Figure 2. The electron neutrino survival probability, P_{ee}, as a function of neutrino energy for the (daytime) LMA oscillation solution. For small values of the parameter β defined in equations (3) and (4), the kinematic (vacuum) oscillation effects are dominant. For values of β greater than unity, the MSW (matter) oscillations are most important. For solar conditions, the transition between vacuum and matter oscillations occurs somewhere in the region of 2 MeV. A p–p (or pep) solar neutrino experiment would, together with the already-available results from ^{8}B solar neutrino experiments, test the predicted existence of the vacuum–matter transition (see discussion in section 6.3).

3.3. Experimentally determined solar neutrino parameters

All the results discussed in this section are taken from an analysis given in [9] for all currently available solar neutrino and reactor anti-neutrino experimental data. In this analysis, all solar neutrino fluxes are treated as free parameters subject only to the restriction that the fluxes satisfy the luminosity constraint. The evolution in the Sun and in the Earth of the neutrino wavefunctions is solved for numerically. The luminosity constraint imposes energy conservation provided that the Sun shines by nuclear fusion reactions among light elements [43]. Where numerical allowed intervals of a given parameter are reported, we marginalize over all other variables including θ_{13} and ΔM^2 atmospheric. At all points in oscillation parameter space, we use the value of all other variables that minimizes χ^2 for that set of parameters.

The best-fit values and the 1σ uncertainties for Δm^2 and $\tan^2\theta_{12}$ are

$$\Delta m^2 = (7.3^{+0.4}_{-0.6}) \times 10^{-5}\,\mathrm{eV}^2, \tag{10}$$

$$\tan^2\theta_{12} = 0.41 \pm 0.05. \tag{11}$$

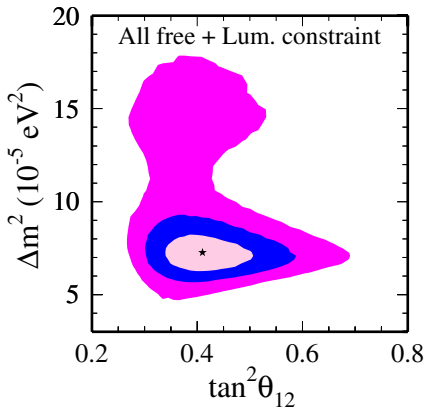

Figure 3. The allowed regions at 1σ, 2σ and 3σ. The allowed regions for neutrino oscillation parameters that are obtained in [9] by a global solution to all the available solar and reactor data. The neutrino fluxes are treated as free parameters subject only to the luminosity constraint.

Figure 3 shows the allowed regions for the oscillation parameters that are obtained at 1σ, 2σ and 3σ from the global solution (free neutrino fluxes subject only to the luminosity constraint) discussed in [9]. The allowed region at 3σ is 'fatter' than the corresponding region that is obtained when the solar neutrino fluxes are required to be consistent with the standard solar model predictions.

In principle, ν_e could oscillate into a state that is a linear combination of active (ν_a) and sterile (ν_s) neutrino states ($\nu_e \to \cos\eta\nu_a + \sin\eta\nu_s$). The allowed range 1σ for the active-sterile admixture is

$$\sin^2\eta \leqslant 0.10. \tag{12}$$

The result given in equation (12) implies that <6% of the ^{8}B flux is in the form of sterile neutrinos in the energy range observed by the Sudbury Solar Neutrino Observatory.

Comparing the measured neutrino fluxes with the theoretical predictions, we find that for BP04:

$$\phi(\mathrm{pp})_{\mathrm{measured}} = (1.02 \pm 0.02 \pm 0.01)\phi(\mathrm{pp})_{\mathrm{theory}}, \tag{13}$$

$$\phi(^8\mathrm{B})_{\mathrm{measured}} = (0.88 \pm 0.04 \pm 0.23)\phi(^8\mathrm{B})_{\mathrm{theory}}, \tag{14}$$

$$\phi(^7\mathrm{Be})_{\mathrm{measured}} = (0.91^{+0.24}_{-0.62} \pm 0.11)\phi(^7\mathrm{Be})_{\mathrm{theory}}. \tag{15}$$

In equations (13) and (15), the 1σ experimental uncertainties are given before the 1σ theoretical uncertainties.

The measured and theoretical values for the fluxes agree within their combined 1σ uncertainties. The measurement error of the ^{8}B neutrino flux is smaller than the uncertainty in the theoretical calculation, but the opposite is true for the p–p and ^{7}Be neutrino fluxes.

The CNO fluxes are poorly constrained by the available solar neutrino data (see [44]). BP04 predictions of the CNO-generated luminosity of the Sun (normalized to the measured

photon luminosity), $L_{\rm CNO} = 1.6 \pm 0.6\,\%$ are well inside the range allowed experimentally, $L_{\rm CNO} = 0.0^{+2.8}_{-0.0}\%$.

The results described above were obtained using the hypothesis that the Sun shines by nuclear fusion reactions among light elements. From neutrino measurements alone, one can measure the solar energy generation rate and then compare this neutrino luminosity with the photon luminosity being radiated from the solar surface. This comparison would test the fundamental idea that nuclear fusion reactions are responsible for the energy radiated by the Sun. Moreover, this same comparison would test a basic inference from the standard solar model, namely, that the Sun is in a quasi-steady state in which the energy currently radiated from the solar surface is balanced by the energy being produced by nuclear reactions in the solar interior at that moment. The ratio of the neutrino-inferred solar luminosity, $L_\odot$ (neutrino-inferred), to the accurately measured photon luminosity, $L_\odot$, is given by

$$\frac{L_\odot\ \text{(neutrino-inferred)}}{L_\odot} = 1.4^{+0.2}_{-0.3}. \tag{16}$$

At present, the neutrino-inferred solar luminosity is still very uncertain. This result reflects once more the need for better determined low-energy neutrino fluxes.

What do we expect from larger data samples in currently running experiments? A global analysis using three years of data simulated for KamLAND shows that the uncertainty of Δm^2 (equation (10)) will be reduced by a factor of 2.5 [9]. SNO neutral current measurements (^{3}He counters) will be able to reduce the uncertainty of $\tan^2\theta_{12}$ by 20%. The neutrino fluxes summarized above are not affected, to the accuracy shown, by the additional simulated KamLAND data and improved SNO neutral current measurement.

4. Neutrinos as dark matter

Neutrinos are the first cosmological dark matter to be discovered. Solar and atmospheric neutrino experiments show that neutrinos have mass but these oscillation experiments only determine the differences between masses, not the absolute values. If we make the plausible but unproven assumption that the lowest neutrino mass, m_1, is much less than the square root of $\Delta m^2_{\rm solar}$, then we can conclude that the mass of cosmological neutrino background is dominated by the mass of the heaviest neutrino. This heaviest neutrino mass is then determined by $\Delta m^2_{\rm atmospheric}$. With this assumption the cosmological mass density in neutrinos is only [20, 39, 45]

$$\Omega_\nu = (0.0009 \pm 0.0001), \qquad m_1 \ll \sqrt{(\Delta m^2_{\rm solar})}. \tag{17}$$

Although the mass density given in equation (17) is small, it is of the same order of magnitude as the observed mass density in stars and gas.

The major uncertainty in determining the value of Ω_ν by neutrino experiments is the unknown value of the lowest neutrino mass. It is possible that neutrino masses are nearly degenerate and cluster around the highest mass scale allowed by direct β-decay experiments. If, for example, all neutrino masses are close to 1 eV, then $\Omega_\nu(1\,\text{eV}) \sim 0.03$, which would be cosmologically significant.

More sensitive neutrino β-decay experiments and neutrinoless double β-decay experiments offer the best opportunities for determining the mass of the lowest mass neutrino and hence establishing the value of Ω_ν from purely laboratory measurements.

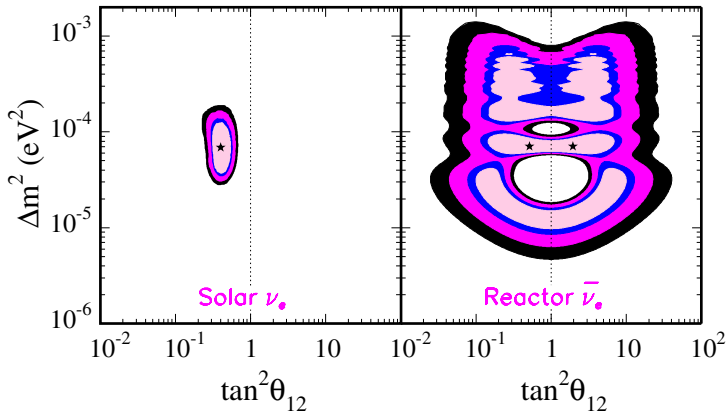

Figure 4. Neutrino and anti-neutrino oscillation constraints. The figure shows the 90, 95, 99%, and 3σ allowed regions for oscillation parameters that are obtained by a global solution to all the available solar data (left panel) or to all the available reactor data (right panel) [31]. The solar neutrino fluxes are treated as free parameters subject only to the luminosity constraint.

5. Test of CPT conservation with reactor and solar neutrino experiments

In this section, we compare the regions of allowed oscillation parameters for neutrinos and anti-neutrinos to constrain the violation of CPT in the neutrino sector [46]–[51]. Our discussion follows the pre-KamLAND analysis of [50], in which expected results from KamLAND were simulated.

Figure 4 shows, in the left-hand panel, the 90, 95, 99% and 3σ allowed regions for oscillation parameters that are obtained by a global solution to all the available solar data and, in the right-hand panel, to all the available reactor data [31]. The juxtaposition of purely solar and purely reactor data in the same figure allows a visual comparison of the constraints on neutrino and on anti-neutrino oscillation parameters. The allowed regions obtained by a global solution to all the available solar and reactor data are described in section 3.3 (see figure 3). The reactor data included in the analysis are from the CHOOZ [37] and KamLAND [33] experiments.

We characterize, following [50], the sensitivity of reactor and solar neutrino experiments to CPT violation by the quantity

$$\langle \Delta CPT \rangle = 2\frac{|\langle P_{\nu\nu}(E, L) - P_{\bar{\nu}\bar{\nu}}(E, L)\rangle|}{\langle P_{\nu\nu}(E, L) + P_{\bar{\nu}\bar{\nu}}(E, L)\rangle}. \tag{18}$$

Here both $P_{\nu\nu}(E, L)$ and $P_{\bar{\nu}\bar{\nu}}(E, L)$ are computed for the same experimental situation, but with different values for $(\Delta m^2_\nu, \theta_\nu)$ and for $(\Delta m^2_{\bar{\nu}}, \theta_{\bar{\nu}})$ that are compatible with the allowed regions at a given CL shown in figure 4. The average in equation (18) is taken for a reactor distance, L, and over all neutrino and anti-neutrino energies, E. Then, $\langle \Delta CPT \rangle$ is the number of events observed in a reactor (anti-neutrino) experiment minus the number of events that would have been observed if neutrinos and anti-neutrinos had exactly the same oscillation parameters, divided by the average number of neutrino and anti-neutrino events.

The maximum value of $\langle \Delta CPT \rangle$ computed by comparing the survival probability in the 1σ (3σ) regions allowed by all solar neutrino data with the anti-neutrino survival probability in

the 1σ (3σ) regions allowed by all reactor data is given by

$$\langle \Delta CPT \rangle \leqslant 0.51\ (1.06) \quad \text{at } 1\sigma\ (3\sigma). \tag{19}$$

Matter effects, which simulate CPT violation, contribute <0.03 (0.08) to $\langle \Delta CPT \rangle$ for neutrino parameters in the 1σ (3σ) allowed regions.

This experimental upper limit on $\langle \Delta CPT \rangle$ can be used to test arbitrary future conjectures of CPT violation. Following [50], we consider an effective interaction which has been discussed by Coleman and Glashow [46, 47] and by Colladay and Kostelecky [48], that violates both Lorentz invariance and CPT invariance. The interaction is of the form

$$\mathcal{L}(\Delta CPT) = \bar{\nu}_{\mathrm{L}}^{\alpha} b_{\mu}^{\alpha\beta} \gamma_{\mu} \nu_{\mathrm{L}}^{\beta}, \tag{20}$$

where α, β are flavour indices, L indicates that the neutrinos are left-handed and b is a Hermitian matrix. We discuss the special case with rotational invariance in which b_0 and the mass-squared matrix are diagonalized by the same mixing angle. We also assume that there are only two interacting neutrinos (or anti-neutrinos) and follow the previous authors in defining η as the difference of the phases in the unitary matrices that diagonalize Δm^2 and the CPT odd quantity δb, which is the difference between the two eigenvalues of b_0.

When the relative phase is $\eta = 0$, the survival probabilities of neutrino and anti-neutrinos take on an especially simple form. For reactor anti-neutrinos, neutrinos oscillate in vacuum (matter effects are negligible in the range of parameters allowed by KamLAND data, see details in [31])

$$P_{\mathrm{ee}} = \cos^4\theta_{13}\left[1 - \sin^2 2\theta_{12}\sin^2\left(\frac{\Delta m^2 L}{4E} - \frac{\delta b L}{2}\right)\right]. \tag{21}$$

For solar neutrinos, sensitivity to δb in the oscillation phase is lost because of the fast oscillations due to the Δm^2 term. In the case of both solar and reactor neutrinos, the mixing in vacuum is unchanged. Equations (5) and (6) are valid with a modified ratio of matter to vacuum effects given by

$$\beta = \frac{2\sqrt{2}G_{\mathrm{F}}\cos^2\theta_{13} n_{\mathrm{e}} E_{\nu}}{\Delta m^2 + 2\delta b E}. \tag{22}$$

We have re-analysed solar and reactor neutrino data with the modified probabilities that contain an extra free parameter δb. We obtain the χ^2 distribution on δb by marginalizing over all other variables. The resulting bounds on violation of CPT invariance are

$$\delta b < 1.5(170) \times 10^{-21}\ \mathrm{GeV}, \qquad \eta = 0 \quad \text{at } 1\sigma\ (3\sigma). \tag{23}$$

The 3σ bound is much weaker than the 1σ bound. The reason is that the available KamLAND spectrum is compatible with no energy dependence at 2σ. Thus KamLAND cannot yet test at 3σ the specific CPT-violating model under discussion. The current bound at 3σ is due to CHOOZ reactor data with a baseline ~100 times shorter (CHOOZ imposes an upper bound on the allowed regions in the right panel of figure 4). If the expected energy dependence is confirmed in KamLAND, the 3σ limit can be significantly improved, to about $\delta b \sim 10^{-21}$ GeV (see [50]).

6. What can be learnt from new solar neutrino experiments?

We begin our discussion of new solar neutrino experiments by presenting in section 6.1 the four primary reasons for doing low-energy solar neutrino experiments. Next we discuss in sections 6.2, 6.3 and 6.4, respectively, what can be learnt from future ^{7}Be, p–p and pep solar neutrino experiments. Finally, we describe in section 6.5 what can be learnt from parasitic solar neutrino experiments that are carried out in connection with a next generation proton-decay experiment. The materials in sections 6.1–6.4 is based on [9].

6.1. Why low-energy solar neutrino experiments?

There are four primary reasons for performing low-energy solar neutrino experiments that measure the energy of individual neutrino-induced events.

First, new phenomena may be revealed at low energies (<3 MeV) that are not discernible at high energies (>5 MeV). According to the currently accepted LMA oscillation solution, the basic oscillation mechanism switches somewhere in the vicinity of 2 MeV (see equation (9) and figure 2) from the MSW matter-dominated oscillations that prevail at high energies to the vacuum oscillations that dominate at low energies. Does this transition from matter-induced to vacuum oscillations actually take place? If the transition does occur, is the ratio (β, see equations (3) and (4)) of the kinematic term in the Hamiltonian (i.e. $\Delta m^2/2E$) to the matter-induced term ($\sqrt{2}G_{\mathrm{F}}n_{\mathrm{e}}\cos^2\theta_{13}$) the only parameter that determines the physical processes that are observed in this energy range?

Secondly, new solar neutrino experiments will provide accurate measurements of the fluxes of the important p–p and ^{7}Be solar neutrino fluxes, which together amount to $>98\%$ of the total flux of solar neutrinos predicted by the standard solar model. These measurements will test the solar model predictions for the main energy-producing reactions, predictions that are more precise than for the higher-energy neutrinos. Using only the measurements of the solar neutrino fluxes, one can determine the current rate at which energy is being produced in the solar interior and can compare that energy generation rate with the observed photon luminosity emitted from the solar surface. This comparison will constitute a direct and accurate test of the fundamental idea that the Sun shines by nuclear reactions among light elements. Moreover, the neutrino flux measurements will test directly a general result of the standard solar model, namely, that the Sun is in a quasi-steady state in which the interior energy generation rate equals the surface radiation rate.

Thirdly, future solar neutrino experiments will make possible a precise measurement of the vacuum mixing angle, θ_{12}, as well as a slightly improved constraint on θ_{13}. The increased robustness in determining mixing angles will be very useful in connection with searches for CP violation. Uncertainties in the CP-conserving neutrino parameters probably compromise the determination of the CP violating phase.

Fourthly, there may be entirely new physical phenomena that show up only at the low energies, the very long baseline, and the great sensitivity to matter effects provided by solar neutrino experiments. It may be recalled that solar neutrino research was initiated to study the solar interior, not to search for neutrino oscillations. Recently, two possibilities have been discussed in which new physics that is compatible with all present data could show up at low energies in solar neutrino experiments. (1) There could be a sterile neutrino with very small mixing to active neutrinos and with a mass splitting smaller than the solar LMA splitting [52]. If so, matter effects in the Sun would resonantly enhance the mixing, producing at energies

around 1 MeV a much stronger deficit than expected from pure LMA oscillations. (2) There could be non-dominant flavour-changing neutrino–matter interactions. In that case, the predicted day–night asymmetry in the lower part of the LMA region ($\Delta m^2 \sim 10^{-5}$) can be very small, making the solar allowed region compatible with the lowest 90% CL region allowed by KamLAND (see the right panel of figure 4). These non-standard interactions would profoundly modify the conversion probability at low energies. The probability that a ν_e neutrino would remain a ν_e could be a factor of two smaller than expected by pure LMA oscillations at the pep line (where $P_{ee}^{LMA} \sim 0.6$), if non-standard interactions are around 10% of the standard coupling (G_F) ([53]). A measurement of the neutrino flux in the pep line will be sensitive to these non-standard interactions, which are unobservable at higher energies. The discovery of either mechanism, sterile neutrinos or flavour-changing neutrino interactions, would have strong particle physics implications.

In this paper, we have assumed the correctness of all solar neutrino and reactor experiments that have been performed so far or which will be performed in the future. But the history of science teaches us that this is a dangerous assumption. Sometimes, unrecognized systematic uncertainties can give misleading results. To be sure that our conclusions are robust, the same quantities must be measured in different ways.

6.2. A ^{7}Be experiment

The existing solar plus reactor experiments provide only loose constraints on the ^{7}Be solar neutrino flux, corresponding to approximately a $\pm 40\%$ uncertainty at 1σ. We need an experiment to measure directly the flux of ^{7}Be solar neutrinos!

How accurate should be the ^{7}Be experiment to provide important new information? A measurement of the ν–e scattering rate accurate to $\pm 10\%$ or better will reduce by a factor of four the uncertainty in the measured ^{7}Be neutrino flux. Moreover, the 10% ^{7}Be flux measurement will reduce the uncertainty in the crucial p–p flux by a factor of about 2.5. That improved determination of the p–p flux by a ^{7}Be measurement is due to the luminosity constraint. A ^{7}Be measurement accurate to $\pm 3\%$ would provide another factor of two improvement in the accuracy of the ^{7}Be and p–p solar neutrino fluxes.

All of these improvements are measured with respect to what we expect can be achieved with three years of operation of the KamLAND experiment. Comparable information can be obtained from a charged-current (neutrino absorption) experiment and from a neutrino–electron scattering experiment if both are performed to the same accuracy.

Contrary to what some authors have stated, a ^{7}Be solar neutrino experiment is not expected to provide significantly more accurate values for the neutrino oscillation parameters than what we think will be available after three years of operation of KamLAND.

6.3. A p–p experiment

According to the standard solar model, about 91% of the total flux of the neutrinos from the Sun is in the form of the low energy (<0.42 MeV) p–p neutrinos. We cannot be sure that we have a correct description of the solar interior until this fundamental prediction is tested. Moreover, the p–p neutrinos are in the range where vacuum oscillations dominate over matter effects, hence observing these low-energy neutrinos is also an opportunity to test in a crucial way our understanding of the neutrino physics.

Figure 2 shows that, for the currently LMA favoured oscillation scenario, the survival probability, P_{ee}, increases by about a factor of two in going from high neutrino energies (at which ^{8}B neutrinos are detected) to low energies (at which p–p neutrinos can be observed). This transition from matter-dominated oscillations to vacuum-dominated oscillations is a fundamental prediction of the favoured LMA oscillation solution. Since we already know the p–p flux to an accuracy of ±2% from existing experiments (see equation (13)), we can use the measured rate of a p–p experiment (or a pep experiment) to test whether the predicted transition from matter-dominated to vacuum-dominated oscillations actually occurs. This test will become even more powerful after a ^{7}Be experiment is performed since the ^{7}Be measurement will, together with the luminosity constraint, make our experimental determination of the p–p neutrino flux even more precise (see the discussion in section 6.2).

If we really know what we think we know, if the standard solar model is correct to the stated accuracy (±1% for the total p–p neutrino flux) and if there is no new physics that shows up below 0.4 MeV, then a measurement of the p–p flux to an accuracy of better than ±3% is necessary to improve significantly our experimental knowledge of $\tan^2\theta_{12}$. The main reason why such a high accuracy is required is that the existing experiments, if they are all correct to their quoted accuracy, already determine the p–p solar neutrino flux to ±2%. (We assume that three years of KamLAND reactor data will be available, as well as a ±5% measurement of the ^{7}Be neutrino–electron scattering rate.)

As described above, an accurate measurement of the p–p solar neutrino flux will provide a direct test of the fundamental ideas underlying the standard solar model. The p–p measurement will make possible the determination of the total solar luminosity from just neutrino experiments alone. The neutrino luminosity can be compared with the photon luminosity to check whether nuclear fusion reactions among light elements is the only discernible source of solar energy and whether the Sun is in an approximate steady state in which the rate of interior energy generation equals the rate at which energy is radiated through the solar surface. The global combination of a ^{7}Be experiment, plus a p–p experiment, plus the existing solar data, and three years of KamLAND would make possible a precise determination of the solar neutrino luminosity. A p–p solar neutrino experiment accurate to 5% would make possible a measurement of the solar neutrino luminosity to 4% and a 1% p–p experiment would determine the solar luminosity to the accuracy implied below:

$$\frac{L_\odot\ (\text{neutrino-inferred})}{L_\odot} = 0.99 \pm 0.02. \tag{24}$$

6.4. A pep experiment

Assuming that the pep neutrino flux (a 1.4 MeV neutrino line) is measured instead of the p–p neutrino flux, we repeated the global analyses of existing and future solar and KamLAND data. The global analyses show that a measurement of the ν–e scattering rate by pep solar neutrinos would, assuming only standard interactions, yield essentially equivalent information about neutrino oscillation parameters and solar neutrino fluxes as a measurement of the ν–e scattering rate by p–p solar neutrinos. The estimated best-estimates and uncertainties in the parameters are almost identical for the analyses we have carried out for p–p and pep neutrinos.

A measurement of pep neutrinos would require a more massive detector than is required to study pp neutrinos, since the pep flux is more than two orders of magnitude smaller than the pp flux. On the other hand, pep neutrinos are more sensitive than pp neutrinos to non-standard matter effects (see discussion in section 6.1).

6.5. Proton decay experiments and solar neutrino measurements

Large water Cherenkov detectors can provide a unique and important test of matter oscillations using ^{8}B solar neutrinos. Only a very large detector will have an event rate that is sufficiently high to detect with statistical confidence the day–night effect with solar neutrinos, an effect which is a characteristic signal of matter-induced neutrino oscillations (the MSW effect).

Motivated by the UNO proposal [54], we suppose for specificity that a future Cherenkov detector will have a fiducial volume seven times that of Super-Kamiokande and that this detector can measure neutrino–electron scattering above 6 MeV. We also assume that the backgrounds and the photo-multiplier coverage ($\sim$40%) will be similar to the Super-Kamiokande experiment.

The best-fit LMA solution predicts a 2% day–night difference in ν–e scattering event rates, which can be observed as a 4σ effect in approximately 10 years. A water Cherenkov proton decay experiment would also provide a much more precise measurement (much better than 1%) of the total event rate for the scattering of ^{8}B solar neutrinos by electrons.

A first detection of the very rare but high energy hep neutrinos should also be possible. We estimate that a measurement of the hep flux with the hypothesized proton decay detector should achieve a 4σ or better accuracy over 10 years. This result assumes that the BP04 predicted hep flux is correct.

For these measurements of solar neutrinos to be successful, the proton decay detector should be placed at a good depth with an active shield. Special care should be taken to make sure that radon contamination is low. Frequent calibrations should be made to ensure that the detector sensitivity and the detector threshold do not vary significantly, in an unknown way, from day to night. The procedure for performing the day–night calibrations should be included in the planning for the next generation proton decay detector.

The study of solar neutrinos using large water Cherenkov detectors is an ideal complement to the study of nucleon decay. The event rate for nucleon decay cannot be predicted with confidence, although the importance of just one or a few events is enormous. The event rate for ^{8}B solar neutrinos can be predicted with great confidence and is enormous, about 31 100 events per year.

Somewhat paradoxically, the study of ^{8}B solar neutrinos could turn out to be the bread and butter project of next generation water Cherenkov proton decay detectors.

Acknowledgments

JNB and CPG acknowledge support from NSF grant no. PHY0070928.

References

[1] Gribov V N and Pontecorvo B M 1969 *Phys. Lett.* B **28** 493
[2] Wolfenstein L 1978 *Phys. Rev.* D **17** 2369
Mikheyev S P and Smirnov A Y 1985 *Sov. J. Nucl. Phys.* **42** 913

[3] Bahcall J N 1989 *Neutrino Astrophysics* (Cambridge: Cambridge University Press)
[4] Bahcall J N, Pinsonneault M H and Basu S 2001 *Astrophys. J.* **555** 990
[5] Cabibbo N 2002 *Int. J. Mod. Phys.* A **17** 3500
[6] Fiorentini G and Ricci B 2002 *Phys. Lett.* B **526** 186
[7] Gonzalez-Garcia M C and Nir Y 2003 *Rev. Mod. Phys.* **75** 345
[8] Smirnov A Yu 2003 *Proc. X Int. Workshop on Neutrino Telescopes, Venice, 11–14 March* ed M B Ceolin
[9] Bahcall J N and Peña-Garay C 2003 *J. High Energy Phys.* **11** 004
[10] Barger V, Marfatia D and Whisnat K 2003 *Int. J. Mod. Phys.* E **12** 569
[11] Bilenky S M, Giunti C, Grifols J A and Masso E 2003 *Phys. Rep.* **379** 69
[12] Kayser B 2003 *Nucl. Phys. Proc.* **118** (Suppl.) 425
[13] Murayama H 2002 *Int. J. Mod. Phys.* A **17** 3403
[14] Fogli G L, Lisi E, Marrone A and Palazzo A 2004 *Phys. Lett.* B **583** 149
[15] Maltoni M, Schwetz T, Tortola M A and Valle J W F 2003 *Phys. Rev.* D **68** 113010
[16] Choubey S, Goswami S, Kar K, Antia H M and Chitre S M 2001 *Phys. Rev.* D **64** 113001
[17] Boothroyd A I and Sackmann I-J 2003 *Astrophys. J.* **583** 1004
[18] Couvidat S, Turck-Chieze S and Kosovichev A G 2003 *Astrophys. J.* **599** 1434
[19] Haxton W C and Holstein B R 2004 *Am. J. Phys.* **72** 18
[20] McDonald A 2004 *New J. Phys.* submitted
[21] Bahcall J N, Pinsonneault M H, Basu S and Christensen-Dalsgaard J 1997 *Phys. Rev. Lett.* **78** 171
[22] Bahcall J N and Pinsonneault M H 2004 *Phys. Rev. Lett.* **92** 121301
[23] Bahcall J N 1997 *Phys. Rev.* C **56** 3391
Bahcall J N, Lisi E, Alburger D E, De Braeckeleer L, Freedman S J and Napolitano J 1996 *Phys. Rev.* C **54** 411
[24] Allende Prieto C, Lambert D L and Asplund M 2002 *Astrophys. J.* **573** L137
Allende Prieto C, Lambert D L and Asplund 2001 *Astrophys. J.* **556** L63
Asplund M, Grevesse N and Sauval A J 2004 *Astron. Astrophys.* in press; see also *Preprint* astro-ph/0312290
Asplund M 2004, private communication
Asplund M, Nordlund A, Trampedach R and Stein R F 2000 *Astron. Astrophys.* **359** 743
Asplund M 2000 *Astron. Astrophys.* **359** 755
[25] Junghans A R *et al* 2003 *Phys. Rev.* C **68** 065803
Baby L T *et al* (ISOLDE Collaboration) 2003 *Phys. Rev. Lett.* **90** 022501
Baby L T *et al* (ISOLDE Collaboration) 2003 *Phys. Rev.* C **67** 065805
Hammache F *et al* 1998 *Phys. Rev. Lett.* **80** 928
Hammache F *et al* 2001 *Phys. Rev. Lett.* **86** 3985
Hass M, Broude C, Fedoseev V, Goldring G, Huber G, Lettry J, Mishin V, Ravn H J, Sebastian V and Weissman L (ISOLDE Collaboration) 1999 *Phys. Lett.* B **462** 237
Strieder F *et al* 2001 *Nucl. Phys.* A **696** 219
Junghans A R, Mohrmann E C, Snover K A, Steiger T D, Adelberger E G, Casandjian J M, Swanson H E, Buchmann L, Park S H and Zyuzin A 2002 *Phys. Rev. Lett.* **88** 041101
[26] Park T S, Marcucci L E, Schiavilla R, Viviani M, Kievsky A, Rosati S, Kubodera K, Min D-P and Rho M 2003 *Phys. Rev.* C **67** 055206
[27] Rogers F J and Nayfonov A 2002 *Astrophys. J.* **576** 1064
Rogers F J 2001 *Contrib. Plasma Phys.* **41** 179
[28] Grevesse N and Sauval A J 1998 *Space Sci. Rev.* **85** 161
[29] Adelberger E G *et al* 1998 *Rev. Mod. Phys.* **70** 1265
[30] Angulo C and Descouvemont P 2001 *Nucl. Phys.* A **690** 755
LUNA Collaboration 2003 *Phys. Lett.* B nucl-ex/0312015 submitted
[31] Bahcall J N, Gonzalez-Garcia M C and Peña-Garay C 2003 *J. High Energy Phys.* **2** 009
[32] Bahcall J N, Fowler W A, Iben I and Sears R L 1963 *Astrophys. J.* **137** 344
Bahcall J N 2003 *Nucl. Phys.* B (Proc. Suppl.) **118** 77

[33] Eguchi K *et al* 2003 *Phys. Rev. Lett.* **90** 021802
[34] Gluza J and Zralek M 2001 *Phys. Lett.* B **517** 158
[35] Kuo T K and Pantaleone J 1986 *Phys. Rev. Lett.* **57** 1805
[36] Shi X and Schramm D N 1992 *Phys. Lett.* B **283** 305
[37] Apollonio M *et al* 1999 *Phys. Lett.* B **466** 415
[38] Boehm F *et al* 2000 *Phys. Rev.* D **62** 072002
[39] Gonzalez-Garcia M C and Peña-Garay C 2003 *Phys. Rev.* D **68** 093003
[40] Bethe H A 1986 *Phys. Rev. Lett.* **56** 1305
[41] Mikheev S P and Smirnov A Y 1986 *Proc. 6th Moriond Workshop on Massive Neutrinos in Astrophysics and Particle Physics* ed O Fackler and J Tran Thanh Van (Gif-sur-Yvette: Editions Frontieres) p 355
[42] Messiah A 1986 *Proc. 6th Moriond Workshop on Massive Neutrinos in Astrophysics and Particle Physics* ed O Fackler and J Tran Thanh Van (Gif-sur-Yvette: Editions Frontieres) p 373
[43] Bahcall J N 2002 *Phys. Rev.* C **65** 025801
[44] Bahcall J N, Gonzalez-Garcia M C and Peña-Garay C 2003 *Phys. Rev. Lett.* **90** 131301
[45] Murayama H and Peña-Garay C 2003 *Phys. Rev.* D **69** 031301
[46] Coleman S R and Glashow S L 1997 *Phys. Lett.* B **405** 249
[47] Coleman S R and Glashow S L 1999 *Phys. Rev.* D **59** 116008
[48] Colladay D and Kostelecky V A 1997 *Phys. Rev.* D **55** 6760
[49] Barger V D, Pakvasa S, Weiler T J and Whisnant K 2000 *Phys. Rev. Lett.* **85** 50555
[50] Bahcall J N, Barger V D and Marfatia D 2002 *Phys. Lett.* B **534** 120
[51] Murayama H 2003 *Preprint* hep-ph/0307127
[52] de Holanda P C and Smirnov A Y 2003 *Preprint* hep-ph/0307266
Berezinsky V, Narayan M and Vissani F 2003 *Nucl. Phys.* B **658** 254
[53] Friedland A, Lunardini C and Peña-Garay C 2004 *Preprint* hep-ph/0402266
[54] UNO Proto-collaboration 2000 UNO Whitepaper: Physics Potential and Feasibility of UNO, SBHEP-01-03(2000), http://nngroup.physics.sunysb.edu/uno/
Jung C K 2002 *Preprint* hep-ex/0005046

New Journal of Physics
An Institute of Physics and Deutsche Physikalische Gesellschaft Journal

Supersymmetric origin of neutrino mass

M Hirsch and J W F Valle

AHEP Group, Instituto de Física Corpuscular—C.S.I.C./Universitat de València
Edificio Institutos de Paterna, Apt 22085, E-46071 Valencia, Spain
E-mail: valle@ific.uv.es

New Journal of Physics **6** (2004) 76
Received 12 May 2004
Published 8 July 2004
Online at http://www.njp.org/
doi:10.1088/1367-2630/6/1/076

Abstract. Supersymmetry with breaking of R-parity provides an attractive way to generate neutrino masses and lepton mixing angles in accordance with the present neutrino data. We review the main theoretical features of the bilinear R-parity breaking (BRpV) model, and stress that it is the simplest extension of the minimal supersymmetric standard model (MSSM), which includes lepton number violation. We describe how it leads to a successful phenomenological model with hierarchical neutrino masses. In contrast with see-saw models, the BRpV model can be probed at future collider experiments, such as the Large Hadron Collider or the Next Linear Collider, since the decay pattern of the lightest supersymmetric particle provides a direct connection with the lepton mixing angles determined by neutrino experiments.

PII: S1367-2630(04)80602-5
© IOP Publishing Ltd and Deutsche Physikalische Gesellschaft

Contents

1. Introduction **2**
2. Formalism **3**
2.1. The superpotential and the soft breaking terms . . . 3
2.2. Radiative breaking of the electroweak symmetry . . . 5
2.3. Neutral fermion mass matrix . . . 7
2.4. Charged fermion mass matrix . . . 8
3. Tree-level neutrino mass: the atmospheric scale **9**
4. One-loop-induced neutrino mass: the solar scale **11**
4.1. Results for the solar mass scale . . . 15
4.2. Analytical approximation for the solar mixing angle . . . 16
5. Testing neutrino properties at high-energy accelerators **18**
6. Discussion and conclusions **19**
Acknowledgments **20**
References **20**

1. Introduction

A combination of solar, atmospheric, reactor and accelerator neutrino experiments [1]–[3] have now firmly established the existence of neutrino masses and therefore the incompleteness of the standard model of electroweak interactions. The determination of neutrino oscillation parameters presented in [4] uses the most recent data and state-of-the-art solar and atmospheric neutrino fluxes;[1] see [5]–[8] for previous reviews and references. We have now learnt that the atmospheric oscillations involving $\nu_\mu \leftrightarrow \nu_\tau$ are characterized by a nearly maximal mixing, whereas the solar neutrino mixing angle is large and significantly non-maximal. With the recent standard solar model fluxes, there is a unique range for the solar mass splitting $\Delta m^2_{\rm SOL}$, determined from the data to be about 30 times smaller than the atmospheric mass splitting $\Delta m^2_{\rm ATM}$.

The discovery of neutrino mass constitutes the only solid hint we currently have of physics beyond the standard model. There are theoretical arguments based on the stability of the gauge hierarchy which suggest the existence of physics at the TeV scale. Supersymmetry [9, 10] provides an answer to both these issues which fits well with unification and string theory ideas [11].

Prompted by these data, there has been a rush of theoretical and phenomenological papers on models of neutrino masses and mixings. The most popular idea is to ascribe neutrino masses to physics at a large mass scale to implement some variant of the see-saw mechanism [12]–[15]. Broken R-parity supersymmetry provides a theoretically interesting and phenomenologically viable alternative to the origin of neutrino mass and mixing [16]–[22]. Here we focus on the case of supersymmetry with bilinear R-parity breaking (BRpV) [23]. This is the simplest of all R-parity violating models. It also provides the simplest extension of the minimal supersymmetric standard model (MSSM) [23] to include the violation of lepton number, as well as a calculable framework for neutrino masses and mixing angles in agreement with the experimental data [24]–[27]. In this model, the atmospheric neutrino mass scale is generated at the tree level through

[1] The results presented in [4] were based on a previous paper published in *Phys. Rev.* D **68**, 113010 (2003), (hep-ph/0309130), which also contains a more extensive list of references.

the mixing of the three neutrinos with the neutralinos, in an effective 'low-scale' variant of the see-saw mechanism [17]. In contrast, the solar mass and mixings are generated radiatively [26]. BRpV can be considered either as a minimal extension of the MSSM [28]–[31] (with no new particles) valid up to some very high unification energy scale, or as the effective description of a more fundamental theory in which the breaking of R-parity occurs in a spontaneous way by minimizing the scalar potential [32]–[34].

This short review is mainly devoted to the generation of neutrino masses and lepton mixing, both the tree-level atmospheric neutrino mass scale as well as a description of the main features of the full one-loop calculation of the neutrino–neutralino mass matrix and its various analytic approximations which, in some cases, can be rather simple. For definiteness we will stick to the case of explicit BRpV only.

However, in contrast with the see-saw mechanism, in BRpV neutrino masses are generated at the electroweak scale [24, 26, 27]. Such low-scale schemes for neutrino masses have the advantage of being testable also outside the realm of neutrino experiments. Although neutrino properties cannot be predicted from first principles, their fit to the data allows for unambiguous tests of the theory at accelerator experiments [27], [35]–[43]. Indeed, the measured lepton mixing angles lead to well-defined predictions of the decay properties of the lightest supersymmetric particle (LSP). This is a very general and robust feature of these theories, which holds irrespective of the nature of the LSP. Here we will illustrate possible phenomenological scenarios by discussing some examples of measurements of decay properties of different LSP candidates.

This paper is organized as follows. In section 2 we introduce the main features of the model, discuss the soft supersymmetry breaking terms, as well as the relevant fermion mass matrices and the main features of the corresponding diagonalizing matrices. In section 3 we discuss the generation of the atmospheric neutrino mass scale at the tree level, whereas in section 4 we analyse the main features of the one-loop-induced solar neutrino mass scale, including a discussion of the relevant Feynman graph topologies. We also give simplified approximation formula for the solar mixing angle. We then turn briefly to collider phenomenology and how the model under discussion could be tested in LSP decays in section 5 before we conclude and summarize our results in section 6.

2. Formalism

In this section, we introduce the main features of the model and the relevant mass matrices. The superpotential of the model and the soft SUSY breaking terms are given, and approximate solutions to the tadpole equations discussed.

2.1. The superpotential and the soft breaking terms

The minimal BRpV model we are working with is characterized by the presence of three extra bilinear terms in the superpotential analogous to the μ term present in the MSSM. Using the conventions of Akeroyd *et al* [31] it may be given as

$$W = \varepsilon_{ab}[h_U^{ij}\widehat{Q}_i^a\widehat{U}_j\widehat{H}_u^b + h_D^{ij}\widehat{Q}_i^b\widehat{D}_j\widehat{H}_d^a + h_E^{ij}\widehat{L}_i^b\widehat{R}_j\widehat{H}_d^a - \mu\widehat{H}_d^a\widehat{H}_u^b + \epsilon_i\widehat{L}_i^a\widehat{H}_u^b], \qquad (1)$$

where the first three terms are the usual MSSM Yukawa terms, μ is the Higgsino mass term of the MSSM and ϵ_i are the three new terms which violate lepton number in addition to R-parity. The couplings h_U, h_D and h_E are 3×3 Yukawa matrices and μ and ϵ_i are parameters with units of mass. The smallness of the bilinear term ϵ_i in equation (1) may arise from a suitable symmetry. In fact, any solution to the μ problem [44] potentially explains also the 'ϵ_i problem' [45]. A common origin for the ϵ_i terms that account for the neutrino oscillation data, and the μ term responsible for electroweak symmetry breaking can be ascribed to a horizontal family symmetry of the type suggested in [46].

The smallness of ϵ_i could also arise dynamically in models with spontaneous breaking of R-parity [32]–[34], where it is given as the product of a Yukawa coupling times a singlet sneutrino vacuum expectation value.

Supersymmetry breaking is parametrized with a set of soft supersymmetry breaking terms. In the MSSM these are given by

$$\begin{aligned}\mathcal{L}_{soft}^{MSSM} = {} & M_Q^{ij2}\widetilde{Q}_i^{a*}\widetilde{Q}_j^a + M_U^{ij2}\widetilde{U}_i\widetilde{U}_j^* + M_D^{ij2}\widetilde{D}_i\widetilde{D}_j^* + M_L^{ij2}\widetilde{L}_i^{a*}\widetilde{L}_j^a + M_R^{ij2}\widetilde{R}_i\widetilde{R}_j^* \\ & + m_{H_d}^2 H_d^{a*}H_d^a + m_{H_u}^2 H_u^{a*}H_u^a - [\tfrac{1}{2}M_s\lambda_s\lambda_s + \tfrac{1}{2}M\lambda\lambda + \tfrac{1}{2}M'\lambda'\lambda' + \text{h.c.}] \\ & + \varepsilon_{ab}[A_U^{ij}\widetilde{Q}_i^a\widetilde{U}_j H_u^b + A_D^{ij}\widetilde{Q}_i^b\widetilde{D}_j H_d^a + A_E^{ij}\widetilde{L}_i^b\widetilde{R}_j H_d^a - B\mu H_d^a H_u^b].\end{aligned} \tag{2}$$

In addition to the MSSM soft SUSY breaking terms in $\mathcal{L}_{soft}^{MSSM}$, the BRpV model contains the following extra terms:

$$V_{soft}^{BRpV} = -B_i\epsilon_i\varepsilon_{ab}\widetilde{L}_i^a H_u^b, \tag{3}$$

where the B_i have units of mass. In what follows, we neglect inter-generational mixing in the soft terms in equation (2).

The electroweak symmetry is broken when the two Higgs doublets H_d and H_u, and the neutral component of the slepton doublets $\widetilde{L}_i^1$ acquire non-zero vacuum expectation values (vevs). These are calculated via the minimization of the effective potential or, in the diagrammatic method, via the tadpole equations. The full-scalar potential at tree level is

$$V_{total}^0 = \sum_i \left|\frac{\partial W}{\partial z_i}\right|^2 + V_D + V_{soft}^{MSSM} + V_{soft}^{BRpV}, \tag{4}$$

where z_i is any one of the scalar fields in the superpotential in equation (1), V_D are the D terms and V_{soft}^{BRpV} is given in equation (3).

The tree-level scalar potential contains the following linear terms:

$$V_{linear}^0 = t_d^0\sigma_d^0 + t_u^0\sigma_u^0 + t_1^0\tilde{\nu}_1^R + t_2^0\tilde{\nu}_2^R + t_3^0\tilde{\nu}_3^R, \tag{5}$$

where the different t^0 are the tadpoles at tree level, and are given by

$$\begin{aligned} t_d^0 &= (m_{H_d}^2 + \mu^2)v_d + v_d D - \mu(Bv_u + v_i\epsilon_i), \\ t_u^0 &= -B\mu v_d + (m_{H_u}^2 + \mu^2)v_u - v_u D + v_i B_i\epsilon_i + v_u\epsilon^2, \\ t_1^0 &= v_1 D + \epsilon_1(-\mu v_d + v_u B_1 + v_i\epsilon_i) + \tfrac{1}{2}(v_i M_{Li1}^2 + M_{L1i}^2 v_i), \\ t_2^0 &= v_2 D + \epsilon_2(-\mu v_d + v_u B_2 + v_i\epsilon_i) + \tfrac{1}{2}(v_i M_{Li2}^2 + M_{L2i}^2 v_i), \\ t_3^0 &= v_3 D + \epsilon_3(-\mu v_d + v_u B_3 + v_i\epsilon_i) + \tfrac{1}{2}(v_i M_{Li3}^2 + M_{L3i}^2 v_i), \end{aligned} \tag{6}$$

where we have introduced the notation

$$H_d = \begin{pmatrix} H_d^0 \\ H_d^- \end{pmatrix}, \qquad H_u = \begin{pmatrix} H_u^+ \\ H_u^0 \end{pmatrix}, \qquad \widetilde{L}_i = \begin{pmatrix} \widetilde{L}_i^0 \\ \tilde{\ell}_i^- \end{pmatrix}, \tag{7}$$

and shifted the neutral fields with non-zero vevs as

$$H_d^0 \equiv \frac{1}{\sqrt{2}}[\sigma_d^0 + v_d + \mathrm{i}\varphi_d^0], \qquad H_u^0 \equiv \frac{1}{\sqrt{2}}[\sigma_u^0 + v_u + \mathrm{i}\varphi_u^0], \qquad \widetilde{L}_i^0 \equiv \frac{1}{\sqrt{2}}[\tilde{\nu}_i^R + v_i + \mathrm{i}\tilde{\nu}_i^I]. \tag{8}$$

The five vacuum expectation values can be expressed in spherical coordinates as

$$\begin{aligned} v_d &= v \sin\theta_1 \sin\theta_2 \sin\theta_3 \cos\beta, \\ v_u &= v \sin\theta_1 \sin\theta_2 \sin\theta_3 \sin\beta, \\ v_3 &= v \sin\theta_1 \sin\theta_2 \cos\theta_3, \\ v_2 &= v \sin\theta_1 \cos\theta_2, \\ v_1 &= v \cos\theta_1, \end{aligned} \tag{9}$$

which preserves the MSSM definition $\tan\beta = v_u/v_d$ with the W boson mass given as $m_W^2 = \frac{1}{4}g^2(v_d^2 + v_u^2 + v_1^2 + v_2^2 + v_3^2)$. We have also defined $D = \frac{1}{8}(g^2 + g'^2)(v_1^2 + v_2^2 + v_3^2 + v_d^2 - v_u^2)$ and $\epsilon^2 = \epsilon_1^2 + \epsilon_2^2 + \epsilon_3^2$. A repeated index i in equation (6) implies summation over $i = 1$–3. The five tree-level tadpoles t_α^0 are equal to zero at the minimum of the tree-level potential, and from there one can determine the tree-level vevs.

2.2. *Radiative breaking of the electroweak symmetry*

A reliable description of electroweak symmetry breaking and Higgs boson physics in supersymmetry requires the inclusion of radiative corrections. In the BRpV model, the full-scalar potential at one-loop level, called effective potential, is

$$V_{total} = V_{total}^0 + V_{RC}, \tag{10}$$

where V_{total}^0 is given in equation (4) and V_{RC} include the quantum corrections. Following Diaz *et al* [24] and Hirsch *et al* [26] we use the diagrammatic method, incorporating the radiative corrections through the one-loop corrected tadpole equations. The one-loop tadpoles are

$$t_\alpha = t_\alpha^0 - \delta t_\alpha^{\overline{\mathrm{DR}}} + T_\alpha(Q) = t_\alpha^0 + \widetilde{T}_\alpha^{\overline{\mathrm{DR}}}(Q), \tag{11}$$

where $\alpha = d, u, 1, 2, 3$ and $\widetilde{T}_\alpha^{\overline{\mathrm{DR}}}(Q) \equiv -\delta t_\alpha^{\overline{\mathrm{MS}}} + T_\alpha(Q)$ are the finite one-loop tadpoles. At the minimum of the potential we have $t_\alpha = 0$, and the vevs calculated from these equations are the renormalized vevs.

Neglecting inter-generational mixing in the soft masses, the five tadpole equations can be conveniently written in matrix form as

$$[t_u^0, t_d^0, t_1^0, t_2^0, t_3^0]^{\mathrm{T}} = \mathbf{M}_{\mathrm{tad}}^2 [v_u, v_d, v_1, v_2, v_3]^{\mathrm{T}}, \tag{12}$$

where the matrix $\mathbf{M}_{\mathrm{tad}}^2$ is given in [26] and depends on the vevs only through the D term defined above.

In the MSSM limit, where $\epsilon_i = v_i = 0$, the angles θ_i are equal to $\pi/2$. In addition to the above MSSM parameters, our model contains nine new parameters, ϵ_i, v_i and B_i. Considering we have three tadpole equations one can take either the three B_i as input and derive the three sneutrino vevs or vice versa, such that we have in total just six new parameters (compared with the MSSM).

To have approximate solutions for the tree-level vevs, consider the following rotation among the H_d and lepton superfields:

$$\mathbf{M}'^2_{\text{tad}} = \mathbf{R}\mathbf{M}^2_{\text{tad}}\mathbf{R}^{-1}, \tag{13}$$

where the rotation $\mathbf{R}$ can be split as

$$\mathbf{R} = \begin{bmatrix} c_3 & 0 & 0 & 0 & -s_3 \\ 0 & 1 & 0 & 0 & 0 \\ 0 & 0 & 1 & 0 & 0 \\ 0 & 0 & 0 & 1 & 0 \\ s_3 & 0 & 0 & 0 & c_3 \end{bmatrix} \times \begin{bmatrix} c_2 & 0 & 0 & -s_2 & 0 \\ 0 & 1 & 0 & 0 & 0 \\ 0 & 0 & 1 & 0 & 0 \\ s_2 & 0 & 0 & c_2 & 0 \\ 0 & 0 & 0 & 0 & 1 \end{bmatrix} \times \begin{bmatrix} c_1 & 0 & -s_1 & 0 & 0 \\ 0 & 1 & 0 & 0 & 0 \\ s_1 & 0 & c_1 & 0 & 0 \\ 0 & 0 & 0 & 1 & 0 \\ 0 & 0 & 0 & 0 & 1 \end{bmatrix}, \tag{14}$$

where the three angles are defined as

$$\begin{aligned} c_1 &= \frac{\mu}{\mu'}, \qquad s_1 = \frac{\epsilon_1}{\mu'}, \qquad \mu' = \sqrt{\mu^2 + \epsilon_1^2}, \\ c_2 &= \frac{\mu'}{\mu''}, \qquad s_2 = \frac{\epsilon_2}{\mu''}, \qquad \mu'' = \sqrt{\mu'^2 + \epsilon_2^2}, \\ c_3 &= \frac{\mu''}{\mu'''}, \qquad s_3 = \frac{\epsilon_3}{\mu'''}, \qquad \mu''' = \sqrt{\mu''^2 + \epsilon_3^2}. \end{aligned} \tag{15}$$

It is clear that this rotation $\mathbf{R}$ leaves the D term invariant. The rotated vevs are given by

$$[v'_u, v'_d, v'_1, v'_2, v'_3]^{\mathrm{T}} = \mathbf{R}[v_u, v_d, v_1, v_2, v_3]^{\mathrm{T}}, \tag{16}$$

and under the assumption that $v'_1, v'_2, v'_3 \ll v$, these three small vevs have the approximate solution

$$\begin{aligned} v'_1 &\approx -\frac{\mu\epsilon_1}{M'^2_{L_1} + D}\left[\frac{m^2_{H_d} - M^2_{L_1}}{\mu'\mu'''}v'_d + \frac{B_1 - B}{\mu'}v'_u\right], \\ v'_2 &\approx -\frac{\mu'\epsilon_2}{M'^2_{L_2} + D}\left[\frac{m'^2_{H_d} - M^2_{L_2}}{\mu''\mu'''}v'_d + \frac{B_2 - B'}{\mu''}v'_u\right], \\ v'_3 &\approx -\frac{\mu''\epsilon_3}{M'^2_{L_3} + D}\left[\frac{m''^2_{H_d} - M^2_{L_3}}{\mu'''^2}v'_d + \frac{B_3 - B''}{\mu'''}v'_u\right], \end{aligned} \tag{17}$$

where we have defined the following rotated soft terms:

$$m'^2_{H_d} = \frac{m^2_{H_d}\mu^2 + M^2_{L_1}\epsilon^2_1}{\mu'^2}, \qquad m''^2_{H_d} = \frac{m'^2_{H_d}\mu'^2 + M^2_{L_2}\epsilon^2_2}{\mu''^2}, \qquad m'''^2_{H_d} = \frac{m''^2_{H_d}\mu''^2 + M^2_{L_3}\epsilon^2_3}{\mu'''^2},$$
$$B' = \frac{B\mu^2 + B_1\epsilon^2_1}{\mu'^2}, \qquad B'' = \frac{B'\mu'^2 + B_2\epsilon^2_2}{\mu''^2}, \qquad B''' = \frac{B''\mu''^2 + B_3\epsilon^2_3}{\mu'''^2}, \tag{18}$$
$$M'^2_{L_1} = \frac{m^2_{H_d}\epsilon^2_1 + M^2_{L_1}\mu^2}{\mu'^2}, \qquad M'^2_{L_2} = \frac{m'^2_{H_d}\epsilon^2_2 + M^2_{L_2}\mu'^2}{\mu''^2}, \qquad M'^2_{L_3} = \frac{m''^2_{H_d}\epsilon^2_3 + M^2_{L_3}\mu''^2}{\mu'''^2}.$$

As can be seen from equation (17), the approximation $v'_1, v'_2, v'_3 \ll v$ is justified if either (i) $\epsilon_i \ll \mu$ and/or (ii) $(m^2_{H_d} - M^2_{L_i})/\mu^2 \ll 1$ and $(B_i - B)/\mu \ll 1$. The latter holds automatically (to some extent) in many models of supersymmetry breaking as, for example, in minimal supergravity [23].

As in the MSSM, the electroweak symmetry is broken because the large value of the top quark mass drives the Higgs mass parameter $m^2_{H_U}$ to negative values at the weak scale via its RGE [47]. In the rotated basis, the parameter μ'''^2 is determined at one loop by

$$\mu'''^2 = -\frac{1}{2}[m^2_Z - \widetilde{A}_{ZZ}(m^2_Z)] + \frac{(m'''^2_{H_d} + \widetilde{T}^{\overline{\mathrm{DR}}}_{v'_d}) - (m^2_{H_u} + \widetilde{T}^{\overline{\mathrm{DR}}}_{v'_u})t'^2_\beta}{t'^2_\beta - 1}, \tag{19}$$

where $t'_\beta = v'_u/v'_d$ is defined in the rotated basis and is analogous to $\tan\beta$ in equation (9) defined in the original basis. The finite $\overline{\mathrm{DR}}$ Z-boson self-energy is $\widetilde{A}_{ZZ}(m^2_Z)$, and the one-loop tadpoles $T^{\overline{\mathrm{DR}}}_{v'_d}$ and $T^{\overline{\mathrm{DR}}}_{v'_u}$ are obtained by applying the rotation $\mathbf{R}$ defined in equation (14) to the original tadpoles in equation (11). The radiative breaking of the electroweak symmetry is valid in the BRpV model in the usual way: the large value of the top quark Yukawa coupling drives the parameter $m^2_{H_U}$ to negative values, breaking the symmetry of the scalar potential.

2.3. Neutral fermion mass matrix

We consider the tree-level structure of the fermion mass matrices in this model. For a more complete discussion of different mass matrices in BRpV see the appendix in [26]. In the basis $\psi^{0\mathrm{T}} = (-\mathrm{i}\lambda', -\mathrm{i}\lambda^3, \widetilde{H}^1_d, \widetilde{H}^2_u, \nu_e, \nu_\mu, \nu_\tau)$ the neutral fermion mass matrix $\mathbf{M}_N$ is given by

$$\mathbf{M}_N = \begin{bmatrix} \mathcal{M}_{\chi^0} & m^{\mathrm{T}} \\ m & 0 \end{bmatrix}, \tag{20}$$

where

$$\mathcal{M}_{\chi^0} = \begin{bmatrix} M_1 & 0 & -\frac{1}{2}g'v_d & \frac{1}{2}g'v_u \\ 0 & M_2 & \frac{1}{2}gv_d & -\frac{1}{2}gv_u \\ -\frac{1}{2}g'v_d & \frac{1}{2}gv_d & 0 & -\mu \\ \frac{1}{2}g'v_u & -\frac{1}{2}gv_u & -\mu & 0 \end{bmatrix} \tag{21}$$

is the standard MSSM neutralino mass matrix (M_2 and M_1 are the SU(2) and U(1) gaugino soft masses) and

$$m = \begin{bmatrix} -\frac{1}{2}g'v_1 & \frac{1}{2}gv_1 & 0 & \epsilon_1 \\ -\frac{1}{2}g'v_2 & \frac{1}{2}gv_2 & 0 & \epsilon_2 \\ -\frac{1}{2}g'v_3 & \frac{1}{2}gv_3 & 0 & \epsilon_3 \end{bmatrix} \tag{22}$$

characterizes the breaking of R-parity. The full 7×7 neutrino/neutralino mass matrix $\mathbf{M}_N$ is diagonalized as

$$\mathcal{N}^* \mathbf{M}_N \mathcal{N}^{-1} = \mathrm{diag}(m_{\chi_i^0}, m_{\nu_j}), \tag{23}$$

where $i = 1, \ldots, 4$ for the neutralinos and $j = 1, \ldots, 3$ for the neutrinos,

$$\mathcal{N}^* \mathbf{M}_{F^0} \mathcal{N}^{-1} = \mathbf{M}_{F^0}^{\mathrm{diag}} \tag{24}$$

and the eigenvectors are given by

$$F_i^0 = \mathcal{N}_{ij} \psi_j \tag{25}$$

using the basis $\psi = (-\mathrm{i}\lambda', -\mathrm{i}\lambda^3, \widetilde{H}_d^1, \widetilde{H}_u^2, \nu_e, \nu_\mu, \nu_\tau)$. As discussed in more detail below, to a very good approximation, the rotation matrix can be written as

$$\mathcal{N}^* \approx \begin{pmatrix} N^* & N^* \xi^\dagger \\ -V_\nu^{\mathrm{T}} \xi & V_\nu^{\mathrm{T}} \end{pmatrix}. \tag{26}$$

Here, N is the rotation matrix that diagonalizes the 4×4 MSSM neutralino mass matrix, V_ν is the rotation matrix that diagonalizes the tree-level neutrino 3×3 mass matrix and $\xi_{ij} \ll 1$ are the relevant small expansion parameters which characterize the violation of R-parity and whose form will be given in section 3.

2.4. Charged fermion mass matrix

The chargino/lepton mass matrix is given by

$$\mathbf{M}_C = \begin{bmatrix} M_2 & \frac{1}{\sqrt{2}}gv_u & 0 & 0 & 0 \\ \frac{1}{\sqrt{2}}gv_d & \mu & -\frac{1}{\sqrt{2}}(h_E)_{11}v_1 & -\frac{1}{\sqrt{2}}(h_E)_{22}v_2 & -\frac{1}{\sqrt{2}}(h_E)_{33}v_3 \\ \frac{1}{\sqrt{2}}gv_1 & -\epsilon_1 & \frac{1}{\sqrt{2}}(h_E)_{11}v_d & 0 & 0 \\ \frac{1}{\sqrt{2}}gv_2 & -\epsilon_2 & 0 & \frac{1}{\sqrt{2}}(h_E)_{22}v_d & 0 \\ \frac{1}{\sqrt{2}}gv_3 & -\epsilon_3 & 0 & 0 & \frac{1}{\sqrt{2}}(h_E)_{33}v_d \end{bmatrix}. \tag{27}$$

We note that the chargino sector decouples from the lepton sector in the limit $\epsilon_i = v_i = 0$. As in the MSSM, the chargino mass matrix is diagonalized by two rotation matrices $\mathbf{U}$ and $\mathbf{V}$

defined by

$$\mathcal{U}^{*}\mathbf{M}_{F^{+}}\mathcal{V}^{-1} = \mathbf{M}_{F^{+}}^{\mathrm{diag}} \tag{28}$$

with the eigenvectors satisfying

$$F_{Ri}^{+} = \mathcal{V}_{ij}\psi_{j}^{+}, \qquad F_{Li}^{-} = \mathcal{U}_{ij}\psi_{j}^{-} \tag{29}$$

in the basis $\psi^{+} = (-\mathrm{i}\lambda^{+}, \widetilde{H}_{2}^{1}, e_{R}^{+}, \mu_{R}^{+}, \tau_{R}^{+})$ and $\psi^{-} = (-\mathrm{i}\lambda^{-}, \widetilde{H}_{1}^{2}, e_{L}^{-}, \mu_{L}^{-}, \tau_{L}^{-})$, with the Dirac fermions being

$$F_{i}^{+} = \left(\begin{array}{c} F_{Ri}^{+} \\ \hline F_{Li}^{-} \end{array}\right). \tag{30}$$

To first order in the R-parity violating parameters we have

$$\mathcal{V} \approx \begin{pmatrix} V & V\xi_{R}^{\mathrm{T}} \\ -V_{R}^{\ell}\xi_{R}^{*} & V_{R}^{\ell} \end{pmatrix}, \qquad \mathcal{U} \approx \begin{pmatrix} U & U\xi_{L}^{\dagger} \\ -V_{L}^{\ell *}\xi_{L} & V_{L}^{\ell *} \end{pmatrix}, \tag{31}$$

where $V_{L}^{\ell *}$ and V_{R}^{ℓ} diagonalize the charged lepton mass matrix according to $V_{L}^{\ell *}\mathbf{M}^{\ell}V_{R}^{\ell\dagger} = \mathbf{M}_{\mathrm{diag}}^{\ell}$. For most purposes it is sufficient to take $\xi_{R} = \mathbf{0}_{2\times 3}$, since it is smaller than ξ_{L} typically by a factor of m_{l}/m_{SUSY}. Note that we can choose $V_{L}^{\ell *} = V_{R}^{\ell\dagger} = \mathbf{1}_{3\times 3}$. We then have

$$\xi_{L}^{i1} = a_{1}^{L}\Lambda_{i}, \qquad \xi_{L}^{i2} = a_{2}^{L}\Lambda_{i} + b\epsilon_{i} \tag{32}$$

and

$$a_{1}^{L} = \frac{g}{\sqrt{2}\Delta_{+}}, \qquad a_{2}^{L} = -\frac{g^{2}v_{u}}{2\mu\Delta_{+}}, \tag{33}$$

where Δ_{+} is the determinant of the 2×2 chargino mass matrix and

$$\Lambda_{i} = \mu v_{i} + v_{d}\epsilon_{i} \propto v_{i}' \tag{34}$$

are the alignment parameters.

3. Tree-level neutrino mass: the atmospheric scale

The tree-level contribution to neutrino masses from broken R-parity supersymmetry has a long history [48]. Owing to the Super-K findings [1], we are interested only in the case where the neutrino mass, determined at the tree level, is small to account for the atmospheric neutrino data. The above form for $\mathbf{M}_{N}$ is especially convenient in this case to provide an approximate analytical discussion valid in the limit of small $\not{R}_{p}$ violation parameters. Indeed, in this case, we perform a perturbative diagonalization of the neutral mass matrix, defining

$$\xi = m \cdot \mathcal{M}_{\chi^{0}}^{-1}. \tag{35}$$

Since the effective RpV parameters are smaller than the weak scale, we can work in a perturbative expansion defined by $\xi \ll 1$, where ξ denotes a 3×4 matrix given as [49]

$$\xi_{i1} = \frac{g' M_2 \mu}{2\det(\mathcal{M}_{\chi^0})}\Lambda_i,$$

$$\xi_{i2} = -\frac{g M_1 \mu}{2\det(\mathcal{M}_{\chi^0})}\Lambda_i,$$

$$\xi_{i3} = -\frac{\epsilon_i}{\mu} + \frac{(g^2 M_1 + g'^2 M_2) v_u}{4\det(\mathcal{M}_{\chi^0})}\Lambda_i,$$

$$\xi_{i4} = -\frac{(g^2 M_1 + g'^2 M_2) v_d}{4\det(\mathcal{M}_{\chi^0})}\Lambda_i. \tag{36}$$

From equations (36) and (34) one can see that $\xi = 0$ in the MSSM limit where $\epsilon_i = 0$, $v_i = 0$.

If the elements of this matrix satisfy

$$\forall \xi_{ij} \ll 1, \tag{37}$$

then one can use it as expansion parameter to find an approximate solution for the mixing matrix $\mathcal{N}$.

In leading order in ξ the mixing matrix $\mathcal{N}$ is given by

$$\mathcal{N}^* = \begin{pmatrix} N^* & 0 \\ 0 & V_\nu^{\mathrm{T}} \end{pmatrix} \begin{pmatrix} 1 - \frac{1}{2}\xi^\dagger\xi & \xi^\dagger \\ -\xi & 1 - \frac{1}{2}\xi\xi^\dagger \end{pmatrix}. \tag{38}$$

The second matrix above block-diagonalizes the mass matrix $\mathbf{M}_N$ approximately to the form $\mathrm{diag}(\mathcal{M}_{\chi^0}, m_{eff})$, where

$$m_{eff} = -m \cdot \mathcal{M}_{\chi^0}^{-1} m^{\mathrm{T}} = \frac{M_1 g^2 + M_2 g'^2}{4\det(\mathcal{M}_{\chi^0})} \begin{pmatrix} \Lambda_e^2 & \Lambda_e\Lambda_\mu & \Lambda_e\Lambda_\tau \\ \Lambda_e\Lambda_\mu & \Lambda_\mu^2 & \Lambda_\mu\Lambda_\tau \\ \Lambda_e\Lambda_\tau & \Lambda_\mu\Lambda_\tau & \Lambda_\tau^2 \end{pmatrix}. \tag{39}$$

The submatrices N and V_ν diagonalize $\mathcal{M}_{\chi^0}$ and m_{eff}

$$N^* \mathcal{M}_{\chi^0} N^\dagger = \mathrm{diag}(m_{\chi_i^0}), \tag{40}$$

$$V_\nu^{\mathrm{T}} m_{eff} V_\nu = \mathrm{diag}(0, 0, m_\nu), \tag{41}$$

where

$$m_\nu = \mathrm{Tr}(m_{eff}) = \frac{M_1 g^2 + M_2 g'^2}{4\det(\mathcal{M}_{\chi^0})}|\vec{\Lambda}|^2. \tag{42}$$

The special form of the neutralino/neutrino mass matrix implies that the effective neutrino mass matrix m_{eff} generated after diagonalizing out the heavy neutralinos has a projective form, a

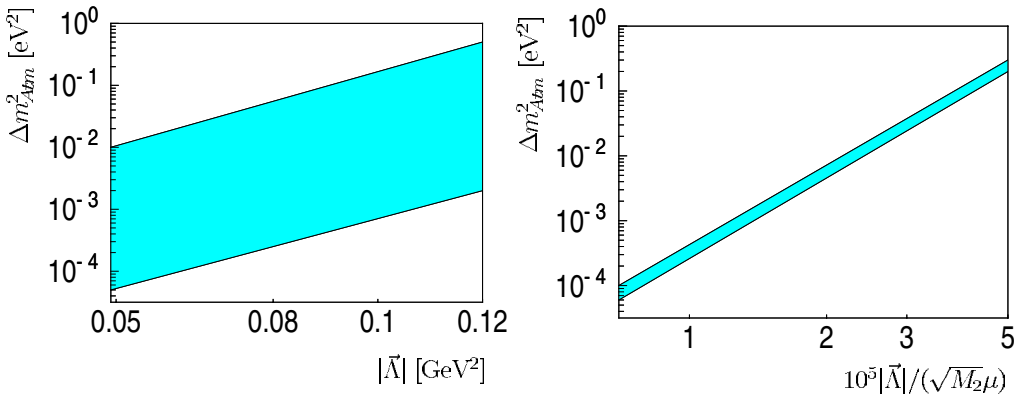

Figure 1. Δm^2_{atm} versus the BRpV alignment parameters.

feature common to many spontaneous R-parity violating models [48]. This implies that only one neutrino acquires a tree-level mass, the other two remaining massless [48]. As a result, at the tree approximation, one can rotate away one of the three angles in the matrix V_ν, leading to

$$V_\nu = \begin{pmatrix} 1 & 0 & 0 \\ 0 & \cos\theta_{23} & -\sin\theta_{23} \\ 0 & \sin\theta_{23} & \cos\theta_{23} \end{pmatrix} \times \begin{pmatrix} \cos\theta_{13} & 0 & -\sin\theta_{13} \\ 0 & 1 & 0 \\ \sin\theta_{13} & 0 & \cos\theta_{13} \end{pmatrix}, \tag{43}$$

where the mixing angles can be expressed in terms of the *alignment vector* $\vec{\Lambda}$ as follows:

$$\tan\theta_{13} = -\frac{\Lambda_e}{(\Lambda_\mu^2 + \Lambda_\tau^2)^{1/2}}, \tag{44}$$

$$\tan\theta_{23} = -\frac{\Lambda_\mu}{\Lambda_\tau}. \tag{45}$$

The non-zero tree-level eigenvalue of the neutrino mass matrix is identified with the atmospheric mass scale. The calculated Δm^2_{atm} can be expressed as a function of the alignment parameter $\vec{\Lambda}$ (left panel in figure 1) or as function of $|\vec{\Lambda}|/(\sqrt{M_2}\mu)$ (right panel in figure 1), all of these expressed in GeV. The figure shows that equation (42) can be used to fix the relative size of R-parity breaking parameters to obtain the correct Δm^2_{atm}. On the other hand, as shown in figure 2, the atmospheric angle can be expressed in terms of Λ_μ/Λ_τ. Its maximality is obtained for $\Lambda_\mu \simeq \Lambda_\tau$ if Λ_e is smaller than the other two. Let us stress once again that there is no solar mass splitting in the tree approximation so that, as a result, the 'solar angle' is not defined, as it can be rotated away by redefining the two degenerate neutrinos [14].

4. One-loop-induced neutrino mass: the solar scale

As we have just seen in the BRpV model the atmospheric mass scale and mixing arises at the tree level. We now discuss the determination of solar neutrino masses and mixings, which are both generated radiatively. One-loop corrections to the neutrino masses can be calculated numerically

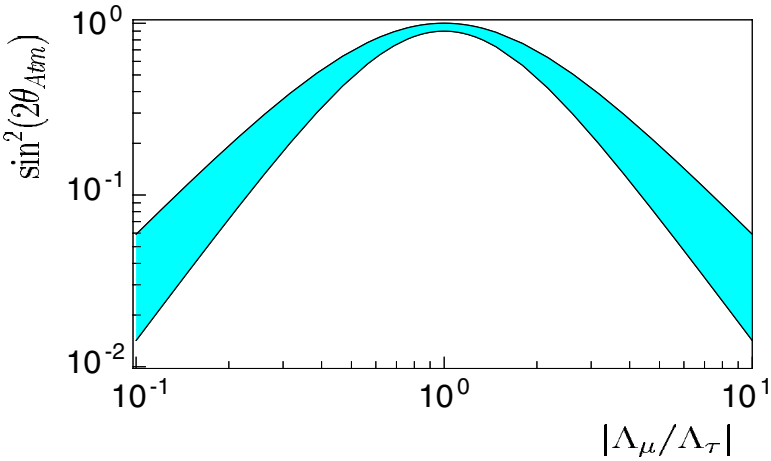

Figure 2. The atmospheric angle versus the ratio of BRpV parameters $|\Lambda_\mu/\Lambda_\tau|$.

[26] or analytically [24]. Whereas the numerical approach can give 'exact' results (exact in the sense of being correct up to higher-order effects), the analytic approach, while being less accurate, gives a better understanding about which parameters control the loops and thus the solar neutrino mass and angles in our model. The discussion will therefore mainly concentrate on the analytical calculations.

In principle, to find the correct neutrino mixing angles one has to diagonalize the one-loop corrected neutralino/neutrino mass matrix. We define

$$M_{ij}^{\text{pole}} = M_{ij}^{\overline{\text{DR}}}(Q) + \Delta M_{ij}, \tag{46}$$

where $M_{ij}^{\overline{\text{DR}}}(Q)$ is the tree-level pole mass and $\overline{\text{DR}}$ indicates the dimensional reduction scheme we used in the numerical calculation. One-loop corrections are

$$\Delta M_{ij} = \tfrac{1}{2}[\widetilde{\Pi}_{ij}^V(m_i^2) + \widetilde{\Pi}_{ij}^V(m_j^2)] - \tfrac{1}{2}[m_{\chi_i^0}\widetilde{\Sigma}_{ij}^V(m_i^2) + m_{\chi_j^0}\widetilde{\Sigma}_{ij}^V(m_j^2)], \tag{47}$$

where the symmetrization is necessary to achieve gauge invariance and consistency with the Pauli principle. Here $\widetilde{\Pi}^V$ and $\widetilde{\Sigma}^V$ are the renormalized self-energies. They contain products of couplings and the usual Passarino–Veltman functions [50].

Diagonalizing the tree-level neutrino mass matrix first and adding then the one-loop corrections before re-diagonalization one finds that the resulting neutrino/neutralino mass matrix has non-zero entries in the neutrino/neutrino, the neutrino/neutralino and in the neutralino/neutralino sectors. We have found [24] that the most important part of the one-loop neutrino masses derives from the neutrino/neutrino sector and that the one-loop induced neutrino/neutralino mixing is usually negligible.

The relevant topologies for the one-loop calculation of neutrino masses are then illustrated in figure 3. Here our conventions are as follows: open circles with a cross inside indicate genuine mass insertions which flip chirality. On the other hand, open circles without a cross correspond to small R-parity violating projections, indicating how much of an Rp-even/odd mass eigenstate is present in a given Rp-odd/even weak eigenstate. In the actual numerical calculation, these projections really belong to the coupling matrices attached to the vertices. However, given the

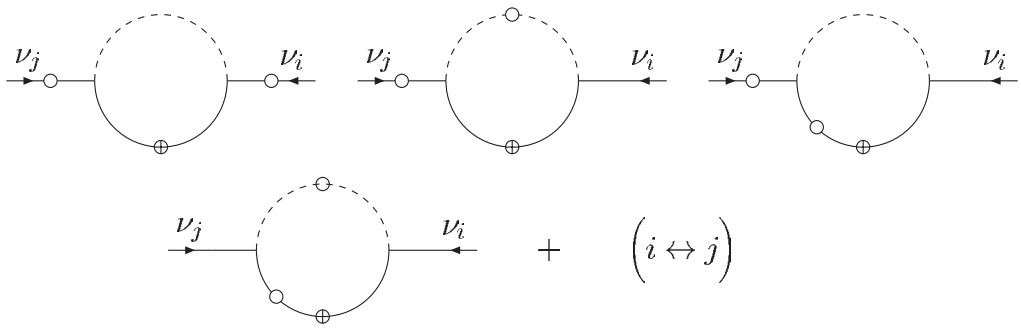

Figure 3. Topologies for neutrino self-energies in the BRpV supersymmetric model.

smallness of Rp-violating effects, the prediagonalization 'insertion method' proves to be a rather useful tool to develop an analytical perturbative expansion and to acquire a simple understanding of the results.

These topologies have then to be 'filled' with all relevant combinations of particles/sparticles. Here we will concentrate on discussing the loop involving bottom/sbottom quarks, since (i) it is in large parts of parameter space the numerically most important one, and (ii) other loops can be calculated in a very similar way [24], although they are more complicated.

The relevant Feynman rules for the bottom–sbottom loops are, in the case of left sbottoms:

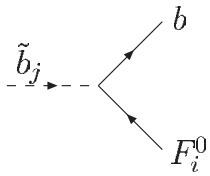

$$= \mathrm{i}\left[O^{bn\tilde{b}}_{Lij}\frac{(1-\gamma_5)}{2} + O^{bn\tilde{b}}_{Rij}\frac{(1+\gamma_5)}{2}\right]$$

with

$$\begin{aligned} O^{bn\tilde{b}}_{Lij} &= -R^{\tilde{b}}_{j1}h_b\mathcal{N}^*_{i3} - R^{\tilde{b}}_{j2}\frac{2g}{3\sqrt{2}}\tan\theta_W\mathcal{N}^*_{i1}, \\ O^{bn\tilde{b}}_{Rij} &= R^{\tilde{b}}_{j1}\frac{g}{\sqrt{2}}(\mathcal{N}_{i2} - \tfrac{1}{3}\tan\theta_W\mathcal{N}_{i1}) - R^{\tilde{b}}_{j2}h_b\mathcal{N}^*_{i3}. \end{aligned} \tag{48}$$

After approximating the rotation matrix $\mathcal{N}$ we find that expressions with the replacement $\mathcal{N} \to N$ are valid when the neutral fermion is a neutralino. When the neutral fermion F^0 is a neutrino, the following expressions hold:

$$\begin{aligned} O^{bn\tilde{b}}_{Lij} &\approx R^{\tilde{b}}_{j1}h_b(a_3|\vec{\Lambda}|\delta_{i'3} + b\tilde{\epsilon}_{i'}) + R^{\tilde{b}}_{j2}\frac{2g}{3\sqrt{2}}\tan\theta_W a_1|\vec{\Lambda}|\delta_{i'3}, \\ O^{bn\tilde{b}}_{Rij} &\approx R^{\tilde{b}}_{j1}\frac{g}{\sqrt{2}}(\tfrac{1}{3}\tan\theta_W a_1 - a_2)|\vec{\Lambda}|\delta_{i'3} + R^{\tilde{b}}_{j2}h_b(a_3|\vec{\Lambda}|\delta_{i'3} + b\tilde{\epsilon}_{i'}), \end{aligned} \tag{49}$$

where $i' = i - 4$ label one of the neutrinos. $R^{\tilde{b}}_{jk}$ are the rotation matrices connecting weak and mass eigenstate basis for the scalar bottom quarks. In case of no inter-generational mixing in the squark sector, $R^{\tilde{b}}_{jk}$ can be parametrized by just one diagonalizing angle $\theta_{\tilde{b}}$.

Putting these couplings together one finds the simplest contribution to the radiatively induced neutrino mass from loops involving bottom quarks and squarks [26]:

$$\widetilde{\Pi}_{ij}(0) = -\frac{N_c}{16\pi^2}\sum_r (O^{bn\tilde{b}}_{Rjr}O^{bn\tilde{b}}_{Lir} + O^{bn\tilde{b}}_{Ljr}O^{bn\tilde{b}}_{Rir})m_b B_0(0, m_b^2, m_r^2), \tag{50}$$

where $B_0(0, m_b^2, m_r^2)$ is a Passarino–Veltman function [50] and can be written as follows:

$$\widetilde{\Pi}_{ij} = -\frac{N_c m_b}{16\pi^2} 2 s_{\tilde{b}} c_{\tilde{b}} h_b^2 \Delta B_0^{\tilde{b}_1\tilde{b}_2}\left(\frac{\tilde{\epsilon}_i\tilde{\epsilon}_j}{\mu^2} + a_3 b(\tilde{\epsilon}_i\delta_{j3} + \tilde{\epsilon}_j\delta_{i3})|\vec{\Lambda}| + \left(a_3^2 + \frac{a_L a_R}{h_b^2}\right)\delta_{i3}\delta_{j3}|\vec{\Lambda}|^2\right). \tag{51}$$

This expression is proportional to the difference of two B_0 functions,

$$\Delta B_0^{\tilde{b}_1\tilde{b}_2} = B_0(0, m_b^2, m_{\tilde{b}_1}^2) - B_0(0, m_b^2, m_{\tilde{b}_2}^2). \tag{52}$$

Parameters Λ_i have been defined above. The $\tilde{\epsilon}$ parameters are defined as $\tilde{\epsilon}_i = (V_\nu^{\mathrm{T}})^{ij}\epsilon_j$, and are given by

$$\begin{aligned}
\tilde{\epsilon}_1 &= \frac{\epsilon_e(\Lambda_\mu^2 + \Lambda_\tau^2) - \Lambda_e(\Lambda_\mu\epsilon_\mu + \Lambda_\tau\epsilon_\tau)}{\sqrt{\Lambda_\mu^2 + \Lambda_\tau^2}\sqrt{\Lambda_e^2 + \Lambda_\mu^2 + \Lambda_\tau^2}},\\
\tilde{\epsilon}_2 &= \frac{\Lambda_\tau\epsilon_\mu - \Lambda_\mu\epsilon_\tau}{\sqrt{\Lambda_\mu^2 + \Lambda_\tau^2}},\\
\tilde{\epsilon}_3 &= \frac{\vec{\Lambda}\cdot\vec{\epsilon}}{\sqrt{\Lambda_e^2 + \Lambda_\mu^2 + \Lambda_\tau^2}}.
\end{aligned} \tag{53}$$

On the other hand, $a_{L,R}$ are defined as

$$a_R = \frac{g}{\sqrt{2}}\left(\frac{1}{3}t_W a_1 - a_2\right), \qquad a_L = \frac{g}{\sqrt{2}}\frac{2}{3}t_W a_1. \tag{54}$$

The different terms in equation (51) can be understood as coming from the graphs corresponding to the first topology of figure 3. They have been depicted in more detail in figure 4, where we have adopted the following conventions: (i) as before, open circles correspond to small R-parity-violating projections, indicating how much of a weak eigenstate is present in a given mass eigenstate, (ii) full circles correspond to R-parity-conserving projections and (iii) open circles with a cross inside indicate genuine mass insertions which flip chirality.

The open and full circles should really appear at the vertices since the particles propagating in the loop are the mass eigenstates. We have however separated them to better identify the origin of the various terms. There is another set of graphs analogous to the previous ones, which corresponds to the heavy sbottom. They are obtained from the previous graphs making the replacement $\tilde{b}_1 \to \tilde{b}_2$, $s_{\tilde{b}} \to c_{\tilde{b}}$ and $c_{\tilde{b}} \to -s_{\tilde{b}}$. Note that for all contributions to the 2×2 sub-matrix corresponding to the light neutrinos the divergence from $B_0(0, m_b^2, m_{\tilde{b}_1}^2)$ is cancelled

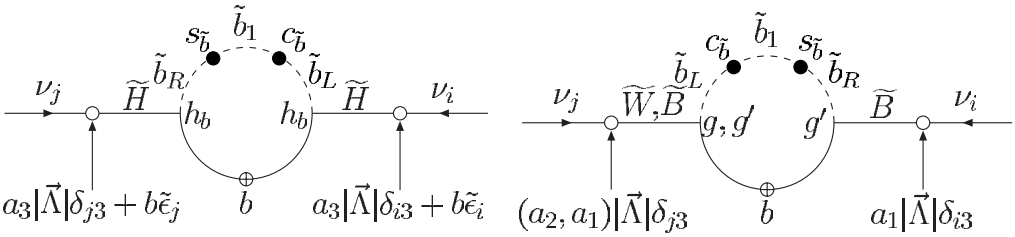

Figure 4. Bottom–sbottom diagrams for solar neutrino mass in the BRpV model.

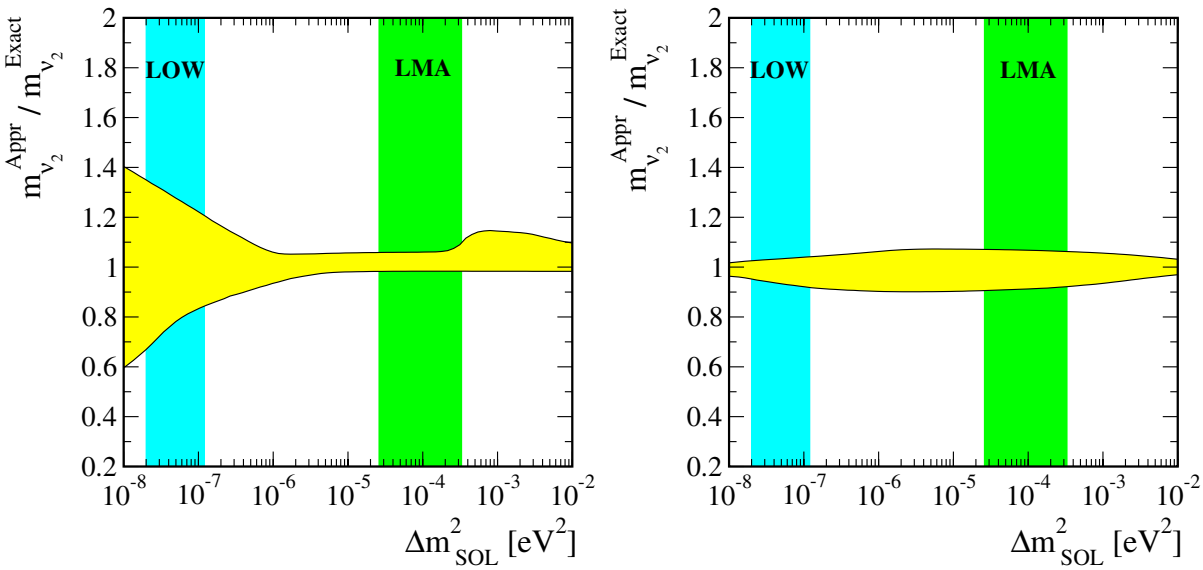

Figure 5. $(m^{Appr}_{\nu_2}/m^{exact}_{\nu_2})$ versus $\Delta m^2_{\rm SOL}$ (eV^2) for the set Ntrl (left panel) and the set Stau (right panel). $m^{Appr}_{\nu_2}$ is the sum of the bottom–sbottom and charged scalar loops, whereas $m^{exact}_{\nu_2}$ is the numerical result for all loops. In case of LMA the approximation works always better than 10%.

by the divergence from $B_0(0, m_b^2, m_{\tilde{b}_2}^2)$, making the contribution from bottom–sbottom loops to this sub-matrix finite, as it should be, since the mass is fully 'calculable'.

The second most important contribution to the radiatively induced neutrino mass usually comes from charged-scalar/charged-fermion loops [26]. Since all possible topologies of figure 3 contribute to this loop the structure of the contribution from charged Higgs/slepton loops is more complex than that of the bottom–sbottom loop considered above. However, the same topology as for the sbottom–bottom loop also contributes to the charged scalar loop. It leads to a final expression similar to equation (51), with appropriate replacements, which is good enough for an order-of-magnitude estimate of the charged scalar loop.

4.1. Results for the solar mass scale

We give a discussion of the analytical versus numerical results of the solar mass scale first. In figure 5 we show a comparison of approximate and exact calculation for two different numerical data sets. In both figures, we show the ratio of the approximate-over-exact solar neutrino mass

parameter $m_{\nu_2}^{Appr}/m_{\nu_2}^{exact}$ versus $\Delta m^2_{\rm SOL}$ in eV^2, where $m_{\nu_2}^{Appr}$ is the approximate loop calculation involving the bottom–sbottom and the charged scalar loop, whereas $m_{\nu_2}^{exact}$ is the exact numerical computation taking into account all loops. The set to the left called 'Ntrl' contains neutralinos being the LSP, whereas the set to the right (Stau) has the charged scalar tau as LSP.

We have found numerically that the terms proportional to $\tilde{\epsilon}_i \times \tilde{\epsilon}_j$ in the self-energies in equation (51) give the most important contribution to m_{ν_2} in the bottom–sbottom loop calculation in most points of our sets. If these terms are dominant, one can find a very simple approximation for the bottom–sbottom loop contribution to m_{ν_2}. It is given by

$$m_{\nu_2} \simeq \frac{3}{16\pi^2}\sin(2\theta_{\tilde{b}})m_b \Delta B_0^{\tilde{b}_2\tilde{b}_1}\frac{(\tilde{\epsilon}_1^2+\tilde{\epsilon}_2^2)}{\mu^2}. \tag{55}$$

Equation (55) works surprisingly well for almost all points in our data sets.

The more complicated structure of the charged scalar loop makes it difficult to give a simple equation for m_{ν_2}, similar to equation (55) for the bottom–sbottom loop. However, we note that equation (55), with appropriate replacements, allows us to estimate the typical contributions to the charged scalar loop within a factor of ∼3. However, such an estimate will be biased towards too small or too large m_{ν_2} depending mainly on which SUSY particle is the LSP [24].

4.2. Analytical approximation for the solar mixing angle

In the basis where the tree-level neutrino mass matrix is diagonal the mass matrix at one-loop level can be written as

$$\tilde{m}_\nu = V_\nu^{(0)\rm T} m_\nu V_\nu^{(0)} = \begin{pmatrix} c_1\tilde{\epsilon}_1\tilde{\epsilon}_1 & c_1\tilde{\epsilon}_1\tilde{\epsilon}_2 & c_1\tilde{\epsilon}_1\tilde{\epsilon}_3 \\ c_1\tilde{\epsilon}_2\tilde{\epsilon}_1 & c_1\tilde{\epsilon}_2\tilde{\epsilon}_2 & c_1\tilde{\epsilon}_2\tilde{\epsilon}_3 \\ c_1\tilde{\epsilon}_3\tilde{\epsilon}_1 & c_1\tilde{\epsilon}_3\tilde{\epsilon}_2 & c_0|\vec{\Lambda}|^2 + c_1\tilde{\epsilon}_3\tilde{\epsilon}_3 \end{pmatrix} + \cdots, \tag{56}$$

where the $\tilde{\epsilon}_i$ were defined before in equation (53). Coefficients c_0 and c_1 contain couplings and supersymmetric masses. Since they cancel in the final expression for the angle their exact definition is not necessary in the following. Dots stand for other terms which we will assume to be less important in the following. This matrix can be diagonalized approximately taking in account that

$$x \equiv \frac{c_1|\vec{\tilde{\epsilon}}|^2}{c_0|\vec{\Lambda}|^2} \ll 1. \tag{57}$$

Then

$$\tilde{m}_\nu = c_0|\vec{\Lambda}|^2 \begin{pmatrix} x\frac{\tilde{\epsilon}_1\tilde{\epsilon}_1}{|\vec{\tilde{\epsilon}}|^2} & x\frac{\tilde{\epsilon}_1\tilde{\epsilon}_2}{|\vec{\tilde{\epsilon}}|^2} & x\frac{\tilde{\epsilon}_1\tilde{\epsilon}_3}{|\vec{\tilde{\epsilon}}|^2} \\ x\frac{\tilde{\epsilon}_2\tilde{\epsilon}_1}{|\vec{\tilde{\epsilon}}|^2} & x\frac{\tilde{\epsilon}_2\tilde{\epsilon}_2}{|\vec{\tilde{\epsilon}}|^2} & x\frac{\tilde{\epsilon}_2\tilde{\epsilon}_3}{|\vec{\tilde{\epsilon}}|^2} \\ x\frac{\tilde{\epsilon}_3\tilde{\epsilon}_1}{|\vec{\tilde{\epsilon}}|^2} & x\frac{\tilde{\epsilon}_3\tilde{\epsilon}_2}{|\vec{\tilde{\epsilon}}|^2} & 1 + x\frac{\tilde{\epsilon}_3\tilde{\epsilon}_3}{|\vec{\tilde{\epsilon}}|^2} \end{pmatrix}. \tag{58}$$

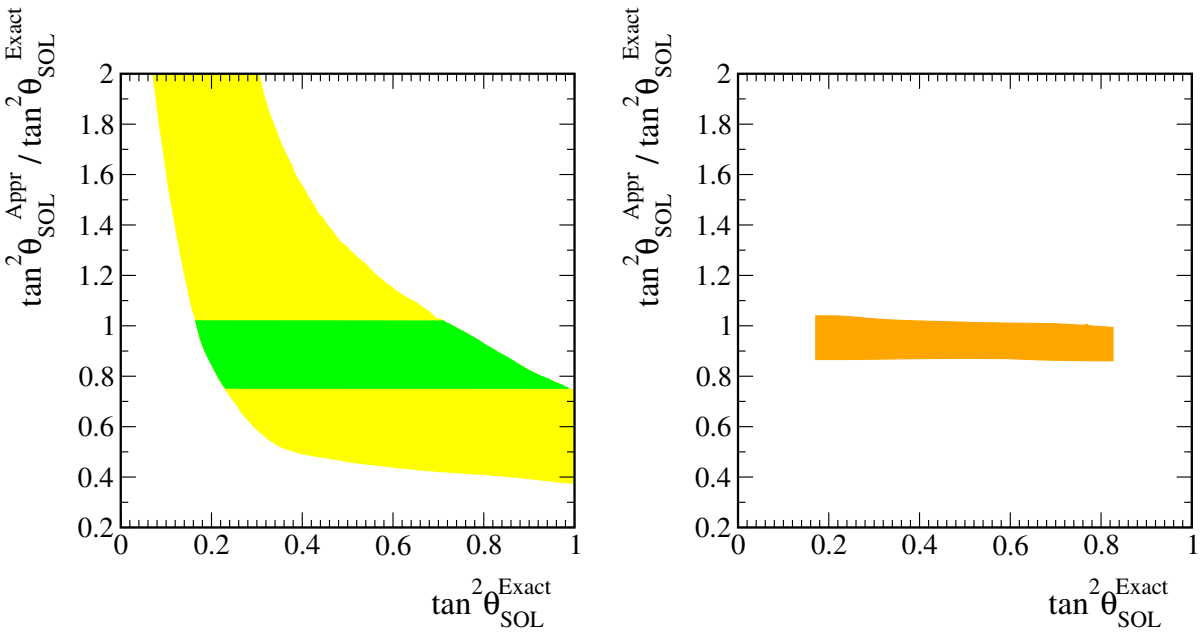

Figure 6. $(\tan^2\theta_{\rm sol}^{Appr}/\tan^2\theta_{\rm SOL}^{exact})$ versus $\tan^2\theta_{\rm SOL}^{exact}$. In the left panel, the darker region contains over 90% of the points in our sample; in the right panel the points in the region shown satisfy the cut $\sin(2\theta_{\tilde b})\Delta B_0^{\tilde\tau_2\tilde\tau_1} > 0.02$.

The rotation matrix that diagonalizes $\tilde m_\nu$ in equation (58) can be written as

$$\widetilde V_\nu^{\rm T}\tilde m_\nu \widetilde V_\nu = {\rm diag}(m_1, m_2, m_3), \tag{59}$$

where

$$\widetilde V_\nu^{\rm T} = \begin{pmatrix} e_{1,1} & e_{1,2} & e_{1,3} \\ e_{2,1} & e_{2,2} & e_{2,3} \\ e_{3,1} & e_{3,2} & e_{3,3} \end{pmatrix}. \tag{60}$$

The lepton mixing matrix is then given by

$$U = (V_\nu^{\rm T}\widetilde V_\nu^{\rm T})^{\rm T}. \tag{61}$$

The expression for the solar mixing angle can be obtained from

$$\tan^2\theta_{\rm SOL} = \frac{U_{e2}^2}{U_{e1}^2}. \tag{62}$$

From the above equations we obtain the very simple expression for the solar mixing angle,

$$\tan^2\theta_{\rm SOL} = \frac{\tilde\epsilon_1^2}{\tilde\epsilon_2^2}. \tag{63}$$

This formula is a very good approximation if the one-loop matrix has the structure $\epsilon_i \times \epsilon_j$, as is the case of the bottom–sbottom loop if $m_{\nu_3} \gg m_{\nu_2}$, as illustrated in figure 6.

In the left panel, we show a calculation comparing for all points the approximate to the exact solar angle in the set with neutralino LSP, whereas the right panel shows a subset of points with the cut $\sin(2\theta_{\tilde{b}})\Delta B_0^{\tilde{\tau}_2\tilde{\tau}_1} > 0.02$. Note that this cut is designed so as to favour points in which there is a sizeable bottom–sbottom loop contribution to the full one-loop neutrino mass. One sees from the right panel that for this case the true solar angle is well approximated by our analytical formula. Note finally that equation (63) will fail completely if $\Lambda_\mu \equiv \Lambda_\tau$ and $\epsilon_\mu \equiv \epsilon_\tau$, since then $\tilde{\epsilon}_2^2 = 0$; see equation (53). This is the origin of the 'sign condition' discussed in [26].

5. Testing neutrino properties at high-energy accelerators

Since R-parity is broken in our model, the lightest supersymmetric particle is unstable and decays. This leads to the exciting possiblity to test the bilinear model at future colliders, such as the LHC or a possible Linear Collider.

The principal idea of such a collider test [39, 41, 43] is easily understood: bilinear R-parity breaking leads to mixing between particles and sparticles with the same quantum numbers, as discussed above extensively for the case of neutrinos/neutralinos. This mixing, however, is not arbitrarily different for each particle/sparticle species. In fact, the bilinear model has just six new parameters, which we choose to be ϵ_i and Λ_i, compared with the MSSM. Essentially five of these six can be fixed from neutrino physics.

Thus, if the MSSM parameters were known, all mixing effects could be calculated and thus all decay properties of the LSP would be fixed—apart from the effects of the last unknown parameter. In reality, however, the MSSM soft SUSY breaking parameters are completely *unknown*. The approach taken in [39, 41, 43] therefore is to calculate ratios of branching ratios of different decays. By taking ratios, one essentially scales out the unknown MSSM parameters approximately and obtains observables which are proportional to either Λ_i/Λ_j or ϵ_i/ϵ_j (or some weird combination thereof). The ratio one measures depends of course on the final state and the LSP under consideration. Since ratios of Λ_i's (or ϵ_i's) are correlated with the neutrino angles, as discussed above, fixing neutrino angles from experimental data therefore gives definite predictions for some ratios of branching ratios.

One example is shown in figure 7, where ratio of branching ratios of neutralino LSP decays are plotted. Note that $\mathrm{Br}(\mu qq')/\mathrm{Br}(\tau qq')$ is directly proportional to $\tan^2(\theta_{atm})$, i.e. should be near $\sim$1 according to current neutrino data. The spread in the points is due to the unknown MSSM parameters. Of course, once SUSY is discovered these unknowns will be measured allowing for much sharper tests of the model than that indicated in figure 7.

A second example is shown in figure 8, where we show $\mathrm{Br}(\tilde{\tau}_1 \to \sum \nu e)/\mathrm{Br}(\tilde{\tau}_1 \to \sum \nu\mu)$ as a function of $(\epsilon_1/\epsilon_2)^2$ (left panel) and as a function of $\tan^2(\theta_\odot)$ (right panel). Obviously this ratio is strongly correlated with the solar angle and, thus, if scalar taus turn out to be the LSP, such a measurement would provide an excellent check of the bilinear model as the origin of the solar neutrino mass scale.

With the LSP unstable, in principle, any sparticle can be the LSP. In [43] the remaining candidates have been discussed: charginos, scalar quarks, gluinos and scalar neutrinos. The main conclusion in [43] is that whichever SUSY particle is the LSP, measurements of branching ratios at future accelerators will provide a definite test of bilinear R-parity breaking as the model of neutrino mass. We just mention that chargino LSPs would be more sensitive to atmospheric

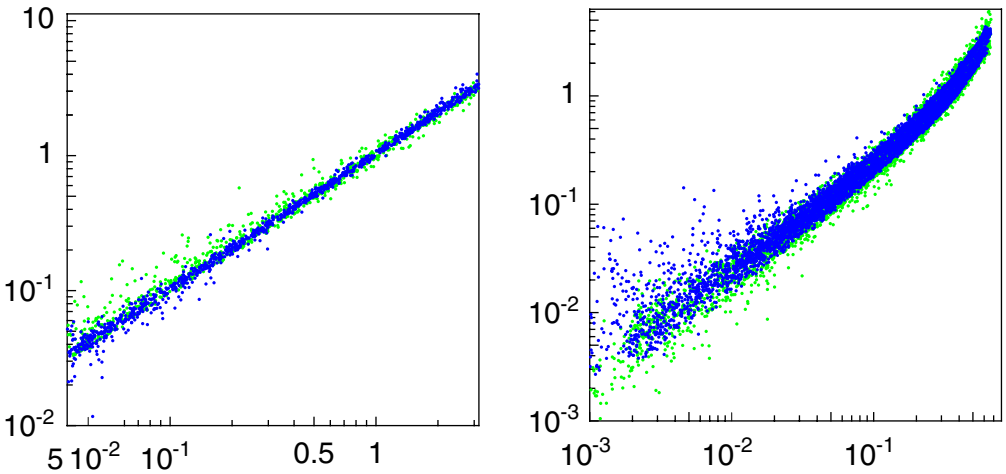

Figure 7. Ratio of branching ratios of neutralino LSP decays. Left panel: $\mathrm{Br}(\mu qq')/\mathrm{Br}(\tau qq')$ as a function of $\tan^2(\theta_{atm})$; right panel: $\mathrm{Br}(eqq')/\mathrm{Br}(\tau qq')$ as a function of U_{e3}^2. Whether bilinear R-parity breaking SUSY is responsible for atmospheric neutrino oscillations can be checked by such a measurement. Note that the spread of the points is entirely due to the unknown MSSM parameters. Even a moderately accurate input of MSSM parameters will lead to much sharper predictions for these decays.

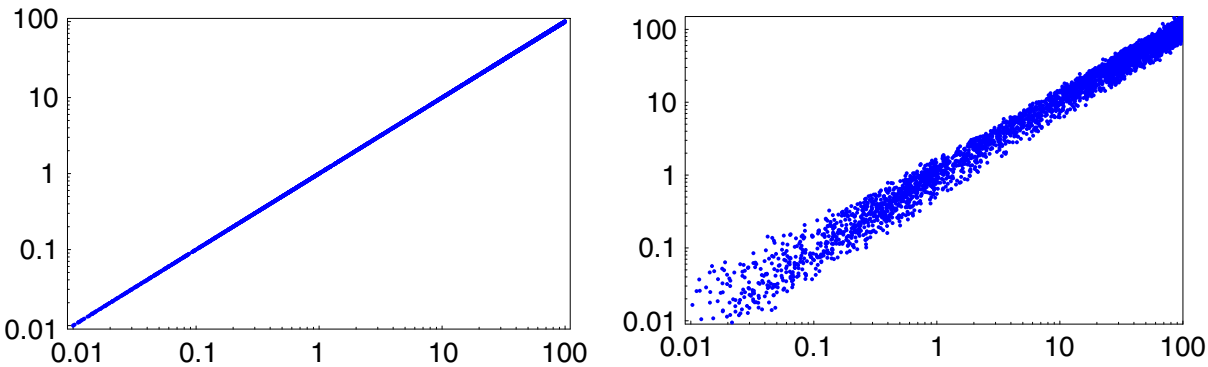

Figure 8. Ratio of branching ratios of scalar tau LSP decays. Left panel: $\mathrm{Br}(\tilde{\tau}_1 \to \sum \nu e)/\mathrm{Br}(\tilde{\tau}_1 \to \sum \nu\mu)$ as a function of $(\epsilon_1/\epsilon_2)^2$; right panel as a function of $\tan^2(\theta_\odot)$. Whether bilinear R-parity breaking SUSY is responsible for solar neutrino oscillations can be checked by such a measurement if scalar taus are the LSP.

neutrino physics (as are neutralinos), whereas the other LSP candidates mentioned above show more dependence on the solar neutrino angle.

6. Discussion and conclusions

We have presented a brief review of the idea that supersymmetry with explicit bilinear breaking of R-parity is the origin of neutrino masses and lepton mixing. The bilinear R-parity breaking

(BRpV) model is the simplest extension of the minimal supersymmetric standard model (MSSM) which includes lepton number violation. We have seen how it leads to a successful phenomenological model for neutrino oscillations, in accordance to present neutrino data. The pattern of neutrino masses is hierarchical, with the atmospheric mass scale arising at the tree level, whereas the solar scale is induced from calculable loop corrections. We have seen how, in contrast with see-saw models, the BRpV model can be probed at future collider experiments, such as the LHC or the NLC. Indeed, we have discussed how, irrespective of the supersymmetric particle which is the lightest, its decay pattern will be directly related to the lepton mixing angles determined in low-energy neutrino experiments.

Acknowledgments

This work was supported by Spanish grant BFM2002-00345, by the European Commission RTN grant HPRN-CT-2000-00148 and the ESF *Neutrino Astrophysics Network*. MH is supported by a Ramon y Cajal contract.

References

[1] Super-Kamiokande, Fukuda Y *et al* 1988 *Phys. Rev. Lett.* **81** 1562 (*Preprint* hep-ex/9807003)
[2] SNO, Ahmad Q R *et al* 2002 *Phys. Rev. Lett.* **89** 011301 (*Preprint* nucl-ex/0204008)
[3] KamLAND, Eguchi K *et al* 2003 *Phys. Rev. Lett.* **90** 021802 (*Preprint* hep-ex/0212021)
[4] Maltoni M, Schwetz T, Tortola M A and Valle J W F 2004 this volume (*Preprint* hep-ph/0405172)
[5] Pakvasa S and Valle J W F *Preprint* hep-ph/0301061
Pakvasa S and Valle J W F 2004 *Proc. of the Indian National Academy of Sciences on Neutrinos, Part A* ed D Indumathi, M V N Murthy and G Rajasekaran, vol 70A, pp 189–222
[6] Barger V, Marfatia D and Whisnant K 2003 *Int. J. Mod. Phys.* E **12** 569
[7] Gonzalez-Garcia M C and Nir Y 2003 *Rev. Mod. Phys.* **75** 34
[8] Fogli G L *et al* 2003 *Talk at 10th Int. Workshop on Neutrino Telescopes, Venice, Italy, 11–14 March 2003* Neutrino Telescopes, pp 151–179
[9] Nilles H P 1984 *Phys. Rep.* **110** 1
[10] Haber H E and Kane G L 1985 *Phys. Rep.* **117** 75
[11] Witten E 2002 *Preprint* hep-ph/0207124
[12] Gell-Mann M, Ramond P and Slansky R 1979 Print-80-0576 (CERN)
[13] Yanagida T 1979 *KEK Lectures* ed O Sawada and A Sugamoto (KEK)
[14] Schechter J and Valle J W F 1980 *Phys. Rev.* D **22** 2227
Schechter J and Valle J W F 1982 *Phys. Rev.* D **25** 774
[15] Mohapatra R N and Senjanovic G 1981 *Phys. Rev.* D **23** 165
[16] Aulakh C S and Mohapatra R N 1982 *Phys. Lett.* B **119** 13
[17] Ross G G and Valle J W F 1985 *Phys. Lett.* B **151** 375
[18] Ellis J R *et al* 1985 *Phys. Lett.* B **150** 142
[19] Abada A, Davidson S and Losada M 2002 *Phys. Rev.* D **65** 075010 (*Preprint* hep-ph/0111332)
[20] Grossman Y and Haber H E 1999 *Preprint* hep-ph/9906310
[21] Bednyakov V, Faessler A and Kovalenko S 1998 *Phys. Lett.* B **442** 203 (*Preprint* hep-ph/9808224)
[22] Joshipura A S, Vaidya R D and Vempati S K 2002 *Nucl. Phys.* B **639** 290 (*Preprint* hep-ph/0203182)
Chang C H and Feng T F 2000 *Eur. Phys. J.* C **12** 137 (*Preprint* hep-ph/9901260)
[23] Diaz M A, Romao J C and Valle J W F 1998 *Nucl. Phys.* B **524** 23 (*Preprint* hep-ph/9706315)
[24] Diaz M A *et al* 2003 *Phys. Rev.* D **68** 013009 (*Preprint* hep-ph/0302021)
[25] Chun E J, Jung D-W and Park J D 2003 *Phys. Lett.* B **557** 233 (*Preprint* hep-ph/0211310)

[26] Hirsch M *et al* 2000 *Phys. Rev.* D **62** 113008 (*Preprint* hep-ph/0004115)
Hirsch M *et al* 2002 *Phys. Rev.* D **65** 119901
[27] Romao J C *et al* 2000 *Phys. Rev.* D **61** 071703 (*Preprint* hep-ph/9907499)
[28] de Campos F *et al* 1995 *Nucl. Phys.* B **451** 3 (*Preprint* hep-ph/9502237)
[29] Banks T, Grossman Y, Nardi E and Nir Y 1995 *Phys. Rev.* D **52** 5319 (*Preprint* hep-ph/9505248)
[30] de Carlos B and White P L 1996 *Phys. Rev.* D **54** 3427 (*Preprint* hep-ph/9602381)
[31] Akeroyd A G *et al* 1998 *Nucl. Phys.* B **529** 3 (*Preprint* hep-ph/9707395)
[32] Masiero A and Valle J W F 1990 *Phys. Lett.* B **251** 273
[33] Romao J C, Santos C A and Valle J W F 1992 *Phys. Lett.* B **288** 311
[34] Romao J C, Ioannisian A and Valle J W F 1997 *Phys. Rev.* D **55** 427 (*Preprint* hep-ph/9607401)
[35] Mukhopadhyaya B, Roy S and Vissani F 1998 *Phys. Lett.* B **443** 191 (*Preprint* hep-ph/9808265)
[36] R-Parity Working Group, Allanach B *et al*, 1999 *Preprint* hep-ph/9906224
[37] Choi S Y, Chun E J, Kang S K and Lee J S 1999 *Phys. Rev.* D **60** 075002 (*Preprint* hep-ph/9903465)
[38] Bartl A *et al* 2001 *Nucl. Phys.* B **600** 39 (*Preprint* hep-ph/0007157)
[39] Porod W, Hirsch M, Romao J and Valle J W F 2001 *Phys. Rev.* D **63** 115004 (*Preprint* hep-ph/0011248)
[40] Restrepo D, Porod W and Valle J W F 2001 *Phys. Rev.* D **64** 055011 (*Preprint* hep-ph/0104040)
[41] Hirsch M, Porod W, Romao J C and Valle J W F 2002 *Phys. Rev.* D **66** 095006 (*Preprint* hep-ph/0207334)
[42] Bartl A *et al* 2003 *JHEP* **11** 005 (*Preprint* hep-ph/0306071)
[43] Hirsch M and Porod W 2003 *Phys. Rev.* D **68** 115007 (*Preprint* hep-ph/0307364)
[44] Giudice G F and Masiero A 1988 *Phys. Lett.* B **206** 480
[45] Nilles H-P and Polonsky N 1997 *Nucl. Phys.* B **484** 33 (*Preprint* hep-ph/9606388)
[46] Mira J M, Nardi E, Restrepo D A and Valle J W F 2000 *Phys. Lett.* B **492** 81 (*Preprint* hep-ph/0007266)
[47] Ibanez L E and Ross G G 1982 *Phys. Lett.* B **110** 215
[48] Santamaria A and Valle J W F 1987 *Phys. Lett.* B **195** 423
Santamaria A and Valle J W F 1988 *Phys. Rev. Lett.* **60** 397
Santamaria A and Valle J W F 1989 *Phys. Rev.* D **39** 1780
[49] Joshipura A S and Nowakowski M 1995 *Phys. Rev.* D **51** 2421 (*Preprint* hep-ph/9408224)
Nowakowski M and Pilaftsis A 1996 *Nucl. Phys.* B **461** 19 (*Preprint* hep-ph/9508271)
Hirsch M and Valle J W F 1999 *Nucl. Phys.* B **557** 60 (*Preprint* hep-ph/9812463)
[50] Passarino G and Veltman M J G 1979 *Nucl. Phys.* B **160** 151

New Journal of Physics
An Institute of Physics and Deutsche Physikalische Gesellschaft Journal

The role of neutrinos, rotations and magnetic fields in collapse-driven supernovae

Shoichi Yamada[1], **Kei Kotake**[2] **and Tatsuya Yamasaki**[3]

[1] Science and Engineering, Waseda University, 3-4-1 Okubo, Shinjuku, Tokyo 169-8555, Japan
[2] Department of Physics, School of Science, University of Tokyo, 7-3-1, Hongo, Bunkyo, Tokyo 113-0033, Japan
[3] Department of Astronomy, Faculty of Science, Kyoto University, Sakyo, Kyoto 606-8502, Japan
E-mail: shoichi@waseda.jp

New Journal of Physics **6** (2004) 79
Received 2 May 2004
Published 9 July 2004
Online at http://www.njp.org/
doi:10.1088/1367-2630/6/1/079

Abstract. Neutrinos are considered to be one of the most important ingredients of collapse-driven supernovae. In the last couple of years, we have seen major progress in both numerical modelling and microphysical understanding of supernova neutrinos. The successful explosion, however, is still elusive. In the former half of this article, we give a brief overview on the current status of the theoretical understanding of the supernova mechanism. In the latter half, we present some new results on multi-dimensional aspects such as rapid rotations, strong magnetic fields and resultant anisotropic neutrino heating, to which our group is currently paying particular attention as an important element for successful explosions. We employ both statical and dynamical approaches. The gravitational waves obtained in the dynamical computations are summarized in an appendix.

PII: S1367-2630(04)80233-7
© IOP Publishing Ltd and Deutsche Physikalische Gesellschaft

Contents

1. Overview **2**
1.1. The importance of neutrino . . . 3
1.2. Multi-dimensional aspects . . . 5
1.3. Magnetic fields . . . 6
2. Accretion shock and its revival **7**
3. Rotations and magnetic fields **11**
3.1. Anisotropic neutrino radiation in rotational core-collapse . . . 11
3.2. Effect of magnetic fields . . . 14
4. Summary **17**
Acknowledgments **18**
Appendix. Gravitational waves from the rotational and magnetorotational core-collapse **18**
References **22**

1. Overview

Substantial effort has been devoted to the study of the mechanism of collapse-driven supernovae during the last 40 years [1]. We know for sure from the observations of SN1987A that they are associated with the death of massive stars ($\gtrsim 10 M_{\odot}$) [2] and that they emit a large number of neutrinos which corresponds to the typical gravitational binding energy of the neutron star over the diffusion time scale of neutrinos in the hot and dense supernova core [3]. Unfortunately, however, we are still not able to tell exactly what drives this explosive phenomenon. Even the most elaborate theoretical models have so far failed to produce successful explosions [4]–[9].

Collapse-driven supernovae are important astrophysical objects in various respects. Most of the heavy elements are synthesized in stars and distributed to the interstellar space by the supernova explosion and the chemical evolution of the galaxy occurs as a result [10]. The collapse-driven supernovae are thought to be one of the most promising sites for r-process [11]. Not only neutrinos but also gravitational waves will be emitted and might be observed if the supernova is not spherically symmetric due to rapid rotation, for example, making the supernova the important target of the looming neutrino and gravitational astronomy [12, 13]. Since the dynamics of the supernova is mainly dictated by microphysics such as weak interactions and nuclear physics as explained below, the revelation of the supernova mechanism will be led or followed by a better understanding of these microphysics.

Recently, the fate of massive stars has attracted considerable attention. This is mainly due to the general recognition that, at least, some of the long-duration gamma-ray bursts (GRB) are associated with the collapse of massive stars and supernova-like events [14]. In particular, the observation of GRB030329/SN2003dh is convincing [15]. The fact that the accompanying supernovae are in general more energetic (they are frequently referred to as 'hypernovae' in the literature and we also employ this term in this sense here) than the canonical collapse-driven supernova is another reason for this frenzy [16]. The comparison of the event rates seems to suggest that most of GRB are accompanied by a hypernova [17]. Although it is supposed that the GRB/hypernova system is partly a result of the black-hole formation, it is not clear how this is

the case. In this context, it is very interesting to know where the boundary between the formation of a neutron star and that of a black hole [18] exists and what causes the difference between the ordinary supernova and the hypernova [19]. All those questions remain to be answered.

In this paper, we focus on the ordinary supernova which will lead to neutron star formation. This may be corresponding to the progenitor mass of about 10–20$M_\odot$ [19, 20]. As will be explained below, the most promising current scenario is the neutrino-driven explosion. In this section, we will first review this scenario briefly, summarizing recent progress in theoretical studies. Then we will discuss some possible boosters, which are expected to help neutrinos to trigger explosions. We pay particular attention to the rotation-induced asymmetry of neutrino emission. We also mention stellar magnetic fields at the end of this section. Our new results on these subjects will be presented in the next two sections.

1.1. The importance of neutrino

The collapse-driven supernova is initiated by the collapse of the stellar core. The pressure deficit due to electron captures and photo-dissociations of nuclei triggers the radial instability. The gravitational stability is not recovered until the nuclear density is reached and the equation of state (EOS) becomes very stiff. In the meantime, the neutrinos emitted by the electron capture are trapped in the core and cannot get out on the dynamical time scale after the density becomes $\gtrsim 10^{11}\,\mathrm{g\,cm^{-3}}$ and the mean free path due to the coherent scattering on nuclei becomes much smaller than the core size. When the core bounce occurs at the central density of a few times the nuclear saturation density, the liberated gravitational energy of $\sim 10^{53}$ erg is stored mostly as the internal energy of the core and is radiated away much later as the trapped neutrinos are getting out of the core on the diffusion time scale [3].

The collapsing core consists of the so-called inner and outer cores; the former contracts in a subsonic and homologous way while the latter falls supersonically on to the former. The bounce of the inner core generates a shock wave at the boundary of these two cores. As the shock wave propagates outwards through the outer core, neutrino emissions and photo-dissociations of nuclei deprive the shock wave of the energy. In the recent sophisticated simulations [4]–[9], the shock wave stalls and becomes an accretion shock inside the core. How far the shock wave can go before stagnation depends on the proportion of the inner and outer cores, which is in turn determined by the electron captures in the collapsing phase [21]. The rates of electron captures on nuclei had been one of the uncertainties in nuclear physics until quite recently [22]. The more suppressed the electron captures are and, as a result, the more lepton-rich the inner core is, the farther the shock wave can go and the easier the explosion may be. The large-scale shell-model calculations by Langanke *et al* [21] have shown that the electron captures proceed further than expected for the standard approximate treatment. Now there seems to be no chance for prompt explosions (see section 1.3, however).

To produce explosions, the stalled shock must be somehow revived. As mentioned above, the neutrino heating is supposed to be the most promising mechanism for that. Due to the neutrino trapping, most of the energy liberated by the gravitational collapse is stored as internal energy in the core and is carried away together with the lepton number by neutrinos diffusing out of the core on the time scale much longer than the dynamical time scale. Although all flavours of neutrinos are emitted, the electron-type neutrinos and anti-neutrinos are mainly responsible for the heating of the matter behind the shock wave via absorptions on nucleons, $\nu_e + n \rightarrow p + e$ and $\bar{\nu}_e + p \rightarrow n + e^+$. The merit of the neutrino-heating mechanism is that neutrinos transport a

great amount of energy equal to the gravitational binding energy of a neutron star, $\sim 10^{53}$ erg, which is about a 100 times the typical kinetic energy of a supernova explosion. The actual available energy will be reduced by a factor of ~ 10, since most of the neutrinos are radiated in the later phase where the luminosity has declined substantially and the neutrino-heating is no longer efficient. Still, the energy that neutrinos can potentially deposit is much greater than the canonical explosion energy.

The problem with this mechanism is that neutrinos interact only weakly with matter and the neutrino-heating is indeed inefficient. In addition, the cooling of matter occurs simultaneously via the very inverse process of the heating reactions, that is, $p + e \rightarrow \nu_e + n$ and $n + e^+ \rightarrow \overline{\nu}_e + p$. Hence the net heating occurs only between the shock wave and the so-called gain radius, at which the heating is just cancelled by the cooling and the net heating vanishes. The issue is the quantitative assessment of whether the heating is sufficient to revive the shock wave. In fact, this is really a subtle problem. In their numerical experiments, Janka and Müller [23] found the shock revival for otherwise failed explosion models if the neutrino luminosity was enhanced artificially by a few tens percent from the original value. On the other hand, Burrows and Goshy [24] demonstrated by studying static configurations after the shock-stagnation that for a given accretion rate there is a critical luminosity for the shock revival. All we have to attain, then, appears to be this relatively small amount of boost of the neutrino luminosity and energy from the values we have obtained in failed explosion models.

In the last couple of years, both numerics and microphysics have been scrutinized. The former, in particular, has seen major progress [4]–[9]. Since Wilson first proposed the neutrino-heating mechanism [25], neutrino transport has been a formidable task and some type of approximation, the multi-group-flux-limited diffusion approximation as the most familiar example, has been employed even in the one-dimensional (1D) spherically symmetric simulations. This is mainly because neutrinos are not in thermal and/or chemical equilibrium with matter except in the central portion of the core and we have to treat not only the spatial but also the momentum distribution of neutrinos as a function of time. This has changed completely lately. A couple of groups [4]–[7], have published the state-of-the-art direct solutions of the Boltzmann equation for neutrinos, and some of them extended even to 2D computations [8, 9, 26]. Although they have still not found successful explosions, the importance of the accurate treatment of neutrino transfer has been confirmed.

The microphysics such as neutrino reaction rates [27] and equations of state have also been studied in detail. The computation of the electron capture rates for various nuclei as mentioned above is one of them [21]. We have at least two equations of state now available based on different realistic descriptions of nuclear interactions [28, 29]. It is easily understood that the neutrino luminosity and/or energy would be increased if the opacity of hot dense matter were somehow smaller than the standard value that we usually use in the numerical modelling. The correlations originating from nuclear interactions have been expected to be promising in reducing the opacity. Although still uncertain, it has been claimed that the opacity of the nuclear matter in the core could be reduced roughly by half [30]–[33]. Relatively small corrections to the standard approximation such as recoil of nucleons and weak magnetism as well as some new reactions like nuclear bremsstrahlung and pair-annihilation/creations among different neutrino flavours have been incorporated and their importance has been evaluated in the recent 1D computations [34]–[36]. Even after these sophistications, the successful explosion has not been found. It seems that the reduction of the neutrino opacity, if any, should occur in the lower-density region much closer to the neutrino sphere, from which neutrinos flow freely. Otherwise, the

enhancement of luminosity and energy will be nullified as neutrinos diffuse towards the neutrino sphere. If the explosion is to occur in the spherically symmetric collapse, we are still missing some important microphysical elements.

1.2. Multi-dimensional aspects

Ever since SN1987A was observed, most researchers think that the dynamics of a supernova is non-spherical one way or another [37]. Hydrodynamical instabilities are supposed to be mainly responsible for this asphericity. The heating region, for example, tends to have a negative entropy gradient because of the neutrino-heating from beneath. It is also pointed out that the accretion shock is subject to large non-spherical oscillations [38]. The region inside the neutrino sphere is also probably unstable. As mentioned in the previous subsection, the neutrino-heating mechanism is very close to explosion as it is in the spherical collapse. Hence, combined with other phenomena such as hydrodynamical instability, it is expected to have a good chance to give a successful explosion. Many multi-dimensional simulations have been made to address this issue, employing different approximations [23], [39]–[42].

The difficulty of multi-dimensional treatment of neutrino transport hampered the definitive answer to this problem. Although some smooth-particle hydrodynamics (SPH) simulations have found explosions induced by the combination of neutrino-heating and convection in the heating region [39, 43], there has been persistent concern with their approximate treatment of neutrino transfer. Other simulations until recently had similar problems [40]. This situation may change soon. A new generation of multi-dimensional simulations has begun to be published [8, 9, 26]. In these simulations, the dynamics of the whole core is computed with a code implemented with the Boltzmann solver. Although they still employ some approximations, this line of research will soon be pursued by other groups.

According to a recently published result [9], successful explosions are still elusive. It should be mentioned that in their models the convective motions are found both inside the neutrino sphere and in the heating region. Hence the maximal boost of heating is expected from these hydrodynamical motions. What effect the employed approximations have on the results remains to be studied further. However, we may have to look for alternatives to the convection.

Our group has been paying attention to stellar rotation [44]–[46]. Apart from the asphericity owing to the convective motion, it has been also recognized that collapse-driven supernovae are in general globally non-spherical [37]. The best example is again SN1987A, the recent pictures of which clearly show the elongated envelope [47, 48]. The spectropolarimetric observations of other supernovae might also support this claim, though still controversial [49]–[51]. It seems most natural to think that this global asphericity is caused by the rotation of the core. Note, however, that the large-amplitude oscillation of the accretion shock as mentioned above may also lead to the global aspherical expansion of the envelope [38, 52].

If the core rotates rapidly, the centrifugal force flattens the core. Then, neutrinos are emitted preferentially in the direction of the rotation axis. Shimizu *et al* [45] pointed out that this anisotropic neutrino radiation may be advantageous to trigger the revival of a shock wave. This is because neutrino-heating is more efficient near the rotation axis than for the spherically symmetric case and the induced global circulative motion supplies cool matter from the equator and carries away heated matter near the rotation axis, which makes the heating process more efficient as a whole. Kotake *et al* [46] estimated the possible anisotropic pattern and amplitude for various rotation laws by 2D simulations of rotational core-collapse with a simplified treatment

of neutrinos and found that the anisotropy assumed in Shimizu *et al* [45] can be obtained if the core is rotating rapidly with the ratio of rotational energy to gravitational energy, $|T/W| \sim 0.5\%$. This will be detailed in section 3.1.

It should be mentioned that this mechanism is important only when the explosion does not occur without global anisotropy. In fact, Fryer and Heger [43] found a minor effect from the anisotropic neutrino radiation in their SPH simulations, where the explosion occurs as a result of convection-boosted neutrino-heating regardless of rotation. It is also added that the rotation of the core may not be so rapid after all. Recent evolution models by Heger *et al* [53, 55] suggest that the transport of angular momentum during the quasi-static evolutionary phase of the progenitor deprives the core of substantial fraction of its angular momentum, particularly when the magnetic torque is taken into account [54, 55]. If this is really the case, the rotation will play no significant role in the dynamics of core-collapse as shown by Buras *et al* [8] (see also Müller *et al* [56]). We had better bear in mind, however, that the evolution models are based on 1D calculations and have some uncertainties in the mechanism and treatment of angular momentum transport.

In the next section, we will consider the effect of rotation on the accretion shock using the analysis of the static configurations. This is an extension of the study by Burrows and Goshy [24] to the rotational case. We will discuss the change of critical luminosity due to rotation and the possible outcome.

1.3. Magnetic fields

Another possible cause for the non-sphericity of supernovae may be stellar magnetic fields. It is a well known fact that pulsars are magnetized neutron stars. Hence it is expected that the core is also magnetized prior to collapse in general. The issue is the strength of magnetic fields. The canonical value for the pulsar, $\sim 10^{12}$ G, is negligibly small in terms of the effect on the dynamics of collapse. In fact, the magnetic field strength should be $\gtrsim 10^{16}$ G if the magnetic stress is to be comparable with the matter pressure in the supernova core. This is mainly the reason why there have been so few papers published so far on the magnetic supernovae [57]–[62].

It is recognized these days that some neutron stars are indeed strongly magnetized, $\gtrsim 10^{15}$ G. There are about 10 of them. Some of them are soft gamma repeaters and others are anomalous x-ray pulsars or high-field radio pulsars [63, 64]. They are collectively referred to as magnetars. At the moment, they are supposed to be a minor subgroup of neutron stars. The origin of this large magnetic field is so far a mystery. The core might have strong magnetic fields prior to collapse already, although the evolution models by Heger *et al* [55] indicate quite the contrary. The magnetic fields that are weak at first might be somehow amplified during the supernova [65].

Yamada and Sawai [61] considered the former case and studied numerically the effect of magnetic fields on the dynamics of the prompt propagation of a shock wave. Their 2D non-relativistic magnetohydrodynamic (MHD) simulations showed that the combination of rapid rotation, $|T/W| \gtrsim 0.1\%$, and strong poloidal magnetic field, $|E_m/W| \gtrsim 0.1\%$, where $|E_m/W|$ is the ratio of the energy of the magnetic field to the gravitational energy, leads in general to jet-like explosions. They found that the magnetic fields are amplified by the wind-up due to differential rotation as well as by the ensuing MRI-like lateral motions of fluid mainly around the boundary of the inner and outer cores near the rotation axis. Intriguingly, the models with the smallest magnetic fields studied still produced a jet-like explosion although it takes longer to launch the jet. This might suggest that even much smaller magnetic fields could be amplified in the collapsed core and play an important role for explosion. Although we do not know if the

strong magnetic fields are common phenomena for the ordinary supernova, it is interesting to see if strong magnetic fields are helpful for the neutrino-heating mechanism.

Kotake *et al* [62] analysed the models with predominantly toroidal magnetic fields, which will be more realistic as suggested by the evolution models. They paid particular attention to the anisotropy of the neutrino radiation, which will be summarized in section 3.2. We also discuss the effect of strong magnetic fields on the heating rates based on our numerical models and the implication for the pulsar kick velocity.

2. Accretion shock and its revival

In this section, we consider the effect of rotation on the post-bounce quasi-static configurations and the revival of stalled shock. After the shock is stalled, the mass accretion rate and neutrino luminosity change slowly and we can approximately describe the state of the core as a steady accretion flow with a standing shock. Assuming spherical symmetry, Burrows and Goshy [24] sought a series of steady-state solutions and found that for a given mass accretion rate there is a critical neutrino luminosity above which there exists no steady-state solution. Using this fact, they argued that the condition for the revival of the stalled shock is that the neutrino luminosity should exceed this critical value.

In this paper, we extend their analysis to the rotational collapse. We seek steady-state solutions of rotating accretion flows with a standing shock, which is non-spherical in general, by solving 2D time-independent hydrodynamical equations. We investigate the effect of rotation on the accretion flow as well as the critical luminosity of neutrinos based on the solutions. Since our purpose here is not to determine the critical values quantitatively but to see qualitatively how rotation affects the flow and the critical luminosity, we adopt a few assumptions and simplifications in solving the steady flow. Formulations are Newtonian and we do not solve neutrino transport assuming that the neutrino luminosity and energy spectrum do not depend on the radius. Although this is mainly for simplicity, the approximation is justified as our computations are limited to the region outside the neutrino sphere. We take into account only absorptions and emissions of neutrinos on nucleons as for heating and cooling processes. Photo-dissociations are neglected. Although there may exist a region where flows are convectively unstable, it is not taken into account.

The basic equations are given as

$$\frac{1}{r^2}\frac{\partial}{\partial r}(r^2\rho u_r) + \frac{1}{r\sin\theta}\frac{\partial}{\partial\theta}(\sin\theta\rho u_\theta) = 0, \tag{1}$$

$$u_r\frac{\partial u_r}{\partial r} + \frac{u_\theta}{r}\frac{\partial u_r}{\partial\theta} - \frac{u_\theta^2+u_\phi^2}{r} = -\frac{1}{\rho}\frac{\partial p}{\partial r} - \frac{GM}{r^2}, \tag{2}$$

$$u_r\frac{\partial u_\phi}{\partial r} + \frac{u_\theta}{r}\frac{\partial u_\phi}{\partial\theta} + \frac{u_\phi u_r}{r} + \frac{u_\theta u_\phi\cot\theta}{r} = 0, \tag{3}$$

$$u_r\frac{\partial u_\theta}{\partial r} + \frac{u_\theta}{r}\frac{\partial u_\theta}{\partial\theta} + \frac{u_r u_\theta}{r} - \frac{u_\phi^2\cot\theta}{r} = -\frac{1}{\rho r}\frac{\partial p}{\partial\theta}, \tag{4}$$

$$u_r\left(\frac{\partial\epsilon}{\partial r} - \frac{p}{\rho^2}\frac{\partial\rho}{\partial r}\right) + \frac{u_\theta}{r}\left(\frac{\partial\epsilon}{\partial\theta} - \frac{p}{\rho^2}\frac{\partial\rho}{\partial\theta}\right) = \dot{q}, \tag{5}$$

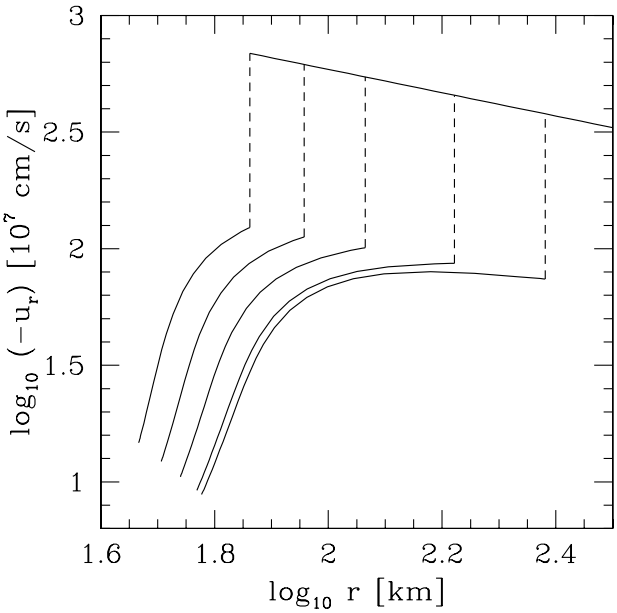

Figure 1. Solution curves of the first branch for steady non-rotating accretion flows with $\dot{M} = 0.2 M_\odot\,\mathrm{s}^{-1}$, $L_{\nu_e} = 5\times10^{52}, 6\times10^{52}, 7\times10^{52}$ and $8\times10^{52}\,\mathrm{erg\,s}^{-1}$ and $8.3165\times10^{52}\,\mathrm{erg\,s}^{-1}$ (critical value), from left to right. Dashed lines denote shock jumps.

where $\boldsymbol{u}$, ρ, p and ϵ denote velocity, density, pressure and specific internal energy, respectively. The gravitational constant, neutron star mass and net heating rate are represented as G, M, $\dot{q}$, respectively.

The outer and inner boundaries are set at the shock surface and the neutrino sphere, respectively. The neutrino sphere is assumed to be spherical for simplicity, though it is not true in reality. We impose the Rankine–Hugoniot relations as the outer boundary conditions. The upwind flow at the shock wave is assumed to be radial and have a free fall velocity. In the rotating case, the angular velocity just outside the shock wave is obtained based on the assumption of the radial infall and the shell-type rotation at the radius of 1000 km, where the model angular velocity is given. The obliqueness of the shock wave is taken into account. At the neutrino sphere, we impose the inner boundary condition that the density is $10^{11}\,\mathrm{g\,cm}^{-3}$. The more desirable condition would be that the neutrino optical depth from the neutrino sphere to infinity equals 2/3. However, these two conditions are almost identical in the case of spherically symmetric flow and we employ the former condition also in the asymmetric case. As for the temperature of neutrino and the electron fraction, we take the values, $T_\nu = 4.5\,\mathrm{MeV}$ and $Y_\mathrm{e} = 0.5$, in the whole region of calculations.

First, we discuss the case with no rotation, i.e., spherically symmetric flow, which was also investigated by Burrows and Goshy [24]. When the neutrino luminosity is below the critical value, there exist two types of solutions (figures 1 and 2). This is common to the adiabatic accretion flow (the so-called Bondi–Hoyle flow), and is a result of the following feature of the accretion flow. When the flow is subsonic, the accreting gas is first accelerated in the outer region, where the gravitational force is dominant, and later decelerated in the inner region, where the pressure gradient becomes more important. As a result of this flow pattern, we can join the outer supersonic flow with the inner subsonic flow via the shock wave at two points, i.e., in the accelerating regime

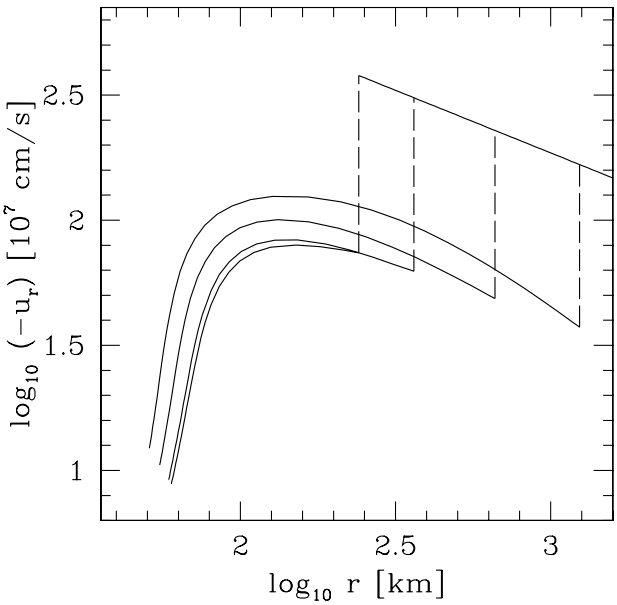

Figure 2. Solution curves of the second branch for steady non-rotating accretion flows with $\dot{M} = 0.2 M_\odot\,\mathrm{s}^{-1}$, $L_{\nu_e} = 6 \times 10^{52}$, 7×10^{52} and $8 \times 10^{52}\,\mathrm{erg\,s}^{-1}$ and $8.3165 \times 10^{52}\,\mathrm{erg\,s}^{-1}$ (critical value), from right to left.

or in the decelerating regime. As the luminosity goes higher, the radius of shock becomes smaller in one of the solutions and gets larger in the other. At the critical luminosity, the radii of shocks in the two solutions merge, and when the luminosity exceeds the critical value, there exists no solution satisfying the boundary conditions, as Burrows and Goshy [24] showed (figure 3). The absence of a solution satisfying the Rankine–Hugoniot relations for the standing shock suggests inevitably that, at this point, the shock is revived and starts to propagate outwards. In fact, when the shock is dislocated either inwards or outwards from the equilibrium position, the downstream pressure becomes always larger than the upstream one. This also suggests the revival of the shock at that point.

Next, we discuss the case of rotation. The centrifugal force plays an important role in the flow in this case. As the theory of Bondi–Hoyle accretion flow tells, it tends to accelerate the subsonic flow and decrease the density and temperature [66]. Since the centrifugal force is greater near the equatorial plane than near the rotation axis, the flows are directed to the equatorial plane (figure 4). At the same time, the shock is deformed into prolate configurations and becomes an oblique shock. As a result, the critical luminosity becomes lower than in the spherically symmetric case (figure 3).

Finally, we discuss what will happen in the rotational case when the neutrino luminosity exceeds the critical value. In the case of spherically symmetric flow, the steady shock condition breaks down on the whole shock surface at the same time. On the other hand, in the case of rotation, the condition is violated pointwisely, first at a certain point on the shock surface in general. Then the shock will start to propagate outwards from that point. In the spherically symmetric flow, we found that, at the critical luminosity, the radii of the shocks in the two branches of solutions coincide with each other. Applying this to the rotational case, we can find at which point on the shock front the steady-state condition breaks down first. We find that this

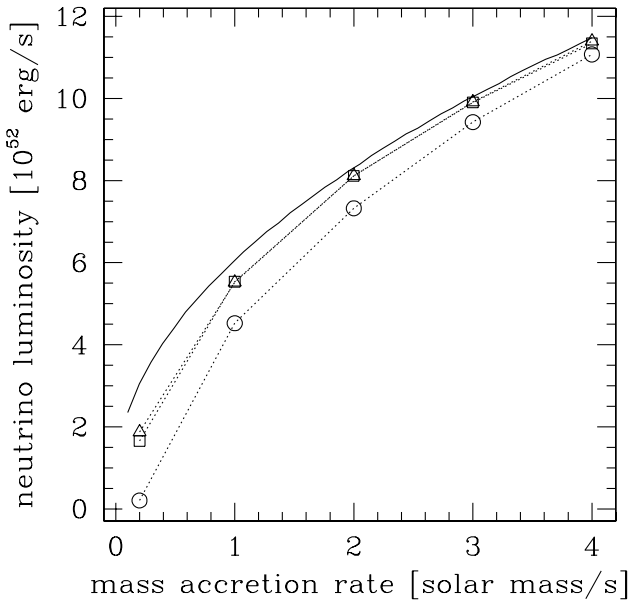

Figure 3. The critical luminosities below which steady accretion flows with a standing shock exist. The solid line corresponds to the spherically symmetric case and open triangles, squares and circles represent the critical luminosities for rotational cases. The rotation frequencies are 0.01, 0.03, 0.10 Hz at 1000 km for triangles, squares and circles, respectively. No steady-state solution exists for a luminosity larger than the critical values.

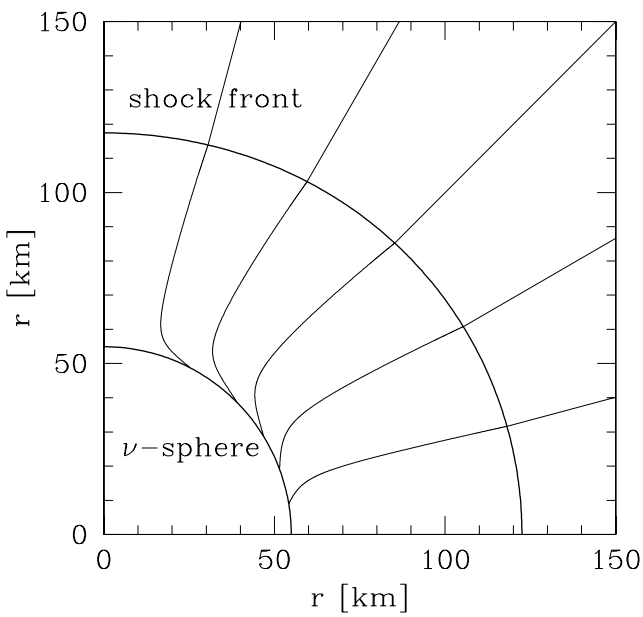

Figure 4. Stream lines for a rotational accretion flow with $\dot{M} = 0.2 M_{\odot}\,\mathrm{s}^{-1}$ and $L_{\nu_e} = 7 \times 10^{52}\,\mathrm{erg\,s}^{-1}$. The rotation frequency is assumed to be 0.1 Hz at a radius of 1000 km.

occurs first at the rotation axis in general. Although time-dependent calculations are necessary to confirm this claim, we think that this suggests that when the luminosity exceeds the critical value in the rotational case, a jet-like explosion will be realized, as suggested by some observations [50]. Detailed results and discussion will be published elsewhere later [67].

3. Rotations and magnetic fields

In this section, we discuss anisotropic neutrino radiations based on our 2D hydrodynamical and MHD simulations.

3.1. Anisotropic neutrino radiation in rotational core-collapse

As stated in the previous sections, recent numerical studies of core collapse supernovae in spherical symmetry have failed to produce explosions [4]–[7]. In the meantime, there are accumulating observations, which require the revision of the spherically symmetric stellar collapse. Spectropolarimetric observations have commonly shown a percent level of linear polarization, which may be interpreted as the asymmetry of core collapse supernovae [49, 51]. It is also well known that SN1987A is globally asymmetric, which is directly observed by the *Hubble Space Telescope* [47, 48]. Provided the facts that the progenitors of collapse-driven supernovae are a rapid rotator on the main sequence [68] and that the recent theoretical studies suggest a fast rotating core prior to the collapse [53] (see, however, [55]), it is important to incorporate rotation in simulations of core collapse.

So far there have been some works devoted to the understanding of the effect of rotation upon the supernova explosion mechanism [8, 43, 44, 57, 59], [69]–[71]. It seems clear that the rotation is not good to prompt shock propagation [44, 71]. This is simply because the centrifugal force tends to halt the core collapse, which then reduces the conversion of gravitational energy into kinetic energy. Here we pay attention to the effect of rotation on the neutrino-heating mechanism. Shimizu *et al* [45] demonstrated that anisotropic neutrino radiations induced by rotation may be able to enhance local heating rates near the rotational axis and trigger globally asymmetric explosions. The required anisotropy of the neutrino luminosity appears to be not very large ($\sim$3%). In their study, the anisotropy of neutrino heating was given by hand and rotation was not taken into account, either. In this paper, we demonstrate how large the anisotropy of neutrino radiation could be, based on the 2D rotational core-collapse simulations from the onset of gravitational collapse of the core through the core bounce to the shock-stall [46]. We not only estimate the anisotropy of neutrino luminosity but also calculate local heating rates based on that.

For the hydrodynamic calculations shown here, we employ the ZEUS-2D code [72]. We made several major changes to the base code to incorporate the microphysics. As for the EOS, we implement a tabulated EOS based on the relativistic mean field (RMF) theory [29] instead of the ideal gas EOS assumed in the original code. We approximate the electron captures and neutrino transport by the so-called leakage scheme. For a more detailed description of the methods, see [46]. As for the initial angular momentum distribution in a core of evolved massive stars, little is known at present about which mode of the instabilities prevails on what time scale during the quasi-static stellar evolution (see [53, 55] for recent developments). Therefore, we assume two possible rotation profiles, shell-type and cylindrical-type. Furthermore, we change the total angular momentum and the degree of differential rotation in a parametric manner. We made the

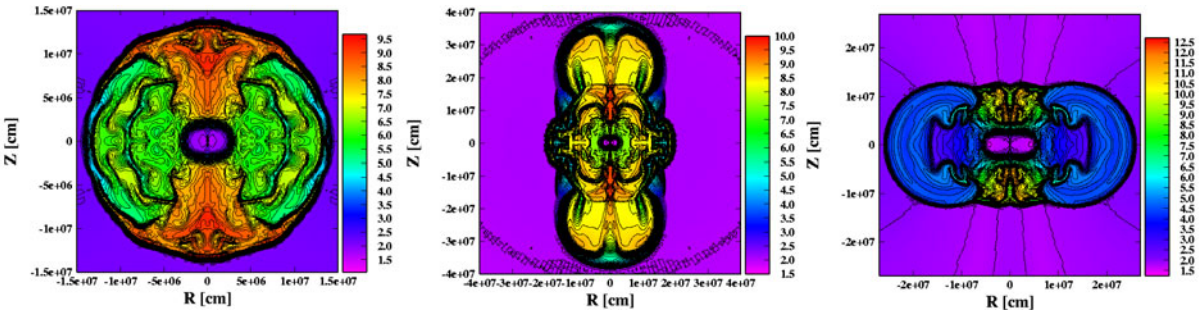

Figure 5. Final profiles of the representative models. They show colour-coded contour plots of entropy (k_B) per nucleon. The initial value of $T/|W|$ is 0.5% for the models of the left (model A) and central panels (model B), 1.5% for the model of the right panel (model C). Here $T/|W|$ is the ratio of rotational to gravitational energy. The model of the central panel has stronger differential rotation than that of the left panel.

pre-collapse models by taking density, internal energy and electron fraction distributions from the spherically symmetric $15M_\odot$ model by Woosley and Weaver [73] and adding angular momentum according to the prescription stated above.

In figure 5, the entropy distributions at the end of computations for some representative models are presented. A variety of the final profiles is immediately seen in the figure. In all the models studied, the shock wave produced by core bounce stalls in the core and no prompt explosion occurs. As the initial rotation rate becomes larger, the shape of the stalled shock wave becomes more oblate due to the stronger centrifugal force (compare the left with the right panel in figure 5). If the initial rotation rate is the same, the shape of the stalled shock is found to be elongated in the direction of the rotational axis as the differential rotation becomes stronger (compare the left with the central panel of figure 5). This is related to the production of high entropy blobs by core bounce. For weak differential rotations, the entropy blob formed near the rotational axis floats up parallel to the axis and then stalls. This makes the shock prolate at first. Then the matter distribution returns to be spherical or oblate due to the centrifugal forces. On the other hand, in the case of strong differential rotations, the shock wave formed first near the rotational axis hardly propagates and stalls very quickly. The high entropy blob begins to grow near the equatorial plane in this case. This then induces the flows towards the rotational axis. As a result, the final configuration becomes prolate. Based on the anisotropic matter distributions after the shock stagnation obtained by these hydrodynamic simulations, we next analyse the neutrino spheres and calculate the degree of anisotropic neutrino radiation.

In the left panel of figure 6, the neutrino spheres for spherical and rotating models are presented. Note that the rotating model in the figure is based on the recent stellar evolution calculation [53]. For the rotating model, it is found that the neutrino sphere forms deeper inside at the pole than for the spherical model. This is a result of the fact that the density is lower on the rotational axis in the rotation models than in the spherical model because the matter tends to move away from the axis due to the centrifugal force. We note that the above features are also true for slower and more rapid rotation models. Furthermore, the configurations are more deformed as the rotation becomes faster due to stronger centrifugal forces. The neutrino temperature profile on the neutrino sphere for the pair is presented in the right panel of figure 6. Note that the neutrino temperature is assumed to be equal to the matter temperature. It is seen from the figure

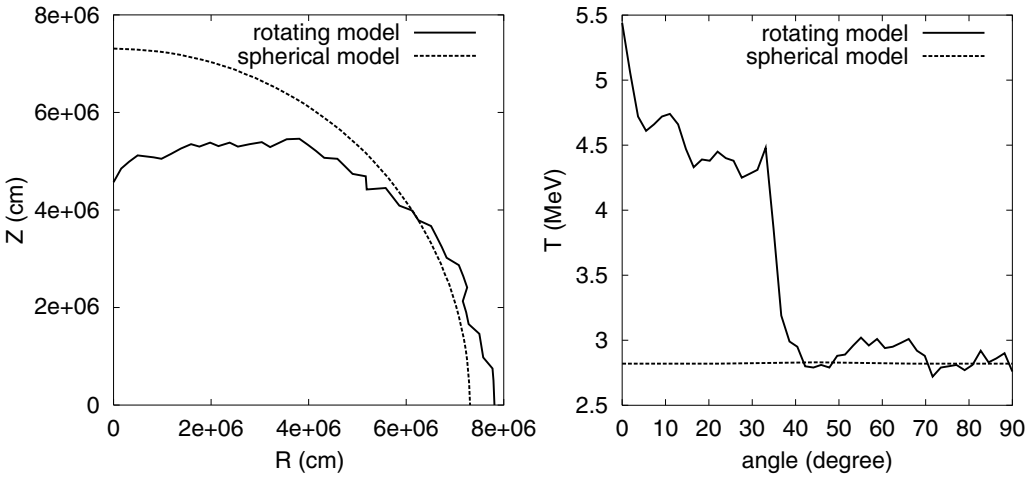

Figure 6. Shapes of neutrino sphere (left panel) and neutrino temperature versus polar angle on the neutrino sphere (right panel) for the rotating model (model A) and the spherical model.

that the temperature varies with the polar angle for the rotating model. The neutrino temperature is higher at the pole for the rotating model than for the spherical model. This can be understood from the fact that the neutrino sphere is formed deeper inside for the rotational model than for the spherical model, as mentioned above.

Based on the above results, we estimate the heating rates outside the neutrino sphere. This is admittedly a very crude estimate, since it is well known [5, 6] that the net heating, the heating minus cooling, becomes positive 50–100 ms after the shock stagnation. We confirmed that the cooling dominates over the heating at the end of simulations in our models also. Since our calculations ended before the heating dominates over the cooling, it is impossible to estimate the location of the gain radius, beyond which the heating dominates over the cooling. Here it is noted that the anisotropy of the heating is found to be similar to that of the cooling in our short runs. It is, thus, expected that the gain radius will be deformed in a similar way in the later phase. If this is true, the bare heating rate discussed below will help us understand the net neutrino heating in the later phase. Bearing this in mind, we consider the bare heating rate for the final configurations (several ten milliseconds after the bounce) in our simulations.

We evaluate the heating rate of the charged-current interaction: $\nu_e + n \rightarrow p + e^-$. The neutrino emission from each point on the neutrino sphere is assumed to be isotropic and take a Fermi–Dirac distribution with a vanishing chemical potential. For the details about the estimation, we refer readers to Kotake *et al* [46]. In figure 7, we show the contour plots of the heating rate for the spherical (top left panel) and some representative rotation models. It is clearly seen from the figure that the neutrino heating occurs anisotropically and is stronger near the rotational axis for the rotation models. This is mainly because the neutrino temperatures at the rotational axis are higher than on the equatorial plane. In addition, the radius of the neutrino sphere tends to be smaller in the vicinity of the rotational axis. As a result, the solid angle of the neutrino sphere is larger when seen from the rotational axis. These two effects make the neutrino heating near the rotational axis more efficient.

By performing the linear analysis for the convective stability in our models, we find that the convective regions appear near the rotational axis (see [46]). This is because the gradient of the

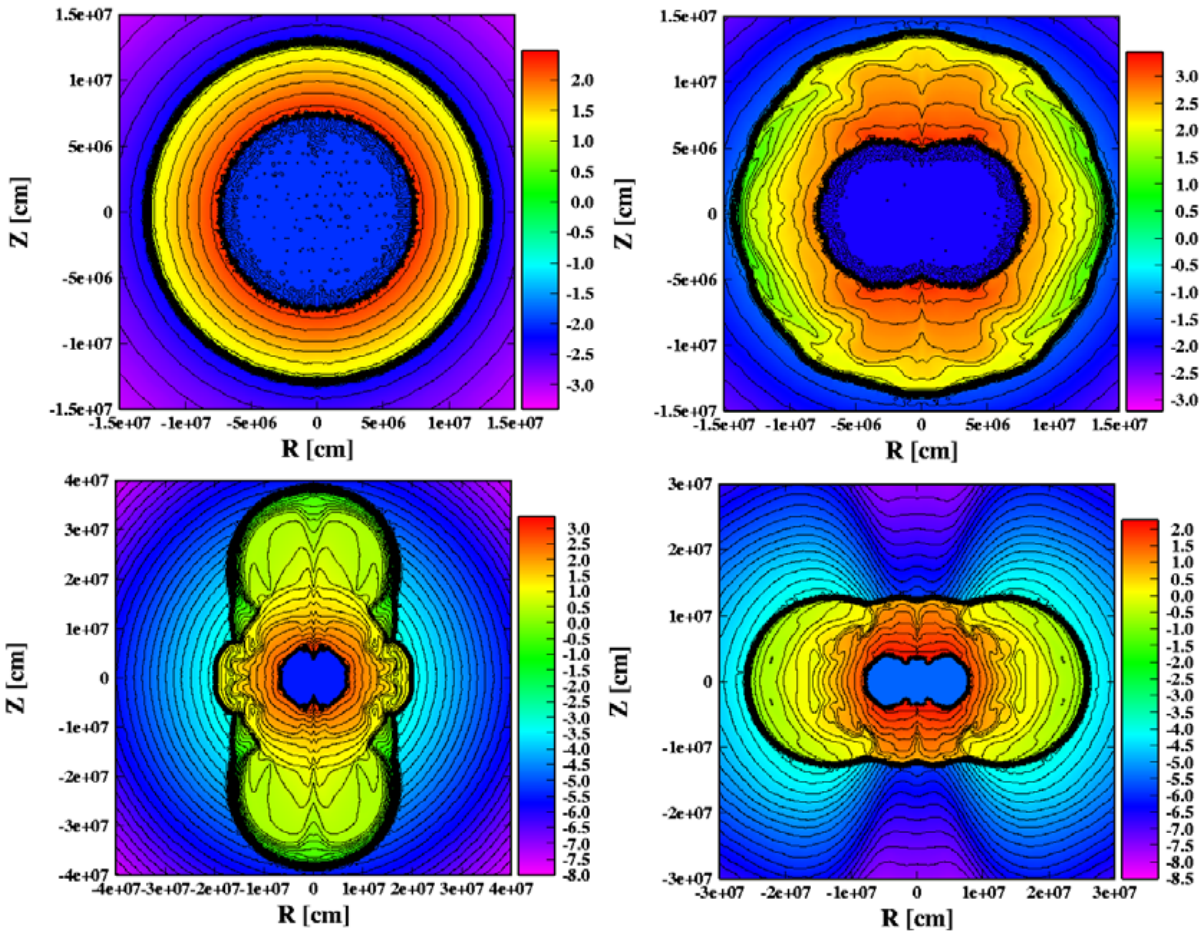

Figure 7. Heating rates outside the neutrino sphere for the spherical model (top left), and also for the models A (top right), B (bottom left) and C (bottom right). All the figures show colour-coded contour plots for the logarithm of the heating rate (MeV nucleon^{-1} s^{-1}). The neutrino sphere and the stalled shock are seen as thick lines separating the bright colour from the dark colour region. Note that the value within the neutrino sphere is artificially modified to dark colours and has no physical meaning.

angular momentum is rather small near the axis and the stabilizing effect of rotation is reduced there. Neutrino heating enhanced near the rotational axis might lead to even stronger convection there later on. Then, the outcome will be a jet-like explosion as considered in Shimizu *et al* [45]. It should be noted that our results suggest that the non-radial neutrino transport should be treated accurately. For this purpose, we are currently preparing 2D radiation-hydrodynamical simulations with an elaborate neutrino transfer scheme [98].

3.2. *Effect of magnetic fields*

Next we discuss the effect of magnetic fields on the rotational collapse described above. While most of the MHD simulations in the context of core-collapse supernovae choose poloidal magnetic fields as initial conditions [57]–[61], [75, 76], recent stellar evolution calculations

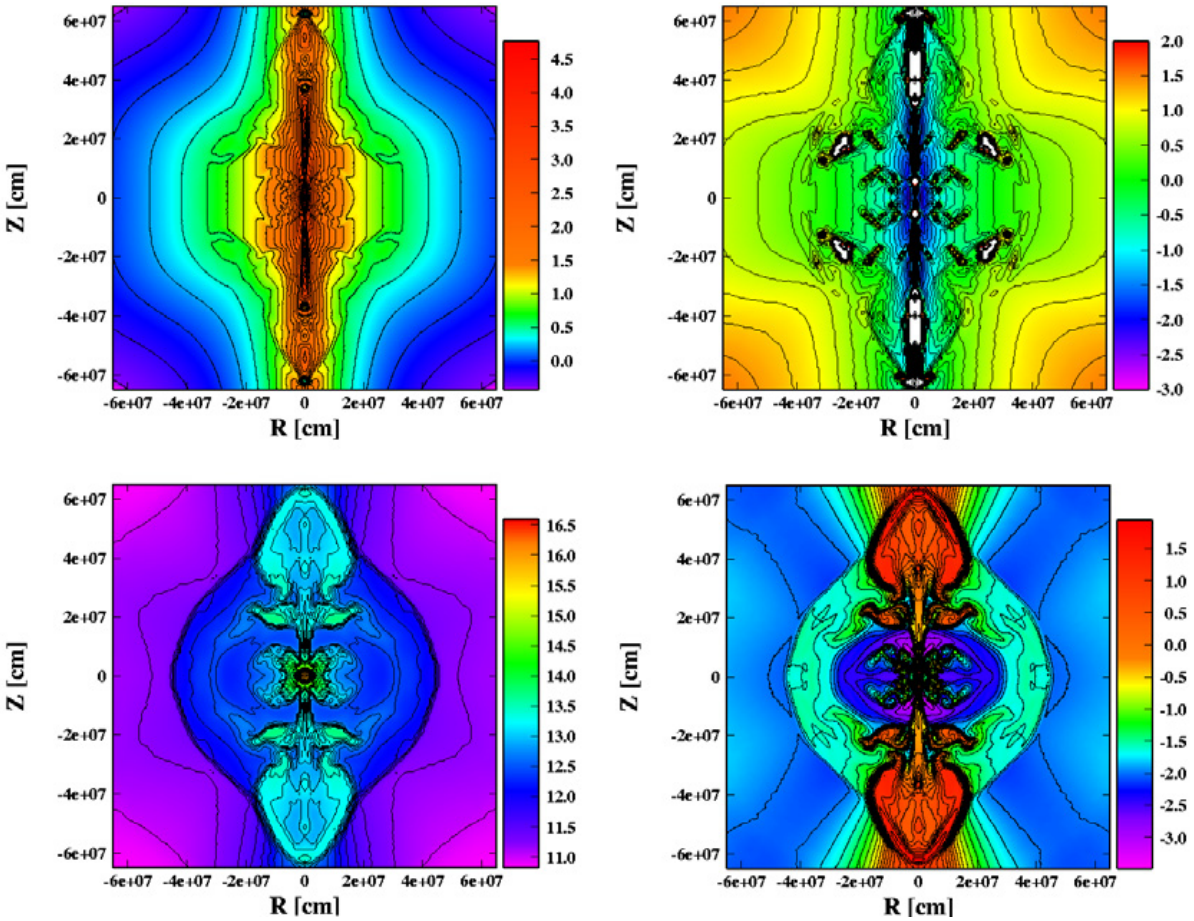

Figure 8. Contour plots of various quantities for the model with the strongest magnetic field in our computations [62]. The top left panel shows the logarithm of the angular velocity (s^{-1}). The top right panel represents the magneto-rotationally unstable regions to non-axisymmetric perturbations. The plot shows the growth time scale (s) of MRI. Note that, in this panel, the regions with white represent stable regions against MRI. The bottom left panel shows the logarithm of magnetic field strength (G). The bottom right panel displays the logarithm of the ratio of magnetic stress to matter pressure in percentage.

show that toroidal magnetic fields may be much stronger than poloidal ones prior to collapse [54, 55]. This situation leads us to investigate the effect of the toroidal magnetic fields on the anisotropic neutrino radiation and convection. We performed a series of 2D MHD core-collapse simulations changing the strength of rotation and the toroidal magnetic fields systematically [62]. We first summarize the results.

The angular velocity profile for the model with the strongest toroidal magnetic fields in our simulations is given in the top left panel of figure 8. The initial values of $T/|W|$ and $E_m/|W|$ are 0.5 and 0.1%, respectively, where $E_m/|W|$ represents the ratio of magnetic field to gravitational field energy. In addition, the initial profiles of rotational and magnetic fields are chosen to be cylindrical with strong differential rotation for this model.

In the top left panel, the negative gradient of angular velocity, $d\Omega/dX < 0$, can be found, where Ω is the angular velocity and X is the distance from the rotational axis. Such a region is known to be unstable to non-axisymmetric perturbations [65, 74]. The characteristic time scale for the growth of the instability called the magneto-rotational instability (MRI) is given as $\tau_{\rm MRI} = 4\pi|d\Omega/d\log X|^{-1}$. The top right panel of figure 8 shows the contour of $\tau_{\rm MRI}$ for the model. The typical time scale is found to be $\sim$O(10) ms near the rotational axis. This suggests that MRI induced by non-axisymmetric perturbations can grow on the prompt shock time scale. The field strengths in the protoneutron star become as high as $\sim 10^{16}$ G (see the bottom left panel of figure 8), and the ratio of magnetic stress to matter pressure gets as high as 0.9 behind the shock wave (see the bottom right panel of figure 8).

As for the anisotropic neutrino radiation, we find that the feature is not changed significantly by the inclusion of very strong toroidal magnetic fields ($\sim 10^{16}$ G in the protoneutron star). Combined with the anisotropic neutrino radiation that heats matter near the rotational axis more efficiently, the growth of the instability is expected to further enhance heating near the axis. Furthermore, the magnetic pressure behind the collimated shock wave is as strong as the matter pressure in the vicinity of the rotational axis. From these results, we expect that the magnetar formation is accompanied by a jet-like explosion if it is formed in the magneto-rotational collapse described above.

In the rest of the section, we present our new results on the effect of poloidal magnetic fields on the neutrino heating. So far we concentrated on the models whose initial magnetic fields are taken to be almost purely toroidal as suggested by the recent stellar evolution calculation [55]. Considering the uncertainties, however, in their models as mentioned before, it should be still important to investigate the effect of poloidal magnetic fields. Here we discuss the model assumed to have strong poloidal magnetic fields ($\sim 10^{12}$ G) prior to core-collapse. In addition, the magnetic field is assumed to be uniform and parallel to the rotational axis initially. During core-collapse, the strength of the magnetic fields substantially exceeds the QED critical value, $B_{\rm QED} = 4.4 \times 10^{13}$ G, and the neutrino reactions are affected by the parity-violating corrections to the weak-interaction rates [77]–[79]. In the following, we estimate the importance of the corrections.

In the left panel of figure 9, the distribution of the poloidal magnetic fields at $t \sim 20$ ms after core bounce is given. The initially uniform magnetic field is deformed to be dipole-like due to core contraction. Using this configuration of magnetic field as a background, we estimate the neutrino heating rate by electron neutrino absorptions on neutron both with and without the parity-violating corrections and compare them by the same procedure as discussed earlier in this paper. As for the cross section with the parity-violating effects, we employ the formula in [78]. The right panel of figure 9 shows the ratio of the heating rate with the corrections to that without the corrections. It is found that the ratio is reduced by $\sim$0.1% due to the corrections near the north pole, whereas it is enhanced $\sim$0.1% in the vicinity of the south pole. If the north/south asymmetry of the neutrino heating persists throughout the later phases, it is expected that the pulsar will be kicked towards the north pole. It is noted that Scheck *et al* [52] recently pointed out that the random velocity perturbation of $\sim$0.1% added artificially several milliseconds after bounce could lead to the global asymmetry of supernova explosion and cause the pulsar-kick. While the orientation of pulsar-kicks is stochastic in their models, the asymmetry of the neutrino heating in the strong magnetic fields considered here will predict the alignment of a pulsar's magnetic axis and the kick velocity. Further numerical investigations are required to see if this is really the case. It is also interesting to study the effect of the anisotropic neutrino

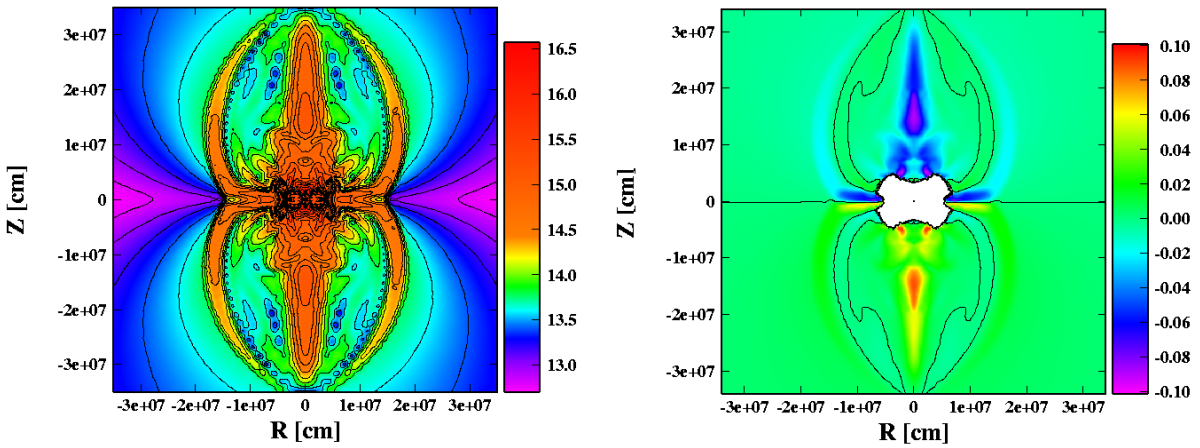

Figure 9. The left panel shows the contour of the logarithm of the magnetic field strength (G). The right panel represents the ratio of the neutrino heating rate with corrections for the parity-violating effect, $Q^{+}_{\nu,\mathrm{B}\neq 0}$, to that without the corrections, $Q^{+}_{\nu,\mathrm{B}=0}$. The values of the colour scale in the right panel are expressed in percentage. Note that the corrections due to the parity-violating effect are $\sim$0.1% on the south and north poles. The surface of the central white region in the right panel represents the neutrino sphere.

radiation in the strong magnetic field on the growth of the convective instability and/or MRI in the later phases [98].

4. Summary

In this article we have reviewed the current status of our theoretical understanding of the collapse-driven supernova. Even the most sophisticated models have not produced a successful explosion so far, although the margin of the theoretical models and the reality seems to have narrowed considerably. We have paid particular attention to the global asymmetry of the dynamics, which may be induced either by rapid rotation or strong magnetic fields of the core. We have solved numerically both static and dynamical equations for rotational cores. Both of them suggest that the rapid rotation and the ensuing anisotropic neutrino radiations are helpful for the shock revival. Strong poloidal magnetic fields may give a substantial kick to the neutron star through the north/south asymmetry of neutrino heating. The origin of the strong magnetic fields remains to be clarified and might be important for the formation of not only magnetars but also ordinary pulsars.

Neutrinos are important from the observational point of view. From the next galactic supernova, we will detect about 10 000 neutrinos, which will reveal the mystery not only of the supernova mechanism but also of neutrino itself. In this respect, the gravitational wave is another important messenger from deep inside massive stars. It will provide us with information, which even the neutrino could not. If the supernova is really asymmetric as considered in this article, we may have a good chance to detect both neutrinos and gravitational waves simultaneously.

We have summarized our recent results on this issue in the appendix, to which we would like to refer interested readers.

As theoreticians, we sincerely hope to be able to make clear the supernova mechanism and the related issues before observations tell us all.

Acknowledgments

This work was partially supported by the Grant-in-Aid for the 21st century COE program 'Holistic Research and Education Center for Physics of Self-organization Systems' and the Grants-in-Aid for Scientific Research (14102004, 14740166, 14079202) of the Ministry of Education, Science, Sports and Culture of Japan. Some of the numerical simulations were done on the supercomputer VPP700E/128 at RIKEN and VPP500/80 at KEK (KEK Supercomputer Projects 02-87 and 03-92).

Appendix. Gravitational waves from the rotational and magnetorotational core-collapse

Here we discuss the gravitational wave from the rotational core-collapse described above. Asymmetric core collapse supernovae have been supposed to be some of the most plausible sources of gravitational radiation for the long-baseline laser interferometers (GEO600, LIGO, TAMA, VIRGO) [80]. The detection of the gravitational signal is important not only for the direct confirmation of general relativity but also for the understanding of supernovae themselves. Combined with neutrino signals, the gravitational wave will enable us to see directly the innermost part of an evolved star, where the angular momentum distribution and the EOS are unknown.

A burst-type gravitational wave is expected to be radiated mainly at the core bounce (see [82, 83] for possible gravitational radiation due to the anisotropic neutrino radiation and the convective motions). Employing the quadrupole formula, we calculated the waveforms of the gravitational wave [84, 85]. First of all, we show the general properties of the waveform with collapse dynamics. The waveform for a typical model is given in the left panel of figure A.1. As the inner core shrinks, the central density increases and the core bounce occurs when the central density reaches its peak at $t_b \cong 243$ ms. At this time, the absolute value of the amplitude becomes maximal. After the core bounce, the core slightly re-expands and oscillates around its equilibrium. As a result, the gravitational wave shows several small bursts and begins to decay. These gross properties are common to all other models. However, there exist some important differences when we compare them in more detail. We will summarize the differences in the following.

In the right panel of figure A.1, the waveform is given for the model, which has a cylindrical rotation law with strong differential rotation. By comparing the left with the right panel of figure A.1, the oscillation period of the inner core for the model in the right panel is clearly longer than that in the left panel. In other words, the pronounced peaks can be seen distinctively in this case. This is because the central density becomes much smaller after the distinct bursts by the strong differential rotation. This effect increases with the initial angular momentum. It is also found that the sign of the second peak is negative in the left panel, while it is

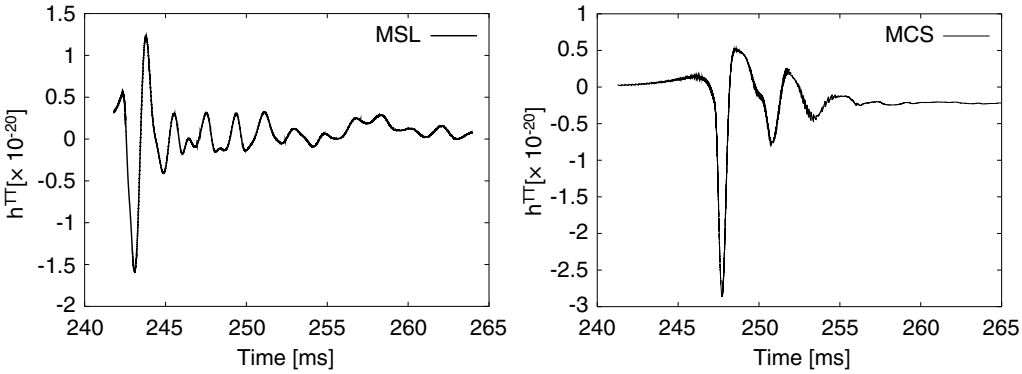

Figure A.1. Time evolutions of the amplitude of gravitational wave for the representative models. Note that the source is assumed to be located at a distance of 10 kpc.

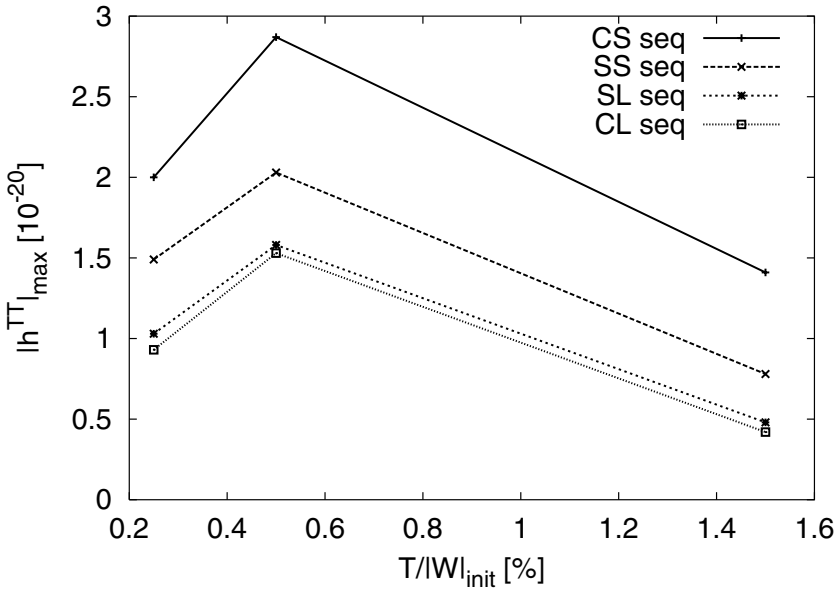

Figure A.2. Relations between $T/|W|_{\rm init}$ and the peak amplitude $|h^{\rm TT}|_{\rm max}$ for all the models [84]. In the figure, CS, SS, SL, CL seq represent the model sequences whose initial rotation profiles differ (see [84] for details). Note that the source is assumed to be located at a distance of 10 kpc.

positive for the model in the right panel. Note that we are speaking of the second peak where the absolute amplitude is the second largest. This characteristic that the sign of the second peak is negative is common to the models with strong differential rotation and the cylindrical rotation law.

Next we discuss the relation between the maximum amplitudes of gravitational wave and the initial $T/|W|$, which is the ratio of the rotational to the gravitational energy. From figure A.2, it is found that the largest amplitude is obtained for the moderate initial rotation rate (i.e. $T/|W|_{\rm init} = 0.5\%$) when one fixes the initial rotation law and the degree of differential

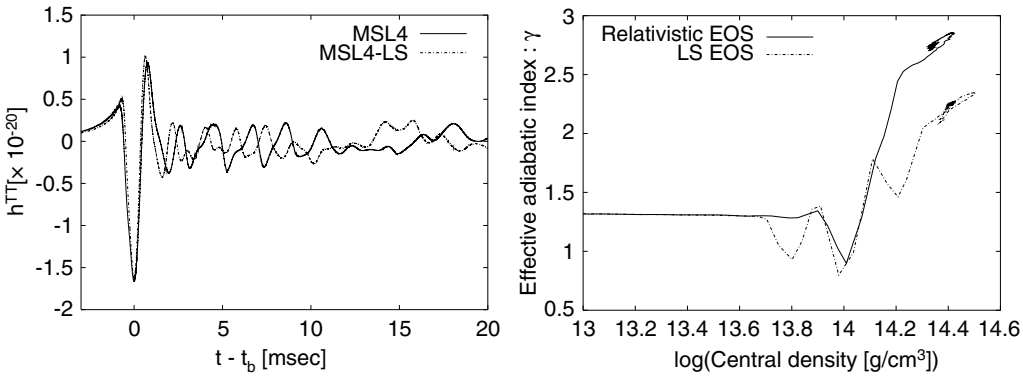

Figure A.3. Waveforms (left panel) for the models with the relativistic EOS (the solid line labelled as MSL4) and with LS EOS (the dashed line labelled as MSL4-LS) and the relation between the central density and the effective adiabatic index γ near core bounce (right panel).

rotation. This is understood as follows. The amplitude of the gravitational wave is roughly proportional to the inverse square of the typical dynamical scale, $t_{\rm dyn}$. Since $t_{\rm dyn}$ is proportional to the inverse square root of the central density ρ, the amplitude is proportional to the density. As a result, the amplitude becomes smaller as the initial rotation rates become larger because the density then decreases. On the other hand, the amplitude is proportional to the quadrupole moment, which becomes larger in turn as the total angular momentum increases. This is because stronger centrifugal forces not only make the mass of the inner core larger, but also deform it. The amplitude of gravitational wave is determined by the competition of these factors. As a result, the amplitudes become maximal for moderate initial rotation rates. According to the study of rotational core collapse by Kotake *et al* [46, 62], considerable anisotropy of neutrino radiation is induced by such rotation rates.

We turn to the effect of the EOS on the gravitational signals. Needless to say, EOS is an important microphysical ingredient for determining the dynamics of core collapse and, eventually, the gravitational wave amplitude. As a realistic EOS, Lattimer–Swesty (LS) EOS [28] has been used in recent papers discussing gravitational radiations from the rotational core collapse [81, 82]. It has been difficult to investigate the effect of EOSs on the gravitational signals because available EOSs based on different nuclear models are limited. Recently, a new complete EOS for supernova simulations has become available [29, 86]. The EOS is based on the RMF theory combined with the Thomas–Fermi approach. By implementing these two realistic EOSs, we look at the differences in the gravitational wave signals. The left panel of figure A.3 shows the waveforms for the models with the relativistic EOS (model MSL4) or the LS EOS (model MSL4-LS). The maximum amplitudes for the two models do not differ significantly. The important difference of the two EOSs is the stiffness. As seen from the right panel of figure A.3, LS EOS is softer than the relativistic EOS. As stated, the amplitude of the gravitational wave is roughly proportional to the central density and, therefore, becomes larger for softer EOS. On the other hand, the amplitude is also proportional to the quadrupole moment, which in turn becomes smaller for softer EOS because the inner core is smaller then. The maximum amplitude is determined by the competition between

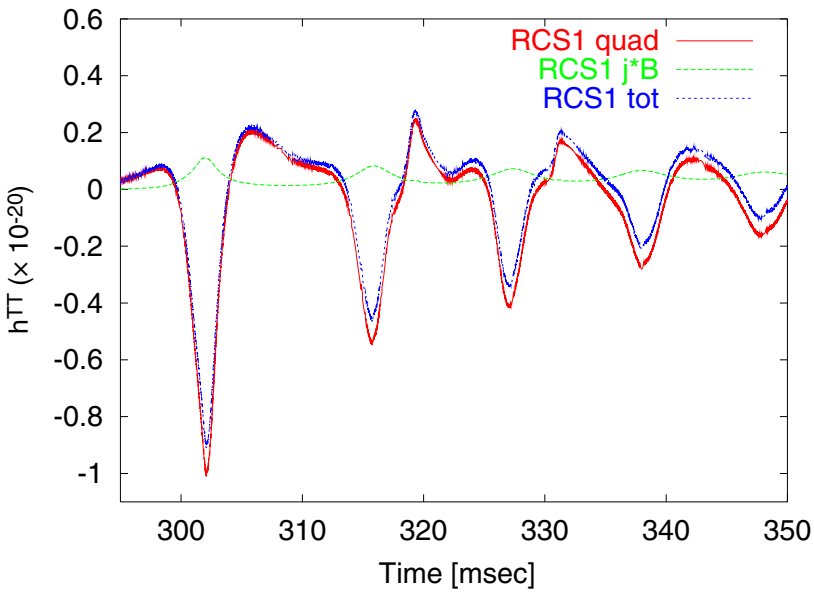

Figure A.4. Waveforms for a model with the strongest magnetic field in our computations [85]. In the figure, quad and $j \times B$ represent the contributions from the mass quadrupole moment and from the electromagnetic field, respectively. The total amplitude is denoted as 'tot'. Note that the source is assumed to be located at a distance of 10 kpc.

these factors. As a result, the peak amplitude becomes almost identical between LS EOS and the relativistic EOS.

We also studied the effect of magnetic fields on the gravitational signals. We derived the quadrupole formula including contributions from the electromagnetic fields [61, 85]. It is found that the amplitude is affected in the strongly magnetized models whose initial $E_m/|W|$ is greater than 0.1%. This is natural because the amplitude contributed from the electromagnetic fields should be of the order of $R_{mag} = (B_c^2/8\pi c^2)/\rho_c \sim 10\%$ $[B_c/(\text{several} \times 10^{17}\,\text{G})]^2[\rho_c/(10^{13}\,\text{g cm}^{-3})]^{-1}$, with B_c and ρ_c being the central magnetic field and the central density, respectively. Thus, strongly magnetized models, whose central magnetic fields at core bounce become as high as $\sim 10^{17}$ G, can affect the amplitude. Furthermore, it is found that the contribution of the electromagnetic fields changes in the opposite phase to the matter contribution (see figure A.4). Together with a slight offset of the electromagnetic part, the negative part of the amplitude becomes less negative, whereas the positive part becomes more positive. The peak amplitude at core bounce is lowered by $\sim$10%.

The maximum amplitudes for all our models with or without magnetic fields range from $5 \times 10^{-21} \leqslant h^{TT} \leqslant 3 \times 10^{-20}$ for a source at the distance of 10 kpc. This is almost the same as obtained in previous studies on rotational core-collapse simulations [61], [87]–[93]. The absolute peak amplitudes are presented in figure A.5. If a source is located within 10 kpc, they are mostly within the detection limits of TAMA and the first LIGO now in operation. The result is not changed even if the central core prior to core collapse has very strong magnetic fields of $\sim 10^{14}$ G. As pointed out earlier, we find that the sign of the second peak is negative for the models with strong differential rotation and cylindrical rotation laws, whereas it is positive

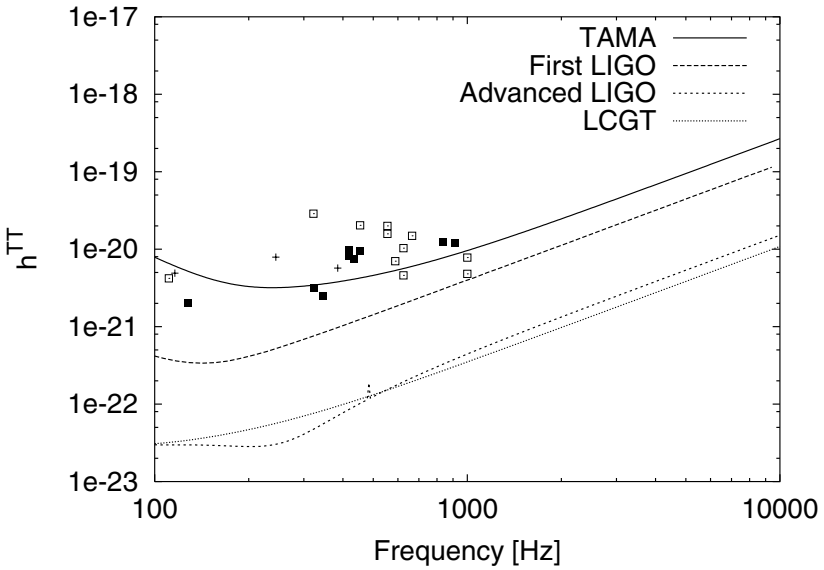

Figure A.5. Detection limits of TAMA [94], first LIGO [95], advanced LIGO [96], and LCGT [97] with the amplitudes from numerical simulations. The open squares represent the maximum amplitudes for all the models, whereas the plus signs and the closed squares stand for the amplitudes of the second peaks for the models with strong differential rotation and cylindrical rotation law and for the other models, respectively. Note that the source is assumed to be located at a distance of 10 kpc.

for the others. The absolute amplitudes of the second peak are also shown in figure A.5. They are also within the detection limit of the first LIGO for a source within 10 kpc. In addition, it seems quite possible for the detectors of next generation such as the advanced LIGO and LCGT to detect the difference in the sign. Therefore, we may be able to obtain in this way the otherwise inaccessible information about the angular momentum distribution of evolved massive stars.

References

[1] Wheeler J C 2003 *Am. J. Phys.* **71** 11
[2] Arnett W D, Bahcall J N, Kirshner R P and Woosley S E 1989 *Ann. Rev. Astron. Astrophys.* **27** 629
[3] Suzuki H 1994 *Physics and Astrophysics of Neutrinos* ed M Fukigita and A Suzuki (Tokyo: Springer) p 763
[4] Rampp M and Janka H T 2000 *Astrophys. J. Lett.* **539** L33
[5] Liebendörfer M, Mezzacappa A, Thilemann F K, Messer O E B, Hix W R and Bruenn S W 2001 *Phys. Rev.* D **63** 103004
[6] Thompson T A, Burrows A and Pinto P A 2003 *Astrophys. J.* **592** 434
[7] Liebendörfer M, Rampp M, Janka H T and Mezzacappa A 2003 *Astrophys. J.* submitted
[8] Buras R, Rampp M, Janka H T and Kifonidis K 2003 *Phys. Rev. Lett.* **90** 241101
[9] Janka H-Th, Buras R, Kifonidis K, Marek A and Rampp M 2004 *Proc. IAU Colloquium 192, 'Supernovae'* ed J M Marcaide and K W Weiler (Berlin: Springer)
[10] Woosley S E, Heger A and Weaver T A 2002 *Rev. Mod. Phys.* **74** 1015
[11] Qian Y-Z 2003 *Prog. Part. Nucl. Phys.* **50** 153

[12] Raffelt G G 2002 *Proc. Texas in Tuscany* December
[13] New K C B 2003 *Living Rev. Rel.* **6** 2
[14] Lazzati D 2004 *Xth Marcel Grossmann Meeting on General Relativity, Rio de Janeiro, Brazil, July 2003*
[15] Hjorth J *et al* 2003 *Nature* **423** 847
[16] Mazzali *et al* 2003 *Astrophys. J. Lett.* **599** L95
[17] Podsiadlowski Ph, Mazzali P A, Nomoto K, Lazzati D and Cappellaro E 2004 *Astrophys. J. Lett.* in press
[18] Fryer C L 1999 *Astrophys. J.* **522** 413
[19] Nomoto K *et al* 2003 *Prog. Theor. Phys. Suppl.* **151** 44
[20] Heger A, Fryer C L, Woosley S E, Langer N and Hartmann D H 2003 *Astrophys. J.* **591** 288
[21] Langanke K *et al* 2004 *Phys. Rev. Lett.* **90** 241102
[22] Bruenn S W 1985 *Astrophys. J. Suppl.* **58** 771
[23] Janka H-Th and Müller E 1996 *Astron. Astrophys.* **306** 167
[24] Burrows A and Goshy J 1993 *Astrophys. J. Lett.* **416** 75
[25] Wilson J R 1982 *Proc. Univ. Illinois Meeting on Numerical Astrophysics*
[26] Livne E, Burrows A, Walder R, Lichtenstadt I and Thompson T A 2003 *Astrophys. J.* submitted
[27] Burrows A, Reddy S and Thompson T A 2004 *Nucl. Phys.* A in press
[28] Lattimer J M and Swesty F D 1991 *Nucl. Phys.* A **535** 331
[29] Shen H, Toki H, Oyamatsu K and Sumiyoshi K 1998 *Nucl. Phys.* A **637** 43
[30] Burrows A and Sawyer R F 1998 *Phys. Rev.* C **58** 554
[31] Reddy S *et al* 1999 *Phys. Rev.* C **59** 2888
[32] Yamada S and Toki H 2000 *Phys. Rev.* C **61** 015803
[33] Mornas L and Perez A 2002 *Eur. Phys. J.* A **13** 383
[34] Thompson T A, Burrows A and Horvath J E 2000 *Phys. Rev.* C **62** 035802
[35] Horowitz C J and Perez-Garcia M A 2003 *Phys. Rev.* C **68** 025803
[36] Keil M Th, Raffelt G G and Janka H-Th 2003 *Astrophys. J.* **590** 971
[37] Wheeler C J 2004 *Proc. on 'Cosmic Explosions in Three Dimensions: Asymmetries in Supernovae and Gamma-Ray Bursts'* ed P Hoeflich, P Kumar and J C Wheeler (Cambridge: Cambridge University Press)
[38] Blondin J M, Mezzacappa A and DeMarino C 2003 *Astrophys. J.* **584** 971
[39] Herant M, Benz W, Hix W R, Fryer C L and Colgate S A 1994 *Astrophys. J.* **435** 339
[40] Burrows A, Hayes J and Fryxell B A 1995 *Astrophys. J.* **450** 830
[41] Keil W, Janka H-Th and Müller E 1996 *Astrophys. J. Lett.* **473** L111
[42] Mezzacappa A *et al* 1998 *Astrophys. J.* **493** 848
[43] Fryer C L and Heger A 2000 *Astrophys. J.* **541** 1033
[44] Yamada S and Sato K 1994 *Astrophys. J.* **434** 268
[45] Shimizu T M, Ebisuzaki T, Sato K and Yamada S 2001 *Astrophys. J.* **552** 756
[46] Kotake K, Yamada S and Sato K 2003 *Astrophys. J.* **595** 304
[47] Pun C S J and The Supernova Intensive Studies (SNIS) Collaboration 2001 *AAS Meeting* 199 94 02
[48] Wang L *et al* 2002 *Astrophys. J.* **579** 671
[49] Wang L, Wheeler J C, Li Z and Clocchiatti A 1996 *Astrophys. J.* **467** 435
[50] Leonard D C, Filippenko A V, Barth A J and Matheson T 2000 *Astrophys. J.* **536** 239
[51] Wang L, Howell D A, Höflich P and Wheeler J C 2001 *Astrophys. J.* **550** 1030
[52] Scheck L, Plewa T, Janka H T, Kifonidis K and Müller E 2004 *Phys. Rev. lett.* **92** 011103
[53] Heger A, Langer N and Woosley S E 2000 *Astrophys. J.* **528** 368
[54] Spruit H C 2002 *Astron. Astrophys.* **381** 923
[55] Heger A, Woosley S E, Langer N and Spruit H C 2003 *Proc. IAU 215 Stellar Rotation* (*Preprint* astro-ph/0301374), to appear
[56] Müller E, Rampp M, Buras R and Janka H-Th 2004 *Astrophys. J.* **603** 221
[57] LeBlanc J M and Wilson J R 1970 *Astrophys. J.* **161** 541
[58] Müller E and Hillebrandt W 1979 *Astron. Astrophys.* **80** 147
[59] Symbalisty E 1984 *Astrophys. J.* **360** 242

[60] Ardeljan N V, Bisnovatyi-Kogan G S and Moiseenko S G 2000 *Astron. Astrophys.* **355** 1181
[61] Yamada S and Sawai H 2004 *Astrophys. J.* in press
[62] Kotake K, Sawai H, Yamada S and Sato K 2004 *Astrophys. J.* in press
[63] Zhang B and Harding A K 2000 *Astrophys. J. Lett.* **535** L51
[64] Guseinov O H, Yazgan E, Ankay A and Tagieva S 2003 *Int. J. Mod. Phys.* D **12** 1
[65] Akiyama S, Wheeler J C, Meier D L and Lichtenstadt I 2003 *Astrophys. J.* **584** 954
[66] Shapiro S L and Teukolsky S A 1983 *Black Holes, White Dwarfs, and Neutron Stars* (New York: Wiley) p 412
[67] Yamasaki T, Yamada S and Kotake K 2004 in preparation
[68] Tassoul J L 1978 *Theory of Rotating Stars* (Princeton, NJ: Princeton University Press)
[69] Müller E and Hillebrandt W 1981 *Astron. Astrophys.* **103** 358
[70] Bodenheimer P and Woosley S E 1983 *Astrophys. J.* **269** 281
[71] Mönchmeyer R M and Müller E 1989 *Timing Neutron Stars, NATO ASI Series* ed H Ögelman and E P J van der Heuvel (New York: ASI)
[72] Stone J M and Norman M L 1992 *Astrophys. J. Suppl.* **80** 753
[73] Woosley S E and Weaver T A 1995 Private communication
[74] Balbus S A and Hawley J F 1992 *Astrophys. J.* **400** 610
[75] Bisnovatyi-Kogan G S and Ruzmaikin A A 1976 *Astrophys. Sp. Sci.* **42** 401
[76] Meier D L, Epstein R I, Arnett W D and Schramm D N 1976 *Astrophys. J.* **204** 869
[77] Horowitz C J and Li G 1998 *Phys. Rev. Lett.* **80** 3694
[78] Arras P and Lai D 1999 *Phys. Rev.* D **60** 43001
[79] Ando S 2003 *Phys. Rev.* D **68** 063002
[80] Cutler C and Thorne K S 2001 *Proc. GR16, Durban, South Africa*
[81] Ott C D, Burrows A, Livne E and Walder R 2004 *Astrophys. J.* in press
[82] Müller E, Rampp M, Buras R, Janka H T and Shoemaker D H 2004 *Astrophys. J.* **603** 221
[83] Burrows A and Hayes J 1996 *Phys. Rev. Lett.* **76** 352
[84] Kotake K, Yamada S and Sato K 2003 *Phys. Rev.* D **68** 044023
[85] Kotake K, Yamada S, Sato K, Sumiyoshi K, Ono H and Suzuki H 2004 *Phys. Rev.* D in press
[86] Sumiyoshi K, Suzuki H, Yamada S and Toki H 2004 *Nucl. Phys.* A **730** 227
[87] Mönchmeyer R, Schäfer G, Müller E and Kates R E 1991 *Astron. Astrophys.* **246** 417
[88] Yamada S and Sato K 1995 *Astrophys. J.* **450** 245
[89] Zweger T and Müller E 1997 *Astron. Astrophys.* **320** 209
[90] Rampp M, Müller E and Ruffert M 1998 *Astron. Astrophys.* **332** 969R
[91] Dimmelmeier H, Font J A and Müller E 2002 *Astron. Astrophys.* **393** 523D
[92] Fryer C L, Holz D E and Hughes S A 2002 *Astrophys. J.* **565** 430
[93] Shibata M 2003 *Phys. Rev.* D **67** 024033
[94] Ando M and TAMA Collaboration 2002 *Class. Quantum Grav.* **19** 1409
[95] Thorne K S 1995 Gravitational waves *Proc. Snowmass 95 Summer Study on Particle and Nuclear Astrophysics and Cosmology* (Singapore: World Scientific) p 398
[96] Weinstein A 2002 *Class. Quantum Grav.* **19** 1575
[97] LCGT Collaboration 1997 *Int. J. Mod. Phys.* D **5** 557
[98] Kotake *et al* 2004 in preparation

New Journal of Physics
An Institute of Physics and Deutsche Physikalische Gesellschaft Journal

Physics of the neutrino mass

R N Mohapatra
Department of Physics, University of Maryland, College Park, MD 20742, USA
E-mail: rmohapat@physics.umd.edu

New Journal of Physics **6** (2004) 82
Received 17 May 2004
Published 14 July 2004
Online at http://www.njp.org/
doi:10.1088/1367-2630/6/1/082

Abstract. Recent neutrino oscillation experiments have yielded valuable information on the nature of neutrino masses and mixings and qualify as the first evidence for physics beyond the standard model. Even though we are far from a complete understanding of the new physics implied by them, there are many useful hints. As the next precision era in neutrino physics is about to be launched, we review the physics of neutrino mass: what we have learned and what we are going to learn.

PII: S1367-2630(04)80842-5
© IOP Publishing Ltd and Deutsche Physikalische Gesellschaft

Contents

Section 1 **3**
1.1. Introduction . . . 3
1.2. Two-component notation for neutrinos . . . 5
1.2.1. Neutrinoless double beta decay and neutrino mass . . . 7
1.2.2. Neutrino mass in two-component notation . . . 7
1.3. Experimental indications for neutrino masses . . . 9
1.3.1. Atmospheric neutrinos . . . 10
1.3.2. Solar neutrinos . . . 10
1.3.3. LSND . . . 11
1.3.4. Neutrinoless double beta decay and tritium decay experiment . . . 11
1.4. Patterns and textures for neutrinos . . . 12
1.5. Neutrino mixing matrix and mass patterns . . . 13
1.6. Neutrino mass textures . . . 15
1.7. Inverted hierarchy and L_e–L_μ–L_τ symmetry . . . 18
1.8. CP violation . . . 19
Section 2 **20**
2.1. Why neutrino mass requires physics beyond the standard model . . . 20
2.2. Seesaw and the right-handed neutrino . . . 22
2.2.1. Why is $M_{\nu_R} \ll M_{P\ell}$? . . . 23
2.2.2. Small neutrino mass using a double seesaw mechanism with ν_R . . . 23
2.3. A gauge model for seesaw mechanism: left–right symmetric unification and type II seesaw . . . 24
2.4. Understanding detailed pattern for neutrinos using the seesaw formula . . . 27
2.5. General consequences of the seesaw formula for neutrino masses . . . 27
2.6. L_e–L_μ–L_τ symmetry and 3×2 seesaw . . . 28
2.7. SO(10) realization of the seesaw mechanism . . . 29
2.7.1. Breaking $B - L$ symmetry: **16** versus **126** . . . 30
2.8. A minimal SO(10) model for neutrinos with **126** . . . 30
2.9. Type II seesaw and quasi-degenerate neutrinos . . . 33
Section 3 **34**
3.1. Lepton flavour violation and neutrino masses . . . 34
3.2. Renormalization group evolution of the neutrino mass matrix . . . 37
3.3. Radiative magnification of neutrino mixing angles . . . 38
3.4. Generation of solar mass difference square in the case of L_e–L_μ–L_τ symmetric models . . . 39
3.5. A horizontal symmetry approach to near bimaximal mixing . . . 40
Section 4 **42**
4.1. Neutrino masses in models with large extra dimensions . . . 42
4.1.1. Neutrino propagation in matter with a bulk neutrino tower . . . 44
4.2. Phenomenological and cosmological constraints on bulk neutrino models . . . 45
4.2.1. Neutrino oscillation constraints . . . 45
4.2.2. Big Bang nucleosynthesis constraints . . . 45
4.2.3. Enhancement of magnetic moments . . . 46
4.2.4. Other implications . . . 46

4.3. Neutrino mass in low-scale gravity models without bulk neutrinos 47
Conclusions and outlook **49**
Acknowledgments **49**
References **49**

Section 1

1.1. Introduction

For a long time, it was believed that neutrinos were massless, spin-half particles, making them drastically different from their other standard model spin-half cousins such as the charged leptons (e, μ, τ) and the quarks (u, d, s, c, t, b), which are known to have mass. In fact, the masslessness of the neutrino was considered so sacred in the 1950s and 1960s that the fundamental law of weak interaction physics, the successful V-A theory for charged current weak processes proposed by Sudarshan, Marshak, Feynman and Gell-Mann, was considered to be intimately linked to this fact. The argument went as follows: a massless fermion field equation is invariant under the γ_5 transformation; since the neutrino is one such particle and it participates exclusively in weak interactions, the weak interactions must somehow reflect invariance under the γ_5-transformation of all fermionic matter (i.e. quarks, charged leptons and the neutrinos) participating in weak interactions. The argument is obviously very heuristic, but it is not hard to see its profound implication: it leads to the resulting four-Fermi weak interaction to involve only V-A currents. This argument remained persuasive for a long time since there was no evidence for neutrino mass for almost the next 50 years and became a celebrated myth in particle theory.

This myth has however been shattered by the accumulating evidence for neutrino mass from the solar and atmospheric neutrino data compiled in the 1990s and still ongoing. One must therefore now be free to look beyond the γ_5 invariance idea for exploring new physics as we proceed to understand the neutrino mass.

The possibility of a nonzero neutrino mass at phenomenological level goes back almost 50 years.[1] In the context of gauge theories, they were discussed extensively in the 1970s and 1980s long before there was any firm evidence for it. For instance, the left–right symmetric theories of weak interactions introduced in 1974 and discussed in those days in connection with the structure of neutral current weak interactions, predicted nonzero neutrino mass as a necessary consequence of parity invariance and quark lepton symmetry.

The existence of a nonzero neutrino mass makes neutrinos more like the quarks, and allows for mixing between the different neutrino species leading to the phenomenon of neutrino oscillation, an idea first discussed by Pontecorvo [2] and Maki *et al* [2] in the 1960s, unleashing a whole new realm of particle physics phenomena to explore. More importantly, the simple fact that neutrino masses vanish in the standard model implies that evidence for neutrino mass is solid evidence for the existence of new physics beyond the standard model.

We are of course far from a complete picture of the masses and mixings of the various neutrinos and cannot therefore have a full outline of the theory of neutrino masses at present.

[1] For a summary of the recent developments in neutrino physics as well as the historical developments in the field, see [1].

However, there exist enough information and indirect indications that constrain the masses and mixings among the neutrinos that we can see a narrowing of the possibilities for the theories beyond the standard model. Combined with other ideas outside the neutrino arena such as supersymmetry and unification, the possibility narrows even further. Many clever experiments now in progress will soon clarify or rule out many of the allowed models. It will be one of the goals of this paper to give a panoramic view of the most likely scenarios for new physics that explain what is now known about neutrino masses.[2] Such discussions are of course by nature very subjective and therefore a sincere apology is due at the beginning of this discussion to all those whose ideas are not cited.

We hope to emphasize two kinds of ideas: one which provides a general framework for understanding of the small neutrino masses, the seesaw mechanism and predicts the existence of superheavy right-handed neutrinos. In the opinion of this author, these ideas are likely to be part of the final theory of neutrino masses. We then touch briefly on some specific models that are based on the above general framework but attempt to provide an understanding of the detailed mass and mixing patterns. These works are instructive for several reasons: first they provide proof of the detailed workability of the general ideas described above (sort of existence proofs that things will work); secondly they often illustrate the kind of assumptions needed and through that provide a unique insight into which directions the next step should be; finally of course nature may be generous in picking one of those models as the final message bearer.

In discussing the neutrino mass, it is instructive to compare it with the other well-known fermion, the electron. The electron and the neutrino are in many ways very similar particles: they are both spin-half objects; they both participate in weak interactions with same strength; in fact they are so similar that in the limit of exact gauge symmetries they are two states of the same object and therefore in principle indistinguishable. Yet there are profound differences between them in the standard model: after gauge symmetry breaking, only the electron has electric charge but the neutrinos come out electrically neutral as they should to match observations. Another difference is that only the left-handed neutrinos of each generation are included in the standard model and not their right-handed counterparts, whereas for the e, μ, τ and all the quark flavours, both helicity states are included. The fact that the right-handed neutrino is excluded from the standard model coupled with the fact that $B - L$ is an exact symmetry of the model implies that neutrino remains massless to all orders in perturbation theory as well as nonperturbatively, as we will discuss later on in this review.

The fact that the neutrino has no electric charge endows it with certain properties not shared by other fermions of the standard model. One can write two kinds of Lorentz-invariant mass terms for the neutrino, the Dirac and Majorana masses, whereas for the charged fermions, conservation of electric charge allows only Dirac-type mass terms. In the four-component notation for the fermions, the Dirac mass has the form $\bar{\psi}\psi$, whereas the Majorana mass is of the form $\psi^{\mathrm{T}}C^{-1}\psi$, where ψ is the four-component spinor and C is the charge conjugation matrix. One can also discuss the two different kinds of mass terms using the two-component notation for the spinors, which provides a very useful way to discuss neutrino masses. We therefore present some of the salient concepts behind the two-component description of the neutrino.

[2] See [3] for a summary of theoretical and phenomenological ideas relating to massive neutrinos.

1.2. Two-component notation for neutrinos

Before we start the discussion of the two-component neutrino, let us write down the Dirac equation for an electron:[3]

$$\mathrm{i}\gamma^{\lambda}\partial_{\lambda}\psi - m\psi = 0. \tag{1}$$

This equation follows from a free Lagrangian

$$\mathcal{L} = \mathrm{i}\bar{\psi}\gamma^{\lambda}\partial_{\lambda}\psi - m\bar{\psi}\psi \tag{2}$$

and leads to the relativistic energy momentum relation $p^{\lambda}p_{\lambda} = m^2$ for the spin-half particle only if the four γ_{λ}s anticommute. If we take γ_{λ}s to be $n \times n$ matrices, the smallest value of n for which four anticommuting matrices exist is four. Therefore, ψ must be a four-component spinor. The physical meaning of the four components is as follows: two components for particle spin-up and spin-down and same for the antiparticle.

A spin-half particle is said to be a Majorana particle if the spinor field ψ satisfies the condition of being self-charge conjugate, i.e.

$$\psi = \psi^{c} \equiv C\bar{\psi}^{\mathrm{T}}, \tag{3}$$

where C is the charge conjugation matrix and has the property $C\gamma_{\lambda}C^{-1} = -\gamma^{\lambda^{\mathrm{T}}}$. This constraint reduces the number of independent components of the spinor by a factor of 2, since the particle and the antiparticle are now the same particle. Using this condition, the mass term in the Lagrangian in equation (2) can be written as $\psi^{\mathrm{T}}C^{-1}\psi$, where we have used the fact that C is a unitary matrix. Writing the mass term in this way makes it clear that if a field carries a $U(1)$ charge and the theory is invariant under those $U(1)$ transformations, then the mass term is forbidden. This means that one cannot impose the Majorana condition on a particle that has a gauge charge. Since the neutrinos do not have electric charge, they can be Majorana particles unlike the quarks, electron or the muon. It is of course well known that the gauge boson interactions in a gauge theory Lagrangian conserve a global $U(1)$ symmetry known as lepton number with the neutrino and electron carrying the same lepton number. If lepton number were to be established as an exact symmetry of nature, the Majorana mass for the neutrino would be forbidden and the neutrino, like the electron, would be a Dirac particle.

The properties of a Majorana fermion can be seen in its free-field expansion in terms of creation and annihilation operators:

$$\psi(x) = \int \frac{\mathrm{d}^3 p}{\sqrt{(2\pi)^3 2E_p}} \Sigma_s (a_s(\mathbf{p})u_s(\mathbf{p})\mathrm{e}^{-\mathrm{i}p\cdot x} + a_s^{\dagger}v_s(\mathbf{p})\mathrm{e}^{\mathrm{i}p\cdot x}). \tag{4}$$

In the γ matrix convention where

$$\gamma_i = \begin{pmatrix} 0 & \sigma_i \\ -\sigma_i & 0 \end{pmatrix} \quad \text{and} \quad \gamma_0 = \begin{pmatrix} 0 & \mathbf{I} \\ \mathbf{I} & 0 \end{pmatrix},$$

the u_s and v_s are given by

$$u_s(\mathbf{p}) = \frac{m}{\sqrt{E}} \begin{pmatrix} \alpha_s \\ \frac{E-\sigma\cdot\mathbf{p}}{m}\alpha_s \end{pmatrix} \tag{5}$$

[3] We follow the discussion in [4].

and

$$v_s(\mathbf{p}) = \frac{m}{\sqrt{E}} \begin{pmatrix} -\frac{E+\sigma\cdot\mathbf{p}}{m}\alpha'_s \\ \alpha'_s \end{pmatrix} \tag{6}$$

α_s and α'_s are two component spinors.

If we choose $\alpha'_s = \sigma_2\alpha_s$, we get the relation among the spinors $u_s(\mathbf{p})$ and $v_s(\mathbf{p})$ $C\gamma_0 u_s^*(\mathbf{p}) = v_s(\mathbf{p})$ and the Majorana condition follows. Note that if ψ were to describe a Dirac spinor, then we would have had a different creation operator $b^\dagger$ in the second term in the free-field expansion above.

The origin of the two-component neutrino is rooted in the isomorphism between the Lorentz group and the SL(2, C) group. The latter is defined as the set of 2×2 complex matrices with unit determinant, whose generators satisfy the same Lie algebra as that of the Lorentz group. Its basic representations are 2- and 2*-dimensional. These are the spinor representations and can be used to describe spin-half particles.

We can therefore write the familiar four-component Dirac spinor used in the text books to describe an electron can be written as

$$\psi = \begin{pmatrix} \phi \\ \mathrm{i}\sigma_2\chi^* \end{pmatrix},$$

where χ and ϕ two two-component spinors. A Dirac mass is given by $\chi^{\mathrm{T}}\sigma_2\phi$ whereas a Majorana mass is given by $\chi^{\mathrm{T}}\sigma_2\chi$, where σ_a are the Pauli matrices. To make correspondence with the four-component notation, we point out that ϕ and $\mathrm{i}\sigma_2\chi^*$ are nothing but the ψ_L and ψ_R, respectively. It is then clear that χ and ϕ have opposite electric charges; therefore the Dirac mass $\chi^{\mathrm{T}}\sigma_2\phi$ maintains electric charge conservation (as well as any other kind of charge like lepton number, etc).

Two-component neutrino is described by the following Lagrangian:

$$\mathcal{L} = \nu^\dagger \mathrm{i}\sigma^\lambda\partial_\lambda\nu - \frac{\mathrm{i}m}{2}\mathrm{e}^{\mathrm{i}\delta}\nu^{\mathrm{T}}\sigma_2\nu + \frac{\mathrm{i}m}{2}\mathrm{e}^{-\mathrm{i}\delta}\nu^\dagger\sigma_2\nu^*. \tag{7}$$

This leads to the following equation of motion for the field χ:

$$\mathrm{i}\sigma^\lambda\partial_\lambda\chi - \mathrm{i}m\sigma_2\chi^* = 0. \tag{8}$$

As is conventionally done in field theories, we can now give a free-field expansion of the two-component Majorana field in terms of the creation and annihilation operators:

$$\chi(x,t) = \sum_{p,s}[a_{\mathbf{p},s}\alpha_{p,s}\mathrm{e}^{-\mathrm{i}p\cdot x} + a^\dagger_{\mathbf{p},s}\beta_{p,s}\mathrm{e}^{\mathrm{i}p\cdot x}], \tag{9}$$

where the sum on s goes over the spin-up and spin-down states.

Using the field equations for a free massive two-component Majorana spinor, one can show that its expansion in terms of the creation and annihilation operators and two-component spinors

$$\alpha = \begin{pmatrix} 1 \\ 0 \end{pmatrix} \quad \text{and} \quad \beta = \begin{pmatrix} 0 \\ 1 \end{pmatrix}$$

is given by the following expression:

$$\chi(x,t) = \sum_p [a_{\mathbf{p},+}\mathrm{e}^{-\mathrm{i}p\cdot x} - a^\dagger_{\mathbf{p},-}\mathrm{e}^{\mathrm{i}p\cdot x}]\alpha\sqrt{E+p}$$
$$+ \sum_p [a_{\mathbf{p},-}\mathrm{e}^{-p\cdot x} + a^\dagger_{\mathbf{p},+}\mathrm{e}^{\mathrm{i}p\cdot x}]\beta\sqrt{E-p}. \tag{10}$$

Note that in a beta decay process, where a neutron is annihilated and proton is created, the leptonic weak current that is involved is $\bar{e}\nu$ (dropping γ matrices); therefore, along with the electron, what is created predominantly is a right-handed particle (with a wave function α), the amplitude being of order $\sqrt{E+p} \approx \sqrt{2E}$. This is the right-handed antineutrino. The left-handed neutrino is produced with a much smaller amplitude $\sqrt{E-p} \approx m_n u/E$. Similarly, in the fusion reaction in the core of the Sun, what is produced is a left-handed state of the neutrino with a very tiny, i.e. $\mathrm{O}(m_\nu/E)$ admixture of the right-handed helicity.

1.2.1. Neutrinoless double beta decay and neutrino mass. As already noted, a Majorana neutrino breaks lepton number by two units. This has the experimentally testable prediction that it leads to the process of neutrinoless double beta decay, where a nucleus (generally even–even nuclei) $(Z, N) \to (Z+2, N-2) + 2e^-$. We will now show by using the above property of the Majorana neutrino that if light neutrino exchange is responsible for this process, then the amplitude is proportional to the neutrino mass.

Double beta decay involves the change of two neutrons to two protons and therefore has to be a second-order weak interaction process. Since each weak interaction process emits an antineutrino, in second-order weak interaction, the final state will involve two anti-neutrinos. But in neutrinoless double beta decay, there are no neutrinos in the final state; therefore the two neutrinos must go into the vacuum state. The vacuum state by definition has no spin whereas the antineutrino emitted in a beta decay has spin. Consider the antineutrino from one of the decays: it must be predominantly right-handed. But to disappear into vacuum, it must combine with a left-handed antineutrino so that the left- and right-handed spin projections add up to zero. In the previous section, we showed that the fraction of left-handed spin projection in a neutrino emitted in beta decay is m_ν/E. Therefore, $\bar{\nu}_e\bar{\nu}_e \to |0\rangle$ must be proportional to the neutrino mass. Thus neutrinoless double beta decay is a very sensitive measure of neutrino mass.

1.2.2. Neutrino mass in two-component notation. Let us now discuss the general neutrino mass for Majorana neutrinos. We have seen earlier that for a Majorana neutrinos, there are two different ways to write a mass term consistent with relativistic invariance. This richness in the possibility for neutrino masses also has a down side in the sense that, in general, there are more parameters describing the masses of the neutrinos than those for the quarks and leptons. For instance, for the electron and quarks, dynamics (electric charge conservation) reduces the number of parameters in their mass matrix. As an example, using the two-component notation for all fermions, for the case of two two-component spinors, a charged fermion mass will be described only by one parameter whereas for a neutrino, there will be three parameters. This difference increases rapidly, e.g. for $2N$ spinors, to describe charged fermion masses, we need N^2 parameters (ignoring CP violation), whereas for neutrinos, we need $2N(2N+1)/2$ parameters. What is more interesting is that for a neutrino-like particle, one can have both even and odd number of two-component objects and have a consistent theory.

In this paper, we will use two-component notation for neutrinos. Thus when we say that there are N neutrinos, we will mean N two-component neutrinos.

In the two-component language, all massive neutrinos are Majorana particles and what is conventionally called a Dirac neutrino is really a very specific choice of mass parameters for the Majorana neutrino. Let us give some examples: if there is only one two-component neutrino (we will drop the prefix two-component henceforth), it can have a mass $m\nu^{\mathrm{T}}\sigma_2\nu$ (to be called $\equiv m\nu\nu$ in short-handed notation). The neutrino is now a self-conjugate object which can be seen if we write an equivalent four-component spinor ψ:

$$\psi = \begin{pmatrix} \nu \\ \mathrm{i}\sigma_2\nu^* \end{pmatrix}. \tag{11}$$

Note that this four-component spinor satisfies the condition

$$\psi = \psi^c \equiv C\bar{\psi}^{\mathrm{T}}. \tag{12}$$

This condition implies that the neutrino is its own anti-particle, a fact more transparent in the four- rather than the two-component notation. The above exercise illustrates an important point, i.e. given any two-component spinor, one can always write a self-conjugate (or Majorana) four-component spinor. Whether a particle is really its own antiparticle or not is therefore determined by its interactions. To see this for the electrons, one may solve the following excercise: i.e. if we wrote two Majorana spinors using the two two-component spinors that describe the charged fermion (electron), then until we turn on the electromagnetic interactions and the mass term, we will not know whether the electron is its own antiparticle or not. Once we turn on the electromagnetism, this ambiguity is resolved.

Let us now go one step further and consider two two-component neutrinos (ν_1, ν_2). The general mass matrix for this case is given by

$$\mathcal{M}_{2\times 2} = \begin{pmatrix} m_1 & m_3 \\ m_3 & m_2 \end{pmatrix}. \tag{13}$$

Note first that this is a symmetric matrix and can be diagonalized by orthogonal transformations. The eigenstates which will be certain admixtures of the original neutrinos now describe self-conjugate particles. One can look at some special cases.

Case (i): If we have $m_{1,2} = 0$ and $m_3 \neq 0$, then one can assign a charge +1 to ν_1 and -1 to ν_2 under some $U(1)$ symmetry other than electromagnetism and the theory is invariant under this extra $U(1)$ symmetry, which can be identified as the lepton number and the particle is then called a Dirac neutrino. The point to be noted is that the Dirac neutrino is a special case of two Majorana neutrinos. In fact, if we insisted on calling this case one with two Majorana neutrinos, then the two will have equal and opposite (in sign) mass as can be seen diagonalizing the above mass matrix. Thus, a Dirac neutrino can be thought of as two Majorana neutrinos with equal and opposite (in sign) masses. Since the argument of a complex mass term in general refers to its C transformation property (i.e. $\psi^c = \mathrm{e}^{\mathrm{i}\delta_m}\psi$, where δ_m is the phase of the complex mass term), the two two-component fields of a Dirac neutrino have opposite charge conjugation properties.

Case (ii): If we have $m_{1,2} \ll m_3$, this case is called pseudo-Dirac neutrino since this is a slight departure from case (i). In reality, in this case also the neutrinos are Majorana neutrinos with their masses $\pm m_0 + \delta$ with $\delta \ll m_0$. The two-component neutrinos will be maximally mixed.

Thus this case is of great current physical interest in view of the atmospheric (and perhaps solar) neutrino data.

Case (iii): There is a third case where one may have $m_1 = 0$ and $m_3 \ll m_2$. In this case, the eigenvalues of the neutrino mass matrix are given, respectively, by $m_\nu \simeq -m_3^2/m_2$ and $M \simeq m_2$. One may wonder under what conditions such a situation may arise in a realistic gauge model. It turns out that if ν_1 transforms as an $SU(2)_L$ doublet and ν_2 is an $SU(2)_L$ singlet, then the value of m_3 is limited by the weak scale, whereas m_2 has no such limit and $m_1 = 0$ if the theory has no $SU(2)_L$ triplet field (as for instance is the case in the standard model). Choosing $m_2 \gg m_3$ then provides a natural way to understand the smallness of the neutrino masses. This is known as the seesaw mechanism [5]. Since this case is very different from cases (i) and (ii), it is generally said that in grand unified theories, one expects the neutrinos to be Majorana particles. The reason is that in most grand unified theories there is a higher scale which under appropriate situations provides a natural home for the large mass m_2.

While we have so far used only two neutrinos to exemplify the various cases including the seesaw mechanism, these discussions generalize when $m_{1,2,3}$ are each $N \times N$ matrices (which we denote by $M_{1,2,3}$). For example, the seesaw formula for this general situation can be written as

$$\mathcal{M}_\nu \simeq -M_{3D}^{\mathrm{T}} M_{2R}^{-1} M_{3D}, \tag{14}$$

where the subscripts D and R are used in anticipation of their origin in gauge theories where M_D turns out to be the Dirac matrix and M_R is the mass matrix of the right-handed neutrinos and all eigenvalues of M_R are much larger than the elements of M_D. It is also worth pointing out that equation (13) can be written in a more general form, where the Dirac matrices are not necessarily square matrices but $N \times M$ matrices with $N \neq M$. We give such examples below.

Although there is no experimental proof that neutrino is a Majorana particle, the general opinion is that since the seesaw mechanism provides such a simple way to understand the glaring differences between the masses of the neutrinos and the charged fermions and since it implies that the neutrinos are Majorana fermions, they indeed are most likely to be Majorana particles.

Even though, for most situations, the neutrino can be treated as a two-component object regardless of whether its mass is of Dirac or Majorana type, there are certain practical situations where differences between the Majorana and Dirac neutrino become explicit: one case is when the two neutrinos annihilate. For Dirac neutrinos, the particle and the antiparticle are distinct and therefore there annihilation is not restricted by Pauli principle in any manner. However, for the case of Majorana neutrinos, the identity of neutrinos and antineutrinos plays an important role and one finds that the annihilation to the Z-bosons occurs only via the P-waves. Similarly, in the decay of the neutrino to any final state, the decay rate for the Majorana neutrino is a factor of 2 higher than for the Dirac neutrino.

1.3. Experimental indications for neutrino masses

Much has been said about the experimental evidences for neutrino masses and their analyses to determine the current favourite values for the various mass differences as well as mixing angles. I will therefore only summarize the main points that are relevant for our present understanding of neutrino masses and for the sake of completeness (see [6] for a detailed discussion).

At present there is no conclusive evidence for neutrino masses from direct search experiments for neutrino masses using tritium beta decay and neutrinoless double beta decay (see later).

There are however many experiments that have measured the flux of neutrinos from the Sun and the cosmic rays and which have provided clear evidences for neutrino oscillations i.e. neutrinos of one flavour transmuting to neutrinos of another flavour. Since such transmutation can occur only if the neutrinos have masses and mixings, these experiments provide evidence for neutrino mass. The expression for vacuum oscillation probability for neutrinos of a given energy E that have travelled a distance L is given by

$$P_{\alpha\beta} = \sum_{i,j} |U_{\alpha i} U^*_{\beta i} U^*_{\alpha j} U_{\beta j}| \cos\left(\frac{\Delta_{ij} L}{2E} - \phi_{\alpha\beta,ij}\right). \tag{15}$$

From this it is clear that neutrino oscillation data yield information about the mass difference squares of the neutrinos ($\Delta_{ij} = m_i^2 - m_j^2$) and mixing angles $U_{\alpha i}$. If the neutrino propagates in dense matter, the Mikheyev–Smirnov–Wolfenstein effect [8] will change this formula but it also depends on the same parameters mass difference square and the $U_{\alpha i}$ [9]. The analysis of the data for the atmospheric neutrinos where the neutrino propagates in vacuum and that for solar neutrinos where the effect of dense matter in the Sun is important therefore leads to the following picture for masses and mixings.

1.3.1. Atmospheric neutrinos. In the Super-Kamiokande experiment [10] which confirms the indications of oscillations in earlier data from the Kamiokande, IMB experiments. More recent data from Soudan II and MACRO experiments provide further confirmation of this evidence. The observation here is the following: in the standard model with massless neutrinos, all the muon and electron neutrinos produced at the top of the atmosphere would be expected to reach detectors on the Earth and would be isotropic; what has been observed is that while that is true for the electron neutrinos, the muon neutrino flux observed on the Earth exhibits a strong zenith angle dependence. A simple way to understand this would be to assume that the muon neutrinos oscillate into another undetected species of neutrino on their way to the earth, with a characteristic oscillation length of order of 10 000 km. Since the oscillation length is roughly given by $E(\mathrm{GeV})/\Delta m^2(\mathrm{eV}^2)$ km, for a GeV neutrino, one would expect the particle physics parameter Δm^2 corresponding to the mass difference between the two neutrinos to be around $10^{-33}\,\mathrm{eV}^2$ corresponding to maximal mixing.

From the existing data several important conclusions can be drawn: (i) the data cannot be fit assuming oscillation between ν_μ and ν_e nor $\nu_\mu - \nu_s$, where ν_s is a sterile neutrino which does not any direct weak interaction; and (ii) the oscillation scenario that fit the data best is $\nu_\mu - \nu_\tau$ for the mass and mixing parameters

$$\Delta m^2_{\nu_\mu - \nu_\tau} \simeq (2\text{–}8) \times 10^{-3}\mathrm{eV}^2, \qquad \sin^2 2\theta_{\mu-\tau} \simeq 0.8\text{–}1. \tag{16}$$

1.3.2. Solar neutrinos. The second evidence for neutrino oscillation comes from the seven experiments that have observed a deficit in the flux of neutrinos from the Sun as compared with the predictions of the standard solar model championed by Bahcall and his collaborators [6] and more recently studied by many groups. The experiments responsible for this discovery are the Chlorine, Kamiokande, Gallex, SAGE, Super-Kamiokande, SNO, GNO [7] experiments conducted at the Homestake mine, Kamioka in Japan, Gran Sasso in Italy and Baksan in Russia and Sudbery in Canada. The different experiments see different parts of the solar neutrino spectrum. The details of these considerations are discussed in other lectures. The oscillation interpretation of the solar

neutrino deficit has more facets to it than the atmospheric case: first the final state particle that the ν_e oscillates into and second what kind of Δm^2 and mixings fit the data. At the moment there is a multitude of possibilities. Let us summarize them now.

As far as the final state goes, it can either be one of the two remaining active neutrinos, ν_μ and ν_τ or it can be the sterile neutrino ν_s. SNO neutral current data announced recently has very strongly constrained the second possibility (i.e. the sterile neutrino in the final state). The global analyses of all solar neutrino data seem to favour the so-called large mixing angle MSW solution with parameters $\Delta m^2 \simeq 1.2 \times 10^{-5}$–$3.1 \times 10^{-4}\,\mathrm{eV}^2$; $\sin^2 2\theta \simeq 0.58$–$0.95$.

1.3.3. LSND. Finally, we come to the last indication of neutrino oscillation from the Los Alamos Liquid Scintillation Detector (LSND) experiment [15], where neutrino oscillations both from a stopped muon (DAR) as well as the one accompanying the muon in pion decay (known as the DIF) have been observed. The evidence from the DAR is statistically more significant and is an oscillation from $\bar{\nu}_\mu$ to $\bar{\nu}_e$. The mass and mixing parameter range that fits data is

$$\text{LSND:} \quad \Delta m^2 \simeq 0.2\text{–}2\,\mathrm{eV}^2, \qquad \sin^2 2\theta \simeq 0.003\text{–}0.03. \tag{17}$$

There are also points at higher masses specifically at $6\,\mathrm{eV}^2$, which are also allowed by the present LSND data for small mixings. KARMEN experiment at the Rutherford laboratory has very strongly constrained the allowed parameter range of the LSND data [16]. Currently, the Miniboone experiment at Fermilab is in progress to probe the LSND parameter region [17].

1.3.4. Neutrinoless double beta decay and tritium decay experiment. Oscillation experiments only depend on the difference of mass squares of the different neutrinos and the mixing angles. Therefore, to have a complete picture of neutrino masses, we need other experiments. Two such experiments are the neutrinoless double beta decay searches and the search for neutrino mass from the analysis of the end point of the electron energy spectrum in tritium beta decay.

Neutrinoless double beta decay measures the following combination of masses and mixing angles:

$$\langle m \rangle_{\beta\beta} = \sum_i U_{ei}^2 m_i. \tag{18}$$

Therefore, naively speaking, it is sensitive to the overall neutrino mass scale. However, in practice, as we will see below, for the case of both normal and inverted hierarchies, it is most likely to settle the question of the overall mass scale at the presently contempleted level of sensitivity in double beta decay searches. Only if the neutrino mass patterns are inverse hierarchical does one expect a visible signal in $\beta\beta_{0\nu}$ decay. We do not go into great detail into this issue, except to mention that in drawing any conclusions about neutrino mass from this process, one has to first have a good calculation of nuclear matrix elements of the various nuclei involved such as ^{76}Ge, ^{136}Xe, ^{100}Mo, etc; secondly, another confusing issue has to do with alternative physics contributions to $\beta\beta_{0\nu}$ which are unrelated to neutrino mass. Nevertheless, neutrinoless double beta decay is a fundamental experiment and a nonzero signal will establish a fundamental result that neutrino is a Majorana particle and that lepton number symmetry is violated. Regardless of whether it tells us anything about the neutrino masses, it would provide a fundamental new revelation about physics beyond the standard model. At present, two experiments, Heidelberg–Moscow and IGEX, that use enriched ^{76}Ge have published limits of $\leqslant 0.3\,\mathrm{eV}$ [12].

More recently, evidence for a double beta signal in the Heidelberg–Moscow data has been claimed [13].

Another important result in further understanding of neutrino mass physics could come from the tritium end-point searches for neutrino masses. This experiment will measure the parameter $m_\nu = \sqrt{\sum_i |U_{ei}|^2 m_i^2}$. This involves a different combination of masses and mixing angles than $\langle m \rangle_{\beta\beta}$. At present, the KATRIN proposal for a high-sensitive search for m_ν has been made and it is expected that it can reach a sensitivity of 0.3 eV.

A third source of information on neutrino mass will come from cosmology, where more detailed study of structure in the universe is expected to provide an upper limit on $\sum_i m_i$ of less than an eV.

Our goal now is to study the theoretical implications of these discoveries. We will proceed towards this goal in the following manner: we will isolate the mass patterns that fit the above data and then look for plausible models that can first lead to the general feature that neutrinos have tiny masses; then we would try to understand in simple manner some of the features indicated by the data in the hope that these general ideas will be part of our final understanding of the neutrino masses. As mentioned earlier, to understand the neutrino masses one has to go beyond the standard model. First we will sharpen what we mean by this statement. Then we will present some ideas which may form the basic framework for constructing the detailed models.

1.4. Patterns and textures for neutrinos

As already mentioned, we will assume two-component neutrinos and therefore their masses will in general be Majorana type. Let us also give our notation to facilitate further discussion: the neutrinos emitted in weak processes such as the beta decay or muon decay are weak eigenstates and are not mass eigenstates. The mass eigenstates determine how a neutrino state evolves in time. Similarly, in the detection process, it is the weak eigenstate that is picked out. This is of course the key idea behind neutrino oscillation and the formula presented in the last section. To set the notation, let us express the weak eigenstates in terms of the mass eigenstates. We will denote the weak eigenstate by the symbol α, β or simply e, μ, τ etc whereas the mass eigenstate will be denoted by the symbols i, j, k, etc. To relate the weak eigenstates to the mass eigenstates, let us start with the mass terms in the Lagrangian for the neutrino and the charged leptons:

$$\mathcal{L}_m = \nu_L^{\mathrm{T}} \mathcal{M}_\nu \nu_L + \bar{E}_L M_\ell E_R + \text{h.c.} \tag{19}$$

Here ν and E, which denote the column vectors for neutrinos and charged leptons, are in the weak basis. To go to the mass basis, we diagonalize these matrices as follows:

$$U_L^{\mathrm{T}} \mathcal{M}_\nu U_L = d_\nu, \qquad V_L M_\ell V_R^\dagger = d_\ell. \tag{20}$$

The physical neutrino mixing matrix is then given by

$$\mathbf{U} = V_L U_L. \tag{21}$$

$\mathbf{U}_{\alpha i}$ and relate the two sets of eigenstates (weak and mass) as follows:

$$\begin{pmatrix} \nu_e \\ \nu_\mu \\ \nu_\tau \end{pmatrix} = U \begin{pmatrix} \nu_1 \\ \nu_2 \\ \nu_3 \end{pmatrix}. \tag{22}$$

Using this equation, one can derive the well-known oscillation formulae for the survival probability of a particular weak eigenstate α discussed in the previous section.

To see the general structure of the mixing matrix $\mathbf{U}$, let us recall that the matrix $\mathcal{M}_\nu$ is complex and symmetric and therefore has six complex parameters describing it for the case of three generations. However, since the neutrino is described by a complex field, we can redefine the phases of three fields to remove three parameters. That leaves nine parameters. In terms of observables, there are three mass eigenvalues (m_1, m_2, m_3) and three mixing angles and phases in the mixing matrix $\mathbf{U}$. The three phases can be split into one Dirac phase, which is analogous to the phase in the quark mixing matrix and two Majorana phases. We can then write the matrix $\mathbf{U}$ as

$$\mathbf{U} = U^{(0)} \begin{pmatrix} 1 & & \\ & \mathrm{e}^{\mathrm{i}\phi_1} & \\ & & \mathrm{e}^{\mathrm{i}\phi_2} \end{pmatrix}. \tag{23}$$

The matrix $\mathbf{U}^{(0)}$ has three real angles $\theta_{12}, \theta_{23}, \theta_{13}$ and a phase. The goal of experiments is to determine all nine of these parameters. The knowledge of the nine observables allows one to construct the mass matrix for the neutrinos and from there one can go in search of the new physics beyond the standard model that leads to such a mass matrix.

The neutrino mass observables given above can be separated into two classes: (i) oscillation observables and (ii) nonoscillation observables. The first class of observables are those accessible to neutrino oscillation experiments and are the two mass differences $\Delta m^2_\odot$ and Δm^2_A; three mixing angles θ_{12} (or $\theta_\odot$), θ_{23} (or θ_A) and θ_{13} (the reactor angle, also called U_{e3}) and the CP phase δ in $U^{(0)}$. The remaining three observables which can only be probed by nonoscillation experiments are the lightest mass of the three neutrinos and the two Majorana phases $\phi_{1,2}$.

1.5. Neutrino mixing matrix and mass patterns

Let us first discuss to what extent the oscillation observables are known. Our discussion will focus on the three neutrino fits to all neutrino data which give as central value for $\Delta m^2_A \simeq 0.0025\,\mathrm{eV}^2$; for solar neutrinos, it gives $\Delta m^2_\odot \simeq (2\text{–}20) \times 10^{-5}\,\mathrm{eV}^2$. It also provides information on the angles in $\mathbf{U}$ which can be summarized by the following mixing matrix (neglecting all CP phases):

$$\mathbf{U} = \begin{pmatrix} c & s & \epsilon \\ -\dfrac{s + c\epsilon}{\sqrt{2}} & \dfrac{c - s\epsilon}{\sqrt{2}} & \dfrac{1}{\sqrt{2}} \\ -\dfrac{s - c\epsilon}{\sqrt{2}} & \dfrac{-c - s\epsilon}{\sqrt{2}} & \dfrac{1}{\sqrt{2}} \end{pmatrix}, \tag{24}$$

where $\epsilon \leqslant 0.16$ from the CHOOZ and PALO-VERDE reactor experiments [14]. s is the solar neutrino mixing angle. Present experiments allow the range $0.6 \leqslant \sin^2 2\theta_\odot \leqslant 0.96$ with the central being near 0.8. The atmospheric mixing angle θ_A is close to maximal i.e. $\sin^2 2\theta_A \simeq 0.8\text{–}1$.

As far as the mass pattern goes however, there are three possibilities:

- normal hierarchy: $m_1 \ll m_2 \ll m_3$,
- inverted hierarchy: $m_1 \simeq -m_2 \gg m_3$ and
- approximately degenerate pattern [18] $m_1 \simeq m_2 \simeq m_3$,

Table 1. Different possible conclusions regarding the nature of the neutrinos and their mass hierarchy from the three.

$\beta\beta_{0\nu}$	Δm^2_{13}	KATRIN	Conclusion
yes	>0	yes	Degenerate, Majorana
yes	>0	no and heavy particle contribution	Degenerate, Majorana
yes	<0	no	Inverted, Majorana
yes	<0	yes	Degenerate, Majorana
no	>0	no	Normal, Dirac or Majorana
no	<0	no	Dirac or Pseudo-Dirac
no	<0	yes	Dirac or Pseudo-Dirac
no	>0	yes	Dirac or Pseudo-Dirac

where m_i are the eigenvalues of the neutrino mass matrix. In the first case, the atmospheric and the solar neutrino data give direct information on m_3 and m_2, respectively. On the other hand, in the last case, the mass differences between the first and the second eigenvalues will be chosen to fit the solar neutrino data and the second and the third to fit the atmospheric neutrino data.

Since Majorana masses violate lepton number, a very important constraint on any discussion of neutrino mass patterns arises from the negative searches for neutrinoless double beta decay [11]. The most stringent present limits are obtained from the Heidelberg–Moscow enriched Germanium-76 experiment at Gran Sasso and implies an upper limit on the following combination of masses and mixings:

$$\langle m_\nu \rangle \equiv \sum_i U_{ei}^2 m_{\nu_i} \leqslant 0.35\,\text{eV}, \quad 95\%\ \text{c.l.} \tag{25}$$

This upper limit depends on the nuclear matrix element calculated by the Heidelberg group [11]. There could be an uncertainty of a factor of 2 in this estimate. This would then relax the above upper bound to at most 0.7 eV in the worst-case scenario. This is still a very useful limit and becomes especially relevant when one considers whether the neutrinos constitute a significant fraction of the hot dark matter of the universe. A useful working formula is $\Sigma_i m_{\nu_i} \simeq 24\Omega_\nu$ eV, where Ω_ν is the neutrino fraction that contributes to the dark matter of the universe. For instance, if the neutrino contribution to dark matter fraction is 20%, then the sum total of neutrino masses must be 4.8 eV. Such large values are apparently in disagreement with present upper limits from structure surveys such as the 2dF survey and others.

Neutrinoless double beta decay limits also imply very stringent constraints on the mixing pattern in the degenerate case.

The inverted hierarchy case (ii) is quite an interesting one and will be discussed from a theoretical perspective in more detail later on; but at the moment we simply note that in this case the value of m_1 is nothing but the $\sqrt{\Delta m_A^2}$. The solar mass difference is an additional parameter in the mass matrix.

In table 1, we describe what we can learn about the nature of the neutrino from the various experiments.

At this point, it is appropriate to stress the theoretical challenges raised by the existing neutrino oscillation data.

- *Ultralight neutrinos:* Why are the neutrino masses so much lighter than the quark and charged lepton masses?
- *Near bimaximal mixing:* How to understand simultaneously two large mixing angles one for the $\mu - \tau$ and another for $e - \mu$?
- *Smallness of* $\Delta m^2_\odot / \Delta m^2_A$: Experimentally, $\Delta m^2_\odot \simeq 10^{-2} \Delta m^2_A$. How does one understand this in a natural manner?
- *Smallness of* U_{e3}: The reactor results also seem to indicate that the angle $\theta_{13} \equiv U_{e3}$ is a very small number. One must also understand this in a framework that simultaneously explains all other puzzles.

Possible other puzzles include a proper understanding of neutrino mass degeneracy if there is a large positive signal for the neutrinoless double beta decay and of course, when we have evidence for CP violating phases in the mass matrix, we must understand their magnitude.

1.6. Neutrino mass textures

From the mixing matrix in equation (24), we can write down the allowed neutrino mass matrix for any arbitrary mass pattern assuming the neutrino is a Majorana fermion. Denoting the matrix elements of $\mathcal{M}_\nu$ as $\mu_{\alpha\beta}$ for $\alpha, \beta = 1, 2, 3$, we have (recall that $\mu_{\alpha\beta} = \mu_{\beta\alpha}$)

$$\begin{aligned}
\mu_{11} &= [c^2 m_1 + s^2 m_2 + \epsilon^2 m_3], \\
\mu_{12} &= (1/\sqrt{2})[-c(s + c\epsilon)m_1 + s(c - s\epsilon)m_2 + \epsilon m_3], \\
\mu_{13} &= (1/\sqrt{2})[-c(s - c\epsilon)m_1 - s(c + s\epsilon)m_2 + \epsilon m_3], \\
\mu_{22} &= \tfrac{1}{2}[(s + c\epsilon)^2 m_1 + (c - s\epsilon)^2 m_2 + m_3], \\
\mu_{23} &= \tfrac{1}{2}[-(s^2 - c^2\epsilon^2)m_1 - (c^2 - s^2\epsilon^2)m_2 + m_3], \\
\mu_{33} &= \tfrac{1}{2}[(s - c\epsilon)^2 m_1 + (c + s\epsilon)^2 m_2 + m_3].
\end{aligned} \tag{26}$$

One can use equation (26) to get information on the nature of the neutrino mass matrix and use it to get clues to the nature of physics beyond the standard model. One technique is to rewrite this mass matrix in a way that reflects some new underlying symmetry of physics beyond the standard model. Below we give some examples of mass matrices that are closely related to this mass matrix but reflect some symmetries of the lepton world. A second utility of equation (26) is to search for mass matrices that lead to testable predictions and thereby test models.

As an example consider the case when $\mu_{11} = \mu_{22} = \mu_{33} = 0$. This is the prediction from the Zee model [19]. Using equation (26), one can easily see that in the leading order the vanishing of all diagonal entries implies that $\Delta m^2_{odot} = 0$, i.e. one must keep higher-order terms in ϵ to get a nonzero $\Delta m^2_\odot$.

An elementary way to proceed in this direction is to start with ways to understand the maximal mixing using only two flavours as in the case of the atmospheric neutrinos (i.e. the 2–3 sector of the neutrino flavour). It is well known that if we have a matrix of the form

$$M = \begin{pmatrix} A & B \\ B & A \end{pmatrix}, \tag{27}$$

then its eigenstates are maximal admixtures of the original 'flavour' states. The eigenvalues are $(A + B)$, $(A - B)$. It is now clear that if we want one of the eigenvalues to be much less than the other, we must have $A \approx B$. We will now have to generalize this discussion to the case of three generations. For this we note that the 'mixing matrix' for this case can be written as

$$U = \begin{pmatrix} 1 & 1 \\ 1 & -1 \end{pmatrix}. \tag{28}$$

We will call this matrix 'maximal mixing matrix'.

Theorem. *The maximal mixing matrix for N generations, if N is a prime number, is given by*

$$U_N = \frac{1}{\sqrt{N}} \begin{pmatrix} 1 & 1 & 1 & \cdot & \cdot \\ 1 & z & z^2 & z^3 & \cdot \\ 1 & z^2 & z^4 & \cdot & \cdot \\ 1 & z^3 & z^6 & \cdot & \cdot \\ 1 & z^4 & z^8 & \cdot & \cdot \end{pmatrix}, \tag{29}$$

where z is the Nth root of unity and the rows and columns extend in an obvious manner to make the matrix $N \times N$.

Note that the general form of an arbitrary element is z^{pq}. When $pq \geqslant N$, the power is simply given by $pq - N$. When the number of generations is not a prime number, then $N = N_1 \cdot N_2 \cdot N_3 \cdots$. In this case,

$$U_N = U_{N_1} \times U_{N_2} \times U_{N_3} \times, \tag{30}$$

where $\times$ stands for a direct product. For example for the case of $N = 4$, we have for the maximal mixing matrix $U_4 = U_2 \times U_2$ which is given by

$$U_4 = \frac{1}{2} \begin{pmatrix} 1 & 1 & 1 & 1 \\ 1 & -1 & 1 & -1 \\ 1 & 1 & -1 & -1 \\ 1 & -1 & -1 & 1 \end{pmatrix} \tag{31}$$

The 4×4 case turns out to be interesting since by decoupling a linear combination of the states from the 4×4 system, we can get the exact bimaximal form [21]. The corresponding 3×3 mass matrix can also be obtained by starting from this discussion. To see how one gets that, note that the matrix in equation (24) for the 2×2 case has a S_{12} symmetry. The corresponding symmetry in the 4×4 case is then $S_{12} \times S_{34}$. Using this property and decoupling one linear combination of the fields, we can get the mass matrix for the 3×3 case that leads to bimaximal mixing [22]. It is left as an exercise to the reader to show that the corresponding mass matrix is given by [21]

$$M_\nu = \begin{pmatrix} A + D & F & F \\ F & A & D \\ F & D & A \end{pmatrix}. \tag{32}$$

Since the present data imply that there are deviations from the exact bimaximal form, this mass matrix must only be treated as a leading-order contribution.

The three different mass patterns can emerge from this mass matrix in various limits: e.g. (i) for $F \ll A \simeq -D$, one gets the normal hierarchy; (ii) for $F \gg A, D$, one has the inverted pattern for masses and (iii) the parameter region $F, D \ll A$ leads to the degenerate case. Clearly, this mass matrix is the leading-order matrix and there will have to be small corrections to this to fit solar neutrino data as well as any possible evidence (or lack of it) for neutrinoless double beta decay. An interesting symmetry of this mass matrix is the $\nu_\mu \leftrightarrow \nu_\tau$ interchange symmetry, which is obvious from the matrix; however in the limit where $A = D = 0$, there appears a much more interesting symmetry, i.e. the continuous symmetry L_e–L_μ–L_τ [23] (see also [55]). If the inverted mass matrix is confirmed by future experiments, this symmetry will provide an important clue to new neutrino-related physics beyond the standard model (see e.g. [24]). There are other ways to proceed towards the same goal. One way inspired by the studies of quark mass matrices is to consider mass matrices with zeros in it and hope that there are sensible symmetries that will guarantee the zeros. One may then be able to obtain relations between different observables such as masses and mixing angles that can be tested in experiments.

To proceed towards this goal, let us recall that in the absence of CP violation, the neutrino mass matrix has six independent entries. In terms of observables there are five oscillation observables, two mass differences ($\Delta m^2_\odot$, Δm^2_A) and three mixing angles: solar, atmospheric and the reactor angle U_{e3}. So if we have more than one vanishing element, we will have nontrivial relations between oscillation observables which can be used as tests of the various ansatzes.

The first point to note is that if there are three zeros or more, the mass matrix cannot describe data. The proof of this is left as an exercise to the reader.

Let us therefore consider some typical two zero mass matrices [25]:

$$M_\nu = \sqrt{\Delta m^2_A} \begin{pmatrix} 0 & 0 & d\epsilon \\ 0 & 1 + a\epsilon & 1 \\ d\epsilon & 1 & 1 + b\epsilon \end{pmatrix} \tag{33}$$

or, alternatively,

$$M_\nu = \sqrt{\Delta m^2_A} \begin{pmatrix} 0 & d\epsilon & 0 \\ d\epsilon & 1 + a\epsilon & 1 \\ 0 & 1 & 1 + b\epsilon \end{pmatrix}. \tag{34}$$

They give a four-parameter fit to all data and yield a relation between $\Delta m^2_\odot / \Delta m^2_A$, U_{e3}, $\theta_\odot$ and θ_A [25]:

$$U^2_{e3} \cos 2\theta_\odot = \frac{\sin^2 2\theta_\odot}{4} \frac{\Delta m^2_\odot}{\Delta m^2_A}. \tag{35}$$

This relation predicts that $U_{e3} \geqslant 0.12$ and can be tested in planned long baseline experiments to be conducted in the near future.

There are also some other two zero textures that predict a degenerate spectrum for neutrinos.

So far we have focused on studying the form of the neutrino mass matrix. The implicit assumption in these discussions has been that the charged lepton mass matrix is diagonal. It may however be that all neutrino mixings are a reflection of structure in the charged lepton mass matrix rather than in the neutrinos. An example of this kind is the democratic mass matrix [27], which also leads to a near bimaximal mixing. As was noted in [28], to get the democratic mixing

matrix, one must choose the charged lepton mass matrix in the following form while keeping the neutrino mass matrix diagonal:

$$M_\ell = \begin{pmatrix} a & 1 & 1 \\ 1 & a & 1 \\ 1 & 1 & a \end{pmatrix}. \tag{36}$$

This form can be derived from a permutation symmetry S_3 operating on the lepton doublets, which may provide another clue to possible gauge model building.

Other models that use charged lepton sector to understand the neutrino have been the focus of several papers [29], especially in the context of grand unified theories [29]. We do not discuss this class of models here.

1.7. Inverted hierarchy and L_e–L_μ–L_τ symmetry

In this section, we consider another interesting clue to model building present in neutrino data if the mass arrangement is inverted. As already noted, if in equation (33), we set $A = D = 0$, this leads to a neutrino mass matrix with two degenerate neutrinos with mass $\pm\sqrt{2}F$ and one massless neutrino. The atmospheric mass difference is given by $\Delta m_A^2 = 2F^2$ and mixing angle $\theta_A = \pi/4$. As far as the solar ν_e oscillation is concerned, $\sin^2 2\,\theta_\odot = 1$ but $\Delta m_\odot^2 = 0$. While this is unphysical, this raises the hope that as corrections to this mass matrix are taken into account, it may be possible to understand the smallness of $\Delta m_\odot^2/\Delta m_A^2$ naturally.

In fact, this hope is fortified by the observation that the $A = D = 0$ limit of the mass matrix in [33] has the leptonic symmetry L_e–L_μ–L_τ; therefore one might hope that as this symmetry is broken by small terms, one will end up with a situation that fits the data well.

This question was studied in [30, 72]. To proceed with the discussion, let us consider the following mass matrix for neutrinos where small L_e–L_μ–L_τ violating terms have been added:

$$\mathcal{M}_\nu = m \begin{pmatrix} z & c & s \\ c & y & d \\ s & d & x \end{pmatrix}. \tag{37}$$

The charged lepton mass matrix is chosen to have a diagonal form in this basis and L_e–L_μ–L_τ symmetric.

In the perturbative approximation, we find the following sum rules involving the neutrino observables and the elements of the neutrino mass matrix. The two obvious relations are

$$\begin{aligned} &\sin^2 2\theta_A = \sin^2 2\theta + \mathrm{O}(\delta^2), \\ &D_3 \equiv \triangle m_A^2 = -m^2 + 2\triangle m_\odot^2 + \mathrm{O}(\delta^2). \end{aligned} \tag{38}$$

The nontrivial relations that also hold for this model are

$$\begin{aligned} &\sin^2 2\theta_\odot = 1 - \left(\frac{\triangle m_\odot^2}{4\triangle m_A^2} - z\right)^2 + \mathrm{O}(\delta^3), \\ &\frac{\triangle m_\odot^2}{\triangle m_A^2} = 2(z + \vec{v}\cdot\vec{x}) + \mathrm{O}(\delta^2), \\ &U_{e3} = \vec{A}\cdot(\vec{v}\times\vec{x}) + \mathrm{O}(\delta^3), \end{aligned} \tag{39}$$

where $\vec{v} = (\cos^2\theta, \sin^2\theta, \sqrt{2}\sin\theta\cos\theta)$, $\vec{x} = (x, y, \sqrt{2}d)$ and $\vec{A} = (1/\sqrt{2})(1, 1, 0)$. δ in the preceding equations represents the small parameters in the mass matrix. These equations represent one of the main results of this paper. Below we study their implications. Finally, there is the relation $\langle m\rangle_{\beta\beta} = mz$. This is an an exact relation true to all orders in the small parameters.

One of the major consequences of these relations is that (i) there is a close connection between the measured value of the solar mixing angle and the neutrino mass measured in neutrinoless double beta decay; and (ii) the present values for the solar mixing angle can be used to predict the $m_{\beta\beta}$ for a value of the $\Delta m^2_\odot$. For instance, for $\sin^2 2\theta_\odot = 0.9$, we would predict $(\Delta m^2_\odot/4\Delta m^2_A - z) = 0.3$. For small $\Delta m^2_\odot$, this implies $m_{\beta\beta} \simeq 0.01$ eV. The second relation involving the $\Delta m^2_\odot/\Delta m^2_A$ in terms of x, y, z, d tells us that for this to be the case, we must have strong cancellation between the various small parameters. Given this, the above $m_{\beta\beta}$ value is expected to be within the reach of new double beta decay experiments contemplated [32]. Note however that the $\sin^2 2\theta_\odot$ cannot be greater than 0.9 in the case of approximate L_e–L_μ–L_τ symmetry.

If the value of $\sin^2 2\theta_\odot$ is ultimately determined to be less than 0.9, the question one may ask is whether the idea of L_e–L_μ–L_τ symmetry is dead. The answer is in the negative since so far we have explored the breaking of L_e–L_μ–L_τ symmetry only in the neutrino mass matrix. It was shown in [30] that if the symmetry is broken in the charged lepton mass, one can lower the $\sin^2 2\theta_\odot$ as long as the value of U_{e3} is sizeable. However, given the present upper limit on U_{e3}, the smallest value is somewhere around $\sin^2 2\theta_\odot \simeq 0.8$.

1.8. CP violation

A not very well-explored aspect of neutrino physics at the moment is CP violation in lepton physics. Unlike the quark sector, CP violation for Majorana neutrinos allows for more phases for neutrinos. Since the Majorana neutrino mass matrix is symmetric, for N generations of neutrinos, there are in general $N(N+1)/2$ phases in it. When the mass matrix is diagonalized, these phases will appear in the unitary matrix U_L that does the diagonalization (i.e. $U^{\mathrm{T}} - \mathcal{M}_\nu U_L = d_\nu$). If we are working in a basis where the charged lepton mass matrix is diagonal, then U_L is a leptonic weak mixing matrix. As we have seen, this has $N(N+1)/2$ phases. Out of them, redefinition of the charged lepton fields in the weak current allows the removal of N phases; so there are $N(N-1)/2$ phases in the neutrino masses. In the quark sector, both up and down fields could be redefined allowing for the number of physical phases that appear in the end to be smaller. However, for Majorana neutrinos, redefinition of the fields does not remove the phases entirely from the theory but rather shifts them to other places where they can manifest themselves physically [33].

Thus, for two generations, there is one and for three generations there are three phases. A convenient parameterization of the mixing matrix with these phases in the mixing matrix for the case of three generations is **UK**:

$$\mathbf{U} = \begin{pmatrix} c & s & \epsilon e^{-i\delta} \\ -\dfrac{s + c\epsilon e^{i\delta}}{\sqrt{2}} & \dfrac{c - s\epsilon e^{i\delta}}{\sqrt{2}} & \dfrac{1}{\sqrt{2}} \\ -\dfrac{s - c\epsilon e^{i\delta}}{\sqrt{2}} & \dfrac{-c - s\epsilon e^{i\delta}}{\sqrt{2}} & \dfrac{1}{\sqrt{2}} \end{pmatrix}, \tag{40}$$

and

$$\mathbf{K} = \mathrm{Diag}(1, \mathrm{e}^{\mathrm{i}\phi_1}, \mathrm{e}^{\mathrm{i}\phi_2}). \tag{41}$$

The phase δ is called the Dirac phase and the ϕ_i are called Majorana phases. Note that the Dirac phase is always multiplied by the small mixing angle ϵ. Its measurability is therefore very closely tied to the absolute magnitude of ϵ. Coming to the Majorana phases, one of the two phases ϕ_i can, in principle, be probed in neutrinoless double beta decay. To see this, let us note that

$$\langle m \rangle_{\beta\beta} = |m_1 c^2 + m_2 s^2 \mathrm{e}^{\mathrm{i}\phi_1} + m_3 \epsilon^2 \mathrm{e}^{-\mathrm{i}(\delta-\phi_2)}|. \tag{42}$$

Since $\epsilon \ll 1$, the last term in the above equation can be dropped. It is then easy to see that one has some chance of seeing the CP phase ϕ_1, once one has a precise knowledge of the Δm_A^2 and the solar mixing angle, provided the nuclear matrix elements are known better [34]. More optimistically, when the phase is zero, the two terms in the expression for $\beta\beta_{0\nu}$ add up and the chances for seeing it is enhanced.

On the whole, there is some chance of measuring the CP phase both for the inverted and the degenerate mass case provided the nuclear matrix elements have much smaller uncertainties than presently known, whereas for the case of normal hierarchy, it depends on how small the smallest neutrino mass is. If it is very close to m_2, the so-called quasi-degenerate case, then one has a good chance to measure the phase if the $\langle m \rangle_{\beta\beta}$ is measured to a precision of 0.001 eV.

A very interesting question relates to the observability of truly CP violating leptonic processes. This question has been addressed in [35]. For instance, although one can probe the CP phase in neutrinoless double beta decay, it is not really a CP violating process; in other words, even in the presence of CP violation, the rate for neutrinoless double beta decay of a nucleus is same as that for the corresponding anti-nucleus. On the other hand, there are genuine CP violating processes where the CP phase can be probed. One is the celebrated example of early universe leptogenesis where one looks at the decay of the Majorana right-handed neutrino into $\ell + H$ and $\bar{\ell} + \bar{H}$ and it is their difference that manifests as the lepton asymmetry. Similarly, one can look at rare decays of $K^\pm$ to $\pi^\mp + \mu^\pm + \mu^\pm$ and similar decay modes for the B meson, where the presence of a physical intermediate state leads to the observability of a truly CP violating difference between decay rates. It however appears that truely CP violating neutrino processes are much too suppressed to be observable.

Section 2

2.1. Why neutrino mass requires physics beyond the standard model

We will now show that in the standard model, the neutrino mass vanishes to all orders in perturbation theory as well as nonperturbatively. The standard model is based on the gauge group $SU(3)_c \times SU(2)_L \times U(1)_Y$ under which the quarks and leptons transform as described in the table 2.

The electroweak symmetry $SU(2)_L \times U(1)_Y$ is broken by the vacuum expectation of the Higgs doublet $\langle H^0 \rangle = v_{wk} \simeq 246$ GeV, which gives mass to the gauge bosons and the fermions, all fermions except the neutrino. Thus, the neutrino is massless in the standard model, at the tree-level. There are several questions that arise at this stage. What happens when one goes beyond

Table 2. The assignment of particles to the standard model gauge group $SU(3)_c \times SU(2)_L \times U(1)_Y$.

Field	Gauge transformation
Quarks Q_L	$(3, 2, \frac{1}{3})$
Right-handed up-quarks u_R	$(3, 1, \frac{4}{3})$
Right-handed down-quarks d_R	$(3, 1, -\frac{2}{3})$
Left-handed leptons L	$(1, 2, -1)$
Right-handed leptons e_R	$(1, 1, -2)$
Higgs boson $\mathbf{H}$	$(1, 2, +1)$
Colour gauge fields G_a	$(8, 1, 0)$
Weak gauge fields $W^{\pm}$, Z, γ	$(1, 3, +1, 0)$

the above simple tree-level approximation? Secondly, do nonperturbative effects change this tree-level result? Finally, how can we judge how this result will be modified when the quantum gravity effects are included?

The first and second questions are easily answered by using the $B - L$ symmetry of the standard model. The point is that since the standard model has no $SU(2)_L$ singlet neutrino-like field, the only possible mass terms that are allowed by Lorentz invariance are of the form $\nu_{iL}^{\mathrm{T}} C^{-1} \nu_{jL}$, where i, j stand for the generation index and C is the Lorentz charge conjugation matrix. Since the ν_{iL} is part of the $SU(2)_L$ doublet field and has lepton number +1, the above neutrino mass term transforms as an $SU(2)_L$ triplet and, furthermore, it violates total lepton number (defined as $L \equiv L_e + L_\mu + L_\tau$) by two units. However, a quick look at the standard model Lagrangian convinces one that the model has exact lepton number symmetry after symmetry breaking; therefore such terms can never arise in perturbation theory. Thus, to all orders in perturbation theory, the neutrinos are massless. As far as the nonperturbative effects go, the only known source is the weak instanton effects. Such effects could affect the result if they broke the lepton number symmetry. One way to see if such breaking occurs is to look for anomalies in lepton number current conservation from triangle diagrams. Indeed, $\partial_\mu j_\ell^\mu = cW\tilde{W} + c'B\tilde{B}$ due to the contribution of the leptons to the triangle involving the lepton number current and Ws or Bs. Luckily, it turns out that the anomaly contribution to the baryon number current nonconservation has also an identical form, so that the $B - L$ current j_{B-L}^μ is conserved to all orders in the gauge couplings. As a consequence, nonperturbative effects from the gauge sector cannot induce $B - L$ violation. Since the neutrino mass operator described above violates also $B - L$, this proves that neutrino masses remain zero even in the presence of nonperturbative effects.

Let us now turn to the effect of gravity. Clearly, as long as we treat gravity in perturbation theory, the above symmetry arguments hold since all gravity coupling respect $B - L$ symmetry. However, once nonperturbative gravitational effects, e.g. black holes and worm holes, are included, there is no guarantee that global symmetries will be respected in the low-energy theory. The intuitive way to appreciate the argument is to note that throwing baryons into a black hole does not lead to any detectable consequence except through a net change in the baryon number of the universe. Since one can throw an arbitrary number of baryons into the black hole, an arbitrary information loss about the net number of missing baryons would prevent us from defining a baryon number of the visible universe—thus baryon number in the presence of a black hole cannot be an exact symmetry. Similar arguments can be made for any global

charge such as lepton number in the standard model. A field-theoretic parameterization of this statement is that the effective low-energy Lagrangian for the standard model in the presence of black holes and worm holes, etc must contain baryon and lepton number violating terms. In the context of the standard model, the only such terms that one can construct are nonrenormalizable terms of the form $LHLH/M_{P\ell}$. After gauge-symmetry breaking, they lead to neutrino masses; however these masses are at most of order $v_{wk}^2/M_{P\ell} \simeq 10^{-5}$ eV [36]. However, as we discussed in the previous section, to solve the atmospheric neutrino problem, one needs masses at least three orders of magnitude higher.

Thus, one must seek physics beyond the standard model to explain observed evidences for neutrino masses. Although there are many possibilities that lead to small neutrino masses of both Majorana as well as Dirac kind, here we focus on the possibility that there is a heavy right-handed neutrino (or neutrinos) that lead to a small neutrino mass. The resulting mechanism is known as the seesaw mechanism and leads to neutrino being a Majorana particle.

The nature and origin of the seesaw mechanism can also be tested in other experiments and we will discuss them below. This will be dependent on the kind of operators that play a role in generating neutrino masses. If the leading-order operator is of dimension 5, then the scale necessarily is very high (of order 10^{12} GeV or greater). On the other hand, in theories with extra space dimensions, this operator may be forbidden and one may be forced to go to higher-dimensional operators, in which case the scale could be lower. In the lecture IV, an example of five- and six-dimensional theory is given, where this indeed happens.

The seesaw mechanism raises a very important question: since we require the mass of the right-handed neutrino to be much less than the Planck scale, a key question is 'what symmetry keeps the right-handed neutrino mass lighter?' We will give two examples of symmetries that can do this.

2.2. *Seesaw and the right-handed neutrino*

The simplest possibility extension of the standard model that leads to nonzero mass for the neutrino is one where only a right-handed neutrino is added to the standard model. In this case ν_L and ν_R can form a mass term, but *a priori*, this mass term is like the mass terms for charged leptons or quark masses and will therefore involve the weak scale. If we call the corresponding Yukawa coupling to be Y_ν, then the neutrino mass is $m_D = Y_\nu v/\sqrt{2}$. For a neutrino mass in the eV range requires that $Y_\nu \simeq 10^{-11}$ or less. Introduction of such small coupling constants into a theory is generally considered unnatural and a sound theory must find a symmetry reason for such smallness. As already alluded to before, the seesaw mechanism [5], where we introduce a singlet Majorana mass term for the right-handed neutrino is one way to achieve this goal. What we have in this case is a (ν_L, ν_R) mass matrix which has the form

$$M = \begin{pmatrix} 0 & m_D \\ m_D & M_R \end{pmatrix}. \tag{43}$$

Since M_R is not constrained by the standard model symmetries, it is natural to choose it to be at a scale much higher than the weak scale. Now diagonalizing this mass matrix for a single neutrino species, we get a heavy eigenstate N_R with mass M_R and a light eigenstate ν with mass $m_\nu \simeq -m^2 v/M_R$. This provides a natural way to understand a small neutrino mass without any unnatural adjustment of parameters of a theory. In a subsequent section, we will discuss a theory which connects the scale M_R to a new symmetry of nature beyond the standard model.

2.2.1. Why is $M_{\nu_R} \ll M_{P\ell}$? The question 'why $M_{\nu_R} \ll M_{P\ell}$?' is in many ways similar to the question in the standard model is 'why is $M_{Higgs} \ll M_{P\ell}$?' It is well known that searches for answer to this question has led us to consider many interesting possibilities for physics beyond the standard model and supersymmetry appears to be the most promising answer to this question. It is hoped that answering this question for ν_R can also lead us to new insight into new symmetries beyond the standard model. There are two interesting answers to our question that I will elaborate later on.

$B - L$: If one adds three right-handed neutrinos to implement the seesaw mechanism, the model admits an anomaly free new symmetry, i.e. $B - L$. One can therefore extend the standard model symmetry to either $SU(2)_L \times U(1)_{I_{3R}} \times U(1)_{B-L}$ or its left–right symmetric extension $SU(2)_L \times SU(2)_R \times U(1)_{B-L}$. In either case, the right-handed neutrino carries the $B - L$ quantum number and its Majorana mass breaks this symmetry. Therefore, the mass of the ν_R can at most be the scale of $B - L$ symmetry breaking, hence answering the question 'why $M_{\nu_R} \ll M_{P\ell}$?'.

$SU(2)_H$: While local $B - L$ is perhaps the most straightforward and natural symmetry that keeps ν_R lighter than the Planck scale, another possibility has recently been suggested in [24]. The main observation here is that if the standard model is extended by including a local $SU(2)_H$ symmetry acting on the first two lepton generations including the right-handed charged leptons, then global Witten anomaly freedom dictates that there must be at least two right-handed neutrinos which transform as a doublet under the $SU(2)_H$ local symmetry. In this class of models, in the limit of exact $SU(2)_H$ symmetry, the ν_Rs are massless and as soon as the $SU(2)_H$ symmetry is broken, they pick up mass. Therefore, 'lightness' of the ν_Rs compared with the Planck scale in these models is related to an $SU(2)_H$ symmetry. These comments are elaborated with explicit examples later on in this review.

2.2.2. Small neutrino mass using a double seesaw mechanism with ν_R. As we have seen from the previous discussion, the conventional seesaw mechanism requires rather high mass for the right-handed neutrino and therefore a correspondingly high scale for $B - L$ symmetry breaking. There is however no way at present to know what the scale of $B - L$ symmetry breaking is. There are, for example model bases on string compactification [37], where the $B - L$ is quite possibly in the TeV range. In this case small neutrino mass can be implemented by a double seesaw mechanism suggested in [38]. The idea is to take a right-handed neutrino N and a singlet neutrino S which has extra quantum numbers which prevent it from coupling with the left-handed neutrino. One can then write a 3×3 neutrino mass matrix in the basis (ν, N, S) of the form

$$M = \begin{pmatrix} 0 & m_D & 0 \\ m_D & 0 & M \\ 0 & M & \mu \end{pmatrix}. \tag{44}$$

For the case $\mu \ll M \approx M_{B-L}$ (where M_{B-L} is the $B - L$ breaking scale) this matrix has one light and two heavy neutrinos per generation and the latter two form a pseudo-Dirac pair with mass of the order of M_{B-L}. The important thing for us is that the light mass eigenvalue is given by $m_D^2\mu/M^2$; for $m_D \approx \mu \simeq$ GeV, a 10 TeV $B - L$ scale is enough to give neutrino masses in the eV range. For the case of three generations, the formula for the light neutrino mass matrix is given by

$$\mathcal{M}_\nu = M_D M^{-1} \mu M^{-1} M_D^{\mathrm{T}}. \tag{45}$$

An example of a model where such a situation can arise is as follows: consider a supersymmetric model with the gauge group $SU(2)_L \times U(1)_{I_{3R}} \times U(1)_{B-L} \times U(1)_X$, with the leptonic sector assignment as $L(2, 0, -1)_0$, $\nu^c(1, -1/2, +1)_0$, $N(1, 0, 0)_{+1}$ and Higgs field assignments as $H_u(2, +1/2, 0)_0$, $\chi(1, +1/2, -1)_{-1}$, $\bar{\chi}(1, -1/2, +1)_1$, $\chi'(1, -1/2, +1)_{-1}$ and $\bar{\chi}'(1, +1/2, -1)_{+1}$. The relevant superpotential that is invariant under this is

$$W = h_\nu L H_u \nu^c + h_{\nu^c} \nu^c \chi N + f \frac{SS\chi\chi'}{M_H}. \tag{46}$$

If we give a vacuum expectation value (vev) to the $\chi\chi'$ and their conjugates of order 10 TeV and choose $M_H \sim 10^{12}$ GeV, then μ in the matrix is of the order of a 100 keV and for $m_D \sim 10$ GeV, we get the light neutrino spectrum of the right order. There are also terms in the superpotential such as $h' L H_u S\chi'/M_H$, which can induce mass terms of the order of a keV if $h' \sim 10^{-3}$ and it will not disturb the small neutrino mass prediction for these models. For further discussion of such effects in SO(10) models, see [39].

2.3. A gauge model for seesaw mechanism: left–right symmetric unification and type II seesaw

Let us now explore the implications of including the right-handed neutrinos into the extensions of the standard model to understand the small neutrino mass by the seesaw mechanism. As already emphasized, if we assume that there are no new symmetries beyond the standard model, the right-handed neutrino will have a natural mass of the order of the Planck scale making the light neutrino masses too small to be of interest in understanding the observed oscillations. We must therefore search for new symmetries that can keep the RH neutrinos at a lower scale than the Planck scale. A new symmetry always helps in making this natural.

To study this question, let us note that the inclusion of the right-handed neutrinos transforms the dynamics of the gauge models in a profound way. To clarify what we mean, note that in the standard model (that does not contain a ν_R) the $B - L$ symmetry is only linearly anomaly free, i.e. $\mathrm{Tr}[(B - L)Q_a^2] = 0$, where Q_a are the gauge generators of the standard model but $\mathrm{Tr}(B - L)^3 \neq 0$. This means that $B - L$ is only a global symmetry and cannot be gauged. However as soon as the ν_R is added to the standard model, one gets $\mathrm{Tr}[(B - L)^3] = 0$ implying that the $B - L$ symmetry is now gaugeable and one could choose the gauge group of nature to be either $SU(2)_L \times U(1)_{I_{3R}} \times U(1)_{B-L}$ or $SU(2)_L \times SU(2)_R \times U(1)_{B-L}$, the latter being the gauge group of the left–right symmetric models [40]. Furthermore, the presence of the ν_R makes the model quark lepton symmetric and leads to a Gell–Mann–Nishijima-like formula for the electric charges [41], i.e.

$$Q = I_{3L} + I_{3R} + \frac{B - L}{2}. \tag{47}$$

The advantage of this formula over the charge formula in the standard model charge formula is that in this case all entries have a physical meaning. Furthermore, it leads naturally to Majorana nature of neutrinos as can be seen by looking at the distance scale where the $SU(2)_L \times U(1)_Y$ symmetry is valid but the left–right gauge group is broken. In that case, one gets

$$\Delta Q = 0 = \Delta I_{3L}, \qquad \Delta I_{3R} = -\Delta \frac{B - L}{2}. \tag{48}$$

Table 3. Assignment of the fermion and Higgs fields to the representation of the left–right symmetry group.

Fields	$SU(2)_L \times SU(2)_R \times U(1)_{B-L}$ representation
Q_L	$(2, 1, +\frac{1}{3})$
Q_R	$(1, 2, \frac{1}{3})$
L_L	$(2, 1, -1)$
L_R	$(1, 2, -1)$
ϕ	$(2, 2, 0)$
Δ_L	$(3, 1, +2)$
Δ_R	$(1, 3, +2)$

We see that if the Higgs fields that break the left–right gauge group carry right-handed isospin of 1, one must have $|\Delta L| = 2$ which means that the neutrino mass must be Majorana type and the theory will break lepton number by two units.

Let us now proceed to give a few details of the left–right symmetric model and demonstrate how the seesaw mechanism emerges in this model.

The gauge group of the theory is $SU(2)_L \times SU(2)_R \times U(1)_{B-L}$ with quarks and leptons transforming as doublets under $SU(2)_{L,R}$. In table 3, we denote the quark, lepton and Higgs fields in the theory along with their transformation properties under the gauge group.

The first task is to specify how the left–right symmetry group breaks to the standard model, i.e. how one breaks the $SU(2)_R \times U(1)_{B-L}$ symmetry so that the success of the standard model including the observed predominant V-A structure of weak interactions at low energies is reproduced. Another question of naturalness that also arises simultaneously is that since the charged fermions and the neutrinos are treated completely symmetrically (quark–lepton symmetry) in this model, how does one understand the smallness of the neutrino masses compared with the other fermion masses.

It turns out that both the above problems of the LR model have a common solution. The process of spontaneous breaking of the $SU(2)_R$ symmetry that suppresses the V + A currents at low energies also solves the problem of ultralight neutrino masses. To see this let us write the Higgs fields explicitly:

$$\Delta = \begin{pmatrix} \Delta^+/\sqrt{2} & \Delta^{++} \\ \Delta^0 & -\Delta^+/\sqrt{2} \end{pmatrix}, \qquad \phi = \begin{pmatrix} \phi_1^0 & \phi_2^+ \\ \phi_1^- & \phi_2^0 \end{pmatrix}. \tag{49}$$

All these Higgs fields have Yukawa couplings to the fermions given symbolically as

$$\mathcal{L}_Y = h_1 \bar{L}_L \phi L_R + h_2 \bar{L}_L \tilde{\phi} L_R + h_1' \bar{Q}_L \phi Q_R + h_2' \bar{Q}_L \tilde{\phi} Q_R + f(L_L L_L \Delta_L + L_R L_R \Delta_R) + \text{h.c.} \tag{50}$$

The $SU(2)_R \times U(1)_{B-L}$ is broken down to the standard model hypercharge $U(1)_Y$ by choosing $\langle \Delta_R^0 \rangle = v_R \neq 0$ since this carries both $SU(2)_R$ and $U(1)_{B-L}$ quantum numbers. It gives mass to the charged and neutral right-handed gauge bosons, i.e. $M_{W_R} = g v_R$ and $M_{Z'} = \sqrt{2} g v_R \cos\theta_W / \sqrt{\cos 2\theta_W}$. Thus by adjusting the value of v_R one can suppress the right-handed current effects in both neutral and charged current interactions arbitrarily leading to an effective near maximal left-handed form for the charged current weak interactions.

The fact that at the same time the neutrino masses also become small can be seen by looking at the form of the Yukawa couplings. Note that the f-term leads to a mass for the right-handed neutrinos only at the scale v_R. Next, as we break the standard model symmetry by turning on the vev's for the ϕ fields as $\mathrm{Diag}\langle\phi\rangle = (\kappa, \kappa')$, we not only give masses to the W_L and the Z bosons but also to the quarks and the leptons. In the neutrino sector, the above Yukawa couplings after $SU(2)_L$ breaking by $\langle\phi\rangle \neq 0$ lead to the so-called Dirac masses for the neutrino connecting the left- and right-handed neutrinos. In the two-component neutrino language, this leads to the following mass matrix for the ν, N (where we have denoted the left-handed neutrino by ν and the right-handed component by N):

$$M = \begin{pmatrix} 0 & h\kappa \\ h\kappa & fv_R \end{pmatrix}. \tag{51}$$

Note that m_D in previous discussions of the seesaw formula (see equation ()) is given by $m_D = h\kappa$, which links it to the weak scale and the mass of the RH neutrinos is given by $M_R = fv_R$, which is linked to the local $B - L$ symmetry. This justifies keeping RH neutrino mass at a scale lower than the Planck mass. It is therefore fair to assume that the seesaw mechanism coupled with observations of neutrino oscillations are a strong indication of the existence of a local $B - L$ symmetry far below the Planck scale.

By diagonalizing this 2×2 matrix, we get the light neutrino eigenvalue to be $m_\nu \simeq (h\kappa)^2/fv_R$ and the heavy one to be fv_R. Note that typical charged fermion masses are given by $h'\kappa$ etc. So since $v_R \gg \kappa, \kappa'$, the light neutrino mass is automatically suppressed. This way of suppressing the neutrino masses is called the seesaw mechanism [5]. Thus, in one stroke, one explains the smallness of the neutrino mass as well as the suppression of the V + A currents.

In deriving the above seesaw formula for neutrino masses, it has been assumed that the vev of the left-handed triplet is zero so that the $\nu_L\nu_L$ entry of the neutrino mass matrix is zero. However, in most explicit models such as the left–right model which provide an explicit derivation of this formula, there is an induced ve for the Δ_L^0 of order $\langle\Delta_L^0\rangle = v_T \simeq v_{wk}^2/v_R$. In the left–right models, this arises from the presence of a coupling in the Higgs potential of the form $\Delta_L\phi\Delta_R^\dagger\phi^\dagger$. In the presence of the Δ_L vev, the seesaw formula undergoes a fundamental change. One can have two types of seesaw formulae depending on whether the Δ_L has vev or not:

Type I seesaw formula:

$$M_\nu \simeq -M_D^{\mathrm{T}} M_{N_R}^{-1} M_D, \tag{52}$$

where M_D is the Dirac neutrino mass matrix and $M_{N_R} \equiv fv_R$ is the right-handed neutrino mass matrix in terms of the Δ Yukawa coupling matrix f.

Type II seesaw formula [42]:

$$M_\nu \simeq f\frac{v_{wk}^2}{v_R} - M_D^{\mathrm{T}} M_{N_R}^{-1} M_D. \tag{53}$$

Note that in the type I seesaw formula, what appears is the square of the Dirac neutrino mass matrix which is, in general, expected to have the same hierarchical structure as the corresponding charged fermion mass matrix. In fact, in some specific GUT models such as SO(10), $M_D = M_u$. This is the origin of the common statement that neutrino masses given by the seesaw formula are hierarchical, i.e. $m_{\nu_e} \ll m_{\nu_\mu} \ll m_{\nu_\tau}$ and even a more model-dependent statement that $m_{\nu_e} : m_{\nu_\mu} : m_{\nu_\tau} = m_u^2 : m_c^2 : m_t^2$.

On the other hand, if one uses the type II seesaw formula, there is no reason to expect a hierarchy and in fact if the neutrino masses turn out to be degenerate as discussed before

as one possibility, one possible way to understand this may be to use the type II seesaw formula.

Secondly, the type II seesaw formula is a reflection of the parity invariance of the theory at high energies. Evidence for it would point more strongly towards left-right symmetry at high energies.

2.4. Understanding detailed pattern for neutrinos using the seesaw formula

Let us now address the question: to what extent can one understand the details of the neutrino masses and mixings using the seesaw formulae? The answer to this question is quite model-dependent. While there exist many models which fit the observations, none (except a few) are completely predictive and almost always they need to invoke new symmetries or new assumptions. The problem in general is that the seesaw formula of type I has 12 parameters in the absence of CP violation (six parameters for a symmetric Dirac mass matrix and six for the M_R) which is why its predictive power is so limited. In the presence of CP violation, the number of parameters double making the situation worse. Specific predictions can be made only under additional assumptions.

For instance, in a class of seesaw models based on the $SO(10)$ group that embodies the left–right symmetric unification model or the $SU(4)$-colour, the mass the tau neutrino mass can be estimated provided one assumes the normal mass hierarchy for neutrinos and a certain parameter accompanying a higher-dimensional operator to be of order 1. To see this, let us assume that in the $SO(10)$ theory, the $B-L$ symmetry is broken by a **16**-dimensional Higgs boson. The RH neutrino mass in such a model arises from the nonrenormalizable operator $\lambda(\mathbf{16}_F\bar{\mathbf{16}}_H)^2/\mathbf{M}_{P\ell}$. In a supersymmetric theory, if **16**-Higgs is also responsible for GUt symmetry breaking, then after symmetry breaking, one obtains the RH neutrino mass $M_R \simeq \lambda(2\times 10^{16})^2/M_{P\ell} \simeq 4\lambda\times 10^{14}$ GeV. In models with $SU(4)_c$ symmetry, $m_{\nu_\tau,D} \simeq m_t(M_U) \sim 100$ GeV. Using the seesaw formula then, one obtains for $\lambda = 1$, tau neutrino mass $m_{\nu_\tau} \simeq 0.025$ eV, which is close to the presently preferred value of 0.05 eV. The situation with respect to other neutrino masses is however less certain and here one has to make assumptions.

The situation with respect to mixing angles is much more complicated. For instance, the striking difference between the quark and neutrino mixing angles makes one doubt whether complete quark lepton unification is truely obeyed in nature. In sections 2.8 and 3.3, two examples are given where very few assumptions are made in getting maximal atmospheric mixing angle.

2.5. General consequences of the seesaw formula for neutrino masses

In this section, we will consider some implications of the seesaw mechanism for understanding neutrino masses. We will discuss two main points. One is the nature of the right-handed neutrino spectrum as dictated by the seesaw mechanism and, secondly, ways to get an approximate L_e–L_μ–L_τ symmetric neutrino mass matrix using the seesaw mechanism and its possible implications for physics beyond the standard model.[4]

For this purpose, we use the type I seesaw formula along with the assumption of a diagonal Dirac neutrino mass matrix to obtain the right-handed neutrino mass matrix M_R:

$$\mathcal{M}_{R,ij} = m_{D,i}\mu_{ij}^{-1}m_{D,j} \tag{54}$$

[4] For discussions of the seesaw formula and attempts to understand neutrino mixings see [54].

with

$$
\begin{aligned}
\mu_{11}^{-1} &= \frac{c^2}{m_1} + \frac{s^2}{m_2} + \frac{\epsilon^2}{m_3}, \\
\mu_{12}^{-1} &= -\frac{c(s+c\epsilon)}{\sqrt{2}m_1} + \frac{s(c-s\epsilon)}{\sqrt{2}m_2} + \frac{\epsilon}{\sqrt{2}m_3}, \\
\mu_{13}^{-1} &= \frac{c(s-c\epsilon)}{\sqrt{2}m_1} - \frac{s(c+s\epsilon)}{\sqrt{2}m_2} + \frac{\epsilon}{\sqrt{2}m_3}, \\
\mu_{22}^{-1} &= \frac{(s+c\epsilon)^2}{2m_1} + \frac{(c_s\epsilon)^2}{2m_2} + \frac{1}{2m_3}, \\
\mu_{23}^{-1} &= -\frac{(s^2-c^2\epsilon^2)}{2m_1} - \frac{(c^2-s^2\epsilon^2)}{2m_2} + \frac{1}{2m_3}, \\
\mu_{33}^{-1} &= \frac{(s-c\epsilon)^2}{2m_1} + \frac{(c+s\epsilon)^2}{2m_2} + \frac{1}{2m_3}.
\end{aligned}
\tag{55}
$$

Since for the cases of normal and inverted hierarchy, we have no information on the mass of the lightest neutrino m_1, we could assume it in principle to be quite small. In that case, the above equation enables us to conclude that quite probably one of the three right-handed neutrinos is much heavier than the other two. The situation is of course completely different for the degenerate case. This kind of separation of the RH neutrino spectrum is very suggestive of a symmetry. In fact, we have recently argued that [24], this indicates the possible existence of an $SU(2)_H$ horizontal symmetry, that leads in the simplest case to an inverted mass pattern for light neutrinos. This idea is discussed in a subsequent section.

2.6. L_e–L_μ–L_τ symmetry and 3×2 seesaw

In this section, we discuss how an approximate L_e–L_μ–L_τ symmetric neutrino mass matrix may arise within a seesaw framework. Consider a simple extension of the standard model by adding two additional singlet right-handed neutrinos [55], N_1, N_2 assigning them L_e–L_μ–L_τ quantum numbers of +1 and −1 respectively. Denoting the standard model lepton doublets by $\psi_{e,\mu,\tau}$, the L_e–L_μ–L_τ symmetry allows the following new couplings to the Lagrangian of the standard model:

$$
\mathcal{L}' = (h_3\bar{\psi}_\tau + h_2\bar{\psi}_\mu)HN_2 + h_1\bar{\psi}_e HN_1 + MN_1^{\mathrm{T}}C^{-1}N_2 + \text{h.c.}, \tag{56}
$$

where H is the Higgs doublet of the standard model and C^{-1} is the Dirac charge conjugation matrix. We add to it the symmetry-breaking mass terms for the right-handed neutrinos, which are soft terms, i.e.

$$
\mathcal{L}_B = \epsilon(M_1 N_1^{\mathrm{T}}C^{-1}N_1 + M_2 N_2^{\mathrm{T}}C^{-1}N_2) + \text{h.c.} \tag{57}
$$

with $\epsilon \ll 1$. These terms break L_e–L_μ–L_τ by two units but since they are dimension 3 terms, they are soft and do not induce any new terms into the theory.

It is clear from the resulting mass matrix for the ν_L, N system that the linear combination $(h_2\nu_\tau - h_3\nu_\mu)$ is massless and the atmospheric oscillation angle is given by $\tan\theta_A = h_2/h_3$; for

$h_3 \sim h_2$, the θ_A is maximal. The seesaw mass matrix then takes the following form (in the basis $(\nu_e, \tilde{\nu}_\mu, N_1, N_2)$ with $\tilde{\nu}_\mu \equiv h_2\nu_\mu + h_3\nu_\tau$):

$$M = \begin{pmatrix} 0 & 0 & m_1 & 0 \\ 0 & 0 & 0 & m_2 \\ m_1 & 0 & \epsilon M_1 & M \\ 0 & m_2 & M & \epsilon M_2 \end{pmatrix}. \tag{58}$$

The diagonalization of this mass matrix leads to the mass matrix of the form discussed before.

2.7. SO(10) realization of the seesaw mechanism

The most natural grand unified theory for the seesaw mechanism is the $SO(10)$ model, although as has been mentioned, the gross dissimilarity between quark and lepton mixings makes additional assumptions necessary to reconcile with the inherent quark–lepton unification in such models. Nevertheless, the $SO(10)$ models are so natural framework for neutrino masses that some salient features may be instructive for any neutrino model building.

The first interesting point to note about the $SO(10)$ models is that the **16**-dimensional spinor representation contains all the fermions of each generation in the standard model plus the right-handed neutrino. Thus, the right-handed neutrino being necessary for the seesaw mechanism is automatic in these models. Secondly, in order to break the $B - L$ symmetry present in the $SO(10)$ group, one may use either the Higgs multiplets in **16**- or **126**-dimensional rep. We will see that either of these representations can be used to implement the seesaw mechanism. To see this note that under the left–right symmetric group $SU(2)_L \times SU(2)_R \times SU(4)_c$, these fields decompose as follows:

$$\begin{aligned} \mathbf{16} &= (2, 1, 4) \oplus (1, 2, 4^*), \\ \mathbf{126} &= (1, 1, 6) \oplus (3, 1, 10) \oplus (1, 3, 10^*) \oplus (2, 2, 15). \end{aligned} \tag{59}$$

Note that to break the $B - L$ symmetry it is the $(1, 2, 4^*)$ and $(1, 3, 10^*)$ in the respective multiplets whose neutral elements need to pick up a large vev. Note however that the $\mathbf{16}_H$ does not have any renormalizable coupling with the **16** spinors which contain the ν_R, whereas there is a renormalizable $SO(10)$ invariant coupling of the form $\mathbf{16}\mathbf{16}\mathbf{1}\bar{\mathbf{2}}\mathbf{6}$ for the second multiplet. Therefore, if we decided to stay with the renormalizable model, then we would need a **126**-dimensional representation to implement the seesaw mechanism, whereas if we used the **16** to break the $B - L$ symmtery, we would require nonrenormalizable couplings of the form $\mathbf{16}^2\bar{\mathbf{16}}^2/M_{P\ell}$. This has important implications for the $B - L$ scale. In the former case, the $B - L$ breaking scale is at an intermediate level such as $\sim 10^{13}$ GeV or so whereas in the latter case, we can have $B - L$ scale coincide with the GUT scale of 2×10^{16} GeV as in the typical SUSYGUT models.[5]

In addition to having the right-handed neutrino as part of the basic fermion representation and the Higgs representations the $SO(10)$ model has several other potential advantages for understanding neutrino masses. For example, if one uses only the **10**-dimensional representation

[5] For a review of SUSY GUTs, see [49].

for giving masses to the quarks and leptons, one has the up-quark mass matrix M_u being equal to the Dirac mass matrix of the neutrinos which goes into the seesaw formula. As a result, if we work in a basis where the up-quark masses are diagonal so that all CKM mixings come from the down mass matrix, then the number of arbitrary parameters in the seesaw formula goes dowm from 12 to 6. Thus, even though one cannot predict neutrino masses and mixings, the parameters of the theory get fixed by their values as inputs. This may then be testable through its other predictions. The **10** only Higgs models have problems of their own, i.e. there are tree-level mass relations in the down sector such as $m_d/m_s = m_e/m_\mu$ which are renormalization group invariant and are in disagreement with observations. It may be possible in supersymmetric models to generate enough one-loop corrections out of the supersymmetry-breaking terms (nonuniversal) to save the situation but they will introduce unknown parameters into the theory.

*2.7.1. Breaking $B - L$ symmetry: **16** versus **126**.* To derive the standard model at low energies from $SO(10)$ symmetry, we must break the $B - L$ symmetry. The breaking of $B - L$ is responsible for the masses of the right-handed neutrino and is therefore intimately connected with neutrino masses via the seesaw mechanism. In an $SO(10)$ model, $B - L$ can be broken by either a **16**-dimensional Higgs boson or by a **126**-dimensional one. The former breaks $B - L$ by one unit whereas the latter does it by two. This has profound implications if the model is supersymmetric. To see this let us remind the reader that in the minimal supersymmetric standard model (MSSM), (unlike the standard model), the tree-level potential can break lepton and baryon number due to the presence of terms like QLd^c, LLe^c and $u^c d^c d^c$ in the superpotential. These terms go by the name of R-parity violating terms where R-parity symmetry is defined by $R_p = (-1)^{3(B-L)+2S}$ and S is the spin of the particle. These terms not only prevent the existence of stable dark matter, but they also lead to catastrophic decay rates for the proton.

In $SO(10)$ models where $B - L$ is broken by **16**-Higgs fields, there exists terms of the form $(\mathbf{16}_m)^3\mathbf{16}_H$ where the subscript m, H denote matter and Higgs respectively. When $\mathbf{16}_H$ field breaks $B - L$, it does so by its ν_R-like component acquiring a vev. When this vev is substituted in the above dim four term in the superpotential, it generates the R-parity violating terms of MSSM. This can also be seen by looking at the formula for R-parity, where for $B - L = 1$, one gets $R_p = -1$ for the field that breaks $B - L$. Hence R-parity is broken.

On the other hand, if $B - L$ is broken by a **126** Higgs field, the only standard model singlet in this multiplet has $B - L = 2$. Therefore when it acquires a vev, it preserves R-parity and therefore no 'unpleasant' R-p violating terms at the MSSM level. One can also see this by writing all terms in the superpotential to all orders that involve **126** field and giving a vev to the $B - L = 2$ field in it to get the MSSM superpotential from it.

It is therefore clear that if one wants the lightest supersymmetric particle to be the dark matter candidate and one wants to work in an $SO(10)$ theory without specific extra symmetries, the better route to model building is to use the **126** Higgs to break $B - L$.

*2.8. A minimal SO(10) model for neutrinos with **126***

It was noted in [43] that if one considers a minimal $SO(10)$ model with a single **10** Higgs (denoted by H) and a single **126** Higgs (Δ) that couple with fermions, then the model not only leads to a naturally stable dark matter but also is remarkably predictive in the neutrino sector. This class of models has only two Yukawa coupling matrices: $h\psi\psi H + f\psi\psi\Delta$. Since $SO(10)$ symmetry implies that h and f are symmetric matrices, if we ignore CP violation, this model has nine

Yukawa coupling parameters. Since **10** and **126** have four Higgs doublets, in principle each one could have a nonzero vev. This leads to only 13 parameters that describe all quark and lepton masses. Noting further the fact that the Higgs standard model doublets in **126** transform as (2, 2, 15) of $SU(2)_L \times SU(2)_R \times SU(4)_c$, one gets the quark and lepton mass matrices to have the following form:

$$\begin{aligned} M_\ell &= h\kappa_d - 3fv_d, \\ M_{\nu_D} &= h\kappa_u - 3fv_u, \end{aligned} \tag{60}$$

where $\kappa_{u,d}$ are the vev's of the up and down type Higgs doublets in the **10** Higgs and $v_{u,d}$ are the corresponding vevs for the standard model doublets in the **126** Higgs multiplet. Note that there are 13 parameters in the above equations and there are 13 inputs (six quark masses, three lepton masses and three quark mixing angles, mass of the Z-boson).

The next important observation on this model is that the same **126** responsible for the fermion masses also has a vev along the $\nu_R\nu_R$ directions so that it generates the right-handed neutrino mass matrix which are proportional to the f matrix. Thus, using the seesaw formula (type I), there are no free parameters in the light neutrino sector.

This model was extensively analysed in [43] before the emergence of all the neutrino oscillation data in late 1990s. It is now known that this minimal $SO(10)$ model without any CP phase cannot fit both the solar and the atmospheric neutrino data simultaneously and is therefore ruled out. It has however been recently noted that once the CP phases are properly included in the discussion, this model can yield a near-bimaximal mixing pattern for neutrinos [44]. However, this version has also now been ruled out.

It was noted in [45] for the case of two generations that if one assumes that the direct triplet term in type II seesaw dominates the seesaw formula, then it provides a very natural understanding of the large atmospheric mixing angle. The simple way to see it is to note that when the triplet term dominates the seesaw formula, then we have the neutrino mass matrix $\mathcal{M}_\nu \propto f$, where f matrix is the **126** coupling with fermions discussed earlier. Using the above equations, one can derive the following sum rule [46]:

$$\mathcal{M}_\nu = c(M_d - M_\ell). \tag{61}$$

Now quark lepton symmetry implies that for the second and third generations, the $M_{d,\ell}$ have the following general form:

$$M_d = \begin{pmatrix} \epsilon_1 & \epsilon_2 \\ \epsilon_2 & m_b \end{pmatrix} \tag{62}$$

and

$$M_\ell = \begin{pmatrix} \epsilon_1' & \epsilon_2' \\ \epsilon_2' & m_\tau \end{pmatrix}, \tag{63}$$

where $\epsilon_i \ll m_{b,\tau}$ as is required by low-energy observations. It is well known that in supersymmetric theories, when low-energy quark and lepton masses are extrapolated to the GUT scale, one gets approximately that $m_b \simeq m_\tau$. One then sees from the above sum rule for neutrino masses that all entries for the neutrino mass matrix are of the same order leading very naturally to the atmospheric mixing angle to be large.

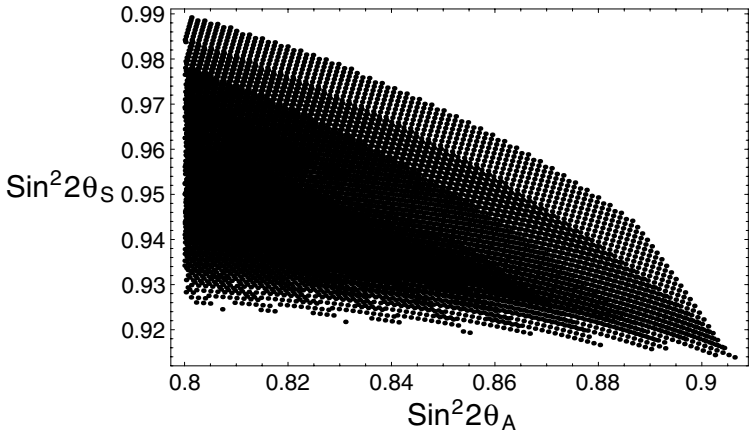

Figure 1. The range of predictions for $\sin^2 2\theta_\odot$ and $\sin^2 2\theta_A$ for the range of quark masses in table 2 that fit the charged lepton spectrum and where all CP phases are set to zero. It was required that the ratio $\Delta m^2_\odot/\Delta m^2_A \leqslant 0.05$. Note that $\sin^2 2\theta_\odot \geqslant 0.9$ and $\sin^2 2\theta_A \leqslant 0.9$.

Since in this model there are no free parameters, it was not clear from the work of Bajc *et al* [45] that the solar mixing angle will fit observations. This question was addressed in [47], where it was shown that the same model can also lead to a large solar mixing angle. A simple way to see this is as follows.

Note that in the basis where the down-quark mass matrix is diagonal, all the quark mixing effects can be put in the down-quark mass matrix, i.e. $M_d = U_{CKM} M_d^d U_{CKM}^{\mathrm{T}}$. Using the Wolfenstein parametrization for quark mixings, we can conclude that we have

$$M_d \approx m_b \begin{pmatrix} \lambda^4 & \lambda^5 & \lambda^3 \\ \lambda^5 & \lambda^2 & \lambda^2 \\ \lambda^3 & \lambda^2 & 1 \end{pmatrix}. \tag{64}$$

In this model, there is a sum rule of the form $M_\ell = c_u M_u + c_d M_d$ which implies that M_ℓ and M_d have roughly similar pattern. In the above equation, the matrix elements are supposed to give only the approximate order of magnitude. As we extrapolate the quark masses to the GUT scale, due to the fact that $m_b - m_\tau \approx m_\tau \lambda^2$ for some value of $\tan\beta$, the neutrino mass matrix $M_\nu = c(M_d - M_\ell)$ takes roughly the form [21]

$$M_\nu = c(M_d - M_\ell) \approx m_0 \begin{pmatrix} \lambda^4 & \lambda^5 & \lambda^3 \\ \lambda^5 & \lambda^2 & \lambda^2 \\ \lambda^3 & \lambda^2 & \lambda^2 \end{pmatrix}. \tag{65}$$

It is then easy to see from this mass matrix that both the θ_{12} (solar angle) and θ_{23} (the atmospheric angle) are large. It also turns out that the ratio of masses $m_2/m_3 \approx \lambda$, which explains the milder hierarchy among neutrinos compared with that among quarks. Mixing angle should be predicted and one has to see whether it is large. In fact, one such attempt before did give a small mixing angle, although there might be other domains of parameters where one may get a large solar mixing angle. Detailed calculations for this have shown that the model is quite consistent with present neutrino mixing data (see figures 1 and 2). Furthermore, it predicts the

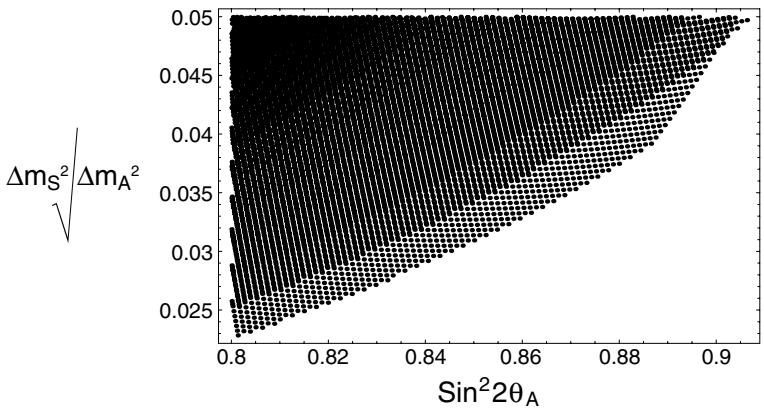

Figure 2. The predictions for $\sin^2 2\theta_A$ and $\Delta m^2_{\odot}/\Delta m^2_A$ for the range of quark masses and mixings that fit charged lepton masses and where all CP phases in the fermion masses are set to zero.

$\theta_{13} = 0.16$ which can be tested in the MINOS as well as other planned long base line neutrino experiments.

Recently, other $SO(10)$ models have been considered where, under different assumptions, the atmospheric and solar neutrino data can be explained together [48].

2.9. Type II seesaw and quasi-degenerate neutrinos

In this subsection we will discuss some issues related to the degenerate neutrino hypothesis, which will be necessary if there is evidence for neutrinoless double beta decay at a significant level (see, for example, the recent results from the Heidelberg–Moscow group [13]) and assuming that no other physics such as R-parity breaking or doubly charged Higgs, etc are not the source of this effect). Thus, it is appropriate to discuss how such models can arise in theoretical schemes and how stable they are under radiative corrections.

There are two aspects to this question: one is whether the degeneracy arises within a gauge theory framework without arbitrary adjustment of parameters and the second aspect is that, given such a degeneracy arises at some scale naturally in a field theory, whether this mass degeneracy is stable under renormalization group extrapolation to the weak scale where we need the degeneracy to be present. In this section we comment on the former aspect.

It has already been alluded to before and first mentioned in [18] that degenerate neutrinos arise naturally in models that employ the type II seesaw since the first term in the mass formula is not connected to the charged fermion masses. One way that has been discussed is to consider schemes where one uses symmetries such as $SO(3)$ or $SU(2)$ or permutation symmetry S_4 [56] so that the Majorana Yukawa couplings f_i are all equal. This then leads to the dominant contribution to all neutrinos being equal. This symmetry however must be broken in the charged fermion sector to explain the observed quark and lepton masses. Such models consistent with known data have been constructed based on $SO(10)$ as well as other groups. The interesting point about the $SO(10)$ realization is that the dominant contributions to the Δm^2s in this model comes from the second term in the type II seesaw formula which in simple models is hierarchical. It is of course known that if the MSW solution to the solar neutrino puzzle is the right solution (or an energy-independent solution), then we have $\Delta m^2_{solar} \ll \Delta m^2_{ATMOS}$. In fact, if we use

the fact that $M_u = M_D$ holds in $SO(10)$ models then we have $\Delta m^2_{ATMOS} \simeq m_0 m_t^2/fv_R$ and $\Delta m^2_{SOLAR} \simeq m_0 m_c^2/fv_R$, where m_0 is the common mass for the three neutrinos. It is interesting that for $m_0 \sim$ few eV and $fv_R \approx 10^{15}$ GeV, both the Δm^2s are close to the required values.

Outside the seesaw framework, there could also be electroweak symmetries that guarantee the mass degeneracy; see [20] for a recent model of this type.

The second question of stability under RGE of such a pattern is discussed in a subsequent section.

Section 3

3.1. Lepton flavour violation and neutrino masses

In the standard model, the masslessness of the neutrino implies that that there is no lepton flavour changing effects unlike in the quark sector. Once one includes the right-handed neutrinos N_R, one for each family, there is lepton mixing and therefore lepton flavour changing effects such as $\mu \to e + \gamma$, $\tau \to e, \mu + \gamma$, etc. However, a simple estimate of the one-loop contribution to such effects shows that the amplitude is of the order

$$A(\ell_j \to \ell_i + \gamma) \simeq \frac{eG_F m_{\ell_j} m_e m_\nu^2}{\pi^2 m_W^2} \mu_B. \tag{66}$$

This leads to an unobservable branching ratio (of the order $\sim 10^{-40}$) for the rare radiative decay modes for the leptons.

The situation however changes drastically as soon as the seesaw mechanism for neutrino masses is embedded into the supersymmetric models. It has been noted in many papers already that in supersymmetric theories, the lepton flavour changing effects get significantly enhanced. They arise from the the mixings among sleptons (superpartners of leptons) of different flavour caused by the renormalization group extrapolations which via loop diagrams lead to lepton flavour-violating (LFV) effects at low energies [58].

The way this happens is as follows. In the simplest $N = 1$ supergravity models [57], the supersymmetry-breaking terms at the Planck scale are taken to have only few parameters: a universal scalar mass m_0, universal A terms and one gaugino mass $m_{1/2}$ for all three types of gauginos. Clearly, a universal scalar mass implies that at the Planck scale, there is no flavour violation anywhere except in the Yukawa couplings (or when the Yukawa terms are diagonalized in the CKM angles). However, as we extrapolate this theory to the weak scale, the flavour mixings in the Yukawa interactions induce nonuniversal flavour-violating scalar mass terms (i.e. flavour-violating slepton and squark mass terms). In the absence of neutrino masses, the Yukawa matrices for leptons can be diagonalized so that there is no flavour violation in the lepton sector even after extrapolation down to the weak scale. On the other hand, when neutrino mixings are present, there is no basis where all leptonic flavour mixings can be made to disappear. In fact, in the most general case, of the three matrices Y_ℓ, the charged lepton coupling matrix, Y_ν, RH neutrino Yukawa coupling and M_{N_R}, the matrix characterizing the heavy RH neutrino mixing, only one can be diagonalizd by an appropriate choice of basis and the flavour mixing in the other two remain. In a somewhat restricted case where the right-handed neutrinos do not have any interaction other than the Yukawa interaction and an interaction that generates the Majorana mass for the right-handed neutrino, one can only diagonalize two out of the three matrices (i.e. Y_ν, Y_ℓ and M_R). Thus, there will always be lepton flavour-violating terms in the basic Lagrangian, no matter what

basis one chooses. These LFV terms can then induce mixings between the sleptons of different flavour and lead to LFV processes. If we keep the M_ℓ diagonal by choice of basis, searches for LFV processes such as $\tau \to \mu + \gamma$ and/or $\mu \to e + \gamma$ can throw light on the RH neutrino mixings/or family mixings in M_D, as has already been observed.

Since in the absence of CP violation, there are at least six mixing angles (nine if M_D is not symmetric) in the seesaw formula and only three are observable in neutrino oscillation, to get useful information on the fundamental high scale theory from LFV processes, it is assumed that M_{N_R} is diagonal so that one has a direct correlation between the observed neutrino mixings and the fundamental high scale parameters of the theory. The important point is that the flavour mixings in Y_ν then reflect themselves in the slepton mixings that lead to the LFV processes via the RGEs.

From the point of view of the LFV analysis, there are essentially two classes of neutrino mass models that need to be considered: (i) the first class is where it is assumed that the RH neutrino mass M_{N_R} is either a mass term in the basic Lagrangian or arises from nonrenormalizable terms such as $\nu^c \chi^{c2}/M_{P\ell}$, as in a class of $SO(10)$ models; and (ii) a second class where the Majorana mass of the right-handed neutrino itself arises from a renormalizable Yukawa coupling, e.g. $f\nu^c\nu^c\Delta$. In the first class of models, in principle, one could decide to have all the flavour mixing effects in the right-handed neutrino mass matrix and keep the Y_ν diagonal. In that case, RGEs would not induce any LFV effects. However, we will bar this possibility and consider the case where all flavour mixings are in the Y_ν so that RGEs can induce LFV effects and estimate them in what follows. In class two models on the other hand, there will always be an LFV effect, although its magnitude will depend on the choice of the seesaw scale (v_{BL}).

Examples of class two models are models for neutrino mixings such as $SO(10)$ with a **126** Higgs field [43] or left–right model with a triplet Higgs, whose vev is the seesaw scale.

In both these examples, the key equations that determine the extent of lepton flavour violation are:

Case (i):

$$\begin{aligned}\frac{\mathrm{d}m_L^2}{\mathrm{d}t} &= \frac{1}{4\pi^2}[(m_L^2 + 2m_{H_d}^2)Y_\ell^\dagger Y_\ell + (m_L^2 + 2H_u^2)Y_\nu^\dagger Y_\nu + 2Y_\ell^\dagger m_{e^c}^2 Y_\ell + Y_\ell^\dagger Y_\ell m_\ell^2 \\ &\quad + 2Y_\nu^\dagger m_{\nu^c}^2 Y_\nu + Y_\nu^\dagger Y_\nu m_\ell^2 + 2A_\ell^\dagger A_\ell + 2A_\nu^\dagger A_\nu - f(g^2)], \\ \frac{\mathrm{d}A_\ell}{\mathrm{d}t} &= \frac{1}{16\pi^2}A_\ell[\mathrm{Tr}(3Y_d^\dagger Y_d + Y_\ell^\dagger Y_\ell) + 5Y_\ell^\dagger Y_\ell + Y_\nu^\dagger Y_\nu - 3g_2^2 - ag_R^2 - bg_{B-L}^2] \\ &\quad + Y_\ell[\mathrm{Tr}(6A_d Y_d^\dagger + A_\ell Y_\ell^\dagger) + 4Y_\ell^\dagger A_\ell + 2Y_\nu^\dagger A_\nu + 6g_2^2 M_2 + \cdots]. \end{aligned} \tag{67}$$

Case (ii): In addition to the above two equations, two more equations are necessary:

$$\begin{aligned}\frac{\mathrm{d}Y_\nu}{\mathrm{d}t} &= \frac{Y_\nu}{16\pi^2}[\mathrm{Tr}(3Y_u Y_u^\dagger + Y_\nu Y_\nu^\dagger) + 3Y_\nu^\dagger Y_\nu + Y_\ell^\dagger Y_\ell + 4f^\dagger f - 3g_2^2 - c_R g_R^2 - c_{B-L} g_{B-L}^2], \\ \frac{\mathrm{d}A_\nu}{\mathrm{d}t} &= \frac{1}{16\pi^2}A_\nu[\mathrm{Tr}(3Y_u^\dagger Y_u + Y_\nu^\dagger Y_\nu) + 5Y_\nu^\dagger Y_\nu + Y_\ell^\dagger Y_\ell + 4f^\dagger f - 3g_2^2 - ag_R^2 - bg_{B-L}^2] \\ &\quad + Y_\ell[\mathrm{Tr}(6A_d Y_d^\dagger + A_\ell Y_\ell^\dagger) + 4Y_\ell^\dagger A_\ell + 6g_2^2 M_2 + \cdots). \end{aligned} \tag{68}$$

To apply these equations, we note that in the basis where the charged lepton masses are diagonal, the seesaw formula involves the right-handed neutrino mass matrix M_R and the neutrino Dirac mass matrix M_D. Assuming the Dirac mass matrix is symmetric, there are 12 parameters (for the case with CP conservation). Since neutrino masses and mixings only provide six observables, there are several different ways that can lead to the observed neutrino mixings. Two distinct extreme ways are as follows: (i) the first case is where the neutrino mixings arise primarily from the off-diagonal elements of the M_D assuming the M_R is diagonal or even an extremely simplified case where it is a unit matrix and (ii) a second case where we can keep the M_D diagonal and all mixings arise from M_R having mixings. In the first case, the RGEs always lead to lepton flavour violation, whereas in the second case, flavour violations arise only if the M_R arises from a Majorana Yukawa coupling of the form $\nu^c\nu^c\Delta$ after $\langle\Delta\rangle \neq 0$ as already explained. We will call this the Majorana case and case (i) as the Dirac case.

In the Dirac case, starting with the simplest supersymmetry breaking assumption of universal scalar masses and proportional A terms, the scalar sleptons develop off-diagonal terms due to the flavour violation in Y_ν and these mass terms have the form

$$m^2_{\tilde{L},ij} \propto \frac{3+a^2}{16\pi^2} \ln \frac{M_{P\ell}}{M_{B-L}} Y^\dagger_\nu Y_\nu + \cdots, \tag{69}$$

where $\cdots$ denote the diagonal terms that cannot cause flavour mixing. If the M_R is diagonal, the $Y^\dagger_\nu Y_\nu$ is nothing but the neutrino mass matrix upto a constant $= M_R$. Using this we can get the Dirac mass dependence of the $B(\ell_j \to e+\gamma)$ (for $\ell_j = \tau, \mu$) to be

$$B(\ell_j \to e+\gamma) \sim \frac{(m_2 cs + m_3\epsilon)^2 v^2_{B-L}}{G_F^2 v^4_{wk} m_0^4} c_{\ell_j}, \tag{70}$$

where $c_\tau = 1/6$ and $c_\mu = 1$, whereas for $B(\tau \to \mu+\gamma) \propto 6m_3^2 v^2_{B-L}/4G_F^2 v^4_{wk} m_0^4$.

Now coming to the second case with Majorana–Yukawa couplings, starting with universal scalar masses at the Planck scale and in the Majorana–Yukawa case all couplings flavour diagonal except the f coupling, it is easy to see that the above equations will induce flavour changing effects in $m^2_{\tilde{L}}$ and A_ℓ. The strength of the slepton flavour mixings depends sensitively on the neutrino mass texture and the resulting texture in the coupling matrix f. Below we give the branching ratio expressions for one extreme case where we assume that the lightest neutrino mass dominates the f matrix elements. We caution the reader that this is by no means the most typical case and results differ significantly as different mass textures are considered [26].

The slepton flavour mixings, via a one-loop diagram involving the winos ($\tilde{W}^+$ and $\tilde{W}^3$) lead to the lepton flavour changing radiative amplitudes. Keeping only the contribution of the $m^2_{\tilde{L}}$ term which dominates for larger $\tan\beta$, we find that roughly speaking the three branching ratios are given by

$$B(\mu \to e+\gamma) \propto \frac{1}{G_F^2 m_0^4 v^4_{B-L}} \frac{m^4_{D3} m^6_{D2} m^2_{D1} \tan^2\beta}{m_1^4 v^4_{wk}}, \tag{71}$$

$$B(\tau \to e+\gamma) \propto \frac{1}{G_F^2 m_0^4 v^4_{B-L}} \frac{m^{10}_{D3} m^2_{D1} \tan^2\beta}{m_1^4 v^4_{wk}}, \tag{72}$$

$$B(\tau \to \mu+\gamma) \propto \frac{1}{G_F^2 m_0^4 v^4_{B-L}} \frac{m^{10}_{D3} m^2_{D2} \tan^2\beta}{m_1^4 v^4_{wk}}. \tag{73}$$

Note an important difference between the predictions for the Dirac case and the Majorana one. Both $\tau \to e + \gamma$ and $\mu \to e + \gamma$ are of the same order of magnitude for the Dirac case, whereas they are very different for the Majorana case where $B(\mu \to e + \gamma)/B(\tau \to e + \gamma) \simeq (m_{D2}/m_{D3})^6$. Therefore, even a mild hierarchy in the Dirac mass sector can make the $\tau \to e + \gamma$ branching ratio much larger than the $\mu \to e + \gamma$ branching ratio. This kind of discrepancy could, in principle, be used to test the origin of the seesaw mechanism.

It must be pointed out that the predictions for the Majorana case are extremely texture-sensitive. In a recent paper [26], calculations have been carried out for a different but consistent texture where $B(\mu \to e + \gamma)$, although much lower than the τ rare decay branching ratios is still found to be within the range of currently planned experiments at PSI.

For completeness, we give the formula for calculating the radiative decay of the leptons. If we express the amplitude for the decay as

$$\mathcal{L} = iem_j(\bar{\ell}_{jL}\sigma_{\mu\nu}\ell_{iR}C_L + \bar{\ell}_{jR}\sigma_{\mu\nu}\ell_{iL}C_R)F^{\mu\nu} + \text{h.c.}, \tag{74}$$

then the branching ratio for the decay $\ell_j \to \ell_i + \gamma$ is given by the formula

$$B(\ell_j \to \ell_i + \gamma) = \frac{48\pi^3\alpha_{em}}{G_F^2}(|C_L|^2 + |C_R|^2)B(\ell_j \to \ell_i + 2\nu). \tag{75}$$

3.2. Renormalization group evolution of the neutrino mass matrix

In the seesaw models for neutrino masses, the neutrino mass arises from the effective operator

$$\mathcal{O}_\nu = -\frac{1}{4}\kappa_{\alpha\beta}\frac{L_\alpha H L_\beta H}{M} \tag{76}$$

after symmetry breaking $\langle H^0 \rangle \neq 0$; here L and H are the leptonic and weak doublets, respectively. α and β denote the weak flavour index. The matrix κ becomes the neutrino mass matrix after symmetry breaking, i.e. $\langle H^0 \rangle \neq 0$. This operator is defined at the scale M since it arises after the heavy field N_R is integrated out. On the other hand, in conventional oscillation experiments, the neutrino masses and mixings being probed are at the weak scale. One must therefore extrapolate the operator down from the seesaw scale M to the weak scale M_Z [59]. The form of the renormalization group extrapolation of course depends on the details of the theory. For simplicity, we will consider only the supersymmetric theories, where the only contributions come from the wave function renormalization and is therefore easy to calculate. The equation governing the extrapolation of the $\kappa_{\alpha\beta}$ matrix is given in the case of MSSM by

$$\frac{\mathrm{d}\kappa}{\mathrm{d}t} = [-3g_2^2 + 6\mathrm{Tr}(Y_u^\dagger Y_u)]\kappa + \frac{1}{2}[\kappa(Y_e^\dagger Y_e) + (Y_e^\dagger Y_e)\kappa]. \tag{77}$$

We note two kinds of effects on the neutrino mass matrix from the above formula: (i) one that is flavour-independent and (ii) a part that is flavour-specific. If we work in a basis where the charged leptons are diagonal, then the resulting correction to the neutrino mass matrix is given by

$$\mathcal{M}_\nu(M_Z) = (1 + \delta)\mathcal{M}(M_{B-L})(1 + \delta), \tag{78}$$

where δ is a diagonal matrix with matrix elements $\delta_{\alpha\alpha} \simeq -m_\alpha^2 \tan^2\beta/16\pi^2 v^2$. In more complicated theories, the corrections will be different. Let us now study some implications of these corrections. For this first note that in the MSSM, this effect can be sizeable if $\tan\beta$ is large (of the order 10 or greater).

3.3. Radiative magnification of neutrino mixing angles

A major puzzle of quark lepton physics is the diverse nature of the mixing angles. Whereas in the quark sector the mixing angles are small, for the neutrinos they are large. One possible suggestion in this connection is that perhaps the mixing angles in both quark and lepton sectors at similar at some high scale; however, due to renormalization effects, they may become magnified at low scales. It was shown in [60] that this indeed happens if the neutrino spectrum is degenerate. This can be seen in a simple way for the $\nu_\mu - \nu_\tau$ sector [60].

Let us start with the mass matrix in the flavour basis:

$$\mathcal{M}_{\mathcal{F}} = \mathcal{U}^* \mathcal{M}_{\mathcal{D}} \mathcal{U}^\dagger = \begin{pmatrix} C_\theta & S_\theta \\ -S_\theta & C_\theta \end{pmatrix} \begin{pmatrix} m_1 & 0 \\ 0 & m_2 e^{-i\phi} \end{pmatrix} \begin{pmatrix} C_\theta & -S_\theta \\ S_\theta & C_\theta \end{pmatrix}. \tag{79}$$

Let us examine the situation when $\phi = 0$ (i.e. CP is conserved), which corresponds to the case when the neutrinos ν_1 and ν_2 are in the same CP eigenstate. Due to the presence of radiative corrections to m_1 and m_2, the matrix $\mathcal{M}_{\mathcal{F}}$ gets modified to

$$\mathcal{M}_{\mathcal{F}} \to \begin{pmatrix} 1+\delta_\alpha & 0 \\ 0 & 1+\delta_\beta \end{pmatrix} \mathcal{M}_{\mathcal{F}} \begin{pmatrix} 1+\delta_\alpha & 0 \\ 0 & 1+\delta_\beta \end{pmatrix}. \tag{80}$$

The mixing angle $\bar{\theta}$ that now diagonalizes the matrix $\mathcal{M}_{\mathcal{F}}$ at the low scale μ (after radiative corrections) can be related to the old mixing angle θ by the following expression:

$$\tan 2\bar{\theta} = \tan 2\theta (1 + \delta_\alpha + \delta_\beta) \frac{1}{\lambda}, \tag{81}$$

where

$$\lambda \equiv \frac{(m_2 - m_1) C_{2\theta} + 2\delta_\beta (m_1 S_\theta^2 + m_2 C_\theta^2) - 2\delta_\alpha (m_1 C_\theta^2 + m_2 S_\theta^2)}{(m_2 - m_1) C_{2\theta}}. \tag{82}$$

If

$$(m_1 - m_2) C_{2\theta} = 2\delta_\beta (m_1 S_\theta^2 + m_2 C_\theta^2) - 2\delta_\alpha (m_1 C_\theta^2 + m_2 S_\theta^2), \tag{83}$$

then $\lambda = 0$ or equivalently $\bar{\theta} = \pi/4$, i.e. maximal mixing. Given the mass heirarchy of the charged leptons, $m_{l_\alpha} \ll m_{l_\beta}$, we expect $|\delta_\alpha| \ll |\delta_\beta|$, which reduces (83) to a simpler form:

$$\epsilon = \frac{\delta m C_{2\theta}}{(m_1 S_\theta^2 + m_2 C_\theta^2)}. \tag{84}$$

For MSSM, the radiative magnification condition can be satisfied provided

$$h_\tau(\mathrm{MSSM}) \approx \sqrt{\frac{8\pi^2 |\Delta m^2(\Lambda)| C_{2\theta}}{\ln(\Lambda/\mu) m^2}}. \tag{85}$$

For $\Delta m^2 \simeq \Delta m_A^2$, this condition can be satisfied for a very wide range of $\tan\beta$.

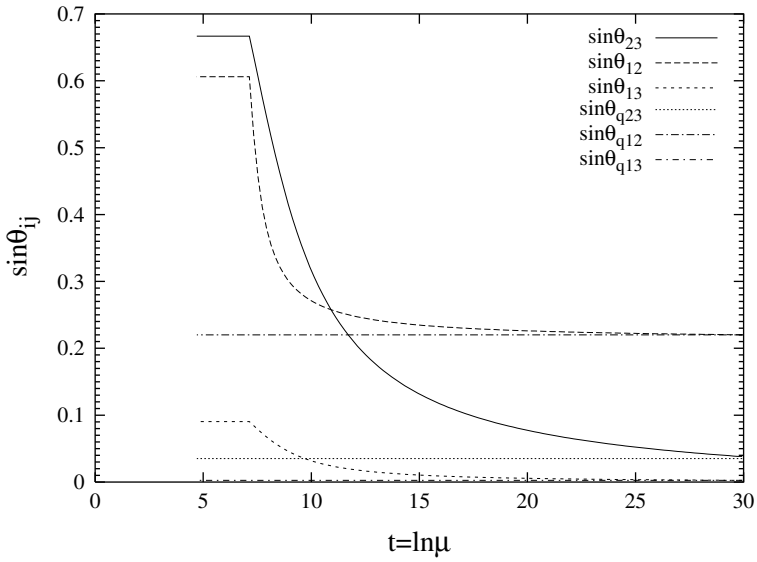

Figure 3. Evolution of small quark-like mixings at the seesaw scale to bi-large neutrino mixings at low energies for the seesaw scale $M_R = 10^{13}$ GeV with $\tan\beta = 55$, $M_{\rm SUSY} = 1$ TeV and mass eigenvalues and mixing angles as given in the first column of table 1. The solid, long-dashed and short-dashed lines represent $\sin\theta_{23}$, $\sin\theta_{13}$ and $\sin\theta_{12}$, respectively, as defined in the text. The evolution of sines of quark mixing angles, $\sin\theta_{qij}$ $(i, j = 1, 2, 3)$, are presented by almost horizontal lines.

A particularly intriguing result was recently found in [61], where it was shown that if one sets the neutrino and quark masses to be equal at the seesaw scale and if the quark masses are quasi-degenerate, then as the mixing angles are extrapolated to the weak scale, they get 'magnified' in such a way that the solar and the atmospheric angles become large and the θ_{13} remains within the present experimental limit. The detailed predictions are given in figure 3.

An important criterion for this to happen is that the common mass for all neutrinos must be above 0.1 eV, a value which can be detected in the planned double beta decay experiments.

It is important to emphasize that this magnification occurs only if at the seesaw scale the neutrino masses are nearly degenerate. A similar mechanism using the right-handed neutrino Yukawa couplings instead of the charged leptons has been carried out recently [62]. Here two conditions must be satisfied: (i) the neutrino spectrum must be nearly degenerate (i.e. $m_1 \simeq m_2$ as in [60]) and (ii) there must be a hierarchy between the right-handed neutrinos.

3.4. Generation of solar mass difference square in the case of L_e–L_μ–L_τ symmetric models

In this section, we give another example where the renormalization group evolution (RGE) of the neutrino mass matrix plays an important role. Consider the following neutrino mass matrix defined at a (unification) scale much above the weak scale as in equation (6):

$$\mathcal{M}_\nu^0 = \begin{pmatrix} 0 & 1 & 1 \\ 1 & 0 & 0 \\ 1 & 0 & 0 \end{pmatrix} m \tag{86}$$

Note that as already emphasized earlier, this matrix has several deficits as far as accomodating neutrino data is concerned. To remind the reader, the problems are twofold: (i) it leads to $\Delta m^2_\odot = 0$ and (ii) solar neutrino mixing angle is maximal. As we show below, RGEs can help to overcome both these defects.

The important point to note is that the RGE depends on the charged lepton mass matrix. Let us assume that the charged lepton mass matrix has the form

$$\mathcal{M}_{\ell^+} = \begin{pmatrix} 0 & 0 & x \\ 0 & y & 0 \\ x' & 0 & 1 \end{pmatrix} m_\tau. \tag{87}$$

For the most part we will take $x' = x$ so that $|x| \simeq \sqrt{m_e/m_\tau}$ and $y \simeq m_\mu/m_\tau$. We will also consider the possibility that $x \gg x'$ (the right-handed singlet leptons multiply the matrix in this equation on the right). In the case $x = x'$; note that there is only a parameter in the leptonic sector (both the charged leptons and neutrinos). We will show that this model can lead to a realistic description of the neutrino oscillations.

At scales below the unification scale, through the renormalization of the effective $d = 5$ neutrino mass operator the form of M^0_ν [30] will be modified. (Analogous corrections in M_{ℓ^+} is negligible.) The modified neutrino mass matrix at the weak scale is given by

$$\mathcal{M}_\nu \simeq \mathcal{M}^0_\nu + \frac{c}{16\pi^2}\ln(M_U/M_Z)(Y_\ell Y^\dagger_\ell M^0_\nu + M^0_\nu (Y_\ell Y^\dagger_\ell)^{\mathrm{T}}). \tag{88}$$

Here $c = -3/2$ for SM while $c = 1$ for SUSY, and Y_ℓ is the charged lepton Yukawa coupling matrix. We have absorbed the flavour-independent renormalization factor into the definition of m in the above equation. Explicitly,

$$\mathcal{M}_\nu \simeq \begin{pmatrix} 2rx & 1 + r(x^2 + y^2) & 1 + r(1 + 2x^2) \\ 1 + r(x^2 + y^2) & 0 & rx \\ 1 + r(1 + 2x^2) & rx & 2rx \end{pmatrix} m. \tag{89}$$

This mass matrix has both an acceptable $\Delta m^2_\odot$ as well as large (but not maximal) solar neutrino mixing angle. This is another example where the renormalization group equations do make a difference in our understanding of the neutrino oscillations.

3.5. A horizontal symmetry approach to near bimaximal mixing

In this section, I present a model [24] which motivates the existence of an $SU(2)_H$ horizontal symmetry acting on leptons to understand the near bimaximal mixing pattern and yields the softly broken L_e–L_μ–L_τ model discussed earlier.

Suppose there is an $SU(2)_H$ horizontal symmetry that acts only on leptons. As already discussed, freedom from global Witten anomaly requires that there must be two right-handed neutrinos that transform as a doublet of $SU(2)_H$. The local $SU(2)_H$ symmetry then implies that the masses of these two right-handed neutrinos are protected and must be at the scale of $SU(2)_H$ breaking. If there is a third right-handed neutrino for reasons of quark lepton symmetry, then it will acquire a mass of the order of the Planck or string scale and decouple

from neutrino physics at lower energies. This therefore provides a physically distinct way of implementing the seesaw mechanism. One has a 3×2 seesaw rather than the usual 3×3 one.

Furthermore, the $SU(2)$ horizontal symmetry restricts both the Dirac mass of the neutrino as well as the right-handed neutrino mass matrix to the forms [24]

$$M_{\nu_L,\nu_R} = \begin{pmatrix} 0 & 0 & 0 & h_0\kappa_0 & 0 \\ 0 & 0 & 0 & 0 & h_0\kappa_0 \\ 0 & 0 & 0 & h_1\kappa_1 & h_1\kappa_2 \\ h_0\kappa_0 & 0 & h_1\kappa_1 & 0 & fv'_H \\ 0 & h_0\kappa_0 & h_1\kappa_2 & fv'_H & 0 \end{pmatrix}. \tag{90}$$

After seesaw diagonalization, it leads to the light neutrino mass matrix of the form

$$\mathcal{M}_\nu = -M_D M_R^{-1} M_D^{\mathrm{T}}, \tag{91}$$

where

$$M_D = \begin{pmatrix} h_0\kappa_0 & 0 \\ 0 & h_0\kappa_0 \\ h_1\kappa_1 & h_1\kappa_2 \end{pmatrix}, \qquad M_R^{-1} = \frac{1}{fv'_H}\begin{pmatrix} 0 & 1 \\ 1 & 0 \end{pmatrix}.$$

The resulting light Majorana neutrino mass matrix $\mathcal{M}_\nu$ is given by

$$\mathcal{M}_\nu = -\frac{1}{fv'_H}\begin{pmatrix} 0 & (h_0\kappa_0)^2 & h_0h_1\kappa_0\kappa_2 \\ (h_0\kappa_0)^2 & 0 & h_0h_1\kappa_0\kappa_1 \\ h_0h_1\kappa_0\kappa_2 & h_0h_1\kappa_0\kappa_1 & 2h_1^2\kappa_1\kappa_2 \end{pmatrix}. \tag{92}$$

To get the physical neutrino mixings, we also need the charged lepton mass matrix defined by $\bar{\psi}_L \mathcal{M}_\ell \psi_R$. This is given in our model by

$$\mathcal{M}_\ell = \begin{pmatrix} h'_2\kappa_0 & 0 & -h'_1\kappa_2 \\ 0 & h'_2\kappa_0 & h'_1\kappa_1 \\ h'_4\kappa_1 & h'_4\kappa_2 & h'_3\kappa_0 \end{pmatrix}. \tag{93}$$

Note that in the limit of $\kappa_1 = 0$, the neutrino mass matrix has exact $(L_e\text{–}L_\mu\text{–}L_\tau)$ symmetry, whereas the charged lepton mass matrix breaks this symmetry. This is precisely the class of inverted hierarchy models that was discussed earlier which provides a realistic as well as a testable model for neutrino oscillations. In particular, this model leads to a relation between the neutrino parameters U_{e3} and the ratio of solar and atmospheric mass difference squared, i.e.

$$U_{e3}^2 \cos 2\theta_\odot = \frac{\Delta m_\odot^2}{2\Delta m_A^2} + \mathrm{O}(U_{e3}^4, m_e/m_\mu), \tag{94}$$

which is testable in proposed long baseline experiments such as NUMI off-axis plan at Fermilab or JHF in Japan.

Section 4

4.1. Neutrino masses in models with large extra dimensions

One of the important predictions of string theories is the existence of more than three space dimensions. For a long time, it was believed that these extra dimensions are small and are therefore practically inconsequential as far as low-energy physics is concerned. However, recent progress in the understanding of the nonperturbative aspects of string theories has opened up the possibility that some of these extra dimensions could be large [66, 67] without contradicting observations. In particular, models where some of the extra dimensions have sizes as large as a millimetre and where the string scale is in the few TeV range have attracted a great deal of phenomenological attention in the past two years [66]. The basic assumption of these models, inspired by the D-branes in string theories, is that the space–time has a brane-bulk structure, where the brane is the familiar (3 + 1)-dimensional space–time, with the standard model particles and forces residing in it, and the bulk consists of all space dimensions where gravity and other possible gauge singlet particles live. One could of course envision $(3 + d + 1)$-dimensional D-branes where d-space dimensions have miniscule ($\leqslant \mathrm{TeV}^{-1}$) size. The main interest in these models has been due to the fact that the low string scale provides an opportunity to test them using existing collider facilities.

A major challenge to these theories comes from the neutrino sector, the first problem being how one understands the small neutrino masses in a natural manner. The conventional seesaw [5] explanation which is believed to provide the most satisfactory way to understand this requires that the new physics scale (or the scale of $SU(2)_R \times U(1)_{B-L}$ symmetry) be around 10^9–10^{12} GeV or higher, depending on the Dirac masses of the neutrinos whose magnitudes are not known. If the highest scale of the theory is a TeV, clearly the seesaw mechanism does not work, so one must look for alternatives. The second problem is that if one considers only the standard model group in the brane, operators such as $LHLH/M_*$ could be induced by string theory in the low-energy-effective Lagrangian. For TeV scale strings this would obviously lead to unacceptable neutrino masses.

One mechanism suggested in [68] is to postulate the existence of one or more gauge singlet neutrinos, ν_B, in the bulk which couple with the lepton doublets in the brane. After electroweak symmetry breaking, this coupling can lead to neutrino Dirac masses, which are suppressed by the ratio $M_*/M_{P\ell}$, where $M_{P\ell}$ is the Planck mass and M_* is the string scale. This is sufficient to explain small neutrino masses and owes its origin to the large bulk volume that suppresses the effective Yukawa couplings of the Kaluza–Klein (KK) modes of the bulk neutrino to the brane fields. In this class of models, naturalness of small neutrino mass requires that one must assume the existence of a global $B - L$ symmetry in the theory, since that will exclude the undesirable higher-dimensional operators from the theory.

To discuss the mechanisms in a concrete setting, let us first focus on TeV scale models. Here, one postulates a bulk neutrino, which is a singlet under the electroweak gauge group. Let us denote the bulk neutrino by $\nu_B(x^\mu, y)$. The bulk neutrino is represented by a four-component spinor and can be split into two chiral Weyl two-component spinors as $\nu_B^{\mathrm{T}} = (\chi^{\mathrm{T}}, -\mathrm{i}\phi^\dagger\sigma_2)$. The two-component spinors χ and ϕ can be decomposed in terms of four-dimensional Fourier components as follows:

$$\chi(x, y) = \frac{1}{\sqrt{2R}}\chi_{+,0} + \frac{1}{\sqrt{R}}\sum_{n=1}^{\infty}\left(\chi_{+,n}\cos\frac{n\pi y}{R} + \mathrm{i}\chi_{-,n}\sin\frac{n\pi y}{R}\right). \tag{95}$$

There is a similar expression for ϕ. It has a five-dimensional kinetic energy term and a coupling with the brane field $L(x^\mu)$. The full Lagrangian involving the ν_B is

$$\mathcal{L} = \mathrm{i}\bar{\nu}_B\gamma_\mu\partial^\mu\nu_B + \kappa\bar{L}H\nu_{BR}(x, y=0) + \mathrm{i}\int \mathrm{d}y\,\bar{\nu}_{BL}(x, y)\partial_5\nu_{BR}(x, y) + \mathrm{h.c.}, \quad (96)$$

where H denotes the Higgs doublet, and $\kappa = hM_*/M_{P\ell}$ is the suppressed Yukawa coupling. This leads to a Dirac mass for the neutrino [68] given by

$$m = \frac{hv_{wk}M_*}{M_{P\ell}}, \quad (97)$$

where v_{wk} is the scale of $SU(2)_L$ breaking. In terms of the two-component fields, the mass term coming from the fifth component of the kinetic energy connects the fields χ_+ with ϕ_- and χ_- with ϕ_+, whereas it is only the ϕ_+ (or $\nu_{B,R,+}$) which couples with the brane neutrino $\nu_{e,L}$. Thus, as far as the standard model particles and forces go, the fields ϕ_- and χ_+ are totally decoupled, and we will not consider them here. The mass matrix that we will write below therefore connects only ν_{eL}, $\phi_{+,n}$ and $\chi_{-,n}$.

From equation (96), we conclude that for $M_* \sim 10\,\mathrm{TeV}$, this leads to $m \simeq 10^{-4}h\,\mathrm{eV}$. It is encouraging that this number is in the right range to be of interest in the discussion of solar neutrino oscillation if the Yukawa coupling h is appropriately chosen. Furthermore, this neutrino is mixed with all the KK modes of the bulk neutrino, with a mixing mass $\sim\sqrt{2}m$; since the nth KK mode has a mass $nR^{-1} \equiv n\mu$, the mixing angle is given by $\sqrt{2}mR/n$. Note that for $R \sim 0.1\,\mathrm{mm}$, this mixing angle is of the right order to be important in MSW transitions of solar neutrinos.

It is worth pointing out that this suppression of m is independent of the number and radius hierarchy of the extra dimensions, provided that our bulk neutrino propagates in the whole bulk. For simplicity, we will assume that there is only one extra dimension with radius of the order of a millimetre.

Secondly, the above discussion can be extended in a very straightforward manner to the case of three generations. The simplest thing to do is to add three bulk neutrinos and consider the Lagrangian to be

$$\mathcal{L} = \mathrm{i}\bar{\nu}_{B,\alpha}\gamma_\mu\partial^\mu\nu_{B,\alpha} + \kappa_{\alpha\beta}\bar{L}_\alpha H\nu_{B\beta R}(x, y=0) + \mathrm{i}\int \mathrm{d}y\,\bar{\nu}_{B\alpha L}(x, y)\partial_5\nu_{B\alpha R}(x, y) + \mathrm{h.c.} \quad (98)$$

One can now diagonalize $\kappa_{\alpha\beta}$ by rotating both the bulk and the active neutrinos. The mixing matrix then becomes the neutrino mixing matrix $\mathbf{U}$ discussed in the text. In this basis (the mass eigenstate basis), one can diagonalize the mass matrix involving the ν_is and the bulk neutrinos to get the mixings between the active and the bulk tower. There are now three mixing parameters, one for each mass eigenstate denoted by $\xi_i \equiv \sqrt{2}m_{,i}R$ and mixing angle for each mass eigenstate to the nth KK mode of the corresponding bulk neutrinos is given by ξ/n. The obseved oscillation data can then be used to put limits on ξ_i; we discuss this in a subsequent section.

It is also worth noting that due to the presence of the infinite tower mixed with the active neutrino, the oscillation probabilities are distorted in a way which is very different from the case of oscillation to a single neutrino level. This has the implication that if at some point the complete oscillation of a neutrino (as opposed to just the overall suppression as is the case now) is observed, it will be possible to put stronger limits on the parameter ξ_i from data.

4.1.1. Neutrino propagation in matter with a bulk neutrino tower. Let us discuss the propagation of a neutrino in matter in the bulk tower neutrino models. For this purpose we have to consider the neutrino mass matrix in the flavour basis in the presence of matter effect, to be denoted by δ_{ee}. This looks as follows in the basis: $(\nu_e, \nu^{(0)}_{BR,+}, \nu^{(1)}_{BL,-}, \nu^{(1)}_{BR,+}, \nu^{(2)}_{BL,-}, \nu^{(2)}_{BR,+}, \ldots)$ is given by

$$\mathcal{M} = \mathcal{M}_{\mathrm{TeV}} \equiv \begin{pmatrix} \delta_{ee} & m & 0 & \sqrt{2}m & 0 & \sqrt{2}m & \cdot & \cdot \\ m & 0 & 0 & 0 & 0 & 0 & \cdot & \cdot \\ 0 & 0 & 0 & \mu & 0 & 0 & \cdot & \cdot \\ \sqrt{2}m & 0 & \mu & 0 & 0 & 0 & \cdot & \cdot \\ 0 & 0 & 0 & 0 & 0 & 2\mu & \cdot & \cdot \\ \sqrt{2}m & 0 & 0 & 0 & 2\mu & 0 & \cdot & \cdot \\ \cdot & \cdot & \cdot & \cdot & \cdot & \cdot & \cdot & \cdot \\ \cdot & \cdot & \cdot & \cdot & \cdot & \cdot & \cdot & \cdot \end{pmatrix}, \tag{99}$$

where δ_{ee} is a possible matter effect. One can evaluate the eigenvalues and the eigenstates of this matrix. The former are the solutions of the transcendental equation

$$m_n = \delta_{ee} + \frac{\pi m^2}{\mu} \cot\left(\frac{\pi m_n}{\mu}\right). \tag{100}$$

The equation for the eigenstates is

$$\tilde{\nu}_n = \frac{1}{N_n}\left[\nu_e + \frac{m}{m_n}\nu^{(0)}_{B,+} + \sum_k \sqrt{2}m\left(\frac{m_n}{m_n^2 - k^2\mu^2}\nu^{(k)}_{B,-} + \frac{k\mu}{m_n^2 - k^2\mu^2}\nu^{(k)}_{B,+}\right)\right], \tag{101}$$

where we have used the notation $\pm$ for the left- and right-handed parts of the KK modes of the bulk neutrino in the two-component notation and dropped the L, R subscripts, the sum over k runs through the KK modes, and N_n is the normalization factor given by

$$N_n^2 = 1 + m^2\pi^2R^2 + \frac{(m_n - \delta_{ee})^2}{m^2}. \tag{102}$$

One of the very striking effects of the KK tower of bulk neutrinos is the presence of multiple MSW resonances each time the neutrino energy is such that one satisfies the resonance condition in a medium. As in the two-neutrino matter resonance, each time there is a level crossing by the ν_e due to its matter effect, there will be a dip in the survival probability of the electron neutrino.

To understand the origin of the dips, note that the MSW resonance condition is given by

$$m_{res}^2 \simeq \frac{4G_F\rho}{\sqrt{2}m_p}E_{res}. \tag{103}$$

As a result, as the neutrino energy E increases the resonance condition is satisfied for higher and higher KK modes of the bulk neutrino. The survival probability at and after the resonance is given by

$$P_{ee} \simeq \exp\left(-\frac{\pi m_n^2 \sin^2 2\theta}{2E}R_{eff}\right) \tag{104}$$

for $E \geqslant E_{res}$ and $P_{ee} \sim 1$ for $E < E_{res}$. The cumulative survival probability is given by $P = P^{(1)}P^{(2)}\cdots P^{(n)}$. Note that due to the exponent being larger than one at the resonance (which can

be checked by putting numbers), as soon as a new KK level is crossed, the P_{ee} dips to a value much less than one and then starts to rise as E increases giving rise to the dip structure. The net effect of the combined dip structure is to flatten the spectrum.

The typical values of the survival probability within the ^8B region ($\sim$6 to $\sim$14 MeV) are quite sensitive to the value of mR. As can be seen from equation (102), higher mR increases $1/N_n \approx m/m_n \approx mR/n$ for various n, and thereby increases ν_e coupling with higher mass eigenstates, strengthens MSW resonances and lowers ν_e survival probability. Thus, searching for dips in solar neutrino spectrum is one way to probe the size of extra dimensions. The same dip phenomena could also appear in higher-energy atmospheric spectra. Since the resonance condition given by the above formula implies that the higher the energy the higher the mass difference squared (or lower the extra dimension radius) probed, search for dips in higher-energy neutrinos can, in principle, reveal the existence of extra dimensions of smaller sizes that cannot be probed by solar neutrinos.

4.2. Phenomenological and cosmological constraints on bulk neutrino models

A generic feature of understanding neutrino mass via bulk neutrinos in models with large flat extra dimension is the presence of an infinite tower of closely spaced sterile neutrinos mixed with active neutrino (say ν_e). Information about the nature of extra dimensions can therefore be obtained by looking at the phenomenological as well as cosmological effects of this mixing with the infinite tower.

4.2.1. Neutrino oscillation constraints. To see the kind of constraints one can derive, let us take a simple model where there are three bulk neutrinos (i.e. three infinite towers), each giving mass to one family of neutrinos. In this minimal model, a simple rotation of the active neutrinos takes the neutrinos to the mass basis and separates three towers. It has been shown in recent papers through detailed analysis [70], that while this minimal model can adequately explain both the solar and atmospheric neutrino oscillation phenomena essentially by arranging the active bulk neutrino mixing, it is not possible to accomodate the LSND results. Furthermore, since generic mixing of the various mass eigenstate neutrinos to the nth KK mode of the corresponding bulk neutrino goes like $m_i R/n$, if R is sizeable, the observable effect simulating a multitude of sterile neutrinos should be present. Since both present atmospheric as well as solar neutral current data from SNO severely constrain the oscillation of the active neutrinos to the sterile ones, this puts a constraint on R. For instance, considering the muon neutrino oscillation to bulk neutrinos in the atmospheric neutrino data, we can take $m_3 R \leqslant 10\%$. This implies that $R \leqslant 2\,\mathrm{eV}^{-1}$ or R less than 40 μm. This constraint is more stringent than the one derived from direct searches for deviations from the inverse square law [71].

4.2.2. Big Bang nucleosynthesis constraints. On the cosmological front, since Big Bang nucleosynthesis is a very sensitive measure of the number of extra neutrino species mixed with the active neutrinos, one should be able to get information about this class of models from these data. The basic idea here is that at the epoch of nucleosynthesis, neutrino oscillation to the bulk modes can bring in the modes into thermodynamic equilibrium with all other relativistic species. If that happens each mode will contribute an amount ρ_ν to the energy density of the universe and speed up the expansion. The faster the expansion of the universe, the earlier the weak interactions go out of equilibrium (to be called freeze-out). Since the neutron to proton ratio depends very

sensitively on the temperature of freeze-out, i.e. $n/p \sim \mathrm{e}^{-(m_n - m_p)/T_*}$, the higher the freeze out temperature T_*, the higher the neutron fraction and hence the helium fraction of the universe.

Higher the mixing strength of the active modes with the bulk modes, the more modes from the bulk that get into thermal equilibrium with the electron. Therefore, to be consistent with observed Helium abundance, one must have a restriction on the mixing parameter $\sqrt{2}mR$.

Very careful analysis of this has been done in two papers [72] by solving the Boltzman equation for the generation of sterile neutrinos from active neutrinos at the BBN epoch. For the case of one space dimension, it was concluded in [72] that the active-bulk mixing and the inverse radius of the extra dimension μ satisfy the constraint

$$\left(\frac{\mu}{\mathrm{eV}}\right)^{0.92} \sin^2 2\theta \leqslant 7.06 \times 10^{-4}. \tag{105}$$

Applying this to the tau neutrino, we find an even more stringent limit on the size of the extra dimensions R than the one just listed, i.e. $R \leqslant 1.5\,\mu\mathrm{m}$.

4.2.3. Enhancement of magnetic moments. Another interesting consequence of the presence of the bulk tower is in its effect on the magnetic moment of the active neutrinos. As is well known [73], if one adds a singlet right-handed neutrino to the standard model to give a Dirac mass to the neutrino, this induces a magnetic moment $\mu_\nu = 10^{-19}(m_n u/eV)\mu_B$, where μ_B is the Bohr magneton ($\mu_B = e/2m_e c$). Since in the bulk neutrino models, there is an infinite tower of neutrinos mixed with the active neutrinos, there is a $\mu_{\nu_e \nu_{B,p}} = 10^{-19}(\sqrt{2}m/eV)\mu_B$ connecting the active neutrino with each KK mode of the bulk neutrino. In a neutrino scattering process $\nu_e + e$ with neutrino energy E_ν, all bulk neutrino modes upto E_ν will be excited [74]. Thus, the effective neutrino magnetic moment will appear to be $\mu_{eff} \simeq 10^{-19}(m/eV)(ER)^{1/2}$ where R is the radius of the extra dimension. For $R \sim$ mm, this enhances the magnetic moment by almost a factor of a million. Thus, this could provide an interesting way to probe the existence of extra dimensions. For example, it has recently been shown that for the case of two extra dimensions, this effect can significantly distort the spectral shape of $\mathrm{d}\sigma/\mathrm{d}T$ versus T (where T is the recoil energy) in $\nu_e - e$ scattering for very low T (in the 1–100 keV range) [75].

A note of caution is that this apparent enhancement is effective only when the KK modes of the bulk neutrino can be excited. For instance, when neutrino spin precesses in a magnetic field, the most of the KK modes do not get excited due to energy momentum conservation and therefore, the magnetic moment enhancement does not take place.

4.2.4. Other implications. Another interesting implication of the bulk neutrino tower appears if the brane model is not the standard model with one Higgs doublet but with two. In this case, the physical charged Higgs can decay into charged lepton and the bulk tower but with the difference that unlike in the normal two Higgs extension, the final state charged lepton emitted in this process will have left-handed helicity, whereas in models without any bulk neutrino, the final state charged lepton will have right-handed helicity [76].

The presence of the bulk neutrino tower also leads to new contributions to flavour changing leptonic rare decays such as $\mu \to e + \gamma$ etc. They in turn lead to constraints on the fundamental scale of nature.[6]

[6] For laboratory constraints on bulk neutrino models, see e.g. [77].

4.3. Neutrino mass in low-scale gravity models without bulk neutrinos

Since the presence of light tower of bulk neutrinos is so constraining and *ad hoc* forbidding of fully allowed operators is theoretically unappealing for the brane bulk picture with the standard model in the brane, it is important to search for alternative ways to solve the neutrino mass problem. In these kinds of scenario, the strategy is to search for higher-dimensional models that will lead to the standard model after compactification of the extra dimensions and yet allow for the possibility of a low fundamental scale. One such alternative has recently been proposed by having the left–right symmetric model or an extension of the standard model with only a local $B - L$ symmetry in the bulk and looking for the standard model in the zero mode part of the spectrum [78]. It is assumed that all fermions are in the bulk. The number of extra space dimensions can either be one or two. The model with two extra space dimensions has additional symmetry which also helps to solve the proton decay problem. So we first give the example of the six-dimensional model with the gauge group $SU(2)_L \times U(1)_{I_{3R}} \times U(1)_{B-L}$. Such models have been called universal extra dimension models [80].

The minimal fermion content of this model is dictated by gravitational anomaly cancellation to be [80]

$$Q_+(2, 0, 1/3), \qquad \psi_+(2, 0, -1), \qquad U_-(1, 1/2, 1/3), \qquad D_-(1, -1/2, 1/3),$$
$$E_-(1, -1/2, -1), \qquad N_-(1, +1/2, -1),$$

where $Q = (u, d)$ and $\psi = (\nu, e)$ and $\pm$ denote the six-dimensional chirality; the numbers in the parentheses are the gauge quantum numbers. Note that each fermion field is a four-component field with two four-dimensional two-component spinors with opposite chirality, e.g. Q has a left chiral Q_L and a right chiral field Q_R. As such the theory is vector like at this stage and we will need orbifold projections to obtain a chiral theory. We choose one Higgs doublet $\phi(2, -1/2, 0)$ and a singlet $B - L$ carrying Higgs boson $\chi(1, 1/2, -1)$. We compactify the theory on a T_2/Z_2 orbifold, where T_2 is defined by the extra coordinates $y_{1,2}$ satisfying the following conditions: $y_{1,2} = y_{1,2} + 2\pi R$ and Z_2 operates on the two extra coordinates as follows: $(y_1, y_2) \to (-y_1, -y_2)$. We now impose the orbifold conditions on the fields as follows. We choose the following fields to be even under the Z_2 symmetry: $Q_L, \psi_L, U_R, D_R, E_R, N_L$; the kinetic energy terms then force the opposite chirality states to be odd under Z_2. Note specifically that, in contrast with the U, D, E fields, it is the N_L which is chosen even under Z_2. This is crucial to our understanding of neutrino masses. As is well known, the even fields when Fourier expanded involve only the $\cos ny/R$ and the odd fields only $\sin ny/R$. As a result only the Z_2 even fields have zero modes. Thus, with the above compactification, below the mass scale R^{-1}, the only fermionic modes are those of the standard model plus the N_L^0. When we give vev to the field $\langle\chi\rangle = v_{BL}$, it breaks the group down to the standard model. We will choose $v_{B-L} \sim 800$ GeV to a TeV.

Before discussing the implications of the model for neutrino masses and proton decay, let us study the extra symmetries of the four-dimensional theory implied by the fact that it derives from a six-dimensional one.

First, the discrete translational symmetry ensures the conservation of the fifth and sixth momentum components, p_a, which are quantized in integer factors of $1/R$.

Secondly, in the full uncompactified six-dimensional theory, there is an extra $U(1)_{45}$ symmetrry associated with the rotations in the y_1, y_2 plane. After compactification, the $U(1)_{45}$ invariance reduces to a Z_4 symmetry. Therefore invariance under the $SO(1, 3) \times Z_4$ space–time

Table 4. $U(1)_{45}$ charges of the various fermions in the $SU(2)_L \times U(1)_{I_{3R}} \times U(1)_{B-L}$ model.

Q_L, ψ_L	+1/2
U_R, D_R, E_R, N_R	+1/2
Q_R, ψ_R, U_L	−1/2
E_L, D_L, N_L	−1/2

Lorentz transformations must be imposed on all possible operators allowed in the effective four-dimensional theory, i.e. the allowed operators will be those that are invariant under the whole $SO(1,5)$ symmetry, plus probably those for which the sum of fermion $U(1)_{45}$ charges is equal to zero modulus 8. The reasoning is as follows: the Z_4 spatial symmetry, actually translates into a Z_8 symmetry group for the spinorial representation. In fact, under a $\pi/2$ rotation of the x_4–x_5 plane a fermion transforms as $\Psi(x') = U\Psi(x)$ with $U = \exp[\mathrm{i}(\pi/2)\Sigma_{45}/2]$, where $\Sigma_{45} = \mathrm{i}[\Gamma^4, \Gamma^5]/2$ is the generator of the $U(1)_{45}$ group.

To see which operators are allowed, we need to know the $U(1)_{45}$ quantum numbers of the theory which can be easily read of from the six-dimensional theory and are given in table 4.

We will use these quantum numbers below.

Let us now turn to understanding the small neutrino mass in this model. Note that in this model due to our orbifold assignments and choice of the gauge group coupled with the residual Z_8 symmetry discussed above, we only have one term that to leading order can contribute to neutrino masses and the term is $\lambda\psi_L^{\mathrm{T}} C^{-1} N_L \phi(\chi^*)^2/M_*^5$.

The following potentially dangerous terms are forbidden for various reasons in this six-dimensional theory:

- $(\psi_L\phi)^2/M_*$ is forbidden by $B-L$ symmetry.
- Terms like $\bar{\psi}_L\phi N_R$, although allowed are also not problematic due to Z_2 quantum numbers which imply that the N_R has no zero modes.
- $(\psi_L\phi)^2(\chi^*)^2/M_*^7$ and $N_L N_L(\chi^*)^2$ are forbidden by the residual Z_8 symmetry.

These operators are written in the six-dimensional field theory. Upon compactification to the four-dimensional theory on our orbifold, the operator that leads to neutrino mass has the form $\lambda\psi_L^{(0)\mathrm{T}} C^{-1} N_L^{(0)} \phi^{(0)} (\chi^{(0)*})^2/M_*^5 R^3$. Using $M_* \simeq 100\,\mathrm{TeV}$ and $R^{-1} \sim \mathrm{TeV}$ and using $\lambda \sim 0.1$, we find for that it leads to $m_\nu \sim \mathrm{eV}$, which is in the right range without any fine tuning. Furthermore, the neutrinos in this model are Dirac particles since all Majorana terms are forbidden to leading order by the Z_8 symmetry.

It is straightforward to have a left–right symmetric embedding of the local $B-L$ symmetry and show in a five-dimensional example how it can lead to small neutrino masses despite the fact that the fundamental scale of the model is in the TeV range. These considerations are easily extended to the six space–time dimensions.

This model does not have a tower of bulk neutrinos with mass gap of meV type; secondly, there is no need to invoke global $B-L$ symmetry to prevent undesirable terms. This argument also carries over to the 6-D extension of this model, which one may want for the purpose of suppressing proton decay.

Conclusions and outlook

At the moment, neutrino oscillation experiments have provided the first evidence for new physics beyond the standard model. The field of neutrino physics therefore has become central to the study of new physics at the TeV scale and beyond. The other area which most theorists believe will be the next one to emerge from experiments is supersymmetry. We have therefore assumed supersymmetry in most of our discussions, although in the last section, we consider low-scale extra dimensional models without supersymmetry.

What have we learned so far? One point that seems very clear is that there is probably a set of three right-handed neutrinos which restore quark lepton symmetry to physics; secondly there must be a local $B - L$ symmetry at some high scale beyond the standard model that is responsible for the RH neutrinos being so far below the Planck scale. While there are very appealling arguments that the scale of $B - L$ symmetry is close to 10^{14}–10^{16} GeVs, in models with extra dimensions, one cannot rule out the possibility that it is around a few TeV. The third point that one may suspect is that the right-handed neutrino spectrum may be split into a heavier one and two others which are nearby. If this suspicion is confirmed, that would point towards an $SU(2)_H$ horizontal symmetry or perhaps even an $SU(3)_H$ symmetry which breaks into an $SU(2)_H$ symmetry (although simple anomaly considerations prefer the first alternative).

The correct theory should explain:

(i) Why are both the solar and atmospheric mixing angles nearly maximal? In particular, is there any significance to the observation that $\theta^{\nu}_{12} + \theta^{q}_{12} = \theta^{\nu}_{23} + \theta^{q}_{23} \simeq \pi/4$ [81]?

(ii) Why is $\Delta m^2_{\odot} \ll \Delta m^2_A$ but $\Delta m^2_{\odot}/\Delta m^2_A \gg m^2_{\mu}/m^2_{\tau}$ as would be expected in a hierarchical scenario?

(iii) What is responsible for the smallness of U_{e3}?

(iv) What is the nature of CP phases in the lepton sector and what is their relation to the CP phases possibly responsible for baryogenesis via leptogenesis?

(v) What is the complete mass spectrum for neutrinos?

As we move into the era of precision neutrino measurement science (PNMS), these and other questions will provide an exciting venue for research in neutrino physics.

Acknowledgments

This work is supported by the National Science Foundation grant number PHY-0099544. Parts of the work were presented at an ICTP summer school on neutrinos. I thank Alexei Smirnov for the invitation and kind hospitality at ICTP during the school, and K S Babu, B Dutta, A Smirnov, G Senjanović, A Perez-Lorenzana, B Kayser, G Fuller and E Akhmedov for discussions.

References

[1] Caldwell D (ed) 2001 *Current Perspectives in Neutrino Physics* (New York: Springer)
Bilenky S M 2001 *Preprint* hep-ph/0103091

[2] Pontecorvo B 1958 *Sov. Phys. JETP* **6** 429
Maki Z, Nakagawa M and Sakata S 1962 *Prog. Theor. Phys.* **28** 870

[3] Mohapatra R N and Pal P B 2004 *Massive Neutrinos in Physics and Astrophysics* 3rd edition (Singapore: World Scientific)
[4] Kayser B and Mohapatra R N 2001 *Current Aspects of Neutrino Physics* ed D Caldwell (Berlin: Springer) p 17
[5] Gell-Mann M, Ramond P and Slansky R 1979 *Supergravity* ed P van Niewenhuizen and D Z Freedman (Amsterdam: North-Holland)
Yanagida T 1979 *Proc. Workshop on Unified Theory and Baryon number in the Universe* ed O Sawada and A Sugamoto (KEK)
Mohapatra R N and Senjanović G 1980 *Phys. Rev. Lett.* **44** 912
Glashow S L 1979 Erice Lectures
[6] Barger V, Whisnant K, Marfatia D and Wood B P 2002 *Preprint* hep-ph/0204253
Bahcall J, Gonzalez-Garcia C and Pena-Garay C 2002 *Preprint* hep-ph/0204314
Bandopadhyay A, Choubey S, Goswami S and Roy D P 2002 *Preprint* hep-ph/0204286
de Holanda P and Smirnov A 2002 *Preprint* hep-ph/0205241
Maltoni M, Schwetz W, Tortola M A and Valle J W F 2002 *Preprint* hep-ph/0207227
Barger V, Whisnant K and Marfatia D 2003 *Int. J. Mod. Phys.* E **12** 569
[7] Cleveland B T *et al* 1998 *Astrophys. J.* **496** 505
Davis R 1994 *Prog. Part. Nucl. Phys.* **32** 13
SuperKamiokande Collaboration, Fukuda Y *et al* 1998 *Phys. Rev. Lett.* **81** 1158
SuperKamiokande Collaboration, Fukuda Y *et al* 1998 *Phys. Rev. Lett.* **81** 4279 (erratum)
SuperKamiokande Collaboration, Fukuda Y *et al* 1999 **82** 1810
Suzuki Y 1999 *Nucl. Phys. Proc. Suppl.* B **77** 35
Fukuda Y *et al* 2001 *Preprint* hep-ex/0103032
SAGE Collaboration, Abdurashitov J N *et al* 1991 *Phys. Rev.* C **60** 055801
GALLEX Collaboration, Hampel W *et al* 1999 *Phys. Lett.* B **447** 127
SNO Collaboration, Ahmed Q R *et al* 2001 *Phys. Rev. Lett.* **87** 071301
[8] Wolfenstein L 1978 *Phys. Rev.* D **17** 2369
Mikheyev S P and Smirnov A Y 1986 *Nuovo Cimento* C **9** 17
[9] Barger V, Whisnant K, Pakvasa S and Phillips R J N 1980 *Phys. Rev.* D **22** 2718
[10] SuperKamiokande Collaboration, Fukuda Y *et al* 1999 *Phys. Rev. Lett.* **82** 2644
IMB Collaboration, Becker-Szendy R *et al* 1995 *Nucl. Phys.* B **38** (*Proc. Suppl.*) 331
Soudan Collaboration, Allison W W M *et al* 1997 *Phys. Lett.* B **391** 491
Macro Collaboration, Ambrosio M *et al* 1998 *Phys. Lett.* B **434** 451
[11] Klapdor-Kleingrothaus H 1999 *Sixty Years of Double Beta Decay* (Singapore: World Scientific)
[12] Baudis L *et al* 1999 *Phys. Rev. Lett.* **83** 41
IGEX Collaboration, Aalseth C *et al* 2002 *Preprint* hep-ex/0202026
[13] Klapdor-Kleingrothaus H *et al* 2001 *Mod. Phys. Lett.* A **16** 2409
[14] CHOOZ Collaboration, Apollonio M *et al* 1999 *Phys. Lett.* B **466** 415
Palo-verde Collaboration, Boehm F *et al* 2000 *Phys. Rev. Lett.* **84** 3764
[15] Athanassopoulos C *et al* 1996 *Phys. Rev.* C **54** 2685
Athanassopoulos C *et al* 1998 *Phys. Rev.* C **58** 2489
Aguilar A *et al* 2001 *Preprint* hep-ex/0104049
[16] KARMEN Collaboration, Eitel K *et al* 2000 *Preprint* hep-ex/0008002
[17] Louis W 2002 Invited talk at the *INT Miniworkshop, Seattle*
Louis W 2002 NeSS2002 workshop, Washington, DC
[18] Caldwell D and Mohapatra R N 1993 *Phys. Rev.* D **48** 3259
Joshipura A 1995 *Phys. Rev.* D **51** 1321
[19] Zee A 1980 *Phys. Lett.* B **93** 389
Wolfenstein L 1980 *Nucl. Phys.* B **175** 93
Koide Y 2001 *Phys. Rev.* D **64** 077301

[20] Babu K S, Ma E and Valle J W F 2002 *Preprint* hep-ph/0206292
[21] Mohapatra R N and Nussinov S 1998 *Preprint* hep-ph/9809415
Mohapatra R N and Nussinov S 1999 *Phys. Rev.* D **60** 013002
Altarelli G and Feruglio F 1998 *Phys. Lett.* B **439** 112
Altarelli G and Feruglio F 1998 *J. High Energy Phys.* JHEP11 (1998) 021
[22] Barger V, Pakvasa S, Weiler T J and Whisnant K 1998 *Phys. Lett.* B **437** 107
Baltz A J, Goldhaber A S and Goldhaber M 1998 *Phys. Rev. Lett.* **81** 5730
Vissani F 1999 *J. High Energy Phys.* JHEP06 (1999) 022
Jezabek M and Sumino Y 1999 *Phys. Lett.* B **457** 139
[23] Joshipura A and Rindani S 2000 *Eur. Phys. J.* C **14** 85
Mohapatra R N, Perez-Lorenzana A and de S Pires C A 2000 *Phys. Lett.* B **474** 355
Kitabayashi T and Yasue M 2001 *Phys. Rev.* D **63** 095002
Kitabayashi T and Yasue M 2001 *Phys. Lett.* B **508** 85
Kitabayashi T and Yasue M 2001 *Preprint* hep-ph/0110303
Lavoura L 2000 *Phys. Rev.* D **62** 093011
Mohapatra R N 2001 *Preprint* hep-ph/0107274
Mohapatra R N 2001 *Phys. Rev.* D **64** 091301
Babu K S and Mohapatra R N 2002 *Phys. Lett.* B **532** 77
Dicus D A, He H-J and Ng J N 2002 *Phys. Lett.* B **536** 83
Shafi Q and Tavartkiladze Z 2000 *Phys. Lett.* B **482** 1451
[24] Kuchimanchi R and Mohapatra R N 2001 *Preprint* hep-ph/0107110
Kuchimanchi R and Mohapatra R N 2002 *Phys. Rev.* D **66** 051301
Kuchimanchi R and Mohapatra R N 2001 *Preprint* hep-ph/0107373
[25] Frampton P, Glashow S L and Marfatia D 2002 *Preprint* hep-ph/0201008
Kageyama A, Kaneko S, Shimoyama N and Tanimoto M 2002 *Phys. Lett.* B **538** 96
Desai B, Roy D P and Vaucher A 2002 *Preprint* hep-ph/0209035
[26] Babu K S, Dutta B and Mohapatra R N 2002 *Preprint* hep-ph/0211068
[27] Fritzsch H and Xing Z Z 1998 *Preprint* hep-ph/9808272
Koide Y 1989 *Phys. Rev.* D **39** 1391
[28] Mohapatra R N and Nussinov S 1998 *Preprint* hep-ph/9808301
Mohapatra R N and Nussinov S 1998 *Phys. Lett.* B **441** 299
[29] Barr S and Dorsner I 2000 *Nucl. Phys.* B **585** 79
Barr S and Dorsner I 2001 *Nucl. Phys.* B **617** 493
[30] Babu K S and Mohapatra R N 2002 *Phys. Lett.* B **532** 77
[31] Goh H S, Mohapatra R N and Ng S-P 2002 *Preprint* hep-ph/0205131
Goh H S, Mohapatra R N and Ng S-P 2002 *Phys. Lett.* B **542** 116
[32] GENIUS Collaboration, Klapdor-Kleingrothaus H *et al* 1998 *J. Phys. G: Nucl. Part. Phys.* **24** 483
CUORE Collaboration, Fiorini E 1998 *Phys. Rep.* **307** 309
MAJORANA Collaboration, Aalseth C E *et al* 2002 *Preprint* hep-ex/0201021
EXO Collaboration, Gratta G *et al* 2002 Invited talk at the *Neutrino Miniworkshop at INT, Seattle* April
MOON Collaboration, Ejiri H *et al* 2000 *Phys. Rev. Lett.* **85** 2917
Cremonesi O 2002 *Proc. of Neutrino* (Munich)
[33] Kayser B 1988 *CP Violation* ed C Jarlskog (Singapore: World Scientific) p 334
Barroso A and Maalampi J 1983 *Phys. Lett.* B **132** 355
[34] Pas H, Klapdor-Kleingrothaus H and Smirnov A 2000 *Preprint* hep-ph/0003219
Farzan Y and Smirnov A Y 2002 *Phys. Rev.* D **65** 113001
Petcov S, Pascoli S and Wolfenstein L 2001 *Preprint* hep-ph/0110287
Frigerio M and Smirnov A Y 2002 *Preprint* hep-ph/0207366
Barger V, Glashow S, Langacker P and Marfatia D 2002 *Preprint* hep-ph/0205290
Petcov S, Pascoli S and Rodejohann W 2002 *Preprint* hep-ph/0209059

Bilenky S, Pascoli S and Petcov S 2001 *Phys. Rev.* D **64** 113003
Rodejohann W 2002 *J. Phys. G: Nucl. Part. Phys.* **28** 1477
Bahcall J N, Murayama H and Pena-Garay C 2004 *Preprint* hep-ph/0403167
[35] de Gouvea A, Kayser B and Mohapatra R N 2003 *Phys. Rev.* D **67** 053004
[36] Barbieri R, Ellis J and Gaillard M K 1980 *Phys. Lett.* B **90** 249
Akhmedov E, Berezhiani Z and Senjanović G 1992 *Phys. Rev. Lett.* **69** 3013
[37] Cvetic M, Langacker P and Shiu G 2002 *Preprint* hep-th/0206115
Langacker P 2002 Invited talk at the Stony Brook Conf. on *Neutrinos and Physics Beyond the Standard Model* October
[38] Mohapatra R N and Valle J W F 1986 *Phys. Rev.* D **34** 1642
[39] Barr S 2003 *Preprint* hep-ph/0309152
Albright C and Barr S 2004 *Phys. Rev.* D **69** 073010
[40] Pati J C and Salam A 1974 *Phys. Rev.* D **10** 275
Mohapatra R N and Pati J C 1975 *Phys. Rev.* D **11** 566 and 2558
Senjanović G and Mohapatra R N 1975 *Phys. Rev.* D **12** 1502
[41] Mohapatra R N and Marshak R E 1980 *Phys. Lett.* B **91** 222
Davidson A 1979 *Phys. Rev.* D **20** 776
[42] Lazarides G, Shafi Q and Wetterich C 1981 *Nucl. Phys.* B **181** 287
Mohapatra R N and Senjanović G 1981 *Phys. Rev.* D **23** 165
[43] Babu K S and Mohapatra R N 1993 *Phys. Rev. Lett.* **70** 2845
Lee D G and Mohapatra R N 1995 *Phys. Rev.* D **51** 1353
[44] Fukuyama T and Okada N 2002 *Preprint* hep-ph/0206118
Fukuyama T, Koide Y, Matsuda K and Nishiura H 2002 *Phys. Rev.* D **65** 033008
[45] Bajc B, Senjanović G and Vissani F 2002 *Preprint* hep-ph/0210207
[46] Brahmachari B and Mohapatra R N 1998 *Phys. Rev.* D **58** 015001
[47] Goh H S, Mohapatra R N and Ng S P 2003 *Phys. Lett.* B **570** 215 (*Preprint* hep-ph/0303055)
Goh H S, Mohapatra R N and Ng S P 2003 *Phys. Rev.* D **68** 115008
Goh H S, Mohapatra R N and Ng S P 2003 *Preprint* hep-ph/0308197
[48] Bludman S, Hata N, Kennedy D and Langacker P 1993 *Nucl. Phys. Proc. Suppl.* **31** 156
Albright C, Babu K S and Barr S 1998 *Phys. Rev. Lett.* **81** 1167
Babu K S, Pati J C and Wilczek F 1998 *Preprint* hep-ph/9812538
Achiman Y 1998 *Preprint* hep-ph/9812389
Bando M, Kugo T and Yoshioka K 1998 *Phys. Rev. Lett.* **80** 3004
Oda K, Takasugi E, Tanaka M and Yoshimura M 1999 *Phys. Rev.* D **59** 055001
[49] Mohapatra R N 1997 TASI Lectures also in Mohapatra R N 1998 *Supersymmetry, Supergravity, Supercolliders* ed J Bagger (Singapore: World Scientific)
[50] Babu K S, Dutta B and Mohapatra R N 1999 *Phys. Lett.* B **458** 93
[51] CLEO Collaboration, Anastassov A *et al* 1999 *Preprint* hep-ex/9908025
[52] Fukugita M and Yanagida T 1986 *Phys. Lett.* B **74** 45
Langacker P, Peccei R D and Yanagida T 1986 *Mod. Phys. Lett.* A **1** 541
Luty M 1999 *Phys. Rev.* D **45** 455
Mohapatra R N and Zhang X M 1992 *Phys. Rev.* **46** 5331
Flanz M, Paschos E and Sarkar U 1995 *Phys. Lett.* B **345** 248
Covi L, Roulet E and Vissani F 1996 *Phys. Lett.* B **384** 169
Buchmuller W and Plumacher M 2000 *Int. J. Mod. Phys.* A **15** 5047
Ma E, Sarkar S and Sarkar U 1998 *Preprint* hep-ph/9812276
Pilaftsis A 1999 *Int. J. Mod. Phys.* A **14** 1811
[53] Kuzmin V, Rubakov V and Shaposnikov M 1985 *Phys. Lett.* B **185** 36
[54] Akhmedov E, Branco G and Rebelo M 2000 *Phys. Rev. Lett.* **84** 3535
Falcone D 2002 *Preprint* hep-ph/0204335

Jezabek M and Urban P 2002 *Preprint* hep-ph/0206080
[55] Grimus W and Lavoura L 2000 *Phys. Rev.* D **62** 093012
Grimus W and Lavoura L 2000 *J. High Energy Phys.* JHEP09 (2000) 007
Grimus W and Lavoura L 2001 *J. High Energy Phys.* JHEP07 (2001) 045
Goh H S, Mohapatra R N and Ng S P 2002 *Phys. Lett.* B **542** 116
[56] Lee D G and Mohapatra R N 1994 *Phys. Lett.* B **329** 463
Bamert P and Burgess C 1994 *Phys. Lett.* B **329** 109
Ionissian A and Valle J W F 1994 *Phys. Lett.* B **332** 93
Joshipura A 1994 *Z. Phys.* C **64** 31
Wu Y L 1998 *Preprint* hep-ph/9810491
Wu Y L 1999 *Preprint* hep-ph/9901320
[57] Arnowitt R, Chamseddine A and Nath P 1984 *Applied $N = 1$ Supergravity* (Singapore: World Scientific)
Barbieri R, Ferrara S and Savoy C 1982 *Phys. Lett.* B **119** 343
Polonyi J 1977 *Budapest Preprint* KFK-1977-93
[58] Borzumati F and Masiero A 1986 *Phys. Rev. Lett.* **57** 961
Hisano J, Moroi T, Tobe K and Yamaguchi M 1996 *Phys. Rev.* D **53** 2442
Hisano J and Nomura D 1999 *Phys. Rev.* D **59** 116005
King S F and Oliviera M 1999 *Phys. Rev.* D **60** 035003
Babu K S, Dutta B and Mohapatra R N 1999 *Phys. Lett.* **458** 93 (*Preprint* hep-ph/9904366)
Lavgnac S, Masina I and Savoy C 2001 *Phys. Lett.* B **520** 269
Chang D, Masiero A and Murayama H 2002 *Preprint* hep-ph/0205111
Rossi A 2002 *Preprint* hep-ph/0207006
Babu K S and Kolda C 2002 *Preprint* hep-ph/0206310
Ellis J, Hisano J, Lola S and Raidal M 2002 *Nucl. Phys.* B **621** 208
Depisch F, Pas H, Redelbach A, Ruckl R and Shimizu Y 2002 *Preprint* hep-ph/0206110
Masiero A, Vempati S and Vives O 2002 *Preprint* hep-ph/0209303
[59] Babu K S, Leung C N and Pantaleone J 1993 *Phys. Lett.* B **319** 191
Chankowski P H and Pluciennik Z 1993 *Phys. Lett.* B **316** 312
Antusch S, Drees M, Kersten J, Lindner M and Ratz M 2001 *Phys. Lett.* B **519** 238
[60] Balaji K R S, Dighe A, Mohapatra R N and Parida M K 2000 *Phys. Rev. Lett.* **84** 5034
Balaji K R S, Dighe A, Mohapatra R N and Parida M K 2000 *Phys. Lett.* B **481** 33
[61] Mohapatra R N, Parida M K and Rajasekaran G 2004 *Phys. Rev.* D **69** 053007
Mohapatra R N, Parida M K and Rajasekaran G 2003 *Preprint* hep-ph/0301234
[62] Antusch S, Kersten J, Lindner M and Ratz M 2002 *Preprint* hep-ph/0206078
[63] Casas J A, Espinosa J R, Ibarra A and Navarro I 1999 *Preprint* hep-ph/9904395
Ellis J and Lola S 1999 *Preprint* hep-ph/9904279
[64] Georgi H and Glashow S L 1998 *Preprint* hep-ph/9808293
[65] Ibarra A and Navarro I 1999 *Preprint* hep-ph/9912282
[66] Antoniadis I 1990 *Phys. Lett.* B **246** 377
Antoniadis I, Benakli K and Quirós M 1994 *Phys. Lett.* B **331** 313
Lykken J 1996 *Phys. Rev.* D **54** 3693
Dienes K R, Dudas E and Gherghetta T 1998 *Nucl. Phys.* B **436** 55
Arkani-Hamed N, Dimopoulos S and Dvali G 1998 *Phys. Lett.* B **429** 263
Arkani-Hamed N, Dimopoulos S and Dvali G 1999 *Phys. Rev.* D **59** 086004
Antoniadis I, Dimopoulos S and Dvali G 1998 *Nucl. Phys.* B **516** 70
[67] Horava P and Witten E 1996 *Nucl. Phys.* B **460** 506
Horava P and Witten E 1996 *Nucl. Phys.* B **475** 94
[68] Dienes K R, Dudas E and Gherghetta T 1999 *Nucl. Phys.* B **557** 25
Arkani-Hamed N, Dimopoulos S, Dvali G and March-Russell J 1998 *Preprint* hep-ph/9811448

[69] Dvali G and Smirnov A Yu 1999 *Nucl. Phys.* B **563** 63
Barbieri R, Creminelli P and Strumia A 2000 *Nucl. Phys.* B **585** 28
Caldwell D, Mohapatra R N and Yellin S 2001 *Phys. Rev. Lett.* **87** 041061
Caldwell D, Mohapatra R N and Yellin S 2002 *Phys. Rev.* D **64** 073001
Lukas A, Ramond P, Romanino A and Ross G 2000 *Phys. Lett.* B **495** 136
Lukas A, Ramond P, Romanino A and Ross G 2000 *Preprint* hep-ph/0011295
Cao Q-H, Gopalakrishna S and Yuan C-P 2003 *Preprint* hep-ph/0312339
[70] Mohapatra R N and Perez-Lorenzana A 2001 *Nucl. Phys.* B **593** 451
Davoudiasl H, Langacker P and Perelstein S 2002 *Phys. Rev.* D **65** 105015
[71] Adelberger E *et al* 2002 *Preprint* hep-ex/0202008
Long J *et al* 2002 *Preprint* hep-ph/0210004
[72] Goh H S and Mohapatra R N 2002 *Phys. Rev.* D **65** 085018
Abajazian K, Fuller G and Patel M 2001 *Preprint* hep-ph/0011048
[73] Fujikawa K and Shrock R 1980 *Phys. Rev. Lett.* **45** 963
[74] McGlaughlin G and Ng J 1999 *Phys. Lett.* B **470** 157
[75] Mohapatra R N, Ng S-P and Yu H 2004 *Preprint* hep-ph/0404274
[76] Agashe K, Deshpande N G and Wu G 2000 *Phys. Lett.* B **489** 367
[77] Ionnissian A and Pilaftsis A 2000 *Phys. Rev.* D **62** 066001
Ionnissian A and Pilaftsis A 2000 *Preprint* hep-ph/0010051
[78] Mohapatra R N and Perez-Lorenzana A 2002 *Phys. Rev.* D **66** 035005
[79] Mimura K and Nandi S 2002 *Preprint* hep-ph/0203126
[80] Appelquist T, Dobrescu B, Ponton E and Yee H 2001 *Phys. Rev. Lett.* **87** 181082
[81] Raidal M 2004 *Preprint* hep-ph/0404046
Minakata H and Smirnov A Y 2004 *Preprint* hep-ph/0405088

New Journal of Physics
An Institute of Physics and Deutsche Physikalische Gesellschaft Journal

New plots and parameter degeneracies in neutrino oscillations

Osamu Yasuda
Department of Physics, Tokyo Metropolitan University, Hachioji, Tokyo 192-0397, Japan
E-mail: yasuda@phys.metro-u.ac.jp

New Journal of Physics **6** (2004) 83
Received 2 May 2004
Published 14 July 2004
Online at http://www.njp.org/
doi:10.1088/1367-2630/6/1/083

Abstract. It is shown that eightfold degeneracy in neutrino oscillations is easily seen by plotting constant probabilities in the $(\sin^2 2\theta_{13}, 1/s_{23}^2)$ plane. Using this plot, we discuss how an additional long baseline measurement resolves degeneracies after the JPARC experiment measures the oscillation probabilities $P(\nu_\mu \to \nu_e)$ and $P(\bar{\nu}_\mu \to \bar{\nu}_e)$ at $|\Delta m_{31}^2|L/4E = \pi/2$. By measuring $P(\nu_\mu \to \nu_e)$ or $P(\bar{\nu}_\mu \to \bar{\nu}_e)$, the $\mathrm{sgn}(\Delta m_{31}^2)$ ambiguity is resolved better at longer baselines and the $\delta \leftrightarrow \pi - \delta$ ambiguity is resolved better when $||\Delta m_{31}^2|L/4E - \pi/2|$ is larger. The θ_{23} ambiguity may be resolved as a by-product if $||\Delta m_{31}^2|L/4E - \pi|$ is small and the CP phase δ turns out to satisfy $|\cos(\delta + |\Delta m_{31}^2|L/4E)| \sim 1$. It is pointed out that the low-energy option ($E \sim 1$ GeV) at the off-axis NuMI experiment may be useful in resolving these ambiguities. The $\nu_e \to \nu_\tau$ channel offers a promising possibility that it would potentially resolve all the ambiguities.

PII: S1367-2630(04)80232-5
© IOP Publishing Ltd and Deutsche Physikalische Gesellschaft

Contents

1. Introduction **2**

2. Plots in the ($\sin^2 2\theta_{13}$, $1/s_{23}^2$) plane **4**

2.1. $\cos 2\theta_{23} = 0$, $\Delta m_{21}^2/\Delta m_{31}^2 = 0$, $AL = 0$ . . . 4

2.2. $\cos 2\theta_{23} \neq 0$, $\Delta m_{21}^2/\Delta m_{31}^2 = 0$, $AL = 0$ . . . 5

2.3. $\cos 2\theta_{23} \neq 0$, $\Delta m_{21}^2/\Delta m_{31}^2 \neq 0$, $AL = 0$ . . . 6

2.4. $\cos 2\theta_{23} \neq 0$, $\Delta m_{21}^2/\Delta m_{31}^2 \neq 0$, $AL \neq 0$ . . . 7

2.5. Oscillation maximum . . . 9

2.6. Fake effects on CP violation due to degeneracies . . . 10

2.6.1. $\sin^2 2\theta_{23} \simeq 1$ . . . 10

2.6.2. $\sin^2 2\theta_{23} < 1$ . . . 12

3. Resolution of ambiguities by the third measurement after JPARC **12**

3.1. $\nu_\mu \to \nu_e$ . . . 13

3.1.1. $\delta \leftrightarrow \pi - \delta$ ambiguity . . . 18

3.1.2. $\Delta m_{31}^2 \leftrightarrow -\Delta m_{31}^2$ ambiguity . . . 18

3.1.3. $\theta_{23} \leftrightarrow \pi/2 - \theta_{23}$ ambiguity . . . 19

3.2. $\bar{\nu}_\mu \to \bar{\nu}_e$ . . . 19

3.3. $\nu_e \to \nu_\tau$ . . . 20

4. Discussion and conclusion **22**

Acknowledgments **22**

Appendix A. Expression for $P(\nu_\mu \to \nu_e) = P$ **23**

Appendix B. Trajectories at the oscillation maximum **24**

References **26**

1. Introduction

From recent experiments on atmospheric [1], solar [2] and reactor [3, 4] neutrinos, we now know the approximately correct values of the mixing angles and mass squared differences for atmospheric and solar neutrino oscillations:

$$(\sin^2 2\theta_{12}, \Delta m_{21}^2) \simeq (0.8, 7 \times 10^{-5}\,\mathrm{eV}^2) \quad \text{for the solar neutrino,}$$

$$(\sin^2 2\theta_{23}, |\Delta m_{31}^2|) \simeq (1.0, 2 \times 10^{-3}\,\mathrm{eV}^2) \quad \text{for the atmospheric neutrino,}$$

where we use the standard parametrization [5] of the MNS mixing matrix

$$U = \begin{pmatrix} c_{12}c_{13} & s_{12}c_{13} & s_{13}\mathrm{e}^{-\mathrm{i}\delta} \\ -s_{12}c_{23} - c_{12}s_{23}s_{13}\mathrm{e}^{\mathrm{i}\delta} & c_{12}c_{23} - s_{12}s_{23}s_{13}\mathrm{e}^{\mathrm{i}\delta} & s_{23}c_{13} \\ s_{12}s_{23} - c_{12}c_{23}s_{13}\mathrm{e}^{\mathrm{i}\delta} & -c_{12}s_{23} - s_{12}c_{23}s_{13}\mathrm{e}^{\mathrm{i}\delta} & c_{23}c_{13} \end{pmatrix},$$

and the case of $\Delta m_{31}^2 > 0$ ($\Delta m_{31}^2 < 0$) corresponds to the normal (inverted) mass hierarchy, as shown in figure 1. In the three-flavour framework of neutrino oscillations, the oscillation parameters that are still unknown to date are the third mixing angle θ_{13}, the sign of the mass

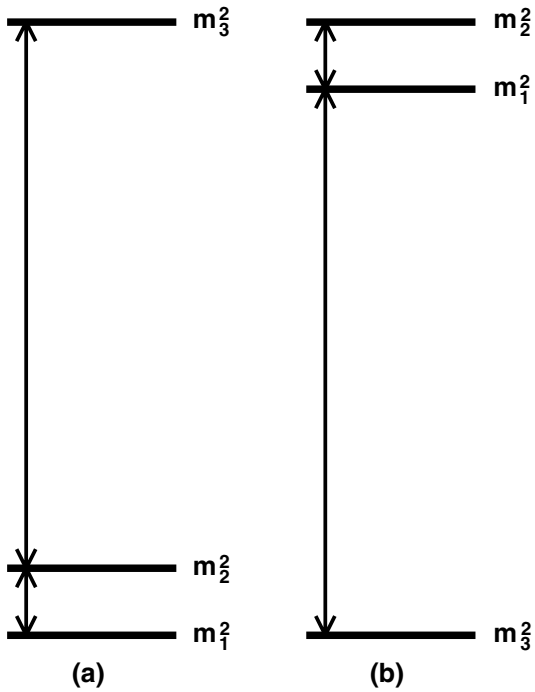

Figure 1. Two mass patterns: (a) normal ($\Delta m^2_{31} > 0$) and (b) inverted ($\Delta m^2_{31} < 0$) hierarchies.

squared difference Δm^2_{31} of the atmospheric neutrino oscillation and the CP phase δ. It is expected that long-baseline experiments in the future will determine these three quantities.

From the work of Burguet-Castell *et al* [6], it is known that even if the values of the oscillation probabilities $P(\nu_\mu \to \nu_e)$ and $P(\bar{\nu}_\mu \to \bar{\nu}_e)$ are exactly given, we cannot determine uniquely the values of the oscillation parameters owing to parameter degeneracies. There are three kinds of parameter degeneracies: intrinsic (θ_{13}, δ) degeneracy [6], the degeneracy of $\Delta m^2_{31} \leftrightarrow -\Delta m^2_{31}$ [7] and the degeneracy of $\theta_{23} \leftrightarrow \pi/2 - \theta_{23}$ [8, 9]. Intrinsic degeneracy is exact when $\Delta m^2_{21}/\Delta m^2_{31}$ is exactly zero. The sgn(Δm^2_{31}) degeneracy is exact when AL is exactly zero, where A ($\equiv\sqrt{2}G_F N_e$) and L stand for the matter effect and the baseline, respectively (G_F is the Fermi constant and N_e the electron density in matter). The θ_{23} degeneracy is exact when $\cos 2\theta_{23}$ is exactly zero. Each degeneracy gives a twofold solution, so that, in total, we will have an eightfold solution if all the degeneracies are exact. In this case, prediction for physics is the same for all the degenerated solutions and there is no problem. However, these degeneracies are lifted slightly in long baseline experiments,[1] and there are in general eight different solutions [9]. When we try to determine the oscillation parameters, ambiguities arise since the values of the oscillation parameters are different for each solution. In particular, this causes a serious problem in the measurement of CP violation, which is expected to be a small effect in the long baseline experiments, and we could mistake a fake effect because of the ambiguities for nonvanishing CP violation if we do not treat the ambiguities carefully.

In previous studies [6, 7, 9], various diagrams have been given to visualize how degeneracies are lifted in the parameter space. To see how the eightfold degeneracy is lifted, it is necessary

[1] $\cos 2\theta_{23}$ may be exactly zero, but the present atmospheric neutrino data [10] allow the possibility of $\cos 2\theta_{23} \neq 0$. Hence, we will assume $\cos 2\theta_{23} \neq 0$ in general in the following discussions.

for the plot to give eight different points for the eight different solutions. An effort was made by Minakata *et al* [11] to visualize the eight different points by plotting the trajectories of constant probabilities in the $(\sin^2 2\theta_{13}, s_{23}^2)$ plane. In the present paper, we propose a plot in the $(\sin^2 2\theta_{13}, 1/s_{23}^2)$ plane, which offers the simplest way to visualize how the eightfold degeneracy is lifted. As a by-product, we show how the third measurement of $\nu_\mu \to \nu_e$, $\bar{\nu}_\mu \to \bar{\nu}_e$ or $\nu_e \to \nu_\tau$ resolves the ambiguities, after the JPARC experiment [12] measures the oscillation probabilities $P(\nu_\mu \to \nu_e)$ and $P(\bar{\nu}_\mu \to \bar{\nu}_e)$ at the oscillation maximum, i.e. at $|\Delta m_{31}^2|L/4E = \pi/2$. Unlike the work of Burguet-Castell *et al* [6], statistical and systematic errors are not taken into account in this paper, and we hope that the present formalism offers a way to understand intuitively how ambiguities appear and how they are resolved by combining other experiments.

In the following discussions, we assume that $|\Delta m_{31}^2|$, Δm_{21}^2 and θ_{12} are sufficiently precisely known. This is justified because the correlation between these parameters and the CP phase δ is not so strong for JPARC [13], and we can safely ignore the uncertainty of these parameters to discuss the ambiguities in δ due to parameter degeneracies.

2. Plots in the $(\sin^2 2\theta_{13}, 1/s_{23}^2)$ plane

As in [14], let us discuss the ambiguities due to degeneracies step by step in the order $(\theta_{23} - \pi/4 = 0, \Delta m_{21}^2 = 0, A = 0) \to (\theta_{23} - \pi/4 \neq 0, \Delta m_{21}^2 = 0, A = 0) \to (\theta_{23} - \pi/4 \neq 0, \Delta m_{21}^2 \neq 0, A = 0) \to (\theta_{23} - \pi/4 \neq 0, \Delta m_{21}^2 \neq 0, A \neq 0)$.

2.1. $\cos 2\theta_{23} = 0,\ \Delta m_{21}^2/\Delta m_{31}^2 = 0,\ AL = 0$

In this case, the oscillation probabilities $P(\nu_\mu \to \nu_e)$ and $P(\bar{\nu}_\mu \to \bar{\nu}_e)$ are equal and are given by

$$P(\nu_\mu \to \nu_e) = P(\bar{\nu}_\mu \to \bar{\nu}_e) = s_{23}^2 \sin^2 2\theta_{13} \sin^2 \Delta,$$

where we have introduced the notation

$$\Delta \equiv \frac{|\Delta m_{31}^2|L}{4E}.$$

To plot the line $P(\nu_\mu \to \nu_e) = P(\bar{\nu}_\mu \to \bar{\nu}_e) = \text{const.}$ in the $(\sin^2 2\theta_{13}, 1/s_{23}^2)$ plane, let us introduce the variables

$$X \equiv \sin^2 2\theta_{13}, \qquad Y \equiv \frac{1}{s_{23}^2}.$$

Then

$$P = s_{23}^2 \sin^2 2\theta_{13} \sin^2 \Delta$$

gives a straight line

$$Y = \frac{\sin^2 \Delta}{P} X, \tag{1}$$

in the (X, Y) plane, where P and $\sin^2 \Delta$ are constant. The intersection of equation (1) and $Y \equiv 1/s_{23}^2 = 2$ in the $(\sin^2 2\theta_{13}, 1/s_{23}^2)$ plane is a unique point that corresponds to a solution with eightfold degeneracy. The solution is depicted in figure 2(a).

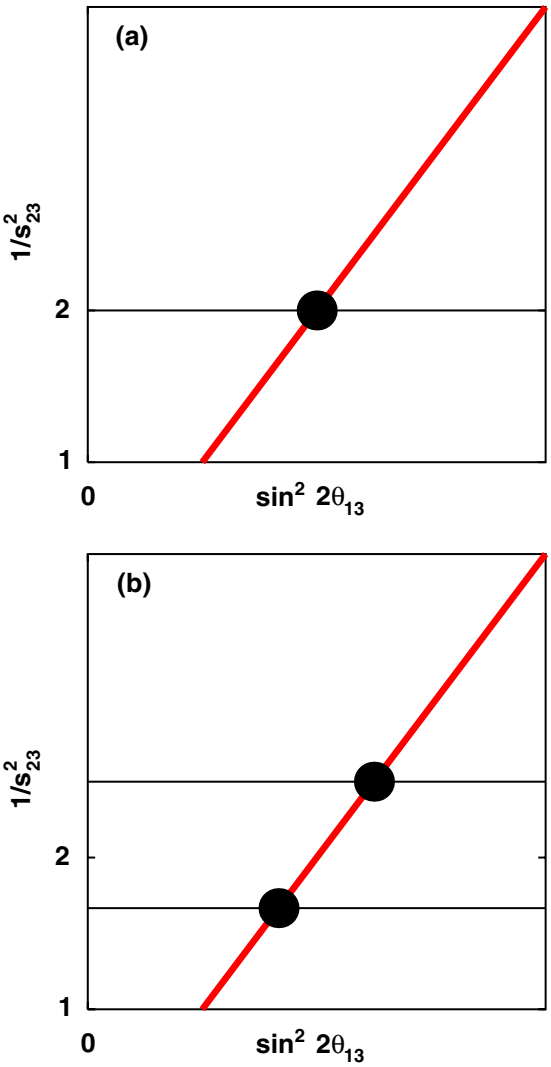

Figure 2. Solutions, marked by black blobs, for the given $P(\nu_\mu \to \nu_e)$, $P(\bar{\nu}_\mu \to \bar{\nu}_e)$ and $P(\nu_\mu \to \nu_\mu)$ for $\Delta m^2_{21}/\Delta m^2_{31} = 0$ and $AL = 0$. (a) For $\cos 2\theta_{23} = 0$, the intersection of $Y \equiv 1/s^2_{23} = 2$ and the trajectory of $P(\nu_\mu \to \nu_e) = P(\bar{\nu}_\mu \to \bar{\nu}_e) =$ const. is a point with eightfold degeneracy. (b) For $\cos 2\theta_{23} \neq 0$, the intersections are two solutions with fourfold degeneracy.

2.2. $\cos 2\theta_{23} \neq 0$, $\Delta m^2_{21}/\Delta m^2_{31} = 0$, $AL = 0$

At present, the Superkamiokande atmospheric neutrino data give the allowed region $0.90 < \sin 2\theta_{23} \leqslant 1.0$ at 90% CL [10], and $\sin^2 2\theta_{23}$ can be, in general, different from 1.0. If $\sin^2 2\theta_{23}$, which is more accurately determined from the oscillation probability $P(\nu_\mu \to \nu_\mu)$ in the future long baseline experiments, deviates from 1, then we have two solutions for $Y \equiv 1/s^2_{23}$:

$$Y_+ = \frac{2}{1 - \sqrt{1 - \sin^2 2\theta_{23}}}, \qquad Y_- = \frac{2}{1 + \sqrt{1 - \sin^2 2\theta_{23}}}.$$

In this case, there are two solutions, one given by equation (1) and $Y = Y_+$ and another given by (1) and $Y = Y_-$. These are two solutions with fourfold degeneracy. The two solutions in the $(\sin^2 2\theta_{13}, 1/s_{23}^2)$ plane are shown in figure 2(b). From this, we see that even if we know precisely the values of $P(\nu_\mu \to \nu_e)$, $P(\bar{\nu}_\mu \to \bar{\nu}_e)$ and $P(\nu_\mu \to \nu_\mu)$, there are two sets of solutions, and this represents the ambiguity due to the $\theta_{23} \leftrightarrow \pi - \theta_{23}$ degeneracy.

2.3. $\cos 2\theta_{23} \neq 0$, $\Delta m_{21}^2/\Delta m_{31}^2 \neq 0$, $AL = 0$

If we turn on the effect of non-zero Δm_{21}^2 in addition to non-zero $\cos 2\theta_{23}$, then the oscillation probabilities are as follows:[2]

$$\begin{Bmatrix} P(\nu_\mu \to \nu_e) \\ P(\bar{\nu}_\mu \to \bar{\nu}_e) \end{Bmatrix} = x^2 \sin^2 \Delta + 2xy\Delta \sin \Delta \cos(\delta \pm \Delta) + y^2 \Delta^2,$$

which are correct to the second-order in the small parameters $|\Delta m_{21}^2/\Delta m_{31}^2|$ and $\sin 2\theta_{13}$, where

$$x \equiv s_{23} \sin 2\theta_{13}, \qquad y \equiv \left| \frac{\Delta m_{21}^2}{\Delta m_{31}^2} \right| c_{23} \sin 2\theta_{12}. \tag{2}$$

In this case, the trajectory of $P(\nu_\mu \to \nu_e) = P$, $P(\bar{\nu}_\mu \to \bar{\nu}_e) = \bar{P}$ (where P and $\bar{P}$ are constant) in the $(X \equiv \sin^2 2\theta_{13}, Y \equiv 1/s_{23}^2)$ plane is given by a quadratic curve:

$$16C_0 X(Y-1)\sin^2 \Delta = \frac{1}{\sin^2 \Delta}(P - \bar{P})^2 Y^2 + \frac{1}{\cos^2 \Delta}[(P + \bar{P} - 2C_0)(Y-1) + P + \bar{P} - 2X \sin^2 \Delta]^2, \tag{3}$$

where

$$C_0 \equiv \left(\frac{\Delta m_{21}^2}{\Delta m_{31}^2} \right)^2 \Delta^2 \sin^2 2\theta_{12}.$$

Equation (3) becomes a hyperbola for most of the region of Δ, but it becomes an ellipse for the region $\Delta \simeq \pi$.

When $\sin^2 2\theta_{23} = 1$, there are two solutions for the intersection of $Y = 2$ and equation (3). This indicates that even if we know the precise values of $P(\nu_\mu \to \nu_e)$, $P(\bar{\nu}_\mu \to \bar{\nu}_e)$ and $P(\nu_\mu \to \nu_\mu)$, there are two sets of solutions for $(\theta_{13}, \theta_{23}, \delta)$ with fourfold degeneracy when $\sin^2 2\theta_{23} = 1$, as shown in figure 3(a). This represents the ambiguity due to intrinsic (θ_{13}, δ) degeneracy. When $\sin^2 2\theta_{23} \neq 1$, there are four sets of solutions with twofold degeneracy, as depicted in figure 3(b).

[2] This result is obtained by taking the limit $A \equiv \sqrt{2} G_F N_e \to 0$ in equation (16) in [15].

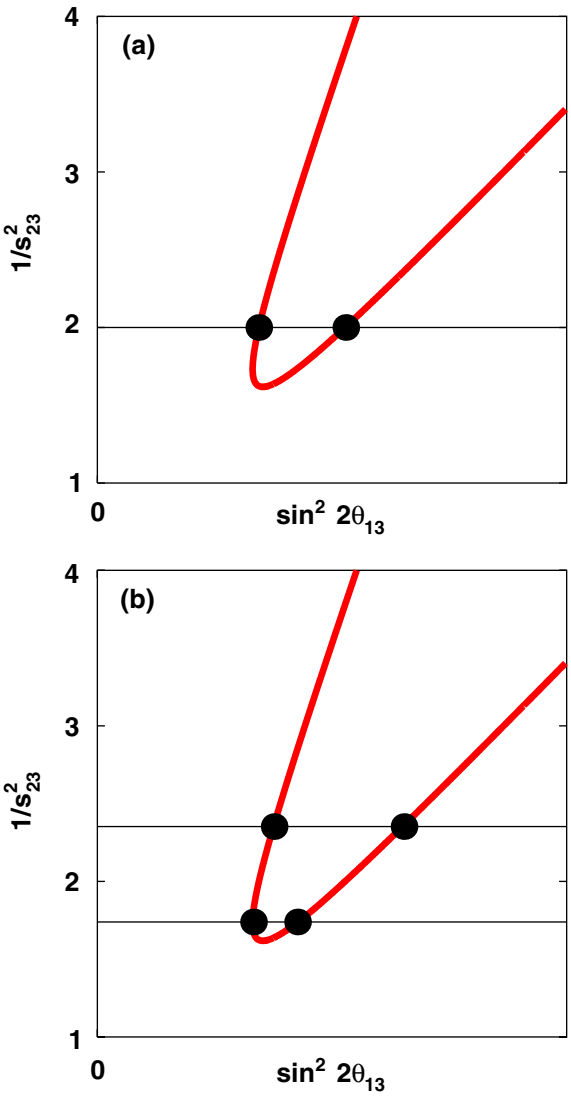

Figure 3. Solutions, marked by black blobs, for the given $P(\nu_\mu \to \nu_e)$, $P(\bar{\nu}_\mu \to \bar{\nu}_e)$ and $P(\nu_\mu \to \nu_\mu)$ for $\Delta m_{21}^2/\Delta m_{31}^2 \neq 0$ and $AL = 0$. (a) For $\cos 2\theta_{23} = 0$, the intersection of $Y \equiv 1/s_{23}^2 = 2$ and the trajectory of $P(\nu_\mu \to \nu_e) =$ const. and $P(\bar{\nu}_\mu \to \bar{\nu}_e) =$ const. are two points with fourfold degeneracy. (b) For $\cos 2\theta_{23} \neq 0$, the intersections are four solutions with twofold degeneracy.

2.4. $\cos 2\theta_{23} \neq 0$, $\Delta m_{21}^2/\Delta m_{31}^2 \neq 0$, $AL \neq 0$

Furthermore, if we turn on the matter effect AL, then the oscillation probabilities are given by [9, 15]

$$\begin{aligned} P(\nu_\mu \to \nu_e) &= x^2 f^2 + 2xyfg\cos(\delta + \Delta) + y^2 g^2, \\ P(\bar{\nu}_\mu \to \bar{\nu}_e) &= x^2 \bar{f}^2 + 2xy\bar{f}g\cos(\delta - \Delta) + y^2 g^2 \end{aligned} \tag{4}$$

for the normal hierarchy and by

$$\begin{aligned} P(\nu_\mu \to \nu_e) &= x^2 \bar{f}^2 - 2xy\bar{f}g\cos(\delta - \Delta) + y^2 g^2, \\ P(\bar{\nu}_\mu \to \bar{\nu}_e) &= x^2 f^2 - 2xyfg\cos(\delta + \Delta) + y^2 g^2, \end{aligned} \tag{5}$$

for the inverted hierarchy, where x and y are given by equation (2) and

$$\begin{Bmatrix} f \\ \bar{f} \end{Bmatrix} \equiv \frac{\sin(\Delta \mp AL/2)}{(1 \mp AL/2\Delta)}, \tag{6}$$

$$g \equiv \frac{\sin(AL/2)}{AL/2\Delta}. \tag{7}$$

Equations (4) and (5) are correct up to the second-order in $|\Delta m^2_{21}/\Delta m^2_{31}|$ and $\sin 2\theta_{13}$, and all orders in AL. The trajectory of $P(\nu_\mu \to \nu_e) = P$, $P(\bar{\nu}_\mu \to \bar{\nu}_e) = \bar{P}$ (where P and $\bar{P}$ are constant) in the $(X \equiv \sin^2 2\theta_{13}, Y \equiv 1/s^2_{23})$ plane is again a quadratic curve for either of the mass hierarchies:

$$\begin{aligned} 16CX(Y-1) = {} & \frac{1}{\cos^2\Delta}\left[\left(\frac{P-C}{f} + \frac{\bar{P}-C}{\bar{f}}\right)(Y-1) - (f+\bar{f})X + \frac{P}{f} + \frac{\bar{P}}{\bar{f}}\right]^2 \\ & + \frac{1}{\sin^2\Delta}\left[\left(\frac{P-C}{f} - \frac{\bar{P}-C}{\bar{f}}\right)(Y-1) - (f-\bar{f})X + \frac{P}{f} - \frac{\bar{P}}{\bar{f}}\right]^2 \end{aligned} \tag{8}$$

for the normal hierarchy, and

$$\begin{aligned} 16CX(Y-1) = {} & \frac{1}{\cos^2\Delta}\left[\left(\frac{P-C}{\bar{f}} + \frac{\bar{P}-C}{f}\right)(Y-1) - (f+\bar{f})X + \frac{P}{\bar{f}} + \frac{\bar{P}}{f}\right]^2 \\ & + \frac{1}{\sin^2\Delta}\left[\left(\frac{P-C}{\bar{f}} - \frac{\bar{P}-C}{f}\right)(Y-1) - (f-\bar{f})X + \frac{P}{\bar{f}} - \frac{\bar{P}}{f}\right]^2 \end{aligned} \tag{9}$$

for the inverted hierarchy, where

$$C \equiv \left(\frac{\Delta m^2_{21}}{\Delta m^2_{31}}\right)^2 \left[\frac{\sin(AL/2)}{AL/2\Delta}\right]^2 \sin^2 2\theta_{12}. \tag{10}$$

Again, these quadratic curves become hyperbolas for most of the region of Δ, but they become ellipses for some $\Delta \simeq \pi$.

If $\sin^2 2\theta_{23} = 1$, there are four solutions with twofold degeneracy, as shown in figure 4(a). If we know for some reason (e.g. from reactor experiments) which solution is selected for each mass hierarchy, then there are only two solutions. This is the ambiguity due to the $\mathrm{sgn}(\Delta m^2_{31})$ degeneracy. If $\sin^2 2\theta_{23} \neq 1$ and if we do not know which solution is favoured with respect to the intrinsic degeneracy for each hierarchy, and if we do not know $\mathrm{sgn}(\Delta m^2_{31})$, then there are eight solutions without any degeneracy, as depicted in figure 4(b). The advantage of our plot is that all the eight solutions for $(\theta_{13}, \theta_{23})$ give different points, and all the lines in the $(\sin^2 2\theta_{13}, 1/s^2_{23})$ plane are described by (at most) quadratic curves so that their behaviours are easy to see.

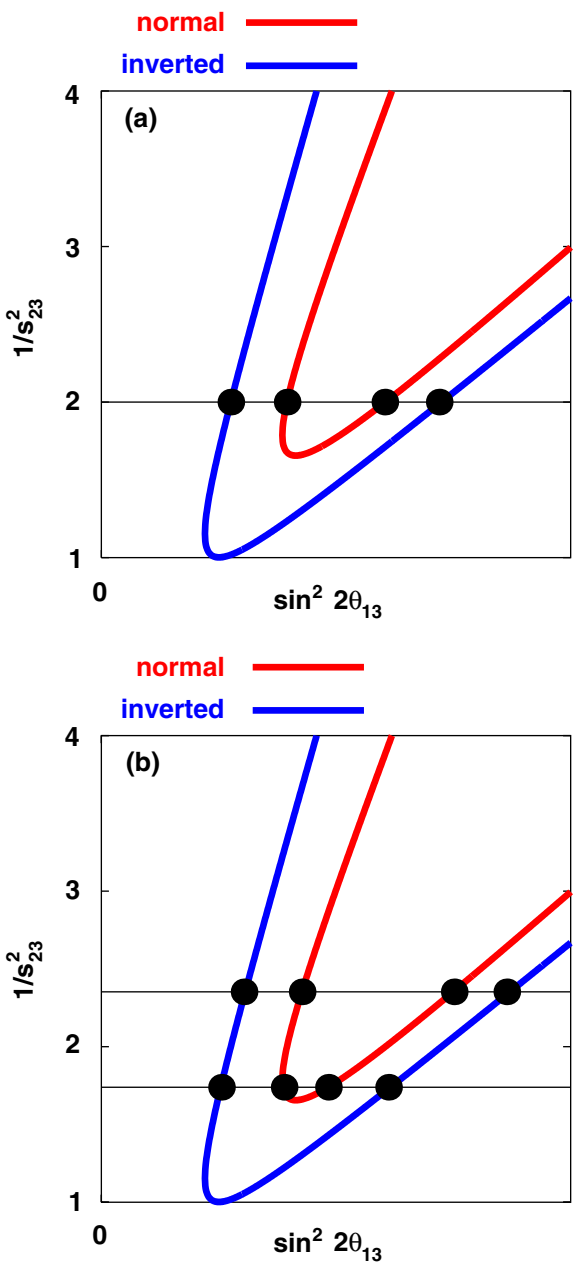

Figure 4. Solutions, marked by black blobs, for the given $P(\nu_\mu \to \nu_e)$, $P(\bar{\nu}_\mu \to \bar{\nu}_e)$ and $P(\nu_\mu \to \nu_\mu)$ for $\Delta m_{21}^2/\Delta m_{31}^2 \neq 0$ and $AL \neq 0$. (a) For $\cos 2\theta_{23} = 0$, the intersection of $Y \equiv 1/s_{23}^2 = 2$ and the trajectory of $P(\nu_\mu \to \nu_e) = \text{const.}$ and $P(\bar{\nu}_\mu \to \bar{\nu}_e) = \text{const.}$ are four points with twofold degeneracy. (b) For $\cos 2\theta_{23} \neq 0$, the intersections are eight solutions without degeneracy.

2.5. *Oscillation maximum*

Finally, consider the case where experiments are done at the oscillation maximum, i.e. when the neutrino energy E satisfies $\Delta \equiv |\Delta m_{31}^2|L/4E = \pi/2$. In this case, the probabilities become

$$P(\nu_\mu \to \nu_e) = x^2 f^2 - 2xyfg \sin\delta + y^2 g^2, \tag{11}$$

$$P(\bar{\nu}_\mu \to \bar{\nu}_e) = x^2 \bar{f}^2 + 2xy\bar{f}g\sin\delta + y^2 g^2 \tag{12}$$

for the normal hierarchy, and

$$P(\nu_\mu \to \nu_e) = x^2 \bar{f}^2 - 2xy\bar{f}g\sin\delta + y^2 g^2, \tag{13}$$

$$P(\bar{\nu}_\mu \to \bar{\nu}_e) = x^2 f^2 + 2xyfg\sin\delta + y^2 g^2 \tag{14}$$

for the inverted hierarchy, where x and y are given by equation (2), and f, $\bar{f}$, g in equations (6) and (7) become

$$\begin{Bmatrix} f \\ \bar{f} \end{Bmatrix} = \pm\frac{\cos(AL/2)}{1 \mp AL/\pi}, \qquad g \equiv \frac{\sin(AL/2)}{AL/\pi}$$

for $\Delta = \pi/2$. The trajectory of $P(\nu_\mu \to \nu_e) = P$, $P(\bar{\nu}_\mu \to \bar{\nu}_e) = \bar{P}$ in the ($X \equiv \sin^2 2\theta_{13}$, $Y \equiv 1/s_{23}^2$) plane becomes a straight line and is given by

$$Y = \frac{f + \bar{f}}{P/f + \bar{P}/\bar{f} - C(1/f + 1/\bar{f})}\left(X - \frac{C}{f\bar{f}}\right) \tag{15}$$

for the normal hierarchy, and

$$Y = \frac{f + \bar{f}}{P/\bar{f} + \bar{P}/f - C(1/f + 1/\bar{f})}\left(X - \frac{C}{f\bar{f}}\right) \tag{16}$$

for the inverted hierarchy, where C is given by equation (10). The straight lines (15) and (16) are very close to each other in relatively short long-baseline experiments such as JPARC, where the matter effect is small. As shown in appendix B, (15) and (16) have the minimum values in $Y \equiv 1/s_{23}^2$, which is larger than the naive value 1 for either of the mass hierarchies. Since equations (15) and (16) are linear in X, there is only one solution between them and $Y = \text{const}$. Thus the ambiguity due to the intrinsic degeneracy is solved by performing experiments at the oscillation maximum, although it is then transformed into another ambiguity due to the $\delta \leftrightarrow \pi - \delta$ degeneracy.

If $\sin^2 2\theta_{23} \simeq 1$, all the four solutions are basically close to each other in the ($\sin^2 2\theta_{13}$, $1/s_{23}^2$) plane, and the ambiguity due to degeneracies are not serious as far as θ_{13} and θ_{23} are concerned (see figure 5(a)). On the other hand, if $\sin^2 2\theta_{23}$ deviates fairly from 1, then the solutions are separated into two groups, those for $\theta_{23} > \pi/4$ and those for $\theta_{23} < \pi/4$ in the ($\sin^2 2\theta_{13}$, $1/s_{23}^2$) plane, as shown in figure 5(b). In this case, resolution of the $\theta_{23} \leftrightarrow \pi/2 - \theta_{23}$ ambiguity is required to determine θ_{13}, θ_{23} and δ.

2.6. Fake effects on CP violation due to degeneracies

2.6.1. $\sin^2 2\theta_{23} \simeq 1$. If the JPARC experiment reveals from the measurement of the disappearance probability $P(\nu_\mu \to \nu_\mu) = P$ that $\sin^2 2\theta_{23} \simeq 1.0$ with a good approximation, then we would not have to worry very much about parameter degeneracy as far as θ_{13} and

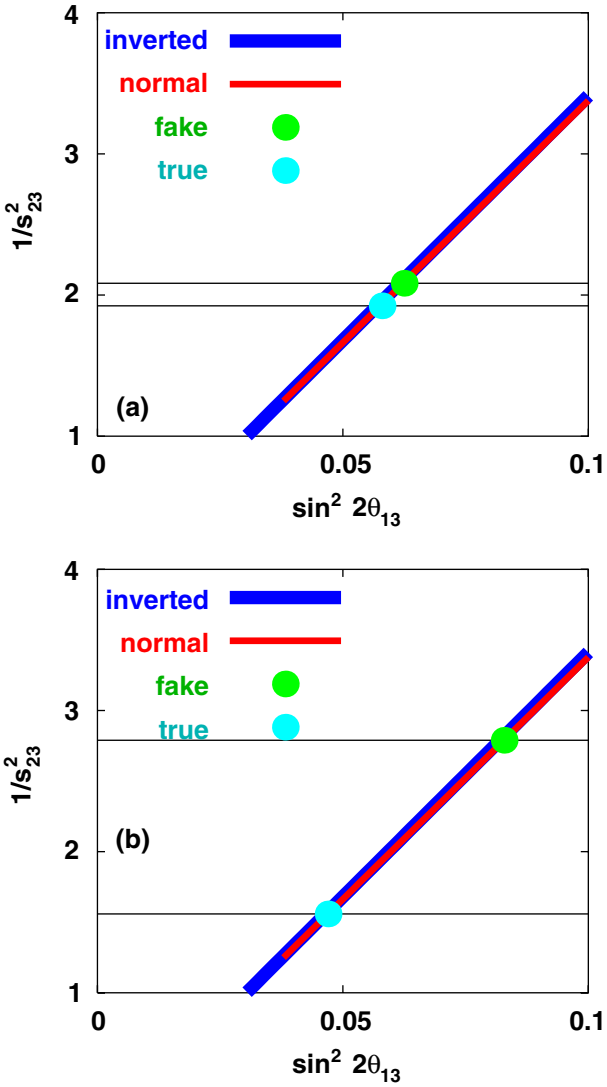

Figure 5. The θ_{23} ambiguity that could arise after JPARC measurements of $P(\nu_\mu \to \nu_e)$, $P(\bar{\nu}_\mu \to \bar{\nu}_e)$ and $P(\nu_\mu \to \nu_\mu)$ at the oscillation maximum. (a) If $\sin^2 2\theta_{23} \simeq 1.0$, the values of θ_{13} and θ_{23} are close to each other for all the solutions and the ambiguity is not serious as far as θ_{13} and θ_{23} are concerned. (b) If $\sin^2 2\theta_{23} < 1$, the θ_{23} ambiguity needs to be resolved to determine θ_{13} and θ_{23} to good precision.

θ_{23} are concerned, since the values of θ_{13} and θ_{23} for all the different solutions are close to each other.

On the other hand, when it comes to the value of the CP phase δ, we have to be careful. From [9], the true value δ and the fake value δ' for the CP phase satisfy the following:

$$x' \sin\delta' = x \sin\delta \frac{f^2 + \bar{f}^2 - f\bar{f}}{f\bar{f}} - \frac{x^2}{\sin\Delta} \frac{f^2 + \bar{f}^2}{f\bar{f}} \frac{f - \bar{f}}{2yg}, \tag{17}$$

where x, y are given by equation (2), f, $\bar{f}$, g are given by (6) and (7) and x' is defined by

$$x'^2 = \frac{x^2(f^2 + \bar{f}^2 - f\bar{f}) - 2yg(f - \bar{f})x \sin\delta \sin\Delta}{f\bar{f}}.$$

Equation (17) indicates that, even if $\sin\delta = 0$, we have nonvanishing fake CP violating effect

$$\sin\delta' = -x\frac{f^2 + \bar{f}^2}{f\bar{f}}\frac{f - \bar{f}}{2yg\sin\Delta}\sqrt{\frac{f\bar{f}}{f^2 + \bar{f}^2 - f\bar{f}}}, \tag{18}$$

if we fail to identify the correct sign of Δm^2_{31}. For the JPARC experiment, equation (18) implies that

$$\sin\delta' \simeq -2.2\sin 2\theta_{13},$$

which is not negligible unless $\sin^2 2\theta_{13} \ll 10^{-2}$. Therefore we have to know the sign of Δm^2_{31} to determine the CP phase to good precision.

2.6.2. $\sin^2 2\theta_{23} < 1$. As explained in section 2.5, if $\sin^2 2\theta_{23}$ deviates fairly from 1, we need to resolve the ambiguity due to the θ_{23} degeneracy to determine the values of θ_{13} and θ_{23}. As for the value of the CP phase δ, we can estimate how serious the effect of the θ_{23} ambiguity on the value of δ could be. If the true value of δ is zero, the CP phase δ' for the fake solution can be estimated as [9]

$$\sin 2\theta'_{13}\sin\delta' = \left|\frac{\Delta m^2_{21}}{\Delta m^2_{31}}\right| \frac{g(f - \bar{f})\sin 2\theta_{12}}{f\bar{f}}\frac{\cot 2\theta_{23}}{\sin\Delta},$$

where

$$\sin^2 2\theta'_{13} = \sin^2 2\theta_{13}\tan^2\theta_{23} + \left(\frac{\Delta m^2_{21}}{\Delta m^2_{31}}\right)^2 \frac{g^2\sin^2 2\theta_{12}}{f\bar{f}}(1 - \tan^2\theta_{23}),$$

and f, $\bar{f}$, g are defined by (6) and (7). For JPARC, we have

$$|\sin\delta'| \sim \frac{1}{200}\frac{|\cot 2\theta_{23}|}{t_{23}}\frac{1}{\sin 2\theta_{13}} \lesssim \frac{1}{500}\frac{1}{\sqrt{\sin^2 2\theta_{13}}}, \tag{19}$$

where we have used the bound $0.90 \leqslant \sin^2 2\theta_{23} \leqslant 1.0$ from the atmospheric neutrino data in the second inequality. Hence, we see that the ambiguity due to the θ_{23} does not cause a serious problem on determination of δ for $\sin^2 2\theta_{13} \gtrsim 10^{-2}$. However, it should be stressed that the effect on CP violation due to the $\mathrm{sgn}(\Delta m^2_{31})$ ambiguity is also serious in this case.

3. Resolution of ambiguities by the third measurement after JPARC

Assuming that the JPARC experiment, which is expected to be the first superbeam experiment, measures $P(\nu_\mu \to \nu_e)$ and $P(\bar{\nu}_\mu \to \bar{\nu}_e)$ at the oscillation maximum $\Delta \equiv |\Delta m^2_{31}|L/4E = \pi/2$, we

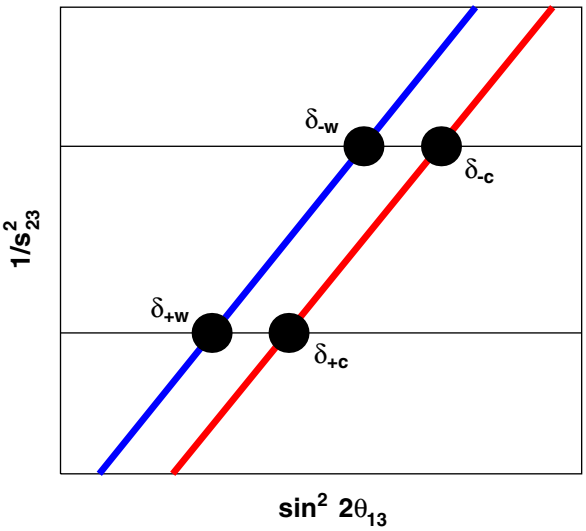

Figure 6. Four possible values for the CP phase δ at the oscillation maximum. The red (blue) line stands for the normal (inverted) hierarchy. Since we are assuming the normal hierarchy here, the red (blue) line corresponds to the correct (wrong) assumption on the mass hierarchy. The + and − signs stand for the choice of $s_{23}^2 = (1 \pm \sqrt{1 - \sin^2 2\theta_{23}})/2$ in the θ_{23} ambiguity and c (w) stands for the correct (wrong) assumption on the mass hierarchy.

will discuss in this section how the third measurement after JPARC can resolve the ambiguities by using the plot in the $(\sin^2 2\theta_{13}, 1/s_{23}^2)$ plane. Resolution of the θ_{23} ambiguity has been discussed previously using the disappearance measurement of $P(\bar{\nu}_e \to \bar{\nu}_e)$ at reactors [8, 11], [16]–[18], the silver channel $\nu_e \to \nu_\tau$ at neutrino factories [19] and the $\nu_\mu \to \nu_e$ channel [21, 22].[3] Here, we take the following reference values for the oscillation parameters:

$$\begin{aligned} &\sin^2 2\theta_{12} = 0.8, \qquad \sin^2 2\theta_{13} = 0.05, \qquad \sin^2 2\theta_{23} = 0.96, \\ &\Delta m_{21}^2 = 7 \times 10^{-5}\,\mathrm{eV}^2, \qquad \Delta m_{31}^2 = 2.5 \times 10^{-3}\,\mathrm{eV}^2 > 0, \qquad \delta = \pi/4. \end{aligned} \tag{20}$$

3.1. $\nu_\mu \to \nu_e$

Let us discuss the case in which another long-baseline experiment measures $P(\nu_\mu \to \nu_e)$. From the measurements of $P(\nu_\mu \to \nu_e)$ and $P(\bar{\nu}_\mu \to \bar{\nu}_e)$ by JPARC at the oscillation maximum, we can deduce the value of δ up to the eightfold ambiguity ($\delta \leftrightarrow \pi - \delta$, $\theta_{23} \leftrightarrow \pi/2 - \theta_{23}$, $\Delta m_{31}^2 \leftrightarrow -\Delta m_{31}^2$).[4] As depicted in figure 6, depending on whether $s_{23}^2 - 1/2$ is positive or negative, we assign subscript + or −, and depending on whether our ansatz for $\mathrm{sgn}(\Delta m_{31}^2)$ is correct or wrong,

[3] There have been a number of studies [20] on how to resolve parameter degeneracies using the $\nu_\mu \to \nu_e$ channel, and they have discussed mainly the intrinsic and $\mathrm{sgn}(\Delta m_{31}^2)$ degeneracies. In [21, 22], the θ_{23} ambiguity as well as others using the $\nu_\mu \to \nu_e$ channel and its combination with $\nu_e \to \nu_\tau$ are discussed. The present scenario, in which the third experiment follows the JPARC results on $P(\nu_\mu \to \nu_e)$ plus $P(\bar{\nu}_\mu \to \bar{\nu}_e)$, measured at the oscillation maximum, has been discussed in [23] from a different viewpoint.

[4] I thank Hiroaki Sugiyama for pointing this out to me.

we assign subscript c or w. Thus, the eight possible values of δ are given by

$$\delta_{+\mathrm{w}}, \delta_{+\mathrm{c}}, \delta_{-\mathrm{w}}, \delta_{-\mathrm{c}}, \pi - \delta_{+\mathrm{w}}, \pi - \delta_{+\mathrm{c}}, \pi - \delta_{-\mathrm{w}}, \pi - \delta_{-\mathrm{c}}. \tag{21}$$

Now, suppose that the third measurement gives the value P for the oscillation probability $P(\nu_\mu \to \nu_e)$. Then, there are in general eight lines in the $(X \equiv \sin^2 2\theta_{13}, Y \equiv 1/s_{23}^2)$ plane, given by

$$f^2 X = [P - C + 2C\cos^2(\delta + \Delta)](Y - 1) + P - 2\cos(\delta + \Delta)\sqrt{C(Y-1)}\sqrt{[P - C\sin^2(\delta + \Delta)](Y-1) + P} \tag{22}$$

for the normal hierarchy and

$$\bar{f}^2 X = [P - C + 2C\cos^2(\delta - \Delta)](Y - 1) + P - 2\cos(\delta - \Delta)\sqrt{C(Y-1)}\sqrt{[P - C\sin^2(\delta - \Delta)](Y-1) + P} \tag{23}$$

for the inverted hierarchy. Here, C is defined by equation (10), Δ $(\equiv |\Delta m_{31}^2| L/4E)$ is defined for the third measurement and δ takes one of the eight values given in equation (21). The derivation of (22) and (23) is given in appendix A. It turns out that the solutions (22) and (23) are hyperbola if $\cos^2(\delta \pm \Delta) > (C - P)/P$, where + and − refer to the normal and inverted hierarchy respectively, and ellipse if $\cos^2(\delta \pm \Delta) < (C - P)/P$. In practice, however, the difference between hyperbola and ellipse is not so important for the present discussions, because we are only interested in the behaviours of these curves in the region $1.52 < Y \equiv 1/s_{23}^2 < 2.92$, which comes from the 90% CL allowed region of the Superkamiokande atmospheric neutrino data for $\sin^2 2\theta_{23}$.

In this context, let us look at three typical cases: $L = 295$, 730 and 3000 km, each of which corresponds to JPARC, off-axis NuMI [24] and a neutrino factory [25].[5]

Figures 7–9 show the trajectories of $P(\nu_\mu \to \nu_e)$ obtained in the third measurement, together with the constraint of $P(\nu_\mu \to \nu_e)$, $P(\bar{\nu}_\mu \to \bar{\nu}_e)$ and $P(\nu_\mu \to \nu_\mu)$, by JPARC for $L = 295, 730$ and 3000 km, respectively, where $\Delta \equiv |\Delta m_{31}^2| L/4E$ takes the values $\Delta = j\pi/8$ $(j = 1, \ldots, 7, j \neq 4)$. The purple (light blue) blob stands for the true (fake) solution given by the JPARC results on $P(\nu_\mu \to \nu_e)$, $P(\bar{\nu}_\mu \to \bar{\nu}_e)$ and $P(\nu_\mu \to \nu_\mu)$. For the correct (wrong) guess on the mass hierarchy, there are in general four red (blue) curves, owing to the fact that the CP phase δ, which is deduced from the JPARC results on $P(\nu_\mu \to \nu_e)$, $P(\bar{\nu}_\mu \to \bar{\nu}_e)$ and $P(\nu_\mu \to \nu_\mu)$, is fourfold: $(\delta_{+\mathrm{c}}, \delta_{-\mathrm{c}}, \pi - \delta_{+\mathrm{c}}, \pi - \delta_{-\mathrm{c}})$ for the correct assumption on the hierarchy and $(\delta_{+\mathrm{w}}, \delta_{-\mathrm{w}}, \pi - \delta_{+\mathrm{w}}, \pi - \delta_{-\mathrm{w}})$ for the wrong assumption. In most cases, the four (red or blue) curves are separated into two pairs

[5] For $L = 3000$ km, the density of the matter may not be treated as constant, and the probability formulae (4) and (5) may no longer be valid. It turns out, however, that the approximation of the formulae becomes good if we replace AL by $AL \to \int_0^L A(x)\,\mathrm{d}x$ everywhere in the formula. In the following discussions, the replacement $AL \to \int_0^L A(x)\,\mathrm{d}x$ is always understood for the baseline $L = 3000$ km. It should be mentioned that the neutrino energy spectrum at neutrino factories is continuous and it is assumed here that we take one particular energy bin whose energy range can be made relatively small. It should also be noted that neutrino factories actually measure the probability $P(\nu_e \to \nu_\mu)$ or $P(\bar{\nu}_e \to \bar{\nu}_\mu)$, instead of $P(\nu_\mu \to \nu_e)$ or $P(\bar{\nu}_\mu \to \bar{\nu}_e)$. Here, we discuss for simplicity the trajectory of $P(\nu_\mu \to \nu_e)$, whose feature is the same as that of $P(\nu_e \to \nu_\mu)$.

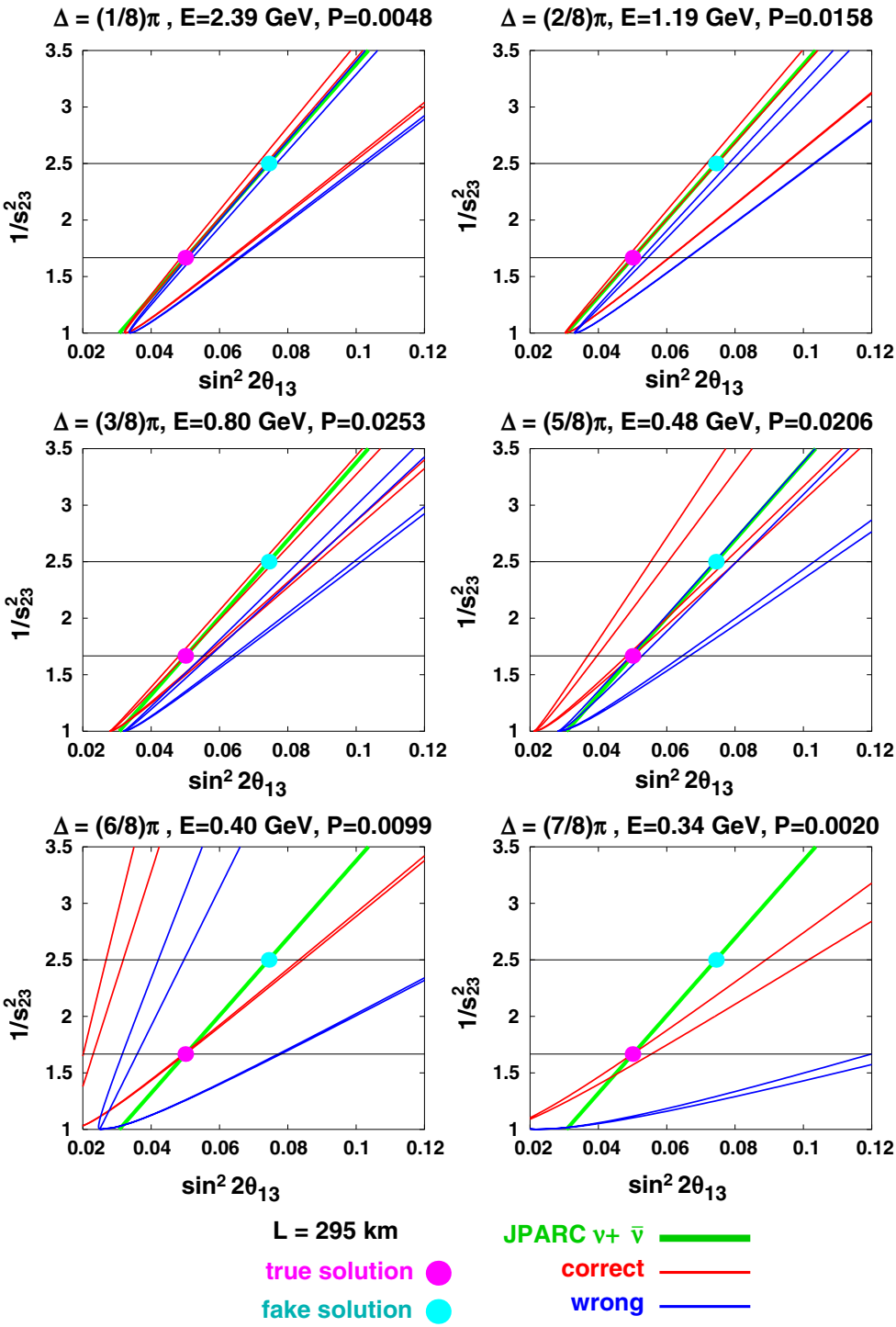

Figure 7. The trajectories of $P(\nu_\mu \to \nu_e) =$ const. of the third experiment at $L = 295\,\mathrm{km}$ with $\Delta \equiv |\Delta m^2_{31}|L/4E = (j/8)\pi$ $(1 \leqslant j \leqslant 7,\ j \neq 4)$ after JPARC. True values are those in (20). The green line is the JPARC result obtained by $P(\nu_\mu \to \nu_e)$ and $P(\bar{\nu}_\mu \to \bar{\nu}_e)$ at the oscillation maximum. The red (blue) lines are the trajectories of $P(\nu_\mu \to \nu_e)$ given by the third experiment assuming the normal (inverted) hierarchy, where δ takes four values for each mass hierarchy.

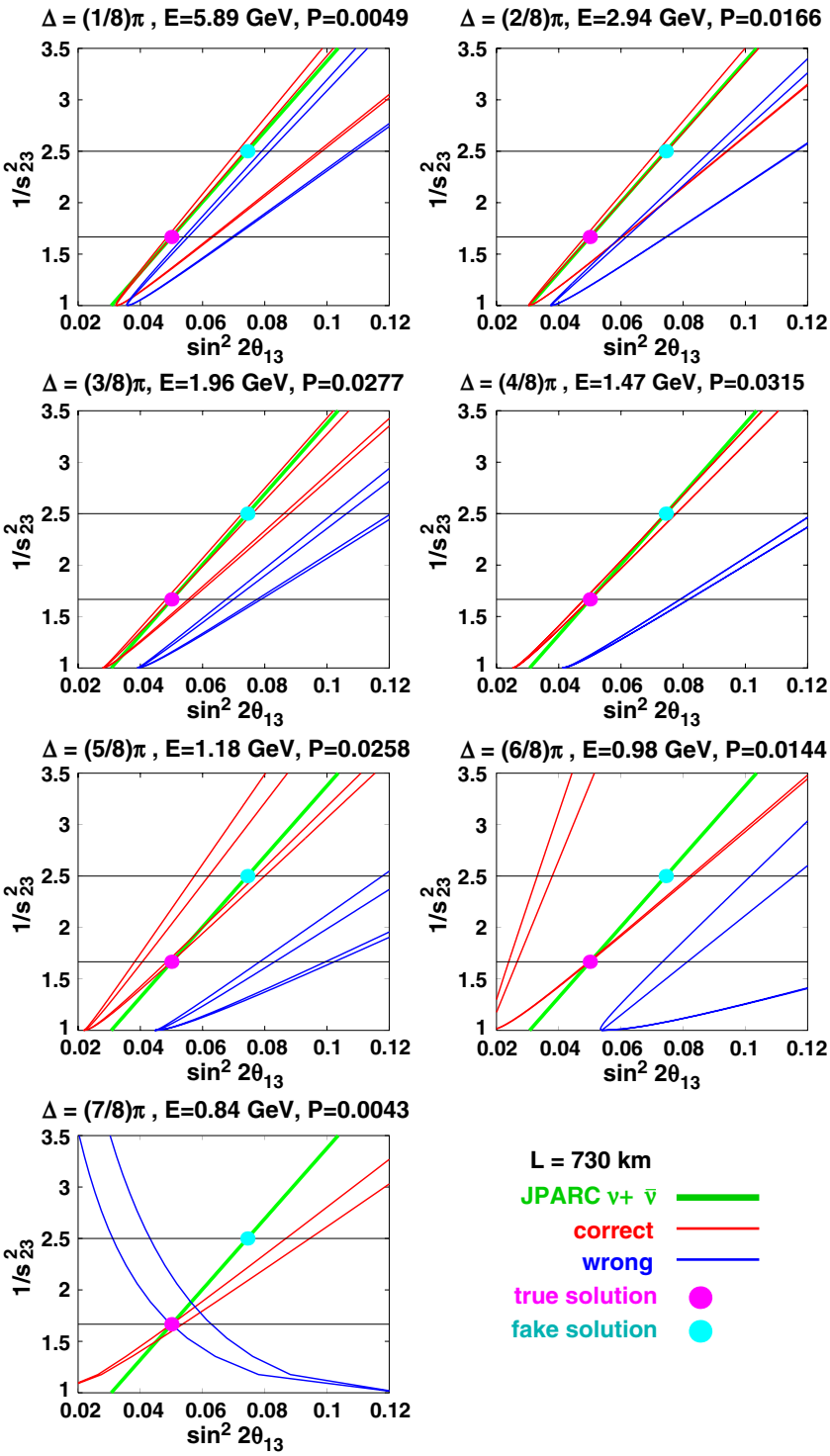

Figure 8. The trajectories of $P(\nu_\mu \to \nu_e) =$ const. of the third experiment at $L = 730\,\mathrm{km}$ with $\Delta \equiv |\Delta m^2_{31}|L/4E = (j/8)\pi$ $(1 \leqslant j \leqslant 7)$ after JPARC. True values are those in (20).

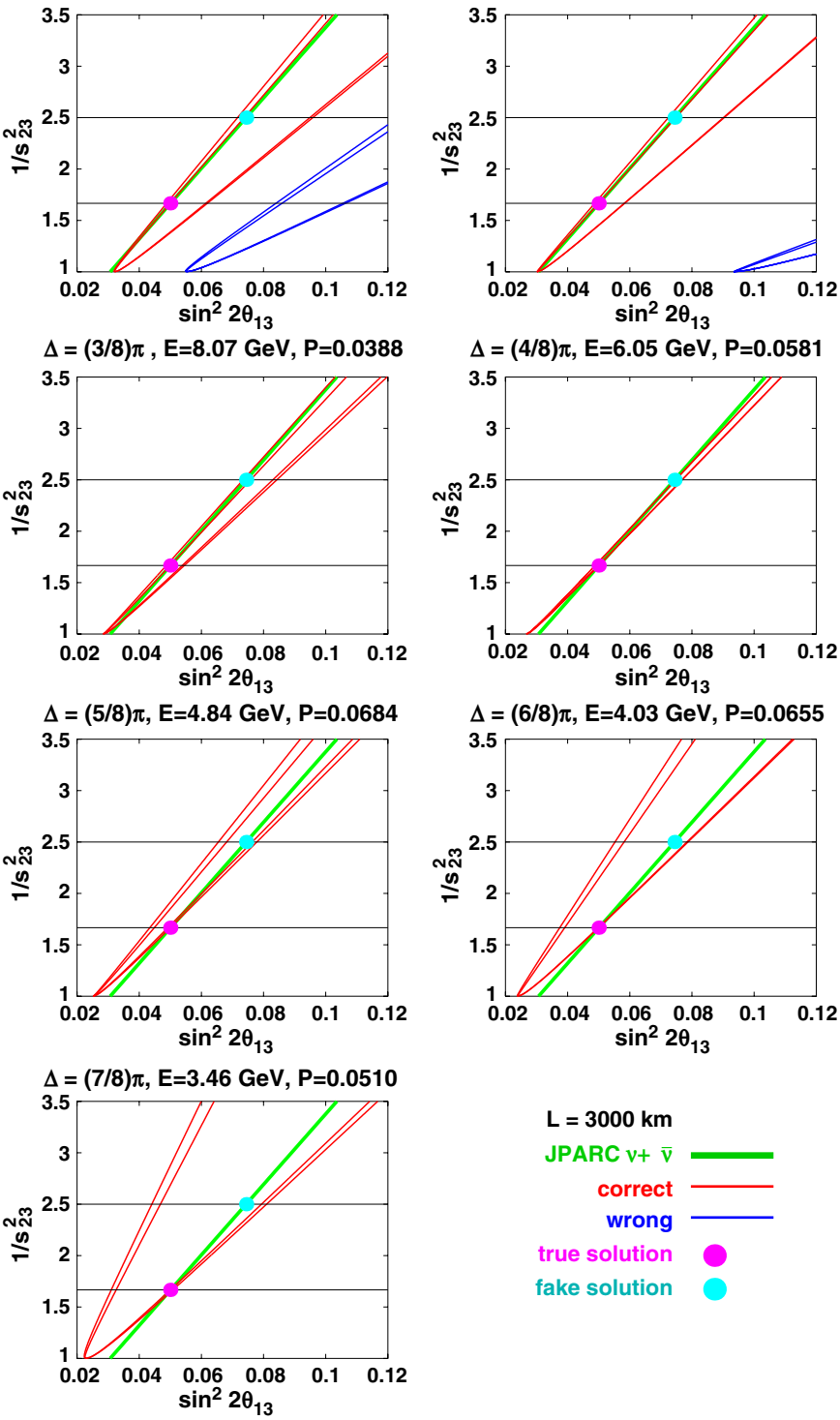

Figure 9. The trajectories of $P(\nu_\mu \to \nu_e) =$ const. of the third experiment at $L = 3000\,\mathrm{km}$ with $\Delta \equiv |\Delta m^2_{31}|L/4E = (j/8)\pi$ $(1 \leqslant j \leqslant 7)$ after JPARC. True values are those in (20). For $\Delta \geqslant (3/8)\pi$, the blue curves (with the wrong assumption for the mass hierarchy) are not seen in the figure because they are far to the right.

of curves. As we will see later, the large split is due to the $\delta \leftrightarrow \pi - \delta$ ambiguity, whereas the small split is due to the $\theta_{23} \leftrightarrow \pi/2 - \theta_{23}$ ambiguity. The reason that the latter splitting is small is because the difference in values for the CP phases is small, as can be seen from (19). In some of the figures in figures 7–9, the number of red or blue curves is less than 4 since not all values of δ give consistent solutions for a set of oscillation parameters.

Let us study the ambiguities one by one.

3.1.1. $\delta \leftrightarrow \pi - \delta$ ambiguity. As mentioned above, the large splitting of four (red or blue) lines into two pair of lines is due to the $\delta \leftrightarrow \pi - \delta$ ambiguity. From (22) and (23), we see that the only difference between the solutions with δ and $\pi - \delta$ appears in $\cos(\delta \pm \Delta)$ or $\sin(\delta \pm \Delta)$. If $\Delta = \pi/2$ (i.e. the oscillation maximum), we have $\cos(\delta + \Delta) = -\sin\delta$ and $\cos(\pi - \delta + \Delta) = -\sin\delta$, so that the values of X with δ and with $\pi - \delta$ are the same, i.e. at oscillation maximum there is exact $\delta \leftrightarrow \pi - \delta$ degeneracy. On the other hand, if $\Delta \neq \pi/2$, we have $\cos(\delta + \Delta) \neq \cos(\pi - \delta + \Delta)$, and the values of X with δ and with $\pi - \delta$ are different. Thus, to resolve the $\delta \leftrightarrow \pi - \delta$ ambiguity, it is advantageous to perform an experiment at Δ farther away from $\pi/2$. Deviation of Δ value from $\pi/2$ implies either high or low energy. In general, the number of events increases for high energy because both the cross-section and the neutrino flux increase. Therefore the high-energy option is preferred in resolving the $\delta \leftrightarrow \pi - \delta$ ambiguity.[6]

3.1.2. $\Delta m^2_{31} \leftrightarrow -\Delta m^2_{31}$ ambiguity. As one can easily imagine, the $\mathrm{sgn}(\Delta m^2_{31})$ ambiguity is resolved better with longer baselines, since the dimensionless quantity $AL \equiv \sqrt{2} G_F N_e L \sim (L/1900\,\mathrm{km})(\rho/2.7\,\mathrm{g\,cm^{-3}})$ becomes of order one for $L \gtrsim 1000\,\mathrm{km}$. On the other hand, from figures 8 and 9, we observe that the split of the curves with different mass hierarchies (the red versus blue curves) is larger for lower energy. Naively, this appears to be counterintuitive, since, at low energy, the matter effect is expected to be less important ($|\Delta m^2_{31}|L/4E \gg AL$). However, this is not the case since we are dealing with the value of $\sin^2 2\theta_{13}$ obtained for a given value of $P(\nu_\mu \to \nu_e)$. To see this, let us consider for simplicity the value of $X \equiv \sin^2 2\theta_{13}$ at $Y \equiv 1/s^2_{23} = 1$, i.e. the X intercept of the quadratic curves at $Y = 1$. $(\sin^2 2\theta_{13})_n((\sin^2 2\theta_{13})_i)$ at $Y = 1$ for the normal (inverted) hierarchy is given by x^2 by putting $y = 0$ in (4) (equation (5)):

$$\left.\begin{aligned} (\sin^2 2\theta_{13})_n &= \frac{P}{f^2} \\ (\sin^2 2\theta_{13})_i &= \frac{P}{\bar{f}^2} \end{aligned}\right\} \qquad \text{for } s^2_{23} = 1.$$

The ratio of these two quantities is given, for small AL, by

$$\frac{(\sin^2 2\theta_{13})_n}{(\sin^2 2\theta_{13})_i} = \frac{f^2}{\bar{f}^2} = \frac{\sin^2(\Delta - AL/2)}{\sin^2(\Delta + AL/2)} \left(\frac{1 + AL/2\Delta}{1 - AL/2\Delta}\right)^2$$
$$\simeq 1 + 2AL\left(\frac{1}{\Delta} - \frac{1}{\tan\Delta}\right).$$

[6] Resolution of $\delta \leftrightarrow \pi - \delta$ ambiguity at neutrino factories has been discussed in [13].

Hence, the larger the Δ (the smaller the neutrino energy), the larger the above ratio, as long as Δ does not exceed π. This phenomenon suggests that it is potentially possible to enhance the matter effect by performing an experiment at low energy ($\Delta > \pi/2$) even with $L = 730\,\mathrm{km}$, and it may enable us to determine the sign of Δm^2_{31} at the off-axis NuMI experiment. Although the neutrino flux decreases for low energy at the off-axis NuMI experiment, the cross-section at $E \sim 1\,\mathrm{GeV}$ is not particularly small compared with higher energy; hence, the low energy possibility at the off-axis NuMI experiment deserves serious study.

3.1.3. $\theta_{23} \leftrightarrow \pi/2 - \theta_{23}$ ambiguity. Figures 7–9, which are plotted for $\delta = \pi/4$, suggest that there is a tendency that, for high energy, the slope of the red curve, which goes through the true point (the purple blob), is almost the same as the slope of the straight green line obtained by JPARC, whereas, for low energy, the slope of the red curve is smaller than that of the JPARC green line. Here, we will discuss the X intercept at $Y = 1$ instead of calculating the slope itself, since it is easier to consider the X intercept and since the difference in the X intercepts inevitably implies different slopes for the two lines with almost all the curves being approximately straight lines. For JPARC, the matter effect is small ($AL \simeq 0.08$), so that we can put $f \simeq \bar{f} \simeq 1$. From equation (15), we have the X intercept at $Y = 1$ as

$$X_{\mathrm{JPARC}} = \frac{P/f + \bar{P}/\bar{f}}{f + \bar{f}} \simeq \frac{P + \bar{P}}{2} \simeq x^2, \tag{24}$$

where the term g^2y^2 has been ignored for simplicity. On the other hand, for the third measurement, from (22), we have

$$X_{\mathrm{3rd}} = \frac{P}{f^2} \simeq x^2 + 2\frac{g}{f}xy\cos(\delta + \Delta), \tag{25}$$

where the term g^2y^2 has been ignored again for simplicity. Equation (25) indicates that it is the second term in (25) that deviates the intercept X_{3rd} of the red line from the intercept X_{JPARC} of the JPARC green line. For the difference between X_{JPARC} and X_{3rd} to be large, f has to be small and $|\cos(\delta + \Delta)|$ has to be large. When AL is small, for f to be small, $||\Delta m^2_{31}|L/4E - \pi|$ has to be small. This is one of the conditions to resolve the θ_{23} ambiguity. Here, we are using the reference value $\delta = \pi/4$; hence, the deviation becomes maximal if $|\delta + \Delta| = |\pi/4 + \Delta| \simeq \pi$. In real experiments, however, nobody knows the value of the true δ in advance and, therefore, it is difficult to design a long baseline experiment to resolve the $\theta_{23} \leftrightarrow \pi/2 - \theta_{23}$ ambiguity. If δ turns out to satisfy $|\cos(\delta + \Delta)| \sim 1$ in the results of the third experiment, then we may be able to resolve the θ_{23} ambiguity as a by-product.

3.2. $\bar{\nu}_\mu \to \bar{\nu}_e$

It turns out that the situation does not change very much even if we use the $\bar{\nu}_\mu \to \bar{\nu}_e$ channel in the third experiment. Typical curves are given for $\bar{\nu}_\mu \to \bar{\nu}_e$ in figure 10, which are similar to those

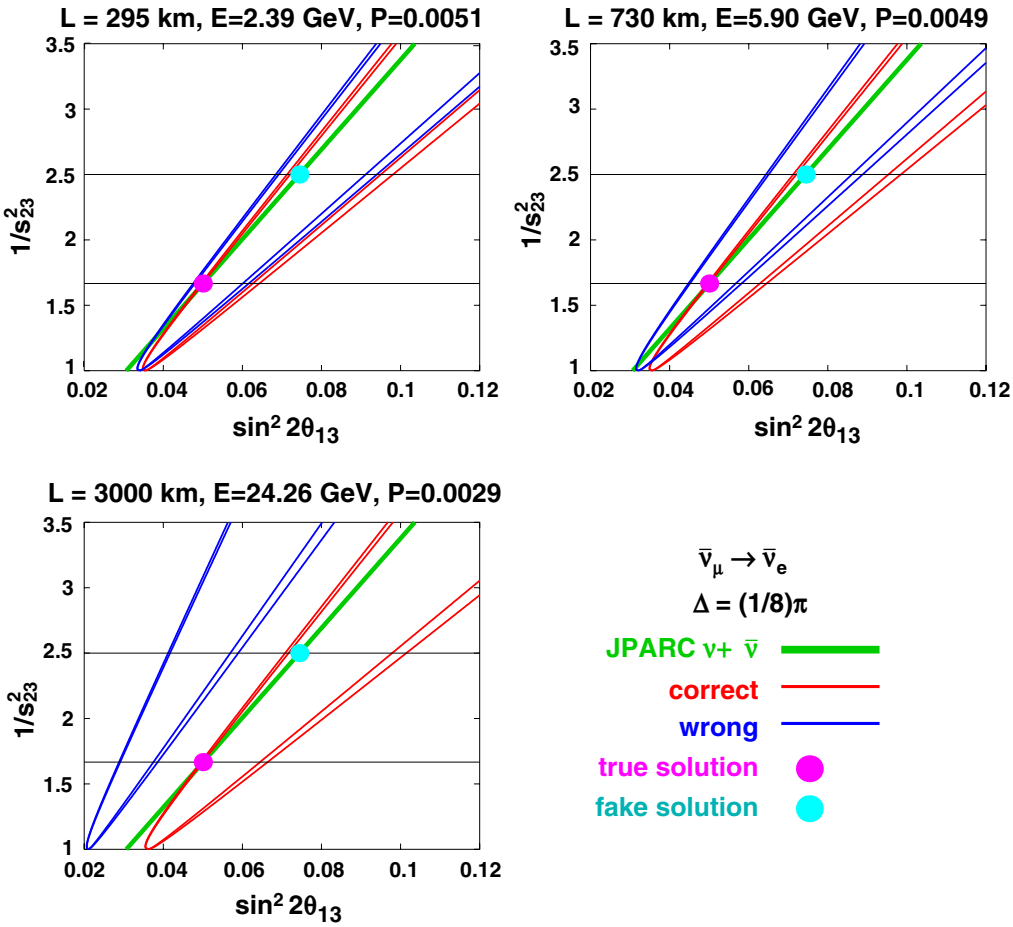

Figure 10. The trajectories of $P(\bar{\nu}_\mu \to \bar{\nu}_e) = \text{const.}$ of the third experiment with $\Delta \equiv |\Delta m^2_{31}|L/4E = \pi/8$ after JPARC. The behaviours are almost similar to those for $P(\nu_\mu \to \nu_e) = \text{const.}$ True values are those in (20).

in figures 7–9. Thus the conclusions we drew on resolution of the ambiguities hold qualitatively for the $\bar{\nu}_\mu \to \bar{\nu}_e$ channel.

3.3. $\nu_e \to \nu_\tau$

The experiment with the channel $\nu_e \to \nu_\tau$ requires intense ν_e beams and it is expected that such measurements can be done at neutrino factories or at beta beam experiments [26]. The oscillation probability $P(\nu_e \to \nu_\tau)$ is given by

$$P(\nu_e \to \nu_\tau) = \tilde{x}^2 f^2 + 2fg\tilde{x}\tilde{y}\cos(\delta + \Delta) + \tilde{y}^2 g^2,$$

where

$$\tilde{x} \equiv c_{23}\sin 2\theta_{23}, \qquad \tilde{y} \equiv \left|\frac{\Delta m^2_{21}}{\Delta m^2_{31}}\right| s_{23}\sin 2\theta_{12},$$

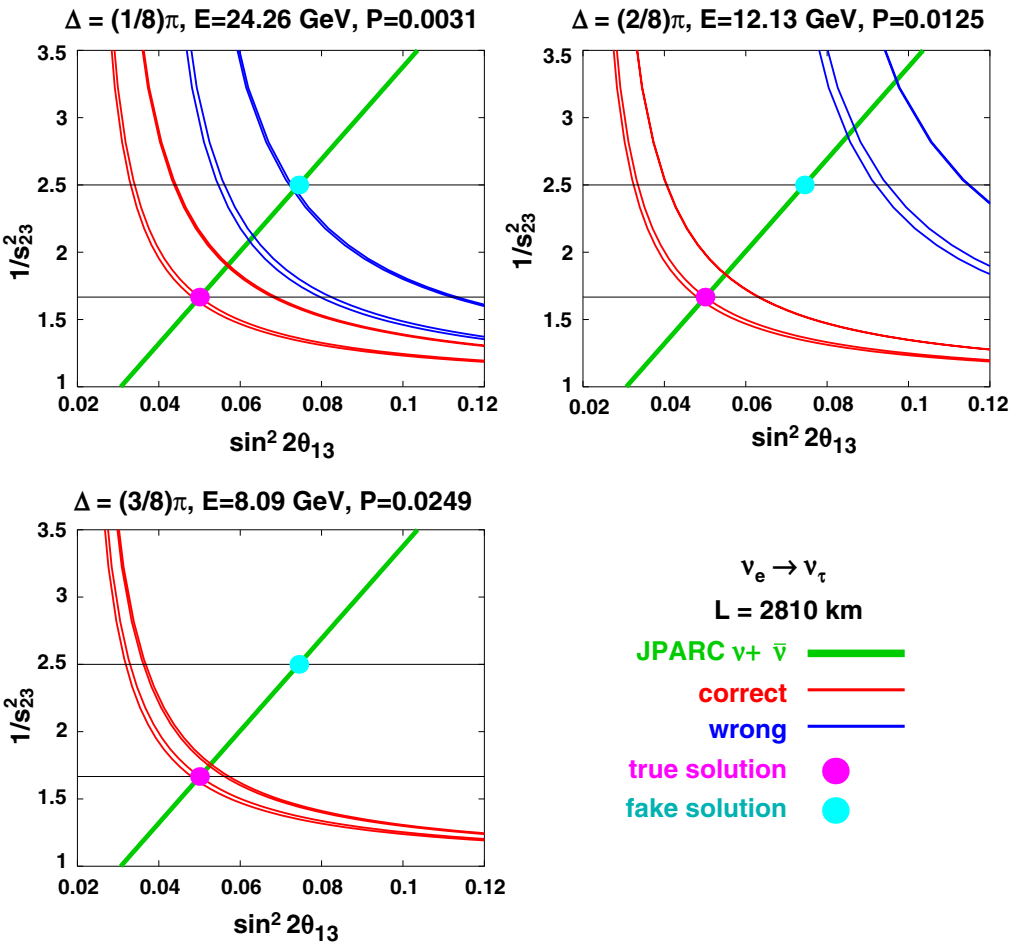

Figure 11. The trajectories of $P(\nu_e \to \nu_\tau) =$ const. of the third experiment at $L = 2810\,\mathrm{km}$ with $\Delta \equiv |\Delta m^2_{31}|L/4E = (j/8)\pi$ $(j = 1, 2, 3)$ after JPARC. True values are those in (20). The curves intersect with the JPARC line perpendicularly; hence, this channel is advantageous to resolve the ambiguities from an experimental point of view.

and f, g are defined in (6) and (7). The solution for $P(\nu_e \to \nu_\tau) = Q$, where Q is constant, is given by

$$X = \frac{Q}{f^2}\left\{\left[1 + \frac{2\cos^2(\delta+\Delta)}{1-C/Q}\right]\frac{1-C/Q}{Y-1} + 1 - \frac{2\cos(\delta+\Delta)}{\sqrt{1-C/Q}}\sqrt{\left[1 + \frac{\cos^2(\delta+\Delta)}{1-C/Q}\right]\frac{1-C/Q}{Y-1} + 1}\right\}, \tag{26}$$

where $X \equiv \sin^2 2\theta_{13}$, $Y \equiv 1/s^2_{23}$ as before and C is given by equation (10). Equation (26) is plotted in figure 11 for $L = 2810\,\mathrm{km}$. From figure 11, we see that the curve $P(\nu_e \to \nu_\tau) = Q$ intersects with the JPARC green line almost perpendicularly, and it is experimentally advantageous: namely,

in real experiments, all the measured quantities have errors and the curves become thick. In this case, the allowed region is a small area around the true solution in the $(\sin^2 2\theta_{13}, 1/s_{23}^2)$ plane and one expects that the fake solution with respect to the θ_{23} ambiguity can be excluded. This contrasts with the case of the $\nu_\mu \to \nu_e$ and $\bar{\nu}_\mu \to \bar{\nu}_e$ channels, where the slope of the red curve is almost the same as that of the JPARC green line and the allowed region can easily contain both the true and fake solutions, so that it becomes difficult to distinguish the true point from the fake one.

Similar to the case of the $\nu_\mu \to \nu_e$ channel, the $\delta \leftrightarrow \pi - \delta$ ambiguity is expected to be resolved more easily for larger values of $|\Delta - \pi/2|$ and the $\mathrm{sgn}(\Delta m_{31}^2)$ ambiguity is resolved easily for larger baseline L (e.g. $L \sim 3000\,\mathrm{km}$).

Thus measurement of the $\nu_e \to \nu_\tau$ channel offers a promising possibility as a potentially powerful candidate to resolve parameter degeneracies in the future.[7]

4. Discussion and conclusion

In this paper, we have shown that the eightfold parameter degeneracy in neutrino oscillations can be easily seen by plotting the trajectory of constant probabilities in the $(\sin^2 2\theta_{13}, 1/s_{23}^2)$ plane. Using this plot, we have seen that the third measurement after the JPARC results on $P(\nu_\mu \to \nu_e)$ and $P(\bar{\nu}_\mu \to \bar{\nu}_e)$ may resolve the $\mathrm{sgn}(\Delta m_{31}^2)$ ambiguity at $L \gtrsim 1000\,\mathrm{km}$, the $\delta \leftrightarrow \pi - \delta$ ambiguity off the oscillation maximum ($|\Delta - \pi/2| \sim \mathcal{O}(1)$) and the θ_{23} ambiguity if $||\Delta m_{31}^2|L/4E - \pi|$ is small and δ turns out to satisfy $|\cos(\delta + \Delta)| \sim 1$. In general, all these constraints on $\Delta \equiv |\Delta m_{31}^2|L/4E$ may be satisfied by taking $\Delta = \pi$. The condition $\Delta = \pi$, however, actually corresponds to the oscillation minimum, and the number of events is expected to be small for a number of reasons: (i) the probability itself is small at the oscillation minimum; (ii) $\Delta = \pi$ implies low energy and the neutrino flux decreases at low energy; and (iii) the cross-section is generally smaller at low energy than at high energy. Therefore, to gain statistics, it is presumably wise to perform an experiment at $\pi/2 < \Delta < \pi$ after JPARC. The off-axis NuMI experiment with $\pi/2 < \Delta < \pi$ ($E \sim 1\,\mathrm{GeV}$) may be advantageous to resolve these ambiguities.

As seen in figures 8 and 9, experiments at the oscillation maximum do not appear to be useful after JPARC, except for the $\mathrm{sgn}(\Delta m_{31}^2)$ ambiguity. To achieve other goals such as resolution of the $\delta \leftrightarrow \pi - \delta$ and θ_{23} ambiguities, it is wise to stay away from $\Delta = \pi/2$ in experiments after JPARC.

Although only oscillation probabilities were discussed here without taking the statistical and systematic errors into account, we hope that the present paper gives some insight on how the ambiguities can be resolved in future long-baseline experiments.

Acknowledgments

We thank Hiroaki Sugiyama for many discussions. This work was partially supported by Grants-in-Aid for Scientific Research Nos 16540260 and 16340078 from Japan Ministry of Education, Culture, Sports, Science and Technology.

[7] Recently, a high γ beta beam option has been proposed [27] and it is concluded that this option may be a serious competitor to neutrino factories.

Appendix A. Expression for $P(\nu_\mu \to \nu_e) = P$

First of all, let us derive equations (22) and (23). For the normal hierarchy, the probability $P(\nu_\mu \to \nu_e) = P$ is given by

$$P = P(\nu_\mu \to \nu_e) = x^2 f^2 + 2xyfg\cos(\delta + \Delta) + y^2 g^2$$

$$= f^2 \frac{X}{Y} + 2f\sqrt{\frac{X}{Y}}\sqrt{C\left(1 - \frac{1}{Y}\right)}\cos(\delta + \Delta) + C\left(1 - \frac{1}{Y}\right), \tag{A.1}$$

where $X \equiv \sin^2 2\theta_{13}$, $Y \equiv 1/s_{23}^2$ as in the text, f is defined in (6) and C is given by (10). Equation (A.1) can be rewritten as

$$(P - C)(Y - 1) + P - f^2 X = 2\sqrt{f^2 X}\sqrt{C(Y - 1)}\cos(\delta + \Delta). \tag{A.2}$$

Taking the square of both left- and right-hand sides of (A.2), we obtain[8]

$$(f^2 X)^2 - 2f^2 X\{[P - C + 2C\cos^2(\delta + \Delta)](Y - 1) + P\} + [(P - C)(Y - 1) + P]^2 = 0.$$

Solving this quadratic equation, we obtain

$$\begin{aligned} f^2 X &= [P - C + 2C\cos^2(\delta + \Delta)](Y - 1) + P \\ &\quad \pm\sqrt{\{[P - C + 2C\cos^2(\delta + \Delta)](Y - 1) + P\}^2 - [(P - C)(Y - 1) + P]^2} \\ &= [P - C + 2C\cos^2(\delta + \Delta)](Y - 1) + P \\ &\quad \pm 2\cos(\delta + \Delta)\sqrt{C(Y - 1)}\sqrt{[P - C + C\cos^2(\delta + \Delta)](Y - 1) + P}. \end{aligned} \tag{A.3}$$

If $\cos(\delta + \Delta) > 0$, then from (A.2) we find that $(P + C)(Y - 1) + P - f^2 X$ has to be positive. On the other hand, (A.3) gives

$$\begin{aligned} (P + C)(Y - 1) + P - f^2 X &= \mp 2\cos(\delta + \Delta)\sqrt{C(Y - 1)} \\ &\quad \times\{\sqrt{[P - C + C\cos^2(\delta + \Delta)](Y - 1) + P} - \cos(\delta + \Delta)\sqrt{C(Y - 1)}\}. \end{aligned} \tag{A.4}$$

From (A.4), we conclude that we have to consider the minus sign in (A.3) for the right-hand side of (A.4) to be positive. Hence, from $P(\nu_\mu \to \nu_e) = P$, we obtain

$$\begin{aligned} f^2 X &= [P - C + 2C\cos^2(\delta + \Delta)](Y - 1) + P \\ &\quad - 2\cos(\delta + \Delta)\sqrt{C(Y - 1)}\sqrt{[P - C\sin^2(\delta + \Delta)](Y - 1) + P}, \end{aligned} \tag{A.5}$$

[8] Here we consider, for simplicity, the case where all the arguments of the square root are positive. After we obtain the final result, we see that the final formula makes sense as long as the whole product of all the arguments is positive.

and, from $P(\bar{\nu}_e \to \bar{\nu}_\mu) = \bar{P}$, we have

$$\bar{f}^2 X = [\bar{P} - C + 2C\cos^2(\delta - \Delta)](Y - 1) + \bar{P} - 2\cos(\delta - \Delta)\sqrt{C(Y-1)}\sqrt{[\bar{P} - C\sin^2(\delta - \Delta)](Y-1) + \bar{P}}. \quad \text{(A.6)}$$

When $P - C\sin^2(\delta + \Delta) > 0$, equation (A.5) is a hyperbola, and the physical region for $Y - 1$ is $Y - 1 \geqslant 0$. On the other hand, when $P - C\sin^2(\delta + \Delta) < 0$, equation (A.5) becomes an ellipse and the physical region for $Y - 1$ is $0 \leqslant Y - 1 \leqslant P/[C\sin^2(\delta + \Delta) - P]$.

Similarly, we obtain for the inverted hierarchy,

$$\bar{f}^2 X = [P - C + 2C\cos^2(\delta - \Delta)](Y - 1) + P + 2\cos(\delta - \Delta)\sqrt{C(Y-1)}\sqrt{[P - C\sin^2(\delta - \Delta)](Y-1) + P}, \quad \text{(A.7)}$$

$$f^2 X = [\bar{P} - C + 2C\cos^2(\delta + \Delta)](Y - 1) + \bar{P} + 2\cos(\delta + \Delta)\sqrt{C(Y-1)}\sqrt{[\bar{P} - C\sin^2(\delta + \Delta)](Y-1) + \bar{P}}. \quad \text{(A.8)}$$

Appendix B. Trajectories at the oscillation maximum

We will assume $\Delta = \pi/2$ throughout this appendix and $\Delta m^2_{31} > 0$ for most part of this appendix. From (A.5), the condition $P(\nu_\mu \to \nu_e) = P$ for the neutrino mode alone gives

$$f^2 X = [P - C + 2C\sin^2\delta](Y - 1) + P + 2\sin\delta\sqrt{C(Y-1)}\sqrt{[P - C\cos^2\delta](Y-1) + P}, \quad \text{(B.1)}$$

whereas the condition $P(\bar{\nu}_\mu \to \bar{\nu}_e) = \bar{P}$ for the anti-neutrino mode alone gives

$$\bar{f}^2 X = [\bar{P} - C + 2C\sin^2\delta](Y - 1) + \bar{P} - 2\sin\delta\sqrt{C(Y-1)}\sqrt{[\bar{P} - C\cos^2\delta](Y-1) + \bar{P}}. \quad \text{(B.2)}$$

When δ ranges from $-\pi/2$ to $\pi/2$, equation (B.1) sweeps out the inside of a hyperbola, as depicted by the red curves in figure B.1(a), whereas (B.2) sweeps out the inside of another hyperbola for the anti-neutrino mode (cf the blue curves in figure B.1(a)). Notice that the left (right) edge of the hyperbola (B.1) for the neutrino mode corresponds to $\delta = -\pi/2$ ($\delta = +\pi/2$), whereas the left (right) edge of the other hyperbola (B.2) for the anti-neutrino mode corresponds to $\delta = +\pi/2$ ($\delta = -\pi/2$). Since the straight line (15) represents the intersection of the two regions (the yellow and light blue regions in figure B.1(b)), the lowest point in the straight line is obtained by putting $\delta = +\pi/2$ ($\delta = -\pi/2$) if $P/f^2 < \bar{P}/\bar{f}^2$ (if $P/f^2 > \bar{P}/\bar{f}^2$), respectively, depending on whether the region for the anti-neutrino mode is to the right of that for the neutrino mode. Therefore, if $P/f^2 < \bar{P}/\bar{f}^2$, then, putting $\delta = +\pi/2$ in (11) and (12) and assuming $xf > yg$, which should

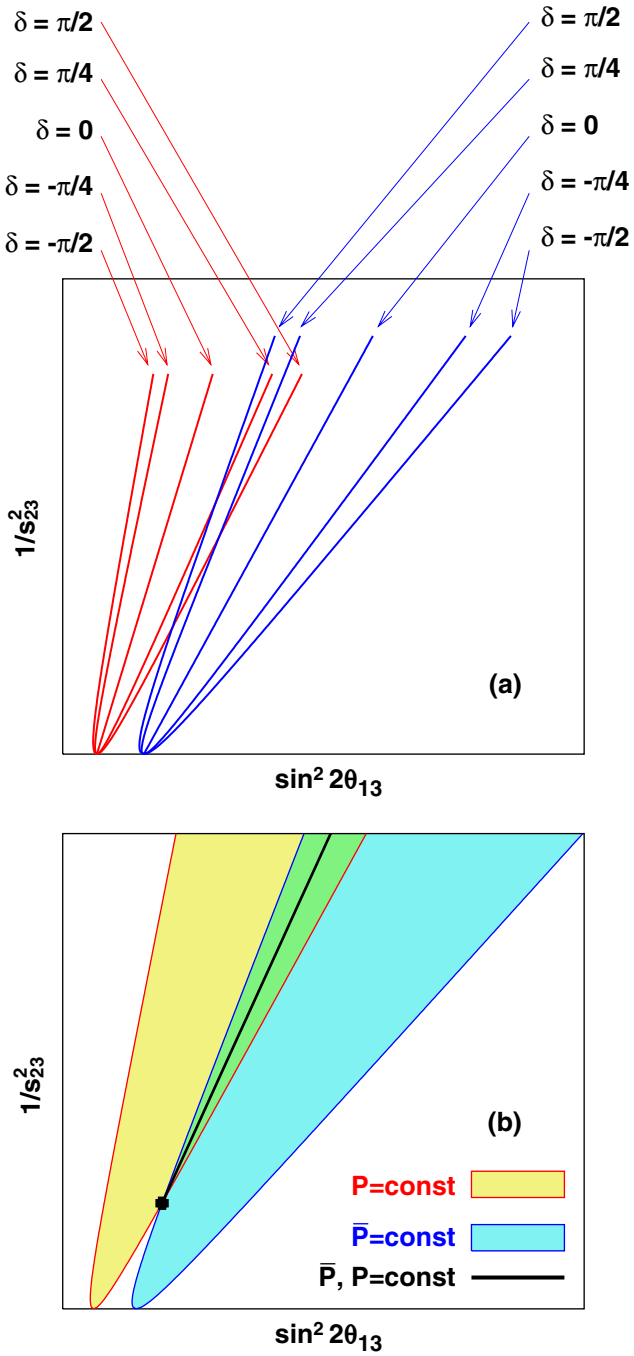

Figure B.1. The region of constant probabilities at the oscillation maximum. (a) Each red (blue) line stands for $P(\nu_\mu \to \nu_e) = \text{const.}$ ($P(\bar{\nu}_\mu \to \bar{\nu}_e) = \text{const.}$) for a specific value of δ. The red line on the right (left) edge corresponds to $\delta = +\pi/2$ ($\delta = -\pi/2$), whereas the blue line on the edge right (left) corresponds to $\delta = -\pi/2$ ($\delta = +\pi/2$). (b) When δ varies from 0 to 2π, the line $P(\nu_\mu \to \nu_e) = \text{const.}$ sweeps out the yellow region, whereas the line $(\bar{\nu}_\mu \to \bar{\nu}_e) = \text{const.}$ sweeps out the light blue region. The black straight line, which is given by $P(\nu_\mu \to \nu_e) = \text{const.}$ and $P(\bar{\nu}_\mu \to \bar{\nu}_e) = \text{const.}$, lies on the overlapping green region.

hold if $\sin^2 2\theta_{13}$ is not very small, we get

$$\sqrt{P} = xf - yg = f\sqrt{\frac{X}{Y}} - \sqrt{C\left(1 - \frac{1}{Y}\right)}, \qquad \sqrt{\bar{P}} = x\bar{f} + yg = \bar{f}\sqrt{\frac{X}{Y}} + \sqrt{C\left(1 - \frac{1}{Y}\right)},$$

which lead to the minimum value of Y,

$$Y_{\min}^{(n)} = \left[1 - \frac{(f\sqrt{\bar{P}} - \bar{f}\sqrt{P})^2}{C(f + \bar{f})^2}\right]^{-1}$$

for the normal hierarchy. On the other hand, for the inverted hierarchy, the corresponding values of δ for the edges for the two modes are the same as those for the normal hierarchy ($\delta = \pm\pi/2$). Hence, if $P/\bar{f}^2 < \bar{P}/f^2$, then putting $\delta = +\pi/2$ in (13) and (14) and assuming $x\bar{f} > yg$, we obtain

$$\sqrt{P} = x\bar{f} - yg, \qquad \sqrt{\bar{P}} = xf + yg,$$

which leads to the minimum value of Y,

$$Y_{\min}^{(i)} = \left[1 - \frac{(\bar{f}\sqrt{\bar{P}} - f\sqrt{P})^2}{C(f + \bar{f})^2}\right]^{-1}$$

for $\Delta m_{31}^2 < 0$.

References

[1] Kajita T and Totsuka Y 2001 *Rev. Mod. Phys.* **73** 85

[2] Bahcall J N 2000 *Phys. Rep.* **333** 47

[3] Apollonio M *et al* (CHOOZ Collaboration) 1999 *Phys. Lett.* B **466** 415 (*Preprint* hep-ex/9907037)

[4] Eguchi K *et al* (KamLAND Collaboration) 2003 *Phys. Rev. Lett.* **90** 021802 (*Preprint* hep-ex/0212021)

[5] Hagiwara K *et al* (Particle Data Group Collaboration) 2002 *Phys. Rev.* D **66** 010001

[6] Burguet-Castell J, Gavela M B, Gomez-Cadenas J J, Hernandez P and Mena O 2001 *Nucl. Phys.* B **608** 301 (*Preprint* hep-ph/0103258)

[7] Minakata H and Nunokawa H 2001 *JHEP* **0110** 001 (*Preprint* hep-ph/0108085)

[8] Fogli G L and Lisi E 1996 *Phys. Rev.* D **54** 3667 (*Preprint* hep-ph/9604415)

[9] Barger V, Marfatia D and Whisnant K 2002 *Phys. Rev.* D **65** 073023 (*Preprint* hep-ph/0112119)

[10] Saji C 2004 Talk at *The 5th Workshop on 'Neutrino Oscillations and their Origin'* 11–15 February, Odaiba, Tokyo, Japan (http://www-sk.icrr.u-tokyo.ac.jp/noon2004/trape/09-Saji.pdf)

[11] Minakata H, Sugiyama H, Yasuda O, Inoue K and Suekane F 2003 *Phys. Rev.* D **68** 033017 (*Preprint* hep-ph/0211111)

[12] Itow Y *et al* 2001 *Preprint* hep-ex/0106019

[13] Pinney J and Yasuda O 2001 *Phys. Rev.* D **64** 093008 (*Preprint* hep-ph/0105087)

[14] Yasuda O 2003 *Preprint* hep-ph/0305295

[15] Cervera A, Donini A, Gavela M B, Gomez-Cadenas J J, Hernandez P, Mena O and Rigolin S 2000 *Nucl. Phys.* B **579** 17 (*Preprint* hep-ph/0002108)

Cervera A, Donini A, Gavela M B, Gomez-Cadenas J J, Hernandez P, Mena O and Rigolin S 2000 *Nucl. Phys.* B **593** 731 (erratum)

[16] Barenboim G and de Gouvea A 2002 *Preprint* hep-ph/0209117
[17] Huber P, Lindner M, Schwetz T and Winter W 2003 *Nucl. Phys.* B **665** 487 (*Preprint* hep-ph/0303232)
[18] Minakata H and Sugiyama H 2004 *Phys. Lett.* B **580** 216 (*Preprint* hep-ph/0309323)
[19] Donini A, Meloni D and Migliozzi P 2002 *Nucl. Phys.* B **646** 321 (*Preprint* hep-ph/0206034)
Autiero D *et al* 2004 *Eur. Phys. J.* C **33** 243 (*Preprint* hep-ph/0305185)
Donini A 2003 *Preprint* hep-ph/0305247
[20] Barger V D, Marfatia D and Whisnant K 2001 *Proc. APS/DPF/DPB Summer Study on the Future of Particle Physics (Snowmass 2001)* ed N Graf, eConf **C010630**, E102 (*Preprint* hep-ph/0108090)
Minakata H and Nunokawa H 2002 *Nucl. Phys. Proc. Suppl.* **110** 404 (*Preprint* hep-ph/0111131)
Kajita T, Minakata H and Nunokawa H 2002 *Phys. Lett.* B **528** 245 (*Preprint* hep-ph/0112345)
Huber P, Lindner M and Winter W 2002 *Nucl. Phys.* B **645** 3 (*Preprint* hep-ph/0204352)
Barger V, Marfatia D and Whisnant K 2002 *Phys. Rev.* D **66** 053007 (*Preprint* hep-ph/0206038)
Minakata H, Nunokawa H and Parke S J 2002 *Phys. Rev.* D **66** 093012 (*Preprint* hep-ph/0208163)
Barger V, Marfatia D and Whisnant K 2003 *Phys. Lett.* B **560** 75 (*Preprint* hep-ph/0210428)
Huber P, Lindner M and Winter W 2003 *Nucl. Phys.* B **654** 3 (*Preprint* hep-ph/0211300)
Whisnant K 2003 *J. Phys. G: Nucl. Part. Phys.* **29** 1843
Mena O 2003 *J. Phys. G: Nucl. Part. Phys.* **29** 1847
Minakata H, Nunokawa H and Parke S J 2003 *Phys. Rev.* D **68** 013010 (*Preprint* hep-ph/0301210)
Huber P and Winter W 2003 *Phys. Rev.* D **68** 037301 (*Preprint* hep-ph/0301257)
Minakata H, Nunokawa H and Parke S J *Preprint* hep-ph/0310023
Winter W *Preprint* hep-ph/0310307
[21] Burguet-Castell J, Gavela M B, Gomez-Cadenas J J, Hernandez P and Mena O 2002 *Nucl. Phys.* B **646** 301 (*Preprint* hep-ph/0207080)
Mena O 2003 *Preprint* hep-ph/0305146
[22] Donini A, Meloni D and Rigolin S 2003 *Preprint* hep-ph/0312072
[23] Whisnant K, Yang J M and Young B L 2003 *Phys. Rev.* D **67** 013004 (*Preprint* hep-ph/0208193)
[24] Ayres D *et al* 2002 *Preprint* hep-ex/0210005
[25] Geer S 1998 *Phys. Rev.* D **57** 6989 (*Preprint* hep-ph/9712290)
Geer S 1999 *Phys. Rev.* D **59** 039903 (erratum)
[26] Zucchelli P 2002 *Phys. Lett.* B **532** 166
[27] Burguet-Castell J, Casper D, Gomez-Cadenas J J, Hernandez P and Sanchez F 2003 *Preprint* hep-ph/0312068

New Journal of Physics
An Institute of Physics and Deutsche Physikalische Gesellschaft Journal

Non-Abelian discrete symmetries and neutrino masses: two examples

Ernest Ma
Physics Department, University of California, Riverside, CA 92521, USA
and Institute for Particle Physics Phenomenology, Physics Department,
University of Durham, Durham DH1 3LE, UK
E-mail: ernest.ma@ucr.edu

New Journal of Physics **6** (2004) 104
Received 17 May 2004
Published 9 August 2004
Online at http://www.njp.org/
doi:10.1088/1367-2630/6/1/104

Abstract. Two recent examples of non-Abelian discrete symmetries (S_3 and A_4) in understanding neutrino masses and mixing are discussed.

Contents

1. Introduction **1**
2. S_3 for two families **2**
2.1. Representations of S_3 2
2.2. Quarks and leptons under S_3 3
3. A_4 for three families **5**
3.1. Representations of A_4 5
3.2. Quarks and leptons under A_4 6
3.3. Three degenerate neutrino masses 7
3.4. Arbitrary neutrino masses 9
4. Conclusion **11**
Acknowledgments **12**
References **12**

1. Introduction

In the standard model of quark and lepton interactions, quark and charged-lepton masses come from the Yukawa couplings of the left-handed doublets $(u, d)_L$ and $(\nu, l)_L$ with the right-handed singlets u_R, d_R and l_R through the vacuum expectation value of the one scalar Higgs doublet

PII: S1367-2630(04)80847-4
© IOP Publishing Ltd and Deutsche Physikalische Gesellschaft

(ϕ^+, ϕ^0). The quark mixing matrix V_{CKM} is then obtained from the mismatch in the diagonalization of the *up* and *down* quark mass matrices. Remarkably, V_{CKM} turns out to be almost identically the unit matrix, i.e. quark mixing angles are all small (for three families, V_{CKM} has three angles and one phase). On the other hand, the analogous $U_{MNS(P)}$, which is obtained from the mismatch in the diagonalization of the charged-lepton mass matrix and that of the neutrino mass matrix, is far from being the unit matrix. Whereas one angle is indeed small, the other two are definitely large. Indeed, to a good first approximation,

$$U_{MNS(P)} \simeq \begin{pmatrix} \sqrt{2/3} & 1/\sqrt{3} & 0 \\ -1/\sqrt{6} & 1/\sqrt{3} & -1/\sqrt{2} \\ -1/\sqrt{6} & 1/\sqrt{3} & 1/\sqrt{2} \end{pmatrix}. \tag{1}$$

In the convention

$$U_{MNS(P)} = \begin{pmatrix} 1 & 0 & 0 \\ 0 & c_{23} & -s_{23} \\ 0 & s_{23} & c_{23} \end{pmatrix} \begin{pmatrix} c_{13} & 0 & s_{13}e^{-i\delta} \\ 0 & 1 & 0 \\ -s_{13}e^{i\delta} & 0 & c_{13} \end{pmatrix} \begin{pmatrix} c_{12} & -s_{12} & 0 \\ s_{12} & c_{12} & 0 \\ 0 & 0 & 1 \end{pmatrix}, \tag{2}$$

this means that

$$\theta_{23} \simeq \pi/4, \qquad \theta_{12} \simeq \tan^{-1}(-1/\sqrt{2}), \qquad \theta_{13} \simeq 0, \tag{3}$$

which are consistent with the present experimental constraints [1]:

$$\sin^2 2\theta_{23} > 0.91 \text{ (90\% CL)}, \qquad 0.30 < \tan^2\theta_{12} < 0.52 \text{ (90\% CL)}, \qquad \sin^2\theta_{13} < 0.067\ (3\sigma). \tag{4}$$

There are a number of approaches in trying to understand the origin of quark and lepton mass matrices. Most of these attempts relate mixing angles with mass ratios. Historically, this was motivated by the phenomenologically successful ansatz $\theta_C \simeq \sqrt{m_d/m_s}$ for the Cabibbo angle. One often assumes that there is a symmetry behind this relationship. In addition, a better question to ask is perhaps whether or not there exists a family symmetry, which tells us that $V_{CKM} = 1$ and $U_{MNS(P)} \neq 1$. Obviously, if each family has its own Abelian (continuous or discrete) symmetry, then there is no mixing among families. That works well for V_{CKM} but not for $U_{MNS(P)}$. If neutrino masses are purely Dirac, then the analogous structure of the quark and lepton sectors would definitely rule out the existence of such a family symmetry. However, if neutrino masses are Majorana, then it is indeed possible to have $V_{CKM} = 1$ and $U_{MNS(P)}$ as given by equation (1) as the result of a symmetry, as shown below. To fit the experimental data, small (radiative) corrections are needed from physics beyond the Standard Model.

2. S_3 for two families

2.1. Representations of S_3

The group of permutations of three objects is S_3. It is isomorphic to the group of three-dimensional rotations of an equilateral triangle to itself, i.e. the dihedral group D_3. It has six elements and three irreducible representations: $\underline{1}$, $\underline{1}'$ and $\underline{2}$. As such, it is ideal for describing two families.

Since $\underline{1}' \times \underline{1}' = \underline{1}$, it is clear that a field transforming as $\underline{1}'$ should have a Z_2 parity of -1, i.e. $\phi \to -\phi$. On the other hand, a doublet (ϕ_1, ϕ_2) under S_3 has a choice of representations as long as it satisfies

$$\underline{2} \times \underline{2} = \underline{1} + \underline{1}' + \underline{2}. \tag{5}$$

Different representations are simply related by a unitary tranformation. The most convenient representation of S_3 is a complex representation [2, 3] such that the products of the doublets $\phi_{1,2}$ and $\psi_{1,2}$ are given by

$$\phi_1\psi_2 + \phi_2\psi_1 \sim \underline{1}, \tag{6}$$

$$\phi_1\psi_2 - \phi_2\psi_1 \sim \underline{1}', \tag{7}$$

$$(\phi_2\psi_2, \phi_1\psi_1) \sim \underline{2}. \tag{8}$$

Note that $\phi_1\phi_1^* + \phi_2\phi_2^*$ is an invariant; hence (ϕ_2^*, ϕ_1^*) is a doublet. Note also that S_3 has the special property that the symmetric product of three doublets, i.e. $\phi_1\psi_1\chi_1 + \phi_2\psi_2\chi_2$ is a singlet.

Specifically, the six group elements are the identity: e, the cyclic and anti-cyclic permutations of three objects: g_c and g_a, and the three interchanges of two objects leaving the third fixed: g_1, g_2, g_3. Their representation matrices are $[1, 1, 1, 1, 1, 1]$ in $\underline{1}$, $[1, 1, 1, -1, -1, -1]$ in $\underline{1}'$ and

$$\left[\begin{pmatrix}1 & 0\\ 0 & 1\end{pmatrix}, \begin{pmatrix}\omega & 0\\ 0 & \omega^2\end{pmatrix}, \begin{pmatrix}\omega^2 & 0\\ 0 & \omega\end{pmatrix}, \begin{pmatrix}0 & \omega^2\\ \omega & 0\end{pmatrix}, \begin{pmatrix}0 & \omega\\ \omega^2 & 0\end{pmatrix}, \begin{pmatrix}0 & 1\\ 1 & 0\end{pmatrix}\right] \tag{9}$$

in $\underline{2}$, respectively, for $[e, g_c, g_a, g_1, g_2, g_3]$, where $\omega = \mathrm{e}^{2\pi\mathrm{i}/3}$.

2.2. *Quarks and leptons under S_3*

Consider a world of only two (i.e. the second and third) families of quarks and leptons. Choosing the convention that all fermions are left-handed, a natural assignment is [4]

$$Q_i = (u_i, d_i), \qquad L_i = (\nu_i, l_i) \sim \underline{2} \quad (i = 2, 3) \tag{10}$$

$$u_2^c, d_2^c, l_2^c \sim \underline{1}, \qquad u_3^c, d_3^c, l_3^c \sim \underline{1}'. \tag{11}$$

To allow u, d and l to have Dirac mass terms, two scalar electroweak doublets $(\phi_i^0, \phi_i^-)\,(i = 2, 3)$ transforming as an S_3 doublet are required. The invariant leptonic Yukawa couplings are then

$$\mathcal{L}_Y = f_2(\phi_2 L_3 + \phi_3 L_2)l_2^c + f_3(\phi_2 L_3 - \phi_3 L_2)l_3^c + \text{h.c.}, \tag{12}$$

resulting in the 2×2 mass matrix linking $l_{2,3}$ to $l_{2,3}^c$ below:

$$\mathcal{M}_{ll^c} = \begin{pmatrix} f_2 v_3 & -f_3 v_3 \\ f_2 v_2 & f_3 v_2 \end{pmatrix}, \tag{13}$$

where $v_i = \langle\phi_i^0\rangle$. On the other hand, the Majorana neutrino mass matrix depends on the product of L_i and L_j, i.e. equation (5). Thus, a choice of scalar representations is available. Suppose two

scalar triplets $(\xi_i^{++}, \xi_i^{+}, \xi_i^{0})$ $(i = 2, 3)$ transforming as an S_3 doublet are used, then

$$\mathcal{L}_Y = h(L_2 L_2 \xi_2 + L_3 L_3 \xi_3) + \text{h.c.}, \tag{14}$$

which leads to

$$\mathcal{M}_\nu = \begin{pmatrix} hu_2 & 0 \\ 0 & hu_3 \end{pmatrix}, \tag{15}$$

where $u_i = \langle \xi_i^0 \rangle$. Comparing equations (13) and (15), the lepton mixing matrix is easily obtained for $v_2 = v_3 = v$, because equation (13) is diagonalized by

$$U^\dagger = \frac{1}{\sqrt{2}} \begin{pmatrix} 1 & 1 \\ -1 & 1 \end{pmatrix} \tag{16}$$

on the left and the unit matrix on the right, which of course means maximal mixing. The charged-lepton mass eigenvalues are then $\sqrt{2} f_2 v$ and $\sqrt{2} f_3 v$, whereas the Majorana neutrino mass eigenvalues are hu_2 and hu_3. They all can be different and yet maximal mixing is ensured. This depends of course on the condition $v_2 = v_3$, which can be maintained in the Higgs potential by the interchange symmetry $\phi_2 \leftrightarrow \phi_3$. The trilinear scalar couplings $\mu_2 \phi_2 \phi_3 \xi_2$ and $\mu_3 \phi_2 \phi_3 \xi_3$ break S_3 softly but are invariant under $\phi_2 \leftrightarrow \phi_3$. Hence, $\mu_2 \neq \mu_3$ would imply $u_2 \neq u_3$. Note that since $m_\tau \gg m_\mu$ means $f_3 \gg f_2$, the charged-lepton matrix is diagonalized by

$$U^\dagger = \frac{1}{\sqrt{v_2^2 + v_3^2}} \begin{pmatrix} v_2 & v_3 \\ -v_3 & v_2 \end{pmatrix} \tag{17}$$

to a good approximation even if $v_2 \neq v_3$. In that case, the mixing angle is given by $\tan^{-1}(v_3/v_2)$, which can differ from $\pi/4$.

In the quark sector, the *down*-quark mass matrix has the same form as equation (13), i.e.

$$\mathcal{M}_{dd^c} = \begin{pmatrix} f_2^d v_3 & -f_3^d v_3 \\ f_2^d v_2 & f_3^d v_2 \end{pmatrix}, \tag{18}$$

but the *up*-quark mass matrix is given by

$$\mathcal{M}_{uu^c} = \begin{pmatrix} f_2^u v_2^* & -f_3^u v_2^* \\ f_2^u v_3^* & f_3^u v_3^* \end{pmatrix} \tag{19}$$

instead, because (ϕ_3^*, ϕ_2^*) must be used in place of (ϕ_2, ϕ_3). This means that there is now a mismatch between the two diagonalized mass matrices and the mixing angle is given by [4]

$$\theta_q = 2\left[\frac{\pi}{4} - \tan^{-1}(v_3/v_2)\right] = \frac{\pi}{2} - 2\theta_l. \tag{20}$$

In this way, the smallness of the quark mixing between the second and third families is related to the deviation from maximal mixing in the μ–τ sector. To include the first family of quarks and leptons, S_3 singlets must be used. Since either $\underline{1}$ or $\underline{1}'$ must be chosen, there has to be mixing of the first family into the 2–3 sector, but its exact form or magnitude cannot be fixed by S_3 alone; see [4] for a specific successful application.

3. A_4 for three families

3.1. Representations of A_4

The group of even permutations of four objects is A_4. It is isomorphic to the group of three-dimensional rotations of a regular tetrahedron, one of five perfect geometric solids known to the ancient Greeks and identified by Plato with the element 'fire'. It is thus a discrete subgroup of SO(3). It is also isomorphic to $\Delta(12)$, which is a discrete subgroup of SU(3) [5]. It has 12 elements and four irreducible reprsentations: $\underline{1}$, $\underline{1}'$, $\underline{1}''$ and $\underline{3}$, with the multiplication rule

$$\underline{3} \times \underline{3} = \underline{1} + \underline{1}' + \underline{1}'' + \underline{3} + \underline{3}, \tag{21}$$

in analogy to equation (5) for S_3. As such, it is ideal for describing three families. Specifically, the products of the triplets $\phi_{1,2,3}$ and $\psi_{1,2,3}$ are given by [6]

$$\phi_1\psi_1 + \phi_2\psi_2 + \phi_3\psi_3 \sim \underline{1}, \tag{22}$$

$$\phi_1\psi_1 + \omega^2\phi_2\psi_2 + \omega\phi_3\psi_3 \sim \underline{1}', \tag{23}$$

$$\phi_1\psi_1 + \omega\phi_2\psi_2 + \omega^2\phi_3\psi_3 \sim \underline{1}'', \tag{24}$$

$$(\phi_2\psi_3, \phi_3\psi_1, \phi_1\psi_2) \sim \underline{3}, \tag{25}$$

$$(\phi_3\psi_2, \phi_1\psi_3, \phi_2\psi_1) \sim \underline{3}, \tag{26}$$

where $\omega = \mathrm{e}^{2\pi\mathrm{i}/3}$. Note that A_4 also has the special property that the symmetric product of three triplets, i.e.

$$\phi_1\psi_2\chi_3 + \phi_1\psi_3\chi_2 + \phi_2\psi_1\chi_3 + \phi_2\psi_3\chi_1 + \phi_3\psi_1\chi_2 + \phi_3\psi_2\chi_1 \tag{27}$$

is a singlet.

Specifically, the 12 group elements are divided into four equivalence classes: C_1 contains only the identity, C_2 has 4 elements of order 3, C_3 also has 4 elements of order 3 and C_4 has 3 elements of order 2. The representation matrices in $\underline{3}$ are given by

$$C_1\colon \quad \begin{pmatrix} 1 & 0 & 0 \\ 0 & 1 & 0 \\ 0 & 0 & 1 \end{pmatrix}, \tag{28}$$

$$C_2\colon \quad \begin{pmatrix} 0 & 0 & 1 \\ 1 & 0 & 0 \\ 0 & 1 & 0 \end{pmatrix}, \quad \begin{pmatrix} 0 & 0 & 1 \\ -1 & 0 & 0 \\ 0 & -1 & 0 \end{pmatrix}, \quad \begin{pmatrix} 0 & 0 & -1 \\ 1 & 0 & 0 \\ 0 & -1 & 0 \end{pmatrix}, \quad \begin{pmatrix} 0 & 0 & -1 \\ -1 & 0 & 0 \\ 0 & 1 & 0 \end{pmatrix}, \tag{29}$$

$$C_3: \quad \begin{pmatrix} 0 & 1 & 0 \\ 0 & 0 & 1 \\ 1 & 0 & 0 \end{pmatrix}, \quad \begin{pmatrix} 0 & 1 & 0 \\ 0 & 0 & -1 \\ -1 & 0 & 0 \end{pmatrix}, \quad \begin{pmatrix} 0 & -1 & 0 \\ 0 & 0 & 1 \\ -1 & 0 & 0 \end{pmatrix}, \quad \begin{pmatrix} 0 & -1 & 0 \\ 0 & 0 & -1 \\ 1 & 0 & 0 \end{pmatrix}, \tag{30}$$

$$C_4: \quad \begin{pmatrix} 1 & 0 & 0 \\ 0 & -1 & 0 \\ 0 & 0 & -1 \end{pmatrix}, \quad \begin{pmatrix} -1 & 0 & 0 \\ 0 & 1 & 0 \\ 0 & 0 & -1 \end{pmatrix}, \quad \begin{pmatrix} -1 & 0 & 0 \\ 0 & -1 & 0 \\ 0 & 0 & 1 \end{pmatrix}. \tag{31}$$

They are [1, 1, 1, 1], [1, ω, ω^2, 1] and [1, ω^2, ω, 1] in $\underline{1}$, $\underline{1}'$ and $\underline{1}''$, respectively.

3.2. *Quarks and leptons under A_4*

In analogy to equations (10) and (11) for S_3, a natural assignment for three families of quarks and leptons is [6]–[10]

$$Q_i = (u_i, d_i), \qquad L_i = (\nu_i, l_i) \sim \underline{3} \quad (i = 1, 2, 3) \tag{32}$$

$$u_1^c, d_1^c, l_1^c \sim \underline{1}, \qquad u_2^c, d_2^c, l_2^c \sim \underline{1}', \qquad u_3^c, d_3^c, l_3^c \sim \underline{1}''. \tag{33}$$

To allow u, d and l to have Dirac mass terms, three scalar electroweak doublets (ϕ_i^0, ϕ_i^-) $(i = 1, 2, 3)$ transforming as an A_4 triplet are required. The invariant leptonic Yukawa couplings are then

$$\begin{aligned} \mathcal{L}_Y = {} & f_1(L_1\phi_1 + L_2\phi_2 + L_3\phi_3)l_1^c + f_2(L_1\phi_1 + \omega L_2\phi_2 + \omega^2 L_3\phi_3)l_2^c \\ & + f_3(L_1\phi_1 + \omega^2 L_2\phi_2 + \omega L_3\phi_3)l_3^c + \text{h.c.}, \end{aligned} \tag{34}$$

where $\underline{1}' \times \underline{1}'' = \underline{1}$ has been used. The resulting 3×3 mass matrix linking $l_{1,2,3}$ to $l_{1,2,3}^c$ is

$$\mathcal{M}_{ll^c} = \begin{pmatrix} f_1 v_1 & f_2 v_1 & f_3 v_1 \\ f_1 v_2 & f_2 \omega v_2 & f_3 \omega^2 v_2 \\ f_1 v_3 & f_2 \omega^2 v_3 & f_3 \omega v_3 \end{pmatrix}, \tag{35}$$

which is diagonalized simply by

$$U_L^\dagger = \frac{1}{\sqrt{3}} \begin{pmatrix} 1 & 1 & 1 \\ 1 & \omega & \omega^2 \\ 1 & \omega^2 & \omega \end{pmatrix} \tag{36}$$

on the left and the unit matrix on the right for $v_1 = v_2 = v_3 = v$. The charged-lepton mass eigenvalues are then $\sqrt{3} f_1 v$, $\sqrt{3} f_2 v$ and $\sqrt{3} f_3 v$, which are of course free to be chosen as m_e, m_μ and m_τ. Since this matrix also diagonalizes the up and down-quark mass matrices, the resulting quark mixing matrix is just the unit matrix, i.e. $V_{CKM} = 1$.

3.3. Three degenerate neutrino masses

Consider now the 3×3 Majorana neutrino mass matrix. Since the product of L_i and L_j is given by equation (21), a choice of scalar representations is available, as for S_3 discussed earlier. The simplest choice is to have one scalar triplet $(\xi_1^{++}, \xi_1^{+}, \xi_1^{0})$ transforming as $\underline{1}$ under A_4. In that case,

$$\mathcal{L}_Y = h_1(L_1L_1 + L_2L_2 + L_3L_3)\xi_1 + \text{h.c.}, \tag{37}$$

resulting in three degenerate neutrino masses, i.e.

$$\mathcal{M}_\nu = \begin{pmatrix} m_0 & 0 & 0 \\ 0 & m_0 & 0 \\ 0 & 0 & m_0 \end{pmatrix}, \tag{38}$$

where $m_0 = 2h_1\langle\xi_1^0\rangle$. In the (e, μ, τ) basis, it becomes

$$\mathcal{M}_\nu^{(e,\mu,\tau)} = U_L^\dagger \mathcal{M}_\nu U_L^* = \begin{pmatrix} m_0 & 0 & 0 \\ 0 & 0 & m_0 \\ 0 & m_0 & 0 \end{pmatrix}. \tag{39}$$

From the high scale where A_4 is broken to the electroweak scale, one-loop radiative corrections will change equation (39) to

$$\begin{pmatrix} m_0 & 0 & 0 \\ 0 & 0 & m_0 \\ 0 & m_0 & 0 \end{pmatrix} + R \begin{pmatrix} m_0 & 0 & 0 \\ 0 & 0 & m_0 \\ 0 & m_0 & 0 \end{pmatrix} + \begin{pmatrix} m_0 & 0 & 0 \\ 0 & 0 & m_0 \\ 0 & m_0 & 0 \end{pmatrix} R^{\mathrm{T}}, \tag{40}$$

where the radiative correction matrix is assumed to be of the most general form, i.e.

$$R = \begin{pmatrix} r_{ee} & r_{e\mu} & r_{e\tau} \\ r_{e\mu}^* & r_{\mu\mu} & r_{\mu\tau} \\ r_{e\tau}^* & r_{\mu\tau}^* & r_{\tau\tau} \end{pmatrix}. \tag{41}$$

Thus, the observed neutrino mass matrix is given by

$$\mathcal{M}_\nu = m_0 \begin{pmatrix} 1 + 2r_{ee} & r_{e\tau} + r_{e\mu}^* & r_{e\mu} + r_{e\tau}^* \\ r_{e\mu}^* + r_{e\tau} & 2r_{\mu\tau} & 1 + r_{\mu\mu} + r_{\tau\tau} \\ r_{e\tau}^* + r_{e\mu} & 1 + r_{\mu\mu} + r_{\tau\tau} & 2r_{\mu\tau}^* \end{pmatrix}. \tag{42}$$

Then using the redefinitions:

$$\delta_0 \equiv r_{\mu\mu} + r_{\tau\tau} - r_{\mu\tau} - r^*_{\mu\tau}, \tag{43}$$

$$\delta \equiv 2r_{\mu\tau}, \tag{44}$$

$$\delta' \equiv r_{ee} - \tfrac{1}{2}r_{\mu\mu} - \tfrac{1}{2}r_{\tau\tau} - \tfrac{1}{2}r_{\mu\tau} - \tfrac{1}{2}r^*_{\mu\tau}, \tag{45}$$

$$\delta'' \equiv r^*_{e\mu} + r_{e\tau}, \tag{46}$$

it becomes

$$\mathcal{M}_\nu = m_0 \begin{pmatrix} 1+\delta_0+\delta+\delta^*+2\delta' & \delta'' & \delta''^* \\ \delta'' & \delta & 1+\delta_0+(\delta+\delta^*)/2 \\ \delta''^* & 1+\delta_0+(\delta+\delta^*)/2 & \delta^* \end{pmatrix}. \tag{47}$$

Without loss of generality, δ may be chosen real by absorbing its phase into ν_μ and ν_τ and δ_0 set equal to zero by redefining m_0 and the other δs. As a result,

$$\sin^2 2\theta_{atm} \simeq 1, \qquad \Delta m^2_{atm} \simeq 4\delta m_0^2, \qquad U_{e3} \simeq \frac{\mathrm{i}\,\mathrm{Im}\,\delta''}{\sqrt{2}\delta}, \tag{48}$$

$$\Delta m^2_{sol} \simeq 4\sqrt{(\tilde{\delta}')^2 + 2(\mathrm{Re}\,\delta'')^2}\,m_0^2, \qquad \tan\theta_{sol} \simeq \frac{\sqrt{2}\,\mathrm{Re}\,\delta''}{\sqrt{(\tilde{\delta}')^2 + 2(\mathrm{Re}\,\delta'')^2} - \tilde{\delta}'}, \tag{49}$$

where $\tilde{\delta}' = \delta' + (\mathrm{Im}\,\delta'')^2/2\delta < 0$.

Thus, this model explains $\theta_{23} \simeq \pi/4$ and predicts three nearly degenerate neutrino masses with neutrinoless double beta decay given by $|m_0|$. Since δ is a radiative correction, it cannot be too large. Given that Δm^2_{atm} is known to be of order $10^{-3}\,\mathrm{eV}^2$, m_0 cannot be much smaller than about 0.3 eV. Remarkably, this is also the upper limit on neutrino mass from the large-scale structure of the Universe [11] and possibly the value of $|m_0|$ as measured in neutrinoless double beta decay [12].

In the Standard Model, there are no flavour-changing leptonic interactions; thus $\delta = \delta'' = 0$ and equation (47) does not lead to neutrino oscillations at all. However, if there is some new physics which allows all the δs to be nonzero, then equation (47) can be realistic. A recent detailed example [9] is available in the context of supersymmetry with arbitrary soft supersymmetry breaking terms.

3.4. Arbitrary neutrino masses

In addition to ξ_1 transforming as $\underline{1}$ under A_4, consider ξ_2, ξ_3 and $\xi_{4,5,6}$ transforming as $\underline{1}'$, $\underline{1}''$ and $\underline{3}$ as well [10]. In that case, $\mathcal{M}_\nu$ in the original basis is given by

$$\mathcal{M}_\nu = \begin{pmatrix} a+b+c & 0 & 0 \\ 0 & a+\omega b+\omega^2 c & d \\ 0 & d & a+\omega^2 b+\omega c \end{pmatrix}, \tag{50}$$

where a comes from $\langle\xi_1^0\rangle$, b from $\langle\xi_2^0\rangle$, c from $\langle\xi_3^0\rangle$ and d from $\langle\xi_4^0\rangle$, assuming that $\langle\xi_5^0\rangle = \langle\xi_6^0\rangle = 0$.

In the basis where the charged-lepton mass matrix is diagonal, the neutrino mass matrix becomes

$$\mathcal{M}_\nu^{(e,\mu,\tau)} = U_L^\dagger \mathcal{M}_\nu U_L^* = \begin{pmatrix} a+(2d/3) & b-(d/3) & c-(d/3) \\ b-(d/3) & c+(2d/3) & a-(d/3) \\ c-(d/3) & a-(d/3) & b+(2d/3) \end{pmatrix}. \tag{51}$$

This matrix has one obvious eigenstate, i.e. $\nu_2 = (\nu_e+\nu_\mu+\nu_\tau)/\sqrt{3}$ with the eigenvalue $m_2 = a+b+c$. Let

$$U = \begin{pmatrix} \sqrt{2/3} & 1/\sqrt{3} & 0 \\ -1/\sqrt{6} & 1/\sqrt{3} & -1/\sqrt{2} \\ -1/\sqrt{6} & 1/\sqrt{3} & 1/\sqrt{2} \end{pmatrix}, \tag{52}$$

then in the basis defined by this transformation, i.e.

$$\nu_1 = \sqrt{\frac{2}{3}}\nu_e - \frac{1}{\sqrt{6}}(\nu_\mu+\nu_\tau), \tag{53}$$

$$\nu_2 = \frac{1}{\sqrt{3}}(\nu_e+\nu_\mu+\nu_\tau), \tag{54}$$

$$\nu_3 = \frac{1}{\sqrt{2}}(-\nu_\mu+\nu_\tau), \tag{55}$$

the neutrino mass matrix of equation (51) rotates to

$$\mathcal{M}_\nu^{(1,2,3)} = U^\dagger \mathcal{M}_\nu^{(e,\mu,\tau)} U^* = \begin{pmatrix} m_1 & 0 & m_4 \\ 0 & m_2 & 0 \\ m_4 & 0 & m_3 \end{pmatrix}, \tag{56}$$

where

$$\begin{pmatrix} m_1 \\ m_2 \\ m_3 \\ m_4 \end{pmatrix} = \begin{pmatrix} 1 & -1/2 & -1/2 & 1 \\ 1 & 1 & 1 & 0 \\ -1 & 1/2 & 1/2 & 1 \\ 0 & -\sqrt{3}/2 & \sqrt{3}/2 & 0 \end{pmatrix} \begin{pmatrix} a \\ b \\ c \\ d \end{pmatrix}. \tag{57}$$

In the limit $m_4 = 0$, equation (56) is diagonal and U becomes the neutrino mixing matrix of equation (1) with the prediction $\tan^2\theta_{12} = 1/2$, as well as $\sin^2 2\theta_{23} = 1$ and $\theta_{13} = 0$. This is of course a well-known ansatz [13], but has only just been derived from the symmetry of a complete theory, without arbitrary assumptions regarding its charged-lepton sector, in [10].

Note that $m_{1,2,3}$ in the above are all arbitrary. In other words, the mixing angles are determined without regard to the masses, just as in the quark sector. There is however an important difference. Whereas all quark mixing angles are zero, the lepton mixing angles are not. Additional small corrections from physics beyond the Standard Model, such as supersymmetry [9, 14], are of course necessary to modify these predictions to coincide with present data.

Experimentally, $|U_{e3}|$ is known to be small, i.e. $m_4 = (\sqrt{3}/2)(c-b)$ may be considered small compared with $|b+c|$. Now $\Delta m^2_{atm} \gg \Delta m^2_{sol}$ implies that either $d \simeq (3/2)(b+c)$ or $d \simeq -2a-(b+c)/2$. If $d \simeq (3/2)(b+c)$, then

$$m_{1,2} \simeq a+b+c, \qquad m_3 \simeq -a+2(b+c). \tag{58}$$

If $d \simeq -2a-(b+c)/2$, then

$$m_{1,2} \simeq a+b+c, \qquad m_3 \simeq -3a. \tag{59}$$

Either one will allow a normal hierarchy or an inverted hierarchy or nearly degenerate masses.

If $m_4 \neq 0$, ν_1 mixes with ν_3, but ν_2 remains the same. Let the new mass eigenstates be

$$\nu'_1 = \nu_1\cos\theta + \nu_3 e^{i\delta}\sin\theta, \qquad \nu'_3 = -\nu_1 e^{-i\delta}\sin\theta + \nu_3\cos\theta, \tag{60}$$

then the new mixing matrix U has elements

$$U_{e1} = \sqrt{\frac{2}{3}}\cos\theta, \qquad U_{e2} = \frac{1}{\sqrt{3}}, \qquad U_{e3} = -\sqrt{\frac{2}{3}}e^{i\delta}\sin\theta, \tag{61}$$

$$U_{\mu 3} = -\frac{1}{\sqrt{2}}\cos\theta + \frac{1}{\sqrt{6}}e^{i\delta}\sin\theta = -\frac{1}{\sqrt{2}}\sqrt{1-\frac{3}{2}|U_{e3}|^2} - \frac{1}{2}U_{e3}. \tag{62}$$

Therefore, the experimental constraint [15]

$$|U_{e3}| < 0.16 \tag{63}$$

implies

$$0.61 < |U_{\mu 3}| < 0.77, \tag{64}$$

or, using $\sin^2 2\theta_{atm} = 4|U_{\mu 3}|^2(1 - |U_{\mu 3}|^2)$,

$$0.94 < \sin^2 2\theta_{atm} < 1. \tag{65}$$

Similarly, using $\tan^2 \theta_{sol} = |U_{e2}|^2/|U_{e1}|^2$,

$$0.5 < \tan^2 \theta_{sol} < 0.52 \tag{66}$$

is obtained. Whereas equation (65) is well satisfied by the current data, equation (66) is at the high end of the 2σ-allowed range centred at $\tan^2 \theta_{sol} \simeq 0.4$ [16].

If future experimental measurements persist in getting a value of $\tan^2 \theta_{sol}$ outside the range predicted by equation (66), one possible explanation within the context of this model is through radiative corrections. Just as equation (39) is radiatively corrected to become equation (47), equation (51) may also get corrected so that ν_1 mixes with ν_2 in equation (56). For example, if $b, c, d < a$, then combining equations (47) and (51) with $b = c$,

$$\tan 2\theta_{sol} \simeq -2\sqrt{2}\left[\frac{b - (d/3) + \delta'' a}{b - (d/3) - 2\delta' a}\right], \tag{67}$$

where

$$\delta'' = \delta_{e\mu} + \delta_{e\tau}, \qquad \delta' = \delta_{ee} - \tfrac{1}{2}(\delta_{\mu\mu} + \delta_{\tau\tau}) - \delta_{\mu\tau}, \tag{68}$$

and $\tan^2 \theta_{sol} \simeq 0.4$ is obtained if $[b - (d/3) + \delta'' a]/[b - (d/3) - 2\delta' a] \simeq 0.75$. Note that, this may occur even if $\delta_{\alpha\beta} = 0$ for $\alpha \neq \beta$, i.e. in the absence of flavour-changing radiative corrections, in contrast with the requirement of [8, 9].

4. Conclusion

The non-Abelian discrete symmetry S_3 is ideal for explaining maximal mixing in the μ–τ sector with a normal hierarchy of neutrino masses. In a specific application [4], it also explains why U_{e3} is small but non-zero.

The non-Abelian discrete symmetry A_4 is a natural candidate for describing three families of quarks and leptons. Whereas Dirac fermion masses come from the decomposition

$$\underline{3} \times (\underline{1} + \underline{1}' + \underline{1}'') = \underline{3}, \tag{69}$$

Majorana neutrino masses come from the decomposition

$$\underline{3} \times \underline{3} = \underline{1} + \underline{1}' + \underline{1}'' + \underline{3}. \tag{70}$$

The mismatch between the quark mass matrices is then naturally given by $V_{CKM} = 1$, whereas that between the charged-lepton and neutrino mass matrices is definitely not the unit matrix, but rather $U_{MNS(P)}$ of equation (1) in a certain symmetry limit, thus predicting a relationship among θ_{23}, θ_{12} and θ_{13}. Specifically, if $\theta_{13} = 0$, then $\sin^2 2\theta_{23} = 1$ and $\tan^2 \theta_{12} = 0.5$, independent of the values of the three neutrino masses. (Note that all six quarks and all three charged leptons have names, but the three neutrinos do not, as yet.) To obtain small nonzero quark mixing angles as well as deviations from the lepton-mixing angles constrained by this model, new physics beyond the Standard Model is expected, such as supersymmetry at the TeV scale.

Acknowledgments

We thank the Institute for Particle Physics Phenomenology, Durham for hospitality. This work was supported in part by the US Department of Energy under grant no. DE-FG03-94ER40837.

References

[1] For a brief review see Smirnov A Yu *Preprint* hep-ph/0402264
[2] Ma E 1991 *Phys. Rev.* D **43** 2761
Ma E 1991 *Phys. Rev.* D **44** 587
[3] Deshpande N G *et al* 1992 *Phys. Rev.* D **45** 953
[4] Chen S-L, Frigerio M and Ma E *Preprint* hep-ph/0404084
[5] Hanany A and He Y-H 1999 *J. High Energy Phys.* JHEP02 (1999) 013
[6] Ma E and Rajasekaran G 2001 *Phys. Rev.* D **64** 113012
[7] Ma E 2002 *Mod. Phys. Lett.* A **17** 289, 627
[8] Babu K S, Ma E and Valle J W F 2003 *Phys. Lett.* B **552** 207
Ma E 2002 *Mod. Phys. Lett.* A **17** 2361
[9] Hirsch M, Romao J C, Skadhauge S, Valle J W F and Villanova del Moral A *Preprint* hep-ph/0312265
[10] Ma E *Preprint* hep-ph/0404199
[11] Spergel D N *et al* 2003 *Astrophys. J.* **148** (Suppl.) 175
Hannestad S 2003 *J. Cosmol. Astropart. Phys.* **0305** 004
[12] Klapdor-Kleingrothaus H V *et al* 2004 *Mod. Phys. Lett.* A **17** 1475
Klapdor-Kleingrothaus H V *et al* 2004 *Phys. Lett.* B **586** 198
[13] Harrison P F, Perkins D H and Scott W G 2002 *Phys. Lett.* B **530** 167
For an updated review see Harrison P F and Scott W G *Preprint* hep-ph/0402006
[14] Babu K S, Dutta B and Mohapatra R N 1999 *Phys. Rev.* D **60** 095004
[15] Apollonio M *et al* 1999 *Phys. Lett.* B **466** 415
Boehm F *et al* 2001 *Phys. Rev.* D **64** 112001
[16] SNO Collaboration, Ahmad Q R *et al* 2002 *Phys. Rev. Lett.* **89** 011301, 011302
KamLAND Collaboration, Eguchi K *et al* 2003 *Phys. Rev. Lett.* **90** 021802
SNO Collaboration, Ahmed S N *et al* 2004 *Phys. Rev. Lett.* **92** 181301

New Journal of Physics
An Institute of Physics and Deutsche Physikalische Gesellschaft Journal

Some aspects of thermal leptogenesis

W Buchmüller[1], P Di Bari[2] and M Plümacher[3]

[1] Deutsches Elektronen-Synchrotron DESY, 22603 Hamburg, Germany
[2] IFAE, Universitat Autònoma de Barcelona, 08193 Bellaterra, Barcelona, Spain
[3] Department of Physics, Theory Division, CERN, 1211 Geneva 23, Switzerland
E-mail: buchmuwi@mail.desy.de

New Journal of Physics **6** (2004) 105
Received 2 June 2004
Published 10 August 2004
Online at http://www.njp.org/
doi:10.1088/1367-2630/6/1/105

Abstract. Properties of neutrinos may be the origin of the matter–antimatter asymmetry of the universe. In the see–saw model for neutrino masses, this leads to important constraints on the properties of light and heavy neutrinos. In particular, an upper bound on the light neutrino masses of 0.1 eV can be derived. We review the present status of thermal leptogenesis with emphasis on the theoretical uncertainties and discuss some implications for lepton and quark mass hierarchies, CP violation and dark matter. We also comment on the 'leptogenesis conspiracy', the remarkable fact that neutrino masses may lie in the range where leptogenesis works best.

PII: S1367-2630(04)81449-6
© IOP Publishing Ltd and Deutsche Physikalische Gesellschaft

Contents

1. Introduction **2**
2. Baryon and lepton number violation in the SM **3**
3. Leptogenesis **4**
3.1. A qualitative overview 4
3.2. Boltzmann equations 6
4. Constraints on neutrino masses **8**
4.1. Final efficiency factor 8
4.2. *CP* asymmetry 11
4.3. Lower bounds on heavy neutrino masses and reheating temperature 12
4.4. Upper bound on light neutrino masses 13
4.5. Leptogenesis conspiracy 14
5. Flavour aspects **16**
6. Cosmological aspects **19**
Acknowledgments **21**
References **21**

1. Introduction

One of the great challenges of modern particle physics and cosmology is to explain the excess of matter over anti-matter observed in the universe. This baryon asymmetry is conveniently expressed as the ratio of baryon minus anti-baryon density to the photon density and has recently been measured to a high degree of accuracy by observations of the cosmic microwave background (CMB) [1] combined with measurements of large-scale structures of the universe [2]:

$$\eta_B^{CMB} = (6.3 \pm 0.3) \times 10^{-10}. \tag{1}$$

In a complete cosmological model, this baryon asymmetry has to be dynamically generated during the evolution of the universe in the hot and dense phase shortly after the big bang. This is possible if the particle interactions violate baryon number (B), charge conjugation (C) and the combined charge and parity conjugation (CP), and if the expansion of the universe leads to a deviation from thermal equilibrium [3].

All these ingredients are present in the Standard Model (SM) of particle interactions. However, the baryon asymmetry that can be generated in the SM falls far short of observations, i.e. an extended model of particle interactions has to be considered. The observation of neutrino masses also requires an extension of the SM and lepton number (L) violating interactions that are introduced in the see–saw model of neutrinos masses [4, 5] can naturally give rise to the observed baryon asymmetry in the leptogenesis scenario [6] that is the topic of this paper.

The rather suprising fact that lepton number violating interactions can give rise to a baryon asymmetry is due to a deep connection between baryon and lepton number in the SM, as discussed in section 2. In section 3, we present the basic mechanism of leptogenesis and introduce some notations that are used in the following. The quantitative solution of the Boltzmann equations and the corresponding bounds on light and heavy neutrino masses are described in section 4.

Here we also comment on the *leptogenesis conspiracy*, the remarkable fact that neutrino masses may lie in the range where leptogenesis works best. In section 5 the connection between low and high energy *CP* violation and implications of leptogenesis for the heavy neutrino mass spectrum are briefly discussed. Section 6 deals with the implications of leptogenesis for dark matter.

2. Baryon and lepton number violation in the SM

In the SM, both baryon and lepton number are classically conserved, since they are protected by global Abelian symmetries. However, due to the chiral nature of weak interactions, these symmetries are anomalous and are violated at the quantum level [7]. This is related to the non-trivial vacuum structure of non-Abelian gauge theories, like the SM. Neglecting fermion masses, there are an infinite number of degenerate ground states whose vacuum field configurations have different topological charges, or Chern–Simons numbers N_{CS} [8, 9]. In the electroweak sector of the SM, a change in the topological charge, i.e. a transition from one vacuum to another one, corresponds to a change in baryon and lepton numbers,

$$\Delta B = \Delta L = n_f \Delta N_{CS}, \tag{2}$$

where n_f is the number of generations of quarks and leptons, i.e. $n_f = 3$ in the SM. Note that, although both baryon and lepton number are violated, the linear combination $B - L$ is still conserved at the quantum level.

At low temperatures, when the electroweak symmetry is broken, the different vacua are separated by a potential barrier, whose height is determined by the vacuum expectation value (VEV) of the Higgs field, $v = \langle\phi\rangle$, i.e. the scale of electroweak symmetry breaking. Hence, processes changing the topological charge are tunnelling processes whose rate is unobservably small, due to the smallness of the electroweak coupling constant. In the low-temperature regime being probed in accelerator experiments, B and L are therefore conserved to a very good approximation, in accordance with experimental observations (cf [10]).

When the standard model particles form a heat bath of temperature T, the situation changes. At high temperatures, $T \geqslant T_{EW} \sim 100$ GeV, the Higgs VEV 'evaporates', leading to a restoration of the electroweak symmetry and the disappearance of the potential barriers separating the different vacua. B and L violating transitions are then no longer suppressed [11].

The rate at which these processes occur is related to the free energy of field configurations which carry topological charge. In the electroweak part of the SM these so-called sphaleron processes lead to an effective interaction of all left-handed fermions [7] (cf figure 1),

$$O_{B+L} = \prod_i (q_{Li} q_{Li} q_{Li} l_{Li}), \tag{3}$$

which indeed violates both baryon and lepton number by three units but conserves the combination $B - L$, in accordance with (2).

The sphaleron transition rate in the symmetric phase of the SM has been evaluated by combining an analytical resummation with numerical lattice techniques [12]. The result is that sphaleron processes are in thermal equilibrium for temperatures in the range

$$100\,\text{GeV} \lesssim T \lesssim 10^{12}\,\text{GeV}. \tag{4}$$

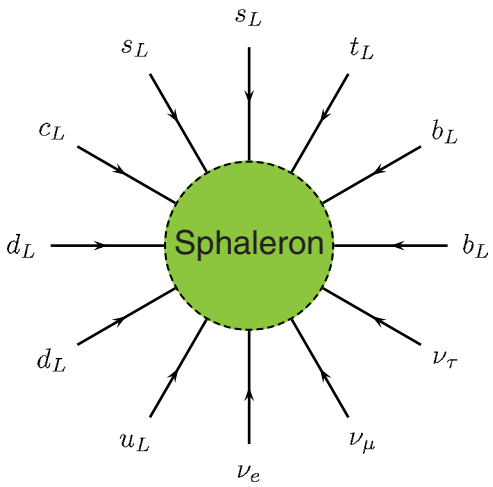

Figure 1. One of the 12-fermion processes which are in thermal equilibrium in the high-temperature phase of the standard model.

These processes have a profound effect on the generation of the cosmological baryon asymmetry. Equation (2) suggests that any $B+L$ asymmetry generated at temperatures $T > T_{EW}$ will be washed out. However, since only left-handed fields couple to sphalerons, a non-zero value of $B+L$ can persist in the high-temperature, symmetric phase if there exists a non-vanishing $B-L$ asymmetry. An analysis of the chemical potentials of all particle species in the high-temperature phase yields the following relation between the baryon asymmetry η_B and the corresponding L and $B-L$ asymmetries η_L and η_{B-L}, respectively [13],

$$\eta_B = a_{sph}\eta_{B-L} = \frac{a_{sph}}{a_{sph}-1}\eta_L. \tag{5}$$

Here a_{sph} is a number $\mathcal{O}(1)$. In the SM with three generations and one Higgs doublet one has $a_{sph} = 28/79$.

3. Leptogenesis

3.1. A qualitative overview

The deep connection between baryon and lepton number in the early universe has led to the realization that lepton number violating processes, whose presence is predicted by the see–saw model for light neutrino masses [4, 5], can be responsible for the observed cosmological baryon asymmetry.

In the see–saw model, the smallness of light neutrino masses is explained through the mixing of left-handed neutrinos with right-handed neutrinos ν_R which are not present in the SM but are predicted in certain models of grand unification. The interactions of the SM are supplemented by the following Yukawa couplings of neutrinos,

$$\mathcal{L}_Y = \overline{l_L} h \nu_R \phi + \overline{\nu_R^c} M \nu_R + \text{h.c.}, \tag{6}$$

where M is the Majorana mass matrix of the right-handed neutrinos, and the Yukawa couplings h yield the Dirac neutrino mass matrix $m_D = hv$ after spontaneous breaking of the electroweak

symmetry. Since the Majorana mass matrix M is independent of electroweak symmetry breaking, one can have $M \gg m_D$, which leads to the mass eigenstates

$$\nu \simeq \nu_L + \nu_L^c = \nu^c, \qquad N \simeq \nu_R + \nu_R^c = N^c, \tag{7}$$

with heavy neutrino masses M and the light neutrino masses

$$m_\nu = -m_D \frac{1}{M} m_D^{\mathrm{T}}. \tag{8}$$

The heavy neutrinos are unstable and decay through their Yukawa couplings into SM lepton and Higgs doublets. Due to their Majorana nature, the heavy neutrinos N can decay both into leptons and anti-leptons, i.e. lepton number is violated in these decays. In conjunction with $B + L$ violating sphaleron transitions, this leads to the required non-conservation of baryon number. Further, violation of C and CP comes about since the Yukawa couplings h are, in general, complex, thereby making possible the generation of a non-vanishing baryon asymmetry in these decays.

A further complication is that the heavy neutrinos also mediate lepton number violating scattering processes which can erase any lepton asymmetry [14, 15]. However, the interaction rates for these processes are suppressed by the large mass of the heavy neutrinos if the temperature T is smaller than their mass. Hence, the lepton asymmetries produced in decays of the heavier neutrinos $N_{2,3}$ will be erased by lepton number violating scatterings mediated by the lightest of the heavy neutrinos, N_1. Therefore, in the simplest case of hierarchical heavy neutrino masses, $M_1 \ll M_{2,3}$, only decays of N_1 can potentially explain the observed baryon asymmetry.

The required deviation from thermal equilibrium is provided by the expansion of the universe. When the universe has cooled down to a temperature of the order of the heavy neutrino mass M_1, the equilibrium number density becomes exponentially suppressed. If the neutrinos are sufficiently weakly coupled, they are not able to follow the rapid change of the equilibrium particle distribution once the temperature falls below their mass. Hence, the deviation from thermal equilibrium consists in a too large number density of heavy neutrinos compared to the equilibrium density [16]. Technically, this requires the total decay width of N_1 to be smaller than the expansion rate, the Hubble parameter H, at the time of decay, i.e. when $T \sim M_1$. This is the case if the *effective neutrino mass*, defined as

$$\tilde{m}_1 = \frac{(m_D^\dagger m_D)_{11}}{M_1}, \tag{9}$$

is smaller than the *equilibrium neutrino mass*

$$m_* = \frac{16\pi^{5/2}}{3\sqrt{5}} g_*^{1/2} \frac{v^2}{M_p} \simeq 10^{-3}\,\mathrm{eV}, \tag{10}$$

where we have used $M_p = 1.2 \times 10^{19}$ GeV and $g_* = 106.75$ as the effective number of relativistic degrees of freedom in the plasma. The effective neutrino mass $\tilde{m}_1$ is a measure of the strength of the coupling of N_1 to the thermal bath.

To see whether this mechanism of leptogenesis [6] can indeed explain the observed baryon asymmetry, a careful numerical study is needed. As we shall see, successful leptogenesis is possible for $\tilde{m}_1 < m_*$ as well as $\tilde{m}_1 > m_*$. A quantitative description of this non-equilibrium process is obtained by means of kinetic equations.

3.2. Boltzmann equations

The evolution of particle number densities in the early universe is influenced not only by interactions but also by the expansion of the universe. It is convenient to scale out the expansion by considering the particle number N_X in some co-moving volume element instead of the number density n_X. For definiteness, we choose the co-moving volume $R_*(t)^3$ which contains one photon at a time t_* before the onset of leptogenesis,

$$N_X(t) = n_X(t) R_*(t)^3. \tag{11}$$

The final baryon asymmetry is expressed in terms of the baryon-to-photon ratio η_B, to be compared with the observed value η_B^{CMB} (cf (1)). This is related to the $B-L$ asymmetry in a co-moving volume element by

$$\eta_B = \frac{a_{sph}}{f} N_{B-L}^f, \tag{12}$$

where $f = 2387/86$ is the dilution factor due to the production of photons from the onset of leptogenesis until recombination, assuming the standard isentropic expansion of the universe.

Further, it is convenient to replace time t by $z = M_1/T$, where M_1 is the mass of the decaying neutrino. This is possible, since in a radiation-dominated universe both variables are related by the expansion rate of the universe, the Hubble parameter H,

$$H = 2t = \sqrt{\frac{4\pi^3 g_*}{45}} \frac{M_1^2}{M_p} \frac{1}{z^2}. \tag{13}$$

In the simplest case of a hierarchical mass spectrum of right-handed neutrinos, $M_1 \ll M_{2,3}$, a numerical description of leptogenesis is provided by a set of two coupled differential equations [17, 18],

$$\frac{\mathrm{d}N_{N_1}}{\mathrm{d}z} = -(D+S)(N_{N_1} - N_{N_1}^{eq}), \tag{14}$$

$$\frac{\mathrm{d}N_{B-L}}{\mathrm{d}z} = -\varepsilon_1 D(N_{N_1} - N_{N_1}^{eq}) - W N_{B-L}, \tag{15}$$

where the terms on the right-hand side describe the effects of particle interactions. There are four classes of processes which contribute: decays, inverse decays, $\Delta L = 1$ scatterings and $\Delta L = 2$ processes mediated by heavy neutrinos. The term D accounts for decays and inverse decays, while the scattering term S represents the $\Delta L = 1$ scatterings. Decays also yield the source term for the generation of the $B-L$ asymmetry, the first term in (15), while all other processes contribute to the total washout term W which competes with the decay source term. Note that, in thermal equilibrium, $N_{N_1} = N_{N_1}^{eq}$, no $B-L$ asymmetry can be generated, illustrating the need for a deviation from thermal equilibrium. The amount of $B-L$ asymmetry being produced by the source term is controlled by the CP asymmetry ε_1 in the decay of N_1.

To understand the dependence of the solutions on the neutrino parameters, it is crucial to note that the interaction terms D and S as well as the contribution from N_1 exchange to W are all proportional to the effective neutrino mass,

$$D, S, W_1 \propto \frac{M_p \tilde{m}_1}{v^2}, \tag{16}$$

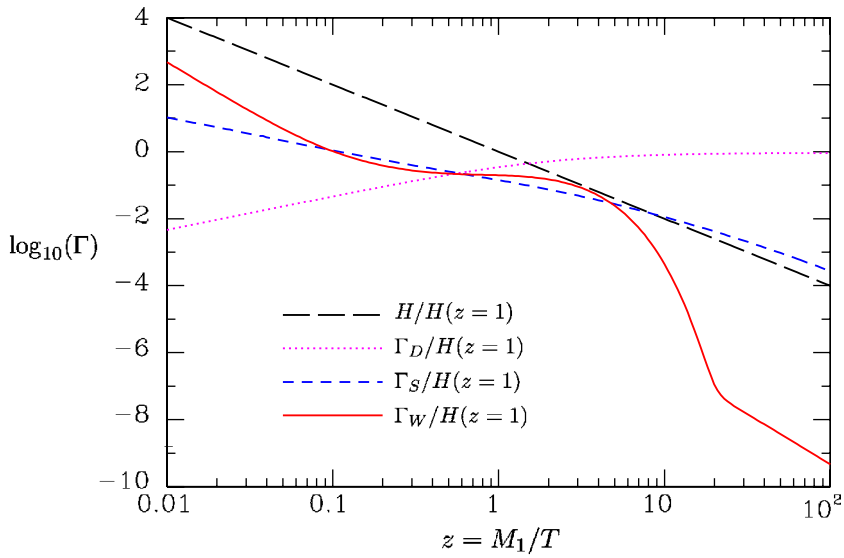

Figure 2. The expansion rate of the universe and the three interaction rates normalized to the expansion rate at $z = 1$ for a typical choice of parameters, $M_1 = 10^{10}$ GeV, $\tilde{m}_1 = 10^{-3}$ eV and $\bar{m} = 0.05$ eV.

whereas the strength of the remaining contribution to the washout term, ΔW, is determined by $\bar{m}^2 = m_1^2 + m_2^2 + m_3^2$, the sum over the squares of light neutrino masses,

$$\Delta W \propto \frac{M_p M_1 \bar{m}^2}{v^4}. \tag{17}$$

If one assumes a vanishing initial $B - L$ asymmetry before the onset of leptogenesis, i.e. at $z \ll 1$, the solution for N_{B-L} has the simple form

$$N_{B-L}(z) = -\tfrac{3}{4}\varepsilon_1 \kappa(z; \tilde{m}_1, M_1\bar{m}^2), \tag{18}$$

where we have introduced the *efficiency factor* κ [19] which does not depend on the *CP* asymmetry ε_1 and parametrizes the effect of scattering and decay processes. It is given by the following integral expression:

$$\kappa(z) = \frac{4}{3}\int_{z_i}^{z} \mathrm{d}z'\, D(N_{N_1} - N_{N_1}^{eq})\mathrm{e}^{-\int_{z'}^{z} \mathrm{d}z'' W(z'')}. \tag{19}$$

It is normalized in such a way that its final value $\kappa_f = \kappa(\infty)$ approaches unity in the limit of thermal initial abundance of heavy neutrinos, $N_{N_1}(z \ll 1) = N_{N_1}^{eq} = 3/4$ and no washout, $W = 0$.

As an example, the three interaction rates, $(\Gamma_D, \Gamma_S, \Gamma_W) = Hz(D, S, W)$, and the Hubble parameter are shown in figure 2 for a typical choice of parameters, $M_1 = 10^{10}$ GeV, $\tilde{m}_1 = 10^{-3}$ eV and $\bar{m} = 0.05$ eV. As can be seen from the figure, the out-of-equilibrium condition $\tilde{m}_1 \lesssim 10^{-3}$ eV is fulfilled at $z = 1$, i.e. all interaction rates are smaller than the Hubble parameter.

The corresponding evolution of the N_1 abundance and the $B - L$ asymmetry is shown in figure 3, starting at $z = 0.1$ with a vanishing initial N_1 abundance. Although the neutrino

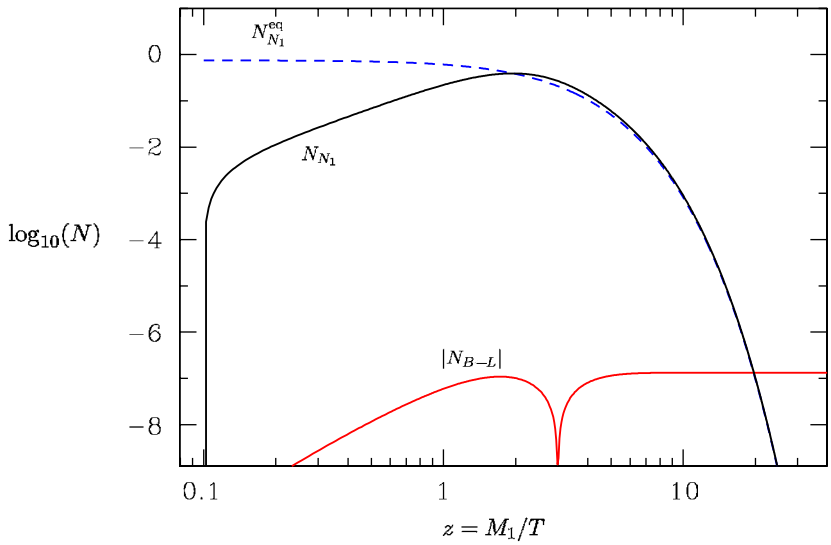

Figure 3. The evolution of the N_1 abundance and the $B - L$ asymmetry for the same choice of parameters as in figure 2 and $\varepsilon_1 = 10^{-6}$.

production rates Γ_D and Γ_S are not in thermal equilibrium, they are still strong enough to produce a non-vanishing abundance of neutrinos at $z \lesssim 1$ and the equilibrium distribution is reached at $z \sim 2$. The required deviation from thermal equilibrium can clearly be seen as a small over-abundance of neutrinos for $z \gtrsim 2$. However, the decay rate Γ_D also comes into thermal equilibrium at $z \sim 2$ leading to a rapid decay of the N_1 abundance and the production of a non-vanishing $B - L$ asymmetry. The change in sign of the asymmetry at $z \sim 3$ is due to the fact that the source term in (15) changes sign once the N_1 abundance becomes larger than the equilibrium abundance, i.e. neutrino production processes at $z \lesssim 2$ lead to a 'wrong sign' asymmetry that partially cancels against the asymmetry produced in the N_1 decays at $z \gtrsim 2$.

4. Constraints on neutrino masses

We are now ready to discuss the implications of thermal leptogenesis for light and heavy neutrino masses. Combining (12) and (18) one obtains

$$\eta_B = -d\varepsilon_1\kappa_f(\tilde{m}_1, M_1\bar{m}^2), \tag{20}$$

where $d = 3\,a_{sph}/(4f) \simeq 10^{-2}$. Hence, determining the amount of baryon asymmetry produced in leptogenesis requires the calculation of both the final efficiency factor κ_f and the *CP* asymmetry ε_1. A comparison with the observed value (cf (1)) then allows one to place stringent constraints on the involved see–saw parameters and, remarkably, on light and heavy neutrino masses.

4.1. Final efficiency factor

Starting from (19) and assuming a high initial temperature, $z_i = M_1/T_i \ll 1$, the final efficiency factor can be calculated analytically [16, 20]. For values $M_1\,\bar{m}^2 \ll 10^{14}$ GeV $[\bar{m}/(0.05\,\text{eV})]^2$ the

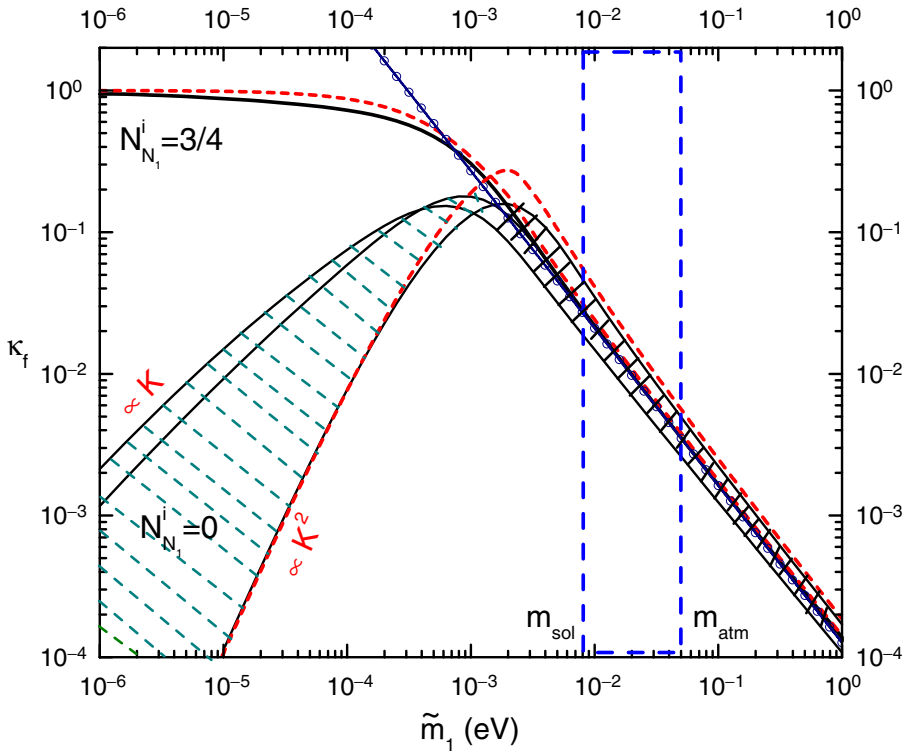

Figure 4. Final efficiency factor when the washout term ΔW is neglected.

washout term ΔW can be neglected and the final efficiency factor depends only on the effective neutrino mass $\tilde{m}_1$.

The results for the efficiency factor are summarized in figure 4. Two different regimes can clearly be distinguished. In the *weak washout regime*, $\tilde{m}_1 \ll 10^{-3}$ eV, the results strongly depend on the initial conditions and on theoretical assumptions, i.e. in that case predictions are strongly model dependent and affected by large theoretical uncertainties. On the other hand, in the *strong washout regime*, $\tilde{m}_1 \gg 10^{-3}$ eV, the dependence on the initial conditions is practically negligible and the theoretical uncertainties are small such that the final asymmetry can be predicted within ~50%.

In both cases, very precise analytical approximations for the final efficiency factor can be obtained. It is instructive to start with a simplified picture where the scattering term S is neglected and only decays and inverse decays contribute. The *decay parameter*,

$$K \equiv \frac{\Gamma_D(z=\infty)}{H(z=1)} = \frac{\tilde{m}_1}{m_*}, \tag{21}$$

controls whether N_1 decays are in thermal equilibirium or not. Here $\Gamma_D(z=\infty)$ is the N_1 decay width and m_* marks the boundary between the weak and strong washout regimes, as discussed in section 3.1.

In the *strong washout regime* inverse decays rapidly thermalize the heavy neutrinos N_1 and the washout due to decays and inverse decays is strong enough to destroy an initial asymmetry that may have been present before the onset of leptogenesis [21], leading to a negligible dependence on

initial conditions. Further, the integrand in (19) is peaked at a value $z_B \gg 1$, implying that the final asymmetry is produced around a well-defined *temperature of baryogenesis* $T_B = M_1/z_B \ll M_1$, where the heavy neutrinos are fully non-relativistic. This contributes to reducing the theoretical uncertainties in the strong washout regime, since it has been shown that the Boltzmann equations employed here can be derived from a fully consistent quantum mechanical treatment in terms of Kadanoff–Baym equations in the non-relativistic limit [22].

In the strong washout regime, the N_1 abundance closely tracks the equilibrium abundance and a simple expression for the final efficiency factor can be obtained,

$$\kappa_f(K) \simeq \frac{2}{Kz_B(K)}(1 - \mathrm{e}^{-(1/2)Kz_B(K)}). \tag{22}$$

Assuming thermal initial N_1 abundance, i.e. $N^i_{N_1} = 3/4$, this expression also reproduces the correct asymptotic limit in the weak washout regime, $K \ll 1$. In figure 4 this analytical result is represented by the short-dashed line which has to be compared to the numerical results, given by the solid lines.

In the weak washout regime, the calculation is more involved if one starts from a vanishing initial N_1 abundance. Indeed, in this case the N_1 production by inverse decays leads to a negative contribution to the efficiency factor, corresponding to a 'wrong-sign' asymmetry, as discussed in section 3.2. The final efficiency factor is thus the sum of a negative contribution, $\kappa_f^-(K)$, and a positive one, $\kappa_f^+(K)$. A very good approximation for these contributions that interpolates between the weak and strong washout regimes is given by

$$\kappa_f^-(K) = -2\mathrm{e}^{-(2/3)N(K)}(\mathrm{e}^{(2/3)\overline{N}(K)} - 1), \tag{23}$$

$$\kappa_f^+(K) = \frac{2}{z_B(K)K}(1 - \mathrm{e}^{-(2/3)z_B(K)K\overline{N}(K)}). \tag{24}$$

Here $N(K) \simeq (9\pi/16)K$ is the maximal N_1 number density being produced in the weak washout regime and $\overline{N}(K)$ interpolates between $N(K)$ and the maximal number density $N_{eq} = 3/4$ in the strong washout regime. For large K the negative contribution is suppressed, while the positive one asymptotically approaches (22). On the other hand, in the weak washout regime, the positive and negative contributions cancel each other to leading order in K, i.e. the total efficiency factor is of order K^2 [23], as shown in figure 4, where the short-dashed line again corresponds to the analytical solution and the solid one to the numerical integration of the Boltzmann equations.

This cancellation of the leading-order contributions to the final efficiency factor in the weak washout regime no longer occurs when the scattering term S is taken into account. Indeed, these scattering processes enhance the N_1 production thereby giving rise to an additional positive contribution to the efficiency factor. On the other hand, these scatterings are CP-conserving, i.e. they do not contribute to the negative part of the efficiency factor, as long as the contribution of $\Delta L = 1$ scatterings to the washout term is negligible which is always the case in the weak washout regime. In this way, scatterings can greatly enhance the final efficiency factor in the weak washout regime [24]. The drawback is that the result is very sensitive to different approximations being used in the computation of the scattering rates and different results, ranging from the case where scatterings are negligible to a behaviour $\kappa_f \propto K$, have been obtained. Potentially important effects that have recently been discussed but are presently controversial include scattering

processes involving gauge bosons [25, 26] and thermal corrections to the decay and scattering rates [26, 27]. The range of different results is represented in figure 4 by the hatched region. An additional uncertainty in the weak washout regime comes about due to the dependence of the final results on the initial N_1 abundance and a possible initial asymmetry created before the onset of leptogenesis.

The situation is very different in the strong washout regime. The final efficiency factor is not sensitive to the neutrino production since a thermal neutrino distribution is always reached at high temperatures, $z \ll 1$. However, $\Delta L = 1$ scatterings also contribute to the washout term but their effect is small and thus the theoretical uncertainty arising from these scattering processes is not larger than about 50%. This uncertainty for values $\tilde{m}_1 > m_* \simeq 10^{-3}$ eV is again indicated by the hatched region in figure 4. A much more important source of uncertainties are *spectator processes* [28], which can change the produced asymmetry by a factor of order one.

In the strong washout regime, the highest efficiency is reached when scatterings are neglected and only decays and inverse decays are taken into consideration, which approximately corresponds to the results obtained in [26]. In this parameter range, the final efficiency factor is given, within theoretical uncertainties, by the simple power-law [20]:

$$\kappa_f = (2 \pm 1) \times 10^{-2} \left(\frac{0.01\,\text{eV}}{\tilde{m}_1} \right)^{1.1 \pm 0.1}. \tag{25}$$

The only model-independent information we have on $\tilde{m}_1$ is that it has to be larger than the smallest neutrino mass m_1 [29]. However, a situation where $m_1 < \tilde{m}_1 \ll m_{sol}$ is rather artificial within neutrino mass models and the leptogenesis predictions are then very model dependent in the weak washout regime. In typical neutrino mass models, values of $\tilde{m}_1$ are usually in the mass range suggested by neutrino oscillations. It is remarkable that both the scale of solar neutrino oscillations, $m_{sol} \equiv \sqrt{\Delta m^2_{sol}} \simeq 8 \times 10^{-3}$ eV, and the scale of atmospheric neutrino oscillations, $m_{atm} \equiv \sqrt{\Delta m^2_{atm}} \simeq 0.05$ eV, are much larger than the equilibrium neutrino mass m_*. Hence, the parameter range suggested by neutrino oscillations, $m_{sol} \lesssim \tilde{m}_1 \lesssim m_{atm}$, lies entirely in the strong washout regime where theoretical uncertainties are small and the efficiency factor is still large enough to allow for successful leptogenesis.

4.2. CP asymmetry

The *CP* asymmetry ε_1 is the second crucial ingredient needed to calculate the baryon asymmetry. To leading order in the Yukawa coupling h, the *CP* asymmetry is determined by the interference between tree level and vertex plus self-energy one-loop diagrams [30, 31] and can be consistently extracted from the $l\phi \to l\phi$ scattering processes [32].

We will be interested in the maximal *CP* asymmetry for given neutrino masses. Assuming a hierarchy of the heavy neutrinos, $M_{2,3} \gg M_1$, $\varepsilon_1^{\max}$ depends on M_1, $\tilde{m}_1$, m_1 and m_3 [21]. It can be expressed as

$$\varepsilon_1^{\max}(M_1, \tilde{m}_1, m_1, m_3) = \varepsilon_1^{\max}(M_1)\beta(\tilde{m}_1, m_1, m_3), \quad \beta \leqslant 1. \tag{26}$$

The maximal asymmetry, i.e. $\beta = 1$, is reached for $m_1 = 0$ and, with $m_3 = \sqrt{m^2_{atm} + m_1^2}$, it is given by [33]

$$\varepsilon_1^{\max}(M_1) = \frac{3}{16\pi} \frac{M_1 m_{atm}}{v^2} \simeq 10^{-6} \left(\frac{M_1}{10^{10}\,\text{GeV}} \right) \left(\frac{m_{atm}}{0.05\,\text{eV}} \right). \tag{27}$$

An improved bound is obtained in the limit $m_1/\tilde{m}_1 \to 0$, where one obtains [34]

$$\beta(m_1) = \frac{m_3 - m_1}{m_{atm}}. \tag{28}$$

Also important is the case of quasi-degenerate neutrinos, $m_3 \simeq m_1$. In this region, one finds [35, 36]

$$\beta(\tilde{m}_1, m_1) \simeq \frac{m_3 - m_1}{m_{atm}} \sqrt{1 - \frac{m_1^2}{\tilde{m}_1^2}}. \tag{29}$$

For all neutrino mass models with moderately hierarchical heavy neutrinos, such that (26) applies, the observed baryon asymmetry yields constraints on the three neutrino parameters $\tilde{m}_1$, m_1 and M_1. In the following two sections we follow mostly the discussion in [20].

4.3. Lower bounds on heavy neutrino masses and reheating temperature

The *maximal baryon asymmetry* $\eta_B^{\max}(M_1, \tilde{m}_1, m_1)$ is the asymmetry corresponding to $\varepsilon_1^{\max}(M_1, \tilde{m}_1, m_1)$. The CMB bound then amounts to the requirement

$$\eta_B^{\max}(M_1, \tilde{m}_1, m_1) \geqslant \eta_B^{CMB}. \tag{30}$$

This represents an interesting constraint on the space of the three parameters M_1, m_1 and $\tilde{m}_1$. We have seen that the absolute maximum of the *CP* asymmetry is obtained for $m_1 = 0$. For $m_1 \neq 0$ the function β suppresses the *CP* asymmetry [34]. Furthermore, the $\Delta L = 2$ washout term becomes stronger when the absolute neutrino mass scale increases (cf (17)). Therefore, the maximal baryon asymmetry $\eta_B^{\max}(M_1, \tilde{m}_1, m_1)$ is maximized for $m_1 = 0$, and in this case the allowed region in the space of the parameters M_1 and $\tilde{m}_1$ is maximal [18].

In this way one finds an important lower bound on the value of M_1 [18, 34], by inserting the expression (27) into the CMB constraint (30) (cf (20)),

$$M_1 \geqslant M_1^{\min} = \frac{1}{d}\frac{16\pi}{3}\frac{v^2}{m_{atm}}\frac{\eta_B^{CMB}}{\kappa_f} \simeq 6.4 \times 10^8\,\text{GeV}\left(\frac{\eta_B^{CMB}}{6 \times 10^{-10}}\right)\left(\frac{0.05\,\text{eV}}{m_{atm}}\right)\kappa_f^{-1}. \tag{31}$$

For *thermal initial abundance*, and in the limit $\tilde{m}_1/m_* \to 0$, one has by definition $\kappa_f = 1$, and therefore

$$M_1 \geqslant (6.6 \pm 0.8) \times 10^8\,\text{GeV} \gtrsim 4 \times 10^8\,\text{GeV}. \tag{32}$$

Here the last inequality is the 3σ bound, with the experimental value of (1) for η_B^{CMB}, and $m_{atm} = (0.051 \pm 0.004)$ eV. In the case of a *dynamically generated* N_1 *abundance* the maximal efficiency factor is $\kappa_f \simeq 0.18$, which yields the more stringent bound

$$M_1 \geqslant (3.6 \pm 0.4) \times 10^9\,\text{GeV} \gtrsim 2 \times 10^9\,\text{GeV}. \tag{33}$$

The most interesting case corresponds to the range $m_{sol} \lesssim \tilde{m}_1 \lesssim m_{atm}$, for which the power law (25) for κ_f can be used. Using the central value of κ_f and neglecting the theoretical

uncertainty, one obtains

$$M_1 \gtrsim (3.3 \pm 0.4) \times 10^{10}\,\mathrm{GeV} \left(\frac{\tilde{m}_1}{10^{-2}\,\mathrm{eV}}\right)^{1.1}, \tag{34}$$

which yields the 3σ bound

$$M_1 \gtrsim (1.5\text{–}10) \times 10^{10}\,\mathrm{GeV}. \tag{35}$$

The lower bound on M_1 is particularly interesting since it can be translated into a lower bound on the initial temperature T_i which, within inflationary models, corresponds to the reheating temperature.

So far, we have assumed that the temperature T_i is larger than M_1. If one relaxes this assumption, the final efficiency factor is in general reduced. For small $\tilde{m}_1$, however, the threshold value for T_i, below which the reduction is appreciable, is given by M_1 itself. Below this temperature the N_1 abundance is either Boltzmann suppressed, for thermal initial abundance, or the N_1 production is considerably suppressed, for zero initial abundance. Therefore, for values $\tilde{m}_1 \lesssim 10^{-3}$ eV, the bounds (32) and (33) apply also to the reheating temperature T_i.

In the more interesting case of strong washout, about 90% of the final baryon asymmetry is produced in a temperature interval $z_B - 2 \lesssim z \lesssim z_B + 2$. Hence the reheating temperature can be about $(z_B - 2)$ times lower than M_1 without any appreciable change in the predicted final asymmetry [20]. In the interesting range $m_{sol} \lesssim \tilde{m}_1 \lesssim m_{atm}$ one has $z_B \simeq 6$–8, and therefore the bound (35) gets relaxed by a factor 4–6, such that

$$T_i \gtrsim (4 \times 10^9\text{–}2 \times 10^{10})\,\mathrm{GeV}. \tag{36}$$

Compared with the small $\tilde{m}_1$ range, $\tilde{m}_1 \lesssim 10^{-3}$ eV, the lower bound on the reheating temperature is slightly more restrictive in the favoured range $m_{sol} \lesssim \tilde{m}_1 \lesssim m_{atm}$ due to the loss in efficiency.

4.4. Upper bound on light neutrino masses

For large values of the absolute neutrino mass scale the ΔW washout term cannot be neglected. The final efficiency factor can be calculated using the approximation that ΔW starts to be effective for $z > z_B$, where the asymmetry generation from decays has already terminated. This works very well in the strong washout regime. Since $\tilde{m}_1 \geqslant m_1$, this does not introduce any restriction if $m_1 \gtrsim m_* \simeq 10^{-3}$ eV. One then has

$$\kappa_f(\tilde{m}_1, M_1\bar{m}^2) \simeq \kappa_f(\tilde{m}_1) \exp\left[-\frac{\omega}{z_B}\left(\frac{M_1}{10^{10}\,\mathrm{GeV}}\right)\left(\frac{\bar{m}}{\mathrm{eV}}\right)^2\right], \tag{37}$$

where $\omega \simeq 0.186$ and $\kappa_f(\tilde{m}_1)$ is the efficiency factor calculated in the regime of small neutrino masses, neglecting the ΔW term. Because of the assumption of strong washout, one can use the simple power law (25). At certain peak values of M_1 and $\tilde{m}_1$, the maximal baryon asymmetry $\eta_B^{\max}$ reaches the absolute maximum

$$\frac{\eta_B^{\mathrm{peak}}(\bar{m})}{\eta_B^{CMB}} \propto \frac{\chi m_* \xi}{\bar{m}^4}, \tag{38}$$

with $\chi \simeq 1.6\,\mathrm{eV}^3$ and $\xi \propto m_{atm}^2$. This finally yields the leptogenesis bound on the neutrino masses, $m_i \lesssim 0.1\,\mathrm{eV}$ [21]. Deviations of the quantity ξ from unity account for a change of the input parameters as well as various corrections, such as a possible enhancement of the *CP* asymmetry or supersymmetry.

A more precise calculation has to take into account the dependence of neutrino masses on the renormalization scale. The running of the atmospheric neutrino mass scale m_{atm} from the Fermi scale $\mu = m_Z$ to the high scale $\mu \sim T_B$ makes the bound less restrictive. On the other hand, the bound on m_i obtained at high energies has to be evolved down to low energies. This second effect is dominant and thus taking the scale dependence into account makes the neutrino mass bound more restrictive [37]. The smallest effect is obtained for a Higgs mass $M_h \simeq 150\,\mathrm{GeV}$, which leads to a ~20% more restrictive bound. Taking into account this effect, one then obtains the 3σ bound [20]

$$m_i \lesssim (0.12\,\mathrm{eV})\xi^{1/4}. \tag{39}$$

Note that the bound $m_i < 0.1\,\mathrm{eV}$ conservatively accounts for the theoretical uncertainties including spectator processes [28] which make the bound more restrictive by about 0.02 eV.[4] The strong suppression of the baryon asymmetry with increasing neutrino mass scale, $\eta_B \propto 1/\bar{m}^4$, which is reflected in the dependence $\xi^{1/4}$, makes the bound rather stable. This is different from the lower bounds on M_1 and T_i which relax as $1/\xi$ [21].

It is important to keep in mind that the neutrino mass bound can be evaded, with some effort. A measurement of the neutrino mass scale above the leptogenesis bound would require significant modifications of the minimal leptogenesis scenario that we described. The possibilities include quasi-degenerate heavy neutrinos [21, 35], non-thermal leptogenesis scenarios [38]–[40] or a non-minimal see–saw mechanism as in theories with Higgs triplets [41]–[43].

4.5. Leptogenesis conspiracy

The upper bound on the neutrino masses (39) arises when the information on m_{atm} from neutrino-mixing experiments is employed. The value of m_{atm} sets the scale for the transition from a hierarchical, with $m_1 \ll m_{atm}$, to a quasi-degenerate neutrino mass spectrum with $m_1 \gtrsim m_{atm}$. The joint action of the *CP* asymmetry suppression for $m_1 \gtrsim m_{atm}$ and $\tilde{m}_1 \approx m_1$ (cf (29)), together with the washout from the ΔW term, place a limit on the level of degeneracy of the light neutrino masses and, using the measured value of the atmospheric neutrino mass scale, an upper bound on the absolute neutrino mass scale.

We now want to study how this upper bound gets relaxed if the experimental measurement of the atmospheric neutrino mass scale is ignored. Since the maximal asymmetry is obtained for hierarchical neutrinos, i.e. $\beta = 1$, we have to use the simple bound (27). This also implies that the upper bound on the absolute neutrino mass scale will coincide with an upper bound on the atmospheric neutrino mass scale itself, since $\bar{m} \simeq m_{atm} \simeq m_3$. The maximal baryon asymmetry is then approximately given by

$$\eta_B^{\max}(M_1, \tilde{m}_1, m_3) = d\varepsilon_1^{\max}(M_1)\kappa_f(\tilde{m}_1, M_1 m_3^2). \tag{40}$$

[4] In [26] the upper bound 0.15 eV has been obtained, which is 0.03 eV weaker than the bound (39). About 0.02 eV of this difference is due to the different treatment of radiative corrections which depend on the top and Higgs masses. The remaining 0.01 eV reflects differences in the treatment of thermal corrections. This is included in the theoretical uncertainty of the efficiency factor $\kappa_f(\tilde{m}_1)$ (cf (25)).

Using (37), it is easy to see that the maximum of the asymmetry is realized for

$$M_1 \simeq 2 z_B 10^{13}\,\mathrm{GeV}\left(\frac{0.05\,\mathrm{eV}}{m_3}\right)^2, \tag{41}$$

and is then given by

$$\eta_B^{\max}(\tilde{m}_1, m_3) \simeq 0.7 \times 10^{-5} z_B(\tilde{m}_1)\kappa_f(\tilde{m}_1)\left(\frac{0.05\,\mathrm{eV}}{m_3}\right). \tag{42}$$

In the case of zero initial N_1 abundance, the maximum is obtained for $\tilde{m}_1 \simeq 2 \times 10^{-3}$ eV, where $k_f \simeq 0.2$ and $z_B \simeq 2$,[5] implying

$$\eta_B^{\mathrm{peak}}(m_3) \simeq 3 \times 10^{-6}\left(\frac{0.05\,\mathrm{eV}}{m_3}\right). \tag{43}$$

Note that the peak lies in the strong washout regime where results do not depend on the initial conditions.

For $m_3 \simeq m_{atm} \simeq 0.05$ eV, (43) is in good agreement with the numerical results of [18]. If we do not make use of the experimental information on m_{atm} and just require that the peak asymmetry is larger than the observed value given by (1), then we obtain the upper bound

$$m_3 \lesssim 250\,\mathrm{eV}. \tag{44}$$

Together with (41) this implies the lower bound for heavy neutrino masses,

$$M_1 \gtrsim 2 \times 10^6\,\mathrm{GeV}. \tag{45}$$

This exercise shows that without the experimental knowledge of m_{atm}, the bound on light neutrino masses would have been much looser. However, it also demonstrates, even more remarkably, that the neutrino oscillation data, together with the laboratory bounds on light neutrino masses, represents a highly non-trivial test of thermal leptogenesis.

As discussed in the previous section, the leptogenesis bound of 0.1 eV appears to have a theoretical uncertainty of about 0.03 eV. For comparison, 10 years ago it was believed, based on the same equations, that Majorana masses $m_3 \sim 10$ keV and $M_1 \sim 1$ TeV were compatible with thermal leptogenesis [17]. During the last few years, both theory and experiment contributed almost equally, on a logarithmic scale, to the progress. On the theoretical side, a better understanding of the Boltzmann equations was important whereas the measurement of the atmospheric neutrino mass scale was the crucial experimental ingredient.

Actually, the successful matching of thermal leptogenesis predictions with experimental data is even more intriguing. From (42) we can derive an upper bound on $\tilde{m}_1$ by using the strong washout behaviour $\kappa_f \simeq 2/(z_B K)$ (cf (22)) and imposing the CMB bound, which yields, with $m_{atm} = \sqrt{m_3^2 - m_1^2}$,

$$\tilde{m}_1 \lesssim 20\,\mathrm{eV}\left(\frac{0.05\,\mathrm{eV}}{m_{atm}}\right), \tag{46}$$

[5] This can be inferred from figures 4 and 5 of [20].

again in very good agreement with the numerical results [18]. From this expression one reads off that only for $m_{atm} \lesssim 1\,\text{eV}$ it is possible to have $\tilde{m}_1 \sim m_{atm}$. If the experiments had found $m_{atm} \gg 1\,\text{eV}$, thermal leptogenesis would have worked only for models with $\tilde{m}_1 \ll m_{atm}$, requiring a large amount of fine tuning, as already pointed out. Furthermore, the favoured strong washout regime implies $m_{atm} > m_*$. Hence, leptogenesis favours for the atmospheric mass scale the range 10^{-3}–1 eV, in remarkable agreement with experimental data. Thanks to this 'conspiracy', the see–saw mechanism, for the same values of the involved parameters, explains equally well both the neutrino masses and the observed baryon asymmetry, with a remarkable independence on the assumptions about the inflationary stage or, more generally, the cosmological stages that precede leptogenesis.

This conspiracy would become even more impressive if the lightest neutrino mass should turn out to be larger than m_*. This would imply, in a completely model independent way, $\tilde{m}_1 \gtrsim m_*$, with thermal leptogenesis in the strong washout regime. Together with the upper bound $m_1 < 0.1\,\text{eV}$, this selects the optimal *leptogenesis window* $10^{-3}\,\text{eV} \lesssim m_1 \lesssim 0.1\,\text{eV}$ for the absolute neutrino mass scale.

5. Flavour aspects

Leptogenesis is closely related to other processes involving neutrinos and charged leptons. The upper bound on the light neutrino masses and the lower bound on the heavy neutrino masses have already been discussed in the previous section. Very interesting are also the connection with neutrino mixing and with lepton flavour changing processes in supersymmetric theories. During the last few years, these subjects have been studied in great detail by many groups (cf [44]–[48]). In the following we shall discuss two important examples, the possible connection between *CP* violation in neutrino oscillations and leptogenesis, i.e. at low and high energies, and the relation between leptogenesis and the heavy neutrino mass spectrum.

In the standard model with right-handed neutrinos, the masses and mixings of leptons are described by three complex matrices,

$$\mathcal{L}_M = \overline{\nu_L} m_D \nu_R + \bar{e}_L m_l e_R + \overline{\nu_R^c} M \nu_R + \text{h.c.}. \tag{47}$$

For the Majorana mass matrix M, one expects $M \gg m_D$, which leads to three light and three heavy Majorana mass eigenstates, $\nu \simeq \nu_L + \nu_L^c = \nu^c$ and $N \simeq \nu_R + \nu_R^c = N^c$.

In the following, we will work in a basis where M is diagonal and real, with $M_1 < M_2 < M_3$, which is appropriate for leptogenesis. The light neutrino mass matrix m_ν and the charged lepton mass matrix m_l are then diagonalized by the unitary transformations,

$$V^{(\nu)\dagger} m_\nu V^{(\nu)*} = -\begin{pmatrix} m_1 & 0 & 0 \\ 0 & m_2 & 0 \\ 0 & 0 & m_3 \end{pmatrix} = m_\nu^{\text{diag}}, \tag{48}$$

$$V^{(e)\dagger} m_e \widetilde{V}^{(e)} = \begin{pmatrix} m_e & 0 & 0 \\ 0 & m_\mu & 0 \\ 0 & 0 & m_\tau \end{pmatrix} = m_l^{\text{diag}}. \tag{49}$$

The leptonic (MNS) mixing matrix

$$U = V^{(e)\dagger} V^{(\nu)} \tag{50}$$

describes the couplings of mass eigenstates in the charged current,

$$\mathcal{L}_{EW}^{(l)} = -\frac{g}{\sqrt{2}} \bar{e}_L \gamma^\mu U \nu_L W_\mu^- + \cdots, \tag{51}$$

which leads to neutrino oscillations.

It is well known that, in general, *CP* violation in neutrino oscillations and in leptogenesis are unrelated [49]. The reason is that the *CP* asymmetries ε_i in heavy neutrino decays depend only on $m_D^\dagger m_D$. Hence, changing m_D to $K m_D$, where K is a general unitary matrix, leaves ε_i invariant whereas the leptonic mixing matrix $U = V^{(e)\dagger} V^{(\nu)}$ is changed to $U = V^{(e)\dagger} K V^{(\nu)}$, and is therefore arbitrary. Still, the question remains whether in some physically well-motivated cases a connection between *CP* violation at low and high energies exists.

CP violating observables are most conveniently described by weak basis invariants which are inert under a unitary transformation, $l \to Kl$, of the lepton doublet $l = (\nu_L, e_L)$. For neutrino oscillations, the appropriate variable is the commutator between the hermitian matrices $H_\nu = m_\nu m_\nu^\dagger$ and $H_l = m_l m_l^\dagger$ [50, 51],

$$\mathrm{Tr}[H_\nu, H_l]^3 \propto \Delta_{\nu 21} \Delta_{\nu 32} \Delta_{\nu 31} \Delta_{l21} \Delta_{l32} \Delta_{l31} J_l, \tag{52}$$

$$\Delta_{\nu 21} = m_2^2 - m_1^2, \ldots, \qquad \Delta_{l21} = m_\mu^2 - m_e^2 \ldots, \tag{53}$$

where J_l is the leptonic Jarlskog invariant [52],

$$J_l = \mathrm{Im}[U_{11} U_{22} U_{12}^* U_{21}^*] \propto \sin\delta, \tag{54}$$

which is proportional to the *CP* violating phase δ of the mixing matrix U. In a basis where the charged lepton matrix m_l is diagonal and real, one has

$$\mathrm{Tr}[H_\nu, H_l]^3 \propto \Delta_{l21} \Delta_{l32} \Delta_{l31} \mathrm{Im}[H_{\nu 12} H_{\nu 23} H_{\nu 31}]; \tag{55}$$

correspondingly, for diagonal and real m_ν one has

$$\mathrm{Tr}[H_\nu, H_l]^3 \propto \Delta_{\nu 21} \Delta_{\nu 32} \Delta_{\nu 31} \mathrm{Im}[H_{l12} H_{l23} H_{l31}]. \tag{56}$$

The *CP* asymmetry in N_1 decays can be conveniently expressed in terms of the weak basis invariant [22]

$$\varepsilon_1 \propto \mathrm{Im}[m_D^\dagger m_\nu m_D^*]_{11}. \tag{57}$$

Comparing (56) and (57) the independence of *CP* violation at low and high energies is obvious. In a basis where m_ν is diagonal and real, *CP* violation in neutrino oscillations is entirely determined by the phases of m_l whereas the lepton asymmetry depends only on the phases of m_D.

An interesting example is the case of only two heavy Majorana neutrinos, N_1 and N_2, which corresponds to the limit where N_3 decouples [53]. For a given texture of m_D one then obtains (cf (55), (57)),

$$\varepsilon_1 \propto \mathrm{Im}[H_{\nu 12} H_{\nu 23} H_{\nu 31}] \propto \sin\delta. \tag{58}$$

Hence, *CP* violation at low and at high energies are both determined by the Dirac phase δ. A further low-energy quantity is the Majorana phase entering neutrinoless double beta decay. In some models with maximal atmospheric neutrino mixing this phase coincides with the leptogenesis phase [54]. All *CP* phases can also be related in models of spontaneous *CP* violation [50, 55].

Another important question is the connection between leptogenesis and the heavy neutrino mass spectrum. In the lepton mass eigenstate basis, the neutrino mass matrix can be reconstructed from data, i.e. the leptonic mixing matrix and the neutrino masses,

$$m_\nu = -U^{(\nu)} m_\nu^{\mathrm{diag}} U^{(\nu)\mathrm{T}}. \tag{59}$$

The heavy neutrino mass matrix is then determined by m_ν and m_D,

$$M^{-1} = -m_D^{-1} m_\nu (m_D^{\mathrm{T}})^{-1}. \tag{60}$$

Using the SO(10) mass relation $m_D = m_u$, where m_u denotes the up-type quark mass matrix, and assuming that in the lepton mass eigenstate basis m_u is also diagonal and real, $m_u = \mathrm{diag}(m_u, m_c, m_t)$, one obtains the heavy neutrino masses in terms of m_ν, m_u, m_c and m_t [56]. Neglecting the hierarchy among the small neutrino masses, one estimates that the hierarchy among the heavy neutrinos is very large,

$$\frac{M_1}{M_3} \sim \left(\frac{m_u}{m_t}\right)^2 \sim 10^{-10}. \tag{61}$$

With $M_3 \sim m_t^2/\sqrt{\Delta m_{atm}^2} \sim 10^{15}$ GeV, this implies $M_1 \sim 10^5$ GeV. A detailed study yields masses in the range $M_1 \sim 10^4$–10^6 GeV. As we saw in the previous section, such small masses are incompatible with conventional thermal leptogenesis. A possible way out are quasi-degenerate heavy neutrino masses [56]. Alternatively, the most naive SO(10) mass relations are not correct.

Parameters consistent with thermal leptogenesis have recently been obtained in a six-dimensional SO(10) GUT model, compactified on an orbifold [57]. Due to mixings with a heavy lepton doublet and a heavy right-handed down-type quark, one finds for the mass matrices in a particular flavour basis the relations,

$$M \propto m_u, \qquad m'_D \sim m'_d \sim m'_e. \tag{62}$$

Here M and m_u are diagonal 3×3 matrices, and m'_D, m'_d and m'_e are 4×4 matrices, due to the mixing with the heavy states. Integrating them out, the neutrino mass matrix can be expressed approximately in terms of the quark mass matrices,

$$m_\nu \propto m_d \frac{1}{m_u} m_d^{\mathrm{T}}. \tag{63}$$

For the light neutrino masses, this leads to the estimate

$$\frac{m_1}{m_3} \sim \left(\frac{m_d}{m_b}\right)^2 \frac{m_t}{m_u} \sim 0.1. \tag{64}$$

A detailed calculation [57] confirms this result. Furthermore, one finds the mixing angle $\Theta_{13} \sim (m_c m_b)/(m_t m_s) \sim 0.1$, and $\varepsilon \sim 10^{-6}$, $\tilde{m}_1 \sim 10^{-2}$ eV, $M_1 \sim (m_u/m_t)M_3 \sim 10^{10}$ GeV, consistent with thermal leptogenesis.

6. Cosmological aspects

It is well known that the temperature required by thermal leptogenesis, $T_B \gtrsim 10^9$ GeV, is potentially in conflict with the thermal production of gravitinos in the early universe [58, 59]. Late gravitino decays after nucleosynthesis significantly alter the successful BBN predictions.

The production of gravitinos is dominated by QCD processes, and the gravitino number density increases linearly with the reheating temperature after inflation,

$$\frac{n_{3/2}}{n_\gamma} \propto \frac{g_3^2}{M_p^2} T_R, \tag{65}$$

where g_3 is the QCD gauge coupling. Correspondingly, the BBN upper bound on the allowed gravitino energy density, $\rho_{3/2} = m_{3/2} n_{3/2}$, implies an upper bound on the reheating temperature. Detailed studies [60, 61] lead to the stringent bounds $T_R < 10^7$–10^9 GeV for gravitino masses in the range $m_{3/2} = 0.1$–1 TeV. Hence, unstable gravitinos are in conflict with thermal leptogenesis, unless the gravitino mass is very large, $m_{3/2} \gtrsim 50$ TeV.

Non-thermal leptogenesis models are still compatible with the above bounds on the reheating temperature. For instance, in some supersymmetric models the scalar partner $\widetilde{N}_1$ of the heavy neutrino N_1 might be the inflaton [62] and its decays could then generate the baryon asymmetry. In this case, the leptogenesis temperature can be below 10^7 GeV [26, 63], which would be consistent with the above gravitino bounds on T_R. However, a recent analysis of the BBN constraints[6] [64] with particular attention to the hadronic decay modes of the gravitino yields the much stronger bound $T_R \ll 10^6$ GeV for gravitino masses $m_{3/2} = 0.1$–1 TeV. Hence, unless the gravitino is extremely heavy, non-thermal leptogenesis also appears to be inconsistent with unstable gravitinos.

Already in connection with thermal leptogenesis, it has therefore been suggested that the gravitino may be the lightest superparticle (LSP) and stable [65]. In this case, gravitino production is enhanced [66],

$$\frac{n_{3/2}}{n_\gamma} \propto \frac{g_3^2}{M_p^2} \left(\frac{m_{\tilde{g}}}{m_{3/2}}\right)^2 T_R, \tag{66}$$

where $m_{\tilde{g}}$ is the gluino mass. Consistency with BBN and the observed amount of dark matter then yields an upper bound on the gravitino mass and a lower bound on the mass of the next-to-lightest superparticle (NSP). In [65], the case of a higgsino NSP was analysed, which is now disfavoured due to the improved BBN bounds on hadronic NSP decays [64]. Still viable is the case where

[6] Note that the analysis strongly depends on the assumed primordial ^{6}Li abundance.

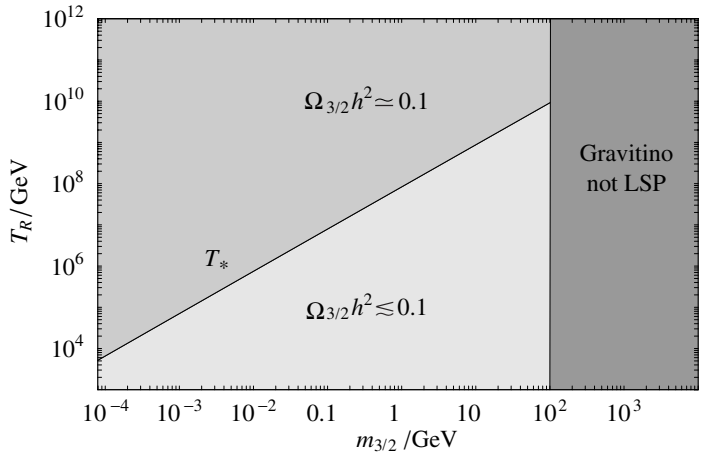

Figure 5. Relic gravitino density for different values of reheating temperature and gravitino mass. $\xi/\eta^2 = 1$. $m_{\tilde{g}} = 1$ TeV, which implies $m_{3/2} < 0.1$ TeV for a stable gravitino. For $T_R > T_*$, $\Omega_{3/2}h^2$ is independent of T_R and $m_{3/2}$.

a scalar lepton is the NSP [67]. For $T_B = 3 \times 10^9$ GeV the upper bound on the gluino mass is $m_{\tilde{g}} < 1.3$ TeV if a scalar tau is the NSP; for a scalar neutrino NSP one finds $m_{\tilde{g}} < 1.8$ TeV [67].

The relic density of gravitinos is determined by thermal production at the reheating temperature T_R after inflation and also by NSP decays after their freeze-out temperature. It is an interesting possibility that the latter process dominates. This would be the case for low reheating temperatures, incompatible with leptogenesis. One then obtains a prediction for the amount of gravitino dark matter which is independent of the reheating temperature [68]. If gravitinos are the only component of dark matter, the superparticles have to be rather heavy. For $\tilde{\tau}_R$ as NSP one finds $m_{3/2} = 0.2$–1TeV and $m_{\tilde{\tau}_R} \geqslant 0.5$ TeV [69].

Recently, it has been pointed out that the thermal production of gravitinos is significantly changed in theories where the gauge coupling depends on the expectation value of a scalar field ϕ [70]. For instance, in the case of gaugino mediation, one has

$$\frac{1}{g_0^2} + \frac{\phi_T}{M} = \frac{1}{g^2(\phi_T)}, \tag{67}$$

where g_0 is the zero-temperature gauge coupling, M is a mass scale between the unification scale and the Planck mass, and ϕ_T is the deviation of the field ϕ from its zero-temperature value at temperature T. At temperatures above a critical temperature,

$$T_* \sim m_{3/2}\left(\frac{M_p}{m_{\tilde{g}}}\right)^{1/2}, \tag{68}$$

the gauge coupling decreases, and the gravitino production is frozen. Remarkably, the relic gravitino density is essentially determined just by the gluino mass [70],

$$\Omega_{3/2}h^2 \simeq (0.05\text{–}0.2) \times \left(\frac{m_{\tilde{g}}}{1\,\text{TeV}}\right)^{3/2}\left(\frac{\xi}{\eta^2}\right)^{1/4}, \tag{69}$$

where the factor[7] ξ/η^2 depends on the mechanism of supersymmetry breaking. For gaugino and gravity mediation one has $\xi/\eta^2 = \mathcal{O}(1)$. The observed amount of dark matter is then obtained for

[7] Here the parameter $\xi^{1/2}$ denotes the ratio of the ϕ mass and the gravitino mass.

a gluino mass $m_{\tilde{g}} \sim 1$ TeV, which will be tested at the LHC. As figure 5 illustrates, the temperature where thermal leptogenesis takes place is probably larger than the critical temperature T_*. For a gluino mass $m_{\tilde{g}} \sim 1$ TeV one then obtains automatically the observed amount of cold dark matter.

Finally, thermal leptogenesis can also be consistent with gravitino dark matter if the gravitino is very light, $m_{3/2} \simeq 0.1$–10 MeV [71, 72], which is realized in gauge mediation models. Alternatively, the gravitino can also be very heavy, $m_{3/2} \sim 100$ TeV [73, 74], as in anomaly mediation.

In summary, leptogenesis strongly constrains the nature of dark matter. For very heavy unstable gravitinos, $m_{3/2} \sim 100$ TeV, where ordinary WIMPs can be the dark matter, the superparticle mass spectrum is strongly restricted. Alternatively, the gravitino has to be the LSP with a mass below $\sim$0.1 TeV; the observed value of $\Omega_{CDM}h^2$ can then be naturally explained. Hence, the identification of the invisible dark matter, which will hopefully take place at colliders in the coming years, will also shed light on baryogenesis and therefore on the origin of the visible matter.

Acknowledgments

We would like to thank K Hamaguchi and M Ratz for helpful discussions and comments.

References

[1] WMAP Collaboration, Spergel D N *et al* 2003 *Astrophys. J.* **148** (Suppl.) 175
[2] Tegmark M *et al* 2004 *Phys. Rev.* D **69** 103501
[3] Sakharov A D 1967 *JETP Lett.* **5** 24
[4] Yanagida T 1979 *Workshop on Unified Theories, KEK Report* 79-18, p 95
[5] Gell-Mann M, Ramond P and Slansky R 1979 *Supergravity* ed P van Nieuwenhuizen and D Freedman (Amsterdam: North Holland) p 315
[6] Fukugita M and Yanagida T 1986 *Phys. Lett.* B **174** 45
[7] 't Hooft G 1976 *Phys. Rev. Lett.* **37** 8
[8] Manton N S 1983 *Phys. Rev.* D **28** 2019
[9] Klinkhammer F R and Manton N S 1984 *Phys. Rev.* D **30** 2212
[10] Rubakov V A and Shaposhnikov M E 1996 *Phys.—Usp.* **39** 461
[11] Kuzmin V A, Rubakov V A and Shaposhnikov M E 1985 *Phys. Lett.* B **155** 36
[12] Bödeker D, Moore G D and Rummukainen K 2000 *Phys. Rev.* D **61** 056003
[13] Khlebnikov S Yu and Shaposhnikov M E 1988 *Nucl. Phys.* B **308** 885
[14] Harvey J A and Turner M S 1990 *Phys. Rev.* D **42** 3344
[15] Fukugita M and Yanagida T 1990 *Phys. Rev.* D **42** 1285
[16] Kolb E W and Turner M S 1990 *The Early Universe* (New York: Addison-Wesley)
[17] Luty M A 1992 *Phys. Rev.* D **45** 455
[18] Buchmüller W, Di Bari P and Plümacher M 2002 *Nucl. Phys.* B **643** 367
[19] Barbieri R, Creminelli P, Strumia A and Tetradis N 2000 *Nucl. Phys.* B **575** 61
[20] Buchmüller W, Di Bari P and Plümacher M 2004 *Preprint* hep-ph/0401240
[21] Buchmüller W, Di Bari P and Plümacher M 2003 *Nucl. Phys.* B **665** 445
[22] Buchmüller W and Fredenhagen S 2000 *Phys. Lett.* B **483** 217
[23] Fry J N and Turner M S 1981 *Phys. Rev.* D **24** 3341
[24] Plümacher M 1997 *Z. Phys.* C **74** 549
[25] Pilaftsis A and Underwood T E J 2003 *Preprint* hep-ph/0309342
[26] Giudice G F, Notari A, Raidal M, Riotto A and Strumia A 2004 *Nucl. Phys.* B **685** 89

[27] Covi L, Rius N, Roulet E and Vissani F 1998 *Phys. Rev.* D **57** 93
[28] Buchmüller W and Plümacher M 2001 *Phys. Lett.* B **511** 74
[29] Fujii M, Hamaguchi K and Yanagida T 2002 *Phys. Rev.* D **65** 115012
[30] Flanz M, Paschos E A and Sarkar U 1995 *Phys. Lett.* B **345** 248
Flanz M, Paschos E A and Sarkar U 1996 *Phys. Lett.* B **384** 487 (E)
[31] Covi L, Roulet E and Vissani F 1996 *Phys. Lett.* B **384** 169
[32] Buchmüller W and Plümacher M 1998 *Phys. Lett.* B **431** 354
[33] Hamaguchi K, Murayama H and Yanagida T 2002 *Phys. Rev.* D **65** 043512
[34] Davidson S and Ibarra A 2002 *Phys. Lett.* B **535** 25
[35] Hambye T, Lin Y, Notari A, Papucci M and Strumia A 2003 *Preprint* hep-ph/0312203
[36] Di Bari P 2003 *Proc. 2nd Int. Workshop on Neutrino Oscillations (Venice, 3–5 December 2003)* ed M Baldo Ceolin
[37] Antusch S, Kersten J, Lindner M and Ratz M 2003 *Nucl. Phys.* B **674** 401
[38] Lazarides G and Shafi Q 1991 *Phys. Lett.* B **258** 305
[39] Murayama H and Yanagida T 1994 *Phys. Lett.* B **322** 349
[40] Giudice G F, Peloso M, Riotto A and Tkachev I 1999 *J. High Energy Phys.* JHEP08 (1999) 014
[41] Hambye T and Senjanovic G 2004 *Nucl. Phys.* B **582** 73
[42] Rodejohann W 2004 *Preprint* hep-ph/0403236
[43] Antusch S and King S F 2004 *Preprint* hep-ph/0405093
[44] Masina I 2002 *Preprint* hep-ph/0210125
[45] Xing Z-Z 2003 *Preprint* hep-ph/0307359
[46] King S F 2003 *Preprint* hep-ph/0310204
[47] Altarelli G and Feruglio F 2004 *New J. Phys.* **6** 106
[48] Ellis J R 2004 *Preprint* hep-ph/0403247
[49] Buchmüller W and Plümacher M 1996 *Phys. Lett.* B **389** 73
[50] Branco G C, Morozumi T, Nobre B M and Rebelo M N 2001 *Nucl. Phys.* B **617** 475
[51] Branco G C 2003 *Preprint* hep-ph/0309215
[52] Jarlskog C 1985 *Phys. Rev. Lett.* **55** 1039
[53] Frampton P H, Glashow S L and Yanagida T 2002 *Phys. Lett.* B **548** 119
[54] Grimus W and Lavoura L 2003 *Preprint* hep-ph/0311362
[55] Achiman Y 2004 *Preprint* hep-ph/0403309
[56] Akhmedov E Kh, Frigerio M and Smirnov A Yu 2003 *J. High Energy Phys.* JHEP09 (2003) 021
[57] Asaka T, Buchmüller W and Covi L 2003 *Phys. Lett.* B **563** 209
[58] Khlopov M Yu and Linde A D 1984 *Phys. Lett.* B **138** 265
[59] Ellis J, Kim J E and Nanopoulos D V 1984 *Phys. Lett.* B **145** 181
[60] Kawasaki M, Kohri K and Moroi T 2001 *Phys. Rev.* D **63** 103502
[61] Cyburt R H, Ellis J, Fields B D and Olive K A 2003 *Phys. Rev.* D **67** 103521
[62] Murayama H, Suzuki H, Yanagida T and Yokoyama J 1993 *Phys. Rev. Lett.* **70** 1912
[63] Ellis J R, Raidal M and Yanagida T 2004 *Phys. Lett.* B **581** 9
[64] Kawasaki M, Kohri K and Moroi T 2004 *Preprint* astro-ph/0402490
[65] Bolz M, Buchmüller W and Plümacher M 1998 *Phys. Lett.* B **443** 209
[66] Moroi T, Murayama H and Yamaguchi M 1993 *Phys. Lett.* B **303** 289
[67] Fujii M, Ibe M and Yanagida T 2004 *Phys. Lett.* B **579** 6
[68] Feng J L, Rajaraman A and Takayama F 2003 *Phys. Rev. Lett.* **91** 011302-1
[69] Feng J L, Su S and Takayama F 2004 *Preprint* hep-ph/0404198
[70] Buchmüller W, Hamaguchi K and Ratz M 2003 *Phys. Lett.* B **574** 156
[71] Fujii M and Yanagida T 2002 *Phys. Lett.* B **549** 273
[72] Fujii M, Ibe M and Yanagida T 2004 *Phys. Rev.* D **69** 015006
[73] Luty M A and Sundrum R 2003 *Phys. Rev.* D **67** 045007
[74] Ibe M, Kitano R, Murayama H and Yanagida T 2004 *Preprint* hep-ph/0403198

New Journal of Physics
An Institute of Physics and Deutsche Physikalische Gesellschaft Journal

Models of neutrino masses and mixings

Guido Altarelli[1] **and Ferruccio Feruglio**[2]

[1] CERN, Department of Physics, Theory Division CH-1211 Genève 23, Switzerland

[2] Dipartimento di Fisica 'G Galilei', Università di Padova and INFN, Sezione di Padova, Via Marzolo 8, I-35131 Padua, Italy

E-mail: guido.altarelli@cern.ch and feruglio@pd.infn.it

New Journal of Physics **6** (2004) 106
Received 5 May 2004
Published 12 August 2004
Online at http://www.njp.org/
doi:10.1088/1367-2630/6/1/106

Abstract. We review theoretical ideas, problems and implications of neutrino masses and mixing angles. We give a general discussion of schemes with three light neutrinos. Several specific examples are analysed in some detail, particularly those that can be embedded into grand unified theories.

Contents

1. Introduction **2**
2. Basic formulae and data for three-neutrino mixing **3**
3. Neutrino masses and lepton number violation **5**
4. Importance of neutrinoless double beta decay **7**
5. Baryogenesis via leptogenesis from heavy ν^c decay **8**
6. Degenerate neutrinos **10**
6.1. Anarchy . . . 13
7. Inverted hierarchy **14**
8. Normal hierarchy **15**
8.1. Semi-anarchy . . . 19
9. Grand unified models of fermion masses **20**
9.1. Models based on horizontal abelian charges . . . 20
9.1.1. F(fermions) $\geqslant 0$ . . . 21
9.1.2. F(fermions) and F(flavons) of both signs . . . 22
9.2. GUT models based on SO(10) . . . 27
10. Conclusion **29**
Acknowledgments **30**
References **30**

PII: S1367-2630(04)80242-8
© IOP Publishing Ltd and Deutsche Physikalische Gesellschaft

1. Introduction

There is by now convincing evidence from the experimental study of atmospheric and solar neutrinos [1]–[3] (the results of the HOMESTAKE experiment are reported in [4]) for the existence of at least two distinct frequencies of neutrino oscillations. This in turn implies non-vanishing neutrino masses and a mixing matrix, in analogy with the quark sector and the CKM matrix. So *a priori* the study of masses and mixings in the lepton sector should be considered at least as important as that in the quark sector. However, actually there are a number of features that make neutrinos especially interesting. In fact, the smallness of neutrino masses is probably related to the fact that νs are completely neutral (i.e. they carry no charge which is exactly conserved) and are Majorana particles with masses inversely proportional to the large scale where lepton number (L) conservation is violated. Majorana masses can arise from the see-saw mechanism [5], in which case there is some relation with the Dirac masses, or from higher-dimensional non-renormalizable operators which come from a different sector of the Lagrangian density than any other fermion mass terms. The relation with L non-conservation and the fact that the observed neutrino oscillation frequencies are well compatible with a large scale for L non-conservation, points to a tantalizing connection with grand unified theories (GUTs). So neutrino masses and mixings can represent a probe into the physics at GUT energy scales and offer a different perspective on the problem of flavour and the origin of fermion masses. There are also direct connections with important issues in astrophysics and cosmology as, for example, baryogenesis through leptogenesis [6] and the possibly non-negligible contribution of neutrinos to hot dark matter in the Universe.

Recently, there have been new important experimental results that have considerably improved our knowledge. The SNO experiment has confirmed that the solar neutrino deficit is due to neutrino oscillations and not to a flaw in our modelling of the Sun [2]: the total neutrino flux is in agreement with the solar model but only about one-third arrives on Earth as ν_e while the remaining part consists of other kinds of active neutrinos, presumably ν_μ and ν_τ. The allowed amount of sterile neutrinos is strongly constrained. The KamLAND experiment has established that $\overline{\nu_e}$ from reactors show oscillations over an average distance of about 180 km which are perfectly compatible with the frequency and mixing angle corresponding to one of the solutions of the solar neutrino problem (the large angle (LA) solution) [7]. Thus, the results from solar neutrinos have been reproduced and improved by a terrestrial experiment. Also the coincidence of the frequency for neutrinos from the Sun and for antineutrinos from reactors is consistent with the validity of CPT invariance. The validity of this symmetry had been questioned because of the puzzling LSND claim of a signal that could indicate a third distinct oscillation frequency (hence implying either more than three light neutrinos or CPT violation). In September 2003 new results have been published by the SNO Collaboration [3], obtained after adding salt to their heavy-water detector in order to increase the sensitivity to the neutral current channels. The previous results have been confirmed with increased accuracy. The allowed region for the LA solution has been further restricted with the elimination of the upper region in Δm^2_{12}. Of great importance have also been the first results from WMAP [8] on the cosmic radiation background. The related determination of cosmological parameters, in combination with other measurements, leads to an upper limit on the cosmological neutrino density $\Omega_\nu \lesssim 0.015$. This is a very important result that indicates that neutrinos are not a major component of the dark matter in the Universe. For three degenerate neutrinos the WMAP limit implies an upper bound on the common mass given by $m_\nu < 0.23$ eV [8]. Given the priors that are assumed for this determination, i.e. a definite

cosmological model, a two-digit value for the bound is not to be taken too seriously [9]. Still the quoted value is about an order of magnitude smaller than the bound from tritium beta decay and of the same order of the upper bound on the Majorana mass that fixes the rate of neutrinoless double beta decay.

In spite of this progress there are many alternative models of neutrino masses [10]. This variety is mostly due to the considerable experimental ambiguities that still exist. One first missing input is the absolute scale of neutrino masses: neutrino oscillations only determine mass-squared differences. For atmospheric neutrinos $\Delta m^2_{atm} \sim 2.6 \times 10^{-3}\,\mathrm{eV}^2$, whereas for solar neutrinos $\Delta m^2_{sol} \sim 7 \times 10^{-5}\,\mathrm{eV}^2$. Another key missing quantity is the value of the third mixing angle s_{13} on which only a bound is known, $s_{13} < 0.22$. Then it is essential to know whether the LSND signal [11], which has not been confirmed by KARMEN [12] and is currently being double-checked by MiniBoone [13], will be confirmed or will be excluded. If LSND is right, we probably need at least four light neutrinos; if not we can do with only the three known ones.

Here we will briefly summarize the main categories of neutrino mass models, discuss their respective advantages and difficulties and give a number of examples. We illustrate how forthcoming experiments can discriminate among the various alternatives. We will devote special attention to a comprehensive discussion in a GUT framework of neutrino masses together with all other fermion masses. This is, for example, possible in models based on SU(5)$\times$ U(1)$_F$ or on SO(10) (we always consider SUSY GUTs) [14, 15].

2. Basic formulae and data for three-neutrino mixing

We assume in the following that the LSND signal [11] will not be confirmed so that there are only two distinct neutrino oscillation frequencies, the atmospheric and the solar frequencies. These two can be reproduced with the known three light neutrino species (see e.g. [16] for more than three neutrinos).

Neutrino oscillations are due to a misalignment between the flavour basis, $\nu' \equiv (\nu_e, \nu_\mu, \nu_\tau)$, where ν_e is the partner of the mass and flavour eigenstate e^- in a left-handed (LH) weak isospin SU(2) doublet (similarly for ν_μ and ν_τ) and the mass eigenstates $\nu \equiv (\nu_1, \nu_2, \nu_3)$ [17, 18]:

$$\nu' = U\nu, \tag{1}$$

where U is the unitary 3×3 mixing matrix. Given the definition of U and the transformation properties of the effective light neutrino mass matrix m_ν,

$$\nu'^{\mathrm{T}} m_\nu \nu' = \nu^{\mathrm{T}} U^{\mathrm{T}} m_\nu U \nu, \qquad U^{\mathrm{T}} m_\nu U = \mathrm{Diag}(m_1, m_2, m_3) \equiv m_{diag}, \tag{2}$$

we obtain the general form of m_ν (i.e. of the light ν mass matrix in the basis where the charged lepton mass is a diagonal matrix):

$$m_\nu = U^* m_{diag} U^\dagger. \tag{3}$$

The matrix U can be parametrized in terms of three mixing angles θ_{12}, θ_{23} and θ_{13} ($0 \leqslant \theta_{ij} \leqslant \pi/2$) and one phase φ ($0 \leqslant \varphi \leqslant 2\pi$) [19], exactly as for the quark mixing matrix V_{CKM}. The following definition of mixing angles can be adopted:

$$U = \begin{pmatrix} 1 & 0 & 0 \\ 0 & c_{23} & s_{23} \\ 0 & -s_{23} & c_{23} \end{pmatrix} \begin{pmatrix} c_{13} & 0 & s_{13}\mathrm{e}^{\mathrm{i}\varphi} \\ 0 & 1 & 0 \\ -s_{13}\mathrm{e}^{-\mathrm{i}\varphi} & 0 & c_{13} \end{pmatrix} \begin{pmatrix} c_{12} & s_{12} & 0 \\ -s_{12} & c_{12} & 0 \\ 0 & 0 & 1 \end{pmatrix}, \tag{4}$$

Table 1. Square mass differences and mixing angles.

	Lower limit (3σ)	Best value	Upper limit (3σ)
$(\Delta m^2_{sun})_{LA}$ (10^{-5} eV^2)	5.4	6.9	9.5
Δm^2_{atm} (10^{-3} eV^2)	1.4	2.6	3.7
$\sin^2\theta_{12}$	0.23	0.30	0.39
$\sin^2\theta_{23}$	0.31	0.52	0.72
$\sin^2\theta_{13}$	0	0.006	0.054

where $s_{ij} \equiv \sin\theta_{ij}$, $c_{ij} \equiv \cos\theta_{ij}$. In addition, if ν are Majorana particles, we have the relative phases among the Majorana masses m_1, m_2 and m_3. If we choose m_3 real and positive, these phases are carried by $m_{1,2} \equiv |m_{1,2}|e^{i\phi_{1,2}}$ [20].[3] Thus, in general, nine parameters are added to the SM when non-vanishing neutrino masses are included: three eigenvalues, three mixing angles and three CP violating phases.

In our notation the two frequencies, $\Delta m^2_I/4E$ ($I = sun, atm$), are parametrized in terms of the ν mass eigenvalues by

$$\Delta m^2_{sun} \equiv |\Delta m^2_{12}|, \qquad \Delta m^2_{atm} \equiv |\Delta m^2_{23}|, \tag{5}$$

where $\Delta m^2_{12} = |m_2|^2 - |m_1|^2 > 0$ and $\Delta m^2_{23} = m_3^2 - |m_2|^2$. The numbering 1, 2, 3 corresponds to our definition of the frequencies and, in principle, may not coincide with the ordering from the lightest to the heaviest state. From experiment, see table 1 [25], we know that s_{13} is small, according to CHOOZ, $s_{13} < 0.22$ (3σ) [22]. Atmospheric neutrino oscillations mainly depend on $(\Delta m^2_{atm}, \theta_{23}, \theta_{13})$, whereas solar oscillations are controlled by $(\Delta m^2_{sol}, \theta_{12}, \theta_{13})$. Therefore, in the ideal limit of exactly vanishing s_{13}, the solar and atmospheric oscillations decouple and depend on two separate sets of two-flavour parameters. For atmospheric neutrinos we have $c_{23} \sim s_{23} \sim 1/\sqrt{2}$, corresponding to nearly maximal mixing. Oscillations of muon neutrinos into tau neutrinos are favoured over oscillations into sterile neutrinos (ν_s). The conversion probability and the zenith angular distribution of high-energy muon neutrinos are sensitive to matter effects, which distinguish ν_τ from ν_s. Moreover, for conversion of ν_μ into pure ν_s, neutral current events would become up/down asymmetric. In both cases data strongly disfavour the pure sterile case. Oscillations into ν_τ are also indirectly supported by a SK data sample that can be interpreted in terms of enriched τ-like charged-current events. The sterile component of the neutrino participating in atmospheric oscillations should amount to less than 0.25 at 90% CL. Disappearance of laboratory-produced muon neutrinos has also been confirmed within expectations by the K2K experiment.

The only surviving solution to the solar neutrino problem after KamLAND and SNO-salt results is LA [23]–[25], with $\Delta m^2_{sol} \approx 7 \times 10^{-5}$ eV^2 and $\sin^2\theta_{12} \approx 0.3$. Before KamLAND the interpretation of solar neutrino data in terms of oscillations required the knowledge of the Boron neutrino flux, f_B. For instance, charged and neutral current data from SNO are sensitive, respectively, to $f_B\langle P_{ee}\rangle$ and to $f_B\langle\sum_a P_{ea}\rangle$ ($a = e, \nu, \tau$), where $\langle P_{ef}\rangle$ denotes the appropriately averaged conversion probability from ν_e to ν_f. KamLAND [7] provides a direct measurement of $\langle P_{ee}\rangle$. Beyond the impact on the oscillation parameters and a check that the solar standard

[3] Mass matrices with a general dependence on ϕ, $\phi_{1,2}$ have been analysed in [21].

model works well ($f_B = (1.00 \pm 0.06) \times 5.05 \times 10^6\,\mathrm{cm}^{-2}\,\mathrm{s}^{-1}$), the comparison among these experiments shows that the conversion of boron solar neutrinos into sterile neutrinos is compatible with zero. Therefore, the LSND indication for a third oscillation frequency associated with one or more sterile neutrinos is not supported by any other experiment, at the moment. Now, after KamLAND, also the possibility that such a frequency originates from a CPT violating neutrino spectrum [26] has no independent support. Data from solar neutrino experiments and KamLAND, involving, respectively, electron neutrinos and electron antineutrinos, are compatible with a CPT invariant spectrum.

If we take maximal s_{23} and keep only linear terms in $u = s_{13}\mathrm{e}^{\mathrm{i}\varphi}$, from experiment we find the following structure of the U_{fi} ($f = e,\mu,\tau$, $i = 1, 2, 3$) mixing matrix, apart from sign convention redefinitions:

$$U_{fi} = \begin{pmatrix} c_{12} & s_{12} & u \\ -(s_{12} + c_{12}u^*)/\sqrt{2} & (c_{12} - s_{12}u^*)/\sqrt{2} & 1/\sqrt{2} \\ (s_{12} - c_{12}u^*)/\sqrt{2} & -(c_{12} + s_{12}u^*)/\sqrt{2} & 1/\sqrt{2} \end{pmatrix}, \tag{6}$$

where θ_{12} is close to $\pi/6$ (for $s_{12} = 1/\sqrt{3}$ and $u = 0$ we have the so-called tri-bimaximal mixing pattern (for models based on discrete symmetries see also [27]), with the entries in the second column all equal to $1/\sqrt{3}$ in absolute value). Given the observed frequencies and our notation in equation (5), there are three possible patterns of mass eigenvalues:

$$\begin{aligned} &\text{Degenerate:} && |m_1| \sim |m_2| \sim |m_3| \gg |m_i - m_j|, \\ &\text{Inverted hierarchy:} && |m_1| \sim |m_2| \gg |m_3|, \\ &\text{Normal hierarchy:} && |m_3| \gg |m_{2,1}|. \end{aligned} \tag{7}$$

Models based on all these patterns have been proposed and studied and all are in fact viable at present. In the following we will first discuss neutrino masses in general and, in particular, Majorana neutrinos. Then we recall the existing constraints on the absolute scale of neutrino masses. We then discuss the importance of neutrinoless double beta decay that, if observed, would confirm the Majorana nature of neutrinos. Also the knowledge of the rate of this process could discriminate among the possible patterns of neutrino masses in (7). The possible importance of heavy Majorana neutrinos for the explanation of baryogenesis through leptogenesis in the early Universe will be briefly discussed. We finally review the phenomenology of neutrino mass models based on the three spectral patterns in (7) and the respective advantages and problems.

3. Neutrino masses and lepton number violation

Neutrino oscillations imply neutrino masses which in turn demand either the existence of right-handed (RH) neutrinos (Dirac masses) or lepton number L violation (Majorana masses) or both. Given that neutrino masses are certainly extremely small, it is really difficult from the theory point of view to avoid the conclusion that L conservation must be violated. In fact, in terms of lepton number violation the smallness of neutrino masses can be explained as inversely proportional to the very large scale where L is violated, of order M_{GUT} or even M_{Pl}.

Once we accept L non-conservation, we gain an elegant explanation for the smallness of neutrino masses. If L is not conserved, even in the absence of heavy RH neutrinos, Majorana masses for neutrinos can be generated by dimension-five operators [28] of the form

$$O_5 = \frac{(Hl)_i^{\mathrm{T}} \lambda_{ij} (Hl)_j}{\Lambda} + \mathrm{h.c.}, \tag{8}$$

with H being the ordinary Higgs doublet, l_i the SU(2) lepton doublets, λ a matrix in flavour space, Λ a large scale of mass of order M_{GUT} or M_{Pl} and a charge conjugation matrix C between the lepton fields is understood. Neutrino masses generated by O_5 are of the order $m_\nu \approx v^2/\Lambda$ for $\lambda_{ij} \approx \mathrm{O}(1)$, where $v \sim \mathrm{O}(100\,\mathrm{GeV})$ is the vacuum expectation value of the ordinary Higgs.

We consider that the existence of RH neutrinos ν^c is quite plausible because all GUT groups larger than SU(5) require them. In particular, the fact that ν^c completes the representation 16 of SO(10): $16 = \bar{5} + 10 + 1$, so that all fermions of each family are contained in a single representation of the unifying group is too impressive not to be significant. At least as a classification group SO(10) must be of some relevance. Thus, in the following, we assume that there are both ν^c and L non-conservation. With these assumptions the see-saw mechanism [5] is possible. Also to fix notations we recall that in its simplest form it arises as follows. Consider the SU(3) $\times$ SU(2) $\times$ U(1) invariant Lagrangian giving rise to Dirac and ν^c Majorana masses (for the time being we consider the ν (versus ν^c) Majorana mass terms as comparatively negligible):

$$\mathcal{L} = -\nu^{c\mathrm{T}} y_\nu (Hl) + \tfrac{1}{2} \nu^{c\mathrm{T}} M \nu^c + \mathrm{h.c.} \tag{9}$$

The Dirac mass matrix $m_D \equiv y_\nu v/\sqrt{2}$, originating from electroweak symmetry breaking, is, in general, non-hermitian and non-symmetric, whereas the Majorana mass matrix M is symmetric, $M = M^{\mathrm{T}}$. We expect the eigenvalues of M to be of order M_{GUT} or more because ν^c Majorana masses are SU(3) $\times$ SU(2) $\times$ U(1) invariant, hence unprotected and naturally of the order of the cutoff of the low-energy theory. Since all ν^c are very heavy we can integrate them away. For this purpose we write down the equations of motion for ν^c in the static limit, i.e. neglecting their kinetic terms,

$$-\frac{\partial \mathcal{L}}{\partial \nu^c} = y_\nu (Hl) - M\nu^c = 0. \tag{10}$$

From this, by solving for ν^c, we obtain

$$\nu^c = M^{-1} y_\nu (Hl). \tag{11}$$

We now replace in the Lagrangian, equation (9), this expression for ν^c and we get the operator O_5 of equation (8) with

$$\frac{2\lambda}{\Lambda} = -y_\nu^{\mathrm{T}} M^{-1} y_\nu, \tag{12}$$

and the resulting neutrino mass matrix reads

$$m_\nu = m_D^{\mathrm{T}} M^{-1} m_D. \tag{13}$$

This is the well-known see-saw mechanism result [5]: the light neutrino masses are quadratic in the Dirac masses and inversely proportional to the large Majorana mass. If some ν^c are massless

or light they would not be integrated away but simply added to the light neutrinos. Notice that the above results hold true for any number n of heavy neutral fermions R coupled to the three known neutrinos. In this more general case, M is an $n \times n$ symmetric matrix and the coupling between heavy and light fields is described by the rectangular $n \times 3$ matrix m_D. Note that for $m_\nu \approx \sqrt{\Delta m^2_{atm}} \approx 0.05\,\text{eV}$ and $m_\nu \approx m_D^2/M$ with $m_D \approx v \approx 200\,\text{GeV}$ we find $M \approx 10^{15}\,\text{GeV}$ which indeed is an impressive indication for M_{GUT}.

If additional non-renormalizable contributions to O_5, equation (8), are comparatively non-negligible, they should simply be added. For instance, in SO(10) or in left–right extensions of the SM, an $\text{SU}(2)_L$ triplet can couple to lepton doublets and may induce a sizeable contribution to neutrino masses. At the level of the low-energy effective theory, such contribution is still described by the operator O_5 of equation (8), obtained by integrating out the heavy $\text{SU}(2)_L$ triplet (which also acquires a VEV due to its coupling to the Higgs doublets). This contribution is called type II to be distinguished from that obtained by the exchange of RH neutrinos (type I). After elimination of the heavy fields, at the level of the effective low-energy theory, the two types of terms are equivalent. In particular, they have identical transformation properties under a chiral change of basis in flavour space. The difference is, however, that in the see-saw mechanism, the Dirac matrix m_D is presumably related to ordinary fermion masses because they are both generated by the Higgs mechanism and both must obey GUT-induced constraints. Thus, if we assume the see-saw mechanism in its simplest type I version, more constraints are implied.

4. Importance of neutrinoless double beta decay

Oscillation experiments do not provide information about the absolute neutrino spectrum and cannot distinguish between pure Dirac and Majorana neutrinos. From the endpoint of tritium beta decay spectrum we have an absolute upper limit of 2.2 eV (at 95% CL) on the mass of electron antineutrino [29], which, combined with the observed oscillation frequencies under the assumption of three CPT-invariant light neutrinos, represents also an upper bound on the masses of the other active neutrinos. Complementary information on the sum of neutrino masses is also provided by the galaxy power spectrum combined with measurements of the cosmic microwave background anisotropies. According to the recent analysis of the WMAP collaboration [8], $\sum_i |m_i| < 0.69\,\text{eV}$ (at 95% CL). More conservative analyses [9] give $\sum_i |m_i| < 1.01\,\text{eV}$, still much more restrictive than the laboratory bound.

The discovery of $0\nu\beta\beta$ decay would be very important because it would establish lepton number violation and the Majorana nature of νs, and provide direct information on the absolute scale of neutrino masses. As already mentioned, the present limit from $0\nu\beta\beta$ is $|m_{ee}| < 0.2\,\text{eV}$ or to be more conservative $|m_{ee}| < 0.3$–$0.5\,\text{eV}$ [30, 31]. Note, however, that the WMAP limit implies for three degenerate νs $|m| < 0.23\,\text{eV}$ and, taken at face value, this limit would pose a direct constraint on m_{ee}.

It is interesting to see what is the level at which a signal can be expected or at least not excluded in the different classes of models in (7) [32, 33]. The quantity which is bound by experiments is the 11 entry of the ν mass matrix, which in general, from equations (2) and (4), is given by

$$|m_{ee}| = |(1 - s_{13}^2)(m_1 c_{12}^2 + m_2 s_{12}^2) + m_3 e^{2i\phi} s_{13}^2|. \tag{14}$$

For three-neutrino models with degenerate, inverse hierarchy or normal hierarchy mass patterns, starting from this general formula it is simple to derive the following bounds.

(a) *Degenerate case.* If $|m|$ is the common mass and we take $s_{13} = 0$, which is a safe approximation in this case, because $|m_3|$ cannot compensate for the smallness of s_{13}, we have $m_{ee} \sim |m|(c_{12}^2 \pm s_{12}^2)$. Here the phase ambiguity has been reduced to a sign ambiguity which is sufficient for deriving bounds. So, depending on the sign we have $m_{ee} = |m|$ or $m_{ee} = |m| \cos 2\theta_{12}$. We conclude that in this case m_{ee} could be as large as the present experimental limit but should be at least of order $\mathrm{O}(\sqrt{\Delta m_{atm}^2}) \sim \mathrm{O}(10^{-2}\,\mathrm{eV})$ unless the solar angle is practically maximal, in which case the minus sign option can be arbitrarily small. However, the experimental 2σ range of the solar angle does not favour a cancellation by more than a factor of 3.

(b) *Inverse hierarchy case.* In this case, the same approximate formula $m_{ee} = |m|(c_{12}^2 \pm s_{12}^2)$ holds because m_3 is small and s_{13} can be neglected. The difference is that here we know that $|m| \approx \sqrt{\Delta m_{atm}^2}$ so that $|m_{ee}| < \sqrt{\Delta m_{atm}^2} \sim 0.05\,\mathrm{eV}$. At the same time, since a full cancellation between the two contributions cannot take place, we expect $|m_{ee}| > 0.01\,\mathrm{eV}$.

(c) *Normal hierarchy case.* Here we cannot in general neglect the m_3 term. However, in this case, $|m_{ee}| \sim |\sqrt{\Delta m_{sun}^2} s_{12}^2 \pm \sqrt{\Delta m_{atm}^2} s_{13}^2|$ and we have the bound $|m_{ee}| <$ a few 10^{-3} eV.

Recently, evidence for $0\nu\beta\beta$ was claimed in [34] at the 4.2σ level corresponding to $|m_{ee}| \sim 0.2$–$0.6\,\mathrm{eV}$ (0.1–0.9 eV in a more conservative estimate of the involved nuclear matrix elements). If confirmed this would rule out cases (b) and (c) and point to case (a) or to models with more than three neutrinos. We recall that further contributions to $0\nu\beta\beta$ transition amplitudes might occur in models with additional L violating interactions, such as R-parity breaking supersymmetry.

5. Baryogenesis via leptogenesis from heavy ν^c decay

In the Universe, we observe an apparent excess of baryons over antibaryons. It is appealing that one can explain the observed baryon asymmetry by dynamical evolution (baryogenesis) starting from an initial state of the Universe with zero baryon number. For baryogenesis, one needs the three famous Sakharov conditions: B violation, CP violation and no thermal equilibrium. In the history of the Universe, these necessary requirements could have occurred at different epochs. Note however that the asymmetry generated by one epoch could be erased at following epochs if not protected by some dynamical reason. In principle, these conditions could be verified in the SM at the electroweak phase transition. B is violated by instantons when kT is of the order of the weak scale (but $\mathrm{B} - \mathrm{L}$ is conserved), CP is violated by the CKM phase and sufficiently marked out-of-equilibrium conditions could be realized during the electroweak phase transition. So the conditions for baryogenesis at the weak scale in the SM superficially appear to be present. However, a more quantitative analysis [35] shows that baryogenesis is not possible in the SM because there is not enough CP violation and the phase transition is not sufficiently strong first-order, unless $m_H < 80\,\mathrm{GeV}$, which is by now completely excluded by LEP. In SUSY extensions of the SM, in particular in the MSSM, there are additional sources of CP violation and the bound on m_H is modified by a sufficient amount by the presence of scalars with large couplings to the Higgs sector, typically the s-top. What is required is that $m_h \sim 80$–$110\,\mathrm{GeV}$, a s-top not heavier

than the top quark and, preferentially, a small $\tan\beta$. However, also this possibility has by now become at best marginal with the results from LEP2.

If baryogenesis at the weak scale is excluded by the data it can occur at or just below the GUT scale, after inflation. However, only that part with $|\mathrm{B}-\mathrm{L}|>0$ would survive and not be erased at the weak scale by instanton effects. Thus baryogenesis at $kT\sim 10^{10}$–10^{15} GeV needs $\mathrm{B}-\mathrm{L}$ violation at some stage like for m_ν if neutrinos are Majorana particles. The two effects could be related if baryogenesis arises from leptogenesis then converted into baryogenesis by instantons [6]. Recent results on neutrino masses are compatible with this elegant possibility [36]. Thus the case of baryogenesis through leptogenesis has been boosted by the recent results on neutrinos [37].

In leptogenesis the baryon asymmetry is produced by the out of equilibrium, CP and L-violating decays of heavy right-handed neutrinos ν^c. In the simplest cases the spectrum of RH neutrinos is assumed to be hierarchical, $M_1 \ll M_{2,3}$ and the mechanism is dominated by the lightest state, ν_1^c. Thus, the expected baryon asymmetry is proportional to the product $\epsilon_1\delta$ between the CP decay asymmetry

$$\epsilon_1 = \frac{\Gamma(\nu_1^c \to l) - \Gamma(\nu_1^c \to \bar{l})}{\Gamma(\nu_1^c \to l) + \Gamma(\nu_1^c \to \bar{l})}, \tag{15}$$

and the efficiency factor $\delta \leqslant 1$, the fraction of the produced asymmetry that survives after ν_1^c decay. To keep δ close to 1 and avoid washing out the developed lepton asymmetry, L-violating interactions should be sufficiently weak to stay out of equilibrium when ν_1^c decays. This in turn happens when the lifetime of ν_1^c exceeds the age of the Universe, which is expressed by the condition [38]

$$\tilde{m}_1 \equiv \frac{(m_D m_D^\dagger)_{11}}{M_1} \leqslant 10^{-3}\,\mathrm{eV}, \tag{16}$$

with $\min\{|m1|, |m2|, |m3|\} \leqslant \tilde{m}_1$. This condition does not provide yet an absolute bound on neutrino masses since, in realistic simulations, the observed baryon asymmetry is achieved for $\delta < 1$. For hierarchical RH neutrino masses the asymmetry ϵ_1 is given by

$$\epsilon_1 \approx -\frac{3\sigma}{8\pi}\frac{1}{(y_\nu y_\nu^\dagger)_{11}}\sum_{j=2,3}\mathrm{Im}[(y_\nu y_\nu^\dagger)^2_{1j}]\frac{M_1}{M_j} \tag{17}$$

($\sigma = 1$ in the supersymmetric case and 1/2 in the non-supersymmetric one) which gives rise to the Davidson–Ibarra (DI) bound [39]:

$$|\epsilon_1| \leqslant \frac{3\sigma}{8\pi}\frac{M_1}{\langle H^0\rangle^2}(\max\{|m1|, |m2|, |m3|\} - \min\{|m1|, |m2|, |m3|\}), \tag{18}$$

where $\langle H^0\rangle$ denotes the VEV of the Higgs doublet giving mass to the up-quarks. Several interesting constraints on the neutrino spectrum emerge from the above discussion. First of all, in the assumed limit $M_{2,3} \gg M_1$, the CP asymmetry vanishes for a completely degenerate light neutrino spectrum (of course, this limit is rather unnatural in the see-saw context). Moreover, depending on the details of the assumed cosmological scenario which fixes the initial abundance of RH neutrinos, the DI bound translates into a lower bound on the lightest RH neutrino mass M_1,

ranging from approximately 10^7 to 10^9 GeV [39, 40]. Finally, an absolute upper bound on light neutrino masses can be derived. Indeed, if we enhance the absolute scale of light neutrino masses, on the one hand we depart from the out-of-equilibrium condition of equation (16) and, on the other, the DI bound, proportional to $\Delta m^2_{atm}/m_3$, becomes more and more stringent. Quantitative studies [40] show that

$$|m_i| < 0.12\text{–}0.15\,\text{eV}. \tag{19}$$

It should be stressed that these bounds hold under the assumption of strict hierarchy in the RH neutrino sector. Indeed, by relaxing the assumption $M_{2,3} \gg M_1$, there are important corrections to the expression of ϵ_1 in equation (17), which may receive a resonant enhancement and which do not vanish any longer for degenerate light neutrinos. For a moderate degeneracy among RH neutrinos, the DI bound is violated and M_1 can be considerably lower than 10^7–10^9 GeV [41]. At the same time, the enhanced CP-violating asymmetry allows a successful leptogenesis even for light neutrino masses around the eV scale [41]. In any case, it is impressive that the resulting range of neutrino masses is fully consistent with the results on neutrino oscillations.

6. Degenerate neutrinos

For degenerate neutrinos the average m^2 is much larger than the splittings. At first sight the degenerate case is the most appealing: the observation of nearly maximal atmospheric neutrino mixing and the more recent result that also the solar mixing is large suggests that all ν masses are nearly degenerate. We shall see that this possibility has become less attractive with the recent new experimental information.

It is clear that in the degenerate case the most probable origin of ν masses is from some dimension 5 operators $(Hl)_i^{\mathrm{T}}\lambda_{ij}(Hl)_j/\Lambda$ not related to the see-saw mechanism $m_\nu = m_D^{\mathrm{T}} M^{-1} m_D$. In fact, we expect the ν Dirac mass m_D not to be degenerate as for all other fermions and a conspiracy to reinstate a nearly perfect degeneracy between m_D and M, which arise from completely different physics, looks very implausible (see, however, [42]). Thus, in degenerate models, in general, there is no direct relation with Dirac masses of quarks and leptons and the possibility of a simultaneous description of all fermion masses within a grand unified theory is more remote [43] (examples of degenerate models are described in [44]).

The degeneracy of neutrinos should be guaranteed by some slightly broken symmetry. Models based on discrete or continuous symmetries have been proposed. For example, in the models of [45, 46], the symmetry is SO(3): in the unbroken limit neutrinos are degenerate and charged leptons are massless. When the symmetry is broken the charged lepton masses are much larger than neutrino splittings because the former are first-order, whereas the latter are second-order in the electroweak symmetry breaking. In this kind of model, the mixing angles are completely undetermined in the symmetric phase and they originate only in the spontaneously broken phase from a misalignment between the symmetry breaking terms for neutrinos and charged leptons.

In principle, when considering models with degenerate masses we must keep in mind that radiative corrections can modify mass splittings and mixing angles in the running from the high scale where neutrino masses are determined at the fundamental level (i.e. the heavy Majorana mass M or M_{GUT}) down to the electroweak scale [47]. These running effects can be evaluated by renormalization group techniques. The effects depend on the parameters

$A_{ab} = (m_a + m_b)/(m_a - m_b)$ and are, with good accuracy, proportional to $\epsilon = y_\tau^2/(16\pi^2)$ $\log(M/m_Z)$, where y_τ is the τ-lepton Yukawa coupling. The value of ϵ is around 10^{-5} in the SM and larger by a factor $1 + \tan^2\beta$ in the MSSM. The corrections are negligible for $|A_{ab}\epsilon| \lesssim 0(1)$. When some of these quantities are large a rapid transition takes place towards a fixed point configuration of mixing angles that does not correspond to the observed pattern. In practice, given the present upper bounds on the degenerate neutrino common mass m_0 and the LA value of Δm^2_{sol}, the corrections are always negligible in the SM and can only become sizable in the MSSM if $\tan^2\beta$ is large, m_0 is close to its absolute upper bound and m_1 and m_2 (those entering in the smallest difference Δm^2_{sol}) are nearly equal in absolute value and sign. Note that these remarks do not include the effects from thresholds that could affect running in a significant way, depending on the details of the heavy and/or light particle spectrum.

The upper limit on the common value $|m|$ becomes particularly stringent if one adopts the cosmological WMAP bound $|m| < 0.23$ eV [8] (or the more conservative one $|m| < 0.34$ eV [9]). The more direct laboratory limit from tritium beta decay is $|m| < 2.2$ eV [29]. In past years degenerate models with ν masses as large as $|m| \sim 1$–2 eV were considered with the perspective of a large fraction of hot dark matter in the universe. In this case, however, the existing limit [30] on the absence of $0\nu\beta\beta$ ($|m_{ee}| < 0.2$ eV or to be more conservative $|m_{ee}| < 0.3$–0.5 eV) implies [31, 48] approximate double maximal mixing (bimixing) for solar and atmospheric neutrinos. As discussed in section 4, for $|m| \gg m_{ee}$, one needs $m_1 \approx -m_2$ and, to a good accuracy, $c^2_{12} \approx s^2_{12}$, to satisfy the bound on m_{ee}. This is exemplified by the following texture:

$$m_\nu = m \begin{pmatrix} 0 & -1/\sqrt{2} & 1/\sqrt{2} \\ -1/\sqrt{2} & (1+\eta)/2 & (1+\eta)/2 \\ 1/\sqrt{2} & (1+\eta)/2 & (1+\eta)/2 \end{pmatrix}, \tag{20}$$

where $\eta \ll 1$, corresponding to an exact bimaximal mixing, $s_{13} = 0$ and the eigenvalues are $m_1 = m$, $m_2 = -m$ and $m_3 = (1+\eta)m$. This texture has been proposed in the context of a spontaneously broken SO(3) flavour symmetry and it has been studied to analyse the stability of the degenerate spectrum against radiative corrections [47, 49]. A more realistic mass matrix can be obtained by adding small perturbations to m_ν in equation (20):

$$m_\nu = m \begin{pmatrix} \delta & -1/\sqrt{2} & (1-\epsilon)/\sqrt{2} \\ -1/\sqrt{2} & (1+\eta)/2 & (1+\eta-\epsilon)/2 \\ (1-\epsilon)/\sqrt{2} & (1+\eta-\epsilon)/2 & (1+\eta-2\epsilon)/2 \end{pmatrix}, \tag{21}$$

where ϵ parametrizes the leading flavour-dependent radiative corrections (mainly induced by the τ Yukawa coupling) and δ controls m_{ee}. Consider first the case $\delta \ll \epsilon$. To first approximation θ_{12} remains maximal. We get $\Delta m^2_{sun} \approx m^2\epsilon^2/\eta$ and

$$\theta_{13} \approx \left(\frac{\Delta m^2_{sun}}{\Delta m^2_{atm}}\right)^{1/2}, \qquad m_{ee} \ll m\left(\frac{\Delta m^2_{atm}\Delta m^2_{sun}}{m^4}\right)^{1/2}. \tag{22}$$

If we instead assume $\delta \gg \epsilon$, we find $\Delta m^2_{sun} \approx 2m^2\delta$, $\theta_{23} \approx \pi/4$, $\sin^2 2\theta_{12} \approx 1 - \delta^2/4$. Also in this case the solar mixing angle remains unacceptably close to $\pi/4$, unless further contributions to the mixing matrix are induced from the diagonalization of the charged lepton sector. We get

$$\theta_{13} \approx 0, \qquad m_{ee} \approx \frac{\Delta m^2_{sun}}{2m}, \tag{23}$$

too small for detection if the average neutrino mass m is around the eV scale. We see that with increasing $|m|$ more and more fine tuning is needed to reproduce the LA solution values of Δm^2_{sun} and θ_{12}. In conclusion, even without invoking the WMAP limit, large ν masses, $|m| \sim 1$–2 eV, are disfavoured by the limit on $0\nu\beta\beta$ decay and by the emerging of the LA solution with the solar angle definitely not maximal. From these considerations, it is possible to derive the bound $|m| < 0.9h$ eV (90% CL) [33], where $h \approx 1$ parametrizes the uncertainties in the nuclear matrix elements. Also, we have seen in section 5 that the attractive mechanism of baryogenesis through leptogenesis appears to disfavour $|m| \gtrsim 0.1$ eV, at least in the simplest realizations. All together, after WMAP and KamLAND, among degenerate models those with $|m| \lesssim 0.23$–1 eV are favoured by converging evidence from different points of view.

For $|m|$ not larger than the $0\nu\beta\beta$ bound, one does not need a cancellation in m_{ee} and m_1 and m_2 can be approximately equal in magnitude and phase. For example, in the limit $s_{13} = 0$, the matrix

$$m_\nu = m \begin{pmatrix} 1 & 0 & 0 \\ 0 & 0 & -1 \\ 0 & -1 & 0 \end{pmatrix} \tag{24}$$

corresponds to maximal θ_{23} (pseudo-Dirac 23 submatrix) with $\mathrm{Diag}[m_\nu] = m(1, 1, -1)$. The angle θ_{12} is unstable and a small perturbation can give any value to it. Note, however, that in this case the non-vanishing matrix elements must be of equal absolute value and not just of order 1. So either this is guaranteed by a symmetry (as, for example, in [45]) or the model is unnaturally fine-tuned.

As a different example (also with no cancellation between m_1 and m_2), a model, which is simple to describe but difficult to derive in a natural way, is one [27, 50] where up-quarks, down-quarks and charged leptons have 'democratic' mass matrices, with all entries equal (in first approximation):

$$m_f = \hat{m}_f \begin{pmatrix} 1 & 1 & 1 \\ 1 & 1 & 1 \\ 1 & 1 & 1 \end{pmatrix} + \delta m_f, \tag{25}$$

where $\hat{m}_f$ ($f = u, d, e$) are three overall mass parameters and δm_f denote small perturbations. If we neglect δm_f, the eigenvalues of m_f are given by $(0, 0, 3\hat{m}_f)$. The mass matrix m_f is diagonalized by a unitary matrix U_f which is in part determined by the small term δm_f. If $\delta m_u \approx \delta m_d$, the CKM matrix, given by $V_{CKM} = U_u^\dagger U_d$, is nearly diagonal, due to a compensation between the large mixings contained in U_u and U_d. When the small terms δm_f are diagonal and of the form $\delta m_f = \mathrm{Diag}(-\epsilon_f, \epsilon_f, \delta_f)$ with $\delta_f \gg \epsilon_f$, the matrices U_f are approximately given by (note the analogy with the quark model eigenvalues π^0, η and η'):

$$U_f^\dagger \approx \begin{pmatrix} 1/\sqrt{2} & -1/\sqrt{2} & 0 \\ 1/\sqrt{6} & 1/\sqrt{6} & -2/\sqrt{6} \\ 1/\sqrt{3} & 1/\sqrt{3} & 1/\sqrt{3} \end{pmatrix}. \tag{26}$$

Note that, due to the degeneracy in the 1, 2 sector in the unperturbed limit, any superposition of the first two rows would also be an eigenvector of zero mass. Thus, the choice $(U_f^\dagger)_{13} = 0$ is unjustified in the unperturbed limit and is only determined by a particular form of the perturbation.

At the same time, the lightest quarks and charged leptons acquire a non-vanishing mass. The leading part of the mass matrix in equation (25) is invariant under a discrete $S_{3L} \times S_{3R}$ permutation symmetry. The same requirement leads to the general neutrino mass matrix:

$$m_\nu = m\left[\begin{pmatrix} 1 & 0 & 0 \\ 0 & 1 & 0 \\ 0 & 0 & 1 \end{pmatrix} + r\begin{pmatrix} 1 & 1 & 1 \\ 1 & 1 & 1 \\ 1 & 1 & 1 \end{pmatrix}\right] + \delta m_\nu, \tag{27}$$

where δm_ν is a small symmetry breaking term and the two independent invariants are allowed by the Majorana nature of the light neutrinos. If r vanishes the neutrinos are almost degenerate. In the presence of δm_ν the permutation symmetry is broken and the degeneracy is removed. If, for example, we choose $\delta m_\nu = \mathrm{Diag}(0, \epsilon, \eta)$ with $\epsilon < \eta \ll 1$ and $r \ll \epsilon$, the solar and the atmospheric oscillation frequencies are determined by ϵ and η, respectively. The problems with this class of models are that the solar angle should be close to maximal (typically more than the atmospheric angle) and that the neutrino spectrum and mixing angles are not determined by the symmetric limit (this applies, for example, to $s_{13} \sim 0$) but only by a specific choice of the parameter r and of the perturbations that cannot be easily justified on theoretical grounds. Notice also that the simplest choice of parameters leads to $\sin^2 2\theta_{23}$ very close to 8/9, value which is now excluded at the 2σ level.

In this model, the mixing angles are almost entirely due to the charged lepton sector. Recently, the question of whether observed neutrino mixings can dominantly arise from the charged lepton sector in a natural way was studied in general in [51]. Of course, one can always choose an *ad hoc* basis where this is true: the point is to decide whether this formal choice can be naturally justified in the physical basis where the symmetries of the Lagrangian are specified. The conclusion is that in presence of two large mixing angles θ_{12} and θ_{23} with the third angle θ_{13} being small, the construction of a natural model with dominance of U_e is made much more difficult than in the case of only the atmospheric angle θ_{23} large. Examples of natural models of this sort can be given [46], [51]–[53] and the stated difficulty is reflected in the relatively complicated symmetry structure required.

In conclusion, the parameter space for degenerate models has recently become smaller because of the indications from WMAP (and also, to some extent, from leptogenesis) that tend to lower the maximum common mass allowed for light neutrinos. It is also rather difficult to reproduce the observed pattern of frequencies and mixing angles, in particular two large and one small mixing angle, with the solar angle large but not maximal. Degenerate models that fit can only arise from a very special dynamics or a non-abelian flavour symmetry with suitable breakings.

6.1. Anarchy

Anarchical models [54] can be considered as particular cases of degenerate models with $m^2 \sim \Delta m^2_{atm}$. In this class of models mass degeneracy is replaced by the principle that all mass matrices are structureless in the neutrino sector (including the LH charged fermions and possibly the RH neutrinos). For the LA solution the ratio of the solar and atmospheric frequencies is not so small: $r = (\Delta m^2_{sun})_{LA}/\Delta m^2_{atm} \sim 1/40$ and two out of three mixing angles are large. The key observation is that the see-saw mechanism tends to enhance the ratio of eigenvalues: it is quadratic in m_D so that a hierarchy factor f in m_D becomes f^2 in m_ν and the presence of the Majorana matrix M results in a further widening of the distribution. Another squaring takes place

in going from the masses to the oscillation frequencies which are quadratic. As a result, a random generation of the m_D and M matrix elements leads to a distribution of r that peaks around 0.1. At the same time, the distribution of $\sin^2\theta_{ij}$ is rather flat for all three mixing angles. Clearly, the smallness of θ_{13} is problematic for anarchy. This can be turned into the prediction that in anarchical models θ_{13} must be near the present bound (after all, the value 0.2 for $\sin\theta_{13}$ is not that smaller than the maximal value 0.707). In conclusion, if θ_{13} is near the present bound, one can argue that the neutrino masses and mixings, interpreted by the see-saw mechanism, can just arise from structureless underlying Dirac and Majorana matrices.

7. Inverted hierarchy

The inverted hierarchy configuration $|m_1| \sim |m_2| \gg |m_3|$ consists of two levels m_1 and m_2 with small splitting $\Delta m^2_{12} = \Delta m^2_{sun}$ and a common mass given by $|m^2_{1,2}| \sim |\Delta m^2_{atm}| \sim 2.6 \times 10^{-3}\,\mathrm{eV}^2$. One particularly interesting example of this sort [55], which leads to double maximal mixing, is obtained with the phase choice $m_1 = -m_2$ so that, approximately,

$$m_{diag} = \mathrm{Diag}(\sqrt{2}m, -\sqrt{2}m, 0). \tag{28}$$

The effective light neutrino mass matrix

$$m_\nu = U^* m_{diag} U^\dagger, \tag{29}$$

which corresponds to the mixing matrix of double maximal mixing $c_{12} = s_{12} = 1/\sqrt{2}$ and $s_{13} = u = 0$ in equation (6):

$$U_{fi} = \begin{pmatrix} 1/\sqrt{2} & 1/\sqrt{2} & 0 \\ -1/2 & 1/2 & 1/\sqrt{2} \\ 1/2 & -1/2 & 1/\sqrt{2} \end{pmatrix}, \tag{30}$$

is given by

$$m_\nu = m \begin{pmatrix} 0 & -1 & 1 \\ -1 & 0 & 0 \\ 1 & 0 & 0 \end{pmatrix}. \tag{31}$$

This texture for m_ν can be reproduced by imposing a U(1) flavour symmetry with charge $L_e - L_\mu - L_\tau$ starting either from $(Hl)^{\mathrm{T}}_i \lambda_{ij} (Hl)_j/\Lambda$ or from RH neutrinos via the see-saw mechanism. However, the absolute values of the 12 and 13 terms would be in general different in this case. As a consequence, while the vanishing of s_{13} and the maximal value of θ_{12} are still valid, the atmospheric angle deviates from the maximal value with $\tan\theta_{23} = x$ where x is the absolute value of the ratio $m_{\nu 13}/m_{\nu 12}$. We also note that the 1–2 degeneracy remains stable under radiative corrections [47, 49].

The leading texture in (31) can be perturbed by adding small terms:

$$m_\nu = m \begin{pmatrix} \delta & -1 & 1 \\ -1 & \eta & \eta \\ 1 & \eta & \eta \end{pmatrix}, \tag{32}$$

where δ and η are small ($\ll 1$), real parameters defined up to coefficients of order 1 that can differ in the various matrix elements. One could also make the absolute values of the 12, 13 terms different by terms of order $s_{13}\delta$. The perturbations leave Δm^2_{atm} and θ_{23} unchanged, in first approximation. We obtain $\tan^2\theta_{12} \approx 1+\delta+\eta$ and $\Delta m^2_{sun}/\Delta m^2_{atm} \approx \eta+\delta$, where coefficients of order one have been neglected. Moreover $\theta_{13} \approx \eta$. If $\eta \gg \delta$, we have

$$\theta_{13} \approx \frac{\Delta m^2_{sun}}{\Delta m^2_{atm}}, \qquad m_{ee} \ll \sqrt{\Delta m^2_{sun}}\left(\frac{\Delta m^2_{sun}}{\Delta m^2_{atm}}\right)^{1/2}. \tag{33}$$

In the other case, $\eta \ll \delta$ we obtain

$$\theta_{13} \ll \frac{\Delta m^2_{sun}}{\Delta m^2_{atm}}, \qquad m_{ee} \approx \frac{1}{2}\sqrt{\Delta m^2_{sun}}\left(\frac{\Delta m^2_{sun}}{\Delta m^2_{atm}}\right)^{1/2}. \tag{34}$$

There is a well-known difficulty of this scenario to fit the LA solution [55]–[57]. Indeed, barring cancellation between the perturbations, in order to obtain a Δm^2_{sun} close to the best-fit LA value, η and δ should be smaller than about 0.1 and this keeps the value of $\sin^2 2\theta_{12}$ very close to 1, in disagreement with global fits of solar data [23]. Notice that the required deviation of the solar mixing angle from the maximal value is of the order of the Cabibbo angle θ_C and indeed the empirical relation $\theta_{12}+\theta_C = \pi/4$ holds within the experimental errors [58]. However, even starting from exact bimixing the pattern of parameters needed to bring the solar angle down from the maximal value can be obtained in a natural way as an effect of the charged lepton matrix diagonalization (see e.g. [56, 57]). This possibility, studied in detail in [51, 59], is not excluded but is strongly constrained by the observed smallness of s_{13}, as in general the amount of deviation from maximal solar angle is typically of order s_{13} (whereas the deviation from maximal atmospheric mixing are of second order).

With the phase choice $m_1 = m_2$, i.e. for $\mathrm{Diag}[m_\nu] = m(1,1,0)$, in the limit $s_{13} = 0$, one obtains the matrix

$$m_\nu = m\begin{pmatrix} 1 & 0 & 0 \\ 0 & 1/2 & -1/2 \\ 0 & -1/2 & 1/2 \end{pmatrix}, \tag{35}$$

which corresponds to large θ_{23} with the solar angle unstable to small perturbations. In this case, fine-tuning or a symmetry is necessary to fix the ratios of the matrix elements as indicated.

In conclusion, also for inverse hierarchy some special dynamics or symmetry is needed to reproduce in detail the observed features of the data.

8. Normal hierarchy

We now discuss the class of models which we consider the simplest approach to neutrino masses and mixings. In particular, in this context, one can formulate the most constrained framework which allows a comprehensive combined study of all fermion masses in GUTs. We start by assuming three widely split νs and the existence of a RH neutrino for each generation, as required to complete a 16-dimensional representation of SO(10) for each generation. We then assume dominance of the see-saw mechanism $m_\nu = m_D^{\mathrm{T}} M^{-1} m_D$. We know that the third-generation eigenvalue of the Dirac mass matrices of up- and down-quarks and of charged leptons

is systematically the largest one. It is natural (although not necessary) to imagine that this property could also be true for the Dirac mass of νs: $m_D^{diag} \sim \mathrm{Diag}(0, 0, m_{D3})$. After see-saw we expect m_ν to be even more hierarchical being quadratic in m_D (barring fine-tuned compensations between m_D and M). Note however that for the LA solution, $r \sim 1/40$, so that the required amount of hierarchy, $r = \Delta m^2_{atm}/\Delta m^2_{sun} = m_3^2/m_2^2$ is quite moderate.

A possible difficulty for hierarchical models is that one is used to expect that large splittings correspond to small mixings because normally only close-by states are strongly mixed. In a 2×2 matrix context the requirement of large splitting and large mixings leads to a condition of vanishing determinant and large off-diagonal elements. For example, the matrix

$$\begin{pmatrix} x^2 & x \\ x & 1 \end{pmatrix} \tag{36}$$

has eigenvalues 0 and $1 + x^2$ and for x of O(1) the mixing is large. Thus, in the limit of neglecting small mass terms of order $m_{1,2}$, the demands of large atmospheric neutrino mixing and dominance of m_3 translate into the condition that the 2×2 subdeterminant 23 of the 3×3 mixing matrix approximately vanishes. The problem is to show that this vanishing can be arranged in a natural way without fine-tuning. Once near-maximal atmospheric neutrino mixing is reproduced the solar neutrino mixing can be arranged to be either small or large without difficulty by implementing suitable relations among the small mass terms.

It is not difficult to imagine mechanisms that naturally lead to the approximate vanishing of the 23 subdeterminant. For example, in [60, 61], it is assumed that one ν^c is particularly light and coupled to μ and τ. In a 2×2 simplified context if we have

$$M \propto \begin{pmatrix} \epsilon & 0 \\ 0 & 1 \end{pmatrix}, \qquad M^{-1} \approx \begin{pmatrix} 1/\epsilon & 0 \\ 0 & 0 \end{pmatrix}, \qquad m_D = \begin{pmatrix} a & b \\ c & d \end{pmatrix}, \tag{37}$$

then for a generic m_D we find

$$m_\nu = m_D^{\mathrm{T}} M^{-1} m_D \approx \frac{1}{\epsilon} \begin{pmatrix} a^2 & ab \\ ab & b^2 \end{pmatrix}. \tag{38}$$

A different possibility that we find attractive is that, in the limit of neglecting terms of order $m_{1,2}$ and, in the basis where charged leptons are diagonal, the Dirac matrix m_D, defined by $\nu^c m_D \nu$, takes the approximate form, called 'lopsided' [62]–[64]:

$$m_D \propto \begin{pmatrix} 0 & 0 & 0 \\ 0 & 0 & 0 \\ 0 & x & 1 \end{pmatrix}. \tag{39}$$

This matrix has the property that for a generic Majorana matrix M one finds

$$m_\nu = m_D^{\mathrm{T}} M^{-1} m_D \propto \begin{pmatrix} 0 & 0 & 0 \\ 0 & x^2 & x \\ 0 & x & 1 \end{pmatrix}. \tag{40}$$

The only condition on M^{-1} is that the 33 entry is non-zero. However, when the approximately vanishing matrix elements are replaced by small terms, one must also assume that no new O(1) terms are generated in m_ν by a compensation between small terms in m_D and large terms in M^{-1}.

It is important for the following discussion to observe that m_D given by equation (39) under a change of basis transforms as $m_D \to V^\dagger m_D U$ where V and U rotate the right and left fields, respectively. It is easy to check that to make m_D diagonal we need large left mixings (i.e. large off-diagonal terms in the matrix that rotates LH fields). Thus, the question is how to reconcile large LH mixings in the leptonic sector with the observed near-diagonal form of V_{CKM}, the quark mixing matrix. Strictly speaking, since $V_{CKM} = U_u^\dagger U_d$, the individual matrices U_u and U_d need not be near-diagonal, but V_{CKM} does, whereas the analogue for leptons apparently cannot be near-diagonal. However, for quarks nothing forbids that, in the basis where m_u is diagonal, the d quark matrix has large non-diagonal terms that can be rotated away by a pure RH rotation. We suggest that this is so and that in some way RH mixings for quarks correspond to LH mixings for leptons.

In the context of (SUSY) SU(5), there is a very attractive hint of how this sort of mechanism can be realized [65, 66]. In the $\bar{5}$ of SU(5) the d^c singlet appears together with the lepton doublet (ν, e). The (u, d) doublet and e^c belong to the 10 and ν^c to the 1 and similarly for the other families. As a consequence, in the simplest model with mass terms arising from only Higgs pentaplets, the Dirac matrix of down-quarks is the transpose of the charged lepton matrix: $m_d = (m_l)^{\mathrm{T}}$. Thus, indeed, a large mixing for RH down-quarks corresponds to a large LH mixing for charged leptons. At leading order we may have the lopsided texture:

$$m_d = (m_l)^{\mathrm{T}} = \begin{pmatrix} 0 & 0 & 0 \\ 0 & 0 & 1 \\ 0 & 0 & 1 \end{pmatrix} v_d. \tag{41}$$

In the same simplest approximation with 5 or $\bar{5}$ Higgs, the up-quark mass matrix is symmetric, so that left and right mixing matrices are equal in this case. Then small mixings for up-quarks and small LH mixings for down-quarks are sufficient to guarantee small V_{CKM} mixing angles even for large d quark RH mixings. It is well known that a model where the down and the charged lepton matrices are exactly the transpose of one another cannot be exactly true because of the e/d and μ/s mass ratios. It is also known that one remedy to this problem is to add some Higgs component in the 45 representation of SU(5) [67]. However, the symmetry under transposition can still be a good guideline if we are only interested in the order of magnitude of the matrix entries and not in their exact values. In models with $\mathrm{U}(1)_F$ flavour symmetry, equal second- and third-generation charges for the $\bar{5}$ could induce a lopsided form for both the charged leptons and the Dirac neutrino mass matrices. Otherwise, in the very crude model where the Higgs pentaplets come from a pure 10 representation of SO(10) one has $m_D = m_u$, i.e. the Dirac neutrino mass matrix m_D is the same as the up-quark mass matrix . For m_D the dominance of the third family eigenvalue as well as a near-diagonal form could be an order of magnitude remnant of this broken symmetry.

To get a realistic mass matrix, we allow for deviations from the symmetric limit of (40) with $x \sim \mathrm{o}(1)$. For instance, we can consider those models where the neutrino mass matrix elements are dominated, via the see-saw mechanism, by the exchange of two right-handed neutrinos [61]. Since the exchange of a single RH neutrino gives a successful zeroth-order texture, we are encouraged to continue along this line. Thus, we add a sub-dominant contribution of a second RH neutrino, assuming that the third one gives a negligible contribution to the neutrino mass matrix, because it has much smaller Yukawa couplings or is much heavier than the first two. The Lagrangian that describes this plausible subset of see-saw models, written in the mass eigenstate

basis of RH neutrinos and charged leptons, is

$$\mathcal{L} = y_i \nu^c H l_i + y'_i \nu^{c\prime} H l_i + \tfrac{1}{2} M \nu^{c2} + \tfrac{1}{2} M' \nu^{c\prime 2}, \tag{42}$$

leading to

$$(m_\nu)_{ij} \propto \frac{y_i y_j}{M} + \frac{y'_i y'_j}{M'}, \tag{43}$$

where $i, j = \{e, \mu, \tau\}$. In particular, if $y_e \ll y_\mu \approx y_\tau$ and $y'_\mu \approx y'_\tau$, we obtain

$$m_\nu = m \begin{pmatrix} \delta & \epsilon & \epsilon \\ \epsilon & 1+\eta & 1+\eta \\ \epsilon & 1+\eta & 1+\eta \end{pmatrix}, \tag{44}$$

where coefficients of order 1 multiplying the small quantities δ, ϵ and η have been omitted. The 23 subdeterminant is generically of order η. The mass matrix in (44) does not describe the most general perturbation of the zeroth-order texture (40). We have implicitly assumed a symmetry between ν_μ and ν_τ which is preserved by the perturbations, at least at the level of the order of magnitudes. The perturbed texture (44) can also arise when the zeros of the lopsided Dirac matrix in (39) are replaced by small quantities. It is possible to construct models along this line based on a spontaneously broken $U(1)_F$ flavour symmetry, where δ, ϵ and η are given by positive powers of one or more symmetry-breaking parameters. Moreover, by playing with the $U(1)_F$ charges, we can adjust, to certain extent, the relative hierarchy between η, ϵ and δ [60, 61], [63]–[66], as we will see in section 8. The texture (44) can also be generated in SUSY models with R-parity violation [68].

Let us come back to the mass matrix m_ν of equation (44). After a first rotation by an angle θ_{23} close to $\pi/4$ and a second rotation with $\theta_{13} \approx \epsilon$, we get

$$m_\nu \approx m \begin{pmatrix} \delta + \epsilon^2 & \epsilon & 0 \\ \epsilon & \eta & 0 \\ 0 & 0 & 2 \end{pmatrix}, \tag{45}$$

up to order 1 coefficients in the small entries. To obtain a large solar mixing angle, we need $|\eta - \delta| < \epsilon$. In realistic models, there is no reason for a cancellation between independent perturbations and thus we assume both $\delta \leqslant \epsilon$ and $\eta \leqslant \epsilon$.

Consider first the case $\delta \approx \epsilon$ and $\eta < \epsilon$. The solar mixing angle θ_{12} is large but not maximal, as indicated by the LA solution. We also have $\Delta m^2_{atm} \approx 4m^2$, $\Delta m^2_{sun} \approx \Delta m^2_{atm}\epsilon^2$ and

$$m_{ee} \approx \sqrt{\Delta m^2_{sun}}. \tag{46}$$

If $\eta \approx \epsilon$ and $\delta \ll \epsilon$, we still have a large solar mixing angle and $\Delta m^2_{sun} \approx \epsilon^2 \Delta m^2_{atm}$, as before. However, m_{ee} will be much smaller than the estimate in (46). This is the case of the models based on the above mentioned $U(1)_F$ flavour symmetry that, at least in its simplest realization, tends to predict $\delta \approx \epsilon^2$. In this class of models we find

$$m_{ee} \approx \sqrt{\Delta m^2_{sun}} \left(\frac{\Delta m^2_{sun}}{\Delta m^2_{atm}} \right)^{1/2}, \tag{47}$$

below the sensitivity of the next generation of planned experiments. It is worth mentioning that in both cases discussed above, we have

$$\theta_{13} \approx \left(\frac{\Delta m^2_{sun}}{\Delta m^2_{atm}}\right)^{1/2}, \tag{48}$$

which might be close to the present experimental limit if the oscillation frequency of the LA solution for solar neutrinos is in the upper part of its allowed range.

If both δ and η are much smaller than ϵ, the 12 block of m_ν has an approximate pseudo-Dirac structure and the angle θ_{12} becomes maximal. This situation is typical of some models where leptons have $U(1)_F$ charges of both signs, whereas the order parameters of $U(1)_F$ breaking have all charges of the same sign [65]. We have two eigenvalues approximately given by $\pm m\epsilon$. As an example, we consider the case where $\eta = 0$ and $\delta \approx \epsilon^2$. We find $\sin^2 2\theta_{12} \approx 1 - \epsilon^2/4$, $\Delta m^2_{sun} \approx m^2\epsilon^3$ and

$$\theta_{13} \approx \left(\frac{\Delta m^2_{sun}}{\Delta m^2_{atm}}\right)^{1/3}, \qquad m_{ee} \approx \sqrt{\Delta m^2_{sun}}\left(\frac{\Delta m^2_{sun}}{\Delta m^2_{atm}}\right)^{1/6}. \tag{49}$$

To recover the LA solution we would need a relatively large value of ϵ. However, this is in general problematic because, on the one hand the presence of a large perturbation raises doubts about the consistency of the whole approach and, on the other, in existing models where all fermion sectors are related to each other, ϵ is never larger than the Cabibbo angle.

Summarizing, within normal hierachical models, there is enough flexibility to reproduce in a natural way the experimental frequencies and mixing angles. In particular, the lopsided matrix solution of the large atmospheric mixing, inspired by SU(5), where the large atmospheric mixing arises from the charged lepton sector, can be extended rather naturally to also account for the solar sector and for the small θ_{13} mixing angle.

8.1. Semi-anarchy

We have seen that anarchy is the absence of structure in the neutrino sector. Here we consider an attenuation of anarchy where the absence of structure is limited to the 23 sector. The typical texture is in this case,

$$m_\nu \approx m \begin{pmatrix} \delta & \epsilon & \epsilon \\ \epsilon & 1 & 1 \\ \epsilon & 1 & 1 \end{pmatrix}, \tag{50}$$

where δ and ϵ are small and by 1 we mean entries of O(1) and also the 23 determinant is of O(1). We see that this texture is similar to equation (44) when $\eta \sim O(1)$. Clearly, in general, we would expect two mass eigenvalues of order 1, in units of m, and one small, of order δ or ϵ^2. This pattern does not fit the observed solar and atmospheric observed frequencies. However, given that the ratio $r = (\Delta m^2_{sun})_{LA}/\Delta m^2_{atm} \sim 1/40$ is not too small, we can assume that the small value of r is generated accidentally, as for anarchy. We see that, if we proceed with the same change of basis as from equation (44) to equation (45), it is sufficient that by chance $\eta \sim \delta + \epsilon^2$ in order to obtain the correct value of r with large θ_{23} and θ_{12} and small $\theta_{13} \sim \epsilon$. The natural smallness of θ_{13} is the main advantage over anarchy. We will come back to this class of models in a following section.

9. Grand unified models of fermion masses

We have seen that the smallness of neutrino masses interpreted via the see-saw mechanism directly leads to a scale Λ for L non-conservation which is remarkably close to M_{GUT}. Thus, neutrino masses and mixings should find a natural context in a GUT treatment of all fermion masses. The hierarchical pattern of quark and lepton masses, within a generation and across generations, requires some dynamical suppression mechanism that acts differently on the various particles. This hierarchy can be generated by a number of operators of different dimensions suppressed by inverse powers of the cut-off Λ_c of the theory. In some realizations, the different powers of $1/\Lambda_c$ correspond to different orders in some symmetry-breaking parameter v_f arising from the spontaneous breaking of a flavour symmetry. In the next subsections, we describe some simplest models based on $\mathrm{SU}(5) \times \mathrm{U}(1)_F$ and on SO(10) which illustrate these possibilities (for models based on non-abelian flavour symmetries see [69]). It is notoriously difficult to turn these models into fully realistic theories, due to well-known problems such as the doublet–triplet splitting, the proton lifetime, the gauge coupling unification beyond leading order and the wrong mass relations for charged fermions of the first two generations. Some of these problems can be solved by adopting the elegant idea of GUTs in extra dimensions [70]. Here we adopt the GUT framework simply as a convenient testing ground for different neutrino mass scenarios.

9.1. Models based on horizontal abelian charges

We discuss here some explicit examples of grand unified models in the framework of a unified SUSY SU(5) theory with an additional $\mathrm{U}(1)_F$ flavour symmetry. The SU(5) generators act 'vertically' inside one generation, whereas the $\mathrm{U}(1)_F$ charges are different 'horizontally' from one generation to the other. If, for a given interaction vertex, the $\mathrm{U}(1)_F$ charges do not add to zero, the vertex is forbidden in the symmetric limit. However, the symmetry is spontaneously broken by the VEVs v_f of a number of 'flavon' fields with non-vanishing charge. Then a forbidden coupling is rescued but is suppressed by powers of the small parameters v_f/Λ_c with the exponents larger for larger charge mismatch [71]. We expect $M_{GUT} \lesssim v_f \lesssim \Lambda_c \lesssim M_{Pl}$. Here we discuss some aspects of the description of fermion masses in this framework.

In these models, the known generations of quarks and leptons are contained in triplets Ψ_i^{10} and $\Psi_i^{\bar{5}}$ $(i = 1, 2, 3)$ corresponding to the three generations, transforming as 10 and $\bar{5}$ of SU(5), respectively. Three more SU(5) singlets Ψ_i^1 describe the RH neutrinos. In SUSY models, we have two Higgs multiplets H_u and H_d, which transform as 5 and $\bar{5}$ in the minimal model. The two Higgs multiplets may have the same or different charges. In all the models that we discuss the large atmospheric mixing angle is described by assigning equal flavour charge to muon and tau neutrinos and their weak SU(2) partners (all belonging to the $\bar{5} \equiv (l, d^c)$ representation of SU(5)). Instead, the solar neutrino oscillations can be obtained with different, inequivalent charge assignments. There are many variants of these models: fermion charges can all be non-negative with only negatively charged flavons, or there can be fermion charges of different signs with either flavons of both charges or only flavons of one charge. We can have that only the top quark mass is allowed in the symmetric limit, or that also other third-generation fermion masses are allowed. The Higgs charges can be equal, in particular both vanishing or can be different. We can arrange that all the structure is in charged fermion masses while neutrinos are anarchical.

9.1.1. F(fermions) $\geqslant$ 0. Consider, for example, a simple model with all charges of matter fields being non-negative and containing one single flavon $\bar{\theta}$ of charge F$= -1$. For a maximum of simplicity we also assume that all the third-generation masses are directly allowed in the symmetric limit. This is realized by taking vanishing charges for the Higgses and for the third-generation components Ψ_3^{10}, $\Psi_3^{\bar{5}}$ and Ψ_3^1. If we define $\mathrm{F}(\Psi_i^R) \equiv q_i^R$ $(R = 10, \bar{5}, 1; i = 1, 2, 3)$, then the generic mass matrix m has the form

$$m = \begin{pmatrix} y_{11}\lambda^{q_1^R+q_1^{R'}} & y_{12}\lambda^{q_1^R+q_2^{R'}} & y_{13}\lambda^{q_1^R+q_3^{R'}} \\ y_{21}\lambda^{q_2^R+q_1^{R'}} & y_{22}\lambda^{q_2^R+q_2^{R'}} & y_{23}\lambda^{q_2^R+q_3^{R'}} \\ y_{31}\lambda^{q_3^R+q_1^{R'}} & y_{32}\lambda^{q_3^R+q_2^{R'}} & y_{33}\lambda^{q_3^R+q_3^{R'}} \end{pmatrix} v, \tag{51}$$

where all the y_{ij} are dimensionless complex coefficients of order 1 and m_u, $m_d = m_l^{\mathrm{T}}$, m_D and M arise by choosing $(R, R') = (10, 10), (\bar{5}, 10), (1, \bar{5})$ and $(1, 1)$, respectively. We have $\lambda \equiv \langle\bar{\theta}\rangle/\Lambda_c$ and the quantity v represents the appropriate VEV or mass parameter. The models with all non-negative charges and one single flavon have particularly simple factorization properties. For instance, in the see-saw expression for $m_\nu = m_D^{\mathrm{T}} M^{-1} m_D$, the dependence on the q_i^1 charges drops out and only that from $q_i^{\bar{5}}$ remains. In addition, for the neutrino mixing matrix U_{ij}, which is determined by m_ν in the basis where the charged leptons are diagonal, one can prove that $U_{ij} \approx \lambda^{|q_i^{\bar{5}} - q_j^{\bar{5}}|}$, in terms of the differences of the $\bar{5}$ charges, when terms that are down by powers of the small parameter λ are neglected. Similarly, the CKM matrix elements are approximately determined by only the 10 charges [71]: $V_{ij}^{CKM} \approx \lambda^{|q_i^{10} - q_j^{10}|}$. If the symmetry-breaking parameter λ is numerically close to the Cabibbo angle, we can choose

$$(q_1^{10}, q_2^{10}, q_3^{10}) = (3, 2, 0), \tag{52}$$

thus reproducing $V_{us} \sim \lambda$, $V_{cb} \sim \lambda^2$ and $V_{ub} \sim \lambda^3$. The same q_i^{10} charges also fix $m_u : m_c : m_t \sim \lambda^6 : \lambda^4 : 1$. The experimental value of m_u (the relevant mass values are those at the GUT scale: $m = m(M_{GUT})$ [72]) would rather prefer $q_1^{10} = 4$. Taking into account this indication and the presence of the unknown coefficients $y_{ij} \sim \mathrm{O}(1)$ it is difficult to decide between $q_1^{10} = 3$ or 4 and both are acceptable. Of course, the charges $(q_1^{10}, q_2^{10}, q_3^{10}) = (2, 1, 0)$ would represent an equally good choice, provided we appropriately rescale the expansion parameter λ. Turning to the $\bar{5}$ charges, if we take [63]–[65], [73, 74]

$$(q_1^{\bar{5}}, q_2^{\bar{5}}, q_3^{\bar{5}}) = (b, 0, 0), \quad b \geqslant 0, \tag{53}$$

together with equation (52) we get the patterns $m_d : m_s : m_b \sim m_e : m_\mu : m_\tau \sim \lambda^{3+b} : \lambda^2 : 1$. Moreover, the 22, 23, 32, 33 entries of the effective light neutrino mass matrix m_ν are all O(1), thus accommodating the nearly maximal value of s_{23}. The small non-diagonal terms of the charged lepton mass matrix cannot change this. We obtain, where arbitrary O(1) coefficients are omitted:

$$m_\nu = \begin{pmatrix} \lambda^{2b} & \lambda^b & \lambda^b \\ \lambda^b & 1 & 1 \\ \lambda^b & 1 & 1 \end{pmatrix} \frac{v_u^2}{\Lambda} \quad (\mathrm{A, SA}), \tag{54}$$

where v_u is the VEVs of the Higgs doublet giving mass to the up-quarks and all the entries are specified up to order 1 coefficients. If we take $v_u \sim 250\,\mathrm{GeV}$, the mass scale Λ of the heavy Majorana neutrinos turns out to be close to the unification scale, $\Lambda \sim 10^{15}\,\mathrm{GeV}$.

If b vanishes, then the light neutrino mass matrix will be structureless and we recover the anarchical (A) picture of neutrinos discussed in section 6.1. In a large sample of anarchical models, generated with random coefficients, the resulting neutrino mass spectrum can exhibit either normal or inverse hierarchy. For down-quarks and charged leptons we obtain a weakened hierarchy, essentially the square root than that of up-quarks.

If b is positive, then the light neutrino mass matrix will be structureless only in the (2, 3) subsector and we get semi-anarchical (SA) models, introduced in section 8.1. In this case, the neutrino mass spectrum has normal hierarchy. However, unless the (2, 3) subdeterminant is accidentally suppressed, atmospheric and solar oscillation frequencies are expected to be of the same order and, in addition, the preferred solar mixing angle is small. Nevertheless, such a suppression can occur in a fraction of semi-anarchical models generated with random, order 1 coefficients. The real advantage over the fully anarchical scheme is represented by the suppression in U_{e3}.

Note that in all previous cases we could add a constant to $q_i^{\bar{5}}$, for example, by taking $(q_1^{\bar{5}}, q_2^{\bar{5}}, q_3^{\bar{5}}) = (2+b, 2, 2)$. This would only have the consequence to leave the top quark as the only unsuppressed mass and to decrease the resulting value of $\tan\beta = v_u/v_d$ down to $\lambda^2 m_t/m_b$. A constant shift of the charges q_i^1 might also provide a suppression of the leading ν^c mass eigenvalue, from Λ_c down to the appropriate scale Λ. One can also consider models where the 5 and $\bar{5}$ Higgs charges are different, as in the 'realistic' SU(5) model of Altarelli *et al* [75]. Also in these models, the top mass could be the only one to be non-vanishing in the symmetric limit and the value of $\tan\beta$ can be adjusted.

9.1.2. F(fermions) and F(flavons) of both signs. Models with naturally large 23 splittings are obtained if we allow negative charges and, at the same time, either introduce flavons of opposite charges or stipulate that matrix elements with overall negative charge are put to zero. For example, we can assign to the fermion fields the set of F charges given by

$$\begin{aligned}
&(q_1^{10}, q_2^{10}, q_3^{10}) = (3, 2, 0),\\
&(q_1^{\bar{5}}, q_2^{\bar{5}}, q_3^{\bar{5}}) = (b, 0, 0), \quad b \geqslant 2a > 0,\\
&(q_1^{1}, q_2^{1}, q_3^{1}) = (a, -a, 0).
\end{aligned} \tag{55}$$

We consider the Yukawa coupling allowed by $\mathrm{U}(1)_F$-neutral Higgs multiplets in the 5 and $\bar{5}$ SU(5) representations and by a pair θ and $\bar{\theta}$ of SU(5) singlets with $\mathrm{F} = 1$ and $\mathrm{F} = -1$, respectively. If $b = 2$ or 3, the up, down and charged lepton sectors are not essentially different than in the SA case. Also in this case the O(1) off-diagonal entry of m_l, typical of lopsided models, gives rise to a large LH mixing in the 23 block which corresponds to a large RH mixing in the d mass matrix. In the neutrino sector, after diagonalization of the charged lepton sector and after integrating out the heavy RH neutrinos we obtain the following neutrino mass matrix in the low-energy effective theory:

$$m_\nu = \begin{pmatrix} \lambda^{2b} & \lambda^b & \lambda^b \\ \lambda^b & 1+\lambda^a\lambda'^a & 1+\lambda^a\lambda'^a \\ \lambda^b & 1+\lambda^a\lambda'^a & 1+\lambda^a\lambda'^a \end{pmatrix} \frac{v_u^2}{\Lambda} \quad \text{(H)}, \tag{56}$$

where λ' is given by $\langle\theta\rangle/\Lambda_c$ and Λ as before denotes the large mass scale associated to the RH neutrinos: $\Lambda \gg v_{u,d}$. The O(1) elements in the 23 block are produced by combining the large LH mixing induced by the charged lepton sector and the large LH mixing in m_D. A crucial property

Table 2. Models and their flavour charges.

Model	Ψ_{10}	$\Psi_{\bar{5}}$	Ψ_1	(H_u, H_d)
Anarchical (A)	(3, 2, 0)	(0, 0, 0)	(0, 0, 0)	(0, 0)
Semi-anarchical (SA)	(2, 1, 0)	(1, 0, 0)	(2, 1, 0)	(0, 0)
Hierarchical (H_I)	(6, 4, 0)	(2, 0, 0)	(1, −1, 0)	(0, 0)
Hierarchical (H_{II})	(5, 3, 0)	(2, 0, 0)	(1, −1, 0)	(0, 0)
Inversely hierarchical (IH_I)	(3, 2, 0)	(1, −1, −1)	(−1, +1, 0)	(0, +1)
Inversely hierarchical (IH_{II})	(6, 4, 0)	(1, −1, −1)	(−1, +1, 0)	(0, +1)

of m_ν is that, as a result of the see-saw mechanism and of the specific $U(1)_F$ charge assignment, the determinant of the 23 block is automatically of $O(\lambda^a\lambda'^a)$ (for this the presence of negative charge values, leading to the presence of both λ and λ' is essential [64, 65]). The neutrino mass matrix of equation (56) is a particular case of the more general pattern presented in equation (44), for $\delta \approx \lambda^{2b}$, $\epsilon \approx \lambda^b$ and $\eta \approx \lambda^a\lambda'^a$. If we take $\lambda \approx \lambda'$, it is easy to verify that the eigenvalues of m_ν satisfy the relations

$$m_1 : m_2 : m_3 = \lambda^{2(b-a)} : \lambda^{2a} : 1. \tag{57}$$

The atmospheric neutrino oscillations require $m_3^2 \sim 10^{-3}\,\mathrm{eV}^2$. The squared-mass difference between the lightest states is of $O(\lambda^{4a})m_3^2$, not far from the LA solution to the solar neutrino problem if we choose $a = 1$. In general, U_{e3} is non-vanishing, of $O(\lambda^b)$. Finally, beyond the large mixing in the 23 sector, m_ν provides a mixing angle $\theta_{12} \sim \lambda^{b-2a}$ in the 12 sector. When $b = 2a$, as for instance in the case $b = 2$ and $a = 1$, the LA solution can be reproduced and the resulting neutrino spectrum is hierarchical (H).

Alternatively, an inversely hierarchical (IH) spectrum can be obtained by choosing

$$\begin{aligned}
&(q_1^{10}, q_2^{10}, q_3^{10}) = (3, 2, 0),\\
&(q_1^{\bar{5}}, q_2^{\bar{5}}, q_3^{\bar{5}}) = (1, -1, -1),\\
&(q_1^{1}, q_2^{1}, q_3^{1}) = (-1, 1, 0),\\
&(q_{H_u}, q_{H_d}) = (0, 1).
\end{aligned} \tag{58}$$

Due to the non-vanishing charge of the H_d Higgs doublet, in the charged lepton sector, we recover the same pattern previously discussed. The light neutrino mass matrix is given by

$$m_\nu = \begin{pmatrix} \lambda^2 & 1 & 1 \\ 1 & \lambda'^2 & \lambda'^2 \\ 1 & \lambda'^2 & \lambda'^2 \end{pmatrix} \quad \text{(IH)}. \tag{59}$$

The ratio between the solar and atmospheric oscillation frequencies is not directly related to the subdeterminant of the block 23, in this case.

A representative set of models is listed in table 2. Note that in some cases the charges for Ψ_{10} have been changed from (3, 2, 0) (our reference values in equations (52), (55) and (58)) to (6, 4, 0) or (5, 3, 0). These values are *a posteriori* better suited to reproduce the moderate level of hierarchy implied by the present neutrino oscillation data. Since the neutrino mixing

parameters are completely independent on the 10 charges, this change is only important for a better fit to quark and charged lepton masses and mixings once a rather large value of λ is derived from the neutrino data. The hierarchical and the inversely hierarchical models may come into several varieties depending on the number and the charge of the flavour symmetry-breaking (FSB) parameters. Above we have considered the case of two (II) oppositely charged flavons with symmetry-breaking parameters λ and λ'. It may be noticed that the presence of two multiplets θ and $\bar{\theta}$ with opposite F charges could hardly be reconciled, without adding extra structure to the model, with a large common VEV for these fields, due to possible analytic terms of the kind $(\theta\bar{\theta})^n$ in the superpotential. Therefore, it is instructive to explore the consequences of allowing only the negatively charged $\bar{\theta}$ field in the theory, case I. In case I, it is impossible to compensate negative F charges in the Yukawa couplings and the corresponding entries in the neutrino mass matrices vanish. Eventually, these zeros are filled by small contributions, arising, for instance, from the diagonalization of the charged lepton sector or from the transformations needed to make the kinetic terms canonical.

Another important ingredient is represented by the see-saw mechanism [5]. Hierarchical models and semi-anarchical models have similar charges in the $(10, \bar{5})$ sectors and, in the absence of the see-saw mechanism, they would give rise to similar results. Even when the results are expected to be independent of the charges of the RH neutrinos, as it is the case for the anarchical and semi-anarchical models, the see-saw mechanism can induce some sizeable effect in a statistical analysis. For this reason, for each type of model, but the normal-hierarchical ones (the mechanism for the 23 subdeterminant suppression is in fact based on the see-saw mechanism), it is interesting to study the case where RH neutrinos are present and the see-saw contribution is the dominant one (SS) and the case where they are absent and the mass matrix is saturated by the non-renormalizable contribution (NOSS).

With this classification in mind, we can distinguish the following type of models, all supported by specific choices of U(1) charges: $\mathrm{A_{SS}}$, $\mathrm{A_{NOSS}}$, $\mathrm{SA_{SS}}$, $\mathrm{SA_{NOSS}}$, $\mathrm{H_{(SS,I)}}$, $\mathrm{H_{(SS,II)}}$, $\mathrm{IH_{(SS,I)}}$, $\mathrm{IH_{(SS,II)}}$, $\mathrm{IH_{(NOSS,I)}}$ and $\mathrm{IH_{(NOSS,II)}}$.

It is interesting to quantify the ability of each model in reproducing the observed oscillation parameters. For anarchy, it has been observed that random-generated, order-one entries of the neutrino mass matrices (in appropriate units), correctly fit the experimental data with a success rate of few per cent. It is natural to extend this analysis to include also the other models based on SU(5) $\times$ U(1) [76], which have mass matrix elements defined up to order-one dimensionless coefficients y_{ij} (see equation (51)). For each model, successful points in parameter space are selected by asking that the four observable quantities $O_1 = r \equiv \Delta m^2_{12}/|\Delta m^2_{23}|$, $O_2 = \tan^2\theta_{12}$, $O_3 = |U_{e3}| \equiv |\sin\theta_{13}|$ and $O_4 = \tan^2\theta_{23}$ fall in the approximately 3σ allowed ranges [23, 24]:

$$0.018 < r < 0.053, \qquad |U_{e3}| < 0.23,$$
$$0.30 < \tan^2\theta_{12} < 0.64, \qquad 0.45 < \tan^2\theta_{23} < 2.57. \tag{60}$$

The coefficients y_{ij} of the neutrino sector are random complex numbers with absolute values and phases uniformly distributed in intervals $\mathcal{I} = [0.5, 2]$ and $[0, 2\pi]$, respectively. The dependence of the results on these choices can be estimated by varying $\mathcal{I}$. For each model, an optimization procedure selects the value of the flavour symmetry-breaking parameter $\lambda = \lambda'$ that maximizes the success rate. The success rates are displayed in figures 1 and 2, separately for the SS and NOSS cases. The two sets of models have been individually normalized to give a total rate 100. From the histograms in figures 1 and 2 we see that normal hierarchy models are neatly

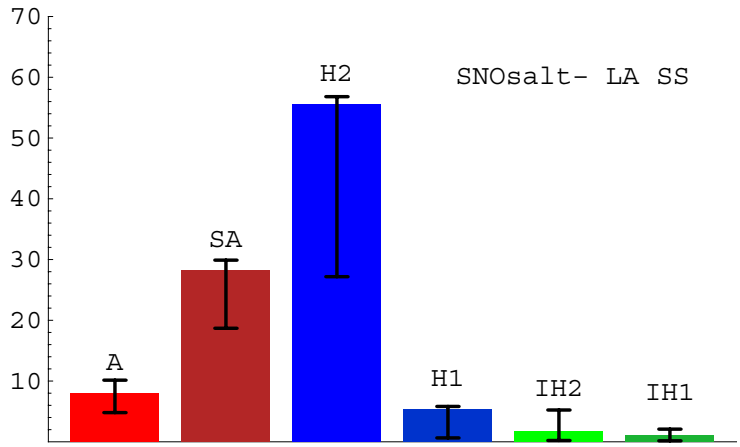

Figure 1. Relative success rates for the LA solution, with see-saw. The sum of the rates has been normalized to 100. The results correspond to the default choice $\mathcal{I} = [0.5, 2]$, and to the following values of $\lambda = \lambda'$: 0.2, 0.25, 0.35, 0.45, 0.45, 0.25 for the models A_{SS}, SA_{SS}, $H_{(SS,II)}$, $H_{(SS,I)}$, $IH_{(SS,II)}$ and $IH_{(SS,I)}$, respectively. The error bars represent the linear sum of the systematic error due to the choice of $\mathcal{I}$ and the statistical error (see text).

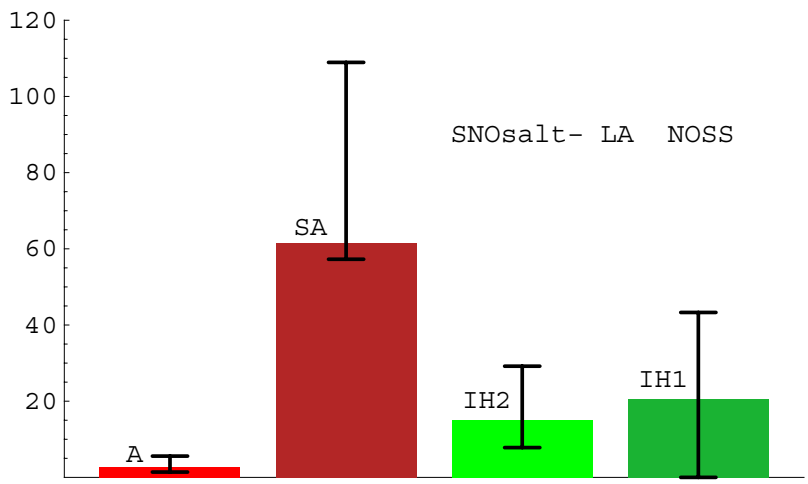

Figure 2. Relative success rates for the LA solution, without see-saw. The sum of the rates has been normalized to 100. The results correspond to the default choice $\mathcal{I} = [0.5, 2]$, and to the following values of $\lambda = \lambda'$: 0.2, 0.2, 0.25, 0.25 for the models A_{NOSS}, SA_{NOSS}, $IH_{(NOSS,II)}$ and $IH_{(NOSS,I)}$, respectively (in our notation there are no $H_{(NOSS,I)}$, $H_{(NOSS,II)}$ models). The error bars represent the linear sum of the systematic error due to the choice of $\mathcal{I}$ and the statistical error (see text).

preferred over anarchy and inverse hierarchy in the context of these SU(5) × U(1) models. In particular, in the SS case, the H_{II} models with normal hierarchy, two oppositely charged flavons and suppressed 23 subdeterminant are clearly preferred. Models of the type H_I are disfavoured. For the relatively large values of the expansion parameter required to fit r, they tend to predict too large $|U_{e3}|$ and $\tan^2\theta_{12} > 1$. We recall that for the chosen charge values the H_{II} model is of

the lopsided type. In the NOSS case the see-saw suppression of the 23 determinant is clearly not operative and all normal hierarchy models coincide with SA.

An interesting question is whether the disfavouring of IH models that we find in our SU(5) × U(1) framework can be extended to a more general context. In the limit of vanishing λ and λ' the IH texture (see equation (59)) becomes close to that of bimaximal mixing and $\theta_{13} = 0$ (actually with $r = 0$). In our U(1) models $r \approx |U_{e3}| \approx |\tan^2\theta_{12} - 1| \approx O(\lambda^2)$ (for $\lambda = \lambda'$). In particular, the charged lepton mixings cannot displace too much θ_{12} from its maximal value because the small value of the electron mass forces a sufficiently large value of the relevant charges, which in turn implies that the charged lepton mixing correction to θ_{12} is small. We have already mentioned that corrections from the charged lepton sector can, in principle, bring the predictions of a neutrino matrix of the bimixing type in agreement with the data and that the smallness of s_{13} induces strong constraints. In the particular set-up of $U(1)_F$ models, we have seen that charged lepton corrections are too small to make the solar angle sufficiently different from maximal.

Leptonic mixing in SUSY GUTs with RH neutrinos are potential sources of lepton flavour violating (LFV) processes beyond neutrino oscillations [79]. The observable effects are difficult to estimate since they are sensitive to both the details of the SUSY-breaking mechanism and to the low-energy superparticle spectrum. In models with gravity-mediated SUSY-breaking and universal boundary conditions for the soft breaking terms at the cut-off scale Λ, running effects give rise to off-diagonal slepton masses $\delta m^{2\,LL}_{\tilde{l}ij}$ proportional, at leading order, to $C_{ij} = (y_\nu^\dagger \log(\Lambda/M) y_\nu)_{ij}$. Current bounds on LFV transitions $l_i \to l_j\gamma$ translate into an upper bound on the combination $|C_{ij}|$, depending on $\tan\beta$ and soft mass parameters. If, for instance, $\tan\beta = 10$, the present experimental bound on $BR(\mu \to e\gamma)$ already excludes $C_{21} > 1$ for the most plausible values of slepton and gaugino masses. In the models considered in this section C_{21} is dominated by the couplings to the RH neutrino of the third generation and, assuming $(\Lambda/M_3) \approx O(100)$, we roughly expect $|y^*_{32} y_{31}| < 0.2$. This constraint is most easily respected by models with inverse hierarchy. For semi-anarchy and normal hierarchy the constraint is almost saturated, whereas anarchy tends to violate it. Future improvements in the experimental sensitivity could lead to a significant selection of the models.

In conclusion, models based on SU(5) × $U(1)_F$ are clearly toy models that can only aim at a semiquantitative description of fermion masses. In fact only the order of magnitude of each matrix entry can be specified. However, it is rather impressive that a reasonable description of fermion masses, now also including neutrino masses and mixings, can be obtained in this simple context, which is suggestive of a deeper relation between gauge and flavour quantum numbers. There are 12 mass eigenvalues and six mixing angles that are specified, modulo coefficients of order 1, in terms of a bunch of integer numbers (from half a dozen to a dozen), the charges, plus 1 or more scale parameters. Moreover, all possible type of mass hierarchies can be reproduced within this framework. In a statistically based comparison, the range of r and the small upper limit on U_{e3} are sufficiently constraining to make anarchy neatly disfavoured with respect to models with built-in hierarchy. If only neutrinos are considered, one might counterargue that hierarchical models have at least one more parameter than anarchy, in our case the parameter λ. However, if one looks at quarks and leptons together, as in the GUT models that we consider, then the same parameter that plays the role of an order parameter for the CKM matrix, for example, the Cabibbo angle, can be successfully used to reproduce also the hierarchy implied by the present neutrino data.

9.2. GUT models based on SO(10)

The fermion sector of SO(10) grand unified theories has remarkable properties. It is automatically anomaly-free, independent of the representation content. The RH neutrino provides the completion of a SM family into a 16 representation, thus offering a natural ground for the see-saw mechanism and baryogenesis through leptogenesis. Moreover, the scale of lepton number violation, determined by the gauge symmetry-breaking pattern, can be smaller than the cut-off Λ_c of the theory, and closer to the grand unification scale itself [80], as suggested by the mass scale associated to atmospheric neutrino oscillations.

In their simplest realizations, SO(10) models are left–right symmetric at the GUT scale and we would expect similar mixing angles for quarks and leptons of both chiralities. In left–right symmetric models, smallness of left mixings implies that also right-handed mixings are small, so that all mixings tend to be small, unless non-renormalizable mass operators with a suitable flavour pattern are introduced. In such a context, accommodating the observed mixing properties of quarks and leptons appear more problematic than in SU(5) theories, at first sight.

One possibility is to exploit the see-saw mechanism to enhance the light neutrino mixing angles. As illustrated in equation (38) in a 2×2 context, to have large or even maximal mixing in m_ν, we do not necessarily need large mixing angles in m_D and M. We can obtain a large mixing starting from nearly diagonal mass matrices m_D and M, provided a RH neutrino, equally coupled to ν_μ and ν_τ, is sufficiently light [81, 82] (for an example in the context of SO(10), see e.g. [83]).

Another possibility is to argue that perhaps what appears to be large is not that large after all. The typical small parameter that appears in the mass matrices is $\lambda \sim \sqrt{m_d/m_s} \sim \sqrt{m_\mu/m_\tau} \sim$ 0.20–0.25. This small parameter is not so small that it cannot become large due to some peculiar accidental enhancement: either a coefficient of order 3, or an exponent of the mass ratio which is less than 1/2 (due, for example, to a suitable charge assignment), or the addition in phase of an angle from the diagonalization of charged leptons and an angle from neutrino mixing. Typically, by exploiting the freedom in the parameter space, in this set of models a large θ_{23} may be accommodated. The large mixing angle for solar neutrinos requires however the introduction of *ad hoc* terms, such as for instance higher-dimensional operators contributing to the light neutrino masses independent of the see-saw mechanism [84]–[86].

Alternatively, to avoid the introduction of *ad hoc* non-renormalizable operators, it is possible to enlarge the Higgs content and consider, for example, an SO(10) model where all fermion mass matrices originate from renormalizable interactions of matter fields in three 16 representations with two Higgs multiplets, a 10_H and a 126_H [87]:

$$\mathcal{L}_Y = 10_H 16 y_{10} 16 + 126_H 16 y_{126} 16, \tag{61}$$

where y_{10} and y_{126} are two symmetric matrices in flavour space. Both y_{10} and y_{126} contribute to the Dirac mass matrices, with the characteristic factor 3 for the y_{126} between the (u, d) and (ν, e) sectors:

$$m_d = \alpha y_{10} + \beta y_{126}, \qquad m_e = \alpha y_{10} - 3\beta y_{126}, \tag{62}$$

and the correct mass relations for first and second generations can be accommodated. In the most general case, when 126_H acquires VEVs in its $SU(2)_L$ singlet and triplet components, both RH and LH Majorana masses can arise in the neutrino sector. They are both proportional to y_{126} and give rise to type I and type II see-saw, respectively. By assuming dominance of the type

II contribution, we find an interesting link between large atmospheric mixing angle and b–τ unification [88]. In this case, the light neutrino mass matrix is proportional to y_{126} and, from equation (62), it can be directly related to m_e and m_d:

$$m_\nu \propto m_d - m_e. \tag{63}$$

If both m_e and m_d have the approximate pattern

$$\begin{pmatrix} \lambda^2 & \lambda^2 \\ \lambda^2 & 1 \end{pmatrix} \tag{64}$$

in the 23 sector, then b–τ unification forces a cancellation in the 33 entry of m_ν, thus allowing for a large 23 neutrino mixing angle. Most of the Yukawa parameters can be determined by the quark masses and mixing angles and from the charged lepton masses. This allows to predict the atmospheric and solar mixing parameters within a range which is still experimentally allowed and $|U_{e3}| \approx 0.16$, not far from the present upper bound [89]. A drawback of the model is the occurrence of two pairs of Higgs doublets with non-vanishing VEVs, of which only one combination is allowed to remain light. This clearly makes the doublet–triplet splitting problem even more complicated than in minimal models.

Finally, we can abandon the idea that the model is left–right-symmetric at the GUT scale. In this case, the mechanism discussed in section 8, based on asymmetric mass matrices, can be embedded in an SO(10) grand-unified theory in a rather economic way [15, 62, 84, 90, 91]. The 33 entries of the fermion mass matrices can be obtained through the coupling $\mathbf{16}_3\mathbf{16}_3\mathbf{10}_H$ among the fermions in the third generation, $\mathbf{16}_3$, and a Higgs tenplet $\mathbf{10}_H$. The two independent VEVs of the tenplet v_u and v_d give mass, respectively, to t/v_τ and b/τ. The key point to obtain an asymmetric texture is the introduction of an operator of the kind $\mathbf{16}_2\mathbf{16}_H\mathbf{16}_3\mathbf{16}'_H$. This operator is supposed to arise by integrating out an heavy $\mathbf{10}$ that couples both to $\mathbf{16}_2\mathbf{16}_H$ and to $\mathbf{16}_3\mathbf{16}'_H$. If the $\mathbf{16}_H$ develops a VEV-breaking SO(10) down to SU(5) at a large scale, then, in terms of SU(5) representations, we get an effective coupling of the kind $\bar{\mathbf{5}}_2\mathbf{10}_3\bar{\mathbf{5}}_H$, with a coefficient that can be of order 1. This coupling contributes to the 23 entry of the down-quark mass matrix and to the 32 entry of the charged lepton mass matrix, realizing the desired asymmetry. To distinguish the lepton and quark sectors, one can further introduce an operator of the form $\mathbf{16}_i\mathbf{16}_j\mathbf{10}_H\mathbf{45}_H$ $(i, j = 2, 3)$, with the VEV of the $\mathbf{45}_H$ pointing in the $\mathrm{B} - \mathrm{L}$ direction. Additional operators, still of the type $\mathbf{16}_i\mathbf{16}_j\mathbf{16}_H\mathbf{16}'_H$ can contribute to the matrix elements of the first generation. The mass matrices appear as

$$m_u = \begin{pmatrix} \eta & 0 & 0 \\ 0 & 0 & \epsilon/3 \\ 0 & -\epsilon/3 & 1 \end{pmatrix} v_u, \qquad m_d = \begin{pmatrix} 0 & \delta & \delta' \\ \delta & 0 & \sigma + \epsilon/3 \\ \delta' & -\epsilon/3 & 1 \end{pmatrix} v_d, \tag{65}$$

$$m_D = \begin{pmatrix} \eta & 0 & 0 \\ 0 & 0 & -\epsilon \\ 0 & \epsilon & 1 \end{pmatrix} v_u, \qquad m_l = \begin{pmatrix} 0 & \delta & \delta' \\ \delta & 0 & -\epsilon \\ \delta' & \sigma + \epsilon & 1 \end{pmatrix} v_d, \tag{66}$$

$$M = \begin{pmatrix} b^2\eta^2 & -b\epsilon\eta & a\eta \\ -b\epsilon\eta & \epsilon^2 & -\epsilon \\ a\eta & -\epsilon & 1 \end{pmatrix} \Lambda, \tag{67}$$

where $\eta \ll \delta, \delta' \ll \epsilon \ll 1$ and a, b and σ are of order O(1). In the charged fermion sector, the parameters η, δ, δ', ϵ and σ are determined from the lepton masses and from a subset of quark masses and mixing angles, leading to six successful predictions. In the neutrino sector, the lopsidedness of m_l is responsible for the large atmospheric mixing angle, whereas the parameters a and b can be adjusted to obtain the solar mixing angle and the ratio between solar and atmospheric squared mass differences. The model predicts small values for $|U_{e3}|$, in a range accessible only to future neutrino factories [92].

Models based on SO(10) times a flavour symmetry are more difficult to construct because a whole generation is contained in the 16, so that, for example for $U(1)_F$, one would have the same value of the charge for all quarks and leptons of each generation, which is too rigid. This problem can be circumvented if not all the observed fermions in a given generation belong to a single 16 representation [93].

10. Conclusion

By now there are rather convincing experimental indications for neutrino oscillations. The direct implication of these findings is that neutrino masses are not all vanishing. As a consequence, the phenomenology of neutrino masses and mixings is brought to the forefront. This is a very interesting subject in many respects. It is a window on the physics of GUTs in that the extreme smallness of neutrino masses can only be explained in a natural way if lepton number conservation is violated. If so, neutrino masses are inversely proportional to the large scale where lepton number is violated. Also, the pattern of neutrino masses and mixings interpreted in a GUT framework can provide new clues on the long-standing problem of understanding the origin of the hierarchical structure of quark and lepton mass matrices.

Neutrino oscillations only determine differences of m_i^2 values and the actual scale of neutrino masses remain to be experimentally fixed. The detection of $0\nu\beta\beta$ decay would be extremely important for the determination of the overall scale of neutrino masses, the confirmation of their Majorana nature and the experimental clarification of the ordering of levels in the associated spectrum. The recent results from cosmology indicate that neutrino masses are not a major fraction of the cosmological mass density $\Omega_\nu \lesssim 1.5\%$. The decay of heavy right-handed neutrinos with lepton number non-conservation can provide a viable and attractive model of baryogenesis through leptogenesis. The measured oscillation frequencies and mixings are remarkably consistent with this attractive possibility.

While the existence of oscillations appears to be on a ground of increasing solidity, many important experimental challenges remain. For atmospheric neutrino oscillations the completion of the K2K experiment, which was delayed by the accident that has seriously damaged the Superkamiokande detector, is important for a terrestrial confirmation of the effect and for an independent measurement of the associated parameters. In the near future the experimental study of atmospheric neutrinos will be further pursued with long baseline measurements by MINOS, OPERA, ICARUS. For solar neutrinos the continuation of SNO, KamLAND and the data from Borexino will lead to a more precise determination of the parameters of the LA solution. Finally, a clarification by MINIBOONE of the issue of the LSND alleged signal is necessary to know if 3 light neutrinos are sufficient or additional sterile neutrinos must be introduced, in spite of the apparent lack of independent evidence in the data for such sterile neutrinos and of the fact that attempts of constructing plausible and natural theoretical models have not led so far to compelling

results. Further in the future there are projects for neutrino factories and/or superbeams aimed at precision measurements of the oscillation parameters and possibly the detection of CP violation effects in the neutrino sector.

Pending the solution of the existing experimental ambiguities a variety of theoretical models of neutrino masses and mixings are still conceivable. Among three-neutrino models we have described a number of possibilities based on degenerate, inverted hierarchy and normal hierarchy type of spectra. The normal hierarchy option appears to us as the most straightforward and flexible framework. In particular, the large atmospheric mixing can arise from lopsided matrices. Then the observed frequencies and the large solar angle can also be obtained without fine-tuning in models where the 23 subdeterminant is automatically suppressed.

The fact that some neutrino mixing angles are large and even nearly maximal, while surprising at the start, was eventually found to be well compatible with a unified picture of quark and lepton masses within GUTs. The symmetry group at M_{GUT} could be either (SUSY) SU(5) or SO(10) or a larger group. For example, we have seen that models based on anarchy, semianarchy, inverted hierarchy or normal hierarchy can all be naturally implemented by simple assignments of $\mathrm{U}(1)_F$ horizontal charges in a semiquantitative unified description of all quark and lepton masses in SUSY $\mathrm{SU}(5) \times \mathrm{U}(1)_F$. Actually, in this context, if one adopts a statistical criterium, hierarchical models appear to be preferred over anarchy and among them normal hierarchy appears the most probable. Note that in almost all of the existing models of neutrino mixings the atmospheric angle is large but not maximal. If it experimentally turned out that indeed θ_{23} is maximal with good accuracy then very special classes of models would be selected [27, 43, 94].

All we know about neutrino masses is well in harmony with the idea and the mass scale of GUTs. As a consequence, neutrino masses have added phenomenological support to this beautiful idea and to the models of physics beyond the Standard Model that are compatible with it. In particular, if we consider the main classes of new physics that are currently contemplated, like supersymmetry, technicolour, large extra dimensions at the TeV scale, little Higgs models, etc, it is clear that the first one is the most directly related to GUTs. SUSY offers a well-defined model computable up to the GUT scale and is actually supported by the quantitative success of coupling unification in SUSY GUTs. For the other examples quoted all contact with GUTs is lost or at least is much more remote. In this sense, neutrino masses fit particularly well in the SUSY picture that so far remains the standard way beyond the Standard Model.

Acknowledgments

FF is partially supported by the European Programs HPRN-CT-2000-00148 and HPRN-CT-2000-00149.

References

[1] The SuperKamiokande collaboration 2000 *Phys. Rev. Lett.* **85** 3999
Toshito T [for the SK collaboration] 2001 *Preprint* hep-ex/0105023
The MACRO collaboration 2001 *Phys. Lett.* B **517** 59
Giacomelli G and Giorgini M [for the MACRO collaboration] 2001 *Preprint* hep-ex/0110021

[2] Ahmad Q R *et al* [SNO Collaboration] 2002 *Phys. Rev. Lett.* **89** 011301 (*Preprint* nucl-ex/0204008)
Ahmad Q R *et al* [SNO Collaboration] 2002 *Phys. Rev. Lett.* **89** 011302 (*Preprint* nucl-ex/0204009)

[3] Ahmed S N *et al* [SNO Collaboration] 2003 *Preprint* nucl-ex/0309004
[4] Cleveland B T *et al* 1998 *Astrophys. J.* **496** 505
The GALLEX collaboration 1999 *Phys. Lett.* B **447** 127
The SAGE collaboration 1999 *Phys. Rev.* C **60** 055801
The SuperKamiokande collaboration 2001 *Preprints* hep-ex/0103032 and hep-ex/0103033
The GNO collaboration 2000 *Phys. Lett.* B **490** 16
The SNO collaboration 2001 *Phys. Rev. Lett.* **87** 71301
[5] Yanagida T 1979 *Proc. of the Workshop on Unified Theory and Baryon Number in the Universe* KEK, March
Glashow S L 1980 *Quarks and Leptons* ed M Lévy *et al* (New York: Plenum) p 707
Gell-Mann M, Ramond P and Slansky R 1979 *Supergravity* Stony Brook
Mohapatra R N and Senjanovic G 1980 *Phys. Rev. Lett.* **44** 912
[6] Fukugita M and Yanagida T 1986 *Phys. Lett.* B **174** 45
[7] Eguchi K *et al* [KamLAND Collaboration] 2003 *Phys. Rev. Lett.* **90** 021802 (*Preprint* hep-ex/0212021)
[8] Bennett C L *et al* 2003 *Astrophys. J. Suppl.* **148** 1
Spergel D N *et al* 2003 *Astrophys. J. Suppl.* **148** 175
Kogut A *et al* 2003 *Astrophys. J. Suppl.* **148** 161
Hinshaw G *et al* 2003 *Astrophys. J. Suppl.* **148** 135
Verde L *et al* 2003 *Astrophys. J. Suppl.* **148** 195
Peiris H V *et al* 2003 *Astrophys. J. Suppl.* **148** 213
[9] Hannestad S 2003 *J. Cosmol. Astropart. Phys.* JCAP05(2003)004
Elgaroy O and Lahav O 2003 *J. Cosmol. Astropart. Phys.* JCAP04(2003)004
Hannestad S 2003 *Preprint* hep-ph/0310220
Hannestad S and Raffelt G 2003 *Preprint* hep-ph/0312154
[10] See e.g. Gonzalez-Garcia M C and Nir Y 2003 *Rev. Mod. Phys.* **75** 345 (*Preprint* hep-ph/0202058)
Mohapatra R N 2002 *Preprint* hep-ph/0211252
Grimus W 2003 *Preprint* hep-ph/0307149
King S F 2004 *Rept. Prog. Phys.* **67** 107 (*Preprint* hep-ph/0310204)
[11] The LSND collaboration 2001 *Preprint* hep-ex/0104049
[12] The Karmen collaboration 2000 *Nucl. Phys. Proc. Suppl.* **91** 191
[13] Spentzouris P 2001 *Nucl. Phys. Proc. Suppl.* **100** 163
[14] Altarelli G and Feruglio F 1999 *Phys. Rep.* **320** 295
[15] Barr S M and Dorsner I 2000 *Nucl. Phys.* B **585** 79
Masina I 2001 *Int. J. Mod. Phys.* A **16** 5101
[16] Gaur N, Ghosal A, Ma E and Roy P 1998 *Phys. Rev.* D **58** 071301
Fogli G L, Lisi E and Marrone A 2001 *Phys. Rev.* D **63** 053008
Peres O L and Smirnov A Y 2001 *Nucl. Phys.* B **599** 3
Giunti C 2001 *Nucl. Phys. Proc. Suppl.* **100** 244
Grimus W and Schwetz T 2001 *Eur. Phys. J.* C **20** 1
Gonzalez-Garcia M C, Maltoni M and Pena-Garay C 2001 *Preprint* hep-ph/0108073
Maltoni M, Schwetz T and Valle J W 2001 *Preprint* hep-ph/0112103
Strumia A 2002 *Preprint* hep-ph/0201134
Maltoni M, Schwetz T, Tortola M A and Valle J W 2003 *Preprint* hep-ph/0305312
Cirelli M, Marandella G, Strumia A and Vissani F 2004 *Preprint* hep-ph/0403158
[17] Pontecorvo B 1957 *Sov. Phys. JETP* **6** 429
Pontecorvo B 1957 *Zh. Eksp. Teor. Fiz.* **33** 549
Maki Z, Nakagawa M and Sakata S 1962 *Prog. Theor. Phys.* **28** 870
Pontecorvo B 1968 *Sov. Phys. JETP* **26** 984
Pontecorvo B 1968 *Zh. Eksp. Teor. Fiz.* **53** 1717
Gribov V N and Pontecorvo B 1969 *Phys. Lett.* B **28** 493

[18] Lee B W, Pakvasa S, Shrock R and Sugawara H 1977 *Phys. Rev. Lett.* **38** 937
Lee B W and Shrock R 1977 *Phys. Rev.* D **16** 1444
[19] Cabibbo N 1978 *Phys. Lett.* B **72** 333
[20] Bilenky S M, Hosek J and Petcov S T 1980 *Phys. Lett.* B **94** 495
Schechter J and Valle J W F 1980 *Phys. Rev.* D **22** 2227
Doi M, Kotani T, Nishiura H, Okuda K and Takasugi E 1981 *Phys. Lett.* B **102** 323
[21] Frigerio M and Smirnov A Y 2002 *Nucl. Phys.* B **640** 233
Frigerio M and Smirnov A Y 2003 *Phys. Rev.* D **67** 013007
[22] The CHOOZ collaboration 1999 *Phys. Lett.* B **466** 415
See also The PALO VERDO collaboration 2000 *Phys. Rev. Lett.* **84** 3764
[23] Fogli G L, Lisi E, Montanino D and Palazzo A 2001 *Phys. Rev.* D **64** 093007
Bahcall J N, Gonzalez-Garcia M C and Pena-Garay C 2001 *J. High Energy Phys.* JHEP08(2001)014
Bahcall J N, Gonzalez-Garcia M C and Pena-Garay C 2001 *Preprint* hep-ph/0111150
Barger V, Marfatia D, Whisnant K and Wood B P 2002 *Preprint* hep-ph/0204253
Bandyopadhyay A, Choubey S, Goswami S and Roy D P 2002 *Preprint* hep-ph/0204286
Bahcall J N, Gonzalez-Garcia M C and Pena-Garay C 2002 *Preprint* hep-ph/0204314
Aliani P, Antonelli V, Ferrari R, Picariello M and Torrente-Lujan E 2002 *Preprint* hep-ph/0205053
Fogli G L, Lisi E, Marrone A, Montanino D, Palazzo A and Rotunno A M 2003 *Phys. Rev.* D **67** 073002 (*Preprint* hep-ph/0212127)
Maltoni M, Schwetz T and Valle J W 2003 *Phys. Rev.* D **67** 093003 (*Preprint* hep-ph/0212129)
Bahcall J N, Gonzalez-Garcia M C and Pena-Garay C 2003 *J. High Energy Phys.* JHEP02(2003)009 (*Preprint* hep-ph/0212147)
Bahcall J N and Pena-Garay C 2003 *Preprint* hep-ph/0305159
Fogli G L, Lisi E, Marrone A and Palazzo A 2004 *Phys. Lett.* B **583** 149
Aliani P, Antonelli V, Picariello M and Torrente-Lujan E 2003 *Preprint* hep-ph/0309156
Bandyopadhyay A, Choubey S, Goswami S, Petcov S T and Roy D P 2004 *Phys. Lett.* B **583** 134
de Holanda P C and Smirnov A Y 2003 *Preprint* hep-ph/0309299
[24] Fogli G L, Lisi E and Marrone A 2001 *Phys. Rev.* D **64** 093005
Gonzalez-Garcia M C, Maltoni M and Pena-Garay C 2001 *Preprint* hep-ph/0108073
Gonzalez-Garcia M C and Nir Y 2002 *Preprint* hep-ph/0202058
Fogli G L, Lisi E, Marrone A and Montanino D 2003 *Phys. Rev.* D **67** 093006 (*Preprint* hep-ph/0303064)
[25] Maltoni M, Schwetz T, Tortola M A and Valle J W F 2003 *Phys. Rev.* D **68** 113010
Mena O and Parke S J 2003 *Preprint* hep-ph/0312131
[26] Murayama H and Yanagida T 2001 *Phys. Lett.* B **520** 263
Barenboim G, Borissov L, Lykken J and Smirnov A Y 2001 *Preprint* hep-ph/0108199
Gouvea A D 2002 *Preprint* hep-ph/0204077
Strumia A 2002 *Preprint* hep-ph/0201134
[27] Harrison P F, Perkins D H and Scott W G 2002 *Phys. Lett.* B **530** 167
Harrison P F and Scott W G 2002 *Phys. Lett.* B **535** 163
Harrison P F and Scott W G 2003 *Phys. Lett.* B **557** 76
Harrison P F and Scott W G 2004 *Preprint* hep-ph/0403278
[28] Weinberg S 1979 *Phys. Rev. Lett.* **43** 1566
[29] Weinheimer C, these Proceedings
[30] The HEIDELBERG–MOSCOW collaboration, Klapdor-Kleingrothaus H V *et al* 2001 *Eur. Phys. J.* A **12** 147
Aalseth C E *et al* [16EX Collaboration] 2002 *Preprint* hep-ex/0202026
[31] Bilenky S M 2004 *Preprint* hep-ph/0403245
[32] Petcov S T and Smirnov A Y 1994 *Phys. Lett.* B **322** 109
Bilenky S M, Bottino A, Giunti C and Kim C W 1996 *Phys. Rev.* D **54** 1881
Bilenky S M, Giunti C, Kim C W and Petcov S T 1996 *Phys. Rev.* D **54** 4432
Vissani F 1999 *J. High Energy Phys.* JHEP06(1999)22

Fukuyama T, Matsuda K and Nishiura H 1998 *Phys. Rev.* D **57** 5884
Barger V D and Whisnant K 1999 *Phys. Lett.* B **456** 194
Vissani F 1999 *Preprint* hep-ph/9904349
Giunti C 2000 *Phys. Rev.* D **61** 036002
Czakon M, Gluza J and Zralek M 1999 *Phys. Lett.* B **465** 211
Bilenky S M, Giunti C, Grimus W, Kayser B and Petcov S T 1999 *Phys. Lett.* B **465** 193
Klapdor-Kleingrothaus H V, Pas H and Smirnov A Y 2001 *Phys. Rev.* D **63** 73005
Rodejohann W 2001 *Nucl. Phys.* B **597** 110
Matsuda K, Takeda N, Fukuyama T and Nishiura H 2001 *Phys. Rev.* D **64** 13001
Falcone D and Tramontano F 2001 *Phys. Rev.* D **64** 077302
Bilenky S M, Pascoli S and Petcov S T 2001 *Phys. Rev.* D **64** 53010
Bilenky S M, Pascoli S and Petcov S T 2001 *Phys. Rev.* D **64** 113003
Osland P and Vigdel G 2001 *Phys. Lett.* B **520** 143
Pascoli S, Petcov S T and Wolfenstein L 2002 *Phys. Lett.* B **524** 319
Pascoli S and Petcov S T 2002 *Preprint* hep-ph/0205022
[33] Feruglio F, Strumia A and Vissani F 2002 *Preprint* hep-ph/0201291
[34] Klapdor-Kleingrothaus H V *et al* 2001 *Mod. Phys. Lett.* A **37** 2409
Klapdor-Kleingrothaus H V, Dietz A, Krivosheina I V and Chkvorets O 2004 *Nucl. Instrum. Methods* A **522** 371
Klapdor-Kleingrothaus H V, Dietz A, Krivosheina I V and Chkvorets O 2004 *Phys. Lett.* B **586** 198
[35] For a review see e.g. Trodden M 1999 *Rev. Mod. Phys.* **71** 1463
[36] Kainulainen K and Olive K A *Neutrino Mass (Springer Tracts in Modern Physics)* ed G Altarelli and K Winter (Berlin: Springer)
[37] Luty M A 1992 *Phys. Rev.* D **45** 455
Murayama H and Yanagida T 1994 *Phys. Lett.* B **322** 349
Flanz M, Paschos E A and Sarkar U 1995 *Phys. Lett.* B **345** 248
Flanz M, Paschos E A and Sarkar U 1995 *Phys. Lett.* B **382** 447 (erratum)
Covi L, Roulet E and Vissani F 1996 *Phys. Lett.* B **384** 169
Ma E and Sarkar U 1998 *Phys. Rev. Lett.* **80** 5716
Pilaftsis A 1999 *Int. J. Mod. Phys.* A **14** 1811
Riotto A and Trodden M 1999 *Ann. Rev. Nucl. Part. Sci.* **49** 35
Ellis J R, Lola S and Nanopoulos D V 1999 *Phys. Lett.* B **452** 87
Giudice G F, Peloso M, Riotto A and Tkachev I 1999 *J. High Energy Phys.* JHEP08(1999)014
Barbieri R, Creminelli P, Strumia A and Tetradis N 2000 *Nucl. Phys.* B **575** 61
Falcone D and Tramontano F 2001 *Phys. Lett.* B **506** 1
Nielsen H B and Takanishi Y 2001 *Phys. Lett.* B **507** 241
Joshipura A S, Paschos E A and Rodejohann W 2001 *J. High Energy Phys.* JHEP08(2001)029
Brahmachari B, Ma E and Sarkar U 2001 *Phys. Lett.* B **520** 152
Hirsch M and King S F 2001 *Phys. Rev.* D **64** 113005
Buccella F, Falcone D and Tramontano F 2002 *Phys. Lett.* B **524** 241
Buchmuller W and Wyler D 2001 *Phys. Lett.* B **521** 291
Garcia-Bellido J and Ruiz Morales E 2002 *Phys. Lett.* B **536** 193
Berger M S and Siyeon K 2002 *Phys. Rev.* D **65** 053019
Branco G C, Gonzalez Felipe R, Joaquim F R and Rebelo M N 2002 *Nucl. Phys.* B **640** 202
Fujii M, Hamaguchi K and Yanagida T 2002 *Phys. Rev.* D **65** 115012
Paschos E A 2002 *Nucl. Phys. Proc. Suppl.* **112** 36 (*Preprint* hep-ph/0204137)
Buchmuller W 2001 Lectures given at European School of High-Energy Physics (ESHEP) *Beatenberg, Switzerland, 26 August–8 September 2001* published in Beatenberg 2001, High-Energy Physics, p 205–47
Akhmedov E K, Frigerio M and Smirnov A Y 2003 *J. High Energy Phys.* JHEP09(2003)021

Buchmuller W, Di Bari P and Plumacher M 2003 *Nucl. Phys.* B **665** 445 (*Preprint* hep-ph/0302092)
Chankowski P H and Turzynski K 2003 *Phys. Lett.* B **570** 198
Velasco-Sevilla L 2003 *J. High Energy Phys.* JHEP10(2003)035
Hambye T and Senjanovic G 2004 *Phys. Lett.* B **582** 73
Barger V, Dicus D A, He H J and Li T J 2004 *Phys. Lett.* B **583** 173
Rodejohann W 2004 *Eur. Phys. J.* C **32** 235
Ibe M, Kitano R, Murayama H and Yanagida T 2004 *Preprint* hep-ph/0403198
Cosme N 2004 *Preprint* hep-ph/0403209
[38] Plumacher M 1997 *Z. Phys.* C **74** 549
Buchmuller W and Plumacher M 1999 *Phys. Rep.* **320** 329
Buchmuller W and Plumacher M 2000 *Int. J. Mod. Phys.* A **15** 5047
[39] Davidson S and Ibarra A 2002 *Phys. Lett.* B **535** 25
[40] Giudice G F, Notari A, Raidal M, Riotto A and Strumia A 2004 *Nucl. Phys.* B **685** 89
Buchmuller W, Di Bari P and Plumacher M 2004 *Preprint* hep-ph/0401240
[41] Pilaftsis A and Underwood T E J 2003 *Preprint* hep-ph/0309342
Hambye T, Lin Y, Notari A, Papucci M and Strumia A 2003 *Preprint* hep-ph/0312203
[42] Jezabek M 2002 *Preprint* hep-ph/0205234
[43] Wetterich C 1999 *Phys. Lett.* B **451** 397
[44] Ioannisian A and Valle J W F 1994 *Phys. Lett.* B **332** 93
Mohapatra R N and Nussinov S 1999 *Phys. Rev.* D **60** 013002
Mohapatra R N and Nussinov S 1998 *Phys. Lett.* B **441** 299
Branco G C, Rebelo M N and Silva-Marcos J I 2000 *Phys. Rev.* D **62** 073004
Perez G 2000 *J. High Energy Phys.* JHEP12(2000)027
[45] Barbieri R, Hall L J, Kane G L and Ross G G 1999 *Preprint* hep-ph/9901228
[46] Antusch S and King S F 2004 *Preprint* hep-ph/0402121
[47] Chankowski P H and Pluciennik Z 1993 *Phys. Lett.* B **316** 312
Babu K S, Leung C N and Pantaleone J 1993 *Phys. Lett.* B **319** 191
Tanimoto M 1995 *Phys. Lett.* B **360** 41
Haba N, Okamura N and Sugiura M 2000 *Prog. Theor. Phys.* **103** 367
Ellis J R and Lola S 1999 *Phys. Lett.* B **458** 310
Haba N, Matsui Y, Okamura N and Sugiura M 1999 *Eur. Phys. J.* C **10** 677
Casas J A, Espinosa J R, Ibarra A and Navarro I 1999 *Nucl. Phys.* B **556** 3
Casas J A, Espinosa J R, Ibarra A and Navarro I 2000 *Nucl. Phys.* B **569** 82
Casas J A, Espinosa J R, Ibarra A and Navarro I 1999 *J. High Energy Phys.* JHEP09(1999)015
Barbieri R, Ross G G and Strumia A 1999 *J. High Energy Phys.* JHEP10(1999)020
Haba N and Okamura N 2000 *Eur. Phys. J.* C **14** 347
Haba N, Matsui Y, Okamura N and Sugiura M 2000 *Prog. Theor. Phys.* **103** 145
Chankowski P H, Krolikowski W and Pokorski S 2000 *Phys. Lett.* B **473** 109
Casas J A, Espinosa J R, Ibarra A and Navarro I 2000 *Nucl. Phys.* B **573** 652
Haba N, Matsui Y and Okamura N 2000 *Prog. Theor. Phys.* **103** 807
Kuo T K, Pantaleone J and Wu G H 2001 *Phys. Lett.* B **518** 101
Chankowski P H and Pokorski S 2002 *Int. J. Mod. Phys.* A **17** 575
Antusch S, Kersten J, Lindner M and Ratz M 2002 *Phys. Lett.* B **538** 87
Frigerio M and Smirnov A Y 2003 *J. High Energy Phys.* JHEP02(2003)004
Antusch S, Kersten J, Lindner M and Ratz M 2003 *Nucl. Phys.* B **674** 401
Casas J A, Espinosa J R and Navarro I 2003 *J. High Energy Phys.* JHEP09(2003)048
Broncano A, Gavela M B and Jenkins E 2004 *Preprint* hep-ph/0406019
Hagedorn C, Kersten J and Lindner M 2004 *Preprint* hep-ph/0406103
[48] Vissani F 1997 *Preprint* hep-ph/9708483
Georgi H and Glashow S L 2000 *Phys. Rev.* D **61** 097301

[49] Barbieri R, Ross G G and Strumia A 1999 *J. High Energy Phys.* JHEP10(1999)020
[50] Fritzsch H and Xing Z Z 1996 *Phys. Lett.* B **372** 265
Fritzsch H and Xing Z Z 1998 *Phys. Lett.* B **440** 313
Fritzsch H and Xing Z Z 2000 *Prog. Part. Nucl. Phys.* **45** 1
Fukugita M, Tanimoto M and Yanagida T 1998 *Phys. Rev.* D **57** 4429
Fukugita M, Tanimoto M and Yanagida T 1999 *Phys. Rev.* D **59** 113016
Tanimoto M, Watari T and Yanagida T 1999 *Phys. Lett.* B **461** 345
Kang S K and Kim C S 1999 *Phys. Rev.* D **59** 091302
Tanimoto M 2000 *Phys. Lett.* B **483** 417
Haba N, Matsui Y, Okamura N and Suzuki T 2000 *Phys. Lett.* B **489** 184
Koide Y and Ghosal A 2000 *Phys. Lett.* B **488** 344
Akhmedov E K, Branco G C, Joaquim F R and Silva-Marcos J I 2001 *Phys. Lett.* B **498** 237
Dermisek R 2003 *Preprint* hep-ph/0312206
[51] Altarelli G, Feruglio F and Masina I 2004 *Preprint* hep-ph/0402155
[52] Antusch S and King S F 2004 *Preprint* hep-ph/0403053
[53] Romanino A 2004 *Preprint* hep-ph/0402258
[54] Hall L J, Murayama H and Weiner N 2000 *Phys. Rev. Lett.* **84** 2572
Haba N and Murayama H 2001 *Phys. Rev.* D **63** 053010
Berger M S and Siyeon K 2001 *Phys. Rev.* D **63** 057302
Hirsch M 2001 *Preprint* hep-ph/0102102
Hirsch M and King S F 2001 *Phys. Lett.* B **516** 103 (*Preprint* hep-ph/0102103)
Vissani F 2001 *Phys. Lett.* B **508** 79
de Gouvea A and Murayama H 2003 *Preprint* hep-ph/0301050
Espinosa J R 2003 *Preprint* hep-ph/0306019
[55] Barbieri R, Hall L J, Smith D R, Strumia A and Weiner N 1998 *J. High Energy Phys.* JHEP12(1998)017
Barbieri R, Hall L J and Strumia A 1999 *Phys. Lett.* B **445** 407
See also Zeldovich Ya B 1952 *Dokl. Akad. Nauk. CCCP* **86** 505
Konopinsky E J and Mahmound H 1953 *Phys. Rev.* **92** 1045
Zee A 1980 *Phys. Lett.* B **93** 389
Petcov S 1982 *Phys. Lett.* B **100** 245
Joshipura A S and Rindani S D 2000 *Eur. Phys. J.* C **14** 85
Mohapatra R N, Perez-Lorenzana A and de Sousa Pires C A 2000 *Phys. Lett.* B **474** 355
Shafi Q and Tavartkiladze Z 2000 *Phys. Lett.* B **482** 145 (*Preprint* hep-ph/0101350)
Ghosal A 2000 *Phys. Rev.* D **62** 092001
Lavoura L 2000 *Phys. Rev.* D **62** 093011
Lavoura L and Grimus W 2000 *J. High Energy Phys.* JHEP09(2000)007
Lavoura L and Grimus W 2000 *Phys. Rev.* D **62** 093012
King S F and Singh N N 2001 *Nucl. Phys.* B **596** 81
Oliver J F and Santamaria A 2002 *Phys. Rev.* D **65** 033003
Babu K S and Mohapatra R N 2002 *Preprint* hep-ph/0201176
[56] Dorsner I and Barr S M 2001 *Nucl. Phys.* B **617** 493
[57] He H J, Dicus D A and Ng J N 2002 *Phys. Lett.* B **536** 83
[58] Raidal M 2004 *Preprint* hep-ph/0404046
[59] Frampton P H, Petcov S T and Rodejohann W 2004 *Preprint* hep-ph/0401206
[60] King S F 1998 *Phys. Lett.* B **439** 350
Davidson S and King S F 1998 *Phys. Lett.* B **445** 191
Shafi Q and Tavartkiladze Z 1999 *Phys. Lett.* B **451** 129
[61] King S F 1999 *Nucl. Phys.* B **562** 57
King S F 2000 *Nucl. Phys.* B **576** 85 (*Preprint* hep-ph/0204360)
Frampton P H, Glashow S L and Yanagida T 2002 *Phys. Lett.* B **548** 119 (*Preprint* hep-ph/0208157)

Raidal M and Strumia A 2003 *Phys. Lett.* B **553** 72 (*Preprint* hep-ph/0210021)
Raby S 2003 *Phys. Lett.* B **561** 119 (*Preprint* hep-ph/0302027)
King S F 2003 Invited talk at *10th Int. Workshop on Neutrino Telescopes, Venice, Italy, 11–14 March* (*Preprint* hep-ph/0306095)
[62] Babu K S and Barr S M 1996 *Phys. Lett.* B **381** 202
Albright C H and Barr S M 1998 *Phys. Rev.* D **58** 013002
Albright C H, Babu K S and Barr S M 1998 *Phys. Rev. Lett.* **81** 1167
Frampton P H and Rasin A 2000 *Phys. Lett.* B **478** 424
[63] Irges N, Lavignac S and Ramond P 1998 *Phys. Rev.* D **58** 035003
[64] Altarelli G and Feruglio F 1998 *Phys. Lett.* B **439** 112
Altarelli G and Feruglio F 1998 *J. High Energy Phys.* JHEP11(1998)021
[65] Altarelli G and Feruglio F 1999 *Phys. Lett.* B **451** 388
[66] Sato J and Yanagida T 1998 *Phys. Lett.* B **430** 127
Elwood J K, Irges N and Ramond P 1998 *Phys. Rev. Lett.* **81** 5064
Berezhiani Z and Rossi A 1999 *J. High Energy Phys.* JHEP03(1999)002
Hagiwara K and Okamura N 1999 *Nucl. Phys.* B **548** 60
Bando M and Kugo T 1999 *Prog. Theor. Phys.* **101** 1313
Grimus W and Lavoura L 2001 *J. High Energy Phys.* JHEP07(2001)045 (*Preprint* hep-ph/0204070)
[67] Georgi H and Jarlskog C 1979 *Phys. Lett.* B **86** 297
[68] Drees M, Pakvasa S, Tata X and ter Veldhuis T 1998 *Phys. Rev.* D **57** 5335
Chun E J, Kang S K, Kim C W and Lee U W 1999 *Nucl. Phys.* B **544** 89
Mukhopadhyaya B, Roy S and Vissani F 1998 *Phys. Lett.* B **443** 191
Kong O C 1999 *Mod. Phys. Lett.* A **14** 903
Bisset M, Kong O C, Macesanu C and Orr L H 2000 *Phys. Rev.* D **62** 035001
Joshipura A S and Vempati S K 1999 *Phys. Rev.* D **60** 111303
Datta A, Mukhopadhyaya B and Roy S 2000 *Phys. Rev.* D **61** 055006
Mukhopadhyaya B 2000 *Pramana* **54** 147
Bhattacharyya G, Klapdor-Kleingrothaus H V and Pas H 1999 *Phys. Lett.* B **463** 77
Romao J C, Diaz M A, Hirsch M, Porod W and Valle J W 2000 *Phys. Rev.* D **61** 071703
Abada A and Losada M 2000 *Nucl. Phys.* B **585** 45
Davidson S and Losada M 2000 *J. High Energy Phys.* JHEP05(2000)021
Abada A and Bhattacharyya G 2001 *Phys. Rev.* D **63** 017701
Barger V D, Han T, Hesselbach S and Marfatia D 2001 *Preprint* hep-ph/0108261
Koide Y and Ghosal A 2002 *Preprint* hep-ph/0203113
[69] Kaplan D B and Schmaltz M 1994 *Phys. Rev.* D **49** 3741
Schmaltz M 1995 *Phys. Rev.* D **52** 1643
Frampton P H and Kephart T W 1995 *Int. J. Mod. Phys.* A **10** 4689
Chou K C and Wu Y L 1996 *Phys. Rev.* D **53** 3492
Frampton P H and Kong O C 1996 *Phys. Rev. Lett.* **77** 1699
Babu K S and Barr S M 1996 *Phys. Lett.* B **387** 87
Barbieri R, Hall L J, Raby S and Romanino A 1997 *Nucl. Phys.* B **493** 3
Barbieri R, Hall L J and Romanino A 1997 *Phys. Lett.* B **401** 47
Blazek T, Raby S and Tobe K 1999 *Phys. Rev.* D **60** 113001
Carone C D and Lebed R F 1999 *Phys. Rev.* D **60** 096002
Frampton P H and Rasin A 2000 *Phys. Lett.* B **478** 424
Dermisek R and Raby S 2000 *Phys. Rev.* D **62** 015007
Aranda A, Carone C D and Lebed R F 2000 *Phys. Rev.* D **62** 016009
Aranda A, Carone C D and Lebed R F 2000 *Phys. Lett.* B **474** 170
Falcone D 2001 *Phys. Rev.* D **64** 117302
Aranda A, Carone C D and Meade P 2002 *Phys. Rev.* D **65** 013011

Aranda A, Carone C D and Meade P 2001 *Phys. Rev.* D **64** 117302
Koide Y and Ghosal A 2001 *Phys. Rev.* D **63** 037301
Ross G G and Velasco-Sevilla L 2003 *Nucl. Phys.* B **653** 3 (*Preprint* hep-ph/0208218)
[70] Kawamura Y 2001 *Prog. Theor. Phys.* **105** 999
Altarelli G and Feruglio F 2001 *Phys. Lett.* B **511** 257
Hall L J and Nomura Y 2001 *Phys. Rev.* D **64** 055003
Hebecker A and March-Russell J 2001 *Nucl. Phys.* B **613** 3
Asaka T, Buchmuller W and Covi L 2001 *Phys. Lett.* B **523** 199
Hall L J, Nomura Y, Okui T and Smith D R 2002 *Phys. Rev.* D **65** 035008
Contino R, Pilo L, Rattazzi R and Trincherini E 2002 *Nucl. Phys.* B **622** 227
Dermisek R and Mafi A 2002 *Phys. Rev.* D **65** 055002
Watari T and Yanagida T 2001 *Phys. Lett.* B **519** 164
Hall L J and Nomura Y 2002 *Phys. Rev.* D **65** 125012
Huang C S, Jiang J, Li T J and Liao W 2002 *Phys. Lett.* B **530** 218
Hebecker A and March-Russell J 2002 *Phys. Lett.* B **539** 119
Asaka T, Buchmuller W and Covi L 2002 *Phys. Lett.* B **540** 295
Hall L J and Nomura Y 2002 *Phys. Rev.* D **66** 075004
Barr S M and Dorsner I 2002 *Phys. Rev.* D **66** 065013
Hall L J and Nomura Y 2002 *Preprint* hep-ph/0207079
Hall L J and Nomura Y 2003 *Ann. Phys.* **306** 132
[71] Froggatt C D and Nielsen H B 1979 *Nucl. Phys.* B **147** 277
[72] Fusaoka H and Koide Y 1998 *Phys. Rev.* D **57** 3986
[73] Bijnens J and Wetterich C 1987 *Nucl. Phys.* B **147** 292
Leurer M, Nir Y and Seiberg N 1993 *Nucl. Phys.* B **398** 319
Leurer M, Nir Y and Seiberg N 1994 *Nucl. Phys.* B **420** 468
Ibanez L E and Ross G G 1994 *Phys. Lett.* B **332** 100
Binetruy P and Ramond P 1995 *Phys. Lett.* B **350** 49
Dudas E, Pokorski S and Savoy C A 1995 *Phys. Lett.* B **356** 45
Leontaris G K and Rizos J 2000 *Nucl. Phys.* B **567** 32
Mira J M, Nardi E and Restrepo D A 2000 *Phys. Rev.* D **62** 016002
[74] Binetruy P, Lavignac S and Ramond P 1996 *Nucl. Phys.* B **477** 353
Binetruy P, Lavignac S, Petcov S T and Ramond P 1997 *Nucl. Phys.* B **496** 3
Berezhiani Z and Tavartkiladze Z 1997 *Phys. Lett.* B **396** 150
Jezabek M and Sumino Y 1998 *Phys. Lett.* B **440** 327
Grossman Y, Nir Y and Shadmi Y 1998 *J. High Energy Phys.* JHEP10(1998)007
Buchmuller W and Yanagida T 1999 *Phys. Lett.* B **445** 399
Froggatt C D, Gibson M and Nielsen H B 1999 *Phys. Lett.* B **446** 256
Choi K, Hwang K and Chun E J 1999 *Phys. Rev.* D **60** 031301
Lola S and Ross G G 1999 *Nucl. Phys.* B **553** 81
Nir Y and Shadmi Y 1999 *J. High Energy Phys.* JHEP05(1999)023
Stech B 2000 *Phys. Rev.* D **62** 093019
King S F and Oliveira M 2001 *Phys. Rev.* D **63** 095004
Tanimoto M 2001 *Phys. Lett.* B **501** 231
Bando M and Maekawa N 2001 *Prog. Theor. Phys.* **106** 1255
Nielsen H B and Takanishi Y 2001 *Phys. Scripta T* **93** 44
[75] Altarelli G, Feruglio F and Masina I 2000 *J. High Energy Phys.* JHEP11(2000)040
[76] Altarelli G, Feruglio F and Masina I 2003 *J. High Energy Phys.* JHEP01(2003)035 (*Preprint* hep-ph/0210342)
[77] Barbieri R, Hambye T and Romanino A 2003 *J. High Energy Phys.* JHEP03(2003)017 (*Preprint* hep-ph/0302118)

[78] Lavignac S, Masina I and Savoy C A 2002 *Nucl. Phys.* B **633** 139 (*Preprint* hep-ph/0202086)
[79] Borzumati F and Masiero A 1986 *Phys. Rev. Lett.* **57** 961
Hisano J, Moroi T, Tobe K, Yamaguchi M and Yanagida T 1995 *Phys. Lett.* B **357** 579
Hisano J, Moroi T, Tobe K and Yamaguchi M 1996 *Phys. Rev.* D **53** 2442
Hisano J and Nomura D 1999 *Phys. Rev.* D **59** 116005
Buchmuller W, Delepine D and Vissani F 1999 *Phys. Lett.* B **459** 171
Feng J L, Nir Y and Shadmi Y 2000 *Phys. Rev.* D **61** 113005
Ellis J R, Gomez M E, Leontaris G K, Lola S and Nanopoulos D V 2000 *Eur. Phys. J.* C **14** 319
Buchmuller W, Delepine D and Handoko L T 2000 *Nucl. Phys.* B **576** 445
Sato J, Tobe K and Yanagida T 2001 *Phys. Lett.* B **498** 189
Sato J and Tobe K 2001 *Phys. Rev.* D **63** 116010
Casas J A and Ibarra A 2001 *Nucl. Phys.* B **618** 171
Lavignac S, Masina I and Savoy C A 2001 *Phys. Lett.* B **520** 269
Kageyama A, Kaneko S, Shimoyama N and Tanimoto M 2002 *Phys. Lett.* B **527** 206
Lavignac S, Masina I and Savoy C A 2002 *Nucl. Phys.* B **633** 139
Masiero A, Vempati S K and Vives O 2003 *Nucl. Phys.* B **649** 189
Babu K S, Dutta B and Mohapatra R N 2003 *Phys. Rev.* D **67** 076006
Blazek T and King S F 2003 *Nucl. Phys.* B **662** 359
Petcov S T, Profumo S, Takanishi Y and Yaguna C E 2004 *Nucl. Phys.* B **676** 453
Barr S M 2004 *Phys. Lett.* B **578** 394
[80] See e.g. Buccella F and Savoy C A 2002 *Mod. Phys. Lett.* A **17** 1239
[81] Smirnov A Y 1993 *Phys. Rev.* D **48** 3264
Altarelli G, Feruglio F and Masina I 2000 *Phys. Lett.* B **472** 382
[82] Dorsner I and Smirnov A Y 2004 *Preprint* hep-ph/0403305
[83] Chen M C and Mahanthappa K T 2003 *Phys. Rev.* D **68** 017301
Chen M C and Mahanthappa K T 2003 *Int. J. Mod. Phys.* A **18** 5819
[84] Babu K S, Pati J C and Wilczek F 2000 *Nucl. Phys.* B **566** 33
[85] See e.g. Lola S and Ross G G 1999 *Nucl. Phys.* B **553** 81
[86] Pati J C 2002 *Preprint* hep-ph/0204240
Pati J C 2003 *Int. J. Mod. Phys.* A **18** 4135
[87] Babu K S and Mohapatra R N 1993 *Phys. Rev. Lett.* **70** 2845
Lee D G and Mohapatra R N 1995 *Phys. Rev.* D **51** 1353
Brahmachari B and Mohapatra R N 1998 *Phys. Rev.* D **58** 015001
Matsuda K, Koide Y, Fukuyama T and Nishiura H 2002 *Phys. Rev.* D **65** 033008
Matsuda K, Koide Y, Fukuyama T and Nishiura H 2002 *Phys. Rev.* D **65** 079904 (erratum)
Fukuyama T and Okada N 2002 *J. High Energy Phys.* JHEP11(2002)011
[88] Bajc B, Senjanovic G and Vissani F 2003 *Phys. Rev. Lett.* **90** 051802
[89] Goh H S, Mohapatra R N and Ng S P 2003 *Phys. Lett.* B **570** 215
Goh H S, Mohapatra R N and Ng S P 2003 *Phys. Rev.* D **68** 115008
Goh H S, Mohapatra R N, Nasri S and Ng S P 2004 *Phys. Lett.* B **587** 105
Dutta B, Mimura Y and Mohapatra R N 2004 *Preprint* hep-ph/0402113
Bajc B, Senjanovic G and Vissani F 2004 *Preprint* hep-ph/0402140
[90] Harvey J A, Reiss D B and Ramond P 1982 *Nucl. Phys.* B **199** 223
Berezhiani Z and Tavartkiladze Z 1997 *Phys. Lett.* B **409** 220
Brahmachari B and Mohapatra R N 1998 *Phys. Rev.* D **58** 015001
Nomura Y and Yanagida T 1999 *Phys. Rev.* D **59** 017303
Oda K Y, Takasugi E, Tanaka M and Yoshimura M 1999 *Phys. Rev.* D **59** 055001
Singh N N 2000 *Preprint* hep-ph/0009087
Maekawa N 2001 *Prog. Theor. Phys.* **106** 401
Babu K S and Barr S M 2002 *Phys. Lett.* B **525** 289

[91] Albright C H and Barr S M 2000 *Phys. Rev. Lett.* **85** 244
Albright C H and Barr S M 2000 *Phys. Rev.* D **62** 093008
Albright C H and Barr S M 2001 *Phys. Rev.* D **64** 073010
[92] Albright C H and Geer S 2002 *Phys. Rev.* D **65** 073004
Albright C H and Geer S 2002 *Phys. Lett.* B **532** 311
Albright C H 2003 *Int. J. Mod. Phys.* A **18** 3947
[93] Asaka T 2003 *Phys. Lett.* B **562** 291
[94] Grimus W and Lavoura L 2001 *J. High Energy Phys.* JHEP07(2001)045
Grimus W and Lavoura L 2001 *Acta Phys. Polon.* B **32** 3719
Grimus W and Lavoura L 2003 *Eur. Phys. J.* C **28** 123
Grimus W and Lavoura L 2003 *Phys. Lett.* B **572** 189
Grimus W and Lavoura L 2003 *Preprint* hep-ph/0305309
King S F and Ross G G 2001 *Phys. Lett.* B **520** 243
Ohlsson T and Seidl G 2002 *Phys. Lett.* B **537** 95
Ohlsson T and Seidl G 2002 *Nucl. Phys.* B **643** 247
Babu K S, Ma E and Valle J W F 2003 *Phys. Lett.* B **552** 207
Kubo J, Mondragon A, Mondragon M and Rodriguez-Jauregui E 2003 *Prog. Theor. Phys.* **109** 795
Chen S L G, Frigerio M and Ma E 2004 *Preprint* hep-ph/0404084
Ma E 2004 *Preprint* hep-ph/0404199

New Journal of Physics
An Institute of Physics and Deutsche Physikalische Gesellschaft Journal

Neutrinos in cosmology

Steen Hannestad
Department of Physics, University of Southern Denmark, Campusvej 55, DK-5230 Odense M, Denmark
E-mail: hannestad@fysik.sdu.dk

New Journal of Physics **6** (2004) 108
Received 27 April 2004
Published 12 August 2004
Online at http://www.njp.org/
doi:10.1088/1367-2630/6/1/108

Abstract. The current status of neutrino cosmology is reviewed, from the question of neutrino decoupling and the presence of sterile neutrinos to the effects of neutrinos on the cosmic microwave background and large scale structure. Particular emphasis is put on cosmological neutrino mass measurements.

Contents

1. Introduction **2**
2. Cosmological data **2**
3. Neutrino decoupling **3**
3.1. Standard model . . . 3
3.2. Big Bang nucleosynthesis and the number of neutrino species . . . 4
3.3. The number of neutrino species—joint CMB and BBN analysis . . . 5
3.4. The effect of oscillations . . . 5
3.5. Low reheating temperature and neutrinos . . . 6
4. Neutrino dark matter **6**
4.1. The Tremaine–Gunn bound . . . 7
4.2. Neutrino hot dark matter . . . 7
4.2.1. Combining measurements of m_ν and N_ν . . . 10
4.2.2. Future neutrino mass measurements . . . 11
4.3. Neutrino warm dark matter . . . 12
4.4. Neutrinos as the source for high-energy cosmic rays . . . 13
5. Neutrinos in the very early universe—leptogenesis **14**
6. Discussion **15**
Acknowledgments **16**
References **16**

PII: S1367-2630(04)79862-6
© IOP Publishing Ltd and Deutsche Physikalische Gesellschaft

1. Introduction

Next to photons, neutrinos are the most abundant particles in the universe. This means that they have a profound impact on many different aspects of cosmology, from the question of leptogenesis in the very early universe, over Big Bang nucleosynthesis, to late-time structure formation. In the present review we focus mainly on late-time aspects of neutrino cosmology, and particularly on issues relevant to cosmological bounds on the neutrino mass.

The absolute value of neutrino masses are very difficult to measure experimentally. On the other hand, mass differences between neutrino mass eigenstates, (m_1, m_2, m_3), can be measured in neutrino oscillation experiments.

The combination of all currently available data suggests two important mass differences in the neutrino mass hierarchy. The solar mass difference of $\delta m_{12}^2 \simeq 7 \times 10^{-5}\,\mathrm{eV}^2$ and the atmospheric mass difference $\delta m_{23}^2 \simeq 2.6 \times 10^{-3}\,\mathrm{eV}^2$ [1]–[3].

In the simplest case, where neutrino masses are hierarchical, these results suggest that $m_1 \sim 0$, $m_2 \sim \delta m_{\mathrm{solar}}$ and $m_3 \sim \delta m_{\mathrm{atmospheric}}$. If the hierarchy is inverted [4]–[9], one instead finds $m_3 \sim 0$, $m_2 \sim \delta m_{\mathrm{atmospheric}}$ and $m_1 \sim \delta m_{\mathrm{atmospheric}}$. However, it is also possible that neutrino masses are degenerate [10]–[20], $m_1 \sim m_2 \sim m_3 \gg \delta m_{\mathrm{atmospheric}}$, in which case oscillation experiments are not useful for determining the absolute mass scale.

Experiments which rely on kinematical effects of the neutrino mass offer the strongest probe of this overall mass scale. Tritium decay measurements have been able to put an upper limit on the electron neutrino mass of 2.3 eV (95% confidence level (CL)) [21]. However, cosmology at present yields a much stronger limit which is also based on the kinematics of neutrino mass.

Very interestingly, there is also a claim of direct detection of neutrinoless double beta decay in the Heidelberg–Moscow experiment [22, 23], corresponding to an effective neutrino mass in the 0.1–0.9 eV range. If this result is confirmed, then it shows that neutrino masses are almost degenerate and well within reach of cosmological detection in the near future.

Another important question which can be answered by cosmological observations is how large the total neutrino energy density is. Apart from the standard model prediction of three light neutrinos, such energy density can be either in the form of additional, sterile neutrino degrees of freedom, or a non-zero neutrino chemical potential.

The paper is organized as follows. In section 2, we review the present cosmological data which can be used for analysis of neutrino physics. In section 3, we discuss neutrino physics around the epoch of neutrino decoupling at a temperature of roughly 1 MeV, including the relation between neutrinos and Big Bang nucleosynthesis. Section 4 discusses neutrinos as dark matter particles, including mass constraints on light neutrinos, and sterile neutrino dark matter. Section 5 contains a relatively short review of neutrino physics in the very early universe from the perspective of leptogenesis. Finally, section 6 contains a discussion.

2. Cosmological data

Large-scale structure (LSS). At present, there are two large galaxy surveys of comparable size: the Sloan Digital Sky Survey (SDSS) [24, 25] and the 2dFGRS (2 degree Field Galaxy Redshift Survey) [26]. Once the SDSS is completed in 2005, it will be significantly larger and more accurate than the 2dFGRS. At present, the two surveys are, however, comparable in precision.

Cosmic microwave background (CMB). The temperature fluctuations are conveniently described in terms of the spherical harmonics power spectrum $C_{T,l} \equiv \langle |a_{lm}|^2 \rangle$, where $\Delta T(\theta, \phi)/T(\theta, \phi) = \sum_{lm} a_{lm} Y_{lm}(\theta, \phi)$. Since Thomson scattering polarizes light, there are also power spectra coming from the polarization. The polarization can be divided into a curl-free (E) and a curl (B) component, yielding four independent power spectra: $C_{T,l}$, $C_{E,l}$, $C_{B,l}$ and the T–E cross-correlation $C_{TE,l}$.

The WMAP experiment has reported data only on $C_{T,l}$ and $C_{TE,l}$ as described in [27]–[32]. Foreground contamination has already been subtracted from their published data.

In addition to the WMAP experiment, there are a number of other current CMB experiments, both ground and balloon based. Wang *et al* [34] have provided a compilation of various data sets, and in addition to these there is the ACBAR experiment [33] which has measured the CMB at small scales.

Other data. Apart from CMB and LSS data there are a number of other cosmological measurements of importance to neutrino cosmology. One is the measurement of the Hubble constant by the HST Hubble Key Project, $H_0 = 72 \pm 8\,\mathrm{km\,s^{-1}\,Mpc^{-1}}$ [35].

The constraint on the matter density coming from measurements of distant type Ia supernovae is also important for neutrino physics. The most recent result is from the Supernova Cosmology Project [36] and yields $\Omega_m = 0.25^{+0.07}_{-0.06}$ (statistical) ± 0.04 (identified systematics).

3. Neutrino decoupling

3.1. Standard model

In the standard model, neutrinos interact via weak interactions with e^+ and e^-. In the absence of oscillations, neutrino decoupling can be followed via the Boltzmann equation for the single particle distribution function [37]

$$\frac{\partial f}{\partial t} - Hp\frac{\partial f}{\partial p} = C_{\mathrm{coll}}, \tag{1}$$

where C_{coll} represents all elastic and inelastic interactions. In the standard model, all these interactions are $2 \leftrightarrow 2$ interactions in which case the collision integral for process i can be written

$$C_{\mathrm{coll,i}}(f_1) = \frac{1}{2E_1}\int \frac{\mathrm{d}^3\boldsymbol{p}_2}{2E_2(2\pi)^3}\frac{\mathrm{d}^3\boldsymbol{p}_3}{2E_3(2\pi)^3}\frac{\mathrm{d}^3\boldsymbol{p}_4}{2E_4(2\pi)^3} \times (2\pi)^4\delta^4(p_1 + p_2 - p_3 + p_4)\Lambda(f_1, f_2, f_3, f_4)S|M|^2_{12\to 34,i}, \tag{2}$$

where $S|M|^2_{12\to 34,i}$ is the spin-summed and -averaged matrix element including the symmetry factor $S = 1/2$ if there are identical particles in the initial or final states. The phase-space factor will be $\Lambda(f_1, f_2, f_3, f_4) = f_3 f_4(1 - f_1)(1 - f_2) - f_1 f_2(1 - f_3)(1 - f_4)$.

The matrix elements for all relevant processes can, for instance, be found in [38]. If Maxwell–Boltzmann statistics is used for all the particles, and neutrinos are assumed to be in complete scattering equilbrium so that they can be represented by a single temperature, then the collision integral can be integrated to yield the average annihilation rate for a neutrino

$$\Gamma = \frac{16G_F^2}{\pi^3}(g_L^2 + g_R^2)T^5, \tag{3}$$

where

$$g_L^2 + g_R^2 = \begin{cases} \sin^4\theta_W + (\frac{1}{2} + \sin^2\theta_W)^2 & \text{for } \nu_e, \\ \sin^4\theta_W + (-\frac{1}{2} + \sin^2\theta_W)^2 & \text{for } \nu_{\mu,\tau}. \end{cases} \tag{4}$$

This rate can then be compared with the Hubble expansion rate

$$H = 1.66 g_*^{1/2} \frac{T^2}{M_{\rm Pl}}, \tag{5}$$

to find the decoupling temperature from the criterion $H = \Gamma|_{T=T_D}$. From this one finds that $T_D(\nu_e) \simeq 2.4\,\text{MeV}$, $T_D(\nu_{\mu,\tau}) \simeq 3.7\,\text{MeV}$, when $g_* = 10.75$, as is the case in the standard model.

This means that neutrinos decouple at a temperature which is significantly higher than the electron mass. When e^+e^- annihilation occurs around $T \sim m_e/3$, the neutrino temperature is unaffected whereas the photon temperature is heated by a factor $(11/4)^{1/3}$. The relation $T_\nu/T_\gamma = (4/11)^{1/3} \simeq 0.71$ holds to a precision of approximately 1%. The main correction comes from a slight heating of neutrinos by e^+e^- annihilation, as well as finite-temperature QED effects on the photon propagator [38]–[51].

3.2. Big Bang nucleosynthesis and the number of neutrino species

Shortly after neutrino decoupling, the weak interactions which keep neutrons and protons in statistical equilibrium freeze out. Again the criterion $H = \Gamma|_{T=T_{\rm freeze}}$ can be applied to find that $T_{\rm freeze} \simeq 0.5 g_*^{1/6}$ MeV [37].

Eventually, at a temperature of roughly 0.2 MeV, deuterium starts to form, and very quickly all free neutrons are processed into ^{4}He. The final helium abundance is therefore roughly given by

$$Y_P \simeq \left.\frac{2n_n/n_p}{1 + n_n/n_p}\right|_{T\simeq 0.2\,\text{MeV}}, \tag{6}$$

where n_n/n_p is determined by its value at freeze out, roughly by the condition that $n_n/n_p|_{T=T_{\rm freeze}} \sim e^{-(m_n-m_p)/T_{\rm freeze}}$.

Since the freeze-out temperature is determined by g_*, this in turn means that g_* can be inferred from a measurement of the helium abundance. However, since Y_P is a function of both $\Omega_b h^2$ and g_*, it is necessary to use other measurements to constrain $\Omega_b h^2$ to find a bound on g_*. One customary method for doing this has been to use measurements of primordial deuterium to infer $\Omega_b h^2$ and from that calculate a bound on g_*. Usually such bounds are expressed in terms of the equivalent number of neutrino species, $N_\nu \equiv \rho/\rho_{\nu_0}$, instead of g_*. The exact value of the bound is quite uncertain because there are different and inconsistent measurements of the primordial helium abundance (see for instance [52] for a discussion of this issue). The most recent analyses are in [52], where a value of $1.7 \leqslant N_\nu \leqslant 3.0$ (95% CL) was found, and in [53], which found the result $N_\nu = 2.5^{+1.1}_{-0.9}$. The difference in these results can be attributed to different assumptions about uncertainties in the primordial helium abundance.

Another interesting parameter which can be constrained by the same argument is the neutrino chemical potential, $\xi_\nu = \mu_\nu/T$ [54]–[57]. At first sight, this looks like it is completely equivalent

Table 1. Various recent limits on the effective number of neutrino species, as well as the data used.

Ref.	Bound on N_ν	Data used
Crotty *et al* [59]	$1.4 \leqslant N_\nu \leqslant 6.8$	CMB, LSS
Hannestad [58]	$0.9 \leqslant N_\nu \leqslant 7.0$	CMB, LSS
Pierpaoli [60]	$1.9 \leqslant N_\nu \leqslant 6.62$	CMB, LSS
Barger *et al* [52]	$0.9 \leqslant N_\nu \leqslant 8.3$	CMB
Hannestad [58]	$2.3 \leqslant N_\nu \leqslant 3.0$	CMB, LSS, BBN
Barger *et al* [52]	$1.7 \leqslant N_\nu \leqslant 3.0$	CMB, BBN

to constraining N_ν. However, this is not true because a chemical potential for electron neutrinos directly influences the $n \leftrightarrow p$ conversion rate. Therefore the bound on ξ_{ν_e} from BBN alone is relatively stringent ($-0.1 \lesssim \xi_{\nu_e} \lesssim 1$ [54]) compared with that for muon and tau neutrinos ($|\xi_{\nu_{\mu,\tau}}| \lesssim 7$ [54]). However, as will be seen in the next section, neutrino oscillations have the effect of almost equilibrating the neutrino chemical potentials prior to BBN, completely changing this conclusion.

3.3. The number of neutrino species—joint CMB and BBN analysis

The BBN bound on the number of neutrino species presented in the previous section can be complemented by a similar bound from observations of the CMB and large scale structure (LSS). The CMB depends on N_ν mainly because of the early Integrated Sachs Wolfe effect which increases fluctuation power at scales slightly larger than the first acoustic peak. The LSS spectrum depends on N_ν because the scale of matter–radiation equality is changed by varying N_ν.

Several recent papers have analysed WMAP and 2dF data for bounds on N_ν [52, 53], [58]–[60], and some of the bounds are listed in table 1. Recent analyses combining BBN, CMB, and LSS data can be found in [52, 58], and these results are also listed in table 1.

Common for all the bounds is that $N_\nu = 0$ is ruled out by both BBN and CMB/LSS. This has the important consequence that the cosmological neutrino background has been positively detected, not only during the BBN epoch, but also much later, during structure formation.

3.4. The effect of oscillations

In the previous section the one-particle distribution function, f, was used to describe neutrino evolution. However, for neutrinos, the mass eigenstates are not equivalent to the flavour eigenstates because neutrinos are mixed. Therefore, the evolution of the neutrino ensemble is not, in general, described by the three scalar functions, f_i, but rather by the evolution of the neutrino density matrix, $\rho \equiv \psi\psi^\dagger$, the diagonal elements of which correspond to f_i.

For three-neutrino oscillations, the formalism is quite complicated. However, the difference in Δm_{12} and δm_{23}, as well as the fact that $\sin 2\theta_{13} \ll 1$ means that the problem effectively reduces to a 2×2 oscillation problem in the standard model. A detailed account of the physics of neutrino oscillations in the early universe is outside the scope of the present paper; however, an excellent and very thorough review can be found in [61].

Without oscillations it is possible to compensate a very large chemical potential for muon and/or tau neutrinos with a small, negative electron neutrino chemical potential [54]. However, since neutrinos are almost maximally mixed, a chemical potential in one flavour can be shared with other flavours, and the end result is that during BBN all three flavours have almost equal chemical potential. This in turn means that the bound on ν_e applies to all species so that [62]–[66]

$$|\xi_i| = \frac{|\eta_i|}{T} \lesssim 0.15 \quad \text{for } i = \mathrm{e}, \mu, \tau. \tag{7}$$

In models where sterile neutrinos are present, even more remarkable oscillation phenomena can occur. However, we do not discuss this possibility further, except for the possibility of sterile neutrino warm dark matter, and instead refer to the review [61].

3.5. Low reheating temperature and neutrinos

In most models of inflation, the universe enters the normal, radiation dominated epoch at a reheating temperature, T_{RH}, which is of order the electroweak scale or higher. However, in principle, it is possible that this reheating temperature is much lower, of the order of MeV. This possibility has been studied many times in the literature, and a very general bound of $T_{\mathrm{RH}} \gtrsim 1$ MeV has been found [67]–[70].

This very conservative bound comes from the fact that the light element abundances produced by big bang nucleosynthesis disagree with observations if the universe was matter-dominated during BBN. However, a somewhat more stringent bound can be obtained by looking at neutrino thermalization during reheating. If a scalar particle is responsible for reheating then direct decay to neutrinos is suppressed because of the necessary helicity flip. This means that if the reheating temperature is too low neutrinos never thermalize. If this is the case, then BBN predicts the wrong light-element abundances. However, even if the heavy particle has a significant branching ratio into neutrinos there are problems with BBN. The reason is that neutrinos produced in decays are born with energies which are much higher than thermal. If the reheating temperature is too low, then a population of high-energy neutrinos will remain and also lead to conflict with the observed light-element abundances. A recent analysis showed that, in general, the reheating temperature cannot be below roughly 4 MeV [71].

4. Neutrino dark matter

Neutrinos are a source of dark matter in the present day universe simply because they contribute to Ω_m. The present temperature of massless standard model neutrinos is $T_{\nu,0} = 1.95\,\mathrm{K} = 1.7 \times 10^{-4}\,\mathrm{eV}$, and any neutrino with $m \gg T_{\nu,0}$ behaves like a standard non-relativistic dark matter particle.

The present contribution to the matter density of N_ν neutrino species with standard weak interactions is given by

$$\Omega_\nu h^2 = N_\nu \frac{m_\nu}{92.5\,\mathrm{eV}}. \tag{8}$$

Just by demanding that $\Omega_\nu \leqslant 1$, one finds the bound [72, 73]

$$m_\nu \lesssim \frac{46\,\mathrm{eV}}{N_\nu}. \tag{9}$$

4.1. The Tremaine–Gunn bound

If neutrinos are the main source of dark matter, then they must also make up most of the galactic dark matter. However, neutrinos can only cluster in galaxies via energy loss due to gravitational relaxation since they do not suffer inelastic collisions. In the distribution function language, this corresponds to phase mixing of the distribution function [74]. By using the theorem that the phase-mixed or coarse-grained distribution function must explicitly take values smaller than the maximum of the original distribution function one arrives at the condition

$$f_{\mathrm{CG}} \leqslant f_{\nu,\max} = \tfrac{1}{2}. \tag{10}$$

Because of this upper bound, it is impossible to squeeze neutrino dark matter beyond a certain limit [74]. For the Milky Way this means that the neutrino mass must be larger than roughly 25 eV *if* neutrinos make up the dark matter. For irregular dwarf galaxies, this limit increases to 100–300 eV [75, 76], and means that standard model neutrinos cannot make up a dominant fraction of the dark matter. This bound is generally known as the Tremaine–Gunn bound.

Note that this phase space argument is a purely classical argument, it is not related to the Pauli blocking principle for fermions (although, by using the Pauli principle $f_\nu \leqslant 1$ one would arrive at a similar, but slightly weaker limit for neutrinos). In fact, the Tremaine–Gunn bound works even for bosons if applied in a statistical sense [75], because even though there is no upper bound on the fine-grained distribution function, only a very small number of particles reside at low momenta (unless there is a condensate). Therefore, although the exact value of the limit is model dependent, the limit applies to any species that was once in thermal equilibrium. A notable counterexample is non-thermal axion dark matter which is produced directly into a condensate.

4.2. Neutrino hot dark matter

A much stronger upper bound on the neutrino mass than the one in (9) can be derived by noticing that the thermal history of neutrinos is very different from that of a WIMP because the neutrino only becomes non-relativistic very late.

In an inhomogeneous universe, the Boltzmann equation for a collisionless species is [77]

$$L[f] = \frac{\mathrm{D}f}{\mathrm{D}\tau} = \frac{\partial f}{\partial \tau} + \frac{\mathrm{d}x^i}{\mathrm{d}\tau}\frac{\partial f}{\partial x^i} + \frac{\mathrm{d}q^i}{\mathrm{d}\tau}\frac{\partial f}{\partial q^i} = 0, \tag{11}$$

where τ is the conformal time, $\mathrm{d}\tau = \mathrm{d}t/a$, and $q^i = ap^i$ is comoving momentum. The second term on the right-hand side has to do with the velocity of the distribution in a given spatial point and the third term is the cosmological momentum redshift.

Following Ma and Bertschinger [77] this can be rewritten as an equation for Ψ, the perturbed part of f

$$f(x^i, q^i, \tau) = f_0(q)[1 + \Psi(x^i, q^i, \tau)]. \tag{12}$$

In synchronous gauge, the equation becomes

$$\frac{1}{f_0}[f] = \frac{\partial \Psi}{\partial \tau} + \mathrm{i}\frac{q}{\epsilon}\mu\Psi + \frac{\mathrm{d}\ln f_0}{\mathrm{d}\ln q}\left[\dot{\eta} - \frac{\dot{h} + 6\dot{\eta}}{2}\mu^2\right] = \frac{1}{f_0}C[f], \tag{13}$$

where $q^j = qn^j$, $\mu \equiv n^j \hat{k}_j$ and $\epsilon = (q^2 + a^2 m^2)^{1/2}$. k^j is the comoving wavevector. h and η are the metric perturbations, defined from the perturbed space–time metric in synchronous gauge [77]

$$\mathrm{d}s^2 = a^2(\tau)[-\mathrm{d}\tau^2 + (\delta_{ij} + h_{ij})\,\mathrm{d}x^i\,\mathrm{d}x^j], \tag{14}$$

$$h_{ij} = \int \mathrm{d}^3k\,\mathrm{e}^{\mathrm{i}\vec{k}\cdot\vec{x}}(\hat{k}_i\hat{k}_j h(\vec{k},\tau) + (\hat{k}_i\hat{k}_j - \tfrac{1}{3}\delta_{ij})6\eta(\vec{k},\tau)). \tag{15}$$

Expanding this in Legendre polynomials one arrives at a set of hierarchy equations

$$\begin{aligned}
&\dot{\delta} = -\tfrac{4}{3}\theta - \tfrac{2}{3}\dot{h}, \qquad \dot{\theta} = k^2\left(\tfrac{1}{4}\delta - \sigma\right), \qquad 2\dot{\sigma} = \tfrac{8}{15}\theta - \tfrac{3}{15}kF_3 + \tfrac{4}{15}\dot{h} + \tfrac{8}{5}\dot{\eta},\\
&\dot{F}_l = \frac{k}{2l+1}(lF_{l-1} - (l+1)F_{l+1}).
\end{aligned} \tag{16}$$

For subhorizon scales ($\dot{h} = \dot{\eta} = 0$), this reduces to the form

$$\begin{aligned}
&\dot{\delta} = -\tfrac{4}{3}\theta, \qquad \dot{\theta} = k^2\left(\tfrac{1}{4}\delta - \sigma\right), \qquad 2\dot{\sigma} = \tfrac{8}{15}\theta - \tfrac{3}{15}kF_3,\\
&\dot{F}_l = \frac{k}{2l+1}(lF_{l-1} - (l+1)F_{l+1}).
\end{aligned} \tag{17}$$

One should notice the similarity between this set of equations and the evolution hierarchy for spherical Bessel functions. Indeed, the exact solution to the hierarchy is

$$F_l(k\tau) \sim j_l(k\tau). \tag{18}$$

This shows that the solution for δ is an exponentially damped oscillation. On small scales, $k > \tau$, perturbations are erased.

This in intuitively understandable in terms of free-streaming. Indeed, the Bessel function solution comes from the fact that neutrinos are considered massless. In the limit of CDM, the evolution hierarchy is truncated by the fact that $\theta = 0$, so that the CDM perturbation equation is simply $\dot{\delta} = -\dot{h}/2$. For massless particles, the free-streaming length is $\lambda = c\tau$ which is reflected in the solution to the Boltzmann hierarchy. Of course, the solution only applies when neutrinos are strictly massless. Once $T \sim m$, there is a smooth transition to the CDM solution. Therefore, the final solution can be separated into two parts: (i) $k > \tau$ ($T = m$): neutrino perturbations are exponentially damped (ii) $k < \tau$ ($T = m$): neutrino perturbations follow the CDM perturbations. Calculating the free streaming wavenumber in a flat CDM cosmology leads to the simple numerical relation (applicable only for $T_{\mathrm{eq}} \gg m \gg T_0$) [37]

$$\lambda_{\mathrm{FS}} \sim \frac{20\,\mathrm{Mpc}}{\Omega_x h^2}\left(\frac{T_x}{T_\nu}\right)^4\left[1 + \log\left(3.9\frac{\Omega_x h^2}{\Omega_m h^2}\left(\frac{T_\nu}{T_x}\right)^2\right)\right]. \tag{19}$$

In figure 1, we have plotted transfer functions for various different neutrino masses in a flat ΛCDM universe ($\Omega_m + \Omega_\nu + \Omega_\Lambda = 1$). The parameters used were $\Omega_b = 0.04$, $\Omega_{\mathrm{CDM}} = 0.26 - \Omega_\nu$, $\Omega_\Lambda = 0.7$, $h = 0.7$ and $n = 1$.

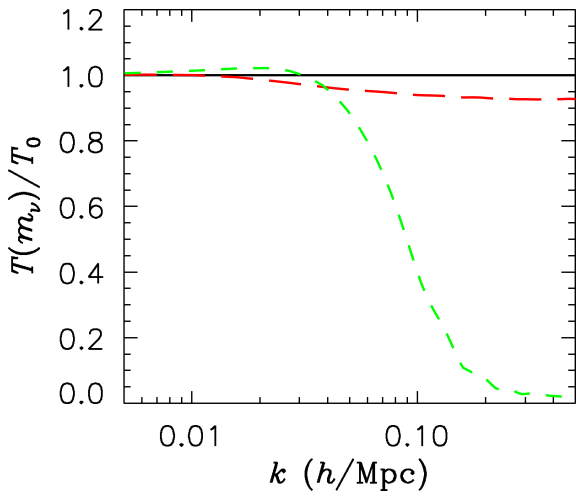

Figure 1. The transfer function $T(k, t = t_0)$ for various different neutrino masses. The solid (black) line is for $m_\nu = 0$, the long-dashed line for $m_\nu = 0.3$ eV, and the dashed line for $m_\nu = 1$ eV.

When measuring fluctuations, it is customary to use the power spectrum, $P(k, \tau)$, defined as

$$P(k, \tau) = |\delta|^2(\tau). \tag{20}$$

The power spectrum can be decomposed into a primordial part, $P_0(k)$, and a transfer function $T(k, \tau)$,

$$P(k, \tau) = P_0(k)T(k, \tau). \tag{21}$$

The transfer function at a particular time is found by solving the Boltzmann equation for $\delta(\tau)$.

At scales much smaller than the free-streaming scale the present matter power spectrum is suppressed roughly by the factor [78]

$$\frac{\Delta P(k)}{P(k)} = \frac{\Delta T(k, \tau = \tau_0)}{T(k, \tau = \tau_0)} \simeq -8\frac{\Omega_\nu}{\Omega_m}, \tag{22}$$

as long as $\Omega_\nu \ll \Omega_m$. The numerical factor 8 is derived from a numerical solution of the Boltzmann equation, but the general structure of the equation is simple to understand. At scales smaller than the free-streaming scale, the neutrino perturbations are washed out completely, leaving only perturbations in the non-relativistic matter (CDM and baryons). Therefore, the *relative* suppression of power is proportional to the ratio of neutrino energy density to the overall matter density. Clearly, the above relation only applies when $\Omega_\nu \ll \Omega_m$, when Ω_ν becomes dominant the spectrum suppression becomes exponential as in the pure hot dark matter model. This effect is shown for different neutrino masses in figure 1.

The effect of massive neutrinos on structure formation applies only to the scales below the free-streaming length. For neutrinos with masses of several eV the free-streaming scale is smaller than the scales which can be probed using the present CMB data and therefore the power spectrum suppression can be seen only in LSS data. On the other hand, neutrinos of sub-eV mass

Table 2. Various recent limits on the neutrino mass from cosmology and the data sets used in deriving them: 1, WMAP data; 2, other CMB data; 3, 2dF data; 4, constraint on σ_8 (different in 4a and 4b); 5, SDSS data; 6, constraint on H_0.

Ref.	Bound on $\sum m_\nu$ (eV)	Data used
Spergel *et al* (WMAP) [27]	0.69	1, 2, 3, 4a, 6
Hannestad [58]	1.01	1, 2, 3, 6
Allen *et al* [83]	$0.56^{+0.3}_{-0.26}$	1, 2, 3, 4b, 6
Tegmark *et al* (SDSS) [25]	1.8	1, 5
Barger *et al* [88]	0.75	1, 2, 3, 5, 6
Crotty *et al* [81]	1.0 (0.6)	1, 2, 3, 5 (6)

behave almost like a relativistic neutrino species for CMB considerations. The main effect of a small neutrino mass on the CMB is that it leads to an enhanced early ISW effect. The reason is that the ratio of radiation to matter at recombination becomes larger because a sub-eV neutrino is still relativistic or semi-relativistic at recombination. With the WMAP data alone it is very difficult to constrain the neutrino mass, and to achieve a constraint which is competitive with current experimental bounds it is necessary to include LSS data from 2dF or SDSS. When this is done the bound becomes very strong, somewhere in the range of 1 eV for the sum of neutrino masses, depending on assumptions about priors. In table 2 the present upper bound on the neutrino mass from various analyses is quoted, as well as the assumptions going into the derivation.

As can be gauged from this table, a fairly robust bound on the sum of neutrino masses is at present somewhere around 1.0 eV, depending somewhat on specific priors and data sets used.

It is also quite interesting to see what exactly provides this bound. It is often stated that the neutrino mass bound comes from LSS data, not from CMB because CMB probes larger scales. However, LSS data alone provides no limit on $\sum m_\nu$ because of degeneracies with other parameters (this is discussed in detail in [79, 82]). On the other hand, WMAP in itself also does not provide a strong limit on the neutrino mass [25], because neutrino mass only has a limited effect on the scales probed by WMAP. Only the combination of the two types of data allows for a determination of $\sum m_\nu$ with any precision. Figure 2 shows the deviation of the best-fit models for $\sum m_\nu = 0$ and 3 eV from WMAP and SDSS data, respectively. From this figure it is obvious that models with high neutrino mass are not ruled out by any single data point, but rather by a general decrease in how well the combined data fits. One fairly evident problem with the high neutrino mass model is that the shape of the LSS power spectrum is not correctly determined. The model spectrum has too much power at intermediate scales and too little at small scales.

In the upper part of this figure the deviation of the best-fit models from other cosmological data is shown. These data is not used in deriving the best-fit models, and therefore the figure shows that the standard concordance model with $\sum m_\nu = 0$ is not only a better fit to CMB and LSS data, but also more consistent with other cosmological data.

4.2.1. Combining measurements of m_ν and N_ν. The limits on neutrino masses discussed above apply only for neutrinos within the standard model, i.e. three light neutrinos with degenerate masses (if the sum is close to the upper bound). However, if there are additional neutrino species sharing the mass, or neutrinos have significant chemical potentials this bound is changed. Models with massive neutrinos have suppressed power at small scale, with suppression proportional to Ω_ν/Ω_m. Adding relativistic energy further suppresses power at scales smaller than the horizon

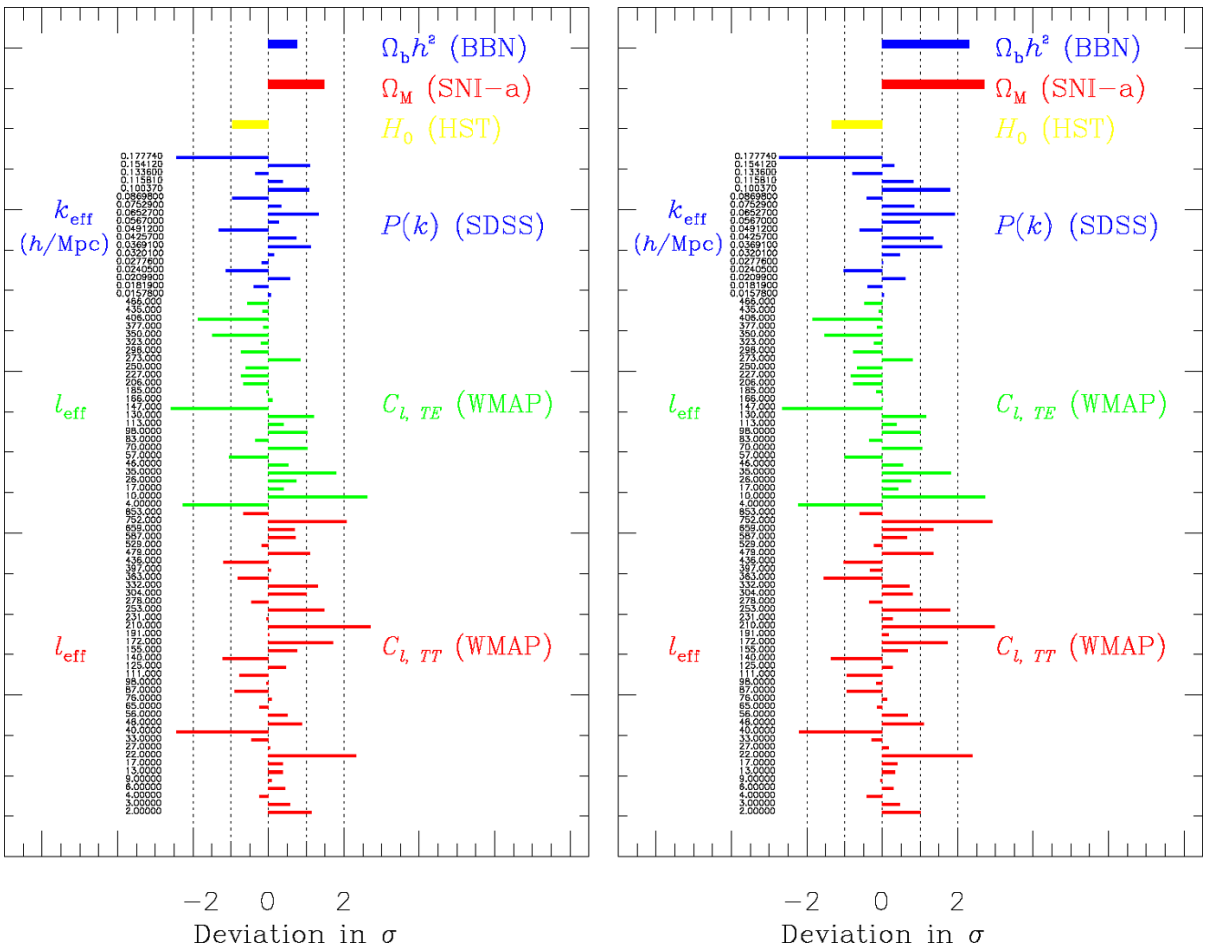

Figure 2. Deviation of the best fit models for $\sum m_\nu = 0$ (left) and $\sum m_\nu = 3\,\mathrm{eV}$ (right). The CMB data shown are the WMAP binned data (http://lambda.gsfc.nasa.gov). The deviation is calculated as 'Deviation in σ' $= (A_{\mathrm{model}} - A_{\mathrm{obs}})/\sigma_{\mathrm{obs}}$.

at matter–radiation equality. For the *same* matter density, such a model would therefore be even more incompatible with data. However, if the matter density is increased, together with m_ν and N_ν, excellent fits to the data can be obtained. This effect is shown in figure 3.

The effect on likelihood contours for (Ω_ν, N_ν) can be seen in figure 4 for the case where N_ν species share the total mass equally.

A thorough discussion of these models can be found in [80, 81].

4.2.2. Future neutrino mass measurements. The present bound on the sum of neutrino masses is still much larger than the mass difference, $\Delta m_{23} \sim 0.05\,\mathrm{eV}$ [3, 89], measured by atmospheric neutrino observatories and K2K. This means that, if the sum of neutrino masses is anywhere close to saturating the bound, then neutrino masses must the almost degenerate. The question is whether in the future it will be possible to measure masses which are of the order of Δm_{23}, i.e. whether neutrino masses can be determined if they are hierarchical.

By combining future CMB data from the Planck satellite with a galaxy survey like the SDSS it has been estimated that neutrino masses as low as about 0.1 eV can be detected [84, 85].

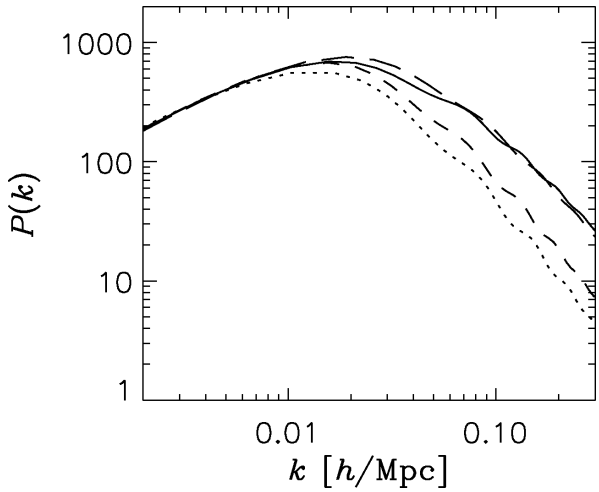

Figure 3. Power spectra for ΛCDM models with $\Omega_b = 0.05, \Omega = 1, h = 0.7, n_s = 1$ and $N_{\nu,\mathrm{massive}} = 1$, and a common large-scale normalization. ——, $\Omega_\nu = 0, \Omega_m = 0.25$ and $N_\nu = 3$; – – –, $\Omega_\nu = 0.05, \Omega_m = 0.25$ and $N_\nu = 3$; - - -, $\Omega_\nu = 0.05, \Omega_m = 0.25$ and $N_\nu = 8$; — —, $\Omega_\nu = 0.05, \Omega_m = 0.35$ and $N_\nu = 8$ (from [80]).

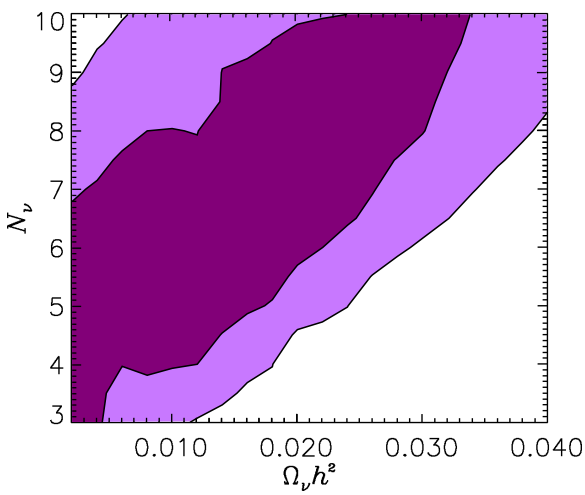

Figure 4. Likelihood contours (68% and 95%) for the case of N_ν neutrinos with equal masses, calculated from WMAP and 2dF data (from [80]).

Another possibility is to use weak lensing of the CMB as a probe of neutrino mass. In this case, it seems likely that a sensitivity below 0.1 eV can also be reached with CMB alone [86, 90].

As noted in [85] the exact value of the sensitivity at this level depends both on whether the hierarchy is normal or inverted, and the exact value of the mass splittings.

4.3. Neutrino warm dark matter

While CDM is defined as consisting of non-interacting particles which have essentially no free-streaming on any astronomically relevant scale, and HDM is defined as consisting of particles

which become non-relativistic around matter–radiation equality or later, warm dark matter is an intermediate. One of the simplest production mechanisms for warm dark matter is active-sterile neutrino oscillations in the early universe [102]–[106].

One possible benefit of warm dark matter is that it does have some free-streaming so that structure formation is suppressed on very small scales. This has been proposed as an explanation for the apparent discrepancy between observations of galaxies and numerical CDM structure-formation simulations. In general, simulations produce galaxy halos which have very steep inner density profiles $\rho \propto r^{\alpha}$, where $\alpha \sim 1$–1.5, and numerous subhalos [91, 92]. Neither of these characteristics are seen in observations and the explanation for this discrepancy remains an open question. If dark matter is warm instead of cold, with a free-streaming scale comparable with the size of a typical galaxy subhalo, then the amount of substructure is suppressed, and possibly the central density profile is also flattened [93]–[99]. In both cases, the mass of the dark matter particle should be around 1 keV [107, 108], assuming that it is thermally produced in the early universe.

On the other hand, from measurements of the Lyman-α forest flux power spectrum, it has been possible to reconstruct the matter power spectrum on relatively small scales at high redshift. This spectrum does not show any evidence for suppression at sub-galaxy scales and has been used to put a lower bound on the mass of warm dark matter particles of roughly 1.1 keV [100, 101]. An even more severe problem lies in the fact that star formation occurs relatively late in warm dark matter models because small scale structure is suppressed. This may be in conflict with the low-l CMB temperature–polarization cross-correlation measurement by WMAP which indicates very early reionization and therefore also early star formation. One recent investigation of this found warm dark matter to be inconsistent with WMAP for masses as high as 10 keV [93].

The case for warm dark matter therefore seems quite marginal, although at present it is not definitively ruled out by any observations.

4.4. Neutrinos as the source for high-energy cosmic rays

Nucleons, with energy above the threshold for photo-pion production on the CMB, rapidly downscatter in energy, the mean free path being of order 20–30 Mpc. At the present CMB temperature of 2.7 K, the threshold, known as the Greisen–Zatzepin–Kuzmin energy [116], is roughly 4×10^{19} GeV. On the other hand, a significant number of particles with energies above the GZK energy have been observed. At present, there is some controversy about the number of such particles observed between different experimental collaborations using different techniques. The HiRes [118] collaboration finds a decline in the number of events beyond the GZK energy which is in fact compatible with a cut-off. On the other hand, the AGASA [117] collaboration finds that the spectrum is consistent with no cut-off, and even with a hardening of the spectrum at very high energies. Recent reviews of these issues can be found in [119].

Either these particles must come from relatively nearby sources or they are not nucleons (or nuclei) with standard model interactions. One explanation which has been proposed is the Z-burst scenario [109]–[113]. In this model, neutrino primaries with very high energy, $E \gg E_{\mathrm{GZK}}$, annihilate with neutrinos in the cosmic background to produce the observed protons. The cross-section is significantly enhanced at $E_{\mathrm{CM}} = m_Z$, corresponding to a neutrino primary energy of $E \sim m_Z^2/2E_{\nu,0} \sim m_Z^2/2m_\nu$. If neutrino masses are hierarchical then the

largest mass is of order $m_\nu \sim \Delta m_{\rm atm} \sim 0.05\,{\rm eV}$, meaning that $E_\nu \sim 10^{23}\,{\rm eV}$. If neutrinos are produced by pion decay in AGNs this must mean that particles of even higher energies are produced there.

On the other hand, if neutrinos have masses close to saturating the cosmological bound then the primary energy can be significantly lower.

Another requirement is that the neutrino annihilation must take place within the GZK sphere. This leads to a too low flux unless the rate is somehow enhanced. It has previously been proposed that this can be explained in models with significant neutrino chemical potential [114]. However, the present cosmological bounds on η rule this out. If neutrinos are of eV mass then they do have significant clustering on GZK scales which can also enhance the rate by a factor of about 2. If ultra-high-energy cosmic rays are explained by the Z-burst, this means that a mass bound on neutrinos can in principle be obtained. In [111, 112] it was estimated that if the annihilations are within the galactic halo it requires a neutrino mass of $m_\nu = 2.34^{+1.29}_{-0.84}\,{\rm eV}$, and if the annihilation happens within the local supercluster the mass must be $m_\nu = 0.26^{+0.20}_{-0.14}\,{\rm eV}$. The first case is already ruled out, but the second possibility might work. It has, however, also been shown that the values obtained in [111, 112] are strongly model dependent [115].

At present the feasibility of the Z-burst scenario remains an open question. One problem is that the annihilation process produces a background of low-energy gamma rays which may be in conflict with EGRET observations, depending on the magnitude of the local neutrino density enhancement.

In any case, the Z-burst scenario is also interesting from the possibility of getting an independent detection of the cosmological neutrino background if the needed very high fluxes of ultra-high-energy neutrinos is measured in future detectors like Auger.

5. Neutrinos in the very early universe—leptogenesis

A particularly attractive model for baryogenesis involves massive, right-handed neutrinos, and is known as baryogenesis via leptogenesis [120]. The basic idea is that the masses of left-handed Majorana neutrinos are generated from couplings to very massive, right-handed neutrinos.

These massive, right-handed states are unstable and because they are Majorana particles their decays violate lepton number conservation. Futhermore, the decays are out of equilibrium and can violate CP which means that all the Sakharov conditions for generating a net lepton number are present. This lepton number can then subsequently be transferred to the baryon sector via Standard Model interactions and account for the observed baryon number of the universe.

A particularly simple model for this is thermal leptogenesis where the right-handed neutrinos are equilibrated at high temperatures directly via their interactions with the thermal plasma. In this case, the correct baryon number is produced only if the following conditions are fulfilled [121]–[126]: (a) masses of the light neutrinos must be less than about 0.1–0.15 eV and (b) masses of the right-handed neutrinos must be larger than about 10^8 GeV. The first condition is interesting because it provides a strong, albeit very model-dependent, bound on the light neutrino masses. The second condition is interesting because it is so high that it might be in conflict with the upper bound on the reheating temperature in supersymmetric models. This bound arises from overproduction and subsequent decay of gravitinos and could probably be relaxed in models where the gravitino is the lightest supersymmetric particle.

Table 3. Summary table of cosmological neutrino mass limits. For completeness, bounds from other sources, astrophysical and experimental, are also listed.

Method	Bound on $\sum m_\nu$	Data used
$\Omega_\nu h^2 \lesssim 0.15$	14 eV	$\Omega_\nu < \Omega_m$
CMB and LSS	0.7–1 eV	WMAP, 2dF, SDSS
SN1987A	$m_{\nu_e} < 5$–20 eV ($\bar{\nu}_e$)	SN1987A cooling curve [127, 128]
β-decay	$m_{\nu_e} < 2.2$ eV (ν_e)	Mainz experiment [21]
$0\nu2\beta$-decay	$m_{\nu,\mathrm{eff}} < 0.35$ eV	Heidelberg–Moscow [129]
	0.1 eV $< m_{\nu,\mathrm{eff}} <$ 0.9 eV	Heidelberg–Moscow [22, 23]

Taken at face value, the thermal leptogenesis constraint on light neutrino masses is the most restrictive cosmological limit known. However, it is *not* a constraint at the same level as experimental bounds, or even bounds from CMB and large-scale structure. The derivation involves a chain of assumptions: (i) leptogenesis is the correct model of baryogenesis, (ii) leptogenesis is thermal and (iii) the heavy neutrino masses are hierarchical. If either of the first two assumptions are relaxed then there is essentially no mass bound from this argument. If the last assumption is relaxed then it has been shown in [126] that the mass bound on the left-handed neutrinos can be relaxed by almost an order of magnitude.

With this in mind, specific mass bounds on neutrino masses from thermal leptogenesis should be taken as both interesting and suggestive, but not as strict and generally applicable bounds.

6. Discussion

In the present paper we have discussed how cosmological observations can be used for probing fundamental properties of neutrinos which are not easily accessible in laboratory experiments. Particularly, the measurement of absolute neutrino masses from CMB and LSS data has received significant attention over the past few years. In table 3 we summarize neutrino mass bounds from cosmological observations and other astrophysical and experimental bounds.

Another cornerstone of neutrino cosmology is the measurement of the total energy density in non-electromagnetically interacting particles. For many years, Big Bang nucleosynthesis was the only probe of relativistic energy density, but with the advent of precision CMB and LSS data it has been possible to complement the BBN measurement. At present, the cosmic neutrino background is seen in both BBN, CMB and LSS data at high significance.

Finally, cosmology can also be used to probe the possibility of neutrino warm dark matter, which could be produced by active-sterile neutrino oscillations.

In the coming years the steady stream of new observational data will continue, and the cosmological bounds on neutrino will improve accordingly. For instance, it has been estimated that with data from the upcoming Planck satellite it could be possible to measure neutrino masses as low as 0.1 eV.

Certainly neutrino cosmology will continue to be a prospering field of research for the foreseeable future.

Acknowledgments

The author acknowledges use of the publicly available CMBFAST package written by Uros Seljak and Matthias Zaldarriaga [87] and the use of computing resources at DCSC (Danish Center for Scientific Computing). He thanks Georg Raffelt for valuable comments on the manuscript.

References

[1] Aliani P, Antonelli V, Picariello M and Torrente-Lujan E 2003 *Preprint* hep-ph/0309156
[2] de Holanda P C and Smirnov A Y 2003 *Preprint* hep-ph/0309299
[3] Maltoni M, Schwetz T, Tortola M A and Valle J W F 2003 *Phys. Rev.* D **68** 113010 (*Preprint* hep-ph/0309130)
[4] Kostelecky V A and Samuel S 1993 *Phys. Lett.* B **318** 127
[5] Fuller G M, Primack J R and Qian Y Z 1995 *Phys. Rev.* D **52** 1288 (*Preprint* astro-ph/9502081)
[6] Caldwell D O and Mohapatra R N 1995 *Phys. Lett.* B **354** 371 (*Preprint* hep-ph/9503316)
[7] Bilenky S M, Giunti C, Kim C W and Petcov S T 1996 *Phys. Rev.* D **54** 4432 (*Preprint* hep-ph/9604364)
[8] King S F and Singh N N 2001 *Nucl. Phys.* B **596** 81 (*Preprint* hep-ph/0007243)
[9] He H J, Dicus D A and Ng J N 2002 *Preprint* hep-ph/0203237
[10] Ioannisian A and Valle J W 1994 *Phys. Lett.* B **332** 93 (*Preprint* hep-ph/9402333)
[11] Bamert P and Burgess C P 1994 *Phys. Lett.* B **329** 289 (*Preprint* hep-ph/9402229)
[12] Mohapatra R N and Nussinov S 1995 *Phys. Lett.* B **346** 75 (*Preprint* hep-ph/9411274)
[13] Minakata H and Yasuda O 1997 *Phys. Rev.* D **56** 1692 (*Preprint* hep-ph/9609276)
[14] Vissani F 1997 *Preprint* hep-ph/9708483
[15] Minakata H and Yasuda O 1998 *Nucl. Phys.* B **523** 597 (*Preprint* hep-ph/9712291)
[16] Ellis J R and Lola S 1999 *Phys. Lett.* B **458** 310 (*Preprint* hep-ph/9904279)
[17] Casas J A, Espinosa J R, Ibarra A and Navarro I 1999 *Nucl. Phys.* B **556** 3 (*Preprint* hep-ph/9904395)
[18] Casas J A, Espinosa J R, Ibarra A and Navarro I 2000 *Nucl. Phys.* B **569** 82 (*Preprint* hep-ph/9905381)
[19] Ma E 1999 *J. Phys. G: Nucl. Part. Phys.* **25** L97 (*Preprint* hep-ph/9907400)
[20] Adhikari R, Ma E and Rajasekaran G 2000 *Phys. Lett.* B **486** 134 (*Preprint* hep-ph/0004197)
[21] Kraus C *et al* 2003 *Eur. J. Phys.* C **33** (Suppl. 1) 805
[22] Klapdor-Kleingrothaus H V, Dietz A, Harney H L and Krivosheina I V 2001 *Mod. Phys. Lett.* A **16** 2409 (*Preprint* hep-ph/0201231)
[23] Klapdor-Kleingrothaus H V, Krivosheina I V, Dietz A and Chkvorets O 2004 *Phys. Lett.* B **586** 198 (*Preprint* hep-ph/0404088)
[24] Tegmark M *et al* [SDSS Collaboration] 2003 *Preprint* astro-ph/0310725
[25] Tegmark M *et al* [SDSS Collaboration] 2003 *Preprint* astro-ph/0310723
[26] Peacock J A *et al* 2001 *Nature* **410** 169 (*Preprint* astro-ph/0103143)
[27] Spergel D N *et al* 2003 *Astrophys. J. Suppl.* **148** 175 (*Preprint* astro-ph/0302209)
[28] Bennett C L *et al* 2003 *Astrophys. J. Suppl.* **148** 1 (*Preprint* astro-ph/0302207)
[29] Kogut A *et al* 2003 *Astrophys. J. Suppl.* **148** 161 (*Preprint* astro-ph/0302213)
[30] Hinshaw G *et al* 2003 *Astrophys. J. Suppl.* **148** 135 (*Preprint* astro-ph/0302217)
[31] Verde L *et al* 2003 *Astrophys. J. Suppl.* **148** 195 (*Preprint* astro-ph/0302218)
[32] Peiris H V *et al* 2003 *Astrophys. J. Suppl.* **148** 213 (*Preprint* astro-ph/0302225)
[33] Kuo C l *et al* [ACBAR collaboration] 2004 *Astrophys. J.* **600** 32 (*Preprint* astro-ph/0212289)
[34] Wang X, Tegmark M, Jain B and Zaldarriaga M 2002 *Preprint* astro-ph/0212417
[35] Freedman W L *et al* 2001 *Astrophys. J.* **553** 47 (*Preprint* astro-ph/0012376)
[36] Knop R A *et al* 2003 *Preprint* astro-ph/0309368
[37] Kolb E W and Turner M S 1990 *The Early Universe* (Reading, MA: Addison-Wesley)
[38] Hannestad S and Madsen J 1995 *Phys. Rev.* D **52** 1764 (*Preprint* astro-ph/9506015)

[39] Dicus D A, Kolb E W, Gleeson A M, Sudarshan E C, Teplitz V L and Turner M S 1982 *Phys. Rev.* D **26** 2694
[40] Rana N C and Mitra B 1991 *Phys. Rev.* D **44** 393
[41] Herrera M A and Hacyan S 1989 *Astrophys. J.* **336** 539
[42] Dolgov A D and Fukugita M 1992 *Phys. Rev.* D **46** 5378
[43] Dodelson S and Turner M S 1992 *Phys. Rev.* D **46** 3372
[44] Fields B D, Dodelson S and Turner M S 1993 *Phys. Rev.* D **47** 4309 (*Preprint* astro-ph/9210007)
[45] Dolgov A D, Hansen S H and Semikoz D V 1997 *Nucl. Phys.* B **503** 426 (*Preprint* hep-ph/9703315)
[46] Dolgov A D, Hansen S H and Semikoz D V 1999 *Nucl. Phys.* B **543** 269 (*Preprint* hep-ph/9805467)
[47] Gnedin N Y and Gnedin O Y 1998 *Astrophys. J.* **509** 11
[48] Esposito S, Miele G, Pastor S, Peloso M and Pisanti O 2000 *Nucl. Phys.* B **590** 539 (*Preprint* astro-ph/0005573)
[49] Steigman G 2001 *Preprint* astro-ph/0108148
[50] Mangano G, Miele G, Pastor S and Peloso M 2001 *Preprint* astro-ph/0111408
[51] Hannestad S 2002 *Phys. Rev.* D **65** 083006
[52] Barger V, Kneller J P, Lee H S, Marfatia D and Steigman G 2003 *Phys. Lett.* B **566** 8 (*Preprint* hep-ph/0305075)
[53] Cuoco A, Iocco F, Mangano G, Miele G, Pisanti O and Serpico P D 2003 *Preprint* astro-ph/0307213
[54] Kang H S and Steigman G 1992 *Nucl. Phys.* B **372** 494
[55] Kohri K, Kawasaki M and Sato K 1997 *Astrophys. J.* **490** 72 (*Preprint* astro-ph/9612237)
[56] Orito M, Kajino T, Mathews G J and Wang Y 2002 *Phys. Rev.* D **65** 123504 (*Preprint* astro-ph/0203352)
[57] Ichikawa K and Kawasaki M 2003 *Phys. Rev.* D **67** 063510 (*Preprint* astro-ph/0210600)
[58] Hannestad S 2003 *J. Cosmol. Astropart. Phys.* JCAP05(2003)004 (*Preprint* astro-ph/0303076)
[59] Crotty P, Lesgourgues J and Pastor S 2003 *Phys. Rev.* D **67** 123005 (*Preprint* astro-ph/0302337)
[60] Pierpaoli E 2003 *Mon. Not. R. Astron. Soc.* **342** L63 (*Preprint* astro-ph/0302465)
[61] Dolgov A D 2002 *Phys. Rep.* **370** 333 (*Preprint* hep-ph/0202122)
[62] Lunardini C and Smirnov A Y 2001 *Phys. Rev.* D **64** 073006 (*Preprint* hep-ph/0012056)
[63] Pastor S, Raffelt G G and Semikoz D V 2001 *Preprint* hep-ph/0109035
[64] Dolgov A D, Hansen S H, Pastor S, Petcov S T, Raffelt G G and Semikoz D V 2002 *Nucl. Phys.* B **632** 363 (*Preprint* hep-ph/0201287)
[65] Abazajian K N, Beacom J F and Bell N F 2002 *Phys. Rev.* D **66** 013008 (*Preprint* astro-ph/0203442)
[66] Wong Y Y 2002 *Phys. Rev.* D **66** 025015 (*Preprint* hep-ph/0203180)
[67] Kawasaki M, Kohri K and Sugiyama N 1999 *Phys. Rev. Lett.* **82** 4168 (*Preprint* astro-ph/9811437)
[68] Kohri K, Yamaguchi M and Yokoyama J 2000 *Phys. Rev.* D **62** 023506 (*Preprint* astro-ph/0002127)
[69] Giudice G F, Kolb E W and Riotto A 2001 *Phys. Rev.* D **64** 023508 (*Preprint* hep-ph/0005123)
[70] Giudice G F, Kolb E W, Riotto A, Semikoz D V and Tkachev I I 2001 *Phys. Rev.* D **64** 043512 (*Preprint* hep-ph/0012317)
[71] Hannestad S 2004 *Preprint* astro-ph/0403291
[72] Gershtein S S and Zeldovich Y B 1966 *JETP Lett.* **4** 120 (*Pisma Zh. Eksp. Teor. Fiz.* **4** 174)
[73] Cowsik R and McClelland J 1972 *Phys. Rev. Lett.* **29** 669
[74] Tremaine S and Gunn J E 1979 *Phys. Rev. Lett.* **42** 407
[75] Madsen J 1991 *Phys. Rev.* D **44** 999
[76] Salucci P and Sinibaldi A 1997 *Astron. Astrophys.* **323** 1
[77] Ma C P and Bertschinger E 1995 *Astrophys. J.* **455** 7 (*Preprint* astro-ph/9506072)
[78] Hu W, Eisenstein D J and Tegmark M 1998 *Phys. Rev. Lett.* **80** 5255 (*Preprint* astro-ph/9712057)
[79] Elgaroy O and Lahav O 2003 *J. Cosmol. Astropart. Phys.* JCAP04(2003)004 (*Preprint* astro-ph/0303089)
[80] Hannestad S and Raffelt G 2003 *Preprint* hep-ph/0312154
[81] Crotty P, Lesgourgues J and Pastor S 2004 *Preprint* hep-ph/0402049
[82] Hannestad S 2002 *Phys. Rev.* D **66** 125011 (*Preprint* astro-ph/0205223)
[83] Allen S W, Schmidt R W and Bridle S L 2003 *Preprint* astro-ph/0306386
[84] Hannestad S 2003 *Phys. Rev.* D **67** 085017 (*Preprint* astro-ph/0211106)
[85] Lesgourgues J, Pastor S and Perotto L 2004 *Preprint* hep-ph/0403296

[86] Abazajian K N and Dodelson S 2003 *Phys. Rev. Lett.* **91** 041301 (*Preprint* astro-ph/0212216)
[87] Seljak U and Zaldarriaga M 1996 *Astrophys. J.* **469** 437 (*Preprint* astro-ph/9603033; see also the CMBFAST website at http://cosmo.nyu.edu/matiasz/CMBFAST/cmbfast.html)
[88] Barger V, Marfatia D and Tregre A 2003 *Preprint* hep-ph/0312065
[89] Fogli G L, Lisi E, Marrone A and Montanino D 2003 *Phys. Rev.* D **67** 093006 (*Preprint* hep-ph/0303064)
[90] Kaplinghat M, Knox L and Song Y S 2003 *Phys. Rev. Lett.* **91** 241301 (*Preprint* astro-ph/0303344)
[91] Kazantzidis S, Mayer L, Mastropietro C, Diemand J, Stadel J and Moore B 2003 *Preprint* astro-ph/0312194
[92] Ghigna S, Moore B, Governato F, Lake G, Quinn T and Stadel J 2000 *Astrophys. J.* **544** 616 (*Preprint* astro-ph/9910166)
[93] Yoshida N, Sokasian A, Hernquist L and Springel V 2003 *Astrophys. J.* **591** L1 (*Preprint* astro-ph/0303622)
[94] Haiman Z, Barkana R and Ostriker J P 2001 *Preprint* astro-ph/0103050
[95] Avila-Reese V, Colin P, Valenzuela O, D'Onghia E and Firmani C 2000 *Preprint* astro-ph/0010525
[96] Bode P, Ostriker J P and Turok N 2001 *Astrophys. J.* **556** 93 (*Preprint* astro-ph/0010389)
[97] Colin P, Avila-Reese V and Valenzuela O 2000 *Astrophys. J.* **542** 622 (*Preprint* astro-ph/0004115)
[98] Hannestad S and Scherrer R J 2000 *Phys. Rev.* D **62** 043522 (*Preprint* astro-ph/0003046)
[99] Sommer-Larsen J and Dolgov A 1999 *Preprint* astro-ph/9912166
[100] Colombi S, Dodelson S and Widrow L M 1996 *Astrophys. J.* **458** 1 (*Preprint* astro-ph/9505029)
[101] Narayanan V K, Spergel D N, Dave R and Ma C P 2000 *Preprint* astro-ph/0005095
[102] Hansen S H, Lesgourgues J, Pastor S and Silk J 2002 *Mon. Not. R. Astron. Soc.* **333** 544 (*Preprint* astro-ph/0106108)
[103] Abazajian K, Fuller G M and Tucker W H 2001 *Astrophys. J.* **562** 593 (*Preprint* astro-ph/0106002)
[104] Abazajian K, Fuller G M and Patel M 2001 *Phys. Rev.* D **64** 023501 (*Preprint* astro-ph/0101524)
[105] Shi X d and Fuller G M 1999 *Phys. Rev. Lett.* **82** 2832 (*Preprint* astro-ph/9810076)
[106] Dodelson S and Widrow L M 1994 *Phys. Rev. Lett.* **72** 17 (*Preprint* hep-ph/9303287)
[107] Hogan C J and Dalcanton J J 2000 *Phys. Rev.* D **62** 063511 (*Preprint* astro-ph/0002330)
[108] Dalcanton J J and Hogan C J 2001 *Astrophys. J.* **561** 35 (*Preprint* astro-ph/0004381)
[109] Weiler T J 1982 *Phys. Rev. Lett.* **49** 234
[110] Weiler T J 1999 *Astropart. Phys.* **11** 303 (*Preprint* hep-ph/9710431)
[111] Ringwald A 2001 *Preprint* hep-ph/0111112
[112] Fodor Z, Katz S D and Ringwald A 2002 *Phys. Rev. Lett.* **88** 171101 (*Preprint* hep-ph/0105064)
[113] Gelmini G and Varieschi G 2002 *Preprint* hep-ph/0201273
[114] Gelmini G and Kusenko A 1999 *Phys. Rev. Lett.* **82** 5202
[115] Kalashev O E, Kuzmin V A, Semikoz D V and Sigl G 2002 *Phys. Rev.* D **65** 103003 (*Preprint* hep-ph/0112351)
[116] Greisen K 1966 *Phys. Rev. Lett.* **16** 748
Zatsepin G T and Kuzmin V A 1966 *JETP Lett.* **4** 78
[117] Hayashida N *et al* 2000 *Preprint* astro-ph/0008102
[118] Abbasi R U *et al* [The High Resolution Fly's Eye Collaboration (HIRES)] 2004 *Preprint* astro-ph/0404137
[119] Sigl G 2004 *Preprint* astro-ph/0404074
[120] Fukugita M and Yanagida T 1986 *Phys. Lett.* B **174** 45
[121] Davidson S and Ibarra A 2002 *Preprint* hep-ph/0202239
[122] Hamaguchi K, Murayama H and Yanagida T 2001 *Preprint* hep-ph/0109030
[123] Buchmuller W, di Bari P and Pluemacher M 2003 *Nucl. Phys.* B **665** 445
[124] Buchmuller W and Pluemacher M 1999 *Phys. Rep.* **320** 329
[125] Giudice G F *et al* 2003 *Preprint* hep-ph/0310123
[126] Hambye T *et al* 2003 *Preprint* hep-ph/0312203
[127] Kernan P J and Krauss L M 1995 *Nucl. Phys.* B **437** 243 (*Preprint* astro-ph/9410010)
[128] Loredo T J and Lamb D Q 2002 *Phys. Rev.* D **65** 063002 (*Preprint* astro-ph/0107260)
[129] Klapdor-Kleingrothaus H V *et al* 2001 *Eur. Phys. J.* A **12** 147 (*Preprint* hep-ph/0103062)

New Journal of Physics
An Institute of Physics and Deutsche Physikalische Gesellschaft Journal

Neutrino masses, mixing, Majorana CP-violating phases and $(\beta\beta)_{0\nu}$ decay

S T Petcov[1]

Scuola Internazionale Superiore di Studi Avanzati, INFN—Sezione di Trieste, I-34014 Trieste, Italy, and Yukawa Institute for Theoretical Physics, Kyoto University, Kyoto 606-8502, Japan
E-mail: petcov@he.sissa.it

New Journal of Physics **6** (2004) 109
Received 29 April 2004
Published 20 August 2004
Online at http://www.njp.org/
doi:10.1088/1367-2630/6/1/109

Abstract. Predictions of the effective Majorana mass $|\langle m\rangle|$ in $(\beta\beta)_{0\nu}$ decay for 3-ν mixing and massive Majorana neutrinos are reviewed in the present study. The physics potential of the experiments, searching for $(\beta\beta)_{0\nu}$ decay and having sensitivity to $|\langle m\rangle| \gtrsim 0.01$ eV for providing information on the type of the neutrino mass spectrum, the absolute scale of neutrino masses and on the Majorana CP-violation phases in the PMNS neutrino mixing matrix, is also discussed.

Contents

1. Introduction **2**
2. Predictions of the effective Majorana mass **8**
2.1. NH neutrino mass spectrum 9
2.2. IH spectrum 9
2.3. Three QD neutrinos 10
3. Constraining the lightest neutrino mass **11**
4. Determining the type of the neutrino mass spectrum **15**
5. Constraining the Majorana CP-violation phases **19**
6. Conclusions **20**
Acknowledgments **20**
References **21**

[1] Also at INRNE, Bulgarian Academy of Sciences, 1789 Sofia, Bulgaria.

PII: S1367-2630(04)80003-X
© IOP Publishing Ltd and Deutsche Physikalische Gesellschaft

1. Introduction

There has been remarkable progress in the study of neutrino oscillations over the last several years. Experiments with solar, atmospheric and reactor neutrinos [1]–[6] have provided compelling evidence for the existence of neutrino oscillations driven by nonzero neutrino masses and neutrino mixing. Evidence for oscillations of neutrinos was obtained also in the first long-baseline accelerator neutrino experiment K2K [7].

The hypothesis of solar neutrino oscillations which, in 1967, were first predicted to cause a solar neutrino deficit [8] and later, in one variety or another, were considered as the most natural explanation for the observed [1, 2] solar neutrino deficit (see e.g. [9]–[11]), has received a convincing confirmation from the measurement of the solar neutrino flux through the neutral current reaction on deuterium by the SNO experiment [3, 4]. Analysis of the solar neutrino data obtained by Homestake, SAGE, GALLEX/GNO, SK and SNO experiments showed that the data favour the large mixing angle (LMA) MSW solution for the solar neutrino problem. The first results of the KamLAND reactor experiment [6] have confirmed (under the very plausible assumption of CPT invariance) the LMA MSW solution, establishing it essentially as a unique solution for the solar neutrino problem. This remarkable result brought us, after more than 30 years of research, initiated by the pioneer works of Pontecorvo [8, 12] and the experiment of Davis *et al* [13], very close to a complete understanding of the true cause of the solar neutrino problem.

A combined two-neutrino oscillation analysis of the solar neutrino and KamLAND data, performed before the latest (salt-phase) SNO results were announced, identified two distinct solution subregions within the LMA solution region, LMA-I and II (see e.g. [14, 15]). The best-fit values of two-neutrino oscillation parameters, namely the solar neutrino mixing angle $\theta_\odot$ and the mass-squared difference $\Delta m^2_\odot$, in the two subregions, LMA-I and -II, read (see e.g. [14]) $\Delta m^{2I}_\odot = 7.3 \times 10^{-5}\,\mathrm{eV}^2$, $\Delta m^{2II}_\odot = 1.5 \times 10^{-4}\,\mathrm{eV}^2$ and $\tan^2\theta^I_\odot = \tan^2\theta^{II}_\odot = 0.46$. The LMA-I solution was preferred statistically by the data. At 90% CL, it was found in (see e.g. [14])

$$\Delta m^2_\odot \cong (5.6 - 17) \times 10^{-5}\,\mathrm{eV}^2, \qquad \tan^2\theta_\odot \cong (0.32 - 0.72). \tag{1}$$

In September 2003, the SNO collaboration published data from the salt phase of the experiment [4]. In particular, for the ratio of the CC and NC event rates, the collaboration found $R_{CC/NC} = 0.306 \pm 0.026 \pm 0.024$ and, correspondingly, $R_{CC/NC} \leqslant 0.41$ at high CL. As was shown in [16], an upper limit of $R_{CC/NC} < 0.5$ implies a significant upper limit on $\Delta m^2_\odot$ smaller than $2 \times 10^{-4}\,\mathrm{eV}^2$: $\Delta m^2_\odot \lesssim 1.7 \times 10^{-4}\,\mathrm{eV}^2$. Thus, the latest SNO data on $R_{CC/NC}$ imply stringent constraints on the LMA-II solution. A combined statistical analysis of data from the solar neutrino and KamLAND experiments, including the latest SNO results, showed [18] (see also e.g. [19]) that the LMA-II solution is allowed only at 99.13% CL. Furthermore, the data have substantially reduced the maximum allowed value of $\sin^2\theta_\odot$ (see [16, 17]), thereby excluding the possibility of maximal mixing[2] at 5.4 standard deviations (S.D.) [4, 18]. The best-fit value of $\theta_\odot$ corresponds to $\cos 2\theta_\odot = 0.40$, whereas, at 90% (95%) CL, one has $\cos 2\theta_\odot \geqslant 0.24$ (0.22). This has very important implications, in particular for predictions of the effective Majorana mass in neutrinoless double-beta decay, $|\langle m \rangle|$ [21]–[24].

[2] Future data from SNO on the day/night effect and the spectrum of e^- from the CC reaction, and future high statistics data from KamLAND, may resolve the LMA-I–LMA-II solution ambiguity and can constrain further the solar neutrino mixing angle (see [16, 18, 20] and references therein).

There is also strong evidence for oscillations of the atmospheric $\nu_\mu(\bar{\nu}_\mu)$ from the Zenith angle dependence of the sub-GeV and multi-GeV μ-like events, which were observed in the Super-Kamiokande experiment [25]. The experimental results are best described in terms of dominant two-neutrino $\nu_\mu \to \nu_\tau$ ($\bar{\nu}_\mu \to \bar{\nu}_\tau$) oscillations with maximal mixing, $\sin^2 2\theta_{\rm atm} \cong 1$. A combined analysis [26] of atmospheric neutrino data and the data from the K2K long-baseline accelerator experiment [7] shows that, at 90% CL, the neutrino mass-squared difference responsible for the atmospheric neutrino oscillations lies in the interval

$$2.0 \times 10^{-3}\,\mathrm{eV}^2 \lesssim \Delta m^2_{\rm atm} \lesssim 3.2 \times 10^{-3}\,\mathrm{eV}^2. \tag{2}$$

The $\Delta m^2_{\rm atm}$ best-fit value found in [26] reads $\Delta m^2_{\rm atm}|_{\rm BF} = 2.6 \times 10^{-3}$ eV. Preliminary results from an improved analysis of the SK atmospheric neutrino data, performed recently by the SK collaboration, gave [25]

$$1.3 \times 10^{-3}\,\mathrm{eV}^2 \lesssim |\Delta m^2_{\rm atm}| \lesssim 3.1 \times 10^{-3}\,\mathrm{eV}^2, \quad 90\%\,\mathrm{CL}, \tag{3}$$

with best-fit value $|\Delta m^2_{\rm atm}| = 2.0 \times 10^{-3}\,\mathrm{eV}^2$. Adding the K2K data [7], Fogli *et al* [27] find the same best-fit value and

$$1.55 \times 10^{-3}\,\mathrm{eV}^2 \lesssim |\Delta m^2_{\rm atm}| \lesssim 2.60 \times 10^{-3}\,\mathrm{eV}^2, \quad 90\%\,\mathrm{CL}. \tag{4}$$

Recently, the SK collaboration presented the first evidence of an 'oscillation dip' in the L/E dependence, where L and E are the distance travelled by neutrinos and the neutrino energy respectively, of a particular selected sample of μ-like events[3] [28]. Such a dip is predicted due to the oscillatory dependence of the $\nu_\mu \to \nu_\tau(\bar{\nu}_\mu \to \bar{\nu}_\tau)$ oscillation probability on L/E: the $\nu_\mu \to \nu_\tau$ ($\bar{\nu}_\mu \to \bar{\nu}_\tau$) transitions of atmospheric neutrinos are predominantly two-neutrino transitions governed by vacuum oscillation probability. The dip in the observed L/E distribution corresponds to the first oscillation minimum of the ν_μ ($\bar{\nu}_\mu$) survival probability, $P(\nu_\mu \to \nu_\mu)(P(\bar{\nu}_\mu \to \bar{\nu}_\mu))$, as L/E increases starting from values for which $\Delta m^2_{\rm atm} L/(2E) \ll 1$ and $P(\nu_\mu \to \nu_\mu) \cong 1$. This beautiful result represents the first ever observation of a direct effect of the oscillatory dependence on L and E of the probability of neutrino oscillations in vacuum.

Interpretation of the solar and atmospheric neutrinos, and of the KamLAND data in terms of neutrino oscillations, requires the existence of three-neutrino mixing in the weak charged lepton current:

$$\nu_{l\mathrm{L}} = \sum_{j=1}^{3} U_{lj}\nu_{j\mathrm{L}}. \tag{5}$$

Here, $\nu_{l\mathrm{L}}$ (where $l = e, \mu, \tau$) are the three left-handed flavour neutrino fields, $\nu_{j\mathrm{L}}$ is the left-handed field of the neutrino ν_j having a mass m_j and U is the Pontecorvo–Maki–Nakagawa–Sakata (PMNS) neutrino mixing matrix [29]. Actually, all existing neutrino oscillation data, except the data of the LSND experiment [30],[4] can be described if we assume the existence of three-neutrino mixing in vacuum, (equation (5)), and we will consider this possibility in what follows.[5]

[3] These are μ-like events for which the relative uncertainty in the experimental determination of the L/E ratio does not exceed 70%.

[4] In the LSND experiment, indications for oscillations $\bar{\nu}_\mu \to \bar{\nu}_e$ with $(\Delta m^2)_{\rm LSND} \simeq 1\,\mathrm{eV}^2$ were obtained. The LSND results are being tested in the MiniBooNE experiment at Fermilab [31].

[5] For a similar analysis taking into account the LSND evidences for neutrino oscillations, see [32].

The PMNS mixing matrix U can be parametrized by three angles $\theta_{\rm atm}$, $\theta_\odot$ and θ and, depending on whether the massive neutrinos ν_j are Dirac or Majorana particles, by one or three CP-violating phases [33]–[35]. In the standard parametrization of U (see e.g. [36]), the three mixing angles are denoted as θ_{12}, θ_{13} and θ_{23}:

$$U = \begin{pmatrix} c_{12}c_{13} & s_{12}c_{13}\,{\rm e}^{{\rm i}\alpha_{21}/2} & s_{13}\,{\rm e}^{{\rm i}\alpha_{31}/2} \\ -s_{12}c_{23} - c_{12}s_{23}s_{13}\,{\rm e}^{{\rm i}\delta} & (c_{12}c_{23} - s_{12}s_{23}s_{13}\,{\rm e}^{{\rm i}\delta})\,{\rm e}^{{\rm i}\alpha_{21}/2} & s_{23}c_{13}\,{\rm e}^{{\rm i}(\delta+\alpha_{31}/2)} \\ s_{12}s_{23} - c_{12}c_{23}s_{13}\,{\rm e}^{{\rm i}\delta} & (-c_{12}s_{23} - s_{12}c_{23}s_{13}\,{\rm e}^{{\rm i}\delta})\,{\rm e}^{{\rm i}\alpha_{21}/2} & c_{23}c_{13}\,{\rm e}^{{\rm i}(\delta+\alpha_{31}/2)} \end{pmatrix}, \tag{6}$$

where we have used the usual notations $s_{ij} \equiv \sin\theta_{ij}$, $c_{ij} \equiv \cos\theta_{ij}$; δ is the Dirac CP-violation phase and α_{21} and α_{31} are two Majorana CP-violation phases [33]–[35]. If we identify the two independent neutrino mass-squared differences in this case, Δm^2_{21} and Δm^2_{31}, with the neutrino mass squared differences that induce the solar and atmospheric neutrino oscillations, $\Delta m^2_\odot = \Delta m^2_{21} > 0$, $\Delta m^2_{\rm A} = \Delta m^2_{31}$, we have $\theta_{12} = \theta_\odot$, $\theta_{23} = \theta_{\rm atm}$ and $\theta_{13} = \theta$. The angle θ is limited by the data from the CHOOZ and Palo Verde experiments [37, 38]. The oscillations between flavour neutrinos are insensitive to the Majorana CP-violating phases α_{21} and α_{31} [33, 39]. Information about these phases can be obtained, in principle, from the $(\beta\beta)_{0\nu}$-decay experiments [22, 24], [40]–[43] (see also [44]–[46]). Majorana CP-violating phases might be at the origin of the baryon asymmetry of the Universe [47].

The precise limit on the angle θ from the CHOOZ and Palo Verde data is $\Delta m^2_{\rm atm}$-dependent (see e.g. [48]). For the values of $\Delta m^2_{\rm atm}$ found in [26] and equation (2), the upper bound on $\sin^2\theta$ at 90% (99.73%) CL reads $\sin^2\theta < 0.03$ (0.05). Using the latest SK preliminary result, one gets, at 90% (99.73%) CL, from a combined 3-ν oscillation analysis of the solar neutrino, CHOOZ and KamLAND data [18],

$$\sin^2\theta < 0.047\ (0.074). \tag{7}$$

Somewhat better limits on $\sin^2\theta$ compared with the existing one can be obtained in the MINOS, OPERA and ICARUS experiments [49, 50]. Various options are currently being discussed (experiments with off-axis neutrino beams, more precise reactor antineutrino and long-baseline experiments, etc; see e.g. [51, 52]) on how to improve the sensitivity to $\sin^2\theta$ by at least a factor of 5 or more, i.e. to values of ~0.01 or smaller.

The combined 3-ν oscillation analysis of the solar neutrino, CHOOZ and KamLAND data also showed [18] that the allowed ranges of the solar neutrino oscillation parameters do not differ substantially for $\sin^2\theta < 0.05$ from those derived in the two-neutrino oscillation analyses. At 90% CL, for instance, one finds

$$0.23 \lesssim \sin^2\theta_\odot \lesssim 0.38 \quad \text{for } \sin^2\theta = 0.0, \tag{8}$$

$$0.25 \lesssim \sin^2\theta_\odot \lesssim 0.36 \quad \text{for } \sin^2\theta = 0.04. \tag{9}$$

The best-fit values in both cases read $\sin^2\theta_\odot = 0.30$. The allowed values of $\Delta m^2_\odot$ in the LMA-I region also do not change considerably with respect to those obtained in the two-neutrino oscillation analyses and are given at 90% CL by [18]

$$5.6 \times 10^{-5}\,{\rm eV}^2 \lesssim \Delta m^2_\odot \lesssim 9.2 \times 10^{-5}\,{\rm eV}^2 \quad \text{for } \sin^2\theta = 0.0, \tag{10}$$

$$6.1 \times 10^{-5}\,{\rm eV}^2 \lesssim \Delta m^2_\odot \lesssim 8.5 \times 10^{-5}\,{\rm eV}^2 \quad \text{for } \sin^2\theta = 0.04. \tag{11}$$

The $\Delta m^2_{\odot}$ best-fit value is practically the same for the two values of $\sin^2\theta$: $\Delta m^2_{\odot} \cong 7.2 \times 10^{-5}\,\mathrm{eV}^2$.

Note that the atmospheric neutrino and K2K data do not allow one to determine the sign of $\Delta m^2_{\mathrm{atm}}$. This implies that if we identify $\Delta m^2_{\mathrm{atm}}$ with Δm^2_{31} for three-neutrino mixing, one can have $\Delta m^2_{31} > 0$ or $\Delta m^2_{31} < 0$. The two possibilities correspond to two different types of neutrino mass spectra: with normal hierarchy, $m_1 < m_2 < m_3$, and with inverted hierarchy, $m_3 < m_1 < m_2$ (see e.g. [40]). We will use the terms normal hierarchical (NH) and inverted hierarchical (IH) for the two types of spectra in the case of strong inequalities between the neutrino masses, i.e. if $m_1 \ll m_2 \ll m_3$ and[6] $m_3 \ll m_1 < m_2$, respectively. The spectrum can also be of quasi-degenerate (QD) type: $m_1 \cong m_2 \cong m_3$ and $m^2_{1,2,3} \gg |\Delta m^2_{\mathrm{atm}}|$.

The sign of $\Delta m^2_{\mathrm{atm}}$ can be determined in very long baseline neutrino oscillation experiments at neutrino factories (see e.g. [54]), e.g. using combined data from long baseline oscillation experiments at the JHF facility and with off-axis neutrino beams [55]. Under some rather special conditions, it might be determined also in experiments with reactor $\bar{\nu}_e$ [53, 56].

As is well known, neutrino oscillation experiments allow one to determine differences of squares of neutrino masses, but not the absolute values of the masses. Information on the absolute values of neutrino masses of interest can be derived in the ^{3}H β-decay experiments studying the electron spectrum [57]–[59] and from cosmological and astrophysical data (see e.g. [60]–[62]). The currently existing most stringent upper bounds on the electron (anti-)neutrino mass $m_{\bar{\nu}_e}$ were obtained in the Troitzk [58] and Mainz [59] ^{3}H β-decay experiments and read

$$m_{\bar{\nu}_e} < 2.2\,\mathrm{eV} \quad (95\%\,\mathrm{CL}). \tag{12}$$

We have $m_{\bar{\nu}_e} \cong m_{1,2,3}$ for the QD neutrino mass spectrum. The KATRIN ^{3}H β-decay experiment [59] is expected to reach a sensitivity of $m_{\bar{\nu}_e} \sim (0.20\text{–}0.35)\,\mathrm{eV}$, i.e. to probe the region of QD neutrino mass spectrum. Data from the WMAP experiment on the cosmic microwave background radiation was used to obtain an upper limit on the sum of neutrino masses [61]:

$$\sum_j m_j < 0.70\,\mathrm{eV} \quad (95\%\,\mathrm{CL}). \tag{13}$$

A conservative estimate of all the uncertainties related to the derivation of this result (see e.g. [63]) leads to a less stringent upper limit, at least by a factor of ~1.5 and possibly by a factor of ~3. The WMAP and future PLANCK experiments can be sensitive to [60] $\sum_j m_j \cong 0.4\,\mathrm{eV}$. Data on weak lensing of galaxies by large-scale structure, combined with data from the WMAP and PLANCK experiments may allow one to determine $(m_1 + m_2 + m_3)$ with an uncertainty of [62] $\delta \sim 0.04\,\mathrm{eV}$.

After the spectacular experimental progress made during the last several years in the studies of neutrino oscillations, further understanding of the structure of the neutrino masses and mixing, of their origins and of the status of the CP symmetry in the lepton sector requires a large and challenging programme of research to be pursued in neutrino physics. The main goals of such a

[6] This definition of the IH spectrum corresponds to a convention we will call A (see e.g. [53]), in which the neutrino masses are not ordered in magnitude according to their index number. We can also always number the neutrinos with definite mass in such a way that [24, 48] $m_1 < m_2 < m_3$. In this convention called B [53], the IH spectrum corresponds to $m_1 \ll m_2 \cong m_3$. We will use convention B in our further analysis.

research programme should include the following:

- High-precision determination of the neutrino mixing parameters which control the solar and the dominant atmospheric neutrino oscillations, $\Delta m^2_{\odot}$, $\theta_{\odot}$ and $\Delta m^2_{\rm A}$, $\theta_{\rm atm}$.
- Measurement of, or improving by at least a factor of 5–10 the existing upper limit on, the value of the only small mixing angle θ ($=\theta_{13}$) in the PMNS matrix U.
- Determination of the type of the neutrino mass spectrum (NH or IH or QD).
- Determining or obtaining significant constraints on the absolute scale of neutrino masses, or on the lightest neutrino mass.
- Determining the nature of massive neutrinos, which can be Dirac or Majorana particles.
- To establish whether the CP symmetry is violated in the lepton sector (i) due to the Dirac phase δ and/or (ii) due to the Majorana phases α_{21} and α_{31} if the massive neutrinos are Majorana particles.
- Searching with increased sensitivity for possible manifestations, other than flavour neutrino oscillations, of the nonconservation of individual lepton charges $L_l, l = e, \mu, \tau$, such as $\mu \to e + \gamma$ and $\tau \to \mu + \gamma$ decays.
- Understanding at a fundamental level the mechanism giving rise to the neutrino masses and mixing and to the L_l nonconservation, i.e. finding the theory of neutrino mixing. Progress in the theory of neutrino mixing might also lead, in particular, to a better understanding of the possible relation between CP violation in the lepton sector at low energies and generation of the baryon asymmetry of the Universe.

Obviously, successful realization of the experimental part of this programme of research would be a formidable task and would require many years.

In the present paper, we will review the potential contribution of studies of neutrinoless double-beta ($(\beta\beta)_{0\nu}$) decay of certain even–even nuclei, $(A, Z) \to (A, Z+2) + \mathrm{e}^- + \mathrm{e}^-$, to the programme of research outlined above. The $(\beta\beta)_{0\nu}$ decay is allowed if the neutrinos with definite mass are Majorana particles (see e.g. [10, 64, 65] for reviews). Let us recall that the nature (Dirac or Majorana) of the massive neutrinos ν_j is related to the fundamental symmetries of particle interactions. The neutrinos ν_j will be Dirac fermions if the particle interactions conserve some lepton charge, e.g. the total lepton charge L. The neutrinos with definite mass can be Majorana particles if there does not exist any conserved lepton charge. As is well known, massive neutrinos are predicted to be of Majorana nature by the see-saw mechanism of neutrino mass generation [66], which also provides a very attractive explanation for the smallness of the neutrino masses and, through the leptogenesis theory [47], for the observed baryon asymmetry of the Universe.

If the massive neutrinos ν_j are Majorana fermions, processes in which the total lepton charge L is not conserved and changes by two units, such as $K^+ \to \pi^- + \mu^+ + \mu^+$ and $\mu^+ + (A, Z) \to (A, Z+2) + \mu^-$, should exist. The process most sensitive to the possible Majorana nature of the massive neutrinos ν_j is the $(\beta\beta)_{0\nu}$ decay (see e.g. [10]). If the $(\beta\beta)_{0\nu}$ decay is generated *only by the (V-A) charged current weak interaction via the exchange of the three Majorana neutrinos ν_j and the latter have masses not exceeding a few MeV*, which will be assumed to hold throughout this paper, the dependence of the $(\beta\beta)_{0\nu}$-decay amplitude $A(\beta\beta)_{0\nu}$ on the neutrino mass and mixing parameters factorizes in the effective Majorana mass $\langle m \rangle$ (see e.g. [10, 65]):

$$A(\beta\beta)_{0\nu} \sim \langle m \rangle M, \tag{14}$$

where M is the corresponding nuclear matrix element (NME) and

$$|\langle m\rangle| = |m_1|U_{e1}|^2 + m_2|U_{e2}|^2\,e^{i\alpha_{21}} + m_3|U_{e3}|^2\,e^{i\alpha_{31}}|, \tag{15}$$

α_{21} and α_{31} being the two Majorana CP-violating phases of the PMNS matrix[7] [33, 35]. Let us note that if CP invariance holds, one has [67] $\alpha_{21} = k\pi, \alpha_{31} = k'\pi$, where $k, k' = 0, 1, 2, \ldots$. In this case,

$$\eta_{21} \equiv e^{i\alpha_{21}} = \pm 1, \qquad \eta_{31} \equiv e^{i\alpha_{31}} = \pm 1 \tag{16}$$

represent the relative CP parities of the Majorana neutrinos ν_1 and ν_2 and ν_1 and ν_3, respectively. It follows from equation (15) that measurement of $|\langle m\rangle|$ will provide information, in particular, on the neutrino masses. As equation (14) indicates, observation of the $(\beta\beta)_{0\nu}$ decay of a given nucleus and measurement of the corresponding half lifetime would allow one to determine $|\langle m\rangle|$ only if the value of the relevant NME M is known with a relatively low uncertainty.

The experimental searches for $(\beta\beta)_{0\nu}$ decay have a long history (see e.g. [64, 65]). Rather stringent upper bounds on $|\langle m\rangle|$ have been obtained in the ^{76}Ge experiments by the Heidelberg–Moscow collaboration [68]:

$$|\langle m\rangle| < 0.35\,\text{eV}, \quad 90\%\,\text{CL}. \tag{17}$$

Taking into account a factor of 3 uncertainty associated with the calculation of the relevant NME [65], we get

$$|\langle m\rangle| < (0.35\text{–}1.05)\,\text{eV}, \quad 90\%\,\text{CL}. \tag{18}$$

The IGEX collaboration has obtained [69]:

$$|\langle m\rangle| < (0.33\text{–}1.35)\,\text{eV}, \quad 90\%\,\text{CL}. \tag{19}$$

Evidence for $(\beta\beta)_{0\nu}$ decay of ^{76}Ge, taking place with a rate corresponding to $0.11\,\text{eV} \leqslant |\langle m\rangle| \leqslant 0.56\,\text{eV}$ (95% CL), is claimed to have been obtained in [70]. The results presented in [70] have been criticized in [71]. Even stronger evidence has reported recently in [72], where the following value of $|\langle m\rangle|$ has been given:

$$0.1\,\text{eV} \leqslant |\langle m\rangle| \leqslant 0.9\,\text{eV}, \quad 99.73\%\,\text{CL}. \tag{20}$$

The results reported in [72] will be checked in the currently running and future $(\beta\beta)_{0\nu}$-decay experiments (see below). However, it may take a very long time before a comprehensive check could be completed.

Higher sensitivity to $|\langle m\rangle|$ is planned to be reached in several $(\beta\beta)_{0\nu}$-decay experiments of a new generation. The NEMO3 experiment [73] with ^{100}M and ^{82}Se, which began to take data in July 2002, and the cryogenics detector CUORICINO [75], which uses ^{130}Te and is already operative, are expected to reach a sensitivity to values of $|\langle m\rangle| \sim 0.2\,\text{eV}$. The first preliminary results from these two experiments were published recently [73, 74] and they respectively read

[7] We assume that $m_j > 0$ and that the fields of the Majorana neutrinos ν_j satisfy the Majorana condition $C(\bar{\nu}_j)^{\mathrm{T}} = \nu_j$, $j = 1, 2, 3$, where C is the charge conjugation matrix.

(90% CL): $|\langle m\rangle| < (1.2–2.7)$ eV and $|\langle m\rangle| < (0.7–1.7)$ eV. Up to an order of magnitude, better sensitivity, i.e. to $|\langle m\rangle| \cong 2.7\times10^{-2}$, 1.5×10^{-2}, 5.0×10^{-2}, 2.5×10^{-2} and 3.6×10^{-2} eV, is expected to be achieved in the CUORE, GENIUS, EXO, MAJORANA and MOON experiments [75][8] with ^{130}Te, ^{76}Ge, ^{136}Xe, ^{76}Ge and ^{100}Mo, respectively. Additional high-sensitivity experiments with ^{136}Xe (XMASS [77]) and ^{48}Ca (CANDLES [78]) are also being considered.

As we will discuss in what follows, the studies of $(\beta\beta)_{0\nu}$ decay and the measurement of a nonzero value of $|\langle m\rangle| \gtrsim$ a few 10^{-2} eV:

- Can establish the Majorana nature of massive neutrinos. The $(\beta\beta)_{0\nu}$ decay experiments are presently the only feasible experiments capable of doing that (see [10]).
- Can give information on the type of the neutrino mass spectrum [21]–[23], [82] (see also [40, 79]–[81]. More specifically, a measured value of $|\langle m\rangle| \gtrsim$ a few $\times\, 10^{-2}$ eV can provide, in particular, unique constraints on, or even can allow one to determine the type of the neutrino mass spectrum if $\nu_{1,2,3}$ are Majorana particles [21, 23].
- Can provide also unique information on the absolute scale of neutrino masses, or on the lightest neutrino mass (see e.g. [21, 22, 79]).
- With additional information from other sources (^{3}H β-decay experiments or cosmological and astrophysical data and considerations) on the absolute neutrino mass scale, the $(\beta\beta)_{0\nu}$-decay experiments can provide unique information on the Majorana CP-violation phases α_{21} and α_{31} [22, 24, 40, 42, 43].

2. Predictions of the effective Majorana mass

The predicted value of $|\langle m\rangle|$ depends, for 3-ν mixing on [83] (see also [40, 79]): (i) $\Delta m^2_{\rm A}$, (ii) $\theta_\odot$ and $\Delta m^2_\odot$, (iii) the lightest neutrino mass and (iv) the mixing angle θ. Using the convention (B), in which always $m_1 < m_2 < m_3$, one has $\Delta m^2_{\rm A} \equiv \Delta m^2_{31}$ and $m_3 = \sqrt{m_1^2 + \Delta m^2_{\rm A}}$, while either $\Delta m^2_\odot \equiv \Delta m^2_{21}$ (normal mass hierarchy) or $\Delta m^2_\odot \equiv \Delta m^2_{32}$ (inverted mass hierarchy). In the first case, we have $m_2 = \sqrt{m_1^2 + \Delta m^2_\odot}$, $|U_{e1}|^2 = \cos^2\theta_\odot(1 - |U_{e3}|^2)$, $|U_{e2}|^2 = \sin^2\theta_\odot(1 - |U_{e3}|^2)$ and $|U_{e3}|^2 \equiv \sin^2\theta$, whereas in the second case, $m_2 = \sqrt{m_1^2 + \Delta m^2_{\rm A} - \Delta m^2_\odot}$, $|U_{e2}|^2 = \cos^2\theta_\odot(1 - |U_{e1}|^2)$, $|U_{e3}|^2 = \sin^2\theta_\odot(1 - |U_{e1}|^2)$ and $|U_{e1}|^2 \equiv \sin^2\theta$. The two possibilities for $\Delta m^2_\odot$ correspond also to the two different *hierarchical* types of neutrino mass spectrum—the NH, $m_1 \ll m_2 \ll m_3$, and the IH, $m_1 \ll m_2 \cong m_3$, respectively. Let us recall that, for the QD neutrino mass spectrum, we have $m_1 \cong m_2 \cong m_3$ and $m^2_{1,2,3} \gg \Delta m^2_{\rm A}$. For the allowed ranges of values of $\Delta m^2_\odot$ and $\Delta m^2_{\rm A}$ (see [25]), the NH (IH) spectrum corresponds to $m_1 \lesssim 10^{-3}$ (2×10^{-2}) eV, whereas one has a QD spectrum if $m_{1,2,3} \cong m_{\bar\nu_e} > 0.20$ eV. For m_1 lying in the interval between $\sim 10^{-3}$ (2×10^{-2}) and 0.20 eV, the neutrino mass spectrum is with partial normal (inverted) hierarchy (see e.g. [40]).

Given $\Delta m^2_\odot$, $\Delta m^2_{\rm A}$, $\theta_\odot$ and $\sin^2\theta$, the value of $|\langle m\rangle|$ depends strongly on the type of the neutrino mass spectrum as well as on the values of the two Majorana CP-violation phases of the PMNS matrix, α_{21} and α_{31} (see equation (15)). Note that for the QD spectrum, $m_1 \cong m_2 \cong m_3$, $m^2_{1,2,3} \gg \Delta m^2_{\rm A}$, $\Delta m^2_\odot$ and $|\langle m\rangle|$ is essentially independent of $\Delta m^2_{\rm A}$ and $\Delta m^2_\odot$.

[8] The quoted sensitivities correspond to values of the relevant NME from [76].

Correspondingly, the two possibilities, $\Delta m^2_\odot \equiv \Delta m^2_{21}$ and $\Delta m^2_\odot \equiv \Delta m^2_{32}$, lead effectively to the same predictions for $|\langle m\rangle|$.[9]

2.1. NH neutrino mass spectrum

For the NH neutrino mass spectrum, one has $m_2 \cong \sqrt{\Delta m^2_\odot}$, $m_3 \cong \sqrt{\Delta m^2_{\rm atm}}$ and $|U_{e3}|^2 \equiv \sin^2\theta$ and, correspondingly,

$$|\langle m\rangle| = \left|(m_1\cos^2\theta_\odot + e^{i\alpha_{21}}\sqrt{\Delta m^2_\odot}\sin^2\theta_\odot)\cos^2\theta + \sqrt{\Delta m^2_{\rm A}}\sin^2\theta\, e^{i\alpha_{31}}\right| \tag{21}$$

$$\simeq \left|\sqrt{\Delta m^2_\odot}\sin^2\theta_\odot\cos^2\theta + \sqrt{\Delta m^2_{\rm A}}\sin^2\theta\, e^{i(\alpha_{31}-\alpha_{21})}\right|, \tag{22}$$

where we have neglected the term $\sim m_1$ in equation (22). In this case, one of the three massive Majorana neutrinos effectively 'decouples' and does not give a contribution to $|\langle m\rangle|$; however, the value of $|\langle m\rangle|$ still depends on the Majorana CP-violation phase $\alpha_{32} = \alpha_{31} - \alpha_{21}$. This is a consequence of the fact that, in contrast with the case of massive Dirac neutrinos (or quarks), CP violation can take place in the mixing of only two massive Majorana neutrinos [33].

From equations (3) and (8)–(11), it follows that $\sqrt{\Delta m^2_\odot} \lesssim 10^{-2}$ eV, $\sin^2\theta_\odot \lesssim 0.40$, $\sqrt{\Delta m^2_{\rm A}} \lesssim 5.5\times 10^{-2}$ eV (at 90% CL) and the largest neutrino mass enters into the expression for $|\langle m\rangle|$ with the factor $\sin^2\theta < 0.05$. For these reasons, the predicted value of $|\langle m\rangle|$ is below 10^{-2} eV: for $\sin^2\theta = 0.04$ (0.02), one finds $|\langle m\rangle| \lesssim 0.006$ (0.005) eV. Using the best-fit values of the indicated neutrino oscillation parameters, we get even smaller values for $|\langle m\rangle|$, $|\langle m\rangle| \lesssim 0.005$ (0.004) eV (see tables 1 and 2). Actually, from equation (21) and the allowed ranges of values of $\Delta m^2_\odot$, $\Delta m^2_{\rm A}$, $\sin^2\theta_\odot$, $\sin^2\theta$ as well as of the lightest neutrino mass m_1 and the CP-violation phases α_{21} and α_{31}, it follows that for the NH spectrum, there can be a complete cancellation between the contributions of the three terms in equation (21) and one can have [22] $|\langle m\rangle| = 0$.

2.2. IH spectrum

One has, for the IH neutrino mass spectrum (see e.g. [40]), $m_2 \cong m_3 \cong \sqrt{\Delta m^2_{\rm A}}$, $|U_{e1}|^2 \equiv \sin^2\theta$. Neglecting $m_1\sin^2\theta$ in equation (15), we find [24, 40, 79]

$$|\langle m\rangle| \cong \sqrt{\Delta m^2_{\rm A}}\cos^2\theta\sqrt{1-\sin^2 2\theta_\odot\sin^2\left(\tfrac{1}{2}\alpha_{32}\right)}. \tag{23}$$

Even though one of the three massive Majorana neutrinos 'decouples', the value of $|\langle m\rangle|$ depends on the Majorana CP-violating phase $\alpha_{32} \equiv (\alpha_{31} - \alpha_{21})$. Obviously,

$$\sqrt{\Delta m^2_{\rm A}}\cos^2\theta|\cos 2\theta_\odot| \leqslant |\langle m\rangle| \leqslant \sqrt{\Delta m^2_{\rm A}}\cos^2\theta. \tag{24}$$

[9] This statement is valid, within the convention $m_1 < m_2 < m_3$ we are using, as long as there are no independent constraints on the CP-violating phases α_{21} and α_{31}, which enter into the expression for $|\langle m\rangle|$. For the spectrum with normal hierarchy, $|\langle m\rangle|$ depends primarily on α_{21} ($|U_{e3}|^2 \ll 1$), whereas if the spectrum is with inverted hierarchy, $|\langle m\rangle|$ will depend essentially on $\alpha_{31} - \alpha_{21}$ ($|U_{e1}|^2 \ll 1$).

Table 1. The maximal values of $|\langle m\rangle|$ (in units of 10^{-3} eV) for the NH and IH spectra, and the minimal values of $|\langle m\rangle|$ (in units of 10^{-3} eV) for the IH and QD spectra, for the best-fit values of the oscillation parameters and $\sin^2\theta = 0.0$, 0.02 and 0.04. The results for the NH and IH spectra are obtained for $\Delta m^2_{\rm atm}|_{\rm BF} = 2.6\times 10^{-3}\,{\rm eV}^2$ ($2.0\times 10^{-3}\,{\rm eV}^2$ for values in parentheses) and $m_1 = 10^{-4}$ eV, whereas those for the QD spectrum correspond to $m_0 = 0.2$ eV (from [23]).

$\sin^2\theta$	$\lvert\langle m\rangle\rvert^{\rm NH}_{\rm max}$	$\lvert\langle m\rangle\rvert^{\rm IH}_{\rm min}$	$\lvert\langle m\rangle\rvert^{\rm IH}_{\rm max}$	$\lvert\langle m\rangle\rvert^{\rm QD}_{\rm min}$
0.0	2.6 (2.6)	19.9 (17.3)	50.5 (44.2)	79.9
0.02	3.6 (3.5)	19.5 (17.0)	49.5 (43.3)	74.2
0.04	4.6 (4.3)	19.1 (16.6)	48.5 (42.4)	68.5

Table 2. Same as table 1, except for the 90% CL allowed values of $\Delta m^2_\odot$ and $\theta_\odot$ obtained in [18], and of $\Delta m^2_{\rm atm}$ given in equation (6) (equation (8) for results in parentheses) (from [23]).

$\sin^2\theta$	$\lvert\langle m\rangle\rvert^{\rm NH}_{\rm max}$	$\lvert\langle m\rangle\rvert^{\rm IH}_{\rm min}$	$\lvert\langle m\rangle\rvert^{\rm IH}_{\rm max}$	$\lvert\langle m\rangle\rvert^{\rm QD}_{\rm min}$
0.0	3.7 (3.7)	10.1 (8.7)	56.3 (50.6)	47.9
0.02	4.7 (4.6)	9.9 (8.6)	55.1 (49.6)	42.8
0.04	5.5 (5.3)	11.4 (9.9)	54.0 (48.6)	45.4

The upper and lower limits correspond respectively to the CP-conserving cases $\alpha_{32} = 0$, or $\alpha_{21} = \alpha_{31} = 0, \pm\pi$, and $\alpha_{32} = \pm\pi$, or $\alpha_{21} = \alpha_{31} + \pi = 0, \pm\pi$. Most remarkably, since $\cos 2\theta_\odot \sim 0.40$ according to the solar neutrino and KamLAND data, we get a significant lower limit on $|\langle m\rangle|$, typically exceeding 10^{-2} eV, in this case [21, 22] (tables 1 and 2). Using, for example, the best-fit values of $\Delta m^2_{\rm A}$ and $\tan^2\theta_\odot$, one finds: $|\langle m\rangle| \gtrsim 0.017$ eV. The maximal value of $|\langle m\rangle|$ is determined by $\Delta m^2_{\rm A}$ and can reach, as it follows from equations (3) and (4), $|\langle m\rangle| \sim 0.050$–$0.055$ eV. The indicated values of $|\langle m\rangle|$ are within the range of sensitivity of the next generation of $(\beta\beta)_{0\nu}$-decay experiments.

The expression for $|\langle m\rangle|$, equation (23), permits us to relate the value of $\sin^2(\alpha_{31}-\alpha_{21})/2$ to the experimentally measured quantities [24, 40] $|\langle m\rangle|$, $\Delta m^2_{\rm atm}$ and $\sin^2 2\theta_\odot$:

$$\sin^2\frac{\alpha_{31}-\alpha_{21}}{2} \cong \left(1 - \frac{|\langle m\rangle|^2}{\Delta m^2_{\rm A}\cos^4\theta}\right)\frac{1}{\sin^2 2\theta_\odot}. \tag{25}$$

A more precise determination of $\Delta m^2_{\rm A}$ and $\theta_\odot$ and a sufficiently accurate measurement of $|\langle m\rangle|$ could allow one to get information about the value of $(\alpha_{31}-\alpha_{21})$, provided the neutrino mass spectrum is of the IH type.

2.3. Three QD neutrinos

In this case, it is convenient to introduce $m_0 \equiv m_1 \cong m_2 \cong m_3$, $m_0^2 \gg \Delta m^2_{\rm A}$, $m_0 \gtrsim 0.20$ eV. The mass m_0 effectively coincides with the electron (anti-)neutrino mass $m_{\bar\nu_e}$ measured in the ^{3}H β-decay experiments: $m_0 = m_{\bar\nu_e}$. Thus, $m_0 < 2.2$ eV, or if we use a conservative cosmological

upper limit [63], $m_0 < 0.7$ eV. The QD neutrino mass spectrum is realized for values of m_0, which can be measured in the ^{3}H β-decay experiment KATRIN.

The effective Majorana mass $|\langle m\rangle|$ is given by

$$|\langle m\rangle| \cong m_0|(\cos^2\theta_\odot + \sin^2\theta_\odot\, e^{i\alpha_{21}})\cos^2\theta + e^{i\alpha_{31}}\sin^2\theta| \tag{26}$$

$$\cong m_0|\cos^2\theta_\odot + \sin^2\theta_\odot\, e^{i\alpha_{21}}| = m_0\sqrt{1-\sin^2 2\theta_\odot \sin^2\left(\frac{\alpha_{21}}{2}\right)}. \tag{27}$$

Similar to the case of the IH spectrum, one has

$$m_0|\cos 2\theta_\odot| \lesssim |\langle m\rangle| \lesssim m_0. \tag{28}$$

For $\cos 2\theta_\odot \sim 0.40$, favoured by the solar neutrino and the KamLAND data, one finds a non-trivial lower limit on $|\langle m\rangle|$, $|\langle m\rangle| \gtrsim 0.07$ eV. For the 90% CL allowed ranges of values of the parameters, one has $|\langle m\rangle| \gtrsim 0.043$ eV (tables 1 and 2). Using the conservative cosmological upper bound on the sum of neutrino masses, we get $|\langle m\rangle| \lesssim 0.70$ eV. Also, in this case, one can obtain, in principle, direct information about one CP-violation phase from the measurement of $|\langle m\rangle|$, m_0 and $\sin^2 2\theta_\odot$:

$$\sin^2\frac{\alpha_{21}}{2} \cong \left(1-\frac{|\langle m\rangle|^2}{m_0^2}\right)\frac{1}{\sin^2 2\theta_\odot}. \tag{29}$$

The specific features of the predictions of $|\langle m\rangle|$ for the three types of neutrino mass spectra discussed above are evident from figures 1 and 2, where the dependence of $|\langle m\rangle|$ on m_1 for the LMA solution is shown. For instance, if $\Delta m^2_\odot = \Delta m^2_{21}$, which corresponds to a spectrum with normal hierarchy, $|\langle m\rangle|$ can lie anywhere between 0 and the currently existing upper limits, given by equations (19) and (20). This conclusion does not change even under the most favourable conditions for the determination of $|\langle m\rangle|$, namely when $\Delta m^2_{\rm atm}$, $\Delta m^2_\odot$, $\theta_\odot$ and θ are known with negligible uncertainty, as seen in figures 1 and 2.

3. Constraining the lightest neutrino mass

By observing the $(\beta\beta)_{0\nu}$ decay of a given nucleus, it would be possible to determine the value of $|\langle m\rangle|$ from the measurement of the associated lifetime of the decay. This would require knowledge of the NME of the process. At present, there exists large uncertainty in the calculation of $(\beta\beta)_{0\nu}$-decay NMEs (see e.g. [65, 84]). This is reflected, in particular, in the factor of ~3 uncertainty in the upper limit on $|\langle m\rangle|$, which is extracted from the experimental lower limits on the $(\beta\beta)_{0\nu}$-decay half lifetime of ^{76}Ge. Recently, encouraging results on the problem of calculating the NMEs have been obtained in [85]. The observation of a $(\beta\beta)_{0\nu}$ decay of one nucleus would probably lead to searches and, eventually, to the observation of decay of other nuclei. One can expect that such a progress, in particular, will help to solve the problem of sufficiently precise calculation of the NMEs for the $(\beta\beta)_{0\nu}$ decay.

In this section, we consider briefly the information that future $(\beta\beta)_{0\nu}$ decay and/or ^{3}H β-decay experiments can provide on the lightest neutrino mass m_1, without taking into account the possible effects of currently existing uncertainties in the evaluation of $(\beta\beta)_{0\nu}$-decay NMEs.

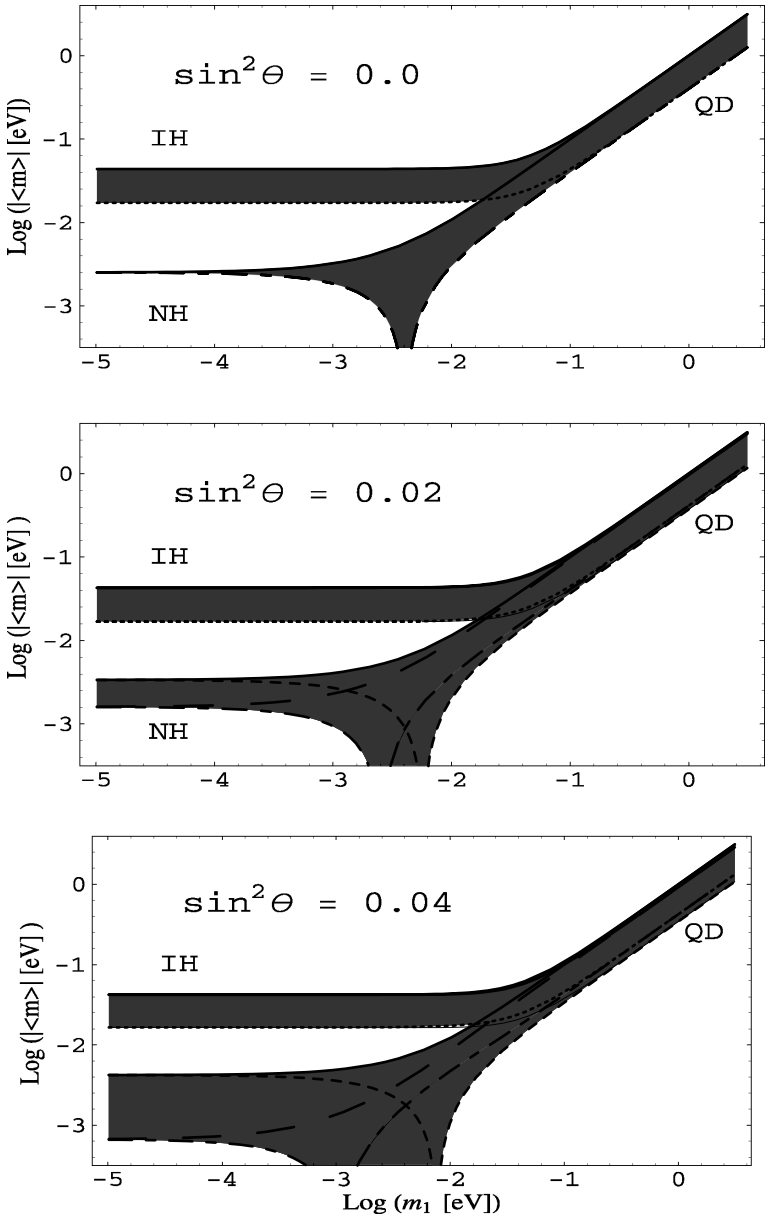

Figure 1. The dependence of $|\langle m\rangle|$ on m_1 for the LMA-I solution, for $\Delta m^2_{\odot} = \Delta m^2_{21}$ and $\Delta m^2_{\odot} = \Delta m^2_{32}$, and for the best-fit values of the solar neutrino oscillation parameters found in [18] and of $\Delta m^2_{\rm atm}$ in [27], and for three fixed values of $\sin^2\theta = 0.0; 0.02; 0.04$ (top, middle and bottom panels). For CP-conservation, the allowed values of $|\langle m\rangle|$ are constrained to lie: for (i) $\Delta m^2_{\odot} = \Delta m^2_{21}$ and the middle and bottom panels (top panel)—(a) on the lower thick solid lines (on the lower thick solid line) if $\eta_{21} = \eta_{31} = 1$, ($b$) on the long-dashed lines (on the lower thick solid line) if $\eta_{21} = -\eta_{31} = 1$, ($c$) on the dash-dotted lines if $\eta_{21} = -\eta_{31} = -1$, ($d$) on the short-dashed lines (on the dash-dotted lines) if $\eta_{21} = \eta_{31} = -1$; and for (ii) $\Delta m^2_{\odot} = \Delta m^2_{32}$ (all panels)—(a) on the upper thick solid line if $\eta_{21} = \eta_{31} = \pm 1$, ($b$) on the dotted lines if $\eta_{21} = -\eta_{31} = \pm 1$. Values of $|\langle m\rangle|$ in the black regions signal CP-violation (from [23]).

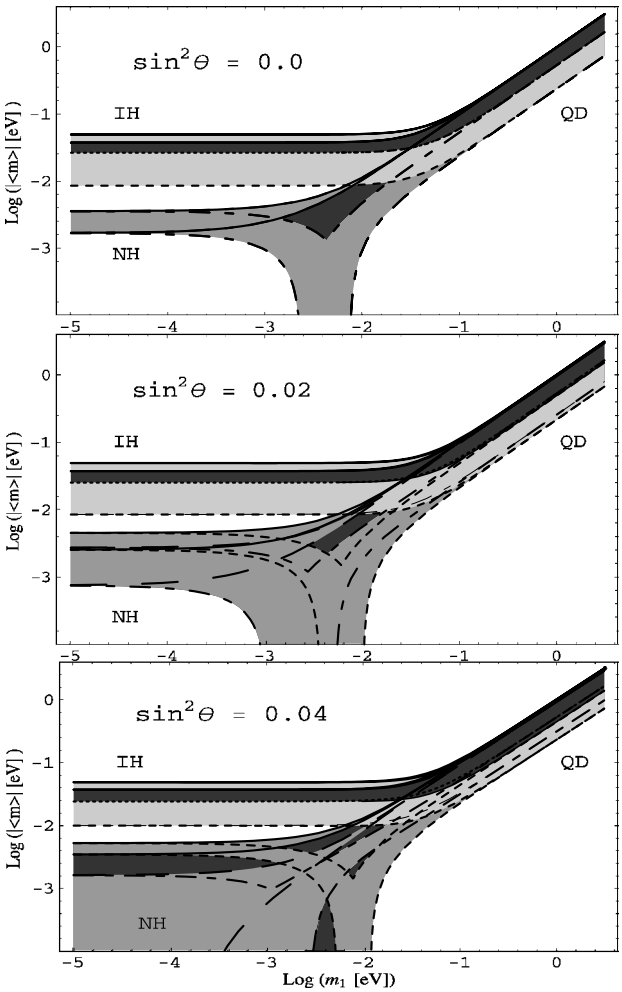

Figure 2. The dependence of $|\langle m\rangle|$ on m_1 for the LMA-I solution, for $\Delta m^2_{\odot} = \Delta m^2_{21}$ and $\Delta m^2_{\odot} = \Delta m^2_{32}$, and for the 90% CL allowed values of $\Delta m^2_{\odot}$ and $\sin^2\theta_{\odot}$ found in [18] and of $\Delta m^2_{\rm atm}$ in [27], and for three values of $\sin^2\theta = 0.0; 0.02; 0.04$ (top, middle and bottom panels). For CP conservation, the allowed values of $|\langle m\rangle|$ are constrained to lie: for (i) $\Delta m^2_{\odot} = \Delta m^2_{21}$ and the middle and bottom panels (top panel), in the medium-gray and light-gray regions (a) between the two lower thick solid lines if $\eta_{21} = \eta_{31} = 1$, ($b$) between the two long-dashed lines (between the two lower thick solid lines) if $\eta_{21} = -\eta_{31} = 1$, ($c$) between the three thick dash-dotted lines and the axes (between the dash-dotted lines and the axes) if $\eta_{21} = -\eta_{31} = -1$, ($d$) between the three thick short-dashed lines and the axes (between the dash-dotted lines and the axes) if $\eta_{21} = \eta_{31} = -1$; and for (ii) $\Delta m^2_{\odot} = \Delta m^2_{32}$ and the middle and bottom panels (top), in the light-grey regions (a) between the two upper thick solid lines if $\eta_{21} = \eta_{31} = \pm 1$, ($b$) between the dotted and the thin dash-dotted (the dotted and the thick short-dashed) lines if $\eta_{21} = -\eta_{31} = 1$, ($c$) between the dotted and the upper thick short-dashed (the dotted and the thick short-dashed) lines if $\eta_{21} = -\eta_{31} = -1$. For CP violation, the allowed regions for $|\langle m\rangle|$ cover all grey + black regions. Values of $|\langle m\rangle|$ in the black regions signal CP violation (from [23]).

An experimental upper limit on $|\langle m\rangle|$, $|\langle m\rangle| < |\langle m\rangle|_{\rm exp}$, will determine a maximal value of m_1, $m_1 < (m_1)_{\rm max}$ for the normal mass hierarchy, $\Delta m^2_\odot \equiv \Delta m^2_{21}$ (figures 1 and 2). For the QD spectrum, for instance, we have $m_1 \gg \Delta m^2_\odot$, $\Delta m^2_{\rm A}$, and up to corrections $\sim\Delta m^2_\odot \sin^2\theta_\odot/(2m_1^2)$ and $\sim\Delta m^2_{\rm A}\sin^2\theta/(2m_1^2)$, one finds [22, 86]

$$(m_1)_{\rm max} \cong \frac{|\langle m\rangle|_{\rm exp}}{|\cos 2\theta_\odot \cos^2\theta - \sin^2\theta|}. \tag{30}$$

We get similar results for inverted mass hierarchy, $\Delta m^2_\odot \equiv \Delta m^2_{32}$, provided the experimental upper limit $|\langle m\rangle|_{\rm exp}$ is larger than the minimal value of $|\langle m\rangle|$, $|\langle m\rangle|^{\rm ph}_{\rm min}$ (figures 1 and 2), predicted by taking into account all uncertainties in the values of the relevant input parameters ($\Delta m^2_{\rm A}$, $\Delta m^2_\odot$, $\theta_\odot$, etc). If $|\langle m\rangle|_{\rm exp} < |\langle m\rangle|^{\rm ph}_{\rm min}$, then either (i) the neutrino mass spectrum is not of the inverted hierarchy type or (ii) there exist contributions to the $(\beta\beta)_{0\nu}$-decay rate other than due to the light Majorana neutrino exchange (see e.g. [87]) that partially cancel the contribution from the Majorana neutrino exchange. The indicated result might also suggest that the massive neutrinos are Dirac particles.

Measurement of $|\langle m\rangle| = (|\langle m\rangle|)_{\rm exp} \gtrsim 0.02\,{\rm eV}$ if $\Delta m^2_\odot \equiv \Delta m^2_{21}$ and measurement of $|\langle m\rangle| = (|\langle m\rangle|)_{\rm exp} \gtrsim \sqrt{\Delta m^2_{\rm A}}\cos^2\theta$ if $\Delta m^2_\odot \equiv \Delta m^2_{32}$ would imply that $m_1 \gtrsim 0.02\,{\rm eV}$ and $0.04\,{\rm eV}$ respectively and, thus, a neutrino mass spectrum with partial hierarchy or of the QD type [40] (figures 1 and 2). The lightest neutrino mass will be constrained to lie in a rather narrow interval, $(m_1)_{\rm min} \leqslant m_1 \leqslant (m_1)_{\rm max}$.[10] The limiting values of m_1 correspond to the case of CP conservation. For $\Delta m^2_\odot \ll m_1^2$, (i.e. for $\Delta m^2_\odot \lesssim 10^{-4}\,{\rm eV}^2$), as can be shown [22], we have $(m_1)_{\rm min} \cong (|\langle m\rangle|)_{\rm exp}$ for $\Delta m^2_\odot \equiv \Delta m^2_{21}$ and $\sqrt{((m_1)_{\rm min})^2 + \Delta m^2_{\rm A}} \cong (|\langle m\rangle|)_{\rm exp}$ for $\Delta m^2_\odot \equiv \Delta m^2_{32}$.

A measured value of $|\langle m\rangle|$, satisfying $(|\langle m\rangle|)_{\rm exp} < (|\langle m\rangle|)_{\rm max}$, where, e.g. for a QD spectrum, $(|\langle m\rangle|)_{\rm max} \cong m_1 \cong m_{\bar\nu_e}$, would imply that at least one of the two CP-violating phases is different from zero: $\alpha_{21} \neq 0$ or $\alpha_{31} \neq 0$.[11]

If the measured value of $|\langle m\rangle|$ lies between the minimal and maximal values of $|\langle m\rangle|$, which are predicted for the IH spectrum,

$$|\langle m\rangle|_\pm = \left|\sqrt{\Delta m^2_{\rm A} - \Delta m^2_\odot}\cos^2\theta_\odot \pm \sqrt{\Delta m^2_{\rm A}}\sin^2\theta_\odot\right|\cos^2\theta, \tag{31}$$

m_1 again would be limited from above, but we would have $(m_1)_{\rm min} = 0$ (figures 1 and 2).

A measured value of $m_{\bar\nu_e}$, $(m_{\bar\nu_e})_{\rm exp} \gtrsim 0.20\,{\rm eV}$, satisfying $(m_{\bar\nu_e})_{\rm exp} > (m_1)_{\rm max}$, where $(m_1)_{\rm max}$ is determined from the upper limit on $|\langle m\rangle|$ if the $(\beta\beta)_{0\nu}$ decay is not observed, might imply that the massive neutrinos are Dirac particles. If $(\beta\beta)_{0\nu}$ decay has been observed and $|\langle m\rangle|$ measured, the inequality $(m_{\bar\nu_e})_{\rm exp} > (m_1)_{\rm max}$, with $(m_1)_{\rm max}$ determined from the measured value of $|\langle m\rangle|$, would lead to the conclusion that there exist contribution(s) to the $(\beta\beta)_{0\nu}$-decay rate other than from the light Majorana neutrino exchange (see e.g. [87] and references therein) that partially cancels the contribution from the Majorana neutrino exchange.

[10] Analytic expressions for $(m_1)_{\rm min}$ and $(m_1)_{\rm max}$ are given in [22].

[11] Note that, in general, the knowledge of the value of $|\langle m\rangle|$ alone will not allow to distinguish the case of CP conservation from that of CP violation.

Table 3. The maximal values of $|\langle m\rangle|$ for the NH and IH spectra and the minimal values of $|\langle m\rangle|$ for the IH and QD spectra (in units of 10^{-3} eV), obtained by using the best-fit values of the solar and atmospheric neutrino oscillation parameters and including 1 S.D. (3 S.D.) uncertainties of 5% (15%) on $\tan^2\theta_\odot$ and $\Delta m^2_\odot$, and of 10% (30%) on $\Delta m^2_{\rm atm}$. Results for $\sin^2\theta = 0.0$, 0.02 and 0.04 are shown. Two values of $\Delta m^2_{\rm atm}|_{\rm BF}$ are used: $\Delta m^2_{\rm atm}|_{\rm BF} = 2.6\times10^{-3}\,{\rm eV}^2$ [$2.0\times10^{-3}\,{\rm eV}^2$]. The results for the NH and IH spectra are obtained for $m_1 = 10^{-4}$ eV, whereas those for the QD spectrum correspond to $m_0 = 0.2$ eV (from [23]).

$\sin^2\theta$	$\lvert\langle m\rangle\rvert^{\rm NH}_{\rm max}$	$\lvert\langle m\rangle\rvert^{\rm IH}_{\rm min}$	$\lvert\langle m\rangle\rvert^{\rm IH}_{\rm max}$	$\lvert\langle m\rangle\rvert^{\rm QD}_{\rm min}$
0.0	2.8 (3.1) [2.8 (3.1)]	17.8 (13.8) [15.5 (12.0)]	53.0 (57.8) [46.4 (50.6)]	78.0 (69.4) [77.6 (69.1)]
0.02	3.8 (4.2) [3.7 (4.1)]	17.4 (13.5) [15.2 (11.7)]	52.0 (56.6) [45.5 (49.6)]	72.5 (64.1) [72.0 (63.7)]
0.04	4.8 (5.3) [4.6 (5.0)]	17.0 (13.3) [14.8 (11.5)]	50.9 (55.5) [44.5 (48.6)]	66.9 (58.7) [66.4 (58.4)]

4. Determining the type of the neutrino mass spectrum

The possibility of distinguishing between the three different types of neutrino mass spectrum, NH, IH and QD, depends on the allowed ranges of values of $|\langle m\rangle|$ for the three spectra. More specifically, it is determined by the maximal values of $|\langle m\rangle|$ for the NH and IH spectra, $|\langle m\rangle|^{\rm NH}_{\rm max}$ and $|\langle m\rangle|^{\rm IH}_{\rm max}$, and by the minimal values of $|\langle m\rangle|$ for the IH and QD spectra, $|\langle m\rangle|^{\rm IH}_{\rm min}$ and $|\langle m\rangle|^{\rm QD}_{\rm min}$. These can be derived from equations (21), (24) and (26) and correspond to CP-conserving values of the Majorana phases [82] α_{21} and α_{31}. The minimal value, $|\langle m\rangle|^{\rm QD}_{\rm min}$, scales to a good approximation with m_0 and, thus, is reached for $m_0 = 0.2$ eV.

In tables 1 and 2 (taken from [23]), we show the values of (i) $|\langle m\rangle|^{\rm NH}_{\rm max}$, (ii) $|\langle m\rangle|^{\rm IH}_{\rm min}$ and (iii) $|\langle m\rangle|^{\rm QD}_{\rm min}$ ($m_0 = 0.2$ eV), calculated for the best-fit and the 90% CL allowed ranges of values of $\tan^2\theta_\odot$ and $\Delta m^2_\odot$ in the LMA solution region. In table 3 (from [23]), we give the same quantities, $|\langle m\rangle|^{\rm NH}_{\rm max}$, $|\langle m\rangle|^{\rm IH}_{\rm min}$ and $|\langle m\rangle|^{\rm QD}_{\rm min}$, calculated using the best-fit values of the neutrino oscillation parameters, including 1 S.D. (3 S.D.) 'prospective' uncertainties[12] of 5% (15%) on $\tan^2\theta_\odot$ and $\Delta m^2_\odot$ and of 10% (30%) on $\Delta m^2_{\rm A}$. As evident from tables 1–3, the possibility of determining the type of the neutrino mass spectrum if $|\langle m\rangle|$ is found to be nonzero in the $(\beta\beta)_{0\nu}$-decay experiments of the next generation depends crucially on the precision with which $\Delta m^2_{\rm A}$, $\theta_\odot$, $\Delta m^2_\odot$, $\sin^2\theta$ and $|\langle m\rangle|$ will be measured. It depends crucially also on the values of $\theta_\odot$ and $|\langle m\rangle|$. The precision itself in the measurement of $|\langle m\rangle|$ in the next generation of $(\beta\beta)_{0\nu}$-decay experiments, given the latter sensitivity limits of $\sim$(1.5–5.0) $\times\,10^{-2}$ eV, depends on the value of $|\langle m\rangle|$. Precision in the measurements of $\tan^2\theta_\odot$ and $\Delta m^2_\odot$, used to derive the numbers in table 3 can be achieved, e.g. in the solar neutrino experiments and/or in the experiments with reactor $\bar\nu_e$ [53, 88]. If $\Delta m^2_{\rm A}$ lies in the interval $\Delta m^2_{\rm A} \cong (2.0\text{–}5.0)\times10^{-3}\,{\rm eV}^2$, as is suggested by the current data [25, 28], its value will be determined with a $\sim$10% error (1 S.D.) by the MINOS experiment [49].

High-precision measurements of $\Delta m^2_{\rm A}$, $\tan^2\theta_\odot$ and $\Delta m^2_\odot$ are expected to take place in the next $\sim$6–7 years. We will assume in what follows that the problem of measuring or tightly constraining $\sin^2\theta$ will also be resolved in the indicated period. Under these conditions, the highest uncertainty in the comparison of the theoretically predicted value of $|\langle m\rangle|$ with

[12] See [43, 82] for further details concerning the calculation of the uncertainty in $|\langle m\rangle|$.

that determined in the $(\beta\beta)_{0\nu}$-decay experiments would be associated with the corresponding $(\beta\beta)_{0\nu}$-decay NMEs. We will also assume in what follows that, by the time one or more $(\beta\beta)_{0\nu}$-decay experiments of the next generation will be operative (2009–2010), at least the physical range of variation of the values of the relevant $(\beta\beta)_{0\nu}$-decay NMEs will be unambiguously determined.

Following [43, 82], we will parametrize the uncertainty in $|\langle m\rangle|$ resulting from imprecise knowledge of the relevant NMEs—we will use the term 'theoretical uncertainty' for the latter—through a parameter ζ, $\zeta \geqslant 1$, defined as

$$|\langle m\rangle| = \zeta((|\langle m\rangle|_{\mathrm{exp}})_{\mathrm{min}} \pm \Delta), \tag{32}$$

where $(|\langle m\rangle|_{\mathrm{exp}})_{\mathrm{min}}$ is the value of $|\langle m\rangle|$ obtained from the measured $(\beta\beta)_{0\nu}$-decay half lifetime of a given nucleus using *the largest NME* and Δ is the experimental error. An experiment measuring a $(\beta\beta)_{0\nu}$-decay half lifetime will thus determine a range of $|\langle m\rangle|$ corresponding to

$$(|\langle m\rangle|_{\mathrm{exp}})_{\mathrm{min}} - \Delta \leqslant |\langle m\rangle| \leqslant \zeta((|\langle m\rangle|_{\mathrm{exp}})_{\mathrm{min}} + \Delta). \tag{33}$$

The currently estimated range of ζ^2 for experimentally interesting nuclei varies from 3.5 for ^{48}Ca to 38.7 for ^{130}Te (see e.g. table 2 in [65, 84]). For ^{76}Ge and ^{82}Se, it is $\sim$10 [65]. The actual uncertainties can be smaller [85].

To be possible to distinguish between the NH and IH spectra, between the NH and QD spectra and between IH and QD spectra, the following inequalities must hold, respectively:

$$\zeta|\langle m\rangle|^{\mathrm{NH}}_{\mathrm{max}} < |\langle m\rangle|^{\mathrm{IH}}_{\mathrm{min}}, \tag{34}$$

$$\zeta|\langle m\rangle|^{\mathrm{NH}}_{\mathrm{max}} < |\langle m\rangle|^{\mathrm{QD}}_{\mathrm{min}}, \tag{35}$$

$$\zeta|\langle m\rangle|^{\mathrm{IH}}_{\mathrm{max}} < |\langle m\rangle|^{\mathrm{QD}}_{\mathrm{min}}, \qquad \zeta \geqslant 1. \tag{36}$$

These conditions imply, as can be demonstrated [82], upper limits on $\tan^2\theta_\odot$ that are a function of neutrino oscillation parameters and of ζ.

In figure 3 (taken from [82]), the upper bounds on $\tan^2\theta_\odot$, for which one can distinguish the NH spectrum from the IH spectrum and from that of the QD type, are shown as a function of $\Delta m^2_\odot$ for $\Delta m^2_{\mathrm{A}} = 3\times10^{-3}\,\mathrm{eV}^2$, $\sin^2\theta = 0.05$ and 0.0 and different values of ζ. For the NH versus IH spectrum, results for $\sin^2\theta = 0.01$ are also shown. For the QD spectrum, values of $m_0 = 0.2$; 1.0 eV are used.

The dependence of the maximal value of $\tan^2\theta_\odot$ of interest on m_0 and $\sin^2\theta$ in the NH versus QD case is rather weak as demonstrated in figure 3. This is not so in what concerns the dependence on $\sin^2\theta$ in the NH versus IH case: the maximal value of $\tan^2\theta_\odot$ under discussion can increase noticeably (e.g. by a factor of $\sim$1.2–1.5) when $\sin^2\theta$ decreases from 0.05 to 0. As it follows from figure 3, it would be possible to distinguish between the NH and QD spectra for the values of $\tan^2\theta_\odot$ favoured by the data for values of $\zeta \cong 3$ or even somewhat higher. In contrast, the possibility of distinguishing between the NH and IH spectra for $\zeta \cong 3$ depends critically on the value of $\sin^2\theta$: as figure 3 indicates, this would be possible for the current best-fit value of $\tan^2\theta_\odot$ and, for instance, $\Delta m^2_\odot = (5.0\text{–}15)\times10^{-5}\,\mathrm{eV}^2$, provided $\sin^2\theta \lesssim 0.01$.

In figure 4 (taken from [82]), we show the maximal value of $\tan^2\theta_\odot$ permitting one to distinguish between the IH and QD spectra as a function of Δm^2_{A}, for $\sin^2\theta = 0.05$ and 0.0,

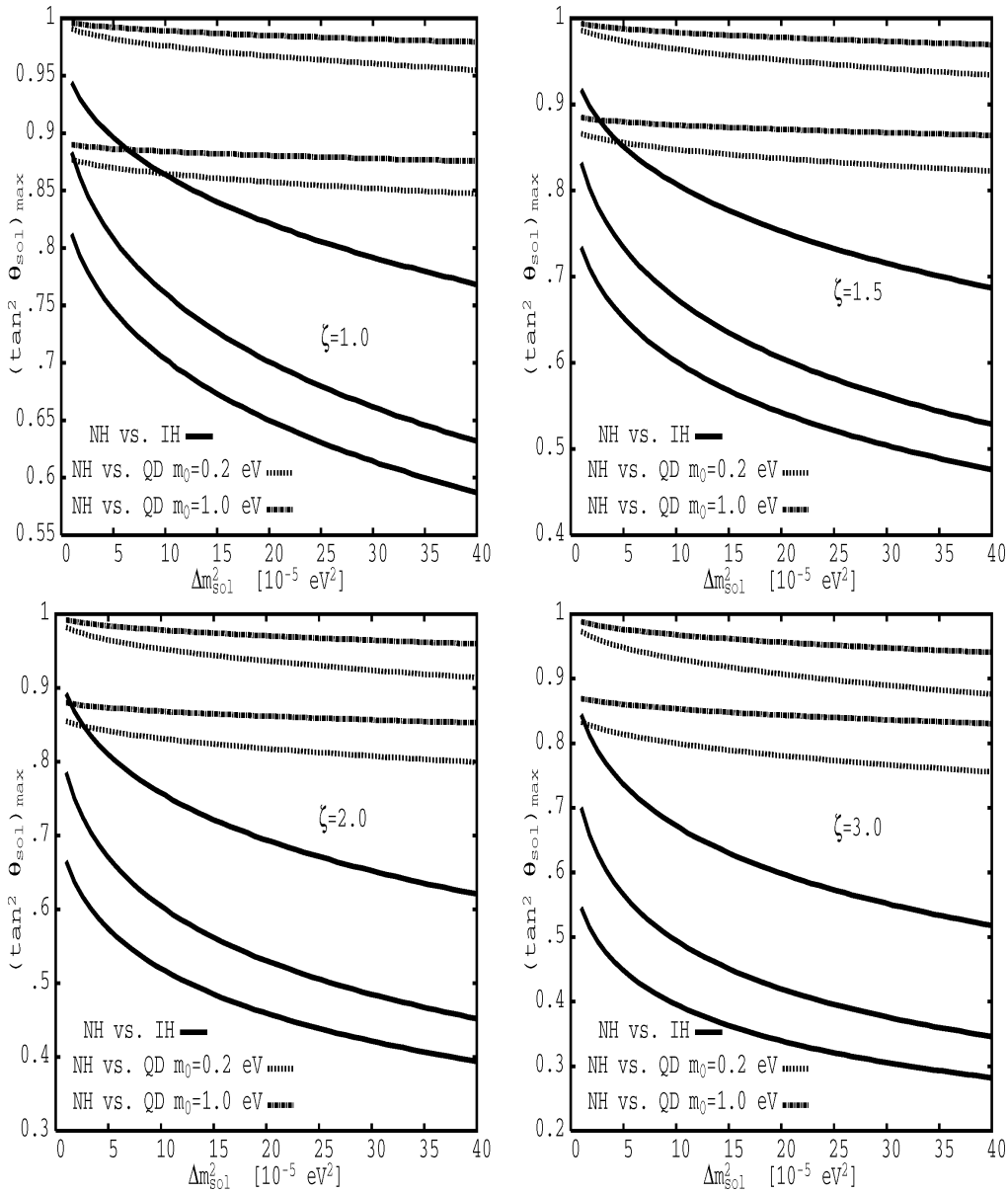

Figure 3. The upper bound on $\tan^2\theta_\odot$, for which one can distinguish the NH spectrum from the IH spectrum and from that of QD type, as a function of $\Delta m^2_\odot$ for $\Delta m^2_{\rm A} = 3\times 10^{-3}\,{\rm eV}^2$ and different values of ζ. The lower (upper) line corresponds to $\sin^2\theta = 0.05$ (0). For NH versus IH, there is a third (middle) line corresponding to $\sin^2\theta = 0.01$ (from [82]).

$\Delta m^2_\odot = 7.0\times 10^{-5}\,{\rm eV}^2$, $m_0 = 0.2, 0.5, 1.0\,{\rm eV}$ and $\zeta = 1.0, 1.5, 2.0, 3.0$. The upper bound on $\tan^2\theta_\odot$ of interest depends strongly on the value of m_0. It decreases with increase in $\Delta m^2_{\rm A}$. As follows from figure 4, for the values of $\Delta m^2_{\rm A}$ favoured by the data and for $\zeta \gtrsim 2$, distinguishing between the IH and QD spectra for $m_0 \cong 0.20\,{\rm eV}$ requires too small, from the point of view of the existing data, values of $\tan^2\theta_\odot$. For $m_0 \gtrsim 0.40\,{\rm eV}$, the values of $\tan^2\theta_\odot$ of interest fall in the ranges favoured by the solar neutrino and KamLAND data even for $\zeta = 3$.

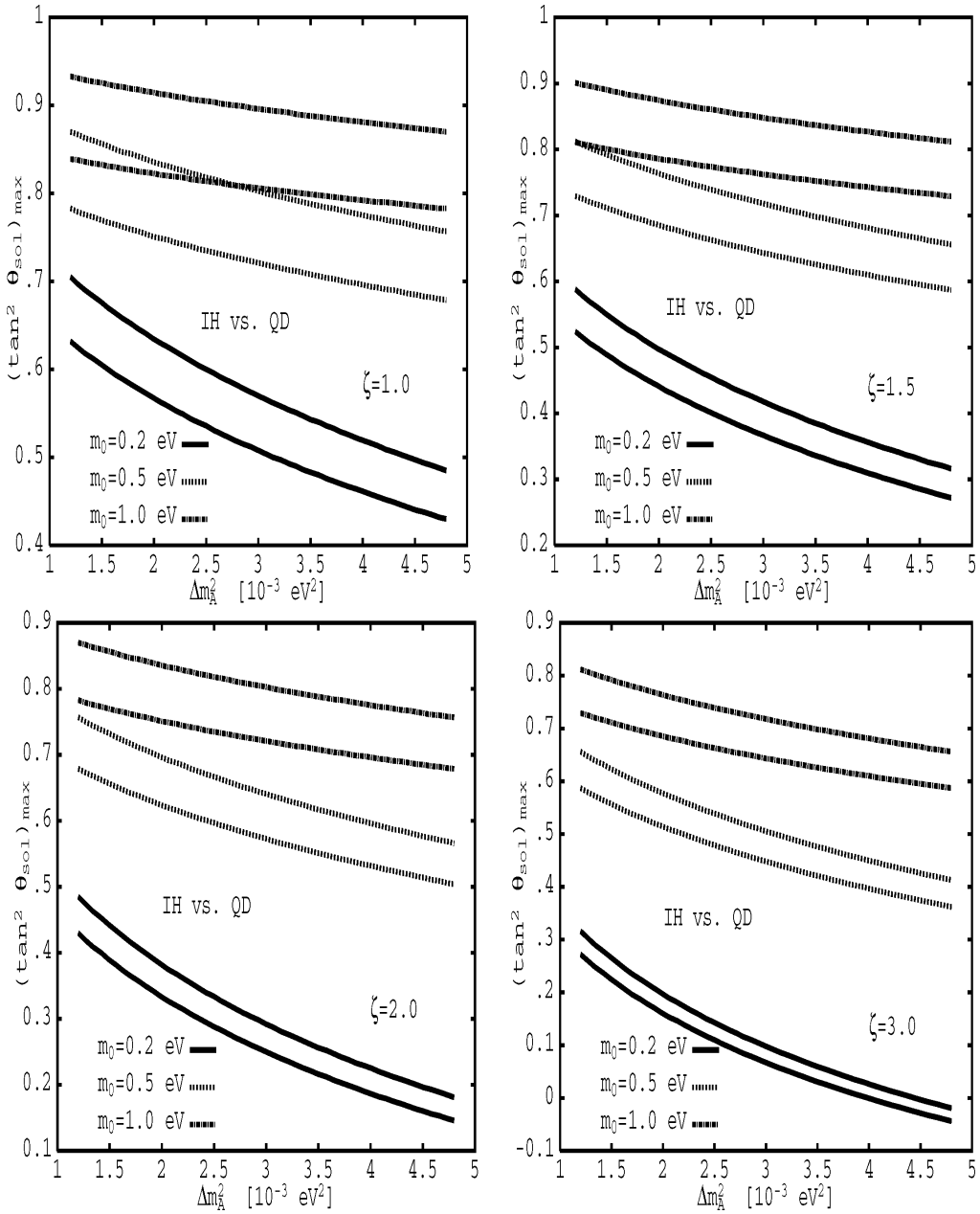

Figure 4. The upper bound on $\tan^2\theta_\odot$ allowing one to discriminate between the IH and QD neutrino mass spectra, as a function of $\Delta m^2_{\rm A}$ for different values of ζ. The lower (upper) line corresponds to $\sin^2\theta = 0.05$ (0) (from [82]).

These quantitative analyses show that if $|\langle m\rangle|$ is found to be nonzero in future $(\beta\beta)_{0\nu}$-decay experiments, it would be easier, in general, to distinguish between the spectrum with NH and those with IH or of QD type using the data on $|\langle m\rangle| \neq 0$ than to distinguish between the IH and QD spectra. Discriminating between the latter would be less demanding if m_0 is sufficiently large.

5. Constraining the Majorana CP-violation phases

The problem of detection of CP violation in the lepton sector is one of the most formidable and challenging problems in the study of neutrino mixing. As was noticed in [22], the measurement of $|\langle m\rangle|$ alone could exclude the possibility that the two Majorana CP-violation phases α_{21} and α_{31}, present in the PMNS matrix, are equal to zero. However, such a measurement cannot rule out, without additional input, the case of the two phases taking different *CP-conserving* values. The additional input needed for establishing CP violation could be, for example, measurement of neutrino mass $m_{\bar{\nu}_e}$ in the ^{3}H β-decay experiment KATRIN [59] or cosmological determination of the sum of the three neutrino masses [62], $\Sigma = m_1 + m_2 + m_3$ or derivation of a sufficiently stringent upper limit on Σ. At present, no viable alternative to the measurement of $|\langle m\rangle|$ for obtaining information on the Majorana CP-violating phases α_{21} and α_{31} exists or can be foreseen to exist in the next ~8 years.

The possibility of obtaining information on the CP violation due to the Majorana phases α_{21} and α_{31} by measuring $|\langle m\rangle|$ was studied by a number of authors [24, 40, 41, 42, 44], and more recently, it was studied in [43, 45]. Barger *et al* [45] considered in their analysis, in particular, the effect of uncertainty in the knowledge of NMEs on the measured value of $|\langle m\rangle|$. After making a certain number of assumptions about the experimental and theoretical developments in the field of interest that may occur by the year 2020,[13] they claim to have shown 'once and for all that it is impossible to detect CP violation from $(\beta\beta)_{0\nu}$ decay in the foreseeable future'. A different approach to the problem was used in [43], where an attempt was made to determine the conditions under which CP violation might be detected from a measurement of $|\langle m\rangle|$ and $m_{\bar{\nu}_e}$ or Σ, or of $|\langle m\rangle|$ and a sufficiently stringent upper limit Σ. We will summarize below results of the latter study.

The analysis in [43] is based on prospective input data on $|\langle m\rangle|$, $m_{\bar{\nu}_e}$, Σ, $\tan^2\theta_\odot$, etc. The effect of the NME uncertainty was included in the analysis. For example, for the IH spectrum ($m_1 \ll m_2 \simeq m_3$, $m_1 < 0.02$ eV), a 'just-CP-violating' region [40]—a value of $|\langle m\rangle|$ in this region would signal unambiguously CP violation in the lepton sector due to Majorana CP-violating phases—would be present if

$$(|\langle m\rangle|_{\rm exp})_{\rm max} < \sqrt{\left(\Delta m^2_{\rm atm}\right)_{\rm min}}, \tag{37}$$

$$(|\langle m\rangle|_{\rm exp})_{\rm min} > \sqrt{\left(\Delta m^2_{\rm atm}\right)_{\rm max}}(\cos 2\theta_\odot)_{\rm max}, \tag{38}$$

where $(|\langle m\rangle|_{\rm exp})_{\rm max(min)}$ is the largest (smallest) experimentally allowed value of $|\langle m\rangle|$, taking into account both the experimental error on the measured $(\beta\beta)_{0\nu}$ decay half lifetime and the uncertainty due to the evaluation of the NMEs. Condition (38) depends crucially on the value of $(\cos 2\theta_\odot)_{\rm max}$ and it is less stringent for smaller values of $(\cos 2\theta_\odot)_{\rm max}$ [22].

Using the parametrization given in equation (32), the necessary condition permitting us to establish, in principle, that the CP symmetry is violated due to the Majorana CP-violating phases reads

$$1 \leqslant \zeta < \frac{\sqrt{\left(\Delta m^2_{\rm atm}\right)_{\rm min}}}{\sqrt{\left(\Delta m^2_{\rm atm}\right)_{\rm max}}(\cos 2\theta_\odot)_{\rm max} + 2\Delta}. \tag{39}$$

[13] It is supposed in [45], in particular, that $|\langle m\rangle|$ will be measured with a 25% (1 S.D.) error and that the uncertainty in the $(\beta\beta)_{0\nu}$-decay NMEs will be reduced to a factor of 2.

Obviously, the smaller the $(\cos 2\theta_\odot)_{\max}$ and Δ values, the larger the 'theoretical uncertainty', which might allow one to make conclusions concerning the CP-violation of interest.

A similar analysis was performed for QD neutrinos mass spectrum. The results can be summarized as follows. The possibility of establishing that the Majorana phases α_{21} and α_{31} have CP-nonconserving values requires quite accurate measurements of $|\langle m\rangle|$ and, e.g. of $m_{\bar{\nu}_e}$ or Σ, and holds only for a limited range of values of the relevant parameters. More specifically, to prove that CP violation associated with Majorana neutrinos takes place requires, in particular, a relative experimental error on the measured value of $|\langle m\rangle|$ not higher than 15–20%, a 'theoretical uncertainty' in the value of $|\langle m\rangle|$ due to imprecise knowledge of the corresponding NMEs smaller than a factor of 2, a value of $\tan^2\theta_\odot \gtrsim 0.55$, and values of the relevant Majorana CP-violating phases $(\alpha_{21}, \alpha_{32})$ typically within the ranges of $\sim(\pi/2\text{–}3\pi/4)$ and $\sim(5\pi/4\text{–}3\pi/2)$.

6. Conclusions

Future $(\beta\beta)_{0\nu}$-decay experiments have a remarkable physics potential. They can establish the Majorana nature of the neutrinos with a definite mass ν_j. If the latter are Majorana particles, the $(\beta\beta)_{0\nu}$-decay experiments can provide unique information on the type of the neutrino mass spectrum and on the absolute scale of neutrino masses. They can also provide unique information on the Majorana CP-violation phases present in the PMNS neutrino mixing matrix. Knowledge of values of the relevant $(\beta\beta)_{0\nu}$-decay NMEs with a sufficiently low uncertainty is crucial for obtaining quantitative information on the neutrino mass and mixing parameters from a measurement of $(\beta\beta)_{0\nu}$-decay half lifetime.

Acknowledgments

The present review is based on the author's joint publications with S M Bilenky, L Wolfenstein, S Pascoli and W Rodejohann. The author is grateful to them for very fruitful and enjoyable collaborations. The author would also like to thank Professors T Kugo and M Nojiri and the other members of the Yukawa Institute for Theoretical Physics (YITP), Kyoto, Japan, where part of this work was done, for the kind hospitality extended to him. This work was partially supported by the Italian INFN under the programme 'Fisica Astroparticellare'.

Notes added. After the submission of this article for publication, the KamLAND experiment reported new data [89] on the spectrum of e^+ produced by reactor $\bar{\nu}_e$: $\bar{\nu}_e + p \to e^+ + n$. The data correspond to a statistics of 766.3 Ty and clearly show a distortion of the e^+ spectrum, compatible with that expected for $\bar{\nu}_e$ oscillations, driven by the neutrino mass-squared difference responsible for the solar neutrino transitions, $\Delta m^2_\odot$ and lying in the LMA-I subregion of the LMA solution region. A combined analysis of the global solar neutrino and KamLAND 766 Ty data in terms of neutrino oscillations reveals [91] that the LMA-II solution is excluded at 4σ. A three-flavour neutrinos oscillation analysis of the data shows [91] that $\sin^2\theta < 0.05$ at 99.73% CL and that, for $\sin^2\theta = 0.0$ (0.02), for instance, one has, at 90% CL, $0.23 \lesssim \sin^2\theta_\odot \lesssim 0.34$ and $7.5\times10^{-5}\,\text{eV}^2 \lesssim \Delta m^2_\odot \lesssim 9.2\ (9.0)\times10^{-5}\,\text{eV}^2$. The corresponding best-fit values read: $\sin^2\theta_\odot \cong 0.28$ and $\Delta m^2_\odot \cong 8.4\times10^{-5}\,\text{eV}^2$. We see that the maximal allowed values of $\sin^2\theta_\odot$ are smaller than those in equations (8) and (9), whereas the best-fit and the minimal values of $\Delta m^2_\odot$ are larger than those used (equations (10) and (11)). The former implies that the minimal

values of $|\langle m \rangle|$ for IH and QD neutrino mass spectra are somewhat larger than those shown in figures 1 and 2; the latter means that the predictions for $|\langle m \rangle|$ in the case of the NH neutrino mass spectrum, illustrated in figures 1 and 2, will be somewhat modified. However, taking into account implications of the new KamLAND data will lead, in general, to minor modifications of the results on the effective Majorana mass $|\langle m \rangle|$ and the physics potential of the $(\beta\beta)_{0\nu}$-decay experiments, presented in this paper.

References

[1] Cleveland B T *et al* 1998 *Astrophys. J.* **496** 505
Abdurashitov J N *et al* [SAGE Collaboration] 2002 *Preprint* astro-ph/0204245
Hampel W *et al* [GALLEX Collaboration] 1999 *Phys. Lett.* B **447** 127
Bellotti E, Talk at Gran Sasso National Laboratories, Italy, 17 May 2002
Kirsten T 2003 *Nucl. Phys. (Proc. Suppl.)* B **118** 33
[2] Fukuda S *et al* [Super-Kamiokande Collaboration] 2001 *Phys. Rev. Lett.* **86** 5651, 5656
[3] Ahmad Q R *et al* [SNO Collaboration] 2001 *Phys. Rev. Lett.* **87** 071301
Ahmad Q R *et al* [SNO Collaboration] 2002 *Phys. Rev. Lett.* **89** 011301
[4] Ahmed S N *et al* [SNO Collaboration] 2003 *Preprint* nucl-ex/0309004
[5] Fukuda Y *et al* [Super-Kamiokande Collaboration] 1998 *Phys. Rev. Lett.* **81** 1562
[6] Eguchi K *et al* [KamLAND Collaboration] 2003 *Phys. Rev. Lett.* **90** 021802
[7] Ahn M H *et al* [K2K Collaboration] 2003 *Phys. Rev. Lett.* **90** 041801
[8] Pontecorvo B 1967 *Zh. Eksp. Teor. Fiz.* **53** 1717
[9] Bilenky S M and Pontecorvo B 1978 *Phys. Rep.* **41** 225
[10] Bilenky S M and Petcov S T 1987 *Rev. Mod. Phys.* **59** 671
[11] Petcov S T 1998 *Lecture Notes in Physics* vol 512 ed H Gausterer and C B Lang (Berlin: Springer) p 281 (*Preprint* hep-ph/9806466)
[12] Pontecorvo B 1946 *Chalk River Laboratory Report PD-205*
[13] Davis R, Harmer D S and Hoffman K C 1968 *Phys. Rev. Lett.* **20** 1205
Davis R, Harmer D S and Hoffman K C 1970 *Acta Physica Acad. Sci. Hung.* **29** (Suppl. 4) 371
Davis R 1972 *Proc. Int. Conf. on 'Neutrino 72' Balatonfured, Hungary* ed A Frenkel and G Marx, OMKDK-TECHNOINFORM, Budapest, p 5
[14] Fogli G L *et al* 2003 *Phys. Rev.* D **67** 073002
[15] Maltoni M, Schwetz T and Valle J W F 2002 *Preprint* hep-ph/0212129
Bandyopadhyay A *et al* 2003 *Phys. Lett.* B **559** 121
Bahcall J N, Gonzalez-Garcia M C and Pena-Garay C 2003 *J. High Energy Phys.* JHEP02(2003)009
Nunokawa H, Teves W J and Zukanovich Funchal R 2002 *Preprint* hep-ph/0212202
Aliani P *et al* 2002 *Preprint* hep-ph/0212212
[16] Maris M and Petcov S T 2002 *Phys. Lett.* B **534** 17
[17] Gonzalez-Garcia M C, Pena-Garay C, Nir Y and Smirnov A Y 2001 *Phys. Rev.* D **63** 013007
[18] Bandyopadhyay A *et al* 2004 *Phys. Lett.* B **583** 134
[19] Maltoni M, Schwetz T, Tortola M A and Valle J W F 2003 *Phys. Rev.* D **68** 113010
Aliani P *et al* 2003 *Preprint* hep-ph/0309156
de Holanda P C and Smirnov A Y 2003 *Preprint* hep-ph/0309299
[20] Maris M and Petcov S T 2000 *Phys. Rev.* D **62** 093006
[21] Pascoli S and Petcov S T 2002 *Phys. Lett.* B **544** 239
[22] Pascoli S, Petcov S T and Wolfenstein L 2002 *Phys. Lett.* B **524** 319
Pascoli S and Petcov S T 2001 *Preprint* hep-ph/0111203
[23] Pascoli S and Petcov S T 2004 *Phys. Lett.* B **580** 280

[24] Bilenky S M *et al* 1996 *Phys. Rev.* D **56** 4432
[25] Saji C *et al* [Super-Kamiokande Collaboration] 2004 Talk given at the *Int. Workshop on Neutrino Oscillations and their Origin (NOON2004) 11–15 February, Tokyo*
[26] Fogli G L *et al* 2003 *Phys. Rev.* D **67** 093006
[27] Fogli G L *et al* 2003 *Preprint* hep-ph/0308055
[28] Ishitsuka M *et al* [Super-Kamiokande Collaboration] 2004 Talk given at the *Int. Workshop on Neutrino Oscillations and their Origin (NOON2004) 11–15 February, Tokyo*
[29] Pontecorvo B 1957 *Zh. Eksp. Teor. Fiz.* **33** 549
Pontecorvo B 1958 *Zh. Eksp. Teor. Fiz.* **34** 247
Maki Z, Nakagawa M and Sakata S 1962 *Prog. Theor. Phys.* **28** 870
[30] Aguilar A *et al* [LSND Collaboration] 2001 *Phys. Rev.* D **64** 112007
[31] Tayloe R [MiniBooNE Collaboration] 2003 *Nucl. Phys. Proc. Suppl.* B **118** 157
[32] Bilenky S M, Pascoli S and Petcov S T 2001 *Phys. Rev.* D **64** 113003
[33] Bilenky S M *et al* 1980 *Phys. Lett.* B **94** 495
[34] Schechter J and Valle J W F 1980 *Phys. Rev.* D **23** 2227
[35] Doi M *et al* 1981 *Phys. Lett.* B **102** 323
[36] Bilenky S M, Giunti C and Grimus W 1999 *Prog. Part. Nucl. Phys.* **43** 1
[37] Apollonio M *et al* 1999 *Phys. Lett.* B **466** 415
[38] Boehm F *et al* 2000 *Phys. Rev. Lett.* **84** 3764
[39] Langacker P *et al* 1987 *Nucl. Phys.* B **282** 589
[40] Bilenky S M, Pascoli S and Petcov S T 2001 *Phys. Rev.* D **64** 053010
[41] Vissani F 2000 *Frascati Phys. Ser.* **16** 337
[42] Rodejohann W 2001 *Nucl. Phys.* B **597** 110
[43] Pascoli S, Petcov S T and Rodejohann W 2002 *Phys. Lett.* B **549** 177
[44] Matsuda K *et al* 2000 *Phys. Rev.* D **62** 093001
Matsuda K *et al* 2001 *Phys. Rev.* D **63** 077301
Nunokawa H *et al* 2002 *Preprint* hep-ph/0206137
[45] Barger V *et al* 2002 *Phys. Lett.* B **540** 247
[46] de Gouvea A, Kayser B and Mohapatra R 2003 *Phys. Rev.* D **67** 053004
[47] Fukugita M and Yanagida T 1986 *Phys. Lett.* B **174** 45
For a recent review see e.g. Buchmüller W and Plümacher M 2000 *Int. J. Mod. Phys.* A **15** 5047
[48] Bilenky S M, Nicolo D and Petcov S T 2002 *Phys. Lett.* B **538** 77
[49] Michael D [MINOS Collaboration] 2003 *Nucl. Phys. Proc. Suppl.* B **118** 189
[50] Komatsu M, Migliozzi P and Terranova F 2003 *J. Phys. G: Nucl. Part. Phys.* **29** 443
[51] Spiro M 2003 *Nucl. Phys. Proc. Suppl.* B **118** 413
[52] Minakata H *et al* 2003 *Phys. Rev.* D **68** 033017
Huber P *et al* 2003 *Nucl. Phys.* B **666** 269
[53] Choubey S, Petcov S T and Piai M 2003 *Phys. Rev.* D **68** 113006
[54] Freund M *et al* 2000 *Nucl. Phys.* B **578** 27
[55] Barger V, Marfatia D and Whisnant K 2002 *Preprint* hep-ph/0210428
Huber P, Lindner M and Winter W 2002 *Preprint* hep-ph/0211300
[56] Petcov S T and Piai M 2002 *Phys. Lett.* B **533** 94
[57] Fermi E 1934 *Nuovo Cim.* **11** 1
[58] Lobashev V *et al* 2001 *Nucl. Phys. Proc. Suppl.* B **91** 280
[59] Weinheimer C *et al* 2003 *Nucl. Phys. Proc. Suppl.* B **118** 279
Weinheimer C *et al* 2003 these proceedings
[60] MAP Collaboration http://map.gsfc.gov/
PLANCK Collaboration http://astro.estec.esa.ne/A-general/Projects/Planck
[61] Spergel D N *et al* [WMAP Collaboration] 2003 *Preprint* astro-ph/0302209

[62] Hu W and Tegmark M 1999 *Astrophys. J. Lett.* **514** 65
[63] Hannestad S 2003 *Preprint* astro-ph/0303076
Elgaroy O and Lahav O 2003 *Preprint* astro-ph/0303089
[64] Morales A and Morales J 2002 *Preprint* hep-ph/0211332
[65] Elliot S R and Vogel P 2002 *Ann. Rev. Nucl. Part. Sci.* **52**
[66] Gell–Mann M, Ramond P and Slansky R 1979 *Supergravity* ed F Nieuwenhuizen and D Friedman (Amsterdam: North-Holland) p 315
Yanagida T 1979 *Proc. Workshop on Unified Theories and the Baryon Number of the Universe* ed O Sawada and A Sugamoto *KEK, Japan*
Mohapatra R N and Senjanovic G 1980 *Phys. Rev. Lett.* **44** 912
[67] Wolfenstein L 1981 *Phys. Lett.* B **107** 77
Bilenky S M, Nedelcheva N P and Petcov S T 1984 *Nucl. Phys.* B **247** 61
Kayser B 1984 *Phys. Rev.* D **30** 1023
[68] Klapdor-Kleingrothaus H V *et al* 2001 *Nucl. Phys. Proc. Suppl.* **100** 309
[69] Aalseth C E, Avignone F T *et al* 2000 *Phys. Atomic Nuclei* **63** 1225
[70] Klapdor-Kleingrothaus H V *et al* 2001 *Mod. Phys. Lett.* **16** 2409
[71] Aalseth C E *et al* 2002 *Mod. Phys. Lett.* **17** 1475
[72] Klapdor-Kleingrothaus H V *et al* 2004 *Phys. Lett.* B **586** 198
[73] Vasiliev V *et al* [NEMO3 Collaboration] 2003 Talk given at the *First Yamada Symp. NDM03, 9–14 June, Nara*
[74] Pavan M *et al* [CUORICINO Collaboration] 2003 Talk given at the *First Yamada Symp. NDM03, 9–14 June, Nara*
[75] Fiorini E 1998 *Phys. Rep.* **307** 309
Klapdor-Kleingrothaus H V *et al* 1998 (GENIUS) *J. Phys. G: Nucl. Part. Phys.* **24** 483
Danilov M *et al* (EXO) 2000 *Phys. Lett.* B **480** 12
De Braeckeleer L (for the Majorana Collaboration) 2000 *Proc. Carolina Conf. on Neutrino Physics, Columbia, SC, March 2000*
Ejiri H *et al* (MOON) 2000 *Phys. Rev. Lett.* **85** 2917
[76] Staudt A *et al* 1990 *Europhys. Lett.* **13** 31
[77] Namba T, Talk given at the *First Yamada Symp. on Neutrinos and Dark Matter in Nuclear Physics (NDM03), 9–14 June, Nara*
[78] Kishimoto T 2003 Talk given at the *NOON2003 Int. Workshop, 9–14 February, Kanazawa*
[79] Bilenky S M *et al* 1999 *Phys. Lett.* B **465** 193
[80] Bilenky S M and Giunti C 1999 *Preprint* hep-ph/9904328
Vissani F 1999 *J. High Energy Phys.* JHEP06(1999)022
Czakon M *et al* 2000 *Preprint* hep-ph/0003161
Klapdor-Kleingrothaus H V, Päs H and Smirnov A Yu 2001 *Phys. Rev.* D **63** 073005
[81] Barger V and Whisnant K 1999 *Phys. Lett.* B **456** 194
Fukuyama T *et al* 2001 *Phys. Rev.* D **64** 013001
Minakata H and Sugiyama H 2002 *Phys. Lett.* B **526** 335
[82] Pascoli S, Petcov S T and Rodejohann W 2003 *Phys. Lett.* B **558** 141
[83] Petcov S T and Smirnov A Yu 1994 *Phys. Lett.* B **322** 109
[84] Bilenky S M and Grifols J A 2002 *Phys. Lett.* B **550** 154
[85] Rodin V A *et al* 2003 *Phys. Rev.* C **68** 044302
[86] Czakon M *et al* 2001 *Preprint* hep-ph/0110166
[87] Babu K S and Mohapatra R N 1995 *Phys. Rev. Lett.* **75** 2276
Päs H *et al* 1999 *Phys. Lett.* B **459** 450
[88] Bandyopadhyay A *et al* 2003 *Phys. Rev.* D **67** 113011
[89] Araki T *et al* [KamLAND Collaboration] 2004 *Preprint* hep-ex/0406035
[90] Bandyopadhyay A *et al* 2004 *Preprint* hep-ph/0406328, version 2

New Journal of Physics
An Institute of Physics and Deutsche Physikalische Gesellschaft Journal

Sequential dominance

Stefan Antusch and S F King
School of Physics and Astronomy, University of Southampton,
Southampton SO17 1BJ, UK
E-mail: santusch@hep.phys.soton.ac.uk and sfk@hep.phys.soton.ac.uk

New Journal of Physics **6** (2004) 110
Received 27 May 2004
Published 20 August 2004
Online at http://www.njp.org/
doi:10.1088/1367-2630/6/1/110

Abstract. We review the mechanism of sequential right-handed neutrino dominance proposed in the framework of the type I see-saw mechanism to account for bi-large neutrino mixing and a neutrino mass hierarchy in a natural way. We discuss how sequential dominance (SD) may also be applied to the right-handed charged leptons, which alternatively allows for bi-large lepton mixing from the charged lepton sector. We review how such SD models may be upgraded to include type II see-saw contributions, resulting in a partially degenerate neutrino mass spectrum with the bi-large lepton mixing arising from SD. We also summarize the model-building applications and the phenomenological implications of SD.

1367-2630/04/010110+21$30.00
PII: S1367-2630(04)81361-2
© IOP Publishing Ltd and Deutsche Physikalische Gesellschaft

Contents

1. Introduction **2**
2. The see-saw mechanism **4**
2.1. Type I see-saw 4
2.2. Type II see-saw 5
3. Sequential right-handed neutrino dominance in the type I see-saw mechanism **6**
3.1. Single right-handed neutrino dominance 6
3.2. Sequential right-handed neutrino dominance 8
3.3. Types of sequential right-handed neutrino dominance 9
4. Sequential right-handed lepton dominance in the type I see-saw mechanism **11**
5. Type II see-saw upgrade **12**
5.1. Type II upgrade of a ISD model 13
6. Model-building applications of SD **15**
6.1. Effective two right-handed neutrino models 15
6.2. GUT and family symmetry models 16
6.3. Sneutrino inflation models 16
7. Phenomenological implications of SD **16**
7.1. RG corrections 16
7.2. Dirac and Majorana CP phases and neutrinoless double beta decay 17
7.3. Theoretical expectations for the mixing angles 17
7.4. Minimal LFV 18
7.5. Leptogenesis 18
8. Discussion and conclusions **19**
Acknowledgments **19**
Appendix. Our conventions **19**
References **20**

1. Introduction

Neutrino masses and mixing angles must now be regarded as unavoidable consequences of the firmly established atmospheric and solar neutrino oscillation experiments [1]. A profound consequence of this is that the minimal Standard Model must necessarily be incomplete, and must be extended in some way to account for neutrino masses and mixings. The simplest way to do this appears to be to add right-handed neutrinos to the Standard Model. Since the right-handed neutrinos are gauge singlets, electroweak symmetry does not prevent them from having large Majorana masses ranging from a few TeV up to the Planck scale. The right-handed neutrinos may also couple with left-handed leptons via the usual Higgs doublets. The combination of very large right-handed neutrino Majorana masses and weak scale Dirac masses from the Higgs couplings leads to suppressed left-handed Majorana neutrino masses, which may be identified with the physical neutrino masses responsible for atmospheric and solar neutrino oscillations. This scenario, proposed some time ago in [2], is known as the see-saw mechanism.

Given the simplicity of the see-saw mechanism, it has been widely applied to understanding the pattern of neutrino masses and mixings implied by the atmospheric and solar neutrino

oscillation data [1]. Although there are alternatives to the see-saw mechanism involving large extra dimensions [3] or R-parity-violating supersymmetry [4], we shall consider only the see-saw mechanism in the present paper, although we shall later consider a more complicated version of the see-saw mechanism, called the type II see-saw mechanism, which also involves heavy Higgs triplets (see e.g. [5]). We shall also only consider the case of three active neutrinos, which is the minimal case consistent with the confirmed atmospheric and solar neutrino oscillation data.

Within the framework as described above, the goal of the see-saw mechanism is to account for large atmospheric neutrino mixing ($\theta_{23} \sim 45^\circ$, close to maximal) and large solar neutrino mixing ($\theta_{12} \sim 30^\circ$, but not maximal) together with the observed atmospheric and solar neutrino mass-squared differences [1]. The solar data are consistent with the so-called large mixing angle (LMA) MSW solution [6]. The third remaining mixing angle associated with the three active neutrinos is so far unmeasured but must be quite small ($\theta_{13} \lesssim 13^\circ$) [7]. The neutrino oscillation data neither determines the absolute scale of neutrino masses nor fixes uniquely the ordering of neutrino masses; however in a normally ordered hierarchical scheme, the neutrino mass values would be roughly given by $m_3 \sim 0.05$ eV, $m_2 \sim 0.008$ eV, with $m_1 \ll m_2$. However m_1 could, in principle, be substantially larger, up to the cosmological limit of about 0.23 eV [8].

It has frequently been observed that the simultaneous appearance of hierarchical neutrino masses and two LMAs is not natural in the see-saw mechanism. An important exception to this is the sequential dominance (SD) mechanism [9]–[13] (see also [14]), which is the subject of this focus. SD is not in itself a model, but is a submechanism within the general framework of the see-saw mechanism, which may be applied to constructing different classes of models. The starting point of SD is to assume that one of the right-handed neutrinos contributes dominantly in the see-saw mechanism to the heaviest neutrino mass, with the atmospheric mixing angle being determined by a simple ratio of two Yukawa couplings [9, 10], which is sometimes referred to as single right-handed neutrino dominance (SRHND). SD corresponds to the further assumption that, together with SRHND, a second right-handed neutrino contributes dominantly to the second heaviest neutrino mass, with the large solar mixing angle interpreted as a ratio of Yukawa couplings [11, 12]. The third right-handed neutrino is effectively decoupled from the see-saw mechanism, and plays no part in determining the neutrino mass spectrum, although it may play a cosmological role. If the decoupled right-handed neutrino is also the heaviest then the SD is effectively equivalent to having two right-handed neutrinos [10, 11].

We also review how SD may be generalized to include the right-handed charged leptons [15], which allows bi-large charged lepton mixing consistent with a neutrino mass hierarchy. We then show how such SD models may be upgraded to include type II see-saw contributions [16], resulting in a partially degenerate neutrino mass spectrum with bi-large lepton mixing arising from SD.

In section 2, we recall the type I and II see-saw mechanisms. Section 3 shows how the type I see-saw mechanism can lead to a hierarchical pattern of neutrino masses, with bi-large neutrino mixing in a natural way using sequential right-handed neutrino dominance. Section 4 shows how the type I see-saw mechanism can lead to bi-large charged lepton mixing, with naturally small neutrino mixing and hierarchical neutrino masses, using SD in the right-handed lepton sector. Section 5 shows how a partially degenerate neutrino mass spectrum could originate from the type II see-saw mechanism, with the neutrino mass splittings and mixings controlled by SD. Section 6 briefly reviews some of the model-building applications, whereas section 7 discusses the phenomenological implications of SD. Section 8 concludes the review. Our conventions are stated in an appendix.

2. The see-saw mechanism

The see-saw mechanism provides a convincing explanation for the smallness of neutrino masses. In this section, we review its simplest form, the type I see-saw mechanism and its generalization to the type II see-saw mechanism.

2.1. Type I see-saw

Before discussing the see-saw mechanism it is worth first reviewing the different types of neutrino mass that are possible. So far, we have been assuming that neutrino masses are Majorana masses of the form

$$m^{\nu}_{\mathrm{LL}}\overline{\nu_{\mathrm{L}}}\nu^{\mathrm{C}}_{\mathrm{L}}, \tag{1}$$

where ν_{L} is a left-handed neutrino field and $\nu^{\mathrm{C}}_{\mathrm{L}}$ is the CP conjugate of a left-handed neutrino field; in other words, a right-handed antineutrino field. Such Majorana masses are possible since both the neutrino and the antineutrino are electrically neutral and so Majorana masses are not forbidden by electric charge conservation. For this reason, a Majorana mass for the electron would be strictly forbidden. However, such Majorana neutrino masses violate lepton number conservation, and in the standard model, assuming only Higgs doublets are present, are forbidden at the renormalizable level by gauge invariance. The idea of the simplest version of the see-saw mechanism is to assume that such terms are zero to begin with, but are generated effectively, after right-handed neutrinos are introduced [2].

If we introduce right-handed neutrino fields then there are two sorts of additional neutrino mass terms that are possible. There are additional Majorana masses of the form

$$M_{\mathrm{RR}}\overline{\nu_{\mathrm{R}}}\nu^{\mathrm{C}}_{\mathrm{R}}, \tag{2}$$

where ν_{R} is a right-handed neutrino field and $\nu^{\mathrm{C}}_{\mathrm{R}}$ is the CP conjugate of a right-handed neutrino field; in other words a left-handed antineutrino field. In addition, there are Dirac masses of the form

$$m^{\nu}_{\mathrm{LR}}\overline{\nu_{\mathrm{L}}}\nu_{\mathrm{R}}. \tag{3}$$

Such Dirac mass terms conserve lepton number, and are not forbidden by electric charge conservation even for the charged leptons and quarks.

Once this is done then the types of neutrino mass discussed in equations (2) and (3) (but not equation (1) since we do not assume direct mass terms, e.g. from Higgs triplets, at this stage) are permitted, and we have the mass matrix

$$(\overline{\nu_{\mathrm{L}}} \quad \overline{\nu^{\mathrm{C}}_{\mathrm{R}}})\begin{pmatrix} 0 & m^{\nu}_{\mathrm{LR}} \\ m^{\nu\mathrm{T}}_{\mathrm{LR}} & M_{\mathrm{RR}} \end{pmatrix}\begin{pmatrix} \nu^{\mathrm{C}}_{\mathrm{L}} \\ \nu_{\mathrm{R}} \end{pmatrix}. \tag{4}$$

Since the right-handed neutrinos are electroweak singlets, the Majorana masses of the right-handed neutrinos M_{RR} may be orders of magnitude larger than the electroweak scale. In the approximation that $M_{\mathrm{RR}} \gg m^{\nu}_{\mathrm{LR}}$, the matrix in equation (4) may be diagonalized to yield effective Majorana masses of the type in equation (1),

$$m^{\nu}_{\mathrm{LL}} = -m^{\nu}_{\mathrm{LR}}M^{-1}_{\mathrm{RR}}m^{\nu\mathrm{T}}_{\mathrm{LR}}. \tag{5}$$

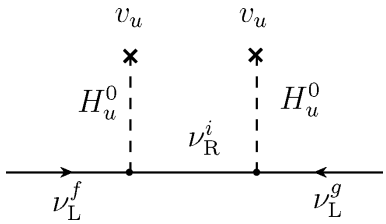

Figure 1. Diagram illustrating the type I see-saw mechanism.

The effective left-handed Majorana masses m^{ν}_{LL} are naturally suppressed by the heavy scale M_{RR}. In a one family example, if we take $m^{\nu}_{LR} = M_W$ and $M_{RR} = M_{GUT}$, then we find $m^{\nu}_{LL} \sim 10^{-3}$ eV which looks good for solar neutrinos. Atmospheric neutrino masses would require a right-handed neutrino with a mass below the grand unified theory (GUT) scale.

With three left-handed neutrinos and three right-handed neutrinos the Dirac masses m^{ν}_{LR} are a 3×3 (complex) matrix and the heavy Majorana masses M_{RR} form a separate 3×3 (complex symmetric) matrix. The light effective Majorana masses m^{ν}_{LL} are also a 3×3 (complex symmetric) matrix and continue to be given from equation (5) which is now interpreted as a matrix product. From a model-building perspective the fundamental parameters which must be input into the see-saw mechanism are the Dirac mass matrix m^{ν}_{LR} and the heavy right-handed neutrino Majorana mass matrix M_{RR}. The light-effective left-handed Majorana mass matrix m^{ν}_{LL} arises as an output according to the see-saw formula in equation (5).

The version of the see-saw mechanism discussed so far is sometimes called the type I see-saw mechanism. It is the simplest version of the see-saw mechanism, and can be thought of as resulting from integrating the heavy right-handed neutrinos to produce the effective dimension 5 neutrino mass operator

$$-\frac{1}{4}(H_u \cdot L^T)\kappa(H_u \cdot L), \tag{6}$$

where the dot indicates the $SU(2)_L$-invariant product and

$$\kappa = 2Y_\nu M_{RR}^{-1} Y_\nu^T \tag{7}$$

with Y_ν being the neutrino Yukawa couplings and $m^{\nu}_{LR} = Y_\nu v_u$ with $v_u = \langle H_u \rangle$. The type I see-saw mechanism is illustrated diagramatically in figure 1.

2.2. Type II see-saw

In models with a left–right symmetric particle content such as minimal left–right symmetric models, Pati-Salam models or GUTs based on SO(10), the type I see-saw mechanism is often generalized to a type II see-saw (see e.g. [5]), where an additional direct mass term m^{II}_{LL} for the light neutrinos is present.

With such an additional direct mass term, the general neutrino mass matrix is given by

$$(\overline{\nu_L} \quad \overline{\nu_R^C}) \begin{pmatrix} m^{II}_{LL} & m^{\nu}_{LR} \\ m^{\nu T}_{LR} & M_{RR} \end{pmatrix} \begin{pmatrix} \nu_L^C \\ \nu_R \end{pmatrix}. \tag{8}$$

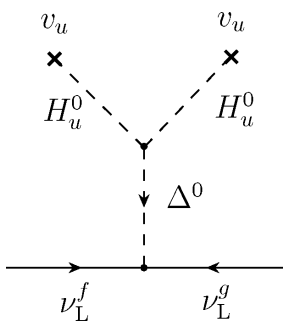

Figure 2. Diagram leading to a type II contribution m_{LL}^{II} to the neutrino mass matrix via an induced vev of the neutral component of a triplet Higgs Δ.

Under the assumption that the mass eigenvalues M_{Ri} of M_{RR} are very large compared with the components of m_{LL}^{II} and m_{LR}, the mass matrix can approximately be diagonalized yielding effective Majorana masses

$$m_{LL}^{\nu} \approx m_{LL}^{II} + m_{LL}^{I} \tag{9}$$

with

$$m_{LL}^{I} \approx -m_{LR}^{\nu} M_{RR}^{-1} m_{LR}^{\nu T} \tag{10}$$

for the light neutrinos. The direct mass term m_{LL}^{II} can also provide a naturally small contribution to the light neutrino masses if it stems, e.g. from a see-saw suppressed induced vev. We will refer to the general case, where both possibilities are allowed, as the II see-saw mechanism. Realizing the type II contribution by generating the dimension 5 operator in equation (6) via the exchange of heavy Higgs triplets of $SU(2)_L$ is illustrated diagrammatically in figure 2.

3. Sequential right-handed neutrino dominance in the type I see-saw mechanism

In this section we discuss an elegant and natural way of accounting for a neutrino mass hierarchy and two LMAs, called SD. The idea of SD is that one of the right-handed neutrinos contributes dominantly to the see-saw mechanism and determines the atmospheric neutrino mass and mixing. A second right-handed neutrino contributes subdominantly and determines the solar neutrino mass and mixing. The third right-handed neutrino is effectively decoupled from the see-saw mechanism.

3.1. Single right-handed neutrino dominance

Consider the case of full neutrino mass hierarchy $m_3 \gg m_2 \gg m_1 \approx 0$. From the appendix we see that in the diagonal charged lepton basis, ignoring phases, the neutrino mass matrix is given by

$$m_{LL}^{\nu} \approx \begin{pmatrix} m_2 s_{12}^2 & \frac{1}{\sqrt{2}}(m_2 s_{12} c_{12} + m_3 \theta_{13}) & -\frac{1}{\sqrt{2}}(m_2 s_{12} c_{12} - m_3 \theta_{13}) \\ . & \frac{1}{2}(m_3 + m_2 c_{12}^2) & \frac{1}{2}(m_3 - m_2 c_{12}^2) \\ . & . & \frac{1}{2}(m_3 + m_2 c_{12}^2) \end{pmatrix}, \tag{11}$$

neglecting terms like $m_2\theta_{13}$ and setting $\theta_{23} \approx \pi/4$. Clearly, this expression reduces to

$$m^{\nu}_{\mathrm{LL}} \approx \begin{pmatrix} 0 & 0 & 0 \\ 0 & 1 & 1 \\ 0 & 1 & 1 \end{pmatrix} \frac{m}{2}, \tag{12}$$

with $m = m_3$ in the approximation that m_2 and θ_{13} are neglected. However, the more exact expression in equation (11) shows that the required form of m_{LL} should have a very definite detailed structure. The requirement $m_2 \ll m_3$ implies that the sub-determinant of the mass matrix m^{ν}_{LL} is small:

$$\det \begin{pmatrix} m_{22} & m_{23} \\ m_{23} & m_{33} \end{pmatrix} \ll m_3^2. \tag{13}$$

This requirement in equation (13) is satisfied by equation (11), as may be readily seen, and this condition must be reproduced in a natural way (without fine-tuning) by any successful theory.

The goal of see-saw model building for hierarchical neutrino masses is therefore to choose input see-saw matrices m^{ν}_{LR} and M_{RR} that will give rise to the form in equation (11). We now show how the input see-saw matrices can be simply chosen to give this form, with the property of a naturally small sub-determinant in equation (13) using a mechanism first suggested in [9] (see also [14]). The idea was developed in [10] where it was called SRHND. SRHND was first successfully applied to the LMA MSW solution in [11].

To understand the basic idea of dominance, it is instructive to begin by discussing a simple 2×2 example, where we have in mind applying this to the atmospheric mixing in the 23 sector:

$$M_{\mathrm{RR}} = \begin{pmatrix} Y & 0 \\ 0 & X \end{pmatrix}, \qquad m^{\nu}_{\mathrm{LR}} = \begin{pmatrix} e & b \\ f & c \end{pmatrix}. \tag{14}$$

The see-saw formula in equation (5), $m^{\nu}_{\mathrm{LL}} = -m^{\nu}_{\mathrm{LR}} M^{-1}_{\mathrm{RR}} m^{\nu\mathrm{T}}_{\mathrm{LR}}$, gives

$$-m^{\nu}_{\mathrm{LL}} = \begin{pmatrix} \frac{e^2}{Y} + \frac{b^2}{X} & \frac{ef}{Y} + \frac{bc}{X} \\ \frac{ef}{Y} + \frac{bc}{X} & \frac{f^2}{Y} + \frac{c^2}{X} \end{pmatrix} \approx \begin{pmatrix} \frac{e^2}{Y} & \frac{ef}{Y} \\ \frac{ef}{Y} & \frac{f^2}{Y} \end{pmatrix}, \tag{15}$$

where the approximation in equation (15) assumes that the right-handed neutrino of mass Y is sufficiently light that it dominates in the see-saw mechanism:

$$\frac{e^2, f^2, ef}{Y} \gg \frac{b^2, c^2, bc}{X}. \tag{16}$$

The neutrino mass spectrum from equation (15) then consists of one neutrino with mass $m_3 \approx (e^2 + f^2)/Y$ and one naturally light neutrino $m_2 \ll m_3$, since the determinant of equation (15) is clearly approximately vanishing, due to the dominance assumption [9]. The atmospheric angle from equation (15) is $\tan\theta_{23} \approx e/f$ [9], which can be large or maximal providing $e \approx f$, even in the case $e, f, b \ll c$ that the neutrino Dirac mixing angles arising from equation (14) are small. Thus, two crucial features, namely a neutrino mass hierarchy $m_3^2 \gg m_2^2$ and a large neutrino mixing angle $\tan\theta_{23} \approx 1$, can arise naturally from the see-saw mechanism assuming the dominance of a single right-handed neutrino. It was also realized that small perturbations from the sub-dominant right-handed neutrinos can then lead to a small solar neutrino mass splitting [9], as we now discuss.

3.2. Sequential right-handed neutrino dominance

To account for the solar and other mixing angles, we must generalize the above discussion to the 3×3 case. The SRHND mechanism is most simply described assuming three right-handed neutrinos in the basis where the right-handed neutrino mass matrix is diagonal although it can also be developed in other bases [10, 11]. In this basis we write the input see-saw matrices as

$$M_{\mathrm{RR}} = \begin{pmatrix} X & 0 & 0 \\ 0 & Y & 0 \\ 0 & 0 & Z \end{pmatrix}, \tag{17}$$

$$m^{\nu}_{\mathrm{LR}} = \begin{pmatrix} a & d & p \\ b & e & q \\ c & f & r \end{pmatrix}. \tag{18}$$

Each right-handed neutrino in the basis of equation (17) couples with a particular column of m^{ν}_{LR} in equation (18). There is no mass ordering of X, Y, Z implied in equation (17). In [9] it was suggested that one of the right-handed neutrinos may dominate the contribution to m^{ν}_{LL} if it is lighter than the other right-handed neutrinos. The dominance condition was subsequently generalized to include other cases where the right-handed neutrino may be heavier than the other right-handed neutrinos but dominates due to its larger Dirac mass couplings [10]. In any case the dominant right-handed neutrino may be taken to be the one with mass Y without loss of generality.

It was subsequently shown how to account for the LMA MSW solution with a large solar angle [11] by careful consideration of the sub-dominant contributions. SD occurs when the right-handed neutrinos dominate sequentially [11],

$$\frac{|e^2|, |f^2|, |ef|}{Y} \gg \frac{|xy|}{X} \gg \frac{|x'y'|}{Z}, \tag{19}$$

which is the straightforward generalization of equation (16) where $x, y \in a, b, c$ and $x', y' \in p, q, r$. Assuming SRHND with sequential sub-dominance as in equation (19), then equations (5), (17) and (18) give

$$-m^{\nu}_{\mathrm{LL}} \approx \begin{pmatrix} \frac{a^2}{X} + \frac{d^2}{Y} & \frac{ab}{X} + \frac{de}{Y} & \frac{ac}{X} + \frac{df}{Y} \\ . & \frac{b^2}{X} + \frac{e^2}{Y} & \frac{bc}{X} + \frac{ef}{Y} \\ . & . & \frac{c^2}{X} + \frac{f^2}{Y} \end{pmatrix}, \tag{20}$$

where the contribution from the right-handed neutrino of mass Z may be neglected according to equation (19). If the couplings satisfy the SD condition in equation (19) then the matrix in equation (20) resembles the Type IA matrix and, furthermore, has a naturally small sub-determinant as in equation (13). This leads to a full neutrino mass hierarchy

$$m_3^2 \gg m_2^2 \gg m_1^2 \tag{21}$$

and, ignoring phases, the solar angle only depends on the sub-dominant couplings and is given by $\tan\theta_{12} \approx a/(c_{23}b - s_{23}c)$ [11]. The simple requirement for large solar angle is then $a \sim b - c$ [11].

Including phases the neutrino masses are given to leading order in m_2/m_3 by diagonalizing the mass matrix in equation (20) using the analytic procedure described in appendix D of [12]. In the case that $d = 0$, corresponding to a 11 texture zero in equation (18), we have [12, 13]

$$m_1 \sim \mathrm{O}\left(\frac{x'y'}{Z}\right), \tag{22}$$

$$m_2 \approx \frac{|a|^2}{Xs_{12}^2}, \tag{23}$$

$$m_3 \approx \frac{|e|^2 + |f|^2}{Y}, \tag{24}$$

where $s_{12} = \sin\theta_{12}$ is given below. Note that with SD each neutrino mass is generated by a separate right-handed neutrino, and the SD condition naturally results in a neutrino mass hierarchy $m_1 \ll m_2 \ll m_3$. The neutrino mixing angles are given to leading order in m_2/m_3 by [12, 13]

$$\tan\theta_{23} \approx \frac{|e|}{|f|}, \tag{25}$$

$$\tan\theta_{12} \approx \frac{|a|}{c_{23}|b|\cos(\tilde{\phi}_b) - s_{23}|c|\cos(\tilde{\phi}_c)}, \tag{26}$$

$$\theta_{13} \approx \mathrm{e}^{\mathrm{i}(\tilde{\phi}+\phi_a-\phi_e)}\frac{|a|(e^*b + f^*c)}{[|e|^2 + |f|^2]^{3/2}}\frac{Y}{X}, \tag{27}$$

where we have written some (but not all) complex Yukawa couplings as $x = |x|\mathrm{e}^{\mathrm{i}\phi_x}$. The phase δ is fixed to give a real angle θ_{12} by

$$c_{23}|b|\sin(\tilde{\phi}_b) \approx s_{23}|c|\sin(\tilde{\phi}_c), \tag{28}$$

where

$$\tilde{\phi}_b \equiv \phi_b - \phi_a - \tilde{\phi} + \delta, \qquad \tilde{\phi}_c \equiv \phi_c - \phi_a + \phi_e - \phi_f - \tilde{\phi} + \delta. \tag{29}$$

The phase $\tilde{\phi}$ is fixed to give a real angle θ_{13} by

$$\tilde{\phi} \approx \phi_e - \phi_a - \arg(e^*b + f^*c). \tag{30}$$

Physically, these results show that in SD the atmospheric neutrino mass m_3 and mixing θ_{23} is determined by the couplings of the dominant right-handed neutrino of mass Y. The solar neutrino mass m_2 and mixing θ_{12} is determined by the couplings of the sub-dominant right-handed neutrino of mass X. The third right-handed neutrino of mass Z is effectively decoupled from the see-saw mechanism and leads to the vanishingly small mass $m_1 \approx 0$.

3.3. Types of sequential right-handed neutrino dominance

Assuming SD, there is still an ambiguity regarding the mass ordering of the heavy Majorana right-handed neutrinos. So far we have assumed that the dominant right-handed neutrino of

Table 1. Types of SD, classified according to the mass ordering of the right-handed neutrinos. LSD corresponds to the dominant right-handed neutrino of mass Y being the lightest, ISD to the dominant right-handed neutrino of mass Y being the intermediate one, and HSD to the dominant right-handed neutrino of mass Y being the heaviest. The fourth column shows the leading-order form for Y_ν under the assumption of a large 33-element in the Yukawa matrix.

Type of SD	M_{RR}	$m^{\nu}_{\mathrm{LR}} = Y_\nu v_{\mathrm{u}}$	Leading Y_ν
LSDa $Y < X < Z$	$\begin{pmatrix} Y & 0 & 0 \\ 0 & X & 0 \\ 0 & 0 & Z \end{pmatrix}$	$\begin{pmatrix} d & a & p \\ e & b & q \\ f & c & r \end{pmatrix}$	$\begin{pmatrix} 0 & 0 & 0 \\ 0 & 0 & 0 \\ 0 & 0 & 1 \end{pmatrix}$
LSDb $Y < Z < X$	$\begin{pmatrix} Y & 0 & 0 \\ 0 & Z & 0 \\ 0 & 0 & X \end{pmatrix}$	$\begin{pmatrix} d & p & a \\ e & q & b \\ f & r & c \end{pmatrix}$	$\begin{pmatrix} 0 & 0 & 1 \\ 0 & 0 & 1 \\ 0 & 0 & 1 \end{pmatrix}$
ISDa $X < Y < Z$	$\begin{pmatrix} X & 0 & 0 \\ 0 & Y & 0 \\ 0 & 0 & Z \end{pmatrix}$	$\begin{pmatrix} a & d & p \\ b & e & q \\ c & f & r \end{pmatrix}$	$\begin{pmatrix} 0 & 0 & 0 \\ 0 & 0 & 0 \\ 0 & 0 & 1 \end{pmatrix}$
ISDb $Z < Y < X$	$\begin{pmatrix} Z & 0 & 0 \\ 0 & Y & 0 \\ 0 & 0 & X \end{pmatrix}$	$\begin{pmatrix} p & d & a \\ q & e & b \\ r & f & c \end{pmatrix}$	$\begin{pmatrix} 0 & 0 & 1 \\ 0 & 0 & 1 \\ 0 & 0 & 1 \end{pmatrix}$
HSDa $Z < X < Y$	$\begin{pmatrix} Z & 0 & 0 \\ 0 & X & 0 \\ 0 & 0 & Y \end{pmatrix}$	$\begin{pmatrix} p & a & d \\ q & b & e \\ r & c & f \end{pmatrix}$	$\begin{pmatrix} 0 & 0 & 0 \\ 0 & 0 & 1 \\ 0 & 0 & 1 \end{pmatrix}$
HSDb $X < Z < Y$	$\begin{pmatrix} X & 0 & 0 \\ 0 & Z & 0 \\ 0 & 0 & Y \end{pmatrix}$	$\begin{pmatrix} a & p & d \\ b & q & e \\ c & r & f \end{pmatrix}$	$\begin{pmatrix} 0 & 0 & 0 \\ 0 & 0 & 1 \\ 0 & 0 & 1 \end{pmatrix}$

mass Y is dominant because it is the lightest one. We emphasize that this need not be the case. The neutrino of mass Y could be dominant even if it is the heaviest right-handed neutrino, providing its Yukawa couplings are strong enough to overcome its heaviness and satisfy the condition in equation (19). In hierarchical mass matrix models, it is natural to order the right-handed neutrinos so that the heaviest right-handed neutrino is the third one, the intermediate right-handed neutrino is the second one and the lightest right-handed neutrino is the first one. It is also natural to assume that the 33 Yukawa coupling is of order unity, due to the large top quark mass. It is therefore possible that the dominant right-handed neutrino is the heaviest (called heavy sequential dominance or HSD), the lightest (called light sequential dominance or LSD) or the intermediate one (called intermediate sequential dominance or ISD). This leads to the six possible types of SD corresponding to the six possible mass orderings of the right-handed neutrinos as shown in table 1. In each case the dominant right-handed neutrino is the one with mass Y, and the leading sub-dominant right-handed neutrino is the one with mass X. The resulting see-saw matrix m^{ν}_{LL} is invariant under re-orderings of the right-handed neutrino columns, but the leading order form of the neutrino Yukawa matrix Y_ν is not.

It is worth emphasizing that, since all the forms above give the same light effective see-saw neutrino matrix m^{ν}_{LL} in equation (20), under the SD assumption in equation (19), this implies

that the analytic results for neutrino masses and mixing angles applies to all of these forms. They are distinguished theoretically by different preferred leading-order forms of the neutrino Yukawa matrix Y_ν shown in the table. These leading-order forms follow from the the LMA requirements $e \sim f$ and $a \sim b - c$.[1] Thus we see that LSDa and ISDa are consistent with a form of Yukawa matrix with small Dirac mixing angles, while HSDa and HSDb correspond to the so-called 'lop-sided' forms.

4. Sequential right-handed lepton dominance in the type I see-saw mechanism

In this section we show how bi-large mixing could originate from the charged lepton sector using a generalization of sequential right-handed neutrino dominance [11, 12] to all right-handed leptons [15]. We write the mass matrices for the charged leptons m_{E} as

$$m_{\mathrm{E}} = \begin{pmatrix} p' & d' & a' \\ q' & e' & b' \\ r' & f' & c' \end{pmatrix}. \tag{31}$$

In our notation, each right-handed charged lepton couples with a column in m_{E}. For the charged leptons, the SD conditions are [15]

$$|a'|, |b'|, |c'| \gg |d'|, |e'|, |f'| \gg |p'|, |q'|, |r'|. \tag{32}$$

They imply the desired hierarchy for the charged lepton masses $m_\tau \gg m_\mu \gg m_e$ and small right-handed mixing of $U_{e_{\mathrm{R}}}$. We assume zero mixing from the neutrino sector which corresponds to the MNS matrix being given by $U_{\mathrm{MNS}} = U_{e_{\mathrm{L}}}\,\mathrm{diag}(1, \mathrm{e}^{\mathrm{i}\beta_2^\nu}, \mathrm{e}^{\mathrm{i}\beta_3^\nu})$ in the conventions in the appendix. A natural possibility for obtaining a small θ_{13} is [15]

$$|d'|, |e'| \ll |f'|. \tag{33}$$

In leading order in $|d'|/|f'|$ and $|e'|/|f'|$, for the mixing angles θ_{12}, θ_{23} and θ_{13}, we obtain

$$\tan(\theta_{12}) \approx \frac{|a'|}{|b'|}, \tag{34a}$$

$$\tan(\theta_{23}) \approx \frac{s_{12}|a'| + c_{12}|b'|}{|c'|}, \tag{34b}$$

$$\tan(\theta_{13}) \approx \frac{s_{12}|e'|\mathrm{e}^{\mathrm{i}(\phi_{a'} - \phi_{b'} + \phi_{e'} + \delta)} - c_{12}|d'|\mathrm{e}^{\mathrm{i}(\phi_{d'} + \delta)}}{|f'|\mathrm{e}^{\mathrm{i}(\phi_{a'} - \phi_{c'} + \phi_{f'})}}, \tag{34c}$$

where the Dirac CP phase δ is determined such that θ_{13} is real, which requires

$$\tan(\delta) \approx \frac{c_{12}|d'|\sin(\phi_{a'} - \phi_{c'} - \phi_{d'} + \phi_{f'}) - s_{12}|e'|\sin(\phi_{b'} - \phi_{c'} - \phi_{e'} + \phi_{f'})}{c_{12}|d'|\cos(\phi_{a'} - \phi_{c'} - \phi_{d'} + \phi_{f'}) - s_{12}|e'|\cos(\phi_{b'} - \phi_{c'} - \phi_{e'} + \phi_{f'})}. \tag{35}$$

[1] Note that the leading-order Y_ν in table 1 only gives the independent order unity entries in the matrix, so that, for example, in LSDb we would expect $b - c \sim 1$ in general, and not zero.

Given $\tan(\delta)$, δ has to be chosen such that $\tan(\theta_{13}) \geqslant 0$ in order to match with the usual convention $\theta_{13} \geqslant 0$. The phases β_2^e and β_3^e from the charge lepton sector are given by

$$\beta_2^e \approx \phi_{a'} - \phi_{b'} + \pi, \tag{36a}$$

$$\beta_3^e \approx \phi_{a'} - \phi_{c'}. \tag{36b}$$

Note that in the case that the neutrino sector induces Majorana phases, the total Majorana phases β_2 and β_3 of the MNS matrix are given by

$$\beta_2 \approx \beta_2^e + \beta_2^\nu, \tag{37a}$$

$$\beta_3 \approx \beta_3^e + \beta_3^\nu. \tag{37b}$$

θ_{13} only depends on d'/f' and e'/f' from the Yukawa couplings to the sub-dominant right-handed muon and on θ_{12}. We find that in the limit $|d'|, |e'| \ll |f'|$, the two LMAs θ_{12} and θ_{23} approximately depend only on a'/c' and b'/c' from the right-handed tau Yukawa couplings. Both mixing angles are large if a', b' and c' are of the same order.

In addition to achieving bi-large mixing from the charged lepton sector, we also require now small mixing from the neutrino sector. Usually, sequential RHND [11, 12] is viewed as a framework for generating large solar mixing θ_{12} and large atmospheric mixing θ_{23} in the neutrino mass matrix. However, given SD in the neutrino sector in equation (19) which guarantees a neutrino mass hierarchy, one can easily find the conditions for small mixing from the neutrinos as well from equations (25) and (26). Using the notation of section 3.2, we need $d, e \ll f$ and $a \ll b, c$. Small mixing from the neutrino sector thus requires three small entries in m_{LR}^ν. As shown in [16], three zero entries in Y_ν might stem from a spontaneously broken SO(3) flavour symmetry and real vacuum alignment. Other realizations might by found via Abelian or discrete symmetries.

5. Type II see-saw upgrade

In type I see-saw models, it seems to be difficult to obtain a partially degenerate or quasi-degenerate neutrino mass spectrum in a natural way, whereas hierarchical masses seem to be natural. The direct mass term in type II models, on the other hand, has the potential to provide a natural way for generating neutrino masses with a partial degeneracy. In this section, we show that it is possible to obtain a partially degenerate neutrino mass spectrum by essentially adding a type II direct neutrino mass contribution proportional to the unit matrix. In this case, the neutrino mass scale is controlled by the type II direct mass term, while the neutrino mass splittings (which are generally now much smaller) and mixings continue to be determined by the type I see-saw matrix using SD as described earlier.

Thus we shall consider a type II upgrade [16], where the mass matrix of the light neutrinos in equation (9) has the particular form

$$m_{\mathrm{LL}}^\nu \approx m^{\mathrm{II}} \begin{pmatrix} 1 & 0 & 0 \\ 0 & 1 & 0 \\ 0 & 0 & 1 \end{pmatrix} + \begin{pmatrix} (m_{\mathrm{LL}}^{\mathrm{I}})_{11} & (m_{\mathrm{LL}}^{\mathrm{I}})_{12} & (m_{\mathrm{LL}}^{\mathrm{I}})_{13} \\ (m_{\mathrm{LL}}^{\mathrm{I}})_{21} & (m_{\mathrm{LL}}^{\mathrm{I}})_{22} & (m_{\mathrm{LL}}^{\mathrm{I}})_{23} \\ (m_{\mathrm{LL}}^{\mathrm{I}})_{31} & (m_{\mathrm{LL}}^{\mathrm{I}})_{32} & (m_{\mathrm{LL}}^{\mathrm{I}})_{33} \end{pmatrix}, \tag{38}$$

in the basis where the mass matrix M_{RR} of the heavy right-handed neutrinos is diagonal.

To understand the effect of the type II contribution $m_{\rm LL}^{\rm II}$, we consider the diagonalization of $m_{\rm LL}^{\rm I}$ by a unitary transformation $(m_{\rm LL}^{\rm I})_{\rm diag} = V m_{\rm LL}^{\rm I} V^{\rm T}$. If we assume for the moment that the type I see-saw mass matrix $m_{\rm LL}^{\rm I}$ is real, which implies that V is an orthogonal matrix, we obtain

$$(m_{\rm LL}^{\nu})_{\rm diag} = m^{\rm II} V V^{\rm T} + V m_{\rm LL}^{\rm I} V^{\rm T} = m^{\rm II} 1 + (m_{\rm LL}^{\rm I})_{\rm diag}. \tag{39}$$

The additional direct mass term leaves the predictions for the mixings from the type I see-saw contribution unchanged in this case. This allows us to transform many type I see-saw models for hierarchical neutrino masses into type II see-saw models for partially degenerate or quasi-degenerate neutrino masses while maintaining the predictions for the mixing angles. Obviously, in the general complex case, it is no longer that simple since for a unitary matrix $VV^{\rm T} \neq 1$ and the phases will have impact on the predictions for the mixings. However, as we will see below, with sequential right-handed neutrino dominance [11, 12] for the type I contribution to the neutrino mass matrix, and a particular phase structure, the known techniques and mechanisms for explaining the bi-large lepton mixings can be directly applied also in the presence of CP phases.

5.1. Type II upgrade of a ISD model

As an example of a type II model where the bi-large lepton mixing stems from the neutrino mass matrix, we now consider explicitly the model A1 of table 4 in [16] with sequential right-handed neutrino dominance [11, 12] for the type I part $m_{\nu}^{\rm I}$ of the neutrino mass matrix. The leading-order Dirac mass matrices are

$$m_{\rm LR}^{\nu} = \begin{pmatrix} a{\rm e}^{{\rm i}\delta_1} & 0 & 0 \\ b{\rm e}^{{\rm i}\delta_1} & e{\rm e}^{{\rm i}\delta_2} & 0 \\ c{\rm e}^{{\rm i}\delta_1} & f{\rm e}^{{\rm i}\delta_2} & r{\rm e}^{{\rm i}\delta_3} \end{pmatrix}, \qquad m_{\rm E} = \begin{pmatrix} a'{\rm e}^{{\rm i}\delta_1'} & 0 & 0 \\ b'{\rm e}^{{\rm i}\delta_1'} & e'{\rm e}^{{\rm i}\delta_2'} & 0 \\ c'{\rm e}^{{\rm i}\delta_1'} & f'{\rm e}^{{\rm i}\delta_2'} & r'{\rm e}^{{\rm i}\delta_3'} \end{pmatrix}, \tag{40}$$

where here a, b, c, e, f, r and a', b', c', e', f', r' are real. $M_{\rm RR}$ and the type II contribution $m_{\rm LL}^{\rm II}$ are given by

$$M_{\rm RR} =: \begin{pmatrix} X & 0 & 0 \\ 0 & Y & 0 \\ 0 & 0 & Z \end{pmatrix}, \qquad m_{\rm LL}^{\rm II} = m^{\rm II} \begin{pmatrix} 1 & 0 & 0 \\ 0 & 1 & 0 \\ 0 & 0 & 1 \end{pmatrix}, \tag{41}$$

denoting the mass of the dominant right-handed neutrino by Y and the mass of the sub-dominant one by X. The sequential RHND condition we impose is then

$$\left|\frac{e^2, f^2}{Y}\right| \gg \left|\frac{a^2, b^2, c^2}{X}\right| \gg \left|\frac{r^2}{Z}\right|. \tag{42}$$

The leading-order type II neutrino mass matrix is given by the type II see-saw formula of equation (9).

The masses of the charged leptons are given by $m_\tau = r'$, $m_\mu = e'$ and $m_e = a'$. In addition we note that the mixings θ_{12}^e, θ_{13}^e and θ_{23}^e, which stem from $U_{e_{\rm L}}$ and could contribute to the MNS matrix, are very small. Furthermore, in leading order each column of M_e has a common complex phase, which can be absorbed by $U_{e_{\rm R}}$. Therefore, the charged leptons do not influence the leptonic CP phases in this approximation.

Using the analytical methods for diagonalizing neutrino mass matrices with small θ_{13} derived in [12], from $m^{\nu}_{\mathrm{LL}} = m^{\mathrm{II}}_{\mathrm{LL}} + m^{\mathrm{I}}_{\mathrm{LL}}$, we find for the mixing angles

$$\tan(\theta_{23}) \approx \frac{|e|}{|f|}, \tag{43a}$$

$$\tan(2\theta_{13}) \approx \frac{2|a|}{X} \frac{|\sin(\theta_{23})|b| + \cos(\theta_{23})|c|\mathrm{sign}(bcef)|}{|2m^{\mathrm{II}}\sin(\tilde{\delta}) + m^{\mathrm{I}}_3 \mathrm{e}^{\mathrm{i}(2\delta_2+3\pi/2-\tilde{\delta})}|}, \tag{43b}$$

$$\tan(\theta_{12}) \approx \frac{|a|}{|\cos(\theta_{23})|b| - \sin(\theta_{23})|c|\mathrm{sign}(bcef)|}, \tag{43c}$$

where m^{I}_i ($i \in \{1, 2, 3\}$) are the mass eigenvalues of the hierarchical $m^{\mathrm{I}}_{\mathrm{LL}}$ given by

$$m^{\mathrm{I}}_1 = \mathcal{O}\left(\frac{r^2}{Z}\right) \approx 0, \tag{44a}$$

$$m^{\mathrm{I}}_2 \approx \frac{(|a|^2 + |\cos(\theta_{23})|b| - \sin(\theta_{23})|c|\mathrm{sign}(bcef)|^2)}{X} \approx \frac{|a|^2}{\sin^2(\theta_{12})X}, \tag{44b}$$

$$m^{\mathrm{I}}_3 \approx \frac{(|e|\sin(\theta_{23}) + |f|\cos(\theta_{23}))^2}{Y}, \tag{44c}$$

and with $\tilde{\delta}$ defined by

$$\tan(\tilde{\delta}) := \frac{m^{\mathrm{I}}_3 \sin(2\delta_2 - 2\delta_1)}{m^{\mathrm{I}}_3 \cos(2\delta_2 - 2\delta_1) - 2m^{\mathrm{II}}\cos(2\delta_1)}. \tag{45}$$

Given $\tan(\tilde{\delta})$, $\tilde{\delta}$ has to be chosen such that

$$\frac{\sin(\theta_{23})|b| + \cos(\theta_{23})|c|\mathrm{sign}(bcef)}{\mathrm{sign}(ab)[2m^{\mathrm{II}}\mathrm{e}^{-\mathrm{i}(2\delta_1+3\pi/2)}\sin(\tilde{\delta}) + m^{\mathrm{I}}_3\mathrm{e}^{-\mathrm{i}(2\delta_1-2\delta_2+\tilde{\delta})}]} \geqslant 0. \tag{46}$$

This does not affect θ_{13}, which we have defined to be $\geqslant 0$; however it is relevant for extracting the Dirac CP phase δ, given by

$$\delta \approx \begin{cases} \tilde{\delta} & \text{for } P \geqslant 0, \\ \tilde{\delta} + \pi & \text{for } P < 0, \end{cases} \tag{47}$$

with P being defined by

$$P := \frac{\cos(\theta_{23})|b| - \sin(\theta_{23})|c|\mathrm{sign}(bcef)}{\mathrm{sign}(ab)[(\cos(\theta_{23})|b| - \sin(\theta_{23})|c|\mathrm{sign}(bcef))^2 - |a|^2]}. \tag{48}$$

The mass eigenvalues of the complete type II neutrino mass matrix are given by

$$m_1 \approx |m^{\mathrm{II}}|, \tag{49a}$$

$$m_2 \approx |m^{\mathrm{II}} - m_2^{\mathrm{I}} \mathrm{e}^{\mathrm{i}2\delta_1}|, \tag{49b}$$

$$m_3 \approx |m^{\mathrm{II}} - m_3^{\mathrm{I}} \mathrm{e}^{\mathrm{i}2\delta_2}|, \tag{49c}$$

and, for $m^{\mathrm{II}} \neq 0$, the Majorana phases β_2 and β_3 can be extracted by

$$\beta_2 \approx \tfrac{1}{2}\arg(m^{\mathrm{II}} - m_2^{\mathrm{I}} \mathrm{e}^{\mathrm{i}2\delta_1}), \tag{50a}$$

$$\beta_3 \approx \tfrac{1}{2}\arg(m^{\mathrm{II}} - m_3^{\mathrm{I}} \mathrm{e}^{\mathrm{i}2\delta_2}). \tag{50b}$$

In the classes of type II see-saw models with sequential right-handed neutrino dominance for the type I contribution to the neutrino mass matrix and real vacuum alignment leading to the phase structure of the Yukawa matrices as in equation (40), the solar and the atmospheric neutrino mixings θ_{12} and θ_{23} are independent of the type II mass scale m^{II} and of the complex phases of the neutrino Yukawa matrix. We can thus upgrade these types of models continously from hierarchical neutrino mass spectra to partially degenerate ones, while maintaining the predictions for the two large lepton mixings.

6. Model-building applications of SD

We have seen that SD is not a model, but is a general sub-mechanism within the see-saw mechanism. SD may be used to obtain hierarchical type I neutrino masses, together with bi-large lepton mixing, in a completely natural way, overcoming the usual naturalness objection to the see-saw mechanism in this case. We have also seen that SD may be extended to the case where the lepton mixing arises from the charged lepton sector. Furthermore, we have seen that the SD mechanism is also useful within the framework of the type II see-saw mechanism in the case that the additional type II mass contributions are proportional to the unit matrix. Despite the successes of SD, the conditions on which it is based have just been stated without any explanation. It also remains to be seen how the mechanism of SD can be used to construct realistic unified models of flavour.

In this section, we discuss some of the model-building applications of SD. We shall see that the use of SD is ideally suited to GUTs and family symmetry models, has already been used in quite a number of works of this nature. SD also makes contact with studies based on two right-handed neutrinos. Finally, there have been some interesting cosmological applications that have recently been proposed. Given the simplicity and naturalness of SD, it is reasonable to expect that it will continue to be exploited increasingly in the future.

6.1. Effective two right-handed neutrino models

In SD we have seen that one of the right-handed neutrinos effectively decouples from the see-saw mechanism. Without loss of generality, we have denoted the mass of this decoupled right-handed neutrino as Z. From table 1 we see that the decoupled right-handed neutrino of mass Z may be

the lightest, the heaviest of the intermediate mass right-handed neutrino. If it is the lightest or the second lightest then it could, in principle, play an important part in leptogenesis or inflation and so have cosmological relevance even though it is decoupled from the see-saw mechanism. However if it is the heaviest right-handed neutrino, as in LSDa or ISDa in table 1, then it would be expected to play no part in phenomenology. In these cases, the heaviest neutrino of mass Z is completely decoupled from physics, and SD reduces to effectively two right-handed neutrino models, as pointed out in [11, 13]. Recently, there have been several studies based on the 'minimal see-saw' involving two right-handed neutrinos [17], and it is worth bearing in mind that such models could naturally arise as the limiting case of SD.

6.2. GUT and family symmetry models

There are many models in the literature based on SRHND or SD. For example, explicit realizations of the small determinant condition of Altarelli and Feruglio implicitly involve SRHND, or SD, together with U(1) family symmetry and SU(5) GUTs [18]. An example of SD of the HSD type in Pati-Salam models with U(1) family symmetry was considered in [19]. Single right-handed neutrino dominance has also been applied to SO(10) GUT models involving a U(2) family symmetry [20]. SD of the LSD type with SU(3) family symmetry and SO(10) GUTs has been considered in [21]. Type II up-gradable models based on SD of the ISD type with SO(3) family symmetry have been considered in [15, 16]. This list is not exhaustive, but represents a subset of models based on single or sequential right-handed neutrino dominance. The main point is that SD can readily be included in a wide range GUT and family symmetry models, and it enhances the naturalness of such models.

6.3. Sneutrino inflation models

SD has recently also been applied to sneutrino inflation [22]. Requiring a low reheat temperature after inflation, in order to solve the gravitino problem, forces the sneutrino inflation to couple very weakly with ordinary matter and its superpartner almost to decouple from the see-saw mechanism. This decoupling of a right-handed neutrino from the see-saw mechanism is a characteristic of SD.

7. Phenomenological implications of SD

We now review phenomenological consequences of type I see-saw models with SD and their type II upgrades for the low-energy neutrino parameters and high-energy mechanisms as leptogenesis and minimal lepton flavour violation (LFV). In order to compare the predictions of see-saw models based on SD with the experimental data obtained at low energy, the renormalization group (RG) running of the effective neutrino mass matrix has to be taken into account.

7.1. RG corrections

For type I models with SD, the running of the mixing angles is generically small [23] since the mass scheme is strongly hierarchical. When the neutrino mass scale is lifted, e.g. via a type II upgrade, a careful treatment of the RG running of the neutrino parameters, including the energy ranges between and above the see-saw scale [23, 24], is required. For convenient estimates of

the running below the see-saw scales, the approximate analytical formulae for the running of the parameters [25] can be used. Dependent on $\tan\beta$ in the MSSM, on the size of the neutrino Yukawa couplings and on the neutrino mass scale, the RG effects can be sizable or cause only small corrections.[2]

7.2. Dirac and Majorana CP phases and neutrinoless double beta decay

At present, the CP phases in the lepton sector are unconstraint by experiment. In type I see-saw models based on SD, there is no restriction on them from a theoretical point of view. The type II upgrade scenario however predicts that all observable CP phases, i.e. the Dirac CP phase δ relevant for neutrino oscillations and the Majorana CP phases β_2 and β_3, become small as the neutrino mass scale increases.

The key process for measuring the neutrino mass scale could be neutrinoless double beta decay. The decay rates depend on an effective Majorana mass defined by $\langle m_\nu\rangle = |\sum_i (U_{\mathrm{MNS}})_{1i}^2 m_i|$. Future experiments which are under consideration at present might increase the sensitivity to $\langle m_\nu\rangle$ by more than an order of magnitude. For type I models with SD, which have a hierarchical mass scheme, $\langle m_\nu\rangle$ can be very small, below the accessible sensitivity.

For models where the neutrino mass scale is lifted via a type II upgrade [16], there is a close relation between the neutrino mass scale, i.e. the mass of the lightest neutrino and $\langle m_\nu\rangle$. Since the CP phases are small, there can be no significant cancellations in $\langle m_\nu\rangle$. This implies that the effective mass for neutrinoless double beta decay is approximately equal to the neutrino mass scale $\langle m_\nu\rangle \approx m^{\mathrm{II}}$ and, therefore, neutrinoless double beta decay will be observable in the next round of experiments if the neutrino mass spectrum is partially degenerate.

7.3. Theoretical expectations for the mixing angles

In order to discriminate between models, precision measurements of the neutrino mixing angles have the potential to play an important role.

One important parameter is the value of the mixing angle θ_{13}, which is at present only bounded from above to be smaller than approximately 13°. In the type I SD case, the mixing angle θ_{13} is typically of the order $\mathcal{O}(m_2^{\mathrm{I}}/m_3^{\mathrm{I}})$. In the type II upgrade scenario this ratio decreases with increasing neutrino mass scale and is smaller than $\approx 5^\circ$ for partially degenerate neutrinos even if it was quite large in the type I limit. Sizable RG corrections, which are usually expected for partially degenerate neutrinos, are suppressed in the type II upgrade scenario due to small CP phases β_2, β_3 and δ [25].

Another important parameter is θ_{23}. Its present best-fit value is close to 45°; however comparably large deviations are experimentally allowed as well. With SD, we expect minimal deviations of θ_{23} from 45° of the order $\mathcal{O}(m_2^{\mathrm{I}}/m_3^{\mathrm{I}})$, which could be observed by future long-baseline experiments in the type I see-saw case.[3] In the type II upgraded version, the corrections can be significantly smaller since the ratio $m_2^{\mathrm{I}}/m_3^{\mathrm{I}}$ decreases with increasing neutrino mass scale [16]. For large $\tan\beta$ in the MSSM, the major source for the corrections can be RG effects [25], which are unsuppressed for small CP phases.

[2] A complete list of references for the β-functions of the neutrino mass operator can be found in [25].

[3] For sensitivities of future long-baseline experiments for measuring deviation from $\theta_{23} = 45^\circ$ and their potential for discriminating between models, see [26].

7.4. Minimal LFV

At leading order in a mass insertion approximation the branching fractions of LFV processes are given by[4]

$$\mathrm{BR}(l_i \to l_j\gamma) \approx \frac{\alpha^3}{G_F^2} f(M_2, \mu, m_{\tilde{\nu}})|m^2_{\tilde{L}_{ij}}|^2 \tan^2\beta, \tag{51}$$

where $l_1 = e, l_2 = \mu, l_3 = \tau$, and where the off-diagonal slepton doublet mass squared is given in the leading log approximation (LLA) by

$$m^{2(\mathrm{LLA})}_{\tilde{L}_{ij}} \approx -\frac{(3m_0^2 + A_0^2)}{8\pi^2} C_{ij}. \tag{52}$$

With SD, using the notation of equations (17) and (18), the leading log coefficients relevant for $\mu \to e\gamma$ and $\tau \to \mu\gamma$ are given approximately as

$$C_{21} = ab \ln\frac{M_U}{X} + de \ln\frac{M_U}{Y}, \qquad C_{32} = bc \ln\frac{M_U}{X} + ef \ln\frac{M_U}{Y}. \tag{53}$$

From table 1 and equation (53) it can be seen which types of SD will lead to large rates for $\mu \to e\gamma$ and $\tau \to \mu\gamma$. For example, the results for HSD show a large rate for $\tau \to \mu\gamma$ which is the characteristic expectation of lop-sided models in general [27] and HSD in particular. A global analysis of LFV has been performed in the constrained minimal supersymmetric standard model (CMSSM) for the case of SD, focusing on the two cases of HSDa and LSDa [28]. The results in [28] are based on an exact calculation, and the error incurred compared with the LLA study [29] can be as much as 100%. For LSDa, $\tau \to \mu\gamma$ is well below observable values. Therefore $\tau \to \mu\gamma$ provides a good discriminator between the HSDa and LSDa types of dominance. In [28] it is shown that the rate for $\mu \to e\gamma$ may determine the order of the sub-dominant neutrino Yukawa couplings in the flavour basis.

7.5. Leptogenesis

Leptogenesis and LFV are important indicators that can help to resolve the ambiguity of right-handed neutrino masses in table 1. In the LSD and HSD cases of SD, leptogenesis has been studied with some interesting results [30]. In general, successful leptogenesis for such models requires the mass of the lightest right-handed neutrino to be quite high, and generally to exceed the gravitino constraints if supersymmetry is assumed. However, putting this to one side for the moment, interesting links between the phase relevant for leptogenesis and the phase δ measurable in neutrino oscillation experiments have been made. The precise link depends on how many 'texture' zeros are assumed to be present in the neutrino Dirac mass matrix. For example, if two texture zeros are assumed then there is a direct link between δ and the leptogenesis phase, with the sign of δ being predicted from the fact that we are made of matter rather than antimatter. On the other hand, if only the physically motivated texture zero in the 11 entry of the Dirac mass matrix is assumed, then the link is more indirect [13].

[4] The mass insertion approximation given in equation (51) is for illustrative purposes only. The conclusions quoted below from [28] do not rely on this approximation.

More generally, in three right-handed neutrino models with SD, if the dominant right-handed neutrino is the lightest one (LSD) then the washout parameter $\tilde{m}_1 \sim \mathrm{O}(m_3)$, which is rather too large compared with the optimal value of around 10^{-3} eV, while if the dominant right-handed neutrino is either the intermediate one or the heaviest one then one finds $\tilde{m}_1 \sim \mathrm{O}(m_2)$ or arbitrary $\tilde{m}_1$, which can be closer to the desired value [30].

8. Discussion and conclusions

Neutrino masses and mixings are now established experimental phenomena which must be included in some extended version of the Standard Model. The simplest mechanism for describing small neutrino masses is the see-saw mechanism; however the simultaneous appearance of hierarchical neutrino masses and two LMAs is not natural in the see-saw mechanism. The simplest solution to this difficulty is to assume SD which has been the subject of this review.

We have reviewed the mechanism of sequential right-handed neutrino dominance which was proposed in the framework of the type I see-saw mechanism to account for bi-large neutrino mixing and a neutrino mass hierarchy in a natural way. We have discussed how SD may also be applied to the right-handed charged leptons, which alternatively allows bi-large lepton mixing in the charged lepton sector. We reviewed how such SD models may be upgraded to include type II see-saw contributions, resulting in a partially degenerate neutrino mass spectrum with bi-large lepton mixing arising from SD. We also saw that the use of SD is ideally suited to GUTs and family symmetry models, and mentioned some examples of such models. We also pointed out the interesting case where SD reduces effectively to the case of two right-handed neutrinos, and mentioned some interesting cosmological applications that have recently been proposed such as sneutrino inflation.

We also reviewed some phenomenological consequences of type I see-saw models with SD and their type II upgrades for the low-energy neutrino parameters and high-energy mechanisms as leptogenesis and minimal LFV, both of which can be probes of different types of SD. While RG effects are expected to be quite small for type I SD, they become increasingly important for the type II upgrade SD as the neutrino mass scale increases. We noted that neutrinoless double beta decay is practically unobservable in type I SD, but may well be observed in the next round of experiments in the type II upgrade sequential models if the neutrino masses are partially degenerate. We have seen that both θ_{13} and the correction to θ_{23} are controlled by the ratio $m_2^{\mathrm{I}}/m_3^{\mathrm{I}}$ which decreases with increasing neutrino mass scale, with interesting consequences.

Given the simplicity and naturalness of SD, we expect it to continue to be used and exploited ubiquitously in the future.

Acknowledgments

We acknowledge the support from the PPARC grant PPA/G/O/2002/00468.

Appendix. Our conventions

For the mass matrix of the charged leptons $m_{\mathrm{E}} = Y_e v_d$, where $v_d = \langle H_d \rangle$, defined by $\mathcal{L}_e = -m_{\mathrm{E}} \bar{e}_{\mathrm{L}}^f e_{\mathrm{R}}^f$ + h.c. and for the neutrino mass matrix m_{LL}^{ν}, the change from flavour basis to mass

eigenbasis can be performed with the unitary diagonalization matrices U_{e_L}, U_{e_R} and U_{ν_L} by

$$U_{e_L} m_E U_{e_R}^\dagger = \begin{pmatrix} m_e & 0 & 0 \\ 0 & m_\mu & 0 \\ 0 & 0 & m_\tau \end{pmatrix}, \qquad U_{\nu_L} m_{LL}^\nu U_{\nu_L}^T = \begin{pmatrix} m_1 & 0 & 0 \\ 0 & m_2 & 0 \\ 0 & 0 & m_3 \end{pmatrix}. \tag{A.1}$$

The MNS matrix is then given by

$$U_{MNS} = U_{e_L} U_{\nu_L}^\dagger. \tag{A.2}$$

We use the parametrization $U_{MNS} = R_{23} U_{13} R_{12} P_0$ with R_{23}, U_{13}, R_{12} and P_0 being defined as

$$R_{12} := \begin{pmatrix} c_{12} & s_{12} & 0 \\ -s_{12} & c_{12} & 0 \\ 0 & 0 & 1 \end{pmatrix}, \qquad U_{13} := \begin{pmatrix} c_{13} & 0 & s_{13} e^{-i\delta} \\ 0 & 1 & 0 \\ -s_{13} e^{i\delta} & 0 & c_{13} \end{pmatrix},$$

$$R_{23} := \begin{pmatrix} 1 & 0 & 0 \\ 0 & c_{23} & s_{23} \\ 0 & -s_{23} & c_{23} \end{pmatrix}, \qquad P_0 := \begin{pmatrix} 1 & 0 & 0 \\ 0 & e^{i\beta_2} & 0 \\ 0 & 0 & e^{i\beta_3} \end{pmatrix} \tag{A.3}$$

and where s_{ij} and c_{ij} stand for $\sin(\theta_{ij})$ and $\cos(\theta_{ij})$, respectively. The matrix P_0 contains the possible Majorana phases β_2 and β_3. δ is the Dirac CP phase relevant for neutrino oscillations.

References

[1] For a review see e.g. King S F 2004 *Rep. Prog. Phys.* **67** 107 (*Preprint* hep-ph/0310204)

[2] Yanagida T 1979 *Proc. Workshop on Unified Theory and Baryon Number of the Universe, KEK, Japan*
Glashow S L 1979 *Cargese Lectures*
Gell-Mann M, Ramond P and Slansky R 1979 *Sanibel Talk, CALT-68-709, February*
Gell-Mann M, Ramond P and Slansky R 1979 *Supergravity* (Amsterdam: North-Holland)
Mohapatra R N and Senjanovic G 1980 *Phys. Rev. Lett.* **44** 912

[3] Arkani-Hamed N, Dimopoulos S, Dvali G R and March-Russell J 2002 *Phys. Rev.* D **65** 024032 (*Preprint* hep-ph/9811448)

[4] Hirsch M and Valle J W F 2004 *Preprint* hep-ph/0405015

[5] Lazarides G, Shafi Q and Wetterich C 1981 *Nucl. Phys.* B **181** 287
Mohapatra R N and Senjanović G 1981 *Phys. Rev.* D **23** 165
Wetterich C 1981 *Nucl. Phys.* B **187** 343

[6] Wolfenstein L 1978 *Phys. Rev.* D **17** 2369
Mikheyev S and Smirnov A Yu 1985 *Sov. J. Nucl. Phys.* **42** 913

[7] Apollonio M *et al* [CHOOZ Collaboration] 1999 *Phys. Lett.* B **466** 415 (*Preprint* hep-ex/9907037)

[8] Elgaroy O *et al* 2002 *Preprint* astro-ph/0204152

[9] King S F 1998 *Phys. Lett.* B **439** 350 (*Preprint* hep-ph/9806440)

[10] King S F 1999 *Nucl. Phys.* B **562** 57 (*Preprint* hep-ph/9904210)

[11] King S F 2000 *Nucl. Phys.* B **576** 85 (*Preprint* hep-ph/9912492)

[12] King S F 2002 *J. High Energy Phys.* JHEP09 (2002) 011 (*Preprint* hep-ph/0204360)

[13] King S F 2003 *Phys. Rev.* D **67** 113010 (*Preprint* hep-ph/0211228)

[14] Davidson S and King S F 1998 *Phys. Lett.* B **445** 191 (*Preprint* hep-ph/9808296)

[15] Antusch S and King S F 2004 *Preprint* hep-ph/0403053

[16] Antusch S and King S F 2004 *Preprint* hep-ph/0402121

[17] Frampton P H, Glashow S L and Yanagida T 2002 *Phys. Lett.* B **548** 119 (*Preprint* hep-ph/0208157)
Raidal M and Strumia A 2003 *Phys. Lett.* B **553** 72 (*Preprint* hep-ph/0210021)
King S F 2003 *Phys. Rev.* D **67** 113010 (*Preprint* hep-ph/0211228)
Ibarra A and Ross G G 2003 *Preprint* hep-ph/0312138
[18] Altarelli G and Feruglio F 1998 *Phys. Lett.* B **439** 112 (*Preprint* hep-ph/9807353)
Altarelli G and Feruglio F 1998 *J. High Energy Phys.* JHEP11 (1998) 021 (*Preprint* hep-ph/9809596)
Altarelli G and Feruglio F 1999 *Phys. Lett.* B **451** 388 (*Preprint* hep-ph/9812475)
Altarelli G, Feruglio F and Masina I 2000 *Phys. Lett.* B **472** 382 (*Preprint* hep-ph/9907532)
[19] King S F and Oliveira M 2001 *Phys. Rev.* D **63** 095004 (*Preprint* hep-ph/0009287)
Blazek T, King S F and Parry J K 2003 *J. High Energy Phys.* JHEP05 (2003) 016 (*Preprint* hep-ph/0303192)
[20] Barbieri R, Creminelli P and Romanino A 1999 *Nucl. Phys.* B **559** 17 (*Preprint* hep-ph/9903460)
Raby S 2003 *Phys. Lett.* B **561** 119 (*Preprint* hep-ph/0302027)
[21] King S F and Ross G G 2001 *Phys. Lett.* B **520** 243 (*Preprint* hep-ph/0108112)
Ross G G and Velasco-Sevilla L 2003 *Nucl. Phys.* B **653** 3 (*Preprint* hep-ph/0208218)
King S F and Ross G G 2003 *Preprint* hep-ph/0307190
[22] Ellis J R, Raidal M and Yanagida T 2004 *Phys. Lett.* B **581** 9 (*Preprint* hep-ph/0303242)
Chankowski P H, Ellis J R, Pokorski S, Raidal M and Turzynski K 2004 *Preprint* hep-ph/0403180
[23] King S F and Singh N N 2000 *Nucl. Phys.* B **591** 3 (*Preprint* hep-ph/0006229)
[24] Antusch S, Kersten J, Lindner M and Ratz M 2002 *Phys. Lett.* B **538** 87 (*Preprint* hep-ph/0203233)
[25] Antusch S, Kersten J, Lindner M and Ratz M 2003 *Nucl. Phys.* B **674** 401 (*Preprint* hep-ph/0305273)
[26] Antusch S, Huber P, Kersten J, Schwetz T and Winter W 2004 *Preprint* hep-ph/0404268
[27] Blazek T and King S F 2001 *Phys. Lett.* B **518** 109 (*Preprint* hep-ph/0105005)
[28] Blazek T and King S F 2003 *Nucl. Phys.* B **662** 359 (*Preprint* hep-ph/0211368)
[29] Lavignac S, Masina I and Savoy C A 2002 *Preprint* hep-ph/0202086
[30] Hirsch M and King S F 2001 *Phys. Rev.* D **64** 113005 (*Preprint* hep-ph/0107014)

New Journal of Physics
An Institute of Physics and Deutsche Physikalische Gesellschaft Journal

Neutrino telescopes in the Mediterranean Sea

J Carr and G Hallewell

Centre de Physique de Particules de Marseille/IN2P3-CNRS 163 Ave. de Luminy, 13288 Marseille, France
E-mail: gregh@cppm.in2p3.fr and carr@cppm.in2p3.fr

New Journal of Physics **6** (2004) 112
Received 5 May 2004
Published 25 August 2004
Online at http://www.njp.org/
doi:10.1088/1367-2630/6/1/112

Abstract. In the Mediterranean Sea there are three sites where neutrino telescopes are being constructed or developed. The collaborations associated with these sites, ANTARES, NEMO and NESTOR, have adopted different technical solutions to implement a deep-sea detector. For these projects the various detector architectures are presented; the technological choices are compared and the current status is described.

PII: S1367-2630(04)80245-3
© IOP Publishing Ltd and Deutsche Physikalische Gesellschaft

Contents

1. Introduction **2**
2. Deep-sea neutrino telescopes **3**
2.1. Detector concepts and site considerations . . . 3
3. Mediterranean Neutrino Telescope projects **5**
3.1. ANTARES detector architecture . . . 6
3.2. NESTOR detector architecture . . . 10
3.3. NEMO detector architecture . . . 11
4. Detector technology issues **12**
4.1. The optical detection modules . . . 12
4.2. Structural and pressure components . . . 14
4.3. Bottom anchors . . . 14
4.4. Electro-optical connection and distribution . . . 16
4.5. Readout systems . . . 19
4.5.1. The NESTOR data acquisition system . . . 19
4.5.2. The ANTARES data acquisition system . . . 20
4.5.3. NEMO readout system R&D . . . 21
4.6. Underwater acoustic survey and navigation . . . 22
4.6.1. The ANTARES acoustic positioning system . . . 22
4.6.2. Semiconductor tiltmeter/compass systems . . . 23
4.7. Site evaluation and underwater and environmental instrumentation . . . 24
4.7.1. The ANTARES instrumentation line . . . 24
4.8. Sea deployment and recovery operations . . . 25
4.8.1. ANTARES deployment procedures . . . 25
4.8.2. NESTOR deployment procedures . . . 27
5. Status in spring 2004 **29**
5.1. ANTARES construction status . . . 29
5.2. NESTOR status . . . 30
6. Conclusion **31**
References **31**

1. Introduction

A number of possible techniques exist to detect high-energy neutrinos from outer space but the most widely exploited method is the detection in large volumes of water or ice of Čerenkov light from the muons and hadrons produced by neutrino interactions with matter around the detector. Water Čerenkov detectors (e.g. IMB, Kamiokande, Super-Kamiokande and SNO) are the only detectors so far to have observed neutrinos produced beyond the earth; these observations being 10^6–10^7 eV neutrinos produced in the sun and supernova 1987a. Experiments are also being developed based on detection of radio wave emission or sound produced in the interactions together with detection of light emission from showers initiated by neutrinos in the atmosphere. These latter techniques are possible for neutrinos with energies above 10^{16} eV. The large sea-based neutrino telescopes described in this paper, as well as the ice-based neutrinos described elsewhere in this review, aim at detection of neutrinos in the 10^{10}–10^{16} eV energy range.

The major scientific objectives of sea-based neutrino telescopes are the discovery and understanding of the sites of acceleration of high-energy particles in the universe. Since their original discovery 100 years ago, the origin of high-energy charged cosmic rays arriving on the earth is unknown. Neutrinos offer a unique possibility to trace cosmic rays back to their origins. Being electric charge neutral they are unperturbed by magnetic fields while, being weakly interacting, they can pass through dense dust clouds which might surround their sources. There are numerous candidate neutrino sources in the cosmos; among the possible sources in the local galaxy are supernova remnants, pulsars and microquasars. Possible extragalactic sources include active galactic nuclei and γ ray bursts. An irreducible background to searches for primary neutrinos from these cosmic sources consists of secondary neutrinos from cosmic ray interactions in the earth's atmosphere.

An important further objective of neutrino telescopes is the search for dark matter in the form of neutralinos. In supersymmetric theories with R-parity conservation, the relic neutralinos from the Big Bang are predicted to concentrate in massive bodies such as the centres of the earth, the sun and the galaxy. At these sites, neutralino annihilations and the subsequent decays of the resulting particles would yield neutrinos detectable in neutrino telescopes of the scale currently in operation and being constructed.

The present paper describes the status of the projects constructing neutrino telescopes in the Mediterranean Sea. Two neutrino telescope projects, ANTARES and NESTOR, are aiming at scientific discoveries with medium-sized detectors while the NEMO project is currently undertaking research and development for the construction of a future larger detector. Sections 1–3 describe the detector techniques and the general concepts of the three projects, section 4 focuses on some technical aspects of the detectors and the concluding sections outline the present status of these projects.

2. Deep-sea neutrino telescopes

A deep sea-water telescope has significant advantages over ice and lake-water experiments due to the better optical properties of the medium. However, serious technological challenges must be overcome to deploy and operate a detector in the deep sea. The pioneering sea-water project, DUMAND, which worked from 1980 to 1995 to deploy a detector off the coast of Hawaii, did not overcome these challenges and the project was cancelled. In contrast, the projects AMANDA and BAIKAL, which deploy from the solid glacial ice and frozen surface lake ice respectively, have developed workable deployment systems. The advantages of sea-water neutrino telescopes are significantly better angular resolution—less than 0.3° for ANTARES compared with 3° for AMANDA—as well as a more uniform efficiency due to the homogeneous medium. A disadvantage of a sea-water detector is the higher optical background due to radioactive decay of ^{40}K and light emission from living organisms: bioluminescence. These backgrounds can be overcome in the design of the detector by having a higher density of optical modules and high bandwidth data readout.

2.1. Detector concepts and site considerations

A deep-sea neutrino telescope detects neutrinos by observing the Čerenkov light produced by muons in the sea water with the muons originating from interactions of the neutrino in the sea

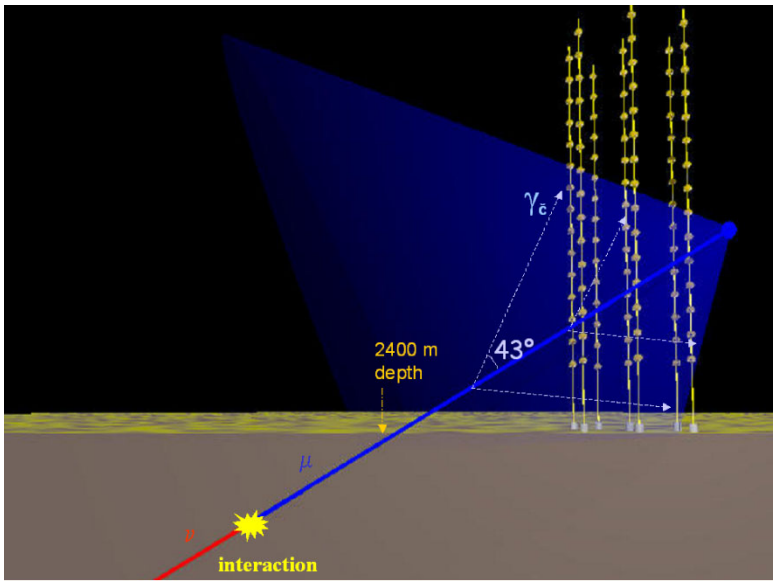

Figure 1. Principle of detection of high-energy neutrinos in an underwater neutrino telescope.

water around the detector or in the rock below it. A matrix of light detectors, in the form of photomultipliers in glass spheres, 'optical modules', is deployed near the seabed. This matrix of light detectors enables the direction of the muon track to be measured with a precision of a few tenths of a degree and at high energies the muon track direction is closely aligned with that of the neutrino such that the neutrino direction is measured with similar precision. Figure 1 illustrates the principle of neutrino detection with the undersea telescope.

The detection of high-energy muon neutrinos exploits three properties:

(i) The directional correlation of the muon and parent neutrino trajectories to within 0.3° for $E_\nu > 10$ TeV.

(ii) The unique upward-going directional signature of muons from cosmic neutrino interactions with respect to the vastly higher muon background from cosmic ray collisions in the atmosphere. Upward-going muons can only originate from local neutrino interactions: the earth filters out all other particles.

(iii) The long range of muons in water and rock over the neutrino energy range of interest. Upward-going muons may be generated far from the instrumented volume and still be detected.

Accurate reconstruction of the trajectory of a neutrino-induced muon relies on tracking over many tens of metres and measurement of the arrival time of the UV-blue component of the Čerenkov wavefront to nanosecond accuracy on photomultiplier tubes (PMTs) whose positions must be known to better than 20 cm.

The detection of electron and tau neutrinos is possible in these telescope optimized for muon neutrino detection but except at very high energy the detection efficiency for these other neutrino types is lower.

The choice of the PMT array spacing depends on the absorption and scattering length in the local deep-water environment and to a lesser degree on the limit set by the chromatic dispersion in arrival time of the Čerenkov photons. Due to the high purity of water at great depth, light absorption and scattering are small. However, the detector is subject to backgrounds from cosmic ray muons, luminescence from deep-water creatures and from Čerenkov light from the β disintegration of ^{40}K, present in sea salt.

The criteria for the site of an underwater neutrino observatory are:

(i) Closeness to the coast to ease deployment and reduce the expense of the power and signal cable connections to the shore.

(ii) A sufficient depth to reduce background from atmospheric muons, and to suppress their miss-reconstruction as up-going. A depth of 1000 m is a minimal requirement; the ANTARES site has a depth of 2400 m, the NEMO site 3400 m and the NESTOR site 4100 m.

(iii) Good optical properties in water: long absorption (>20 m) and scattering (∼50 m) lengths[1] for light in the range ($350 < \lambda < 550$ nm).

(iv) Low level of bioluminescence.

(v) Low rates of biofouling (bacterial film deposition and marine life accretion) on optical surfaces.

(vi) Low rates of sedimentation (for any upward-looking optical components).

(vii) Low velocity bottom current (∼few cm s^{-1}), since rate of bioluminescence is dependent on this parameter.

3. Mediterranean Neutrino Telescope projects

In the Mediterranean Sea, three sites are under evaluation for Neutrino Telescope projects at the locations shown in figure 2. The most advanced project is that of the ANTARES collaboration which is building a detector with initially 900 optical modules and effective area 50 000 m^2 at a site off the south coast of France near Toulon. The NEMO collaboration is exploring a site off Sicily. Since 2000 the ANTARES and NEMO collaborations have been working together on the detector at the Toulon site with an agreement to choose the optimal site in the Mediterranean for a future larger telescope. In addition, the NEMO group has a test site in the bay of Catania used to perform R&D for the future large detector. The NESTOR collaboration intends to build a detector with 168 optical modules and around 20 000 m^2 effective area at a site near Pylos off the coast of Greece. The different projects have chosen different solutions for the technical implementation of the deep-sea neutrino telescope concept.

The ANTARES collaboration started in 1996 to explore sites off the French coast. The site chosen is at 42°50′N 6°10′E with a depth of 2400 m. The ANTARES detector array will suspend optical modules on individual mooring lines, with readout via cables connected to the bottom of the lines. This configuration is similar to that originally chosen by the DUMAND collaboration.

As with DUMAND, the ANTARES detector requires connections to be made on the seabed by underwater vehicles. However, in the last 10 years, the relevant underwater technology has

[1] The absorption coefficient, a, is defined as $1/L_a$; the scattering coefficient, $b = 1/L_b$. Their combination, $c = (L_a + L_b)/(L_a \cdot L_b)$, is the attenuation coefficient. Due to the combination of absorption and scattering phenomena, light intensity scales with distance L as $I = (I_0/L^2)\mathrm{e}^{-cx}$.

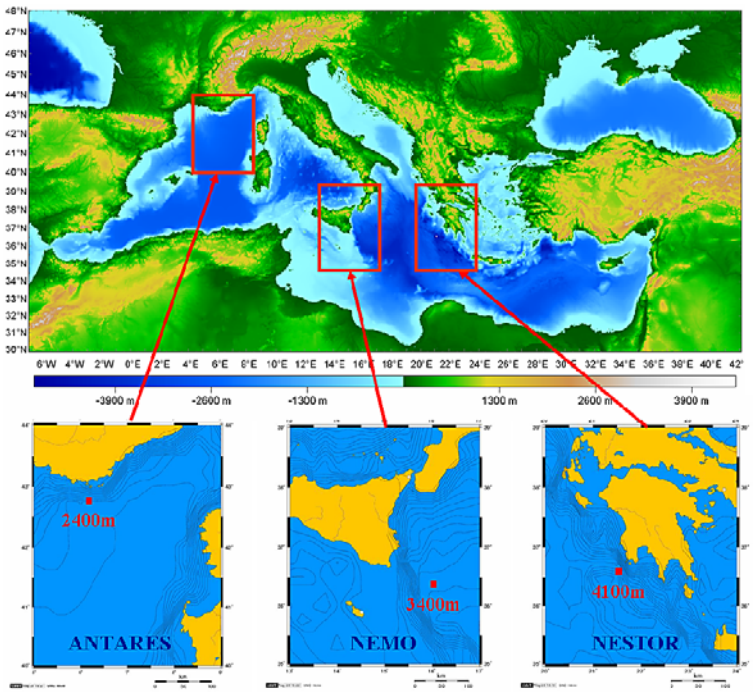

Figure 2. Locations of the sites of the three Mediterranean Neutrino Telescope projects.

advanced significantly due to the needs of the offshore-oil industry, facilitating the ANTARES configuration. Currently, a wide range of suitable deep-sea connectors is available and extensively used in industry, including electro-optical connectors wet mateable at depth on the site. Many commercial underwater vehicles now exist that are capable of making these connections. The ANTARES readout design maximizes the reliability of the detector by dividing the system into independent sections such that the failure of no single active component can cause the loss of the whole detector. The detector signals are digitized in local electronics and transmitted to the shore over high bandwidth optical links. On shore, a computer farm will take the trigger decisions to decide which data are recorded on tape. An advantage of the ANTARES approach is the possibility to quickly recover and repair all elements of the detector deployed in the sea.

The NESTOR detector will be installed at a depth of 4100 m. A key concept of the NESTOR project, and a significant difference with ANTARES, is the arrangement of the optical modules on a tower structure with all internal connections made on the surface during deployment, hereby avoiding the need for underwater connections. The NESTOR towers will contain 12 hexagonal floors of 16 m radius with photomultipliers looking both upward and downward. Test deployments have been performed and many detector elements exist, including the data/power cable connection from the site to the shore.

3.1. ANTARES detector architecture

The geometrical layout and readout architecture of the ANTARES detector have been optimized using four criteria: total detection efficiency, neutrino direction precision and background rejection and cost.

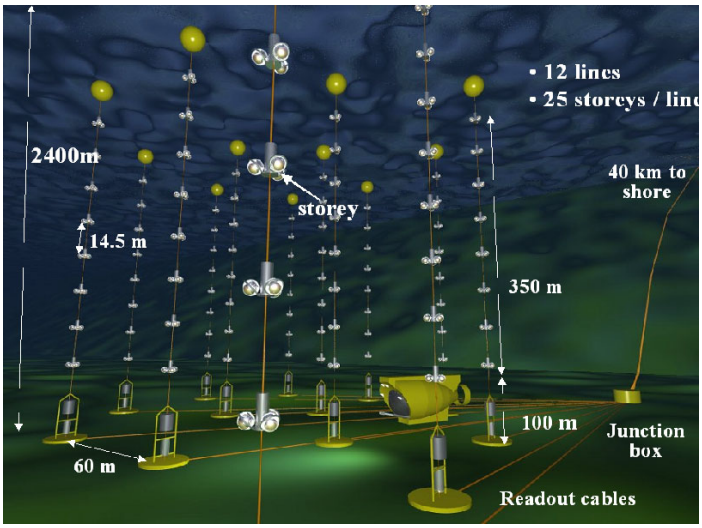

Figure 3. The layout of the ANTARES Neutrino Telescope on the sea floor.

The maximum detection efficiency requires the maximum instrumented volume and is optimal with a homogeneous distribution of light detectors; a configuration which also assures the best precision on neutrino direction. The background reduction requires optical modules closely spaced enough to be able to recognize tracks by timing associations within the distribution of random hits due to the light backgrounds in the sea water from radioactive decays in ^{40}K and bioluminescence. Cost considerations also lead to a close grouping of the light detectors.

The detector geometry chosen by ANTARES is a compromise between the homogenous spacing indicated by the efficiency and precision criteria and the clustering indicated by the background and cost criteria. The layout of the detector is shown in figure 3. The optical modules are arranged in groups of three on lines with a total height of 420 m, which are weighted to the seabed and held nearly vertical by syntactic foam buoys at the top. The seabed at the site is at a depth of 2400 m and the optical modules positioned at depths between 2300 and 2000 m. A line has a total of 75 optical modules arranged in 25 storeys containing three light detectors.

The default readout mode of ANTARES is to transmit the time and amplitude of any light signal above a threshold corresponding to 1/3 of a photo-electron for each optical module. These signals are then treated in a computer farm on shore to find hit patterns corresponding to physics events. The grouping of three optical modules in a storey allows local coincidences to be made for this pattern finding and also, under certain circumstances, local triggers to be formed to reduce the readout rate. The bioluminescence rate at the site varies with season. It is planned that when the singles rate is too high for the throughput of the data acquisition system the local trigger will be used to reduce the data flow to acceptable levels. In addition, the front-end electronics allows a more detailed readout of the light signal than the standard time and amplitude mode. With this detailed readout it is possible to sample the full waveform of the signal with 128 samples separated by $\sim$2 ns, enabling special calibration studies of the electronics.

The readout architecture of the detector has several levels of multiplexing of the photomultiplier signals. The first level is in the 'local control module' (LCM) in each storey of the detector, where the analogue electrical outputs of the photomultipliers are digitized in a

custom-built ASIC chip, the analogue ring sampler (ARS) before being treated by a data acquisition card containing an FPGA and microprocessor, which outputs the multiplexed signals of the three local optical modules on an Ethemet optical link. These links from five storeys, forming a 'Sector', are combined in an Ethemet switch in the master local control module (MLCM) at every fifth storey and the combined link output is sent on a particular wavelength to a dense wavelength division multiplexing (DWDM) system in an electronics container, the string control module (SCM) at the bottom of each line. In the SCM, the outputs from the five MLCMs along the line are multiplexed on to one pair of optical fibres. These fibres are then connected to a junction box on the seabed via interlink cables. In the junction box the outputs from up to 16 lines are gathered onto a 48 fibre electro-optical submarine cable and sent to the experiment shore station at La Seyne-sur-Mer. The optical links between each MLCM and the shore station are connected using only passive components.

The electrical supply system has a similar architecture to the readout system. The submarine cable supplies up to 4400 V, 10 A ac to a transformer in the junction box. The 16 independent secondary outputs from the transformer provide up to 500 V, 4 A to the lines via the interlink cables. At the base of each line a string power module (SPM) power supply shares the same container as the SCM. The SPM distributes up to 400 V dc to the MLCMs and LCMs in each storey each of which contains a local power box (LPB) to provide the various low voltages required by each electronics card.

The 45 km electro-optical undersea cable[2] linking the detector to the shore station was laid in October 2001. The cable was terminated in December 2002 with the deployment of the central electro-optical junction box respectively.

A series of site evaluation campaigns has been carried out by the ANTARES collaboration [1, 2]. At the array depth of 2400 m, the expected background rate from atmospheric cosmic ray muons is around 30 Hz. This rate is insignificant in comparison with the ^{40}K β background from sea salt, which adds a singles rate of 60 kHz to each 10-in PMT, or with occasional bio-luminescence, which can peak during short bursts up to MHz rates, and is seasonally and ocean current dependent. Since the PMTs in the ANTARES array will be angled 45° downward towards the seabed, fouling is not a serious problem. The combined signal loss due to bio-deposition and sedimentation has been measured [1] to be less than 2% per year.

The attenuation and scattering lengths in water at the ANTARES site have been measured in several campaigns between 1998 and 2000. At 466 nm, attenuation (scattering) lengths have varied between 45 and 60 m (37 and 79 m). The seasonal variation in these figures is significant, and the ANTARES array will incorporate an 'instrumentation' line which will deploy underwater instruments including transparency and current profile monitors.

The construction of optical modules for 12 detection lines is well advanced. The commissioning of a full readout chain is in progress: a prototype 'sector line' of five optical module triplets was deployed in late 2002 following the deployment of the electro-optical junction box. A site instrumentation line was deployed in early 2003. The commissioning of the array of 12 detection lines is planned for completion in 2006.

The performance of an undersea neutrino detector is characterized by the effective area: the angular resolution and the energy resolution. The effective area is given either as the effective area for muons or the effective area for neutrinos. The latter quantity is most easily used to

[2] Manufactured and deployed by Alcatel.

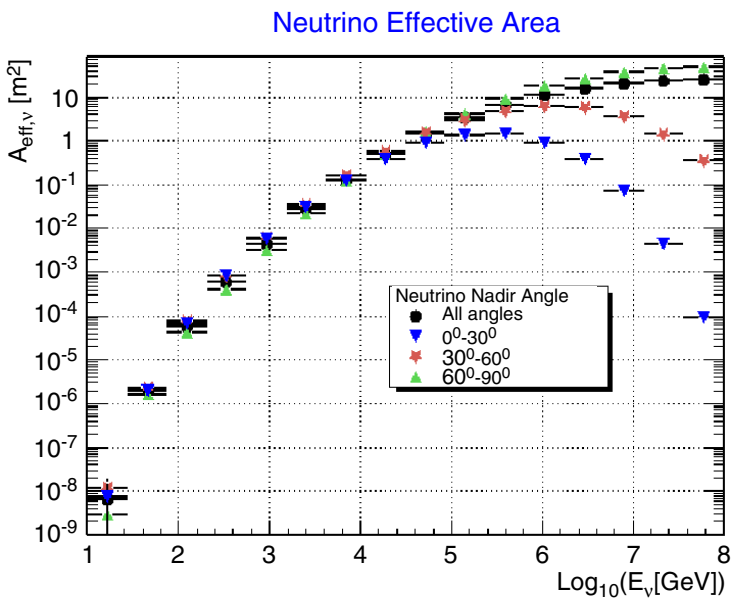

Figure 4. Neutrino effective area for the ANTARES detector as a function of neutrino energy and for various ranges of incident neutrino directions.

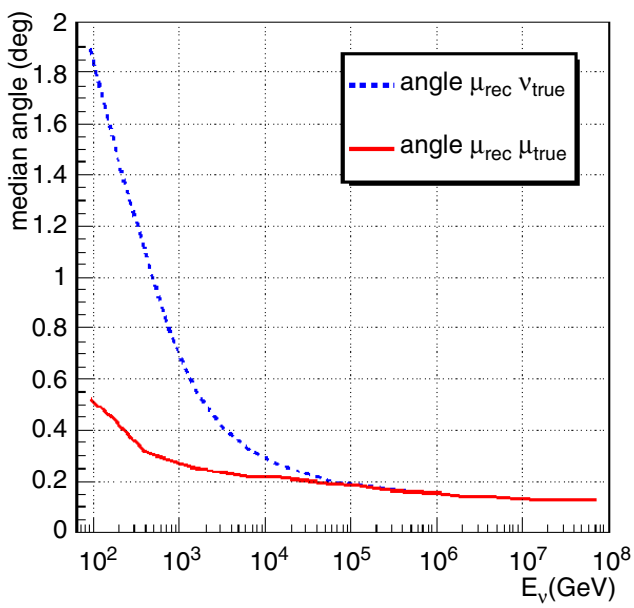

Figure 5. Angular resolution: (red solid line) resolution of the reconstruction of the muon track; (blue dotted line) resolution of the reconstructed muon track relative to the neutrino direction taking into account the kinematics of the neutrino interaction.

calculate the events rates; for this the number of events in the detector is just the product of the neutrino flux and the neutrino effective area. Figure 4 shows the neutrino effective area as simulated for the ANTARES detector. The angular resolution is shown in figure 5 and the energy resolution in figure 6.

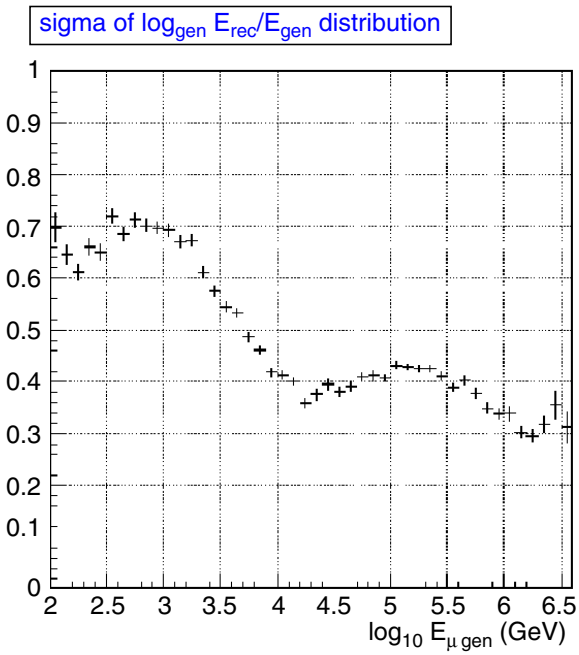

Figure 6. Energy resolution: the value plotted is the sigma of the logarithm of the energy resolution.

3.2. NESTOR detector architecture

The NESTOR array will be located near Pylos on the Greek Ionian Sea coast. An electro-optical cable has been laid from a shore station at Methoni to a site at a depth of 4100 m around 15 km from the shore. The array, shown conceptually in figure 7, will comprise a series of 'towers', each rising 360 m from a seabed anchor, held in tension by an underwater buoy. Each tower will contain 144 PMTs mounted on 12 titanium-framed 32 m diameter 'floors' in the form of six-pointed stars. A pair of PMTs will be mounted on each arm, one looking up and the other down. The array is intended to be installed and extended without the need for underwater electro-optical connections by submarine vehicles.

The water in this region of the Ionian basin is very clear, with ∼55 m attenuation length [3] for blue light. Bottom currents have been measured to be below 10 cm s^{-1}. Extremely low rates of sedimentation and biofouling permit a significant number of upward-looking optical sensors.

The NESTOR cable to shore was deployed in June 2000, but was damaged by the ship during the cable lay. In January 2002 the end of the cable was recovered; the cable was repaired and redeployed at 4100 m with an electro-optical junction box and associated instruments including an underwater current meter, an ocean bottom seismometer, a nephelometer to monitor light scattering, temperature and pressure sensors, a compass and a tilt-meter. Instrument data were transferred to the shore for nearly a year; the first long-duration real-time data readout from a component of deep-sea neutrino detector. The first detector floor was deployed in March 2003 and has allowed the reconstruction of muons as described in section 5.2. After this engineering run, a detector consisting of four floors will be deployed for more tests and physics data taking, followed by the complete tower.

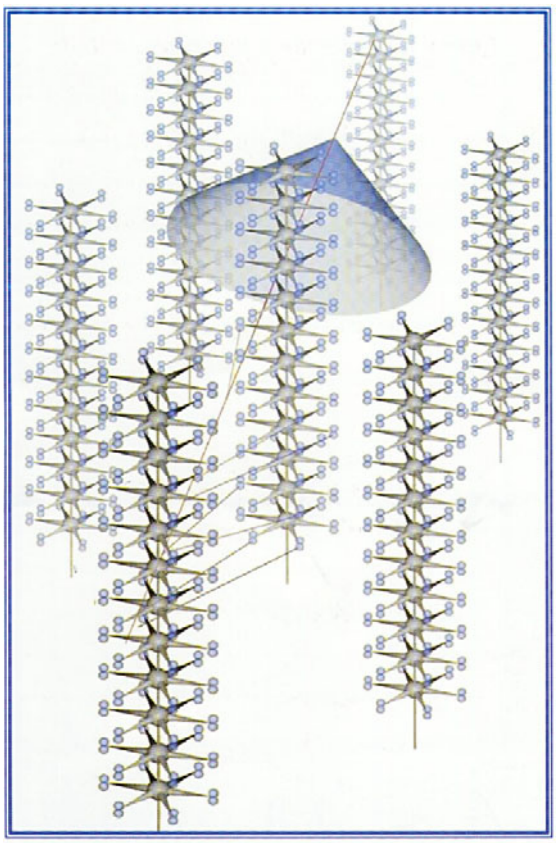

Figure 7. Conceptual layout of the NESTOR array.

3.3. NEMO detector architecture

The NEMO collaboration has identified a possible site for a km^3-scale array at a depth of 3500 m, distant of 80 km from the Sicilian coast near Capo Passero. At this location in the Ionian Sea, bacterial concentration is relatively low, with the consequent advantages of low expected bioluminescence background and biofouling rate. Preliminary studies over a period of 40 days have shown no evidence for biofouling. At the site, the light attenuation (absorption) length exceeds 35 m (70 m) [4]. The average bottom current is around 3 cm s^{-1}, with a measured sedimentation rate of $\sim$20 m g^{-1} d^{-1}. It remains to be proven that this low rate would not seriously degrade the performance of upward-looking PMTs after $\sim$1 year, should the detector design include them.

The NEMO concept is for a 1-km^3-scale array with 4096 optical modules hung from 64 'towers' laid in a square grid with 200 m spacing. Each tower, shown in figure 8, would rise 750 m from a seabed anchor, and would contain 16 'floors' separated in height by 40 m, each with a pair of PMTs at each end of a 20 m composite support arm. A matrix of support cables would ensure that successive floors deploy orthogonally under the force of the suspension buoy. The NEMO collaboration has also brought into service a test site at a depth of 2031 m. A 28 km electro-optical cable from Catania in Sicily [5] splits 23 km from the shore, a second branch running 5 km to the 'Geostar' underwater environmental platform. Each site is serviced by 10 optical fibres and six electrical conductors.

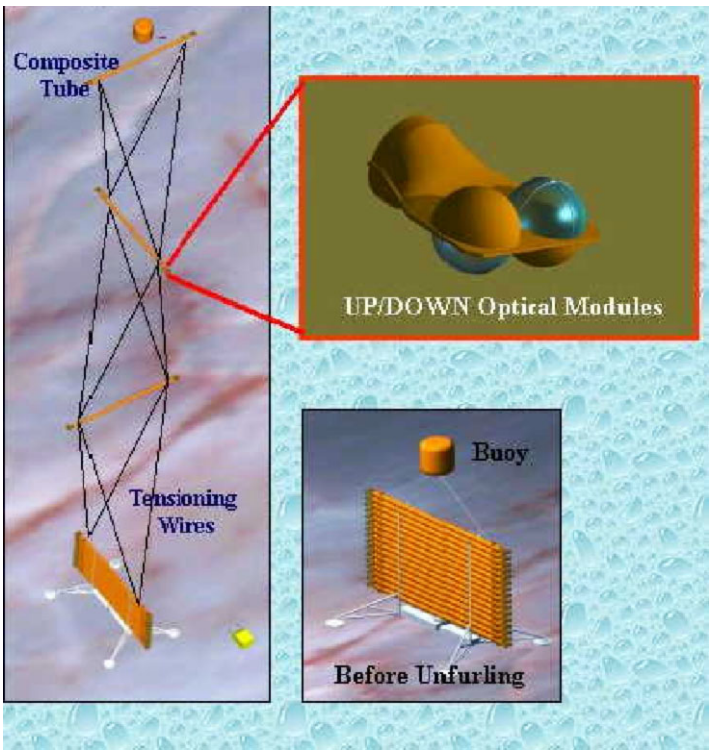

Figure 8. Concept for a NEMO tower.

4. Detector technology issues

In the following sections (see also [6]), the technology of underwater neutrino detectors is discussed in more detail.

4.1. The optical detection modules

As in existing water neutrino detectors such as Super-Kamiokande and SNO, Čerenkov light will be detected using PMTs with single photon sensitivity. The extreme pressure at the operating depths requires that the PMTs be housed in pressure-resistant glass spheres. Such spheres are readily available in diameters up to 43 cm with depth ratings up to 7000 m from several suppliers[3] and may be purchased in a variety of glasses, including low potassium (low β activity) variants. Spheres are supplied as matched hemispheres and can be predrilled with electrical and pump-out penetrations. Leak tightness at high pressures is given by plastic deformation of the ground glass contact surfaces of the hemispheres: no 'O' ring joint is used.

Figure 9 illustrates the components of a generic optical module of an underwater neutrino detector. In ANTARES [7] and NESTOR [8], the pressure spheres from different manufacturers exhibit very similar characteristics: 43 cm diameter with 1.5 cm thick, low activity (<0.5% K content) borosilicate glass having $n = 1.47$ and transmission >87% for $\lambda > 400$ nm. A PMT

[3] Benthos type 2040-17V used in NESTOR (Benthos Corp, North Falmouth, MA 02556, USA), Vitrovex type 8330 used in ANTARES ('Vitrovex' ® by Nautilus Marine Service GmbH, D-28357, Bremen, Germany) and 'EKRAN' (Novosibirsk) and Vitrovex used at Lake Baikal.

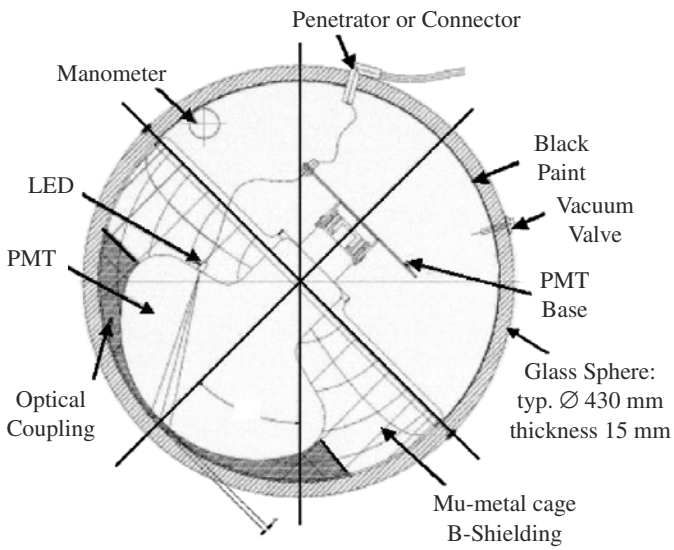

Figure 9. A generic underwater optical module.

Table 1. Parameters of Hamamatsu 7081-20 PMT.

Photocathode-sensitive area	500 cm^2
Combined efficiency (quantum Å collection: $400 < \lambda < 700$ nm)	>16%
Gain at 2500 V	2×10^8
Pulse amplitude at nominal working gain of 5×10^7	60 mV/50 W
Transit time	~60 ns
Transit time spread (TTS: FWHM)	<3 ns
Dark count rate (at 0.3 × single PE threshold)	<10 kHz
Pulse rise time	<5 ns
Pulse width (FWHM: single PE)	<12 ns

with single photon sensitivity is shielded from earth's magnetic field by a two-part mu-metal wire cage, and is mounted and optically coupled onto one hemisphere using an index matching gel.[4] Since power consumption is critical in large detector arrays powered through very long shore cables, the HV bias for the dynode array is usually generated in a custom PMT base from a dc input, using a Cockcroft–Walton chain. A light flasher system consisting of a blue LED and pulser circuit may be added to monitor the PMT transit time, which can exceed 60 ns in large photocathode PMTs. The pulser trigger signal is referenced to the detector master clock.

Table 1 illustrates the performance of the Hamamatsu R7081-20 10-in PMT used by the ANTARES collaboration. Its performance is fairly typical of PMTs used in deep-water neutrino detectors.

[4] In ANTARES, 'Silgel' ® 612 A/B by Wacker-Chemic GmbH (Munich, Germany): two-component silicon rubber, room temperature cure: $n = 1.404$ (transmission >88% for $(400 < \lambda < 700)$ nm). In NESTOR, Wacker Semicosil gel $\{n \sim 1.4\}$ (gel or liquid glycerine, $n = 1.478$) with polyurethane (gel) containment gasket.

Figure 10. Partially folded titanium frame of a NESTOR 'floor' (at NESTOR Institute, Pylos).

4.2. Structural and pressure components

In the present generation of deep underwater neutrino arrays, the requirements of pressure and corrosion resistance have predicated the almost exclusive use of glass and titanium for pressure vessels. Structural supports are in titanium or composites, which will offer important cost savings in km^3-scale arrays. Figures 10, 11 and 12 illustrate the use of titanium in the NESTOR and ANTARES optical module support frames and electro-optical junction box respectively.

Each 32-m-diameter NESTOR titanium floor frame [8, 9] will incorporate a central titanium sphere containing data acquisition, power conversion and monitor and control system electronics. The six arms are composed of folding 5 m tubular frames as shown in figure 10.

Although uncoated ferrous-metal structures (including stainless steel) are unsuitable for use in deep-sea water, possible cost reductions relative to titanium might be achieved by decoupling the problems of pressure and corrosion resistance. Figure 12 illustrates a junction box being considered by NEMO [10] in which a main electro-optical cable is split into parallel outputs for an array of detection lines. Cables exit the walls of the spherical steel pressure vessel through 'penetrators' and pass through an oil volume to terminate in underwater-mateable connectors arranged around the circumference of an oil bath built in composite GRP. An internal flexible water bladder[5] ensures the equi-pressure of water and oil by compensating the slight compressibility of the oil.

4.3. Bottom anchors

The NESTOR, ANTARES and NEMO underwater neutrino detectors tension their detection lines between anchors and a buoy, usually composed of a pressure (compression)-resistant syntactic

[5] Manufactured, for example, by Pronal SA (Leers, France).

Figure 11. Titanium optical module support frames for 'triplet' stories of the ANTARES detector.

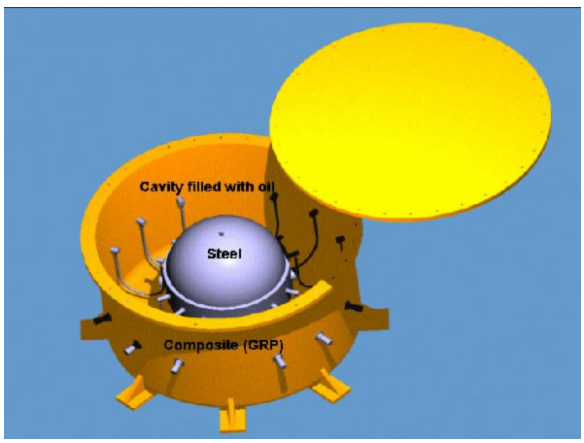

Figure 12. Example of an oil barrier/steel deep-sea junction box pressure vessel (NEMO).

foam.[6] Bottom anchors for deep-water detectors are often sophisticated devices, incorporating an acoustic release system allowing the line to float to the surface for recovery. In this event a 'disposable' deadweight is left on the seabed. In ANTARES and NEMO, an underwater mateable/breakable connector[7] automatically disconnects with the unrestrained line buoyant force.

[6] Glass micro-spheres in resin: manufactured, for example, by BMTI s.a. (La Seyne-sur-Mer, France).
[7] MkII Hybrid (Electro-optical) Connector (Ocean Design Inc, Ormond Beach, FL, USA).

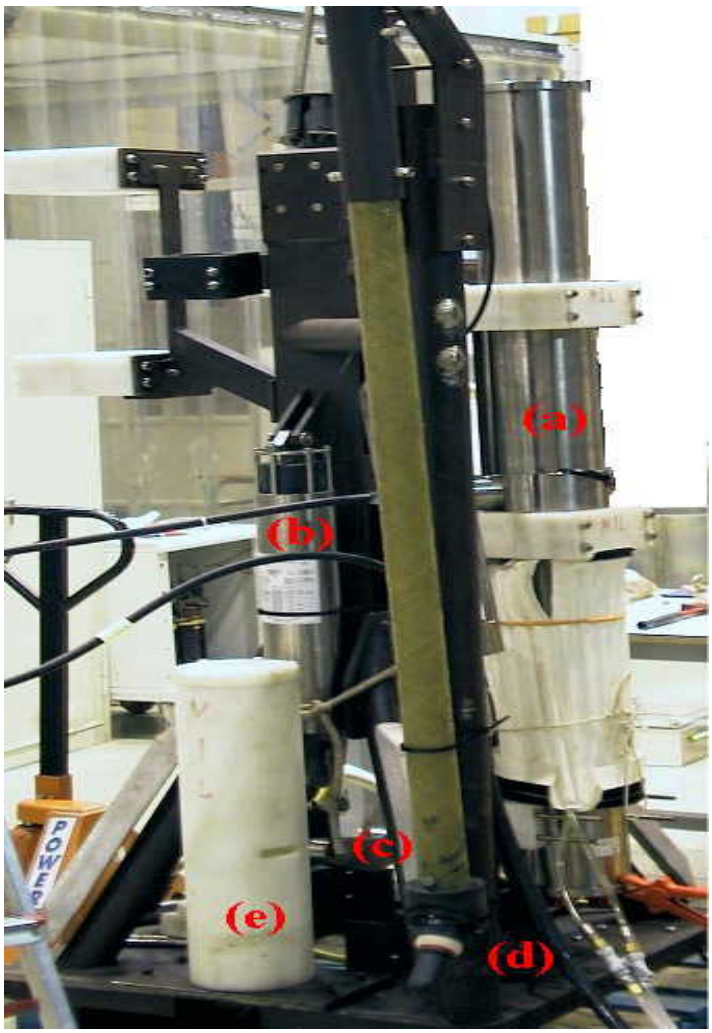

Figure 13. ANTARES 'bottom string socket' anchor.

Figure 13 illustrates the recoverable part of the ANTARES anchor. This incorporates the detection line power converter (a); the acoustically activated release (b) the release shackle (c) and the acoustic survey system transponder[8] (d). The disconnect speed of the underwater-mateable connector is regulated by a pair of sea-water dashpots (e).

4.4. Electro-optical connection and distribution

The present generation underwater neutrino arrays are deployed in stages on sites where an electro-optical shore cable has already been deployed. Unless terminating in deep underwater-mateable connectors, the shore cable must be dredged to the surface for connection to be made to it. Shore cables are deployed with dredging tails and acoustic transponders to enable them to be located for this operation. Options for the connection of additional

[8] Model RT861-B2T (Oceano Technologies, Brest, France; http://www.oceano-technologies.fr).

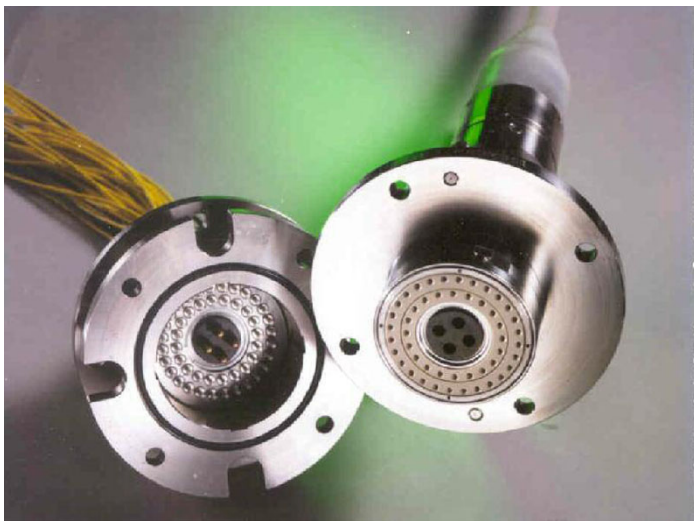

Figure 14. Example of a commercial (dry-mate) undersea cable electro-optical connector (Photo courtesy Sea Con Inc.).

detector lines are:

(i) Underwater hook-up to the connector on the seabed anchor of a previously deployed line, or more safely, to a previously deployed junction box. Both require the use of underwater-mateable electro-optical connectors and a manned or remotely operated submarine vehicle (ROV). This is the option chosen by ANTARES.

(ii) Deployment of each detection line with a dredgeable or buoy-anchor released cable pigtail of length exceeding the water depth (4–5 km). This allows a dry connection to be made at the surface with less-expensive connectors, without the need for a ROV. This would represent an extension to the present NESTOR recovery/deployment concept using a recoverable rope (ReRo: section 4.8.2), which is not, in its present form, an interlink cable. However, under such a connection strategy, the seabed would risk becoming cluttered with very long cables whose descent would need to be carefully controlled to avoid damage to already-deployed detector elements.

Electro-optical distribution is a significant component of the cost of undersea neutrino detectors, particularly where the shore link cable is long or custom made. In an effort to minimise this cost, ANTARES (NESTOR) have deployed standard telecommunications cables with 48 (18) optical fibres and a *single* power conductor.[9] Figure 14 illustrates the (dry-mateable) electro-optical connector[10] of the ANTARES undersea cable. The connector shell is titanium with an outer diameter of 25 cm. The four electrical contacts (in equipotential in the ANTARES cable) are grouped at the centres. In both detectors, power returns to the shore station via a deep-sea electrode[11] and a shore electrode located below the low tide level. NESTOR uses monopolar dc

[9] In long undersea telephone cables, optical signal repeaters are often powered by series wiring using the single power conductor: one (the other) end station supplying a +ve (−ve) voltage w.r.t. the sea.

[10] SeaCon/Inc, El Cajon, CA, USA.

[11] In ANTARES via a 40-mm diameter titanium bar anode: length 1.7 m with 'KERAMOX®-MMO' coating (Magneto Special Anodes BV, BA Schiedam, Netherlands).

Figure 15. Left: ANTARES junction box with penetrators and underwater-mateable connectors. Right: ANTARES junction box during deployment, illustrating acoustic transponder titanium support frame and undersea cable attachment.

while ANTARES will be powered with 4200 V 50 Hz ac at ∼8 A: a central transformer in an underwater junction box reducing and distributing the voltage to the detector lines.

The ANTARES 50 Hz distribution system is rather conservative and may not be optimal for a km^3-scale detector such that groups are performing R&D for future systems. At the NEMO test site the main electro-optical cable splits into two drops, each with 10 optical fibres and six power conductors [11], which will facilitate studies of a variety of ac and dc powering scenarios.

Figure 15 shows the ANTARES central junction box, which is based on a 1 m diameter titanium sphere with a central cylindrical connector belt through which enter the shore electro-optical cable, the sea electrode cable and 16 'penetrators' with 2.5 m electro-optical cable pigtails ending in underwater-mateable connectors. The junction box is installed in a titanium frame providing strain relief for the re-descent of the shore cable. The frame also contains an acoustic transponder[12] to locate the junction box following deployment.

For undersea connections the Ocean Design MkII Hybrid connector system[13] is used. The receptacle and cable-mounting plug are oil-filled with conductors and fibre ends shuttered in the oil volume in the unmated condition. Upon connection, the shutters open and oil is displaced into bladders at the rear of the receptacle and plug.

The ANTARES junction box is the underwater hub of the detector, splitting the power between the detector lines, distributing clock signals and gathering the data signals from the detector lines onto the shore cable. Its 24 kW transformer has 16 separate 500 V secondaries

[12] Model ET861T by Oceano Technologies: 9 kHz → 14 kHz & v.v.

[13] MkII Hybrid Connector, Titanium shell (2 conductors, 4 fibres). Fibreoptic insertion loss <0.2 dB, HV standoff (pin-shell) 500 V unmated, 1000 V mated (Ocean Design Inc, Ormond Beach, FL 32174, USA). Rated >100 insertions <6000 depth before oil refurbishment.

to power and galvanically isolate each detection or instrumentation line. Each output may be switched on/off or reset by a remotely controllable circuit breaker handled via the triply redundant junction box slow control system. Passive fibre-optic splitters distribute the master clock signals in duplicate to the 16 output lines. Lines will be connected to the junction box as they are deployed, using a ROV equipped with a manipulator arm. Power arriving at a detection line from the junction box is converted from 500 V ac to 380 V dc at the anchor for passage up the cable to the 25 electronic containers. In these, it is further reduced via dc/dc converters for use in optical modules and readout electronics.

Very high reliability is required of critical underwater electronics and power distribution components, MTBF (mean time between failures) $\gg$10 year typical operational life, due to the very high cost of recovery and repair of damaged components, particularly should submarine vehicles be required.

In contrast to the situation with electro-optical connectors, a wider variety of underwater all-electrical or all-fibre connectors exists. Relatively inexpensive dry-mateable types for 500 bar + ambient pressure are available from several manufacturers, including Sea-Con Inc and Gisma.[14]

4.5. Readout systems

The principal problem for the readout systems of undersea neutrino telescopes is the separation of single photoelectron (SPE)-like PMT signals along muon trajectories from background due to ^{40}K disintegrations and PMT dark current pulses and occasional bioluminescence. The bioluminescence rate is very variable in time, pulses lasting a few seconds with rates up to MHz being produced by fish while bacteria and plankton give rates which vary with sea current. Pulses from bioluminescence represent the main contribution to PMT dead time, but these high rates are usually correlated over only a few adjacent PMTs.

Data may be uploaded to the shore with or without the application of local ('off-shore') triggering or local bioluminescence-rejecting coincidences. The 'all-to-shore' option allows trigger decisions to be taken in on-shore electronics which can be upgraded to profit from technology advances during the lifetime of the detector.

4.5.1. The NESTOR data acquisition system. The NESTOR readout [9] and data acquisition system (RDAQ) follows a data-driven architecture with waveform capture and capabilities for forming local (per floor) coincidences to reduce on-shore processing requirements.

Within the central titanium sphere of each floor, a 'floor board' implements PMT pulse sensing, majority logic event triggering, waveform capture and digitization for 12 PMTs. The board extracts data, formats events and transmits data via the single bi-directional optical fibre up-/downlink per floor to the shore. Its FPGA/PLDs can be reprogrammed through the downlink.

The heart of the board is the four-channel analogue transient waveform digitizer (ATWD) ASIC, developed at LBNL. Each channel contains 128 10-bit ADCs, which after activation simultaneously digitize 128 samples of a selected channel. At the chosen sampling rate of 282 MHz, each channel has a time range of 453 ns. One channel in each ATWD is retained for synchronization, digitizing the waveform of a 40 MHz clock signal. A 'shore board' at the

[14] Gisma, Neumuenster, Germany: http://www.gisma-connectors.de.

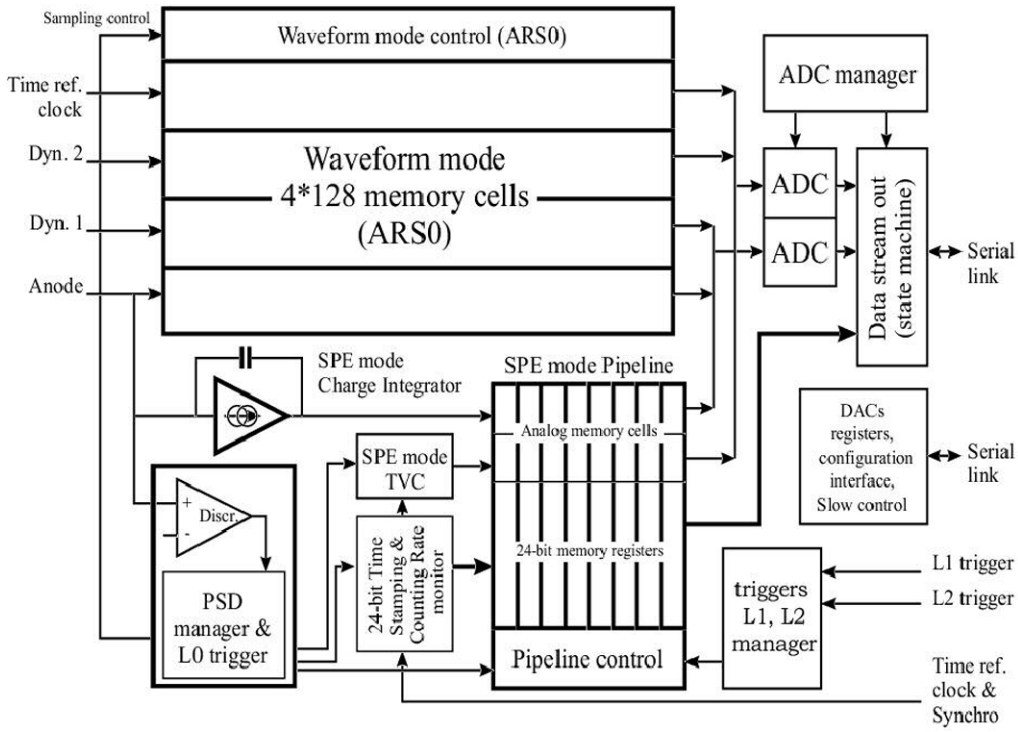

Figure 16. ANTARES ARS functionality.

shore counting room, broadcasts a global 40 MHz clock signal via downlink to the floor board, receives the uplink data and transmits them to the second level triggering system.

A 'floor-trigger' occurs when the programmed local coincidence requirement is satisfied on the floor. The time-stamp of a floor-trigger is defined as the leading edge of the majority logic signal, and the occurrence of such a trigger initiates waveform capture by the ATWD. This time stamp will also be used at the shore to build a global event combining experimental information from several floors.

The performance of the RDAQ electronics and the online software has been extensively studied in the laboratory using an LED calibration system. The robustness of the system has been demonstrated under near-realistic immersion conditions at the NESTOR Navarino Bay Test Station. The rms time stability of ATWD sampling at frequency of 282 MHz has been measured to be 6.4 ps [9], negligible compared with the sampling period of 3.54 ns.

4.5.2. The ANTARES data acquisition system. In the ANTARES array, the functions of the detector readout system are to time-stamp (accepted) analogue PMT signals, to digitize their charge and to merge the data from the 90 PMTs on each detector line onto each single fibre-optic uplink to the shore station. The first stage of PM signal processing is performed by the analogue ring sampler (ARS) ASIC [12] (figure 16). The ARS chips associated with each optical module triplet are housed in a common electronics container, together with (depending on the position of the triplet along the detection line) the compass and tiltmeter and/or hydrophone signal processing cards of the line positioning system.

The ARS ASIC is implemented in AMS 0.8 μm CMOS technology, and is based on a four-channel mixed analogue/digital pipeline memory. The ARS also implements a waveform

shape-sensitive discriminator to distinguish single photoelectron-like (SPE) pulse shapes from superimposed pulses or from larger pulses characteristic of background. The PMT direct anode signal enters one of the four inputs. Although each input can handle pulses up to 4.5 V, an attenuated anode signal, and a signal from the 12th dynode are used to extend dynamic range in the case of large signals. The distributed 20 MHz master clock signal enters the fourth input. A signal from the PMT anode triggers the ARS by crossing an amplitude threshold set to a fraction of the SPE average amplitude (the L0 threshold). The signal is time-stamped and its charge integrated to a precision of ∼10% to compensate for time walk effects. A time to voltage converter (TVC) interpolates between 20 MHz clock pulses to give a time resolution of ∼0.4 ns. Integrated charge and time stamp are then stored in the mixed analogue/digital pipeline memory. At the ARS output, an SPE tag consists of a header (1 byte), the integrated charge (1 byte), TVC (1 byte) and the time stamp (3 bytes).

In recent tests [13, 14] with signals from a PMT illuminated with mainly single photoelectrons at a single point on the photocathode, a time resolution of ∼1.1 ns has been achieved, comparing favourably with the PMT TTS of $\sigma \sim 1.3$ ns with full photocathode illumination. The intrinsic time resolution of the ARS was determined to be $\sigma \sim 350$ ps from measurement of the separation of two pulses injected into the ARS with a known time difference.

Analogue pulse shape discrimination separates SPE pulses, which are charge-integrated, from waveform (WF) pulse shapes, which are WF-sampled in 128 samples at up to 1 GHz. This processing is implemented when the pulse height exceeds several photoelectrons, when the time over the L0 threshold is longer than normal, or when the L0 threshold is crossed more than once in the charge integration time. With 128 analogue samples of the waveform, at the ARS output, a WF event can typically contain >250 bytes.

SPE events are expected to represent more than 98% of the ANTARES data, while WF events will be mainly generated by background phenomena, primarily ^{40}K disintegrations and bioluminescence. The pipeline memory of each ARS can store up to 16 SPE hits or 4 WF hits.

With a singles rate of 70 kHz, and 2% fraction of WF events, the (typical) data rate will be ∼7 Mbytes s^{-1} per PMT. Two ARS chips are connected to each PMT to reduce dead time. This data rate is shared between the (fast) output ports of the two ARSs and is well within the 20 Mbytes s^{-1} bandwidth limit of each. The PMT readout system is intended to handle an average singles rate of up to 100 kHz with surges of up to 250 kHz due to bioluminescence bursts.

Data from five PMT triplets (five levels) will be merged onto a single descendant fibre with a typical bandwidth of 105 Mbytes s^{-1}. Data from six such fibres will be dense wavelength division (DWD)-multiplexed onto a single fibre at the bottom of each detection line, resulting in a typical data rate to shore of 700 Mbytes s^{-1} per line. These fibres pass through the junction box and onto the 40 km electro-optical cable linking the detector array to the shore.

An on-shore data switchyard will de-multiplex up to 70 incoming data streams and pass data to a processing farm consisting of up to 100 PCs running at an input data rate in the range 50–100 Mbytes s^{-1}.

4.5.3. NEMO readout system R&D. The NEMO collaboration is studying a readout system for a km^3-scale array of 4096 PMTs. An event rate of 50 kHz per PMT (dark current + 40K + SPE signals + average bioluminescence contribution) has been assumed [11]. A PMT signal-processing ASIC ('LIRA01', built in AMS 0.35 μm CMOS technology: [11]) with three channels of 256-deep switched capacitor array analogue memory and 200 MHz sampling rate is under

development. The ASIC channels sample the PMT anode, a dynode and the 20 MHz master clock. LIRA01 will also incorporate a twin threshold (0.25 SPE, 5 SPE) discriminator trigger and single photon classifier. The ASIC is aimed at a temporal resolution of 300 ps. The DAQ output rate (after zero suppression and packing) is ∼5 Mbytes s^{-1}per PMT. Two LIRA ASICs will be used in each optical module: while one is sampling the PMT, the other will push data out towards a 20 MHz sampling ADC.

A synchronous digital hierarchy (SDH) protocol is being considered for data transmission and reception. An STM-1 tributary: (up to 155 Mbytes s^{-1}) might be used for the readout of a floor (4 PMTs) onto a single descending optical fibre. In electronics at the tower base, the 16 floor STM-1 streams would be multiplexed onto a single optical fibre running the STM-16 protocol (up to 2.5 Gbytes s^{-1}).

The array power and readout architecture envisions eight secondary junction boxes (SJBs) and a primary junction box (PJB) to which the shore electro-optical cable is connected. The principal data paths from the SJBs to the PJB follow a star network, with a redundant data ring between the SJBs. Data from each subarray of eight towers would be DWD-interleaved[15] in its SJB onto a single optical fibre, thence passing to the PJB (with the additional redundant highway between SJBs), before being retransmitted onto the 100 km shore electro-optical cable following a + 17 dB m amplification.[16]

4.6. Underwater acoustic survey and navigation

The reconstruction of muon tracks in an underwater neutrino detector is based on precise measurements (∼1 ns) of the arrival times of Čerenkov photons at optical modules. This reconstruction requires knowledge of the positions of the optical modules relative to each other or, more practically, with respect to fixed reference points such as the detector line anchors. The precision of this spatial positioning should be better than the corresponding dispersive uncertainty in the arrival time of Čerenkov light detection (e.g. ∼1.6 ns over a typical flight distance of 40 m in ANTARES). Since 1 ns is equivalent to 22 cm of light travel path in water, the relative position of every OM should be known to ∼10–20 cm.

Since detection lines will be suspended between sea anchors and submerged buoys subject to movement by deep ocean currents, the positions of individual optical modules will need to be regularly determined from measurements of line curvature and twist. In ANTARES, the relative positions of the OMs will be obtained from fits to position data determined by two independent systems: a high-frequency long base line LBL acoustic system [14, 15] and a series of semiconductor tiltmeter-compass sensors disposed along each detection line. The relative positions of the OMs will then be deduced from this reconstructed line shape and from the geometry of the OM frame. Additionally, a network of laser and LED beacons producing narrow, time-stamped blue light flashes will be used to give redundancy in the on-line calibration of PMT timing.

4.6.1. The ANTARES acoustic positioning system. An array of four 40–60 kHz acoustic transponders [15][17] delineating a 300 × 300 m LBL square, has been deployed on the seabed at

[15] Candidate device: AWG/CI008 by E-Tek Dynamics.
[16] Candidate device: type 1738U Erbium-doped Fiber Amplifier by Agere Systems.
[17] Frequency range 44–60 kHz, 2 kHz channel spacing (Genisea/ECA, Toulon, France).

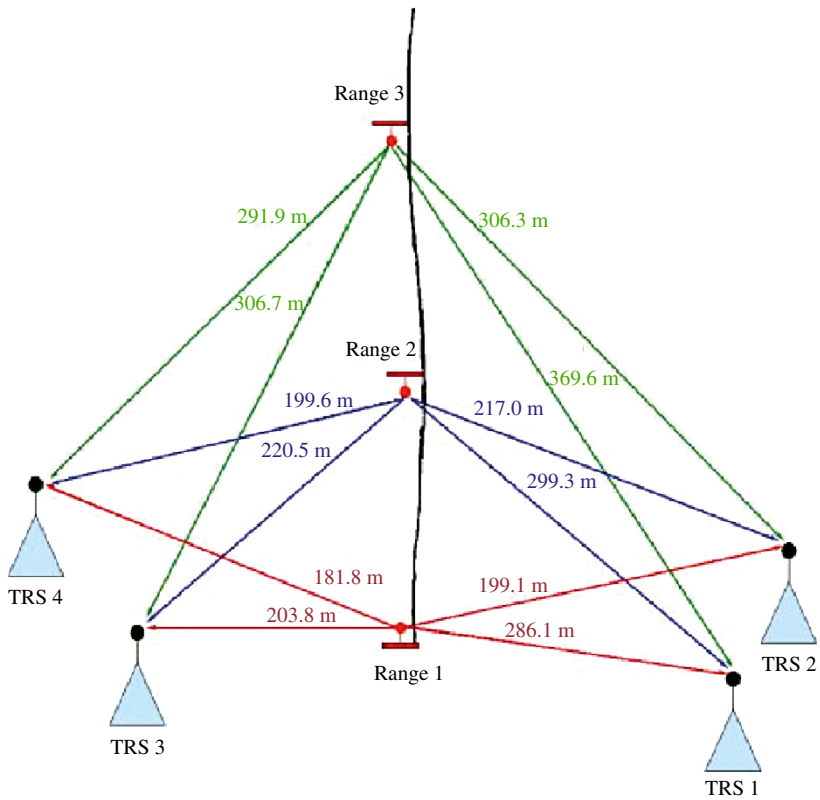

Figure 17. Illustration of relative positions of hydrophone rangefinders and transponders.

the ANTARES site. Additional transponders will be added (on sea anchors) as detection lines are deployed. The LBL transponders will transmit sound signals to hydrophones mounted at six positions (altitudes 100, 184, 256, 328, 388 and 448 m) along each detection line. The 3D positions of the hydrophones will be obtained by triangulation. The seabed transponders will interrogate each other and the seabed anchors to determine their relative positions. Figure 17 illustrates a recent implementation of the acoustic survey system with rangemeter hydrophones at three elevations on a deployed line. The precision of vertical height measurement between two hydrophone rangemeters was measured to be better than 5 cm as can be seen in figure 18. The transmission and reception of each sound pulse must be time-referenced relative to the master clock signal used to time-stamp PMT data. The conversion of acoustic transit times to distances requires accurate knowledge of the sound velocity within the detector. This in turn depends on the temperature, salinity and pressure [16].

Instrumentation to monitor these parameters will be needed, and has been extensively studied in the ANTARES-NEMO collaboration. These instruments are included on a dedicated instrumentation line.

4.6.2. Semiconductor tiltmeter/compass systems. The detection lines of ANTARES will incorporate combined bi-axial tiltmeter and compass sensors[18] to give the localtilt angles of

[18] Model TCM2-20 (Precision Navigation Inc., Santa Rosa, CA, USA; http://www.pnicorp.com).

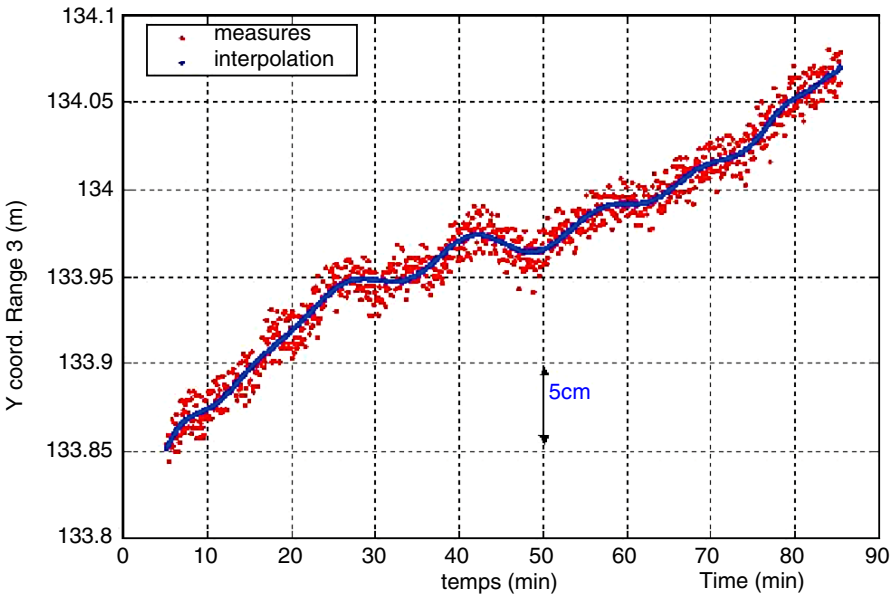

Figure 18. Time variation of vertical displacement between hydrophone rangefinders due to deep ocean current.

each OM triplet level with respect to the horizontal plane (range/precision; $\pm 20/\pm 0.2^\circ$ in pitch and roll), as well as its orientation relative to Earth Magnetic North (heading range/precision; $0\text{–}360^\circ/\pm 0.5 \rightarrow 1^\circ$), caused by cable torsion.

The performance of the positioning system has been studied in various configurations (varying the number of acoustic sensors and tiltmeters; the locations and precision of sensors, positions of missing sensors, etc), with differing values of deep water current and detector line twist as a function of altitude. These studies indicate that the proposed combination of acoustic triangulation and tiltmeter compasses should allow the positions of all OMs to be determined with an accuracy $\sigma < 10$ cm in deep water currents up to 15 cm s^{-1}.

4.7. Site evaluation and underwater and environmental instrumentation

NEMO and ANTARES, together with the Lake Baikal experiment, have a common programme of site measurements and instrument cross-calibration [4, 17]. Some instruments have been used at all three sites. Additionally, many of the results from the instruments used in site characterization are of interest to the oceanographic, deep-sea biology and geophysics communities. The NESTOR collaboration has, for example, been acquiring real-time seismograph and ocean current data at its Ionian Sea site since January 2002. The NEMO test site lab at Catania will acquire real-time data from the GEOSTAR-Poseidon underwater seismic station.

One output of the ANTARES junction box (two conductors at 500 V ac, and four optical fibres; DAQ Tx, Rx and two carrying GPS-referenced clocks) will be made available for oceanographic collaborators, while on another output a comprehensive array of environmental monitoring instruments for the ANTARES site, some developed by the NEMO collaboration, will be incorporated onto a dedicated instrumentation line.

4.7.1. The ANTARES instrumentation line. One of the 16 junction box outputs will be reserved for an 'instrumentation line' containing equipment for monitoring the detector array and

deep-sea environmental parameters including salinity, sound velocity, water transparency and current profile. For detector-wide timing calibration, a laser beacon will illuminate the array with fast (900 ps), time-stamped laser[19] pulses at a wavelength of 456 nm. Its action will complement shorter-range blue LED beacons distributed among the detection lines.

The deep-sea current profile (velocity, direction) will be sampled over 256 intervals over the full detector depth of 300 m by a pair of 300 kHz acoustic Doppler current profilers[20] with a velocity range (resolution) of 5 m s^{-1} (1 mm s^{-1}).

The optical attenuation of water at 470 nm will be measured over a 25 cm path length using a commercial photodiode-based water transmission meter.[21] The line will be equipped with sound velocity meters of the same type as installed close to the sea anchors of some detection lines. These devices[22] have a flight path of 20 cm and a precision of ± 0.05 m s^{-1} for typical velocities in the range 1400–1600 m s^{-1}. Several velocity meters will also be equipped with conductivity–temperature[23] and depth (pressure) probes.[24] A seismometer will also be connected to the instrumentation line. A preliminary version of the instrumentation line with a single current profiler, shown in figure 19, was deployed in early 2003.

4.8. Sea deployment and recovery operations

An essential feature of undersea neutrino telescopes is the necessity to have access to significant naval resources. These naval resources include surface boats and structures together with submersible vehicles of different types. The three Mediterranean projects have taken very different detector design choices implying the need for different naval resources; in particular, NESTOR wishes to avoid the necessity for undersea vehicles while ANTARES and NEMO choose to use them. The success of the two projects currently building detectors will in large part be conditioned by these choices and the naval resources used.

4.8.1. ANTARES deployment procedures. Table 2 illustrates the equipment necessary in the installation and repair of the ANTARES detector array which is centred on a junction box linked to a shore cable.

Connections of underwater detection lines require the plugging of cables with underwater-mateable connectors through the use of a manned submarine or ROV. In all cases, an already-deployed seabed acoustic transponder net and a ship with a GPS-referenced dynamical positioning system are required. Objects to be deployed on the seabed are equipped with their own acoustic transponders, allowing their positions to be triangulated with respect to an already deployed acoustic transponder net, of which the ANTARES LBL is an example.

During the deployment of the ANTARES junction box at a depth of 2400 m, the undersea electro-optical cable was first located through shop-borne interrogation of the acoustic

[19] Incorporating a NG-10120-120 laser head (Nanolase, Meylin, France).
[20] Workhorse Monitor (RD Instruments, San Diego, CA, USA).
[21] C-STAR (WETlabs Inc.; http://www.wetlabs.com).
[22] Model QUUX-3A(A) (Genisea, France).
[23] OEM-OT sensor by Falmouth Scientific (Cataumet, MA, USA; http://www.falmouth.com; precision of ± 0.001 mS cm^{-1}).
[24] Druck S A (Asnières sur Seine, France).

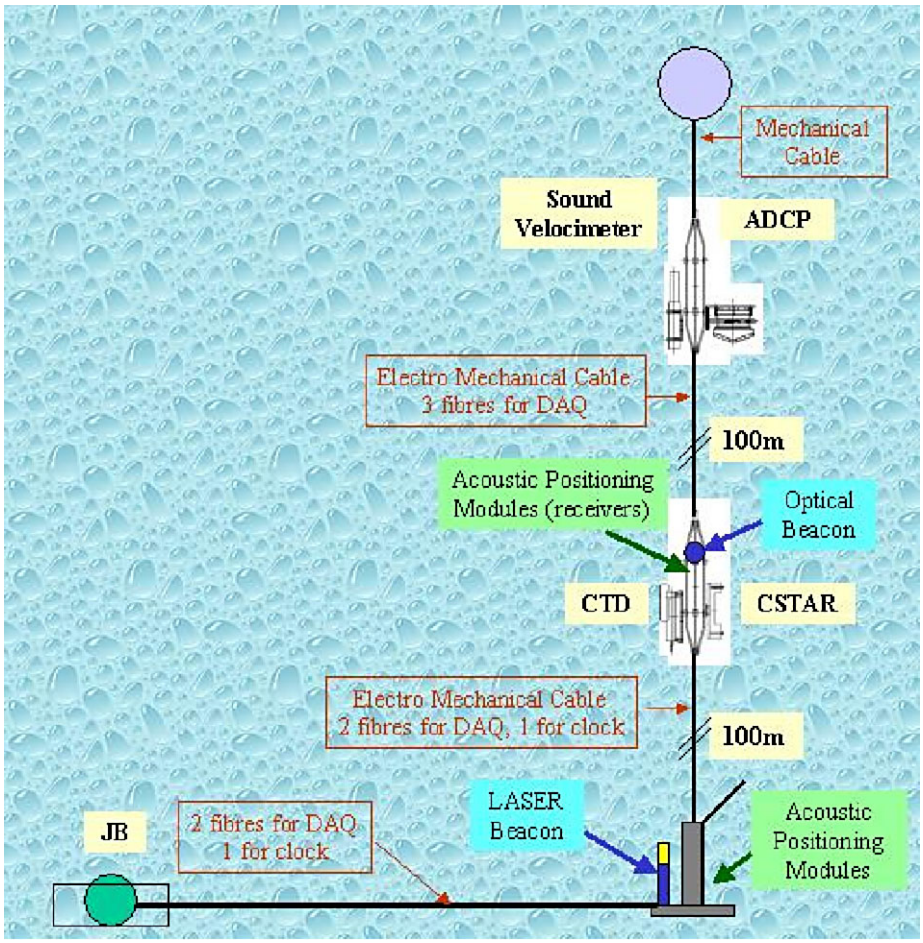

Figure 19. Configuration of a prototype instrumentation line to be deployed at the ANTARES site.

Table 2. Resources required for detector installation and detector repairs in ANTARES.

	Underwater resource required		
Deployed object	GPS/acoustic navigation	Grapple	Submarine vehicle
(a) *Detector installation*			
Shore site E/O cable	YES	NO	NO
Junction box	YES	YES	NO
Detection line	YES	NO	NO
Line-JB cable connect	YES	NO	YES
(b) *Detector repairs*			
Shore site E/O cable	YES	YES	NO
Junction box	YES	YES	YES
Detection line	YES	NO	NO
Line-JB cable connect	YES	NO	YES

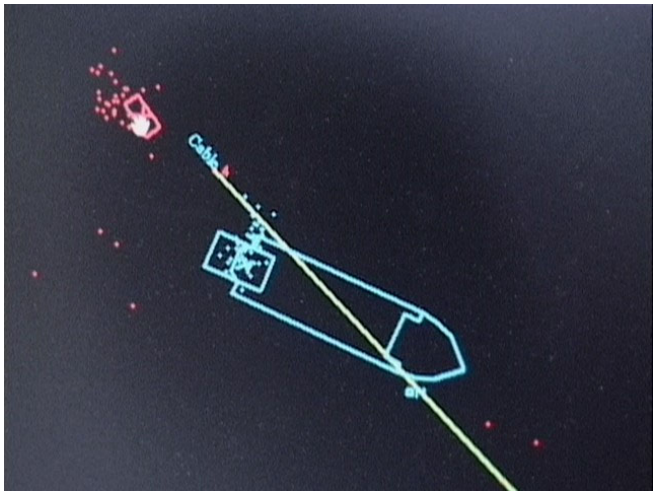

Figure 20. Acoustic transponder positioning of the ANTARES junction box during descent to seabed.

transponder attached to its 400-m-long dredging tail. Movement of this transponder confirmed when the lowered grapple had successfully snagged the dredging tail. The descent of the junction box to the seabed was monitored in real time by triangulation of the position of its individual acoustic transponder relative to the deployed LBL net.

In figure 20, the most recent position of the junction box is shown by a rectangle, while previous positions (at differing heights) are indicated by spots. During the descent, the dynamical positioning ship adjusted its position 2.5 km along the track of the undersea cable as 2.5 km of cable were re-laid on the seabed with the junction box attached.

4.8.2. NESTOR deployment procedures. In contrast, the NESTOR array will be deployed without the need for ROVs to perform underwater cable connections. Instead, underwater connections require that the last 5 km of the underwater cable from the shore station be raised with the seafloor instrument package. Several times in tests, the collaboration has deployed and recovered payloads composed of its base station and several floors from a depth of 4000-m using cable-laying ships or platforms. The collaboration is constructing a highly specialized deployment platform. The self-propelled and ballasted platform shown in figure 21 has an equilateral triangular form of side 51 m, with a central well. It will be equipped with a GPS-related dynamical positioning system capable of maintaining its position at sea to a precision of several metres, and can be used to deploy structures with diameters as large as 100 m.

Figure 22 illustrates the NESTOR deployment/recovery concept [18] using a 5000 m neutral buoyancy (recovery rope, ReRo) rope equipped with an anchor, buoy and acoustic release at its free end. During deployment, a NESTOR tower is lowered to the sea bottom (together with the final 5 km of undersea cable) and the ReRo is laid across the sea floor with its anchor and buoy positioned around 5 km from the tower base. During recovery the ReRo anchor is released with a coded acoustic signal and the buoy floats to the surface for capture. Once the 5000 m ReRo has been winched aboard the ship the tower will be at the surface for connection of additional floors or the removal or replacement of components.

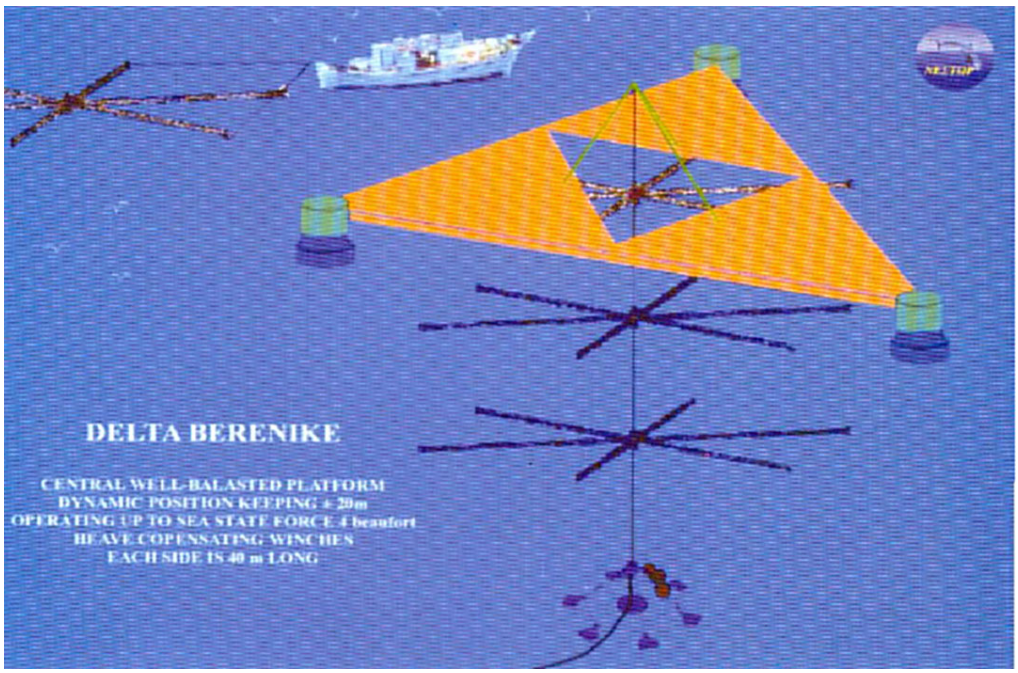

Figure 21. NESTOR deployment platform.

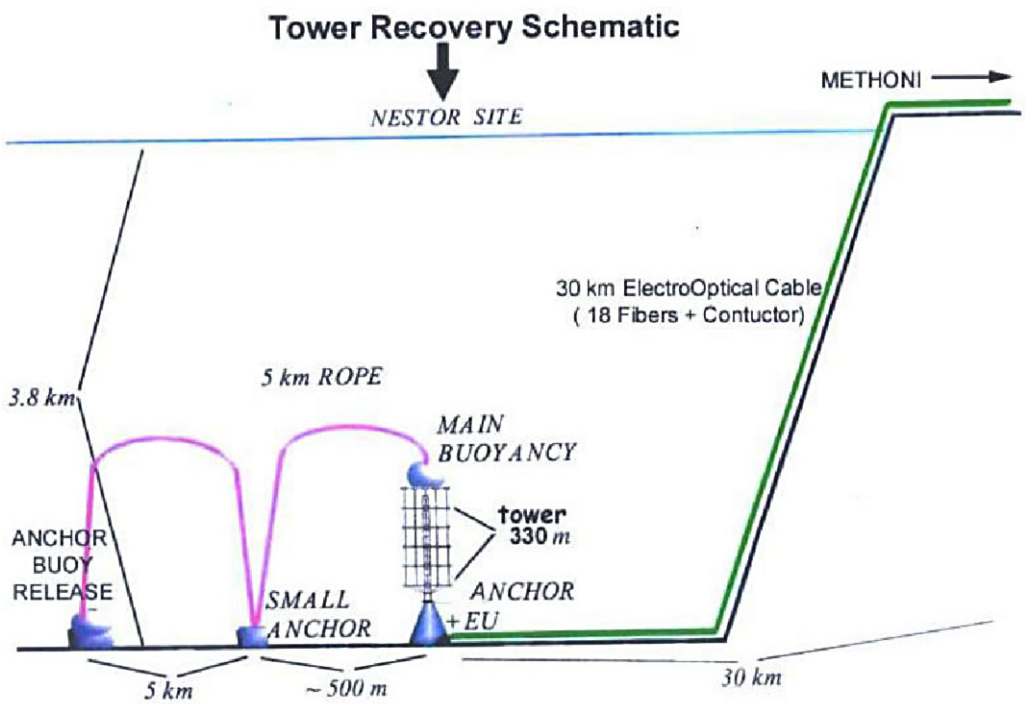

Figure 22. NESTOR tower deployment and recovery using a 5 km recovery rope.

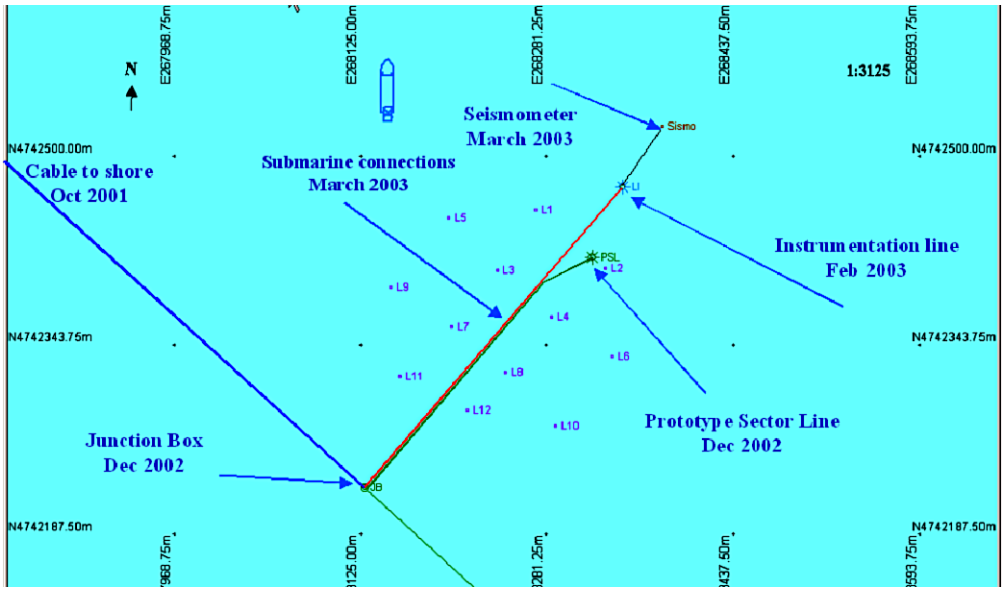

Figure 23. Configuration of ANTARES Telescope on seabed March 2003. The Shore cable and Junction Box installations are permanent. The MIL was recovered in May 2003 and the PSL was recovered in July 2003.

5. Status in spring 2004

ANTARES and NESTOR which have finished their R&D activities and the prototype stages are now in the process of full detector construction. NEMO is continuing R&D towards a km^3 detector.

5.1. ANTARES construction status

In October 2001, the first permanent element of the ANTARES telescope, the submarine cable of length 45 km, was laid between the site and the beach of Les Sablettes in La Seyne-sur-Mer. On land, the electrical energy for the detector is supplied from a power supply in a cabin close to the beach and the optical fibre continue to the shore station in the Institute Michel Pasha at a distance of 45 km. In December 2002, the junction box was connected to the cable and deployed on the seabed.

During 2002, a final short prototype optical line, prototype sector line (PSL), and a prototype instrumental line, mini instrumentation line (MIL), were constructed and extensively tested in a dark room in the laboratory. The two lines were deployed and connected on the ANTARES site in sea operations between December 2002 and March 2003. Figure 23 illustrates the items deployed on the ANTARES site up to March 2003.

Following the line connections, data taking started with both of the lines functioning successfully. Extensive data were taken with the PSL until July 2003 when it was recovered. The MIL developed a water leak and was recovered in May after 1 month of operation.

The prototype testing showed a number of problems during the sea operation and these have been diagnosed in the laboratory after the line recoveries. The water leak in the MIL was due to a type of commercial connector which we now believe has a design fault; for the future, the corrective action will be to avoid using this type of connector. In both lines, there were faults in

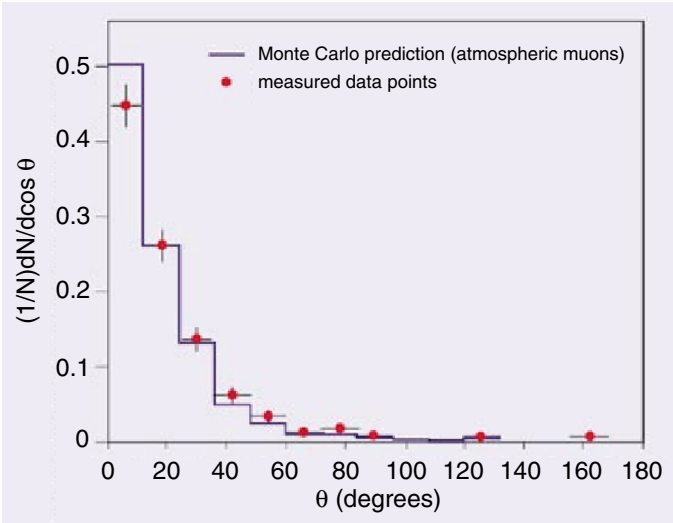

Figure 24. Comparison between the measured zenith angular distribution of muon tracks reconstructed in the NESTOR floor and the expected distribution.

the distribution in the line of the time reference clock due to broken optical fibres. The cause of the broken fibre is understood as the use of a substandard plastic tube in the line cables; for the future, steel tubes will be used to protect the optical fibres.

The background light levels in an undersea neutrino telescope are dominated from radioactive decay of ^{40}K in the sea-water salt and from bioluminescence. During the operation of the PSL the rates of background light from bioluminescence were higher than the values measured during the initial site explorations in which the measurements were made with autonomous mooring lines which recorded PMT counting rates in a memory. Following the evaluation of the data from the PSL tests, it is concluded that averaged over a year of operation of the full detector the data loss due to the bioluminescence would be 10–20% in neutrino detection efficiency.

The next step in the construction of the ANTARES telescope will be the installation of a new instrumentation line towards the end of 2004. Many elements of the full detector such as optical modules, mechanical structure and line cables are in production while the full orders for the electronics of the system will be placed in mid-2004. The installation of the full 12 lines of the detector will take place during 2005 and 2006. It is expected that the first exciting science results of the detector, opening up this new field of astroparticle physics in the northern hemisphere, will be available during 2006.

5.2. NESTOR status

At the end of March 2003 the first floor of a NESTOR tower was deployed at a depth of 4100 m. More than 5 million events consisting of a 4-fold coincidence between signals in the optical modules were recorded [19]. These data have been analysed in order to reconstruct muon tracks. The distribution of muons is shown in figure 24 compared with the predictions from flux calculations [20] using the Monte Carlo simulation of the detector. After operation of the floor for a period of time a fault developed in the submarine cable, which is now awaiting repair or replacement. The NESTOR collaboration plans to continue installation of the first tower during 2004.

6. Conclusion

The three Mediterranean projects have all made very significant progress in recent years. ANTARES and NESTOR will have completed detectors in the next few years. Together with the NEMO group they have combined in the 'KM3NET' design project for the next stage towards a km^3 Mediterranean Neutrino Telescope.

References

[1] Amram P *et al* 2003 *Astropart. Phys.* **19** 253
[2] Amram P *et al* 2000 *Astropart. Phys.* **13** 127
[3] Anassontzis E *et al* 1994 *Nucl. Instrum. Methods* A **349** 242
[4] Capone A 2002 *ANTARES Collaboration Meeting, Catania, 24–28 September*
[5] Sedita M 2002 *ANTARES Collaboration Meeting, Catania, 24–28 September*
[6] Hallewell G 2002 *ICFA Instrument. Bull.* **25** 17
[7] Amram P *et al* 2002 *Nucl. Instrum. Methods* A **484** 369
[8] Anassontzis E *et al* 2002 *Nucl. Instrum. Methods* A **479** 439
[9] Tzamarias S *et al* 2002 *Proc. 4th Workshop on Ring Imaging Čerenkov Detectors (RICH 2002), Pylos, June*
Tzamarias S *et al* 2003 *Nucl. Instrum. Methods* A **502** 150
[10] Musumeci N 2002 *ANTARES Collaboration Meeting, Catania, 24–28 September*
[11] Lo Nigro L 2002 *ANTARES Collaboration Meeting, Catania, 24–28 September*
[12] Druillole F *et al* 2001 *Proc. IEEE Symp. on Nuclear Science, 4–10 November, San Diego, CA*
[13] Feinstein F 2002 *Proc. 3rd Conf. on New Developments in Photo-detection, Beaune, June*
Feinstein F 2003 *Nucl. Instrum. Methods* A **504** 258
[14] Hallewell G 2002 *Proc. 4th Workshop on Ring Imaging Čerenkov Detectors (RICH 2002), Pylos, June*
Hallewell G 2003 *Nucl. Instrum. Methods* A **502** 258
[15] Bertin V, Genisea 2000 *ANTARES Report 3INS0103B*
[16] Chen C and Millero F 1977 *J. Acoust. Soc. Am.* **62** 1129
[17] Schuller J-P 2002 *ANTARES Collaboration Meeting, Catania, 24–28 September*
[18] Anassontzis E G and Koske P 2003 *Sea Technol.* **44** 10
[19] Ball A and Tsirigotis A 2003 *CERN Courier* **43** 23
[20] Okuda A 1994 *Astropart. Phys.* **2** 393

New Journal of Physics
An Institute of Physics and Deutsche Physikalische Gesellschaft Journal

SNEWS: the SuperNova Early Warning System

Pietro Antonioli[1], Richard Tresch Fienberg[2], Fabrice Fleurot[3], Yoshiyuki Fukuda[4], Walter Fulgione[5], Alec Habig[6], Jaret Heise[7], Arthur B McDonald[8], Corrinne Mills[9,13], Toshio Namba[10], Leif J Robinson[2], Kate Scholberg[11,14], Michael Schwendener[3], Roger W Sinnott[2], Blake Stacey[11], Yoichiro Suzuki[10], Réda Tafirout[3,15], Carlo Vigorito[5], Brett Viren[12], Clarence Virtue[3] and Antonino Zichichi[1]

[1] University of Bologna and INFN Bologna, Via Irnerio 46, 40126 Bologna, Italy
[2] Sky & Telescope, 49 Bay State Road, Cambridge, MA 02138-1200, USA
[3] Department of Physics and Astronomy, Laurentian University, Sudbury, Ont. P3E 2C6, Canada
[4] Department of Physics, Miyagi University of Education, Sendai, Miyagi 980-0845, Japan
[5] IFSI-CNR Torino, University of Torino and INFN Torino, Via P Giuria 1, 10125 Torino, Italy
[6] Department of Physics, University of Minnesota, Duluth, MN 55812-2496, USA
[7] Los Alamos National Laboratory, Los Alamos, NM 87545, USA
[8] Department of Physics, Queen's University, Kingston, Ont. K7L 3N6, Canada
[9] Department of Physics, Boston University, Boston, MA 02215, USA
[10] Institute for Cosmic Ray Research, University of Tokyo, Kashiwa, Chiba 277-8582, Japan
[11] Department of Physics, Massachusetts Institute of Technology, Cambridge, MA 02139, USA
[12] Brookhaven National Laboratory, PO Box 5000, Upton, NY 11973-5000, USA
E-mail: schol@mit.edu

New Journal of Physics **6** (2004) 114
Received 1 May 2004
Published 1 September 2004
Online at http://www.njp.org/
doi:10.1088/1367-2630/6/1/114

[13] Current address: Department of Physics, University of California, Santa Barbara, CA 93106, USA.
[14] Author to whom all correspondence should be addressed.
[15] Current address: Department of Physics, University of Toronto, Toronto, Ont. M5S 1A7, Canada.

PII: S1367-2630(04)80237-4
© IOP Publishing Ltd and Deutsche Physikalische Gesellschaft

Abstract. This paper provides a technical description of the SuperNova Early Warning System (SNEWS), an international network of experiments with the goal of providing an early warning of a galactic supernova.

Contents

1. Introduction **2**
2. SNEWS overview **3**
3. The supernova signal and current detectors **4**
4. The three Ps **5**
4.1. Prompt . . . 5
4.2. Pointing . . . 6
4.3. Positive . . . 6
4.3.1. False alerts . . . 7
4.4. Privacy . . . 8
5. Description of individual experiments' supernova triggers **8**
5.1. Super-K supernova online monitor . . . 9
5.2. SNO supernova online monitor . . . 9
5.3. LVD supernova online monitor . . . 10
6. SNEWS coincidence implementation **11**
6.1. The coincidence server . . . 11
6.2. Coincidence software . . . 11
6.3. SNEWS shifts . . . 12
6.4. SNEWS operational modes . . . 12
6.5. SNEWS packet types and flags . . . 12
6.6. Coincidence definition . . . 13
6.7. Rate-dependent GOLD coincidence suppression . . . 13
6.8. Demotion and promotion . . . 15
7. High rate test results **16**
8. The alert to the astronomical community **20**
8.1. Amateur astronomers . . . 21
8.2. SNEWS alerts . . . 21
9. Status and future prospects **22**
10. Summary **22**
Acknowledgments **22**
References **22**

1. Introduction

The famous supernova SN1987A in the Large Magellanic Cloud (LMC) brought the field of supernova neutrino astrophysics to life. Two water Cherenkov detectors, Kamiokande II and IMB, detected 20 events between them [1]–[4]; two scintillator detectors, Baksan and LSD [5, 6] also reported observations. The sparse SN1987A neutrino data were sufficient to confirm the

baseline model of gravitational collapse causing type II SNe and to put limits on neutrino properties (such as a $\bar{\nu}_e$ mass limit of around 20 eV.) To make distinctions between different theoretical models of core collapse and supernova explosions and to extract more information about neutrino properties, we await the more copious neutrino signal which the new generation of large neutrino experiments will detect from the next such event in our Galaxy.

When the core of a massive star at the end of its life collapses, less than 1% of the gravitational binding energy of the neutron star will be released in the forms of optically visible radiation and the kinetic energy of the expanding remnant. The remainder of the binding energy is radiated in neutrinos, of which ~1% will be electron neutrinos from an initial 'neutronization' burst and the remaining 99% will be neutrinos from the later cooling reactions, roughly equally distributed among flavours. Average neutrino energies are expected to be about 13–14 MeV for ν_e, 14–16 MeV for $\bar{\nu}_e$ and 20–21 MeV for all other flavours. The neutrinos are emitted over a total timescale of tens of seconds, with roughly half of them emitted during the first 1–2 s. The expected features of a core collapse neutrino signal are summarized in [7]; more recent simulation work can be found e.g. in [8, 9].

A core-collapse supernova in our Galaxy will bring a wealth of scientific information. The neutrino signal will provide information about the properties of neutrinos themselves and astrophysicists will learn about the nature of the core collapse. One unique feature of the neutrino signal is that it is *prompt*: neutrinos emerge on a timescale of tens of seconds, while the first electromagnetic signal may be hours or days after the stellar collapse. Therefore, neutrino observation can provide an *early alert* that could allow astronomers a chance to make unprecedented observations of the very early turn-on of the supernova light curve; even observations of SNe as young as a few days are rare for extra-galactic supernovae. The environment immediately surrounding the progenitor star is probed by the initial stages of the supernova. For example, any effects of a close binary companion upon the blast would occur very soon after shock breakout. UV and soft x-ray flashes are predicted at very early times. Finally, there may be entirely unexpected effects—no supernova has ever been observed very soon after its birth. Although the neutrino signal will be plentiful in practically all galactic core collapses, it is possible that there will be little or no optical fireworks (the supernova 'fizzles'); the nature of any observable remnant would then be very interesting.

This paper focuses on the prompt alert which is possible using the neutrino signal. We will describe the technical aspects of the system.

Section 2 gives an overview of SNEWS, and section 3 briefly covers the expected signal in current detectors. Section 4 discusses some issues associated with SNEWS. Section 5 introduces the individual experiments' monitors. Section 6 covers SNEWS implementation and defines the coincidence conditions and alert scheme. Section 7 describes the results of the 'high-rate' system test performed in 2001. Section 8 describes the alert to the astronomical community. Section 9 gives future directions. The final section summarizes the results obtained.

2. SNEWS overview

The SNEWS (SuperNova Early Warning System) collaboration is an international group of experimenters from several supernova neutrino-sensitive experiments. The primary goal of SNEWS is to provide the astronomical community with a prompt alert for a galactic supernova. An additional goal is to optimize global sensitivity to supernova neutrino physics, by such cooperative work as downtime coordination.

The idea of a blind central coincidence computer receiving signals from several experiments has been around for some time (see e.g. [10]). In addition to the basic early warning advantages of a neutrino detector, there are several benefits from a system involving neutrino signals from two or more different detectors. First, if the supernova is distant and only weak signals are recorded, a coincidence between signals from different detectors effectively increases the sensitivity by allowing reductions in alarm thresholds and allowing one to impose a minimum of (possibly model-dependent) expectations on the form of the signal. Secondly, even if a highly sensitive detector such as Super-K is online, *requiring a coincidence among several detectors effectively reduces the non-Poissonian background present for any given detector and enormously increases the confidence in an alert.*[16] Background alarms at widely separated laboratories are highly unlikely to be correlated. Without the additional confidence from coincident neutrino observations, it would be very difficult for any individual detector to provide an *automated* alert to astronomers. Finally, using signals from more than one detector, there is some possibility for determining the direction of the source when a single detector alone can provide no information (see [11]). Unfortunately, triangulation is, in practice, quite difficult to do promptly, and cannot point as well as individual detectors.

An important question for SNEWS is: how often is a galactic supernova likely to occur? Estimates vary widely, but are typically in the range of about one per 30 years (see e.g. [12]). This is frequent enough to have a reasonable hope of observing one during the next five or 10 years, but rare enough to mean that we must take special care not to miss anything when one occurs.

The charter member experiments of SNEWS are Super-Kamiokande (Super-K) in Japan, the Sudbury Neutrino Observatory (SNO) in Canada and the Large Volume Detector (LVD) in Italy.[17] Representatives from AMANDA, IceCube, KamLAND, Borexino, Mini-BooNE, Icarus, OMNIS and LIGO participate in the SNEWS Working Group, and we hope will eventually join the active coincidence.

There is currently a single coincidence server, hosted by Brookhaven National Laboratory. We expect that additional machines will be deployed in the future. The BNL computer continuously runs a coincidence server process, which waits for alarm datagrams from the experiments' clients, and provides an alert if there is a coincidence within a specified time window (10 s for normal running.) We have implemented a scheme of 'GOLD' and 'SILVER' alerts: GOLD alerts are intended for automated dissemination to the community; SILVER alerts will be disseminated among the experimenters, and require human checking.

At the time of this writing, no inter-experiment coincidence, real or accidental, has ever occurred (except in high rate test mode), nor has any core collapse event been detected within the lifetimes of the currently active experiments.

3. The supernova signal and current detectors

There are several classes of detectors capable of observing neutrinos from gravitational collapse. Most supernova neutrino detectors are designed primarily for other purposes, e.g. for proton

[16] 'Non-Poissonian' refers to background alarms whose rate cannot be well predicted according to a constant-background-rate Poisson distribution. Detector effects such as flashing phototubes and electronics problems fall under this category. Rates may also be locally Poissonian, just non-stationary.

[17] MACRO [13] was another charter member, and was involved with SNEWS until it turned off in 2000.

Table 1. Supernova neutrino detector types and their primary capabilities.

Detector type	Material	Energy	Time	Point	Flavour
Scintillator	C, H	y	y	n	$\bar{\nu}_e$
Water Cherenkov	H_2O	y	y	y	$\bar{\nu}_e$
Heavy water	D_2O	NC: n	y	n	All
		CC: y	y	y	ν_e, $\bar{\nu}_e$
Long string water Cherenkov	H_2O	n	y	n	$\bar{\nu}_e$
Liquid argon	Ar	y	y	y	ν_e
High Z/neutron	Pb, Fe	y	y	n	All
Radio-chemical	^{37}Cl, ^{127}I, ^{71}Ga	n	n	n	ν_e

decay searches, solar and atmospheric neutrino physics, accelerator neutrino oscillation studies and high-energy neutrino source searches.

Table 1 gives a brief overview of the supernova neutrino detector types. More detailed information about supernova detection capabilities can be found in [14]. To summarize briefly: scintillator and water Cherenkov detectors are sensitive primarily to $\bar{\nu}_e$; those with neutral current capabilities (heavy water, high Z/neutron, and also water Cherenkov and scintillator to some extent) are sensitive to all flavours. Water Cherenkov and heavy water detectors have significant pointing capabilities. All except radiochemical detectors can see neutrinos in real-time. All have energy resolution except long string water Cherenkov and radiochemical detectors.

Table 2 lists specific supernova neutrino detectors and their capabilities [15]–[23]. For a summary of supernova neutrino capabilities of future detectors, see [24, 25].[18,19]

4. The three Ps

To make the best use of a neutrino burst supernova alert, the astronomical community needs the 'three Ps': 'prompt', 'pointing' and 'positive'. We comment on each of these below.

4.1. Prompt

The alert must be as prompt as possible to catch the early stages of shock breakout, which occurs within hours (or less) of core collapse. We estimate an alert dissemination time of 5 min or less

[18] Note that the currently running Super-K II (after reconstruction in 2002) has nearly the same supernova sensitivity as Super-K I; a slight increase in energy threshold due to loss of phototubes will cause only a few percent loss of total signal events.

[19] Gravitational wave detectors deserve some note here. Large interferometer experiments such as LIGO, Virgo, GEO, TAMA and ACIGA [26] as well as cryogenic antennas belonging to the IGEC collaboration [27] may have the capability of detecting gravitational wave signals from asymmetric supernova explosions (although the details of a stellar collapse gravitational wave signal are not yet well understood). When these detectors reach maturity over the next several years, they will become an important part of a stellar collapse network, and combined neutrino and gravitational wave data will be an extremely valuable source of information for testing supernova models. The gravitational wave signal may be even more prompt than the neutrino signal, and in fact, may provide a $t = 0$ for a neutrino time-of-flight mass measurement (see e.g. [28]). The scientific potential from combined gravitational wave and neutrino signals from stellar collapse is an exciting and largely unexplored territory.

Table 2. Specific supernova neutrino detectors. The expected numbers of events are approximate, and refer to yields in the dominant channels.

Detector	Type	Mass (kton)	Location	No. of events @8.5 kpc	Status
Super-K	H_2O Ch.	32	Japan	7000	Running
SNO	H_2O,	1.4	Canada	300	Running
	D_2O	1		450	
LVD	Scint.	1	Italy	200	Running
AMANDA	Long string	$M_{\mathrm{eff}} \sim 0.4\,\mathrm{pmt}^{-1}$	Antarctica		Running
Baksan	Scint.	0.33	Russia	50	Running
Mini-BooNE	Scint.	0.7	USA	200	Running
KamLAND	Scint.	1	Japan	300	Running
Borexino	Scint.	0.3	Italy	100	200 ×
Icarus	Liquid argon	2.4	Italy	200	200 ×
OMNIS	High Z (Pb)	2	USA	2000	Proposed
LANNDD	Liquid argon	70	USA	6000	Proposed
UNO/Hyper-K	H_2O Ch.	600–1000	USA/Japan	>100 000	Proposed

for an automated (GOLD) alert. A SILVER alert involving human-checked alarms would take longer, optimistically 20 min or so, but perhaps longer.

4.2. Pointing

Clearly, the more accurately we can point to a core collapse event using neutrino information, the more likely it will be that early light turn-on will be observed by astronomers. Even for the case when no directional information is available (e.g. for a single scintillator detector online) it is still useful for astronomers to know that a gravitational collapse event has occurred. However, any pointing information is extremely valuable. The question of pointing to the supernova using the neutrino data has been examined in detail in [11]. There are two ways of pointing with neutrinos: first, individual detectors can make use of asymmetric reactions for which the products 'remember' the direction of the incoming neutrino. Second, the timing of the neutrino signals in several detectors can be used to do triangulation. In [11], estimates of roughly 5° pointing accuracy for Super-K and 20° pointing accuracy for SNO have been given for a galactic centre core collapse. Triangulation is less promising, and presents practical difficulties: it requires immediate and complete exchange of event-by-event information, which is difficult in practice, and we do not plan to attempt it promptly.

We do not anticipate that SNEWS will disseminate pointing information as part of the initial alert message in the short term (although this may change); this information will come from the individual experiments, and may not be available immediately. Each experiment establishes its own protocol for making estimated pointing information available.

4.3. Positive

There must be no false supernova alerts to the astronomical community. A single experiment cannot realistically decrease the false alert rate to zero, since there will always be some residual

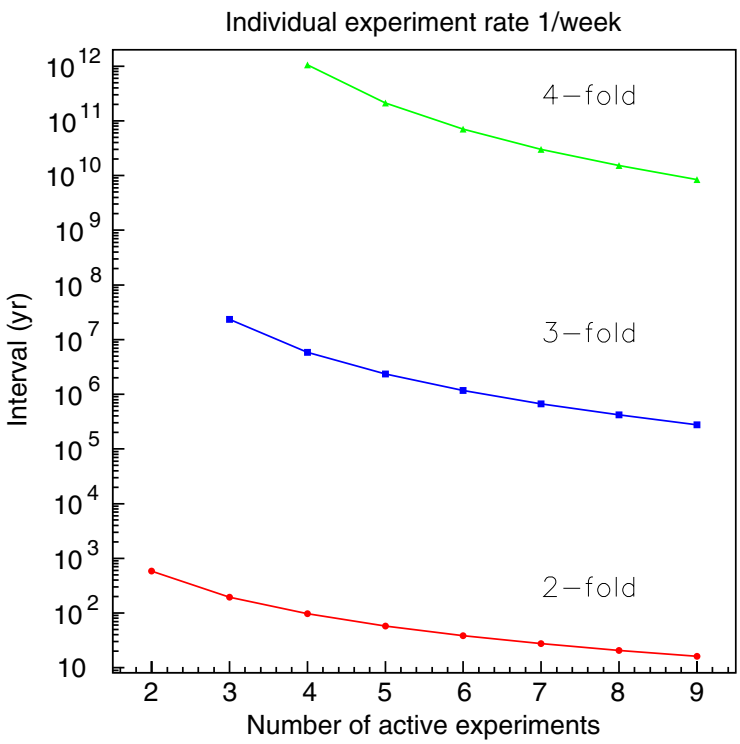

Figure 1. Average interval between accidental alerts for an n-fold coincidence of N experiments, for a 10 s coincidence window and a uniform individual experiment background alarm rate of one per week.

rate of false alerts from Poissonian and non-Poissonian sources. However, by requiring an inter-experiment coincidence, the false alert rate can be decreased to nearly zero: this is the great strength of SNEWS. We have chosen the nominal acceptable average false alert rate to be *one per century*. The following section is devoted to the question of ensuring a false alert rate which is sufficiently low.

4.3.1. False alerts. The fundamental motivation for the SNEWS coincidence is the reduction of false alerts. We categorize the possibilities for false alerts below:

(i) *Accidental coincidences*: accidental (random) coincidences imply that there was no actual association with an astronomical event and that the coincidence occurred by chance. The rough expected rate of accidental coincidences can be calculated by assuming equal, constant, uncorrelated alarm rates for each experiment.

Figure 1 shows the average interval between accidental alerts for an n-fold coincidence of N experiments, for a 10 s coincidence window and an individual experiment background alarm rate of one per week. This plot shows that an individual experiment alarm rate of one per week is acceptable only if four or fewer experiments are online, or if a three-fold coincidence if required; otherwise a lower individual experiment rate is required. Based on these considerations, the requirement for an experiment to participate in SNEWS is an average alarm rate of *no more than one per week*. We may adjust the criteria defined in

this paper if more than four experiments are running. In reality, individual alarm rates are not strictly Poissonian and change with time. However, they may be Poissonian on shorter time scales, and so long as instantaneous individual rates do not exceed a certain value, the accidental coincidence rate can be made as small as desired. In section 6.6, we detail how we deal with potentially changing alarm rates.

(ii) *Non-astrophysical correlated bursts*: the possibility of some correlation between bursts seen in the individual detectors, which is not astrophysical in origin, exists to the extent that some credible coupling can be shown to exist between detectors. For participating detectors that may be physically close to one another there are a large number of possible couplings from a shared local environment (electrical noise, ambient pressure, seismic, etc). For participating detectors that are very well separated from one another one has to invoke more fanciful and substantially less probable couplings such as solar activity, solar flares, or widescale upper atmospheric electrical disturbances. The most credible coupling for separated detectors may well be the seismic one, but even that is not really plausible.

(iii) *Malicious actions*: a fake alert sent to the astronomical community by hackers breaking into our machines is a remote possibility, but one which we view seriously. Breaching several machines at the individual experiments and creating false alarms at the client datagram level would have the same end effect, but would require more knowledge of the detailed and widely different operation of several detectors, so we feel this is much less of a concern. To prevent malicious actions, we take a serious approach to the security of the server and the connections to it. We require that the server be housed at a national laboratory with designated personnel to take responsibility for the security and maintenance of the machine.

4.4. Privacy

Another 'P' (relevant to experimenters more than to astronomers) is 'Privacy'. To satisfy inter-experiment privacy needs (and in addition to help ensure secure data transmission), we have set up a formal set of rules for data sharing and have structured the collaboration around these rules. The 'SNEWS subgroup' is a working group of a few people per experiment, designated by our Advisory Board (spokespeople of the active experiments). Only subgroup members have access to the alarm data from all experiments. Subgroup members agree not to propagate information without explicit approval from the Advisory Board.

5. Description of individual experiments' supernova triggers

In this section we will describe briefly the online supernova monitoring systems of Super-K, SNO and LVD, which provide alarm input to the SNEWS coincidence. The supernova capabilities of the detectors are well known and details can be found elsewhere [14]; other details of the triggers, monitoring systems and analyses are also described elsewhere [29]–[31]. Although each of these three experiments takes a somewhat different approach to real-time monitoring, every one is sensitive to a galactic supernova and can provide an alarm on a timescale of minutes.

A note on SNEWS terminology: an 'alarm' refers to a supernova neutrino burst candidate detected by an individual experiment, according to conditions defined for that experiment. An

'alert' refers to a coincidence between alarms, and the conditions which define an alert are described in section 6. This section describes the individual experiment alarm conditions only. The detailed neutrino event information comprising the alarm bursts is not sent to the coincidence server.

5.1. Super-K supernova online monitor

The Super-K supernova alarm system involves software that does a prompt pre-analysis before full reconstruction. Roughly 2-min chunks of data called 'subruns' are sent from the event builder via 'express-line' to a dedicated supernova burst monitor machine, skipping the usual steps required before data are sent to the offline processes. The low energy trigger events are then searched for clusters in several time windows (0.5, 2 or 10 s).

If the 'pre-multiplicity' thresholds are exceeded for any of these time windows, then the 'pre-candidate' is passed to a second monitor program for further analysis. Standard noise reduction algorithms similar to those applied for solar neutrino analysis [32] are applied, and the search is performed again, this time on events passing the cuts and with a higher energy threshold. Full energy reconstruction is not done (to save time), but vertices and directions are reconstructed. If any cluster passes a second pass multiplicity threshold, the multiplicity N in a 20 s time window is counted; in addition, the mean distance between event positions in the cluster, $R_{\mathrm{mean}} = (1/C)\sum_{i=1}^{N-1}\sum_{j=i+1}^{N}|\vec{r}_i - \vec{r}_j|$, where C is the number of pairs, is calculated. Background supernova alarms arise from muon spallation events and 'flashing' tubes. Both of these types of fake clusters have event vertex distributions which are highly non-uniform, and which will yield small R_{mean} values. Candidate clusters with sufficiently high N and R are considered to be supernova candidates.

Because reconstruction of thousands of events in a real supernova burst (~5000 events) could require an hour or more to analyse fully, pre-alarms are generated after 100 events if a candidate is found (roughly a 1 min timescale).

If an alarm burst candidate is found, a datagram is sent to the SNEWS server, and shiftworkers are alerted. Detailed information about the candidate is made available to shiftworkers (present 24 h a day onsite). The shiftworker checks for the existence of spallation muons, examines reconstructed vertices and their goodness, and also checks the exploded view of the PMT hit pattern. A preliminary estimate of the supernova direction from elastic scattering is available at this point. If a good supernova candidate is identified, an offline process will re-analyse to provide full, precise reconstruction within a few hours.

5.2. SNO supernova online monitor

At SNO, custom readout electronics collect the PMT data underground and pass that information to an event builder. Built events are then sent to an event dispatcher process running on a surface computer, which is used for online monitoring. A fully detailed description will be found elsewhere [30]. Summarized here is the basic machinery of the trigger, which consists of three distinct levels which are fast and completely automated:

- *Level 1*: this is the burst monitor which looks in the datastream for a certain number of events above a certain energy threshold within a certain time window. At present, the multiplicity threshold is set to 30 events above approximately 4 MeV in a 2 s time window which provides

a good sensitivity to a galactic supernova. Dynamic thresholds are used whenever calibration sources are introduced in the detector. Bursts satisfying the multiplicity criteria are written to a data file and then transferred to an analysis machine.

- *Level 2*: at this level events are calibrated and analysed on an event-by-event basis. The main task of this second-level trigger is to identify events with anomalous time and charge as well as events with geometric signatures of particular detector pathologies in order to cut them from the burst data set. For example, events with low charge to number-of-hits ratio usually indicate electrical pickup. A set of data cleaning cuts are applied which are meant to reject known instrumental background with a very high efficiency. Cherenkov events pass those cuts with very little sacrifice.
- *Level 3*: if more than 35% of the events composing a burst survive the data cleaning cuts, an alert is sent to the SNEWS server and a dialout computer contacts the members of the SNO supernova trigger group. In the meantime, a more in-depth analysis is performed to extract fitted vertices and direction cosines. The relative event fractions occurring in the D_2O/H_2O volumes are extracted and a search algorithm uses the events' direction cosines to find the electron scattering (ES) events, which are expected to best convey information about the direction of the possible supernova.

The Level 2 analysis produces a set of histograms which are mainly useful for a quick burst diagnostic by the operator and any interested party. Besides hit and time distributions, crate/slot/channel occupancies are provided, which are expected to be flat for a supernova signal. The Level 3 analysis produces a set of histograms using fitted vertices in both the light and heavy water volumes as well as angular distribution of the events' fitted directions. Each burst is catalogued and automatically archived on the SNO private WWW server.

5.3. LVD supernova online monitor

In the LVD experiment the scintillator counting rate is continuously monitored by a DAQ task, which examines all data collected in real time. A simple and fast muon rejection algorithm makes a pre-selection of ν-candidate signals, registered by the experiment with a 12.5 ns time precision. This first selection level does not apply cuts on pulse energy and topological distribution.

A separate on-line monitor task looks for burst candidates from the reduced data stream. The search algorithm is based on a pure statistical analysis of the time sequence of events including some additional cuts. The code processes the sequence in order to extract significant clusters of pulses having an expected frequency, induced by the accidental background, lower than a predefined threshold.

At this level, pulse energy is required to be in the 7–100 MeV range in order to avoid fluctuation effects at the edge of energy threshold and problems due to electronic noise, as well as to reject single counter muon signals. After these cuts the background pulse frequency is found to be very stable and corresponds, for the full LVD configuration, to $f_B = 0.2$ Hz. The resulting ν -pulse candidate time sequence, collected inside a 1000-pulse deep circular buffer, is processed by the alarm module of the monitoring code. Buffered events are processed in fixed time windows $\Delta T = 20$ s originating at the start run time. For each asynchronous window the number N_ν of contained single pulses is obtained. Then the Poissonian probability P_C to have $k \geqslant N_\nu$ events in the cluster is calculated according to $P_C(k \geqslant N_\nu, \lambda) = \sum_{k=N_\nu}^{\infty} \lambda^k e^{-\lambda}/k!$, where $\lambda = f_B \times 20$ is the mean expected number of pulses due to background rate. To optimize

sensitivity, the online frequency f_B is evaluated each time a new pulse is inserted into the buffer. The alarm threshold probability is obtained from the above expression by fixing a global alarm frequency f_A. The predictive capability of the selection algorithm has been checked with real and simulated data as a function of the required global alarm frequency ($f_A = 1\ \mathrm{h}^{-1}, \ldots, 1\ \mathrm{yr}^{-1}$).

Finally, to reduce the number of false alarms, for each selected candidate a topological check is applied. For a real supernova burst candidate, a uniform distribution of pulses between involved counters is expected. If not, counters with abnormal high counting are excluded and the resulting cluster is re-analysed. Surviving clusters are considered to be candidate alarms, and corresponding datagrams are sent to the SNEWS servers; all related information is saved for further analysis. Online event buffering and processing gives less than 2 min delay between the burst time and the alarm notification. The LVD shiftworker and experts within the collaboration are notified.

6. SNEWS coincidence implementation

This section describes the hardware setup and software developed for SNEWS.

6.1. The coincidence server

There is currently a single SNEWS workstation running Linux at Brookhaven National Laboratory, which serves as the coincidence server. Previously, we had servers at LNGS and Kamioka, but moved to BNL in the fall of 2003, for ease of security and maintenance with the resources available there. The software has capabilities for dealing with multiple servers, and more may be added in the future. A second, identical machine is kept running and in synch with the primary server, so that immediate failover is possible in case of a problem with the primary server.

The coincidence server remains behind the BNL firewall. Only very limited access to SNEWS subgroup members and the BNL system administrator is permitted. In addition, the server is housed in a physically secure location. If additional servers are added to the network, they will be subject to similar security requirements.

6.2. Coincidence software

The SNEWS software involves client and server programs which implement a simple datagram exchange via socket, employing TCP/IP protocol, and encrypted via OpenSSL. The code is designed to be easily portable to diverse operating systems.

The client software is provided to the individual experiments in the form of a library of subroutines that may be called by an experiment's supernova watch software to initiate a datagram transfer. The package also provides standalone tools for testing.

The server software runs in a standalone mode, and most of the time simply waits to receive datagrams from the clients. It maintains two queues: a normal queue and a 'high-rate' queue, for test alarms. When an alarm datagram is received, it is placed on a queue according to its flag (see section 6.5). One month's worth of alarms are stored in the queue. Received alarms are written to disk, and are read in from disk if the server is stopped and restarted.

Every time an alarm is received, the last 24 hours' worth of alarms on the queue is searched for a coincidence. See section 6.6 for detailed coincidence conditions.

When a client initiates a connection, the server employs several layers of checks to validate the origin of the datagram. Only the IP addresses of the client machines of the involved experiments are allowed to submit packets. In addition, the client and server exchange certificates which have been verified by the SNEWS Certificate Authority, and the server rejects the connection if any check fails.

6.3. SNEWS shifts

SNEWS subgroup members share shiftwork on a regular cycle. Shift duties include a check twice daily to ensure that the server is running, that network connectivity is up, and that communication capability is in good order.

Individual experiment alarm rates are monitored by SNEWS subgroup members, so that any long term increase of rate over the one per week limit may be addressed.

6.4. SNEWS operational modes

We have established a well-defined operational mode for SNEWS, which we expect to develop in a series of managed transitions between operational modes. For instance, new experiments or new coincidence servers will be added or removed. Each operational mode is identified by a number and the date when it came into effect, and will specify in detail the participants, the coincidence conditions, the alert classifications, and the procedures for action in case of different alarm conditions. The following sections outline the conditions for the operational mode we anticipate for the near future.

6.5. SNEWS packet types and flags

Each participating experiment may generate and send to the server different types of alarm datagrams. The alarm datagrams include a packet type and a level flag. The packet type can be PING, ALARM, or RETRACTION. The level flag can be TEST, GOOD, POSSIBLE, RETRACTED or OVERRIDE. Datagrams having packet field values which do not belong to any of these categories are discarded by the server.

Packet types

- PING: these packets are used for test purposes only and cause nothing more than a message printed to the coincidence server log.
- ALARM: these packets contain information about individual experiment alarms; what the server does with them depends on the level flag.
- RETRACTION: these packets contain information about previously sent alarms to be retracted from the server's alarm queues.

Level flags

- TEST: this flag indicates a datagram packet intended for test use as well as for any high-rate test mode.
- POSSIBLE: this flag indicates an alarm generated during scheduled operations (i.e. maintenance, calibration, tests, etc) or other known anomalous conditions. It is up to each experimental collaboration to set this flag inside the packet when appropriate.

- GOOD: this flag indicates an alarm generated during normal detector conditions.
- RETRACTED: this flag is set for retraction packets. (Note that this information is redundant—all packets of RETRACTION type will be retracted regardless of level flag.)
- OVERRIDE: this flag indicates an alarm that has been confirmed as good.

6.6. Coincidence definition

The general coincidence definition implemented in the coincidence code may generate either of the two types of alert: GOLD or SILVER.

A GOLD alert is generated if *all* of the following conditions (1–4) are met.

(1) There is a two- or more-fold coincidence (by UT time stamp) within 10 s, involving at least two different experiments. (The time window refers to the maximum separation of any of the alarms in the coincidence.)

(2) At least two of the experiments involved are at physically separated laboratories. This condition is automatically satisfied for the current operational mode.

(3) Two or more of the alarms in the coincidence are flagged as GOOD. It is the responsibility of each participant experiment to flag the alarm sent to the SNEWS server(s) appropriately. The specific criteria for GOOD/POSSIBLE alarms are locally defined by each experiment.

(4) For at least two of the experiments involved in the coincidence, the rate of good alarms for several past time intervals $\{T_i\} = \{10\,\text{min}, 1\,\text{h}, 10\,\text{h}, 1\text{ day}, 3\text{ days}, 1\text{ week}, 1\text{ month}\}$ preceding the first alarm of the coincidence candidate, must be consistent with the $\lambda_{\max} = 1\text{ week}^{-1}$ requirement.[20] We define the precise condition as follows: if an experiment sent $\{n_i\}$ alarms in each of the last intervals $\{T_i\}$ before the first event of the coincidence, then the Poisson probabilities $\mathcal{P}_i$ for n_i or more alarms in T_i,

$$\mathcal{P}_i = \sum_{n=n_i}^{\infty} (\lambda_{\max} T_i)^n \mathrm{e}^{-\lambda_{\max} T_i}/n!,$$

for each interval T_i, must each be greater than $\mathcal{P}_{thr} = 0.5\%$. This corresponds to the condition that each $\{n_i\}$ must be less than $\{1, 2, 2, 3, 4, 5, 11\}$ for the preceding intervals $\{T_i\}$ for an alarm to be GOLD.

When the first criterion is satisfied, but at least one of the other criteria is not satisfied, the generated alert is flagged as SILVER. In this case the alert has to be checked by the individual experiment collaborations before any public announcement. No alert will be sent to the community by SNEWS until (and if) there is an upgrade to GOLD.

6.7. Rate-dependent GOLD coincidence suppression

The last criterion—demotion to SILVER based on past rate history—deserves some additional discussion. The purpose of this criterion is to protect against short term rate increases from one or more experiments. The suppression is effective: see figure 2. However, it comes at a slight

[20] These intervals represent real time, not live time, since full live time information will not be available to the coincidence server.

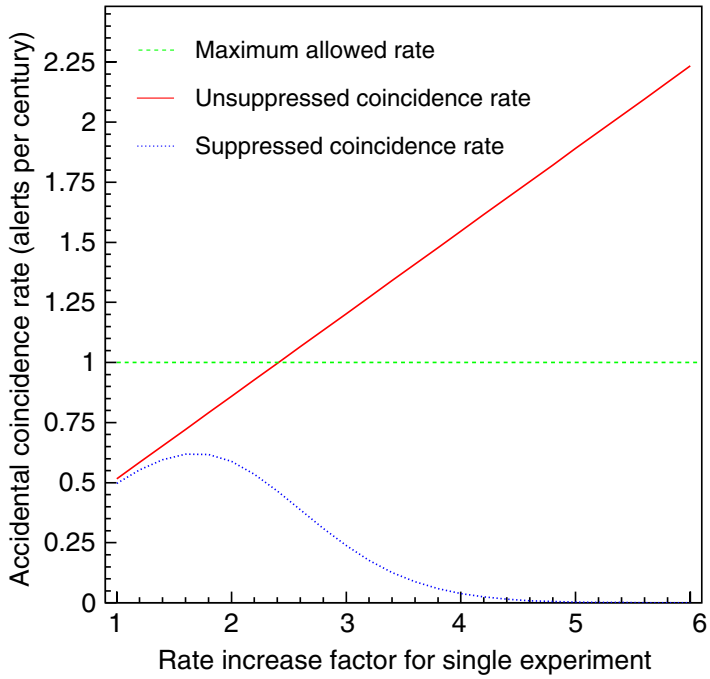

Figure 2. The green dashed line shows the maximum allowed accidental coincidence rate (one per century). The red line shows the expected accidental coincidence rate of 2 out of 3 experiments (for a 10 s coincidence window), under the assumption that one of the three experiences an increase in rate by a factor f (and the others maintain a one per week rate), as a function of rate increase factor f. The blue dotted line shows the expected coincidence rate after the past rate history suppression has been applied.

cost: if one assumes a constant Poisson background rate of one per week for all three experiments, criterion 4 will result in demotion of about 4% of true GOLD alerts to SILVER, just due to Poisson fluctuations in the previous time windows. However, the protection against unexpected increases in background rate is probably worth this small loss (note that typically individual experiment alarm rates will be less than one per week in any case).

One might also worry that long term rate increases might cause increased demotion of true GOLD to SILVER. We have evaluated the overall average rate increase from any single experiment that would result in 90% of true coincidences being demoted. Figure 3 shows the effect of changing $\mathcal{P}_{thr}$. The value of $\mathcal{P}_{thr}$ chosen was 0.5%, which gives fairly low true GOLD suppression (4%); and at this threshold any overall single experiment rate increase of more than a factor of 4 will result in demotion of 90% of coincidences.[21]

We feel that this GOLD and SILVER scheme strikes the right balance between danger of losing true coincidences due to too-stringent criteria and danger of issuing false alerts to astronomers.

[21] Note that long-term average alarm rates will be monitored by shiftworkers, and *subgroup members will be notified if rates of their experiments exceed the nominal one per week limit*, so any such rate increase will be temporary. Also note that if alarm rate increases have clearly been corrected, by subgroup agreement on a case-by-case basis individual alarms may be retracted after the fact, so as not to decrease true GOLD coincidence efficiency.

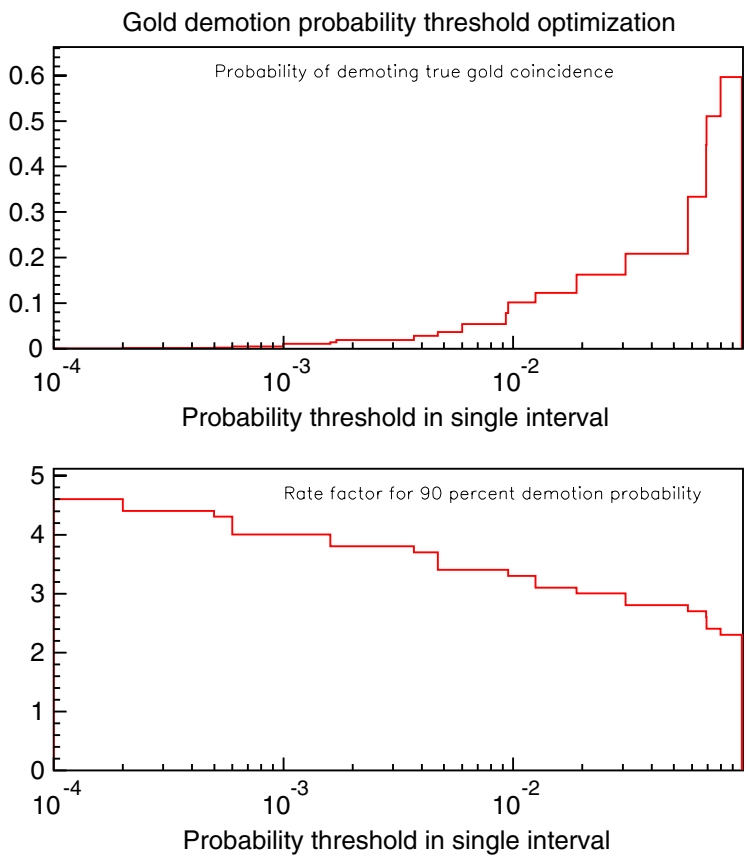

Figure 3. Upper panel: total probability of demoting a true GOLD coincidence as a function of $\mathcal{P}_{thr}$, assuming three experiments with the one per week alarm rate. Lower panel: factor by which average rate of any single experiment would have to increase in order for 90% of coincidences to be demoted. The $\mathcal{P}_{thr}$ chosen is 0.005.

6.8. Demotion and promotion

Although we hope to avoid ever being in the situation where retraction of a GOLD alert is necessary, any experiment may reflag from GOOD (or POSSIBLE) to RETRACTED its own alarm after data checking. The server will then automatically reevaluate and reissue the alert based on alarms in the previous day of its memory: the result may be still GOLD, demotion to SILVER, or no alert at all. For the latter case, the SNEWS subgroup is notified, and a RETRACTED alert will be issued to the same mailing list as for GOLD and posted on the public web page.

Experiments may also send OVERRIDE packets: a GOLD alert may also be generated if condition 1 is satisfied and at least one alarm in the coincidence is OVERRIDE and at least one is GOOD, regardless of whether the other conditions are satisfied. This case allows an override of past high-rate history demotion (or other conditions that could tag an alarm as POSSIBLE) for a human-checked alert.

Figure 4 summarizes the sequence of events and GOLD versus SILVER decisions.

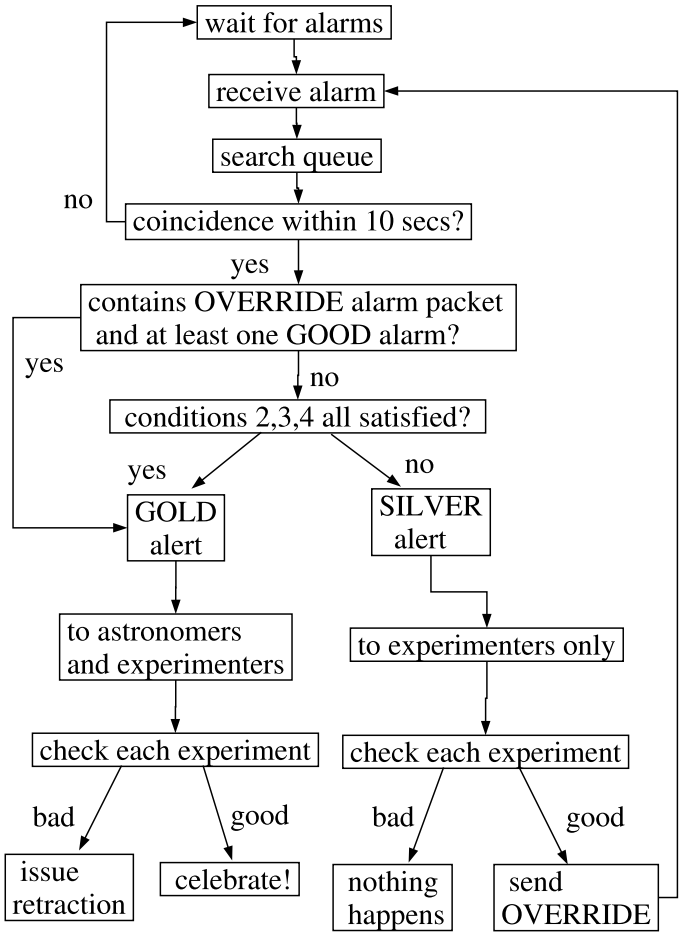

Figure 4. Flowchart summarizing the sequence of events and decisions that determine whether an alert is GOLD or SILVER.

7. High rate test results

During an approximate two-month period in April–June of 2001, Super-K, LVD and SNO subgroup members performed a 'high rate test' of the coincidence software. The purpose was two-fold: first, to check the robustness of the software and work out any remaining bugs; and second, to increase confidence in our understanding of the expected coincidence rates. The test was highly successful.

The idea of the high rate test was to lower the thresholds of the experiments' supernova monitors such that coincidence alerts increased to a non-negligible rate, due to the Poissonian nature of the data. Each experiment set its supernova monitor burst search parameters to yield a test alarm rate somewhere in the range of 10–100 per day. In addition, to increase artificially the coincidence rate, the coincidence window was increased from its standard value of 10–400 s.

The individual experiment alarm and coincidence rates were somewhat non-stationary, which was not unexpected. The results were analysed via a 'time-shift' method (see below) to show that alarms were uncorrelated, and that recorded coincidences were consistent with expected rates.

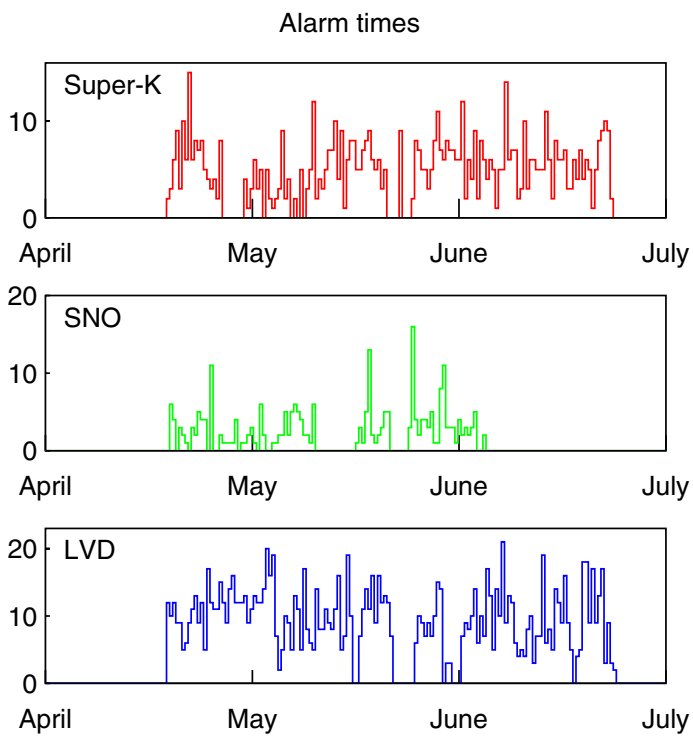

Figure 5. Number of alarms received from the individual experiments, plotted in 11 h bins.

The alarms received as a function of time, and coincidences as a function of time, are shown in figures 5 and 6. The numbers of individual alarms, and numbers of 2- and 3-fold coincidences are shown in table 3. The rates are roughly constant over most periods, although there is clearly some 'burstiness'.

Experiments can be 'dead' to SNEWS for many reasons: actual detector deadtime, online supernova monitor problems, network problems, or coincidence server problems. To estimate the deadtime, we used the data themselves and counted improbably long gaps as deadtime. This method automatically takes into account dead time from all causes.

After removing the dead intervals, we calculated the overlapping live periods for each pair of detectors, as well as the three-experiment overlap time. Note that there are some dead intervals common to all detectors due to network trouble; in particular, the period 22–25 May represents a problem with network availability to the test server at the Kamioka site. (Note that we expect very high uptime at the current BNL server site.)

Based on these known alarm rates and live periods, we then calculate expected accidental coincidence rates. For the purpose of comparison with expected coincidence rates, we have calculated the 'raw' number of coincidences from the individual experiment alarms arriving at the server: the number of raw coincidences is defined as the number of times the individual experiment alarms are separated by a maximum test time window of $\tau = 400$ s.

Note that in the real case, according to the rate history-based demotion algorithm described above, the coincidence server will suppress redundant alerts. If there is more than one alarm from a given experiment within the time window, the server will send only one GOLD alert, corresponding to the coincidence of the first alarm from each experiment (assuming all conditions

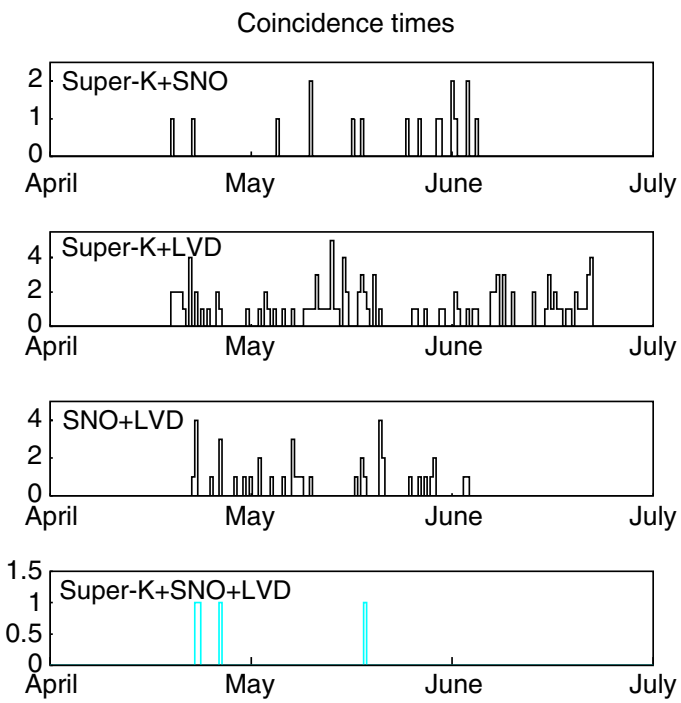

Figure 6. 2- and 3-fold coincidences, plotted in 11 h bins. 'Unique' coincidences only are shown.

Table 3. Alarm and coincidence summary.

Experiment combination[a]	Common live time (days)[b]	SK/SNO/LVD alarms[c]	N_{coinc} expected (eqn)[d]	N_{coinc} expected (shift)[e]	N_{coinc} observed raw (unique)[f]
SK/SNO	$24.1^{+1.1}_{-0.5}$	334/187/–	$24.1^{+1.0}_{-2.2}$	24.9 ± 7.0	30 (17)
SK/LVD	$44.6^{+1.1}_{-0.9}$	576/–/1025	$122.6^{+4.9}_{-5.8}$	133.8 ± 13.7	149 (112)
SNO/LVD	$27.7^{+0.7}_{-0.6}$	–/189/646	$40.8^{+1.6}_{-2.0}$	46.4 ± 9.2	52 (41)
SK/SNO/LVD	$19.6^{+1.1}_{-0.6}$	276/144/431	$2.9^{+0.3}_{-0.5}$	4.2 ± 2.9	4 (4)

[a] Indicates the 2- or 3-fold experiment combination.
[b] The overlap live time for the combination in column 1 with estimated uncertainties.
[c] The numbers of alarms from the experiments which are within the overlap live time.
[d] The number of expected coincidences according to equation (1); the error reported is the systematic error only, from uncertainty in the live-time estimate.
[e] The expectation and its RMS based on the time-shift method.
[f] The observed number of coincidences during the test; the number outside parentheses indicates the 'raw' number of coincidences defined as the number of alarms with maximum time separation of 400 s (to be compared with the predictions); the number in parentheses is the number of 'unique' coincidences tagged by the coincidence server (see text).

are satisfied), whereas multiple 'raw' coincidences would be counted for this cluster. Subsequent coincidences would be demoted to SILVER. The number of 'unique' coincidences is the number of coincidences with different first alarm times.

The final column of table 3 shows both 'raw' and 'unique' (in parentheses) numbers of coincidences. Figure 6 shows 'unique' coincidences. The coincidence server output was checked to verify consistency with the calculated raw coincidences.

For stationary, uncorrelated Poisson point processes, the rate of N-fold coincidences between N detectors is given by

$$\lambda_{\text{coinc}} = N\left(\frac{\tau^{N-1}}{T_{\text{obs}}^{N}}\right)\prod_{i=1}^{N}\mathcal{N}_i, \tag{1}$$

where τ is the coincidence window (the maximum separation of events for a coincidence), T_{obs} is the total common observing time and $\mathcal{N}_i$ is the number of events observed by the ith detector. For example, for a 2-fold coincidence between detectors i and j, the expected number of coincidences is $2\mathcal{N}_i\mathcal{N}_j\tau/T_{\text{obs}\,ij}$.

The uncertainties on the expectated rate values are calculated by propagating the uncertainties on the live time.

However, (1) is strictly valid only for stationary processes, and this assumption is clearly violated in our case (see figure 5). Therefore, we take a different approach to calculate expected coincidence rates: to predict more generally the number of accidental coincidences from these non-stationary alarm sequences, we apply a 'time-shift' method [33]–[35]: for any pair of detectors, we shift all of one experiment's alarm time values by an offset Δt, and determine the number of coincidences n_c for that time offset value. This procedure is repeated for many values of Δt; the mean and standard deviation of the distribution of n_c values then gives both the expected number of observed coincidences and its expected spread, which we then compare with the observed number of raw coincidences. Similarly, we time-shift one of the three experiment's alarm time series by Δt to determine the expected 3-fold coincidence rate.

The plot of n_c versus time offset value should be flat, and show no spike at zero (or any other) offset, if there are no correlations between the different experiments' alarm times. The results of this analysis for 2-fold coincidences are shown in figure 7 (a similar plot, although with lower statistics, results for 3-fold coincidences). We use time shifts ranging from -150 to 150 h at 1000 s intervals. Live time is taken into account in the time-shifted sample by shifting the offset experiment's live period by the same offset and then re-evaluating the overlap time. The mean and RMS values of the resulting shifted coincidence rates are used to determine the expected number of coincidences for each combination in table 3.

Table 3 shows the expected and observed numbers of events. The expected numbers of coincidences from (1) do not exactly match the expected numbers from the time-shift method, even after considering the live-time estimate uncertainty. Presumably, this is due to the somewhat non-stationary nature of the alarm sequence. The number of observed coincidences do match the time-shift expectations well within the expected spread. In addition, the time shift plots show no evidence of correlations between experiments, as expected.

Although these somewhat non-stationary data, taken at lowered threshold, do not necessarily imply that rates will also be non-stationary when thresholds are raised and running conditions are normal, one can never be completely sure that individual experiment rates will not increase unexpectedly. This is the motivation for the rate-dependent GOLD suppression scheme of section 6.7.

The coincidence server now has capability for continuous high rate testing, using tagged TEST alarms in parallel with normal alarms.

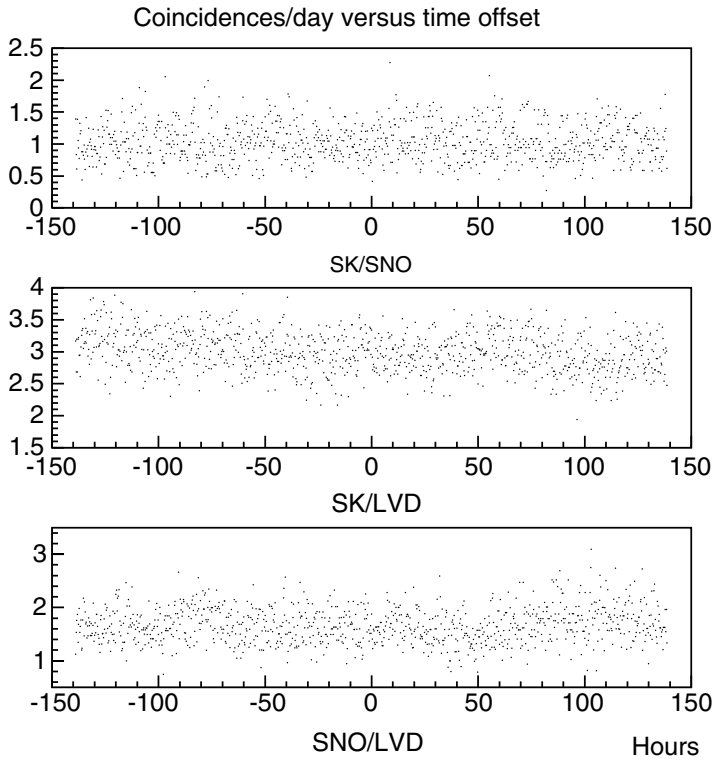

Figure 7. Rate of 2-fold coincidences for each experiment pair, as a function of time offset in hours. The rate was determined using overlap live time after the time offset.

8. The alert to the astronomical community

At the supernova early alert workshop of 1998, the conclusion from the astronomer working group [36] was that 'the message will spread itself' and that SNEWS will need to do no more than send out e-mails to as many astronomers as possible. SNEWS maintains a mailing list of interested parties, including both professionals and amateurs, to be alerted in the case of a coincidence.

In an ideal case, the coincidence network provides the astronomical community with an event time and an error box on the sky at which interested observers could point their instruments. In a realistic case, the size of the error box is dependent on the location of the supernova and the experiments which are online, and may be very large (and at this time will not be available in the initial alert message). However, members of the mailing list with wide-angle viewing capability (satellites, small telescopes) should be able to pinpoint an optical event quickly. Although an unknown fraction of galactic supernovae will be obscured by dust, many will be visible to amateurs with modest equipment.

Regardless of the quality of neutrino pointing available, however, the advance warning alone gives observers of all kinds valuable time to get to their observatories and prepare to gather data as soon as an accurate position is determined.

A Target of Opportunity proposal for the Hubble Space Telescope, 'Observing the Next Nearby Supernova', aiming to take advantage of early supernova light based on an early warning, was approved [37] for Cycle 13 and was operational for Cycles 8–12.

8.1. Amateur astronomers

The large pool of skilled and well-equipped amateur astronomers is also prepared to help locate a nearby supernova. The editors of *Sky & Telescope* magazine have set up a clearinghouse for amateur observers in search for first light (and a precise optical position as early as possible) [38], via their AstroAlert service [39]. This was started by former editor-in-chief Leif Robinson, and has the continued support of current editor-in-chief Rick Fienberg. In collaboration with the American Association of Variable Star Observers, they have developed a set of criteria for evaluating amateur responses to an alert, so that a reliable precise position can be disseminated as early as possible. For instance, there must be at least two consistent reports, demonstrated lack of motion, lack of identification with known asteroid and variable star databases, variability consistent with supernova light curves and, if the information is available, a spectrum consistent with known supernova types.

On 14 February 2003, *Sky & Telescope* performed a test for amateurs. A transient target (the asteroid Vesta at a near-stationary point in its retrograde loop) was selected, which at the time was about magnitude 6.7. *Sky & Telescope* issued an alert (very carefully tagged as a test) to their mailing list, with a given 13° uncertainty radius. They received 83 responses via the web response form, and more by e-mail. The responses were of world-wide distribution, and although many observers experienced poor conditions, six were successful in identifying the target. From this experience, they have suggested refinements to optimize amateur astronomer strategy. A second test is planned soon, and should be a regular occurrence.

8.2. SNEWS alerts

We maintain two alert mailing lists which will be sent automatically by the SNEWS coincidence software in the case of an alert. The first is the GOLD alert list, which includes all astronomers who have signed up, including *Sky & Telescope* and the HST astronomers, and will be an 'automated' alert. The second mailing list will be for SILVER alerts, and will be sent to neutrino experimenters only. These alerts will be checked out by shiftworkers at their respective experiments before an alert is issued; each experiment is responsible for making sure the SILVER alert messages reach shiftworkers. Each experimental collaboration defines its own protocol for acting on a SNEWS SILVER or GOLD alert.

For both SILVER and GOLD cases, a message containing the following information will be automatically sent by the server to the SNEWS subgroup members:

- UTC time of the coincidence,
- all detectors involved in the coincidence, and
- the types of alarms (GOOD, POSSIBLE) for each experiment involved in the coincidence.

The information may also be posted to a restricted SNEWS subgroup page for SILVER, and a public page for GOLD.

To allow the confirmation of a SNEWS alert as really coming from SNEWS, any alerts will be public key signed using the SNEWS key. This key has the ID# 68DF93F7, and is available on the network of public PGP keyservers such as http://pgp.mit.edu/.

Note that there is no restriction on individual experiments making any announcement based on individual observation in the case of absence of a SNEWS alert, SILVER or GOLD, or

preceding or following any SNEWS alert message. Any individual experiment may publicly announce a supposed supernova signal following a dispatched SILVER alert which has not yet been upgraded to GOLD. In this case, the information that a previous SILVER alert from the SNEWS server(s) has been received should be cited.

9. Status and future prospects

At the time of this writing, SILVER alerts only between Super-K and LVD have been activated. We are working towards having the operational mode described in this paper to be activated in a very short term, comprising automated GOOD alarms from Super-K and LVD, but automated POSSIBLE alarms only from SNO, such that SNO will participate in a GOLD alert only if at least two other experiments' GOOD alarms are present.

We also expect SNEWS to incorporate more galactic-supernova-sensitive neutrino detectors over the next few years. In addition, we may expand the network of servers with additional secure sites.

10. Summary

In summary, several supernova neutrino detectors are now online. If a stellar core collapse occurs in our Galaxy, these detectors will record signals from which a wealth of physical and astrophysical information can be mined.

An early alert of a gravitational collapse occurrence is essential to give astronomers the best chance possible of observing the physically interesting and previously poorly observed early turn-on of the supernova light curve. A coincidence of several neutrino experiments is a very powerful technique for reducing 'non-Poissonian' false alarms to the astronomical community, in order to allow a prompt alarm. We have implemented such a system, currently incorporating several running detectors: LVD, SNO and Super-K. We expect to expand the network in the near future, and move to a more automated mode in the near future.

Acknowledgments

We thank the members of the Super-K, SNO and LVD experimental collaborations, without whose hard work the SNEWS project would not be possible. We thank Sam Aronson and Tom Schlagel of Brookhaven National Laboratory for providing a secure home for the server. We are grateful to John Bahcall, Barry Barish, John Beacom, Janet Conrad, Ed Kearns, Janet Mattei, Jim Stone and Larry Sulak for advice and support; others from the early days of SNEWS are Adam Burrows, Robert Kirschner and Mark Vagins. We also thank the members of the SNEWS working group from other experiments. SNEWS is funded by the National Science Foundation awards PHY-0303196 and PHY-0302166.

References

[1] Hirata K S *et al* 1987 *Phys. Rev. Lett.* **58** 1490
[2] Bionta R M *et al* 1987 *Phys. Rev. Lett.* **58** 1494

[3] Bratton C B *et al* 1988 *Phys. Rev.* D **37** 3361
[4] Hirata K S *et al* 1988 *Phys. Rev.* D **38** 448
[5] Alekseev E N *et al* 1987 *JETP Lett.* **45** 589
[6] Aglietta M *et al* 1987 *Europhys. Lett.* **3** 1315
[7] Burrows A *et al* 1992 *Phys. Rev.* D **45** 3361
[8] Thompson T *et al* 2003 *Astrophys. J.* **592** 434
[9] Liebendorfer M *et al* 2002 *Preprint* astro-ph/0207036
[10] Cline D B1990 *Proc. Supernova Watch Workshop (Santa Monica)*
[11] Beacom J and Vogel P 1999 *Phys. Rev.* D **60** 033007 (*Preprint* astro-ph/9811350)
[12] Tammann G A *et al* 1994 *Astrophys. J. Suppl.* **92** 487
[13] Ahlen S *et al* 1992 *Astropart. Phys.* **1** 11
Ambrosio M *et al* 1998 *Astropart. Phys.* **8** 123
[14] Scholberg K 2000 *Nucl. Phys. Proc. Suppl.* **91** 331 (*Preprint* hep-ex/0008044)
[15] Aglietta M *et al* 1992 *Nuovo Cimento* A **105** 1793
[16] Fukuda S *et al* 2003 *Nucl. Instrum. Methods* A **501** 418
[17] Boger J *et al* 2000 *Nucl. Instrum. Methods* A **449** 172 (*Preprint* nucl-ex/9910016)
[18] Jacobsen J E, Halzen F and Zas E 1994 *Phys. Rev.* D **49** 1758
Jacobsen J E, Halzen F and Zas E 1996 *Phys. Rev.* D **53** 7359
[19] Bueno A, Gil-Botella I and Rubbia A 2003 *Preprint* hep-ph/0307222
[20] Sharp M *et al* 2002 *Phys. Rev.* D **66** 013012 (*Preprint* hep-ph/0205035)
[21] Cadonati L *et al* 2002 *Astropart. Phys.* **16** 361 (*Preprint* hep-ph/0012082)
[22] Boyd R N *et al* 2003 *Nucl. Phys.* A **718** 222
[23] Jung C K 2000 *Preprint* hep-ex/0005046
[24] Homestake Collaboration 2003 *NUSEL Science Book Preprint* nucl-ex/0308018
[25] Scholberg K 2003 http://mocha.phys.washington.edu/∼int_talk/WorkShops/Neutrino02/Working_Groups/People/Scholberg_K/scholberg_thurs_solarstellarwg.pdf
[26] Hughes S A *et al* 2001 *Preprint* astro-ph/0110349
[27] Astone P *et al* 2003 *Phys. Rev.* D **68** 022001 (*Preprint* astro-ph/0302482)
[28] Arnaud N *et al* 2000 *Phys. Rev.* D **65** 033010 (*Preprint* hep-ph/0109027)
[29] Fukuda Y 2003 *Proc. Origin of Matter and Evolution of Galaxies 2000* (Singapore: World Scientific) p 209
Super-K Collaboration, in preparation
[30] Virtue C 2001 *Nucl. Phys. Proc. Suppl.* **100** 326 (*Preprint* astro-ph/0103324)
SNO Collaboration, in preparation
[31] Fulgione W 1999 *Nucl. Phys. Proc. Suppl.* **70** 469
[32] Fukuda S *et al* 2001 *Phys. Rev. Lett.* **86** 5651 (*Preprint* hep-ex/0103032)
[33] Amaldi E *et al* 1989 *Astron. Astrophys.* **216** 325
[34] Prodi G A *et al* 2000 *Int. J. Mod. Phys.* D **9** 237 (*Preprint* astro-ph/0003106)
[35] Allen Z A *et al* 2000 *Phys. Rev. Lett.* **85** 5046 (*Preprint* astro-ph/0007308)
[36] http://hep.bu.edu/∼schol/workshop/workshop_summary.html
[37] Bahcall J (P.I.) 2003 Observing the next nearby supernova, HST proposal 10264 http://presto.stsci.edu/public/propinfo.html
[38] Robinson L J 1999 *Sky & Telescope* **30** (August)
[39] http://SkyandTelescope.com/observing/proamcollab/astroalert/

New Journal of Physics
An Institute of Physics and Deutsche Physikalische Gesellschaft Journal

BBN for pedestrians

James P Kneller[1] **and Gary Steigman**[2,3,4]

[1] Department of Physics, North Carolina State University, Raleigh, NC 27695-8202, USA
[2] Department of Physics, The Ohio State University, Columbus, OH 43210, USA
[3] Department of Astronomy, The Ohio State University, Columbus, OH 43210, USA
E-mail: steigman@mps.ohio-state.edu

New Journal of Physics **6** (2004) 117
Received 14 June 2004
Published 17 September 2004
Online at http://www.njp.org/
doi:10.1088/1367-2630/6/1/117

Abstract. The simplest, 'standard' model of Big Bang nucleosynthesis (SBBN) assumes three light neutrinos ($N_\nu = 3$) and no significant electron neutrino asymmetry ($\nu_e - \bar{\nu}_e$ asymmetry parameter $\xi_e \equiv \mu_e/kT$, where μ_e is the chemical potential of ν_e) leaving only one adjustable parameter: the baryon to photon ratio $\eta \equiv n_B/n_\gamma$. The primordial abundance of any one nuclide can, therefore, be used to measure η and the value derived from the observationally inferred primordial abundance of deuterium closely matches that from current non-BBN data, primarily from the WMAP survey. However, using this same estimate for η, there is a tension between the SBBN-predicted abundances of ^{4}He and ^{7}Li and their current, observationally inferred primordial abundances, suggesting that N_ν may differ from the standard model value of three and/or that ξ_e may differ from zero (or, that systematic errors in the abundance determinations have been underestimated or overlooked). The differences are not large and the allowed ranges of the BBN parameters (η, N_ν and ξ_e) permitted by the data are quite small. Within these ranges, the BBN-predicted abundances of D, ^{3}He, ^{4}He, and ^{7}Li are very smooth, monotonic functions of η_{10}, $\Delta N_\nu \equiv N_\nu - 3$ and ξ_e. As a result, it is possible to describe the dependence of these abundances (or powers of them) upon the three parameters by simple, *linear* fits which, over their ranges of applicability, are accurate to a few per cent or even better. The fits presented here have *not* been maximized for their accuracy but, rather, for their *simplicity*. To identify the ranges of applicability and relative accuracies, they are compared with detailed BBN calculations; their utility is illustrated with several examples.

[4] Author to whom all correspondence should be addressed.

PII: S1367-2630(04)82025-1
© IOP Publishing Ltd and Deutsche Physikalische Gesellschaft

Given the tension within BBN, these fits should prove useful in facilitating studies of the viability of various options for non-standard physics and cosmology, prior to undertaking detailed BBN calculations.

Contents

1. Big Bang nucleosynthesis **2**
1.1. The baryon density η . . . 3
1.2. Early-Universe expansion rate S . . . 3
1.3. Lepton asymmetry ξ . . . 5
1.4. BBN predictions . . . 5
2. Observed primordial abundances **6**
3. Fits **8**
3.1. ^{4}He . . . 8
3.2. D . . . 9
3.3. ^{3}He . . . 12
3.4. ^{7}Li . . . 12
4. Applications **12**
4.1. SBBN . . . 13
4.2. Non-standard expansion $S \neq 1, \xi_e = 0$ . . . 14
4.3. Non-zero lepton number $\xi_e \neq 0, S = 1$ . . . 17
4.4. Non-standard expansion rate and non-zero lepton number $S \neq 1, \xi_e \neq 0$ . . . 18
5. Summary and conclusions **21**
Acknowledgments **21**
References **21**

1. Big Bang nucleosynthesis

Shortly after the emergence of the Big Bang model, it was realized that conditions were ripe during the early Universe for a brief period of nucleosynthesis. Just as in every other setting where nuclear reactions occur, the yields of the emerging nuclides are governed by three environmental characteristics: the duration of the event, the density of the reactants, and their thermal properties. A brief, dilute and cool environment would yield a very different set of abundances compared with those that would emerge if Big Bang nucleosynthesis (BBN) had been long-lasting, dense and hot. Although it is possible to characterize BBN in such broad generality (with some success; see, e.g. [1, 2]), the paradigm most frequently encountered uses the Friedman equation to relate the BBN expansion rate, H, to the thermal properties of the particles present at that epoch

$$H^2 = \frac{8\pi G_N}{3}\rho, \tag{1}$$

with G_N being Newton's constant and ρ the total energy density. The standard model of particle physics provides the candidate particles whose energy density contribute to ρ, but it is possible that this may fall short of the actual particle content at that time. Even so, after blueshifting

the currently observed Cosmic Background Radiation (CBR) energy density back to the epoch of BBN, it emerges that the energy density of the Universe was dominated during BBN by the relativistic particles. The thermal properties of each particle species are described by a temperature and a chemical potential, but thermal coupling among the constituents equilibrates the temperatures while chemical coupling relates the chemical potentials. Charge neutrality provides additional relations. This reduces the number of independent quantities with the result that BBN can be described by a minimal set of parameters, typically taken to be: the density of the nucleons/baryons, the chemical potentials of the three, active neutrinos, and the energy density in unaccounted particles (and/or additional terms on the right-hand side of (1)). In what follows, the role of each is discussed and the parameters used to describe them are introduced.

1.1. The baryon density η

The simplest, 'standard' model for BBN (SBBN) sets any 'extra' energy density and the chemical potentials of the three neutrinos to zero leaving just the density of the baryons, n_{B}, as the only adjustable/free parameter. But since n_{B} drops as the Universe expands, it is useful to introduce the baryon-to-photon ratio $\eta \equiv n_{\mathrm{B}}/n_{\gamma}$ ($\eta_{10} \equiv 10^{10}\eta$), since this quantity is dimensionless and constant, except during the period of $\mathrm{e}^{\pm}$ annihilation.

From an inspection of the flow of nuclei through the reaction network in SBBN it can be seen that the primordial abundances of the relic light nuclides D, ^{3}He and ^{7}Li are determined by the competition between the nuclear production and destruction rates, which scale with the nucleon density. To an extent which varies from nuclide to nuclide, these three nuclei are all potential baryometers. In contrast, as the light nucleus with the largest binding energy per nucleon, the ^{4}He relic abundance is relatively *insensitive* to the magnitudes of the nuclear reaction rates because, for the range in baryon density of interest here, they are sufficiently rapid to burn nearly all neutrons present initially to ^{4}He. The sensitivity it does possess is due to the role that η plays in determining the temperature at which the D abundance becomes significant: it is the build up of a large D abundance that leads to the most rapid phase of nuclear burning in BBN and the termination of free neutron decay as an important process.

1.2. Early-Universe expansion rate S

The early Universe is radiation-dominated, with its expansion rate determined by the energy density in the relativistic particles, ρ_{R}. Prior to BBN, e.g., at a temperature of a few MeV, before $\mathrm{e}^{\pm}$ annihilation, the standard model of particle physics provides photons, $\mathrm{e}^{\pm}$ pairs and three flavours of left-handed (i.e., one helicity state) neutrinos (and their right-handed, antineutrinos) as constituents of this dominant component. With all chemical potentials set to zero, the energy densities are related by thermal equilibrium so that

$$\rho_{\mathrm{R}} = \rho_{\gamma} + \rho_{e} + 3\rho_{\nu} = \tfrac{43}{8}\rho_{\gamma}, \tag{2}$$

where ρ_{γ} is the energy density in the CBR photons (which, today, have redshifted to become the CBR photons observed at a temperature of 2.7 K). In this case, the time–temperature relation (derived from the Friedman equation) is,

$$\text{Pre-e}^{\pm}\text{ annihilation:} \quad tT_{\gamma}^{2} = 0.738\,\mathrm{MeV}^{2}\,\mathrm{s}. \tag{3}$$

In SBBN it is often assumed that the neutrinos are fully decoupled prior to $e^{\pm}$ annihilation and that they do not share in the energy transferred from the annihilating $e^{\pm}$ pairs to the CBR photons. In this approximation, the photons are hotter than the neutrinos in the post-$e^{\pm}$ annihilation universe by a factor $T_\gamma/T_\nu = (11/4)^{1/3}$, and the relativistic energy density is

$$\rho_{\rm R} = \rho_\gamma + 3\rho_\nu = 1.68\rho_\gamma, \tag{4}$$

corresponding to a new time–temperature relation,

$$\text{Post-e}^{\pm}\text{ annihilation:}\quad tT_\gamma^2 = 1.32\,\text{MeV}^2\,\text{s}. \tag{5}$$

In quite general terms, one possible consequence of new physics beyond the standard model could be a non-standard, early Universe expansion rate, parametrized by an expansion rate factor S,

$$H \to H' \equiv SH. \tag{6}$$

Although the introduction of S here is quite general, in practice one must adopt a specific scheme through which this occurs. Such a non-standard expansion rate might, but need not, be due to a change in the energy density: a change in the strength of gravity would also alter the expansion rate of the early Universe [3] as would non-standard, higher-dimensional models which modify the expansion rate versus energy density relation (the Friedman equation (1)) in our $(3+1)$-dimensional world [12]. Different gravitational couplings for fermions and bosons [4] would have similar effects. These different mechanisms for implementing a non-standard expansion rate are not necessarily equivalent.

If consideration is restricted to only the possibility of additional energy density, then

$$\rho_{\rm R} \to \rho'_{\rm R} \equiv S^2\rho_{\rm R}, \tag{7}$$

where $\rho'_{\rm R} = \rho_{\rm R} + \rho_X$ and X identifies the extra component. With the further restriction that X are also relativistic, this extra component behaves just like an additional neutrino though we emphasize that 'X' need not be additional flavours of active or sterile neutrinos. In these circumstances S is a constant prior to $e^{\pm}$ annihilation and it is convenient to account for the extra contribution to the standard-model energy density by normalizing it to that of an 'equivalent' neutrino flavour [11], so that

$$\rho_X \equiv \Delta N_\nu \rho_\nu = \tfrac{7}{8}\Delta N_\nu \rho_\gamma. \tag{8}$$

For this case,

$$S \equiv S_{pre} = (1 + \tfrac{7}{43}\Delta N_\nu)^{1/2}. \tag{9}$$

However, the expansion rate is more fundamental to BBN than is ΔN_ν, so we parametrize this class of non-standard models using S (but, for comparison, we will often also quote the corresponding value of ΔN_ν as given by (9)).

Not every additional energy density component can be accommodated this way since we require that ρ_X is proportional to ρ_ν as the Universe evolves. An example that breaks this mold is if the 'X' were not 'decoupled', in the sense that X shared in the energy released

when the $e^{\pm}$ pairs annihilate. Other examples are found within some quintessence models [3], [5]–[7].

As we discussed above, D, ^{3}He and ^{7}Li act as the principal baryometers for BBN since the ^{4}He relic abundance does not vary considerably with η. But ^{4}He is very sensitive to the competition between the weak interaction rates (interconverting neutrons and protons) and the universal expansion rate which, during the early, radiation-dominated evolution is fixed by the energy density in relativistic particles ('radiation'). As a result, while D, ^{3}He and ^{7}Li probe the baryon density, consistency between their abundances and that of ^{4}He *tests* the standard model and provides *constraints* on (and, perhaps, hints of) physics beyond the standard model.

1.3. Lepton asymmetry ξ

The baryon-to-photon ratio $\eta = n_{\rm B}/n_\gamma$ provides a dimensionless measure of the universal baryon asymmetry which is very small ($\eta \lesssim 10^{-9}$). By charge neutrality, the asymmetry in the charged leptons must also be of this order. However, there are no direct observational constraints (see [10, 13, 14] and further references therein), on the magnitude of any asymmetry among the neutral leptons (neutrinos). A dimensionless measure of the magnitude of the neutral lepton asymmetry is provided by ξ, the ratio of the neutral lepton chemical potential to the temperature (in energy units): $\xi \equiv \mu/kT$. For example, for a neutrino flavour α, the asymmetry ('neutrino degeneracy') L_α, between the numbers of ν_α and $\bar{\nu}_\alpha$ is

$$L_\alpha \equiv \frac{n_{\nu_\alpha} - n_{\bar{\nu}_\alpha}}{n_\gamma} = \frac{\pi^2}{12\zeta(3)}\left(\xi_\alpha + \frac{\xi_\alpha^3}{\pi^2}\right). \tag{10}$$

Note that for $\xi_\alpha \ll 1$, $L_\alpha \approx 0.684\xi_\alpha$. Mixing among the three active neutrinos (ν_e, ν_μ, ν_τ) ensures that at the time of BBN, $L_e \approx L_\mu \approx L_\tau$ ($\xi_e \approx \xi_\mu \approx \xi_\tau$) [15].

While any neutrino degeneracy ($\xi_\alpha < 0$ as well as > 0) will *increase* the energy density in the relativistic neutrinos and, hence, the early Universe expansion rate, the discussion here is limited to sufficiently small values of ξ_α so that the effect on S of a non-zero ξ_α is negligible. Even so, a non-zero but relatively small asymmetry between *electron* type neutrinos and antineutrinos ($\xi_e \gtrsim 10^{-2}$), while large compared with the baryon asymmetry, can still have a significant impact on the early Universe. The interconversion of neutrons to protons is affected by the ν_e so that any non-zero ξ_e will alter the n/p ratio, thereby affecting the yields of the light nuclides formed during BBN.

Of the light nuclei, the neutron limited ^{4}He abundance is the most sensitive to ξ_e and, together with the D, ^{3}He, and ^{7}Li baryometers, again provides a test of the consistency of the standard model.

1.4. BBN predictions

The BBN-predicted D, ^{4}He and ^{7}Li isoabundance curves for S versus η and for ξ_e versus η are shown in figures 1 and 2. For D, the curves represent the ratio (to hydrogen) by number $y_{\rm D} \equiv 10^5({\rm D/H}) = 2, 3, 4$; similarly, for ^{7}Li, the curves correspond to $y_{\rm Li} \equiv 10^{10}({\rm Li/H}) = 3, 4, 5$; for ^{4}He, the curves correspond to the mass fraction $Y_{\rm P} = 0.23, 0.24, 0.25$. These figures show clearly that D and ^{7}Li are good baryometers, sensitive to η, while ^{4}He is a good chronometer, sensitive to S, as well as a good leptometer, sensitive to ξ_e.

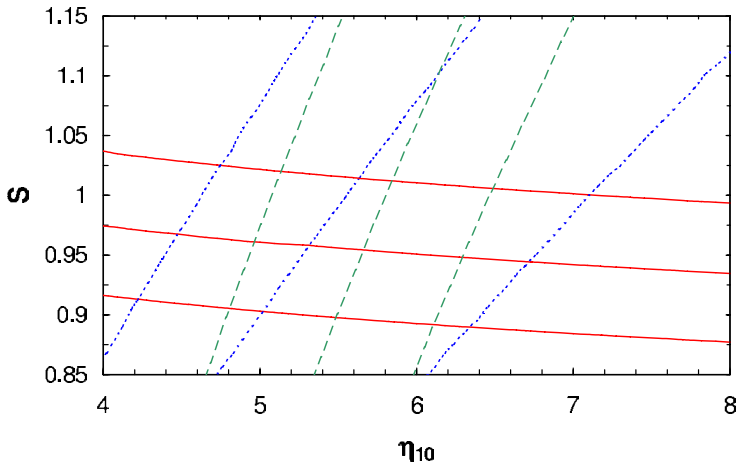

Figure 1. BBN-predicted isoabundance curves for D (dotted), ^{7}Li (dashed) and ^{4}He (solid) in the expansion-rate parameter (S), baryon density parameter (η) plane. From left to right, for D, $y_{\rm D} = 4, 3, 2$, while for ^{7}Li, $y_{\rm Li} = 3, 4, 5$. For ^{4}He, from bottom to top, $Y_{\rm P} = 0.23, 0.24, 0.25$.

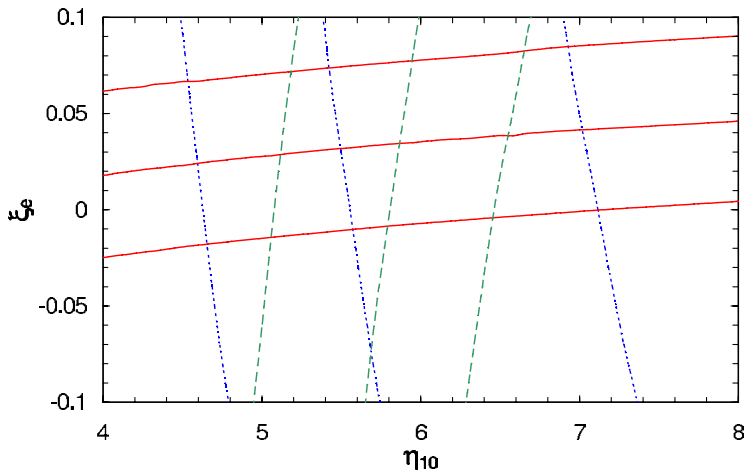

Figure 2. BBN-predicted isoabundance curves for D (dotted), ^{7}Li (dashed) and ^{4}He (solid) in the lepton asymmetry parameter (ξ_e), baryon density parameter (η) plane. From left to right, for D, $y_{\rm D} = 4, 3, 2$, and for ^{7}Li, $y_{\rm Li} = 3, 4, 5$. For ^{4}He, from top to bottom, $Y_{\rm P} = 0.23, 0.24, 0.25$.

2. Observed primordial abundances

The success of BBN relies on its ability to predict the observed primordial abundances and, conversely, to learn about the cosmological parameters using these same abundances. However, the comparison of predictions and observations is far from trivial because of the further processing of the nuclei since the end of BBN.

Deuterium is the baryometer of choice, primarily because BBNs observed abundance should have only decreased as gas is cycled through stars where D is burned to heavier, more tightly bound, nuclei [18]. As a result, D observed anywhere in the Universe, at any time during its

evolution, should provide a *lower* bound to its primordial abundance. Further, the deuterium observed in the high redshift, low metallicity QSO absorption line systems (QSOALS) should be very nearly primordial. In contrast, the post-BBN evolution of ^{3}He and of ^{7}Li are considerably more complicated, involving the competition between production, destruction and survival. As a result, at least so far, the current, locally observed (in the Galaxy) abundances of these nuclides have been of less value than that of deuterium. Indeed, over the range in y_D to be adopted below, the primordial abundance of ^{3}He is predicted to lie in the narrow range, $1.0 \lesssim y_3 \lesssim 1.1$, in excellent agreement with that inferred from galactic observations [19]. Thus, ^{3}He provides similar, but less compelling constraints than does D. While current estimates of primordial lithium, based on observations of very metal-poor (nearly primordial) stars, are problematic, ^{7}Li is retained here to highlight this challenge. For ^{4}He the post-BBN evolution is straightforward, but difficult to quantify at a sufficient level of accuracy. As gas is cycled through stars, hydrogen is burned to helium; only a very small fraction of the helium is burned to heavier nuclei. If material is sampled 'here and now', a correction based on models of the chemical evolution of galaxies would need to be made for post-BBN produced ^{4}He. To avoid the model-dependent uncertainties associated with such corrections, which would surely overwhelm the observational errors, the best strategy is to search for ^{4}He in the least evolved objects, in this case the metal-poor, extragalactic H_{II} regions.

Inferring the primordial D abundance from the QSOALS has not been without its difficulties, with some of the original abundance claims having been withdrawn or revised. Presently, there are 5–6 QSOALS with reasonably firm deuterium detections [20]–[25]. However, there is significant dispersion among the abundances and the data fail to reveal the anticipated 'deuterium plateau' at low metallicity or at high redshift [26]. Here we adopt the five abundance determinations collected in the recent paper of Kirkman *et al* [25]. The weighted mean value of y_D is 2.6.[5] The dispersion among these five data points is very large, resulting in a $\chi^2 = 15.3$ for four degrees of freedom, suggesting that one or more of these abundance determinations may be in error, or affected by unidentified and unaccounted systematic errors. To allow for this, we follow the approach advocated by [22, 25] and adopt for the uncertainty in y_D the dispersion among the data points divided by the square root of the number of them. Thus, the primordial abundance of deuterium to be used here is chosen to be $y_D = 2.6 \pm 0.4$.

A somewhat less than clear situation also exists for the determinations of the primordial abundance of ^{4}He. There have been two, largely independent, estimates of Y_P based on analyses of large data sets of low-metallicity, extragalactic H_{II} regions. The 'IT' [27, 28] estimate of Y(IT) $= 0.244 \pm 0.002$, and the 'OS' determination [29]–[31] of Y(OS) $= 0.234 \pm 0.003$ differ by nearly 3σ. Very recently, IT have expanded their original data set and attempted to account for some (but not all) of the systematic uncertainties [32]; see e.g., [33]. For their full data set of 89 H_{II} regions, IT find $Y_P = 0.2429 \pm 0.0009$. To provide a contrast with previous results, this value is adopted for our analysis here.

As with ^{4}He, the abundance of ^{7}Li grows in the course of post-BBN evolution, with lithium being produced in some stars (at some distinct times in their evolution) as well as in cosmic ray spallation reactions (where CNO nuclei are broken down to, among other nuclides, lithium). So, as for D and ^{4}He, lithium should be observed in the least evolved, most metal-poor objects. While lithium has been observed in the Sun and in the solar system, as well as in the interstellar

[5] This differs from the result quoted in Kirkman *et al* [25] because they have taken the mean of $\log(y_D)$ and then used it to infer y_D ($y_D \equiv 10^{\langle \log(y_D) \rangle}$).

medium of the Galaxy, these provide evolved, metal-enriched samples of little use in estimating the primordial abundance of lithium. The most relevant data come from studies of the very metal-poor stars in the halo of the Galaxy or in globular clusters. While this material should be very nearly primordial, it must be kept in mind that these are observations of the surfaces of the oldest stars in the Galaxy. If, during the course of their evolution, the surface material of these stars were mixed with the lithium-depleted interiors, the currently observed surface lithium abundances may not reflect the lithium abundances in these stars at their birth. The most recent data from studies of halo stars is from Ryan *et al* [34] who find $y_{\rm Li} = 1.23^{+0.34}_{-0.16}$. In contrast, and in some conflict with this result, Bonifacio *et al* [35] derive from a sample of Globular Cluster stars, $y_{\rm Li} = 2.19^{+0.46}_{-0.38}$.

Below we compare each of these estimates of the primordial abundances with the BBN predictions, standard as well as non-standard, fixed by the adopted D and ^{4}He abundances.

3. Fits

The non-linear, coupled differential equations of BBN are not conducive to analytic solution so that detailed comparison of the theoretical predictions with the observed/derived abundances of the light nuclei can only be achieved after resorting to a lengthy process of numerical calculations. This necessity blurs the connection between the parameter set $\{\eta, S, \xi_e\}$ and the data set $\{y_{\rm D}, Y_{\rm P}, y_{\rm Li}\}$, and, conversely, the parameter values the data recommend. Yet, it is clear from figures 1 and 2 that the relic light nuclide abundances are smoothly varying, monotonic functions of η, S and ξ_e, so it is not surprising that over limited but substantial ranges, simple relations exist between the predicted abundances and these parameters. While the BBN-predicted primordial abundances are certainly *not* linearly related to the baryon density, the expansion rate or the lepton asymmetry, our goal here is to find simple, linear fits to the predicted abundances (or powers of them) as functions of these parameters (to be defined more carefully below). These fits work well, sometimes remarkably well, over limited ranges in the parameters (and/or over limited ranges in the predicted abundances of D, ^{4}He, and ^{7}Li).

Since the domains over which our fits are applicable are restricted, we must focus upon specific values for η, S and ξ_e. The 'target' value/range of the baryon density is motivated by the (non-BBN) results from the WMAP constraints from the CBR temperature fluctuations [8], where, for SBBN, $\eta_{10} = 6.14 \pm 0.25$. As shown in [9, 10] (and references therein), this estimate is little affected by a non-standard expansion rate and/or any (small) lepton asymmetry. As a result, a limited range in η_{10}, centred around $\eta_{10} = 6$, is chosen here: $4 \leqslant \eta_{10} \leqslant 8$. For our simple, linear fits to the BBN-predicted abundances as a function of S to be sufficiently accurate, we must restrict the range in S. This is the case for the fits we adopt provided that $0.85 \leqslant S \leqslant 1.15$ corresponding to $-1.7 \lesssim \Delta N_\nu \lesssim 2.0$ ($1.3 \lesssim N_\nu \lesssim 5.0$). For an 'interesting' range in ξ_e over which the fits are reasonably accurate, $-0.1 \leqslant \xi_e \leqslant 0.1$ is adopted.

Before presenting our fits, it is worth re-emphasizing that figures 1 and 2 show clearly that D and ^{7}Li are good baryometers, sensitive to η, while ^{4}He is a good chronometer, sensitive to S, as well as a good leptometer, sensitive to ξ_e.

3.1. ^{4}He

The ^{4}He abundance (mass fraction: $Y_{\rm P}$) is very insensitive to the baryon density at BBN, varying roughly logarithmically with η over the range of η adopted here ($4 \lesssim \eta_{10} \lesssim 8$). Thus, while for

SBBN ($S = 1$ and $\xi_e = 0$) to a very good approximation $Y = Y(\eta) \propto \ln \eta$, we prefer to find a *linear* relation between Y_P and η. Motivated by simplicity, the following linear fit for Y versus η agrees with the SBBN-predicted abundance to within 0.0006 ($\lesssim 0.25\%$) over our adopted range in η.

$$Y_P^{FIT} \equiv 0.2384 + 0.0016\eta_{10} = 0.2384 + \eta_{10}/625. \tag{11}$$

We note that over the same range in η this fit also agrees with the BNT [16] predictions for Y_P to within 0.0002 ($\lesssim 0.1\%$) or better. While the accuracy of this fit is certainly not perfect, the difference is still smaller than the current errors in the observationally inferred primordial value of Y_P.

As with the Y_P–η relation, the following linear fits to the Y_P–S and ξ_e relations work very well over the adopted parameter ranges (see figures 1–4).

$$Y_P^{FIT} \equiv 0.2384 \pm 0.0006 + 0.0016\eta_{10} + 0.16(S-1) - 0.23\xi_e. \tag{12}$$

Notice that for fixed η_{10} and $\Delta N_\nu \ll 1$, $\Delta Y \approx 0.013\Delta N_\nu$.

It is convenient to rewrite this fit of $Y_P(\eta, S, \xi_e)$ (given by (12)) in a form which will facilitate comparison with comparable fits to the $y_D(\eta, S, \xi_e)$ and $y_{Li}(\eta, S, \xi_e)$ relations. To this end, we introduce η_{He}, defined as follows:

$$\eta_{He} \equiv 625(Y_P - 0.2384 \pm 0.0006). \tag{13}$$

Then,

$$\eta_{He} = \eta_{10} + 100(S-1) - \tfrac{575}{4}\xi_e. \tag{14}$$

The meaning of η_{He} is clear; η_{He} is the SBBN ($S = 1$ and $\xi_e = 0$) value of η_{10} corresponding to the adopted value of Y_P. Once Y_P is chosen, the resulting value of η_{He} provides a linear constraint on the combination of η, S, and ξ_e shown in (14). As may be seen in figures 3 and 4, this fit works well (for $4 \leqslant \eta_{10} \leqslant 8$) for $0.23 \lesssim Y_P \lesssim 0.25$, corresponding to $-5 \lesssim \eta_{He} \lesssim 7$.

Adopting the IT [32] value $Y_P = 0.2429 \pm 0.0009$ (see section 2), leads to $\eta_{He} = 2.81 \pm 0.68$ ($\Omega_B^{He} h^2 = 0.0103 \pm 0.0025$). Note that if, indeed, the very small IT error estimate is realistic, then helium is a competitive baryometer to deuterium! The comparisons of this fit with the results from our BBN code are shown in figures 3 and 4. As these figures and equation (14) show, η_{He}, which is 'linear' in Y_P, is very sensitive to S and ξ_e, but relatively insensitive to η.

3.2. D

Over the restricted range in η under study here, the deuterium abundance $y_D \equiv 10^5(D/H)$, is well described by a power law in η with $y_D \propto \eta^{-1.6}$. For our adopted range of η, $y_D = y_D(\eta)$ fits well by

$$y_D^{FIT} \equiv 46.5\eta_{10}^{-1.6}. \tag{15}$$

While the true y_D–η relation is not precisely a power law, for $4 \lesssim \eta_{10} \lesssim 8$, this fit is accurate (compared with our detailed SBBN calculation) to better than 1%, three times smaller than the

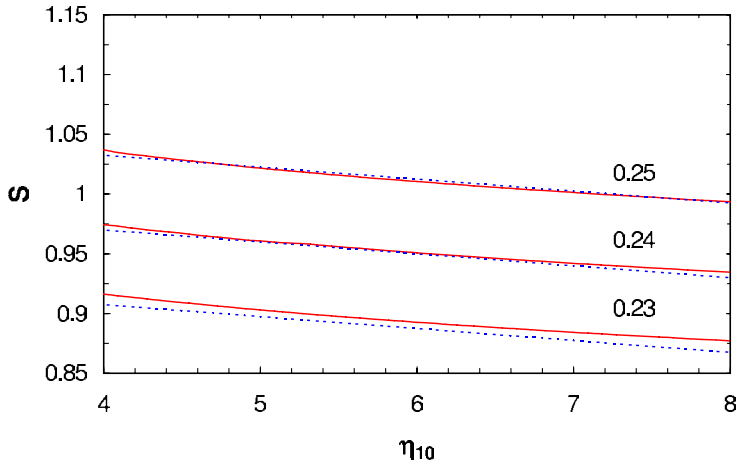

Figure 3. BBN-predicted isoabundance curves for ^{4}He in the expansion-rate parameter (S), baryon density parameter (η) plane. From bottom to top, $Y_P = 0.23, 0.24, 0.25$. The solid curves are the BBN-predicted results, while the dotted curves are our fits (see the text).

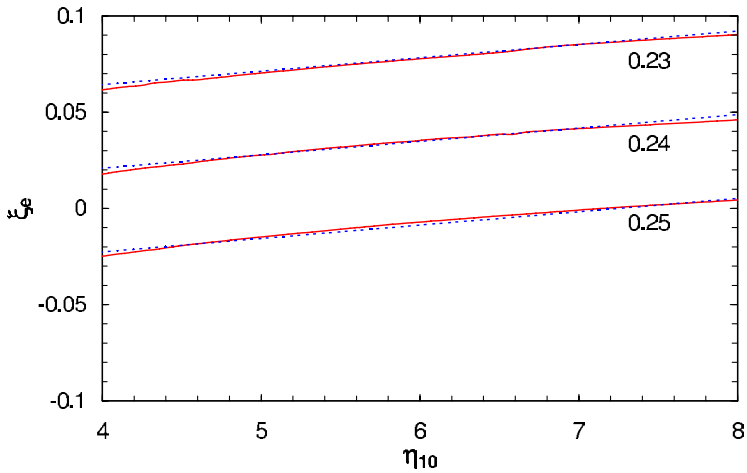

Figure 4. BBN-predicted isoabundance curves for ^{4}He (solid) in the lepton asymmetry parameter (ξ_e), baryon density parameter (η) plane. From top to bottom, $Y_P = 0.23, 0.24, 0.25$. The solid curves are the BBN-predicted results, while the dotted curves are our fits (see the text).

$\sim$3% BBN uncertainty estimated by BNT [16]; this fit (and our SBBN calculation) agrees with the BNT prediction to 2% or better over this range in η. We note that different BBN codes are largely independent and often use somewhat different nuclear reaction data sets, so that the *differences* in their predicted abundances can provide an estimate of the overall uncertainties.

In analogy with η_{He} defined by the ^{4}He abundance (see (12)), it is useful to define a similar parameter, η_D, for D (including a 3% error estimate),

$$\eta_D \equiv \left(\frac{46.5(1 \pm 0.03)}{y_D}\right)^{1/1.6}. \tag{16}$$

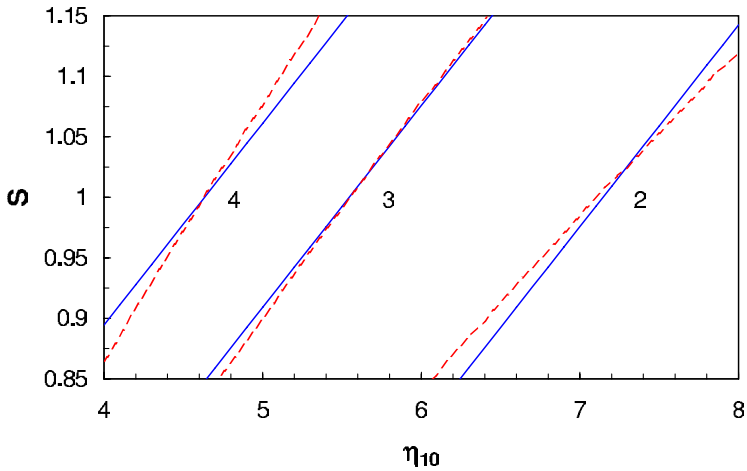

Figure 5. BBN-predicted isoabundance curves for D in the expansion-rate parameter (S), baryon density parameter (η) plane. From left to right, $y_{\rm D} = 4$, 3, 2. The solid curves are the BBN-predicted results, while the dotted curves are our fits (see the text).

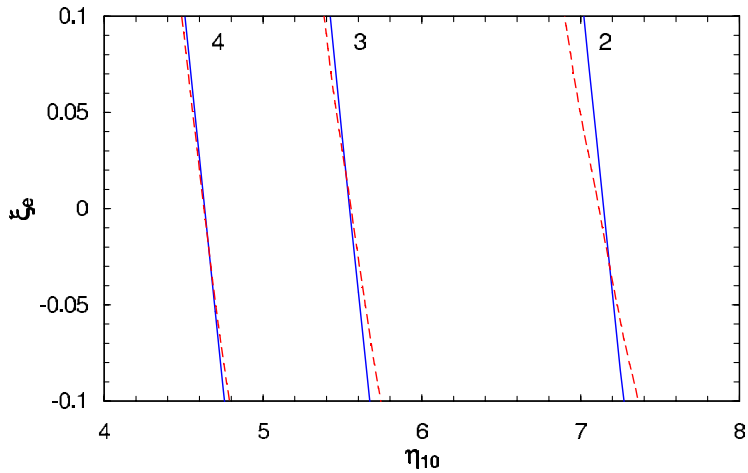

Figure 6. BBN-predicted isoabundance curves for D in the lepton asymmetry parameter (ξ_e), baryon density parameter (η) plane. From left to right, $y_{\rm D} = 4$, 3, 2. The solid curves are the BBN-predicted results, while the dotted curves are our fits (see the text).

Substituting the abundance estimate (section 2) for primordial D into this equation leads to our adopted value for $\eta_{\rm D} = 6.06^{+0.68}_{-0.53}$ ($\Omega_{\rm B}^{\rm D} h^2 = 0.0221^{+0.0025}_{-0.0019}$).

For the adopted ranges in η, S and ξ_e, a simple linear relation which provides a good fit to $\eta_{\rm D}$ (see figures 5 and 6) is,

$$\eta_{\rm D} = \eta_{10} - 6(S-1) + \tfrac{5}{4}\xi_e. \tag{17}$$

As may be seen from figures 5 and 6, this fit works quite well (for $4 \leqslant \eta_{10} \leqslant 8$) for $2 \lesssim y_{\rm D} \lesssim 4$, corresponding to $5 \lesssim \eta_{\rm D} \lesssim 7$. Given the restricted ranges for S and ξ_e, it is clear from figures 5 and 6 and equation (17) that D is a sensitive baryometer ($\eta_{\rm D} \approx \eta_{10}$).

3.3. ^3He

The dependence of the BBN-predicted abundance of ^{3}He on the baryon density, expansion rate, and lepton asymmetry is similar to that of D, but ^{3}He is considerably less sensitive to them than is D. Indeed, over the parameter ranges adopted here, the ^{3}He abundance is well fit by $y_3 \propto y_{\rm D}^{0.35}$. As a result, along with its more complicated post-BBN evolution, ^{3}He provides complementary but less compelling constraints than does D. In our subsequent analysis, ^{3}He is set aside in favour of D.

3.4. ^7Li

As with D, the ^{7}Li abundance[6] is well described by a power law in η over the range in baryon abundance explored here: $y_{\rm Li} \equiv 10^{10}({\rm Li/H}) \propto \eta^2$. The following fit agrees with the BBN predictions to better than 3% over the adopted range in η:

$$y_{\rm Li}^{FIT} \equiv \frac{\eta_{10}^2}{8.5}. \tag{18}$$

While this fit predicts slightly smaller lithium abundances compared with those of BNT [16], the differences are at the 5–8% level, small compared with the BNT uncertainty estimates as well as those of Hata *et al* [17] (∼10–20%).

In analogy with $\eta_{\rm D}$ and $\eta_{\rm He}$ defined above, we introduce $\eta_{\rm Li}$ (allowing for a 10% uncertainty), defined by,

$$\eta_{\rm Li} \equiv (8.5(1 \pm 0.1)y_{\rm Li})^{1/2}. \tag{19}$$

Using the Ryan *et al* [34] estimate (section 2) $y_{\rm Li} = 1.23^{+0.34}_{-0.16}$, $\eta_{\rm Li} = 3.23^{+0.44}_{-0.28}$ ($\Omega_{\rm B}^{\rm Li} h^2 = 0.0118^{+0.0016}_{-0.0010}$), while the Bonifacio *et al* [35] result of $y_{\rm Li} = 2.19^{+0.46}_{-0.38}$ gives $\eta_{\rm Li} = 4.31^{+0.48}_{-0.46}$ ($\Omega_{\rm B}^{\rm Li} h^2 = 0.0157 \pm 0.0017$).

A simple, linear relation for $\eta_{\rm Li}$ as a function of η, S and ξ_e, which works reasonably well over the adopted parameter ranges (see figures 7 and 8) is,

$$\eta_{\rm Li} = \eta_{10} - 3(S-1) - \tfrac{7}{4}\xi_e. \tag{20}$$

As figures 7 and 8 reveal, this fit works well (for $4 \leqslant \eta_{10} \leqslant 8$) for $3 \lesssim y_{\rm Li} \lesssim 5$, corresponding to $5 \lesssim \eta_{\rm Li} \lesssim 7$. We note that this fit breaks down for $y_{\rm Li} \lesssim 2$ ($\eta_{\rm Li} \lesssim 4$). In addition, figures 7 and 8, along with (20), show that, as is the case for deuterium, lithium can be an excellent baryometer (for the restricted ranges of S and ξ_e, $\eta_{\rm Li} \approx \eta_{10}$).

4. Applications

In this section the application of our simple, linear fits (among η, S, ξ_e and $y_{\rm D}$, $y_{\rm Li}$, $Y_{\rm P}$) is illustrated by considering several standard and non-standard BBN options.

[6] It is common in the astronomical literature to present the lithium abundance logarithmically: $[{\rm Li}] \equiv 12 + \log({\rm Li/H}) = 2 + \log(y_{\rm Li})$.

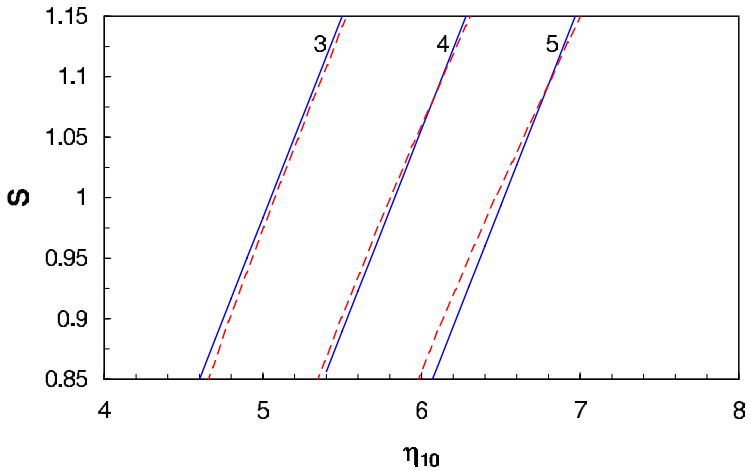

Figure 7. BBN-predicted isoabundance curves for ^{7}Li in the expansion-rate parameter (S), baryon density parameter (η) plane. From left to right, $y_{\rm Li} = 3$, 4, 5. The solid curves are the BBN-predicted results, while the dotted curves are our fits (see the text).

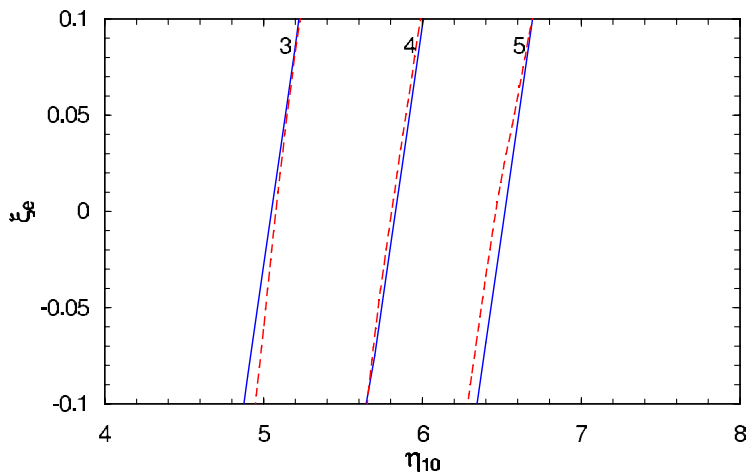

Figure 8. BBN-predicted isoabundance curves for ^{7}Li in the lepton asymmetry parameter (ξ_e), baryon density parameter (η) plane. From left to right, ^{7}Li, $y_{\rm Li} = 3$, 4, 5. The solid curves are the BBN-predicted results, while the dotted curves are our fits (see the text).

4.1. SBBN

As a first application of our simple fits to the predicted primordial abundances, consider the case of SBBN ($S = 1$, $\xi_e = 0$). In this case, the predicted abundances depend on only one adjustable parameter, the baryon abundance parameter η. For SBBN we may adopt the WMAP-inspired value [8] of $\eta_{10} = 6.14 \pm 0.25$ ($\Omega_{\rm B}h^2 = 0.0224 \pm 0.009$). For $S = 1$ and $\xi_e = 0$ we expect, for SBBN

$$\eta_{\rm D} = \eta_{\rm He} = \eta_{\rm Li} = \eta_{10}. \tag{21}$$

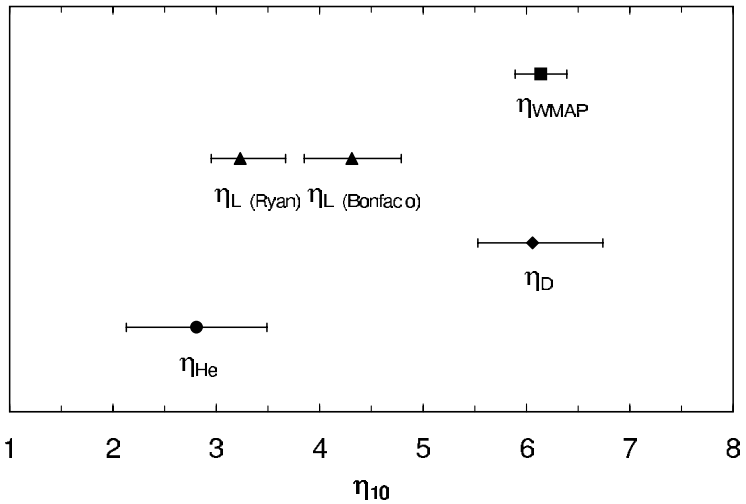

Figure 9. The baryon abundance parameters (see section 3) corresponding to the D, ^{4}He and ^{7}Li abundances adopted here (from section 2), and from WMAP [8].

It is clear from figure 9, using the abundances identified in section 2, that (21) is not satisfied ($\eta_{\rm D} \approx \eta_{10} \neq \eta_{\rm He} \approx \eta_{\rm Li}$). However, SBBN does work for deuterium: $\eta_{\rm D} = 6.06^{+0.68}_{-0.53} \approx \eta_{10} = 6.14 \pm 0.25$. In addition, we note that for the WMAP baryon abundance the SBBN-predicted value of the ^{3}He primordial abundance, $1.1 \pm 0.1 \times 10^{-5}$, is in excellent agreement with that inferred from the study of Galactic $H_{\rm II}$ regions [19]. The problems arise for ^{4}He and ^{7}Li.

For ^{4}He, the recent Izotov and Thuan [32] determination of the primordial mass fraction leads to $\eta_{\rm He} = 2.81 \pm 0.68$ (section 3.1), which is $\sim 6\sigma$ below the WMAP baryon density parameter. While Izotov and Thuan have attempted to account for some of the potential systematic errors in their $Y_{\rm P}$ determination, it may well be that they have underestimated the residual error; see e.g. [33]. If not, this disagreement may provide a hint of new physics beyond the standard model ($S \neq 1$ and/or $\xi_e \neq 0$).

As may be seen from figures 1, 2, 5–8, along with (17) and (20), the BBN-predicted abundance of ^{7}Li is closely tied to that of D, $y_{\rm Li} \approx 4.3(y_{\rm D}/2.6)^{-5/4}$. For $y_{\rm D}$ in its observed range (and/or for η_{10} in the WMAP range), $y_{\rm Li} \approx 4$–5 ([Li] ≈ 2.6–2.7). For the WMAP baryon abundance, the SBBN prediction is $y_{\rm Li} = 4.44^{+0.58}_{-0.57}$, to be compared with the halo star estimate from [34] of $y_{\rm Li} = 1.23^{+0.34}_{-0.16}$, or with the globular cluster estimate from Bonifacio *et al* [35] of $y_{\rm Li} = 2.19^{+0.46}_{-0.38}$. The SBBN-predicted ^{7}Li abundance is much higher, by factors of $\sim$2–4, than those inferred from the studies of the oldest halo and/or globular cluster stars in the Galaxy. It will be seen in more detail below that it is unlikely that any of the 'simple' non-standard effects ($S \neq 1$, $\xi_e \neq 0$) can resolve this conflict (since the ^{7}Li and D abundances are so tightly coupled). It may well be that for these oldest stars in the Galaxy, mixing surface material with the lithium-depleted interior has reduced their observed, surface lithium abundances from the primordial value [36, 37].

4.2. Non-standard expansion $S \neq 1$, $\xi_e = 0$

The previous section has reminded us of the tension between the observationally inferred primordial abundances of D, ^{4}He and ^{7}Li; see e.g. [38]. While it is not unlikely that the resolution

of these conflicts may be found in systematic uncertainties of the astronomy (e.g. corrections to the derived helium abundance and/or lithium depletion/dilution via mixing), they may be providing hints of new physics. Since the BBN abundance of ^{4}He is sensitive to the early-Universe expansion rate and that of D probes the baryon density, a combination of the two abundances permits us to investigate constraints on models with non-standard expansion rates [11, 39]. Setting aside ^{7}Li for the moment and only using D and ^{4}He, we may use equations (14) and (17) to find

$$S - 1 = \frac{\eta_{\rm He} - \eta_{\rm D}}{106} \tag{22}$$

and

$$\eta_{10} = \frac{100\eta_{\rm D} + 6\eta_{\rm He}}{106}. \tag{23}$$

It is clear from (23) that D is the dominant baryometer. While it may appear from (22) that D and ^{4}He make comparable contributions to constraining the expansion rate, recall that $\eta_{\rm He}$ is linear in $Y_{\rm P}$ while $\eta_{\rm D}$ varies only as a fractional power of $y_{\rm D}$. Whereas reconciling $Y_{\rm P}$ with $y_{\rm D}$ requires an increase in $Y_{\rm P}$ of $\Delta Y_{\rm P} \approx 0.006$ ($\sim$2.5%), reconciling D with ^{4}He would require that $y_{\rm D}$ increase by a factor of $\sim$4–5 (and, the resulting $\eta_{\rm D}$ would then be in conflict with the WMAP determination of η_{10}). From (22), for $\Delta N_\nu \ll 1$ and with $y_{\rm D}$ ($\eta_{\rm D}$) fixed, $\Delta Y \approx 0.014\Delta N_\nu$. Note that, depending on the quantity held fixed (η_{10} or $\eta_{\rm D}$), the coefficients in the ΔY–ΔN_ν relations differ slightly.

For the values adopted in sections 3.1 and 3.2 (and their uncertainties), $\eta_{\rm D} = 6.06^{+0.68}_{-0.53}$ and $\eta_{\rm He} = 2.81 \pm 0.68$, we find

$$\eta_{10} = 5.88^{+0.64}_{-0.50} \quad \text{and} \quad S = 0.969^{+0.008}_{-0.009}. \tag{24}$$

If the non-standard expansion rate factor is associated with an equivalent number of neutrinos, $\Delta N_\nu = -0.37^{+0.10}_{-0.11}$. These results, along with the D and ^{4}He isoabundance curves, are shown in figure 10. Notice that although ΔN_ν is now closer to zero than in, e.g., [9], the smaller adopted uncertainty in $Y_{\rm P}$ results in a larger, $\sim$3–4σ discrepancy. However, these BBN results for the baryon density and the expansion rate are in excellent agreement with those from WMAP which, while sensitive to the baryon density parameter, is relatively insensitive to the expansion rate factor; see [9].

Although the above combination of η_{10} and S can reconcile the inferred primordial abundances of D and ^{4}He, it cannot resolve the lithium problem. Combining equations (14), (17) and (20), it follows that the predicted lithium abundance may be related to the abundances of D and He by

$$\eta_{\rm Li} = \frac{103\eta_{\rm D} + 3\eta_{\rm He}}{106} = 5.97^{+0.66}_{-0.52}. \tag{25}$$

Accounting for the theoretical uncertainty in the BBN lithium production and in our fit, and using (19) with this estimate for $\eta_{\rm Li}$, the predicted lithium abundance is

$$y_{\rm Li} = 4.20^{+1.07}_{-0.81} \quad \text{and} \quad [{\rm Li}]_{\rm P} = 2.62^{+0.10}_{-0.09}. \tag{26}$$

The resulting conflict is shown in figure 11 where the D and ^{4}He constraints on η_{10} and S are shown along with isoabundance curves for ^{7}Li. It is clear that $y_{\rm Li} < 3$ is strongly disfavoured.

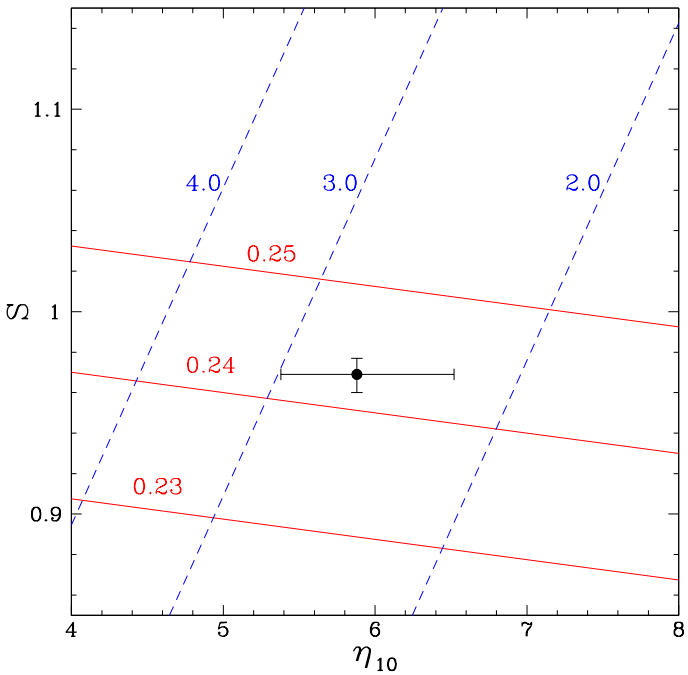

Figure 10. BBN-predicted isoabundance curves for D (dashed) and ^{4}He (solid) in the expansion-rate parameter (S), baryon density parameter (η) plane. The point with error bars corresponds to the adopted abundances for D and ^{4}He ($\xi_e = 0$); see the text and equation (23).

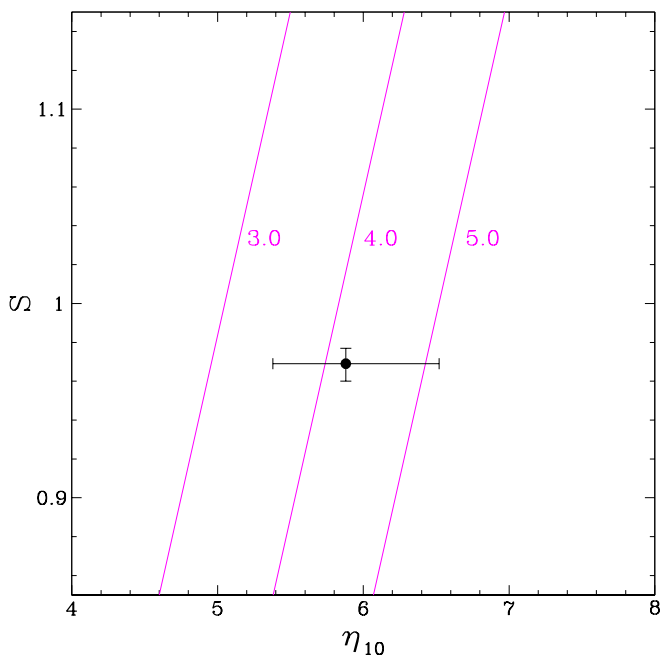

Figure 11. BBN-predicted isoabundance curves ^{7}Li in the expansion-rate parameter (S), baryon density parameter (η) plane. The numbers next to the curves are for $y_{\rm Li}$. The point with error bars corresponds to the adopted abundances for D and ^{4}He (ξ_e =0) as in figure 9.

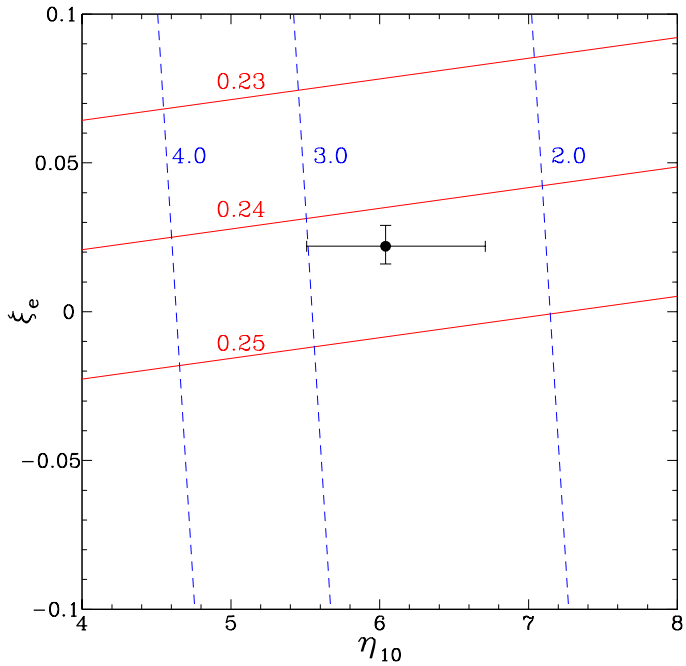

Figure 12. BBN-predicted isoabundance curves for D (dashed) and ^{4}He (solid) in the lepton asymmetry parameter (ξ_e), baryon density parameter (η) plane. The point with error bars corresponds to the adopted abundances for D and ^{4}He ($S = 1$); see the text and equation (28).

4.3. Non-zero lepton number $\xi_e \neq 0$, $S = 1$

In an attempt to relieve the tension between the BBN predicted and observed D and ^{4}He abundances, a non-zero lepton number ($\nu_e - \bar{\nu}_e$ asymmetry; $\xi_e \neq 0$) is an alternative to the non-standard expansion rate explored in the previous section. An excess of ν_e over $\bar{\nu}_e$ will drive down the pre-BBN neutron-to-proton ratio, leaving fewer neutrons to be incorporated in ^{4}He. The resulting, lower, BBN-predicted ^{4}He abundance will be closer to that observed. At the same time, the effect of an e-neutrino asymmetry on the abundances of D and/or ^{7}Li is small.

As for the case of $S \neq 1$, we set aside ^{7}Li and use D and ^{4}He to constrain η_{10} and ξ_e. For $S = 1$,

$$\eta_{10} = \frac{115\eta_{\rm D} + \eta_{\rm He}}{116} \tag{27}$$

and

$$\xi_e = \frac{\eta_{\rm D} - \eta_{\rm He}}{145}. \tag{28}$$

Using the D and ^{4}He abundances adopted here,

$$\eta_{10} = 6.04^{+0.67}_{-0.53} \quad \text{and} \quad \xi_e = 0.022^{+0.007}_{-0.006}. \tag{29}$$

These results, along with the D and ^{4}He isoabundance curves, are shown in figure 12.

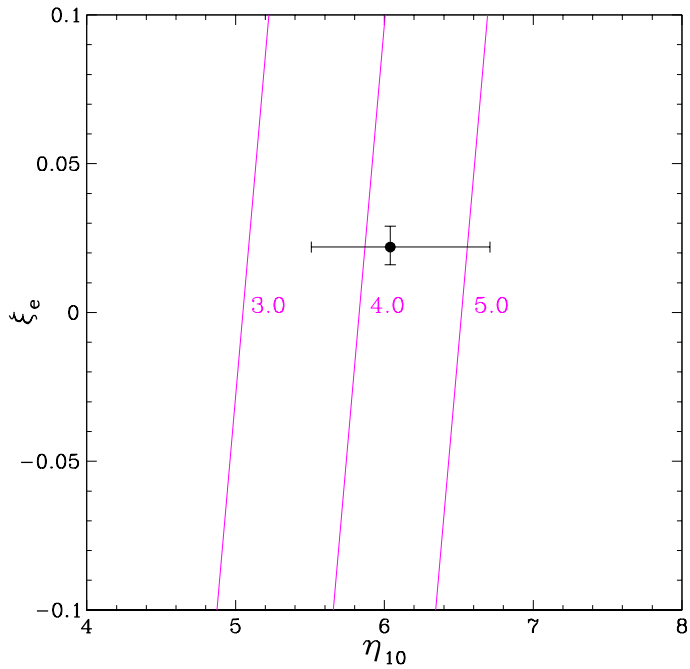

Figure 13. BBN-predicted isoabundance curves ^{7}Li in the lepton asymmetry parameter (ξ_e), baryon density parameter (η) plane. The numbers next to the curves are for $y_{\rm Li}$. The point with error bars corresponds to the adopted abundances for D and ^{4}He ($S = 1$) as in figure 11.

A 'small' lepton asymmetry, $\xi_e \approx 0.02$, which is very large compared with the baryon asymmetry ($\sim\eta \lesssim 10^{-9}$), can reconcile the observationally inferred primordial D and ^{4}He abundances with the predictions of BBN. But this lepton asymmetry will not resolve the conflict between the BBN-predicted and observed ^{7}Li abundances since

$$\eta_{\rm Li} = \frac{142\eta_{\rm D} + 3\eta_{\rm He}}{145} = 5.99^{+0.67}_{-0.52} \tag{30}$$

and

$$y_{\rm Li} = 4.23^{+1.08}_{-0.82} \quad \text{and} \quad [{\rm Li}]_{\rm P} = 2.63^{+0.10}_{-0.09}. \tag{31}$$

As is the case for a non-standard expansion rate, the BBN-predicted abundance of ^{7}Li is very tightly tied to that of D, and a non-zero lepton number cannot resolve the conflict between theory and data. This is illustrated in figure 13, where it is clear that here, too, $y_{\rm Li} < 3$ is strongly disfavoured.

4.4. Non-standard expansion rate and non-zero lepton number $S \neq 1$, $\xi_e \neq 0$

In section 4.2 it was seen that, in the absence of a non-zero lepton number, the D and ^{4}He abundances severely restrict deviations of the early universe expansion rate from its standard value. When associated with the effective number of neutrinos, this constraint (for the choice of D and ^{4}He abundances adopted here) is nearly 4σ away from the standard value of $N_\nu = 3$.

If the LSND result [40] is interpreted in terms of a 4th, 'sterile', neutrino, the mixing of such a neutrino with the active neutrinos would bring it into equilibrium in the early universe prior to BBN [41], resulting in $N_\nu = 4$ at BBN.[7] Clearly (see section 4.2), the current best estimates of the primordial abundances cannot tolerate the corresponding speed-up in the expansion rate at BBN. However, in section 4.3 it was shown that $N_\nu = 3$ is perfectly acceptable provided that there is a small but significant $\nu_e - \bar{\nu}_e$ asymmetry. It is, therefore, not unexpected that for $\xi_e \neq 0$, the BBN constraints on S (ΔN_ν) are considerably expanded (see e.g. [9] and references therein). In implementing for BBN $S \neq 1$ as well as $\xi_e \neq 0$, there is a problem. Because of concerns about the primordial ^{7}Li (and ^{3}He) abundances as inferred from current observational data, the analysis here has been restricted to employing only the D and ^{4}He abundances. But, with three free parameters (η_{10}, S (or ΔN_ν) and ξ_e) and only two constraints ($\eta_{\rm D}$ and $\eta_{\rm He}$), non-BBN data (restricting η_{10}) is required to proceed further. Retaining the constraints from D and ^{4}He, S and ξ_e are then functions of the baryon density parameter,

$$590(S-1) = 116\eta_{10} - (115\eta_{\rm D} + \eta_{\rm He}) \tag{32}$$

and

$$145\xi_e = 106(S-1) + \eta_{\rm D} - \eta_{\rm He}. \tag{33}$$

For the abundances adopted here (section 2), this leads to

$$590(S-1) = 116\eta_{10} - 700^{+78}_{-61}, \tag{34}$$

and

$$\xi_e = 0.731(S-1) + 0.0224^{+0.0066}_{-0.0059}. \tag{35}$$

This ξ_e–S relation is shown in figure 14.

A constraint on the baryon density is possible utilizing CBR data, provided that the corresponding values of $S-1$ and ξ_e are sufficiently small, so that the expansion rate at recombination, some 400 kyr after BBN, does not deviate significantly from the standard value. For the WMAP recommended baryon abundance [8], $\eta_{10} = 6.14$, $S \approx 1.0203$, corresponding to $\Delta N_\nu \approx 0.25$ and $\xi_e \approx 0.037$. This point is shown in figure 14.

It is now possible to address the question of whether or not BBN permits $N_\nu = 4$ ($S = 1.0783$). This choice for S requires $\xi_e = 0.080$ and $\eta_{10} = 6.43$, only $\sim 1\sigma$ away from the WMAP value. This point is shown in figure 15 where the $\xi_e - \Delta N_\nu$ relation is displayed. While BBN constraints on more extreme cases (e.g., $\Delta N_\nu \geqslant 2$) can be explored (see e.g. [10]), our simple fits begin to become inaccurate for $\xi_e \geqslant 0.1$, limiting our analysis here to $\Delta N_\nu \lesssim 1.2$ (see figure 15).

For the general case studied here, the BBN-predicted lithium abundance depends on the baryon density (as well as on the D and ^{4}He abundances),

$$\eta_{\rm Li} = 0.159\eta_{10} + 0.822\eta_{\rm D} + 0.019\eta_{\rm He}. \tag{36}$$

Notice that here, too, the ^{7}Li abundance is tightly tied to that of D. Indeed,

$$\eta_{\rm Li} = \eta_{\rm D} + 3[(S-1) - \xi_e] \approx \eta_{\rm D}. \tag{37}$$

[7] Provided that ξ_e is very small. A non-zero lepton asymmetry can prevent the mixing between active and sterile neutrinos [42].

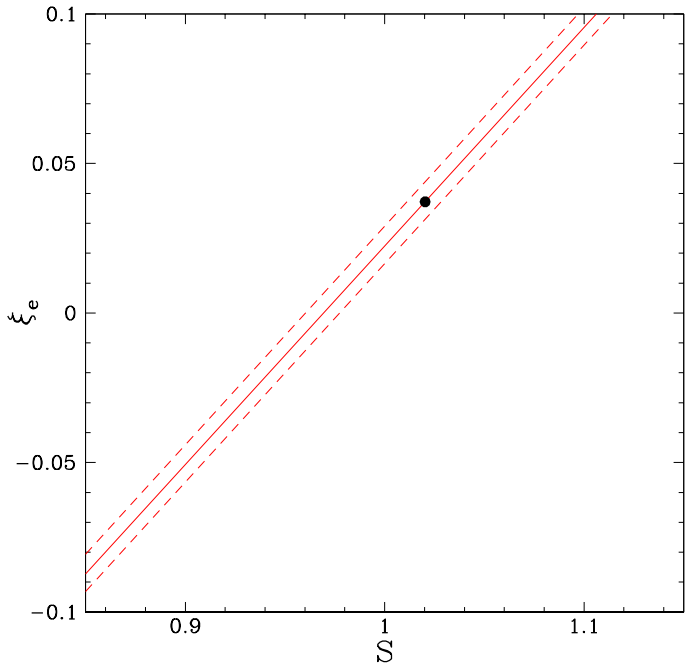

Figure 14. BBN-predicted ξ_e–S relation corresponding to the adopted D and ^{4}He abundances. The solid curve is for the central value and the dashed curves represent the 1σ uncertainties. The point indicated corresponds to the WMAP value for the baryon density; see the text.

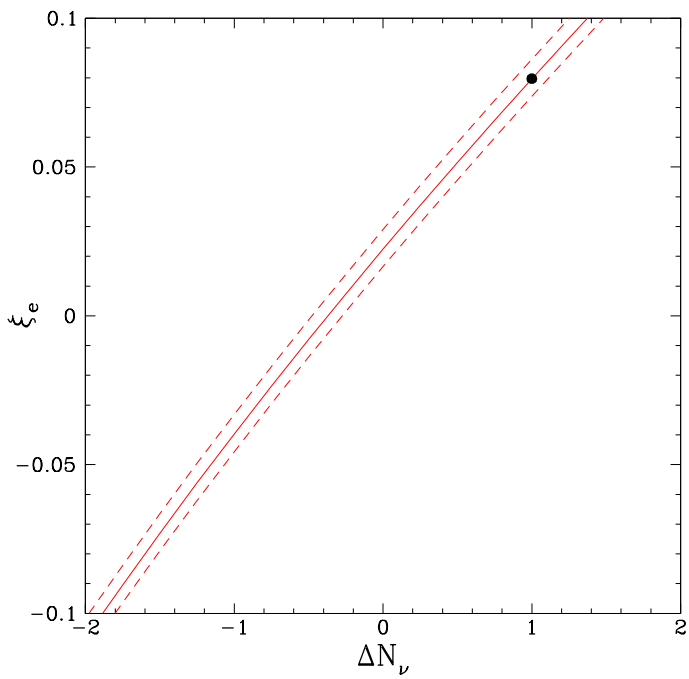

Figure 15. BBN-predicted ξ_e–ΔN_ν relation corresponding to the adopted D and ^{4}He abundances. The solid curve is for the central value and the dashed curves represent the 1σ uncertainties. The point indicated corresponds to $N_\nu = 4$.

As before, there are lithium 'problems' for the two cases studied above. For the WMAP combination of parameters (see equation (19)), $\eta_{\rm Li} = 6.01$, so that $y_{\rm Li} = 4.25$ ([Li] = 2.63). For $N_\nu = 4$, $\eta_{\rm Li} = 6.06$, corresponding to $y_{\rm Li} = 4.32$ ([Li] = 2.64). At least for these combinations of non-standard physics (as well as for SBBN), there is an apparent conflict between the BBN predicted and observed primordial abundances of lithium.

5. Summary and conclusions

In the toolbox of a particle phenomenologist, BBN is a venerable and valuable tool, providing complementary constraints on, or hints of, new physics beyond the standard model. As the models change and the data are updated, not every phenomenologist on the street may have easy access to a BBN code to enable quick revision of previous bounds or investigation of new hints. It may, then, be of value to have simple fits to the BBN-predicted abundances as functions of the key variables (baryon density, expansion rate or neutrino number and neutral lepton asymmetry). For interesting but limited ranges of the parameters such fits have been presented here and applied to several simple examples. We have seen that the observed D and ^{4}He abundances, while apparently inconsistent with SBBN (modulo systematic errors in the data), can be reconciled if non-standard expansion rates and/or non-zero lepton number are allowed. It was also shown how non-zero lepton number allows one, or more, sterile neutrinos while maintaining the consistency of BBN. Finally, by revealing the clear connections between the BBN-predicted abundances of D and ^{7}Li, we showed that none of these non-standard physics solutions can reconcile the observed and predicted lithium abundances.

Acknowledgments

This work has been supported by the US Department of Energy under grants DE-FG02-02ER41216 at NCSU and DE-FG02-91ER40690 at OSU.

References

[1] Carroll S M and Kaplinghat M 2002 *Phys. Rev.* D **65** 063507
[2] Massó E and Rota F 2003 *Phys. Rev.* D **68** 123504
[3] Kneller J P and Steigman G 2003 *Phys. Rev.* D **67** 063501
[4] Barrow J D and Scherrer R J 2004 *Preprint* astro-ph/0406088
[5] Serna A, Dominguez-Tenreiro R and Yepes G 1992 *Astrophys. J.* **391** 433
[6] Serna A and Dominguez-Tenreiro R 1993 *Phys. Rev.* D **48** 1591
[7] Bean R, Hansen S H and Melchiorri A 2001 *Phys. Rev.* D **64** 103508
[8] Spergel D N *et al* 2003 *Astrophys. J. Suppl.* **148** 175
[9] Barger V, Kneller J P, Marfatia D, Langacker P and Steigman G 2003 *Phys. Lett.* B **569** 123
[10] Barger V, Kneller J P, Lee H-S, Marfatia D and Steigman G 2003 *Phys. Lett.* B **566** 8
[11] Steigman G, Schramm D N and Gunn J E 1977 *Phys. Lett.* B **66** 202
[12] Randall L and Sundrum R 1999 *Phys. Rev. Lett.* **83** 3370 and 4690
[13] Kang H S and Steigman G 1992 *Nucl. Phys.* B **372** 494
[14] Kneller J P, Scherrer R J, Steigman G and Walker T P 2001 *Phys. Rev.* D **64** 123506
[15] Lunardini C and Smirnov A Y 2001 *Phys. Rev.* D **64** 073006
Dolgov A D, Hansen S H, Pastor S, Petcov S T, Raffelt G G and Semikoz D V 2002 *Nucl. Phys.* B **632** 363

Wong Y Y 2002 *Phys. Rev.* D **66** 025015
Abazajian K N, Beacom J F and Bell N F 2002 *Phys. Rev.* D **66** 013008
[16] Burles S, Nollett K M and Turner M S 2001 *Phys. Rev.* D **63** 063512
[17] Hata N, Scherrer R J, Steigman G, Thomas D, Walker T P, Bludman S and Langacker P 1995 *Phys. Rev. Lett.* **75** 3977
[18] Epstein R, Lattimer J and Schramm D N 1976 *Nature* **263** 198
[19] Bania T M, Rood R T and Balser D 2002 *Nature* **415** 54
[20] Burles S and Tytler D 1998 *Astrophys. J.* **499** 699
[21] Burles S and Tytler D 1998 *Astrophys. J.* **507** 732
[22] O'Meara J M *et al* 2001 *Astrophys. J.* **552** 718
[23] Pettini M and Bowen D V 2001 *Astrophys. J.* **560** 41
[24] D'Odorico S, Dessauges-Zavadsky M and Molaro P 2001 *Astron. Astrophys.* **338** L1
[25] Kirkman D, Tytler D, Suzuki N, O'Meara J and Lubin D 2003 *Astrophys. J. Suppl.* **149** 1
[26] Steigman G 2004 *STScI Symp. Ser.* **15** 46; also in *Proc. STScI Symp. on 'The Dark Universe: Matter, Energy, and Gravity'* ed M Livio, May
[27] Izotov Y I, Thuan T X and Lipovetsky V A 1997 *Astrophys. J. Suppl.* **108** 1
[28] Izotov Y I, Thuan T X and Lipovetsky V A 1998 *Astrophys. J.* **500** 188
[29] Olive K A and Steigman G 1995 *Astrophys. J. Suppl.* **97** 49
[30] Olive K A, Skillman E and Steigman G 1997 *Astrophys. J.* **483** 788
[31] Fields B D and Olive K A 1998 *Astrophys. J.* **506** 177
[32] Izotov Y I and Thuan T X 2004 *Astrophys. J.* **602** 200
[33] Olive K A and Skillman E D 2004 *Preprint* astro-ph/0405588
[34] Ryan S G, Beers T C, Olive K A, Fields B D and Norris J E 2000 *Astrophys. Lett.* **530** L57
[35] Bonifacio P and Molaro P 1997 *Mon. Not. R. Astron. Soc.* **285** 847
Bonifacio P, Molaro P and Pasquini L 1997 *Mon. Not. R. Astron. Soc.* **292** L1
[36] Pinsonneault M H, Walker T P, Steigman G and Narayanan V K 1999 *Astrophys. J.* **527** 180
[37] Pinsonneault M H, Steigman G, Walker T P and Narayanan V K 2002 *Astrophys. J.* **574** 398
[38] Olive K A, Steigman G and Walker T P 2000 *Phys. Rep.* **333** 389
[39] Olive K A, Schramm D N, Steigman G and Walker T P 1990 *Phys. Lett.* B **236** 454
[40] Aguilar A *et al* [LSND Collaboration] 2001 *Phys. Rev.* D **64** 112007
[41] di Bari P 2002 *Phys. Rev.* D **65** 043509
[42] Foot R and Volkas R R 1995 *Phys. Rev. Lett.* **75** 4350

New Journal of Physics
An Institute of Physics and Deutsche Physikalische Gesellschaft Journal

Solar neutrinos

A B McDonald

Physics Department, SNO Institute, Queen's University, Kingston K7L 3N6, Canada

E-mail: mcdonald@owl.phy.queensu.ca

New Journal of Physics **6** (2004) 121
Received 10 May 2004
Published 23 September 2004
Online at http://www.njp.org/
doi:10.1088/1367-2630/6/1/121

Abstract. A review of solar neutrino experiments is provided, including experimental measurements to date and proposed future measurements. Experiments to date have provided a clear indication that solar neutrinos are undergoing flavour transformation and that the dominant mechanism for this transformation is oscillation. The mixing parameters are well defined and limits are placed on sub-dominant modes. The measurements also provide strong confirmation of solar model calculations. New experiments under development will study neutrino oscillation parameters and sub-dominant modes with greater precision and will investigate solar fluxes further, concentrating primarily on the low energy pp, ^{7}Be, pep and CNO reactions.

PII: S1367-2630(04)80371-9
© IOP Publishing Ltd and Deutsche Physikalische Gesellschaft

Contents

1. Introduction **2**
2. General description of solar neutrino measurements **2**
3. Measurements to date **4**
3.1. Radiochemical detectors 4
3.1.1. Homestake Cl experiment 4
3.1.2. Ga-based experiments: SAGE, GALLEX, GNO 5
3.2. Real-time solar neutrino detectors 5
3.2.1. Kamiokande and Super-Kamiokande 5
3.2.2. SNO 6
3.3. Summary of results for solar neutrino measurements to date 9
4. Future solar neutrino experiments **10**
4.1. Physics motivation 10
4.2. General description of experiments 12
4.2.1. Target materials 12
4.2.2. Radioactive backgrounds 12
4.3. Constructed experiments 13
4.4. Next generation experiments 14
4.4.1. ES measurements 14
4.4.2. CC measurements 15
4.5. Summary 16
References **16**

1. Introduction

The study of solar neutrinos was initiated by the pioneering experimental efforts of R Davis coupled with the theoretical work of J Bahcall. The original objective was to study the physics of the Sun. The set of measurements that have been carried out over more than 35 years have provided detailed information on solar properties and have confirmed the accuracy of the Standard Solar Model. These measurements have also provided extensive information on the physics of neutrinos themselves, including observations of flavour change that extend beyond the Standard Model of Elementary Particle Physics. The theoretical aspects of solar neutrino measurements and their impact on solar models and neutrino properties are described in detail by Bahcall and Pena-Garay [1]. The present paper will describe the experiments that have been carried out to date and will provide a description of potential future experiments and their objectives.

2. General description of solar neutrino measurements

The models of the Sun have been developed to a high degree of detail over many years. Reactions that describe the thermonuclear power of the Sun also emit copious numbers of neutrinos with energies ranging up to about 18 MeV (see figure 1 and table 1 in [1]). These neutrinos are very difficult to detect because of the very low neutrino cross-sections and invariably require deep underground locations to get away from radioactive backgrounds induced by cosmic rays.

The detection reactions that have been used for solar neutrinos are of two types:

- Radiochemical measurements involving the transformation of atoms of an element such as Cl or Ga into another radioactive element through inverse beta decay induced by electron neutrinos. These reactions can be observed by sweeping the radioactive elements from the detector volume and observing the subsequent decay. The measurements on Cl by R Davis *et al* [2] and on Ga by SAGE [3], GALLEX and GNO [4] experiments typically involve collection periods of the order of a month and subsequent decay measurement periods of many months.
- The observation of events in real time produced by neutrino interactions in light water (Kamiokande [5] and Super-Kamiokande [6]) and heavy water (Sudbury Neutrino Observatory (SNO)) [7] via the Cherenkov process. The reactions that have been used involve elastic scattering of neutrinos from electrons, the inverse beta decay reaction on deuterium producing energetic electrons and inelastic scattering on deuterium producing free neutrons. The inverse beta decay on deuterium is sensitive only to electron neutrinos, the inelastic scattering on deuterium is equally sensitive to all neutrino types and the elastic scattering on electrons is predominantly sensitive to electron neutrinos, with a small (about 14%) sensitivity to other active neutrino types.

These experiments have a variety of neutrino energy thresholds and are therefore sensitive to different combinations of the neutrino-producing reactions in the Sun. Figure 1 of [1] shows the thresholds for the above experiments and illustrates that the Ga experiments have about one-half of their sensitivity from the pp reaction, the Cl-based measurements have sensitivity primarily to the ^{8}B neutrinos with some sensitivity to ^{7}Be and the light and heavy-water-based experiments are sensitive almost exclusively to the ^{8}B neutrinos with a negligible contribution from the hep neutrinos.

Starting with the measurements on Cl and continuing with measurements on Ga and light water, too few neutrinos were observed in comparison with the predictions of solar models. This came to be known as the Solar Neutrino Problem and was extensively discussed in the scientific literature. Attempts to explain the experimental data generally involved either changes to the solar models to modify the predicted neutrino fluxes or proposals for new physical properties of neutrinos, such as oscillations among neutrino types leading to a smaller flux of electron neutrinos reaching the detectors. The initial detectors were either exclusively or predominantly sensitive to electron neutrinos and so neutrino oscillations would result in lower observed fluxes. Oscillations of massive neutrinos can be modified by interactions with electrons in the Sun (or the Earth) (the Mikheyev–Smirnov–Wolfenstein or MSW effect [8]) that can result in neutrino-energy-dependent probabilities for oscillation. In addition, other mechanisms such as neutrino decay [9] or resonant spin-flavour precession (RSFP) [10], were considered as explanations for the small observed fluxes. Very detailed measurements of the energy dependence and time-dependence of ^{8}B fluxes were carried out by the Super-Kamiokande experiment with no statistically significant effects observed. Calculations of possible changes to solar models did not provide modifications to neutrino fluxes that agreed with the observed data. A firm conclusion on whether neutrino flavour change was taking place depended on solar model calculations of the relative size of the various neutrino fluxes. Although solar models provided very good agreement with all other solar properties, including helioseismology measurements [11], it was difficult to be certain whether changes to solar models or changes to neutrino properties might be required to explain the discrepancy between experiment and theory.

Subsequently, the SNO experiment performed measurements of the interactions of ^{8}B neutrinos with deuterium and was able to demonstrate in a manner independent of detailed solar model flux calculations that neutrino flavour change was definitely taking place. The measurement showed that the flux of all active neutrinos was about three times the flux of electron neutrinos, clearly indicating the transformation of electron neutrinos to other active types. In addition, the measurement of the total active ^{8}B neutrino flux was found to be in excellent agreement with the prediction of the Standard Solar Model calculations.

The set of solar neutrino measurements to date defines a well-localized region of parameter space for neutrino mixing that also describes the oscillation of reactor anti-neutrinos observed recently by the KamLAND experiment. The observation of similar parameters for oscillation in these two cases provides restrictions on CPT, as well as restricting possible contributions from sterile neutrinos, RSFP, neutrino decay and flavour-changing neutral current interactions. This overall set of measurements has thereby made a significant impact on our understanding of the Sun and on the basic properties of neutrinos. Neutrino physics has now moved to a precision phase and future measurements are aimed at the definition of neutrino properties and parameters of the Maki–Nakagawa–Sakahata–Pontecorvo (MNSP) [12] mixing matrix with higher precision. They will also improve our knowledge of possible sub-dominant processes mentioned above. Future solar neutrino measurements are primarily aimed at observation of low-energy fluxes and will thereby extend our detailed understanding of the neutrino processes in the Sun. The following sections will describe the measurements to date as well as further experiments that are being developed.

3. Measurements to date

3.1. Radiochemical detectors

3.1.1. Homestake Cl experiment. In the late 1960s, Davis *et al* [2] began their pioneering solar neutrino measurements using 680 tons of liquid perchlorethylene, sited 1480 m underground (4300 m of water equivalent: m.w.e) in the Homestake gold mine near Lead, SD, USA, to observe electron neutrinos from the Sun. The electron neutrino capture reaction on ^{37}Cl produces radioactive ^{37}Ar atoms (half-life 35 days) in the liquid. The ^{37}Ar atoms were flushed with He gas every 100 days and condensed into sensitive proportional counters. About 0.5 Ar atom day^{-1} was produced. The capture reaction on ^{37}Cl was calculated to be sensitive primarily to neutrinos from ^{8}B decay in the Sun, but there is substantial sensitivity to neutrinos from ^{7}Be as well.

The detector is sited underground to reduce ^{37}Ar production by cosmic rays. Detector and proportional counter materials were carefully selected to minimize contributions from background radioactivity. Background rates of ^{37}Ar from sources other than the Sun were restricted to about 0.02 atom day^{-1}. Non-radioactive tracer isotopes ^{36}Ar and ^{38}Ar were injected during successive runs to determine the argon extraction efficiency and were measured by mass spectrometry. Pulse-shape analysis was used on the pulses from the proportional counter to reduce counter backgrounds from other than ^{37}Ar decay.

The detector has been operated from 1968 until 2001 and the cumulative average of the data [2], with statistical and systematic uncertainties, was $2.56 \pm 0.16(stat) \pm 0.16(syst)$ SNU, where a Solar Neutrino Unit (SNU) is defined as one electron neutrino capture per 10^{+36} atoms of ^{37}Cl s^{-1}. This result is substantially smaller than the predictions of the Standard Solar Model [1] of $8.5^{+1.8}_{-1.8}$ SNU (model BP04).

3.1.2. Ga-based experiments: SAGE, GALLEX, GNO. Experiments studying the electron neutrino capture reaction on Ga (^{71}Ga(ν_e,e$^-$)^{71}Ge) are being carried out in the Baksan laboratory (depth of 4700 m.w.e.) in Russia (SAGE) [3] with about 60 tons of liquid Ga metal and in the Gran Sasso laboratory (3300 m.w.e) in Italy (GALLEX, GNO) [4] with 30.3 tons of Ga in a concentrated $GaCl_3$–HCl solution.

The radioactive decay of ^{71}Ge (half-life 11.4 days) is observed after extraction and deposition into low-background proportional counters. Somewhat different extraction techniques are used for the two experiments. In SAGE, the Ge is removed by extraction into an aqueous solution via an oxidation reaction, followed by concentration, conversion to $GeCl_4$ and synthesis to GeH_4 for use in the proportional counter. In GALLEX and GNO, volatile $^{71}GeCl_4$ is formed directly in the target solution, swept out by N_2 gas, absorbed in water and then converted into GeH_4. The detectors were very carefully made from low radioactivity materials and external background is carefully controlled in the counting facilities. Intense ^{51}Cr sources [13] have been used to calibrate the sensitivity of the detector to neutrinos.

The results from these experiments to date [3, 4] are as follows: GALLEX + GNO: $70.8 \pm 4.5(stat) \pm 3.8(syst)$ SNU, SAGE: $70.9 + 5.3/-5.2(stat) + 3.7/-3.2(syst)$ SNU. These numbers are in excellent agreement and are much smaller than the predictions of the Standard Solar Model (131 SNU) [1].

3.2. Real-time solar neutrino detectors

3.2.1. Kamiokande and Super-Kamiokande. From 1983 to 1996 the 1 kton (680 ton fiducial) light water neutrino detector, Kamiokande [5] (1000 m underground, 2600 m.w.e.) in the Kamioka mine in Japan, studied solar neutrinos, as well as other physical processes such as proton decay and atmospheric neutrinos. In 1996, the much larger (22.5 kton light water) Super-Kamiokande detector [14] began operation at the same site, studying solar neutrinos and other physics with higher sensitivity. Solar neutrinos are observed through the elastic scattering of neutrinos from electrons, by the detection of Cherenkov light from the recoiling electron. The energy threshold for Kamiokande was about 7 MeV and about 5 MeV for Super-Kamiokande. Therefore, the sensitivity of these detectors is almost entirely for ^{8}B solar neutrinos with a tiny contribution from the hep reaction.

For Kamiokande, the flux of neutrinos from the ^{8}B decay was measured [5] to be $2.8 \pm 0.19(stat) \pm 0.33(syst) \times 10^{+6}\,\mathrm{cm}^{-2}\,\mathrm{s}^{-1}$, clearly less than the solar model prediction [1] of $5.82(1 \pm 0.23) \times 10^{+6}\,\mathrm{cm}^{-2}\,\mathrm{s}^{-1}$. Studies of the variation in flux as a function of time showed no statistically significant effects.

The solar neutrino flux from ^{8}B decay measured by Super-Kamiokande [6] is $2.35 \pm 0.02(stat) \pm 0.08(syst) \times 10^{+6}\,\mathrm{cm}^{-2}\,\mathrm{s}^{-1}$, and is also significantly smaller than the solar model prediction. The neutrino energy spectrum is very similar to that expected from ^{8}B decay and no distortion due to the MSW effect [8] has been observed. Figure 1 shows a comparison of the observed spectrum with the spectrum from ^{8}B decay.

To look for indications of the MSW effect through regeneration of neutrinos while passing through the Earth [15], an analysis of the spectra including solar zenith angle has been performed. Figure 1 also shows the asymmetry between day and night and it is clear that there is no significant effect observed. A maximum likelihood analysis of this 1496 days of data shows a day–night asymmetry of $-1.8 \pm 1.6(stat)^{+1.3}_{-1.2}(syst)\%$, consistent with zero and with the expected value (2.1%) from the most recent analysis of the LMA solution for neutrino oscillations as discussed

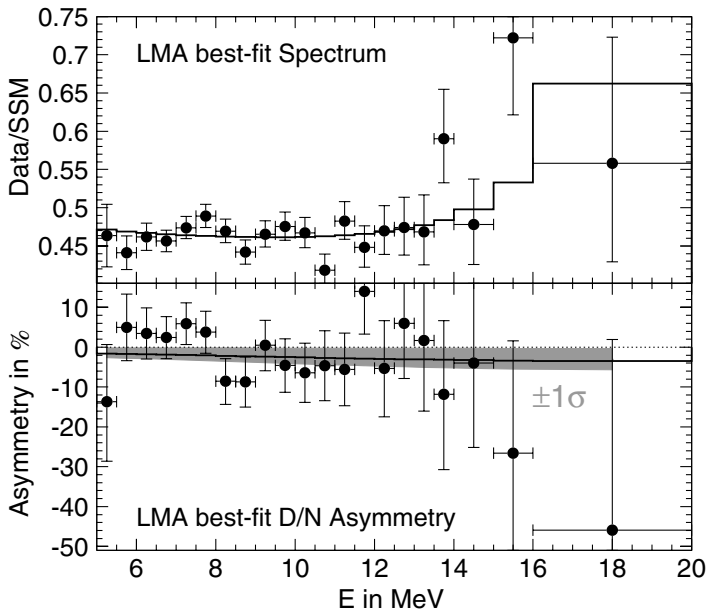

Figure 1. Solar neutrino elastic scattering energy spectrum (top) and day/night (D/N) Asymmetry (bottom) as measured by Super-Kamiokande. The predictions (solid lines) are for the LMA solution. The grey bands are the $\pm\sigma$ ranges for the asymmetry over the entire energy range.

in [1]. A further analysis of the data was carried out, seeking distortion of the ^{8}B energy spectrum from magnetic scattering associated with a finite neutrino magnetic moment. Potential distortions of the weak elastic scattering (ES) spectrum from oscillation of ^{8}B neutrinos were taken into account by incorporating data from other solar neutrino experiments and an upper limit for the neutrino magnetic moment of $1.1 \times 10^{-10}\mu_B$ was obtained for 90% confidence level [16].

If there were a significant neutrino magnetic moment, this could couple with solar magnetic field distributions and produce different observed fluxes through flavour change as neutrinos pass through different solar regions at various times of year. However, the neutrino flux as a function of time of year is observed by the Super-Kamiokande measurements to follow the variation expected for the Earth–Sun distance variation with no observable additional effects as shown in figure 2. With the full 1496 day data set, the amplitude of the neutrino flux variation is measured to be 1.51 ± 0.43 (consistent with one) times the amplitude expected from the eccentricity of the Earth's orbit. The perihelion shift is measured to be 13 ± 17 days (consistent with zero). Studies over longer periods of time to seek correlations between the data and the sunspot numbers (indicative of magnetic fields in the outer regions of the Sun) also show no correlations [6].

3.2.2. SNO. The principal objective of the SNO has been the clear observation of flavour change for ^{8}B solar neutrinos by a comparison of the total flux of active neutrinos with the total flux of electron neutrinos. The measurement of flavour change does not rely on solar model calculations and, in fact, the total flux of active neutrinos can be compared with the predicted flux of ^{8}B neutrinos as a test of those calculations. The fluxes are measured through the following reactions

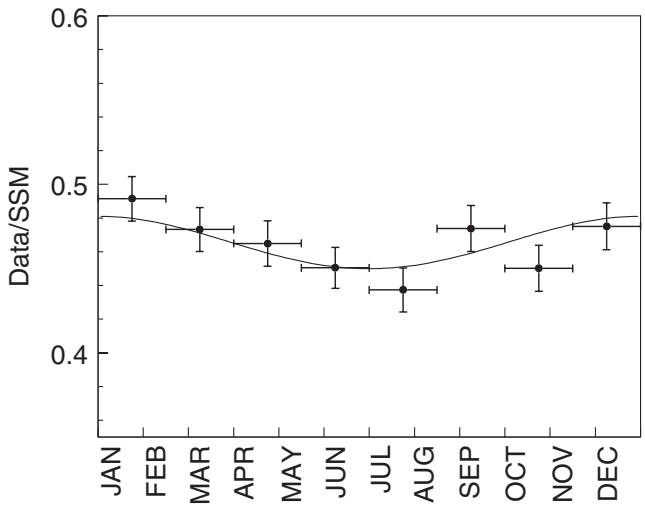

Figure 2. Seasonal variation of the solar neutrino flux as measured by Super-Kamiokande. The curve shows the expected seasonal variation of the flux introduced by the eccentricity of the Earth's orbit.

in a heavy-water-based Cherenkov detector:

$$\nu_e + \mathrm{d} \rightarrow \mathrm{p} + \mathrm{p} + \mathrm{e}^- \qquad \text{(charged current: CC)}$$
$$\nu_x + \mathrm{d} \rightarrow \mathrm{p} + \mathrm{n} + \nu_x \qquad \text{(neutral current: NC)}$$
$$\nu_x + \mathrm{e}^- \rightarrow \nu_x + \mathrm{e}^- \qquad \text{(ES)}$$

The CC reaction is sensitive exclusively to electron neutrinos, whereas the NC reaction is equally sensitive to all neutrino flavours ($x = \mathrm{e}, \mu, \tau$) above the energy threshold of 2.2 MeV. The ES reaction is sensitive to all flavours as well, but with reduced sensitivity to ν_μ and ν_τ. Comparison of the ^{8}B flux deduced from the CC reaction with the total flux of active neutrinos observed with the NC reaction (or the ES reaction with reduced sensitivity) can provide clear evidence of neutrino flavour transformation without reference to solar model flux calculations.

The SNO detector [17] uses 1100 tons of heavy water sited 2000 m underground (6200 m water equivalent) near Sudbury, Ontario, Canada. Neutrinos are detected via the Cherenkov process in the central heavy water volume or in the surrounding volume of light water. The CC and ES reactions are observed through the Cherenkov light produced by the electrons. The NC reaction is observed through the detection of the neutron in the final state of the reaction. The SNO experimental plan involves three phases wherein different techniques are employed for the detection of neutrons from the NC reaction. During the first phase, with pure heavy water, neutrons were observed through the Cherenkov light produced when neutrons are captured on deuterium, producing 6.25 MeV gammas. For the second phase, about 2.2 tons of salt was added to the heavy water and neutron detection was enhanced through capture on Cl, with about 8.6 MeV gamma energy release and a higher capture efficiency. The neutrons from the NC reaction capture on Cl and provide a more isotropic pattern at the PMTs for these events than for the CC events. This enables the fluxes from the CC and NC reactions to be extracted on a statistical basis with no constraint on the shape of the CC energy spectrum. For the third phase, the salt was removed

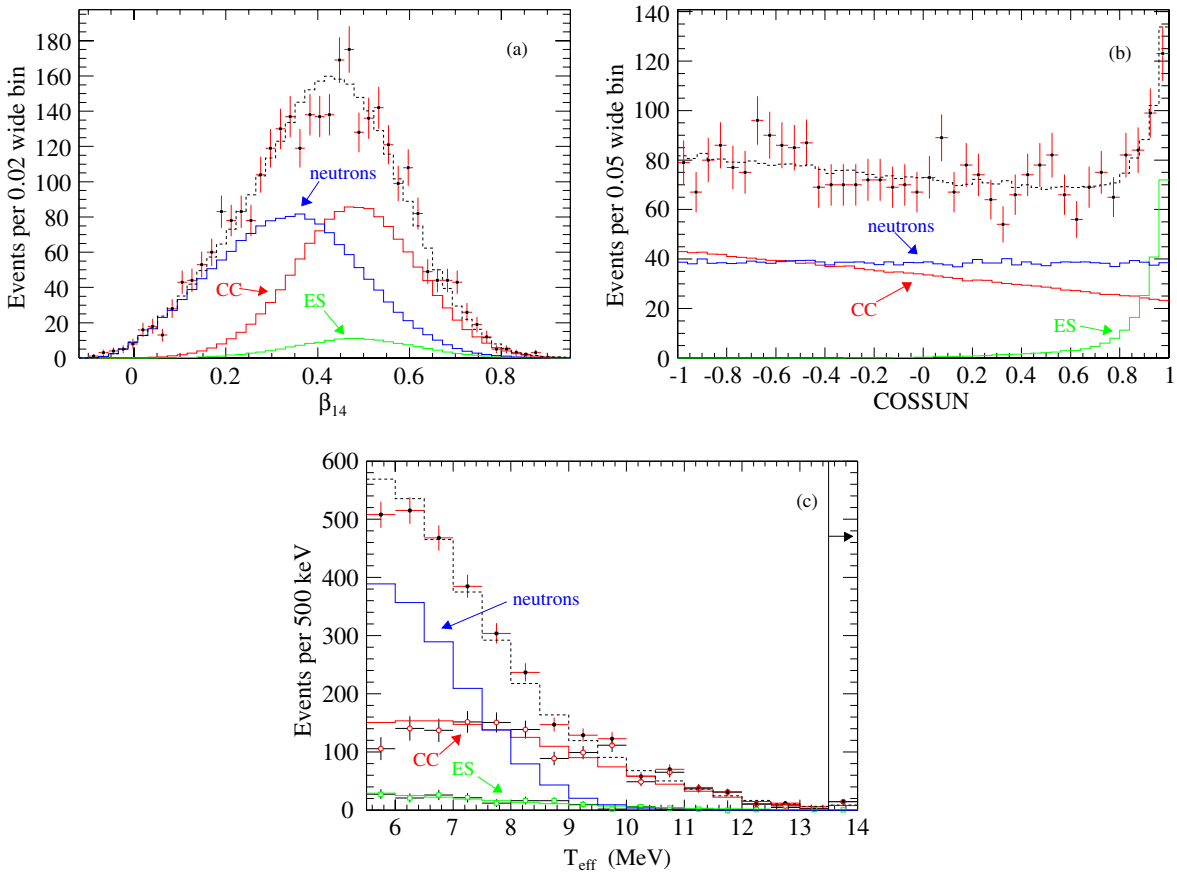

Figure 3. Distribution of (a) β_{14}, (b) $\cos\theta_{\odot}$ and (c) kinetic energy, for the selected events. The CC and ES spectra are extracted from the data using β_{14} and $\cos\theta_{\odot}$ distributions in each energy bin. Also shown are the Monte Carlo predictions for CC, ES, NC +internal and external-source neutron events, all scaled to the fit results. The broken lines represent the summed components. All distributions are for events with $T_{\rm eff} \geqslant 5.5$ MeV and $R_{\rm fit} \leqslant 550$ cm. Differential systematics are not shown.

and an array of ^{3}He-filled proportional counters has been installed to provide neutron detection independent of the PMT array.

During operation to date, radioactivity levels were achieved that result in background events for the NC reaction from photodisintegration of deuterium by gamma rays that are <5% of the predicted rate from the Standard Solar Model neutrino flux. The threshold for observation of the CC and ES reactions in the salt phase is 5.5 MeV in equivalent electron kinetic energy.

Results from the initial phase of the experiment with pure heavy water [18]–[20] showed clear evidence for neutrino flavour change, without reference to solar model calculations. The hypothesis of no flavour change was tested assuming an undistorted CC spectrum and found to be violated using summed data for the CC and NC reactions observed through Cherenkov processes in the heavy water. With the addition of salt it was possible to break the strong correlation between the CC and NC event types because the pattern of light on the PMTs is different for the two reactions. An event angular distribution parameter β_{14} (defined in [7]) was used to separate NC and CC events on a statistical basis. Data from the salt phase are shown in figure 3, together with

the best fit to the data of the NC (8.6 MeV gamma cascade) shape, the CC and ES reactions and a small background component determined from independent measurements.

The fluxes inferred for this fit are

$$\phi_{CC}^{SNO} = 1.59^{+0.08}_{-0.07}(stat)^{+0.06}_{-0.08}(syst),$$

$$\phi_{ES}^{SNO} = 2.21^{+0.31}_{-0.26}(stat) \pm 0.10(syst),$$

$$\phi_{NC}^{SNO} = 5.21 \pm 0.27(stat) \pm 0.38(syst),$$

where these fluxes and those following in this section are quoted in units of $10^6\ \mathrm{cm}^{-2}\ \mathrm{s}^{-1}$.

By comparison of the CC and NC fluxes it is clear that only about one-third of the neutrinos reaching the Earth are electron neutrinos. These results violate the hypothesis test for no flavour change at $>7\sigma$. Previous measurements with pure heavy water had reached similar conclusions of flavour change at levels of 5.5σ [19, 20] (by consideration of the summed CC and NC and ES data) and 3.3σ [18] (by comparison of the CC data with ES measurements by Super-Kamiokande). The measurements from the salt phase, combined with the results of other solar neutrino experiments indicate that the mixing is non-maximal (mixing angle $<\pi/4$) with a CL corresponding to 5.5 SD. The measured total flux of active ^{8}B neutrinos measured with the NC reaction in the salt phase is in very good agreement with and more accurate than the SSM prediction [1] of $5.82(1 \pm 0.23)$.

3.3. Summary of results for solar neutrino measurements to date

The measurements to date have provided convincing evidence for flavour change of neutrinos and matter enhancement of these effects in the Sun. The data for solar neutrinos have been analysed by many authors. Figure 4(a) shows the results for an analysis assuming ν_1, ν_2 mixing is dominant [7], following the SNO salt data.

Measurements of reactor anti-neutrinos by the KamLAND detector reported in 2002 show oscillation parameters matching well with the LMA region for the solar neutrino case (assuming CPT conservation). Figure 4(b) shows the remaining acceptable region when the KamLAND data is combined with the solar data.

The KamLAND detector [21] is a 1 kton liquid scintillator detector constructed in the former Kamiokande location with the initial objective to look for oscillations for neutrinos produced in the power reactors in Japan and Korea. Work is in progress to reduce the radioactive background in the detector and use it for measurements of low energy solar neutrinos. These measurements will be discussed below.

The observation of anti-neutrino disappearance with similar oscillation parameters to those observed for solar neutrinos places strong restrictions on flavour change mechanisms other than oscillation arising from finite neutrino mass. Mechanisms such as resonant spin-flavour procession, flavour-changing neutral currents and neutrino decay are strongly disfavoured as explanations for the low fluxes observed on Earth for solar electron neutrinos. Oscillation to sterile neutrinos is also strongly disfavoured and sub-dominant oscillations to sterile neutrinos are restricted by comparison of the active total flux of ^{8}B solar neutrinos observed by the NC reaction in SNO with the ^{8}B flux calculated with solar models. If CPT conservation is assumed, a limit on sub-dominant sterile components can be obtained without reference to solar model flux calculations [22] by using KamLAND data combined with SNO CC and

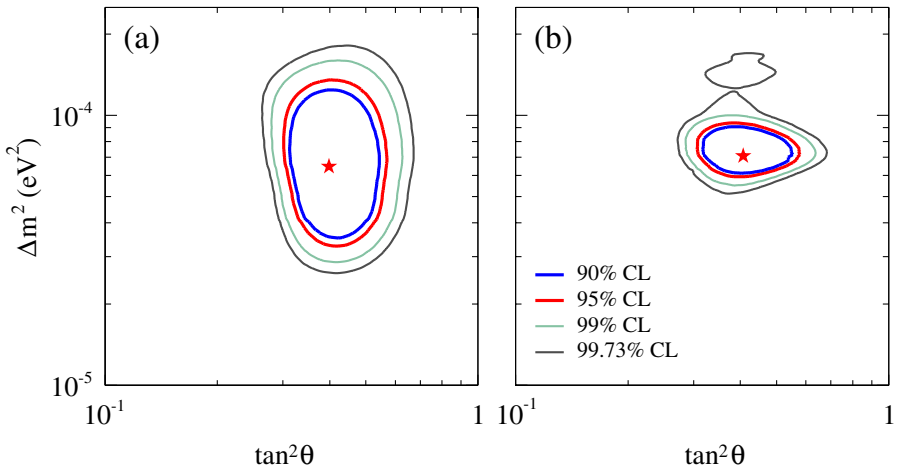

Figure 4. Global neutrino oscillation contours. (a) Solar global: D_2O day and night spectra, salt CC, NC, ES fluxes, SK, Cl, Ga. The best-fit point is $\Delta m^2 = 6.5 \times 10^{-5}$, $\tan^2\theta = 0.40$, $f_B = 1.04$, with χ^2/d.o.f. = 70.2/81. (b) Solar global + KamLAND. The best-fit point is $\Delta m^2 = 7.1 \times 10^{-5}$, $\tan^2\theta = 0.41$, $f_B = 1.02$. In both (a) and (b) the ^{8}B flux is free, the hep flux is fixed at its solar model value and the other solar fluxes are included with the central value and uncertainty calculated with the solar model.

NC measurements. Conceptually, the oscillation parameters defined by Kamland are used to determine the initial ^{8}B solar neutrino flux from the SNO CC measurement. That flux can then be compared with the SNO NC measurement to set limits on oscillation to sub-dominant sterile components.

The KamLAND data have also been analysed [23] to place restrictions on electron anti-neutrinos from the Sun. This provides strong restrictions on processes that change ^{8}B solar electron neutrinos into anti-neutrinos, including spin-flavour precession and neutrino decay. The analysis sets a limit of 2.8×10^{-4} of the Standard Solar Model flux for the flux of electron anti-neutrinos (90% CL).

4. Future solar neutrino experiments

4.1. Physics motivation

As can be seen from figure 4, the solar measurements to date, combined with KamLAND are providing strong constraints on the parameters for the mixing of active neutrinos. This is discussed in more detail in [1]. The main physics motivations for future solar neutrino measurements are as follows:

(i) *Improvement in accuracy for the mixing parameters for three active neutrino types.* The improvement of the 1–2 mixing parameters provides an important objective for future measurements of solar neutrinos. In addition, improvement in the accuracy for the solar neutrino measurements leads to improvement in the knowledge of other parameters in the full MNSP mixing matrix [12] for three active neutrinos. For example, as discussed by

Maltoni *et al* [24] measurements of solar neutrinos and KamLAND provide the dominant constraints on the θ_{13} parameter for the lowest mass part of the allowed range of Δm^2_{23} for fits to the atmospheric neutrino measurements. Therefore, improvements in solar neutrino measurements can provide valuable information prior to direct measurements of the θ_{13} parameter that are planned for the future.

(ii) *Further study of matter-enhanced oscillation.* As shown in figure 1 of [1], the oscillation situation for the LMA parameters is very different for neutrino energies above a few MeV where matter-enhanced oscillation dominates and below this energy, where the oscillation is close to the vacuum case. Therefore, it is of interest to study the energy dependence across this transition for solar neutrinos to confirm the present understanding of the oscillation situation for LMA parameters as well as to provide more accurate parameters for the oscillation.

A CC and a NC measurement for the same neutrino reaction below a few MeV would provide a measure of electron neutrino survival without reference to solar model calculations. This survival probability could then be compared with the SNO results for ^{8}B neutrinos to demonstrate directly the difference for vacuum oscillation and the energy-dependent matter enhancement.

Improvement in the accuracy of existing experiments could provide direct evidence for matter enhancement in the Sun through the distortion of the neutrino spectrum for ^{8}B neutrinos or a clear day–night difference in observed flux, arising from matter-enhancement in the Earth. The effects are expected to be small for the LMA solution and hence the measurements are difficult.

(iii) *Search for physics beyond three active neutrino types.* In addition, improvements in the 1–2 parameters are of value in seeking evidence for physics beyond three active neutrino types, through tests of the unitarity of the MNSP matrix. At present, these tests are limited by the lack of knowledge of other mixing parameters but when future measurements are made, the unitarity of the MNSP matrix will place restrictions on possible contributions from sterile neutrinos and other physics, such as CPT violation when KamLAND data is included [25].[1] In addition, as has been pointed out by some authors [26], distortion of the energy spectrum could be possible for certain cases involving sterile neutrinos.

(iv) *Further information on solar models.* With a clear knowledge of the oscillation parameters for solar neutrinos, further information could be obtained on solar models by individual observations of pp, ^{7}Be, pep and CNO neutrinos. Although solar models appear to work very well, improved accuracy on neutrinos from these reactions can test model parameters with extreme accuracy, including radial profile information, since the various reactions are concentrated in different radial sections of the Sun.

This physics motivation leads to the following experimental objectives for future measurements of solar neutrinos:

(i) Improvement in the accuracy of currently running solar neutrino experiments to reduce the experimental uncertainties and improve the restrictions on the 1–2 mixing parameters. (This also is the objective of the KamLAND experiment with reactor anti-neutrinos.)

[1] I thank S Pakvasa and V Barger for discussions on this topic.

(ii) Measurements of lower-energy solar neutrinos (pp, pep, ^{7}Be and CNO) including real-time measurements via CC and ES reactions. The objective would be to perform a measurement of neutrino flavour change for neutrinos with energy below a few MeV without reference to solar model calculations. These measurements of solar electron neutrino fluxes for the individual low-energy reactions will also test solar models in much greater detail.

(iii) Study of the ES process for the lowest energy solar neutrinos to measure the neutrino magnetic moment with a sensitivity greater than present measurements with terrestrial or solar neutrinos.

4.2. General description of experiments

4.2.1. Target materials. In addition to the materials that have been used (water, heavy water, gallium and chlorine), there are a number of materials proposed for future experiments whose properties are matched to the objectives for lower-energy neutrinos. For the CC inverse electron-capture reaction $\nu_e + (A, Z) \rightarrow e^- + (A, Z+1)^*$, the nuclear properties are very important and targets with low-energy thresholds for inverse beta decays of electron neutrinos are being considered, including ^{115}In, ^{100}Mo, ^{82}Se, ^{160}Gd, ^{176}Yb and ^{7}Li. For the ES reaction, $\nu_{e,\mu,\tau} + e^- \rightarrow \nu_{e,\mu,\tau} + e^-$ hydrocarbon liquid scintillators are considered to obtain significantly more light than can be obtained from the Cherenkov process.

However, for pep and CNO neutrinos, background from cosmogenically produced ^{11}C can be a problem requiring a muon veto and imposition of dead time following such an event, except perhaps for sites as deep as SNO and its future extension, SNOLAB. For pp neutrinos, naturally occurring ^{14}C is prohibitive in hydrocarbons and so several proposed experiments are based on other materials such as liquid He, Ne or Xe or gaseous He. Very accurate measurements are necessary to measure the total flux of all active neutrinos, because the Neutral Current interaction only contributes about one-sixth of the ES cross-section.

For ES measurements, the expected interaction rates corresponding to about 0.6 of the SSM are about 1.2 ton^{-1} day^{-1} for pp-neutrinos, 0.024 ton^{-1} day^{-1} for pep-neutrinos and 0.3 ton^{-1} day^{-1} for ^{7}Be-neutrinos. Therefore, detector masses of 20–500 tons are required to obtain event rates greater than about 10 day^{-1} for these solar reactions. The CC reaction rates depend on the matrix elements for the inverse electron capture processes. As an example, the interaction rate in ^{115}In for 0.6 of the SSM would be about 0.2 ton^{-1} day^{-1} for pp-neutrinos and about 0.04 ton^{-1} day^{-1} for ^{7}Be-neutrinos.

4.2.2. Radioactive backgrounds. The neutrino signals of interest, below a few MeV, are inevitably affected by radioactive backgrounds from naturally occurring radioisotopes in detector materials (^{14}C, ^{40}K, ^{238}U, ^{232}Th and related decay products), from cosmogenically produced isotopes (^{11}C and ^{39}Ar) and by other man-made isotopes from the atmosphere (^{85}Kr). Control of these backgrounds is accomplished by extreme care in detector manufacture, as well as the use of very deep locations and *in situ* purification techniques.

For ES measurements, the signal is a single recoil electron. Therefore, background from radioactive decays can mimic a neutrino signal directly. As an example, for a signal-to-background ratio of about 1 for ^{7}Be-neutrinos, Th and U impurity levels of less than about 5×10^{-17} g U(Th) g^{-1}(hydrocarbon) are required. For CC measurements, there are coincidence requirements for the signals that can result in somewhat less stringent radioactive impurity requirements.

4.3. Constructed experiments

SAGE, Super-Kamiokande and SNO are continuing operation and GNO has finished its measurements. In addition, KamLAND is working on the reduction of radioactive impurities with the objective of performing measurements of ^{7}Be-neutrinos. The BOREXINO experiment [27, 28] is a 300 ton hydrocarbon liquid scintillation detector that has been constructed in the Gran Sasso laboratory with the primary objective of measuring ^{7}Be-neutrinos. Extensive work has been done on the reduction of radioactive impurities as demonstrated in preliminary measurements in a smaller test detector [29]. It is expected that detector filling for Borexino could take place later in 2004.

The SAGE detector will be continuing with sensitivity in the pp-neutrino region. Improved accuracy for this region will be valuable for further restricting oscillation parameters. The Super-Kamiokande detector will shut down in 2005 to complete the refurbishment of the phototubes destroyed in the accident in 2002. This will re-establish the phototube coverage that was being used prior to the accident and should restore the analysis threshold for solar neutrinos to 5 MeV.

The SNO detector is entering its third phase, using ^{3}He-filled proportional counters to make a fully independent measurement of the neutrons from the NC reaction. About 2.5 years of operation in this configuration is planned. Projected accuracy for the NC measurement is potentially improved by about a factor of two and the removal of the correlated signals should also improve the accuracy of CC flux measurement by possibly as much as 1.5 and provide more sensitivity for the study of ^{8}B spectral distortion. With this improvement in the SNO results and with the future running planned for the KamLAND experiment and other solar neutrino experiments, one can expect that the allowed region in figure 4(b) will be reduced in both parameters, with the improvements in SNO reducing the θ_{12} range by about a factor of two and improvements in KamLAND accuracy from future running with reactor neutrinos reducing the range of Δm^2_{12} by about a factor of three [30] for 3 years of data. This improvement in the accuracy of the 1–2 parameters will provide significant constraints on θ_{13} and on sterile neutrinos as discussed above. In addition, further measurements of low-energy solar neutrinos by experiments to be discussed below all improve on this accuracy, particularly if it is possible to measure both CC and NC processes for these low-energy cases.

The KamLAND detector is improving the purification of their 1000 ton central volume of liquid scintillator with the particular objective of measuring ^{7}Be neutrinos [31]. The principal backgrounds that must be reduced are ^{210}Pb, ^{85}Kr and ^{40}K, which affect the region below 1 MeV, as well as U and Th chain elements, particularly Rn and ^{210}Pb. Measurements of U and Th chain elements in the fiducial volume indicate impurity levels at present of about 5×10^{-17} g(Th) g^{-1} and 4×10^{-18} g(U) g^{-1} (equilibrium equivalents). Techniques for reduction of these contaminants from the liquid scintillator are being developed, using gas stripping with nitrogen gas that has been purified of Kr, Ar and Rn, as well as stripping of ^{210}Pb with extraction techniques with ultra-pure water. The expected fiducial volume for solar neutrinos is on the order of 500 tons. The relatively shallow depth of the KamLAND site will probably prevent observation of pep and CNO solar neutrinos due to ^{11}C background induced by muons.

The Borexino detector [27] should be in operation in 2004, incorporating the many radiopurification techniques developed for this experiment that has always had a primary aim of measuring the flux of ^{7}Be neutrinos. The Borexino collaboration have pioneered many techniques for reducing radioactive background in liquid scintillators and used a Counting Test Facility (CTF) [29] to obtain the design objectives for a number of radioactive contaminants. The

Table 1. Future projects.

Experiment	Reaction	Target and technique
XMASS [33]	ES	Liquid scintillator (Xe)
HERON [34]	ES	Liquid scintillator (He)
CLEAN [35]	ES	Liquid scintillator (Ne)
TPC [36]	ES	Gas time projection chamber (He +hydrocarbon)
LENS [37, 38]	CC: ^{115}In,^{176}Lu	Liquid scintillator (metallo-organic)
MOON [39]	CC: ^{100}Mo	Fibre-optic and/or liquid scintillator (metallo-organic)

results from the CTF have been used to develop purification techniques (including distillation of the scintillator as well as water and nitrogen stripping) that will be applied for the full scale detector. Techniques [32] for isolating production locations for muon-induced ^{11}C may make it possible to observe pep and CNO neutrinos if other radioactivity, particularly ^{210}Pb, can be reduced sufficiently. Radiopurity objectives are 10^{-16} g g^{-1} for uranium and thorium, and their progenies (assuming secular equilibrium), 10^{-14} g g^{-1} for potassium, 10^{-10} g g^{-1} for argon and 4×10^{-16} g g^{-1} for krypton to obtain background rates less than the expected signals for ^{7}Be.

The possibility of replacing the heavy water in the SNO detector with liquid scintillator is being considered as an option when the heavy water phase is completed. The deep location would provide a significant reduction of ^{11}C for potential measurements of pep and CNO solar neutrinos and there could be other advantages for observation of geoneutrinos, reactor neutrinos and possibly double beta decay with added isotopes.

4.4. Next generation experiments

Future projects under development are aimed primarily at measurements of pp and ^{7}Be neutrinos by the CC and ES reactions. Table 1 lists the largest of the projects under development.

4.4.1. ES measurements. Measurements at the Borexino CTF [40] indicate ^{14}C/^{12}C ratios of about 10^{-18} in organic scintillators. This background is a problem for the measurement of pp-neutrinos in ES experiments because of the 156 keV β-decay endpoint for ^{14}C. Therefore, a number of experiments under development are based on inorganic materials, principally a noble gas scintillator. Such scintillators can provide over four times as many photons as a typical liquid scintillator but the photons are at UV wavelengths and so wavelength shifters are required.

The XMASS experiment [41] proposes to use 10 tons of liquid xenon to observe pp and ^{7}Be solar neutrinos via scintillation light. This mass could provide 10 events day^{-1} for pp and 5 events day^{-1} for ^{7}Be neutrinos. The experiment is being developed in stages. Presently, a 100 kg prototype detector is in operation and has confirmed initial Monte Carlo calculations for detector performance. It is proposed to build a 1 ton detector before moving to the full scale experiment. The detector is located in an ultra-clean facility in the Kamioka mine near the Super-Kamiokande detector. For the 10 ton detector, a 2.5 m diameter spherical design is planned using low-background steel photomultiplier tubes with quartz windows that can operate at liquid xenon temperature. Distillation techniques have been developed and applied to reduce ^{85}Kr background by up to a factor of 300 in one pass. The two-neutrino double beta decay of

^{136}Xe has not been measured to date and will be one of the objectives of the first two phases. If its magnitude is too high, isotope separation may be necessary to remove the ^{136}Xe for the solar neutrino measurements. Neutrinoless double beta decay is also one of the future experimental objectives, using ^{136}Xe isotope. For 5 years of operation of the full scale XMASS detector, for the detection of pp-neutrinos, Nakahata has indicated [42] an expected sensitivity to $\sin^2\theta_{12}$ of about ± 0.03.

The HERON experiment [34] design uses liquid helium with detection via scintillation and/or observation with wafer calorimeters of rotons or 'electron-bubbles' formed at the surface of the helium. Tests have been performed of this innovative technology and detector simulations performed including background estimates. The use of helium provides an inherently very low-background medium for the measurements. A 20 ton detector is planned with pp-neutrino rates of more than 1000 year^{-1} in the fiducial volume. With spectral measurements on the pp spectrum, the shape could provide a sensitive probe of neutrino magnetic moment.

Liquid neon is the basis for the CLEAN experimental design [35]. Neon has no long-lived radioactive isotopes, is an excellent scintillator, has a higher density than liquid helium, can be readily purified and is relatively inexpensive. A spherical design with a full radius of 3 m and a fiducial radius of 1.5 m is being considered. Monte Carlo simulations indicate that the detector would be capable of sensitive dark matter measurements as well as accurate measurements of the pp- and ^{7}Be flux.

A large (18 m $\times$ 20 m) high-pressure (10 atmosphere) time projection chamber using 97% helium gas has been proposed [36] to measure the spectra for low-energy solar neutrinos. The detector technology would build on the MuNu detector experience and could provide directional identification of the ES reaction through the strong angular distribution for the recoil electrons. As with the other detectors, dark matter detection would also be one of the objectives of the design.

4.4.2. CC measurements. The LENS experiment [37] has been working with a low-background test facility to develop a CC measurement based on ^{115}In (with a threshold energy 120 keV) in a metallo-organic scintillator. Scintillators have been developed with over 5% loading by weight of In and acceptable light attenuation lengths. A detector with high granularity is required to identify the background events. Therefore, the detector design has many modules. The neutrino events will be tagged by two gammas from a cascade in the final nucleus, reducing background from natural and from contaminant ^{115}In radioactivity significantly. A total volume of about 60 tons of In in 3000 tons of liquid scintillator is planned [38]. This would provide about 3 events per day for either a pp or a ^{7}Be flux at 0.6 of the Standard Solar Model. The nuclear matrix element for the low-energy neutrino absorption reaction has been measured through the (p, n) reaction. However, to provide an accurate calibration, a measurement with an ^{37}Ar radioactive neutrino source is planned.

The MOON [39] experiment proposes to use a low-energy inverse electron capture reaction on ^{100}Mo to observe pp neutrinos with excellent sensitivity and a threshold energy of 168 keV. The daughter nucleus ^{100}Tc beta decays with a half-life of 16 s, so the signature of the CC reaction is two localized electrons. ^{100}Mo itself undergoes two-neutrino double beta decay at a rate that constitutes a background for the detection of solar neutrinos and so a detector with small modules is used to discriminate double beta decays from neutrino events. A design is under development using optical fibers for an extensive modular structure. A counting rate of 0.4 events per day for pp-neutrinos is projected for a detector containing about 3 tons of ^{100}Mo isotope.

4.5. Summary

Measurements of solar neutrinos have contributed substantially to our knowledge of neutrino properties and of the physics of the Sun. Neutrino flavour change has been clearly observed in an appearance measurement. A series of sensitive measurements with different energy thresholds have tested the Standard Solar Model for the dominant reactions and there is very good agreement assuming neutrino flavour change. The measurements to date, combined with reactor anti-neutrino measurements have defined the flavour change mechanism to be the oscillation of massive neutrinos and defined the acceptable range of oscillation parameters with reasonable accuracy. They have also provided limits at the 10% level for sub-dominant components such as sterile neutrinos.

Future experiments will provide improved accuracy for neutrino oscillation parameters as well as providing the first measurements of individual neutrino reactions in real time at low energy to probe solar models with greater sensitivity.

References

[1] Bahcall J N and Pena-Garay C 2004 *New J. Phys.* **6** 63

[2] Davis R *et al* 1968 *Phys. Rev. Lett.* **14** 20
Cleveland B T, Daily T, Davis R Jr, Distel J R, Lande K, Lee C K, Wildenhain P S and Ullman J 1998 *Astrophys. J.* **496** 505

[3] Gavrin V N *et al* 2003 *Nucl. Phys.* B (*Proc. Suppl.*) **118** 39

[4] Hampel W *et al* 1999 *Phys. Lett.* B **447** 127
Altmann *et al* 2000 *Phys. Lett.* B **490** 16

[5] Fukuda Y *et al* 1996 *Phys. Rev.* D **44** 1683

[6] Fukuda S *et al* 2001 *Phys. Rev. Lett.* **86** 5651
Fukuda S *et al* 2002 *Phys. Lett.* B **539** 179
Smy M (Super-Kamiokande Collaboration) 2003 *Nucl. Phys.* B (*Proc. Suppl.*) **118** 25

[7] Ahmed S N *et al* 2003 *Preprint* nucl-ex/0309004

[8] Mikheyev S P and Smirnov A Y 1986 *Massive Neutrinos in Astrophysics and in Particle Physics, Proc. Moriond Workshop* ed O Fackler and J Tran Thanh Van (Gif-sur-Yvette: Editions Frontières) p 335
Mikheyev S P and Smirnov A Yu 1985 *Sov. J. Nucl. Phys.* **42** 1441
Wolfenstein L 1978 *Phys. Rev.* D **17** 2369

[9] Beacom J F and Bell N F 2002 *Phys. Rev.* D **65** 113009

[10] Miranda O G *et al* 2001 *Nucl. Phys.* B **595** 360
Chauhan B C and Pulido J 2002 *Phys. Lett.* **66** 053006
Akhmedov E Kh and Pulido J 2003 *Phys. Lett.* B **553** 7

[11] Bahcall J N *et al* 1997 *Phys. Rev. Lett.* **78** 171

[12] Maki Z, Nakagawa N and Sakata S 1962 *Prog. Theor. Phys.* **28** 870
Pontecorvo B 1957 *J. Exp. Theor. Phys.* **33** 549
Pontecorvo B 1958 *J. Exp. Theor. Phys.* **34** 247
Gribov V and Pontecorvo B 1969 *Phys. Lett.* B **28** 493

[13] Anselmann P *et al* 1995 *Phys. Lett.* B **342** 440
Abdurashitov J N *et al* 1996 *Phys. Rev. Lett.* **77** 4708
Hampel W *et al* 1998 *Phys. Lett.* B **420** 114

[14] Fukuda S *et al* 2003 *Nucl. Instrum. Methods* A **501** 418

[15] Baltz A J and Weneser J 1988 *Phys. Rev.* D **37** 3364
Gonzalez-Garcia M C, Peña-Garay C and Smirnov A Y 2001 *Phys. Rev.* D **63** 113004

[16] Liu D W *et al* 2004 *Preprint* hep-ex/040215 v1
[17] Boger J *et al* 2000 *Nucl. Instrum. Methods* A **449** 72
[18] Ahmad Q R *et al* 2001 *Phys. Rev. Lett.* **87** 071301
[19] Ahmad Q R *et al* 2002 *Phys. Rev. Lett.* **89** 011301
[20] Ahmad Q R *et al* 2002 *Phys. Rev. Lett.* **89** 011302
[21] Eguchi E *et al* 2003 *Phys. Rev. Lett.* **90** 021802
[22] Bahcall J N, Gonzales-Garcia M C and Peña-Garay C 2003 *J. High Energy Phys.* JHEP02(2003)009
[23] Eguchi K *et al* 2004 *Phys. Rev. Lett.* **92** 071301 (*Preprint* hep-ex/0310047)
[24] Maltoni M, Schwetz T, Tortola M A and Valle J W F 2003 *Phys. Rev.* D **68** 113010
[25] Bahcall J N, Barger V and Marfatia D 2002 *Phys. Lett.* B **534** 120 (*Preprint* hep-ph/0201211)
[26] Holanda P C and Smirnov A Yu 2003 *Preprint* hep-ph/0307266
[27] Borexino collaboration, Alimonti G *et al* 2002 *Astropart. Phys.* **16** 205
[28] Borexino collaboration, Arpesella C *et al* 2002 *Astropart. Phys.* **18** 1
[29] Borexino collaboration, Alimonti G *et al* 1998 *Astropart. Phys.* **8** 141
Borexino collaboration, Alimonti G *et al* 1998 *Nucl. Instrum. Methods* A **406** 411
[30] Balantekin A B, Barger V, Marfatia D, Pakvasa S and Yuksel H 2004 private communication
[31] Suzuki A 2004 private communication
[32] Franco D, Rannucci G and Schoenert S (Borexino Collaboration) 2004 private communication
[33] Suzuki Y 2000 *LowNu2 Workshop, Tokyo* http://www-sk.icrr.u-tokyo.ac.jp/neutlowe/
[34] Lanou B 2002 *LowNu 2002 Workshop, Heidelberg* http://www.mpi-hd.mpg.de/nubis/www_lownu2002/
[35] McKinsey D N and Doyle J M 2000 *J. Low Temp. Phys.* **118** 153
[36] Bonvicini G *et al* 2001 Contributed paper, Snowmass *Preprints* hep-ex/0109199, hep-ex/0109032
[37] Raghavan R S 1997 *Phys. Rev. Lett.* **78** 3618
LENS Collaboration 1999 Letter of Intent, Laboratori Nazionali del Gran Sasso http://www.mpi-hd.mpg.de/nubis/www_lownu2002/
[38] Raghavan R S 2004 *NOON2004 Conf., Tokyo, Japan* http://www-sk.icrr.u-tokyo.ac.jp/noon2004/
[39] Ejiri H *et al* 2000 *Phys. Rev. Lett.* **85** 2917
[40] Borexino Collaboration, Alimonti G *et al* 1998 *Phys. Lett.* B **422** 349
[41] Namba T 2004 *NOON2004 Conf., Tokyo, Japan* http://www-sk.icrr.u-tokyo.ac.jp/noon2004/
[42] Nakahata M 2002 *LowNu 2002 Workshop, Heidelberg* http://www.mpi-hd.mpg.de/nubis/www_lownu2002/

New Journal of Physics
An Institute of Physics and Deutsche Physikalische Gesellschaft Journal

Status of global fits to neutrino oscillations

Michele Maltoni[1], **Thomas Schwetz**[2], **Mariam Tórtola**[3] **and José W F Valle**[3]

[1] CN Yang Institute for Theoretical Physics, SUNY at Stony Brook, Stony Brook, NY 11794-3840, USA
[2] Physik-Department, Technische Universität München, James-Franck-Strasse, D-85748 Garching, Germany
[3] AHEP Group, Instituto de Física Corpuscular—CSIC/Universitat de València, Edificio Institutos de Paterna, Apt 22085, E-46071 Valencia, Spain
E-mail: maltoni@insti.physics.sunysb.edu, schwetz@ph.tum.de, mariam@ific.uv.es and valle@ific.uv.es

New Journal of Physics **6** (2004) 122
Received 18 May 2004
Published 28 September 2004
Online at http://www.njp.org/
doi:10.1088/1367-2630/6/1/122

Abstract. We review the present status of global analyses of neutrino oscillations, taking into account the most recent neutrino data including the latest KamLAND and K2K updates presented at Neutrino 2004, as well as state-of-the-art solar and atmospheric neutrino flux calculations. We give the two-neutrino solar + KamLAND results, and the two-neutrino atmospheric + K2K oscillation regions, discussing in each case the robustness of the oscillation interpretation against departures from the Standard Solar Model and the possible existence of non-standard neutrino physics. Furthermore, we give the best-fit values and allowed ranges of the three-flavour oscillation parameters from the current worlds' global neutrino data sample and discuss in detail the status of the small parameters $\alpha \equiv \Delta m^2_{\rm SOL}/\Delta m^2_{\rm ATM}$ as well as $\sin^2\theta_{13}$, which characterize the strength of CP violating effects in neutrino oscillations. We also update the degree of rejection of four-neutrino interpretations of the LSND evidence in view of the most recent developments.

PII: S1367-2630(04)80908-X
© IOP Publishing Ltd and Deutsche Physikalische Gesellschaft

Contents

1. Introduction **2**

2. Leading oscillations with $\Delta m^2_{\mathrm{ATM}}$ **3**

2.1. Atmospheric neutrino oscillations . . . 3

2.2. The K2K accelerator experiment . . . 5

2.3. Atmospheric and K2K combined . . . 5

2.4. Robustness of oscillation interpretation: atmospheric neutrinos . . . 6

3. Leading oscillations with $\Delta m^2_{\mathrm{SOL}}$ **9**

3.1. Solar neutrino oscillations . . . 9

3.2. The KamLAND reactor neutrino experiment . . . 10

3.3. Solar and KamLAND combined . . . 12

3.4. Robustness of oscillation interpretation: solar neutrinos . . . 14

3.4.1. Beyond the SSM . . . 14

3.4.2. Beyond solar neutrino oscillations: spin flavour precession . . . 15

3.4.3. Beyond SM neutrino cross sections: constraining neutrino magnetic moments . . . 17

4. Three-flavour neutrino oscillations **19**

4.1. Global three-neutrino analysis . . . 19

4.2. The small parameters $\alpha \equiv \Delta m^2_{\mathrm{SOL}}/\Delta m^2_{\mathrm{ATM}}$ and θ_{13} . . . 20

5. Four-neutrino oscillations and LSND **24**

5.1. A common parametrization for four-neutrino schemes . . . 24

5.2. (2 + 2): ruled out by solar and atmospheric data . . . 26

5.3. (3 + 1): strongly disfavoured by SBL data . . . 27

5.4. Comparing (3 + 1), (2 + 2) and (3 + 0) hypotheses . . . 28

6. Summary and conclusions **30**

Acknowledgments **31**

Appendix. The new KamLAND results **31**

References **34**

1. Introduction

The discovery of neutrino masses by the combination of a variety of data from solar [1]–[10], atmospheric [11]–[13], reactor [14, 15] and accelerator [16, 17] neutrino experiments was the major recent achievement in astroparticle, high energy, and nuclear physics, which culminates a heroic effort dating back over about four decades. This has now firmly established the incompleteness of the Standard Model of electroweak interactions, expected on theoretical grounds since long ago [18]–[22]. The determination of neutrino oscillation parameters is now a flourishing industry (see, e.g., [23]) which has finally entered the high precision age, with many experiments underway and a new generation coming. Apart from a careful understanding of solar and atmospheric neutrino fluxes, nuclear physics, neutrino cross sections and experimental response functions, an interpretation of the data relies heavily on the proper description of neutrino propagation properties both in the Sun and the Earth, including the so-called matter effects [24, 25].

The avalanche of data in a field where these have been traditionally so scarce, given the feebleness of neutrino interactions, has prompted a rush of phenomenological papers on the interpretation of neutrino data. A number of reviews are already available [26]–[29]. Here we revisit the latest global analysis of neutrino oscillation parameters presented in [30] in view of the most recent solar [31] and atmospheric [32] neutrino flux calculations and of the new data presented at Neutrino 2004.

This paper is organized as follows. In section 2, we briefly discuss the analysis of the atmospheric neutrino data including the state-of-the-art three-dimensional calculation of the atmospheric neutrino flux given in [32]. In order to obtain the allowed ranges for the oscillation parameters $\Delta m^2_{\rm ATM}$ and $\theta_{\rm ATM}$ we combine the atmospheric neutrino data from the Super-K experiment with the accelerator data from the KEK to Kamioka (K2K) experiment, which provides the first independent confirmation of the oscillation evidence from atmospheric neutrinos. We give also a short description of robustness of the atmospheric data with respect to non-standard neutrino interactions in section 2.4.

In section 3 we briefly describe the solar neutrino experiments and the KamLAND reactor neutrino experiment, and discuss the two-neutrino interpretation of the data described by $\Delta m^2_{\rm SOL}$ and $\theta_{\rm SOL}$. We comment on the implications of the recent update of the Standard Solar Model (SSM) neutrino fluxes from [31]. Furthermore, in section 3.4 we discuss the robustness of the oscillation interpretation of solar neutrino data when going beyond the SSM framework or invoking non-standard neutrino properties. As examples, we consider the effects of solar radiative-zone density fluctuations, convective-zone magnetic fields and the prospects of probing electromagnetic neutrino properties with current and future experiments.

After discussing the dominant oscillations in the two-flavour approximation in sections 2 and 3 we devote section 4 to the global three-neutrino analysis of the data, combining all current neutrino oscillation data except LSND. In addition to presenting the best fit values and allowed ranges for the oscillation parameters, we update the status of the three-flavour parameters $\alpha \equiv \Delta m^2_{\rm SOL}/\Delta m^2_{\rm ATM}$ and θ_{13} in view of the new data reported at Neutrino 2004. In section 6 we give an update of the status of attempts to account for the LSND data in terms of four-neutrino oscillations. Finally, we conclude and summarize our results in section 6. A detailed discussion of the recent KamLAND results is given in an appendix.

2. Leading oscillations with $\Delta m^2_{\rm ATM}$

2.1. Atmospheric neutrino oscillations

In 1998 the Super-K experiment obtained evidence for neutrino oscillations [11] from the observation of the zenith angle dependence of their μ-like atmospheric neutrino data. This effect has been confirmed also by other atmospheric neutrino experiments; see, e.g., [12, 13]. Recently, Super-K has reported a dip in the L/E distribution of the atmospheric ν_μ survival probability [33], which provides a clear signature for neutrino oscillations.

In our atmospheric neutrino analysis we include the most recent charged-current atmospheric neutrino data from Super-K [34], including the e-like and μ-like data samples of sub- and multi-GeV contained events (each grouped into 10 bins in zenith angle), as well as the stopping (5 angular bins) and through-going (10 angular bins) up-going muon data events. As before, we do not use the information on ν_τ appearance, multi-ring μ and neutral-current events since an efficient Monte Carlo simulation of these data would require a more detailed

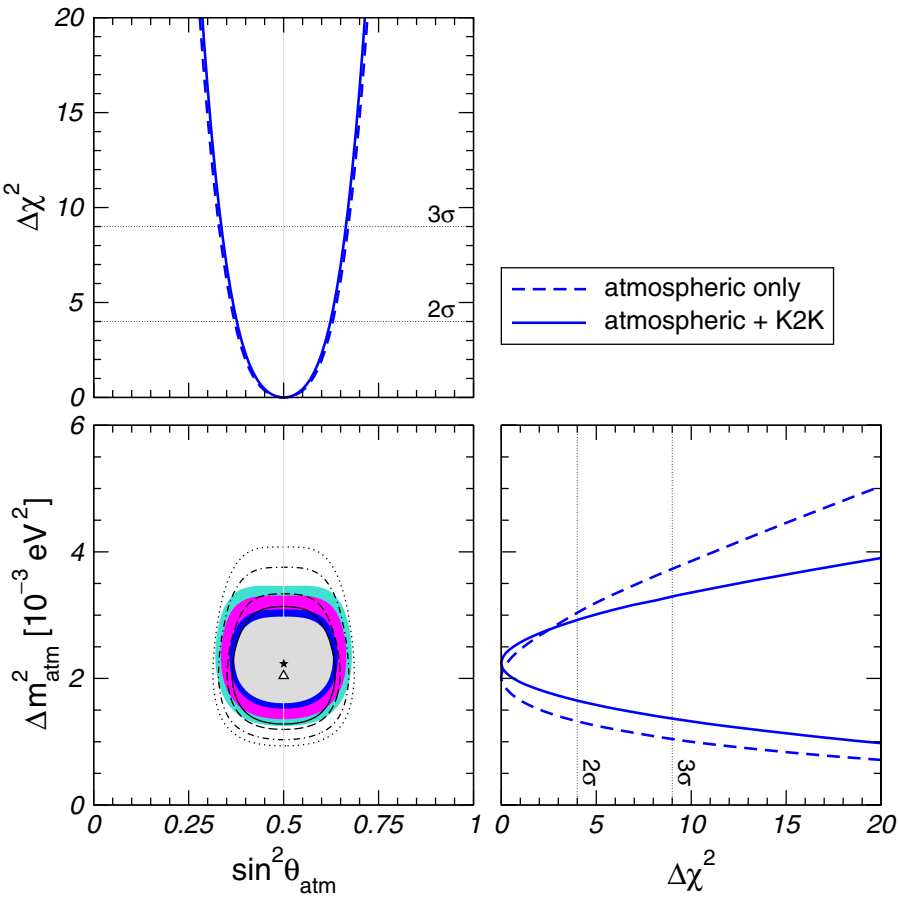

Figure 1. Allowed ($\sin^2\theta_{\rm ATM}$, $\Delta m^2_{\rm ATM}$) regions at 90, 95 and 99%, and 3σ CL for 2 d.o.f. The regions delimited by the lines correspond to atmospheric data only, while for the coloured regions K2K data are also added. The best-fit point of atmospheric (atmospheric + K2K) data is marked by a triangle (star). Also shown is the $\Delta\chi^2$ as a function of $\sin^2\theta_{\rm ATM}$ and $\Delta m^2_{\rm ATM}$, minimized with respect to the undisplayed parameter.

knowledge of the Super-K experiment, and in particular of the way the neutral-current signal is extracted from the data. For details of our analysis see [35, 36] and references therein. With respect to our previous atmospheric neutrino analysis [30] we have now taken into account the new three-dimensional atmospheric neutrino fluxes given in [32]. Furthermore, we have updated our statistical analysis following closely [37], taking special care of systematical errors, like uncertainties in the neutrino fluxes and detection cross sections. Details on the χ^2 analysis can also be found in [38]. With these updates our results are in excellent agreement with those of the Super-K collaboration [34].

In figure 1 we show the results of our analysis of atmospheric data in the framework of two-flavour $\nu_\mu \to \nu_\tau$ oscillations. The regions delimited by the hollow contours correspond to the allowed regions for the oscillation parameters $\sin^2\theta_{\rm ATM}$ and $\Delta m^2_{\rm ATM}$. The current best fit point occurs at

$$\sin^2\theta_{\rm ATM} = 0.50, \qquad \Delta m^2_{\rm ATM} = 2.0\times 10^{-3}\,{\rm eV}^2 \quad \text{(ATM data)}. \tag{1}$$

The main difference from the results of [30] is the relatively lower values of $\Delta m^2_{\rm ATM}$ implied by the use of the new three-dimensional atmospheric neutrino fluxes reported in [32] instead of the one-dimensional Bartol fluxes [39] used previously.

2.2. The K2K accelerator experiment

The K2K long-baseline neutrino oscillation experiment [16] probes the ν_μ disappearance oscillation channel in the same region of Δm^2 as explored by atmospheric neutrinos. The neutrino beam is produced by a 12 GeV proton beam from the KEK proton synchrotron, and consists of 98% muon neutrinos with a mean energy of 1.3 GeV. The beam is controlled by a near detector 300 m away from the proton target. Information on neutrino oscillations is obtained by the comparison of this near detector data with the ν_μ content of the beam observed by the Super-Kamiokande detector at a distance of 250 km.

The data sample called K2K-I [16] has been collected in the period from June 1999 to July 2001 (4.8×10^{19} protons on target). K2K-I has observed 56 events in Super-K, whereas $80.1^{+6.2}_{-5.4}$ have been expected in the case of no oscillations. This gives clear evidence for ν_μ disappearance: the probability that the observed flux at Super-K is explained by a statistical fluctuation without neutrino oscillations is less than 1% [16]. Recently, at the Neutrino 2004 conference, new data from the K2K-II period have been presented [17]. K2K-II started in the autumn of 2002, and the released data corresponds to 4.1×10^{19} protons on target, comparable to the K2K-I sample. From the combined analysis of K2K-I and K2K-II, 108 events have been observed in Super-K, whereas $150.9^{+11.6}_{-10.0}$ have been expected for no oscillations. Out of the 108 events, 56 are the so-called single-ring muon events. This data sample contains mainly muon events from the quasi-elastic scattering $\nu_\mu + \mathrm{p} \to \mu + \mathrm{n}$, and the reconstructed energy is closely related to the true neutrino energy. Hence these data can be used for a spectral analysis. Using the Kolmogorov–Smirnov test, the K2K collaboration finds that the observed spectrum is consistent with the spectrum expected for no oscillation only at a probability of 0.11%, whereas the spectrum predicted by the best-fit oscillation parameters has a probability of 52% [17].

In our re-analysis of K2K data we use the energy spectrum of the 56 single-ring muon events from K2K-I + K2K-II.[4] Similar to [38] we use a phenomenological parametrization of the spectrum expected for no oscillation. Adopting reasonable assumptions on the energy resolution function and on systematical errors, we fit the data divided into 15 bins in reconstructed neutrino energy, as given in [17]. The allowed regions for the oscillation parameters from K2K data are shown in figure 2 in comparison to the ones from atmospheric neutrino data. This figure illustrates that the neutrino mass-squared difference indicated by the ν_μ disappearance observed in K2K is in perfect agreement with atmospheric neutrino oscillations. Hence, K2K data provide the first confirmation of oscillations with $\Delta m^2_{\rm ATM}$ from a man-made neutrino source. K2K gives a rather weak constraint on the mixing angle due to low statistics in the current data sample.

2.3. Atmospheric and K2K combined

In figure 1 the allowed regions in the ($\sin^2\theta_{\rm ATM}$, $\Delta m^2_{\rm ATM}$) plane from the combined analysis of K2K and Super-K atmospheric neutrino data are shown as shaded regions. As expected from figure 2 we find that, apart from providing an independent confirmation, K2K data start already

[4] We cannot use the full K2K data sample of 108 events, since not enough information is available to analyse these data outside the K2K collaboration.

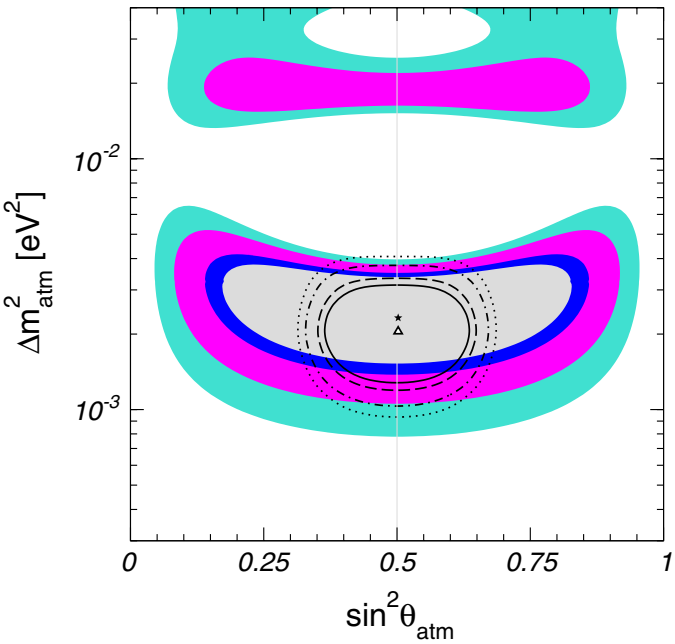

Figure 2. Allowed K2K regions in the ($\sin^2\theta_{\rm ATM}$, $\Delta m^2_{\rm ATM}$) plane at 90, 95 and 99% and 3σ CL for 2 d.o.f. The hollow lines delimit the region determined from the atmospheric data only. The star (triangle) corresponds to the K2K (atmospheric) best-fit point.

to constrain the allowed region of $\Delta m^2_{\rm ATM}$, whereas the determination of the mixing angle is completely dominated by atmospheric data. From the projections of χ^2 onto the $\Delta m^2_{\rm ATM}$ and $\sin^2\theta_{\rm ATM}$ axes shown in figure 1 we find the best-fit point

$$\sin^2\theta_{\rm ATM} = 0.5, \qquad \Delta m^2_{\rm ATM} = 2.2\times 10^{-3}\,{\rm eV}^2 \quad ({\rm ATM + K2K\ data}) \tag{2}$$

with the corresponding allowed ranges at 3σ (5σ) for 1 degree of freedom (d.o.f.):

$$\begin{aligned} &0.34\,(0.27) \leqslant \sin^2\theta_{\rm ATM} \leqslant 0.66\,(0.73), \\ &1.4\,(0.85)\times 10^{-3}\,{\rm eV}^2 \leqslant \Delta m^2_{\rm ATM} \leqslant 3.3\,(4.2)\times 10^{-3}\,{\rm eV}^2. \end{aligned} \tag{3}$$

Note that despite the downward shift of the atmospheric mass-splitting implied by the new neutrino fluxes from [32] our new quoted value for $\Delta m^2_{\rm ATM}$ in (2) is statistically compatible both with our previous result [30] and the value obtained by the new Super-K L/E analysis [33]. Let us remark that the K2K constraint on $\Delta m^2_{\rm ATM}$ from below is important for future long-baseline experiments, since the performance of such experiments is drastically affected if $\Delta m^2_{\rm ATM}$ is in the lower part of the 3σ range allowed by atmospheric data (see e.g. [40]).

2.4. Robustness of oscillation interpretation: atmospheric neutrinos

We now turn to the issue of the robustness of the oscillation interpretation of the atmospheric neutrino data. Non-standard physics may in principle affect atmospheric neutrino fluxes, as

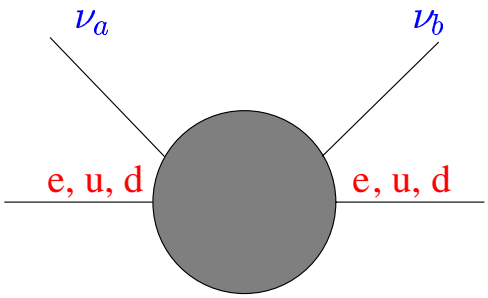

Figure 3. Effective flavour-changing NSI operator.

well as neutrino propagation and detection cross sections [26]. Apart from the issue of their theoretical viability [41], neutrino decays have been considered since long ago [42]. Non-standard interactions arising from the SU(2) ⊗ U(1) charged and neutral currents [20] or from new particles [43]–[49], as well as quantum mechanical decoherence [38] might also affect atmospheric neutrino results. Although strongly rejected by recent atmospheric data as the dominant mechanisms [33, 38, 50], non-standard phenomena might still be present at a sub-leading level in addition to oscillations and, to this extent, have some impact on the determination of the oscillation parameters.

In the following we illustrate the stability of the measurement of $\Delta m^2_{\rm ATM}$ and $\sin^2\theta_{\rm ATM}$ by assuming the presence of non-standard interactions of the neutrinos with earth matter. New neutrino interactions beyond the Standard Model are a natural feature in most neutrino mass models [51] and can be of two types: flavour-changing (FC) and non-universal (NU). These interactions (called NSI for short) may be schematically represented as effective dimension-6 terms of the type εG_F, as illustrated in figure 3, where ε specifies their sub-weak strength. Such interactions may arise from a non-trivial structure of charged and neutral current weak interactions characterized by a non-unitary lepton mixing matrix [20]. These gauge-induced NSI may lead to flavour and CP violation, even with massless or degenerate neutrinos [45], [47]–[49]. Alternatively, such non-standard neutrino interactions may also arise in models where neutrino masses are 'calculable' from radiative corrections [43, 44] and in some supersymmetric models with broken R parity [52]. Finally, in supersymmetric unified models, the strength of non-standard neutrino interactions may be a calculable renormalization effect [46].

The impact of non-standard neutrino interactions on atmospheric neutrinos was considered in [50] treating the NSI strengths as free phenomenological parameters. This analysis takes into account both the effect of $\nu_\mu \to \nu_\tau$ oscillations (OSC) as well as the existence of non-standard neutrino–matter interactions (NSI) in this channel. In addition to the standard term in the Hamiltonian describing oscillations, a term $H_{\rm NSI}$ is introduced, accounting for an effective potential induced by the NSI with earth matter:

$$H_{\rm NSI} = \pm\sqrt{2}G_F N_f \begin{pmatrix} 0 & \varepsilon \\ \varepsilon & \varepsilon' \end{pmatrix}. \tag{4}$$

Here +(−) holds for neutrinos (anti-neutrinos) and ε and ε' parametrize the NSI: $\sqrt{2}G_F N_f \varepsilon$ is the forward scattering amplitude for the FC process $\nu_\mu + f \to \nu_\tau + f$ and $\sqrt{2}G_F N_f \varepsilon'$ represents the difference between $\nu_\mu + f$ and $\nu_\tau + f$ elastic forward scattering. The quantity N_f is the number

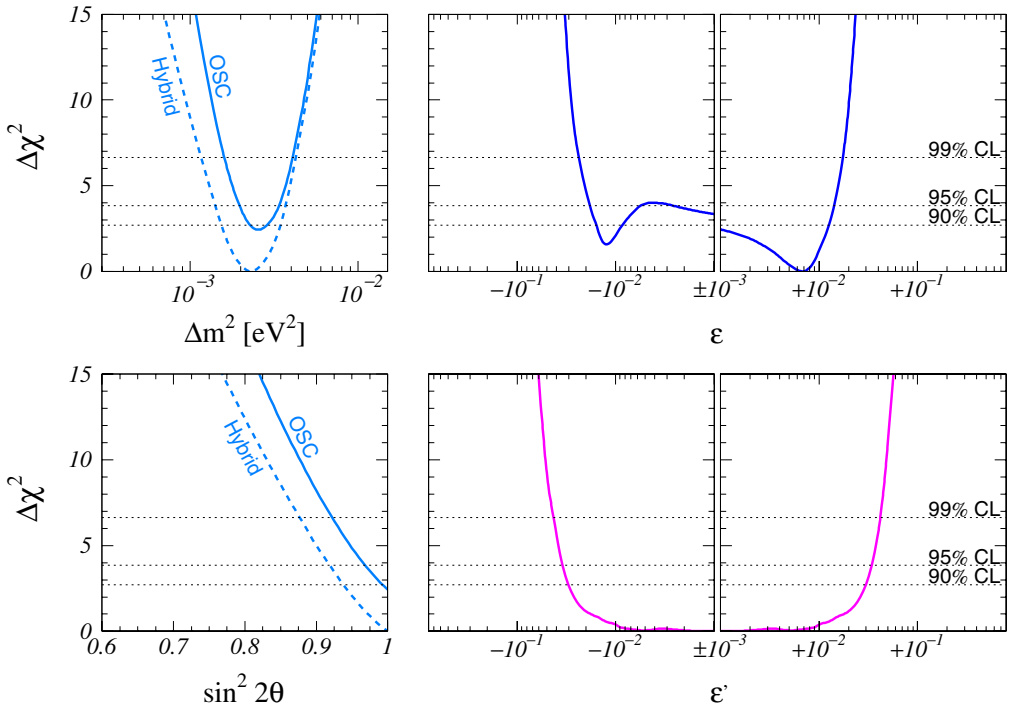

Figure 4. Atmospheric neutrino oscillation parameters from [50] fitted in the presence of non-standard interactions using the Bartol flux [39]. We show the behaviour of χ^2 as a function of the four parameters $\Delta m^2_{\rm ATM}$ (upper left), $\sin^2 2\theta_{\rm ATM}$ (lower left), the FC parameter ε (upper right) and the NU parameter ε' (lower right). In each panel, χ^2 is minimized with respect to the three undisplayed parameters. In the left panels, we also show the pure oscillation case (OSC), with ε and ε' set to zero.

density of the fermion f along the neutrino path. For definiteness, we take for f the down-type quark.

In figure 4 we show the results of a fit to atmospheric neutrino data for the four parameters $\Delta m^2_{\rm ATM}$, $\sin^2 2\theta_{\rm ATM}$, ε and ε'.[5] In the left panels the pure oscillation case ($\varepsilon = \varepsilon' = 0$) is compared to the case where some NSI are also allowed. We find that the χ^2 improves slightly (2.4 units) in the presence of NSI, but the determination of the oscillation parameters is practically unaffected. This is an important result, since it shows that the allowed ranges derived for $\Delta m^2_{\rm ATM}$ and $\sin^2 2\theta_{\rm ATM}$ are rather stable with respect to non-standard physics.[6] In turn, the high preference of the data for oscillations allows us to set strong bounds on NSI. From the right panels of figure 4 we deduce the bounds at 3σ

$$-0.03 \leqslant \varepsilon \leqslant 0.02, \qquad |\varepsilon'| \leqslant 0.05. \tag{5}$$

[5] Here we assume that the parameter ε is real; for the more general case of complex ε, see [53].

[6] Note that the analysis of [50] is based on the neutrino fluxes of [39], and in addition to the Super-K data described in section 2.1, the up-going muon data from the MACRO experiment [12] is also used. This explains the slight difference between the best-fit values of $\Delta m^2_{\rm ATM}$ from figure 4 for the pure oscillation case and equation (1).

Before closing we stress that, apart from its intrinsic theoretical importance, the study of non-standard neutrino interactions has an astrophysical interest, as these can affect the propagation of neutrinos in a variety of astrophysical environments, such as supernovae [54, 55] and pulsars [56]. They could lead to 'deep-inside' neutrino conversions, in addition to those expected from conventional neutrino oscillations.

3. Leading oscillations with $\Delta m^2_{\mathrm{SOL}}$

3.1. Solar neutrino oscillations

In this section we consider oscillations of solar neutrinos in the two-flavour framework. A detailed discussion of experimental and theoretical aspects of solar neutrino physics can be found in other contributions to this volume [57, 58]. Therefore, we focus in the following on the determination of the oscillation parameters from the fit to solar neutrino data. In our analysis we take into account the rates of the chlorine experiment at the Homestake mine [2, 1] ($2.56 \pm 0.16 \pm 0.16$ SNU), the most up-to-date results [59] of the gallium experiments SAGE [3, 60] ($66.9^{+3.9+3.6}_{-3.8-3.2}$ SNU) and GALLEX/GNO [4]–[6] ($69.3 \pm 4.1 \pm 3.6$ SNU), as well as the 1496-day Super-K data sample [7] in the form of 44 bins (eight energy bins, six of which are further divided into seven zenith angle bins). From the SNO experiment we include the most recent data from the salt phase [10] in the form of the neutral current (NC), charged current (CC) and elastic scattering (ES) fluxes, as well as the 2002 spectral day/night data [8, 9] (17 energy bins for each day and night period).

The analysis methods used here are similar to the ones described in [30, 36] and references therein, including the use of the so-called pull approach for the χ^2 calculation, as described in [61]. In this method all systematic uncertainties are included by introducing new parameters in the fit and adding a penalty function to χ^2. For example, for each of the eight solar neutrino fluxes a parameter is introduced, and the predictions from the SSM including the correlated errors are taken into account by means of a penalty function. The method described in [61] is extended in two respects. First, it is generalized to the case of correlated statistical errors [62] as necessary to treat the SNO-salt data. Second, we do not consider the χ^2 only up to first order in the pulls, but instead each pull parameter is treated exactly to all orders. This is particularly interesting in the case of the solar ^{8}B flux. In our approach, it is possible to include the SSM prediction for this flux as well as the SNO NC measurement on the same footing, without pre-selecting a particular value, as implied by expanding around the predicted value. In this way, the fit itself can choose the best compromise between the SNO NC data and the SSM prediction.

In figure 5 we compare the allowed regions for the oscillation parameters using the solar neutrino fluxes given in the BP00 SSM [63] and the recent update (BP04) presented in [31]. One finds that the change in the flux predictions has a negligible impact on the allowed regions. This illustrates that, thanks to the good experimental accuracy, the determination of the oscillation parameters is rather robust with respect to changes in the SSM. The current best-fit values for solar neutrino oscillation parameters are

$$\sin^2\theta_{\mathrm{SOL}} = 0.29, \qquad \Delta m^2_{\mathrm{SOL}} = 6.0 \times 10^{-5}\,\mathrm{eV}^2 \quad \text{(solar data, BP04)}. \tag{6}$$

Also the rejection against maximal solar mixing is 5.6σ, the same as found previously [30] using the BP00 solar model. This is the significance at which bi-maximal models of neutrino mass, such as the CP conserving version of the neutrino unification model given in [64], are ruled out.

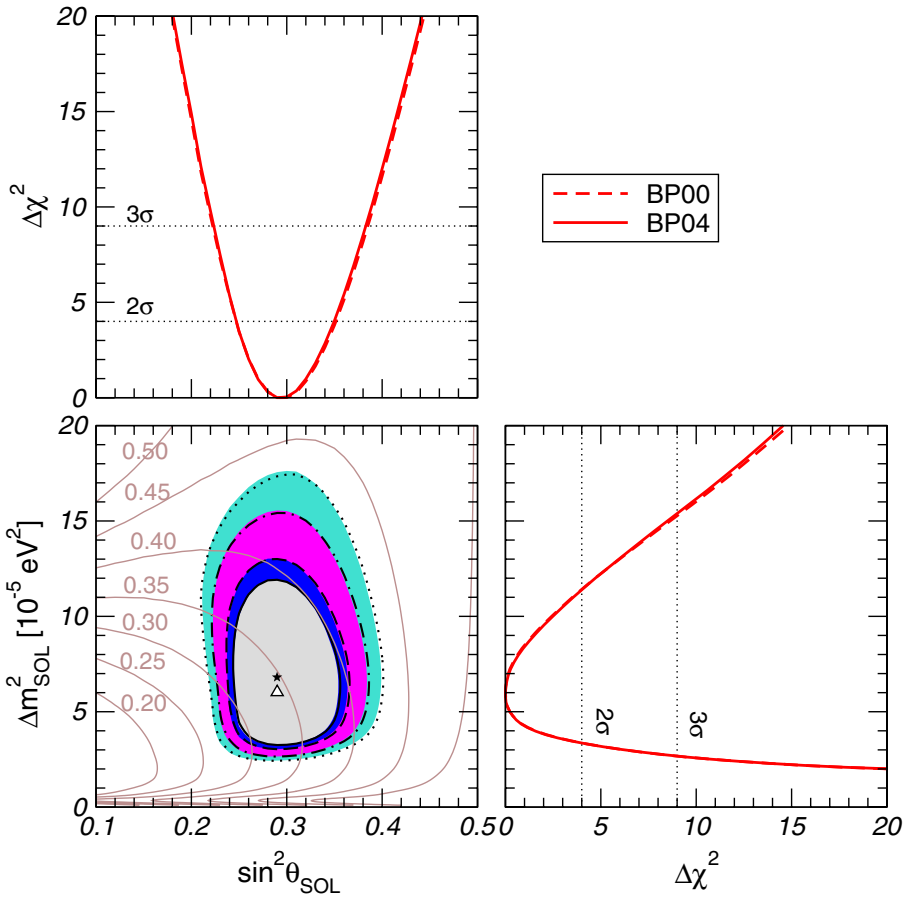

Figure 5. Allowed regions from all solar neutrino data at 90, 95 and 99%, and 3σ CL for 2 d.o.f. in the plane of $\sin^2\theta_{SOL}$ and Δm^2_{SOL}. The regions delimited by the curves correspond to the BP00 SSM [63], whereas for the coloured regions the BP04 SSM [31] has been used. Also shown is $\Delta\chi^2$ as a function of $\sin^2\theta_{SOL}$ and Δm^2_{SOL}, minimized with respect to the undisplayed parameter. The labelled contours denote constant CC/NC ratio in the SNO experiment.

Despite the fact that the BP04 model does not imply any significant change in the solar neutrino parameters, we will use it in our subsequent discussion of solar neutrino results.

3.2. The KamLAND reactor neutrino experiment

The KamLAND experiment [14, 15] is a reactor neutrino experiment with its detector located at the Kamiokande site. Most of the $\bar{\nu}_e$ flux incident at KamLAND comes from nuclear plants at distances of 80–350 km from the detector, making the average baseline of about 180 km, long enough to provide a sensitive probe of the LMA solution of the solar neutrino problem. The KamLAND collaboration has for the first time measured the disappearance of neutrinos travelling to a detector from a power reactor. They observe a strong evidence for the disappearance of neutrinos during their flight over such distances, giving the first terrestrial confirmation of

the solar neutrino anomaly and also establishing the oscillation hypothesis with man-produced neutrinos.

In KamLAND, the reactor anti-neutrinos are observed by the process $\bar{\nu}_e + \mathrm{p} \rightarrow \mathrm{e}^+ + \mathrm{n}$, where the delayed coincidence of the prompt energy from the positron and a characteristic gamma from the neutron capture allows an efficient reduction of backgrounds. The neutrino energy is related to the prompt energy by $E_\nu = E_{\mathrm{pr}} + \Delta - m_e$, where Δ is the neutron–proton mass difference and m_e is the positron mass. In the lower part of the energy spectrum there is a relevant contribution from geo-neutrino events to the signal (see e.g. [65, 66]). To avoid large uncertainties associated with the geo-neutrino flux, an energy cut at 2.6 MeV prompt energy is applied for the oscillation analysis.

First results from KamLAND were published in [14]. In the period from March to October 2002 data corresponding to a 162 ton-year exposure have been collected, and after all cuts 54 anti-neutrino events remained in the final sample. This number has to be compared to 86.8 ± 5.6 reactor neutrino events predicted for no oscillations and 0.95 ± 0.99 background events, which gives a probability that the KamLAND result is consistent with the no-disappearance hypothesis of less than 0.05% [14]. Recently, new results have been presented by KamLAND [15]. With a somewhat larger fiducial volume of the detector an exposure corresponding to 766.3 ton-year has been obtained between March 2002 and January 2004 (including a reanalysis of the 2002 data from [14]). A total of 258 events have been observed, in comparison to the expectation of 356.2 ± 23.7 reactor neutrino events in the case of no disappearance and 7.5 ± 1.3 background events. This leads to a confidence level of 99.995% for $\bar{\nu}_e$ disappearance, and the averaged survival probability is $0.686 \pm 0.044(\mathrm{stat}) \pm 0.045(\mathrm{syst})$. Moreover, evidence for spectral distortion consistent with oscillations is obtained [15].

It was shown in [67] in relation to the first KamLAND data that most information on the neutrino oscillation parameters $\sin^2\theta_{\mathrm{SOL}}$ and $\Delta m^2_{\mathrm{SOL}}$ can be extracted from the data by using an event-based likelihood analysis. This requires a knowledge of the prompt energy of each observed event. Unlike the first data sample, it is not possible to recover this information for the latest KamLAND data sample from publicly available material. Therefore only χ^2-analyses based on binned data can be performed outside the KamLAND collaboration. Details of our KamLAND simulation based on 2002 data can be found in [67, 68], a discussion of our updated analysis method for the current data sample is given in appendix A. Here we briefly summarize the main features: instead of the traditional bins of equal size in E_{pr} we use the data binned equally in $1/E_{\mathrm{pr}}$, which can be obtained from [15], and which allows to extract more relevant information on the oscillation parameters. We adopt the improved anti-neutrino flux parametrization from [69], and include various systematic errors associated to the neutrino fluxes, reactor fuel composition and individual reactor powers. Furthermore, we include matter effects, a careful treatment of backgrounds and information on the average contribution to the total reactor neutrino signal as a function of the distance to the detector.

The KamLAND allowed regions for $\sin^2\theta_{\mathrm{SOL}}$ and $\Delta m^2_{\mathrm{SOL}}$ are shown in figure 6 in comparison to the regions from solar data. One observes beautiful agreement between KamLAND data and the region implied by the LMA solution to the solar neutrino problem, which in this way has been singled out as the only viable one. Before this experiment we had a very complex pattern of alternative oscillation solutions like LOW, SMA or VAC; see e.g. [35, 36]. All of these are completely ruled out by the KamLAND data. From this point of view, the KamLAND experiment has played a fundamental role in the resolution of the solar neutrino problem.

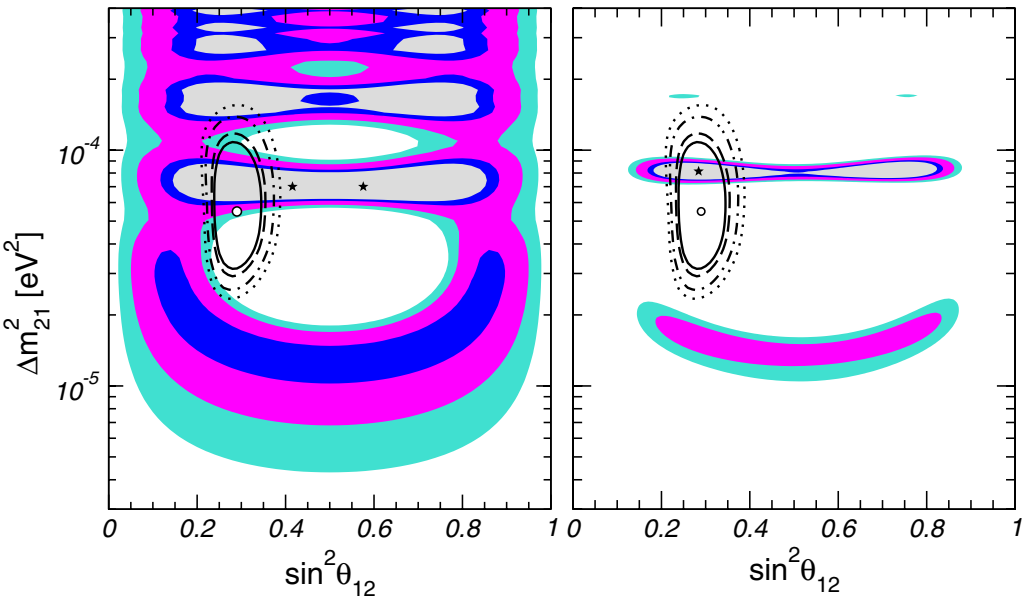

Figure 6. Allowed regions from KamLAND data at 90, 95 and 99%, and 3σ CL for 2 d.o.f. for the 2002 data sample [14] (left panel) and the latest 766.3 ton-year data sample [15] (right panel). The regions delimited by the lines correspond to solar data. The KamLAND best-fit points are marked with a star, the solar best-fit point with a dot.

Comparing the left and right panels of figure 6 one can appreciate the improvement implied by the recent KamLAND data. The allowed region is drastically reduced, and in particular the mass-squared difference is very well determined by recent data. We find the best-fit point

$$\begin{aligned} \Delta m^2_{\rm SOL} &= 8.1^{+0.4}_{-0.3} \times 10^{-5}\,{\rm eV}^2\ (1\sigma) \\ \sin^2\theta_{\rm SOL} &= 0.29 \end{aligned} \qquad \text{(KamLAND data).} \tag{7}$$

The solution at low values of $\Delta m^2_{\rm SOL}$ is present at the 99% CL, with the local minimum at $\Delta m^2_{\rm SOL} = 1.6 \times 10^{-5}\,{\rm eV}^2$ and $\sin^2\theta_{\rm SOL} = 0.31$ and $\Delta\chi^2 = 7.5$ relative to the best-fit point. The so-called high-LMA solution is present only marginally at the 3σ level at $\Delta m^2_{\rm SOL} = 1.7 \times 10^{-4}\,{\rm eV}^2$, $\sin^2\theta_{\rm SOL} = 0.25$ and $\Delta\chi^2 = 11.3$. Although not statistically significant, we note that the small matter effect favours slightly values of $\sin^2\theta_{\rm SOL} < 0.5$ over the 'mirror solution' with $\sin^2\theta_{\rm SOL} > 0.5$. The high values of $\Delta m^2_{\rm SOL} \gtrsim 3 \times 10^{-4}\,{\rm eV}^2$ in the averaging regime, which have been allowed by first KamLAND data [14] at 90% CL, are now ruled out at more than 3σ. This indicates that the spectral distortion associated to neutrino oscillations has been observed [15] (see also the appendix for further discussion).

3.3. Solar and KamLAND combined

Under the fundamental assumption of CPT invariance we can directly compare the information obtained from solar neutrino experiments and the KamLAND reactor experiment. In figure 7 we show the allowed regions from the combined solar and KamLAND data. The current best-fit

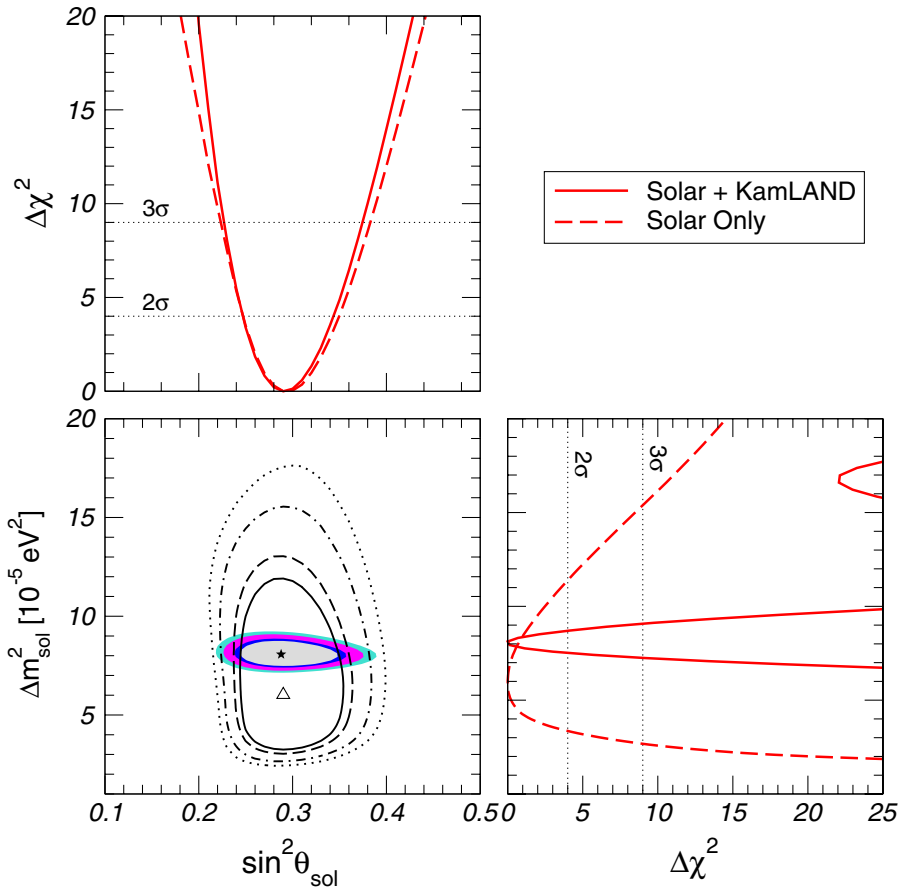

Figure 7. Allowed regions from combined solar and KamLAND data at 90, 95 and 99%, and 3σ CL for 2 d.o.f. The regions shown with lines correspond to solar data only, from figure 5.

point of the global analysis occurs at

$$\sin^2\theta_{\rm SOL} = 0.29, \qquad \Delta m^2_{\rm SOL} = 8.1 \times 10^{-5}\,{\rm eV}^2 \quad \text{(solar + KamLAND data)}. \tag{8}$$

From the projections of χ^2 onto the $\Delta m^2_{\rm SOL}$ and $\sin^2\theta_{\rm SOL}$ axes also shown in figure 7 we find the following allowed ranges at 3σ (5σ) for 1 d.o.f.:

$$\begin{aligned} &0.23\,(0.19) \leqslant \sin^2\theta_{\rm SOL} \leqslant 0.37\,(0.45), \\ &7.3\,(6.7) \times 10^{-5}\,{\rm eV}^2 \leqslant \Delta m^2_{\rm SOL} \leqslant 9.1\,(9.9) \times 10^{-5}\,{\rm eV}^2. \end{aligned} \tag{9}$$

As expected from figure 6 the determination of the mixing angle is completely dominated by the solar neutrino data, whereas KamLAND significantly reduces the allowed range for $\Delta m^2_{\rm SOL}$. Also the so-called high-LMA region, which previously was present around $\Delta m^2_{\rm SOL} \simeq 1.4 \times 10^{-4}\,{\rm eV}^2$ at 3σ (see, e.g., [30]) is now ruled out with a $\Delta\chi^2 = 22.1$ with respect to the global minimum, which corresponds to an exclusion at about 4.3σ for 2 d.o.f. Notice also that the day/night data are treated as previously [30, 36]. An improved analysis of the day/night asymmetry data along the lines followed by the Super-K collaboration in [70] would lead to an even more pronounced

rejection of the high $\Delta m^2_{\rm SOL}$ region. Currently not enough information is available to reproduce this result outside the Super-K collaboration. Finally we note that the use of the BP04 fluxes has not changed significantly the allowed regions.

3.4. Robustness of oscillation interpretation: solar neutrinos

The oscillation interpretation of solar neutrino data depends both on astrophysical input (the model of the Sun) as well as on the physics characterizing both the propagation as well as neutrino interaction properties. Either may differ from the SSM and Standard Electroweak Model expectations. How robust is the oscillation interpretation of solar neutrino data in view of this?

3.4.1. Beyond the SSM. In the following we will briefly discuss consequences of departures from the SSM. The effect of varying solar neutrino fluxes has been widely discussed, thus, as a case study we consider the possibility of solar density fluctuations. Even though this possibility was suggested in a number of papers [71]–[73] it has been traditionally neglected for several reasons. First, helioseismic measurements constrain deviations of solar properties from SSM predictions at better than the per cent level. Second, preliminary studies of the implications for neutrino oscillations of radiative-zone helioseismic waves [73] indicated that they are unlikely to have observable effects. Third, no other known sources of fluctuations seemed to have the properties required to influence neutrino oscillations.

Recently, all of these points have been re-examined, with the result that the presence of solar fluctuations appears more likely than previously thought. First, direct helioseismic bounds turn out to be insensitive to fluctuations whose size is as small as those to which neutrinos are sensitive [74, 75] typically several hundreds of km. Second, recent studies have shown how such solar density fluctuations can arise near the solar equatorial plane in the presence of magnetic fields deep within the solar radiative zone due to a resonance between Alfvén waves and helioseismic g-modes [76].

It has been shown in [77] that such density fluctuations can affect neutrino propagation in an important way. The effect of random matter density fluctuations on the electron-neutrino survival probability for LMA oscillations has been shown to be sizeable if the correlation length L_0 (we take $L_0 = 100$ km) is comparable to the neutrino oscillation length in the Sun. This is illustrated in figure 8. The fluctuation's amplitude ξ at the position of neutrino resonance is zero in the left panel, and it is 4 and 8% in the middle and right panels, respectively. The corresponding solar neutrino oscillation parameters obtained in our global fit are shown in figure 9 before and after the new KamLAND data presented at Neutrino 2004. One sees that these new data have a rather strong impact on the stability of the oscillation parameters. With 2002 KamLAND data an additional allowed region was present for $\Delta m^2_{\rm SOL} \sim 2 \times 10^{-5}\,{\rm eV}^2$ at the 99% CL [78], whereas the new KamLAND data pin down the oscillation parameters such that the allowed regions in figure 9 are practically stable, and the new solar noise-induced solution appears only marginally at the 3σ CL.

Conversely, as shown in [78], the quality of current solar neutrino measurements after the SNO-salt and KamLAND results is sufficiently good so as to place important constraints on fluctuations in the solar medium, deep within the solar radiative zone. In other words, neutrinos may be used as an astrophysical probe of the solar interior, beyond the framework of the SSM. As illustrated in figure 10, density fluctuations are strongly constrained if the correlation length lies in the range of several hundred km. Comparing the curves for free and fixed oscillation parameters,

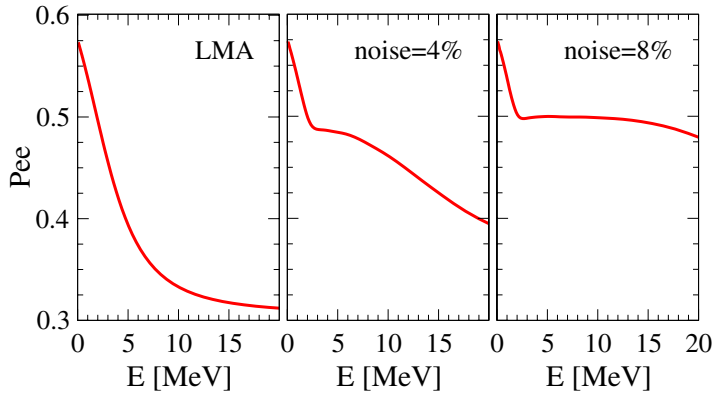

Figure 8. Effect of random matter density fluctuations with a correlation length of $L_0 = 100$ km on the electron-neutrino survival probability for LMA oscillations.

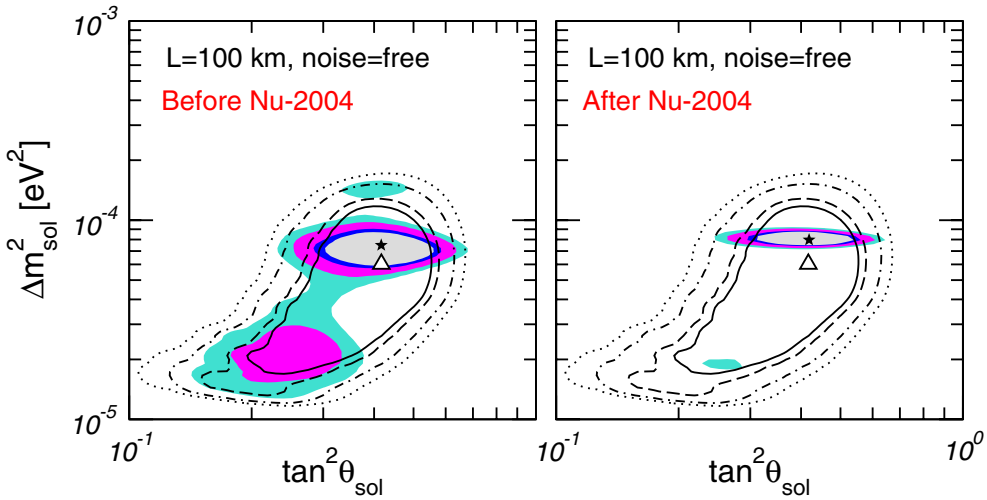

Figure 9. Solar neutrino oscillation parameters with an arbitrary noise amplitude and a correlation length $L_0 = 100$ km from combining solar data with 2002 KamLAND data (left panel) and 2004 KamLAND data (right panel). The contour lines refer to solar data only.

one notes that the bounds on fluctuations have already become rather stable, a situation that may still improve when the accuracy on $\Delta m^2_{\rm SOL}$ and $\theta_{\rm SOL}$ gets improved by future neutrino experiments. Because oscillations are sensitive to correlation lengths which are so short, such solar neutrino results will complement the constraints that come from helioseismology.

3.4.2. Beyond solar neutrino oscillations: spin flavour precession. In extensions of the Standard Model (SM) neutrino masses are in general accompanied also by non-standard interactions and/or electromagnetic properties. In the minimal extension of the SM with Dirac neutrino masses one expects very tiny neutrino magnetic moments (MMs) [79], well below current experimental sensitivities. However, the theoretically preferred case of Majorana neutrinos leads to potentially larger transition magnetic moments closer to the present sensitivities. These can affect neutrino

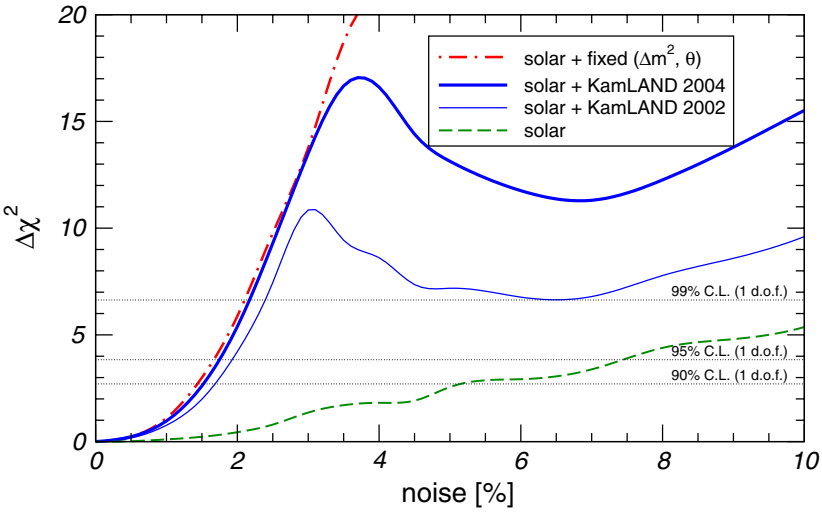

Figure 10. Bounds on random matter density fluctuations for a correlation length of $L_0 = 100$ km from solar neutrino data, solar + KamLAND data, and solar data for oscillation parameters fixed at the best-fit point.

propagation properties in the Sun beyond the oscillation mechanism, due to the possible presence of solar magnetic fields. Alternatively, they can affect the determination of neutrino oscillation parameters due to non-standard neutrino cross sections inside the detectors.

The most general form of the electromagnetic current of massive (Majorana) neutrinos has been given in [80]. The magnetic piece is characterized by a 3×3 complex antisymmetric matrix, the so-called Majorana transition moment (TM) matrix, that contains MMs as well as electric dipole moments of the neutrinos. Their existence would affect neutrino propagation inside the solar convective zone due to a spin-flavour precession (SFP) effect [80]–[82]. This, in general, depends on the assumed magnetic field profile. In order to quantify the extent to which the oscillation regions can be altered by the sub-leading spin-flavour precession effect, a χ^2 analysis was performed in [83] taking into account the global solar + KamLAND disappearance data. We assumed that neutrino conversions are driven mainly by LMA oscillations, and used the same self-consistent [84] convective-zone solar magnetic field profile employed in [85]. The results we obtain indicate that, even though small, current bounds on neutrino magnetic moments and solar magnetic fields still leave room for slight modifications in the determinations of solar neutrino oscillation parameters, in the presence of large magnetic moments.[7]

However, in the general Majorana case, where theory may give rise to higher moments, there is a characteristic feature of the spin flavour precession which will lead to more stringent constraints, and hence increase the robustness of the oscillation parameter determination. The argument is based on the presence of anti-neutrinos in the solar flux [80]–[82]. Recently, the KamLAND collaboration [86] has reported a result which greatly improves the bound on an anti-neutrino component in the solar flux from 0.1% of the solar boron ν_e flux to 2.8×10^{-2}% at the 90% CL, about 30 times better than the recent Super-K limit [87]. This implies that, in practical terms, extremely good stability of the solar neutrino oscillation parameters against the possible existence of sub-leading SFP conversions is obtained. As a result, we conclude

[7] Note that our analysis of solar neutrino data applies also to the special case of Dirac neutrinos.

that solar neutrino oscillation parameters can be inferred without any reference to neutrino magnetic properties nor solar magnetic fields. We refer the reader to [83] for quantitative details.

All in all, our analysis of solar neutrino data indicates pretty good stability of the oscillation parameter determination for the case of Majorana neutrinos, due to the solar anti-neutrino limit from KamLAND. In contrast, for the special case of Dirac neutrinos, this limit does not apply and the determination of oscillation parameters is potentially more fragile. However, we note that the gauge theoretic expectations for Dirac magnetic moments are typically lower than those for Majorana neutrino transition moments.

3.4.3. Beyond SM neutrino cross sections: constraining neutrino magnetic moments. Neutrino transition magnetic moments are basic properties of neutrinos [80]. Although they do not substantially affect neutrino propagation, even in the presence of solar magnetic fields, non-trivial electromagnetic neutrino properties could still show up in the detection process and to this extent affect the determination of oscillation parameters. Experiments based on the neutrino detection via neutrino–electron elastic scattering are a sensitive probe of the electromagnetic properties. In [88] it was shown that current data from solar neutrinos (in particular from Super-K) in combination with reactor neutrino–electron scattering data provides strong bounds on all the elements of the TM matrix (for similar analyses see [89]–[92]).

In several experiments such as Super-K, Borexino and some reactor experiments [93]–[95], neutrinos are detected via the elastic neutrino–electron scattering, whose electromagnetic cross section is [96, 97] given by

$$\frac{\mathrm{d}\sigma_{\mathrm{em}}}{\mathrm{d}T} = \frac{\alpha^2\pi}{m_e^2\mu_B^2}\left(\frac{1}{T} - \frac{1}{E_\nu}\right)\mu_{\mathrm{eff}}^2, \tag{10}$$

where μ_{eff} is an effective MM [98], T denotes the kinetic energy of the recoil electron and E_ν is the incoming neutrino energy. The electromagnetic cross section adds to the weak cross section and allows to extract information about the TM matrix, which we denote by λ in the following. Taking into account the antisymmetry of λ for Majorana neutrinos, it is useful to define vectors $\mathbf{\Lambda}$ by $\lambda_{jk} = \varepsilon_{jkl}\Lambda_l$, where λ_{jk} are the elements of the TM matrix in the mass basis. The effective MM square μ_{eff}^2 takes on different forms in the cases of solar and reactor neutrino experiments. The detailed derivation of the following expressions can be found in [88]. For the case of solar neutrino experiments one obtains the effective MM square

$$\mu_{\mathrm{LMA}}^2 = |\mathbf{\Lambda}|^2 - |\Lambda_2|^2 + P_{e1}^{2\nu}(|\Lambda_2|^2 - |\Lambda_1|^2), \tag{11}$$

where $P_{e1}^{2\nu}$ corresponds to the probability that an electron neutrino produced in the core of the sun arrives at the detector as the mass eigenstate ν_1 in a two-neutrino scheme. In contrast, the μ_{eff}^2 relevant in reactor experiments is given as

$$\mu_{\mathrm{R}}^2 = |\mathbf{\Lambda}|^2 - \cos^2\theta_{\mathrm{SOL}}|\Lambda_1|^2 - \sin^2\theta_{\mathrm{SOL}}|\Lambda_2|^2 - \sin 2\theta_{\mathrm{SOL}}|\Lambda_1||\Lambda_2|\cos\delta, \tag{12}$$

where $\delta = \arg(\Lambda_1^*\Lambda_2)$ is the relative phase between Λ_1 and Λ_2.

In the following we discuss the constraints on neutrino TMs from solar and reactor neutrino experiments [88]. The χ^2 obtained from the data is minimized with respect to all TM parameters

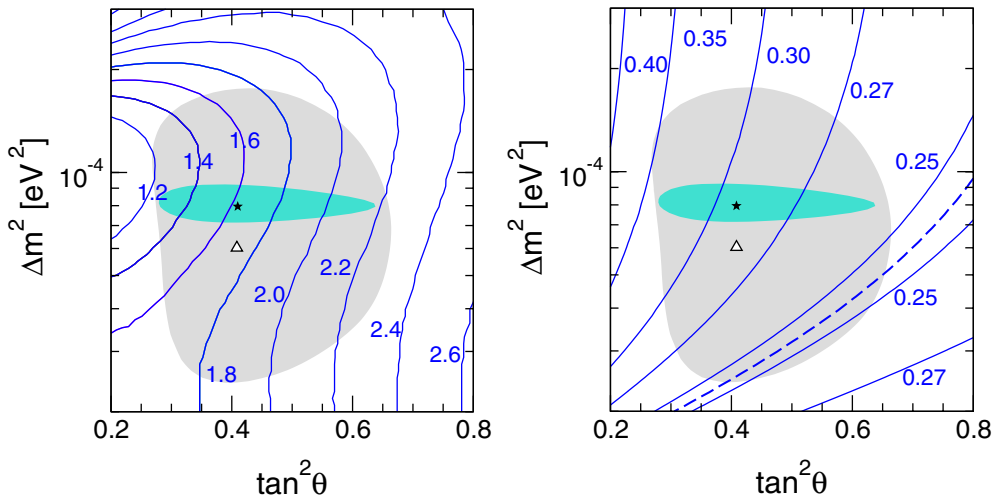

Figure 11. Contours of the 90% CL bound on $|\mathbf{\Lambda}|$ in units of $10^{-10}\mu_B$ from combined solar and reactor data (left panel) and after 3 years of Borexino data-taking (right panel). The grey (light) shaded region is the 3σ LMA region obtained in the global analysis of solar neutrino data (best-fit point marked with a triangle), whereas the green (dark) one corresponds to the 3σ region obtained after including the KamLAND results (best-fit point marked with a star). The dashed line in the right panel corresponds to $P_{e1} = 0.5$ for ^{7}Be neutrinos, and shows the strongest attainable limit.

except the modulus $|\mathbf{\Lambda}|$. To take into account the physical boundary $|\mathbf{\Lambda}| \geqslant 0$ we use Bayesian methods to calculate an upper bound on $|\mathbf{\Lambda}|$. Let us stress that these bounds apply to *all* elements of the TM matrix, including MMs and electric dipole moments of all neutrino flavours, since $|\mathbf{\Lambda}|^2 = |\Lambda_1|^2 + |\Lambda_2|^2 + |\Lambda_3|^2$. Furthermore, since $|\mathbf{\Lambda}|$ is independent of the basis these bounds apply also for the TMs in the flavour basis.

In the left panel of figure 11 we show contours of the 90% CL bound on $|\mathbf{\Lambda}|$ in the $(\tan^2\theta_{\rm SOL}, \Delta m^2_{\rm SOL})$ plane for the combination of solar and reactor data. We note that in the upper parts of the LMA region, the solar data alone give already a strong bound on $|\mathbf{\Lambda}|$, see [88] for details. In contrast, for low $\Delta m^2_{\rm SOL}$ values the inclusion of reactor data plays an important role in improving the bound. From our analysis we find at 90% CL:

$$|\mathbf{\Lambda}| < \begin{cases} 3.4 \times 10^{-10}\mu_B & \text{(solar + KamLAND data)}, \\ 1.7 \times 10^{-10}\mu_B & \text{(solar + KamLAND + reactor data)}, \end{cases} \tag{13}$$

where for each value of $|\mathbf{\Lambda}|$ we have minimized the χ^2 with respect to $\tan^2\theta_{\rm SOL}$ and $\Delta m^2_{\rm SOL}$.

Finally we note that the Borexino experiment [99] will improve these bounds roughly by one order of magnitude. This experiment is mainly sensitive to the solar ^{7}Be neutrino flux, which will be measured by elastic neutrino–electron scattering. Therefore, Borexino is similar to Super-K, the main difference is the mono-energetic line of the ^{7}Be neutrinos, with an energy of 0.862 MeV, which is roughly one order of magnitude smaller than the energies of the ^{8}B neutrino flux relevant in Super-K. Owing to the lower neutrino energy, the sensitivity to electromagnetic properties is

increased, as can be seen from (10). Details about our Borexino simulation can be found in [88]. At the best-fit point one finds the sensitivity

$$|\mathbf{\Lambda}| \leqslant 0.29 \times 10^{-10} \mu_B \quad \text{at } 90\% \text{ CL} \tag{14}$$

after three years of Borexino data taking. In the right panel of figure 11 we show contours of the 90% CL bound in the $(\tan^2\theta_{\rm SOL}, \Delta m^2_{\rm SOL})$ plane.

4. Three-flavour neutrino oscillations

4.1. Global three-neutrino analysis

In this section the three-neutrino oscillation parameters are determined from a global analysis of the most recent neutrino oscillation data. For earlier three-neutrino analyses see [35, 100, 101]. To fix the notation, we define the neutrino mass-squared differences $\Delta m^2_{\rm SOL} \equiv \Delta m^2_{21} \equiv m^2_2 - m^2_1$ and $\Delta m^2_{\rm ATM} \equiv \Delta m^2_{31} \equiv m^2_3 - m^2_1$, and use the convenient form of the parametrization for the leptonic mixing matrix given in [20] and now adopted as standard by the PDG [102]:

$$U = \begin{pmatrix} c_{13}c_{12} & s_{12}c_{13} & s_{13} \\ -s_{12}c_{23} - s_{23}s_{13}c_{12} & c_{23}c_{12} - s_{23}s_{13}s_{12} & s_{23}c_{13} \\ s_{23}s_{12} - s_{13}c_{23}c_{12} & -s_{23}c_{12} - s_{13}s_{12}c_{23} & c_{23}c_{13} \end{pmatrix}, \tag{15}$$

where $c_{ij} \equiv \cos\theta_{ij}$ and $s_{ij} \equiv \sin\theta_{ij}$. Furthermore, we use the notations $\theta_{12} \equiv \theta_{\rm SOL}$ and $\theta_{23} \equiv \theta_{\rm ATM}$. Because of the hierarchy $\Delta m^2_{\rm SOL} \ll \Delta m^2_{\rm ATM}$ it is a good approximation to set $\Delta m^2_{\rm SOL} = 0$ in the analysis of atmospheric and K2K data,[8] and to set $\Delta m^2_{\rm ATM}$ to infinity for the analysis of solar and KamLAND data. This implies furthermore that the effect of a possible Dirac CP-violating phase [20] in the lepton mixing matrix can be neglected.[9] We perform a general fit to the global data in the five-dimensional parameter space $s^2_{12}, s^2_{23}, s^2_{13}, \Delta m^2_{21}, \Delta m^2_{31}$, and show projections onto various one- or two-dimensional sub-spaces.

We include in our analysis the global solar neutrino oscillation data from all solar neutrino experiments and the KamLAND reactor experiment as described in section 3, the atmospheric neutrino data from Super-K, as well as spectral data from the K2K long-baseline experiment (see section 2). In addition, in our fit, we take into account the constraints from the CHOOZ reactor experiment [105].

The results of the global three-neutrino analysis are summarized in figure 12 and in table 1. In the upper panels of the figure, the $\Delta\chi^2$ is shown as a function of the parameters $\sin^2\theta_{12}, \sin^2\theta_{23}, \sin^2\theta_{13}, \Delta m^2_{21}, \Delta m^2_{31}$, minimized with respect to the undisplayed parameters. The lower panels show two-dimensional projections of the allowed regions in the five-dimensional parameter space. The best-fit values and the allowed ranges of the oscillation parameters from the global data are given in table 1. This table summarizes the current status of the three-flavour neutrino oscillation parameters.

[8] See [103] for a two-mass scale analysis of atmospheric data.

[9] The two Majorana phases [20] do not show up in oscillations but do appear in lepton number violating processes [104].

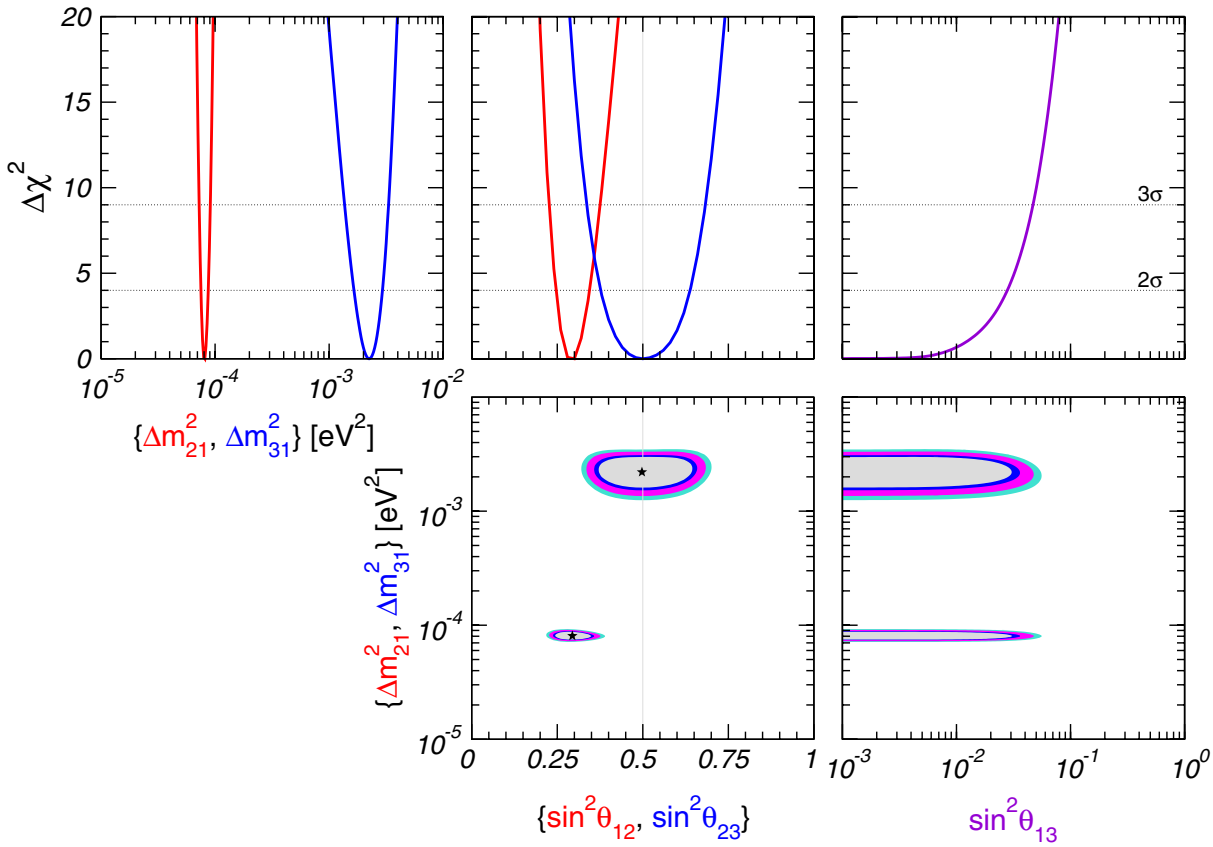

Figure 12. Projections of the allowed regions from the global oscillation data at 90, 95 and 99%, and 3σ CL for 2 d.o.f. for various parameter combinations. Also shown is $\Delta\chi^2$ as a function of the oscillation parameters $\sin^2\theta_{12}$, $\sin^2\theta_{23}$, $\sin^2\theta_{13}$, Δm^2_{21}, Δm^2_{31}, minimized with respect to all undisplayed parameters.

Table 1. Best-fit values, 2σ, 3σ, and 4σ intervals (1 d.o.f.) for the three-flavour neutrino oscillation parameters from global data including solar, atmospheric, reactor (KamLAND and CHOOZ) and accelerator (K2K) experiments.

Parameter	Best fit	2σ	3σ	4σ
Δm^2_{21} (10^{-5} eV^2)	8.1	7.5–8.7	7.2–9.1	7.0–9.4
Δm^2_{31} (10^{-3} eV^2)	2.2	1.7–2.9	1.4–3.3	1.1–3.7
$\sin^2\theta_{12}$	0.30	0.25–0.34	0.23–0.38	0.21–0.41
$\sin^2\theta_{23}$	0.50	0.38–0.64	0.34–0.68	0.30–0.72
$\sin^2\theta_{13}$	0.000	$\leqslant$0.028	$\leqslant$0.047	$\leqslant$0.068

4.2. The small parameters $\alpha \equiv \Delta m^2_{\rm SOL}/\Delta m^2_{\rm ATM}$ and θ_{13}

Genuine three-flavour effects are associated to the mass hierarchy parameter $\alpha \equiv \Delta m^2_{\rm SOL}/\Delta m^2_{\rm ATM}$ and the mixing angle θ_{13}. In particular, in a three-neutrino scheme, CP violation disappears in the limit where two neutrinos become degenerate [20, 106] and in the limit where $\theta_{13} \to 0$. We discuss in this subsection the present status of these small parameters.

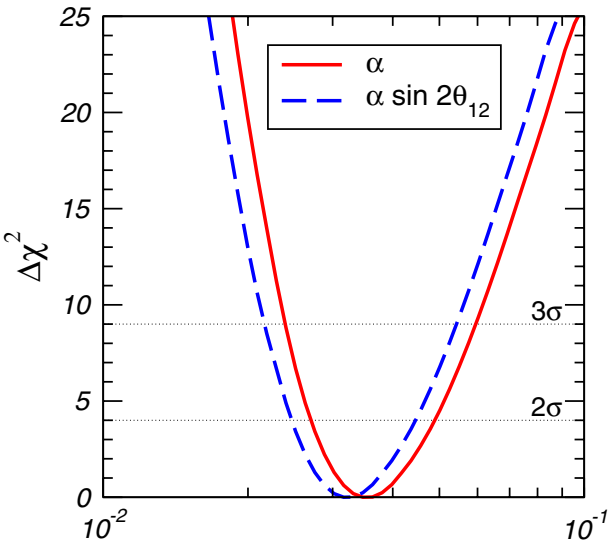

Figure 13. $\Delta\chi^2$ from global oscillation data as a function of $\alpha \equiv \Delta m^2_{\rm SOL}/\Delta m^2_{\rm ATM}$ and $\alpha \sin 2\theta_{12}$.

In figure 13 the $\Delta\chi^2$ from the global data is shown as a function of the mass hierarchy parameter α. Also shown in this figure is the $\Delta\chi^2$ as a function of the parameter combination $\alpha \sin 2\theta_{12}$, since to leading order in the long baseline $\nu_e \to \nu_\mu$ oscillation probability, solar parameters appear in this particular combination [107, 108]. We obtain the following best-fit values and 3σ intervals:

$$\begin{aligned} &\alpha = 0.035, && 0.024 \leqslant \alpha \leqslant 0.060, \\ &\alpha \sin 2\theta_{12} = 0.032, && 0.022 \leqslant \alpha \sin 2\theta_{12} \leqslant 0.054. \end{aligned} \tag{16}$$

Let us now discuss the status of the mixing angle θ_{13}, which at the moment is the last unknown angle in the three-neutrino leptonic mixing matrix. Only an upper bound exists, which used to be dominated by the CHOOZ [105] and Palo Verde [109] reactor experiments. Currently, considerable effort is being put to determine this angle in future experiments (see, e.g., [26, 27, 40]).

In figure 14 we show the $\Delta\chi^2$ as a function of $\sin^2\theta_{13}$ for different data sample choices. From this figure we find the following bounds at 90% CL (3σ) for 1 d.o.f.:

$$\sin^2\theta_{13} \leqslant \begin{cases} 0.041\ (0.079) & \text{(solar + KamLAND)}, \\ 0.029\ (0.067) & \text{(CHOOZ + atmospheric + K2K)}, \\ 0.022\ (0.047) & \text{(global data)}. \end{cases} \tag{17}$$

We find that the new data from KamLAND have a surprisingly strong impact on this bound. Before the 2004 KamLAND data the bound on $\sin^2\theta_{13}$ from global data was dominated by the CHOOZ reactor experiment, together with the determination of Δm^2_{31} from atmospheric data (see, e.g., [30]). However, using most recent data the combined bound from solar + KamLAND becomes comparable to the CHOOZ bound, and these data contribute notably to the final bound. A detailed discussion of the reason for such improvement on $\sin^2\theta_{13}$ from the 2004 KamLAND

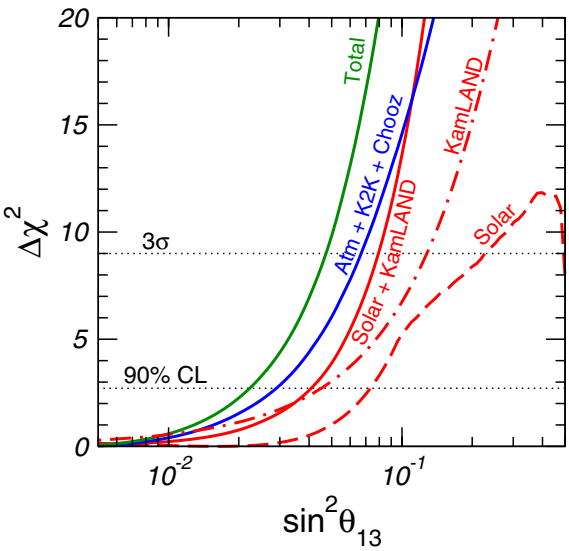

Figure 14. $\Delta\chi^2$ profiles projected onto the $\sin^2\theta_{13}$ axis, for solar, KamLAND, solar + KamLAND, atmospheric + K2K + CHOOZ, and for the global data.

data is given in section of the appendix A.2. One reason is the rather strong signal for spectral distortion in the current sample.

As noted in [30], the bound from solar + KamLAND is especially important for the relatively lower values of $\Delta m^2_{\rm ATM}$ implied by the use of the new three-dimensional atmospheric fluxes [32], since the CHOOZ bound on $\sin^2\theta_{13}$ deteriorates quickly when $\Delta m^2_{\rm ATM}$ decreases (see figure 15). Such loosening in sensitivity for low $\Delta m^2_{\rm ATM}$ values is prevented first, by the lower bound on $\Delta m^2_{\rm ATM}$ from K2K (see figure 2) and second, by the bound from solar + KamLAND, which is independent of $\Delta m^2_{\rm ATM}$. In figure 15 we show the upper bound on $\sin^2\theta_{13}$ as a function of $\Delta m^2_{\rm ATM}$ from CHOOZ data alone compared to the bound from an analysis including solar and reactor neutrino data (CHOOZ and KamLAND). One finds that, although for larger $\Delta m^2_{\rm ATM}$ values the bound on $\sin^2\theta_{13}$ is dominated by the CHOOZ data, for $\Delta m^2_{\rm ATM} \lesssim 2\times10^{-3}\,{\rm eV}^2$ the solar + KamLAND data start being important. For illustration we show in figure 15 also the bound as implied by the old 2002 KamLAND data to highlight the improvement of the new data. We note that, as before, the bound from solar data is rather stable under the recent SSM update.

Let us discuss in some more detail the constraint on $\sin^2\theta_{13}$ from solar data, which emerges from a subtle interplay of various solar neutrino observables. In figure 16 we show the results of a three-parameter fit ($\sin^2\theta_{\rm SOL}$, $\Delta m^2_{\rm SOL}$, $\sin^2\theta_{13}$) to solar and KamLAND data. Allowed regions are shown for various values of $\sin^2\theta_{13}$ in the ($\sin^2\theta_{\rm SOL}$, $\Delta m^2_{\rm SOL}$) plane with respect to the global minimum. Note that here we calculate the allowed regions at a given confidence level for 3 d.o.f. The shape of $\Delta\chi^2$ from solar data shown in figure 14 can be understood from figure 16. Indeed, one observes that, for solar data, increasing θ_{13} can be compensated to some extent by increasing $\Delta m^2_{\rm SOL}$. Since solar data disfavour large values of $\Delta m^2_{\rm SOL}$, the bound improves. Also the combination with KamLAND has a similar effect, since recent KamLAND data essentially fix $\Delta m^2_{\rm SOL}$ at roughly $8\times10^{-5}\,{\rm eV}^2$ such that the continuous rise of $\Delta m^2_{\rm SOL}$ with $\sin^2\theta_{13}$ preferred by solar data is prevented. On the other hand, solar data break a correlation of $\sin^2\theta_{13}$ and $\sin^2\theta_{12}$ in the KamLAND data (see section A.2 of the appendix), which again leads to an improvement of the combined bound on $\sin^2\theta_{13}$.

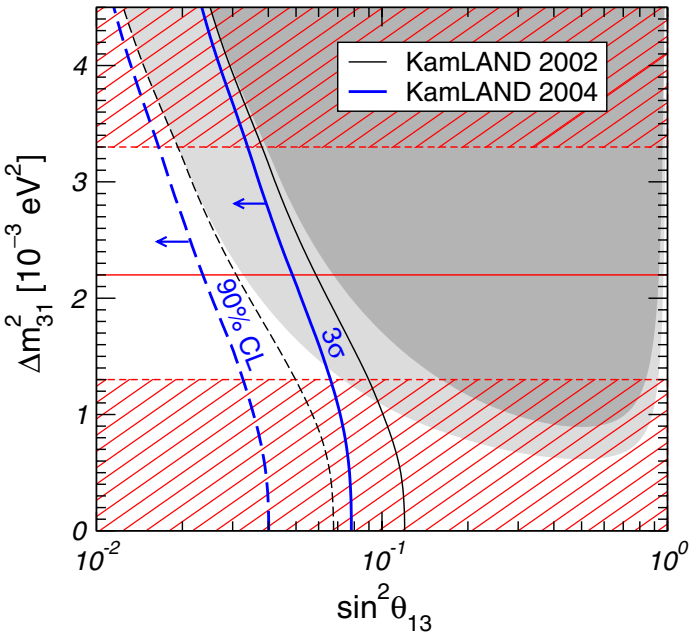

Figure 15. Upper bound on $\sin^2\theta_{13}$ (1 d.o.f.) from solar + KamLAND + CHOOZ data as a function of $\Delta m^2_{\rm ATM}$. The dashed (solid) curve corresponds to the 90% (3σ) CL bound, the thin curves have been obtained with 2002 KamLAND data, whereas the thick curves follow from the recent 2004 KamLAND update. The light (dark) shaded region is excluded by CHOOZ data alone at 90% (3σ) CL. The horizontal line corresponds to the best-fit value of $\Delta m^2_{\rm ATM}$ from atmospheric + K2K data given in (2), and the hatched regions are excluded by atmospheric + K2K data at 3σ according to (3).

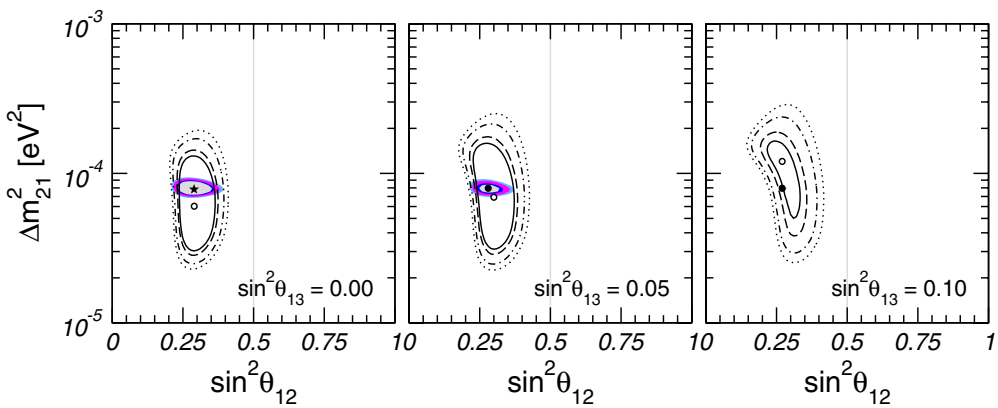

Figure 16. Sections of the three-dimensional allowed regions in the ($\sin^2\theta_{\rm SOL}$, $\Delta m^2_{\rm SOL}$) plane at 90, 95 and 99% and 3σ CL for 3 d.o.f. for various $\sin^2\theta_{13}$ values from solar data (lines) and solar + KamLAND data (coloured regions). The local minima in each plane from solar + KamLAND (solar only) data are marked by filled (open) dots.

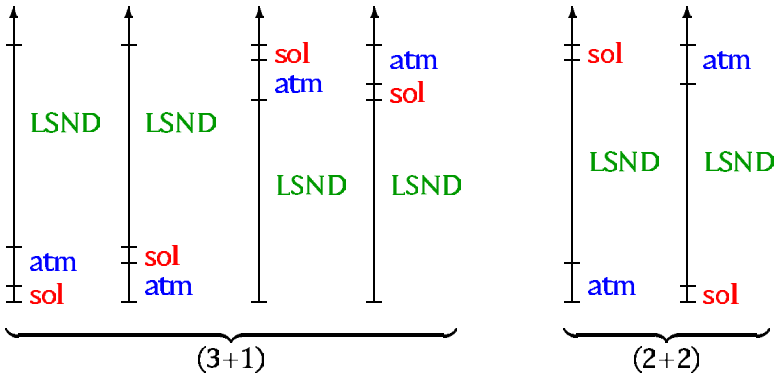

Figure 17. The two classes of six four-neutrino mass spectra, (3 + 1) and (2 + 2).

The difference in the day/night solar neutrino fluxes due to the regeneration effect in the earth in the three-flavour framework has been considered recently in [110, 111]. This observable may provide valuable information on θ_{13} in the context of future solar neutrino experiments like UNO or Hyper-K [112].

5. Four-neutrino oscillations and LSND

In addition to the strong evidence for oscillations due to the mass-squared differences $\Delta m^2_{\rm SOL}$ and $\Delta m^2_{\rm ATM}$, there is also a hint for oscillations with a much larger mass-squared difference from the LSND experiment [113]. This accelerator experiment performed at Los Alamos observed $87.9 \pm 22.4 \pm 6.0$ excess events in the $\bar{\nu}_\mu \to \bar{\nu}_e$ appearance channel, corresponding to a transition probability of $P = (0.264 \pm 0.067 \pm 0.045)\%$, which is $\sim 3.3\sigma$ away from zero. To explain this signal with neutrino oscillations requires a mass-squared difference $\Delta m^2_{\rm LSND} \sim 1\,{\rm eV}^2$. Such a value is inconsistent with the mass-squared differences required by solar/KamLAND and atmospheric/K2K experiments within the standard three-flavour framework. In this section we consider four-neutrino schemes, where a sterile neutrino [114]–[116] is added to the three active ones to provide the additional mass scale needed to reconcile the LSND evidence. We include in our analysis data from the LSND experiment, as well as from short-baseline (SBL) accelerator [117, 118] and reactor [105, 109, 119] experiments reporting no evidence for oscillations (see [120] for details of our SBL data analysis). We update our previous four-neutrino analyses (see, e.g., [121, 122]) by including the most recent solar and KamLAND [15] data, the improved atmospheric neutrino fluxes [32] and latest data from the K2K long-baseline experiment [17].

5.1. A common parametrization for four-neutrino schemes

Four-neutrino mass schemes are usually divided into the two classes (3 + 1) and (2 + 2), as illustrated in figure 17. We note that (3 + 1) mass spectra include the three active-neutrino scenario as a limiting case. In this case, solar and atmospheric neutrino oscillations are explained by active neutrino oscillations, with mass-squared differences $\Delta m^2_{\rm SOL}$ and $\Delta m^2_{\rm ATM}$, and the fourth neutrino state gets completely decoupled. We will refer to such a limiting scenario as (3 + 0). In contrast, the (2 + 2) spectrum is intrinsically different, as the sterile neutrino must take part in either solar or in atmospheric neutrino oscillations, or in both.

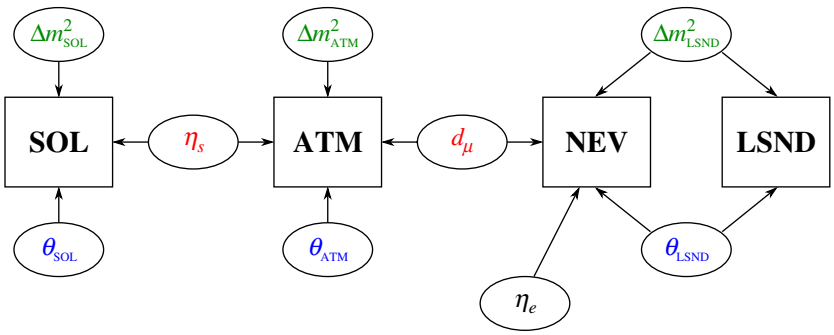

Figure 18. Parameter dependence of the different data sets in our parametrization.

Neglecting CP violation, neutrino oscillations in four-neutrino schemes are generally described by nine parameters: three mass-squared differences and six mixing angles in the lepton mixing matrix [20]. We use the parametrization introduced in [123], in terms of $\Delta m^2_{\rm SOL}$, $\theta_{\rm SOL}$, $\Delta m^2_{\rm ATM}$, $\theta_{\rm ATM}$, $\Delta m^2_{\rm LSND}$ and $\theta_{\rm LSND}$. These six parameters are similar to the two-neutrino mass-squared differences and mixing angles and are directly related to the oscillations in solar, atmospheric and the LSND experiments. For the remaining three parameters we use η_s, η_e and d_μ. These quantities are defined by

$$\eta_\alpha = \sum_i |U_{\alpha i}|^2 \quad \text{with } i \in \text{solar mass states}, \tag{18}$$

$$d_\alpha = 1 - \sum_i |U_{\alpha i}|^2 \quad \text{with } i \in \text{atmospheric mass states}, \tag{19}$$

where $\alpha = e, \mu, \tau, s$. Note that in (2 + 2) schemes the relation $\eta_\alpha = d_\alpha$ holds, whereas in (3 + 1) schemes η_α and d_α are independent. The physical meaning of these parameters is the following: η_α is the fraction of ν_α participating in solar oscillations, and $(1 - d_\alpha)$ is the fraction of ν_α participating in oscillations with $\Delta m^2_{\rm ATM}$ (for further discussions see [123]). For the analysis we adopt the following approximations:

(i) We make use of the hierarchy $\Delta m^2_{\rm SOL} \ll \Delta m^2_{\rm ATM} \ll \Delta m^2_{\rm LSND}$. This means that for each data set we consider only one mass-squared difference; the other two are set either to zero or to infinity.

(ii) In the analyses of solar and atmospheric data (but not for SBL data) we set $\eta_e = 1$, which is justified because of strong constraints from reactor experiments [105, 109, 119].

Within this approximation, the parameter structure of the four-neutrino analysis gets rather simple. The parameter dependence of the four data sets solar, atmospheric, LSND and NEV is illustrated in figure 18. In this section, except where explicitly noted otherwise, we tacitly consider KamLAND as part of the solar data sample and K2K as part of the atmospheric data sample. The NEV data set contains the experiments KARMEN [117], CDHS [118], Bugey [119], CHOOZ [105], and Palo Verde [109], reporting no evidence for oscillations. We see that only η_s links solar and atmospheric data and d_μ links atmospheric and NEV data, while LSND and NEV data are coupled by $\Delta m^2_{\rm LSND}$ and $\theta_{\rm LSND}$. With the definitions (18) and (19) and in our approximation the parameter structure shown in figure 18 holds for both types of mass spectra, (3 + 1) as well as (2 + 2) [123].

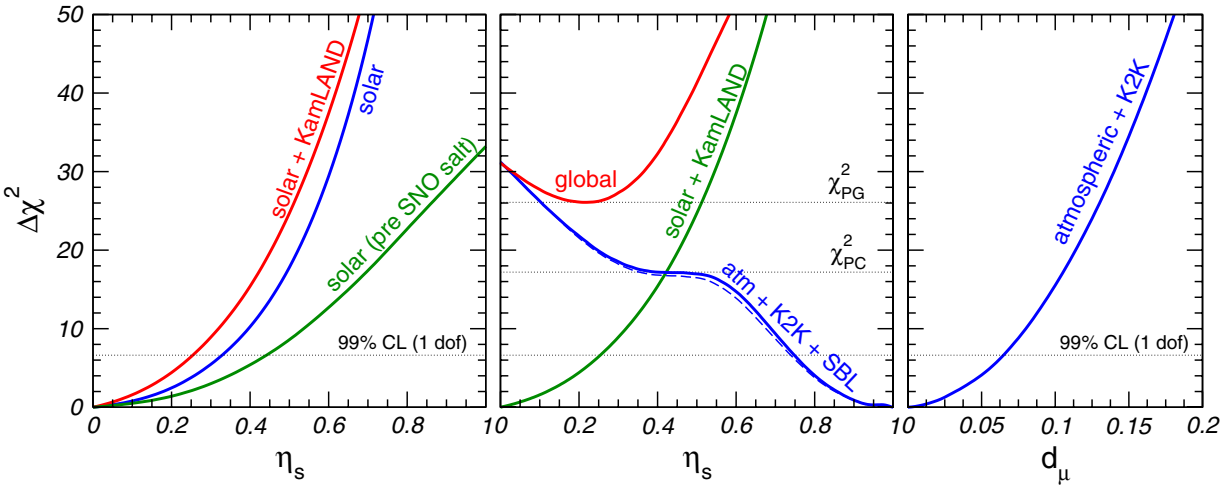

Figure 19. Left: $\Delta\chi^2$ as a function of η_s from solar data before the SNO salt-phase results, from current solar data, and from solar + KamLAND data. Middle: $\Delta\chi^2_{\rm SOL}$, $\Delta\chi^2_{\rm ATM+K2K+SBL}$ and $\bar{\chi}^2_{\rm global}$ as a function of η_s in (2 + 2) oscillation schemes. The dashed line corresponds to atmospheric and K2K data only (without SBL data). Right: $\Delta\chi^2_{\rm ATM+K2K}$ as a function of d_μ.

5.2. (2 + 2): ruled out by solar and atmospheric data

The strong preference for oscillations into active neutrinos in solar and atmospheric oscillations [36] leads to a direct conflict in (2 + 2) oscillation schemes. We will now show that thanks to recent solar neutrino data (in particular from the SNO-salt phase [10]) in combination with the KamLAND experiment [14], and the latest Super-K data on atmospheric neutrinos [11] the tension in the data has become so strong that (2 + 2) oscillation schemes are essentially ruled out.[10]

In the left panel of figure 19 we show the $\Delta\chi^2$ from solar neutrino data as a function of η_s, the parameter describing the fraction of the sterile neutrino participating in solar neutrino oscillations. It is clear from the figure that the improved determination of the neutral current event rate from the solar ^{8}B flux implied by the salt enhanced measurement in SNO [10] substantially tightened the constraint on a sterile contribution: the 99% CL bound improves from $\eta_s \leqslant 0.44$ for pre-SNO-salt to $\eta_s \leqslant 0.31$ (BP00). The boron flux predicted in the current BP04 SSM is slightly larger than the NC flux measured in SNO, which leaves more room for a sterile component in the solar neutrino flux. Indeed, using the BP04 SSM the bound deteriorates slightly to $\eta_s \leqslant 0.33$ at the 99% CL. This effect illustrates that in schemes beyond minimal three-flavour oscillations the data still shows some sensitivity to the theoretical SSM input. Although KamLAND on its own is insensitive to a sterile neutrino contamination, it contributes indirectly to the bound because of the better determination of $\Delta m^2_{\rm SOL}$ and $\theta_{\rm SOL}$ [36]. The combined analysis leads to the 99% CL bound

$$\eta_s \leqslant 0.25 \quad \text{(solar + KamLAND, BP04)}. \tag{20}$$

[10] For an earlier four-neutrino analysis of solar and atmospheric data see [124].

In contrast, in (2 + 2) schemes atmospheric data prefer values of η_s close to 1. From the combined analysis of Super-K atmospheric data, K2K and SBL neutrino data we obtain the bound $\eta_s \geqslant 0.75$ at 99% CL, in clear disagreement with the bound from solar data. In the middle panel of figure 19 we show $\Delta\chi^2$ for solar data and for atmospheric + K2K combined with SBL data as a function of η_s. Note that the main effect comes from atmospheric + K2K data; SBL experiments contribute only marginally, as visible from the dashed line. From this figure we also see that the 'solar + KamLAND' and the 'atm + K2K + SBL' allowed domains overlap only at $\chi^2_{\rm PC} = 17.2$, i.e. at the 4.1σ level.

In the middle panel of figure 19 we also show the 'global' $\bar{\chi}^2$ function defined as follows:

$$\bar{\chi}^2(\eta_s) \equiv \Delta\chi^2_{\rm SOL+KAM}(\eta_s) + \Delta\chi^2_{\rm ATM+K2K+SBL}(\eta_s). \tag{21}$$

In [121, 125] we have proposed a statistical method to evaluate the disagreement of different data sets in global analyses. The *parameter goodness of fit* (PG) makes use of the $\bar{\chi}^2$ defined in (21). This criterion is very useful to evaluate the GOF of the *combination* of data sets, avoiding dilution by the large number of data points, as it happens for the usual GOF criterion (for details see [125]). We find $\chi^2_{\rm PG} \equiv \bar{\chi}^2_{\rm min} = 26.1$, which corresponds to 5.1σ. We conclude that (2 + 2) mass schemes are ruled out by the disagreement between the latest solar and atmospheric neutrino data. This is a very robust result, independent of whether LSND is confirmed or disproved.[11]

Let us note that we now obtain a slightly smaller $\chi^2_{\rm PG}$ than previously [122], and the disagreement gets slightly weaker. The reason is that in the present analysis we have not included the atmospheric neutrino data from the MACRO experiment [12]. As discussed in [36], these data have some sensitivity to η_s and enhance the rejection against a sterile component in atmospheric oscillations. Since relevant information to perform a consistent combined analysis of Super-K and MACRO using the new fluxes is presently not available, we prefer to use only Super-K data, which allows us to derive simpler and more robust results.[12] Let us mention that we are also neglecting neutral current and tau appearance data from Super-K, which would also increase the rejection against a sterile component, since the detailed information needed to use these data are presently not available outside the Super-K collaboration.

5.3. (3 + 1): strongly disfavoured by SBL data

It is known for a long time [120], [129]–[134] that (3 + 1) mass schemes are disfavoured by the comparison of SBL disappearance data [118, 119] with the LSND result. The reason is

[11] Sub-leading effects beyond the approximations adopted here should not affect this result significantly. Allowing for additional parameters to vary at the percent level might change the *ratio* of some observables [126]; however, we expect that the absolute number of events relevant for the fit will not change substantially.

[12] The reason for this is the presence of some conflict between theoretical predictions from three-dimensional fluxes and MACRO as well as Super-K thru-going muon data (see discussion in the second reference of [12]). This difference did not appear with older one-dimensional fluxes, and makes it particularly important to properly take into account all the correlations between different data sets. For Super-K, detailed information on the correlation between various sub-samples (sub-GeV, multi-GeV, stopping and thru-going muons) can be extracted from [37], whereas the relevant information to include MACRO is not available. Since in this analysis we are more interested in the *robustness* rather than in the *strength* of our results, we restrict our analysis to Super-K data only. A consistent way of combining Super-K and MACRO data using three-dimensional fluxes is however under investigation.

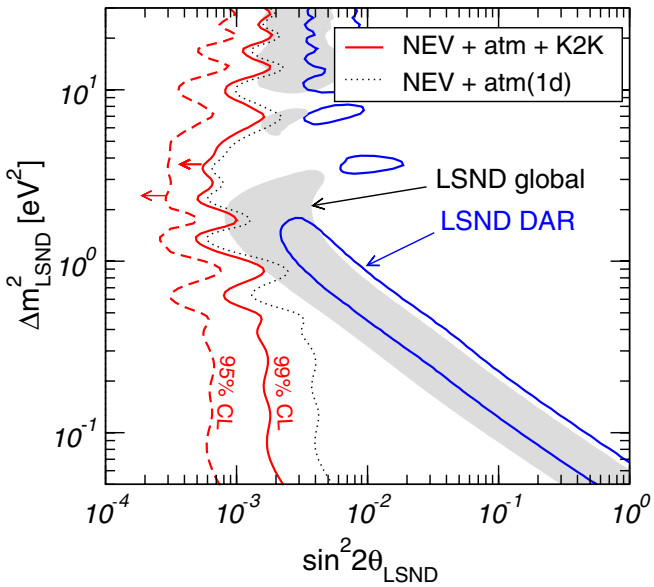

Figure 20. Upper bound on $\sin^2 2\theta_{\rm LSND}$ from NEV, atmospheric and K2K neutrino data in (3 + 1) schemes. The bound is calculated for each $\Delta m^2_{\rm LSND}$ using the $\Delta\chi^2$ for 1 d.o.f. The dotted line corresponds to the bound at 99% CL without K2K and using one-dimensional atmospheric fluxes. Also shown are the regions allowed at 99% CL (2 d.o.f.) from global LSND data [113] and decay-at-rest (DAR) LSND data [128].

that in (3 + 1) schemes the relation $\sin^2 2\theta_{\rm LSND} = 4d_e d_\mu$ holds, and the parameters d_e and d_μ (see (19)) are strongly constrained by ν_e and ν_μ disappearance experiments, leading to a double suppression of the LSND amplitude. In [132] it was realized that the up–down asymmetry observed in atmospheric μ events leads to an additional constraint on d_μ. The $\Delta\chi^2(d_\mu)$ from the fit to atmospheric + K2K data is shown in the right panel of figure 19. We find that the use of the new atmospheric fluxes [32] as well as K2K data [17] considerably strengthen the constraint on d_μ: the new bound $d_\mu \leqslant 0.065$ at 99% CL decreases roughly by a factor 2 with respect to the previous bound $d_\mu \leqslant 0.13$ [36, 127], as implied by fitting atmospheric data with one-dimensional fluxes [39] and without K2K. Following [127] we show in figure 20 the upper bound on the LSND oscillation amplitude $\sin^2 2\theta_{\rm LSND}$ from the combined analysis of NEV and atmospheric neutrino data. This figure illustrates that the improvement implied by the stronger bound on d_μ is mostly relevant for lower values of $\Delta m^2_{\rm LSND}$. From this figure we see that the bound is incompatible with the signal observed in LSND at the 95% CL. Only marginal overlap regions exist between the bound and global LSND data if both are taken at 99% CL. On using only the decay-at-rest LSND data sample [128] the disagreement is even more severe. These results show that (3 + 1) schemes are strongly disfavoured by SBL disappearance data.

5.4. Comparing (3 + 1), (2 + 2) and (3 + 0) hypotheses

Using the methods developed in [123] we perform a global fit to the oscillation data in the four-neutrino framework. This approach allows to statistically compare the different hypotheses. Let us first evaluate the GOF of (3 + 1) and (2 + 2) spectra using the PG method described in [125].

Table 2. Parameter GOF and the contributions of different data sets to $\chi^2_{\rm PG}$ in (3 + 1) and (2 + 2) neutrino mass schemes.

	SOL	ATM	LSND	NEV	$\chi^2_{\rm PG}$	PG
(3 + 1)	0.0	0.4	5.7	10.9	17.0	1.9×10^{-3} (3.1σ)
(2 + 2)	5.3	20.8	0.6	7.3	33.9	7.8×10^{-7} (4.9σ)

We divide the global oscillation data into the four data sets SOL, ATM, LSND and NEV. Then we use the PG method to test the statistical compatibility of these data sets assuming a given neutrino mass scheme. Following [121] we consider

$$\bar{\chi}^2 = \Delta\chi^2_{\rm SOL}(\theta_{\rm SOL}, \Delta m^2_{\rm SOL}, \eta_s) + \Delta\chi^2_{\rm ATM}(\theta_{\rm ATM}, \Delta m^2_{\rm ATM}, \eta_s, d_\mu) + \Delta\chi^2_{\rm NEV}(\theta_{\rm LSND}, \Delta m^2_{\rm LSND}, d_\mu, \eta_e) + \Delta\chi^2_{\rm LSND}(\theta_{\rm LSND}, \Delta m^2_{\rm LSND}), \quad (22)$$

where $\Delta\chi^2_X = \chi^2_X - (\chi^2_X)_{\rm min}$ ($X = $ SOL, ATM, NEV, LSND). In table 2 we show the contributions of the four data sets to $\chi^2_{\rm PG} \equiv \bar{\chi}^2_{\rm min}$ for (3 + 1) and (2 + 2) oscillation schemes. As expected we observe that in (3 + 1) schemes the main contribution comes from SBL data due to the tension between LSND and NEV data in these schemes. For (2 + 2) oscillation schemes a large part of $\chi^2_{\rm PG}$ comes from solar and atmospheric data, due to the rejection against a sterile neutrino contribution of these two data sets, as discussed in section 5.2. The contribution from NEV data in (2 + 2) comes mainly from the tension between LSND and KARMEN [128], which does not depend on the mass scheme.

The parameter goodness-of-fit is obtained by evaluating $\chi^2_{\rm PG}$ for four d.o.f. [125]. This number of degrees of freedom corresponds to the four parameters $\eta_s, d_\mu, \theta_{\rm LSND}, \Delta m^2_{\rm LSND}$ describing the coupling of the different data sets (see equation (21) and figure 18). The best GOF is obtained in the (3 + 1) case. However, even in this best case the PG is only 0.19%. This PG value is slightly reduced with respect to our previous result 0.56% [121, 122] because of the improved limit on d_μ from atmospheric + K2K data (see section 5.3). The PG of 7.8×10^{-7} for (2 + 2) schemes shows that these mass schemes are essentially ruled out by the disagreement between the individual data sets. As mentioned in section 5.2 the exclusion of (2 + 2) schemes is slightly weaker as previously [122] since we now do not include MACRO data in our analysis.

Although we have seen that none of the four-neutrino mass schemes provides a good fit to the global oscillation data including LSND, it is interesting to consider the *relative* status of the three hypotheses (3 + 1), (2 + 2) and the three-active neutrino scenario (3 + 0). This can be done by comparing the χ^2 value of the best-fit point—which occurs for the (3 + 1) scheme—with the ones corresponding to (2 + 2) and (3 + 0). First we observe that (2 + 2) schemes are strongly disfavoured with respect to (3 + 1) with a $\Delta\chi^2 = 16.9$. For four d.o.f. this is equivalent to an exclusion at 3.1σ. Furthermore, we find that (3 + 0) is disfavoured with a $\Delta\chi^2 = 17.5$ (corresponding to 3.2σ for four d.o.f.) with respect to (3 + 1). This reflects the high statistical significance of the LSND result, since in a (3 + 0) scheme no effect is predicted for LSND.

To summarize, we find that four-neutrino schemes do not provide a satisfactory fit to the global data. The strong rejection of non-active oscillation in the solar + KamLAND and atmospheric + K2K neutrino data rules out (2 + 2) schemes, irrespective of whether LSND is confirmed or not. Using an improved goodness-of-fit method, especially sensitive to the combination of data sets, we find that (2 + 2) schemes are ruled out at the 4.9σ level. On

the other hand, (3 + 1) spectra are disfavoured by the disagreement of LSND with short-baseline disappearance data, leading to a marginal GOF of 1.9×10^{-3} (3.1σ). Should LSND be confirmed it would be very desirable to have more data on ν_e and/or ν_μ SBL disappearance to decide about the status of (3 + 1) schemes. In that case, a positive signal is predicted right at the sensitivity edge of existing experiments.

More drastic attempts to reconcile the LSND signal with the rest of neutrino oscillation data have been reviewed in [26]. For example, in [135] a five-neutrino scheme is invoked to reconcile all the data. In [136] it has been shown that even the rather drastic assumption of CPT violation in a three-neutrino framework [137, 138] does not provide a satisfactory description of the global neutrino data set including LSND. Similarly, an interpretation of the LSND signal in terms of a non-standard muon decay is disfavoured by KARMEN [139].

We conclude that currently no convincing explanation for the LSND result exists, and how to reconcile this evidence with the rest of the data remains a puzzle. It is therefore very important to settle this issue experimentally. A confirmation of the LSND signal by the MiniBooNE experiment [140] would be very exciting and would require some novel physics ideas.

6. Summary and conclusions

We have given a brief review of the status of global analyses of neutrino oscillations, taking into account the latest neutrino data, including the most recent updates of KamLAND and K2K presented at Neutrino2004, as well as state-of-the-art solar and atmospheric neutrino flux calculations. We presented two-neutrino solar + KamLAND results, as well as two-neutrino atmospheric + K2K oscillation regions, and a discussion in each case of the robustness with which the oscillation hypothesis can be established, in view of possible modifications. These might come from the assumed theoretical fluxes, the non-validity of the SM neutrino interaction cross sections or the existence of non-trivial neutrino propagation properties beyond oscillations. As case studies we have mentioned the robustness of the solar neutrino oscillation hypothesis *vis à vis* the possible existence of radiative-zone solar density fluctuations, non-zero convective-zone solar magnetic fields and neutrino transition magnetic moments. For the atmospheric + K2K analysis we have considered explicitly the robustness of the oscillation hypothesis against the possible existence of flavour or universality violating non-standard neutrino interactions.

Furthermore, we have performed a fit to the most recent world neutrino data sample in the three-flavour framework. The results of this global analysis are summarized in figure 12 and table 1, where we give the best-fit values and allowed ranges of the three-flavour oscillation parameters. In addition, we discussed in detail the status of the small parameters $\alpha \equiv \Delta m^2_{\rm SOL}/\Delta m^2_{\rm ATM}$ and $\sin^2\theta_{13}$, which characterize the strength of CP violating effects in neutrino oscillations, highlighting the improvement of the bound on $\sin^2\theta_{13}$ implied by the inclusion of the recent KamLAND data. Finally, we gave a review over the current status of four-neutrino interpretations of the LSND anomaly, in view of the most recent experimental and theoretical advances.

All in all, we can say beyond reasonable doubt that neutrino masses, discovered through atmospheric neutrino oscillations, have now also been confirmed in the solar neutrino oscillation channel thanks to the important input of the KamLAND experiment. Theory-wise, while the SSM was necessary in order to establish the need for physics beyond the SM, it has now been made to some extent irrelevant by the high precision of the experiments which currently dominate the determination of solar neutrino oscillation parameters. The next goal in the agenda is the

determination of the small parameter $\sin^2\theta_{13}$ that characterizes the strength of CP violating effects in neutrino oscillations, and the exploration of the Majorana nature of the neutrino which will be sensitive to the other leptonic CP phases.

Acknowledgments

This review is based on work with a number of collaborators with whom we have had many (sometimes passionate) discussions. The list includes E Kh Akhmedov, J Barranco, C P Burgess, N S Dzhalilov, N Fornengo, M C González-García, W Grimus, M Guzzo, P C de Holanda, O Miranda, H Nunokawa, C Peña-Garay, T I Rashba, A I Rez, V B Semikoz and R Tomàs. This work was supported by Spanish grant BFM2002-00345, by the European Commission RTN grant HPRN-CT-2000-00148 and the ESF *Neutrino Astrophysics Network*. MM is supported by the National Science Foundation grant PHY0098527. TS has been supported by the Sonderforschungsbereich 375 für Astro-Teilchenphysik der Deutschen Forschungsgemeinschaft. MT has been supported by FPU fellowship AP2000-1953.

Appendix. The new KamLAND results

In this appendix we discuss in some detail the most recent data from KamLAND [15]. In section A.1 we give the details of our data analysis, whereas in section A.2 we discuss the physics results.

A.1. Analysis details of the new data

We have modified our previous KamLAND analysis methods [67, 68] applied to the first published KamLAND data [14] in various aspects to take into account the characteristics of the new data. First, to analyse KamLAND data one has to know the contribution of the various power reactors to the signal. We extract the relevant information from figure 1(b) of [15], where the no-oscillation signal is given as a function of the distance to the detector. Second, we use an improved parametrization [69] of the anti-neutrino flux emitted by the isotopes ^{235}U, ^{239}Pu, ^{238}U and ^{241}Pu in the nuclear reactors. Third, we include 2.69 accidental background events in the lowest energy bin. For the 4.8 ± 0.9 background events expected from the beta-decay of ^{9}Li and ^{8}He we assume regular beta-spectra with endpoints of 13.6 and 10.7 MeV, respectively (see, e.g., figure 11 of [40]). Fourth, we include the small matter effects.

In general most information can be extracted from data by un-binned likelihood methods (see [67] for the case of the first KamLAND data). Unfortunately, it is not possible to obtain event-based energy information for the current KamLAND sample, and one has to stick with binned data outside the collaboration. Traditionally, data is given in bins of equal size in the prompt energy $E_{\rm pr}$ (see figure 2(b) of [15]). However, it turns out that in the case of KamLAND more information can be obtained if data is binned equally in $1/E_{\rm pr}$. The relevant information can be extracted from figure 3 of [15], where the ratio of the observed spectrum to the expectation for no oscillation is given in 13 bins of 180 km E_ν^{-1} [MeV]. We show the data binned in $1/E_{\rm pr}$ as well as in $E_{\rm pr}$ in figure A.1. The $1/E_{\rm pr}$ binning is more useful for two reasons. First, it is more natural to make the bins smaller in the region of many events (low energy) and wider in the high-energy region, where there are very few events. This maintains more energy information in the region

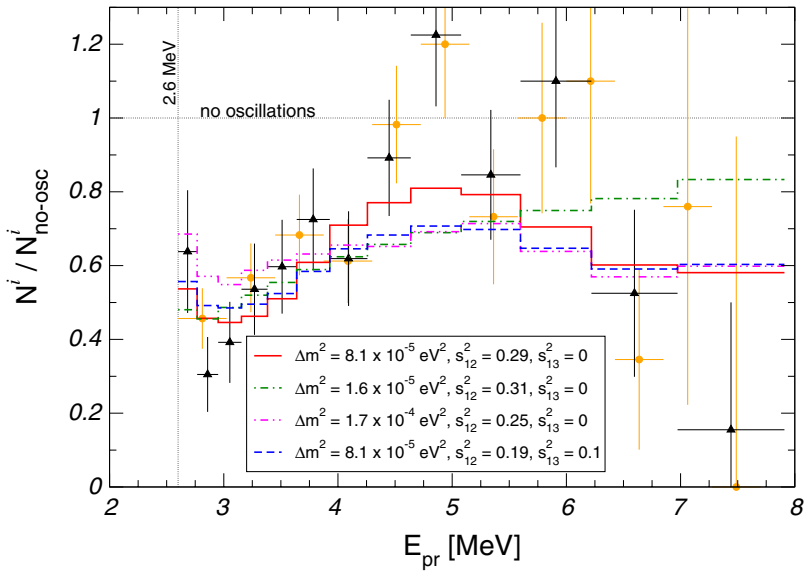

Figure A.1. Data divided by the expectation for no oscillations for equal bins in $1/E_{\rm pr}$ (triangles) and in $E_{\rm pr}$ (dots). Also shown is the spectrum for the best-fit point (solid), the local best-fit points in the low Δm^2 (dash-dotted) and high Δm^2 (dash-dot-dotted) regions, and for a large value of $\sin^2\theta_{13}$ (dashed).

of greater statistics. Second, since the frequency of neutrino oscillations is proportional to $1/E_\nu$ this binning is more appropriate for the signal we are interested.

Concerning the statistical analysis, we adopt a Poisson χ^2-function, and make extensive use of the pull-method to implement various systematical errors. In the overall normalization uncertainty we include only the detector-specific contributions by summing up the errors of the left column of table 1 from [15], which gives $\sigma_{\rm det} = 5.47\%$. The uncertainties associated to the anti-neutrino flux are treated according to the method presented in [69]. We include an uncertainty on the thermal power (2%) and the fuel composition (1%) of each individual reactor, as well as the spectral uncertainty of the emitted anti-neutrino fluxes. In agreement with [69] we find that flux related uncertainties play only a minor role in the KamLAND analysis.

A.2. Discussion of the KamLAND results

In figure A.1 we show the predictions for the probabilities in the various bins $P_i \equiv N^i_{\rm osc}/N^i_{\rm no\text{-}osc}$ compared to the data $P_i^{\rm obs} \equiv N^i_{\rm obs}/N^i_{\rm no\text{-}osc}$. From this figure one can see that the probabilities are rather low for low energies, whereas in the region around 4.5 MeV even slightly more events than expected for no oscillations have been observed. This is a very characteristic pattern indicating rather strong spectral distortion, and only the best fit parameters (solid line) can reproduce this shape. All other parameter choices shown in the figure have problems to accommodate the high data points in the middle of the spectrum. This holds for the solution around $\Delta m^2 \simeq 1.6 \times 10^{-5}$ eV^2 as well as for the high-LMA solution at $\Delta m^2 \simeq 1.7 \times 10^{-4}$ eV^2 (compare figure 6). The rejection power to these two 'solutions' is significantly increased by the $1/E_{\rm pr}$ binning with respect to the $E_{\rm pr}$ binning: in our analysis we obtain a $\Delta\chi^2 = 7.5(11.3)$ for the local minimum at $1.6(17) \times 10^{-5}$ eV^2, whereas with the traditional $E_{\rm pr}$ binning we

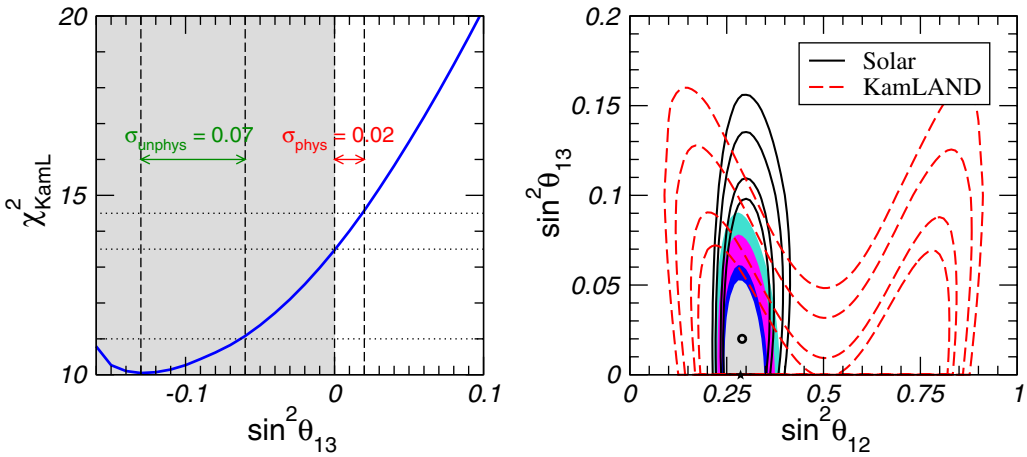

Figure A.2. Left panel: χ^2 from KamLAND data as a function of $\sin^2\theta_{13}$ including the unphysical region $\sin^2\theta_{13} < 0$. Right panel: allowed regions at 90, 95 and 99% and 3σ of $\sin^2\theta_{13}$ and $\sin^2\theta_{12}$ (2 d.o.f.) for fixed $\Delta m^2_{\rm SOL} = 8.1 \times 10^{-5}\,{\rm eV}^2$ from KamLAND data (dashed), solar data (solid), and KamLAND + solar data combined (shaded regions).

find $\Delta\chi^2 = 4.0(8.5)$. In particular, to disfavour the high-LMA region the more precise energy information at low energies provided by the $1/E_{\rm pr}$ bins is crucial, whereas for the low region the high energy part seems to be important.

Let us now discuss the bound on $\sin^2\theta_{13}$ from the KamLAND data. From figure A.1 one can see that turning on $\sin^2\theta_{13}$ leads to a flatter energy spectrum and it gets more difficult to accommodate the low probabilities for low energies simultaneously with the high data points in the middle part of the spectrum. It is also clear from the relevant three-flavour survival probability in vacuum

$$P_{ee} = 1 - \frac{1}{2}\sin^2 2\theta_{13} - \cos^4\theta_{13}\sin^2 2\theta_{12}\sin^2\frac{\Delta m^2_{21}L}{4E_\nu} \tag{A.1}$$

that values of $\sin^2\theta_{13} > 0$ suppress the oscillatory term. In fact, if a fit to the KamLAND data is performed without imposing the constraint $\sin^2\theta_{13} \geqslant 0$ one finds a best-fit point within the unphysical region at $\sin^2\theta_{13} = -0.13$ (see figure A.2). Because of the rather large difference in the probability between the low and medium energy bins, the fit is improved by a $\Delta\chi^2 \simeq 3.5$ by allowing an enhancement of the oscillatory term in (A.1) due to values of $\cos^4\theta_{13} > 1$, i.e. $\sin^2\theta_{13} < 0$. Figure A.2 illustrates that this fact leads to a rather strong bound on $\sin^2\theta_{13}$ if the analysis is restricted to the physical region. Just from the statistical power of the data one would expect a 1σ error on $\sin^2\theta_{13}$ of $\sigma \simeq 0.07$. However, due to the particular fluctuation observed in the actual data, the best-fit point lies in the unphysical region. This implies that for $\sin^2\theta_{13} = 0$ there is already some tension in the fit, and a significantly smaller error of $\sigma = 0.02$ is obtained within the physical region.[13]

[13] We note that in such a case a reliable bound can be calculated by performing a Monte Carlo simulation of many synthetic data sets. This is beyond the scope of the present paper, and we throughout use the naive method of calculating bounds by considering $\Delta\chi^2$-values as implied by Gaussian statistics and restricting the analysis to the physical region.

Finally, in the right-hand panel of figure A.2, we illustrate, why the combination of KamLAND and solar data leads to a further notable improvement of the bound on $\sin^2\theta_{13}$. From (A.1) one expects for KamLAND a correlation between $\sin^2\theta_{13}$ and $\sin^2 2\theta_{12}$. Solving (A.1) for $\sin^2 2\theta_{12}$ and expanding up to first order in $\sin^2\theta_{13}$ one finds

$$\sin^2 2\theta_{12}\sin^2\frac{\Delta m^2_{21}L}{4E_\nu} \simeq 1 - P_{ee} - 2P_{ee}\sin^2\theta_{13}. \tag{A.2}$$

For a given survival probability, (23) implies a negative correlation between $\sin^2\theta_{13}$ and $\sin^2 2\theta_{12}$. This trend is visible also in the actual fit, see figure A.2, where the allowed region for these two parameters is shown for fixed Δm^2. One observes that increasing $\sin^2\theta_{13}$ can be compensated to some extent by decreasing $\sin^2\theta_{12}$ (within the 'light side' $\sin^2\theta_{12} < 0.5$). This, however, is in disagreement with solar data, which provide a stable lower bound on $\sin^2\theta_{12}$ due to the fundamentally different conversion mechanism (MSW matter effect in the sun versus vacuum oscillations). The combined analysis of KamLAND and solar data leads essentially to the intersection of the two individual allowed regions, which further improves the bound on $\sin^2\theta_{13}$.

References

[1] Davis R 1994 *Prog. Part. Nucl. Phys.* **32** 13
[2] Cleveland B T *et al* 1998 *Astrophys. J.* **496** 505
[3] SAGE Collaboration, Abdurashitov J N *et al* 1999 *Phys. Rev.* C **60** 055801 (*Preprint* astro-ph/9907113)
[4] GNO Collaboration 2002 *Nucl. Phys. Proc. Suppl.* **110** 311
[5] GALLEX Collaboration, Hampel W *et al* 1999 *Phys. Lett.* B **447** 127
[6] GNO Collaboration, Altmann M *et al* 2000 *Phys. Lett.* B **490** 16 (*Preprint* hep-ex/0006034)
[7] Super-Kamiokande Collaboration, Fukuda S *et al* 2002 *Phys. Lett.* B **539** 179 (*Preprint* hep-ex/0205075)
[8] SNO Collaboration, Ahmad Q R *et al* 2002 *Phys. Rev. Lett.* **89** 011301 (*Preprint* nucl-ex/0204008)
[9] SNO Collaboration, Ahmad Q R *et al* 2002 *Phys. Rev. Lett.* **89** 011302 (*Preprint* nucl-ex/0204009)
[10] SNO Collaboration, Ahmed S N *et al* 2003 *Phys. Rev. Lett.* 041801 (*Preprint* nucl-ex/0309004)
[11] Super-Kamiokande Collaboration, Fukuda Y *et al* 1998 *Phys. Rev. Lett.* **81** 1562 (*Preprint* hep-ex/9807003)
[12] MACRO Collaboration, Surdo A 2002 *Nucl. Phys. Proc. Suppl.* **110** 342
Giacomelli G and Margiotta A 2004 *Phys. At. Nucl.* **67** 1139 (*Preprint* hep-ex/0407023)
[13] Soudan 2 Collaboration, Sanchez M *et al* 2003 *Phys. Rev.* D **68** 113004 (*Preprint* hep-ex/0307069)
[14] KamLAND Collaboration, Eguchi K *et al* 2003 *Phys. Rev. Lett.* **90** 021802 (*Preprint* hep-ex/0212021)
[15] KamLAND Collaboration, Araki T *et al* 2004 *Preprint* hep-ex/0406035
G Gratta 2004 Talk at *Neutrino 2004, 14–19 June 2004, Paris* (http://neutrino2004.in2p3.fr/)
[16] K2K Collaboration, Ahn M H *et al* 2003 *Phys. Rev. Lett.* **90** 041801 (*Preprint* hep-ex/0212007)
[17] Nakaya T 2004 Talk at *Neutrino 2004, 14–19 June 2004, Paris* (http://neutrino2004.in2p3.fr/)
[18] Gell-Mann M, Ramond P and Slansky R 1979 Print-80-0576 (CERN)
[19] Yanagida T 1979 *KEK Lectures* ed Sawada and Sugamoto (Tsukuba, Ibaraki: KEK)
[20] Schechter J and Valle J W F 1980 *Phys. Rev.* D **22** 2227
[21] Mohapatra R N and Senjanovic G 1981 *Phys. Rev.* D **23** 165
[22] For a short review see Valle J W F 2003 Neutrino masses twenty-five years later *AIP Conf. Proc.* **687** 16 (*Preprint* hep-ph/0307192)
[23] Goodman M *Neutrino Oscillation Industry* http://neutrinooscillation.org/
[24] Mikheev S P and Smirnov A Y 1985 *Sov. J. Nucl. Phys.* **42** 913
[25] Wolfenstein L 1978 *Phys. Rev.* D **17** 2369
[26] Pakvasa S and Valle J W F 2004 *Proc. Indian National Academy of Sciences, Part A* ed D Indumathi, M V N Murthy and G Rajasekaran, vol 70A, No 1, pp 189–222 (*Preprint* hep-ph/0301061)

[27] Barger V, Marfatia D and Whisnant K 2003 *Int. J. Mod. Phys.* E **12** 56
[28] Gonzalez-Garcia M C and Nir Y 2003 *Rev. Mod. Phys.* **75** 34
[29] Fogli G L *et al* 2003 *Proc. Int. Workshop on Astroparticle and High Energy Physics, 14–18 October 2003, Valencia, Spain* Published in *J. High Energy Phys.* PRHEP-AHEP2003/071, accessible from http://ific.uv.es/ahep/
[30] Maltoni M, Schwetz T, Tortola M A and Valle J W F 2003 *Phys. Rev.* D **68** 113010 (*Preprint* hep-ph/0309130)
[31] Bahcall J N and Pinsonneault M H 2004 *Phys. Rev. Lett.* **93** 121301 (*Preprint* astro-ph/0402114)
[32] Honda M, Kajita T, Kasahara K and Midorikawa S 2004 *Preprint* astro-ph/0404457
[33] Super-Kamiokande Collaboration, Ashie Y 2004 *Preprint* hep-ex/0404034
[34] Hayato Y 2003 http://eps2003.physik.rwth-aachen.de
[35] Gonzalez-Garcia M, Maltoni M, Pena-Garay C and Valle J W F 2001 *Phys. Rev.* D **63** 033005 (*Preprint* hep-ph/0009350)
[36] Maltoni M, Schwetz T, Tortola M A and Valle J W F 2003 *Phys. Rev.* D **67** 013011 (*Preprint* hep-ph/0207227 version v3)
[37] Kameda J 2002 *PhD Thesis* University of Tokyo, available at http://www-sk.icrr.u-tokyo.ac.jp/doc/sk/pub/
[38] Fogli G L, Lisi E, Marrone A and Montanino D 2003 *Phys. Rev.* D **67** 093006 (*Preprint* hep-ph/0303064)
[39] Barr G, Gaisser T K and Stanev T 1989 *Phys. Rev.* D **39** 3532
[40] Huber P, Lindner M, Rolinec M, Schwetz T and Winter W 2004 *Preprint* hep-ph/0403068
[41] Schechter J and Valle J W F 1982 *Phys. Rev.* D **25** 774
Valle J W F 1983 *Phys. Lett.* B **131** 87
Gelmini G B and Valle J W F 1984 *Phys. Lett.* B **142** 181
Gonzalez-Garcia M C and Valle J W F 1989 *Phys. Lett.* B **216** 360
[42] Pakvasa S and Tennakone K 1972 *Phys. Rev. Lett.* **28** 1415
[43] Zee A 1980 *Phys. Lett.* B **93** 389
[44] Babu K S 1988 *Phys. Lett.* B **203** 132
[45] Mohapatra R N and Valle J W F 1986 *Phys. Rev.* D **34** 1642
[46] Hall L J, Kostelecky V A and Raby S 1986 *Nucl. Phys.* B **267** 415
[47] Bernabeu J *et al* 1987 *Phys. Lett.* B **187** 303
[48] Branco G C, Rebelo M N and Valle J W F 1989 *Phys. Lett.* B **225** 385
[49] Rius N and Valle J W F 1990 *Phys. Lett.* B **246** 249
[50] Fornengo N *et al* 2002 *Phys. Rev.* D **65** 013010 (*Preprint* hep-ph/0108043)
[51] Valle J W F 1991 *Prog. Part. Nucl. Phys.* **26** 91
[52] Hirsch M and Valle J W F 2004 *New J. Phys.* **6** 76 (*Preprint* hep-ph/0405015)
[53] Gonzalez-Garcia M C and Maltoni M 2004 *Phys. Rev.* D at press (*Preprint* hep-ph/0404085)
[54] Nunokawa H, Qian Y Z, Rossi A and Valle J W F 1996 *Phys. Rev.* D **54** 4356 (*Preprint* hep-ph/9605301)
[55] Fogli G L, Lisi E, Mirizzi A and Montanino D 2002 *Phys. Rev.* D **66** 013009 (*Preprint* hep-ph/0202269)
[56] Grasso D, Nunokawa H and Valle J W F 1998 *Phys. Rev. Lett.* **81** 2412 (*Preprint* astro-ph/9803002)
[57] McDonald A 2004 *New J. Phys.* **6** 121
[58] Bahcall J N and Pena-Garay C 2004 *New J. Phys.* **6** 63 (*Preprint* hep-ph/0404061)
[59] Bellotti E and Gavrin V http://mocha.phys.washington.edu/
[60] SAGE Collaboration, Abdurashitov J N *et al* 2002 *J. Exp. Theor. Phys.* **95** 181 (*Preprint* astro-ph/0204245)
The latest number was presented by
Cattadori C M 2004 Talk at *Neutrino 2004, 14–19 June 2004, Paris* http://neutrino2004.in2p3.fr/
[61] Fogli G L, Lisi E, Marrone A, Montanino D and Palazzo A 2002 *Phys. Rev.* D **66** 053010 (*Preprint* hep-ph/0206162)
[62] Balantekin A B and Yuksel H 2003 *Phys. Rev.* D **68** 113002 (*Preprint* hep-ph/0309079)
[63] Bahcall J N, Pinsonneault M H and Basu S 2001 *Astrophys. J.* **555** 990 (*Preprint* astro-ph/0010346)
[64] Chankowski P, Ioannisian A, Pokorski S and Valle J W F 2001 *Phys. Rev. Lett.* **86** 3488 (*Preprint* hep-ph/0011150)

[65] Fiorentini G, Lasserre T, Lissia M, Ricci B and Schonert S 2003 *Phys. Lett.* B **558** 15 (*Preprint* hep-ph/0301042)
[66] Nunokawa H, Teves W J C and Zukanovich Funchal R 2003 *J. High Energy Phys.* JHEP11(2003)020 (*Preprint* hep-ph/0308175)
[67] Schwetz T 2003 *Phys. Lett.* B **577** 120 (*Preprint* hep-ph/0308003)
[68] Maltoni M, Schwetz T and Valle J W F 2003 *Phys. Rev.* D **67** 093003 (*Preprint* hep-ph/0212129)
[69] Huber P and Schwetz T 2004 *Preprint* hep-ph/0407026
[70] Super-Kamiokande Collaboration, Smy M B *et al* 2004 *Phys. Rev.* D **69** 011104 (*Preprint* hep-ex/0309011)
[71] Balantekin A B, Fetter J M and Loreti F N 1996 *Phys. Rev.* D **54** 3941 (*Preprint* astro-ph/9604061)
[72] Nunokawa H, Rossi A, Semikoz V B and Valle J W F 1996 *Nucl. Phys.* B **472** 495 (*Preprint* hep-ph/9602307)
[73] Bamert P, Burgess C P and Michaud D 1998 *Nucl. Phys.* B **513** 319 (*Preprint* hep-ph/9707542)
[74] Castellani V, Degl'Innocenti S, Dziembowski W A, Fiorentini G and Ricci B 1999 *Nucl. Phys. Proc. Suppl.* **70** 301 (*Preprint* astro-ph/9712174)
[75] Christensen-Dalsgaard J 2003 *Rev. Mod. Phys.* **74** 1073 (*Preprint* astro-ph/0207403)
[76] Burgess C P *et al* 2004 *Mon. Not. R. Astron. Soc.* **348** 609 (*Preprint* astro-ph/0304462)
[77] Burgess C *et al* 2003 *Astrophys. J.* **588** L65 (*Preprint* hep-ph/0209094)
[78] Burgess C P *et al* 2004 *J. Cosmol. Astropart. Phys.* JCAP01(2004)007 (*Preprint* hep-ph/0310366)
[79] Fujikawa K and Shrock R 1980 *Phys. Rev. Lett.* **45** 963
[80] Schechter J and Valle J W F 1981 *Phys. Rev.* D **24** 1883
Schechter J and Valle J W F 1982 *Phys. Rev.* D **25** 283 (erratum)
[81] Akhmedov E K 1988 *Phys. Lett.* B **213** 64
[82] Lim C-S and Marciano W J 1988 *Phys. Rev.* D **37** 1368
[83] Miranda O G, Rashba T I, Rez A I and Valle J W F 2004 *Phys. Rev. Lett.* **93** 051304 (*Preprint* hep-ph/0311014)
[84] Kutvitskii V A and Solov'ev L S 1994 *J. Exp. Theor. Phys.* **78** 456
[85] Miranda O G *et al* 2001 *Nucl. Phys.* B **595** 360 (*Preprint* hep-ph/0005259)
[86] KamLAND Collaboration, Eguchi K *et al* 2004 *Phys. Rev. Lett.* **92** 071301 (*Preprint* hep-ex/0310047)
[87] Super-Kamiokande Collaboration, Gando Y *et al* 2003 *Phys. Rev. Lett.* **90** 171302 (*Preprint* hep-ex/0212067)
[88] Grimus W *et al* 2003 *Nucl. Phys.* B **648** 376 (*Preprint* hep-ph/0208132)
[89] Beacom J F and Vogel P 1999 *Phys. Rev. Lett.* **83** 5222 (*Preprint* hep-ph/9907383)
[90] Joshipura A S and Mohanty S 2002 *Phys. Rev.* D **66** 012003 (*Preprint* hep-ph/0204305)
[91] Grifols J A, Masso E and Mohanty S 2004 *Phys. Lett.* B **587** 184 (*Preprint* hep-ph/0401144)
[92] Super-Kamiokande Collaboration, Liu D W *et al* 2004 *Phys. Rev. Lett.* **93** 021802 (*Preprint* hep-ex/0402015)
[93] Derbin A V 1994 *Phys. At. Nucl.* **57** 222
[94] TEXONO Collaboration, Li H B *et al* 2002 *Preprint* hep-ex/0212003
[95] MUNU Collaboration, Daraktchieva Z *et al* 2003 *Phys. Lett.* B **564** 190 (*Preprint* hep-ex/0304011)
[96] Bardin D Y, Bilenky S M and Pontecorvo B 1970 *Phys. Lett.* B **32** 68
[97] Kyuldjiev A V 1984 *Nucl. Phys.* B **243** 387
[98] Grimus W and Schwetz T 2000 *Nucl. Phys.* B **587** 45 (*Preprint* hep-ph/0006028)
[99] Borexino Collaboration, Alimonti G *et al* 2002 *Astropart. Phys.* **16** 205 (*Preprint* hep-ex/0012030)
[100] Fogli G L *et al* 2003 *Phys. Rev.* D **67** 073002 (*Preprint* hep-ph/0212127)
[101] Gonzalez-Garcia M C and Pena-Garay C 2003 *Preprint* hep-ph/0306001
[102] Particle Data Group, Hagiwara K *et al* 2002 *Phys. Rev.* D **66** 010001
[103] Gonzalez-Garcia M C and Maltoni M 2003 *Eur. Phys. J.* C **26** 417 (*Preprint* hep-ph/0202218)
[104] Doi M, Kotani T, Nishiura H, Okuda K and Takasugi E 1981 *Phys. Lett.* B **102** 323
[105] CHOOZ Collaboration, Apollonio M *et al* 1999 *Phys. Lett.* B **466** 415 (*Preprint* hep-ex/9907037)
[106] Schechter J and Valle J W F 1980 *Phys. Rev.* D **21** 309
[107] Freund M 2001 *Phys. Rev.* D **64** 053003 (*Preprint* hep-ph/0103300)
[108] Akhmedov E K, Johansson R, Lindner M, Ohlsson T and Schwetz T 2004 *J. High Energy Phys.* JHEP04(2004)078 (*Preprint* hep-ph/0402175)
[109] Palo Verde Collaboration, Boehm F *et al* 2001 *Phys. Rev.* D **64** 112001 (*Preprint* hep-ex/0107009)

[110] Akhmedov E K, Tortola M A and Valle J W F 2004 *J. High Energy Phys.* JHEP05(2004)057 (*Preprint* hep-ph/0404083)
[111] Blennow M, Ohlsson T and Snellman H 2004 *Phys. Rev.* D **69** 073006 (*Preprint* hep-ph/0311098)
[112] Yanagisawa C 2003 *Proc. Int. Workshop on Astroparticle and High Energy Physics, 14–18 October 2003, Valencia, Spain* Published in *J. High Energy Phys.* PRHEP-AHEP2003/062, accessible from http://ific.uv.es/ahep/
[113] LSND Collaboration, Aguilar A *et al* 2001 *Phys. Rev.* D **64** 112007 (*Preprint* hep-ex/0104049)
[114] Peltoniemi J T and Valle J W F 1993 *Nucl. Phys.* B **406** 409 (*Preprint* hep-ph/9302316)
[115] Peltoniemi J T, Tommasini D and Valle J W F 1993 *Phys. Lett.* B **298** 383
[116] Caldwell D O and Mohapatra R N 1993 *Phys. Rev.* D **48** 3259
[117] KARMEN Collaboration, Armbruster B *et al* 2002 *Phys. Rev.* D **65** 112001 (*Preprint* hep-ex/0203021)
[118] CDHS Collaboration, Dydak F *et al* 1984 *Phys. Lett.* B **134** 281
[119] Declais Y *et al* 1995 *Nucl. Phys.* B **434** 503
[120] Grimus W and Schwetz T 2001 *Eur. Phys. J.* C **20** 1 (*Preprint* hep-ph/0102252)
[121] Maltoni M, Schwetz T, Tortola M A and Valle J W F 2002 *Nucl. Phys.* B **643** 321 (*Preprint* hep-ph/0207157)
[122] Schwetz T 2003 *Preprint* hep-ph/0311217
[123] Maltoni M, Schwetz T and Valle J W F 2002 *Phys. Rev.* D **65** 093004 (*Preprint* hep-ph/0112103)
[124] González-García M C, Maltoni M and Peña-Garay C 2001 *Phys. Rev.* D **64** 093001 (*Preprint* hep-ph/0105269)
[125] Maltoni M and Schwetz T 2003 *Phys. Rev.* D **68** 033020 (*Preprint* hep-ph/0304176)
[126] Paes H, Song L-G and Weiler T J 2003 *Phys. Rev.* D **67** 073019 (*Preprint* hep-ph/0209373)
[127] Maltoni M, Schwetz T and Valle J W F 2001 *Phys. Lett.* B **518** 252 (*Preprint* hep-ph/0107150)
[128] Church E D, Eitel K, Mills G B and Steidl M 2002 *Phys. Rev.* D **66** 013001 (*Preprint* hep-ex/0203023)
[129] Bilenky S M, Giunti C and Grimus W 1998 *Eur. Phys. J.* C **1** 247 (*Preprint* hep-ph/9607372)
[130] Okada N and Yasuda O 1997 *Int. J. Mod. Phys.* A **12** 3669 (*Preprint* hep-ph/9606411)
[131] Barger V D, Pakvasa S, Weiler T J and Whisnant K 1998 *Phys. Rev.* D **58** 093016 (*Preprint* hep-ph/9806328)
[132] Bilenky S M, Giunti C, Grimus W and Schwetz T 1999 *Phys. Rev.* D **60** 073007 (*Preprint* hep-ph/9903454)
[133] Peres O L G and Smirnov A Y 2001 *Nucl. Phys.* B **599** 3 (*Preprint* hep-ph/0011054)
[134] Giunti C and Laveder M 2001 *J. High Energy Phys.* JHEP02(2001)001 (*Preprint* hep-ph/0010009)
[135] Sorel M, Conrad J M and Shaevitz M 2003 *Preprint* hep-ph/0305255
[136] Gonzalez-Garcia M C, Maltoni M and Schwetz T 2003 *Phys. Rev.* D **68** 053007 (*Preprint* hep-ph/0306226)
[137] Murayama H and Yanagida T 2001 *Phys. Lett.* B **520** 263 (*Preprint* hep-ph/0010178)
[138] Barenboim G, Borissov L and Lykken J 2002 *Preprint* hep-ph/0212116
[139] Armbruster B *et al* 2003 *Phys. Rev. Lett.* **90** 181804 (*Preprint* hep-ex/0302017)
[140] BooNE Collaboration, Zimmerman E D 2002 eConf C0209101 TH05 (*Preprint* hep-ex/0211039)

New Journal of Physics
An Institute of Physics and Deutsche Physikalische Gesellschaft Journal

Unity of CP and T violation in neutrino oscillations

Martin Blom[1] **and Hisakazu Minakata**

Department of Physics, Tokyo Metropolitan University, 1-1 Minami-Osawa, Hachioji, Tokyo 192-0397, Japan
E-mail: martin@phys.metro-u.ac.jp and minakata@phys.metro-u.ac.jp

New Journal of Physics **6** (2004) 130
Received 21 April 2004
Published 7 October 2004
Online at http://www.njp.org/
doi:10.1088/1367-2630/6/1/130

Abstract. In a previous work, a simultaneous P–$CP[P]$ and P–$T[P]$ bi-probability plot was proposed as a useful tool for a unified graphical description of CP and T violation in neutrino oscillations. The diamond-shaped structure of the plot is understood as a consequence of the approximate CP–CP and T–CP relations obeyed by the oscillation probabilities. In this paper, we take a step forward towards a deeper understanding of the unified graphical representation by showing that these two relations are identical in their content, suggesting a truly unifying view of CP and T violation in neutrino oscillations. We suspect that the unity reflects the underlying CPT theorem. We also present a calculation of corrections to the CP–CP and the T–CP relations to leading order in $\Delta m^2_{21}/\Delta m^2_{31}$ and s^2_{13}.

[1] Also at: Division of Mathematical Physics, Department of Physics, Royal Institute of Technology (KTH), AlbaNova University Center, Roslagstullsbacken 11, 106 91 Stockholm, Sweden.

PII: S1367-2630(04)79572-5
© IOP Publishing Ltd and Deutsche Physikalische Gesellschaft

Contents

1. Introduction 2
2. CP and T violation in neutrino oscillation 3
3. Unified graphical representation of CP and T violation 4
4. Diamond shaped structure of CP and T bi-probability plot 6
5. Equivalence between the CP–CP and the T–CP relations 7
6. Leading-order corrections to the CP–CP and the T–CP relations 8
7. Concluding remarks 9

Acknowledgments 9

Appendix. No δ-dependence in the two-flavour limit 9

References 11

1. Introduction

Exploring leptonic CP and T violation is one of the most challenging endeavours in particle physics. Confirming (or refuting) unsuppressed CP violation analogous to that in the quark sector must shed light on a deeper understanding of the lepton–quark correspondence, a concept whose importance was recognized early in the 1960s [1]. We should note, however, that it is only after the KamLAND experiment [2], which confirmed the MSW large mixing-angle (LMA) solution [3, 4] of the solar neutrino problem, that we are able to talk about detecting CP or T violation in an experimentally realistic setting. An almost maximal mixing of θ_{23} discovered by the atmospheric neutrino observation by Super-Kamiokande [5], which broke new ground in the field of research, also greatly encourages attempts towards measuring the leptonic Kobayashi–Maskawa phase δ.

Yet, we might have the last impasse to observing leptonic CP violation, a too-small value of θ_{13}, which lives in the unique unexplored (1–3) sector of the MNS matrix [6]. Currently, it is bounded from above by a modest constraint $\sin^2 2\theta_{13} \leqslant 0.15-0.25$ obtained by the Chooz reactor experiment [7]. Towards removing the last impasse, two different methods for measuring θ_{13} are proposed and materialized into a number of concrete experimental programs. The first is the measurement of appearance probability $P(\nu_\mu \to \nu_e)$ in long-baseline (LBL) experiments using an accelerator neutrino beam, being and to be performed by ongoing [8, 9] and next-generation projects [10]–[12]. The second is the reactor measurement of θ_{13}. It is a pure measurement of θ_{13} independent of other oscillation parameters, δ and θ_{23}, and thus will play a role complementary to the LBL experiments [13]. This property is expected to help in resolving the parameter degeneracy [14]–[19] related to θ_{23} [13]. A spur of experimental projects that took place worldwide for the relatively new opportunity are now summarized in the White Paper Report [20].

If such challenges are blessed by nature we will be able to proceed to measure the leptonic CP or T violating phase δ. The relatively large value of θ_{13} will allow us to measure it via ν_e and $\bar{\nu}_e$ appearance measurement using conventional superbeam experiments, an idea which may be traced back to [21]. Feasible experimental programs for such appearance measurement with upgraded beams as well as detectors are proposed. See e.g., [10, 22] for the JPARC-Hyper-Kamiokande project and [11] for NOνA. It is also proposed that a fast search for CP violation

can be performed by combining neutrino mode operation of such experiments with high statistics reactor measurement of θ_{13} [23].

If θ_{13} is too small to be seen in the above experiments, an entirely new strategy is called for. We will probably need a more aggressive approach with ambitious beam technologies, neutrino factory [24] or beta beam [25] or even both. Here also, vigorous worldwide activities for developing beam and target technologies as well as studying physics capabilities are underway [26]–[28]. Intense neutrino beams from a muon storage ring and the clean background for wrong sign muon detection are expected to lead to an enormous sensitivity of θ_{13} up to $\sim 1^\circ$. Enriched by the golden ($\nu_e \to \nu_\mu$) [29] as well as the silver ($\nu_e \to \nu_\tau$) [30] channels, it will be able to resolve all the parameter degeneracies, as claimed in [31]. See [32] for a review of old and new ideas on how to measure leptonic CP violation.

How does T violation measurement fit into the scene? In our understanding, it will probably come later than CP violation measurement because the measurement is more difficult to carry out. In neutrino factories it requires electron charge identification which is highly non-trivial, if not impossible. The beta beam, if built, would give us an ideal apparatus because it can deliver a pure ν_e beam which comes from decaying radioactive nuclei. By combining with superbeam (or neutrino factory) measurement of $P(\nu_\mu \to \nu_e)$, it will provide us with a unique opportunity for exploring leptonic T violation.

Keeping in mind the scope of experimental realization of CP and T violation measurement in the future, we discuss in this paper a unified view of leptonic CP and T violation, one of the most fundamental problems in particle physics. We hope that our discussion is illuminating and contributes to a deeper understanding of the problem. In this paper we use, except for the appendix, the standard notation of the MNS matrix [33].

2. CP and T violation in neutrino oscillation

It has been known for a long time that CP and T conservation are intimately related to each other by the CPT theorem. For neutrino oscillation in vacuum the invariance leads to a relation between neutrino and antineutrino oscillation probabilities

$$P(\nu_\alpha \to \nu_\beta; \delta) = P(\bar{\nu}_\beta \to \bar{\nu}_\alpha; \delta). \tag{1}$$

Then, the question might be 'does there exist an analogous relation in neutrino oscillation in matter?'. It was shown in [34] that indeed there exists such a relationship,

$$P(\nu_\alpha \to \nu_\beta; \Delta m^2_{31}, \Delta m^2_{21}, \delta, a) = P(\bar{\nu}_\beta \to \bar{\nu}_\alpha; \Delta m^2_{31}, \Delta m^2_{21}, \delta, -a), \tag{2}$$

which comes from the classical time reversal and the complex conjugate of the neutrino evolution equation assuming that the matter profile is symmetric about the mid-point between production and detection. Let us call (2) the CPT relation in matter. Here, $a = 2\sqrt{2}G_F N_e E$ is the fundamental quantity which is related to the neutrino's index of refraction in matter [3] with G_F being the Fermi constant, E the neutrino energy, and $N_e(x)$ an electron number density on Earth. The mass-squared difference of neutrinos is defined as $\Delta m^2_{ij} \equiv m^2_i - m^2_j$ where m_i is the mass of the ith eigenstate.

There is an immediate consequence of the CPT relation in matter, equation (2). If we define ΔP_{CPT} as

$$\Delta P_{CPT} \equiv P(\nu_\alpha \to \nu_\beta; \Delta m^2_{31}, \Delta m^2_{21}, \delta, a) - P(\bar{\nu}_\beta \to \bar{\nu}_\alpha; \Delta m^2_{31}, \Delta m^2_{21}, \delta, a), \tag{3}$$

then, ΔP_{CPT} is an odd function of a. The property may be used to formulate the method for detecting extrinsic CPT violation in neutrino oscillation due to the matter effect [35].

Do the CPT relation and various other relationships between oscillation probabilities give a unified picture of CP and T violation in neutrino oscillation in matter? In this paper we argue that the answer is indeed yes. Although our argument in this paper is based on the line of thought in [34], we believe that we have taken a step forward from the previous work.

3. Unified graphical representation of CP and T violation

Towards the goal of this paper, let us introduce a graphical representation of the characteristic features of neutrino oscillations relevant for leptonic CP violation [15]. For simplicity of notation let us define the symbols for CP and T conjugate probabilities, $CP[P] \equiv P(\bar{\nu}_\alpha \to \bar{\nu}_\beta)$ and $T[P] \equiv P(\nu_\beta \to \nu_\alpha)$, for a given probability $P(\nu_\alpha \to \nu_\beta)$. It is the CP trajectory diagram in the P–$CP[P]$ bi-probability space, which can be extended to incorporate the P–$T[P]$ bi-probability plot [34].

Given two observables P and $CP[P]$, one can draw a dot in P–$CP[P]$ space, and it becomes a closed ellipse when δ is varied. In figure 1 the ellipses labelled $V_\pm$ are the ones for vacuum oscillation probabilities where the subscripts $\pm$ denote the sign of Δm^2_{31}. When the matter effect is turned on they split into two ellipses labelled $CP_\pm$ in the CP bi-probability plot and into $T_\pm$ in the T bi-probability plot, both of which are simultaneously depicted in figure 1.

Let us first focus on the P–$CP[P]$ bi-probability plot. We first note that the oscillation probability $P(\nu_\alpha \to \nu_\beta)$ can be written on very general grounds (for $\alpha = e$, $\beta = \mu, \tau$, or vice versa)[2] as [38, 39]

$$P(\nu_\alpha \to \nu_\beta) = A \cos\delta + B \sin\delta + C, \tag{4}$$

where A, B, and C are functions of Δm^2_{31}, Δm^2_{21} and a. (Of course, the previously obtained approximate formulae do have such a form; see, e.g., [29, 40, 41].) It is nothing but (4) that guarantees the elliptic nature of the trajectories. Then, one can show that the lengths of major and minor axes (the 'polar' and 'radial' thickness of the ellipses) represent the size of the $\sin\delta$ and the $\cos\delta$ terms, respectively, whereas the distance between two ellipses with positive and negative Δm^2_{31} displays the size of the matter effect [15]. Finally, the distance to the centre of the ellipse from the origin is essentially given by $\sin^2 2\theta_{13}$. Notice that all the features of the bi-probability plot except for the distance between $\Delta m^2_{31} = \pm$ ellipses are essentially determined by the vacuum parameters in the setting of E and L relevant for the superbeam experiments. Therefore, one can easily guess how it looks like in the other experimental settings. As indicated in figure 1, the CP violating and CP conserving effects of δ are comparable in size with the matter effect even at such high energy and long baseline.

[2] In the $\nu_\mu - \nu_\tau$ channel, there exist $\sin 2\delta$ and $\cos 2\delta$ terms in the oscillation probability, and the bi-probability diagrams are no longer elliptic.

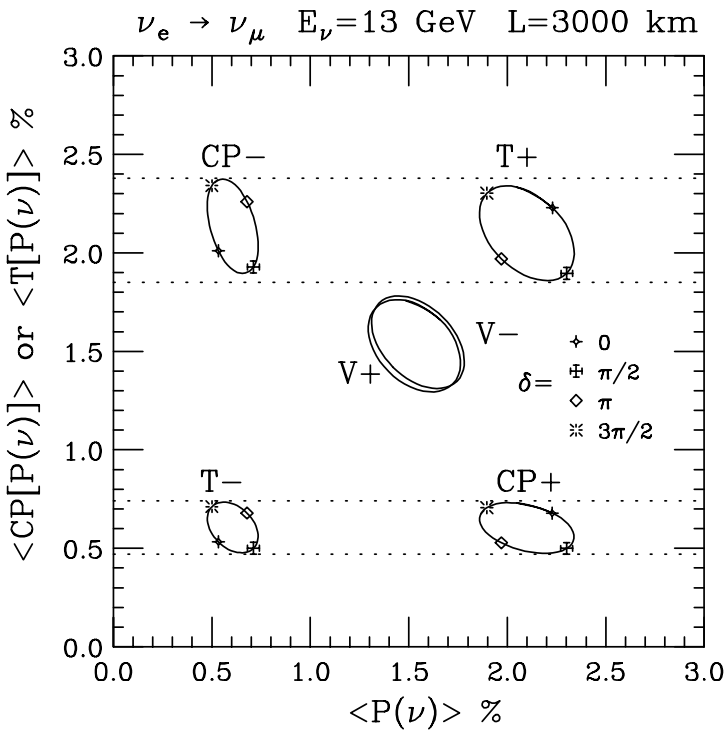

Figure 1. A simultaneous P–$T[P]$ and P–$CP[P]$ bi-probability plot with experimental parameters corresponding to the baseline distance and about twice the optimal energy corresponding to maximal exhancement of T violating effect [36]. Notice the difference between movement of the direction in P–$T[P]$ and P–$CP[P]$ plot; they are orthogonal to each other for reasons explained in the text. The figure is the same as figure 1 of [34]; apart from that we have changed the convention of δ to the standard one used in the text of the paper. The convention is employed by almost everybody who works in the field (see, e.g., [14, 18]) including all our previous works, [15, 19, 34, 37], but is different from that of [33]. Although the convention of the MNS matrix is the same, the latter takes a convention such that U in the neutrino evolution equation (A.1) is replaced by U^*.

We notice that in the P–$T[P]$ bi-probability plot, the matter effect splits the vacuum ellipses $V_\pm$ in quite a different way from the P–$CP[P]$ bi-probability plot. This is because the T violating measure ΔP_T, which is given by

$$\Delta P_T \equiv P(\nu_\alpha \to \nu_\beta; \Delta m^2_{13}, \delta, a) - P(\nu_\beta \to \nu_\alpha; \Delta m^2_{13}, \delta, a) = 2B \sin\delta \tag{5}$$

for symmetric matter profiles, vanishes at $\delta = 0$. Therefore, the T (or CP) conserving point must remain on the diagonal line in the P–$T[P]$ bi-probability plot.

Equation (5) stems from the fact that the coefficients except for B are symmetric under the interchange $\alpha \leftrightarrow \beta$. Therefore, if $\Delta P_T \neq 0$, then $\delta \neq 0$ even in matter. The matter effect cannot create a fake T violation for symmetric matter profiles [42]. For modifications which occur for asymmetric matter profiles, see e.g. [43]–[45].

Notice that the matter effect cannot create fake T violation; it does modify the coefficient B in equation (5), whose feature is made transparent in [36]. Among other things, it was shown in [36] that the matter effect can enhance the T asymmetry up to a factor of 1.5. Other earlier references on T violation in neutrino oscillation include [46]–[49].

4. Diamond shaped structure of CP and T bi-probability plot

In view of figure 1 we notice a remarkable feature of the simultaneous P–$CP[P]$ and P–$T[P]$ diagrams; it has a square or diamond shape. The diamond-shaped structure of combined P–$CP[P]$ and P–$T[P]$ diagrams can be understood by the following two relations which are called the CP–CP and the T–CP relations in [34]. Their precise statements are:

CP–CP relation:

$$\begin{aligned} P(\nu_e \to \nu_\mu; \Delta m^2_{31}, \Delta m^2_{21}, \delta, a) &= P(\bar{\nu}_e \to \bar{\nu}_\mu; -\Delta m^2_{31}, -\Delta m^2_{21}, \delta, a) \\ &\approx P(\bar{\nu}_e \to \bar{\nu}_\mu; -\Delta m^2_{31}, +\Delta m^2_{21}, \pi + \delta, a). \end{aligned} \tag{6}$$

T–CP relation:

$$\begin{aligned} P(\nu_\mu \to \nu_e; \Delta m^2_{31}, \Delta m^2_{21}, \delta, a) &= P(\bar{\nu}_e \to \bar{\nu}_\mu; -\Delta m^2_{31}, -\Delta m^2_{21}, 2\pi - \delta, a) \\ &\approx P(\bar{\nu}_e \to \bar{\nu}_\mu; -\Delta m^2_{31}, +\Delta m^2_{21}, \pi - \delta, a). \end{aligned} \tag{7}$$

These relations are meant to be valid to leading order in $\Delta m^2_{21}/\Delta m^2_{31}$, i.e., to zeroth order in δ-independent and to first order in δ-dependent terms, respectively.

Roughly speaking, the CP–CP relation guarantees that the locations of the first and the third bases are approximately symmetric under reflection with respect to the diagonal line in P–$CP[P]$ space, whereas the T–CP relation guarantees that the ordinates of the $T_\pm$ ellipse are approximately the same as those of $CP_\mp$. Of course, one has to specify the values of the CP phase δ to make the relationship precise, and that is why the change in δ is involved between the RHS and the LHS of equations (6) and (7).

A rough sketch of the argument given in [34] is as follows. The first equality in (6) is obvious by noticing

$$P(\nu_e \to \nu_\mu; \Delta m^2_{31}, \Delta m^2_{21}, \delta, a) = P(\nu_e \to \nu_\mu; -\Delta m^2_{31}, -\Delta m^2_{21}, -\delta, -a), \tag{8}$$

which follows from the fact that a complex conjugate of the neutrino evolution equation gives the same oscillation probability, and the simple relation (see e.g. [41])

$$P(\bar{\nu}_e \to \bar{\nu}_\mu; \Delta m^2_{31}, \Delta m^2_{21}, \delta, a) = P(\nu_e \to \nu_\mu; \Delta m^2_{31}, \Delta m^2_{21}, -\delta, -a). \tag{9}$$

Then, the second approximate equality follows to leading order in $\Delta m^2_{21}/\Delta m^2_{31}$ after an appropriate shift of δ which takes care of the sign change in δ-dependent terms.

For the T–CP relation, the first equality in (7) can be derived by using (8) in the CPT relation in matter (2). Then, the second approximate equality holds for small $\Delta m^2_{21}/\Delta m^2_{31}$ with the same adjustment of the phase δ.

5. Equivalence between the CP–CP and the T–CP relations

We now point out that the CP–CP and the T–CP relations are equivalent to each other in their physics contents. Roughly speaking, the T–CP relation is a 'T conjugate' of the CP–CP relation. It reflects the relationships among various neutrino oscillation probabilities discussed in the previous section. Their equivalence again testifies to the unity of CP and T violation in neutrino oscillations.

We present the proof of the above statement through the computation of the corrections to the CP–CP and the T–CP relations. Let us define for clarity of notation the deviation from the CP–CP and the T–CP relations as

$$\Delta P_{CP-CP} \equiv P(\nu_e \to \nu_\mu; \Delta m^2_{31}, \Delta m^2_{21}, \delta, a) - P(\bar{\nu}_e \to \bar{\nu}_\mu; -\Delta m^2_{31}, +\Delta m^2_{21}, \pi + \delta, a), \tag{10}$$

$$\Delta P_{T-CP} \equiv P(\nu_\mu \to \nu_e; \Delta m^2_{31}, \Delta m^2_{21}, \delta, a) - P(\bar{\nu}_e \to \bar{\nu}_\mu; -\Delta m^2_{31}, +\Delta m^2_{21}, \pi - \delta, a). \tag{11}$$

Because of the first equality in (6), ΔP_{CP-CP} can be written as

$$\Delta P_{CP-CP} = P(\nu_e \to \nu_\mu; \Delta m^2_{31}, \Delta m^2_{21}, \delta, a) - P(\nu_e \to \nu_\mu; +\Delta m^2_{31}, -\Delta m^2_{21}, \pi + \delta, a). \tag{12}$$

On the other hand, by using the first equality in (6) and the relation

$$P(\nu_\mu \to \nu_e; \Delta m^2_{31}, \Delta m^2_{21}, \delta, a) = P(\nu_e \to \nu_\mu; \Delta m^2_{31}, \Delta m^2_{21}, -\delta, a), \tag{13}$$

which is valid for symmetric matter density profiles, ΔP_{T-CP} can be cast into the form

$$\Delta P_{T-CP} = P(\nu_e \to \nu_\mu; \Delta m^2_{31}, \Delta m^2_{21}, -\delta, a) - P(\nu_e \to \nu_\mu; +\Delta m^2_{31}, -\Delta m^2_{21}, \pi - \delta, a). \tag{14}$$

Therefore, it holds that

$$\Delta P_{T-CP}(\delta) = \Delta P_{CP-CP}(-\delta) \pmod{2\pi}. \tag{15}$$

Namely, the relation (11) is the T-conjugate of (10). This completes the proof that the CP–CP and the T–CP relations are identical in their content.

In passing, we note the following: it was noted in [15] that there exists an approximate symmetry in the vacuum oscillation probability under the simultaneous transformations $\Delta m^2_{31} \to -\Delta m^2_{31}$ and $\delta \to \pi - \delta$ which explains the almost overlap of V_+ and V_- trajectories as in figure 1. A generalization of the approximate symmetry in the case with matter effect has been obtained [34],

$$P(\nu_\alpha \to \nu_\beta; \Delta m^2_{31}, \Delta m^2_{21}, \delta, a) \approx P(\nu_\alpha \to \nu_\beta; -\Delta m^2_{31}, \Delta m^2_{21}, \pi - \delta, -a), \tag{16}$$

from which the CP–CP and the T–CP relations also follow. Clearly, the correction to the approximate symmetry is also related to ΔP_{CP-CP}. To show this, we define the difference ΔP_{flip} between the LHS and RHS of (16),

$$\Delta P_{flip} \equiv P(\nu_\alpha \to \nu_\beta; \Delta m^2_{31}, \Delta m^2_{21}, \delta, a) - P(\nu_\alpha \to \nu_\beta; -\Delta m^2_{31}, \Delta m^2_{21}, \pi - \delta, -a). \tag{17}$$

Using the frequently used identity, one can show that

$$\Delta P_{flip} = P(\nu_\alpha \to \nu_\beta; \Delta m^2_{31}, \Delta m^2_{21}, \delta, a) - P(\nu_\alpha \to \nu_\beta; +\Delta m^2_{31}, -\Delta m^2_{21}, \pi + \delta, a). \tag{18}$$

Thus, $\Delta P_{flip} = \Delta P_{CP-CP}$; they are identical.

6. Leading-order corrections to the CP–CP and the T–CP relations

We now compute the leading-order corrections to the CP–CP and the T–CP relations. During the course of the computation, we will give an explicit proof of these relations. We start from the Kimura–Takamura–Yokomakura (KTY) formula [38] of the oscillation probability, equation (4). We note that the coefficients A, B and C are functions of Δm^2_{21}, Δm^2_{31}, and the matter coefficient a, but we here suppress dependences on the latter two quantities. We also note that A and B start from first order in Δm^2_{21}, so that we can write $A(x) = x\alpha(x)$ and $B(x) = x\beta(x)$. Using the fact that $\sin(\pi+\delta) = -\sin(\delta)$ and $\cos(\pi+\delta) = -\cos(\delta)$, we obtain

$$\begin{aligned}\Delta P_{CP-CP} &\equiv P(\Delta m^2_{21}, \delta) - P(-\Delta m^2_{21}, \pi+\delta)\\ &= [A(\Delta m^2_{21}) + A(-\Delta m^2_{21})]\cos\delta + [B(\Delta m^2_{21}) + B(-\Delta m^2_{21})]\sin\delta\\ &\quad + [C(\Delta m^2_{21}) - C(-\Delta m^2_{21})]\\ &= [\alpha(\Delta m^2_{21}) - \alpha(-\Delta m^2_{21})]\Delta m^2_{21}\cos\delta + [\beta(\Delta m^2_{21}) - \beta(-\Delta m^2_{21})]\Delta m^2_{21}\sin\delta\\ &\quad + [C(\Delta m^2_{21}) - C(-\Delta m^2_{21})]. \end{aligned} \tag{19}$$

Therefore, we have shown that the RHS of (19) is of order $\epsilon \equiv \Delta m^2_{21}/\Delta m^2_{31}$ (C term), or ϵ^2 (A and B terms). This is an explicit proof of the CP–CP relation, and hence also the T–CP relation.

We are now left with the computation of the first-order terms of α, β and C. The exact form of these coefficients are calculated in [38].[3] Therefore, it is straightforward to compute the RHS of (19). It reads

$$\begin{aligned}\Delta P_{CP-CP} = &+ 16\frac{a\Delta m^2_{21}\Delta m^2_{31}}{(\Delta m^2_{31}-a)^3}s^2_{13}c^2_{13}s^2_{12}s^2_{23}\sin^2\left[\frac{(\Delta m^2_{31}-a)L}{4E}\right]\\ &- 8\left(\frac{\Delta m^2_{21}L}{4E}\right)\left(\frac{\Delta m^2_{31}}{\Delta m^2_{31}-a}\right)^2 s^2_{13}c^2_{13}s^2_{12}s^2_{23}\sin\left[\frac{(\Delta m^2_{31}-a)L}{2E}\right]\\ &- 16J_r\left(\frac{\Delta m^2_{21}}{\Delta m^2_{31}-a}\right)^2\left[\left(\frac{\Delta m^2_{31}}{a}\right)^2(s^2_{12}-c^2_{12}) + \left(\frac{\Delta m^2_{31}}{a}\right)(c^2_{12}-s^2_{12}) - s^2_{12}\right]\\ &\times \sin\left(\frac{aL}{4E}\right)\sin\left(\frac{(\Delta m^2_{31}-a)L}{4E}\right)\cos\left(\delta - \frac{\Delta m^2_{31}L}{4E}\right)\\ &+ 8J_r\left(\frac{\Delta m^2_{21}L}{4E}\right)\left(\frac{\Delta m^2_{21}}{a}\right)\left(\frac{\Delta m^2_{31}}{\Delta m^2_{31}-a}\right)\left[(s^2_{12}-c^2_{12})\sin\left(\delta - \frac{aL}{2E}\right)\right.\\ &\left.+ c^2_{12}\sin\left(\delta - \frac{\Delta m^2_{31}L}{2E}\right) - s^2_{12}\sin\left(\delta - \frac{(\Delta m^2_{31}-a)L}{2E}\right)\right], \end{aligned} \tag{20}$$

where $J_r \equiv c_{12}s_{12}c_{23}s_{23}c^2_{13}s_{13}$. ΔP_{T-CP} can be obtained by replacing δ by $2\pi - \delta$ in ΔP_{CP-CP}, as dictated in (15). We have kept in the expression of the oscillation probability the terms up to order $O(\epsilon s^2_{13})$ and $O(s^4_{13})$ in C, and to $O(\epsilon^2 s_{13})$ and $O(\epsilon s^3_{13})$ in A and B. But the contributions from higher order terms in s_{13} cancel in (20).

[3] Note, however, that there is an error in the sign of the term denoted as $A^{(1)}_k$ in equation (44) of the first reference in [38].

The feature that the coefficients A and B start with first-order terms of Δm^2_{21} played an important role in proving the CP–CP relation to leading order. It comes from the fact that they vanish in the two-flavour limit $\Delta m^2_{21} \to 0$ and that the probabilities allow Taylor expansion in terms of the variable. The former statement is proved in the appendix on very general grounds without assuming adiabaticity or constant matter density.

7. Concluding remarks

In this paper, we have presented a new unified view of the leptonic CP and T violation in neutrino oscillations. Based on the CPT relation in matter and other relations obeyed by the oscillation probabilities which are derived in [34] we were able to complete our understanding of the structure of a unified description of CP and T violation in terms of the bi-probability plot. Namely, the diamond-shaped structure of simultaneous P–$CP[P]$ and P–$T[P]$ bi-probability plot is now understood as a consequence of a unique relation, the CP–CP (or equivalently, the T–CP) relation. Based on this observation and relying on the KTY formula we have computed leading-order corrections to the CP–CP relation.

We have also briefly touched upon the basic features of the T violating measure which are in contrast with those of CP violation. They include vanishing T violating measure at vanishing CP phase δ, and the enhancement of T-violating asymmetry by the matter effect up to a factor of 1.5. Though measurement of T violation should give us a cleaner way of detecting genuine CP violating effects, it is not easy to carry out experimentally. We must wait for the construction of an intense electron (anti-) neutrino beam either by beta beam [25] or in neutrino factories [24].

Acknowledgments

We thank Hiroshi Nunokawa and Stephen Parke for kindly redrawing the figure and for the useful comments. MB wishes to thank the Sweden–Japan Foundation for financing his visit to Tokyo Metropolitan University. This work was supported by the Grant-in-Aid for Scientific Research in Priority Areas No. 12047222, Japan Ministry of Education, Culture, Sports, Science, and Technology, and the Grant-in-Aid for Scientific Research, No. 16340078, Japan Society for the Promotion of Science.

Appendix. No δ-dependence in the two-flavour limit

Although it should be the case on physics grounds, it is not entirely trivial to show that δ-dependence disappears from the oscillation probabilities in the two-flavour limit $\Delta m^2_{21} \to 0$. We carry it out explicitly in this appendix. It is a slight modification of the method [50] that allows us to show that δ-dependence disappears in the survival probability $P(\nu_e \to \nu_e)$.

We write down the evolution equation of three flavour neutrinos in matter which is valid to leading order in electroweak interaction:

$$\mathrm{i}\frac{\mathrm{d}}{\mathrm{d}x}\begin{bmatrix}\nu_e\\ \nu_\mu\\ \nu_\tau\end{bmatrix} = \frac{1}{2E}\left\{U\begin{bmatrix}0 & 0 & 0\\ 0 & \Delta m^2_{21} & 0\\ 0 & 0 & \Delta m^2_{31}\end{bmatrix}U^+ + \begin{bmatrix}a(x) & 0 & 0\\ 0 & 0 & 0\\ 0 & 0 & 0\end{bmatrix}\right\}\begin{bmatrix}\nu_e\\ \nu_\mu\\ \nu_\tau\end{bmatrix}. \tag{A.1}$$

In this appendix we take a slightly different parametrization of the mixing matrix

$$U = \mathrm{e}^{\mathrm{i}\lambda_7\theta_{23}}\Gamma_\delta \mathrm{e}^{\mathrm{i}\lambda_5\theta_{13}}\mathrm{e}^{\mathrm{i}\lambda_2\theta_{12}}, \tag{A.2}$$

where λ_i are SU(3) Gell-Mann's matrices and Γ contains the CP-violating phase

$$\Gamma_\delta = \begin{bmatrix} 1 & 0 & 0 \\ 0 & 1 & 0 \\ 0 & 0 & e^{i\delta} \end{bmatrix}. \tag{A.3}$$

We then rewrite the evolution equation (A.1) in terms of the new basis defined by

$$\tilde{\nu}_\alpha = [\Gamma^{-1}\, e^{-i\lambda_7\theta_{23}}]_{\alpha\beta}\nu_\beta \equiv (T^t)_{\alpha\beta}\nu_\beta. \tag{A.4}$$

In the vanishing Δm^2_{12} limit, it reads

$$i\frac{d}{dx}\begin{bmatrix} \tilde{\nu}_e \\ \tilde{\nu}_\mu \\ \tilde{\nu}_\tau \end{bmatrix} = \frac{1}{2E}\left\{ e^{i\lambda_2\theta_{13}} \begin{bmatrix} 0 & 0 & 0 \\ 0 & 0 & 0 \\ 0 & 0 & \Delta m^2_{31} \end{bmatrix} e^{-i\lambda_2\theta_{13}} + a(x) \begin{bmatrix} 1 & 0 & 0 \\ 0 & 0 & 0 \\ 0 & 0 & 0 \end{bmatrix} \right\} \begin{bmatrix} \tilde{\nu}_e \\ \tilde{\nu}_\mu \\ \tilde{\nu}_\tau \end{bmatrix}. \tag{A.5}$$

Now we observe that the CP phase δ disappears from the equation. It is due to the specific way that the matter effect comes in; $a(x)$ only appears in the (1.1) element in the Hamiltonian matrix and therefore the matter matrix diag(a, 0, 0) is invariant under rotation in 2–3 space by $e^{i\lambda_7\theta_{23}}$. Then the rotation by the phase matrix Γ does nothing. Notice that $\tilde{\nu}_\mu$ does not have time evolution due to (A.5).

It is clear from (A.5) that any transition amplitude computed in the $\tilde{\nu}_\alpha$ basis is independent of the CP violating phase. Of course, it does not immediately imply that the CP violating phase δ disappears in the physical transition amplitude $\langle \nu_\beta \mid \nu_\alpha \rangle$. The latter is related to the transition amplitude defined in the $\tilde{\nu}_\alpha$ basis as

$$\langle \nu_\beta \mid \nu_\alpha \rangle = T_{\alpha\gamma} T^*_{\beta\delta} \langle \tilde{\nu}_\delta \mid \tilde{\nu}_\gamma \rangle, \tag{A.6}$$

where T is defined in (A.4) and its explicit form in our parametrization (A.2) of the mixing matrix reads

$$T = \begin{bmatrix} 1 & 0 & 0 \\ 0 & c_{23} & s_{23}e^{i\delta} \\ 0 & -s_{23} & c_{23}e^{i\delta} \end{bmatrix}. \tag{A.7}$$

One can show that the amplitude of $\nu_e \to \nu_\mu$ has a pure phase factor $e^{i\delta}$ and hence $P(\nu_e \to \nu_\mu)$ is independent of phase δ;

$$\langle \nu_\mu(x) \mid \nu_e(0) \rangle = c_{23} \langle \tilde{\nu}_\mu(x) \mid \tilde{\nu}_e(0) \rangle + s_{23}e^{i\delta} \langle \tilde{\nu}_\tau(x) \mid \tilde{\nu}_e(0) \rangle. \tag{A.8}$$

The first term, however, vanishes because $\langle \tilde{\nu}_\mu(x) \mid \tilde{\nu}_e(0) \rangle = \langle \tilde{\nu}_\mu(0) \mid \tilde{\nu}_e(0) \rangle = 0$. (No evolution in $\tilde{\nu}_\mu$.) Notice that the same statement does apply to the $P(\nu_e \to \nu_\tau)$ and $P(\nu_\mu \to \nu_\tau)$ as well. One can show that the same conclusion holds for different choices of the phase matrix from that in (A.2).

Since absence or presence of T violation should not depend on the parametrization used, this completes the proof that the δ dependence disappears from all the oscillation probabilities in the limit $\Delta m^2_{12} \to 0$.

References

[1] Gamba A, Marshak R E and Okubo S 1959 *Proc. Natl Acad. Sci.* **45** 881
Maki Z, Nakagawa M, Ohnuki Y and Sakata S 1960 *Prog. Theor. Phys.* **23** 1174

[2] Eguchi K *et al* (KamLAND Collaboration) 2003 *Phys. Rev. Lett.* **90** 021802 (*Preprint* hep-ex/0212021)
Araki T *et al* (KamLAND Collaboration) 2004 *Preprint* hep-ex/0406035

[3] Wolfenstein L 1978 *Phys. Rev.* D **17** 2369

[4] Mikheyev S P and Smirnov A Yu 1985 *Yad. Fiz.* **42** 1441 (*Sov. J. Nucl. Phys.* **42** 913)
Mikheyev S P and Smirnov A Yu 1986 *Nuovo Cimento* **9** 17

[5] Fukuda Y *et al* (Kamiokande Collaboration) 1994 *Phys. Lett.* B **335** 237
Fukuda Y *et al* (Super-Kamiokande Collaboration) 1998 *Phys. Rev. Lett.* **81** 1562 (*Preprint* hep-ex/9807003)
Fukuda S *et al* (Super-Kamiokande Collaboration) 2000 *Phys. Rev. Lett.* **85** 3999 (*Preprint* hep-ex/0009001)
Ashie Y *et al* (Super-Kamiokande Collaboration) 2004 *Preprint* hep-ex/0404034

[6] Maki Z, Nakagawa M and Sakata S 1962 *Prog. Theor. Phys.* **28** 870

[7] Apollonio M *et al* (CHOOZ Collaboration) 1999 *Phys. Lett.* B **466** 415 (*Preprint* hep-ex/9907037)
See also The Palo Verde Collaboration, Boehm F *et al* 2001 *Phys. Rev.* D **64** 11200 (*Preprint* hep-ex/0107009)

[8] The MINOS Collaboration, Adamson P *et al* 1998 *MINOS Detectors Technical Design Report Version 1.0* NuMI-L-337 (October)

[9] Komatsu M, Migliozzi P and Terranova F 2003 *J. Phys. G: Nucl. Part. Phys.* **29** 443 (*Preprint* hep-ph/0210043)

[10] Itow Y *et al* 2001 *Preprint* hep-ex/0106019
For an updated version, see http://neutrino.kek.jp/jhfnu/loi/loi.v2.030528.pdf

[11] Ayres D *et al* 2002 *Preprint* hep-ex/0210005
Ambats I *et al* (NOνA Collaboration) 2004 FERMILAB-PROPOSAL-0929

[12] Gomez-Cadenas J J *et al* (CERN working group on Super Beams Collaboration) 2001 *Preprint* hep-ph/0105297

[13] Minakata H, Sugiyama H, Yasuda O, Inoue K and Suekane F 2003 *Phys. Rev.* D **68** 033017 (*Preprint* hep-ph/0211111)

[14] Burguet-Castell J, Gavela M B, Gomez-Cadenas J J, Hernandez P and Mena O 2001 *Nucl. Phys.* B **608** 301 (*Preprint* hep-ph/0103258)

[15] Minakata H and Nunokawa H 2001 *J. High Energy Phys.* JHEP10(2001)001 (*Preprint* hep-ph/0108085)
Minakata H and Nunokawa H 2002 *Nucl. Phys. Proc. Suppl.* **110** 404 (*Preprint* hep-ph/0111131)

[16] Kajita T, Minakata H and Nunokawa H 2002 *Phys. Lett.* B **528** 245 (*Preprint* hep-ph/0112345)

[17] Fogli G and Lisi E 1996 *Phys. Rev.* D **54** 3667 (*Preprint* hep-ph/9604415)

[18] Barger V, Marfatia D and Whisnant K 2002 *Phys. Rev.* D **65** 073023 (*Preprint* hep-ph/0112119)

[19] Minakata H, Nunokawa H and Parke S 2002 *Phys. Rev.* D **66** 093012 (*Preprint* hep-ph/0208163)

[20] Anderson K *et al* 2004 White Paper Report on Using Nuclear Reactors to Search for a Value of θ_{13} *Preprint* hep-ex/0402041

[21] Minakata H and Nunokawa H 2000 *Phys. Lett.* B **495** 369 (*Preprint* hep-ph/0004114)
Sato J 2001 *Nucl. Instrum. Methods* A **472** 434 (*Preprint* hep-ph/0008056)
Richter B 2000 *Preprint* hep-ph/0008222

[22] Shiozawa M 2003 Talk given at *8th Intl Workshop on Topics in Astroparticle and Underground Physics* (TAUP2003) *5–9 September, Seattle, Washington*

[23] Minakata H and Sugiyama H 2004 *Phys. Lett.* B **580** 216 (*Preprint* hep-ph/0309323)

[24] Geer S 1998 *Phys. Rev.* D **57** 6989
Geer S 1999 *Phys. Rev.* D **59** 039903 (erratum) (*Preprint* hep-ph/9712290)
De Rujula A, Gavela M B and Hernandez P 1999 *Nucl. Phys.* B **547** 21 (*Preprint* hep-ph/9811390)

[25] Zucchelli P 2002 *Phys. Lett.* B **532** 166

[26] Apollonio M *et al* 2002 *Preprint* hep-ph/0210192

[27] Albright C *et al* 2000 *Preprint* hep-ex/0008064

[28] Bouchez J, Lindroos M and Mezzetto M 2003 *Preprint* hep-ex/0310059

[29] Cervera A, Donini A, Gavela M B, Gomez Cadenas J J, Hernandez P, Mena O and Rigolin S 2000 *Nucl. Phys.* B **579** 17 (*Preprint* hep-ph/0002108)
Cervera A, Donini A, Gavela M B, Gomez Cadenas J J, Hernandez P, Mena O and Rigolin S 2000 *Nucl. Phys.* B **593** 731 (erratum)
[30] Donini A, Meloni D and Migliozzi P 2002 *Nucl. Phys.* B **646** 321 (*Preprint* hep-ph/0206034)
[31] Donini A 2003 *Preprint* hep-ph/0310014
[32] Minakata H 2004 *Proc. 2nd Workshop on Neutrino Oscillations (NO-VE 2003), Venice, Italy, 3–5 December 2003, Preprint* hep-ph/0402197
[33] Hagiwara K *et al* (Particle Data Group Collaboration) 2002 *Phys. Rev.* D **66** 010001
[34] Minakata H, Nunokawa H and Parke S J 2002 *Phys. Lett.* B **537** 249 (*Preprint* hep-ph/0204171)
[35] Jacobson M and Ohlsson T 2004 *Phys. Rev.* D **69** 013003 (*Preprint* hep-ph/0305064)
[36] Parke S J and Weiler T J 2001 *Phys. Lett.* B **501** 106 (*Preprint* hep-ph/0011247)
[37] Minakata H, Nunokawa H and Parke S J 2003 *Phys. Rev.* D **68** 013010 (*Preprint* hep-ph/03012101)
[38] Kimura K, Takamura A and Yokomakura H 2002 *Phys. Lett.* B **537** 86 (*Preprint* hep-ph/0203099)
Kimura K, Takamura A and Yokomakura H 2002 *Phys. Rev.* D **66** 073005 (*Preprint* hep-ph/0205295)
[39] Yokomakura H, Kimura K and Takamura A 2002 *Phys. Lett.* B **544** 286 (*Preprint* hep-ph/0207174)
[40] Arafune J, Koike M and Sato J 1997 *Phys. Rev.* D **56** 3093
Arafune J, Koike M and Sato J 1999 *Phys. Rev.* D **60** 119905 (erratum) (*Preprint* hep-ph/9703351)
[41] Minakata H and Nunokawa H 1998 *Phys. Rev.* D **57** 4403 (*Preprint* hep-ph/9705208)
Minakata H and Nunokawa H 1997 *Phys. Lett.* B **413** 369
[42] Krastev P I and Petcov S T 1988 *Phys. Lett.* B **205** 84
[43] Miura T, Takasugi E, Kuno Y and Yoshimura M 2001 *Phys. Rev.* D **64** 013002 (*Preprint* hep-ph/0102111)
[44] de Gouvea A 2001 *Phys. Rev.* D **63** 093003 (*Preprint* hep-ph/0006157)
[45] Akhmedov E K, Huber P, Lindner M and Ohlsson T 2001 *Nucl. Phys.* B **608** 394 (*Preprint* hep-ph/0105029)
[46] Kuo T K and Pantaleone J 1987 *Phys. Lett.* B **198** 406
[47] Toshev S 1989 *Phys. Lett.* B **226** 335
Toshev S 1991 *Mod. Phys. Lett.* A **6** 455
[48] Yasuda O 1999 *Acta Phys. Pol.* B **30** 3089 (*Preprint* hep-ph/9910428)
[49] Koike M and Sato J 2000 *Phys. Rev.* D **61** 073012
Koike M and Sato J 2000 *Phys. Rev.* D **62** 079903 (erratum) (*Preprint* hep-ph/9909469)
Koike M and Sato J 2000 *Phys. Rev.* D **62** 073006 (*Preprint* hep-ph/9911258)
[50] Minakata H and Watanabe S 1999 *Phys. Lett.* B **468** 256 (*Preprint* hep-ph/9906530)

New Journal of Physics
The open–access journal for physics

Neutral currents and tests of three-neutrino unitarity in long-baseline experiments

V Barger[1], S Geer[2] and K Whisnant[3]

[1] Department of Physics, University of Wisconsin, Madison, WI 53706, USA
[2] Fermi National Accelerator Laboratory, PO Box 500, Batavia, IL 60510, USA
[3] Department of Physics, Iowa State University, Ames, IA 50011, USA
E-mail: barger@pheno.physics.wisc.edu

New Journal of Physics **6** (2004) 135
Received 13 July 2004
Published 20 October 2004
Online at http://www.njp.org/
doi:10.1088/1367-2630/6/1/135

Abstract. We examine a strategy for using neutral current measurements in long-baseline neutrino oscillation experiments to put limits on the existence of more than three light, active neutrinos. We determine the relative contributions of statistics, cross-section uncertainties, event misidentification and other systematic errors to the overall uncertainty of these measurements. As specific case studies, we make simulations of beams and detectors that are like the K2K, T2K and MINOS experiments. We find that the neutral current cross-section uncertainty and contamination of the neutral current signal by charge current events allow a sensitivity for determining the presence of sterile neutinos at the 0.10–0.15 level in probablility.

1367-2630/04/010135+18$30.00
PII: S1367-2630(04)83356-1
© IOP Publishing Ltd and Deutsche Physikalische Gesellschaft

Contents

1. Introduction **2**

2. Using NC data to determine sterile content **3**

2.1. Formalism . . . 3

2.2. Ignore ν_e's . . . 4

2.2.1. Below τ threshold . . . 5

2.2.2. Above τ threshold . . . 6

2.3. Do not ignore ν_e's . . . 7

2.3.1. Below τ threshold . . . 7

2.3.2. Above τ threshold, no τ measurement . . . 8

2.3.3. Above τ threshold with a τ measurement . . . 8

3. Detector simulations **8**

3.1. K2K- and T2K-like experiments . . . 9

3.2. A MINOS-like experiment . . . 10

4. Results **11**

4.1. A perfect detector . . . 11

4.2. More realistic K2K- and T2K-like experiments . . . 12

4.3. The MINOS-like detector . . . 13

4.4. Exclusion limit when $P_{\mu s} = 0$ . . . 13

5. Summary **14**

Acknowledgments **15**

References **15**

1. Introduction

In recent years, a series of exciting experimental results have shown that neutrinos have finite masses and mixings. For a recent review of the status see [1]. Solar neutrino and atmospheric neutrino results indicate that all three known neutrino flavours (e, μ, τ) participate in neutrino mixing and, hence, neutrino oscillations. Consequently, the standard framework to describe the experimental results and analyse neutrino oscillation data is that of three-flavour mixing in which the three flavour eigenstates are related to three mass eigenstates by a 3×3 mixing matrix [2]. The positive signal for $\bar{\nu}_\mu \to \bar{\nu}_e$ oscillations from the LSND experiment [3] challenges the three-flavour mixing paradigm [4]. However, the neutrino oscillation interpretation of the LSND observations is yet to be confirmed. Independent of whether or not the LSND results are confirmed by MiniBooNE [5], the three-flavour mixing framework deserves further experimental scrutiny in the coming years. Much of the focus on future experiments so far has been directed to the determination of the three-mixing angles and the CP-violating phase with long-baseline oscillation experiments[4] and reactor experiments.[5] Of interest in this paper is the measurement of the neutral current, which could allow tests of the unitarity of the 3×3 mixing matrix and thus indirectly probe the existence of sterile neutrinos.

[4] Representative long-baseline studies are given in [6].

[5] Representative reactor oscillation studies are given in [7].

In a three-flavour neutrino model, the sum of the oscillation probabilities

$$\sum_{y=e,\mu,\tau} P(\nu_x \to \nu_y)$$

is unity. If there are more than three light neutrinos, we know from measurements of the invisible width of Z [8] that the additional neutrinos must be sterile. If additional light neutrinos mix with the three known flavours we can expect a non-zero oscillation probability to sterile neutrinos, $P(\nu_x \to \nu_s) \neq 0$. To test the three-flavour neutrino-mixing paradigm, it is important to search for a sterile neutrino component within the neutrino flux from natural and manmade sources. Since sterile neutrinos have no strong or electroweak interactions, they cannot be detected directly. However, neutral current (NC) measurements allow $\sum_{y=e,\mu,\tau} P(\nu_x \to \nu_y)$ to be determined which, by probability conservation, is equal to $1 - P(\nu_x \to \nu_s)$. Therefore, in principle, a NC measurement alone is sufficient to determine $P(\nu_x \to \nu_s)$. However, in a realistic detector misidentifications of CC and NC events, together with systematic uncertainties on the relevent neutrino interaction cross-sections, complicate the analysis.

In this paper, we study the use of NC measurements to determine limits on the sterile neutrino content in long-baseline neutrino oscillation experiments. First we consider the sensitivity to the sterile content that might be obtained in a K2K- [9], T2K- [10] and MINOS-like [11] experiment with a 'perfect' detector and 'perfect' beam if there are no systematic uncertainties. We then consider the impact on the sensitivity of event misidentification and systematic uncertainties. Our study is based on a simple simulation of the long-baseline neutrino beams, neutrino interactions [12], and detector responses. We present our results versus event rates and the size of the cross-section uncertainty in order to show the dependence on these quantities.

2. Using NC data to determine sterile content

2.1. Formalism

The present and proposed long-baseline neutrino oscillation experiments exploit conventional neutrino beams that are produced by the decay of charged pions in a long channel. This produces a beam which is initially almost entirely ν_μ. Kaons and muons decaying in the channel introduce a small (typically $\sim$1%) ν_e component in the neutrino beam. As the neutrino beam travels towards a distant detector its flavour content will evolve. In our analysis, we will consider three active neutrinos (ν_e, ν_μ, ν_τ) and one sterile neutrino (ν_s), with oscillation probabilities $P(\nu_\mu \to \nu_x) \equiv P_{\mu x}$, $x = e, \mu, \tau, s$. We begin by considering an oscillation experiment that has an initially pure ν_μ beam with well-known neutrino spectrum and flux, and a detector with perfect identification of the produced events. Then the event rates at the far detector will be

$$N_{NC} = N_\mu^0 (1 - P_{\mu s}) \sigma_{NC}/\sigma_\mu, \tag{1}$$

$$N_\mu = N_\mu^0 P_{\mu\mu}, \tag{2}$$

$$N_e = N_\mu^0 P_{\mu e} \sigma_e/\sigma_\mu, \tag{3}$$

$$N_\tau = N_\mu^0 P_{\mu\tau} \sigma_\tau/\sigma_\mu, \tag{4}$$

where N_μ^0 is the predicted number of ν_μ CC interactions in the detector in the absence of oscillations and the σ_x denote the interaction cross-sections $(\sigma_e, \sigma_\mu, \sigma_\tau)$ for $(\nu_e, \nu_\mu, \nu_\tau)$ CC interactions and σ_{NC} for ν_x NC interactions.

In an ideal experiment, N_{NC} determines $P_{\mu s}$ and $N_{\rm CC}$ determines $P_{\mu\mu}$. In practice, the presence of ν_e and ν_τ CC events complicates the analysis if these events are not distinguished from NC events. Under that circumstance, the NC events provide a measure of $1 - P_{\mu s} + \epsilon_e P_{\mu e} + \epsilon_\tau P_{\mu\tau}$, where the factors ϵ_e and ϵ_τ reflect the contaminations.

Probability conservation ($P_{\mu e} + P_{\mu\mu} + P_{\mu\tau} + P_{\mu s} = 1$) can be used to eliminate $P_{\mu\tau}$ or $P_{\mu e}$, but not both. If the beam energy is below the threshold for τ production or the probability $P_{\mu e}$ is small and can be neglected, then $P_{\mu s}$ can still be determined. However, for a realistic detector with particle misidentifications and/or a ν_e component at the far detector that cannot be neglected, the problem of determining $P_{\mu s}$ can be complex but still solvable, as we shall discuss.

In general, let the probability that an event of type x (NC, ν_e CC, ν_μ CC or ν_τ CC) be identified in the detector as an event of type y be given by ζ_{xy}, where $x, y =$ (NC, e, μ, τ) (note that ζ_{xx} is the efficiency for detecting an event of type x). If N_μ^0 is the predicted number of ν_μ CC interactions in the detector in the absence of oscillations, then after including oscillations, detector efficiencies and mis-identifications, and integrating over the energy dependence, the number of measured events of type y will be

$$N_y = \frac{N_\mu^0}{\sigma_\mu}\left[(1 - P_{\mu s})\sigma_{NC}\zeta_{NC,y} + \sum_{x=e,\mu,\tau} P_{\mu x}\sigma_x\zeta_{xy}\right], \tag{5}$$

where the interaction cross-sections for ν_e CC, ν_μ CC, ν_τ CC and NC events are given by σ_e, σ_μ, σ_τ and σ_{NC}, respectively.

In (5), we do not include explicitly a term that accounts for the ν_e contamination of the beam. In practice, this contamination could be added to $P_{\mu e}$ and subtracted from $P_{\mu\mu}$. The contamination is expected to be of order 1% or less, which is small compared to the misidentification factors, as we subsequently will show. Therefore we neglect this small correction.

2.2. Ignore ν_e's

We consider first the situation in which the ν_e component in the beam at the far detector is so small that ν_e CC interactions can be neglected. In this case, we let $P_{\mu e} \to 0$ (it is known to be small, at the 5% level or less from the CHOOZ experiment [13]). It is convenient to define the following two ratios:

$$R_{NC} \equiv \frac{N_{NC}}{\zeta_{NCNC}N_{NC}^0} = (1 - P_{\mu s}) + f_{\mu,NC}P_{\mu\mu} + f_{\tau,NC}P_{\mu\tau}, \tag{6}$$

$$R_\mu \equiv \frac{N_\mu}{\zeta_{\mu\mu}N_\mu^0} = f_{NC,\mu}(1 - P_{\mu s}) + P_{\mu\mu} + f_{\tau,\mu}P_{\mu\tau}, \tag{7}$$

where

$$N_x^0 \equiv \sigma_x N_\mu^0/\sigma_\mu \tag{8}$$

and

$$f_{x,y} \equiv \zeta_{xy}\sigma_x/\zeta_{yy}\sigma_y \tag{9}$$

is a normalized misidentification factor that gives the ratio of the number of events of type x identified as type y to the number of events of type y that are identified as type y. Measuring R_{NC} and R_μ is sufficient for deducing $P_{\mu s}$ (and $P_{\mu\mu}$). The analysis depends on whether or not we are above the ν_τ CC interaction threshold, i.e., whether or not there are ν_τ CC events produced in the detector.

2.2.1. Below τ threshold. For neutrino energies below the τ threshold, $\sigma_\tau = 0$ and $f_{\tau,j} = 0$. In this case we can invert (6) and (7) to obtain

$$P_{\mu\mu} = \frac{R_\mu - R_{NC} f_{NC,\mu}}{1 - f_{\mu,NC} f_{NC,\mu}}, \tag{10}$$

$$P_{\mu s} = 1 - \frac{R_{NC} - R_\mu f_{\mu,NC}}{1 - f_{\mu,NC} f_{NC,\mu}}. \tag{11}$$

Adding uncertainties in quadrature we get

$$\delta P_{\mu\mu} = \frac{\sqrt{(\delta R_\mu)^2 + f_{NC,\mu}^2 (\delta R_{NC})^2}}{1 - f_{\mu,NC} f_{NC,\mu}}, \tag{12}$$

$$\delta P_{\mu s} = \frac{\sqrt{(\delta R_{NC})^2 + f_{\mu,NC}^2 (\delta R_\mu)^2}}{1 - f_{\mu,NC} f_{NC,\mu}}, \tag{13}$$

where in the limit of Gaussian statistical uncertainties

$$\delta R_j = R_j \sqrt{\frac{1}{N_j} + \epsilon_j^2} \tag{14}$$

and

$$\epsilon_j \equiv \delta N_j^0 / N_j^0. \tag{15}$$

The first term in each δR_j is the usual statistical uncertainty, the second comes from the normalization uncertainty (flux *and* cross-section).

Note that the normalized misidentification factors $f_{\mu,NC}$ and $f_{NC,\mu}$ will be sensitive to the neutrino energy spectrum and the detector technology, and therefore must be evaluated for each experimental set-up. Most of the misidentification terms are suppressed by f^2; if $f \leqslant 0.1$ then $f^2 \leqslant 0.01$. If the experimental set-up is such that we can ignore all terms of order f^2 (see table 1), we have

$$\frac{P_{\mu s}}{\delta P_{\mu s}} \simeq \frac{1 - R_{NC} + f_{\mu,NC} R_\mu}{\delta R_{NC}}, \tag{16}$$

which measures the significance of the deviation of $P_{\mu s}$ from zero.

In (16) we have not included the effects of uncertainties of the f factors. By considering subsamples in our Monte Carlo calculations of the $f_{x,y}$, we estimate the uncertainties from the Monte Carlo to be about 2% for the most significant f factors. This has a small effect since

Table 1. Signal efficiencies (ζ_{jj}) and normalized misidentification factors ($f_{i,j}$) in selected long-baseline experiments.

Experiment	j (channel)	Signal	ζ_{jj}	$f_{NC,j}$	$f_{\mu,j}$	$f_{e,j}$	$f_{\tau,j}$
K2K-like	NC	Two e-like, no μ-like	0.391	–	0.068	0.052	–
(basic)	μ	One μ-like, no e-like	0.520	0.087	–	0.0007	–
	e	One e-like, no μ-like	0.497	0.003	0.0004	–	–
K2K-like	NC	Even e-like, no μ-like	0.437	–	0.078	0.060	–
(aggressive)	μ	Even e-like, $\geqslant 1$ μ-like	0.989	0.086	–	0.003	–
	e	Odd e-like	0.993	0.002	0.005	–	–
K2K-like	NC	Even e-like, no μ-like	0.494	–	0.081	0.011	–
(Gaussian	μ	Even e-like, $\geqslant 1$ μ-like	0.994	0.073	–	0.0007	–
beam)	e	Odd e-like	0.999	0.0003	0.0004	–	–
T2K-like	NC	Even e-like, no μ-like	0.420	–	0.25	0.006	–
(Gaussian	μ	Even e-like, $\geqslant 1$ μ-like	0.988	0.036	–	0.0014	–
beam)	e	Odd e-like	0.944	0.00002	0.00001	–	–
MINOS-like	NC	No $\mu > 1$ GeV	1.000	–	0.903	–	0.429
$P_{\mu e} = 0$	μ	Any $\mu > 1$ GeV	0.749	0	–	–	0
MINOS-like	NC	No e, μ, or γ	0.520	–	1.067	0.005	0.347
$P_{\mu e} \neq 0$	μ	Any $\mu > 1$ GeV	0.749	0	–	0	0
	e	No $\mu > 1$ GeV, $\geqslant 1e$ or γ	0.999	0.125	0.090	–	0.064

the systematic uncertainty of the NC cross-section (i.e., ϵ_{NC}) is expected to be at least three times larger; this is especially true when the uncertainties are added in quadrature. If there is a systematic uncertainty for an f that is not small compared to ϵ_{NC}, in practice it can be incorporated into ϵ_{NC}, weighted by the value of f itself.

For a perfect detector that can identify each event correctly, $f_{x,y} = \delta_{xy}$. In this limit $P_{\mu s} = 1 - R_{NC}$ and

$$\frac{P_{\mu s}}{\delta P_{\mu s}} \simeq \frac{P_{\mu s}}{\sqrt{(1 - P_{\mu s})(1/\zeta_{NCNC} N^0_{NC}) + (1 - P_{\mu s})^2 \epsilon^2_{NC}}}. \tag{17}$$

This ratio depends only on $P_{\mu s}$, the experimental statistics and the systematic uncertainty on the NC measurement. Thus, (17) defines the maximum sensitivity that is in principle achievable for a given N^0_{NC} and ϵ_{NC}.

2.2.2. Above τ threshold. If the neutrino energy is above the τ threshold and there is not a clean signature for ν_τ CC events, we can still deduce $P_{\mu\mu}$ and $P_{\mu s}$ by using the identity $P_{\mu\mu} + P_{\mu\tau} + P_{\mu s} = 1$ to eliminate $P_{\mu\tau}$ in (6) and (7) (we are still assuming $P_{\mu e} = 0$), which gives

$$P_{\mu\mu} = \frac{R_\mu(1 + f_{\tau,NC}) + R_{NC}(f_{NC,\mu} + f_{\tau,\mu})}{1 + f_{\tau,NC} - f_{\tau,\mu} + f_{\tau,NC} f_{NC,\mu} - f_{\mu,NC}(f_{NC,\mu} + f_{\tau,\mu})}, \tag{18}$$

$$P_{\mu s} = 1 - \frac{R_{NC}(1 - f_{\tau,\mu}) - R_\mu(f_{\mu,NC} - f_{\tau,NC})}{1 + f_{\tau,NC} - f_{\tau,\mu} + f_{\tau,NC} f_{NC,\mu} - f_{\mu,NC}(f_{NC,\mu} + f_{\tau,\mu})}. \tag{19}$$

If no other process contaminates the ν_μ CC events (i.e., $f_{j,\mu} = 0$ as appears to be the case for a MINOS-like experiment; see section 3), then

$$\frac{P_{\mu s}}{\delta P_{\mu s}} \simeq \frac{1 + f_{\tau,NC} - R_{NC} + R_\mu(f_{\mu,NC} - f_{\tau,NC})}{\sqrt{(\delta R_{NC})^2 + (f_{\mu,NC} - f_{\tau,NC})^2(\delta R_\mu)^2}}. \tag{20}$$

For a perfect detector, $P_{\mu s}/\delta P_{\mu s}$ is again given by (17).

2.3. Do not ignore ν_e's

If the ν_e CC interaction rate in the far detector is not negligible (which could be the case if $\sin^2 2\theta_{13}$ is near its upper bound and we want to push the uncertainty in the measurement of $P_{\mu s}$ down to the few per cent level), then we need three measurements to be able to solve for all of the probabilities. The potential measurables are

$$R_{NC} \equiv \frac{N_{NC}}{\zeta_{NCNC} N^0_{NC}} = (1 - P_{\mu s}) + f_{\mu,NC} P_{\mu\mu} + f_{e,NC} P_{\mu e} + f_{\tau,NC} P_{\mu\tau}, \tag{21}$$

$$R_\mu \equiv \frac{N_\mu}{\zeta_{\mu\mu} N^0_\mu} = f_{NC,\mu}(1 - P_{\mu s}) + P_{\mu\mu} + f_{e,\mu} P_{\mu e} + f_{\tau,\mu} P_{\mu\tau}, \tag{22}$$

$$R_e \equiv \frac{N_e}{\zeta_{ee} N^0_e} = f_{NC,e}(1 - P_{\mu s}) + f_{\mu,e} P_{\mu\mu} + P_{\mu e} + f_{\tau,e} P_{\mu\tau}, \tag{23}$$

and, if we are above the ν_τ CC interaction threshold,

$$R_\tau \equiv \frac{N_\tau}{\zeta_{\tau\tau} N^0_\tau} = f_{NC,\tau}(1 - P_{\mu s}) + f_{\mu,\tau} P_{\mu\mu} + f_{e,\tau} P_{\mu e} + P_{\mu\tau}. \tag{24}$$

2.3.1. Below τ threshold. Below the ν_τ CC threshold energy, the three measurements must be R_μ, R_{NC} and R_e. Then $f_{\tau,j} = 0$, the $P_{\mu\tau}$ terms drop out, and we can invert equations (21)–(23) to obtain

$$P_{\mu\mu} = \frac{R_\mu(1 - f_{e,NC} f_{NC,e}) - R_{NC}(f_{NC,\mu} - f_{NC,e} f_{e,\mu}) - R_e(f_{e,\mu} - f_{e,NC} f_{NC,\mu})}{1 - f}, \tag{25}$$

$$P_{\mu e} = \frac{R_e(1 - f_{\mu,NC} f_{NC,\mu}) - R_{NC}(f_{NC,e} - f_{NC,\mu} f_{\mu,e}) - R_\mu(f_{\mu,e} - f_{\mu,NC} f_{NC,e})}{1 - f}, \tag{26}$$

$$P_{\mu s} = 1 - \frac{R_{NC}(1 - f_{\mu,e} f_{e,\mu}) - R_\mu(f_{\mu,NC} - f_{\mu,e} f_{e,NC}) - R_e(f_{e,NC} - f_{e,\mu} f_{\mu,NC})}{1 - f}, \tag{27}$$

where $f \equiv f_{\mu,NC} f_{NC,\mu} + f_{e,NC} f_{NC,e} + f_{\mu,e} f_{e,\mu} - f_{\mu,NC} f_{NC,e} f_{e,\mu} - f_{NC,\mu} f_{\mu,e} f_{e,NC}$. The calculation of the δP's is straightforward; each R term has a statistical and systematic uncertainty given by (14).

Note that for an idealized detector in which no other processes significantly contaminate ν_e CC events (i.e., $f_{j,e} \simeq 0$) and ν_e CC events do not contaminate ν_μ CC events (i.e., $f_{e,\mu} \simeq 0$), then $P_{\mu e} = R_e$. Since $P_{\mu e}$ is small (of order 0.1 or less, as indicated by current oscillation limits), eliminating terms of order f^2 and $fP_{\mu e}$ in this case will recover the situation where we ignored ν_e (i.e., (16)).

2.3.2. Above τ threshold, no τ measurement. For energies above the ν_τ CC interaction threshold the $P_{\mu\tau}$ terms do not drop out of equations (21)–(23). If we do not have the means to measure ν_τ CC events but can measure ν_e CC events, then we can use probability conservation to eliminate $P_{\mu\tau}$, giving

$$R_{NC} = (1 - P_{\mu s})(1 + f_{\tau,NC}) + P_{\mu\mu}(f_{\mu,NC} - f_{\tau,NC}) + P_{\mu e}(f_{e,NC} - f_{\tau,NC}), \tag{28}$$

$$R_\mu = (1 - P_{\mu s})(f_{NC,\mu} + f_{\tau,\mu}) + P_{\mu\mu}(1 - f_{\tau,\mu}) + P_{\mu e}(f_{e,\mu} - f_{\tau,\mu}), \tag{29}$$

$$R_e = (1 - P_{\mu s})(f_{NC,e} + f_{\tau,e}) + P_{\mu\mu}(f_{\mu,e} - f_{\tau,e}) + P_{\mu e}(1 - f_{\tau,e}). \tag{30}$$

The general solution for the probabilities is somewhat messy, but if we assume that no other processes contaminate the ν_μ CC signal (i.e., $f_{j,\mu} \simeq 0$) and the ν_e CC events do not contaminate the other signals ($f_{e,j} \simeq 0$) (see section 3), then $P_{\mu\mu} = R_\mu$ and we can invert (28) and (30) to obtain

$$P_{\mu s} = 1 - \frac{R_{NC}(1 - f_{\tau,e}) + R_e f_{\tau,NC} + R_\mu[f_{\tau,NC}(1 - f_{\mu,e}) - f_{\mu,NC}(1 - f_{\tau,e})]}{1 + f_{\tau,NC}(1 + f_{NC,e}) - f_{\tau,e}}. \tag{31}$$

The calculation of $\delta P_{\mu s}$ is straightforward.

If no other processes contaminate the ν_e CC signal (i.e., $f_{j,e} \to 0$), then $P_{\mu e} = R_e$ and we obtain

$$\frac{P_{\mu s}}{\delta P_{\mu s}} = \frac{1 + f_{\tau,NC} - R_{NC} + R_\mu(f_{\mu,NC} - f_{\tau,NC}) - R_e f_{\tau,NC}}{\sqrt{(\delta R_{NC})^2 + (f_{\mu,NC} - f_{\tau,NC})^2(\delta R_\mu)^2 + f_{\tau,NC}^2(\delta R_e)^2}}. \tag{32}$$

2.3.3. Above τ threshold with a τ measurement. If R_τ is also measured, in addition to R_e, then there are four measurements (R_μ, R_{NC}, R_e and R_τ), but there are only three independent quantities (since $P_{\mu\mu} + P_{\mu e} + P_{\mu\tau} + P_{\mu s} = 1$). One possible approach would be to assume that $P_{\mu s}$ is independent of the other probabilities and use these four measurements to test probability conservation. We do not pursue this option here. Instead, we use probability conservation to eliminate one of the probabilities and use three of the four measurements to determine $P_{\mu s}$ (the fourth measurement could be used to check probability conservation afterwards). Since $P(\nu_\mu \to \nu_\tau)$ is most likely much larger than $P(\nu_\mu \to \nu_e)$ in the L/E regime we are considering, we use R_τ as the third measurement (along with R_μ and R_{NC}). Then the appropriate formulae for the measurables R_{NC}, R_μ and R_τ can be found by the interchange $\tau \leftrightarrow e$ in (28)–(30).

3. Detector simulations

We wish to explore how well in principle a neutrino three-flavour unitarity test can be performed with a given muon-neutrino beam as a function of dataset size, and study which systematic uncertainties are likely to be important, and their impact.

We consider first a 'perfect' experiment in which the sensitivity of the unitarity test is determined only by the statistical uncertainties, calculated using a parametrization of the known

beam flux and spectrum, together with a simulation of neutrino interactions in the detector. An event simulation is used to determine the relevent detection efficiencies and misidentification factors. We use the NEUGEN Monte Carlo code [12] to simulate neutrino interactions in the detector. Events are classified as ν_μ CC, ν_e CC or NC. In practice, the requirements used to identify events of a given type will depend upon the detector technology. For example, for a water Cherenkov detector in our simple analysis, we will define a ν_e CC event candidate as an event with an electron candidate above threshold. An electron candidate is either a real electron or a π^0 with an energy exceeding 1 GeV (in which case the two daughter photons from the high-energy π^0 produce Cherenkov rings that overlap in the detector and cannot be distinguished from a single electromagnetically showering particle). A NC event candidate would be an event containing a π^0 candidate but no muon candidate, where a π^0 candidate has two e-like rings above threshold (which come from a π^0 with energy less than 1 GeV). The definition of CC and NC events can of course be varied, and then tuned to give favourable values for the signal efficiencies and misidentification factors. Examples are shown in table 1.

3.1. K2K- and T2K-like experiments

To identify the most important systematic uncertainties, it is useful to compare the sensitivity of our 'perfect experiment' with that of a realistic experiment. We begin with the K2K experiment. K2K uses a beam from the KEK laboratory in Japan. The neutrinos in the KEK beam have a mean energy of 1.3 GeV [9], and the neutrinos travel 250 km to the Super-K water Cerenkov detector. A new experiment T2K is being planned that will exploit a more intense neutrino source that is presently under construction at Tokai, Japan. T2K will also use the Super-K detector, but with a slightly longer baseline (300 km) and narrow-band beam with an axis displaced slightly from pointing directly at the far detector (an 'off-axis' beam). The real experimental sensitivities of the K2K and T2K experiments can only be determined by the experimental collaborations. In the following, we use the NEUGEN Monte Carlo program to simulate neutrino interactions together with a simple model for the response of a Super-K-like detector. Although this is inadequate to predict precisely the real K2K and T2K sensitivities, it does enable us to identify the dominant sources of systematic uncertainties, and hence explore how the experimental results will depend upon the sizes of these systematics. We use the following parametrization of a Super-K-like detector response:

(a) A threshold of 197 MeV c^{-1} for the detection and measurement of muons [14], and 100 MeV c^{-1} for electrons and π^0's. These thresholds approximate those used for the atmospheric neutrino analysis of Super-K [14, 15].

(b) Energy resolutions given by [15]

$$\frac{\Delta E_{rms}}{E} = 0.005 + \frac{0.025}{\sqrt{E(\mathrm{GeV})}} \tag{33}$$

for electrons and π^0's and

$$\frac{\Delta p_{rms}}{p} = 0.03 \tag{34}$$

for charged pions and muons.

In addition, we use a parametrization of the spectra for the K2K and T2K neutrino beams.

In our analysis, we will use only simulated events with visible energy greater than 0.1 GeV. For our 'basic' signals we define a ν_μ CC event candidate as an event with a single muon-like

ring, a ν_e CC event candidate as an event with a single e-like ring, and a NC event candidate as an event with two e-like rings, which are assumed to be two photons from a single π^0 decay. Given these definitions, the detector efficiencies and misidentification factors determined from our simulations are listed in table 1. As shown in the table, the efficiencies ζ_{jj} are of order one-half, and there is no significant contamination of one signal by another due to misidentification. Also shown are the results of a more aggressive signal definition, where a simulated event with an odd number of e-like rings is labelled as a ν_e CC event candidate, and the remaining events (those with an even number of e-like rings) are labelled as ν_μ CC event candidates if they have one or more μ-like rings or NC if they do not. In this more aggressive scenario no events are discarded, i.e., all events were used for one of the targeted signals. Although some of the misidentification factors are slightly larger for the aggressive scenario, overall they are not greatly changed, while there is a significant improvement in the efficiencies for the CC events.

To investigate whether our analysis is sensitive to the assumed details of the neutrino spectrum, we have repeated the calculation of efficiencies and misidentification factors for a K2K-like experiment with a beam that has the same average energy and beam spread as the KEK beam, but with a Gaussian energy spectrum (no long high-energy tail). For the Gaussian beam, the misidentification factors involving ν_e were greatly reduced (since backgrounds from the high-energy tail are now suppressed), but $f_{\mu,NC}$ and $f_{NC,\mu}$ were only slightly affected. Since $f_{\mu,NC}$ is the dominant f factor for a K2K-like experiment, we conclude that our results are not very sensitive to the detailed beam spectrum we assume.

We now consider a T2K-like experiment, where we have used a beam spectrum that corresponds to a detector 2° off-axis. The resulting misidentification factors for a T2K-like experiment are shown in table 1. All of the misidentification factors are reduced except for $f_{\mu,NC}$, which is now 0.25. Therefore, in both the K2K- and T2K-like experiments, the most important contamination is ν_μ CC events being misidentified as NC events.

3.2. A MINOS-like experiment

The MINOS experiment is a long-baseline oscillation experiment that will use a neutrino beam from the Fermilab Main Injector and an iron-scintillator sampling calorimeter 730 km away in Minnesota. MINOS is expected to begin data taking early in 2005 with the so-called Low Energy NuMI horn configuration. With a beam energy that is about a factor of three higher than the KEK beam, and a detector that is very different from the water Cherenkov detector used by K2K and T2K, the efficiencies and misidentification factors for MINOS will be very different than those for the experiments in Japan. To compute the numbers given in table 1 we have used a parametrization of the NuMI neutrino beam spectrum for the Low Energy horn configuration, the NEUGEN Monte Carlo Program to simulate neutrino interactions in an iron detector, and a simple parametrization of the response of a MINOS-like detector. In particular we assume:

(a) An energy threshold of 50 MeV for the detection and measurement of electrons, and charged and neutral pions, and a threshold of 1 GeV for the identification and measurement of muons. Note that the MINOS detector is expected to be able to determine the charge and measure the momenta of muons from 0.5 to 100 GeV c^{-1}, and to distinguish ν_μ CC events from NC events if the muons have momenta exceeding about 1 GeV c^{-1} [16]. Our final results are insensitive to the exact values chosen for the energy thresholds; the most significant changes occur in $f_{e,NC}$, which doubles in size when the thresholds are increased to 100 MeV. However,

$f_{e,NC}$ is very small and consequently does not significantly affect our results. The significant f factors change at most by 5%.

(b) Energy resolutions given by

$$\frac{\Delta E_{rms}}{E} = \frac{0.23}{\sqrt{E(\mathrm{GeV})}} \tag{35}$$

for electrons and π^0's

$$\frac{\Delta E_{rms}}{E} = \frac{0.55}{\sqrt{E(\mathrm{GeV})}}, \tag{36}$$

for charged pions and

$$\frac{\Delta p_{rms}}{p} = 0.05 \tag{37}$$

for muons. Note that in practice the muon energy resolution for the MINOS experiment is expected to be somewhat better (worse) than described by (37) if the muon ranges out (does not range out) in the detector. We found that $\Delta p_{rms}/p$ values as high as 0.10 do not appreciably change our results.

As shown in the table, for a MINOS-like experiment there is a very large contamination of the NC channel by ν_μ CC events, and misidentification of ν_τ CC events as NC events is also significant. The efficiency for identifying NC events is about one-half, similar to the K2K-like and T2K-like experiments.[6]

The size of $f_{\mu,NC}$ may be understood as follows: f depends not only on the misidentification fraction, but also on the relative cross-sections and efficiency of the signal. For $f_{\mu,NC}$ in the case where electron neutrinos are being ignored, the probability of a μ event being misidentified as a NC event is about 0.25 and the μ cross-section is about 3.5 times larger than the NC cross-section, which leads to $f_{\mu,NC} \simeq 0.9$.

We have not considered the effect of τ decays into muons or electrons, each of which occurs with branching fraction of about 18%. If all of the τ decays to muons were identified as muons, then $f_{\tau,\mu}$ would be at most about 0.08; this has only a small effect because $f_{\tau,\mu}$ is proportional to $\sigma_\tau/\sigma\mu \sim 0.3$. In practice, many muons from τ decays would not pass the muon minimum energy cut, and $f_{\tau,\mu}$ would be even smaller. Since $f_{\tau,\mu}$ is much smaller than $f_{\mu,NC}$ and $f_{\tau,NC}$, we do not consider the effects of τ decays.

4. Results

4.1. A perfect detector

We first find the sensitivity of the NC unitarity test for a perfect detector, i.e., a detector that can categorize each event correctly as CC muon or NC, with no misidentification and 100%

[6] Although to first order for MINOS all events with an electron or photon candidate will be classified as NC events, there are three independent probabilities, and it is necessary to extract a separate ν_e signal, in addition to ν_μ and NC signals, to be able to solve for all of the probabilities. Hence we must try to select genuine ν_e interactions from the large NC background. In the table we also show misidentification factors when all non-μ events are classified as NC events, which could be used when $P_\mu e$ is very small.

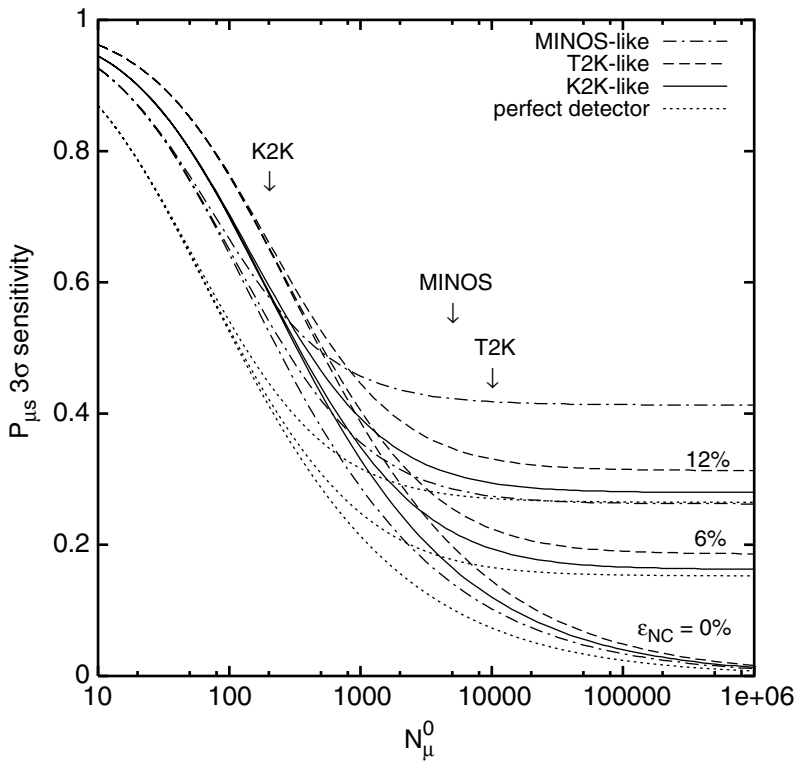

Figure 1. Assuming Gaussian statistical uncertainties, the 3σ sensitivity for measuring $P_{\mu s}$ versus N_μ^0 for fixed values of the NC systematic error for a perfect detector (dotted curves, using equation (17), the K2K-like experiment with our basic signal definition (solid), the T2K-like experiment (dashed), and the MINOS-like experiment (dash-dotted). The number of NC events without oscillations is $N_{NC}^0 = 0.156 N_\mu^0$. The systematic uncertainties $\delta N_\mu^0/N_\mu^0$ and $\delta N_e^0/N_e^0$ are assumed to be 2%, except when $\epsilon_{NC} \equiv \delta N_{NC}^0/N_{NC}^0 = 0$, in which case they are 0. The arrows indicate the approximate statistical sensitivities expected for the K2K, T2K and MINOS experiments.

efficiency. The figure of merit for a perfect detector is given by (17) with $\zeta_{NCNC} = 1$. We show the 3σ sensitivity for $P_{\mu s}$ (i.e., the minimum value of $P_{\mu s}$ for which $P_{\mu s} = 3\delta P_{\mu s}$) versus N_μ^0 (the number of CC muons expected in the detector with no oscillations) for several values of the NC systematic error in figure 1 (the dotted curves). At low statistics the sensitivity is very poor, and for high statistics the sensitivity approaches the asymptotic limit of $3\epsilon_{NC}/(1 + 3\epsilon_{NC})$, where $\epsilon_{NC} \equiv \delta N_{NC}^0/N_{NC}^0$ is the fractional NC normalization uncertainty.

4.2. More realistic K2K- and T2K-like experiments

Next we find the NC sensitivity for the K2K-like detector described in section 3.1 for the case $P_{\mu e} \simeq 0$. We generated 400 000 neutrino events using the NEUGEN simulator, from which the normalized misidentification factors $f_{x,y}$ were calculated. For a given set of probabilities P_{xy}, the values of R_{NC} and R_μ were calculated, and the corresponding measured value of $P_{\mu s}$ was determined from (11). The uncertainty on $P_{\mu s}$ was calculated using (14), assuming the

uncertainties δR_{NC} and δR_μ are uncorrelated and add in quadrature. The 3σ sensitivity for $P_{\mu s}$ is shown in figure 1 (solid curves) for various values of ϵ_{NC} for the case $P_{\mu s} = 1 - P_{\mu\mu}$ (all ν_μ oscillating to ν_s; we will consider cases with nonzero $P_{\mu\tau}$ later). For both low and high statistics the K2K-like 3σ sensitivity can be approximated by

$$P_{\mu s}^{min} \simeq \frac{3(1 + f_{\mu,NC})(\delta R_{NC}/R_{NC})}{1 + 3(1 + f_{\mu,NC})(\delta R_{NC}/R_{NC})}, \tag{38}$$

which can be derived from (16), where factors quadratic in the $f_{x,y}$ are ignored. Since $f_{\mu,NC} \simeq 0.08$ for our K2K-like experiment, the NC sensitivity is at most about 1.08, worse than that of the perfect detector for large numbers of events where the statistical uncertainty becomes negligible compared to the systematic uncertainty. At low statistics the efficiency becomes important and the K2K-like performance will be more than 1.08, worse than a perfect detector.

The K2K-like curves in figure 1 are plotted for the simple K2K signals in table 1. The corresponding curves for the more aggressive K2K-like signals are very similar to the simple case; the improved efficiencies are partially compensated for by the slightly higher value of $f_{\mu,NC}$. Thus the result is fairly insensitive to the exact signal criteria used.

We next consider the effects of nonzero $P_{\mu\tau}$. If we assume $P_{\mu\tau} = 1 - P_{\mu s}$ (i.e., $P_{\mu\mu} = P_{\mu e} = 0$), the curves are very close to those of the perfect detector, since the dominant misidentification term $f_{\mu,NC}$ does not contribute to R_{NC} when $P_{\mu\mu} = 0$. If both $P_{\mu\mu}$ and $P_{\mu\tau}$ are both nonzero (with $P_{\mu e} \simeq 0$), the results will lie somewhere between the curves for K2K-like and the perfect detector.

Finally, we consider nonzero $P_{\mu e}$, in which case R_e must also be measured and $P_{\mu s}$ is determined using (27). As discussed in section 2.3.1 if $P_{\mu e}$ is of order 0.1 or less (as indicated by oscillation bounds such as from the CHOOZ reactor), and if the misidentification factors are also of order 0.1 or less, then this case reduces to that where the ν_e are ignored. We have verified this numerically for the K2K-like misidentification factors in table 1.

In summary, the sensitivity of the K2K-like detector to the NC signal is only slightly worse than that of a perfect detector, with the dominant loss of sensitivity coming from the misidentification of CC muon events as NC. For comparison, in figure 1, we have also shown sensitivity curves for the T2K-like experiment with a Gaussian beam spread. Since $f_{\mu,NC} = 0.25$ in this case, the sensitivity is about a factor of $1.25/1.08 = 1.16$ worse than for K2K.

4.3. The MINOS-like detector

For the MINOS-like case, we generated 320 000 neutrino events using the NEUGEN simulator, and calculated the corresponding misidentification factors. The 3σ sensitivity for $P_{\mu s}$ was calculated as described above for the case $P_{\mu s} = 1 - P_{\mu\mu}$; the results are shown in figure 1. At low statistics, the MINOS-like experiment does better than the K2K- and T2K-like experiments because of the higher NC efficiency, but at high statistics it does worse because of the larger misidentification factors.

4.4. Exclusion limit when $P_{\mu s} = 0$

If a 3σ signal for $P_{\mu s}$ is not observed, then an exclusion limit (upper bound) for $P_{\mu s}$ can then be obtained. The 90% CL exclusion limit for $P_{\mu s}$ is shown in figure 2 for a perfect detector (dotted curves), K2K-like with basic signals (solid curves), and T2K-like with basic signals (dashed

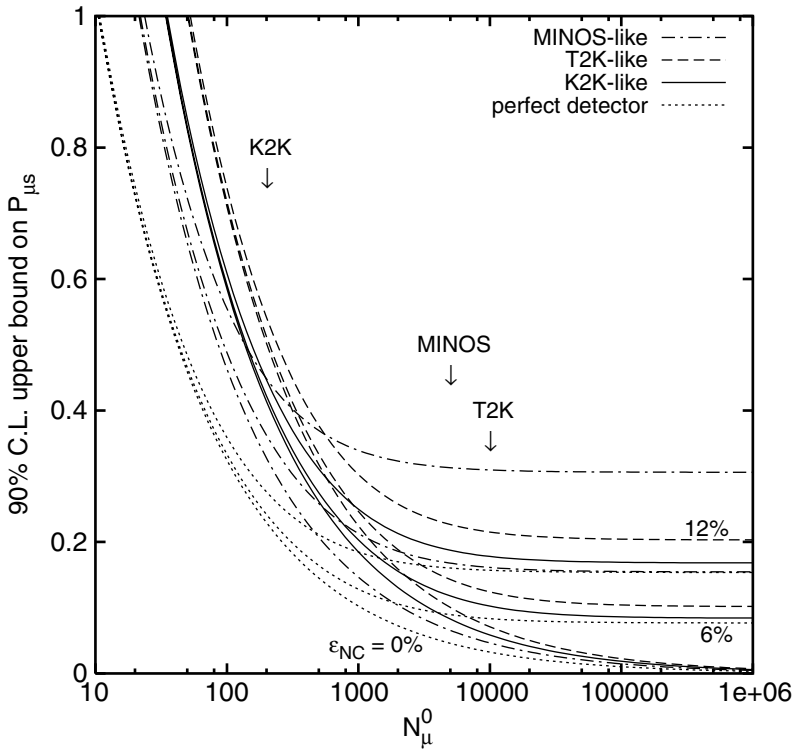

Figure 2. Assuming Gaussian statistical uncertainties, the 90% CL exclusion limit for $P_{\mu s}$ versus N_μ^0 for fixed values of the NC systematic error for a perfect detector (dotted curves), the K2K-like experiment with basic signals (solid), the T2K-like experiment with basic signals (dashed), and the MINO-like experiment (dash-dotted). Other assumptions are the same as in figure 1.

curves). To model realistic oscillation probabilities we have assumed a three-neutrino model assuming the parameters $\delta m_{31}^2 = 2.0 \times 10^{-3}$ eV^2, $\sin^2 2\theta_{23} = 1.0$, and $\sin^2 2\theta_{13} = 0.1$. At high statistics the relative values of the exclusion limits are approximately proportional to $(1 + f_{\mu,NC})$, similar to the 3σ sensitivity levels calculated previously. As was the case for the 3σ sensitivity, the MINOS-like detector does better than the K2K- and T2K-like detectors at low statistics, due to the higher NC efficiency, but not as well at high statistics due to larger misidentification factors.

5. Summary

At low statistics ($\lesssim$1000 events), experiments with a larger NC efficiency, such as our MINOS-like example, tend to have better sensitivity to the sterile oscillation probability $P_{\mu s}$. At high statistics, the sensitivity in the cases we considered is primarily limited by the systematic uncertainty in the NC rate, ϵ_{NC}, and the contamination of the NC signal from CC μ events, $f_{\mu,NC}$ (and NC contamination from CC τ events, $f_{\tau,NC}$, above τ threshold). The best anticipated ϵ_{NC} is of order a few per cent, so the best 3σ sensitivity and 90% CL exclusion limits that can be expected for the sterile oscillation probability will be of order 0.10–0.15 (0.2–0.3 for the oscillation amplitude).

The lowest contamination rates are realized for the K2K- and T2K-like cases. Very fine-grain detectors, such as a liquid argon TPC, will be subject to much less event misidentification than the K2K- or MINOS-like detectors. However, even when event misidentification is eliminated, at most an 8% improvement is possible over the K2K-like detectors. Therefore, significant improvements in these sterile probability sensitivities or limits can only be achieved by lowering the uncertainty in NC cross-sections or improving the event selection criteria, both of which could prove to be challenging but very worthwhile.

Acknowledgments

We thank D Harris for a critical reading of the paper and H Gallagher for assistance with NEUGEN. VB thanks the Aspen Center for Physics for hospitality during the completion of this paper. This research was supported in part by the US Department of Energy under Grant nos. DE-FG02-95ER40896, DE-AC02-76CH03000 and DE-FG02-01ER41155, and in part by the Wisconsin Alumni Research Foundation.

References

[1] Barger V, Marfatia D and Whisnant K 2003 *Int. J. Mod. Phys.* **12** 569 (*Preprint* hep-ph/0308123)
[2] Maki Z, Nakagawa M and Sakata S 1962 *Prog. Theor. Phys.* **28** 870
Pontecorvo B 1968 *Sov. Phys. JETP* **26** 984
Gribov V N and Pontecorvo B 1969 *Phys. Lett.* B **28** 493
[3] Athanassopoulos C *et al* (LSND Collaboration) 1996 *Phys. Rev.* C **54** 2685 (*Preprint* nucl-ex/9605001)
Athanassopoulos C *et al* (LSND Collaboration) 1996 *Phys. Rev. Lett.* **77** 3082 (*Preprint* nucl-ex/9605003)
Athanassopoulos C *et al* (LSND Collaboration) 1998 *Phys. Rev.* C **58** 2489 (*Preprint* nucl-ex/9706006)
Athanassopoulos C *et al* (LSND Collaboration) 1998 *Phys. Rev. Lett.* **81** 1774 (*Preprint* nucl-ex/9709006)
Aguilar A *et al* 2001 *Phys. Rev.* D **64** 112007 (*Preprint* hep-ex/0104049)
Church E D, Eitel K, Mills G B and Steidl M 2002 *Phys. Rev.* D **66** 013001 (*Preprint* hep-ex/0203023)
[4] Barger V, Kayser B, Learned J, Weiler T J and Whisnant K 2000 *Phys. Lett.* B **489** 345 (*Preprint* hep-ph/0008019)
Maltoni M, Schwetz T, Tortola M A and Valle J W 2002 *Nucl. Phys.* B **643** 321 (*Preprint* hep-ph/0207157)
Bahcall J N, Gonzalez-Garcia M C and Pena-Garay C 2002 *Phys. Rev.* C **66** 035802 (*Preprint* hep-ph/0204194)
[5] Stancu I *et al* (MiniBooNE collaboration) FERMILAB-TM-2207
[6] Fogli G L and Lisi E 1996 *Phys. Rev.* D **54** 3667 (*Preprint* hep-ph/9604415)
Arafune J and Sato J 1997 *Phys. Rev.* D **55** 1653 (*Preprint* hep-ph/9607437)
Geer S 1998 *Phys. Rev.* D **57** 6989
Geer S 1999 *Phys. Rev.* D **59** 039903 (erratum) (*Preprint* hep-ph/9712290)
Autin B *et al* 1998 CERN-SPSC-98-30
De Rujula A, Gavela M B and Hernandez P 1999 *Nucl. Phys.* B **547** 21 (*Preprint* hep-ph/9811390)
Blondel A *et al* 2000 *Nucl. Instrum. Methods* A **451** 102
Barger V D, Dai Y B, Whisnant K and Young B L 1999 *Phys. Rev.* D **59** 113010 (*Preprint* hep-ph/9901388)
Dick K, Freund M, Lindner M and Romanino A 1999 *Nucl. Phys.* B **562** 29 (*Preprint* hep-ph/9903308)
Lipari P 2000 *Phys. Rev.* D **61** 113004 (*Preprint* hep-ph/9903481)
Campanelli M, Bueno A and Rubbia A 1999 *Preprint* hep-ph/9905240
Barger V D, Geer S and Whisnant K 2000 *Phys. Rev.* D **61** 053004 (*Preprint* hep-ph/9906487)
Donini A, Gavela M B, Hernandez P and Rigolin S 2000 *Nucl. Phys.* B **574** 23 (*Preprint* hep-ph/9909254)
Freund M and Ohlsson T 2000 *Mod. Phys. Lett.* A **15** 867 (*Preprint* hep-ph/9909501)
Koike M and Sato J 2000 *Phys. Rev.* D **62** 073006 (*Preprint* hep-ph/9911258)

Barger V D, Geer S, Raja R and Whisnant K 2000 *Phys. Rev.* D **62** 013004 (*Preprint* hep-ph/9911524)
Freund M, Lindner M, Petcov S T and Romanino A 2000 *Nucl. Phys.* B **578** 27 (*Preprint* hep-ph/9912457)
Cervera A, Donini A, Gavela M B, Gomez-Cadenas J J, Hernandez P, Mena O and Rigolin S 2000 *Nucl. Phys.* B **579** 17
Cervera A, Donini A, Gavela M B, Gomez-Cadenas J J, Hernandez P, Mena O and Rigolin S 2001 *Nucl. Phys.* B **593** 731 (erratum) (*Preprint* hep-ph/0002108)
Mocioiu I and Shrock R 2000 *Phys. Rev.* D **62** 053017 (*Preprint* hep-ph/0002149)
Barger V D, Geer S, Raja R and Whisnant K 2000 *Phys. Rev.* D **62** 073002 (*Preprint* hep-ph/0003184)
Freund M, Huber P and Lindner M 2000 *Nucl. Phys.* B **585** 105 (*Preprint* hep-ph/0004085)
Barger V D, Geer S, Raja R and Whisnant K 2000 *Phys. Lett.* B **485** 379 (*Preprint* hep-ph/0004208)
Bueno A, Campanelli M and Rubbia A 2000 *Nucl. Phys.* B **589** 577 (*Preprint* hep-ph/0005007)
Barger V D, Pakvasa S, Weiler T J and Whisnant K 2000 *Phys. Rev. Lett.* **85** 5055 (*Preprint* hep-ph/0005197)
Dick K, Freund M, Huber P and Lindner M 2001 *Nucl. Phys.* B **598** 543 (*Preprint* hep-ph/0008016)
Albright C *et al* 2000 *Preprint* hep-ex/0008064
Richter B 2000 *Preprint* hep-ph/0008222
Yokomakura H, Kimura K and Takamura A 2000 *Phys. Lett.* B **496** 175 (*Preprint* hep-ph/0009141)
Parke S J and Weiler T J 2001 *Phys. Lett.* B **501** 106 (*Preprint* hep-ph/0011247)
Koike M, Ota T and Sato J 2002 *Phys. Rev.* D **65** 053015 (*Preprint* hep-ph/0011387)
Barger V D, Geer S, Raja R and Whisnant K 2001 *Phys. Rev.* D **63** 113011 (*Preprint* hep-ph/0012017)
Blondel A *et al* 2001 *Nucl. Instrum. Methods* A **503** 173
Miura T, Takasugi E, Kuno Y and Yoshimura M 2001 *Phys. Rev.* D **64** 013002 (*Preprint* hep-ph/0102111)
Barger V D *et al* 2001 *Preprint* hep-ph/0103052
Burguet-Castell J, Gavela M B, Gomez-Cadenas J J, Hernandez P and Mena O 2001 *Nucl. Phys.* B **608** 301 (*Preprint* hep-ph/0103258)
Chen H S *et al* (VLBL Study Group H2B-1 Collaboration) 2001 *Preprint* hep-ph/0104266
Akhmedov E K, Huber P, Lindner M and Ohlsson T 2001 *Nucl. Phys.* B **608** 394 (*Preprint* hep-ph/0105029)
Freund M, Huber P and Lindner M 2001 *Nucl. Phys.* B **615** 331 (*Preprint* hep-ph/0105071)
Pinney J and Yasuda O 2001 *Phys. Rev.* D **64** 093008 (*Preprint* hep-ph/0105087)
Gomez-Cadenas J J *et al* (CERN working group on Super Beams Collaboration) 2001 *Preprint* hep-ph/0105297
Miura T, Shindou T, Takasugi E and Yoshimura M 2001 *Phys. Rev.* D **64** 073017 (*Preprint* hep-ph/0106086)
Mocioiu I and Shrock R 2001 *J. High Energy Phys.* JHEP11(2001)050 (*Preprint* hep-ph/0106139)
Ota T, Sato J and Kuno Y 2001 *Phys. Lett.* B **520** 289 (*Preprint* hep-ph/0107007)
Minakata H and Nunokawa H 2001 *J. High Energy Phys.* JHEP10(2001)001 (*Preprint* hep-ph/0108085)
Barger V D, Marfatia D and Whisnant K 2001 *Proc. APS/DPF/DPB Summer Study on the Future of Particle Physics (Snowmass)* ed N Graf, eConf C010630, E102 (*Preprint* hep-ph/0108090)
Wang Y f, Whisnant K and Young B L 2002 *Phys. Rev.* D **65** 073006 (*Preprint* hep-ph/0109053)
Barger V D, Gago A M, Marfatia D, Teves W J, Wood B P and Zukanovich Funchal R 2002 *Phys. Rev.* D **65** 053016 (*Preprint* hep-ph/0110393)
Adams T *et al* 2001 *Proc. APS/DPF/DPB Summer Study on the Future of Particle Physics (Snowmass)* ed N Graf, eConf C010630, E1001 (*Preprint* hep-ph/0111030)
Wang Y F, Whisnant K, Xiong Z H, Yang J M and Young B L (VLBL Study Group H2B-4 Collaboration) 2002 *Phys. Rev.* D **65** 073021 (*Preprint* hep-ph/0111317)
Barger V, Marfatia D and Whisnant K 2002 *Phys. Rev.* D **65** 073023 (*Preprint* hep-ph/0112119)
Skadhauge S 2002 *Nucl. Phys.* B **639** 281 (*Preprint* hep-ph/0112189)
Bilenky S M, Freund M, Lindner M, Ohlsson T and Winter W 2002 *Phys. Rev.* D **65** 073024 (*Preprint* hep-ph/0112226)
Bueno A, Campanelli M, Navas-Concha S and Rubbia A 2002 *Nucl. Phys.* B **631** 239 (*Preprint* hep-ph/0112297)

Aoki M, Hagiwara K, Hayato Y, Kobayashi T, Nakaya T, Nishikawa K and Okamura N 2003 *Phys. Rev.* D **67** 093004 (*Preprint* hep-ph/0112338)
Kajita T, Minakata H and Nunokawa H 2001 *Preprint* hep-ph/0112345
Zucchelli P 2002 *Phys. Lett.* B **532** 166
Bahcall J N, Barger V and Marfatia D 2002 *Phys. Lett.* B **534** 120 (*Preprint* hep-ph/0201211)
Mocioiu I and Pospelov M 2002 *Phys. Lett.* B **534** 114 (*Preprint* hep-ph/0202160)
Gomez-Cadenas J J and Harris D A 2002 *Ann. Rev. Nucl. Part. Sci.* **52** 253
Minakata H, Nunokawa H and Parke S 2002 *Phys. Lett.* B **537** 249 (*Preprint* hep-ph/0204171)
Barenboim G, De Gouvea A, Szleper M and Velasco M 2002 *Preprint* hep-ph/0204208
Huber P, Lindner M and Winter W 2002 *Nucl. Phys.* B **645** 3 (*Preprint* hep-ph/0204352)
Beavis D *et al* 2002 *Preprint* hep-ex/0205040
Donini A, Meloni D and Migliozzi P 2002 *Nucl. Phys.* B **646** 321 (*Preprint* hep-ph/0206034)
Barger V, Marfatia D and Whisnant K 2002 *Phys. Rev.* D **66** 053007 (*Preprint* hep-ph/0206038)
Alsharoa M M *et al* (Muon Collider/Neutrino Factory Collaboration) 2002 *Preprint* hep-ex/0207031
Burguet-Castell J, Gavela M B, Gomez-Cadenas J J, Hernandez P and Mena O 2002 *Nucl. Phys.* B **646** 301 (*Preprint* hep-ph/0207080)
Rubbia A and Sala P 2002 *J. High Energy Phys.* JHEP09(2002)004 (*Preprint* hep-ph/0207084)
Minakata H, Nunokawa H and Parke S 2002 *Phys. Rev.* D **66** 093012 (*Preprint* hep-ph/0208163)
Whisnant K, Yang J M and Young B L 2003 *Phys. Rev.* D **67** 013004 (*Preprint* hep-ph/0208193)
Aoki M, Hagiwara K and Okamura N 2003 *Phys. Lett.* B **554** 121 (*Preprint* hep-ph/0208223)
Ayres D *et al* 2002 *Preprint* hep-ex/0210005
Apollonio M *et al* 2002 *Preprint* hep-ph/0210192
Barger V, Marfatia D and Whisnant K 2003 *Phys. Lett.* B **560** 75 (*Preprint* hep-ph/0210428)
Diwan M *et al* 2002 *Preprint* hep-ex/0211001
Huber P, Lindner M and Winter W 2003 *Nucl. Phys.* B **654** 3 (*Preprint* hep-ph/0211300)
Minakata H, Nunokawa H and Parke S 2003 *Preprint* hep-ph/0301210
Leung C N and Wong Y Y 2003 *Phys. Rev.* D **67** 056005 (*Preprint* hep-ph/0301211)
Huber P and Winter W 2003 *Preprint* hep-ph/0301257
Mezzetto M 2003 *J. Phys. G: Nucl. Part. Phys.* **29** 1771 (*Preprint* hep-ex/0302007)
Autin B, Harris D A, King S F, McFarland K S and Yasuda O 2003 *Preprint* hep-ph/0302218
Asratyan A, Davidenko G, Dolgolenko A, Kaftanov V, Kubantsev M and Verebryusov V 2003 *Preprint* hep-ex/0303023
Diwan M *et al* 2003 *Phys. Rev.* D **68** 012002 (*Preprint* hep-ph/0303081)
For a recent discussion of iron scintillator detectors at Fermilab, see Barenboim G *et al* 2003 *Preprint* hep-ex/0304017
For a discussion of iron scintillator detectors at the Indian Neutrino Observatory, see http://www.imsc.ernet.in/∼ino
Jacobson M and Ohlsson T 2003 *Preprint* hep-ph/0305064
Autiero D *et al* 2003 *Preprint* hep-ph/0305185
Zucchelli P 2002 *Phys. Lett.* B **532** 166
Mezzetto M 2003 *J. Phys. G: Nucl. Part. Phys.* **29** 1771 (*Preprint* hep-ex/0302007)
An analysis of oscillation signals generated by one extra sterile neutrino has been made by Cirelli M *et al* 2004 *Preprint* hep-ph/0403158
[7] Kozlov Y, Mikaelyan L and Sinev V 2003 *Yad. Fiz.* **66** 497 (*Preprint* hep-ph/0109277)
Kozlov Y, Mikaelyan L and Sinev V 2003 *Phys. Atom. Nucl.* **66** 469 (Engl. Transl.)
Martemyanov V, Mikaelyan L, Sinev V, Kopeikin V and Kozlov Y 2002 *Preprint* hep-ex/0211070
Minakata H, Sugiyama H, Yasuda O, Inoue K and Suekane F 2002 *Preprint* hep-ph/0211111
Huber P, Lindner M, Schwetz T and Winter W 2003 *Preprint* hep-ph/0303232
Shaevitz M H and Link J M 2003 *Preprint* hep-ex/0306031
Huber P, Lindner M, Rolinec M, Schwetz T and Winter W 2004 *Preprint* hep-ph/0403068

[8] Hagiwara K *et al* (Particle Data Group Collaboration) 2002 *Phys. Rev.* D **66** 010001
[9] Ahn S H *et al* (K2K Collaboration) 2001 *Phys. Lett.* B **511** 178 (*Preprint* hep-ex/0103001)
Ahn M H *et al* (K2K Collaboration) 2003 *Phys. Rev. Lett.* **90** 041801 (*Preprint* hep-ex/0212007)
[10] See http://neutrino.kek.jp/jhfnu for Letter of Intent (2003) and other information
Itow Y *et al* 2001 *Preprint* hep-ex/0106019
[11] MINOS Collaboration 1998 Fermilab Report No. NuMI-L-375
[12] Gallagher H 2002 *Nucl. Phys. Proc. Suppl.* **112** 188
[13] Apollonio M *et al* (CHOOZ Collaboration) 1998 *Phys. Lett.* B **420** 397 (*Preprint* hep-ex/9711002)
Apollonio M *et al* (CHOOZ Collaboration) 1999 *Phys. Lett.* B **466** 415 (*Preprint* hep-ex/9907037)
Apollonio M (CHOOZ Collaboration) 2003 *Eur. Phys. J.* C **27** 331 (*Preprint* hep-ex/0301017)
[14] Yamada S 2003 *PhD Thesis* University of Tokyo
[15] Fukuda Y *et al* (Super-K Collaboration) 1998 *Phys. Lett.* B **433** 9
[16] Michael D 2003 Talk at *the Fermilab User's Meeting, 3 June*

New Journal of Physics
The open-access journal for physics

Evidence for the MSW effect

Gianluigi Fogli and Eligio Lisi
Dipartimento di Fisica and Sezione INFN di Bari, Via Amendola 173, 70126 Bari, Italy
E-mail: gianluigi.fogli@ba.infn.it and eligio.lisi@ba.infn.it

New Journal of Physics **6** (2004) 139
Received 9 July 2004
Published 25 October 2004
Online at http://www.njp.org/
doi:10.1088/1367-2630/6/1/139

Abstract. Recent solar and reactor neutrino data have convincingly established that electron neutrinos and antineutrinos are subject to flavour transitions driven by neutrino masses and mixing. In addition, such data can be used to prove that the interaction of neutrinos in matter modifies the flavour transition pattern with respect to the case of propagation in vacuum, as predicted long ago by Mikheyev, Smirnov and Wolfenstein (MSW). We present a brief review of how the current evidence for MSW solar neutrino transitions has developed in recent years, and how it has been strengthened by the latest reactor neutrino data presented at the Neutrino 2004 Conference.

Contents

1. Introduction and notation **1**
2. The impact of solar and reactor data during the period 2001–2003 **3**
2.1. Converging towards the LMA MSW solution 3
2.2. Proving MSW effects in the LMA solution 6
3. The impact of KamLAND 2004 data **8**
4. Bounds on the size of MSW effects: evolution from 2002 to 2004 **9**
5. Conclusions and prospects **12**
Acknowledgments **13**
References **13**

1. Introduction and notation

The Cl [1], Ga [2, 3], Super-Kamiokande (SK) [5]–[7] and Sudbury Neutrino Observatory (SNO) [8]–[11] solar neutrino experiments have established that the deficit of the observed solar ν_e flux

PII: S1367-2630(04)83352-4
© IOP Publishing Ltd and Deutsche Physikalische Gesellschaft

with respect to expectations [12, 13] implies new neutrino physics beyond the standard model. In particular, the charged and neutral current (CC and NC) data from SNO have proven the occurrence of ν_e transitions into a different active state ν_a with high statistical significance [11].

Such transitions were predicted long ago as a consequence of possible flavour oscillations [14] in the $\nu_e \to \nu_a$ channel (ν_a being a linear combination of ν_μ and ν_τ) driven by nonzero ν squared mass difference and mixing angle parameters $(\delta m^2, \theta_{12})$ [15]. We now know that the (ν_μ, ν_τ) combination orthogonal to ν_a is probed by atmospheric ν oscillations [16], with different parameters $(\Delta m^2, \theta_{23})$ [17]. We also know that the third mixing angle θ_{13}, needed to complete the 3×3 mixing matrix, is bound to be rather small ($\sin^2\theta_{13} <$ few %) by additional reactor results [17, 18], and we can set it to zero to a good approximation for our purposes (unless otherwise noticed). An updated overview of such a 'standard' neutrino oscillation scenario can be found in [19].

The first (2003) results from the Kamioka Liquid scintillator AntiNeutrino Detector (KamLAND) [20] have provided a beautiful and crucial confirmation of the solar ν_e oscillation picture through a search for long-baseline oscillations of reactor $\bar{\nu}_e$'s. Also the recent KamLAND data released at the Neutrino 2004 Conference [21, 22] clearly indicate that the observed disappearance of $\bar{\nu}_e$ in KamLAND is consistent with the same region of the $(\delta m^2, \theta_{12})$ parameter space which explains the solar neutrino deficit, the so-called large mixing angle (LMA) solution.

In the LMA parameter range, flavour transitions between ν_e and ν_a should be significantly affected by the neutrino interaction energy difference $V = V_e - V_a$ arising in solar (and possibly Earth) background matter [23, 24],

$$V(x) = \sqrt{2} G_F N_e(x), \tag{1}$$

where N_e is the electron number density at the point x. The associated flavour change, known as Mikheyev–Smirnov–Wolfenstein (MSW) effect [23], should occur adiabatically [25] in the solar matter, for LMA parameters (see [26] for a recent discussion).

In the context of the Hamiltonian ($\mathcal{H}$) evolution of 2ν active flavours, the MSW effect enters through a dynamical term $\mathcal{H}_{\rm dyn}$ in matter, in addition to the kinetic term $\mathcal{H}_{\rm kin}$ in vacuum:

$$\mathrm{i}\frac{\mathrm{d}}{\mathrm{d}x}\begin{pmatrix}\nu_e\\ \nu_a\end{pmatrix} = (\mathcal{H}_{\rm dyn} + \mathcal{H}_{\rm kin})\begin{pmatrix}\nu_e\\ \nu_a\end{pmatrix}, \tag{2}$$

where

$$\mathcal{H}_{\rm dyn} = \frac{V(x)}{2}\begin{pmatrix}1 & 0\\ 0 & -1\end{pmatrix} \tag{3}$$

and

$$\mathcal{H}_{\rm kin} = \frac{\delta m^2}{4E}\begin{pmatrix}-\cos 2\theta_{12} & \sin 2\theta_{12}\\ \sin 2\theta_{12} & \cos 2\theta_{12}\end{pmatrix}, \tag{4}$$

E being the neutrino energy.

In this work, we review the current evidence for $\mathcal{H}_{\rm dyn} \neq 0$, i.e., for the occurrence of dynamical MSW effects in the solar matter, induced by the interaction energy V in equation (1).

In order to quantify such evidence, we introduce [27, 28] a free parameter $a_{\rm MSW}$ which modulates the overall amplitude of the dynamical term $\mathcal{H}_{\rm dyn}$ through the substitution

$$V \to a_{\rm MSW} \cdot V, \tag{5}$$

whenever matter is traversed by neutrinos (both in the Sun and in the Earth). This parameter formally interpolates between the case of no matter effect,

$$a_{\rm MSW} = 0 \quad \text{(no MSW effect)}, \tag{6}$$

and the case of standard matter effects,

$$a_{\rm MSW} = 1 \quad \text{(standard MSW effect)}. \tag{7}$$

We will show that the case $a_{\rm MSW} = 0$ is ruled out, the data globally prefer $a_{\rm MSW} \sim 1$, and that the previously large uncertainties in the allowed range of $a_{\rm MSW}$ are significantly reduced by including the recent (2004) KamLAND data.

In the following, we discuss the evidence for the MSW effect in historical perspective, by showing the impact of four data sets which, in combination with previous results from the Cl, Ga and SK experiments [1]–[3], [5, 6] (as well from the CHOOZ reactor experiment [18]), have been crucial to test and constrain the MSW effect: the SNO-I data in 2001–2002 [8]–[10], the first KamLAND data in 2002 [20], the SNO-II data in 2003 [11] and the KamLAND data presented at the Neutrino 2004 Conference [21, 22]. As a useful complement to such a historical overview, the reader is referred to [19] for a detailed global analysis of neutrino oscillation data.

2. The impact of solar and reactor data during the period 2001–2003

Figure 1, based on the works [28]–[30], shows the dramatic progress in constraining the 2ν oscillation parameters $(\delta m^2, \theta_{12})$ during the years 2001–2003. This progress is relevant also for the emerging evidence in favour of the MSW effect, as discussed below.

2.1. Converging towards the LMA MSW solution

For many years, the physics of the MSW effect has been mostly investigated in the limit of small θ_{12} (see, e.g., the review in [31]), for at least two reasons. The first was the theoretical prejudice in favour of small neutrino mixing, in analogy with the quark case. The second was the fact that, for small θ_{12}, the MSW effect can become dramatically large; in particular, when V is such that the diagonal elements of $\mathcal{H}$ vanish, the Hamiltonian becomes maximally off-diagonal in the flavour basis, thus inducing large flavour transition amplitudes—despite the smallness of θ_{12}. This so-called 'resonance' condition can be easily realized in the Sun (where V spans several orders of magnitude from the core to the photosphere [12]) and predicts strong distortions in the neutrino energy spectrum. Figure 1(a) shows the 2ν fit to 2001 solar neutrino data (Cl + Ga + SK), prior to SNO-I data [29, 32], where mixing angle values as small as $\tan^2\theta_{12} \sim 10^{-4}$–$10^{-3}$ are allowed.

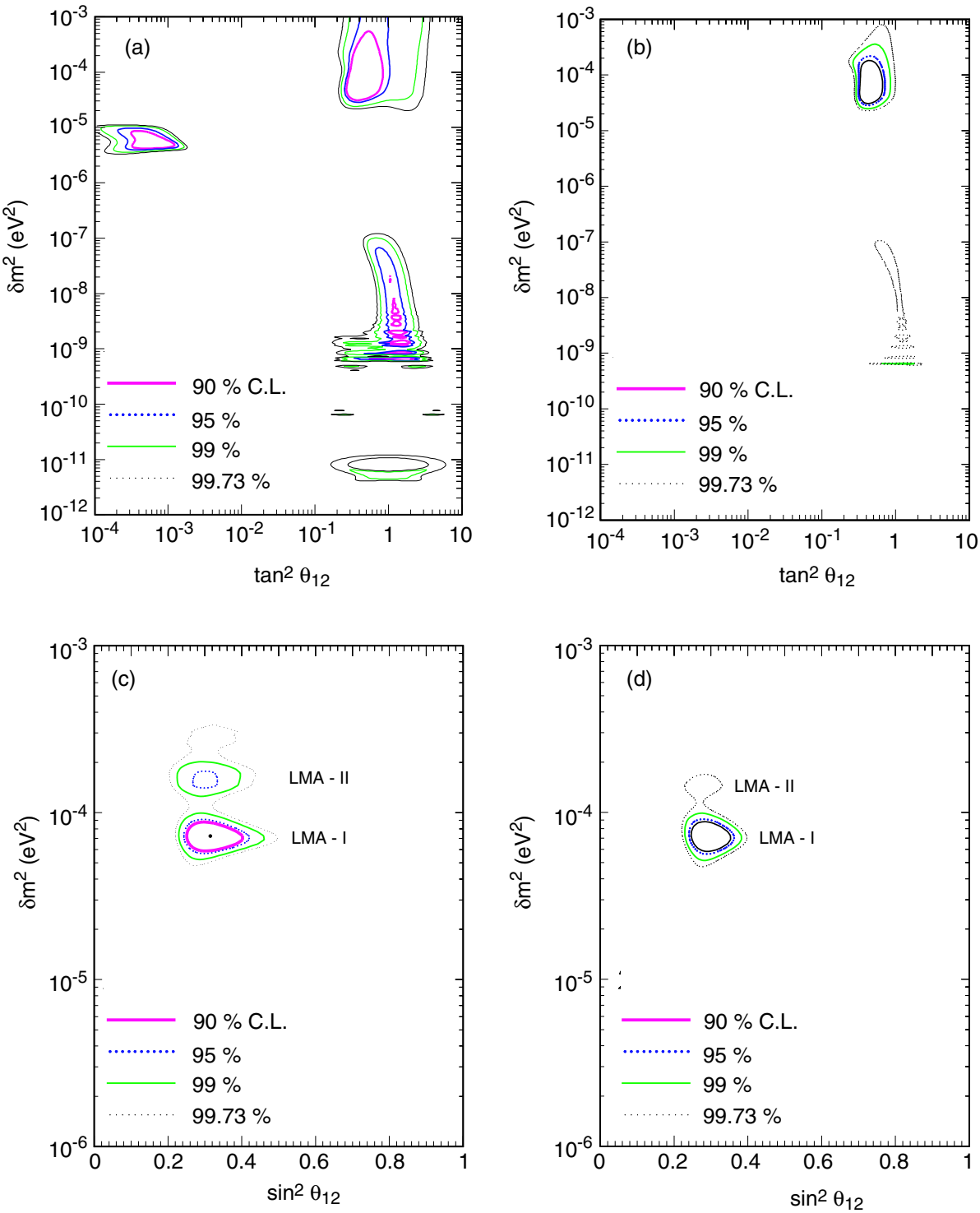

Figure 1. Results of global analyses of solar and terrestrial neutrino experiments during the years 2001–2003. (a) All solar neutrino data (Cl + Ga + SK) before SNO (2001), (b) including SNO-I data (2001–2002), (c) including first KamLAND data (2002), (d) including SNO-II data (2003). Based on [28]–[30].

At the turn of the millennium, however, the increasing evidence for no spectral distortions in the SK solar neutrino experiment [5, 6] started to decrease the likelihood of small mixing solutions to the solar neutrino problem, in favour of large mixing ones. At about the same time, theoretical prejudices against large mixing had to face the increasing evidence in favour of $\theta_{23} \sim \pi/4$ from atmospheric neutrino data [16]. Eventually, small solar neutrino mixing was ruled out in 2001–2002 by the data from the SNO experiment (SNO-I phase [9]), which strongly enhanced the tension between total rate and spectrum shape data at small θ_{12} (see, e.g., [29, 32, 33]).

Figure 1(b) shows the combination of all solar neutrino experiments as of 2002 (Cl + Ga + SK + SNO-I) [29], which allows only solutions at relatively large values of θ_{12}. At 99% CL, the figure shows a best-fit solution at $\delta m^2 \sim$ few $\times\, 10^{-5}$ eV^2 (called LMA), where MSW effects are expected to modulate the energy profile of the solar neutrino survival probability [26, 34]. However, figure 1(b) also shows other (non-LMA) solutions at lower δm^2, where the observability of the MSW effect is more problematic. For example, for δm^2 as low as a few $\times 10^{-10}$ eV^2, matter effects are dominant in principle inside the Sun (since $V \gg \delta m^2/E$, i.e., $\|\mathcal{H}_{\rm dyn}\| \gg \|\mathcal{H}_{\rm kin}\|$); in practice, however, they simply inhibit flavour transitions up to the Sun's surface (since $\mathcal{H} \sim \mathcal{H}_{\rm dyn}$ is approximately flavour-diagonal inside the Sun), so that observable flavour transition effects are actually dominated by vacuum oscillations outside the Sun, where $\mathcal{H} \sim \mathcal{H}_{\rm kin}$ (see [35] and references therein).

Therefore, from the solar neutrino data available in 2002 we have learned that MSW effects should be sought at large, and not small, values of the mixing angle θ_{12}, and most likely in the so-called LMA region. However, there was still room for other regions of the mass-mixing parameter space where, from the phenomenological viewpoint, MSW effects would be unobservably small, i.e., where $a_{\rm MSW} \simeq 0$ would be allowed. It is thus fair to say that the 2002 solar neutrino data did not provide compelling evidence in favour of matter effects in the Sun.

At the end of 2002, however, the allowed parameter space in figure 1(b) was dramatically reduced by the first evidence for $\bar{\nu}_e$ disappearance in the long-baseline reactor experiment KamLAND [20]. Figure 1(c) shows that the combination of all solar + reactor 2002 data uniquely selects the LMA region and splits it into (at least) two subregions, conventionally called LMA-I (at best fit, $\delta m^2 \sim 6 \times 10^{-5}$ eV^2 and $\sin^2\theta_{12} \sim 0.3$) and LMA-II (at somewhat higher δm^2), see e.g. [30]. The reduction of the parameter space around the LMA region(s) is very important, when combined with the SK + SNO preference for $P_{ee} \sim 1/3 < 1/2$, where P_{ee} is the average ν_e survival probability in the SK–SNO energy range [29, 32].

Indeed, for typical LMA parameters and for $a_{\rm MSW} = 1$ (standard matter effects), MSW transitions occur adiabatically in the Sun [23, 25], leading to a survival probability of the form (up to residual Earth matter effects):

$$P_{ee} \simeq \cos^2\theta'_{12}\cos^2\theta_{12} + \sin^2\theta'_{12}\sin^2\theta_{12} \quad (a_{\rm MSW} = 1), \tag{8}$$

where θ'_{12} is the rotation angle which diagonalizes $\mathcal{H}$ at the ν_e production point in the solar core. On the other hand, for hypothetically zeroed matter effects ($a_{\rm MSW} = 0$), one would get an energy-independent form for P_{ee} in the LMA region,

$$P_{ee} \simeq 1 - \tfrac{1}{2}\sin^2 2\theta_{12} \quad (a_{\rm MSW} = 0), \tag{9}$$

as originally suggested by Gribov and Pontecorvo [36] prior to the MSW papers [23] (see also [37, 38]).

In the SK and SNO energy range (approximately $E > 5$ MeV), the above two expressions lead to comparable results in the second octant of the mixing angle ($\theta_{12} > \pi/4$), but differ considerably in the first octant, where $P_{ee}(a_{\rm MSW} = 1) < 1/2$, while $P_{ee}(a_{\rm MSW} = 0) > 1/2$. Therefore, within the LMA region, proving the occurrence of MSW effects in the Sun is equivalent to proving that $P_{ee} < 1/2$, which can only happen if the second octant ($\theta_{12} \geqslant \pi/4$) is ruled out. The 2002 SK + SNO data favoured $P_{ee} \sim 1/3$ [29], but the case $P_{ee} = 1/2$ (as well as $\theta_{12} = \pi/4$) was not convincingly ruled out; indeed, figure 1(c) shows that, combining all 2002 solar + reactor data, the LMA-I solution is still marginally compatible with maximal mixing. The discrimination of the cases $a_{\rm MSW} = 0$ and $a_{\rm MSW} = 1$ thus required a more precise determination of the experimental-to-theoretical ratio of CC to NC events in SNO, which is independent of standard solar model predictions, and directly measures the average of P_{ee} over the SNO and SK energy response functions with appropriate thresholds [29], [39]–[41].

In summary, from 2002 solar + reactor data we have learned that the solar neutrino deficit is explained by neutrino flavour transitions with mass-mixing parameters in the LMA region. In this region, the SNO and SK experiments can prove the occurrence of MSW effects in the Sun by showing that the energy-averaged survival probability $\langle P_{ee}\rangle$ is smaller than 1/2 (which can only happen if $\theta_{12} < \pi/4$). In 2002, however, the emerging SNO + SK indications in favour of $\langle P_{ee}\rangle < 1/2$, although intriguing, were not compelling in our opinion [27].

2.2. *Proving MSW effects in the LMA solution*

In 2003, the SNO experiment finally provided compelling evidence for $\langle P_{ee}\rangle < 1/2$ through the so-called phase-II data, which allowed a better statistical separation of CC and NC events [11, 42]. In particular, a model-independent combination of SNO + SK data provided the following upper bound [28]:

$$\langle P_{ee}\rangle < 0.43\ (3\sigma). \tag{10}$$

The above model-independent limit is crucial to our discussion, and its derivation deserves some comments. As already mentioned, it has been shown in [40] (see also [29]) that the SK and SNO experiments probe the same energy-averaged ν_e survival probability $\langle P_{ee}\rangle$ to a good accuracy, provided that the detector thresholds are appropriately chosen. For the SNO-II kinetic energy threshold ($T_{\rm SNO} = 5.5$ MeV) and energy resolution [11], we find that the equivalent SK threshold is $E_{\rm SK} \simeq 7.8$ MeV in total energy [27]. For equalized thresholds, the SK elastic scattering (ES) flux and the SNO NC and CC fluxes are linked by the exact relations [40]

$$\Phi_{\rm ES}^{\rm SK} = \Phi_B[\langle P_{ee}\rangle + r(1 - \langle P_{ee}\rangle)], \tag{11}$$

$$\Phi_{\rm CC}^{\rm SNO} = \Phi_B\langle P_{ee}\rangle, \tag{12}$$

$$\Phi_{\rm NC}^{\rm SNO} = \Phi_B, \tag{13}$$

where $r = 0.154$ is the ratio of (properly averaged) $\nu_{\mu,\tau}$ and ν_e CC cross-sections, and Φ_B is the true ^{8}B neutrino flux from the Sun. From the above equations, one can (over)constrain both Φ_B and $\langle P_{ee}\rangle$ in a truly model-independent way, namely, without any prior assumption about the energy profile of P_{ee} or about Φ_B predictions in standard solar models (SSMs).

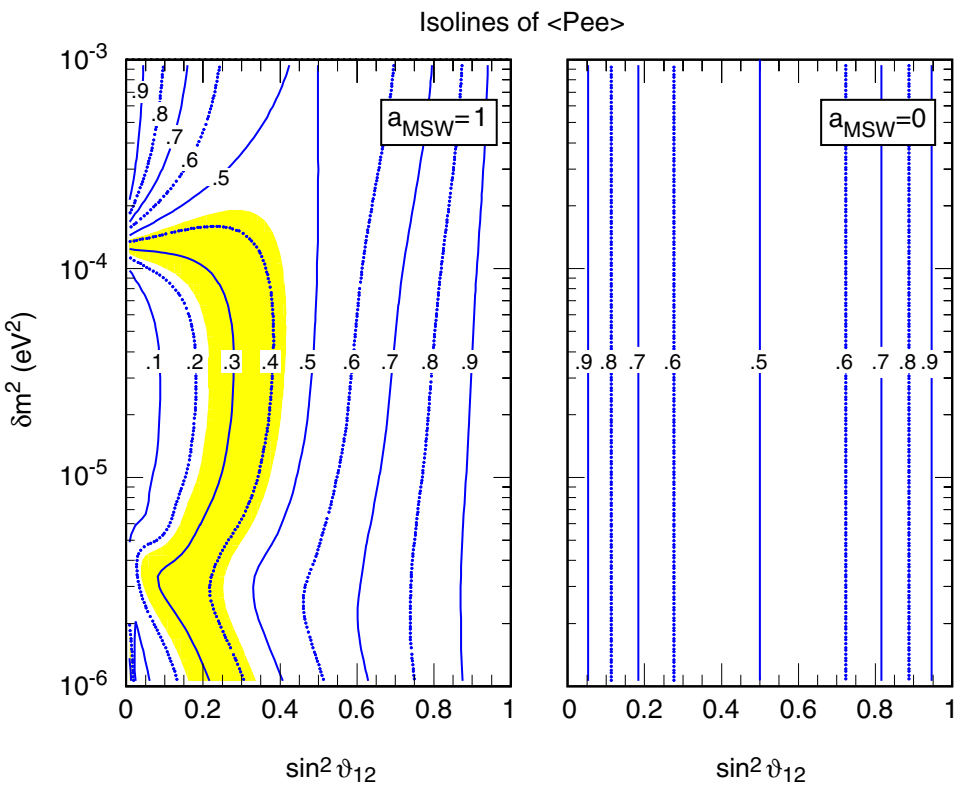

Figure 2. Isolines of the energy-averaged solar ν_e survival probability $\langle P_{ee}\rangle$ with standard MSW effects ($a_{\rm MSW} = 1$) and with no matter effects ($a_{\rm MSW} = 0$). The grey region is allowed by the current SK + SNO combination (dominated by SNO-II data). No such region exists in the absence of MSW effects. See also [28].

Using the above set of equations one gets

$$\Phi_B = (5.5 \pm 1.2) \times 10^6\,{\rm cm}^{-2}\,{\rm s}^{-1}\,(3\sigma), \tag{14}$$

in good agreement with SSM predictions [12, 13], and

$$\langle P_{ee}\rangle = 0.31^{+0.12}_{-0.08}\,(3\sigma), \tag{15}$$

from which equation (10) is derived. The above 3σ limits on $\langle P_{ee}\rangle$ are in very good agreement with the '3σ range' obtained by naively triplicating the errors of the SNO CC/NC flux ratio, which is a direct measurement of $\langle P_{ee}\rangle$: $\Phi^{\rm SNO}_{\rm CC}/\Phi^{\rm SNO}_{\rm NC} = 0.306 \pm 0.105\,(3\sigma)$ [11]. However, as emphasized in [42], the errors of the CC/NC ratio are not normally distributed, and should not be used in fits. Conversely, our bounds in equation (15) are statistically safe and well-defined [28].

Figure 2 illustrates the impact of the above bounds through isolines of $\langle P_{ee}\rangle$ in the $(\delta m^2, \sin^2\theta_{12})$ parameter range relevant to the LMA region, for both $a_{\rm MSW} = 1$ (left panel) and $a_{\rm MSW} = 0$ (right panel) [28]. The superposed grey region is allowed by the 3σ model-independent bounds in equation (15). No such region exists in the case $a_{\rm MSW} = 0$, which is therefore rejected

at the 3σ level (at least). In the standard MSW case (left panel), the allowed region appears to confine δm^2 below $\sim 2 \times 10^{-4}\,\mathrm{eV}^2$ and $\sin^2\theta_{12}$ below ~ 0.4. In particular, the SNO-II data significantly contribute to reject maximal mixing ($\sin^2\theta_{12} = 1/2$) and to reduce the likelihood of the 'high δm^2' LMA-II parameter region, as also evident in the global fit of figure 1(d).

In conclusion, from the combination of 2003 solar and reactor data—including the crucial contribution of SNO-II data—we have obtained the first compelling evidence in favour of MSW effects, by ruling out the null hypothesis of no matter effects in the Sun ($a_{\mathrm{MSW}} = 0$). The evidence is closely related to the evidence for $\langle P_{ee}\rangle < 1/2$ in SK and SNO (figure 2), and to the confinement of the LMA solution(s) in the first octant, $\theta_{12} < \pi/4$ (figure 1(d)). The reader is referred to [28] for further details.

3. The impact of KamLAND 2004 data

At the Neutrino 2004 Conference, the KamLAND Collaboration has released new reactor neutrino data, which not only confirm disappearance of electron neutrino flavour, but also show the first imprint of energy spectrum distortions due to an oscillatory pattern [21, 22]. These new spectral data have greatly reduced the multiplicity of solutions and the uncertainties on δm^2 as compared with previous KamLAND-only fits [20], especially in the region of relatively high δm^2 (LMA-II and higher), where the KamLAND event energy spectrum would be undistorted. This fact helps the observability of MSW effects in the Sun, which would vanish at relatively high δm^2 (i.e., for $\mathcal{H}_{\mathrm{kin}} \gg \mathcal{H}_{\mathrm{dyn}}$) in the LMA region. The 2004 KamLAND data, in combination with solar neutrino data, are thus expected to enhance the evidence for MSW effects that emerged [27] from 2003 data.[1]

In our analysis of the KamLAND 2004 data, we fit the 13-bin energy spectrum reported in [22] with the same statistical procedure as in [30], but taking into account the new estimate of the accidental and cosmogenic backgrounds [22] as in [19], and the updated detector energy resolution, average reactor fuel composition, and unoscillated reactor neutrino flux distribution from [22]. A more accurate (event-by-event) likelihood analysis could be performed if the KamLAND collaboration would disclose further (but currently unpublished) information about time variations of reactor neutrino fluxes and of the detector lifetime, as well as about the energy and time tagging of each event, as emphasized in [43, 44].[2]

Figure 3 shows our analysis of the updated 2004 solar neutrino data (including the SSM input from [13]) at 99.73% CL for 2 d.o.f. (degrees of freedom), superposed to our fit to 2004 KamLAND data at the same CL. The combined solar + KamLAND region (shown at four different CLs) is in good agreement with the one shown in the official KamLAND 2004 analysis [22], as well as in other recent papers [19, 46]. The global best fit $[(\delta m^2/\mathrm{eV}^2, \sin^2\theta_{12}) = (8.3 \times 10^{-5}, 0.29)]$ is controlled by the intersection of the KamLAND LMA-I horizontal band with the 'vertical' solar allowed region. The 'LMA-II' KamLAND-only solution is borderline ($\mathrm{CL} \simeq 3\sigma$) and may marginally appear (as in [22]) or marginally disappear (as in figure 3) at 3σ, depending on small variations in the analysis. The separate solar and KamLAND best-fit δm^2 values are not coincident, the latter ($\delta m^2 = 8.3 \times 10^{-5}\,\mathrm{eV}^2$) being a factor 1.5 higher than the former ($\delta m^2 = 5.5 \times 10^{-5}\,\mathrm{eV}^2$) in our analysis. Such small mismatch [22], although not

[1] It should also be noted that the recent KamLAND data can help to improve the upper bounds on θ_{13}, see [19].

[2] We also mention that background estimates are currently being revised by the KamLAND Collaboration, and that minor changes in the best-fit values of δm^2 and $\sin^2\theta_{12}$ can be expected accordingly [45].

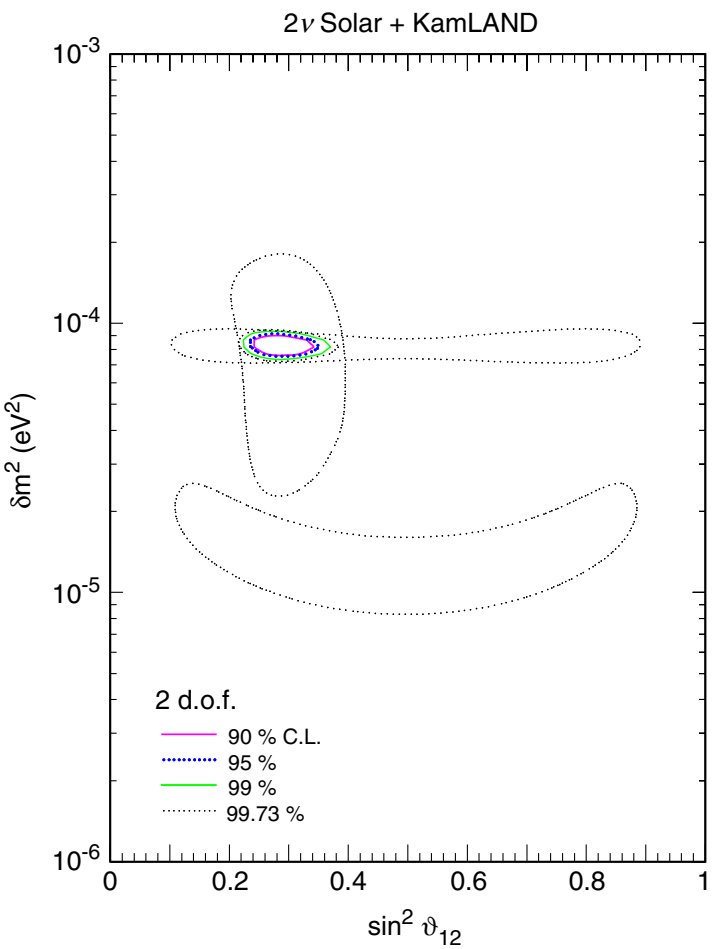

Figure 3. Our global analysis of solar and KamLAND data in the 2ν oscillation case, including the new results presented at the Neutrino 2004 Conference [4, 21, 22], as well as the updated standard solar model input from [13].

alarming from a statistical viewpoint, governs the deviation of the best-fit value of $a_{\rm MSW}$ from unity, as discussed in the next section.

In conclusion, the combination of solar and reactor neutrino data (as available at the Neutrino 2004 Conference) leads to a very satisfactory situation: KamLAND and solar data are highly consistent with each other, and select a single LMA solution in the oscillation parameter space, where the null hypothesis of no MSW effects in the Sun is ruled out. In the next section we go beyond the test of the null hypothesis, and quantify how well the magnitude of the MSW contribution to the hamiltonian ($\mathcal{H}_{\rm dyn}$) is determined by experimental data.

4. Bounds on the size of MSW effects: evolution from 2002 to 2004

According to equations (3) and (4) the size of the dynamical (MSW) and kinematical (vacuum) terms in the neutrino propagation Hamiltonian is governed by the prefactors V and $\delta m^2/E$, respectively. The relative ratio $V/(\delta m^2/E)$ is small for KamLAND neutrinos propagating in the Earth, while it can be of $O(1)$ for solar neutrinos propagating in the Sun (within LMA parameters).

This means that KamLAND data are crucial to fix the kinematical part of the Hamiltonian ($\mathcal{H}_{\rm kin}$), while only solar neutrinos can really test the dynamical part ($\mathcal{H}_{\rm dyn}$). So far, we have shown that the combination of all data constrains the mass-mixing parameters of $\mathcal{H}_{\rm kin}$ around a single 'LMA point' (figure 3), and that the null case $\mathcal{H}_{\rm dyn} = 0$ is ruled out at $>3\sigma$ (figure 2).

However, one can do better than just switching the MSW effect on ($a_{\rm MSW} = 1$) and off ($a_{\rm MSW} = 0$). By treating the parameter $a_{\rm MSW}$ (equation (5)) as a continuous variable, one can check whether the 'solar + KamLAND' combination of data can constrain matter effects in the Sun to have the right size [$a_{\rm MSW} \sim O(1)$]. We have thus performed global analyses with (δm^2, $\sin^2\theta_{12}$, $a_{\rm MSW}$) unconstrained, including solar and reactor data as available in 2002 [27], 2003 [28] and 2004 (this work). The results are marginalized with respect to (δm^2, $\sin^2\theta_{12}$), in order to obtain the relevant bounds on $a_{\rm MSW}$.[3] In a sense, such bounds tell us how well the Fermi constant is 'measured' through MSW effects ($V = \sqrt{2}\, G_F\, N_e$) on solar neutrino flavour transitions, i.e., $a_{\rm MSW}$ can be interpreted as

$$a_{\rm MSW} = \frac{G_F(\nu_\odot)}{G_F}. \tag{16}$$

Figure 4 shows the statistical $\Delta\chi^2$ variations as a function of $a_{\rm MSW}$, derived by our analysis of 2002 data (including SNO-I and first KamLAND results) [27], 2003 data (including SNO-II results) [28] and 2004 data (including the latest KamLAND results [22]). The horizontal dotted lines at $\Delta\chi^2 = n^2$ correspond to n–σ bounds ($n = 1, 2, 3$ and 4). CHOOZ data [18] are also included, being relevant in setting upper limits to δm^2 (from reactor data only) in the 2002 and 2003 fits; they are currently less relevant, since KamLAND 2004 data place an upper bound on δm^2 by themselves. The three curves are discussed below in historical sequence.

With 2002 data, upper and lower bounds on $a_{\rm MSW}$ are already visible. In particular, the hypothetical case of zeroed matter effects is already disfavoured at a formal $\sim 3.5\sigma$ level, thus providing an indirect indication in favour of matter effects in the Sun. However, the 2002 $\Delta\chi^2$ curve also presents several quasi-degenerate minima, and allows a $\pm 3\sigma$ range for $a_{\rm MSW}$ which spans about three orders of magnitude. The width of this range can be understood by recalling the following facts [27]: (1) The LMA range of δm^2 constrained by solar neutrino data, which covers about one decade (figure 3), can be shifted up or down by shifting $a_{\rm MSW}$ with respect to 1, since the LMA oscillation physics depends on $V/\delta m^2 \propto a_{\rm MSW}/\delta m^2$. (2) The range of δm^2 constrained by KamLAND + CHOOZ 2002 data, which covers about two decades [30], is much less affected by $a_{\rm MSW}$ variations. As a consequence, by appropriately shifting $a_{\rm MSW}$, it is possible to overlap the reconstructed ranges of δm^2 from solar and from reactor data over about 1 + 2 decades. When the overlap sweeps through the degenerate δm^2 intervals allowed by KamLAND [30], the fit is locally improved, leading to a 'wavy' structure in $\Delta\chi^2$. In conclusion, although 2002 solar + reactor data strongly disfavoured $a_{\rm MSW} = 0$ (zeroed matter effects) and provided a best fit close to $a_{\rm MSW} = 1$ (standard matter effects), the presence of other local minima in the $\Delta\chi^2$ function, as well as the broad 3σ allowed range for $a_{\rm MSW}$, did not provide a clear evidence of standard matter effects [27].

In 2003, the previous 2002 'indication' in favour of matter effects has become a real 'evidence' [28] by means of the SNO-II data, as already mentioned in section 2. In fact, the 2003 curve in figure 4 puts both upper and lower bounds on $a_{\rm MSW}$ at a safe CL ($>5\sigma$), and shows an intriguing (although weak) preference for $a_{\rm MSW} \sim 1$. However, as for the 2002 curve, also

[3] We refer the reader to [27, 28] for technical details of this kind of analysis.

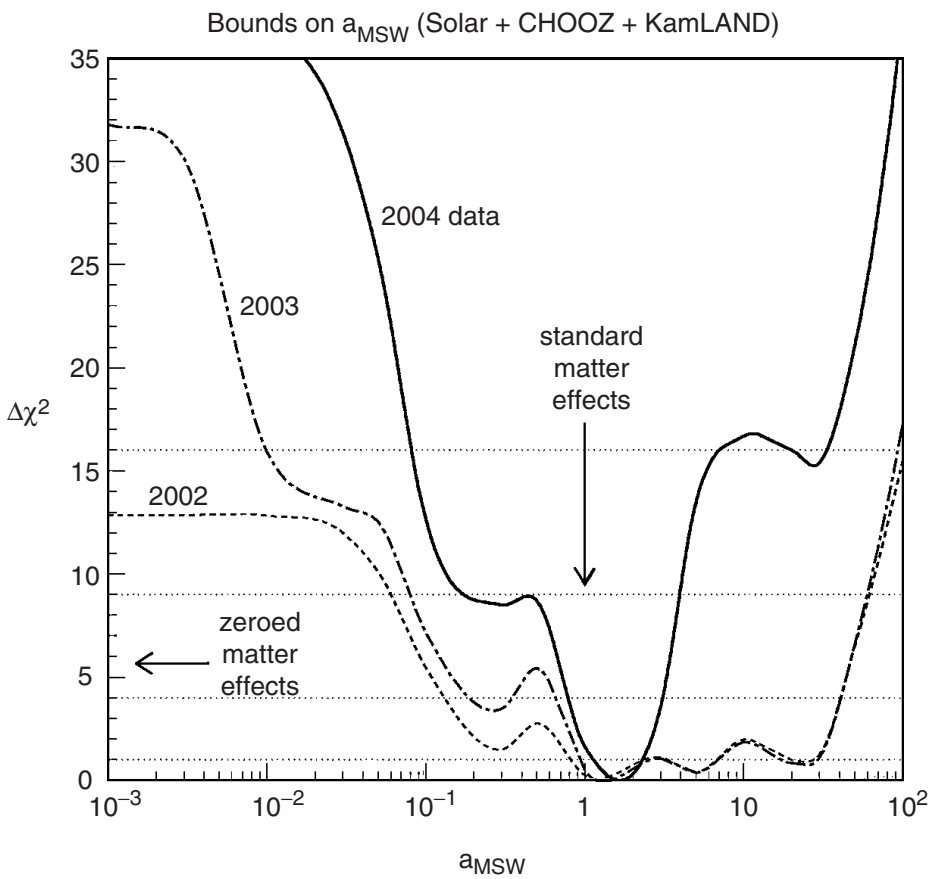

Figure 4. Bounds on a_{MSW}, considered as a continuous free parameter, from the combination of all solar, CHOOZ and KamLAND data, as available in the years 2002, 2003 and 2004 (Neutrino 2004 Conference). For the '2002' and '2003' curves, see also [27] and [28], respectively. Horizontal short dashed lines are drawn at the 1, 2, 3 and 4σ CL ($\Delta\chi^2 = 1$, 4, 9 and 16). A clear trend emerges in favour of MSW effects with standard magnitude ($a_{\mathrm{MSW}} = 1$), and against the hypothetical case of no matter effects (now excluded at $>6\sigma$). In particular, using the Neutrino 2004 data, the case $a_{\mathrm{MSW}} = 1$ is confirmed within a factor of ~ 2 uncertainty at 2σ (95% CL).

the 2003 allowed 3σ range of a_{MSW} appears to be rather large and with several quasi-degenerate minima, basically governed by the multiplicity of KamLAND-only solutions (unchanged from 2002 to 2003). Therefore, although 2003 solar + reactor data provided clear evidence in favour of the MSW effect, they did not allow us to 'measure' the magnitude of MSW effects [28].

Finally, the solid curve in figure 4 shows the most recent bounds on a_{MSW}, as obtained by our analysis of the solar + reactor data, updated after the Neutrino 2004 Conference [4, 21, 22]. The null hypothesis ($a_{\mathrm{MSW}} = 0$) is now rejected at $>6\sigma$. Moreover, the dramatic reduction of the multiplicity of KamLAND solutions (figure 3) leads to a corresponding reduction of the allowed range for a_{MSW}, which can now be 'measured' within a factor of ~ 2 (at the $\pm 2\sigma$ level) around the best fit, which is found at $a_{\mathrm{MSW}} \simeq 1.6$. The slight deviation of the best fit from 1 reflects the slight mismatch of the best fit values of δm^2 from solar and KamLAND data separately

(see previous section), which is traded for an increase of $a_{\rm MSW}$, when this parameter is left free. Within the uncertainties, it can be claimed that the size of standard MSW effects in solar neutrino flavour transitions has been experimentally determined within a factor of ∼2 at 95% CL. Neutrino oscillation data thus provide an alternative (although inherently coarse) way to probe the magnitude of standard electroweak interactions (equation (16)) through the MSW effect—a very satisfactory result.

A final remark is in order. We have assumed for simplicity 2ν flavour oscillations in the channel $\nu_e \to \nu_a$ (ν_a being a linear combination of ν_μ and ν_τ) driven by the $(\delta m^2, \theta_{12})$ parameters. The (ν_μ, ν_τ) combination orthogonal to ν_a is probed by atmospheric $\nu_\mu \to \nu_\tau$ oscillations, with different parameters $(\Delta m^2, \theta_{23})$. As far as the third mixing angle θ_{13} is zero (and $\delta m^2/\Delta m^2 \ll 1$), the two oscillation channels are practically decoupled, and all our previous considerations hold without changes. However, for small but nonzero θ_{13}, the 3ν survival probability slightly deviates from the 2ν case for both solar and KamLAND ν_e oscillations:

$$P_{ee}^{3\nu} \simeq (1 - 2\sin^2\theta_{13})\, P_{ee}^{2\nu}. \tag{17}$$

This deviation is expected to lead to a slight relaxation of all previous bounds. For instance, in testing the null hypothesis $a_{\rm MSW} = 0$ (section 2.2), the minimum value of $\langle P_{ee}\rangle$ in the right panel of figure 2 can slightly decrease from 1/2 to $1/2 - \sin^2\theta_{13}$. Since the 3σ upper bound on $\sin^2\theta_{13}$ is at the level of a few per cent only (0.05–0.07, depending on details of global analyses, see e.g. [19, 47]), the relaxation of the upper bound on $\langle P_{ee}\rangle$ is marginal, and does not change our conclusions. In the more general case of variable $a_{\rm MSW}$, we have not performed the 3ν generalization of the analysis presented in this section and in figure 4. Our educated guess is that an allowance for small values of θ_{13} should only slightly weaken—but should not spoil—the main results presented in this work.

5. Conclusions and prospects

In recent years, solar and reactor neutrino data have been shown to be consistent with (and to favour) MSW effects in the flavour evolution of solar neutrinos. We have witnessed the emergence of indications in favour of MSW effects in the Sun in 2002, of compelling evidence for such effects in 2003, and of a first 'measurement' of the magnitude of such effects (within a factor of ∼2 at 95% CL) in 2004. In particular, the rejection of the null hypothesis of no MSW effect in 2003 (figure 2) and the increasingly stringent bounds on the size of the MSW dynamical term $\mathcal{H}_{\rm dyn}$ in equation (5) during the years 2002–2004 (figure 4) show a dramatic progress in this sense. At the same time, figures 1 and 3 testify the progress in constraining the mass-mixing parameters which govern the kinematical term $\mathcal{H}_{\rm kin}$ in equation (4).

We conclude by observing that, although MSW effects are an expected and unavoidable consequence of the standard theory of electroweak interactions, their basic confirmation in the current neutrino phenomenology represents an important and reassuring experimental accomplishment, which strengthen our confidence in the emerging picture of neutrino masses and mixings. Further confirmation of the MSW effects in the Sun might come from more precise solar and reactor data, as well as from possible future indications for slight MSW-induced distortions in the low-energy part of the SK and SNO spectra. Finally, in a more distant future, one might also hope to prove the occurrence of MSW effects in the Earth through very accurate determinations of day–night differences in the solar neutrino flux (not discussed in this work).

Acknowledgments

We thank A Marrone, A Palazzo and A M Rotunno for earlier collaboration on the topic of this paper and for their help in the updated analysis of 2004 data. We thank G Fiorentini and B Ricci the authors of [48], for graphically editing figure 1, and A Yu Smirnov for bringing [45] to our attention. Finally, we would like to thank the organizers of the Neutrino 2004 Conference in Paris, where this work was initiated, for kind hospitality.

References

[1] Homestake Collaboration, Cleveland B T *et al* 1998 *Astrophys. J.* **496** 505
[2] SAGE Collaboration, Abdurashitov J N *et al* 2002 *J. Exp. Theor. Phys.* **95** 181 (*Zh. Eksp. Teor. Fiz.* **95** 211)
[3] Kirsten T (for the GALLEX/GNO Collaboration) 2003 *Proc. of Neutrino 2002, 20th Int. Conf. on Neutrino Physics and Astrophysics (Munich, Germany 2002)* ed F von Feilitzsch and N Schmitz *Nucl. Phys.* B *Proc. (Suppl.)* **118** 33
[4] Cattadori C 2004 *Neutrino 2004, 21st Int. Conf. on Neutrino Physics and Astrophysics (Paris 2004)* neutrino2004.in2p3.fr
[5] SK Collaboration, Fukuda S *et al* 2001 *Phys. Rev. Lett.* **86** 5651, 5656
[6] SK Collaboration, Fukuda S *et al* 2002 *Phys. Lett.* B **539** 179
[7] SK Collaboration, Smy M B *et al* 2004 *Phys. Rev.* D **69** 011104
[8] SNO Collaboration, Ahmad Q R *et al* 2001 *Phys. Rev. Lett.* **87** 071301
[9] SNO Collaboration, Ahmad Q R *et al* 2002 *Phys. Rev. Lett.* **89** 011301
[10] SNO Collaboration, Ahmad Q R *et al* 2002 *Phys. Rev. Lett.* **89** 011302
[11] SNO Collaboration, Ahmed S N *et al* 2004 *Phys. Rev. Lett.* **92** 181301
[12] Bahcall J N 1989 *Neutrino Astrophysics* (Cambridge: Cambridge University Press)
[13] Bahcall J N and Pinsonneault M H 2004 *Phys. Rev. Lett.* **92** 121301
See also J N Bahcall's homepage www.sns.ias.edu/~jnb
[14] Pontecorvo B 1968 *Zh. Eksp. Teor. Fiz.* **53** 1717 (*Sov. Phys.—JETP* **26** 984)
[15] Maki Z, Nakagawa M and Sakata S 1962 *Prog. Theor. Phys.* **28** 870
[16] Kajita T and Totsuka Y 2001 *Rev. Mod. Phys.* **73** 85
[17] See, e.g., the reviews in Gonzalez-Garcia M C and Nir Y 2003 *Rev. Mod. Phys.* **75** 345
Barger V, Marfatia D and Whisnant K 2003 *Int. J. Mod. Phys.* E **12** 569
[18] CHOOZ Collaboration, Apollonio M *et al* 1999 *Phys. Lett.* B **466** 415
CHOOZ Collaboration Apollonio M *et al* 2003 *Eur. Phys. J.* C **27** 331
[19] Maltoni M, Schwetz T, Tortola M and Valle J W F 2004 *New J. Phys.* this issue (*Preprint* hep-ph/0405172)
[20] KamLAND Collaboration, Eguchi K *et al* 2003 *Phys. Rev. Lett.* **90** 021802
[21] Gratta G 2004 *Neutrino 2004, 21st Int. Conf. on Neutrino Physics and Astrophysics (Paris 2004)* neutrino2004.in2p3.fr
[22] KamLAND Collaboration, Araki T *et al* 2004 *Preprint* hep-ex/0406035
[23] Wolfenstein L 1978 *Phys. Rev.* D **17** 2369
Mikheev S P and Smirnov A Yu 1985 *Yad. Fiz.* **42** 1441 (*Sov. J. Nucl. Phys.* **42** 913)
[24] Barger V D, Whisnant K, Pakvasa S and Phillips R J N 1980 *Phys. Rev.* D **22** 2718
[25] Wolfenstein L 1978 *Neutrino '78, 8th Int. Conf. on Neutrino Physics and Astrophysics (Purdue University West Lafayette, Indiana 1978)* ed E C Fowler (Purdue, IN: Purdue University Press) p C3
[26] de Holanda P C, Liao W and Smirnov A Yu 2004 *Preprint* hep-ph/0404042
[27] Fogli G L, Lisi E, Palazzo A and Rotunno A M 2003 *Phys. Rev.* D **67** 073001
[28] Fogli G L, Lisi E, Marrone A and Palazzo A 2004 *Phys. Lett.* B **583** 149
[29] Fogli G L, Lisi E, Marrone A, Montanino D and Palazzo A 2002 *Phys. Rev.* D **66** 053010
[30] Fogli G L, Lisi E, Marrone A, Montanino D, Palazzo A and Rotunno A M 2003 *Phys. Rev.* D **67** 073002

[31] Kuo T K and Pantaleone J 1989 *Rev. Mod. Phys.* **61** 937
[32] Fogli G L, Lisi E, Montanino D and Palazzo A 2001 *Phys. Rev.* D **64** 093007
[33] Maltoni M, Schwetz T, Tortola M and Valle J W F 2003 *Phys. Rev.* D **67** 013011
[34] See also Bahcall J N and Peña-Garay C 2004 *New J. Phys.* **6** 63
[35] Lisi E, Marrone A, Montanino D, Palazzo A and Petcov S T 2001 *Phys. Rev.* D **63** 093002
[36] Gribov V N and Pontecorvo B 1969 *Phys. Lett.* B **28** 493
Bilenky S M and Pontecorvo B 1978 *Phys. Rep.* **41** 225
[37] Choubey S, Goswami S, Gupta N and Roy D P 2001 *Phys. Rev.* D **64** 053002
Choubey S, Goswami S and Roy D P 2002 *Phys. Rev.* D **65** 073001
[38] Berezinsky V, Gonzalez-Garcia M C and Peña-Garay C 2001 *Phys. Lett.* B **517** 149
[39] Smirnov A Yu 2002 *Neutrino 2002, 20th Int. Conf. on Neutrino Physics and Astrophysics (Munich 2002)* ed F von Feilitzsch and N Schmitz, p 87
[40] Villante F L, Fiorentini G and Lisi E 1999 *Phys. Rev.* D **59** 013006
[41] Maris M and Petcov S T 2002 *Phys. Lett.* B **534** 17
[42] SNO Collaboration, 'HOWTO use the SNO Salt flux results'? available at www.sno.phy.queensu.ca
[43] Lisi E, talk at *NOON 2003, 4th Int. Workshop on Neutrino Oscillations and their OrigiN (Kanazawa 2003)* www-sk.icrr.u-tokyo.ac.jp/noon2003
[44] Lisi E, Palazzo A and Rotunno A M 2004 *Astropart. Phys.* in press (*Preprint* hep-ph/0403036)
[45] Suzuki A 2004 talk at *Nobel Symp. on Neutrino Physics (Enköping 2004)* available at www.physics.kth.se/nobel2004
[46] Bandyopadhyay A, Choubey S, Goswami S, Petcov S T and Roy D P 2004 *Preprint* hep-ph/0406328
Bahcall J N, Gonzalez-Garcia M C and Pena-Garay C 2004 *Preprint* hep-ph/0406294
Miranda O G, Tortola M A and Valle J W F 2004 *Preprint* hep-ph/0406280
Aliani P, Antonelli V, Ferrari R, Picariello M and Torrente-Lujan E 2004 *Preprint* hep-ph/0406182
[47] Goswami S 2004 *Neutrino 2004, 21st Int. Conf. on Neutrino Physics and Astrophysics (Paris 2004)* neutrino2004.in2p3.fr
[48] Fiorentini G and Ricci B 2003 *Preprint* astro-ph/0310753

New Journal of Physics
The open-access journal for physics

Extra-galactic sources of high-energy neutrinos

Eli Waxman
Physics Faculty, Weizmann Institute of Science, Rehovot 76100, Israel
E-mail: waxman@wicc.weizmann.ac.il

New Journal of Physics **6** (2004) 140
Received 23 June 2004
Published 25 October 2004
Online at http://www.njp.org/
doi:10.1088/1367-2630/6/1/140

Abstract. The existence of extra-galactic high-energy neutrino sources is implied by observations of ultra-high energy, $>10^{19}$ eV, cosmic-rays (UHECRs). Phenomenological, model-independent constraints imposed on the characteristics of the extra-galactic neutrino sources are presented. It is argued that high-energy neutrino telescopes under construction may reach the sensitivity required for detecting the extra-galactic neutrino signal. Such detection will allow to identify the sources of UHECRs and to test models of these sources. It will also provide information on fundamental neutrino properties.

Contents

1. Introduction and summary **1**
2. Phenomenological considerations **4**
2.1. The luminosity constraint for UHECR sources and its implications for high-energy neutrino telescopes . . . 4
2.2. The WB bound . . . 7
2.3. GZK neutrinos . . . 9
3. GRBs **11**
3.1. The fireball model . . . 11
3.2. The association of GRBs and UHECRs . . . 11
3.3. 100 TeV neutrinos . . . 12
3.4. TeV neutrinos . . . 13
References **13**

1. Introduction and summary

The detection of MeV neutrinos from the Sun enabled direct observations of nuclear reactions in the core of the Sun, as well as studies of fundamental neutrino properties [1]. Existing MeV

PII: S1367-2630(04)82530-8
© IOP Publishing Ltd and Deutsche Physikalische Gesellschaft

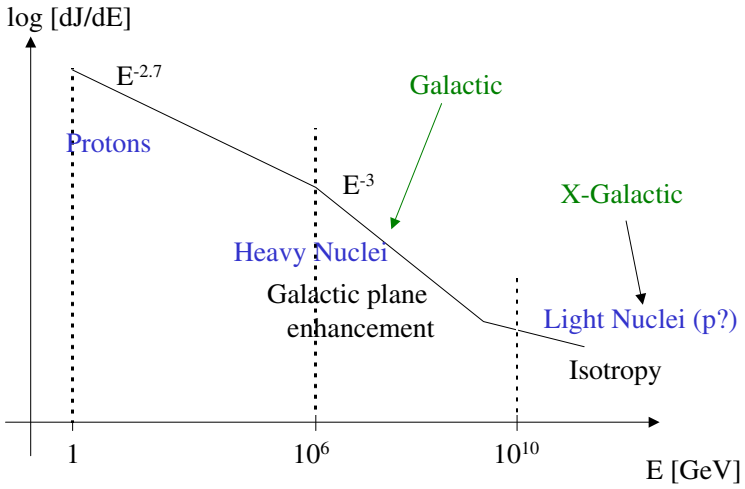

Figure 1. A schematic description of the differential spectrum and of the composition of cosmic rays observed on Earth.

neutrino 'telescopes' are also capable of detecting neutrinos from supernova explosions in our local galactic neighbourhood, at distances <100 kpc, such as supernova 1987A. The detection of neutrinos emitted by SN1987A provided a direct observation of the core collapse process and constraints on neutrino properties [2]. The main goal of the construction of high energy, >1 TeV, neutrino telescopes [3] is the extension of the distance accessible to neutrino astronomy to cosmological scales.

The existence of extra-galactic high-energy neutrino sources is implied by cosmic-ray observations. The cosmic-ray spectrum extends to energies $\sim 10^{20}$ eV [4] (see figure 1), and is likely dominated beyond $\sim 10^{19}$ eV by extra-galactic sources of protons. The flattening of the cosmic-ray spectrum at $\sim 10^{19}$ eV, accompanied by the evidence for a composition change from heavy nuclei to light ones at this energy and the lack of any anisotropy signal, suggest that a heavy nuclei galactic component, dominant below $\sim 10^{19}$ eV, is overtaken by an extra-galactic proton component at higher energy. The origin of the highest energy, $>10^{19}$ eV, cosmic rays (UHECRs) is a mystery. However, irrespective of the sources some fraction of the protons are expected to produce pions as they escape their source by either hadronic collisions with ambient gas or photoproduction with source photons, leading to electron and muon neutrino production through the decay of charged pions.

In section 2 a phenomenological, model-independent discussion of extra-galactic high-energy neutrino sources is presented. In section 2.1 we show that the stringent constraints, which are imposed on the properties of possible UHECR sources by the high energies observed, rule out almost all source candidates and also suggest that the UHECR sources may be detectable at ~ 1 TeV to ~ 1 PeV neutrino energies by km-scale (i.e. Gt scale) neutrino telescopes. These constraints suggest that γ-ray bursts and active galactic nuclei are the most plausible sources of UHECRs, and may be detectable by km-scale neutrino telescopes. The required large effective volume will be achieved by optical Cerenkov detectors being constructed under ice (AMANDA [5] and IceCube [6]) and water (ANTARES [7], NESTOR [8] and NEMO [9]).

In section 2.2 we discuss the constraints imposed by cosmic-ray observations on the extra-galactic high-energy neutrino intensity produced by sources which, like γ-ray bursts and jets of

active galactic nuclei, are optically thin for high-energy nucleons to p, γ and p–p(n) interactions. For sources of this type, the energy generation rate of neutrinos cannot exceed the energy generation rate of high-energy protons implied by the observed cosmic-ray flux, setting an upper bound of $E_\nu^2\Phi_\nu < 2 \times 10^{-8}$ GeV cm^{-2} s^{-1} sr^{-1} to the extra-galactic high-energy neutrino intensity [10, 11] (figure 4, equation (7)). This upper bound, which came to be known in the literature as the Waxman–Bahcall (WB) bound, implies that km-scale (i.e. Gt) neutrino telescopes are needed to detect the expected extra-galactic flux in the energy range of ∼1 TeV to ∼1 PeV, and much larger effective volume is required to detect the flux at higher energy. We note that the WB bound may be evaded by postulating the existence of sources which are optically thick for protons to p, γ or p–p(n) interactions [10]–[12]. However, the existence of such 'hidden' or 'neutrino only' factories is not motivated by measurements of the cosmic-ray flux or by any electromagnetic observations.

In section 2.3, we discuss 'GZK neutrinos'. If the sources of UHECRs are extra-galactic and the particles are indeed protons, then these particles lose energy by interacting with the cosmic microwave background photons [13]. Protons of energy exceeding the threshold for pion production, $\sim 5 \times 10^{19}$ eV, lose most of their energy over a time, short compared to the age of the universe (the 'GZK effect'). The decay of the pions generates a background of high-energy neutrinos ([14]; for detailed updated discussion see [15] and references therein). The intensity of this background, at neutrino energies $\sim 10^{19}$ eV, should be similar to the WB bound, $E_\nu^2\Phi_\nu \sim 2 \times 10^{-8}$ GeV cm^{-2} s^{-1} sr^{-1}. Coherent radio Cerenkov detectors (ANITA [16] and RICE [17]), and possibly large air-shower detectors (Auger [18] and OWL-AIRWATCH [19]), may provide the large effective volume required for the detection of the 'GZK neutrinos'. Their detection will help to determine the identity of the cosmic-ray particles and will constrain the redshift evolution of UHECR sources.

The rapid energy loss of $>5 \times 10^{19}$ eV protons implies, in addition to the generation of high-energy neutrinos, a strong suppression of UHECR flux above 5×10^{19} eV (the 'GZK suppression'). The flux measurements of all UHECR experiments are in agreement below 10^{20} eV, and consistent with the expected GZK suppression [20] (figure 3). At higher energy, $\sim 2 \times 10^{20}$ eV, the flux reported by one experiment is higher by a factor of ∼3 than that reported by other experiments, which report a flux consistent with the GZK suppression. At still higher energy, $>3 \times 10^{20}$ eV, the exposure of all experiments is insufficient to derive a reliable estimate of the flux. The uncertainty in the experimental determination of the UHECR flux at energies $>10^{20}$ eV lead many authors to speculate that there may be a new source of ultra-high-energy cosmic rays and neutrinos beyond 10^{20} eV, producing a neutrino intensity higher than the WB bound at these neutrino energies (see section 2.3). Since, however, we do not have direct experimental evidence for a rapid increase beyond 3×10^{20} eV of the cosmic-ray energy generation rate with cosmic-ray energy, it is reasonable in our view to extend the WB limit beyond 10^{19} eV by simply extrapolating the horizontal line in figure 4 to higher energies. The validity of this extrapolation will be tested by future measurements of the spectrum of ultra-high-energy cosmic rays and neutrinos.

In section 3, we discuss high-energy neutrino emission from gamma-ray bursts (GRBs). This discussion illustrates the applicability of the phenomenological, model-independent arguments presented in section 2 through a discussion of (a model of) a particular, plausible extra-galactic source of UHECRs and high-energy neutrinos (for discussion of AGN models, see [21] and references therein). In section 3.1 we present a brief discussion of the fireball model of GRBs, which has recently gained strong support from 'afterglow' observations (for more complete

discussions see [22]–[24]), and in section 3.2 we briefly present the arguments suggesting a connection between GRBs and UHECR sources (see [23, 24] for more detailed discussion). In section 3.3 we show that the production of 100 TeV neutrinos in the region where GRB in γ-rays are produced is a generic prediction of the fireball model. It is a direct consequence of the assumptions that energy is carried from the underlying engine as kinetic energy of protons and that γ-rays are produced by synchrotron emission of shock accelerated particles. The predicted neutrino intensity is $\approx$20% of the WB intensity bound, implying a detection of $\sim$20 muon induced neutrino events per year in a km-scale neutrino detector [25, 26] (since these events should be correlated in time and direction with GRB in γ-rays, the search for GRB neutrinos is essentially background-free). Neutrinos may also be produced in other stages of fireball evolution, at energies different than 100 TeV. The production of these neutrinos is dependent on additional model assumptions. As an example, we discuss in section 3.4 the production of TeV neutrinos expected in the 'collapsar' scenario, where GRB progenitors are associated with the collapse of massive stars. (A more detailed and comprehensive discussion can be found in [23, 24].)

The discussion of GRB neutrino emission demonstrates that in addition to identifying the sources of UHECRs, high-energy neutrino telescopes can also provide a unique probe of these sources. Moreover, the detection of high-energy neutrinos from extra-galactic sources may also provide information on fundamental neutrino properties [25]. High-energy neutrinos are expected to be produced in astrophysical sources by the decay of charged pions, which lead to the production of muon and electron neutrinos. However, oscillation to ν_τ's [27] implies that neutrino telescopes should detect equal numbers of ν_μ's and ν_τ's. Up-going τ's, rather than μ's, would be a distinctive signature of such oscillations. The detection of neutrinos from GRBs could be used to test the simultaneity of neutrino and photon arrival to an accuracy of $\sim$1 s, checking the assumption of special relativity that photons and neutrinos have the same limiting speed. These observations would also test the weak equivalence principle, according to which photons and neutrinos should suffer the same time delay as they pass through a gravitational potential. With 1 s accuracy, a burst at 1 Gpc would reveal a fractional difference in limiting speed of 10^{-17}, and a fractional difference in gravitational time delay of order 10^{-6} (considering the galactic potential alone). Previous applications of these ideas to supernova 1987A (see [28] for a review), yielded much weaker upper limits of orders 10^{-8} and 10^{-2}, respectively.

2. Phenomenological considerations

2.1. The luminosity constraint for UHECR sources and its implications for high-energy neutrino telescopes

A detailed discussion of particle acceleration is beyond the scope of this paper. However, the essence of the challenge of accelerating particles to $>10^{19}$ eV can be understood using the following simple arguments. Consider an astrophysical source driving a flow of magnetized plasma, with characteristic magnetic field strength B and velocity v. Imagine now a conducting wire encircling the source at radius R, as illustrated in figure 2. The potential generated by the moving plasma is given by the time derivative of the magnetic flux Φ and is therefore given by $V = \beta BR$ where $\beta = v/c$. A proton which is allowed to be accelerated by this potential drop would reach energy $E_p \sim \beta eBR$. The situation is somewhat more complicated in the case

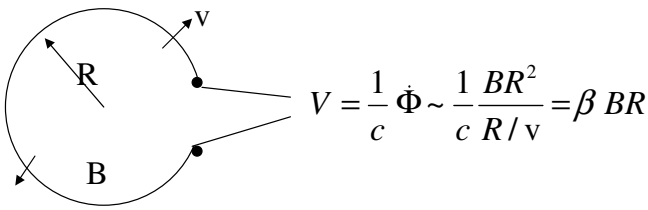

Figure 2. Potential drop generated by an outflow of magnetized plasma.

of a relativistic outflow, where $\Gamma \equiv (1-\beta^2)^{-1/2} \gg 1$. In this case, the proton is allowed to be accelerated only over a fraction of the radius R, comparable to R/Γ. To see this, one must realize that as the plasma expands, its magnetic field decreases, so the time available for acceleration corresponds, say, to the time of expansion from R to $2R$. In the observer frame this time is R/c, while in the plasma rest frame it is $R/\Gamma c$. Thus, a proton moving with the magnetized plasma can be accelerated over a transverse distance $\sim R/\Gamma$. This sets a lower limit to the product of the magnetic field and source size, which is required to allow acceleration to E_p,

$$BR > \Gamma E_p/e\beta. \tag{1}$$

Equation (1) also sets a lower limit to the rate L at which energy should be generated by the source. The magnetic field carries with it an energy density $B^2/8\pi$, and the flow therefore carries with it an energy flux $> vB^2/8\pi$ (some energy is also carried as plasma kinetic energy), which implies $L > vR^2B^2$. Using equation (1), we find

$$L > \frac{\Gamma^2}{\beta}\left(\frac{E_p}{e}\right)^2 c = 10^{45.5}\frac{\Gamma^2}{\beta}\left(\frac{E_p}{10^{20}\,\mathrm{eV}}\right)^2 \mathrm{erg\,s^{-1}}. \tag{2}$$

Only two types of sources are known to satisfy this requirement. The brightest steady sources are active galactic nuclei (AGN). For them Γ is typically between 3 and 10, implying $L > 10^{47}\mathrm{erg\,s^{-1}}$, which may be satisfied by the brightest AGN.[1] The brightest transient sources are GRBs. For these sources $\Gamma \simeq 10^{2.5}$ implying $L > 10^{50.5}\,\mathrm{erg\,s^{-1}}$, which is generally satisfied since the typical observed MeV-photon luminosity of these sources is $L_\gamma \sim 10^{52}\,\mathrm{erg\,s^{-1}}$.[2]

It is instructive to compare equation (2) to the constraints imposed on a neutrino source by requiring it to be detectable by a km-scale neutrino telescope. Consider the minimum flux of a source that can be detected by a neutrino telescope with effective area A (in the plane perpendicular to the source direction) and exposure time T. The probability that a muon

[1] Phenomenological arguments similar to those used here were applied by Lovelace [29] to a specific model of AGN jets, in which the relation between proton energy and source luminosity may be written as $L \sim 10^{46}(E_p/10^{20}\,\mathrm{eV})^2\,\mathrm{erg\,s^{-1}}$, consistent with equation (2). The derivation given here is more general, as it does not assume a specific model and includes the dependence on characteristic plasma velocity.

[2] It was recognized earlier (see [30] and references therein) that while highly magnetized neutron stars may also satisfy equation (1), it is hard to utilize the potential drop in their electromagnetic winds for proton acceleration to ultra-high energy. The mechanisms recently proposed for acceleration in 'magnetars' (see [31] and references therein) also face serious difficulties. In [31], for example, the electromagnetic wind must penetrate through a supernova envelope shell without losing energy to acceleration of the shell and without 'contaminating' the wind with baryons. The mechanism by which such penetration may be achieved is unclear.

produced by the interaction of a muon neutrino with a nucleon will cross the detector is given by the ratio of the muon and neutrino mean free paths.[3] For water and ice, this probability is $P_{\nu\mu} \approx 10^{-4}(E_\nu/100\,\mathrm{TeV})^\alpha$, with $\alpha = 1$ for $E_\nu < 100\,\mathrm{TeV}$ and $\alpha = 0.5$ for $E_\nu > 100\,\mathrm{TeV}$ (see e.g. [32]). Thus, the neutrino flux required for the detection of N events is

$$f_\nu \approx 5 \times 10^{-12} N \left(\frac{E_\nu}{100\,\mathrm{TeV}}\right)^{1-\alpha} \left(\frac{AT}{\mathrm{km}^2\,\mathrm{yr}}\right)^{-1} \mathrm{erg\,cm^{-2}\,s^{-1}}. \tag{3}$$

A lower limit to the source flux is also set by the requirement that the signal would exceed the background produced by atmospheric neutrinos. The flux of atmospheric neutrinos, averaged over zenith angle, is approximately given by $\Phi_\nu^A \approx 5 \times 10^{-8}(E_\nu/100\,\mathrm{TeV})^{-\beta}\,\mathrm{GeV\,cm^{-2}\,s^{-1}\,sr^{-1}}$, with $\beta = 1.7$ for $E_\nu < 100\,\mathrm{TeV}$ and $\beta = 2.0$ for $E_\nu > 100\,\mathrm{TeV}$. For a neutrino detector with angular resolution $\Delta\theta$, the source flux for which the signal constitutes a 5σ detection over the atmospheric background flux is

$$f_\nu \approx 3 \times 10^{-12} \left(\frac{E_\nu}{100\,\mathrm{TeV}}\right)^{-\beta/2} \left(\frac{\Delta\theta}{1^\circ}\right) \left(\frac{AT}{\mathrm{km}^2\,\mathrm{yr}}\right)^{-1/2} \mathrm{erg\,cm^{-2}\,s^{-1}}. \tag{4}$$

Comparing equations (3) and (4), we find that for km-scale detectors, the atmospheric neutrino background poses a less stringent constraint on source flux than the requirement of a detectable signal, except at low energies $\ll 100\,\mathrm{TeV}$.

The luminosity of a cosmologically distant source which corresponds to the flux of equation (3) is

$$L_\nu \approx 10^{46} N d_{L,28}^2 \left(\frac{E_\nu}{100\,\mathrm{TeV}}\right)^{1-\alpha} \left(\frac{AT}{\mathrm{km}^2\,\mathrm{yr}}\right)^{-1} \mathrm{erg\,s^{-1}}. \tag{5}$$

Here, $d_L = 10^{28} d_{L,28}\,\mathrm{cm}$ is the luminosity distance and $d_{L,28} \sim 1$ for sources at redshift $z = 1$. The neutrino luminosity is, of course, a lower limit to the total energy output rate from the source. The lower limit set by equation (5) to the luminosity of a steady source that may be detectable at $\sim 10^{1\pm1}$ TeV neutrino energies by a km-scale neutrino detector, $L > 10^{46}\,\mathrm{erg\,s^{-1}}$, is similar to the constraint of equation (2) imposed by requiring proton acceleration to $\sim 10^{20}$ eV. As mentioned following equation (2), the only steady sources bright enough to possibly satisfy these constraints are AGN. Equations (2) and (5) also imply similar luminosity constraints on GRBs. For a typical GRB duration of $10^{1.5}$ s, equation (5) implies $L > 10^{52}\,\mathrm{erg\,s^{-1}}$, similar to the constraint imposed by equation (2) for the typical Lorentz factor appropriate for these sources, $\gamma \simeq 10^{2.5}$.

The phenomenological arguments presented above imply that the luminosity that must be produced by a source of UHECRs, equation (2), may allow such a source to be detectable by a km-scale neutrino detector at $\sim 10^{1\pm1}$ TeV neutrino energy (see equation (5)). Equation (5) also implies that the detection of sources at $\gg 10^2$ TeV neutrino energy would require detectors with effective volume $\gg 1\,\mathrm{km}^3$. The most plausible sources of UHECRs, GRBs and AGN, are therefore also the most likely to be detectable neutrino sources. Such detection would be possible only if the neutrino luminosity of the source constitutes a significant fraction of the total source luminosity. For GRBs, this issue is discussed in some more detail in section 3, within the context of current GRB models.

[3] Note that the mean free path of muons of energy >0.3 TeV is of order 1 km. Thus, a detector with effective cross-sectional area A corresponds to a detector with an effective volume $\sim A \times (1\,\mathrm{km})$.

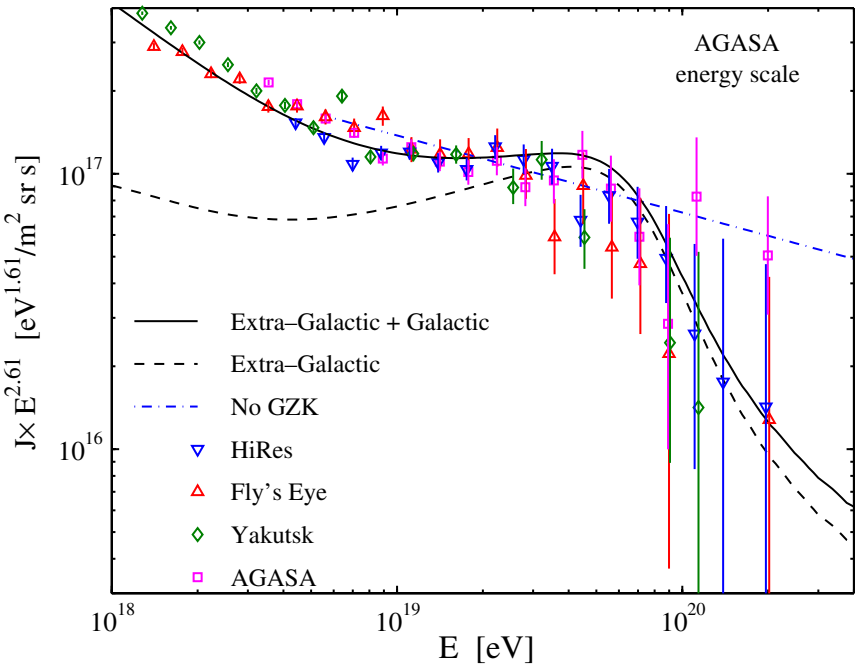

Figure 3. The solid curve shows the energy spectrum derived from the two-component model discussed in section 2.2 (the energy generation rate of the extra-galactic component, equation (6), was assumed to evolve rapidly, $\phi(z) \propto (1+z)^3$ up to $z = 2$, following the evolution of QSOs [40] and star formation rate [41]). The dashed curve shows the extra-galactic component contribution. The 'No GZK' curve is an extrapolation of the $E^{-2.75}$ energy spectrum derived for the energy range 6×10^{18}–4×10^{19} eV [4]. Data taken from [35]–[38] (AGASA's energy scale was chosen).

The current upper limits provided by the AMANDA experiment on neutrino fluxes from steady point sources, $\sim 10^{-10}$ erg cm^{-2} s^{-1} [33], indicate that the sensitivity required to detect the fluxes expected from cosmological sources will be achieved by km-scale detectors.

2.2. The WB bound

As explained in section 1, cosmic-ray observations suggest that the cosmic-ray flux is dominated above 10^{19} eV by extra-galactic sources of protons (and at lower energy by galactic heavy nuclei sources). Under the assumption that the UHECRs are extra-galactic protons, the observed flux of UHECRs allows one to determine the rate (per unit time and volume) at which high-energy protons are produced. Such analysis was carried out in [34], based on Fly's Eye [35] and AGASA [36] data available at the time, constraining the rate of energy production in protons in the energy range of 10^{19} eV $< E_p < 10^{21}$ eV to $4.5 \pm 1.5 \times 10^{44}$ erg Mpc^{-3} yr^{-1}. Assuming the production spectrum to follow a power-law, $\mathrm{d}N/\mathrm{d}E_p \propto E_p^{-n}$, the same analysis constrained n to $1.8 < n < 2.8$. A recent analysis, with larger AGASA exposure and including data from Yakutsk [37] and new data from HiRes [38], gives consistent results [20]. Figure 3 presents a comparison of available UHECR data with the predictions of a model, where extra-galactic protons in the

energy range 10^{19}–10^{21} eV are produced by cosmologically distributed sources at a rate and spectrum given by

$$E_p^2 \frac{\mathrm{d}\dot{N}_p}{\mathrm{d}E_p} = 0.65 \times 10^{44}\,\mathrm{erg\,Mpc^{-3}\,yr^{-1}}\phi(z), \tag{6}$$

corresponding to energy production rate of $3 \times 10^{44}\,\mathrm{erg\,Mpc^{-3}\,yr^{-1}}$ in protons in the energy range of $10^{19}\,\mathrm{eV} < E_p < 10^{21}\,\mathrm{eV}$ and spectral index $n = 2$.[4] Here, $\phi(z)$ accounts for redshift evolution and $\phi(z = 0) = 1$. The spectrum above 10^{19} eV is only weakly dependent on $\phi(z)$ since proton energy loss limits their propagation distance. For the heavy nuclei component dominating at lower, $<10^{19}$ eV, energy we have taken the Fly's Eye experimental fit [35], $\mathrm{d}N/\mathrm{d}E \propto E^{-3.50}$.

Figure 3 demonstrates that model predictions are in good agreement with the data of all experiments in the energy range 10^{19}–10^{20} eV. The uncertainty in the derived energy production rate, equation (6), due to systematic uncertainties in the absolute energy calibration of the experiments is ≈20% [20].[5] Above 10^{20} eV the Fly's Eye, HiRes and Yakutsk experiments are in agreement with each other and with the model, while the AGASA experiment reports a flux higher by a factor ∼3.

The energy production rate, equation (6), sets an upper bound to the neutrino intensity produced by sources which, like GRBs and AGN jets, are optically thin for high-energy nucleons to p, γ and p–p(n) interactions. For sources of this type, the energy generation rate of neutrinos cannot exceed the energy generation rate implied by assuming that all the energy injected as high-energy protons is converted to pions (via p, γ and p–p(n) interactions). The resulting upper bound (for muon and anti-muon neutrinos, neglecting mixing) is [10]

$$E_\nu^2 \Phi_\nu \;<\; 2 \times 10^{-8} \xi_z \left[\frac{(E_p^2\,\mathrm{d}\dot{N}_p/\mathrm{d}E_p)_{z=0}}{10^{44}\,\mathrm{erg\,Mpc^{-3}\,yr^{-1}}} \right] \mathrm{GeV\,cm^{-2}\,s^{-1}\,sr^{-1}}. \tag{7}$$

ξ_z is (a dimensionless parameter) of order unity, which depends on the redshift evolution of $E_p^2\,\mathrm{d}\dot{N}_p/\,\mathrm{d}E_p$ (see equation (6)). In order to obtain a conservative upper bound, we adopt $(E_p^2\,\mathrm{d}\dot{N}_p/\,\mathrm{d}E_p)_{z=0} = 10^{44}\,\mathrm{erg\,Mpc^{-3}\,yr^{-1}}$ and a rapid redshift evolution, $\Phi(z) = (1+z)^3$ up to $z = 2$, following the evolution of QSOs [40], which exhibit the fastest (known) source evolution. This evolution, which also approximately describes the evolution of star formation rate [41], yields $\xi_z \approx 3$.

Below $\sim 10^{19}$ eV, the extra-galactic proton flux is dominated by the galactic cosmic-ray background. In our derivation of the neutrino intensity bound, we have assumed that the generation rate of extragalactic protons extends to energies lower than $\sim 10^{19}$ eV as $\mathrm{d}\dot{N}_p/\mathrm{d}E_p \propto E_p^{-2}$. The energy generation rate at these energies may, however, be higher, since part of the

[4] An energy spectrum similar to the assumed $\mathrm{d}N/\mathrm{d}E_p \propto E_p^{-2}$ has been observed for both non-relativistic [4] and relativistic [39] shocks. It is believed to be due to Fermi acceleration in collisionless shocks [4, 39], although a first principles understanding of the process is not yet available.

[5] As explained in detail in [20], the various experiments are consistent with each other when systematic errors in the absolute energy scale of the events are taken into account. The relative systematic shifts in absolute energy calibration between Fly' Eye and the other experiments, required to bring into agreement the fluxes measured at 10^{19} eV by the different experiments, are {−11%, +7.5%, −19%} for {AGASA, HiRes, Yakutsk}, respectively. All shifts are well within the published systematic errors.

cosmic-ray flux below $\sim 10^{19}$ eV may be produced by extra-galactic sources of protons. The available observational evidence suggests that only a small fraction of the cosmic-ray flux in the energy range 10^{14}–10^{17} eV is composed of protons. Direct (balloon) composition measurements at 10^{14} eV [42] show that the fraction of cosmic-ray flux composed of protons at this energy is $\sim$20%. Air-shower and cosmic-ray tracking detectors measurements indicate [43] that the proton fraction decreases in the energy range 10^{14}–10^{16} eV. In fact, the Fly's Eye and AGASA experiments support [44] a composition strongly dominated by (consistent with 100%) heavy nuclei at 10^{17} eV. Assuming, conservatively, that $\sim$10% of the cosmic rays in this energy region are protons, the neutrino bound may be raised at energies $E_\nu < 10^{16}$ eV. (Since the cosmological model we have used accounts for $\sim$10% of the total cosmic-ray flux at 10^{17} eV, and a progressively larger fraction at higher energies, one cannot increase the upper bound on neutrino fluxes at energies $\geqslant 10^{16}$ eV.) Since the energy density in cosmic rays is approximately proportional to E^{-1} for energies less than 10^{18} eV, the actual extra-galactic neutrino flux could exceed the most stringent WB limit by a factor of $(10^{16}\,\mathrm{eV}/E_\nu)$ for neutrino energies $E_\nu < 10^{16}$ eV [10, 11].

The WB upper bound is compared in figure 4 with current limits of the lake Baikal and of the AMANDA experiments on the diffuse neutrino intensity, and with the expected sensitivity of planned neutrino telescopes.

The figure indicates that km-scale (i.e. Gt) neutrino telescopes are needed to detect the expected extra-galactic flux in the energy range of $\sim$1 TeV to $\sim$1 PeV, and that much larger effective volume is required to detect the flux at higher energy.

2.3. GZK neutrinos

Protons of energy exceeding the threshold for pion production, $\sim 5 \times 10^{19}$ eV, lose most of their energy over a time, short compared to the age of the universe: $>10^{20}$ eV protons, for example, lose most of their energy over $<3 \times 10^8$ yr. Assuming that high-energy protons are produced by extra-galactic sources at the rate implied by UHECR observations (equation (6)), the proton energy loss to pion production produces a neutrino intensity similar to the WB bound. The expected GZK neutrino intensity is schematically shown in figure 4. Since most of the pions are produced in interactions with photons of energy corresponding to the Δ-resonance, each of the resulting neutrinos carry approximately 5% of the proton energy. The neutrino background is therefore close to the WB bound above $\sim 5 \times 10^{18}$ eV, where neutrinos are produced by $\sim 10^{20}$ eV protons. The intensity at lower energies is lower, since protons of lower energy do not lose all their energy over the age of the universe. The GZK intensity in figure 4 decreases at the highest energies since it was assumed that the maximum energy of protons produced by UHECR sources is 10^{21} eV. The results of detailed calculations of the expected GZK neutrino intensity [15] are in agreement with the qualitative analysis presented above. Recently, it was pointed out that the GZK neutrino spectrum at the low energy end, $<10^{18}$ eV, is expected to be modified due to the interaction of high-energy protons with the infrared background [47].

The detection of GZK neutrinos will be a milestone in neutrino astronomy. Most important, neutrino detectors with sensitivity better than the WB bound at energies $>10^{18}$ eV will test the hypothesis that the UHECR are protons (possibly somewhat heavier nuclei) of extra-galactic origin. Measurements of the flux and spectrum would constrain the redshift evolution of the sources. The GZK neutrino intensity presented in figure 4 is obtained for rapidly evolving sources. For non-evolving sources the intensity is lower by a factor of $\approx$5.

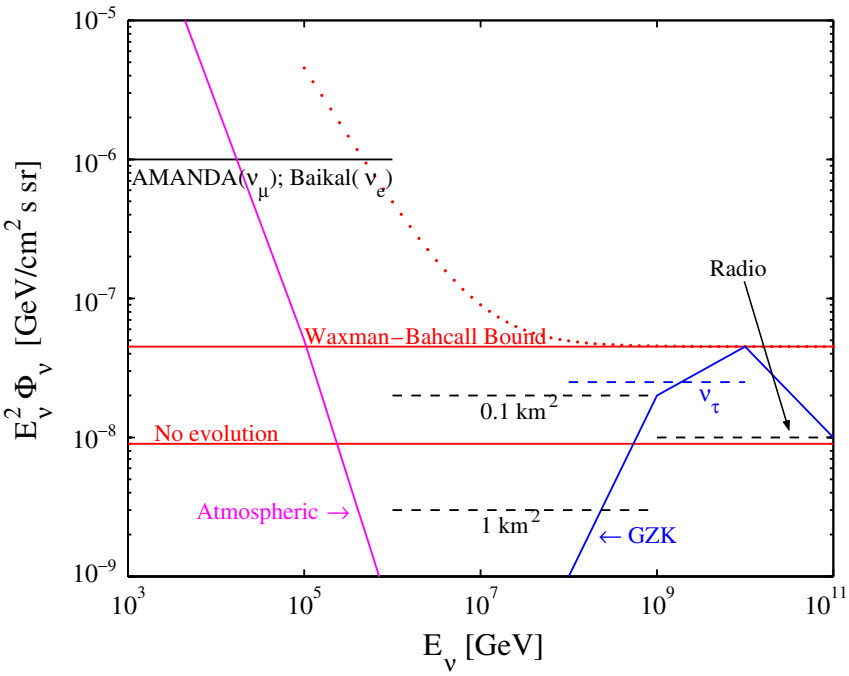

Figure 4. The upper bound imposed by UHECR observations on the extra-galactic high-energy muon neutrino intensity (lower-curve: no evolution of the energy production rate of equation (6); upper curve: assuming evolution following star formation rate), compared to the atmospheric neutrino background and to the experimental upper bounds of BAIKAL [45] and AMANDA [46]. The dotted curve is the maximum contribution due to possible extra-galactic component of lower-energy, $<10^{17}$ eV, protons as first discussed in [10] (see text). The curve labelled 'GZK' shows the intensity due to interaction with micro-wave background photons. Dashed curves show the expected sensitivity of 0.1 Gt (AMANDA, ANTARES, NESTOR) [5]–[8] and 1 Gt (IceCube, NEMO) [6, 9] optical Cerenkov detectors, of the coherent radio Cerenkov (balloon) experiment ANITA [16] and of the Auger air-shower detector (sensitivity to ν_τ) [18]. Radio Cerenkov detectors in ice (RICE [17]) and space air-shower detectors (OWL-AIRWATCH [19]) may also achieve the sensitivity required to detect fluxes lower than the WB bound at energies $>10^{18}$ eV.

The uncertainty in the experimental determination of the UHECR flux at energies $>10^{20}$ eV lead many authors to speculate that there may be a new source of ultra-high-energy cosmic rays and neutrinos beyond 10^{20} eV, producing a neutrino intensity higher than the WB bound at these neutrino energies. Most of these models involve 'new physics': decay of super-massive dark matter particles (see e.g. [48]) and topological defects (see e.g. [49]) have been proposed to produce ultra-high-energy neutrinos with small associated cosmic-ray proton flux, thus possibly producing a flux of neutrinos exceeding the WB bound. Other models postulate the existence of 'neutrino-only' sources, producing ultra-high-energy neutrinos with small associated proton or γ-ray flux, without specifying a model for such sources [50]. In our view, it is reasonable to extend the WB limit beyond 10^{20} eV by simply extrapolating the horizontal line in figure 4 to

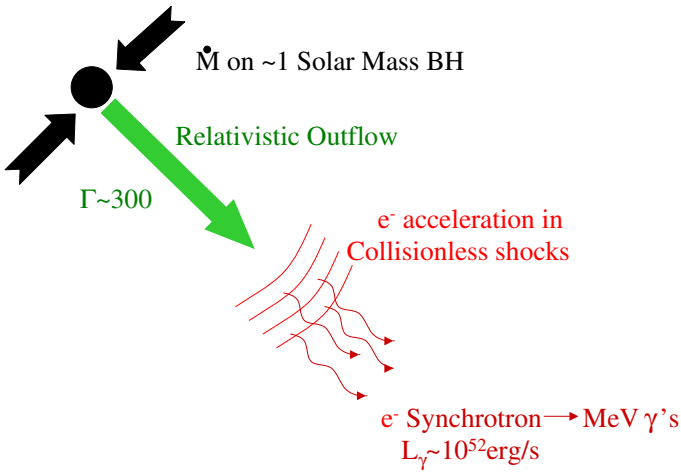

Figure 5. The fireball scenario of GRB production.

higher energies. The validity of this extrapolation will be tested by future measurements of the spectrum of ultra-high-energy cosmic rays and neutrinos.

3. GRBs

3.1. The fireball model

GRBs are short, typically tens of seconds long, flashes of γ rays, carrying most of their energy in >1 MeV photons. The detection in the past few years of 'afterglows', delayed x-ray, optical and radio emission from GRB sources, proved that the sources lie at cosmological distances, and provided strong support for the scenario of GRB production described in figure 5 [22]–[24]. The energy source is believed to be rapid mass accretion on a newly formed solar-mass black hole (or, possibly, neutron star). Recent observations suggest that the formation of the central compact object is associated with type Ib/c supernovae [51].

The energy release drives an ultra-relativistic, $\Gamma \sim 10^{2.5}$, plasma outflow. The emission of γ-rays is assumed to be due to internal collisionless shocks within the relativistic wind, the 'fireball,' which occur at a large distance from the central black hole due to variability in the wind emitted from the central 'engine'. It is commonly assumed that electrons are accelerated to high energy within the collisionless shocks, and that synchrotron emission from these shock accelerated electrons produces the observed γ-rays. At still larger distances, the wind impacts on surrounding medium. Here too, the collisionless shock driven into the ambient gas is believed to accelerate electrons to high energy, leading to synchrotron emission which accounts for the 'afterglow'.

3.2. The association of GRBs and UHECRs

GRBs were suggested to be UHECR sources in [52, 53]. The GRB–UHECR association was based on two major arguments in [52]: (i) the constraints imposed on the relativistic wind by requiring that it would produce the observed γ-rays are remarkably similar to those imposed by

Table 1. Constraints on GRB wind parameters from photon observations and from the requirement for proton acceleration to 10^{20} eV.

Wind property	MeV γ-rays	10^{20} eV protons
u_B/u_e	$\geqslant 0.1$	$\geqslant 0.02$
Γ	$\geqslant 300$	$\geqslant 100$
$\mathrm{d}N/\mathrm{d}E$	$\mathrm{d}N_e/\mathrm{d}E_e \propto E_e^{-2}$	$\mathrm{d}N_p/\mathrm{d}E_p \propto E_p^{-2}$

the requirement that the wind would allow proton acceleration to 10^{20} eV; (ii) the rate (per unit volume) at which energy is generated by GRBs in γ-rays is similar to the rate at which energy should be generated in high-energy protons in order to account for the observed UHECR flux. Both arguments have been strengthened by more recent GRB and UHECR observations [54].

The constraints on wind parameters are summarized in table 1 (for a pedagogical discussion see [23, 24]). γ-ray observations require the ratio of magnetic field and electron energy densities, u_B/u_e, to exceed 0.1 in order to produce electron synchrotron emission in the MeV range, $\Gamma > 300$ to avoid pair production by high-energy photons which would make the wind opaque, and $\mathrm{d}N_e/\mathrm{d}E_e \propto E_e^{-2}$ to account for the synchrotron spectrum. Acceleration of protons to 10^{20} eV requires $u_B/u_e > 0.02$ to satisfy equation (1); $\Gamma > 100$ to avoid synchrotron losses of protons on a time scale shorter than the acceleration time; and $\mathrm{d}N_p/\mathrm{d}E_p \propto E_p^{-2}$ to reproduce the observed UHECR spectrum (see equation (6)). The constraints on wind parameters imposed by requiring proton acceleration to $>10^{20}$ eV are largely independent of the details of the assumed acceleration process (as illustrated, e.g., by the analysis of [55]).

The fact that similar constraints are obtained from independent arguments, related to γ-ray emission and to proton acceleration, suggests that GRBs and UHECRs are associated. The association is further supported by the similarity of energy generation rates. The energy generation rate of GRBs (at $z = 0$) is $\approx 10^{44}\,\mathrm{erg\,Mpc^{-3}\,yr^{-1}}$ [54], comparable to the energy generation rate in UHECRs (equation (6)).

We note that GRBs have also been suggested as the sources of galactic cosmic rays above the 'knee', i.e. above $\sim 10^{15}$ eV [56]. The discussion of this issue is beyond the scope of this paper.

3.3. 100 TeV neutrinos

Protons accelerated in the fireball to high energy lose energy through photo-meson interaction with fireball photons. The decay of charged pions produced in this interaction results in the production of high-energy neutrinos. The key relation is between the observed photon energy, E_γ, and the accelerated proton's energy, E_p, at the threshold of the Δ-resonance. In the observer frame,

$$E_\gamma E_p = 0.2\,\mathrm{GeV}^2\,\Gamma^2. \tag{8}$$

For $\Gamma \approx 10^{2.5}$ and $E_\gamma = 1$ MeV, we see that characteristic proton energies $\sim 10^{16}$ eV are required to produce pions. Since neutrinos produced by pion decay typically carry 5% of the proton energy, the production of $\sim 10^{14}$ eV neutrinos is expected [25].

The fraction of energy lost by protons to pions, f_π, is $f_\pi \approx 0.2$ [23]–[25], [57]. Assuming that GRBs generate the observed UHECRs, the expected GRB muon-neutrino flux may be

estimated using equation (7) [10, 25],

$$E_\nu^2 \Phi_\nu \approx 0.3 \times 10^{-8} \frac{f_\pi}{0.2} \,\mathrm{GeV\,cm^{-2}\,s^{-1}\,sr^{-1}}. \tag{9}$$

This neutrino spectrum extends to $\sim 10^{16}$ eV, and is suppressed at higher energy due to energy loss of pions and muons [10, 25, 58]. Equation (9) implies a detection rate of $\sim$20 neutrino-induced muon events per year (over 4π sr) in a cubic-km detector. Since GRB neutrino events are correlated both in time and in direction with γ-rays, their detection is practically background-free.

3.4. TeV neutrinos

The 100 TeV neutrinos discussed in the previous section are produced at the same region where GRB γ-rays are produced. Their production is a generic prediction of the fireball model. It is a direct consequence of the assumptions that energy is carried from the underlying engine as kinetic energy of protons and that γ-rays are produced by synchrotron emission of shock accelerated particles. Neutrinos may be produced also in other stages of fireball evolution, at energies different than 100 TeV. The production of these neutrinos is dependent on additional model assumptions. We discuss below some examples related to the GRB progenitor. For a more detailed discussion see [23, 24] and references therein.

The most widely discussed progenitor scenarios for long-duration GRBs involve core collapse of massive stars. In these 'collapsar' models, a relativistic jet breaks through the stellar envelope to produce a GRB. For extended or slowly rotating stars, the jet may be unable to break through the envelope. Both penetrating (GRB producing) and 'choked' jets can produce a burst of $\sim$5 TeV neutrinos by interaction of accelerated protons with jet photons, while the jet propagates in the envelope [59]. The estimated event rates may exceed $\sim 10^2$ events yr^{-1} in a km-scale detector, depending on the ratio of non-visible to visible fireballs. A clear detection of non-visible GRBs with neutrinos may be difficult due to the low-energy resolution for muon-neutrino events, unless the associated supernova photons are detected. In the two-step 'supranova' model, interaction of the GRB blast wave with the supernova shell can lead to detectable neutrino emission, either through nuclear collisions with the dense supernova shell or through interaction with the intense supernova and backscattered radiation field [60].

References

[1] See the following reviews in this issue, and references therein:
Bahcall J N and Peña-Garay C 2004 *New J. Phys.* **6** 63
Fogli G and Lisi E 2004 *New J. Phys.* **6** 139
McDonald A B 2004 *New J. Phys.* **6** 121

[2] See the following reviews in this issue, and references therein:
Yamada S, Kotake K and Yamasaki T 2004 *New J. Phys.* **6** 79
Balantekin A B *New J. Phys.* to be published

[3] See the following reviews in this issue, and references therein:
Carr J and Hallewell G 2004 *New J. Phys.* **6** 112
Karle A *New J. Phys.* to be published
Starev T *New J. Phys.* to be published
Zas E *New J. Phys.* to be published

[4] Blandford R and Eichler D 1987 *Phys. Rep.* **154** 1
Axford W I 1994 *Astrophys. J. Suppl.* **90** 937
Nagano M and Watson A A 2000 *Rev. Mod. Phys.* **72** 689
Abu-Zayyad T *et al* 2001 *Astrophys. J.* **557** 686
[5] Andres E *et al* 2000 *Astropart. Phys.* **13** 1; http://amanda.uci.edu/
[6] Ahrens J *et al* 2004 *New Astron. Rev.* **48** 519; http://icecube.wisc.edu/
[7] Katz U F 2004 *Eur. Phys. J.* C **33** 971; http://antares.in2p3.fr/
[8] Tsirigotis A G 2004 *Eur. Phys. J.* C **33** 956; http://www.nestor.org.gr/
[9] Capone A 2003 *SPIE* **4858** 64; http://nemoweb.lns.infn.it/
[10] Waxman E and Bahcall J N 1999 *Phys. Rev.* D **59** 023002
[11] Bahcall J N and Waxman E 2001 *Phys. Rev.* D **64** 023002
[12] Mannheim K, Protheroe R J and Rachen J P 2001 *Phys. Rev.* D **63** 023003 (*Preprint* astro-ph/9812398, v1, v2 and v3)
[13] Greisen K 1966 *Phys. Rev. Lett.* **16** 748
Zatsepin G T and Kuzmin V A 1966 *JETP* **4** 78
[14] Berezinsky V S and Zatsepin G T 1969 *Phys. Lett.* B **28** 423
[15] Engel R, Seckel D and Stanev T 2001 *Phys. Rev.* D **64** 093010
[16] Barwick S W *et al* 2003 *SPIE* **4858** 265; http://www.ps.uci.edu/anita/
[17] Kravchenko I *et al* 2003 *Astropart. Phys.* **19** 15; http//www.bartol.udel.edu/∼spiczak/rice/rice.html
[18] Argiró S 2004 *Eur. Phys. J.* C **33** 947; http://www.auger.org/admin/
[19] Scarsi L *et al* 1998 *SPIE* **3445** 505; http://hep.fi.infn.it/AIRWATCH/
[20] Bahcall J N and Waxman E 2003 *Phys. Lett.* B **556** 1
[21] Stanev T 2004 *New J. Phys.* **6** to be published
[22] Piran T 2000 *Phys. Rep.* **333** 529
[23] Mészáros P 2002 *Annu. Rev. Astron. Astrophys.* **40** 137
[24] Waxman E 2001 *Physics and Astrophysics of Ultra-High-Energy Cosmic Rays* (*Lecture Notes in Physics* vol 576) ed M Lemoine and G Sigl (Berlin: Springer) p 122
Waxman E 2003 *Supernovae and Gamma-Ray Bursters* (*Lecture Notes in Physics* vol 598) ed K Weiler (Berlin: Springer) p 393
[25] Waxman E and Bahcall J N 1997 *Phys. Rev. Lett.* **78** 2292
[26] Alvarez-Muñiz J and Halzen F 1999 *Astrophys. J.* **521** 928
Guetta D, Hooper D, Alvarez-Muñiz J, Halzen F and Reuveni E 2004 *Astropart. Phys.* **20** 429
[27] Casper D *et al* 1991 *Phys. Rev. Lett.* **66** 2561
Fukuda Y *et al* 1994 *Phys. Lett.* B **335** 237
Fogli G L and Lisi E 1995 *Phys. Rev.* D **52** 2775
[28] Bahcall J N 1989 *Neutrino Astrophysics* (New York: Cambridge University Press) pp 438–60
[29] Lovelace R V E 1976 *Nature* **262** 649
[30] Hillas A M 1984 *Ann. Rev. Astron. Astrophys.* **22** 425
[31] Arons J 2003 *Astrophys. J.* **589** 871
[32] Gaisser T K, Halzen F and Stanev T 1995 *Phys. Rep.* **258** 173
[33] Ahrens J *et al* 2004 *Phys. Rev. Lett.* **92** 071102
[34] Waxman E 1995 *Astrophys. J.* **452** L1
[35] Bird D J *et al* 1994 *Astrophys. J.* **424** 491
[36] Hayashida N *et al* 1999 *Astrophys. J.* **522** 225 (*Preprint* astro-ph/0008102)
[37] Efimov N N *et al* 1991 *Proc. Int. Symp. on Astrophysical Aspects of the Most Energetic Cosmic-Rays* ed M Nagano and F Takahara (Singapore: World Scientific) p 20
[38] Abu-Zayyad T *et al* 2002 *Preprint* astro-ph/0208243
[39] Bednarz J and Ostrowski M 1998 *Phys. Rev. Lett.* **80** 3911
Achterberg A *et al* 2001 *Mon. Not. R. Astron. Soc.* **328** 393
Waxman E 1997 *Astrophys. J.* **485** L5
[40] Boyle B J and Terlevich R J 1998 *Mon. Not. R. Astron. Soc.* **293** L49

[41] Lilly S J, Le Fevre O, Hammer F and Crampton D 1996 *Astrophys. J.* **460** L1
Madau P *et al* 1996 *Mon. Not. R. Astron. Soc.* **283** 1388
Steidel C C, Adelberger K L, Giavalisco M, Dickinson M and Pettini M 1999 *Astrophys. J.* **519** 1
[42] Burnett T H *et al* (the JACEE collaboration) 1990 *Astrophys. J.* **349** L25
Asakimori K *et al* (the JACEE collaboration) 1995 *Proc. 24th Cosmic-Ray Conf. (Rome, 1995)* vol 2, p 707
[43] Bernlohr K *et al* 1998 *Astropart. Phys.* **8** 253
[44] Gaisser T K *et al* 1993 *Phys. Rev.* D **47** 1919
Dawson B R, Meyhandan R and Simpson K M 1998 *Astropart. Phys.* **9** 331
[45] Balkanov V *et al* 2002 *Nucl. Phys.* B (*Proc. Suppl.*) **110** 504
[46] Andres E *et al* 2001 *Nucl. Phys.* B (*Proc. Suppl.*) **91** 423
Ahrens J *et al* 2003 *Phys. Rev. Lett.* **90** 251101
[47] Stanev T 2004 *Preprint* astro-ph/04045353
Bugaev E V, Misaki A and Mitsui K 2004 *Preprint* astro-ph/0405109
[48] Ellis J, Gaisser T K and Steigman G 1981 *Nucl. Phys.* B **177** 427
Berezinsky V, Kachelriess M and Vilenkin A 1997 *Phys. Rev. Lett.* **79** 4302
[49] Vilenkin A 1985 *Phys. Rep.* **121** 263
Hill C T and Schramm D N 1985 *Phys. Rev.* D **31** 564
Bhattacharjee P, Hill C T and Schramm D N 1992 *Phys. Rev. Lett.* **69** 567
Berezinsky V S and Vilenkin A 2000 *Phys. Rev.* D **62** 083512 (*Preprint* hep-ph/9908257)
Alvarez-Mumiz A and Halzen F 2001 *Phys. Rev.* D **63** 037302 (*Preprint* astro-ph/0007329)
Letessier-Selvon A 2000 *Nucl. Phys. (Proc. Suppl.)* **91** 473–9 (*Preprint* astro-ph/0000416)
[50] Weiler T 1999 *Astropart. Phys.* **11** 303
Gelmini G and Kusenko A 2000 *Phys. Rev. Lett.* **84** 1378
[51] Galama T J *et al* 1998 *Nature* **395** 670
Stanek K Z *et al* 2003 *Astrophys. J.* **591** L17
Hjorth J *et al* 2003 *Nature* **423** 847
[52] Waxman E 1995 *Phys. Rev. Lett.* **75** 386
[53] Vietri M 1995 *Astrophys. J.* **453** 883
Milgrom M and Usov V 1995 *Astrophys. J.* **449** L37
[54] Waxman E 2004 *Astrophys. J.* **606** 988
[55] Gialis D and Pelletier G 2004 *Astron. Astrophys.* at press (*Preprint* astro-ph/0402586)
Gialis D and Pelletier G 2004 *Astrophys. J.* submitted (*Preprint* astro-ph/0405547)
[56] Milgrom M and Usov V 1996 *Astropart. Phys.* **4** 365
Wick S D, Dermer C D and Atoyan A 2004 *Astropart. Phys.* **21** 125
[57] Guetta D, Spada M and Waxman E 2001 *Astrophys. J.* **559** 101
[58] Rachen J P and Mészáros P 1998 *Phys. Rev.* D **58** 123005
[59] Mészáros P and Waxman E 2001 *Phys. Rev. Lett.* **87** 171102
Razzaque S, Mészáros P and Waxman E 2003 *Phys. Rev.* D **68** 083001
Razzaque S, Mészáros P and Waxman E 2004 *Phys. Rev.* D **69** 023001
[60] Guetta D and Granot J 2003 *Phys. Rev. Lett.* **90** 191102
Guetta D and Granot J 2003 *Phys. Rev. Lett.* **90** 201103
Razzaque S, Mészéros P and Waxman E 2003 *Phys. Rev. Lett.* **90** 241103
Dermer C D and Atoyan A 2003 *Phys. Rev. Lett.* **91** 071102

New Journal of Physics
The open-access journal for physics

Reactor neutrino oscillation studies with KamLAND

K Inoue

Research Center for Neutrino Science, Tohoku University, Aramaki Aoba, Aoba, Sendai, Miyagi 980-8578, Japan
E-mail: inoue@awa.tohoku.ac.jp

New Journal of Physics **6** (2004) 147
Received 6 July 2004
Published 28 October 2004
Online at http://www.njp.org/
doi:10.1088/1367-2630/6/1/147

Abstract. KamLAND, the 1000 t liquid scintillator detector utilizing nuclear power reactors distributing effectively ∼180 km from the experimental site, has performed a search for reactor neutrino oscillations. Results obtained from the baseline show evidence for reactor neutrino disappearance, while previous searches at less than 1 km showed consistent flux, as expected. This provides a resolution for the long-standing solar neutrino problem if combined with results from solar neutrino experiments. KamLAND with increased statistics also provided evidence of spectral distortion as expected from the neutrino oscillation and, if converted to the L/E distribution, it shows clear oscillatory behaviour of neutrino propagation. Consequently, the results have a good sensitivity on neutrino oscillation parameters and a precise determination of Δm^2 has been realized.

1367-2630/04/010147+24$30.00
PII: S1367-2630(04)83052-0
© IOP Publishing Ltd and Deutsche Physikalische Gesellschaft

Contents

1. Introduction **2**

2. Reactor neutrinos **3**

2.1. Neutrino spectra and cross-section 3

2.2. Reactors around the Kamioka site 5

3. KamLAND detector **7**

3.1. Apparatus 7

3.2. Event trigger 8

3.3. Impurity level 8

3.4. Energy calibrations 8

3.5. Vertex calibrations 9

3.6. Analysis and systematic errors 12

4. Results **13**

4.1. Evidence for reactor neutrino disappearance 13

4.2. Evidence of spectral distortion 16

4.3. Measurement of neutrino oscillation parameters 19

5. Overlooked background **20**

6. Summary **23**

References **23**

1. Introduction

KamLAND has obtained evidence for reactor anti-neutrino disappearance [1] and of its spectral distortion [2]. This paper describes the KamLAND detector and reviews these important breakthroughs in neutrino physics.

Nuclear power reactors are intense $\bar{\nu}_e$ sources and useful for neutrino studies. In fact, the first discovery of neutrino existence was carried out with reactor neutrinos. Since then, vigorous efforts have been made to investigate neutrino properties with nuclear reactors. Knowledge of the intensity of neutrinos and neutrino spectra from nuclear fission has accumulated with various experiments. Theoretical calculations on neutrino cross-section and non-thermal fission neutrino spectra have also been improved along with the experimental progress. Finally, the interaction rate of reactor $\bar{\nu}_e$ has become predictable at a few % level without a near detector for normalization. The baseline of reactor neutrino experiments has then extended [3, 4] to ∼1000 m to look for neutrino oscillations. However, no significant deficit from neutrino oscillations has been observed so far.

In parallel with the progress in reactor neutrino study, the observation of solar neutrinos was started in 1968. The unexpected new problem—that the observed neutrino flux was much smaller than predicted by standard solar models [5]—has not been resolved for more than 30 years. Several experiments followed the solar neutrino observation with various neutrino reactions. In addition to the first radiochemical ^{37}Cl experiment [6], neutrino–electron elastic scattering in real-time water Cherenkov detectors [7, 8], low reaction threshold ^{71}Ga radiochemical experiments [9]–[11], and a real-time heavy water Cherenkov detector [12]. All the experiments except for the neutral current measurement of the heavy water experiment have obtained a clear deficit of

neutrino flux. These experiments are purely or mainly sensitive to the ν_e component while the neutral current measurement is equally sensitive to all neutrino flavours, ν_e, ν_μ and ν_τ. Before the neutral current measurement, the possibility of some deficiency in standard solar model calculations or of unknown neutrino properties have both been forceful arguments. The obtained agreement of the neutral current result with the prediction of standard solar models established flavour transition of neutrinos during their travel from the Sun to the Earth and thus it was found that the deficits were caused by a neutrino property not included in the standard model of elementary particle physics. The most popular hypothesis to explain the deficit was a neutrino oscillation, but other models such as resonant spin flavour precession [13], neutrino decay [14], flavour changing neutral current and so on also remained possibilities at that time. Even assuming the neutrino oscillation hypothesis, one of the oscillation parameters, mass squared difference, could vary by many orders of magnitude from 10^{-10} to several $\times 10^{-4}$ eV^2. In order to conclude that neutrino oscillation was the right solution and to restrict the allowed oscillation parameter region, a terrestrial neutrino experiment with a well-understood artificial neutrino source was required.

The common important feature of those solar experiments are that the sites are deep underground in order to avoid cosmogenic backgrounds and that detectors are very large to overcome the very small interaction probability of neutrinos. These features are also relevant for reactor neutrino measurements when one wants to extend its baseline. In order to explore the small mass difference region allowed by solar neutrino results, baselines of more than 100 km are necessary. For an experiment with such a baseline, much more powerful reactors, a bigger detector and a deeper underground site were necessary. A new experiment, KamLAND, occupied the location where the former Kamiokande experiment existed. KamLAND is an abbreviation of Kamioka Liquid-scintillator Anti-Neutrino Detector. It holds about 1200 m^3 of liquid scintillator and is located 1000 m underground; 80% of reactor neutrino contribution $\sim 5 \times 10^6$ cm^{-2} s^{-1} is coming from reactors distributing 130–220 km away from the detector. Total thermal power output generated over that distance range amounts to 70 GW. It corresponds to 7% of the world total nuclear power generation. Compared with the pioneering 'Poltergeist' experiment which first established neutrino existence, LS amount is scaled up from 1400 l to 1200 m^3 (1000 times), effective reactor power from 700 MW to 70 GW (100 times), depth from 12 to 1000 m (100 times) and effective distance from 11 m to $\sim$180 km (more than 10000 times!). These many orders of magnitude extensions became possible by various important improvements on the knowledge of reactor neutrinos by previous experiments. And most importantly, this baseline is the right distance to explore the LMA solution which was the most favourable oscillation parameter with solar neutrino results (see figure 1).

Now, the terrestrial KamLAND experiment using a well-understood artificial neutrino source can explore the oscillation parameters relevant for the phenomena found in the 1.5×10^{11} m astronomical-scale distance.

2. Reactor neutrinos

2.1. Neutrino spectra and cross-section

The total power generation of world-wide reactors amounts to $\sim$1.1 TW and it corresponds to one-third mole $\bar{\nu}_e$ creation per second. These very intense neutrinos are freely available and are really useful if one could find a good location for their measurement.

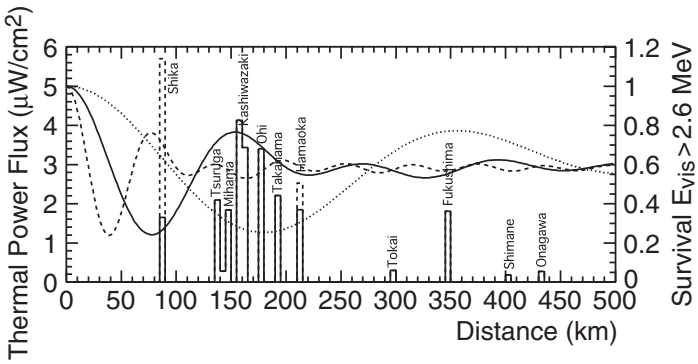

Figure 1. Distribution of nuclear power reactors as a function of distance from the KamLAND site. The solid histogram is the current operation and the dashed histogram is the expected operation in 2006 (Shika at 88 km increases by a factor 3). The height of the histogram shows the thermal power flux contribution at Kamioka. Also shown as solid ($\Delta m^2 = 7 \times 10^{-5}\,\mathrm{eV}^2$), dashed ($3 \times 10^{-5}$) and dotted ($1.4 \times 10^{-4}$) lines are the survival probability of $\bar{\nu}_e$ as a function of distance (all for $\sin^2 2\theta = 0.84$). The probability is calculated for events above 2.6 MeV in visible energy.

In the observation of reactor neutrinos, four fissile nuclei (^{235}U, ^{239}Pu, ^{238}U and ^{241}Pu) are important and the others contribute only at the 0.1% level. Fission fragments from these nuclei sequentially β decay and emit anti-electron–neutrinos. The purity of the 'anti' neutrinos is very high and electron–neutrino contamination is only at the 10 ppm level above an inverse β decay threshold, 1.8 MeV. These four nuclei release similar energy when they undergo fission [15] (^{235}U 201.8 ± 0.5 , ^{239}Pu 210.3 ± 0.6, ^{238}U 205.0 ± 0.7 and ^{241}Pu 212.6 ± 0.7 MeV). Thus, the fission rate is strongly correlated with the thermal power output that is measurable at much better than 2% even without any special care. Then, one fission causes about six neutrino emissions on average and, therefore, the neutrino intensity can be roughly estimated to be $\sim 2 \times 10^{20}\,\bar{\nu}_e\,\mathrm{GW}_{\mathrm{th}}^{-1}\,\mathrm{s}^{-1}$. Fission spectra reach equilibrium within a day above ~2 MeV. This delay is a possible cause of systematic error. Also, attention to the long-lived nuclei such as

$$^{106}\mathrm{Ru} \xrightarrow{T_{1/2}=372\,\mathrm{d}} \mathrm{Rh} \xrightarrow[E_{\max}=3.541\,\mathrm{MeV}]{} \mathrm{Pd},$$

$$^{144}\mathrm{Ce} \xrightarrow{T_{1/2}=285\,\mathrm{d}} \mathrm{Pr} \xrightarrow[E_{\max}=2.996\,\mathrm{MeV}]{} \mathrm{Nd}$$

is necessary [16]. They affect the correlation between thermal power and neutrino flux at low-energy region by <1% level.

The beta spectra from ^{235}U, ^{239}Pu and ^{241}Pu have been measured with a spectrometer irradiating thermal neutrons at ILL [17]. They fitted the observed beta spectra from 30 hypothetical beta branches and converted each branch to a neutrino spectrum [18]. In the case of ^{238}U, it does not undergo fission with thermal neutrons and only a theoretical calculation [19] is available. This calculation traces 744 unstable fission products and obtains the corresponding neutrino spectrum. The error on the calculated spectrum is larger than the measurement, but it

contributes only ∼8% on average for ordinary reactor cores. And knowing the time evolution of the fuel composition, the uncertainty of the neutrino event rate coming from the calculation of these spectra is only ∼2.3%.

The neutrino reaction commonly used since 'Poltergeist' and subsequent experiments is the inverse β decay:

$$\bar{\nu}_e + p \rightarrow e^+ + n.$$

Advantages of this reaction are the rich target number, low reaction threshold

$$E_{lab} = \frac{(M_n + m_e)^2 - M_p^2}{2M_p} = 1.806\,\text{MeV},$$

very precisely known cross-section and the delayed two-fold coincidence signal. The cross-section is closely related to the neutron life-time ($n \rightarrow p + e^- + \bar{\nu}_e$) as follows:

$$\sigma_{tot}^{(0)} = \frac{2\pi^2/m_e^5}{f_{p.s.}^R \tau_n} E_e^{(0)} p_e^{(0)}.$$

Recent precise studies on neutrons provided a very accurate lifetime of $\tau_n = 885.7 \pm 0.8$ s and as a result the precision of the neutrino cross-section on proton is 0.2% with order $1/M$ corrections (Coulomb, weak magnetism, recoil, inner and outer radiative corrections) [20]. The prompt signal is the positron and its annihilation gammas with a material electron, thus the prompt signal has energies always larger than 1 MeV (two electron masses). The delayed signal is the capture of the neutron on an environmental atom such as hydrogen, gadolinium, cadmium or ^{3}He. It provides clear tagging and very good background discrimination in timing, position and energy. Effective neutrino energy of reactor neutrinos via the inverse decay is about 4 MeV.

The validity of the neutrino spectra and cross-sectional calculations have been experimentally tested. The most accurate measurement has been performed by the Bugey experiment [15]. It measured an overall reaction rate with 1.4% accuracy and the result ($\sigma_f = 5.750 \times 10^{-43}$ cm^2 fission^{-1} $\pm$ 1.4%) was in very good agreement with the calculation ($\sigma_{V-A} = 5.824 \times 10^{-43}$ cm^2 fission^{-1} $\pm$ 2.7%). The ratio $\sigma_f/\sigma_{V-A} = 0.987 \pm 1.4\% \pm 2.7\%$. Also, Bugey-3 tested models of neutrino spectra and the ILL ones showed an excellent agreement [21]. Finally, a few % precision became possible without a near detector for flux normalization with the above calculation models and procedures.

2.2. Reactors around the Kamioka site

There are 52 commercial power reactor cores distributed in 16 sites in Japan and the nominal thermal power output 152 GW is 15% of the world total. The reactor complex located at about 160 km from Kamioka site, Kashiwazaki Kariwa, is the world's strongest reactor and its full thermal power generation is 24.3 GW. A fortunate characteristic of the Kamioka site is that 80% of neutrino contribution comes from 130 to 220 km, the distance relevant for the solar LMA solution.

As described above, the thermal power output has a direct relation with neutrino flux and the accuracy of the thermal power output is currently taken as 2%. Thermal power is measured by temperature change and flow rate of cooling water and the error is dominated by the precision

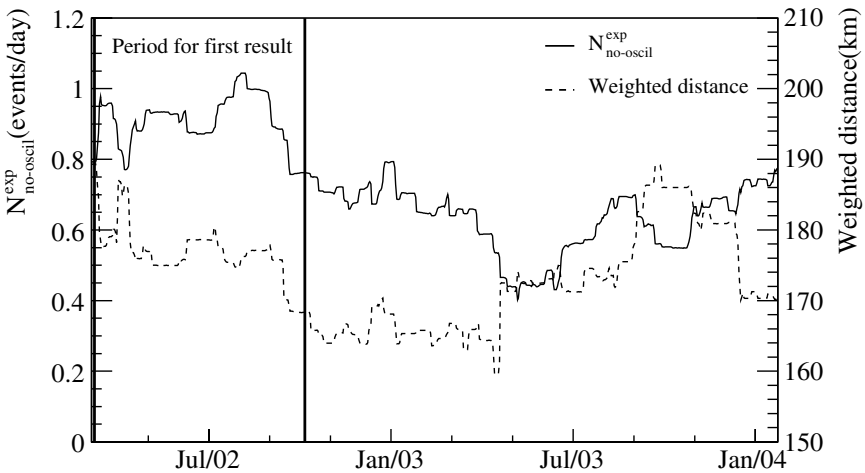

Figure 2. Time variation of expected reactor neutrino event rate at KamLAND and of average distance weighted by event rate for reactors up to 400 km are shown for the data period from March 2002 to January 2004.

of the flow meter. While the error is very conservatively taken now, it may be improved in future by investigating properties of flow meters in detail.

In addition, the composition of four fissile nuclei is also important to predict the reactor neutrino spectrum. On burning the fuel, the contribution of four nuclei changes in time, the so-called burn-up effect. This effect is calculable knowing the initial ^{235}U enrichment, fraction of new fuel and history of thermal power output for each reactor core. The systematic error of the neutrino event rate coming from this calculation is much smaller than 1%.

Detailed thermal power history and enrichment information for all the Japanese commercial reactor cores and one of the research cores have been obtained from the companies for the analysis periods, the first result from 4 March to 6 October 2002 and the second result from 9 March 2002 to 11 January 2004. Also histories of electric power output from Korean reactors were obtained (http://www.insc.anl.gov/). Since many reactor cores were inspected in 2003, the expected neutrino signal rate has decreased to ∼40% level of 2002 as shown in figure 2. Contribution of Korean and rest-of-the-world reactors over the live time has changed between the analysis periods from 2.5 to 3.4% (Korean) and from 0.7 to 1.1% (rest). But the average fuel composition ^{235}U : ^{238}U : ^{239}Pu : ^{241}Pu changed only slightly from 0.568 : 0.078 : 0.297 : 0.057 to 0.563 : 0.079 : 0.301 : 0.057. These average compositions are used to estimate neutrino spectra from Korean and rest-of-the-world reactors. As the operation pattern changes, the average distance weighted by the expected no-oscillation event rate for reactors up to 400 km is also changed, as shown in figure 2.

Some of the systematic errors discussed in the previous subsection depend on experiment. Considering the observation periods and analysis threshold, KamLAND specific errors are calculated as follows. In addition to 2% thermal power error of Japanese reactor cores, we assigned 10% error for cores for which only the electric power history is available (Korean reactors) and 50% error for cores for which only nominal power is known (rest-of-the-world and research reactors) and the combined error from thermal power was estimated to be 2.1%. The effect of time lag from the slow β decay component was estimated by sliding the operation time window up to 1 day and was obtained as 0.01% and the effect of ^{106}Ru and ^{144}Ce is less than 0.02% above 2.6 MeV visible energy.

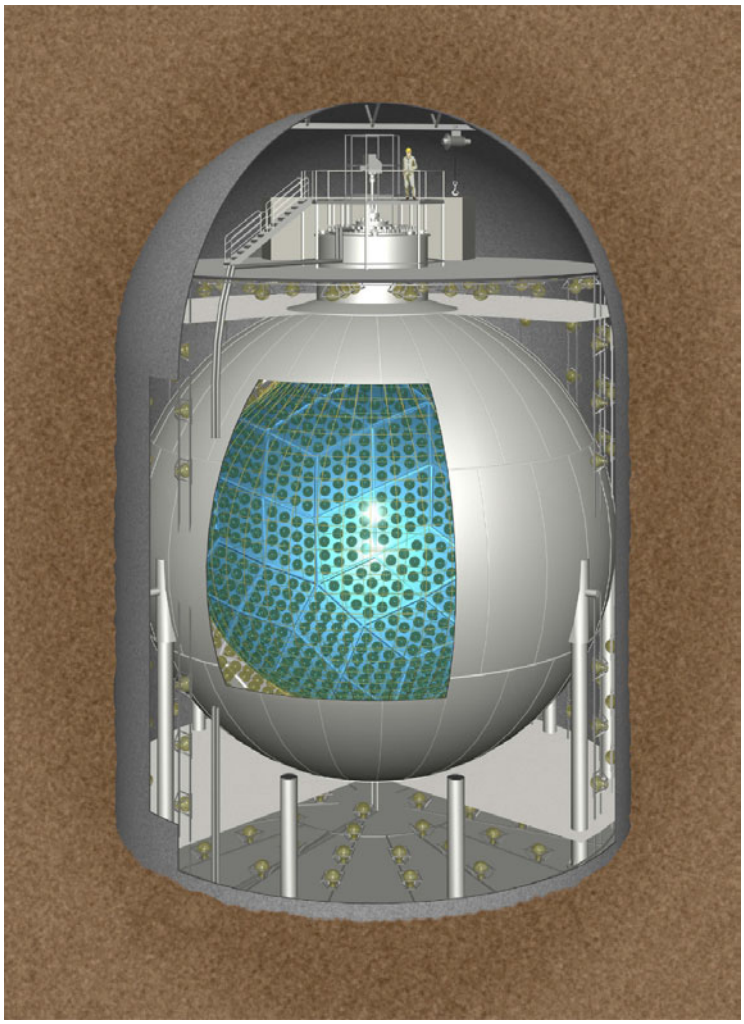

Figure 3. Schematic view of the KamLAND detector.

The analysis threshold of 2.6 MeV for visible energy increases the error from anti-neutrino spectra from 2.3 to 2.5%. Then, the total systematic error of the anti-neutrino signal rate except for a detector part was obtained as 3.4%.

3. KamLAND detector

3.1. Apparatus

KamLAND is a monolithic liquid-scintillator detector located at longitude 137°18′43.495″, latitude 36°25′35.562″ in the Japanese geodetic system 2000 based on international terrestrial reference frame and geodetic reference system 1980. Its altitude is 358 m and it is covered by 2700 m water-equivalent mountain rock under Mt. Ikenoyama (1368 m). As shown in figure 3, the detector contains 1200 m^3 liquid scintillator (LS: 1,2,4-trimethylbenzene, 20%; dodecane, 80% and PPO, 1.52 g l^{-1} as a fluor) and 1800 m^3 buffer oil (BO: dodecane, 50% and isoparaffin, 50%)

in an 18-m-diameter stainless-steel tank. Free protons in the LS are the $\bar{\nu}_e$ targets. A positron from the inverse β decay reaction ($\bar{\nu}_e + p \rightarrow e^+ + n$) and a 2.2 MeV γ ray from the neutron capture on a proton (mean capture time is ~210 μs) make clear a two-fold-delayed-coincidence signal. The LS is suspended by a Kevlar rope network in the BO with a 13-m-diameter spherical balloon made of 135-μm-thick transparent film (EVOH–Nylon–Nylon–Nylon–EVOH). The buoyancy of the BO is controlled to be slightly (0.04%) lighter than LS to keep the balloon shape. Photons emitted in the detector are monitored by 1325 newly developed 17" tubes and 554 old Kamiokande 20" tubes. While the total photocoverage is 34%, only the 17" tubes corresponding to 22% were used until 27 February 2003. The photon yield of the LS is about 8000 photons MeV^{-1} and the photoelectron yield is ~300 and ~470 p.e. MeV^{-1} without and with 20" tubes, respectively. All these PMTs are isolated from the inner region by a 3-mm-thick acrylic sphere at 16.6 m diameter for preventing radon emanation from these materials. The outer detector (OD) is a water Cherenkov detector with 3.2 kt pure water and 225 old Kamiokande 20" tubes for purposes of external background absorption and cosmic-ray muon tag.

3.2. Event trigger

Each phototube is connected to two sets of three range analogue-transient-waveform-digitizers recording whole pulse shape from one to thousands of photoelectrons for about 200 ns. The global event trigger is issued based on the number of hit channels (each channels has about 0.3 p.e. threshold) and currently set at 200 hits corresponding to ~700 keV. Also a delayed trigger (120 hits, ~400 keV) is enabled for 1 ms after each global event trigger to perform real-time impurity measurements of uranium and thorium using delayed coincidence events such as

$$^{214}\mathrm{Bi} \xrightarrow{\beta,\gamma} {}^{214}\mathrm{Po}(\tau = 237\,\mu\mathrm{s}) \xrightarrow[7.687\,\mathrm{MeV}]{\alpha} {}^{210}\mathrm{Pb}.$$

The latter α decay is observed with a quench of about a factor 14 and the low threshold delayed trigger is necessary to tag this α decay. The lowest trigger threshold is limited by data size but is sufficiently low for the reactor neutrino analysis (all phenomena have visible energies of more than two electron masses). The OD trigger threshold is set to provide more than 99% muon tagging efficiency.

3.3. Impurity level

The primary target, in reactor neutrino measurements, requires a radioactive impurity level of lower than $10^{-13}\,\mathrm{g\,g^{-1}}$ for uranium and thorium. The measured impurity level is listed in table 1 together with the requirements. The achieved impurity levels of uranium ($3.5 \pm 0.5 \times 10^{-18}\,\mathrm{g\,g^{-1}}$) and thorium ($5.2 \pm 0.8 \times 10^{-17}\,\mathrm{g\,g^{-1}}$), assuming radioactive equilibrium, are much better than the initial requirement and even better than that of the future ^{7}Be solar neutrino measurement. However, an extra purification of ^{85}Kr and ^{210}Pb (daughter of ^{222}Rn) contamination is necessary to start solar neutrino observation in the second stage. Vigorous efforts are being made to develop an efficient purification method and ways to measure their concentration.

3.4. Energy calibrations

Energy calibrations are performed suspending radioactive sources (^{68}Ge: two 511 keV γ, ^{65}Zn: 1.11 MeV γ, ^{60}Co: 1.17 + 1.33 MeV γ) along the z-axis. Spallation products (neutron,

Table 1. Requirements and achievements of radioactive impurities.

Impurities	Achievements	Requirements (reactor)	Requirements (solar)
^{222}Rn	$0.03\,\mu$Bq m^{-3}		
^{238}U	$3.5 \pm 0.5 \times 10^{-18}$ g g^{-1}	10^{-13} g g^{-1}	10^{-16} g g^{-1}
^{232}Th	$5.2 \pm 0.8 \times 10^{-17}$ g g^{-1}	10^{-13} g g^{-1}	10^{-16} g g^{-1}
^{40}K	$<2.7 \times 10^{-16}$ g g^{-1}	10^{-14} g g^{-1}	10^{-18} g g^{-1}
^{85}Kr	$\sim$1 Bq m^{-3}		1 μBq m^{-3}
^{210}Pb	$\sim$100 mBq m^{-3}		1 μBq m^{-3}
On the balloon		Equiv. mine dust	
^{222}Rn	4.0×10^{-4} Bq		
^{238}U	3.1×10^{-8} g	0.9 g	
^{232}Th	9.7×10^{-4} g	0.1 g	

^{12}B/^{12}N) are also utilized to know the behaviour at off z-axis. Neutrons are created at the rate of $\sim$3000 events (kt-day)$^{-1}$ and are captured on proton or on ^{12}C ($\sim$0.5%) and provide 2.22 or 4.95 MeV γ. ^{12}B ($Q = 13.4$ MeV, $T_{1/2} = 20.2$ ms) and ^{12}N ($Q = 17.3$ MeV, $T_{1/2} = 11.0$ ms) are β decays and are produced at the rate of 80 events (kt-day)$^{-1}$. Fits to the energy distribution and decay time result in the relative contribution of ^{12}N being only $\sim$1%. These wide range energy calibrations cover up to $\sim$13 MeV well above the relevant energies of reactor neutrino measurement, 1.0–8.5 MeV as shown in figure 4. Spallation events distribute uniformly both in time and space and are thus very useful to monitor space uniformity and time variation. γ rays (^{40}K and ^{208}Tl) from external material also provides a good monitor of time variations.

The energy resolution achieved so far is $7.3\%/\sqrt{E(\mathrm{MeV})}$ and $6.2\%/\sqrt{E(\mathrm{MeV})}$ with only 17" tubes and with both 17" and 20" tubes, respectively. The observed uniformity of the energy scale with the latest energy estimator is better than 0.3% in 5.5-m-radius fiducial volume and time variation of the scale was controlled within 1.3%. In addition to these wide energy range calibrations, α decays in the Bi–Po chain provide a wide variety of $\mathrm{d}E/\mathrm{d}x$ and this helped in a detailed study of the quenching effect of LS (thus a linearity study of the energy scale). Extracting $\mathrm{d}E/\mathrm{d}x$ dependence of photon yield and Cherenkov contribution from these calibrations, a positron energy scale relevant for the reactor neutrino analysis has been made. Finally, the systematic error of the energy scale at the 2.6 MeV threshold was estimated to be 2.0% and the systematic error on the neutrino event rate above 2.6 MeV was then obtained as 2.33%.

3.5. Vertex calibrations

The fiducial cut is applied based on the reconstructed vertices from the relative times of PMT hits. The vertex resolution is $\sim 23\,\mathrm{cm}/\sqrt{E(\mathrm{MeV})}$ and $\sim 20\,\mathrm{cm}/\sqrt{E(\mathrm{MeV})}$ for a point source before and after the 20" PMT inclusion. The vertex reconstruction tool has been tuned using γ ray sources along the z-axis and vertex biases are less than 5 cm in the region $-5.5 < z < 5.5$ m as shown in figure 5. It corresponds to less than 3% fiducial volume error if one assumes spherical symmetry of the detector. This uniform performance of the vertex fitter together with the energy estimator made it possible to expand the fiducial volume from 5 m radius in the first results [1] to 5.5 m radius in the second results [2] and resulted 33% increase in the number of free target

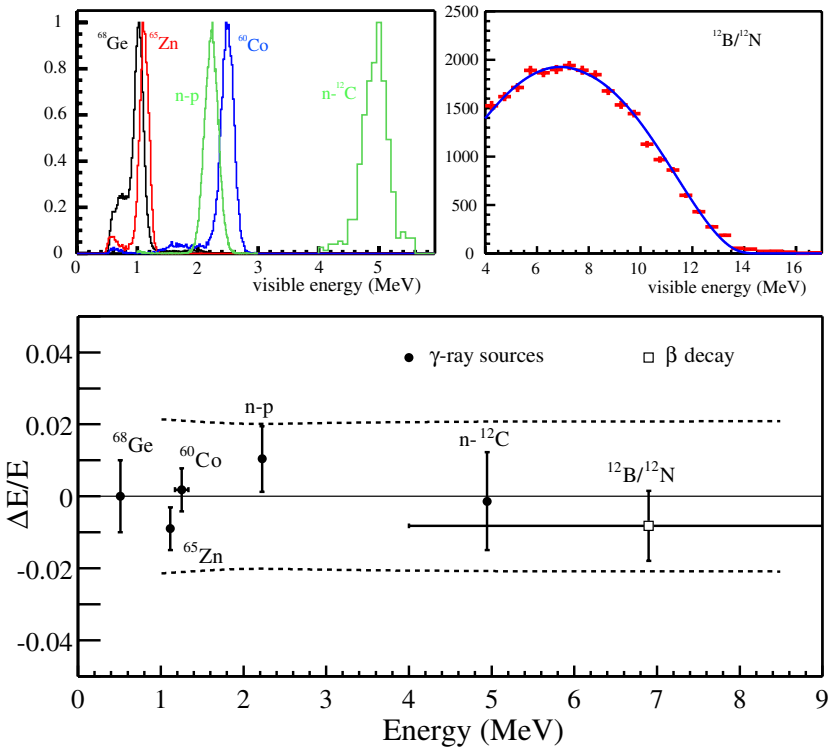

Figure 4. Energy calibrations with discrete γ rays and β decays of ^{12}B/^{12}N are shown. Average energies for multiple γ are used for ^{68}Ge and ^{60}Co and the horizontal bar for ^{12}B/^{12}N in the bottom panel is the energy range used for the calibration.

protons in the fiducial volume from 3.46×10^{31} (408.5 t LS) to 4.61×10^{31} (543.7 t LS) taking into account the LS density of 0.780 g cm^{-3} at 11.5° and chemical composition of the LS listed in table 2.

This systematic error was verified with uniformly distributing cosmogenic nuclei (^{12}B β decays). The number of events observed in the fiducial volume was compared with the total number of events observed in the whole LS volume. The total LS volume has been measured at three independent places during detector filling and resulted in 1171 ± 25 m^3. The 'nominal' 5.5 m radius fiducial volume corresponds to 0.595 ± 0.013 of the total LS volume. The number of ^{12}B events observed in the fiducial volume compared to the whole volume was 0.607 ± 0.006 (stat) $\pm$ 0.006 (syst), where the systematic error arises from events near the balloon edge that deposit a fraction of their energy outside the LS. Similarly, spallation neutron events were counted for a consistency check and the consistent ratio 0.587 ± 0.013 (stat) was obtained. Since ^{12}B provides calibration for energy more than 4 MeV, ^{8}He/^{9}Li delayed coincidence events (β + neutron) were used to relatively extend vertex calibration down to 2.2 MeV. Comparing the radius of each pair of high energy prompt event and 2.2 MeV delayed event, the energy dependence of a possible vertex bias was found to be less than 5 cm in the fiducial volume. The bias corresponds to 2.7% systematic error. Combining errors from the LS volume measurement, ^{12}B and ^{8}He/^{9}Li calibrations, total fiducial volume error was estimated as 4.7%.

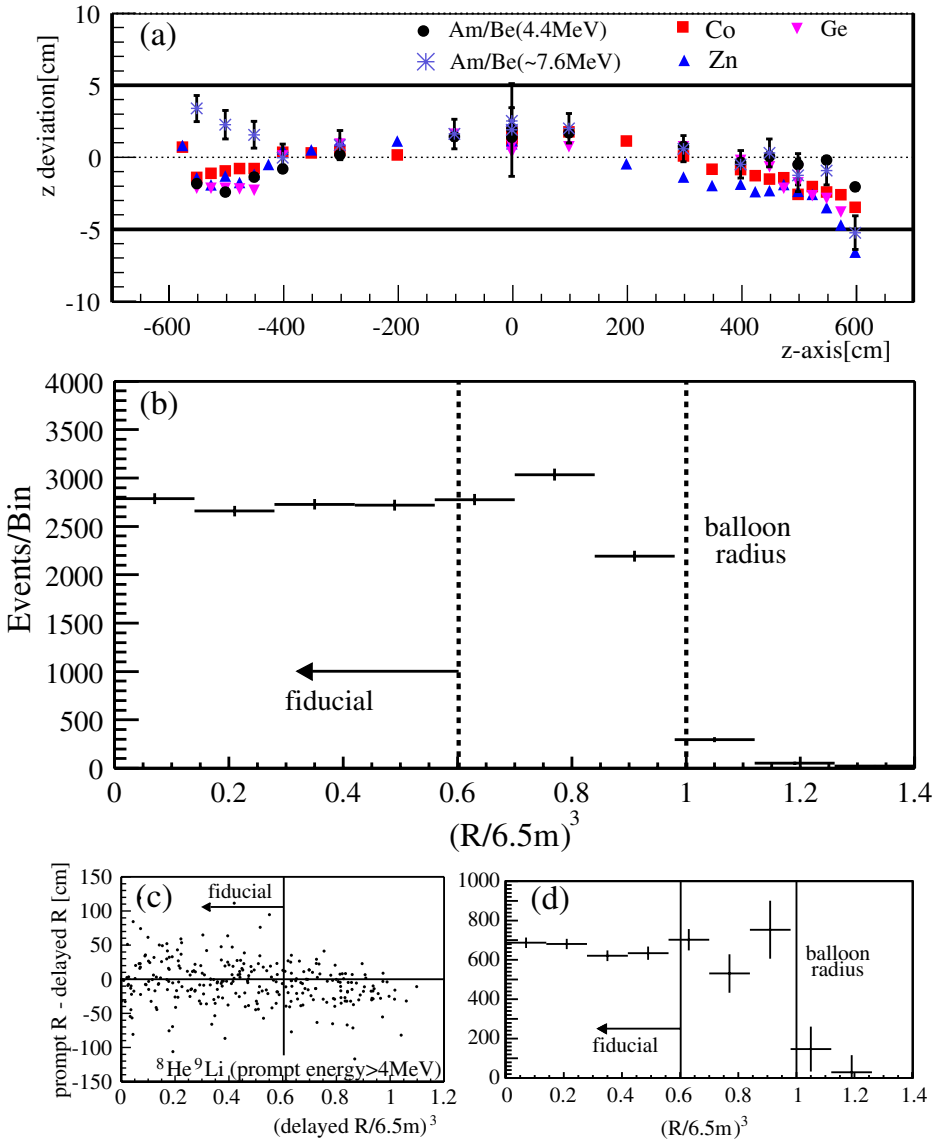

Figure 5. Vertex calibrations: (a) vertex biases of source calibrations along the z-axis; (b) the R^3 distribution of cosmogenic $^{12}B/^{12}N$ events; (c) the vertex correlation of high-energy prompt and 2.2 MeV γ events from $^{8}He/^{9}Li$ data sample; (d) the R^3 distribution of spallation neutron events.

Table 2. Chemical composition of the LS.

Atoms	Number (kt)	Nuclei	Natural abundance	Number (kt)
H	8.470×10^{31}	^{1}H	0.99985	8.469×10^{31}
		^{2}H	0.00015	1.271×10^{28}
C	4.302×10^{31}	^{12}C	0.989	4.255×10^{31}
		^{13}C	0.011	4.732×10^{29}
N	1.593×10^{28}	^{14}N	0.99634	1.587×10^{28}
O	7.064×10^{27}	^{16}O	0.99762	7.074×10^{27}

3.6. Analysis and systematic errors

Detection and tagging efficiencies of delayed coincidence signals are measured by a LED pulser, intensity measurements of radioactive sources, AmBe delayed coincidence signals and so on. For the specific selection criteria applied in this analysis: (i) a 5.5 m radius fiducial cut for both prompt and delayed, (ii) a time correlation cut (0.5–1000 μs), (iii) a vertex correlation cut (2.0 m), (iv) a delayed energy cut (1.8–2.6 MeV) and (v) a prompt energy cut (2.6–8.5 MeV visible energy), the total efficiency for the reactor neutrino signals was obtained as $89.8 \pm 1.5\%$. A major inefficiency comes from the space correlation at the fiducial edge events (91.3%) because the 5.5 m radius cut is applied for both the prompt and the delayed events. Cuts for the delayed coincidence signal have been extracted from the first results (0.5–660 μs and 1.6 m) to increase the detection efficiency and it reduced the systematic error at the same time, and an 1.2 m radius cylinder cut around z-axis for delayed events applied in the first result is not used in the new analysis. By extracting cuts and extending fiducial volume, accidental background increases rapidly and the selection is not applicable below 2.6 MeV where geo-neutrino signals are expected. The main sources of error are from ^{210}Bi as prompt and ^{208}Tl as delayed events.

The earth has 44 TW heat flow at the surface: 20 TW of it is thought to come from radio-activity in the earth, 16 TW from uranium and thorium and 4 TW from ^{40}K. In U and Th decay chains, there are β decays emitting observable $\bar{\nu}_e$ with inverse decay (1.806 MeV threshold). Their sharp edges at the end-points and their constant flux, independent of thermal power variation of reactors, will be useful to distinguish them if there are enough statistics. Subtraction of geo-neutrino contributions cannot be done blindly using inaccurate predictions. Therefore, the analysis threshold of visible energy, 2.6 MeV, is for now set above the geo-neutrino end-point energy, 2.49 MeV. On the other hand, U and Th contributions can be separately obtained from their characteristic energy spectra when sufficient statistics is acquired. Subtraction of nearby contributions with a radio-activity map will make it possible to investigate the interior of the earth with neutrinos. This is the start of the new field of 'neutrino geophysics'. The lower threshold covering all $\bar{\nu}_e$ events (0.9 MeV) was also used for a consistency check and for a geo-neutrino search in the first paper. An updated analysis below 2.6 MeV will be presented elsewhere.

There are also two types of correlated backgrounds associating with showering cosmic-ray muons. One is fast neutrons from outside and another is long-lived β-decay-nuclei accompanied by neutron emission in the detector. Fast neutrons from outside are strongly suppressed by multiple layers of absorbers: the OD itself, the 2.5 m of non-scintillating oil surrounding the LS and the 1–1.5 m LS layer outside the fiducial volume. The contribution of fast neutrons is estimated by tagging muons in the OD and looking for a delayed coincidence signal in the ID. Vertices of such events are concentrated close to the wall, and there are very few events entering the fiducial volume. Therefore, the upper limit of the fast neutron background is obtained by considering 8% inefficiency of the OD tagging (number of good OD hits larger than 5), and also estimating contribution of rock penetrating muons by simulation with restriction of the measurement. Long-lived neutron emitter candidates are ^{8}He and ^{9}Li. Their half-lives are 0.12 and 0.18 s and 16 and 50% of their β decays emit neutrons. The production rate of these nuclei with neutron emission mode was obtained as $\sim$1.5 events (kt-day)$^{-1}$ looking at correlations with preceding muons. From fits to the decay time and β decay spectra of those events, mostly ^{9}Li decays (more than 85 at 90% CL) are observed. In order to eliminate these backgrounds, spallation cuts are employed. We apply a 2 ms veto after any muons. For muons with extra energy losses from minimum ionization larger than 10^6 p.e. on 17" PMTs ($\sim$3 GeV) and for

Table 3. Background summary (number of events).

Background	First result, 0.9 MeV	First result, 2.6 MeV	Second result, 2.6 MeV
Accidental	1.81 ± 0.08	0.0086 ± 0.00005	2.69 ± 0.02
^{9}Li/^{9}He	1.1 ± 1.0	0.94 ± 0.85	4.8 ± 0.9
Fast neutron	<0.5	<0.5	<0.89
Total	2.9 ± 1.1	1 ± 1	7.5 ± 1.3

Table 4. Estimated systematic uncertainties (%) of the new analysis.

Fiducial volume	4.7	Reactor power	2.1
Energy threshold	2.3	Fuel composition	1.0
Cut efficiency	1.6	$\bar{\nu}_e$ spectra	2.5
Live time	0.06	Cross-section	0.2
Total			6.5

muons tracked with poor reliability, a 2 s veto is additionally applied. For smaller energy losses, the 2 s veto is applied only in the 3 m radius cylinder around the muon track. These spallation cuts caused 11.4% (5 m radius fiducial volume) and 9.7% (5.5 m radius) dead time.

Considering dead time from the spallation cuts, the total live time used for the reactor neutrino analysis became 145.1 days for the first result and 515.1 days for the second result. The total exposures are 162 and 766.3 t-year, respectively. Estimated non-neutrino backgrounds during the periods are summarized in table 3. Accidental backgrounds are estimated by an off-timing window, 10 ms to 20 s, and by swapping the prompt and the delayed selection criteria [4]. Known neutrino backgrounds are small enough except for geoneutrinos in the 0.9 MeV analysis. An earth model with 16 TW heat from uranium and thorium predicts 9 events in the 0.9 MeV threshold sample of the first result.

The estimated systematic uncertainties of the new analysis for the rate analysis above 2.6 MeV are listed in table 4. The total systematic error becomes slightly larger than the previous analysis from 6.4 to 6.5%. The largest systematic error is still the fiducial volume error and it will be improved by future full-volume source calibrations.

4. Results

4.1. Evidence for reactor neutrino disappearance

The expected reactor anti-neutrino event rate for no oscillation and the observed rate during the first result period, from 4 March to 6 October 2002 (162 t-year exposure) are plotted in figure 6. The observed rates are always smaller than the no-oscillation expectation. While the expected number of neutrino events above 2.6 MeV is 86.8 ± 5.6 signal events and 1 ± 1 background events, only 54 events were observed. The significance of neutrino disappearance calculated with the following formula

$$P = \frac{1}{\sqrt{2\pi}\sigma} \int_0^\infty \mathrm{d}x \exp\left(-\frac{(N_{\mathrm{no\cdot osc}} + N_{\mathrm{BG}} - x)^2}{2\sigma^2}\right) \sum_{n=0}^{N_{\mathrm{obs}}} \frac{x^n \mathrm{e}^{-x}}{n!}$$

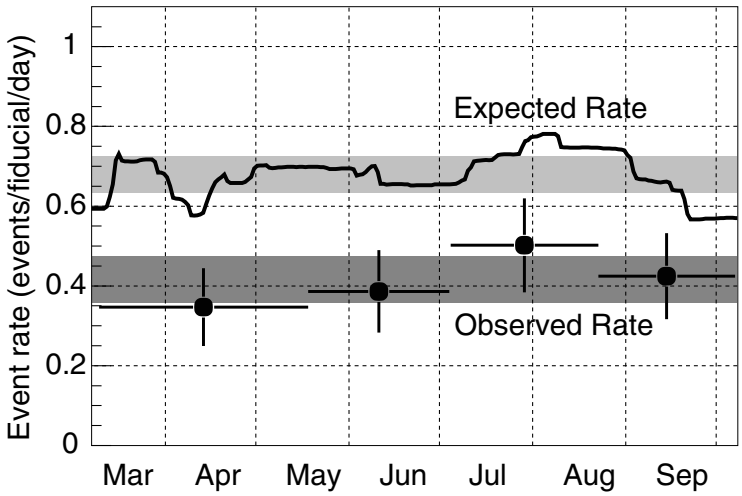

Figure 6. Reactor neutrino event rate in 2002. The plots and line are the observed and expected event rate, respectively, and the grey hatches are their average. The structure in the expected rate reflects the change in the reactor operations.

is 99.95%, where $N_{\text{no-osc}}$ and N_{BG} are the mean number of expected signal and background (86.8 and 1, respectively) and x run possibilities constrained by the Gaussian term, σ is the systematic and background total error $\sqrt{(86.8 \times 0.064)^2 + 1^2} = 5.66$ and N_{obs} $(= 54)$ is the observed number of events. The possibility of observing less than 54 events with x expected is integrated for all possible x; it gives 0.05% in this case. The ratio of observed to expected number of events is

$$R = \frac{N_{\text{obs}} - N_{\text{BG}}}{N_{\text{no-osc}}} = 0.611 \pm 0.085\ (\text{stat}) \pm 0.041\ (\text{syst}).$$

The expected signal for the 0.9 MeV threshold is 124.8 ± 7.5 events and the background rate is 2.9 ± 1.1 events without the uncertain geo-neutrino contribution of ~9 events. The observed number of signal events $(= 86)$, is consistent with the neutrino disappearance observed above 2.6 MeV. Figure 7 shows the observed ratios of reactor neutrino flux from KamLAND and previous experiments. The band shows the allowed range of the oscillatory pattern from various LMA parameters and the deficit at KamLAND is in good agreement with the LMA solution. This evidence of neutrino disappearance supports the LMA solution of the solar neutrino problem and all the other oscillation solutions are excluded at 99.95% CL under the CPT invariance. Also the other exotic models (RSFP, neutrino decay, etc) cannot be the leading phenomena of the solar neutrino problem. Adding the KamLAND results to the solar neutrino observations, the solar neutrino problem has been finally solved and the LMA solution is found to be the right one.

The spectrum information in figure 8 helps to shrink the allowed region of the oscillation parameters. An unbinned maximum likelihood method was applied using the following χ^2:

$$\chi^2_{\text{rate+shape}} = \chi^2_{\text{rate}}(\theta, \Delta m^2, N_{\text{BG1}\sim2}, \alpha_{1\sim4}) - 2\log L_{\text{shape}}(\theta, \Delta m^2, N_{\text{BG1}\sim2}, \alpha_{1\sim4}) + \chi^2_{\text{BG}}(N_{\text{BG1}\sim2}) + \chi^2_{\text{distortion}}(\alpha_{1\sim4}),$$

$$\chi^2_{\text{rate}} = \frac{(N_{\text{obs}} - N_{\text{osc}}(\theta, \Delta m^2, \alpha_{1\sim4}) - N_{\text{BG1}\sim2})^2}{\sigma^2_{\text{stat}} + \sigma^2_{\text{syst}}},$$

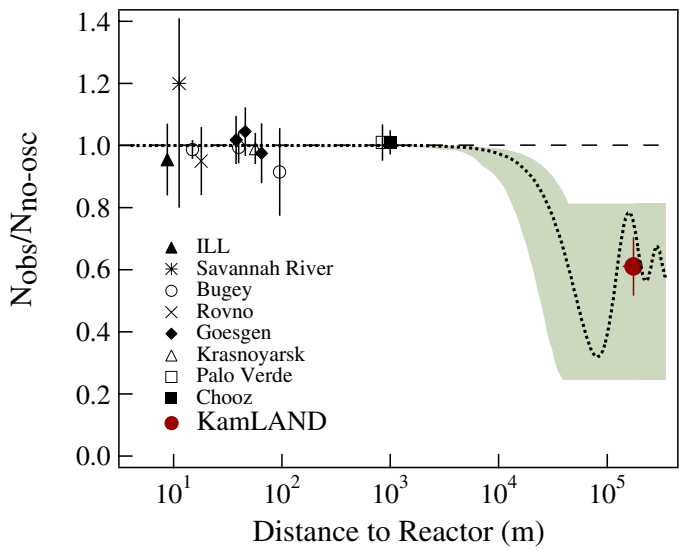

Figure 7. Observed neutrino rate at various baselines. The bands are for the various LMA parameters and the dotted line is for $(\sin^2 2\theta, \Delta m^2) = (0.833, 5.5 \times 10^{-5}\,\mathrm{eV}^2)$. The dashed lines are for no oscillation, the SMA, LOW and VAC solutions and the other hypothesis.

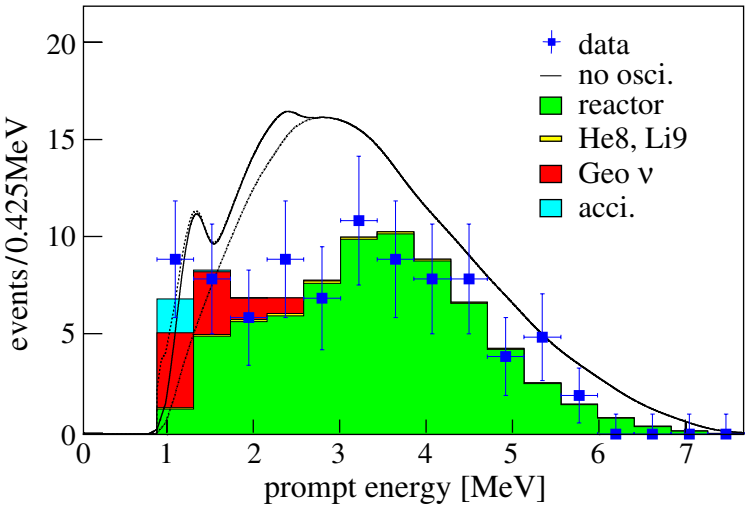

Figure 8. Energy spectrum at KamLAND. The curves are for no oscillation and the histograms are for the best-fit oscillation spectrum and the various background estimations.

where θ and Δm^2 are the oscillation parameters, $N_{\mathrm{BG1\sim2}}$ the number of ^{9}Li/^{8}He backgrounds floated with an constraint of $\chi^2_{\mathrm{BG}}(N_{\mathrm{BG1\sim2}})$ term, $\alpha_{1\sim4}$ floating parameters to account for the spectral effects of energy scale uncertainty, finite resolution, $\bar{\nu}_e$ spectrum uncertainty, and fiducial volume error, respectively also constrained by the $\chi^2_{\mathrm{distortion}}(\alpha_{1\sim4})$ term. Figure 9 shows the excluded region from the rate analysis and the allowed region from rate + shape analysis with two different threshold data. Only two bands overlap with the LMA region [22] from solar

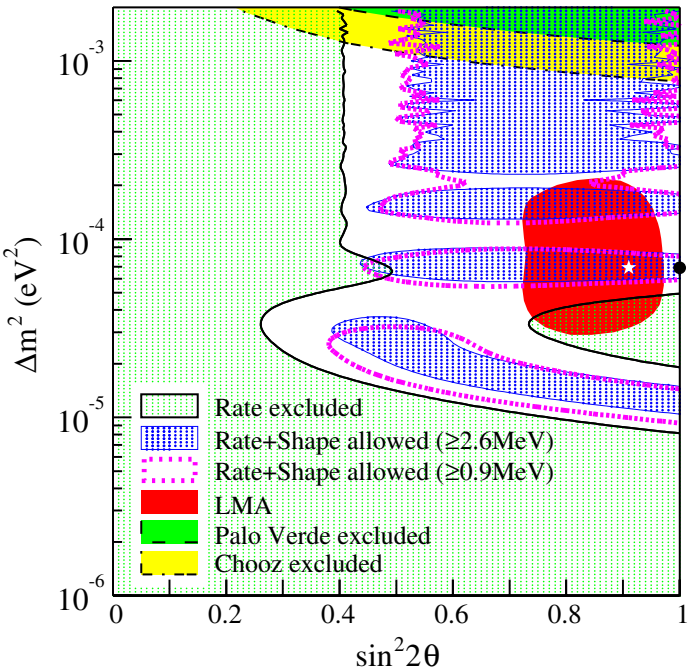

Figure 9. Excluded region by rate analysis and allowed region by rate + shape analysis from the first result. All regions are shown for a 95% confidence level. The black dot is the best-fit parameter from the rate + shape analysis above 2.6 MeV and the star is from the 0.9 MeV threshold.

observations. Two different thresholds give similar allowed region and it means data below and above 2.6 MeV are consistent with each other. When using data below 2.6 MeV, both uranium and thorium geo-neutrino contributions are treated as free parameters. This is the reason that the allowed region does not shrink with larger statistics in the 0.9 MeV threshold. The best-fit parameters are met at $(\sin^2 2\theta,\ \Delta m^2) = (1.0, 6.9 \times 10^{-5}\mathrm{eV}^2)$ with the 2.6 MeV threshold and $(0.91,\ 6.9 \times 10^{-5})$ with the 0.9 MeV threshold. The mass difference is stable but the mixing angle changes easily. There is an excess from the expected reactor spectrum below 2.6 MeV but the statistics is yet insufficient to discuss geo-neutrinos and a thorough background study is necessary.

4.2. Evidence of spectral distortion

The first results shrank the allowed region of oscillation parameters to two bands, LMA1 ($\Delta m^2 \sim 7 \times 10^{-5}\,\mathrm{eV}^2$) and LMA2 ($\Delta m^2 \sim 1.4 \times 10^{-4}\,\mathrm{eV}^2$), but the spectral distortion was not yet significant.

The second result increased the exposure by factor 4.7 ($\times$3.55 from live time and $\times$1.33 from expanded fiducial volume) from 162 to 766.3 t-year. Also the unusually low reactor operation in 2003 is used to see a correlation between the thermal power flux and neutrino event rate.

The expected number of signals without oscillation above 2.6 MeV ($E_{\bar{\nu}_e} = 3.4$ MeV) is 365.2 ± 23.7 (syst) and the estimated number of backgrounds is 7.5 ± 1.3 while 258 events are

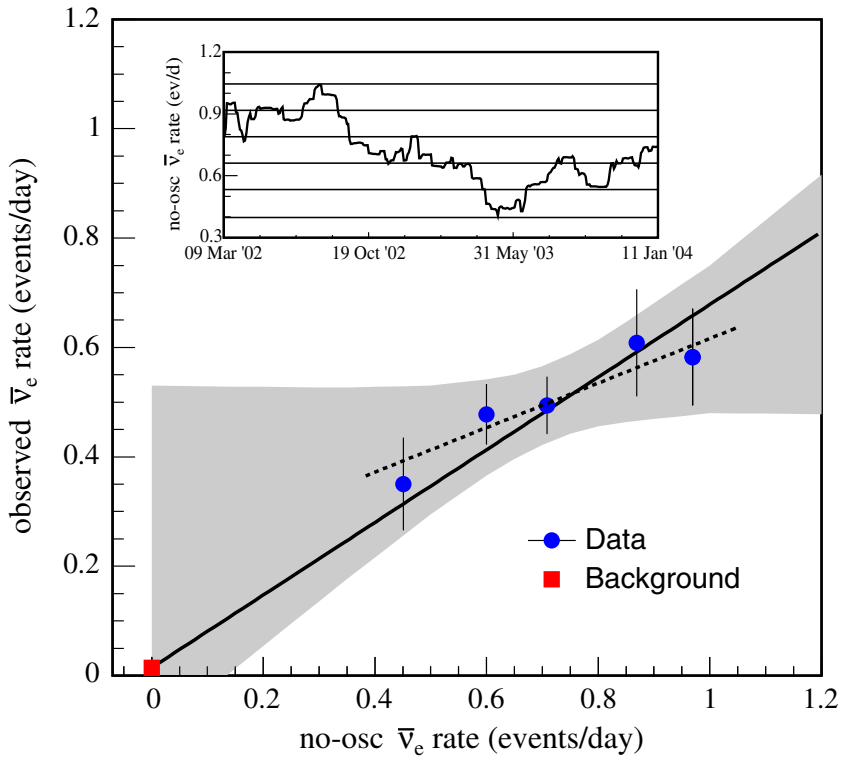

Figure 10. A plot of the observed $\bar{\nu}_e$ event rate versus no-oscillation expectation. The dashed line is the best linear fit, the grey region is the associated 90% CL. The solid line shows a fit constrained to the expected background at zero reactor anti-neutrino flux. The inset shows a division of the data set into five bins.

observed. It confirms reactor neutrino disappearance at the 99.995% CL, and the average survival probability during the live time is

$$R = 0.686 \pm 0.044\ (\text{stat}) \pm 0.045\ (\text{syst}).$$

The statistical error is already comparable with the systematic error. If the new analysis is applied for the period covered by the first result, the ratio 0.582 ± 0.069 (stat) $\pm$ 0.039 (syst) is obtained and is in good agreement with the first result.

The data set was divided into five bins according to the expected signal rate without oscillation and the observed number of events was compared with that expected for each set as shown in figure 10. The statistics is not enough to extract the uncorrelated component of $\bar{\nu}_e$ flux to reactor operation and the intercept is consistent with the estimated background rate.

The reactor neutrino spectra obtained with the updated data set is shown in figure 11 together with the lego plot of delayed energy versus prompt energy after all the selections except for the delayed energy cut. Events observed at delayed energy $\sim$5 MeV are consistent with the probability of neutron capture on ^{12}C ($\sim$0.5%). Three events are observed where $\sim$1.5 events are expected.

The observed spectrum does not agree with the no-oscillation spectrum at all. The goodness-of-fit was tested by binning the data into 20 equal-probability bins and by calculating the Pearson-χ^2 statistic for the data. The method helps to avoid the difficulty of treating small statistics bins. The χ^2_P was calculated for the scaled no-oscillation spectrum to see the statistical significance of

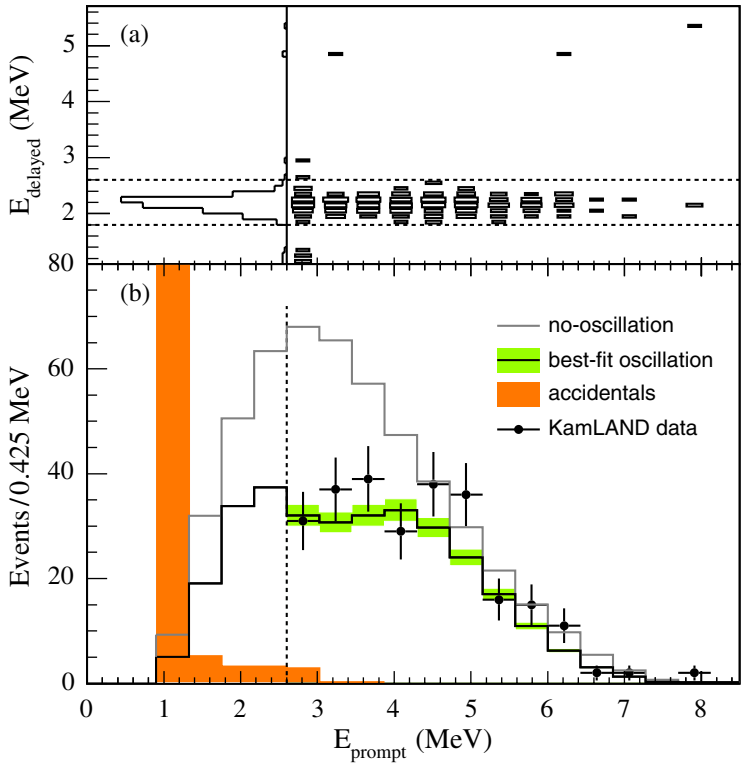

Figure 11. (a) Delayed energy versus prompt energy distribution after all selections except for the delayed energy cut. (b) Prompt energy spectrum along with the spectrum of accidental backgrounds. Other backgrounds are too few and cannot be seen. The solid histogram with shaded band indicates the best-fit oscillation spectrum of reactor neutrinos and the systematic error.

the spectral distortion. Then, the probability of exceeding the observed χ^2_P, the goodness-of-fit was estimated by MC simulation. The χ^2_P of the scaled no-oscillation is 43.4 with 19 d.o.f. and the goodness-of-fit is only 0.1%. This means the no-oscillation is excluded at 99.9% CL with only spectral shape information. This is evidence of spectral distortion. Considering the significance of deficit of 99.995%, no-oscillation is excluded at a great confidence level.

The obtained spectral distortion can be well reproduced by a neutrino oscillation. The best-fit oscillation parameter was surveyed using the unbinned method, the same way as with the first result but adding new background term for non-negligible accidental events. The best-fit values for Δm^2 and $\tan^2\theta$ are $8.3 \times 10^{-5}\,\mathrm{eV}^2$ and 0.41, respectively. If the flux is scaled freely, the best-fit parameter of a shape-only analysis gives $\Delta m^2 = 8.3 \times 10^{-5}\,\mathrm{eV}^2$ and $\tan^2\theta = 0.78$. The allowed region of the oscillation parameter is mostly determined by the shape information and an addition of rate information does not change the sensitivity very much. The best-fit oscillation spectrum is also shown in figure 11, and the χ^2_P and the goodness-of-fit of the best-fit spectrum are 18.3 with 18 d.o.f. and 42%. The oscillation spectrum explains the observed spectral distortion very well.

The goodness of the oscillation hypothesis can be seen more easily with a L/E plot as shown in figure 12. The energy spectrum is rebinned according to L_0 over $E_{\bar{\nu}_e} \sim E_{\mathrm{prompt}} + 0.8\,\mathrm{MeV}$ where the constant L_0 is chosen at 180 km as a relevant distance. The observed oscillatory behaviour agrees very well with the expected pattern from the best-fit oscillation parameters

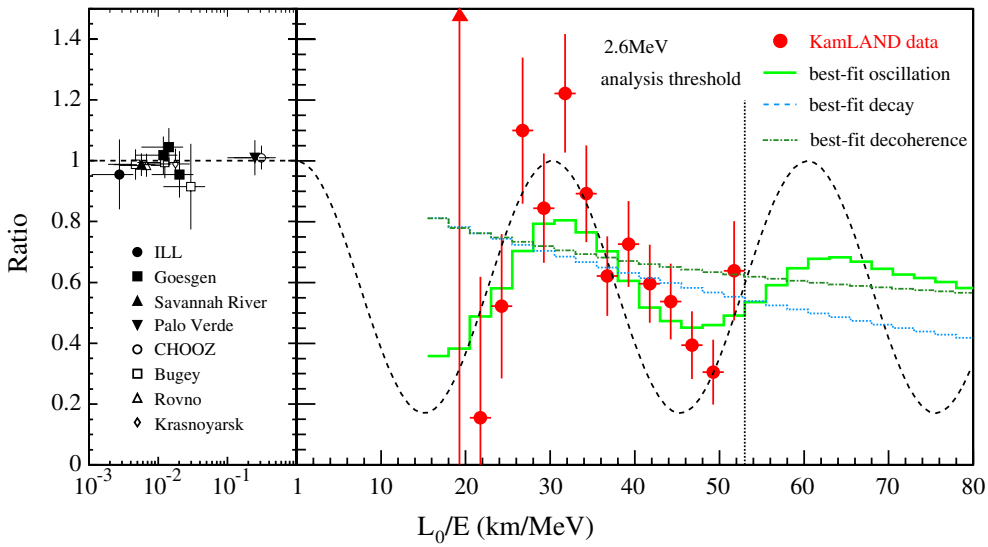

Figure 12. The ratio of observed event rate to no-oscillation expectation is plotted as a function of $L_0/E_{\bar{\nu}_e}$. The energy spectrum is rebinned according to L_0 over $E_{\bar{\nu}_e}$ and the constant L_0 is chosen at 180 km as a relevant distance. Histograms are for the best-fit-oscillation, decay and decoherence considering real distance distribution of reactors and detector responses. Only the dashed sine curve represents oscillatory behaviour for the best-fit oscillation parameter as if only one reactor existed at a 180 km distance. Results from previous short baseline experiments are also plotted.

as shown by the green solid histogram in the figure. It clearly shows about one full phase of the oscillation. The oscillatory behaviour is compared with a neutrino decay model [23] and a decoherence model [24]. Surveys of parameter spaces resulted in the best-fit parameters of decay and decoherence as $(\sin^2\theta, m/c\tau) = (1.0, 0.011\,\mathrm{MeV\,km^{-1}})$ and $(\sin^2 2\theta, \gamma^0) = (1.0, 0.028\,\mathrm{MeV\,km^{-1}})$, respectively. The expected L/E dependences of these parameters are also plotted in figure 12. Their monotonically decreasing ratio does not agree with the observed oscillatory pattern, and the goodness-of-fit for these parameters using the Pearson-χ^2 are only 5% ($\chi^2_{\mathrm{P}}/\mathrm{d.o.f.} = 30.1/18$) for decay and 6% ($\chi^2_{\mathrm{P}}/\mathrm{d.o.f.} = 28.6/18$) for decoherence. Naively considering $\Delta\chi^2$ from the oscillation ($\chi^2_{\mathrm{P}}/\mathrm{d.o.f.} = 18.3/18$), the oscillation is favoured over decay and decoherence more than 99% level. Now, KamLAND alone can conclude the observation of neutrino oscillation without a help of solar neutrino results and an assumption of CPT invariance.

4.3. Measurement of neutrino oscillation parameters

The allowed region of two neutrino oscillation parameters from the updated data set is shown in figure 13. Comparing with the first result, the precision of the parameter determination has been significantly improved. The allowed region from solar neutrino results shown in the figure uses the neutrino flux from BP2004 [5]. The best-fit point from KamLAND is $(\sin^2 2\theta, \Delta m^2) = (0.83, 8.3 \times 10^{-5}\,\mathrm{eV}^2)$ and sits in the LMA1 region. Maximal mixing of the LMA1 region is allowed at the 79% CL. The LMA2 region barely appears at the 99.73% CL (allowed at the 99.6% CL) while the LMA0 is allowed at the 94% CL.

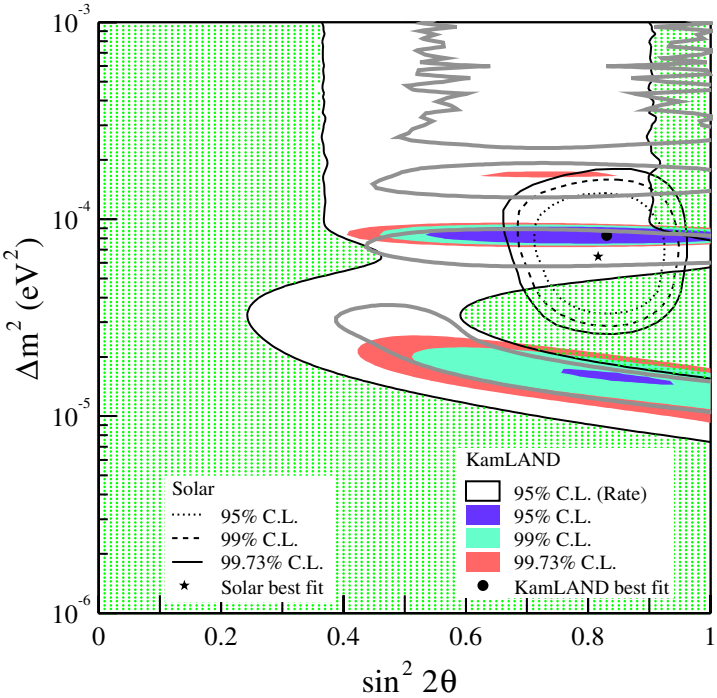

Figure 13. Allowed regions of neutrino oscillation parameters from the second result. The region shaded green is excluded by the rate analysis at 95% CL. Allowed regions by rate + shape analysis are shown in three different colours for 95, 99 and 99.73% CL. The thick grey curve is the 95% CL allowed region by rate + shape analysis of the first result.

In order to see the dark side of the oscillation parameters, the allowed region is plotted on the Δm^2 versus $\tan^2\theta$ space in figure 14. A small asymmetry seen between the light side and the dark side in the figure comes from the matter effect during a neutrino propagation. A constant matter density 2.7 of g cm^{-3} was used in the analysis. The best-fit has been obtained in the light side but the difference with the local minimum in the dark side is very small.

Assuming the CPT invariance, KamLAND result and the solar global analysis can be combined. Figure 15 shows the allowed region from the solar + KamLAND global analysis. There is only one region allowed at 99.73% CL and the parameter space is very much scaled up in the figure. The measured value of the two neutrino oscillation parameters are $\Delta m^2 = 8.2^{+0.6}_{-0.5} \times 10^{-5}\,\mathrm{eV}^2$ and $\tan^2\theta = 0.40^{+0.09}_{-0.07}$. The sensitivity in Δm^2 is dominated by the observed spectral distortion in KamLAND while the mixing angle is mainly constrained by the solar neutrino results. Further improvement of the precision of the neutrino oscillation parameters will require an improvement of the systematic error already larger than the statistical error in KamLAND.

5. Overlooked background

In a survey of possible background sources, various neutron-producing reactions such as photo-neutron production, spontaneous fission, neutral current interaction of atmospheric neutrinos,

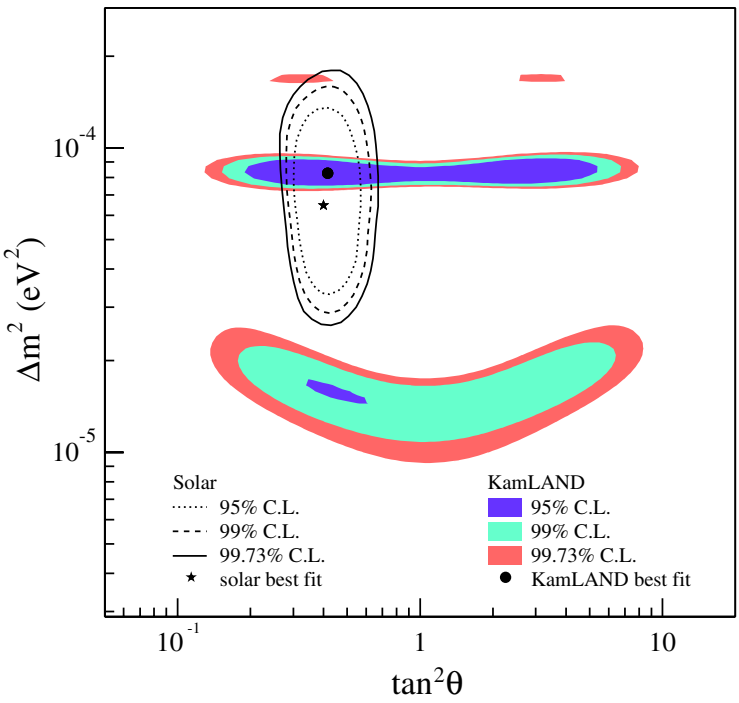

Figure 14. Allowed region of neutrino oscillation parameters from the second result. Horizontal axis is now $\tan^2\theta$ and the dark side ($\tan^2\theta > 1$) is also shown.

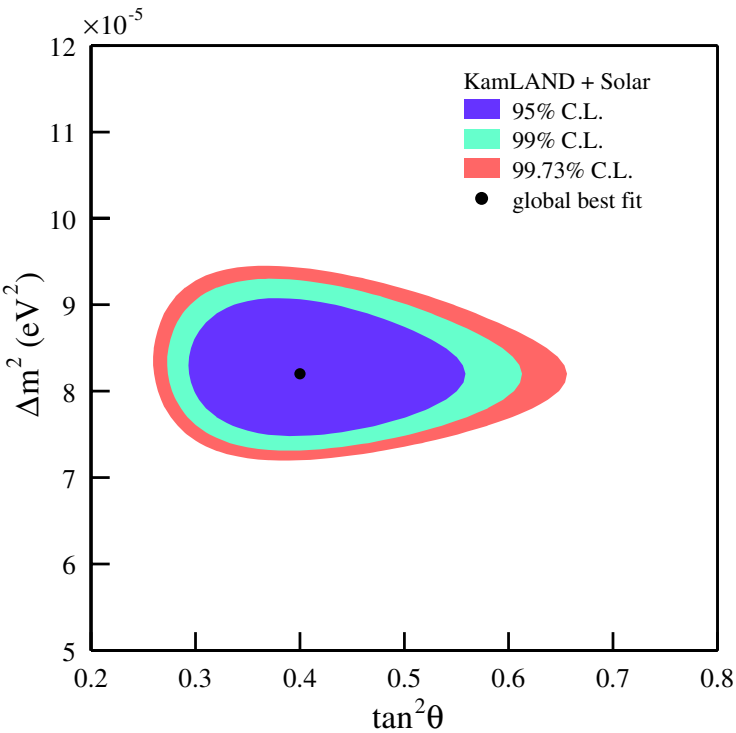

Figure 15. Allowed region of neutrino oscillation parameters from the solar + KamLAND global analysis. The global best-fit point with 1σ error is $(\tan^2\theta, \Delta m^2) = (0.40^{+0.09}_{-0.07},\ 8.2^{+0.6}_{-0.5} \times 10^{-5}\,\mathrm{eV}^2)$.

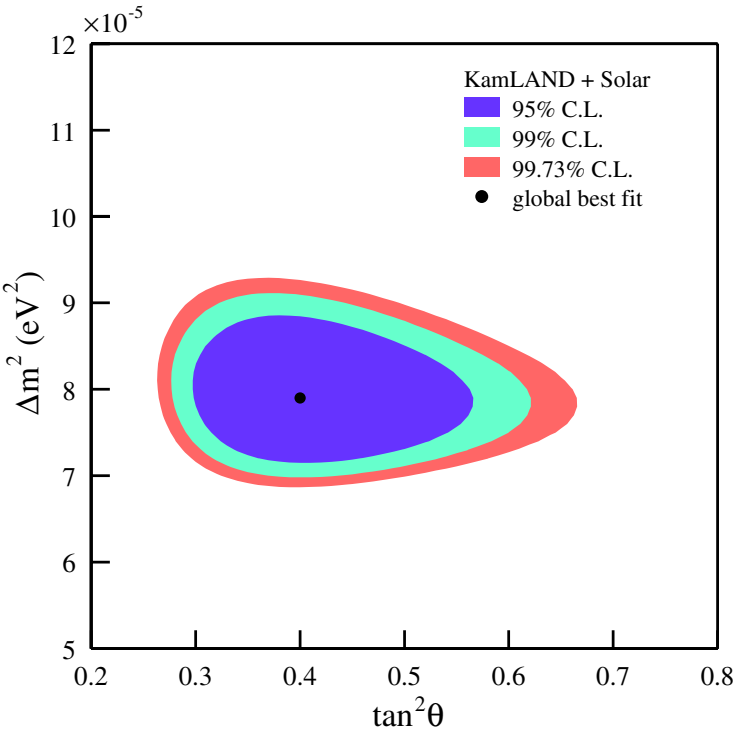

Figure 16. Preliminary allowed region of neutrino oscillation parameters from the solar + KamLAND global analysis. A preliminary estimation of previously unnoticed background ^{13}C (α, n) is included. The result does not change much but the best fit Δm^2 moves a little downward.

deuteron disintegration by solar neutrinos and (α, n) interactions were additionally investigated. And it turned out that the previously unnoticed background from ^{13}C(α, n)^{16}O$^{(*)}$ is not negligible [25].

A number of ^{222}Rn have decayed in the liquid scintillator before the experiment starts and long-lived ^{210}Pb ($T_{1/2} = 22.3$ yr) have accumulated in the detector. Daughter nuclei, ^{210}Po ($T_{1/2} = 138.4$ d), are almost in equilibrium with ^{210}Pb and they emit 5.3 MeV α-rays. The natural abundance of ^{13}C is only 1.1% but neutrons are created with $Q = 2.2$ MeV at a probability of about one per 10 million α decays. Neutron energy ranges from 0 to 7.5 MeV depending on the final states of ^{16}O. Hard recoil of a proton by neutron elastic scattering has the possiblity of faking a prompt event of the neutrino signal although the quenching effect of the liquid scintillator makes the visible energy very low and mostly subthreshold. A ^{12}C(n, n$'$)^{12}C*(4.44 MeV, 2$^+$) reaction, if it took place successively, could make a 4.4 MeV γ ray as a prompt signal from the decay of the excited state. Also internal pair conversion of ^{16}O*(6.05 MeV, 0$^+$) and γ ray emission from ^{16}O*(6.13 MeV, 3$^-$) effectively mimic the prompt signal. Considering these reactions, a preliminary background estimation of about 10 events in the 5.5 m radius fiducial volume has been obtained. Their effect on the oscillation parameter determination was tested with the global analysis and the result did not change much as shown in figure 16. The allowed region slightly shifted to smaller Δm^2.

6. Summary

KamLAND first observed evidence of reactor neutrino disappearance at ∼180 km baseline. It excluded all but the LMA solution of the solar neutrino problem, which has lasted for more than 30 years. Improved analysis and increased run time provided 4.7 times larger exposure and the significance of the reactor neutrino disappearance was strengthened to 99.995% CL. In addition, the scaled no-oscillation spectrum was excluded at the 99.9% CL and the observed L/E distribution matches very well with the expected oscillatory behaviour of the neutrino oscillation. This evidence of spectral distortion can conclude the observation of neutrino oscillation by KamLAND alone. Combining the great sensitivity of KamLAND in Δm^2 with the solar neutrino results, the neutrino oscillation parameters have been determined to drastically improved value $(\tan^2\theta, \Delta m^2) = (0.40^{+0.09}_{-0.07},\ 8.2^{+0.6}_{-0.5} \times 10^{-5}\,\mathrm{eV}^2)$. A terrestrial experiment using a well-understood artificial neutrino source has finally confirmed the neutrino oscillations suggested by the solar neutrino experiments and provided a resolution of the long-standing solar neutrino problem, and it has now entered a precision measurement of the neutrino oscillation parameters.

References

[1] The KamLAND Collaboration 2003 *Phys. Rev. Lett.* **90** 021802
[2] The KamLAND Collaboration 2004 *Preprint* hep-ex/0406035
[3] Apollonio M *et al* 2003 *Eur. Phys. J.* C **27** 331
[4] Boehm F *et al* 2001 *Phys. Rev.* D **61** 112001
[5] For example, Bahcall J N and Peña-Garay C 2004 *New J. Phys.* **6** 63 (*Preprint* hep-ph/0404061)
[6] Cleveland B T *et al* 1998 *Astrophys. J.* **496** 505
[7] The Kamiokande Collaboration 1999 *Phys. Rev. Lett.* **77** 415
[8] The Super-Kamiokande Collaboration 2004 *Phys. Rev.* D **69** 011104
[9] The SAGE Collaboration 2002 *J. Exp. Theor. Phys.* **95** 181
[10] The Gallex Collaboration 1999 *Phys. Lett.* B **447** 127
[11] The GNO Collaboration 2000 *Phys. Lett.* B **490** 16
[12] The SNO Collaboration 2004 *Phys. Rev. Lett.* **92** 181301
[13] Lim C S and Marciano W J 1988 *Phys. Rev.* D **37** 1368
Akhmedov E Kh 1988 *Phys. Lett.* B **213** 64
Akhmedov E Kh 1989 *Sov. Phys.—JETP* **68** 690
Barranco J *et al* 2002 *Phys. Rev.* D **66** 093009
[14] Berezhiani Z *et al* 1992 *JETP Lett.* **55** 371
Raghavan R S *et al* 1988 *Phys. Rev.* D **38** 1317
Beacom J F and Bell N F 2002 *Phys. Rev.* D **65** 113009
[15] Declais Y *et al* 1994 *Phys. Lett.* B **338** 383
[16] Kopeikin V I *et al* 2001 *Phys. At. Nucl.* **64–65** 849
[17] Mampe M *et al* 1978 *Nucl. Instrum. Methods* **154** 127
[18] Schreckenbach K *et al* 1985 *Phys. Lett.* B **160** 325
Hahn A A *et al* 1989 *Phys. Lett.* B **218** 365
[19] Vogel P *et al* 1981 *Phys. Rev.* C **24** 1543
[20] Vogel P and Beacom J F 1999 *Phys. Rev.* D **60** 053003
Kurylov A *et al* 2003 *Phys. Rev.* C **67** 035502

[21] Achkar B *et al* 1996 *Phys. Lett.* B **374** 243
[22] Fogli G L *et al* 2002 *Phys. Rev.* D **66** 053010
[23] Barger V D *et al* 1999 *Phys. Rev. Lett.* **82** 2640
[24] Lisi E *et al* 2000 *Phys. Rev. Lett.* **85** 1166
[25] Shimizu I, talk given at *ICHEP2004, August 16–22, 2004, Beijing, China*
Suzuki A, talk given at *Nobel Symposium on Neutrino Physics, 19–24 August, 2004, Haga Slott, Sweden*

New Journal of Physics
The open-access journal for physics

The particle physics reach of high-energy neutrino astronomy

Tao Han[1] **and Dan Hooper**[2]

[1] Physics Department, University of Wisconsin, 1150 University Ave., Madison, WI 53706, USA

[2] Astrophysics Department, University of Oxford, Denys Wilkinson Laboratory, Oxford OX1 3RH, UK

E-mail: than@physics.wisc.edu and hooper@astro.ox.ac.uk

New Journal of Physics **6** (2004) 150
Received 31 August 2004
Published 28 October 2004
Online at http://www.njp.org/
doi:10.1088/1367-2630/6/1/150

Abstract. We discuss the prospects for high-energy neutrino astronomy to study particle physics in the energy regime comparable to and beyond that obtainable at the current and planned colliders. We describe the various signatures of high-energy cosmic neutrinos expected in both neutrino telescopes and air shower experiments and discuss these measurements within the context of theoretical models with a quantum gravity or string scale near a TeV, supersymmetry and scenarios with interactions induced by electroweak instantons. We attempt to access the particle physics reach of these experiments.

1367-2630/04/010150+24$30.00
PII: S1367-2630(04)85536-8
© IOP Publishing Ltd and Deutsche Physikalische Gesellschaft

Contents

1. Introduction **2**
2. The high-energy cosmic neutrino flux **3**
3. Particle physics with high-energy neutrino astronomy **6**
3.1. Neutrino telescopes . . . 7
3.2. Neutrinos in air shower experiments . . . 8
4. Signatures of new physics **10**
4.1. Contributions of KK gravitons . . . 10
4.2. TeV string resonances . . . 11
4.3. Microscopic black hole production . . . 13
4.4. p-brane production . . . 15
4.5. Electroweak instanton-induced processes . . . 16
4.6. Signatures of SUSY . . . 19
5. Conclusions and summary **20**
Acknowledgments **21**
References **21**

1. Introduction

In recent endeavours, exploration of high-energy particle physics has largely been conducted in accelerator experiments, and for good reason. Accelerator laboratories provide controlled, high-luminosity environments in which very precise levels of measurement can be reached. Despite these advantages, astrophysics experiments have also revealed a great deal of particle physics beginning with Anderson's discovery of the positron in 1932, then the muon, the pion, etc, predating accelerator experiments and continuing to the observation of neutrino masses and mixings. It is clear that astrophysics has much to offer in studying the fundamental aspects of particle physics.

Particle physics has entered an exciting era. The standard model (SM) of the strong and electroweak interactions has been experimentally verified to high precision, while the mechanisms for electroweak symmetry breaking and mass generation remain largely unknown. Theoretical arguments and indirect experimental evidence imply the existence of new physics near the electroweak scale below a few TeV (for a recent review on the status of the SM and beyond, see e.g. [1]). The leading candidates of theoretical models beyond the SM include weak-scale supersymmetry (SUSY) (for an introductory review on SUSY, see e.g. [2]), strongly interacting dynamics (for a recent review on strong dynamics in the electroweak sector, see e.g. [3]) and low-scale string or quantum gravity [4, 5]. It is encouraging that all of the above scenarios often lead to observable signatures in next-generation colliders such as the CERN Large Hadron Collider (LHC) and an e^+e^- linear collider.

The field of high-energy neutrino astronomy finds itself in a position to contribute to two very different areas of science: astronomy and particle physics (for recent reviews of high-energy neutrino astronomy, see e.g. [6]). On the one hand, the next generation of neutrino telescopes may reveal the origins of the highest energy cosmic rays, help us understand the progenitors of γ-ray bursts and provide other insights into some of the greatest outstanding astrophysical

puzzles. On the other, very-high-energy cosmic neutrinos present a unique opportunity to study the interactions of elementary particles at energies comparable to and beyond those obtainable in current or planned colliders. This is the main advantage of such experiments over traditional collider experiments. Currently, the highest energy achieved in collider experiments is at Fermilab's Tevatron, with $E_{CM} \approx 2$ TeV. This centre-of-mass energy roughly corresponds to a PeV neutrino striking a nucleon at rest, $E_\nu = E_{CM}^2/2m_N$. Even the LHC at CERN will only reach energies that correspond to 100 PeV cosmic neutrinos. It is certainly plausible, as we will discuss, that there is a neutrino flux at energies well beyond 1 EeV. Even crude measurements of neutrino cross-sections at extremely high energies would provide powerful tests of fundamental physics at and beyond a scale of 1–10 TeV. Additionally, sources of high-energy neutrinos may be observed from distances of hundreds or thousands of Mps, providing baselines for tests of neutrino oscillations or decays that could not be carried out using accelerator, atmospheric or solar neutrinos.

The experimental status of high-energy neutrino astronomy is developing rapidly. Current technologies such as the AMANDA-II [7] and RICE [8] experiments at the South Pole have proven successful, but with too little sensitivity to reach many of the most interesting physics goals. Several new experiments are soon to enter the field fortunately. IceCube [9] will expand the effective area of AMANDA-II by more than a factor of 20 while also improving both the angular and energy resolution. ANTARES [10], in the Mediterranean, will use a similar technique, but with sensitivity to neutrino-induced muons of lower energy (down to 10 GeV). Radio techniques will be employed in the balloon-based ANITA [11] experiment, which has its first flight scheduled in the next year or two. High-energy cosmic-ray experiments, such as the Pierre Auger observatory [12] and space-based observatories such as OWL [13] or EUSO [14], will also be sensitive to ultrahigh-energy cosmic neutrinos. Other proposals, such as using acoustic techniques [15] or natural salt domes as a Cerenkov medium [16] or expanding IceCube into a multi-kilometre ultrahigh-energy experiment [17], have been discussed as well. With the development of these many and varied techniques, a new window into fundamental particle physics will be opened [6], possibly predating the LHC experiments.

This paper is a mini review on the potential of high-energy neutrino astronomy in studying particle physics beyond the SM. We first present the current theoretical predictions on the high-energy cosmic neutrino flux in section 2. We then discuss methods for exploring particle physics via high-energy neutrino astronomy in section 3, paying particular attention to future neutrino telescopes and air shower observatories. We summarize in section 4 the predicted experimental signatures from various new physics scenarios, including models with low-scale quantum gravity, low-scale string resonances, black holes and p-branes, electroweak instantons and SUSY. We draw our conclusions in section 5.

2. The high-energy cosmic neutrino flux

Just as the performance of an accelerator experiment crucially depends on its luminosity, the particle physics reach of high-energy neutrino astronomy will depend on the incoming flux of cosmic neutrinos. Here, we will briefly review some of the arguments for various neutrino fluxes from cosmic accelerators.

The spectrum of cosmic rays has been well measured up to energies near 10^{20} eV (10^8 TeV in the laboratory frame) where the experiments become limited by poor statistics. The spectrum

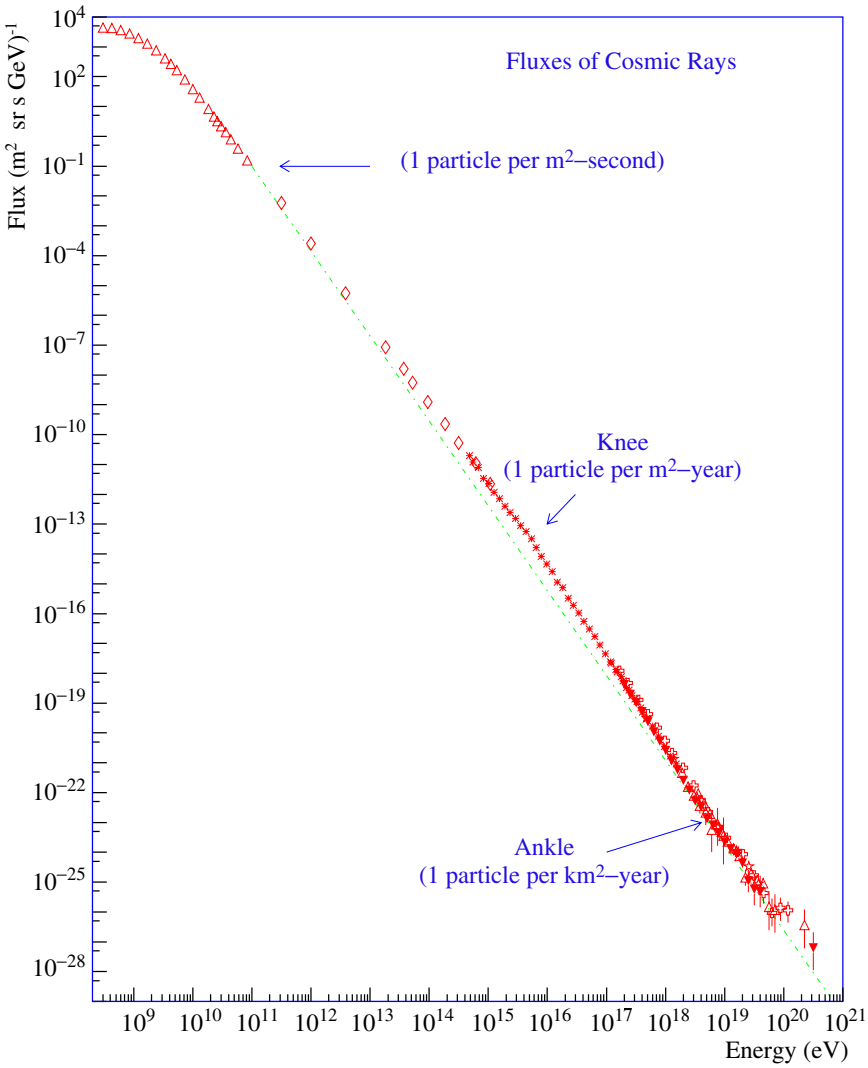

Figure 1. The observed cosmic ray spectrum.

consists of a series of power laws that change at energies called as the 'knee' and 'ankle' (see figure 1). The standard process believed to be responsible for the observed spectrum of cosmic rays is the acceleration of charged particles via second-order Fermi acceleration (for a discussion of Fermi acceleration, see [18]). In Fermi's original paper on the subject, he proposed that cosmic rays were accelerated by the reflecting off of time-varying magnetic fields associated with galactic clouds moving with randomly distributed velocities. Although this process will statically accelerate charged particles, it does so very slowly and is generally not capable of even countering the effects of energy losses by ionization and other processes. If instead we consider a compact region of dense plasma, however, the random motion of the matter and the associated magnetic fields can be sufficient to accelerate charged cosmic rays to very high energies. Although there is no strong evidence as of yet, it is likely that supernova remnants accelerate most of the cosmic rays up to the knee in the spectrum, occurring around 10^{15} eV, by this mechanism. A generic feature of Fermi acceleration is a power-law spectrum, $\mathrm{d}N/\mathrm{d}E \propto E^{-\alpha}$, where $\alpha \simeq 2$ [19].

The maximum energy to which a cosmic ray source may accelerate particles can be estimated by a simple argument. First, we assume that, to accelerate a proton to a given energy in a given magnetic field, the size of the accelerator must be larger than the gyroradius of the orbit of the particle:

$$R > R_{\mathrm{gyro}} = \frac{E}{B}. \tag{1}$$

This condition yields a maximum energy of

$$E_{\mathrm{max}} = \gamma BR, \tag{2}$$

where γ is the Lorentz factor of the cosmic accelerator. To produce cosmic rays with energies near the highest observed ($\sim 10^{20}$ eV), very compact objects are required. For the most compact objects, we can consider $R \sim GM/c^2$ or the Schwartzchild radius of the object. For such a source, we find a maximum energy of

$$E_{\mathrm{max}} \propto \gamma BM. \tag{3}$$

With only micro-Gauss galactic magnetic fields, we must turn to extragalactic sources to accelerate cosmic rays to energies above the EeV scale. Extragalactic sources potentially capable of accelerating particles to such energies include the relativistic jets of active galactic nuclei or gamma-ray bursts.

As protons are accelerated to very high energies in such sources, they may undergo photo-meson interactions with the surrounding radiation fields. In such interactions, both charged and neutral pions are produced. These pions then decay, producing neutrinos and γ rays, respectively. This process essentially guarantees the existence of the accompanying neutrinos and γ rays given the observed cosmic-ray flux. Alternatively, bounds can be placed on the cosmic neutrino flux by relating it to the cosmic-ray spectrum. Using this method, Waxman and Bahcall [20] have placed a upper bound for each neutrino flavour,

$$E_\nu^2\, \mathrm{d}N_\nu/\mathrm{d}E_\nu \lesssim 10^{-8}\,\mathrm{GeV}(\mathrm{cm}^2\,\mathrm{s\,sr})^{-1}. \tag{4}$$

This assumes that the sources in question are optically thin or transparent to protons. If sources are optically thick to protons however, the bound on the neutrino flux can be based only on γ-ray observations by EGRET and is thus weaker by a factor of about 40 [21]. Furthermore, if some sources were truly 'hidden', implying that neither nucleons nor photons could escape, no upper bound could be made on the corresponding neutrino flux. For a further discussion of these and similar arguments, see [22].

In addition to the neutrino production from cosmic-ray interactions in or near cosmic accelerators, ultrahigh-energy cosmic rays produce neutrinos during propagation over cosmological distances [23]. Protons of energy above a few times 10^{19} eV can scatter off cosmic microwave background photons with a centre-of-mass energy roughly equal to the resonance corresponding to the mass of the Δ-hadron (1.232 GeV). Again, both charged and neutral pions can be produced this way, yielding neutrinos and γ rays. The neutrino flux corresponding to this process is called the 'cosmogenic neutrino flux'. Unlike the flux of neutrinos from cosmic accelerators, the spectrum of cosmogenic neutrinos depends only on the spectrum of ultrahigh-energy protons and the distribution of their sources and thus can be reliably calculated [24].

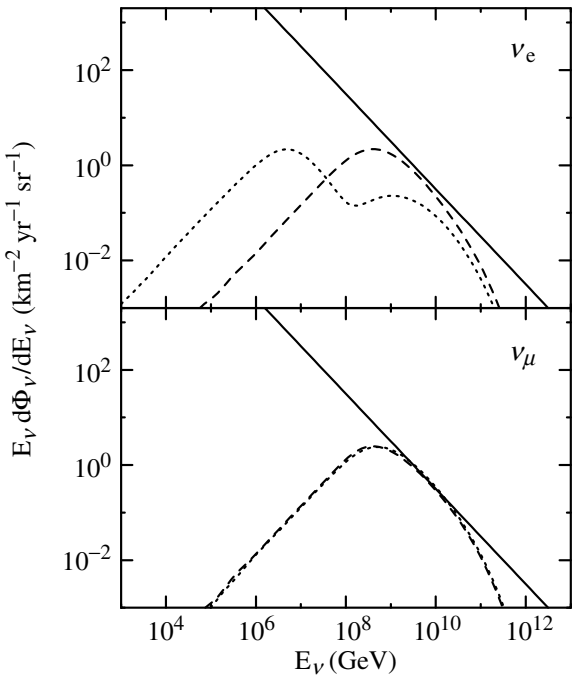

Figure 2. The cosmic neutrino flux corresponding to the bound of Waxman and Bahcall [20] (solid line) and the cosmogenic neutrino flux (dashed curve for ν and dotted curve for $\bar{\nu}$) [27]. Note that, after neutrino oscillations are considered, these fluxes will contain all the three neutrino flavours (ν_e, ν_μ, ν_τ) in equal quantities. The figure was taken from [28].

The cosmogenic neutrino flux is often thought of as a 'guaranteed' source of ultrahigh-energy neutrinos, assuming that the cosmic-ray primaries at the highest observed energies are protons and not heavy nuclei [25].

There are ways in which neutrino fluxes larger than those described here could be produced. For example, in models of non-accelerator cosmic-ray origins, i.e., models in which the highest energy cosmic rays are produced in the decay or annihilations of superheavy objects. In such models, the resulting neutrino flux is not constrained by the arguments shown here. Although such scenarios are certainly interesting, we will not consider them in this paper. For a further discussion on cosmic neutrino fluxes and their constraints, see [26].

Throughout the remainder of this paper, we will primarily consider two representative choices for the cosmic neutrino spectrum. The first is a flux equal to the bound set by Waxman and Bahcall [20], which we call the Waxman–Bahcall flux of equation (4). The second is the cosmogenic neutrino flux, as calculated in [27]. Each of these is shown in figure 2.

3. Particle physics with high-energy neutrino astronomy

To identify potential signatures of new physics in high-energy neutrino interactions, one must first understand the phenomenology predicted by the SM, in particular the features of charged and neutral current interactions between high-energy neutrinos and target nuclei. The SM predicts

the cross-sections for neutrino–nucleon interactions, up to uncertainties in parton distribution functions at extremely small values of the momentum fraction x, to energies beyond those probed by any planned neutrino telescopes [29]. In this section, we will describe the experimental features predicted by the SM in neutrino telescopes and air shower experiments.

3.1. Neutrino telescopes

Neutrino telescopes are essentially arrays of detectors distributed over a large volume of a Cerenkov medium, such as water or ice. These detectors may be sensitive to optical Cerenkov radiation, as are AMANDA-II, IceCube and ANTARES, or to radio, as is RICE. We will focus on optical Cerenkov detectors here, although the treatment of shower detection is quite easily generalized to include radio.

Muons produced in the charged current interactions of muon neutrinos can travel several kilometres through a detector medium, producing a 'track' of Cerenkov light that can be observed and accurately reconstructed by neutrino telescopes.

The rate of muon events observed in a large volume neutrino telescope is given by

$$N = \iiint \mathrm{d}E_\nu\,\mathrm{d}y\,\mathrm{d}\cos\theta_z N_A \frac{\mathrm{d}N_{\nu_\mu}(E_\nu)}{\mathrm{d}E_{\nu_\mu}\mathrm{d}t\,\mathrm{d}\Omega} R_\mu(E_\mu,\theta_z)\frac{\mathrm{d}\sigma}{\mathrm{d}y}(E_{\nu_\mu})P_S(E_\nu,\theta_z)A_{\mathrm{eff}}T, \tag{5}$$

where θ_z is the zenith angle of an event ($\theta = 0$ is vertically down-going), N_A the Avogadro number, $\mathrm{d}N_\nu/\mathrm{d}E_\nu\,\mathrm{d}t\,\mathrm{d}\Omega$ the flux of muon neutrinos (per unit energy, per unit time, per solid angle), $\mathrm{d}\sigma/\mathrm{d}y$ the differential neutrino–nucleon cross-section (where y is defined such that $E_\mu = (1-y)E_{\nu_\mu}$), $P_S(E_\nu,\theta_z)$ the survival probability of a neutrino travelling through the Earth, A_{eff} the effective area of the detector ($\simeq 1\,\mathrm{km}^2$ for IceCube), T the length of time observed and $R_\mu(E_\mu,\theta_z)$ is either the muon range or the length of material (i.e. ice) between the detector and the Earth's surface, whichever is smaller. The muon range is defined as the distance a muon propagates in the medium surrounding the detector before falling below a cutoff energy. The muon range is given by [30]

$$R_\mu = \frac{1}{\beta}\ln\left(\frac{\alpha+\beta E_\mu}{\alpha+\beta E_\mu^{\mathrm{cut}}}\right), \tag{6}$$

where E_μ^{cut} is the minimum muon energy required to produce an event. This value is selected to reduce the number of background events while retaining as many signal events as possible. In optical Cerenkov neutrino telescopes, muons with energy as low as 10–100 GeV can be observed, although cuts well above this energy are often imposed when searching for high-energy neutrinos. In ice, $\alpha \simeq 2\times10^{-6}\,\mathrm{TeV\,cm^2\,g^{-1}}$ and $\beta \simeq 4.2\times10^{-6}\,\mathrm{cm^2\,g^{-1}}$ [30]. For a PeV muon in ice and a 100 GeV muon energy threshold, the range is approximately 1.7 km. For muons with energies of 10 PeV, 100 PeV or 1 EeV, the range increases to 7, 13 and 18 km, respectively. Thus, for very energetic muon neutrinos, the target volume of the experiment becomes a long cylinder, rather than a box. This is particularly relevant for neutrinos coming from a direction near the horizon.

Unlike in accelerator experiments, the flux (or luminosity) of a cosmic neutrino beam may be unknown. Therefore, simply counting the number of events will not provide sufficient information to measure a neutrino cross-section. Instead, information from the angular and energy distributions of events must be used [31]. For a cross-section of about 2×10^{-7} mb, a particle's

interaction length as it travels through the Earth is equal to the Earth's diameter. This cross-section is reached near $E_\nu \sim 100$ TeV according to the SM prediction. Thus, as the neutrino–nucleon cross-section is increased from its SM value, the effect of absorption in the Earth becomes more pronounced and fewer of the observed events will come from neutrinos travelling through the Earth. A crude way to measure the neutrino–nucleon cross-section could, therefore, be a comparison of the up-going and down-going (or Earth-skimming, etc) events in a high-energy neutrino telescope. However, a more sophisticated analysis of the angular distribution of events as a function of energy would be more useful.

In addition to muon tracks, neutrino telescopes are sensitive to electromagnetic and hadronic showers. These events can be produced by all three neutrino flavours in neutral current interactions, or in some charged current interactions. For example, electromagnetic showers are produced in the charged current interaction of an electron neutrino. The rate of shower events is calculated in an expression similar to equation (5), but the muon range, R_μ, together with the effective area, $A_{\rm eff}$, are replaced by the effective volume of the detector. Also, the shower's energy is given by $E_{\rm sh} = yE_\nu$ for neutral current events and $E_{\rm sh} = E_\nu$ for electron neutrino charged current events. The minimum energy a shower must have to be observed by an optical Cerenkov neutrino telescope is of the order of a few TeV. For radio detectors, the shower threshold is much higher, in the PeV–EeV range.

Finally, very large volume neutrino telescopes, such as IceCube, are also capable of observing events uniquely associated with tau neutrinos. Tau neutrinos that interact via charged current in the detector medium produce a shower and a charged tau lepton. Below a few PeV, the tau lepton's lifetime is sufficiently short that it decays, producing a second shower essentially spatially coincident with the first one. Such an event is indistinguishable from a single shower. At higher energies, however, the tau lifetime can be long enough to distinguish these two showers. For example, at 10 PeV, a tau travels, on average, about 500 m before decaying. If both showers occur within the detector volume, such an event is called a 'double bang' and is a clear signature of a tau neutrino [32]. If the first of these showers occurs outside of the detector, with only the second shower being observed, the event is called a 'lollipop'. Here, the observation of the shower with a minimum ionizing track (produced by the tau) constitutes the candy and the stick of the 'lollipop', respectively. Again, this is a clear signature of a tau neutrino.

Standard cosmic accelerators produce neutrinos via charged pion decay (see section 2). Pion decays produce flavours of neutrinos in the ratio $\phi_{\nu_e} : \phi_{\nu_\mu} : \phi_{\nu_\tau} = 1 : 2 : 0$. Over the long baselines such neutrinos travel before reaching the Earth, neutrino oscillations modify this ratio to $\phi_{\nu_e} : \phi_{\nu_\mu} : \phi_{\nu_\tau} \cong 1 : 1 : 1$ or nearly equal quantities of all three flavours. Considering only SM neutrino interactions, these incoming flavour ratios can be translated to ratios of observed muon tracks, electromagnetic and hadronic showers and tau unique events [33]. By measuring the ratios of these event types observed in IceCube, the presence of interactions beyond the SM may be tested.

3.2. Neutrinos in air shower experiments

Very high-energy cosmic neutrinos can occasionally interact with particles in the Earth's atmosphere producing extended air showers observable in high-energy cosmic ray experiments such as AGASA, HiRes or the next generation Pierre Auger Observatory [12] (for a review of ultrahigh-energy air shower experiments, see e.g. [34]). Although the characteristics of neutrino-induced showers do, in principle, differ from those initiated by hadronic cosmic rays [35],

significantly more hadronic showers are expected, thus making showers from neutrino primaries difficult to conclusively identify.

Primary particles that have a near-horizontal trajectory can provide an opportunity to distinguish neutrinos from hadronic events, however. In contrast to hadronic cosmic rays (which interact at the top of the atmosphere), neutrino primaries have considerably smaller cross-sections and thus interact with nearly equal probability throughout the atmosphere. If a shower is observed that was initiated deep inside the atmosphere, it can be associated with a neutrino (or other weakly interacting particle) primary. For there to be sufficient column depth to make this distinction (typically 3000–4000 g cm^{-2} is required), only primaries within about 15° of the horizon can be considered [36, 37]. The class of cosmic ray events that can be associated with neutrino primaries are called 'deeply penetrating, quasi-horizontal showers'.

To calculate the rate of neutrino-induced deeply penetrating, quasi-horizontal showers in an air shower experiment, one must estimate the acceptance to neutrino detection. This quantity is essentially the effective target mass multiplied by the accessible solid angle. It is often given in km^3 water equivalent steradians (km^3 we sr), where, for example, 1 km^3 water equivalent would be the target mass contained in 1 km^3 of water or ice. Anchordoqui *et al* [37] estimates the acceptance of the AGASA experiment to deeply penetrating, quasi-horizontal showers to be 0.05 km^3 we sr at 10^8 GeV, rising to 1.0 km^3 we sr at 10^{10} GeV and above. They estimate the acceptance of Auger to be larger than AGASA by a factor of 20, 20 and 50 at 10^8, 10^{10} and 10^{12} GeV, respectively. These estimates consider showers within 15° of the horizon and with a maximum height of 15 km. For a discussion of the HiRes acceptance, see [38].

The number of neutrino events observed as deeply penetrating, quasi-horizontal showers is given by

$$N = \int \mathrm{d}E_\nu N_A \frac{\mathrm{d}N_\nu(E_\nu)}{\mathrm{d}E_\nu\,\mathrm{d}t\,\mathrm{d}\Omega}\sigma(E_\nu)A(E_\nu)T, \tag{7}$$

where N_A is Avogadro's number, $\mathrm{d}N_\nu/\mathrm{d}E_\nu\,\mathrm{d}t\,\mathrm{d}\Omega$ is the flux of neutrinos (per unit energy, per unit time, per solid angle), $\sigma(E_\nu)$ is the neutrino–nucleon scattering cross-section, $A(E_\nu)$ is the acceptance of the detector and T is the length of time observed. This expression assumes that roughly all of the energy of the neutrino goes into the produced shower. If this is not the case, such as with neutral current interactions, a differential cross-section should be used as in equation (5) and the acceptance be written as a function of the shower energy rather than neutrino energy.

At the very high energies at which air shower experiments are most effective (0.1 EeV and higher), a reasonable and conservative flux of neutrinos to consider is the cosmogenic flux (see section 2). This flux peaks at about 0.1 EeV, but is substantial at 1 EeV and above. If we insert this flux, an experimental acceptance and the neutrino–nucleon cross-section, we can predict the number of neutrino-induced deeply penetrating, quasi-horizontal events that would be observed in an air shower experiment.

In addition to deeply penetrating quasi-horizontal showers, it may be possible to identify showers produced by Earth-skimming tau neutrinos using the fluorescence detectors of the Auger experiment [39]. Earth-skimming, ultrahigh-energy tau neutrinos produce tau leptons in charged current interactions. Since, at ultrahigh energies, the tau decay length is comparable to its interaction length, a shower produced in the tau decay can be observed as an extended air shower if the tau is produced not too deep beneath the Earth's surface. The rates for this class of events is expected to be rather small however, and we will not study this signature in further detail here.

4. Signatures of new physics

In high-energy cosmic neutrino experiments, the new physics enters the neutrino–nucleon scattering cross-section $\sigma_{\nu N}(E_\nu)$ as in equations (5) and (7). It is given by

$$\sigma_{\nu N}(E_\nu) = \sum_i \int_{x_{min}}^{1} \mathrm{d}x\, \hat{\sigma}_i(xs)\, f_i(x, Q), \tag{8}$$

where $\hat{\sigma}_i$ is the scattering cross-section for the neutrino–parton subprocesses, which reflects the fundamental dynamics of neutrino interactions. The sum is over all the contributing partons i and f_i are the parton distribution functions. The cross-sections are insensitive to the choice of momentum transfer Q. The cross-sections are also insensitive to uncertainties in the parton distribution functions at low x if there is a TeV scale threshold. For instance, the highest energy neutrino fluxes, which are large at $E_\nu \sim 10^{10}$ GeV, probe $x \sim (1\,\mathrm{TeV})^2/10^{10}\,\mathrm{GeV}^2 \approx 10^{-4}$, within the range of validity of the parton distribution functions that we take as CTEQ5 [40].

There are many interesting scenarios in which neutrino–nucleon interactions would be substantially enhanced over the SM prediction at high energies. In this section, we summarize the literature on these models, describing how their signatures may be observed in high-energy cosmic neutrino experiments.

4.1. Contributions of KK gravitons

The most significant proposal, perhaps, is that of TeV scale gravity with the existence of extra spatial dimensions. The motivation for such a scenario can be traced to the understanding of the large hierarchy between the electroweak scale, below about $\mathcal{O}(1\ \mathrm{TeV})$, and the Planck scale $M_{PL} \sim 10^{19}$ GeV. If there are n extra spatial dimensions, then the four-dimensional Planck scale is related to the D-dimensional Planck scale M_D by

$$M_{PL}^2 \sim V_n M_D^{n+2}, \tag{9}$$

where $V_n \sim R^n$ is the volume of the extra dimensions if they are flat with a compactification scale R [4]; and $V_n \sim \int \mathrm{e}^{-kx_i}\, \mathrm{d}^n x$ if the ith extra dimension is 'warped' with a curvature k [5]. An immediate implication of this scenario would be to naturally understand the largeness of the Planck scale in comparison with the electroweak scale. Namely, it can be interpreted as due to the large volume of the extra dimensions while the fundamental D-dimensional Planck scale M_D may be low, possibly at the TeV scale.

In models with large and flat extra dimensions, often called the large extra dimensions (ADD) scenario [4], the fundamental Planck scale is assumed to be of the order of 1 TeV and a large number of Kaluza-Klein (KK) graviton states of mass $1/R$ of sub-eV become accessible. Their couplings to the SM particles at an energy E are enhanced to $(ER)^n/M_{PL}^2 \sim E^n/M_D^{n+2}$, and thus potentially large effects on high-energy processes may occur [41]. High-energy neutrinos can exchange these KK gravitons with quarks or gluons in target nucleons, resulting in an enhancement. For a scale of gravity near 1 TeV, neutrinos above PeV energies begin to interact largely by the effects of new physics. In the Randall–Sundrum scenario, an anti-de Sitter dimension with a non-factorizable warped geometry is introduced [5]. Again, KK gravitons become accessible at the TeV scale [42], enhancing the neutral current neutrino interaction rate above this scale.

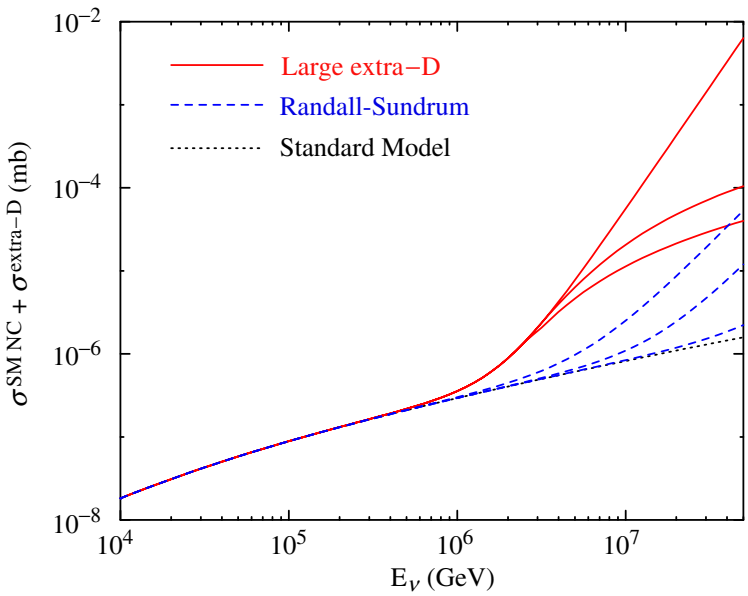

Figure 3. The neutrino–nucleon cross-section for models of TeV-scale gravity. The solid lines represent models with ADD (ADD scenario), with varying choices for the unitarization scheme of the partial wave amplitudes [43]. Short dashed lines represent Randall–Sundrum models with varied scales (1–3 TeV) and KK graviton masses (500 GeV–1 TeV). Dotted lines represent the prediction of the SM.

The effect on the neutral current neutrino–nucleon cross section in these scenarios is shown in figure 3 [43]. The solid lines represent models with ADD for the quantum gravity scale taken as 1 TeV. The three curves correspond to different choices for the unitarization scheme of the partial wave amplitudes proposed in [43], as compared to some other calculations [44]. Short dashed lines represent the Randall–Sundrum model with a varied AdS scale (Λ =1–3 TeV) and KK graviton masses (500 GeV–1 TeV). Dotted lines represent the prediction of the SM. In the scenarios considered here, neutrino telescopes expect to observe more neutral current events per charged current event than predicted by the SM. This effect sets in right above the threshold near M_D, providing a clear indication for new physics. Furthermore, the ratio of down-going to up-going events will be enhanced over the SM prediction as more neutrinos are absorbed as they propagate through the Earth [43]. The behaviour of the energy spectrum due to these effects is shown in figure 4.

4.2. TeV string resonances

At energies above the compactification scale $1/R$, the extra dimensions and KK effects may become observable if M_D is not too high as discussed in the previous section. At even higher energies near the string scale M_S, string effects dominate over gravitational effects based on string perturbation arguments [45, 46]. The string scale may be related to the D-dimensional gravity scale by

$$M_S = \kappa M_D, \tag{10}$$

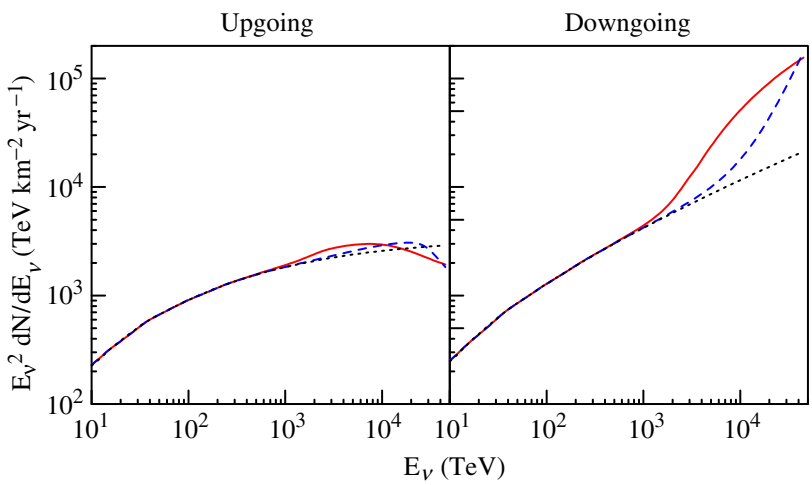

Figure 4. The energy distribution of $\nu_\mu + \bar{\nu}_\mu$ events in Icecube. The left and right panels show the up-going and down-going events, respectively. The Waxman–Bahcall flux has been used (see section 2). In each panel, the solid line is the event rate when the neutrino–nucleon cross-section $\sigma^{\rm SM} + \sigma^{\rm ADD}$ is used; the dashed line uses $\sigma^{\rm SM} + \sigma^{\rm RS}$ with a KK graviton mass 500 GeV and $\Lambda = 1$ TeV; the dotted line corresponds to $\sigma^{\rm SM}$ alone. The figure is a modified version from [43].

with $\kappa \lesssim 1$, depending on the string coupling and compactification of the extra dimensions. Large effects from string resonances may be produced when $E \gtrsim M_S$.

General tree-level open-string amplitudes can be constructed based on the Veneziano amplitude [45],

$$S(s,t) = \frac{\Gamma(1-\alpha' s)\Gamma(1-\alpha' t)}{\Gamma(1-\alpha' s-\alpha' t)}, \tag{11}$$

where $\alpha' = M_S^{-2}$ is the string tension. This amplitude develops simple poles at $\sqrt{s} = \sqrt{n} M_S$ with $n = 1, 2, \ldots,$ leading to resonances in the matrix elements. The physical effects of these resonances have been explored [46, 47], including their signatures in cosmic neutrino experiments [48, 49]. We present the neutrino–nucleon cross-sections due to Veneziano amplitude resonances in figure 5 [49]. The solid curve shows the prediction for the SM neutral current process, while the dashed and dot-dashed curves represent string excitations with and without the gluon contribution, respectively. We see that neutrino–gluon scattering can be the dominant process, 5–10 times larger than the neutrino-quark-induced processes. It is interesting to note that, even for processes that vanish in the SM at tree level, there can still be substantial stringy contributions to their amplitudes at high energies. Generally speaking, the energy dependence of the cross-sections for string resonances are weaker than those for KK states.

The event rates expected in IceCube and Auger have been calculated for these models [48, 49]. With the SM interactions, only about 0.2 (0.7) shower events per year are expected in the experiment from a cosmogenic (Waxman–Bahcall) neutrino flux. These rates can be enhanced by a factor of 5–6 due to string excitations with $M_S = 1$ TeV or a factor of about 1.5–1.7 with $M_S = 2$ TeV.

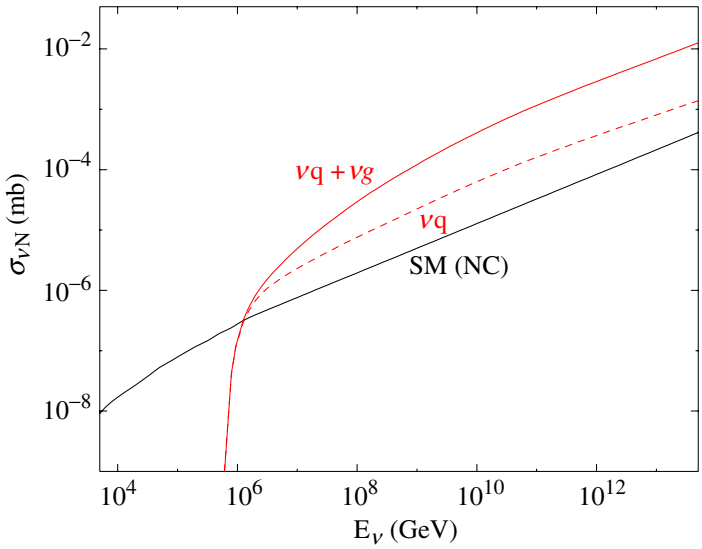

Figure 5. νN cross-sections via TeV string resonances considering νq and νg contributions (dashed curved) [49] and the νq contribution only (dot-dashed curve). The string scale is taken to be $M_S = 1$ TeV and the Chan–Paton factor used is $T = 1/2$. Also plotted is the SM neutral current prediction (solid curve).

4.3. Microscopic black hole production

At trans-Planckian energies $E \gg M_D$, it has been argued that black hole production will be the leading process [50] (for a recent review black holes in theories with extra dimensions, see e.g. [51]). This is because the energy dependence of the black hole production cross-section grows faster than for sub-Planckian processes and the number of non-perturbative states grows faster than the perturbative string states. The cross-section for black hole production can be naively estimated by the geometric description,

$$\sigma(E_{\rm CM}) = \pi r_{\rm sch}^2(E_{\rm CM}), \tag{12}$$

where $r_{\rm sch}(E_{\rm CM})$ is the Schwarzchild radius of a black hole formed with a mass equal to the centre-of-mass energy of the collision. In $4+n$ dimensions, the Schwarzchild radius of a black hole of mass $M_{\rm BH}$ is given by

$$r_{\rm sch}(M_{\rm BH}) = \frac{1}{M_D}\left[\frac{M_{\rm BH}}{M_D}\right]^{1/(1+n)}\left[\frac{2^n\pi^{(n-3)/2}\Gamma(\frac{3+n}{2})}{2+n}\right]^{1/(1+n)}. \tag{13}$$

Although some studies support the validity of the geometric cross-section argument [52], it is possible that a substantial fraction of the total energy will be radiated away in the form of gravitational waves, reducing the mass of any black hole that may be formed and reducing the corresponding cross-section [53].

Although the lowest mass possible for the black hole creation is approximately the fundamental Planck scale M_D, the effective centre-of-mass energy should be several times larger

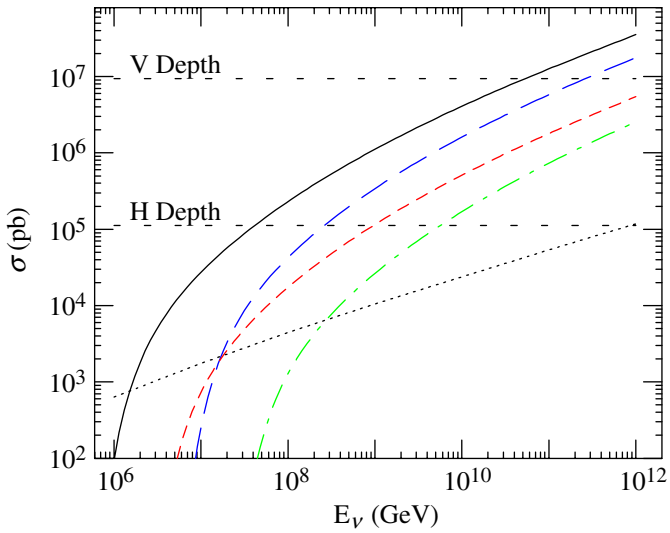

Figure 6. The neutrino–nucleon cross-section for black hole production in models of TeV-scale gravity. The lines represent models with a scale (M_D) of 1 TeV and a minimum black hole mass of 1 TeV (solid line), a scale of 1 TeV and a minimum black hole mass of 3 TeV (long dashes), a scale of 2 TeV and a minimum black hole mass of 2 TeV (short dashes) and a scale of 2 TeV and a minimum black hole mass of 6 TeV (dot-dashes). The dotted line represents the prediction of the SM. The number of extra dimensions was assumed to be six. The figure is taken from [28].

for the semi-classical argument to be valid. To parametrize this effect, we introduce the quantity, $x_{\min} = M_{\rm BH}^{\min}/M_D > 1$. In addition to the ambiguity of the value of $x_{\min}$, other uncertainties can possibly arise in the estimation of the cross-section [54], which we do not consider further here. In figure 6, we show the cross-section for black hole production in neutrino–nucleon interactions for different choices of M_D and $x_{\min}$. As a result of the sum over all partons and the lack of suppression from small perturbative couplings, the black hole cross-section may exceed SM interaction rates by two or more orders of magnitude. The cross-sections corresponding to neutrino interaction lengths equal to the horizontal and vertical depths of IceCube position are also given in figure 6 by the horizontal dotted lines. We see that, for the geometric cross-section $M_D \sim 1$ TeV and neutrino energies $E_\nu \sim 10^9$ GeV where the cosmogenic flux peaks, black hole production increases the probability of conversion in down-going neutrinos without increasing the cross-section so much that vertical neutrinos would be shadowed before reaching the detector. We therefore expect significantly enhanced rates in neutrino telescopes. The energy dependence of the black hole production cross-section is stronger than that for the other processes we have discussed so far, thus confirming the argument that black hole production is likely to be the dominant effect of low-scale gravity at higher energies.

Black holes decay via Hawking evaporation almost instantly (with a lifetime of the order 10^{-27} s). The Hawking radiation follows a thermal distribution with temperature $T_H = (1+n)/4\pi r_{\rm sch}$ with an average multiplicity of the particles radiated of approximately $\langle N\rangle \cong M_{\rm BH}/2T_H$. Naively, the particles are radiated in numbers proportional to their degrees of freedom,

i.e. 75% hadronic, 10% to charged leptons, etc.[3] Assume that the signals in a neutrino telescope produced in black hole decays follow these ratios [28, 57]. The 10% of Hawking radiation that produces charged leptons generates equal numbers of muons, taus and electrons, which can be observed as muon tracks, tau unique events and electromagnetic showers, respectively. The full 75% of Hawking radiation that goes into hadronic modes results in hadronic showers. This is in contrast to the ratios of event types predicted for SM interactions. Taking into account the degrees of freedom corresponding to each channel and the factors effecting the probability of detection (i.e. muon range, etc), the ratios of muons to taus to showers can be predicted for a particular black hole production model. For example, for a model with $M_D = 1$ TeV and $x_{\min} = 1$, about twice as many showers are expected than muon tracks (considering a $\mathrm{d}N_\nu/\mathrm{d}E_\nu \propto E_\nu^{-2}$ flux). In contrast, the SM prediction is about 20% more muons than showers [28]. By combining flavour ratio measurements with angular and energy distributions, large-volume neutrino telescopes such as IceCube will be capable of searching for evidence of black hole production in models with a fundamental Planck scale up to 1–2 TeV.

The angular distributions of muon tracks above 500 TeV in a kilometre-scale neutrino telescope, such as IceCube, in models of black hole production are shown in figure 7. While the enhanced cross-section significantly increases the down-going event rate ($\cos\theta_z > 0$) over the SM prediction (dotted curves), the rate of up-going events is suppressed due to absorption in the Earth.

Air shower experiments, unlike neutrino telescopes, do not have the ability to observe muon tracks or identify tau unique events. They are, however, very sensitive to EeV scale cosmic neutrinos and are thus capable of placing valuable limits on models of black hole production. Currently, the strongest such limit comes from the AGASA air shower experiment. AGASA has reported the observation of one neutrino-like (deeply penetrating, quasi-horizontal) event, and predicts a background to this signal of 1.7 events from misidentifying hadronic primaries [37]. At the 95% confidence level, this places an upper limit of 3.5 black hole events. This can be directly translated into a limit on the fundamental Planck scale, M_D. For values of $x_{\min}$ over the range 1–3, AGASA can place a lower limit on M_D of 1.0–1.4 TeV [37, 58], a limit which is competitive to the strongest bounds from collider experiments [59]. Auger, with considerably higher acceptance to these events, is expected to improve this sensitivity to 3–4 TeV for $n \gtrsim 4$ [37].

4.4. p-brane production

p-branes are p-dimensional, spatially extended solutions of gravitational theories. The existence of such objects is a generic prediction of theories with extra dimensions. If the fundamental scale of gravity is of the order of 1 TeV, then it is reasonable to expect that, in addition to black holes (a spherically symmetric 0-brane), higher dimensional states may also be generated in high-energy collisions [60, 61]. The cross-section for p-brane production is argued to be geometrical, similar to that for black hole production, except that it may have a lower threshold near the quantum gravity scale. If the p-brane wraps only around the small (compact) dimensions, the cross-section for p-brane production can be comparable to, or even larger than, the cross-section for black hole production (for a recent review on p-brane production, see e.g. [62]). If the p-brane wraps around

[3] The greybody factors as the corrections for the black hole decays were calculated in [55]. Also, specific models may give a somewhat different ratio of black hole decays when taking into account the constraint from nucleon stability [56].

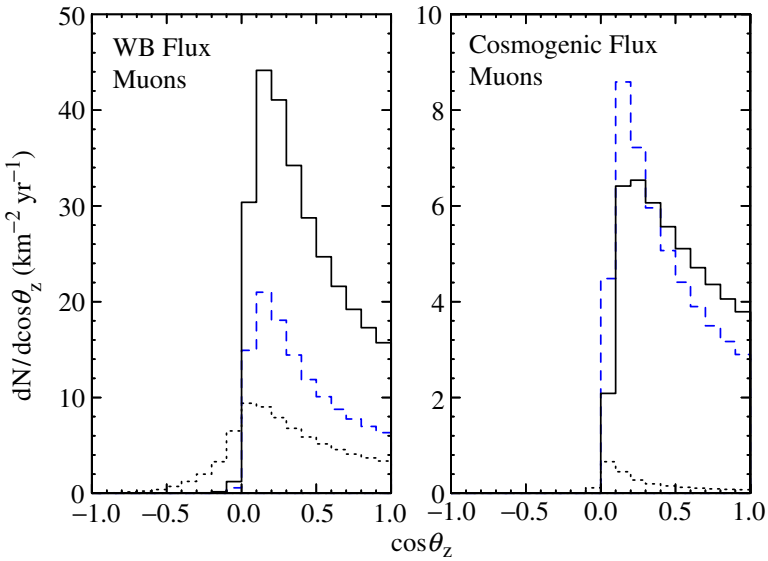

Figure 7. The angular distribution of muon tracks above 500 TeV in a kilometre-scale neutrino telescope, such as IceCube, in models of black hole production [28]. The dotted line represents the prediction for the SM prediction, while the solid and dashed lines are for the black hole production models with $x_{\min} = 1$ and 3, respectively. All models shown have $n = 1$ and $M_D = 1$ TeV. The Waxman–Bahcall and cosmogenic neutrino fluxes were used in the left and right frames, respectively (see section 2). $\cos\theta_z = 0$ corresponds to a horizontal event, while positive and negative values correspond to down-going and up-going muons, respectively. While the enhanced cross-section significantly increases the down-going event rate, the rate of up-going events is suppressed due to absorption in the Earth. The figure is taken from [28].

large dimensions as well, their production will be suppressed by powers of $M_D/M_{\rm PL}$ [60, 61]. Typical cross-sections for p-brane production in νN collisions are presented in figure 8 [63], which could be higher when compared with the black hole production by orders of magnitude.

Unlike the standard Hawking radiation picture for black hole evaporation, the decay of p-branes is not well understood. p-branes may decay into branes of lower dimension. Alternatively, they may decay directly into a combination of brane and bulk particles.

Below the energy threshold for p-brane or black hole production, lighter states, called 'string balls' may also be produced [64]. We do not study these objects further here, since we consider our presentation to be already quite representative for the conservative scenario as in the string resonances in section 4.2, and for the more optimistic scheme in this section.

4.5. Electroweak instanton-induced processes

SM electroweak instantons represent tunnelling transitions between topologically inequivalent vacua, leading to baryon plus lepton number $(B + L)$ violating processes. Such processes are exponentially suppressed below the so-called 'Sphaleron' energy, $E_{sph} \sim \pi M_W/\alpha_W \sim 8$ TeV. Above this scale, however, such process may be unsuppressed and the corresponding

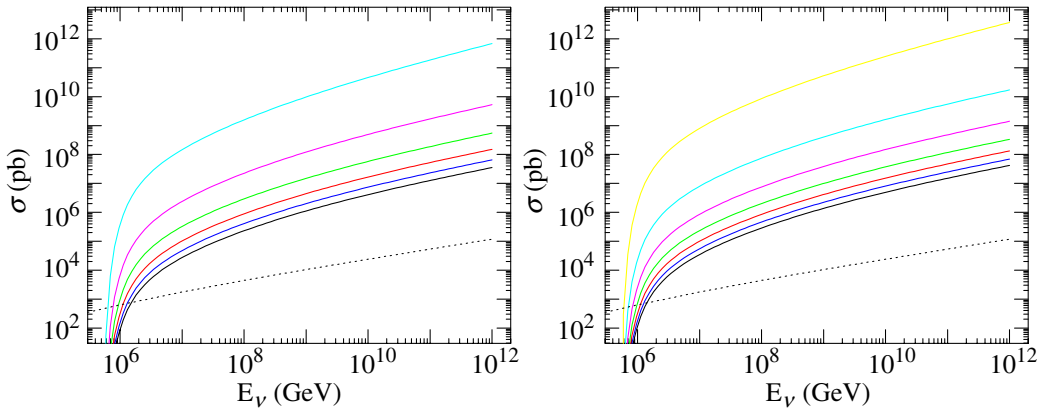

Figure 8. The total cross-section for p-brane production for $n = 6$ (left), $n = 7$ (right), $M_D = M_p^{min} = 1$ TeV and $m = 0, \ldots, n-1$ (from bottom to top). The SM cross-section, $\sigma(\nu N \to \ell X)$, is also shown (dotted line). The figure is taken from [63].

cross-sections can be quite large [65], potentially resulting in enhanced neutrino scattering signals in cosmic neutrino experiments.

The neutrino–nucleon cross-section corresponding to electroweak instanton-induced interactions is difficult to reliably calculate. One approach to this problem is to use a perturbative method in close analogy to QCD [66]. Alternatively, this calculation has been performed using a generalized semi-classical approach [67]. In this second approach, these interactions remain suppressed to much higher energies up to about 30 times the Sphaleron energy. The estimated neutrino–nucleon cross-sections corresponding to these two approaches are shown in figure 9 [68].

From the standpoint of neutrino phenomenology, it is important to note the extremely rapid increase of the neutrino–nucleon cross-section demonstrated in these models. This is in contrast to the more gradual growth predicted for the cross-sections for black hole production, KK exchanges, etc. Below the energy thresholds for such interactions, the SM predictions are accurate. At energies roughly a factor of 10 higher, the cross-section becomes sufficiently large that the Earth efficiently absorbs the incoming neutrino flux, as indicated above the horizontal dotted lines (horizontal and downward depths) in figure 9. Thus, in a neutrino telescope, a sharp enhancement in a fairly narrow range of energies is predicted for these models, as depicted in figure 10. Although spectacular, the ability of planned experiments to observe such features is limited, however. Even with the more optimistic of the models considered here, an experiment such as IceCube is expected to see only of the order of 1 event/year from instanton-induced processes [68]. Future experiments with very large volumes will be required to further probe such models.

Another interesting characteristic feature of instanton-induced processes is the large multiplicity of final state particles and the violation of $B + L$. The basic operators involving quark and lepton fields are of the form $\langle (qqq\ell)^{n_g} \rangle$ [65], where $n_g = 3$ is the number of fermion generations. It has been argued that the processes involving multiple gauge bosons and Higgs bosons, such as $\langle (qqq\ell)^{n_g} W^n H^m \rangle$, can be significantly enhanced [69]. A typical neutrino-induced

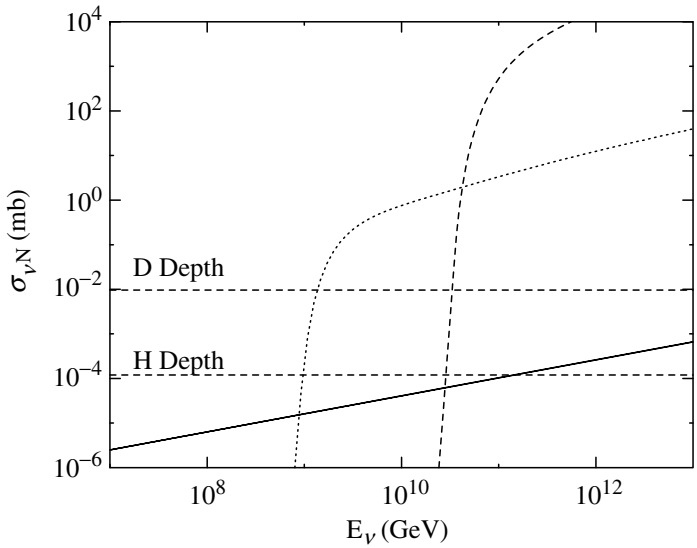

Figure 9. The neutrino–nucleon cross-section for electroweak instanton-induced interactions. The dotted line represents the perturbative approach of [66]. The dashed line represents the semi-classical approach of [67]. The solid lines represent the SM neutral+charged current prediction. The figure is taken from [68].

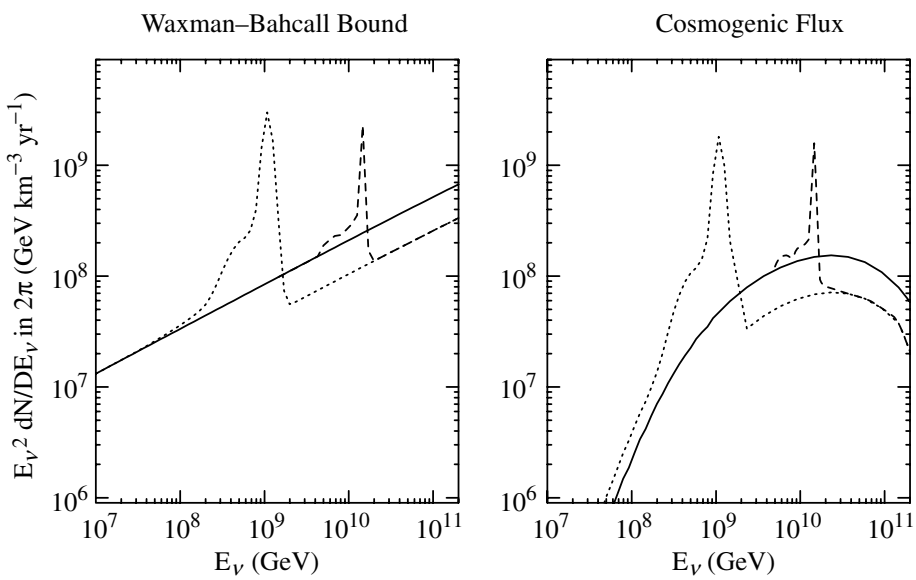

Figure 10. The spectrum of neutrino (shower) events predicted in a neutrino telescope including the electroweak instanton-induced interactions for the models described in the text. The dotted line represents the perturbative approach of [66]. The dashed line represents the semi-classical approach of [67]. The solid lines is the SM prediction. The figure is taken from [68].

event could thus be

$$\nu_e u \rightarrow \bar{d}\bar{d} + \bar{c}\bar{c}\bar{s}\mu^+ + \bar{t}\bar{t}\bar{b}\tau^+ + nW + mH. \tag{14}$$

With both quarks and leptons of all three generations involved simultaneously in the primary production, this type of events should look quite unique. It is difficult to predict how such events would appear to the IceCube detector however, given the fact that the particles will be highly collimated and difficult to separate.

4.6. Signatures of SUSY

SUSY remains a leading candidate for physics beyond the SM. Although weak-scale SUSY is only weakly coupled to the SM and generally would not lead to substantially enhanced neutrino scattering cross-sections, certain charged particles produced by cosmic neutrinos may be long lived and may provide observable signatures. This scenario could naturally be realized when the gravitino is the stable lightest supersymmetric particle (LSP) and a charged slepton (such as stau) is the next-to-lightest supersymmetric particle (NLSP) [70, 71]. Interactions of high-energy neutrinos may be able to produce pairs of sparticles, which rapidly decay to charged slepton NLSPs, which can only decay further into states including a gravitino. With only highly suppressed couplings allowing this decay, the NLSP stau can be sufficiently long-lived to be potentially observable in a large volume neutrino telescope such as IceCube [70]. Similar features may appear in supersymmetric models with R-parity violation [72].

Sparticle pair production in neutrino–nucleon interactions is dominated by the t-channel chargino exchange, resulting in a slepton and a squark. The squark then quickly decays into a slepton NLSP. The cross-section for this process is rather small however, typically 2–3 orders of magnitude below the SM processes in the energy range well above the kinematic threshold as shown in figure 11. The key observation here is that sleptons produced in neutrino interactions travel through the Earth, losing energy via ionization processes and radiation. Due to their much greater mass, sleptons lose far less energy than muons produced in SM charged current interactions. The 'slepton range' can extend to hundreds or thousands of kilometres, thus in part making up for the low cross-section for their production.

The two sparticles produced in these interactions travel from their point-of-origin separated by an angle of $\theta \simeq 2m_{\tilde{l}}/E_\nu$. Therefore, the signature of this process consists of a pair of Cerenkov tracks, separated by a distance $L\theta$, where L is the distance between the detector and the sparticles' point-of-origin. Considering a PeV neutrino, for example, two sleptons separated by $\theta \simeq 10^{-3}$–10^{-4} could be produced. After travelling $\sim$1000 km, their tracks would be separated by $\sim$100–1000 m, which could be potentially distinguished in a neutrino telescope. This 'double track' signature would provide a method of distinguishing sparticle tracks from ordinary muon tracks.

Typical models with stau-NLSP predict only a one-track or a few double-track events per year in IceCube [70]. Larger volume detectors, e.g. extensions of IceCube, may be needed to further explore this possibility.

As a final remark on the possibility of observing supersymmetric particles in high-energy cosmic-ray interactions, neutrino experiments may be able to identify particles that are part of the cosmic-ray spectrum, such as in cosmic ray models of top–down origin [73]. For instance, if a neutralino is the LSP, it will interact with nucleons in a manner that somewhat resembles a neutrino neutral current interaction. Thus, without very large fluxes of high-energy cosmic

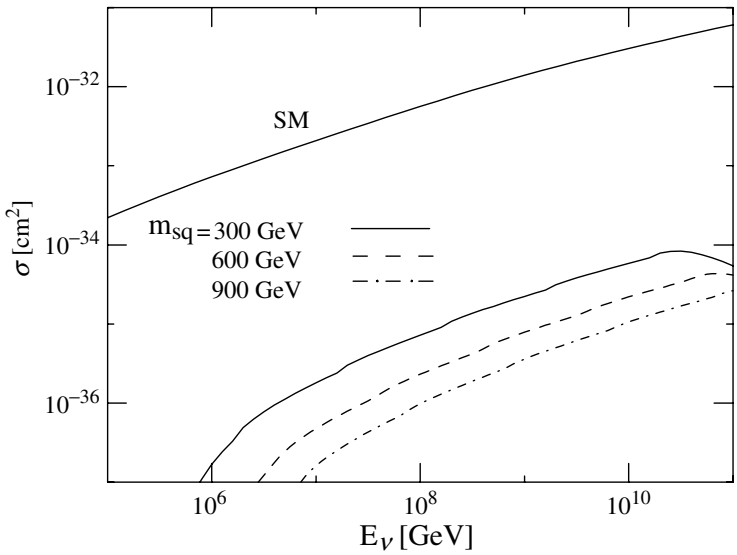

Figure 11. The νN cross-section in the scenario of stau-NLSP. Curves are shown for squarks of mass 250, 600 and 900 GeV. A stau mass of 250 GeV was used. The chargino mass used was also 250 GeV. The top curve corresponds to the SM charged current interactions. The figure is taken from [70].

neutralinos, it would be very difficult to distinguish any such particle from neutrinos. Neutralinos can have considerably smaller cross-sections with nucleons than neutrinos however, allowing them to travel through the Earth at energies at which neutrinos will be efficiently absorbed [73]. Thus ultrahigh-energy, neutralino-induced showers provide a low background signal in the direction of the Earth. Future space-based air shower experiments, such as OWL or EUSO, may be sensitive to this signature in some scenarios [73, 74].

5. Conclusions and summary

In this paper, we have reviewed the ability of neutrino telescopes and air shower experiments to study particle physics with high-energy cosmic neutrinos. The main advantage of such experiments over traditional collider experiments is the higher energy at which interactions can be studied. Several of the experiments we describe in this paper could expect multiple events per year at energies above 1 EeV, corresponding to about 40 TeV in the centre-of-mass frame of a neutrino–nucleon collision. Clearly, collider experiments have advantages over astroparticle techniques as well. Most notably, the high luminosities and well-controlled conditions of collider experiments are luxuries astronomers do not often enjoy.

Together, these advantages and disadvantages determine the areas of particle physics in which neutrino astronomy can be most useful. In particular, models in which significant deviations from the SM occur at energies beyond the reach of colliders can often be tested in such experiments. In this paper, we have reviewed several of such scenarios, summarized as follows:

- KK gravitons in low-scale quantum gravity scenarios: sensitive near the threshold, presumably $E_{CM} \approx M_D \sim 1$ TeV or $E_\nu \sim 1$ PeV.

- TeV string resonances in low string-scale scenarios: near and above the string scale, presumably $M_S \sim 1$ TeV, thus $E_\nu > 1$ PeV.
- p-brane production in low-scale quantum gravity scenarios: near and above the quantum gravity scale, presumably $M_D \sim 1$ TeV, thus $E_\nu > 1$ PeV.
- Black hole production in low-scale quantum gravity scenarios: likely, the dominant signature at trans-Planckian energies $E_{CM} \gg M_D \sim 1$ TeV, thus $E_\nu \gg 1$ PeV.
- Electroweak instanton-induced processes: above the sphaleron energy $E_{CM} > 10$ TeV, thus $E_\nu > 100$ PeV.
- SUSY with a charged slepton as a long-lived NLSP.

Although not discussed in this paper, other probes of exotic particle physics are possible using neutrino astronomy. These include searches for particle dark matter and neutrinos associated with models of top-down cosmic ray origin.

Although astronomy, and not particle physics, is the primary objective of neutrino telescopes and air shower experiments, upcoming experiments such as IceCube, AUGER, ANITA, OWL and EUSO will each study interactions at energies well beyond the reach of colliders and provide complementary probes to the traditional techniques used to study our Universe at the smallest scales.

Acknowledgments

We thank Jaime Alvarez-Muniz for his assistance with the figures and Jonathan Feng for helpful comments. TH is supported in part by DOE grant no. DE-FG02-95ER40896 and the Wisconsin Alumni Research Foundation. DH is supported by the Leverhulme Trust.

References

[1] Altarelli G 2004 *Nucl. Instrum. Methods* A **518** 1 (*Preprint* hep-ph/0306055)
[2] Martin S P 1997 *Preprint* hep-ph/9709356
[3] Hill C T and Simmons E H 2003 *Phys. Rep.* **381** 235 (*Preprint* hep-ph/0203079)
[4] Arkani-Hamed N, Dimopoulos S and Dvali G 1998 *Phys. Lett.* B **429** 263
Arkani-Hamed N, Dimopoulos S and Dvali G 1999 *Phys. Rev.* D **59** 086004
Antoniadis I, Arkani-Hamed N, Dimopoulos S and Dvali G 1998 *Phys. Lett.* B **436** 257
[5] Randall L and Sundrum R 1999 *Phys. Rev. Lett.* **83** 3370
[6] Learned J G and Mannheim K 2000 *Ann. Rev. Nucl. Part. Sci.* **50** 679
Halzen F and Hooper D 2002 *Rep. Prog. Phys.* **65** 1025 (*Preprint* astro-ph/0204527)
Weiler T J 2003 *Int. J. Mod. Phys.* A **18** 4065 (*Preprint* astro-ph/0304180)
[7] Andres E *et al* 2001 *Nature* **410** 441
[8] Kravchenko I 2003 *Preprint* astro-ph/0306408
Kravchenko I *et al* 2003 *Astropart. Phys.* **20** 195 (*Preprint* astro-ph/0206371)
[9] Ahrens J *et al* [The IceCube Collaboration] 2003 *Nucl. Phys. Proc. Suppl.* **118** 388 (*Preprint* astro-ph/0209556)
Ahrens J *et al* 2003 *Part. Astrophys.* to be published (*Preprint* astro-ph/0305196) IceCube Preliminary Design Document, online at http://icecube.wisc.edu/science/sci-tech-docs/
[10] Blanc F *et al* [ANTARES Collaboration] 2003 *Presented by L. Thompson on behalf of the ANTARES Collaboration, to appear in the Proc. 28th Int. Cosmic Ray Conf. (ICRC 2003) (Tsukuba, Japan, 31 July–7 August 2003)*
Katz U F [ANTARES Collaboration] 2003 *Preprint* astro-ph/0310736

[11] ANITA Proposal, Gorham P, Principle Investigator
ANITA home page http://www.ps.uci.edu/anita/index.html
[12] Blumer J [AUGER Collaboration] 2003 *Prepared for 28th Int. Cosmic Ray Conf. (ICRC 2003) (Tsukuba, 31 July–7 August 2003)*
Coutu S, Bertou X and Billoir P [AUGER Collaboration] 1999 *Prepared for 23rd Johns Hopkins Workshop on Current Problems in Particle Theory: Neutrinos in the New Millennium (Baltimore, MD, 10–12 June 1999)*
Capelle K S, Cronin J W, Parente G and Zas E 1998 *Astropart. Phys.* **8** 321 (*Preprint* astro-ph/9801313)
[13] Stecker F W, Krizmanic J F, Barbier L M, Loh E, Mitchell J W, Sokolsky P and Streitmatter R E 2004 *Preprint* astro-ph/0408162
Dutta S I, Reno M H and Sarcevic I 2002 *Phys. Rev.* D **66** 033002 (*Preprint* hep-ph/0204218)
[14] Scarsi L 2001 *Nuovo Cimento* C **24** 471
Cline D B and Stecker F W 2000 *Preprint* astro-ph/0003459
[15] Dedenko L G, Zheleznykh I M, Karaevsky S K, Mironovich A A, Svet V D and Furduev A V 1997 *Bull. Russ. Acad. Sci. Phys.* **61** 469
Dedenko L G, Zheleznykh I M, Karaevsky S K, Mironovich A A, Svet V D and Furduev A V 1997 *Izv. Ross. Akad. Nauk.* **61** 593
Riccobene G, Cosentino L, Musumeci M, Pavan G and Speziale F [NEMO Collaboration] 2004 *Nucl. Instrum. Methods* A **518** 220
[16] Gorham P, Saltzberg D, Odian A, Williams D, Besson D, Frichter G and Tantawi S 2002 *Nucl. Instrum. Methods* A **490** 476 (*Preprint* hep-ex/0108027)
[17] Halzen F and Hooper D 2003 *J. Cosmol. Astropart. Phys.* JCAP08(2003)006 (*Preprint* astro-ph/0310152)
[18] Longair M S 1994 *High Energy Astrophysics* vol 2 (New York: Cambridge University Press) ch 21
[19] Waxman E 1995 *Astrophys. J.* **452** L1
[20] Waxman E and Bahcall J N 1999 *Phys. Rev.* D **59** 023002 (*Preprint* hep-ph/9807282)
Bahcall J N and Waxman E 2001 *Phys. Rev.* D **64** 023002 (*Preprint* hep-ph/9902383)
Coppi P S and Aharonian F A 1997 *Astrophys. J.* **487** L9 (*Preprint* astro-ph/9610176)
[21] Mannheim K, Protheroe R J and Rachen J P 2001 *Phys. Rev.* D **63** 023003 (*Preprint* astro-ph/9812398)
[22] Albuquerque I F M, Lamoureux J and Smoot G F 2002 *Astrophys. J. Suppl.* **141** 195 (*Preprint* hep-ph/0109177)
[23] Stecker F W 1979 *Astrophys. J.* **228** 919
[24] Fodor Z, Katz S D, Ringwald A and Tu H 2003 *J. Cosmol. Astropart. Phys.* JCAP0311(2003)015 (*Preprint* hep-ph/0309171)
[25] Hooper D, Taylor A and Sarkar S 2004 *Preprint* astro-ph/0407618
Ave M, Busca N, Olinto A V, Watson A A and Yamamoto T 2004 *Preprint* astro-ph/0409316
[26] Kalashev O E, Kuzmin V A, Semikoz D V and Sigl G 2002 *Phys. Rev.* D **66** 063004 (*Preprint* hep-ph/0205050)
[27] Engel R, Seckel D and Stanev T 2001 *Phys. Rev.* D **64** 093010 (*Preprint* astro-ph/0101216)
[28] Alvarez-Muniz J, Feng J L, Halzen F, Han T and Hooper D 2002 *Phys. Rev.* D **65** 124015 (*Preprint* hep-ph/0202081)
[29] Gandhi R, Quigg C, Reno M H and Sarcevic I *Phys. Rev.* D **58** 093009 (*Preprint* hep-ph/9807264)
Gandhi R, Quigg C, Reno M H and Sarcevic I 1996 *Astropart. Phys.* **5** 81 (*Preprint* hep-ph/9512364)
[30] Dutta S I, Reno M H, Sarcevic I and Seckel D *Phys. Rev.* D **63** 094020 (*Preprint* hep-ph/0012350)
[31] Tyler C, Olinto A and Sigl G *Phys. Rev.* D **63** 055001
Hooper D 2002 *Phys. Rev.* D **65** 097303 (*Preprint* hep-ph/0203239)
Kusenko A and Weiler T J 2002 *Phys. Rev. Lett.* **88** 161101 (*Preprint* hep-ph/0106071)
Jain P, Kar S, McKay D W, Panda S and Ralston J P 2002 *Phys. Rev.* D **66** 065018 (*Preprint* hep-ph/0205052)
[32] Learned J G and Pakvasa S 1995 *Astropart. Phys.* **3** 267 (*Preprint* hep-ph/9405296)
Halzen F and Saltzberg D 1998 *Phys. Rev. Lett.* **81** 4305 (*Preprint* hep-ph/9804354)
[33] Beacom J F, Bell N F, Hooper D, Pakvasa S and Weiler T J 2003 *Preprint* hep-ph/0307025
Beacom J F, Bell N F, Hooper D, Pakvasa S and Weiler T J 2003 *Phys. Rev. Lett.* **90** 181301 (*Preprint* hep-ph/0211305)

[34] Anchordoqui L, Paul T, Reucroft S and Swain J 2003 *Int. J. Mod. Phys.* A **18** 2229 (*Preprint* hep-ph/0206072)
[35] Jain A, Jain P, McKay D W and Ralston J P 2000 *Preprint* hep-ph/0011310
Anchordoqui L, Goldberg H, McCauley T, Paul T, Reucroft S and Swain J 2001 *Phys. Rev.* D **63** 124009 (*Preprint* hep-ph/0011097)
[36] Anchordoqui L and Goldberg H 2002 *Phys. Rev.* D **65** 047502 (*Preprint* hep-ph/0109242)
Ahn E J, Ave M, Cavaglia M and Olinto A V 2003 *Phys. Rev.* D **68** 043004 (*Preprint* hep-ph/0306008)
[37] Anchordoqui L A, Feng J L, Goldberg H and Shapere A D 2002 *Phys. Rev.* D **65** 124027 (*Preprint* hep-ph/0112247)
Feng J L and Shapere A D 2002 *Phys. Rev. Lett.* **88** 021303 (*Preprint* hep-ph/0109106)
[38] Yoshida S, Dai H Y, Jui C C and Sommers P 1997 *Astrophys. J.* **479** 547
[39] Aramo C, Insolia A, Leonardi A, Miele G, Perrone L, Pisanti O and Semikoz D V 2004 *Preprint* astro-ph/0407638
Feng J L, Fisher P, Wilczek F and Yu T M 2002 *Phys. Rev. Lett.* **88** 161102 (*Preprint* hep-ph/0105067)
Bertou X, Billoir P, Deligny O, Lachaud C and Letessier-Selvon A 2002 *Astropart. Phys.* **17** 183 (*Preprint* astro-ph/0104452)
[40] Lai H L *et al* [CTEQ Collaboration] 2000 *Eur. Phys. J.* C **12** 375 (*Preprint* hep-ph/9903282)
[41] Guidice G, Rattazzi R and Wells J 1999 *Nucl. Phys.* B **544** 3
Han T, Lykken J D and Zhang R 1999 *Phys. Rev.* D **59** 105006
Mirabelli E A, Perelstein M and Peskin M E 1999 *Phys. Rev. Lett.* **82** 2236
Hewett J 1999 *Phys. Rev. Lett.* **82** 4765
Rizzo T 1999 *Phys. Rev.* D **59** 115010
[42] Davoudiasl J H, Hewett J L and Rizzo T G 2000 *Phys. Rev. Lett.* **84** 2080
[43] Alvarez-Muniz J, Halzen F, Han T and Hooper D 2002 *Phys. Rev. Lett.* **88** 021301 (*Preprint* hep-ph/0107057)
[44] Nussinov S and Shrock R 2001 *Phys. Rev.* D **64** 047702 (*Preprint* hep-ph/0103043)
Domokos G and Kovesi-Domokos S 1999 *Phys. Rev. Lett.* **82** 1366 (*Preprint* hep-ph/9812260)
Jain P, McKay D W, Panda S and Ralston J P 2000 *Phys. Lett.* B **484** 267 (*Preprint* hep-ph/0001031)
Tyler C, Olinto A V and Sigl G 2001 *Phys. Rev.* D **63** 055001 (*Preprint* hep-ph/0002257)
[45] Polchinski J 1998 *String Theory* vols I and II (Cambridge: Cambridge University Press)
[46] Shiu G and Tye S H 1998 *Phys. Rev.* D **58** 106007
Ibanez L E, Rabadan R and Uranga A M 1999 *Nucl. Phys.* B **542** 112
Antoniadis I, Bachas C and Dudas E 1999 *Nucl. Phys.* B **560** 93
Benakli K 1999 *Phys. Rev.* D **60** 104002
Accomando E, Antoniadis I and Benakli K 2000 *Nucl. Phys.* B **579** 3
[47] Cullen S, Perelstein M and Peskin M E 2000 *Phys. Rev.* D **62** 055012 (*Preprint* hep-ph/0001166)
[48] Cornet R, Illana J L and Masip M 2001 *Phys. Rev. Lett.* **86** 4235
[49] Friess J J, Han T and Hooper D 2002 *Phys. Lett.* B **547** 31 (*Preprint* hep-ph/0204112)
[50] Amati D, Ciafaloni M and Veneziano G 1987 *Phys. Lett.* B **197** 81
Amati D, Ciafaloni M and Veneziano G 1992 *Phys. Lett.* B **289** 87
Argyres P C, Dimopoulos S and March-Russell J 1998 *Phys. Lett.* B **441** 96 (*Preprint* hep-th/9808138)
Banks T and Fischler W 1999 *Preprint* hep-th/9906038
[51] Kanti P 2003 *Preprint* hep-ph/0402168
[52] D'Eath P D and Payne P N 1992 *Phys. Rev.* D **46** 658
D'Eath P D and Payne P N 1992 *Phys. Rev.* D **46** 675
D'Eath P D and Payne P N 1992 *Phys. Rev.* D **46** 694
Eardley D M and Giddings S B 2002 *Phys. Rev.* D **66** 044011 (*Preprint* gr-qc/0201034)
Solodukhin S N 2002 *Phys. Lett.* B **533** 153 (*Preprint* hep-ph/0201248)
[53] Anchordoqui L A, Feng J L, Goldberg H and Shapere A D 2003 *Preprint* hep-ph/0311365
Yoshino H and Nambu Y 2003 *Phys. Rev.* D **67** 024009 (*Preprint* gr-qc/0209003)
[54] Ahn E J, Cavaglia M and Olinto A V 2003 *Preprint* hep-ph/0312249

[55] Kanti P and March-Russell J 2002 *Phys. Rev.* D **66** 024023 (*Preprint* hep-ph/0203223)
Kanti P and March-Russell J 2003 *Phys. Rev.* D **67** 104019 (*Preprint* hep-ph/0212199)
[56] Han T, Kribs G D and McElrath B 2003 *Phys. Rev. Lett.* **90** 031601 (*Preprint* hep-ph/0207003)
[57] Kowalski M, Ringwald A and Tu H 2002 *Phys. Lett.* B **529** 1 (*Preprint* hep-ph/0201139)
[58] Anchordoqui L A, Feng J L, Goldberg H and Shapere A D 2003 *Phys. Rev.* D **68** 104025 (*Preprint* hep-ph/0307228)
[59] Dimopoulos S and Landsberg G 2001 *Phys. Rev. Lett.* **87** 161602 (*Preprint* hep-ph/0106295)
Giddings S B and Thomas S 2002 *Phys. Rev.* D **65** 056010 (*Preprint* hep-ph/0106219)
[60] Ahn E J, Cavaglia M and Olinto A V 2003 *Phys. Lett.* B **551** 1 (*Preprint* hep-th/0201042)
[61] Cheung K and Chou C H 2002 *Phys. Rev.* D **66** 036008 (*Preprint* hep-ph/0205284)
[62] Cavaglia M 2003 *Int. J. Mod. Phys.* A **18** 1843 (*Preprint* hep-ph/0210296)
[63] Anchordoqui L A, Feng J L and Goldberg H 2002 *Phys. Lett.* B **535** 302 (*Preprint* hep-ph/0202124)
[64] Dimopoulos S and Emparan R 2002 *Phys. Lett.* B **526** 393 (*Preprint* hep-ph/0108060)
[65] 't Hooft G 1976 *Phys. Rev. Lett.* **37** 8
't Hooft G 1976 *Phys. Rev.* D **14** 3432
't Hooft G 1978 *Phys. Rev.* D **18** 2199
Ringwald A 1990 *Nucl. Phys.* B **330** 1
Khoze V V and Ringwald A 1991 *Phys. Lett.* B **259** 106
[66] Ringwald A 2003 *Phys. Lett.* B **555** 227 (*Preprint* hep-ph/0212099) and references therein
[67] Bezrukov F, Levkov D, Rebbi C, Rubakov V and Tinyakov P 2003 *Phys. Lett.* B **574** 75 (*Preprint* hep-ph/0305300)
Bezrukov F, Levkov D, Rebbi C, Rubakov V and Tinyakov P 2003 *Phys. Rev.* D **68** 036005 (*Preprint* hep-ph/0304180)
[68] Han T and Hooper D 2004 *Phys. Lett.* B **582** 21 (*Preprint* hep-ph/0307120)
[69] Arnold P and McLerran L 1988 *Phys. Rev.* D **37** 1020
Ringwald A 1990 *Nucl. Phys.* B **330** 1
Espinosa O 1990 *Nucl. Phys.* B **343** 310
Khoze V A and Ringwald A 1991 *Phys. Lett.* B **259** 106
[70] Albuquerque I, Burdman G and Chacko Z 2004 *Phys. Rev. Lett.* **92** 221802 (*Preprint* hep-ph/0312197)
[71] Feng J L, Rajaraman A and Takayama F 2003 *Phys. Rev. Lett.* **91** 011302 (*Preprint* hep-ph/0302215)
Feng J L, Su S and Takayama F 2004 *Preprint* hep-ph/0404231
[72] Carena M, Choudhury D, Lola S and Quigg C 1998 *Phys. Rev.* D **58** 095003 (*Preprint* hep-ph/9804380)
[73] Barbot C, Drees M, Halzen F and Hooper D 2003 *Phys. Lett.* B **563** 132 (*Preprint* hep-ph/0207133)
[74] Anchordoqui L, Goldberg H and Nath P 2004 *Preprint* hep-ph/0403115

New Journal of Physics
The open-access journal for physics

Relic neutrino background from cosmological supernovae

Shin'ichiro Ando[1] **and Katsuhiko Sato**[1,2]

[1] Department of Physics, School of Science, The University of Tokyo, 7-3-1 Hongo, Bunkyo-ku, Tokyo 113-0033, Japan
[2] Research Center for the Early Universe, School of Science, The University of Tokyo, 7-3-1 Hongo, Bunkyo-ku, Tokyo 113-0033, Japan
E-mail: ando@utap.phys.s.u-tokyo.ac.jp and sato@phys.s.u-tokyo.ac.jp

New Journal of Physics **6** (2004) 170
Received 24 September 2004
Published 16 November 2004
Online at http://www.njp.org/
doi:10.1088/1367-2630/6/1/170

Abstract. Present and future observations of supernova relic neutrinos (SRNs), i.e., a cosmological neutrino background from past core-collapse supernova explosions, potentially give us useful information concerning various fields of astrophysics, cosmology and particle physics. We review recent progress of theoretical and observational studies of SRNs, particularly focusing on the detectability, and also on implications for cosmic star formation history and neutrino physics.

PII: S1367-2630(04)86971-4
© IOP Publishing Ltd and Deutsche Physikalische Gesellschaft

Contents

1. Introduction **2**
2. Formulation and models **4**
2.1. Formulation . . . 4
2.2. Models for cosmic SFR . . . 5
2.3. Neutrino spectrum from supernova explosions . . . 7
2.4. Neutrino spectrum after neutrino oscillation . . . 8
3. Flux and event rate of SRNs **9**
3.1. Flux of SRNs . . . 9
3.2. Event rate at water Čerenkov detectors . . . 10
4. Detectability and observational upper limit **12**
4.1. Background events against detection . . . 12
4.2. Detectability at pure-water Čerenkov detectors . . . 14
4.3. Detectability at other detectors . . . 15
4.4. Current observational limit and future prospects . . . 15
5. Implication for cosmic star formation history **16**
5.1. Constraints from the current observational limit . . . 16
5.2. Performance of Gd-loaded detectors . . . 16
6. Implication for neutrino properties **20**
6.1. Inverted mass hierarchy . . . 20
6.2. Resonant spin–flavour conversion . . . 21
6.3. Decaying neutrinos . . . 22
7. Conclusions **24**
Acknowledgments **25**
References **25**

1. Introduction

A core-collapse supernova explosion is one of the most spectacular events in astrophysics, and it attracts a great deal of attention from many physicists and astronomers. It also produces a number of neutrinos and 99% of its gravitational binding energy is transformed into neutrinos; detection of the galactic supernova neutrino burst by ground-based large water Čerenkov detectors, such as Super-Kamiokande (SK) and Sudbury Neutrino Observatory (SNO), would provide valuable information on the nature of neutrinos as well as supernova physics. In addition, because supernova explosions have occurred very commonly in both the past and present universe, tracing the cosmic star-formation rate (SFR), they should have emitted a great number of neutrinos, which now make a diffuse background, i.e., supernova relic neutrinos (SRNs). The physics involved in SRN ranges quite widely—from cosmic SFR and supernova physics to neutrino properties as elementary particles. Therefore, detecting SRNs or even setting limits on their flux can give us quite useful and unique implications for various fields of astrophysics, cosmology and particle physics. Detectability of SRNs in various detectors and its implications have been discussed in many theoretical papers [1]–[19] from various points of view, which we discuss in detail in the following part of the present paper.

Flux estimation requires models of neutrino spectrum emitted from each supernova explosion and cosmic SFR. Furthermore, it is experimentally established that neutrinos mix among different flavours, altering the neutrino spectrum at detectors from the original one after neutrinos propagate inside a supernova envelope; this effect should now be taken into account appropriately. In addition to a flux estimation as precise as possible, a detailed discussion of background events, which hinder the SRN detection, is essential; this has been thoroughly studied by Ando *et al* [12] and we follow their discussion later in this paper. A stringent observational upper limit on the SRN flux has been obtained by the SK group [20] and its value is only a factor of 3–6 larger than several theoretical predictions [8]–[10], [12], being consistent with (and more stringent than) the theoretical upper limit given by Kaplinghat *et al* [11] using conservative models. In order to make the SRN detection more likely, a promising method was proposed by Beacom and Vagins [21]. Their basic idea is to dissolve gadolinium trichloride ($GdCl_3$) in water in Čerenkov detectors, which greatly reduces the background events if it is applied to the currently working or proposed future detectors such as SK, Hyper-Kamiokande (HK) and Underground Nucleon Decay and Neutrino Observatory (UNO). Therefore, we are now at an exciting stage, where SRNs would soon be actually detected, and be used in many applications for various fields of astrophysics as a unique and complementary method to the usual observations of light.

Since we have promising prospects for SRN detection, it is timely to discuss the SRN potential for probing the universe or for particle physics. Cosmic SFR is one such possibility. The most popular method inferring SFR is to use the galaxy luminosity function of rest-frame ultraviolet (UV) radiation [22]–[30], in addition to far-infrared (FIR)/sub-millimetre dust emission [31, 32] and near-infrared (NIR) Hα line emission [33]–[36]. In these traditional approaches, however, there are a fair number of ambiguities when the actual observables are converted into the cosmic SFR [37]. The most serious problem is that the effects of dust extinction are non-negligible, especially for rest-frame UV observations. For the approach using SRNs, on the other hand, we are not troubled by such a problem, because neutrinos are completely free of dust extinction. This point is the same with observations in the sub-millimetre wave band; however, neutrinos are emitted directly from stars, whereas sub-millimetre radiation comes from dust and is an indirect process. Another advantage is that supernovae are directly connected with the death of massive stars with $M \gtrsim 8M_\odot$, whose lifetime is expected to be very short compared with the Hubble time-scale H_0^{-1}. It enables direct inference of the cosmic SFR assuming the initial mass function (IMF), not bothering with uncertainty concerning the galaxy luminosity function, which sometimes causes difficulty in the case of rest-frame UV observation [37]. Motivated by all of these reasons, many researchers have investigated the dependence of the SRN flux on various models of cosmic SFR or to what extent the SFR can be probed from future SRN observations. Totani *et al* [8] estimated flux using several theoretical models of galaxy evolution. After the bursting release of the observational SFR data points since the pioneering study by Madau *et al* [23], the SRN flux has been estimated using these SFR results [9, 10, 12]. More recently, theoretical SRN flux calculations have been compared with the observational upper limit by SK [20]. Fukugita and Kawasaki [13] used the limit to obtain constraints on the cosmic SFR; Strigari *et al* [16] adopted the latest SFR model based on the Sloan Digital Sky Survey [38] and concluded that their median SRN flux is slightly below the current SK upper limit. Following the proposal to dissolve Gd into detectors [21], Ando [17] investigated potential performance of the Gd-loaded water Čerenkov detectors such as SK, HK and UNO, using the Monte Carlo (MC) simulation, especially focusing on how reliably an assumed SFR model can be reproduced from the SRN observation.

Neutrino properties can also be probed by the SRN observation in principle. It is pointed out that the resulting SRN signal depends on neutrino oscillation models [14]; particularly, if the mass hierarchy is inverted, i.e., the first mass eigenstate that most strongly couples to electron flavour is heavier than the third state, $m_1 > m_3$, and the value of θ_{13}, which has not yet been well constrained, is sufficiently large, then the flavour conversion during propagation inside the supernova envelope could considerably change the neutrino signal. Another interesting possibility is that a stringent constraint can be set on neutrino decay models from the SRN observation as first pointed out by Ando [15] and subsequently studied by Fogli *et al* [18]. Non-radiative neutrino decay can be induced by the interaction between neutrinos and massless or very light particles such as Majoron. The strongest lower limit to the neutrino lifetime-to-mass ratio is obtained from the solar neutrino observation [39]–[41] and meson decay [42]–[44] to be $\tau/m \gtrsim 10^{-4}\,\mathrm{s\,eV^{-1}}$. SRN observation, on the other hand, is sensitive to $\sim 10^{10}\,\mathrm{s\,eV^{-1}}$, which is many orders of magnitude larger than the current limit. This is because of the much longer baseline between the Earth and cosmological supernovae, from which SRNs are emitted, compared to 1 AU in the case of solar neutrino observations. Neutrino decay could also change the detected signal from high-energy astrophysical objects [45] or the galactic supernova explosions [46]–[48], and could alter usual discussions on the early universe and structure formation [49] as well as on supernova coolings [50]–[52]; but we stress that, in principle, we can obtain the most stringent constraints on the neutrino lifetime from the SRN observations.

This paper is organized as follows. We first introduce the formulation for calculating the SRN flux in section 2. Models of cosmic SFR, supernova neutrino spectrum calculated by various groups are given in the same section. Neutrino oscillation inside the supernova envelope is briefly described there. SRN flux and event rate at ground-based detectors calculated with our reference models are given in section 3. Section 4 is devoted to a detailed discussion on background events against the SRN detection and detectability at various detectors. Current observational limit by SK, which is obtained by a statistical argument including background events, is also briefly summarized in the same section. We discuss implications of the SRN observation for cosmic SFR and neutrino properties such as oscillation and decay in sections 5 and 6, respectively. Finally, we conclude this paper by giving a brief summary in section 7. Throughout this paper, we only consider electron anti-neutrinos ($\bar{\nu}_e$) at detectors because this kind of flavour is most easily detected by the water Čerenkov detectors, on which we mainly focus.

2. Formulation and models

2.1. Formulation

The present number density of SRNs ($\bar{\nu}_e$), whose energy is in the interval $E_\nu \sim E_\nu + \mathrm{d}E_\nu$, emitted in the redshift interval $z \sim z + \mathrm{d}z$, is given by

$$\mathrm{d}n_\nu(E_\nu) = R_{\mathrm{SN}}(z)(1+z)^3 \frac{\mathrm{d}t}{\mathrm{d}z}\,\mathrm{d}z \frac{\mathrm{d}N_\nu(E'_\nu)}{\mathrm{d}E'_\nu}\,\mathrm{d}E'_\nu (1+z)^{-3} = R_{\mathrm{SN}}(z)\frac{\mathrm{d}t}{\mathrm{d}z}\mathrm{d}z \frac{\mathrm{d}N_\nu(E'_\nu)}{\mathrm{d}E'_\nu}(1+z)\,\mathrm{d}E_\nu, \tag{1}$$

where $E'_\nu = (1+z)E_\nu$ is the energy of neutrinos at redshift z, which is now observed as E_ν; $R_{\mathrm{SN}}(z)$ represents the supernova rate per comoving volume at z, and hence the factor $(1+z)^3$ should be multiplied to obtain the rate per physical volume at that time; $\mathrm{d}N_\nu/\mathrm{d}E_\nu$ is the

number spectrum of neutrinos emitted by one supernova explosion; and the factor $(1+z)^{-3}$ comes from the expansion of the universe. The Friedmann equation gives the relation between t and z as

$$\frac{\mathrm{d}z}{\mathrm{d}t} = -H_0(1+z)\sqrt{\Omega_\mathrm{m}(1+z)^3+\Omega_\Lambda}, \tag{2}$$

and we adopt the standard ΛCDM cosmology ($\Omega_\mathrm{m}=0.3$, $\Omega_\Lambda=0.7$, and $H_0=70h_{70}\,\mathrm{km\,s^{-1}\,Mpc^{-1}}$).[3] We now obtain the differential number flux of SRNs, $\mathrm{d}F_\nu/\mathrm{d}E_\nu$, using the relation $\mathrm{d}F_\nu/\mathrm{d}E_\nu = c\,\mathrm{d}n_\nu/\mathrm{d}E_\nu$:

$$\frac{\mathrm{d}F_\nu}{\mathrm{d}E_\nu} = \frac{c}{H_0}\int_0^{z_\mathrm{max}} R_\mathrm{SN}(z)\frac{\mathrm{d}N_\nu(E'_\nu)}{\mathrm{d}E'_\nu}\frac{\mathrm{d}z}{\sqrt{\Omega_\mathrm{m}(1+z)^3+\Omega_\Lambda}}, \tag{3}$$

where we assume that gravitational collapses begin at the redshift $z_\mathrm{max}=5$.

2.2. Models for cosmic SFR

As our reference model for the SFR, we adopt a model that is based on recent progressive results of rest-frame UV, NIR Hα, and FIR/sub-millimetre observations; a simple functional form for the SFR per unit comoving volume is given as [53]

$$\psi_*(z) = 0.32 f_* h_{70}\frac{\exp(3.4z)}{\exp(3.8z)+45}\frac{\sqrt{\Omega_\mathrm{m}(1+z)^3+\Omega_\Lambda}}{(1+z)^{3/2}} M_\odot\,\mathrm{year}^{-1}\,\mathrm{Mpc}^{-3}, \tag{4}$$

where f_* is a factor of order unity, which we illustrate below. Figure 1 shows the SFR $\psi_*(z)$ with the various data points from rest-frame UV [22, 23, 30], Hα line [33]–[35], and FIR/sub-millimetre [31, 32] observations; these data points are not corrected for dust extinction. In the local universe, all studies show that the comoving SFR monotonically increases with z out to a redshift of at least 1. Although there is such a general observational tendency, even the local ($z=0$) SFR density is far from precise determination; it ranges fairly widely as $\psi_*(0) = (0.5\text{–}2.9)\times10^{-2}h_{70}M_\odot\,\mathrm{year}^{-1}\,\mathrm{Mpc}^{-3}$ [54]. For this reason, we introduce the correction factor f_*. Our reference model (4) with $f_*=1$ is consistent with mildly dust-corrected UV data at low redshift; on the other hand, it may underestimate the results of the other wave band observations. In fact, it predicts the local SFR value of $0.7\times10^{-2}h_{70}M_\odot\,\mathrm{year}^{-1}\,\mathrm{Mpc}^{-3}$, which is close to the lower limit of the estimation by Baldry and Glazebrook [54], but we stress that the SRN flux given below using this model can be simply applied to the other cases if we adjust the correction factor f_*, and would be quite general. Calculations by Strigari *et al* [16] are based on the SFR model giving a local value of $1.6\times10^{-2}M_\odot\,\mathrm{year}^{-1}\,\mathrm{Mpc}^{-3}$, which corresponds to $f_*=2.3$ in our notation. Although the SFR-z relation generally tends to increase from $z=0$ to ∼1, behaviours at the higher redshift region $z>1$ are not clear at all. Ando *et al* [12] also investigated the dependence on the several adopted SFR models, which were only different at high-redshift regions ($z\gtrsim1.5$); our reference model (4) was referred to as the 'SF1' model there.

[3] Although we use the specific cosmological model here, the SRN flux itself is completely independent of such cosmological parameters, as long as we use observationally inferred SFR models; see their cancellation between equations (3) and (4).

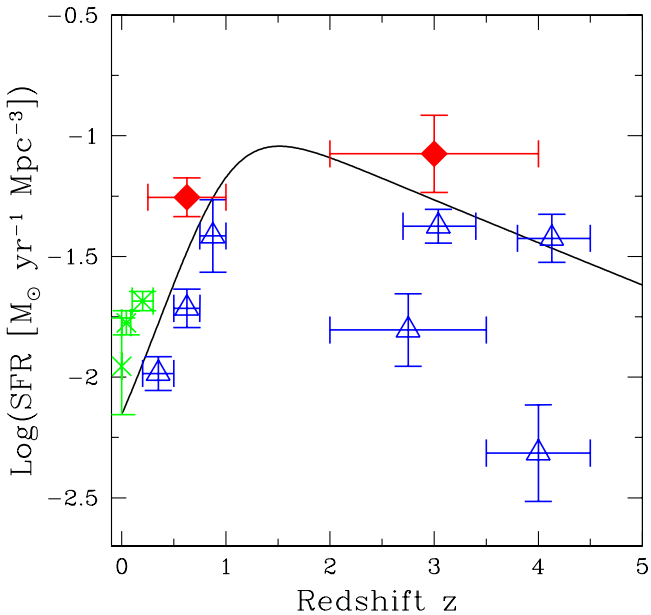

Figure 1. Cosmic SFR as a function of redshift. Data points are given by rest-frame UV (△) [22, 23, 30], NIR Hα (×) [33]–[35], and FIR/sub-millimetre (♦) [31, 32] observations. The solid line represents our reference model given by equation (4) with $f_* = 1$. The standard ΛCDM cosmology is adopted ($\Omega_{\rm m} = 0.3$, $\Omega_\Lambda = 0.7$, $H_0 = 70\,{\rm km\,s^{-1}\,Mpc^{-1}}$).

They showed that the SRN flux at $E_\nu > 10\,{\rm MeV}$ is highly insensitive to the difference among the SFR models (owing to the energy redshift, as discussed in section 3.1).

We obtain the supernova rate ($R_{\rm SN}(z)$) from the SFR by assuming the Salpeter IMF ($\phi(m) \propto m^{-2.35}$) with a lower cutoff around $0.5M_\odot$, and that all stars with $M > 8M_\odot$ explode as core-collapse supernovae, i.e.,

$$R_{\rm SN}(z) = \frac{\int_{8M_\odot}^{125M_\odot} {\rm d}m\,\phi(m)}{\int_0^{125M_\odot} {\rm d}m\,m\phi(m)}\psi_*(z) = 0.0122M_\odot^{-1}\psi_*(z). \tag{5}$$

Here we assume that the IMF does not change with time, which may be a good approximation provided there are no significant correlations between the IMF and the environment in which stars are born; extant evidence seems to argue against such correlations over the redshift range of interest ($z \lesssim 2$) [55]. The resulting local supernova rate evaluated with $f_* = 1$ agrees within errors with the observed value of $R_{\rm SN}(0) = (1.2 \pm 0.4) \times 10^{-4} h_{70}^3\,{\rm year^{-1}\,Mpc^{-3}}$ (see e.g., [56] and references therein). In fact, the totally time-integrated neutrino spectrum from massive stars ($\gtrsim 30M_\odot$) could be very different from the models that we use (and give in the next subsection), possibly because of, e.g., black hole formation. However, the conversion factor appearing in equation (5) is highly insensitive to the upper limit of the integral in the numerator; for instance, if we change the upper limit of the numerator to $25M_\odot$, the factor becomes $0.010M_\odot^{-1}$, which is only slightly different from the value in equation (5).

Table 1. Fitting parameters for supernova neutrino spectrum.

Model	Mass ($M_\odot$)	$\bar{E}_{\bar{\nu}_e}$ (MeV)	$\bar{E}_{\nu_x}$ (MeV)	$\beta_{\bar{\nu}_e}$	β_{ν_x}	$L_{\bar{\nu}_e}$ (erg)	L_{ν_x} (erg)
LL [57]	20	15.4	21.6	3.8	1.8	4.9×10^{52}	5.0×10^{52}
TBP [58]	11	11.4	14.1	3.7	2.2	–	–
	15	11.4	14.1	3.7	2.2	–	–
	20	11.9	14.4	3.6	2.2	–	–
KRJ [59]	–	15.4	15.7	4.2	2.5	–	–

2.3. Neutrino spectrum from supernova explosions

For the neutrino spectrum from each supernova, we adopt three reference models by different groups, i.e., simulations by the Lawrence Livermore (LL) group [57] and Thompson, Burrows and Pinto [58] (hereafter TBP), and the MC study of spectral formation by Keil, Raffelt and Janka [59] (hereafter KRJ). In this field, however, the most serious problem is that the recent sophisticated hydrodynamic simulations have not obtained the supernova explosion itself; the shock wave cannot penetrate the entire core. Therefore, many points still remain controversial, e.g., the average energy ratio among neutrinos of different flavours, or how the gravitational binding energy is distributed to each flavour. All these problems are quite serious for our estimation, since the binding energy released as $\bar{\nu}_e$ changes the normalization of the SRN flux, and the average energy affects the SRN spectral shape. Traditionally, neutrino spectrum is assumed to have a Fermi–Dirac spectral shape with $T_{\bar{\nu}_e} \simeq 5$ MeV and $T_{\nu_x} \simeq 8$ MeV, where ν_x represents non-electron neutrinos and anti-neutrinos, as adopted in many studies including recent ones [7]–[11], [13, 16, 19]. This approximation is roughly consistent with the LL model, although slight difference exists at both high- and low-energy regions [12, 57]. The other two models (TBP and KRJ) that are more sophisticated, however, are not consistent with such simple treatment at all as we describe below or as already discussed in [17]. For all these reasons stated above, we believe that these three models from different groups will be complementary.

The numerical simulation by the LL group [57] is considered to be the most appropriate for our estimation, because it is the only model that succeeded in obtaining a robust explosion and in calculating the neutrino spectrum during the entire burst (∼15 s). According to their calculation, the average energy difference between $\bar{\nu}_e$ and ν_x was rather large and the complete equipartition of the binding energy was realized $L_{\nu_e} = L_{\bar{\nu}_e} = L_{\nu_x}$, where L_{ν_α} represents the released gravitational energy as α-flavour neutrinos. The neutrino spectrum obtained by their simulation is well fitted by a simple formula, which was originally given by KRJ as

$$\frac{\mathrm{d}N_\nu}{\mathrm{d}E_\nu} = \frac{(1+\beta_\nu)^{1+\beta_\nu} L_\nu}{\Gamma(1+\beta_\nu)\bar{E}_\nu^2} \left(\frac{E_\nu}{\bar{E}_\nu}\right)^{\beta_\nu} \mathrm{e}^{-(1+\beta_\nu)E_\nu/\bar{E}_\nu}, \tag{6}$$

where $\bar{E}_\nu$ is the average energy; the values of the fitting parameters for the $\bar{\nu}_e$ and ν_x spectrum are summarized in table 1.

Although the LL group succeeded in obtaining a robust explosion, their result has recently been criticized because it lacked many relevant neutrino processes that are now recognized as important. Thus, we adopt the recent result of another hydrodynamic simulation, the TBP

one, which included all the relevant neutrino processes, such as neutrino bremsstrahlung and neutrino–nucleon scattering with nucleon recoil. Their calculation obtained no explosion, and the neutrino spectrum ends at 0.25 s after core bounce. In the strict sense, we cannot use their result as our reference model because the fully time-integrated neutrino spectrum is definitely necessary in our estimate. However, we adopt their result in order to confirm the effects of recent sophisticated treatments of neutrino processes in the supernova core on the SRN spectrum. The TBP calculations include three progenitor mass models, i.e., 11, 15 and $20M_{\odot}$; all of these models are well-fitted by equation (6), and the fitting parameters are summarized in table 1. The average energy for both $\bar{\nu}_e$ and ν_x is much smaller than that by the LL calculation. Although we do not show this in table 1, it was also found that at least for the early phase of the core-collapse, the complete equipartition of the gravitational binding energy for each flavour was not realized. However, it is quite unknown whether these trends hold during the entire burst. In this study, we adopt the average energy given in table 1 as our reference model, while we assume perfect equipartition between flavours, i.e., $L_{\bar{\nu}_e} = L_{\nu_x} = 5.0 \times 10^{52}$ erg.

In addition, we also use the model by KRJ. Their calculation did not couple with the hydrodynamics, but it focused on the spectral formation of neutrinos of each flavour using an MC simulation. Therefore, the static model was assumed as a background of neutrino radiation, and we use their 'accretion phase model II', in which the neutrino transfer was solved in the background of a 150 ms postbounce model by way of a general relativistic simulation. The fitting parameters for their MC simulation are also summarized in table 1. Unlike the previous two calculations, their result clearly shows that the average energy of ν_x is very close to that of $\bar{\nu}_e$. It also indicates that the equipartition among each flavour was not realized, but rather $L_{\nu_e} \simeq L_{\bar{\nu}_e} \simeq 2L_{\nu_x}$. Since the totally time-integrated neutrino flux is unknown from such temporary information, in this case also, we assume perfect equipartition, $L_{\bar{\nu}_e} = L_{\nu_x} = 5.0 \times 10^{52}$ erg, as well as that the average energies are the same as those in table 1.

2.4. Neutrino spectrum after neutrino oscillation

The original $\bar{\nu}_e$ spectrum is different from what we observe as $\bar{\nu}_e$ at Earth, owing to the effect of neutrino oscillation. Since the specific flavour neutrinos are not mass eigenstates, they mix with other flavour neutrinos during their propagation. The behaviour of flavour conversion inside the supernova envelope is well understood, because the relevant mixing angles and mass square differences are fairly well determined by recent solar [60, 61], atmospheric [62], and reactor neutrino experiments [63]. The remaining ambiguities concerning the neutrino oscillation parameters are the value of θ_{13}, which is only weakly constrained ($\sin^2\theta_{13} \lesssim 0.1$ [64]), and the type of mass hierarchy, i.e., normal ($m_1 \ll m_3$) or inverted ($m_1 \gg m_3$). We first discuss the case of normal mass hierarchy as our standard model; in this case, the value of θ_{13} is irrelevant. The case of inverted mass hierarchy is addressed in section 6.1. In addition, other exotic mechanisms, such as resonant spin–flavour conversion (see [65] and references therein) and neutrino decay [15, 18], which possibly change the SRN flux and spectrum, might work in reality, and these topics are also discussed later in sections 6.2 and 6.3, respectively.

The produced $\bar{\nu}_e$ at the supernova core are coincident with the lightest mass eigenstate $\bar{\nu}_1$ owing to the large matter potentials. Since this state $\bar{\nu}_1$ is the lightest in vacuum also, there are no resonance regions in which one mass eigenstate can change into another state, and therefore $\bar{\nu}_e$ at production arrives at the stellar surface as $\bar{\nu}_1$. Thus, the $\bar{\nu}_e$ spectrum observed by

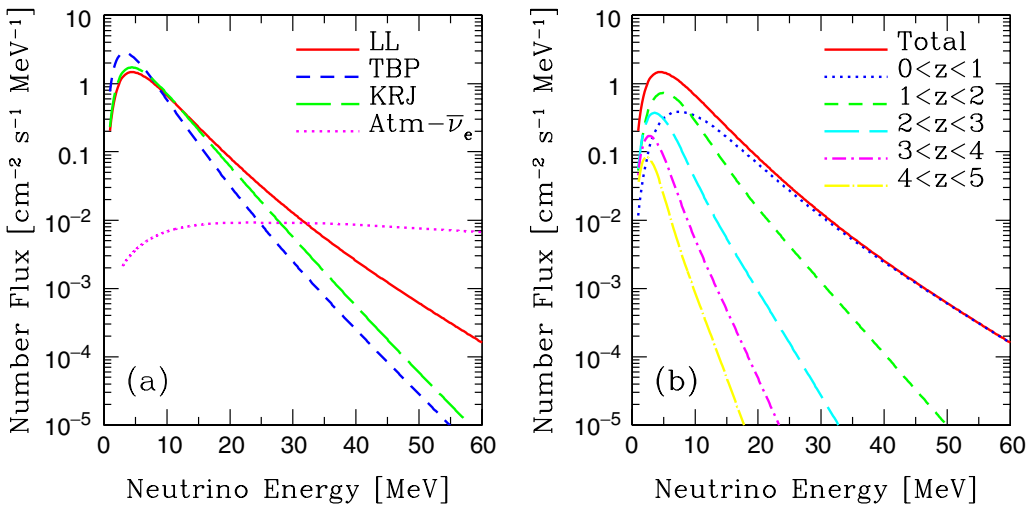

Figure 2. (a) SRN flux in units of $f_* \,\mathrm{cm}^{-2}\,\mathrm{s}^{-1}\,\mathrm{MeV}^{-1}$ calculated with three reference models of original neutrino spectrum: LL, TBP and KRJ. The flux of atmospheric neutrinos [66, 67] is also shown for comparison. (b) The same as (a), but indicating contribution from various redshift ranges. LL is adopted as the supernova model. These figures are taken from [17].

the distant detector is

$$\frac{\mathrm{d}N_{\bar{\nu}_\mathrm{e}}}{\mathrm{d}E_{\bar{\nu}_\mathrm{e}}} = |U_{\mathrm{e}1}|^2 \frac{\mathrm{d}N_{\bar{\nu}_1}}{\mathrm{d}E_{\bar{\nu}_1}} + |U_{\mathrm{e}2}|^2 \frac{\mathrm{d}N_{\bar{\nu}_2}}{\mathrm{d}E_{\bar{\nu}_2}} + |U_{\mathrm{e}3}|^2 \frac{\mathrm{d}N_{\bar{\nu}_3}}{\mathrm{d}E_{\bar{\nu}_3}} = |U_{\mathrm{e}1}|^2 \frac{\mathrm{d}N^0_{\bar{\nu}_\mathrm{e}}}{\mathrm{d}E_{\bar{\nu}_\mathrm{e}}} + (1 - |U_{\mathrm{e}1}|^2) \frac{\mathrm{d}N^0_{\nu_\mathrm{x}}}{\mathrm{d}E_{\nu_\mathrm{x}}}, \tag{7}$$

where the quantities with superscript 0 represent those at production, $U_{\alpha i}$ is the mixing matrix element between the α-flavour state and ith mass eigenstate, and observationally $|U_{\mathrm{e}1}|^2 = 0.7$. In other words, 70% of the original $\bar{\nu}_\mathrm{e}$ survives; on the other hand, the remaining 30% comes from the other component ν_x. Therefore, both the original $\bar{\nu}_\mathrm{e}$ and ν_x spectra are necessary for the estimation of the SRN flux and spectrum; since the original ν_x spectrum is generally harder than that of the original $\bar{\nu}_\mathrm{e}$, as shown in table 1, the flavour mixing is expected to harden the detected SRN spectrum.

3. Flux and event rate of SRNs

3.1. Flux of SRNs

The SRN flux can be calculated by equation (3) with our reference models given in section 2. Figure 2(a) shows the SRN flux as a function of neutrino energy for the three supernova models, LL, TBP and KRJ. The flux of atmospheric $\bar{\nu}_\mathrm{e}$, which becomes a background event for SRN detection, is shown in the same figure [66, 67]. The SRN flux peaks at $\lesssim$5 MeV, and around this peak, the TBP model gives the largest SRN flux because the average energy of the original $\bar{\nu}_\mathrm{e}$ is considerably smaller than in the other two models but the total released energy is assumed to be the same. On the other hand, the model gives a smaller contribution at high-energy regions, $E_\nu > 10$ MeV. In contrast, the high-energy tail of the SRN flux with the LL model extends

Table 2. Flux of SRNs.

		Flux (f_* cm^{-2} s^{-1})		
Model	Redshift range	Total	$E_\nu > 11.3$ MeV	$E_\nu > 19.3$ MeV
LL	Total	11.7	2.3	0.46
	$0 < z < 1$[a]	4.1 (35.3)	1.6 (70.9)	0.39 (85.2)
	$1 < z < 2$[a]	4.9 (42.0)	0.6 (26.3)	0.06 (14.0)
	$2 < z < 3$[a]	1.8 (15.1)	0.1 (2.5)	0.0 (0.7)
	$3 < z < 4$[a]	0.6 (5.3)	0.0 (0.2)	0.0 (0.0)
	$4 < z < 5$[a]	0.2 (2.1)	0.0 (0.0)	0.0 (0.0)
TBP	Total	16.1	1.3	0.14
KRJ	Total	12.7	2.0	0.28

[a] Contribution from each redshift range to the total ($0 < z < 5$) value are shown in parentheses as percentages.

farther than with the other models, and it gives flux more than an order of magnitude larger at $E_\nu = 60$ MeV. This is because the high-energy tail was mainly contributed by the harder component of the original neutrino spectrum; in the case of the LL calculation, the average energy of the harder component ν_x is significantly larger than that of the other two calculations, as shown in table 1. We show the values of the SRN flux integrated over the various energy ranges in table 2. The total flux is expected to be (11–16) f_* cm^{-2} s^{-1} for our reference models, although this value is quite sensitive to the shape of the assumed SFR, especially at high-z. The energy range in which we are more interested is high-energy regions such as $E_\nu > 19.3$ MeV and 11.3 MeV, because as discussed below, the background events are less critical and the reaction cross section increases as $\propto E_\nu^2$. In such a range, the SRN flux is found to be (1.3–2.3) f_* cm^{-2} s^{-1} ($E_\nu > 11.3$ MeV) and (0.14–0.46) f_* cm^{-2} s^{-1} ($E_\nu > 19.3$ MeV). Thus, the uncertainty about the supernova neutrino spectrum and its luminosity gives at least a factor of 2–4 ambiguity compared to the expected SRN flux in the energy region of our interest.

Figure 2(b) shows the contribution by supernova neutrinos emitted from various redshift ranges. At the high-energy region $E_\nu > 10$ MeV, the dominant flux comes from the local supernovae ($0 < z < 1$), while the low-energy side is mainly contributed by the high-redshift events ($z > 1$). This is because the energy of neutrinos that were emitted from a supernova at redshift z is reduced by a factor of $(1 + z)^{-1}$ reflecting the expansion of the universe, and therefore high-redshift supernovae only contribute to low-energy flux. We also show the energy-integrated flux from each redshift range in table 2 in the case of the LL supernova model. From the table, it is found that in the energy range of our interest, more than 70% of the flux comes from local supernova explosions at $z < 1$, while the high-redshift ($z > 2$) supernova contribution is very small.

3.2. Event rate at water Čerenkov detectors

The water Čerenkov neutrino detectors have greatly succeeded in probing the properties of neutrinos as elementary particles, such as neutrino oscillation. The SK detector is one of these detectors, and its large fiducial volume (22.5 kton) might enable us to detect the diffuse background of SRNs. Furthermore, much larger water Čerenkov detectors such as HK and UNO

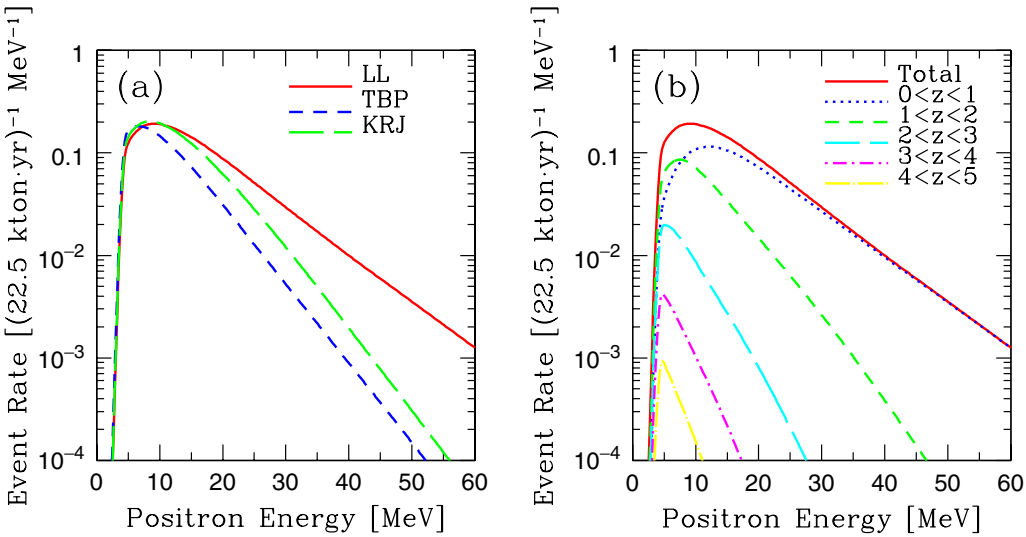

Figure 3. (a) Event rate at water Čerenkov detectors in units of f_* (22.5 kton year)$^{-1}$ MeV^{-1} for three supernova models. (b) The same as (a), but indicating contribution from various redshift ranges. LL is adopted as the supernova model. These figures are taken from [17].

Table 3. Event rate of SRNs.

		Event rate [f_* (22.5 kton year)$^{-1}$]	
Model	Redshift range	$E_e > 10$ MeV	$E_e > 18$ MeV
LL	Total	2.3	1.0
	$0 < z < 1$[a]	1.7 (77.5)	0.9 (87.5)
	$1 < z < 2$[a]	0.5 (20.6)	0.1 (11.9)
	$2 < z < 3$[a]	0.0 (1.7)	0.0 (0.5)
	$3 < z < 4$[a]	0.0 (0.1)	0.0 (0.0)
	$4 < z < 5$[a]	0.0 (0.0)	0.0 (0.0)
TBP	Total	0.97	0.25
KRJ	Total	1.7	0.53

[a] Contribution from each redshift range to the total ($0 < z < 5$) value are shown in parentheses as percentages.

are being planned. SRN detection is most likely with the inverse β-decay reaction with protons in water, $\bar{\nu}_e\, p \rightarrow e^+ n$, and its cross section is precisely understood [68, 69]. In our calculation, we use the trigger threshold of SK-I (before the accident).

The expected event rates at such detectors are shown in figures 3(a) and (b) in units of f_* (22.5 kton year)$^{-1}$ MeV^{-1}; with SK, it takes a year to obtain the shown SRN spectrum, while with HK and UNO, much less time (1 year $\times$ (22.5 kton $V_{\rm fid}^{-1}$), where $V_{\rm fid}$ is the fiducial volume of HK or UNO) is necessary because of their larger fiducial volume. Figure 3(a) compares the three models of the original supernova neutrino spectrum, and figure 3(b) shows the contribution to the total event rate from each redshift range. In table 3 we summarize the event rate integrated over various energy ranges for three supernova models. The expected event

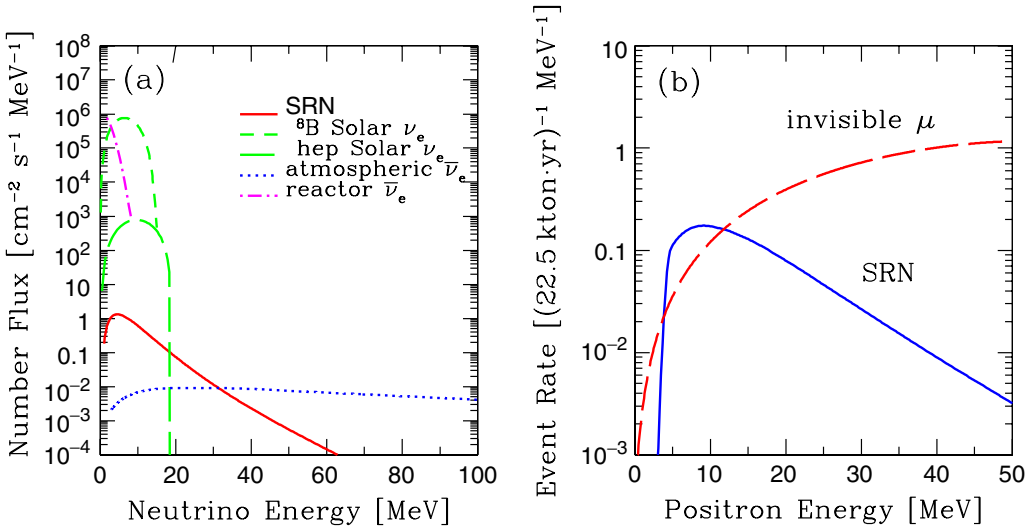

Figure 4. (a) Number flux of SRNs compared with other background neutrinos. (b) Event rate of SRNs and invisible muon decay products. In both panels, LL is adopted as the original neutrino spectrum. These figures are taken from [12].

rate is (0.97–2.3) f_* (22.5 kton year)$^{-1}$ for $E_e > 10$ MeV and (0.25–1.0) f_* (22.5 kton year)$^{-1}$ for $E_e > 18$ MeV. This clearly indicates that if the background events that hinder the detection are negligible, the SK has already reached the required sensitivity for detecting SRNs; with the future HK and UNO, a statistically significant discussion would be possible. This also shows that the current shortage of our knowledge concerning the original supernova neutrino spectrum and luminosity gives at least a factor of 2 ($E_\nu > 10$ MeV) to 4 ($E_\nu > 18$ MeV) uncertainty to the event rate at the high-energy range (actual detection range). We also summarize the contribution from each redshift range in the same table, especially for the calculation with the LL model. The bulk of the detected events will come from the local universe ($z < 1$), but the considerable flux is potentially attributed to the range $1 < z < 2$.

4. Detectability and observational upper limit

4.1. Background events against detection

In the previous section, we calculated the expected SRN spectrum at the water Čerenkov detectors on the Earth, but the actual detection is quite restricted because of the presence of other background events. In this paper, we follow a detailed consideration of these backgrounds by Ando *et al* [12]. There are atmospheric and solar neutrinos, anti-neutrinos from nuclear reactors, spallation products induced by cosmic-ray muons and decay products of invisible muons. We show in figures 4(a) and (b) the flux and event rate of SRNs and these background events.

The flux of the atmospheric neutrinos is usually calculated using MC method including various relevant effects (flux of primary cosmic rays, solar modulation, geomagnetic field, interaction of cosmic rays in the air, and so on), and in that simulation one-dimensional approximation is used, i.e., after the interaction of primary cosmic ray particles with air nuclei,

all the particles are assumed to be moving along the line of the momentum vector of the primary cosmic ray particles [70]. There are many authors who calculated the atmospheric neutrino flux (see [71]–[73] for recent one-dimensional results). We use in this paper the flux calculated by Gaisser *et al* [66, 67]. More recently, results of three-dimensional flux calculations have been reported by several groups (see [74, 75] and references therein). These calculations show slight increase of the flux at low-energy regions, although the flux below 100 MeV is not given. Therefore, it should be noted that there is possibility that the flux of atmospheric neutrinos in the relevant energy regime is higher than that adopted in this paper by about 20–30%.

Solar neutrino flux is dominant in the energy range below 19 MeV. We use the flux predicted by the standard solar model (SSM) in figure 4 [76]. Since the solar neutrinos are not $\bar{\nu}_e$ but ν_e, the cross section for them is about two orders of magnitude smaller than that for $\bar{\nu}_e$. Furthermore, recoil electrons scattered by solar neutrinos strongly concentrate to the opposite direction of the Sun, in contrast to the isotropic distribution of $\bar{\nu}_e$ events. Therefore, the solar neutrinos are an avoidable background, not as critical as other events. At the same energy range corresponding to $E_\nu \lesssim 19$ MeV, there is another serious background that becomes an obstacle for solar neutrino detection, i.e., spallation products induced by cosmic ray muons. The event rate of the spallation background is several hundred per day per 22.5 kton, and it is extremely difficult to reject all of these events. Therefore, the solar neutrino range ($E_\nu \lesssim 19$ MeV), cannot be used as an energy window.

The third background which we must consider is anti-neutrinos from nuclear reactors. In each nuclear reactor, almost all the power comes from the fissions of the four isotopes, ^{235}U (∼75%), ^{238}U (∼7%), ^{239}Pu (∼15%) and ^{241}Pu (∼3%) [77]. Each isotope produces a unique electron anti-neutrino spectrum through the decay of its fission fragments and their daughters. The $\bar{\nu}_e$ spectrum from ^{235}U, ^{239}Pu and ^{241}Pu can be derived using the semi-empirical formula with which we fit the data of detected β-spectrum from fission by thermal neutrons [78, 79]. (^{238}U undergoes only fast neutron fission and hence electron spectrum from ^{238}U cannot be measured by this kind of experiment.) Above 7 MeV, the number of β counts drops dramatically and fitting error becomes large. In addition, with this method, as we determine the maximum β energy and derive the energy distribution below that energy, it is difficult to estimate the errors at the high-energy range. While the $\bar{\nu}_e$ spectra in [78, 79] are given as tables, we use for simplicity a somewhat less accurate analytical approximation given in [80]. As a normalization factor we use energy-integrated $\bar{\nu}_e$ flux at Kamioka, $1.34 \times 10^6\ \mathrm{cm}^{-2}\ \mathrm{s}^{-1}$, which is the total flux from various nuclear reactors in Japan and Korea [77].

With the backgrounds that we discussed above and from figure 4(a), we expect the energy window of SRN events to be in the range 19–30 MeV. However, electrons or positrons from invisible muons are the largest background in the energy window from 19 to 60 MeV. This invisible muon event is illustrated as follows. Atmospheric neutrinos produce muons by interaction with the nucleons (both free and bound) in the fiducial volume. If these muons are produced with energies below Čerenkov radiation threshold (kinetic energy less than 53 MeV), then they will not be detected ('invisible muons'), but successively produced electrons and positrons from the muon decay will be visible. Since this muon decay signal will mimic the $\bar{\nu}_e\,\mathrm{p} \rightarrow \mathrm{e}^+\mathrm{n}$ process in SK, it is difficult to distinguish SRN from these events. The spectrum of this invisible muon events is shown in figure 4(b), compared with the SRN spectrum. Therefore, even at the remaining part of the energy window 19–30 MeV, there is a huge background due to the invisible muons, resulting in a 'no energy window' for the SRN detection at present.

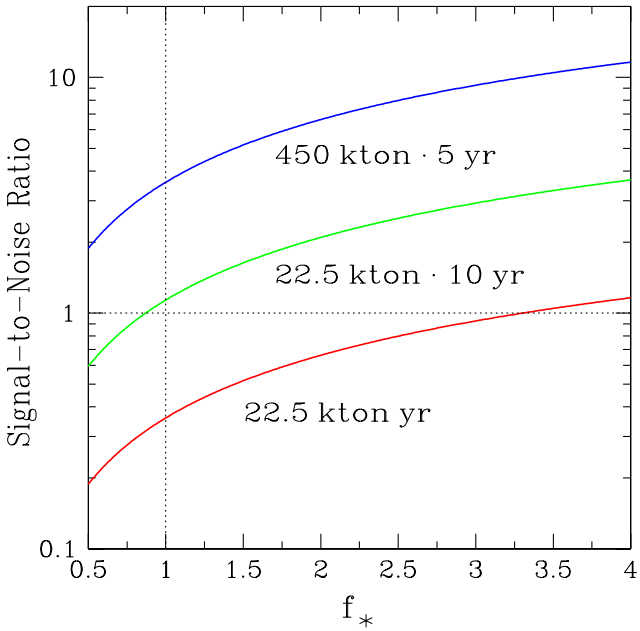

Figure 5. Signal-to-noise ratio S/N of SRNs at pure-water Čerenkov detectors (8), as a function of a correction factor f_* for the SFR model (4). LL is assumed for the original neutrino spectrum. Each line is labelled by the value of the effective volume $V_{\rm eff}$.

4.2. Detectability at pure-water Čerenkov detectors

We expect that SRNs could most likely be detected at water Čerenkov detectors such as SK, because the largest class of volume can be realized, enabling the most statistically significant discussions. The most serious problem is that there is no energy window as we described in the previous subsection. In the energy range 19–30 MeV, the SRN event number is estimated to be $N_{\rm SRN} = 0.73 f_* \, (V_{\rm eff}\, 22.5\,{\rm kton}^{-1}\,{\rm year}^{-1})$ for the LL model, where we define the effective volume of detectors $V_{\rm eff}$ as (fiducial volume)×(time)×(efficiency), which is the relevant quantity representing the detector performance. On the other hand, the background level would be as large as $N_{\rm bg} \sim 3.4\,(V_{\rm eff}\, 22.5\,{\rm kton}^{-1}\,{\rm year}^{-1})$, contributed mainly by the invisible muon decay products. Therefore, signal-to-noise ratio S/N can be written as

$$S/N \equiv \frac{N_{\rm SRN}}{\sqrt{N_{\rm SRN} + N_{\rm bg}}} = \frac{0.73 f_*}{\sqrt{0.73 f_* + 3.4}} \left(\frac{V_{\rm eff}}{22.5\,{\rm kton\,year}} \right)^{1/2}, \tag{8}$$

plotted in figure 5 as a function of f_* for several values of the effective volume. For detectors with the size of SK, one-year observation is found to be insufficient to obtain significant SRN detection. Further data-taking for about 10 years may reach $S/N \lesssim$ a few, but this number is still insufficient in statistical significance. Future mega-ton class detectors such as HK and UNO, now under planning, potentially give us a considerable number of SRN detection, by data-taking for a couple of years, as can be seen from the upper curve in figure 5.

4.3. Detectability at other detectors

In this subsection, we discuss the SRN detectability at SNO (the heavy water Čerenkov detector) and KamLAND (the scintillation detector), which is mainly discussed in [11, 12] and [12, 16], respectively. An advantage of these detectors is that we are able to identify $\bar{\nu}_e$ events using delayed coincidence signals; neutrons produced via $\bar{\nu}_e d \rightarrow e^+ nn$ (SNO) and $\bar{\nu}_e p \rightarrow e^+ n$ (KamLAND) are tagged by deuterons, Cl or He (SNO) and by protons (KamLAND), resulting in γ-ray cascades, identified with the preceded positron signal. Using this technique, we can remove other backgrounds of non-$\bar{\nu}_e$ origin (solar neutrinos, invisible muons and spallation products), opening up an energy window in the range of 10–30 MeV. Unfortunately, because the detector volume is small (both detectors are about 1 kton), the expected SRN rate is quite small, $0.03 f_* \text{ year}^{-1}$ for SNO and $0.1 f_* \text{ year}^{-1}$ for KamLAND [12]. More recently, Strigari *et al* [16] estimated the event rate at KamLAND to be $\sim$0.4 year^{-1}, but they used the energy range above 6 MeV, simply because there have been no events seen above this energy at KamLAND [63]. In addition, the detectability at liquid argon detectors has been discussed in [19]; although the detection is still challenging, potential advantage is that these detectors can mainly capture ν_e, which is difficult with other detectors.

4.4. Current observational limit and future prospects

The most stringent upper limit on the SRN flux is obtained by the observation for 1496 days (4.1 years) at the SK detectors [20]. This limit is obtained by the statistical analysis including the background events from atmospheric neutrinos and invisible muons, and is $<1.2\,\text{cm}^{-2}\,\text{s}^{-1}$ over the energy region of $E_\nu > 19.3$ MeV (90% CL). Comparing with the prediction for the same energy range given in table 2, we find that the current SK limit is only about a factor 2.5–8.5 larger than our prediction using the reference model for the cosmic SFR with $f_* = 1$, depending on the adopted original neutrino spectrum. This strong constraint motivated many theoretical studies [13]–[16] and has been translated into constraints on various quantities as we further discuss in the following sections.

Although the SK limit was derived by a careful analysis of the spectral data over the energy range $E_e > 18$ MeV, we here show that a very rough statistical argument using equation (8) can fairly well reproduce the same limit. In equation (8), we consider setting a limit at 90% CL, which corresponds to 1.64σ level (or $S/N < 1.64$), as a result of no SRN detection for $V_{\text{eff}} = 22.5\,\text{kton} \cdot 4.1$ year observation. Substituting these values into equation (8), it is solved for f_*, resulting in the upper limit $f_* < 2.6$ (90% CL). This value is then translated into the flux limit using the relation between the SRN flux and f_* (for the LL model) given in table 2, i.e., $F_\nu < 1.2\ \text{cm}^{-2}\ \text{s}^{-1}$ for $E_\nu > 19.3$ MeV (90% CL), which is in remarkable agreement with the actual result reported by the SK group [20].

In the near future, sensitivity of water Čerenkov detectors for the SRN detection would be significantly improved by the promising technique proposed recently [21]. The basic idea is the same as the delayed coincidence technique actually adopted by SNO or KamLAND (see discussions in section 4.2), but $GdCl_3$ is dissolved into the pure-water of SK (or other future detectors), which enables us to actively identify $\bar{\nu}_e$ by capturing neutrons produced by the $\bar{\nu}_e\, p \rightarrow e^+ n$ reaction. Owing to this proposal, the range 10–30 MeV would be an energy window because we can positively distinguish the $\bar{\nu}_e$ signal from other backgrounds such as solar neutrinos (ν_e), invisible muon events and spallation products. The neutron capture efficiency by Gd is estimated to be 90% with the proposed 0.2% admixture by mass of $GdCl_3$ in water,

Table 4. Constraints on supernova rate and SFR models. Upper part shows the SK limit on the SRN observation [20], whereas the lower part shows the results of local supernova surveys [56] and observational inference of the local SFR [54].

	f_*	$R_{\rm SN}(0)$ (year^{-1} Mpc^{-3})	$\psi_*(0)$ ($M_\odot$ year^{-1} Mpc^{-3})
LL	<2.6	$<2.2 \times 10^{-4}$	$<1.8 \times 10^{-2}$
TBP	<8.6	$<7.3 \times 10^{-4}$	$<6.0 \times 10^{-2}$
KRJ	<4.3	$<3.6 \times 10^{-4}$	$<3.0 \times 10^{-2}$
[56]	0.9–1.9	$(0.8–1.6) \times 10^{-4}$	–
[54]	0.7–4.2	–	$(0.5–2.9) \times 10^{-2}$

and subsequently 8 MeV γ-cascade occurs from the excited Gd. The single-electron energy equivalent to this cascade was found to be 3–8 MeV by a careful simulation [81], and with the trigger threshold adopted in SK-I, only about 50% of such cascades can be detected actually. However, it is expected that SK-III, which will begin operation in mid-2006, will trigger at 100% efficiency above 3 MeV, with good trigger efficiency down to 2.5 MeV [21]. In that case most of the γ-cascades from Gd will be detected with their preceding signal of positrons. From this point on, we assume 100% efficiency; even if we abandon this assumption, it does not affect our physical conclusion, since the relevant quantity representing the detector performance is the effective volume $V_{\rm eff}$ that already includes efficiency.

5. Implication for cosmic star formation history

5.1. Constraints from the current observational limit

The current SK upper limit on the SRN flux is already stringent to give some physical or astronomical consequences. In this subsection, we discuss a constraint on the cosmic SFR from the SRN limit; similar arguments have been given in [13]. Comparing with our flux predictions using several supernova models (table 2), the SK limit can be directly translated into a bound on the correction parameter f_* to the cosmic SFR introduced in (4), since the redshift dependence is roughly consistent among various observations. Further, the constraint on f_* can then be used as that on the local supernova rate and SFR. The results are summarized in table 4 for various supernova models. For comparison, in the lower part of the same table, we also show the result of local supernova surveys, $R_{\rm SN}(0) = (0.8–1.6) \times 10^{-4}$ year^{-1} Mpc^{-3} [56], and the observationally inferred SFR $\psi_*(0) = (0.5–2.9) \times 10^{-2} M_\odot$ year^{-1} Mpc^{-3} [54]. In particular, for the local SFR, the SK limit on the SRN flux may rule out some fraction of the observationally inferred value, if we choose the LL model for the original neutrino spectrum; for the other two supernova models, the SK limit is very close to the current upper bound on the cosmic SFR by observations with the light. Therefore, we stress that the neutrino observation has already reached sensitivity to the cosmic SFR comparable with the usual and traditional approaches using light.

5.2. Performance of Gd-loaded detectors

Performance of the proposed Gd-loaded detectors as an SFR probe is of interest to us, and has recently been investigated in detail by Ando [17] using the MC simulation; in this subsection, we

briefly introduce his discussion. Although we focus here on how far the SFR can be probed by SRN observation, the uncertainty from the supernova neutrino spectrum would give a fair amount of error. However, this problem can be solved if a supernova explosion occurs in our galaxy; the expected event number is about 5000–10 000 at SK, when a supernova neutrino burst occurs at 10 kpc, and it will enable a statistically significant discussion concerning the neutrino spectrum from supernova explosions. Even if there are no galactic supernovae in the near future, remarkable development of the supernova simulation can be expected with the growth of computational resources and numerical technique. With such developments, the supernova neutrino spectrum and luminosity may be uncovered, and the ambiguity is expected to be reduced significantly. Thus, in this paper we assume that the supernova neutrino spectrum is well understood and that our reference models are fairly good representatives of nature; we analyse the SFR alone with several free parameters.

The basic procedure adopted in [17] is as follows. (1) The expected signal (spectrum) at a Gd-loaded detector in the range 10–30 MeV is simulated, assuming that there are no background events. In that process, the SFR given by equation (4) with $f_* = 1$ and the LL model as neutrino spectrum are used for the generation of the SRN signal. (2) Then the SRN spectrum is analysed using the maximum likelihood method with two free parameters of the SFR and a set of the best-fit values for those parameters is obtained; they are concerned with the supernova rate as

$$R_{\rm SN}(z) = \begin{cases} R^0_{\rm SN}(1+z)^\alpha & \text{for } z < 1, \\ 2^\alpha R^0_{\rm SN} & \text{for } z > 1, \end{cases} \tag{9}$$

where $R^0_{\rm SN}$ represents the local supernova rate and α determines the slope of supernova rate evolution. Although a constant SFR at $z > 1$ is assumed, it is found that the result would be the same even if this assumption is changed. This is because the bulk of the detected event comes from local supernova as already shown. (3) 10^3 such MC simulations are performed and 10^3 independent sets of best-fit parameters are obtained. Then we discuss the standard deviation of the distributions of such best-fit parameter sets and the implications for the cosmic SFR.

Using this procedure, we discuss the performance of Gd-SK for 5 years, or an effective volume of 22.5 kton · 5 year. As the expected event number is only ∼10, the parameters $R^0_{\rm SN}$ and α both cannot be well determined at once. Therefore, one of those parameters should be fixed in advance at some value inferred from other observations. Firstly, the value of $R^0_{\rm SN}$ was fixed to be 1.2×10^{-4} year^{-1} Mpc^{-1}, which was inferred from the local supernova survey [56], and the distribution of the best-fit values of the parameter α was obtained. The result of 10^3 MC simulations are shown in figure 6(a) as a histogram of the distribution of best-fit parameters α (solid histogram). The average value of these 10^3 values for α is found to be 2.7, and the standard deviation is 0.8, i.e., $\alpha = 2.7 \pm 0.8$. Secondly, in turn, the value of α was fixed to be 2.9 in order to obtain the distribution of best-fit values for the local supernova rate $R^0_{\rm SN}$ from the SRN observation. The result of 10^3 MC generations and analyses in this case is shown in figure 6(b). The average value for $R^0_{\rm SN}$ is 1.2×10^{-4} year^{-1} Mpc^{-3}, and the standard deviation is 0.4×10^{-4} year^{-1} Mpc^{-3}, i.e., $R^0_{\rm SN} = (1.2 \pm 0.4) \times 10^{-4}$ year^{-1} Mpc^{-3}. Figure 7 shows the comparison between the supernova rate model, in which the parameter is inferred from the MC simulations, and the 'true' reference model; the cases of fixed $R^0_{\rm SN}$ and α are shown in figures 7(a) and (b), respectively. The allowed region at the 1σ level is located between the two dotted curves, while the solid curve represents the reference model, from which MC data were generated. Thus, with the Gd-SK detector we can roughly reproduce the supernova rate profile at $z < 1$ for 5 years' operation.

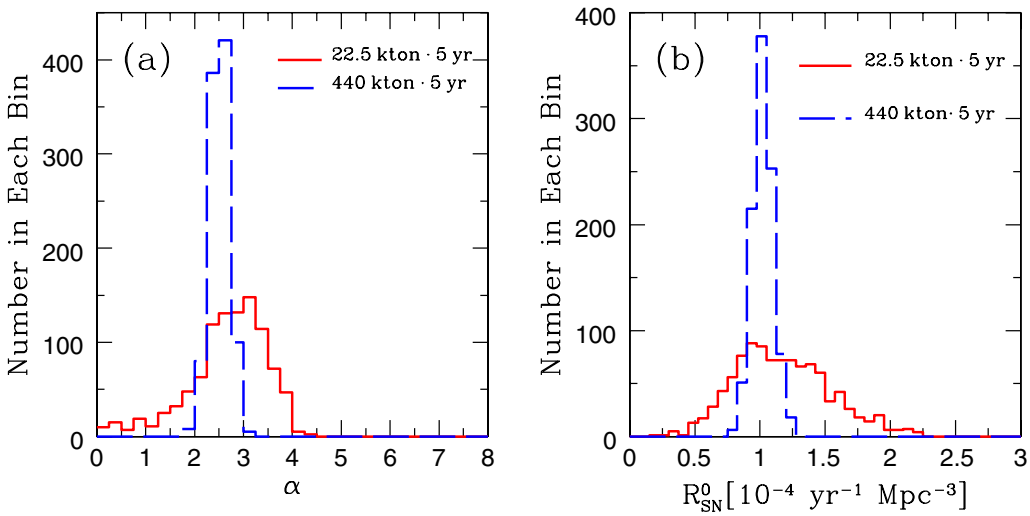

Figure 6. Distribution of 10^3 best-fit values for (a) α and (b) R^0_{SN}, which are obtained from the analyses of each MC generation. The effective volume is 22.5 kton · 5 year for solid histogram and 440 kton · 5 year for dashed histogram. (a) The value of the local supernova rate is fixed to be $R^0_{SN} = 1.2 \times 10^{-4}$ year^{-1} Mpc^{-3}. The resulting distributions are characterized by $\alpha = 2.7 \pm 0.8$ for an effective volume of 22.5 kton · 5 year and $\alpha = 2.5 \pm 0.2$ for 440 kton · 5 year. (b) The value of α is fixed to be 2.9. The resulting distributions are characterized by $R^0_{SN} = (1.2 \pm 0.4) \times 10^{-4}$ year^{-1} Mpc^{-3} for 22.5 kton · 5 year and $R^0_{SN} = (1.0 \pm 0.1) \times 10^{-4}$ year^{-1} Mpc^{-3} for 440 kton · 5 year. These figures are taken from [17].

Now, we turn our attention to future mega-ton class detectors such as Gd-HK or Gd-UNO. With these detectors, the effective volume considered, 440 kton · 5 year, is expected to be realized in several years from the start of their operation. Firstly, the same analysis as illustrated above was performed; i.e., one of relevant parameters, α or R^0_{SN}, was fixed and the dependence on the remaining parameter was investigated. The result of these cases are also shown in figures 6(a) and (b) as dashed histograms, which give $\alpha = 2.5 \pm 0.2$ and $R^0_{SN} = (1.0 \pm 0.1) \times 10^{-4}$ year^{-1} Mpc^{-3}, respectively. The statistical errors are considerably reduced compared with the case of 22.5 kton · 5 year, because of the ∼20 times larger effective volume. Thus, future maga-ton detectors will probably pin down, within 10% statistical error, either the index of supernova rate evolution α or the local supernova rate R^0_{SN} if the other is known in advance. The dashed curves in figure 7 set the allowed region of the supernova rate at the 1σ level by the considered detectors, well reproducing the assumed model. In principle, we can determine both parameters by SRN observation, because R^0_{SN} is concerned with the absolute value of the flux alone but α is concerned with both the absolute value and the spectral shape; i.e., these two parameters are not degenerate with respect to each other. Thus, the same procedure was repeated but without fixing the values of α or R^0_{SN}. The distribution of 10^3 best-fit parameter sets of (α, R^0_{SN}) was calculated assuming a detector with an effective volume of 440 kton · 5 year; the mean values and the standard deviations were found to be $\alpha = 3.5 \pm 1.3$ and $R^0_{SN} = (8.8 \pm 4.8) \times 10^{-5}$ year^{-1} Mpc^{-3}. Even though the effective volume is as large as 440 kton · 5 year, it is still insufficient for determining both parameters at once.

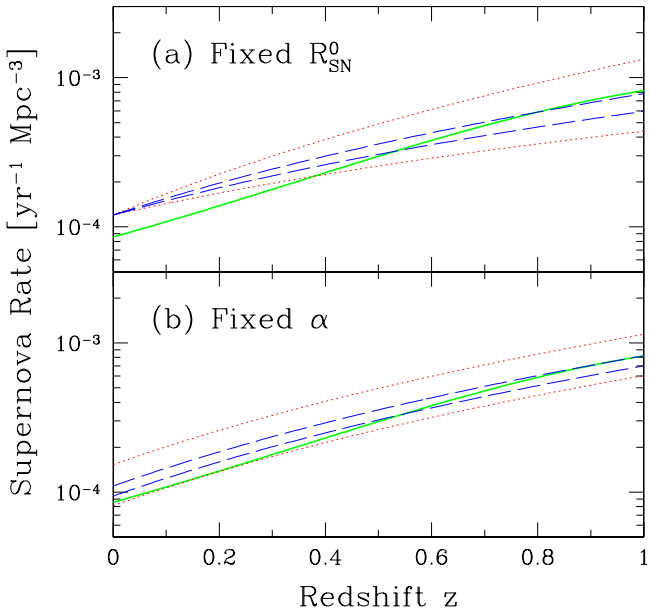

Figure 7. Supernova rate as a function of redshift. In both panels, solid curves represent the reference model, from which MC data were generated. (a) The allowed region at the 1σ level, concerning the fitting parameter α with fixed R^0_{SN}, is shown as the area between the two dotted curves for an effective volume of 22.5 kton · 5 year and as the area between the two dashed curves for an effective volume of 440 kton · 5 year. (b) The same as (a) but for fitting parameter R^0_{SN} with fixed α. This figure is taken from [17].

Throughout the above arguments or those in [17], the reference SFR model with $f_* = 1$ was assumed and they seem to be dependent on the adopted values of f_*. However, the results can easily be applied to the case with other values of f_*. This is because the statistical errors are inversely proportinal to the square root of the event number, which is simply proportional to $f_* V_{\rm eff}$ in our arguments; i.e., $\delta\alpha/\langle\alpha\rangle, \delta R^0_{SN}/\langle R^0_{SN}\rangle \propto (f_* V_{\rm eff})^{-1/2}$. In consequence, we find that the discussions given above and in [17] are quite general and can be easily modified in the other cases of f_* using the following relations:

$$\frac{\delta\alpha}{\langle\alpha\rangle} \simeq 0.3\left(\frac{f_* V_{\rm eff}}{22.5\,\text{kton}\cdot 5\,\text{year}}\right)^{-1/2}, \qquad \frac{\delta R^0_{SN}}{\langle R^0_{SN}\rangle} \simeq 0.3\left(\frac{f_* V_{\rm eff}}{22.5\,\text{kton}\cdot 5\,\text{year}}\right)^{-1/2}. \tag{10}$$

As a next step, it would be useful to investigate the possibility of how far (to which z) we can probe the cosmic SFR by the SRN observations. As we have already shown, the main contribution to the SRN event rate at 10–30 MeV comes from the low-redshift region $0 < z < 1$. Signals from further high-redshift universe would become enhanced if we could reduce the lower energy threshold $E_{\rm th}$ of the SRN detection range. The value of $E_{\rm th}$ is restricted to 10 MeV because at energy regions lower than this, there is a large background of reactor neutrinos; its removal is impossible with the current detection methods. Since the SK and HK detectors are (will be) located at Kamioka in Japan, they are seriously affected by background neutrinos from

many nuclear reactors. If some large-volume detectors were built at a location free from such background, the lower threshold energy could be reduced, enabling us to probe the high-redshift supernova rate. Ando [17] also discussed the performance of future mega-ton class of detectors as a function of the value of $E_{\rm th}$ and found that the behaviour of SFR at $1 < z < 2$ affects more and more the detected event number at $E_{\rm th} < E_{\rm e} < 30$ MeV, as we reduce the threshold energy.

6. Implication for neutrino properties

6.1. Inverted mass hierarchy

Throughout the above discussions, we have assumed normal hierarchy of neutrino masses ($m_1 \ll m_3$). However, the case of inverted mass hierarchy has not yet been experimentally excluded, and we explore this possibility in this subsection following the discussion given by Ando and Sato [14]. In this case, flavour conversions inside the supernova envelope change dramatically, compared with the normal mass hierarchy already discussed in section 2.4. Since $\bar{\nu}_3$ is the lightest, $\bar{\nu}_{\rm e}$ are created as $\bar{\nu}_3$, owing to a large matter potential. In that case, it is well known that at a so-called resonance point, there occurs a level crossing between $\bar{\nu}_1$ and $\bar{\nu}_3$ (for a more detailed discussion, see, e.g., [82]). At this resonance point, complete $\bar{\nu}_1 \leftrightarrow \bar{\nu}_3$ conversion occurs when the so-called adiabaticity parameter is sufficiently small compared to unity (it is said that resonance is 'non-adiabatic'), while conversion never occurs when it is large (adiabatic resonance). The adiabaticity parameter γ is quite sensitive to the value of θ_{13}, i.e., $\gamma \propto \sin^2 2\theta_{13}$; when $\sin^2 2\theta_{13} \gtrsim 10^{-3}$ ($\sin^2 2\theta_{13} \lesssim 10^{-5}$), the resonance is known to be completely adiabatic (non-adiabatic) [82]. When the resonance is completely non-adiabatic (because of small θ_{13}), the situation is the same as in the case of normal mass hierarchy already discussed in section 2.4 (because $\bar{\nu}_{\rm e}$ at production becomes $\bar{\nu}_1$ at the stellar surface), and the $\bar{\nu}_{\rm e}$ spectrum after oscillation is represented by equation (7). On the other hand, adiabatic resonance (due to large θ_{13}) forces $\bar{\nu}_{\rm e}$ at production become $\bar{\nu}_3$ when they escape from the stellar surface, and therefore the observed $\bar{\nu}_{\rm e}$ spectrum is given by

$$\frac{{\rm d}N_{\bar{\nu}_{\rm e}}}{{\rm d}E_{\bar{\nu}_{\rm e}}} = |U_{\rm e3}|^2 \frac{{\rm d}N^0_{\bar{\nu}_{\rm e}}}{{\rm d}E_{\bar{\nu}_{\rm e}}} + (1 - |U_{\rm e3}|^2) \frac{{\rm d}N^0_{\nu_{\rm x}}}{{\rm d}E_{\nu_{\rm x}}} \simeq \frac{{\rm d}N^0_{\nu_{\rm x}}}{{\rm d}E_{\nu_{\rm x}}}. \tag{11}$$

The second equality follows from the fact that the value of $|U_{\rm e3}|^2$ is constrained to be much smaller than unity from reactor experiments [64]. Thus, equation (11) indicates that complete conversion takes place between $\bar{\nu}_{\rm e}$ and $\nu_{\rm x}$. When the value of θ_{13} is large enough to induce adiabatic resonance ($\sin^2 2\theta_{13} \gtrsim 10^{-3}$), the obtained SRN flux and spectrum should be very different from those obtained in sections 3.1 and 3.2. The SRN flux and event rate in this case were calculated with equations (3) and (11), and the results are summarized in tables 5 and 6. The values (with the LL model) shown in this table are consistent with the calculation by [14], in which numerically calculated conversion probabilities were adopted with some specific oscillation parameter sets (which include a model with inverted mass hierarchy and $\sin^2 2\theta_{13} = 0.04$), as well as realistic stellar density profiles; they also included the shock wave propagation and the Earth matter effect in their calculations, but both were found to affect only by a few percent and thus irrelevant.

The total flux becomes (9.4–14) $f_*\,{\rm cm}^{-2}\,{\rm s}^{-1}$, somewhat smaller than the values given in table 2, because the total flux is dominated by the low-energy region. The fluxes at $E_\nu > 19.3$ MeV are enhanced to be (0.30–0.94) $f_*\,{\rm cm}^{-2}\,{\rm s}^{-1}$, but this is still below the current

Table 5. Flux of SRNs in the case of inverted mass hierarchy. Values given in this table are applicable only when the value of θ_{13} is large enough to induce completely adiabatic resonance, i.e., $\sin^2 2\theta_{13} \gtrsim 10^{-3}$. If $\sin^2 2\theta_{13} \lesssim 10^{-5}$, on the other hand, the results become the same as those given in table 2.

	Flux (f_* cm^{-2} s^{-1})		
Model	Total	$E_\nu > 11.3$ MeV	$E_\nu > 19.3$ MeV
LL	9.4	3.1	0.94
TBP	13.8	1.9	0.30
KRJ	12.7	2.2	0.38

Table 6. Event rate of SRNs in the case of inverted mass hierarchy. Values given in this table are applicable only when the value of θ_{13} is large enough to induce completely adiabatic resonance, i.e., $\sin^2 2\theta_{13} \gtrsim 10^{-3}$. If $\sin^2 2\theta_{13} \lesssim 10^{-5}$, on the other hand, the results become the same as those in table 3.

	Event rate [f_* (22.5 kton year)$^{-1}$]	
Model	$E_e > 10$ MeV	$E_e > 18$ MeV
LL	3.8	2.3
TBP	1.6	0.58
KRJ	2.0	0.76

90% CL upper limit of 1.2 cm^{-2} s^{-1} obtained by the SK observation if $f_* = 1$ is adopted. The event rate at the future detectable energy range, $E_\nu > 10$ MeV, is expected to become (1.6–3.8) f_* (22.5 kton year)$^{-1}$, which is considerably larger than the values in the case of normal mass hierarchy, (0.97–2.3) f_* (22.5 kton year)$^{-1}$. The increase (decrease) of the flux and event rate integrated over the high (total) energy region is due to the very high efficiency of the flavour conversion, $\nu_x \to \bar{\nu}_e$, inside the supernova envelope; because the original ν_x are expected to be produced with larger average energy as shown in table 1, the efficient conversion makes the SRN spectrum harder, which enhances the flux and event rate at the high-energy region. Thus, if the inverted mass hierarchy, as well as the large value for θ_{13}, were realized in nature, SRN detection would be rather easier, compared with the other cases. Although we do not repeat the MC simulations that were introduced in section 5.2, the results can be easily inferred; the statistical errors in this case would be $\sim (3.8/2.3)^{1/2} = 1.3$ times smaller than the values given in equation (10), because they are inversely proportional to the square root of the event number.

6.2. Resonant spin–flavour conversion

If neutrinos have non-zero magnetic moment as large as $10^{-12}\mu_B$, where μ_B is the Bohr magneton, it potentially changes a supernova neutrino signal owing to an additional effect of the flavour conversions. In particular, if neutrinos are Majorana particles, the interaction between the Majorana magnetic moment and supernova magnetic fields induces a spin–flavour conversion (e.g., $\bar{\nu}_e \leftrightarrow \nu_{\mu,\tau}$, $\nu_e \leftrightarrow \bar{\nu}_{\mu,\tau}$) resonantly (see [65] and references therein). This mechanism could

potentially give quite a characteristic supernova neutrino signal at detectors, and is also expected to affect the SRN spectrum significantly. However, it is still premature to estimate the SRN flux including the spin–flavour conversions for several reasons. Firstly, the shock wave propagation can change the magnetic field structure as well as the density profile of supernova progenitors, both of which are essential for calculating flavour-conversion probabilities [83]. Because there is no reliable supernova simulation that succeeded in pushing the shock wave outside the core, we are not even at the stage to start the calculation. Furthermore, calculating how the propagating shock wave changes the magnetic field structure would be quite a difficult task. The second reason is that the spin–flavour conversion probabilities strongly depend on the metallicity of progenitor stars [84]. Because SRN is the accumulation of neutrinos from past supernova explosions, it should be quite natural that the poor metal stars give some contribution to the SRN flux. In consequence, it would be difficult to obtain some implication for the neutrino magnetic moment or supernova magnetic fields from the SRN detection at present; instead, a future galactic supernova neutrino burst might give some clues by its time profile or spectrum [65, 85].

6.3. Decaying neutrinos

Non-radiative neutrino decay, which is not satisfactorily constrained, potentially and significantly changes the SRN flux and spectrum. The most stringent lower limit on the neutrino lifetime-to-mass ratio comes from the solar neutrino observations [39]–[41] as well as the meson decay experiments [42]–[44], which is $\tau/m \gtrsim 10^{-4}\,\mathrm{s\,eV^{-1}}$. Since this limit is still very weak, neutrino decay could also change the detected signal from high-energy astrophysical objects [45] or the galactic supernova explosions [46]–[48], and could alter usual discussions on the early universe and structure formation [49] as well as on supernova coolings [50]–[52]. In this subsection, we discuss the potential consequence of the neutrino decay on the SRN flux, with which we can obtain the most stringent limit on the neutrino lifetime in principle, as pointed out by Ando [15].

Since the flux estimation of SRNs including the neutrino decay is somewhat complicated, we rather follow a simple and intuitive argument given in [15]; exact formulation was recently derived by Fogli *et al* [18]. Ando [15] assumed the following conditions: (i) daughter neutrinos are active species; (ii) neutrino mass spectrum is quasi-degenerate ($m_1 \approx m_2 \approx m_3$); and neutrino mass hierarchy is normal. This is because the SRN flux would be most strongly enhanced owing to the decay and it might give a larger flux than the current observational limit by SK [20]; in that case the flux limit can be translated into the limit on the neutrino lifetime. He also restricted his discussion only to the helicity-conserving mode of $\bar{\nu}_3 \to \bar{\nu}_1$ and $\bar{\nu}_2 \to \bar{\nu}_1$ for simplicity, characterized by lifetimes τ_3 and τ_2 of each mode; in models discussed in [86]–[88], the above condition (ii) strongly suppresses the helicity-flip mode. In the actual calculation, instead of these lifetimes, he introduced the 'decay redshift' z_i^{d} ($i = 2, 3$) of the mass eigenstate $\bar{\nu}_i$ as two free parameters. If the source redshift z is larger than the decay redshift z_i^{d}, all the neutrinos $\bar{\nu}_i$ were assumed to decay; on the other hand, if $z < z_i^{\mathrm{d}}$, completely survive. The relation between z_i^{d} and τ_i/m can be written as

$$\tau_i = \frac{mc^2}{E_\nu}\int_{z_i^{\mathrm{d}}}^{0}\frac{\mathrm{d}t}{\mathrm{d}z}\,\mathrm{d}z = \frac{mc^2}{E_\nu H_0}\int_0^{z_i^{\mathrm{d}}}\frac{\mathrm{d}z}{(1+z)\sqrt{\Omega_{\mathrm{m}}(1+z)^3+\Omega_\Lambda}}, \tag{12}$$

where we assume $E_\nu = 10\,\mathrm{MeV}$ as a typical neutrino energy when evaluating the lifetime τ_i from z_i^{d}.

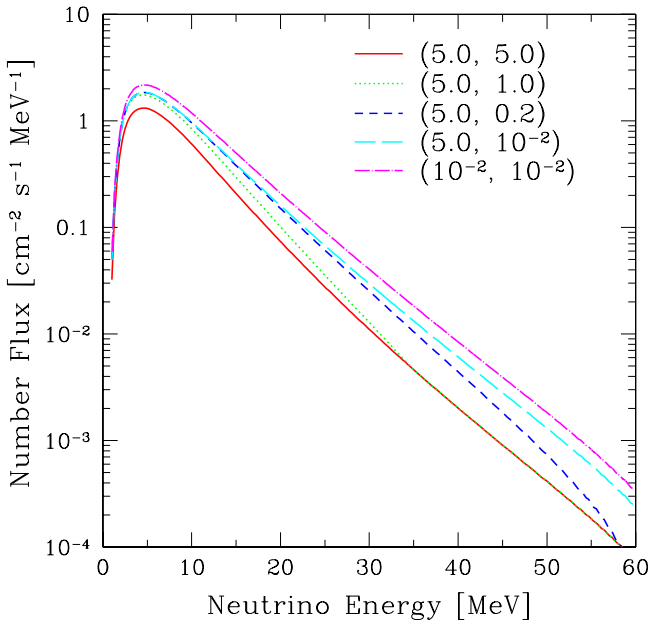

Figure 8. SRN flux for various parameter sets of decay redshifts, calculated with the LL model and $f_* = 1$. Each label represents $(z_2^{\rm d}, z_3^{\rm d})$. This figure is taken from [15].

Figure 8 shows the SRN flux for various parameter sets of decay redshifts $(z_2^{\rm d}, z_3^{\rm d})$ as a function of neutrino energy; the LL model as the original neutrino spectrum and $f_* = 1$ were assumed. The solid curve in figure 8 shows the SRN flux for $z_2^{\rm d} = z_3^{\rm d} = z_{\rm max}(=5)$, which represents the same flux as that without the neutrino decay. Then, the decay of the heaviest mass eigenstate $\bar{\nu}_3$ was included by reducing the value of $z_3^{\rm d}$, but keeping $\bar{\nu}_2$ stable. When $z_3^{\rm d} = 1.0$ (dotted curve), the SRN flux at the low-energy region ($E_\nu \lesssim 35\,{\rm MeV}$) deviates from the no-decay model. This is because the neutrinos from supernovae at redshift larger than $z_3^{\rm d} = 1.0$ are affected by the $\bar{\nu}_3 \to \bar{\nu}_1$ decay and it results in the increase of $\bar{\nu}_{\rm e}$. Since the neutrino energies are redshifted by a factor of $(1+z)^{-1}$ owing to an expansion of the universe, the decay effect can be seen at low energy alone. When the value of $z_3^{\rm d}$ is reduced to 10^{-2}, the neutrinos even from the nearby sources are influenced by the $\bar{\nu}_3 \to \bar{\nu}_1$ decay, resulting in a deviation over the entire energy range as shown by the long-dashed curve in figure 8. If the $\bar{\nu}_2 \to \bar{\nu}_1$ decay is added, it further enhances the SRN flux. In table 7, the SRN flux integrated over the energy range of $E_\nu > 19.3\,{\rm MeV}$ is summarized, for the each decay models. In the second column, the lifetime-to-mass ratio is indicated, which corresponds to each decay redshift, which is obtained using equation (12). The ratio between the predicted flux and the 90% CL upper limit given by the SK observation [20] is also shown in the fourth column. This result shows that several decaying models may have already been excluded or severely constrained by the current SRN limit by SK. It also proves that the SRN observation can potentially give us a lower limit on the neutrino lifetime as strong as $\sim 10^{10}\,{\rm s\,eV^{-1}}$, which is many orders of magnitude stronger than that by the solar neutrino observations. In addition, future detectors such as the HK and UNO (may be loaded with Gd) is expected to greatly improve our knowledge of the SRN spectral shape as well as its flux; if a number of data were actually acquired by such detectors, the most general and model-independent discussions concerning the neutrino decay would become accessible.

Table 7. Predicted SRN flux for various decay models. The LL model is assumed as the original neutrino spectrum and the integrated energy range is $E_\nu > 19.3$ MeV. The ratio of the prediction and the limit is shown in the fourth column.

Model $(z_2^{\rm d}, z_3^{\rm d})$	$\tau_2/m, \tau_3/m$ (s eV^{-1})	Predicted flux (f_* cm^{-2} s^{-1})	Prediction/limit
(5.0, 5.0)	$3.9 \times 10^{10}, 3.9 \times 10^{10}$	0.43	$0.35 f_*$
(5.0, 1.0)	$3.9 \times 10^{10}, 2.4 \times 10^{10}$	0.55	$0.42 f_*$
(5.0, 0.2)	$3.9 \times 10^{10}, 7.7 \times 10^{9}$	0.93	$0.75 f_*$
$(5.0, 10^{-2})$	$3.9 \times 10^{10}, 4.4 \times 10^{8}$	1.0	$0.88 f_*$
$(10^{-2}, 10^{-2})$	$4.4 \times 10^{8}, 4.4 \times 10^{8}$	1.4	$1.2 f_*$

7. Conclusions

As stressed several times in this paper, we are in an exciting era of the SRN observation. This is because the current SK upper limit [20] is *just above* several theoretical predictions using realistic models for the cosmic SFR and supernova neutrino spectrum, and also because of the promising technique proposed in [21] could greatly improve performance of the presently working or planned future detectors, especially for detecting SRNs. Having arrived at such a situation, we believe that it is time to review recent progress of theoretical and observational researches concerning SRNs from various points of view. Many physical and astronomical consequences can be derived from the constraints on the SRNs as we have reviewed throughout this paper.

The basics of SRN calculation were given in sections 2 and 3. Models involved in the SRN calculations are those of the cosmic SFR and original supernova neutrino spectrum. Although, the SFR-z relation has been intensively studied in recent years, there remains a fair amount of uncertainty; in fact, the best estimate of the local SFR density ranges fairly widely as $(0.5\text{–}2.9) \times 10^{-2} h_{70}$ year^{-1} Mpc^{-3} [54]. In order to take this uncertainty into account, we have introduced the correction factor f_* in equation (4), for which a wide range (0.7–4.2) is still allowed from the SFR observation. As for the original supernova spectrum, contrary to the traditional approach using the Fermi–Dirac distribution, we followed the approach taken by our group [12, 17], i.e., adopting the results of numerical simulations. In particular, following [17], we used three neutrino spectra by different groups, i.e., LL [57], TBP [58] and KRJ [59], and performed comparison among models. Recent progress in neutrino experiments has proven that neutrinos are massive and mix among different flavours. This effect was also taken into account appropriately. As a result, it was found that the uncertainty concerning the original neutrino spectrum gives difference in the resulting SRN flux by at least a factor of 2–4. The expected event rate at a water Čerenkov detector with a fiducial volume of 22.5 kton was found to be $0.25\text{–}1\, f_*$ year^{-1} (for $E_{\rm e} > 19.3$ MeV) and $1\text{–}2\, f_*$ year^{-1} (for $E_{\rm e} > 10$ MeV), depending on these supernova models (see table 3).

Besides the flux estimation, a careful discussion about background events is definitely necessary in order to investigate the detectability. This has been thoroughly argued in [12] and we followed them in section 4. The most serious background comes from decay products of invisible muons, which are produced almost at rest inside the detector and that is why 'invisible.' Because of the background, the detection is severely restricted; for a pure-water Čerenkov detector with

the size of SK, it would take about (may be more than) 10 years in order to reach a signal-to-noise ratio with a small value (see figure 5). We also discussed the performance of other detectors such as SNO and KamLAND in the same section, by mainly following [12, 16]. The current observational upper limit by SK [20] and the proposed technique that potentially improves the performance of water Čerenkov detectors [21] were briefly introduced there. In addition, we showed that the SK limit on the SRN flux can be fairly well reproduced by a simple statistical argument using equation (8).

Section 5 was devoted to the discussion on the current status and future prospects for obtaining limits on the cosmic SFR from the SRN observations. We first showed that the current SRN limit from SK [20] already sets a stringent limit on the local SFR value, as discussed in [13]. Surprisingly, it might rule out a part of local SFR value allowed by the current observations using the light as shown in table 4. Performance of future detectors loaded with Gd as proposed in [21] was investigated in detail using the MC simulation, following the discussion in [17]. The distribution of the best-fit values of two parameters concerning SFR (9) was obtained by the generated 10^3 MC data and by accompanying likelihood analyses. If one of the two free parameters was fixed somehow in advance using other observations, then the SRN observation can constrain the remaining parameter by accuracy of $\sim 0.3\,(f_* V_{\rm eff}/22.5\,{\rm kton}\cdot 5\,{\rm year})^{-1/2}$; this number would soon become quite significant if the future mega-ton class detectors such as HK or UNO loaded with Gd started data-taking.

Finally, in section 6, SRN constraints on particle physics models of neutrinos were discussed. Neutrino oscillations in the case of inverted mass hierarchy [14], resonant spin–flavour conversions induced by the neutrino magnetic moment (see [65] and references therein) and neutrino decay [15, 18] are expected to considerably change the SRN signal at the detectors. In particular, for the neutrino decay model, the SRN observation potentially gives the most stringent constraint on the neutrino lifetime, compared with a galactic supernova [46]–[48], high-energy astrophysical objects [45] as well as the most reliable (but weak) limit at present by the solar neutrino observations [39]–[41].

Acknowledgments

SA was supported by a Grant-in-Aid for JSPS Fellows and KS was partially supported by a Grant-in-Aid for Scientific Research provided by the Ministry of Education, Culture, Sports, Science and Technology of Japan through Research Grant No. S14102004 and a Grant-in-Aid for Scientific Research on priority Areas No. 14079202.

References

[1] Bisnovatyi-Kogan G S and Seidov S F 1984 *Ann. N.Y. Acad. Sci.* **422** 319
[2] Krauss L M, Glashow S L and Schramm D N 1984 *Nature* **310** 191
[3] Woosley S E, Wilson J R and Mayle R 1986 *Astrophys. J.* **302** 19
[4] Hirata K S 1991 *PhD Thesis* University of Tokyo
[5] Totsuka Y 1992 *Rep. Prog. Phys.* **55** 377
[6] Suzuki H 1994 *Physics and Astrophysics of Neutrinos* ed M Fukugita and A Suzuki (Tokyo: Springer) p 764
[7] Totani T and Sato K 1995 *Astropart. Phys.* **3** 367
[8] Totani T, Sato K and Yoshii Y 1996 *Astrophys. J.* **460** 303
[9] Malaney R A 1997 *Astropart. Phys.* **7** 125

[10] Hartmann D H and Woosley S E 1997 *Astropart. Phys.* **7** 137
[11] Kaplinghat M, Steigman G and Walker T P 2000 *Phys. Rev.* D **62** 043001
[12] Ando S, Sato K and Totani T 2003 *Astropart. Phys.* **18** 307
[13] Fukugita M and Kawasaki M 2003 *Mon. Not. R. Astron. Soc.* **340** L7
[14] Ando S and Sato K 2003 *Phys. Lett.* B **559** 113
[15] Ando S 2003 *Phys. Lett.* B **570** 11
[16] Strigari L E, Kaplinghat M, Steigman G and Walker T P 2004 *J. Cosmol. Astropart. Phys.* JCAP03(2004)007
[17] Ando S 2004 *Astrophys. J.* **607** 20
[18] Fogli G L, Lisi E, Mirizzi A and Montanino D 2004 *Phys. Rev.* D **70** 013001
[19] Cocco A G, Ereditato A, Fiorillo G, Mangano G and Pettorino V 2004 *Preprint* hep-ph/0408031
[20] Malek M *et al* 2003 *Phys. Rev. Lett.* **90** 061101
[21] Beacom J F and Vagins M R 2004 *Phys. Rev. Lett.* **93** 171101
[22] Lilly S, Fèvre O L, Hammer F and Crampton D 1996 *Astrophys. J.* **460** L1
[23] Madau P, Ferguson H C, Dickinson M E, Giavalisco M, Steidel C C and Fruchter A 1996 *Mon. Not. R. Astron. Soc.* **283** 1388
[24] Cowie L, Songaila A, Hu E and Cohen J 1996 *Astron. J.* **112** 839
[25] Connolly A, Szalay A, Dickinson M, Rao M S and Brunner R 1997 *Astrophys. J.* **486** L11
[26] Sawicki M J, Lin H and Yee H K C 1997 *Astron. J.* **113** 1
[27] Treyer M, Ellis R, Milliard B, Donas J and Bridges T 1998 *Mon. Not. R. Astron. Soc.* **300** 303
[28] Madau P, Pozzetti L and Dickinson M 1998 *Astrophys. J.* **498** 106
[29] Pascarelle S M, Lanzetta K M and Fernandez-Soto A 1998 *Astrophys. J.* **508** L1
[30] Steidel C C, Adelberger K L, Giavalisco M, Dickinson M and Pettini M 1999 *Astrophys. J.* **519** 1
[31] Hughes D H *et al* 1998 *Nature* **394** 241
[32] Flores H *et al* 1999 *Astrophys. J.* **517** 148
[33] Gallego J, Zamorano J, Aragón-Salamanca A and Rego M 1995 *Astrophys. J.* **455** L1
[34] Gronwall C 1998 *Proc. 33rd Rencontres de Moriond, Dwarf Galaxies and Cosmology* ed T Thuan *et al* (Gif-sur-Yvette: Editions Frontiéres) p 41
[35] Tresse L and Maddox S 1998 *Astrophys. J.* **495** 691
[36] Glazebrook K, Blake C, Economou F, Lilly S and Colless M 1999 *Mon. Not. R. Astron. Soc.* **306** 843
[37] Somerville R S, Primack J R and Faber S M 2001 *Mon. Not. R. Astron. Soc.* **320** 504
[38] Glazebrook K *et al* 2003 *Astrophys. J.* **587** 55
[39] Beacom J F and Bell N F 2002 *Phys. Rev.* D **65** 113009
[40] Bandyopadhyay A, Choubey S and Goswami S 2003 *Phys. Lett.* B **555** 33
[41] Eguchi K *et al* 2003 *Phys. Rev. Lett.* **92** 071301
[42] Barger V D, Keung W Y and Pakvasa S 1982 *Phys. Rev.* D **25** 907
[43] Picciotto C E *et al* 1988 *Phys. Rev.* D **37** 1131
[44] Britton D I *et al* 1994 *Phys. Rev.* D **49** 28
[45] Beacom J F, Bell N F, Hooper D, Pakvasa S and Weiler T J 2003 *Phys. Rev. Lett.* **90** 181301
[46] Frieman J A, Haber H E and Freese K 1988 *Phys. Lett.* B **200** 115
[47] Raghavan R S, He X G and Pakvasa S 1988 *Phys. Rev.* D **38** 1317
[48] Ando S 2004 *Phys. Rev.* D **70** 033004
[49] Beacom J F, Bell N F and Dodelson S 2004 *Phys. Rev. Lett.* **93** 121302
[50] Fuller G M, Mayle R and Wilson J R 1988 *Astrophys. J.* **332** 826
[51] Kachelriess M, Tomàs R and Valle J W F 2000 *Phys. Rev.* D **62** 023004
[52] Farzan Y 2003 *Phys. Rev.* D **67** 073015
[53] Porciani C and Madau P 2001 *Astrophys. J.* **548** 522
[54] Baldry I K and Glazebrook K 2003 *Astrophys. J.* **593** 258
[55] Scalo J 1998 *Proc. 38th Herstmonceux Conf. (ASP Conf. Ser.* Vol. 142: *The Stellar Initial Mass Function)* p 201
[56] Madau P, della Valle M and Panagia N 1998 *Mon. Not. R. Astron. Soc.* **297** 17

[57] Totani T, Sato K, Dalhed H E and Wilson J R 1998 *Astrophys. J.* **496** 216
[58] Thompson T A, Burrows A and Pinto P 2003 *Astrophys. J.* **592** 434
[59] Keil M T, Raffelt G G and Janka H T 2003 *Astrophys. J.* **590** 971
[60] Fukuda S *et al* 2002 *Phys. Lett.* B **539** 179
[61] Ahmed S N *et al* 2004 *Phys. Rev. Lett.* **92** 181301
[62] Fukuda Y *et al* 1999 *Phys. Rev. Lett.* **82** 2644
[63] Eguchi K *et al* 2003 *Phys. Rev. Lett.* **90** 021802
[64] Apollonio M *et al* 1999 *Phys. Lett.* B **466** 415
[65] Ando S and Sato K 2003 *J. Cosmol. Astropart. Phys.* JCAP10(2003)001
[66] Gaisser T K, Stanev T and Barr G 1988 *Phys. Rev.* D **38** 85
[67] Barr G, Gaisser T K and Stanev T 1989 *Phys. Rev.* D **39** 3532
[68] Vogel P and Beacom J F 1999 *Phys. Rev.* D **60** 053003
[69] Strumia A and Vissani F 2003 *Phys. Lett.* B **564** 42
[70] Kajita T and Totsuka Y 2001 *Rev. Mod. Phys.* **73** 85
[71] Lipari P, Stanev T and Gaisser T K 1998 *Phys. Rev.* D **58** 073003
[72] Agrawal V, Gaisser T K, Lipari P and Stanev T 1996 *Phys. Rev.* D **53** 1314
[73] Honda M, Kajita T, Kasahara K and Midorikawa S 1995 *Phys. Rev.* D **52** 4985
[74] Barr G D, Gaisser T K, Lipari P, Robbins S and Stanev T 2004 *Phys. Rev.* D **70** 023006
[75] Honda M, Kajita T, Kasahara K and Midorikawa S 2004 *Phys. Rev.* D **70** 043008
[76] Bahcall J N 1989 *Neutrino Astrophysics* (Cambridge: Cambridge University Press)
[77] Bemporad C, Gratta G and Vogel P 2002 *Rev. Mod. Phys.* **74** 297
[78] Schreckenbach K *et al* 1985 *Phys. Lett.* B **160** 325
[79] Hahn A A *et al* 1989 *Phys. Lett.* B **218** 365
[80] Vogel P and Engel J 1989 *Phys. Rev.* D **39** 3378
[81] Hargrove C K, Blevis I, Paterson D and Earle E D 1995 *Nucl. Instrum. Methods.* A **357** 157
[82] Dighe A S and Smirnov A Yu 2000 *Phys. Rev.* D **62** 033007
[83] Ando S and Sato K 2003 *Phys. Rev.* D **67** 023004
[84] Ando S and Sato K 2003 *Phys. Rev.* D **68** 023003
[85] Akhmedov E Kh and Fukuyama T 2003 *J. Cosmol. Astropart. Phys.* JCAP12(2003)007
[86] Kim C W and Lam W P 1990 *Mod. Phys. Lett.* A **5** 297
[87] Berezhiani Z G, Fiorentini G, Moretti M and Rossi A 1992 *Z. Phys.* C **54** 581
[88] Giunti C, Kim C W, Lee U W and Lam W P 1992 *Phys. Rev.* D **45** 1557

New Journal of Physics
The open-access journal for physics

Atmospheric neutrinos

Takaaki Kajita
Research Center for Cosmic Neutrinos, Institute for Cosmic Ray Research, University of Tokyo, Kashiwa-no-ha 5-1-5, Kashiwa, Chiba 277-8582, Japan
E-mail: kajita@icrr.u-tokyo.ac.jp

New Journal of Physics **6** (2004) 194
Received 23 August 2004
Published 10 December 2004
Online at http://www.njp.org/
doi:10.1088/1367-2630/6/1/194

Abstract. Neutrino oscillation was discovered through the study of atmospheric neutrinos. Atmospheric neutrinos are produced as decay products in hadronic showers resulting from collisions of cosmic rays with nuclei in the atmosphere. Electron neutrinos and muon neutrinos are produced mainly by the decay chain of charged pions to muons and electrons. Depending on the energy of the neutrinos, atmospheric neutrinos are observed as fully contained events, partially contained events and upward-going muon events. The energy range covered by these events is from a few hundred MeV to >1 TeV. Data from various experiments showed zenith angle- and energy-dependent deficit of ν_μ events, while ν_e events did not show any such effect. It was also shown that the ν_μ survival probability obeys the sinusoidal function as predicted by neutrino oscillations. Two-flavour $\nu_\mu \leftrightarrow \nu_\tau$ oscillations, with $\sin^2 2\theta > 0.90$ and Δm^2 in the region of 1.9×10^{-3} to 3.0×10^{-3} eV^2, explain all these data. Various detailed studies using high statistics atmospheric neutrino data excluded the alternative hypotheses that were proposed to explain the ν_μ deficit.

1367-2630/04/010194+34$30.00
PII: S1367-2630(04)85325-4
© IOP Publishing Ltd and Deutsche Physikalische Gesellschaft

Contents

1. Introduction **2**
2. Atmospheric neutrino flux **6**
3. Neutrino interactions **9**
4. Atmospheric neutrino experiments **9**
4.1. Water Cherenkov detectors . . . 10
4.2. Fine-grained tracking detectors . . . 12
5. Observation of atmospheric neutrinos **13**
5.1. Selection of atmospheric neutrino events . . . 13
5.2. General features . . . 15
5.3. μ/e ratio . . . 16
5.4. Zenith angle distribution . . . 18
5.5. Two-flavour neutrino oscillation analysis . . . 21
5.6. L/E analysis . . . 21
5.7. Three-flavour neutrino oscillation analysis . . . 23
5.8. Search for CC ν_τ events . . . 25
5.9. Constraints on $\nu_\mu \leftrightarrow \nu_{\text{sterile}}$ oscillations . . . 26
5.10. Other interpretations . . . 29
6. Prospects of future atmospheric neutrino experiments **29**
6.1. Measurement of $\sin^2 2\theta_{23}$ and Δm^2_{23} . . . 30
6.2. θ_{13} . . . 31
6.3. Sign of Δm^2 . . . 31
6.4. Effects of the solar oscillation terms . . . 31
7. Summary **31**
Acknowledgments **32**
References **32**

1. Introduction

Studies of the neutrino have played essential roles in the understanding of elementary particle physics. In the standard model of elementary particle physics, neutrinos have been assumed to have zero mass. It has been recognized that the small but finite neutrino masses can be understood naturally by the see-saw mechanism [1, 2] by introducing super-heavy neutral particles. The neutrino mass inferred from atmospheric and other experiments suggests that the mass of the super-heavy neutral particle could be close to the energy scale of the Grand Unification [3, 4]. Therefore, it is widely understood that an experimental study of neutrino masses and mixing angles is one of the few ways to explore physics beyond the standard model, especially physics at the Grand Unification scale.

One of the most sensitive methods to observe small neutrino masses is to study neutrino flavour oscillations [5, 6]. If neutrinos have a finite mass, each flavour eigenstate (for example, ν_μ) can be expressed by a combination of mass eigenstates (ν_1, ν_2 and ν_3). The relation between the

mass eigenstates (ν_1, ν_2, ν_3) and the flavour eigenstates (ν_e, ν_μ, ν_τ) can be expressed by

$$\begin{pmatrix} \nu_e \\ \nu_\mu \\ \nu_\tau \end{pmatrix} = U \begin{pmatrix} \nu_1 \\ \nu_2 \\ \nu_3 \end{pmatrix}, \tag{1}$$

where U is the mixing matrix. This matrix is often called the MNSP (or MNS, or PMNS) matrix taking the initials of the authors who discussed neutrino oscillations for the first time [5, 6]. For simplicity, let us discuss two-flavour neutrino oscillations. The probability for a neutrino produced in a flavour state ν_α to be observed in a flavour state ν_β after travelling a distance L through the vacuum is:

$$P(\nu_\alpha \to \nu_\beta) = \sin^2 2\theta \sin^2 \left(\frac{1.27 \Delta m^2(\mathrm{eV}^2) L(\mathrm{km})}{E_\nu(\mathrm{GeV})} \right), \tag{2}$$

where E_ν is the neutrino energy, θ is the mixing angle between the flavour eigenstates and mass eigenstates and Δm^2 is the mass-squared difference of the neutrino mass eigenstates.

The above description has to be generalized to three-flavour oscillations. In the three-flavour oscillation framework, neutrino oscillations are parametrized by three mixing angles (θ_{12}, θ_{23} and θ_{13}), three mass-squared differences (Δm^2_{12}, Δm^2_{23} and Δm^2_{13}; of the three Δm^2's, only two are independent) and one CP phase (δ). In this case, the mixing matrix U is expressed by

$$U = \begin{pmatrix} c_{12}c_{13} & s_{12}c_{13} & s_{13}\mathrm{e}^{-\mathrm{i}\delta} \\ -s_{12}c_{23} - c_{12}s_{23}s_{13}\mathrm{e}^{\mathrm{i}\delta} & c_{12}c_{23} - s_{12}s_{23}s_{13}\mathrm{e}^{\mathrm{i}\delta} & s_{23}c_{13} \\ s_{12}s_{23} - c_{12}c_{23}s_{13}\mathrm{e}^{\mathrm{i}\delta} & -c_{12}s_{23} - s_{12}c_{23}s_{13}\mathrm{e}^{\mathrm{i}\delta} & c_{23}c_{13} \end{pmatrix}, \tag{3}$$

where c_{ij} and s_{ij} represent $\cos\theta_{ij}$ and $\sin\theta_{ij}$, respectively. See, e.g., [7] for more detailed discussions on the neutrino mixing.

If a neutrino mass hierarchy is assumed, the three Δm^2's are approximated by two Δm^2's, and neutrino oscillation lengths are significantly different for the two Δm^2's. One $\Delta m^2 (\Delta m^2_{12})$ is related to solar neutrino experiments and the KamLAND reactor experiment. The other Δm^2 (Δm^2_{23} or Δm^2_{13}) is related to atmospheric, reactor and long-baseline neutrino oscillation experiments. It is known that it is approximately correct to assume two-flavour oscillations for analyses of the present neutrino oscillation data. Therefore, in this paper, we mostly discuss two-flavour neutrino oscillations assuming two significantly different Δm^2's.

Atmospheric neutrinos arise from the decay of secondaries (π, K and μ) produced by primary cosmic ray interactions in the atmosphere. These neutrinos can be detected by underground neutrino detectors. Interactions of low-energy neutrinos, around 1 GeV, have all of the final state particles 'fully contained (FC)' in the detector. Higher energy charged current ν_μ interactions may result in the muon exiting the detector; these are referred to as 'partially contained (PC)'. In order to reject the background from cosmic ray particles, as well as to cleanly reconstruct the details of the event, the vertex position of the interaction is typically defined to be within some fiducial volume. In addition, some of the detectors are equipped with outer detectors (also referred to as veto- or anti-detectors) to easily identify penetrating particles.

There is a third category of charged current ν_μ events, where the interaction occurs outside the detector, and the muon enters and either passes through the detector or stops in the detector.

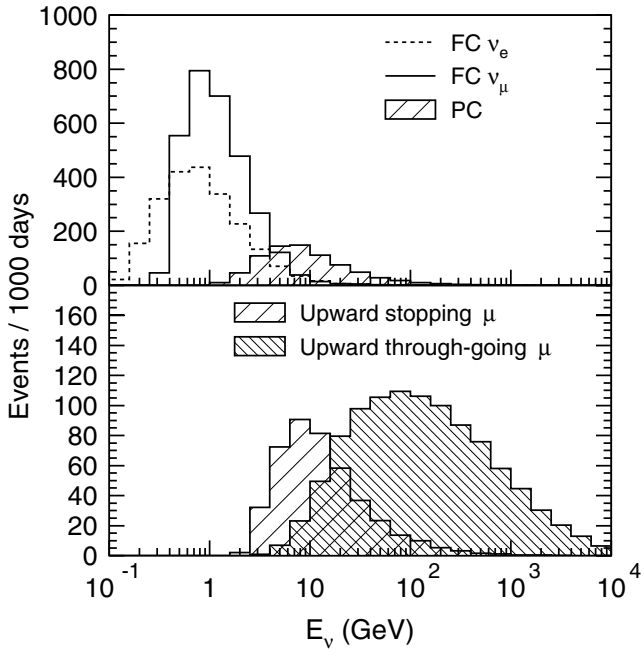

Figure 1. The parent neutrino energy distributions for several different classifications of atmospheric neutrino events. These distributions are for the Super-Kamiokande analysis; for other detectors they will be similar but different depending on detector size, which controls the maximum energy of a fully contained event and the minimum energy of a through-going muon.

These are referred to as 'upward-going muons' because one generally requires that they originate from below the horizon to ensure that a sufficient amount of rock absorbs ordinary cosmic ray muons. Each of the fully contained partially contained and upward-going muon event samples has a certain range of parent neutrino energies. As an example, figure 1 shows the distribution of parent neutrino energies for each category of event samples for the Super-Kamiokande analysis. The energies of atmospheric neutrinos observed in underground detectors range from about 100 MeV to >1 TeV.

Atmospheric neutrino experiments started in the 1960s. One experiment was carried out in the Kolar Gold Field in India [8]. Other experiments were carried out at the East Rand Proprietary Mine in South Africa [9, 10]. In all these experiments, neutrino events occurring in the rock surrounding a neutrino detector were measured. Since the experiments were carried out in extremely deep underground (about 8000 metres water equivalent (m.w.e.)), the charged particles traversing the detectors almost horizontally were essentially of atmospheric neutrino origin. Also, since it was required that the particle should penetrate through the rock and the detector, most of these neutrinos were expected to be charged current (CC) ν_μ events.

In the early 1980s, the first massive underground detectors (of the order of 1 kt) were constructed, primarily to search for proton decay with a lifetime of less than 10^{32} years, as predicted by early Grand Unified Theories [3, 4]. The most serious background for proton decay searches is atmospheric neutrino events, at a rate of approximately 10^2 events year^{-1} kt^{-1}.

Therefore, these experiments studied details of the observed atmospheric neutrino events [11, 12].

Current interest in the atmospheric neutrinos was initiated by the study of the ν_μ/ν_e flux ratio in the late 1980s [13]. The Kamiokande water Cherenkov experiment measured the number of e-like and μ-like events, which were mostly CC ν_e and ν_μ interactions, respectively. They found that the number of μ-like events had a significant deficit compared with the Monte Carlo prediction, while the number of e-like events had, in good agreement with the prediction [13]. The flavour ratio of the atmospheric neutrino flux, $(\nu_\mu + \bar{\nu}_\mu)/(\nu_e + \bar{\nu}_e)$, has been calculated to an accuracy of better than 5% in the relevant energy range. Because of the small $(\mu/\mathrm{e})_{\mathrm{Data}}/(\mu/\mathrm{e})_{\mathrm{Prediction}}$ ratio, it was concluded: 'We are unable to explain the data as the result of the systematic detector effects or uncertainties in the atmospheric neutrino fluxes. Some as-yet-accounted-for physics such as neutrino oscillations might explain the data'. This result triggered the interest in atmospheric neutrinos.[1] Consistent results were reported in the early 1990s from the IMB water Cherenkov experiment [14]. On the other hand, fine-grained iron calorimeter experiments, NUSEX [15] and Ferjus [16, 17], did not observe any significant ν_μ deficit within their statistics. Therefore, the situation was unclear in the early 1990s.

Another important hint towards the understanding of atmospheric neutrino phenomena was given in the mid-1990s [18]. Zenith angle distributions for multi-GeV fully-contained events and partially contained events were studied in Kamiokande. For detectors near the surface of the Earth, the neutrino flight distance, and thus the neutrino oscillation probability, is a function of the zenith angle of the neutrino direction. Vertically downward-going neutrinos travel about 15 km while vertically upward-going neutrinos travel about 13 000 km before interacting in the detector. The Kamiokande data showed that the deficit of μ-like events depended on the neutrino zenith angle. However, due to the relatively poor event statistics, the statistical significance of the up–down asymmetry in the Kamiokande data was 2.9 standard deviations and, therefore, the data were not conclusive. In 1998, the Super-Kamiokande experiment, with substantially larger data statistics than those in the previous experiments, concluded that the atmospheric neutrino data gave evidence for neutrinos oscillations [19]. Various detailed studies of neutrino oscillations have been made using atmospheric neutrino data. The atmospheric neutrino experiments are still contributing substantially to our understanding of neutrino masses and mixing angles.

In the following sections, details of the atmospheric neutrino observations are described. Section 2 describes the calculation of atmospheric neutrino fluxes. Section 3 outlines the simulation of neutrino interactions relevant to the energy range of atmospheric neutrinos. Sections 4 and 5 describe the details of the atmospheric neutrino data and the neutrino oscillation analyses. Then, in section 6, future prospects of the atmospheric neutrino experiments are briefly described. Section 7 summarizes the paper. In most of this paper, when mention is made of neutrinos, we imply both neutrinos and anti-neutrinos.

[1] We, however, note that a deficit of ν_μ events was already observed in the late 1970s [10]. The observed ν_μ flux in the South Africa experiment was only about 60% of that expected. This result is approximately consistent with data from the present experiments. However, due to the uncertainty in the predicted flux, no strong conclusion was made. Also, in 1986, IMB noticed that the observed fraction of events with electrons from muon decay was smaller than expected [11]. This can be explained by the deficit of CC ν_μ events. However, detailed study of the cause for the deficit was not made. A similar, but statistically less significant, effect was observed in Kamiokande (figure 19 of [12]) as well.

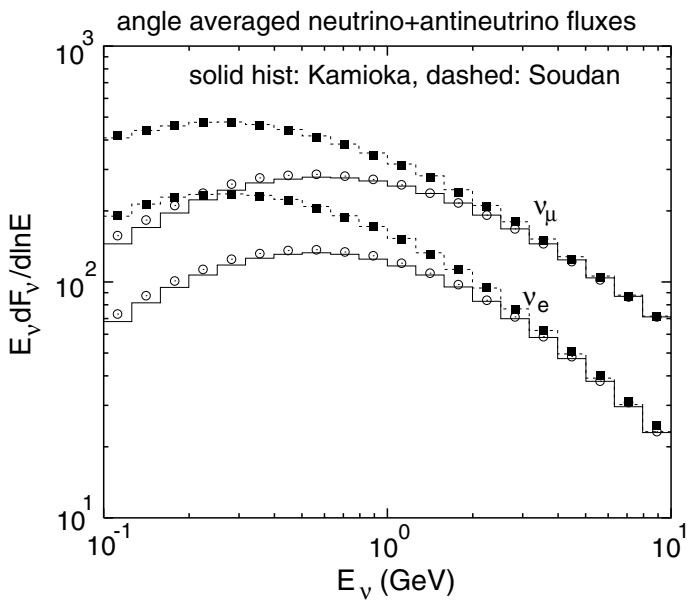

Figure 2. (a) The atmospheric neutrino energy spectrum calculated for the Kamioka and Soudan-2 sites [21]. The $(\nu_\mu + \overline{\nu}_\mu)$ and $(\nu_e + \overline{\nu}_e)$ fluxes are plotted for the three-dimensional (⊙) and one-dimensional (■) calculations. ——, histograms for Kamioka site and - - - -, histograms for the Soudan-2 site.

2. Atmospheric neutrino flux

To carry out detailed studies of neutrino oscillations using atmospheric neutrinos, it is important to know the expected flux in the absence of neutrino oscillations. The difficulties and uncertainties in the calculation of atmospheric neutrino fluxes differ between high and low energies. For low-energy neutrinos with energies of about 1 GeV, the primary fluxes of cosmic ray components are relatively well known. On the other hand, the low-energy cosmic ray fluxes of $\lesssim$10 GeV are modulated by solar activity, and affected by the geomagnetic field through a rigidity (momentum/charge) cutoff. The cutoff is lower near the poles and, therefore, the low energy flux is higher for detector locations near the poles than for those near the equator. For high-energy neutrinos with energies $\gtrsim$100 GeV, primary cosmic rays with energies >1000 GeV are relevant. At these energies, solar activity and the rigidity cutoff do not affect the cosmic rays, but details of the higher energy primary cosmic ray flux are not as well measured.

We outline the methods and results of the three most detailed atmospheric neutrino flux calculations [20]–[22]. More detailed description of the flux calculation can be found in [23]. Unlike older calculations [24, 25] in which the secondary particles were assumed to travel in the direction of the primary cosmic ray (one-dimensional calculations), in these calculations three-dimensional Monte Carlo methods were used. Also, primary cosmic ray flux data were used; solar modulation and geomagnetic field effects were taken into account; and the interaction of cosmic ray particles with the air nucleus, the propagation of the secondary particles in the air and the decay of them are simulated.

The calculated energy spectra of atmospheric neutrinos, by the one- and three-dimensional methods, at Kamioka (Japan) and the Soudan mine (USA) are shown in figure 2. The accuracy

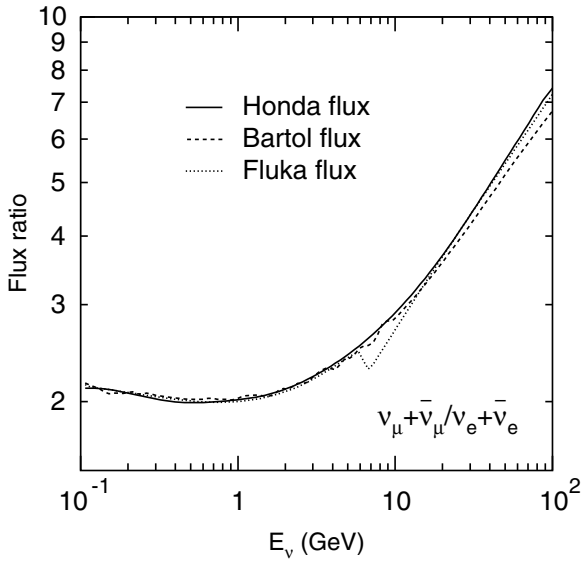

Figure 3. The flux ratio of $\nu_\mu + \overline{\nu}_\mu$ to $\nu_e + \overline{\nu}_e$ versus neutrino energy. Solid, broken and dotted lines show predictions of [20], [21] and [22], respectively.

in recent primary cosmic ray flux measurements [26, 27] below 100 GeV is about 5% and the data from independent experiments agree within the quoted uncertainties. However, the primary cosmic ray data are much less accurate above 100 GeV. Therefore, for neutrino energies $\lesssim$10 GeV, the calculated absolute flux should have a small uncertainty of about 10%. Indeed, calculated fluxes by [20], [21] and [22] agree within 10%. However, at much higher than 10 GeV, the uncertainties in the absolute neutrino flux must be substantially larger.

Figure 3 shows the calculated flux ratio of $\nu_\mu + \overline{\nu}_\mu$ to $\nu_e + \overline{\nu}_e$ as a function of the neutrino energy, integrated over solid angle. This ratio is essentially independent of the primary cosmic ray spectrum. The calculated flux ratio has a value of about 2 for energies less than a few GeV and increases with increase in neutrino energy. This is because a π-decay produces a ν_μ and a μ; the μ, when it decays, produces another ν_μ and a ν_e. Furthermore, three neutrinos produced in the chain decay of a π have approximately the same average energy. In the higher energy regions, the probability of a muon not to decay before reaching the ground increases with increase in muon energy. In the energy region of less than $\sim$10 GeV, most of the neutrinos are produced by the decay chain of pions and the expected uncertainty of this ratio is about 3%. In the higher energy region (>10 GeV), the contribution of K decay to the neutrino production is more important. There, the ratio depends more on the K production cross sections and the uncertainty of the ratio is expected to be larger.

Figure 4 shows the zenith angle dependence of the atmospheric neutrino fluxes for several neutrino energies and for two locations. At low energies and at the Kamioka location, the fluxes of downward-going neutrinos are lower than those of upward-going neutrinos. This is due to the cutoff of primary cosmic rays by the geomagnetic field. On the other hand, in North America, the fluxes of the downward-going neutrinos are higher than those of the upward-going neutrinos due to the very low rigidity cutoff. For neutrino energies higher than a few GeV, the calculated fluxes are essentially up–down symmetric, because the primary particles are more energetic than the rigidity cutoff. The enhancement of the flux near the horizon for low-energy neutrinos is a

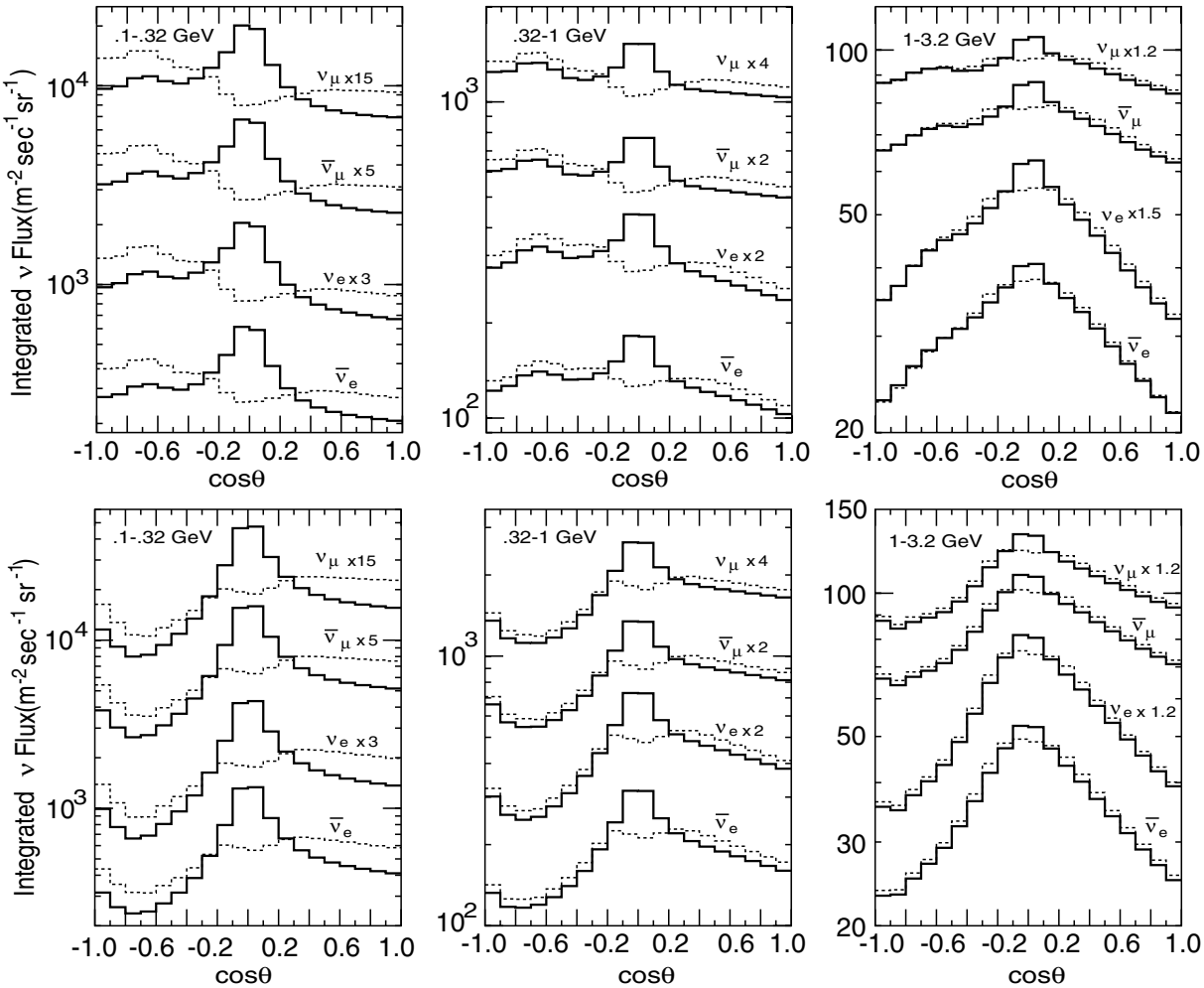

Figure 4. The flux of atmospheric neutrinos versus zenith angle for three neutrino energy ranges. Solid and broken lines show the prediction by three-dimensional and one-dimensional calculations [20], respectively. The upper panels are for the Kamioka site and the lower panels are for the North America sites (SNO and Soudan-2).

feature characteristic of full three-dimensional flux calculations, first reported in [22, 28] and confirmed by other calculations [20, 21]. The mechanism for the enhancement is discussed in [29]. The three-dimensional effect is only important below ∼1 GeV as seen in figure 4. However, the horizontal enhancement cannot be seen in the lepton zenith angle distribution, due to the relatively poor angular correlation between neutrinos and leptons below 1 GeV.

The uncertainties in the up–down and vertical–horizontal ratios of the number of events can be estimated by comparing the predicted ratios by various flux models. These uncertainties generally depend on the energy and the neutrino flavour. The uncertainty in the up–down event ratio is about 1–2% in the energy region below 1 GeV and is less than 1% above 1 GeV. The main source of the uncertainty in the vertical–horizontal ratio around a GeV is the size of the horizontal enhancement of the flux due to the three-dimensional effect; the uncertainty is estimated to be a few per cent. In the higher energy region, where upward through-going muons are relevant,

the largest source of the uncertainty in the vertical–horizontal ratio is the K production cross section, and the vertical–horizontal uncertainty is estimated to be 3% [30].

Summarizing the details of the atmospheric neutrino flux, we remark that, while the absolute flux value has a relatively large, energy-dependent uncertainty of about 10–30%, the $(\nu_\mu + \overline{\nu}_\mu/(\nu_e + \overline{\nu}_e)$ flux ratio is predicted to an accuracy of about 3%. The zenith-angle dependence of the flux is well understood, and especially, above a few GeV neutrino energies, the flux is predicted to be up–down symmetric.

3. Neutrino interactions

The important energy range for atmospheric neutrino interactions is between 0.1 GeV and 10 TeV. The Monte Carlo technique is used to simulate the neutrino interactions.

Usually, the following charged and neutral current (NC) neutrino interactions are considered in the simulation program.

- (quasi-)elastic scattering, $\nu\,\mathrm{N} \rightarrow \mathrm{l}\,\mathrm{N}'$,
- single-meson production, $\nu\,\mathrm{N} \rightarrow \mathrm{l}\,\mathrm{N}'\mathrm{m}$,
- coherent π production, $\nu\,{}^{16}\mathrm{O} \rightarrow \mathrm{l}\,\pi\,{}^{16}\mathrm{O}$,
- deep inelastic scattering, $\nu\,\mathrm{N} \rightarrow \mathrm{l}\,\mathrm{N}'$ hadrons.

Here, N and N′ are the nucleons (proton or neutron), l is the lepton and m is the meson, respectively. The most dominantly produced mesons are pions. If the neutrino interaction occurred in a nucleus, generated particles like pions and kaons interact with the nucleus before escaping from nuclei.

In the lowest energy range of <1 GeV, the quasi-elastic scattering [31] is dominant. For scattering off nucleons in ${}^{16}\mathrm{O}$, the Fermi motion of the nucleons and Pauli exclusion principle are taken into account. Usually, these effects are treated based on the relativistic Fermi gas model [32]. In the GeV energy range, the single-pion production processes [33, 34] are also important. In the multi-GeV or higher energy ranges, the deep inelastic scattering is dominant. Finally, it should be mentioned that high statistics neutrino interaction data taken by recent neutrino oscillation experiments are very important to improve the simulation of atmospheric neutrino interactions.

The total CC cross sections, together with the cross sections for quasi-elastic scattering, single meson productions and deep inelastic scattering, are shown in figure 5.

4. Atmospheric neutrino experiments

The rate of the atmospheric neutrino interactions is about 200 $\mathrm{kt}^{-1}\,\mathrm{year}^{-1}$. Since the background rate at the surface due to cosmic ray particles is very frequent, namely $\sim 2 \times 10^2\,\mathrm{m}^{-2}\,\mathrm{s}^{-1}$, it is unrealistic to carry out atmospheric neutrino experiments at the surface with the present technology. The hadrons, electrons and gammas still remaining at the surface are quickly absorbed by several metres of rock. Muons, consisting of a large fraction of the secondary cosmic rays at the surface, on the other hand, lose their energy only by ionization. If one wants to decrease the atmospheric muon flux significantly, the detector must be located deep underground.

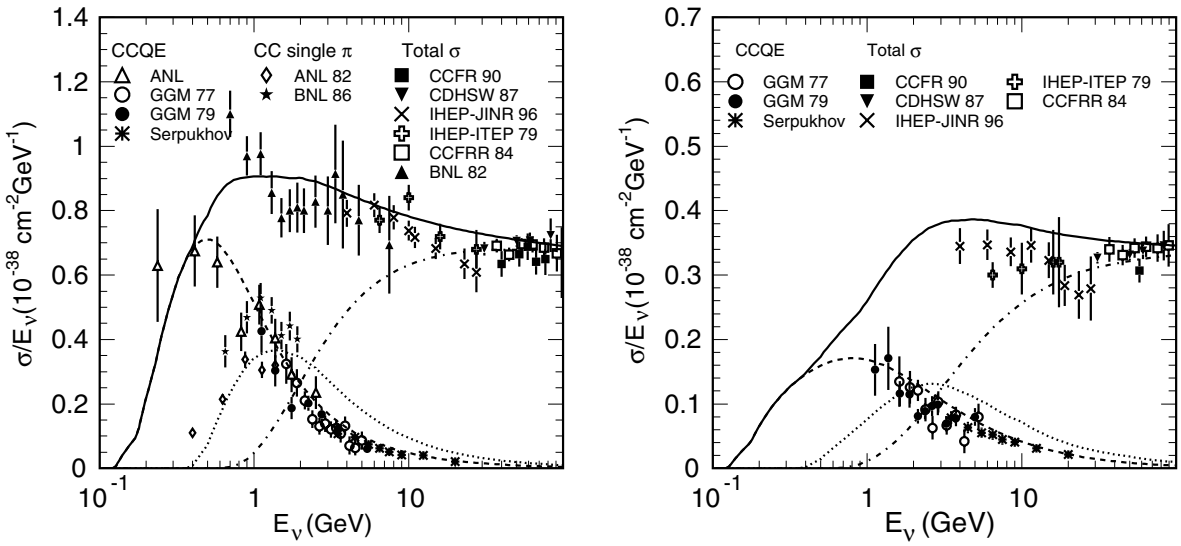

Figure 5. CC total cross section divided by E_ν for (a) neutrino and (b) anti-neutrino nucleon interactions. Solid lines show the calculated total cross sections. The broken, dotted and dash-dotted lines show the calculated quasi-elastic, single-meson and deep-inelastic scattering cross sections, respectively. Data points from various experiments are also shown. (The reference can be found in [44].)

Figure 6 shows the depth of the detectors and the cosmic ray muon rate. Even at a depth of 2700 m.w.e. (1000 m underground for the standard rock), Super-Kamiokande observes about two muons s^{-1}. This rate should be compared with the observed atmospheric neutrino rate in the fiducial volume of the same detector, about nine events day^{-1}. The rate of muons is $\sim 2 \times 10^4$ times more frequent than that of atmospheric neutrino events in Super-Kamiokande.

To date, two significantly different techniques, water Cherenkov detectors and fine-grained tracking detectors, have been used to observe atmospheric neutrino events. Each of these techniques will be described below.

4.1. Water Cherenkov detectors

In water Cherenkov detectors, an atmospheric neutrino event is detected by observing Cherenkov radiation from relativistic charged particles produced by the neutrino interaction with the nucleus. A two-dimensional array of photomultiplier tubes on the inside surface of the detector detects the photons. The hit time and the pulse height from each PMT are recorded. The timing information, with a typical resolution of a few nanoseconds for a single photoelectron pulse, is useful for reconstruction of the vertex position. The total number of photo-electrons gives information on the energy of the particles above the Cherenkov threshold. Figure 7 shows fully contained atmospheric neutrino events observed in the Super-Kamiokande detector.

The first-generation water Cherenkov detectors were IMB and Kamiokande. IMB [36] started taking data in 1982 and ended in 1991 after two major upgrades. The first phase of the detector (IMB-1) was equipped with 2048 PMTs each of 5-inch diameter. The light collection was improved by the addition of 2 feet × 2 feet × 0.5 inch wave-shifting plates, for a brief

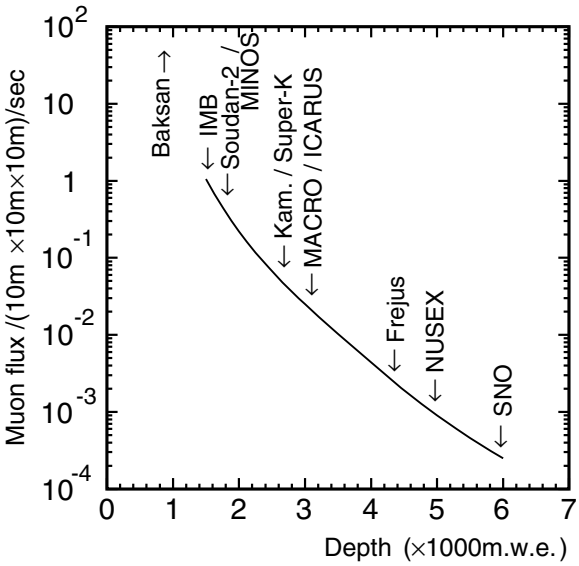

Figure 6. Depth of the detectors and the calculated cosmic ray muon rate (——). This figure is modified from [35].

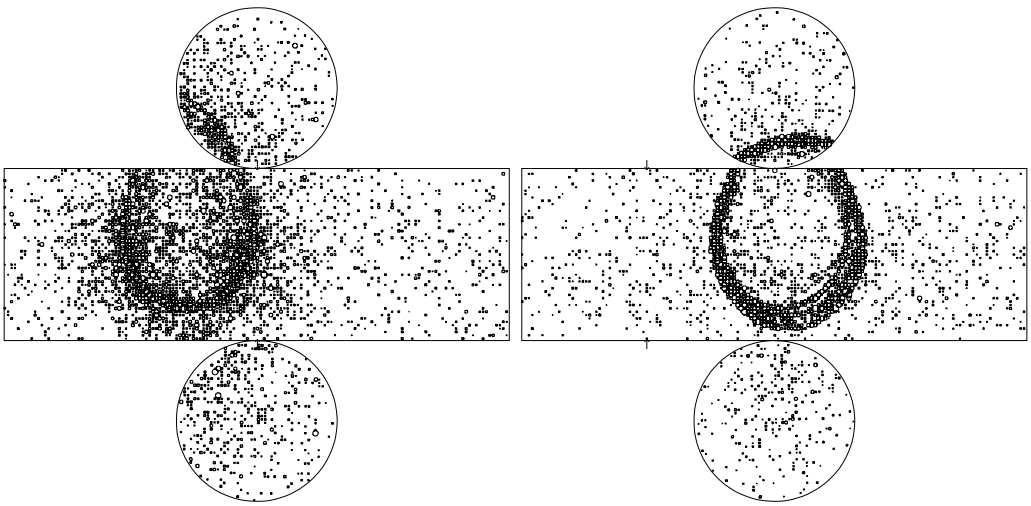

Figure 7. Example event displays from the Super-Kamiokande detector. Signals observed by the inner detector are shown. The left figure shows an electron event and the right one shows a muon event. The size of the circles shows the observed intensity of the photons by the PMTs that are installed at the position of the circles.

running period (IMB-2). Finally, the detector was equipped with 2048 8-inch PMTs, again with a wavelength shifter plate (IMB-3). It had a total mass and fiducial mass of 8 and 3.3 kt, respectively.

Kamiokande [37] started taking data in 1983 and ended in 1996. The Kamiokande detector used 1000 PMTs with 20-inch diameter, a photo cathode coverage of 20%. For the second phase, Kamiokande had an outer detector with thickness of the water between 0.5 and 1.5 m. The outer detector made it possible to identify the exiting atmospheric neutrino events (partially

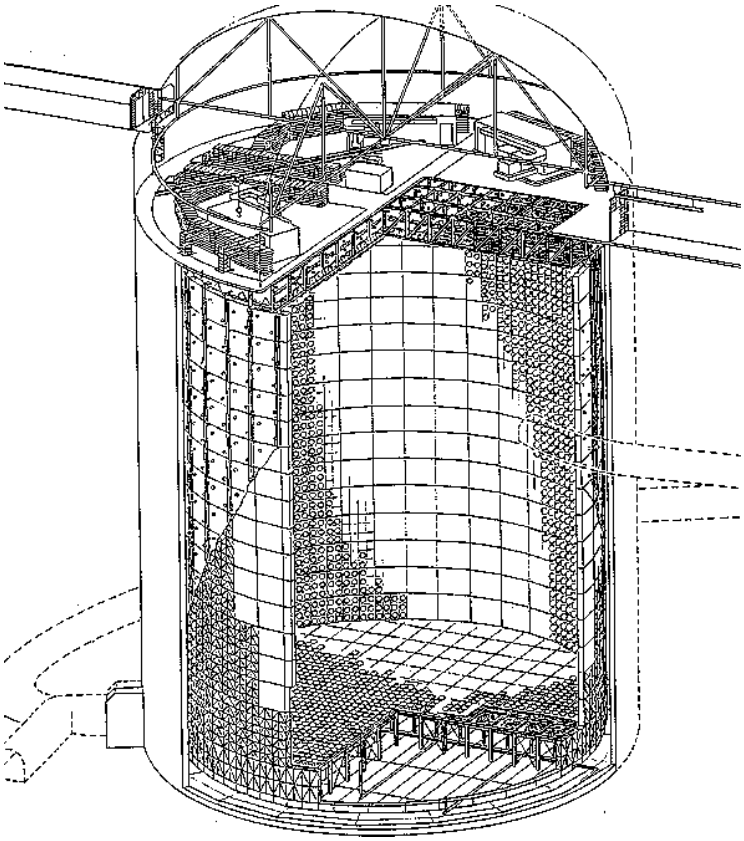

Figure 8. The Super-Kamiokande detector. It is a 50 kt water Cherenkov detector and is located 1000 m underground.

contained events) [18]. The detector was smaller than IMB: the total and fiducial masses were 4.5 and 1.04–1.35 kt, respectively. This detector showed that a water Cherenkov detector is able to separate electrons and muons very efficiently, thereby providing the possibility of studying neutrino oscillations using atmospheric neutrinos.

The present generation water Cherenkov detector is Super-Kamiokande [38] (see figure 8), whose results dominate our understanding of atmospheric neutrinos. It began taking data in 1996. It has a total mass of 50 kt. It uses 11 146 PMTs, each of 20-inch diameter with a photo-cathode coverage of 40% of the inner detector surface, a factor of two higher than that of Kamiokande. An outer detector surrounds the inner detector with 2 m thickness of water, equipped with 1885 8-inch PMTs with wavelength-shifting plates. The fiducial volume for neutrino vertices is 2 m from the plane of photomultiplier tubes, resulting in a 22.5 kt mass. The large mass and photocathode coverage allow for high statistics and detailed studies of atmospheric neutrinos.

4.2. Fine-grained tracking detectors

The second category of atmospheric neutrino detectors consists of comparatively fine resolution tracking detectors. The first generation of these experiments includes NUSEX [39] and Frejus [40]. These detectors were smaller than the water Cherenkov detectors in the 1980s. Tracking detectors have an advantage in sensitivity because they can detect low momentum charged

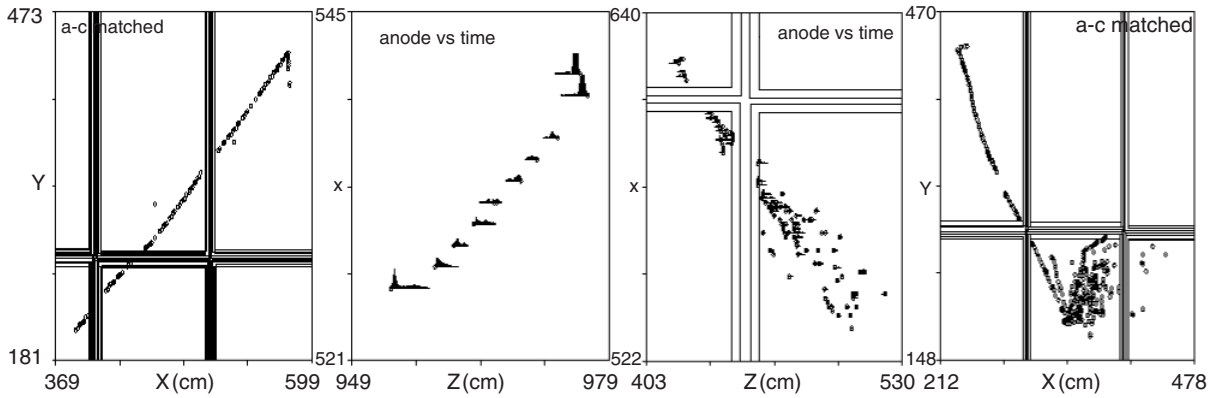

Figure 9. Example event displays from the Soudan-2 detector, showing the long track from a muon and a shorter, more heavily ionizing track from a recoil proton.

particles that would be below the Cherenkov threshold in water. In particular, the Soudan-2 detector [41] is able to reconstruct the short and heavily ionizing trajectory of recoil protons from atmospheric neutrino events such as $\nu n \rightarrow \mu p$, as shown in figure 9. The Soudan-2 detector is equipped with anti-counters. The anti-counter was useful to estimate the fraction of non-neutrino background events in the atmospheric neutrino sample as well as to eliminate cosmic ray background events easily.

There is a second type of fine-grained tracking detector that is mostly sensitive to muon neutrinos in the form of upward-going muons. These include the Baksan [42] and MACRO [43] experiments, which have fairly small absorber mass (a few hundred tons). These detectors identify the direction of the muon by resolving the time-of-flight as it traverses two or more layers of the liquid scintillator. The MACRO detector is composed of three horizontal planes with the lower section filled with crushed rock absorber and a hollow upper section. In addition to through-going muons, MACRO has analysed partially contained and stopping muon topologies, where the crushed rock in the lower section acts as neutrino target or muon stopper, respectively.

Table 1 summarizes major atmospheric neutrino detectors.

5. Observation of atmospheric neutrinos

5.1. Selection of atmospheric neutrino events

In very deep underground experiments such as Frejus [40] and NUSEX [39], the trigger rates were very low, about 7 and 45 events h^{-1} for NUSEX and Frejus, respectively. Hence, atmospheric neutrino events were simply selected by requiring the primary vertex in the fiducial volume.

Typically, detectors located at less deep places consisted of an outer anti-counter and an inner detector. In Kamiokande and Super-Kamiokande, most of the cosmic ray muons were rejected by requiring no signal in the anti-counter in selecting FC events. In Kamiokande, the remaining events were doubly scanned by physicists to select atmospheric neutrino events. In Super-Kamiokande, additional software cuts were applied to eliminate the remaining background events. The event scanning is not used to reject background events [44]. The selection of PC events is more complicated, because these events have anti-counter signals. However, even for

Table 1. Summary of the atmospheric neutrino experiments which observed fully contained (FC), partially contained (PC), upward-stopping muon and upward-through-going muon events.

Experiment	Detection technique	Type of events	Fiducial mass (kt)	Total exposure	Number of events
Baksan	Liquid scintillator	Up-through-μ	–	10.55 year	424
NUSEX	Gas counter-iron plate	FC	0.13	0.74 kt · year	50
Frejus	Gas counter-iron plate	FC	0.7	2.0 kt · year	158
		PC	0.7	2.0 kt · year	58
Kamiokande	Water Cherenkov	FC	1.04–1.35	7.7–8.2 kt · year	885
		PC	1.04	6.0 kt · year	118
		Up-through-μ	–	6.7 year	372
IMB	Water Cherenkov	FC	3.3	7.7 kt · year	935
		Up-through-μ	–	3.6 year	532
		Up-stopping-μ	–	3.6 year	85
Soudan-2	Gas counter-iron plate	FC	0.77	5.9 kt · year	379.5[a]
		PC		5.9 kt · year	57.7[a]
MACRO	Liquid scintillator + gas counter	Up-through-μ	–	6.17 year[b]	857[c]
			–	5.6 year	262[c]
			–	5.8 year	157[c]
Super-Kamiokande	Water Cherenkov	FC	22.5	92 kt · year	12180
		PC	22.5	92 kt · year	911
		Up-through-μ	–	4.5 year	1841.6[c]
		Up-stopping-μ	–	4.5 year	417.7[c]

[a] >300 MeV/c is required. Background events are statistically subtracted.
[b] Exposure with the partial detector configuration is normalized to the full detector configuration [45, 52].
[c] Background events are statistically subtracted.

these events, the information of the anti-counter is very useful. For example, by requiring only one anti-counter signal cluster, most of the cosmic ray muons are eliminated, because they typically produce two signal clusters at their entrance and exit points, while PC events typically have only one signal cluster. In Super-Kamiokande, various software cuts eliminate these background events and the event sample of PC events was selected without event scanning [44].

In Soudan-2, a different approach was taken. Events with reconstructed vertices in the fiducial volume were selected without using any anti-counter information. Then, the events were classified into 'quiet shield' and 'rock' events according to the anti-counter information. 'Quiet shield' events have no anti-counter hit signal and should be primarily neutrino events. The 'rock' events have anti-counter hits and are background events. Since there could be some contamination of background events among the 'quiet shield' events, the distribution of the minimum distance between the event vertex and the detector surface was studied. Generally, the vertex positions of the background events should cluster near the surface of the detector. About 90% of the 'quiet shield' events with the minimum momentum of 300 MeV/ c were fitted as neutrino events, and were used for further analyses.

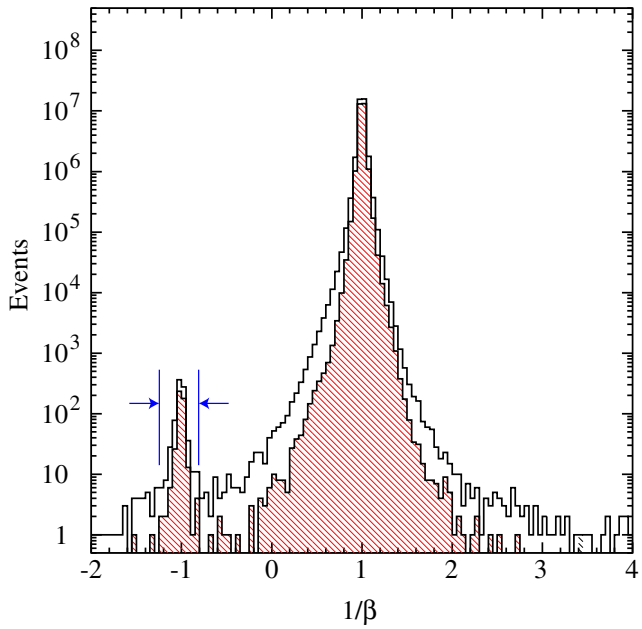

Figure 10. Reconstructed $1/\beta$ distribution for through-going particles observed in MACRO. $1/\beta = 1$ (-1) means downward-going (upward-going) particles with $\beta = 1$.

The selection of upward-going muons relies on a completely different algorithm. Typically, the track of every muon that enters the detector is reconstructed. Only muons that travel upward are selected. Figure 10 shows the reconstructed inverse velocity $(1/\beta)$ distribution for through-going particles observed in MACRO. Two clusters of events are seen near $1/\beta = -1$ and 1. They correspond to the downward-going muons $(1/\beta = 1)$ and upward-going muons $(1/\beta = -1)$. The contaminations of non-neutrino background events in the upward-going muon samples are generally small in the present generation atmospheric neutrino experiments. Estimated background contaminations range from $<1\%$ to several per cent, depending on the location of the detector and the category of events.

5.2. General features

Before discussing the data related to neutrino oscillations, we briefly discuss data statistics and some distributions that are relatively insensitive to neutrino oscillations.

The number of observed events and the detector exposures from each experiment are summarized in table 1.

The vertex positions of atmospheric neutrino interactions must be distributed uniformly within the detector. On the other hand, the vertex positions of background events should be clustered near the surface of the detector. The distribution of vertex positions is therefore an important check for background contamination. Figure 11 shows the distribution of the vertex position for fully contained events in Super-Kamiokande. The observed event rate was lower than that for the Monte Carlo prediction. We note that the Monte Carlo does not include neutrino oscillations. An excess of events near the walls of the inner detector is seen. However, this excess rapidly disappears as the vertex position moved to the inner region. Within the fiducial volume of 2 m from the inner detector walls, there is no evidence for background contamination.

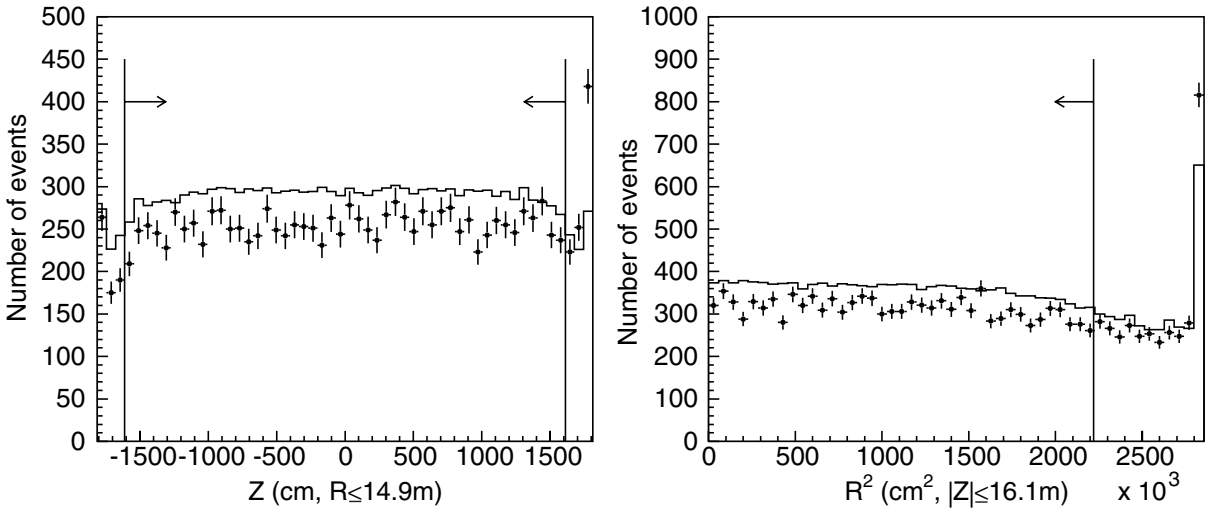

Figure 11. The distribution of fully contained event vertices in the vertical (left) and horizontal (right) coordinates, compared with the Super-Kamiokande data and atmospheric neutrino Monte Carlo prediction. The points show the data and the histogram shows the Monte Carlo prediction. Arrows indicate the fiducial region for the contained events. Neutrino oscillation is not included in the Monte Carlo calculation.

A similar study was carried out by the Soudan-2 experiment (see section 4). The background contamination in the Soudan-2 FC sample was estimated to be about 10%. The larger background contamination in Soudan-2 compared with Super-Kamiokande can be understood to be due to the shallower detector position and the thinner detector region outside of the fiducial volume in Soudan-2.

Figure 12 shows the momentum distribution for fully contained single-ring e-like and μ-like events observed in Super-Kamiokande. The shape of these distributions agreed well with the corresponding Monte Carlo predictions over a wide momentum range. The cutoff of the high-energy muon spectrum is due to the requirement of full-containment in the detector. A deficit of μ-like events in the whole momentum range is seen. This deficit is explained by neutrino oscillations.

In summary, the atmospheric neutrino data samples have, generally, high purity, and the Monte Carlo prediction reasonably reproduces the basic distributions of the data.

5.3. μ/e ratio

The atmospheric (ν_μ/ν_e) flux ratio has been measured by identifying electrons and muons produced by CC ν_e and CC ν_μ interactions, respectively. Electrons produce electromagnetic showers while propagating in matter. On the other hand, muons slowly lose their energy by $\mathrm{d}E/\mathrm{d}x$ while propagating in matter. The different propagation of these particles in matter is used to separate electrons and muons.

In tracking calorimeters, the event pattern is recorded in a three-dimensional view, and the separation of electrons and muons is carried out by event pattern recognition. Figure 9 shows examples of events observed by the Soudan-2 detector. CC ν_μ events are clearly recognized

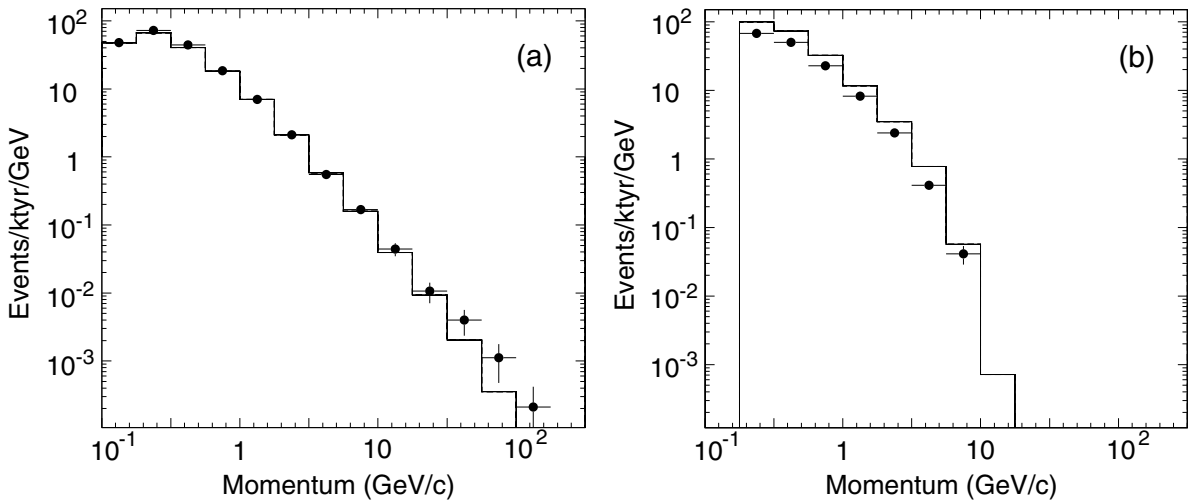

Figure 12. Momentum distributions for fully-contained single-ring (a) e-like and (b) μ-like events observed in Super-Kamiokande during 92 kt · year exposure of the detector. The Monte Carlo prediction does not include neutrino oscillations.

by a long straight track, which is a candidate muon. A CC ν_e event, on the other hand, has an electromagnetic shower linked to the vertex point.

In water Cherenkov detectors, CC ν_e and CC ν_μ events are distinguished by the difference in the characteristic shape of the Cherenkov ring. Figure 7 shows an e-like and a μ-like event observed in the Super-Kamiokande detector. A clear outer edge of the Cherenkov light is identified for a μ-like event, while the edge is relatively unclear for an e-like event due to an electromagnetic shower and the multiple scattering of low-energy electrons.

On the basis of the particle identification technique, the flavour ratio in the atmospheric neutrino flux was measured. The $(\nu_\mu + \overline{\nu}_\mu)/(\nu_e + \overline{\nu}_e)$ flux ratio has been calculated to an accuracy of about 3%, and therefore the measurement of this ratio is sensitive to neutrino oscillations. Experimentally, the μ-like/e-like ratio for the data is compared with that for the MC. Therefore, $(\mu\text{-like/e-like})_{\text{Data}}/(\mu\text{-like/e-like})_{\text{MC}}$ should be consistent with unity within the errors for the case of no neutrino oscillations. Figure 13 summarizes the $(\mu/\text{e})_{\text{Data}}/(\mu/\text{e})_{\text{MC}}$ measurements from various experiments. Measurements from Kamiokande (both sub- and multi-GeV data samples) [18, 46], IMB-3 (sub-GeV) [14], Soudan-2 [47] and Super-Kamiokande [19, 44] (both sub- and multi-GeV data samples) showed $(\mu/\text{e})_{\text{Data}}/(\mu/\text{e})_{\text{MC}}$ ratios which were smaller than unity. The sub-GeV (multi-GeV) sample in Kamiokande and Super-Kamiokande was defined to include events with $E_{\text{vis}} < 1.33$ (>1.33) GeV, where E_{vis} is the visible energy. $E_{\text{vis}} = 1.33$ GeV corresponds to an electron (muon) momentum of 1.33 (about 1.4) GeV/c. There were a few measurements [15, 17, 48] suggesting a ratio consistent with unity. However, these measurements had relatively large statistical errors.

Since many of the uncertainties of the prediction and the experiment cancel when taking this ratio, the systematic error of this measurement was relatively small. Neither a statistical fluctuation nor systematic uncertainties can explain the small (μ/e) ratio of the data.

The small μ/e ratio could be interpreted as due to neutrino oscillations between $\nu_\mu \leftrightarrow \nu_\tau$ or $\nu_\mu \leftrightarrow \nu_e$ with a large mixing angle. However, there were other possibilities that could explain the data. For example, Mann *et al* [49] suggested that the data could be explained by proton decay

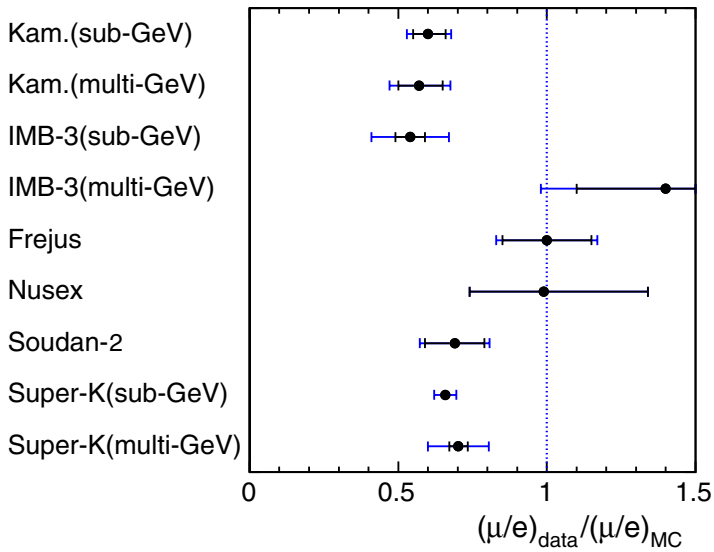

Figure 13. Summary of the measurements of the double ratio μ-like/e-like (data) to μ-like/e-like (Monte Carlo) by various atmospheric neutrino experiments. The inner and outer error bars show the statistical and statistical + systematic errors, respectively.

into $e^+\nu\nu$, since the observed small μ/e ratio could be interpreted as due to an excess of e-like signal by these positrons.

5.4. Zenith angle distribution

The atmospheric neutrino flux is predicted to be up–down symmetric above a few GeV neutrino energies. For downward-going neutrinos, the flight length is about 15 km, while that for vertically upward-going neutrinos it is 13 000 km. Therefore, if the neutrino oscillation length is O(100–1000 km), it should be possible to observe up–down asymmetry of the flux while the prediction is up–down symmetric. Early data from Kamiokande [18] showed that the upward-going multi-GeV μ-like events had substantially lower event rate than the downward-going ones, while an approximate up–down symmetry was expected.

The zenith angle distributions for e-like and μ-like events observed in Super-Kamiokande (92 kt · year) are shown in figure 14 [44, 50]. The μ-like data have exhibited a strong deficit of upward-going events, while no significant deficit has been observed in the e-like data. For further discussion, we define the up–down ratio U/D, where U is the number of upward-going events ($-1 < \cos\Theta < -0.2$, where Θ is the zenith angle) and D is the number of downward-going events ($0.2 < \cos\Theta < 1$). The ratio is expected to be near unity independent of flux model for $E_\nu > 1$ GeV, above which effects due to the Earth's magnetic field on cosmic rays are small. The U/D value for the multi-GeV FC + PC μ-like events from Super-Kamiokande, $0.55^{+0.035}_{-0.033}$(stat.) ± 0.005 (syst.) deviates from unity by 10 standard deviation (SD). Many systematic errors are cancelled for the U/D ratio. Hence the estimated systematic error in the U/D ratio is about 1% [44]. The observed up–down ratio suggests a near maximal neutrino mixing, because U/D can be approximately expressed as $U/D = 1 - \sin^2 2\theta_{23}/2$. For sub-GeV μ-like events, the observed ratio is larger than that in the multi-GeV sample due to the poorer angular resolution. Below 400 MeV c, the ratio is close to unity due to the very poor angular resolution.

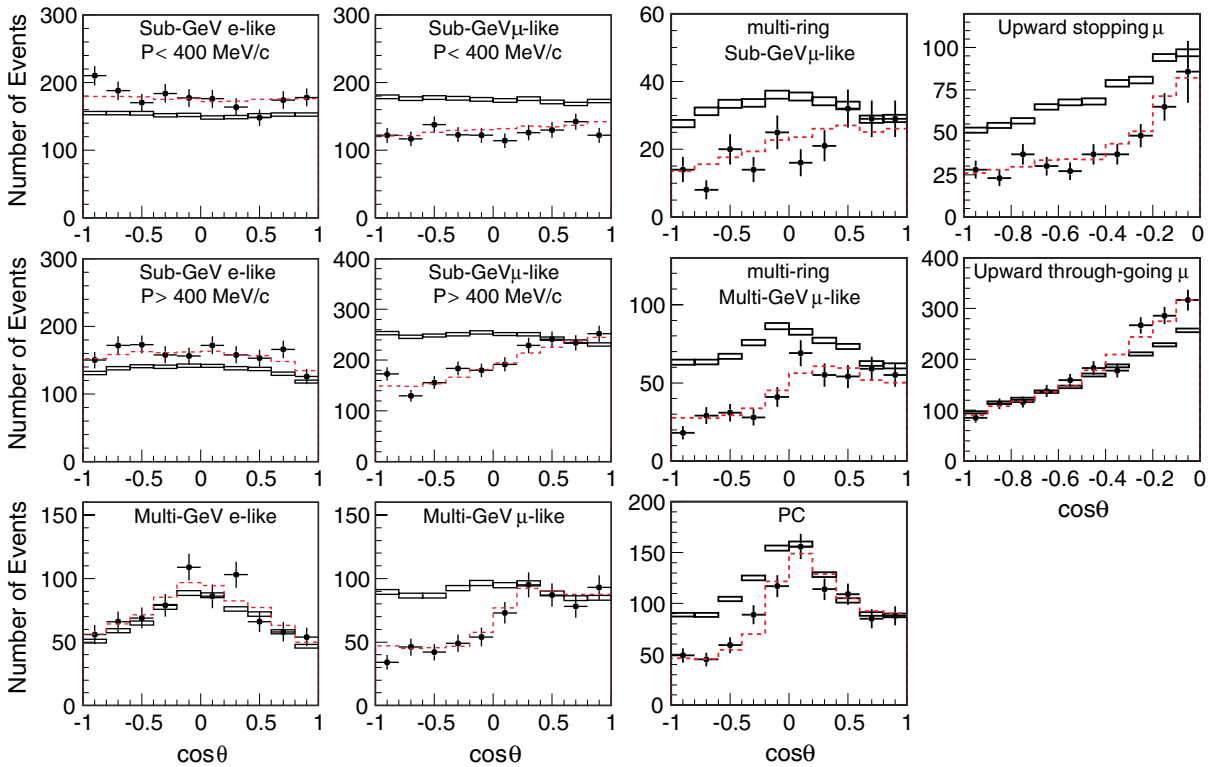

Figure 14. Zenith-angle distributions observed in Super-Kamiokande based on 92 kt · year data for various data samples; $\cos\Theta = 1\,(-1)$ corresponds to down-going (up-going). The solid line histograms show the prediction without neutrino oscillations. The broken line histograms show the prediction with $\nu_\mu \to \nu_\tau$ oscillations ($\Delta m^2_{23} = 2.1 \times 10^{-3}\,\mathrm{eV}^2$, $\sin^2 2\theta_{23} = 1.0$). In the oscillation prediction, various uncertainty parameters such as the absolute normalization were adjusted to give the best fit to the data.

The observed number of events for upward through-going muons was slightly higher than the no-oscillation prediction. We note that the predicted neutrino flux has more than 20% uncertainty in the energy range of >100 GeV. The observed zenith angle distribution is explained well by neutrino oscillations, if the large systematic uncertainty in the absolute flux is taken into account.

Figure 15 shows the zenith angle distributions observed in Soudan-2 (5.9 kt · year) [51]. Due to the geomagnetic field effect and the zenith angle-dependent detection efficiency for PC events, more downward-going events are predicted than the upward-going ones even for the no-oscillation case. Although the statistics of the Soudan-2 data are limited, the observed deficit of upward-going μ-like events is consistent with the Super-Kamiokande data.

Figure 16 shows the zenith angle distributions for three data samples observed in MACRO [52, 53]. The predicted and observed numbers of events near the horizon are small (or the error bars are large if the efficiency is corrected to estimate the flux in figure 16 (left panel)) due to the lower efficiency for near-horizontal events. The zenith angle distribution for upward-going PC events (figure 16, middle panel) shows a relatively large deficit of the data events, while that for upward-going stopping μ plus downward-going PC events shows only a small deficit

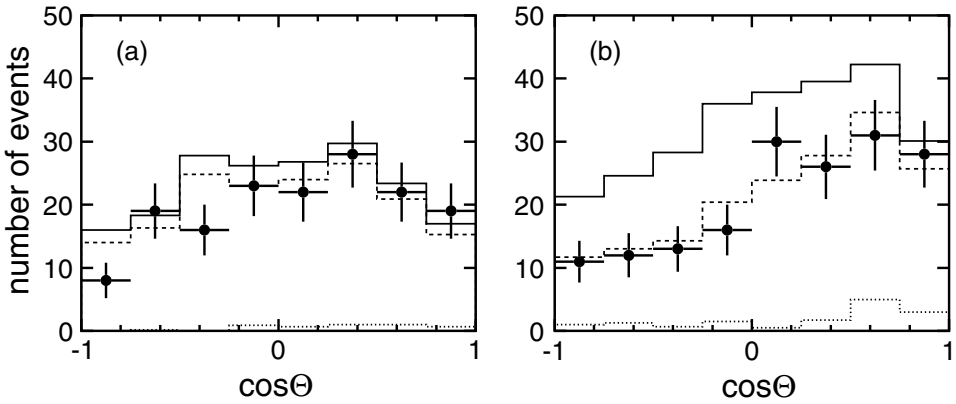

Figure 15. Zenith-angle distributions observed in Soudan-2 based on 5.9 kt · year data for the (a) CC ν_e and (b) CC ν_μ samples. The solid, broken and dotted line histograms show the Monte Carlo prediction without neutrino oscillations, with neutrino oscillations and the estimated background events, respectively.

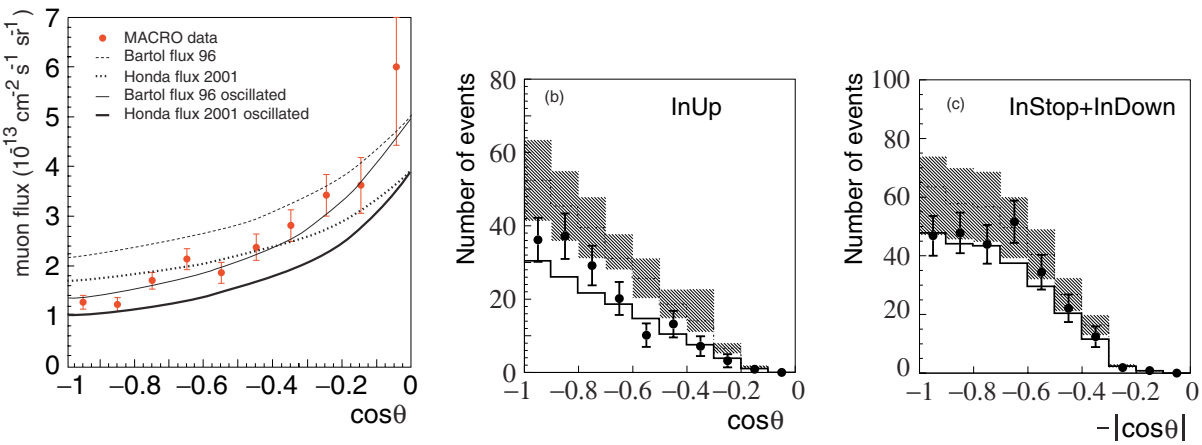

Figure 16. Zenith-angle distributions for the upward through-going muon flux (left), upward PC events (middle), and upward stopping muons plus downward PC events (right) observed in MACRO. For the middle and right panels, the lines with the shaded regions show the expectation for null oscillations with the absolute normalization uncertainty. The flux model used in the middle and right panels [22] gives a very similar flux prediction as the lower flux model in the left figure for upward-through-going muons. The solid lines show the expected flux for $\nu_\mu \to \nu_\tau$ oscillations with ($\sin^2 2\theta_{23} = 1.0,\ \Delta m^2_{23} = 2.3 \times 10^{-3}\,\mathrm{eV}^2$).

of the data events. This can be understood by neutrino oscillations, since about a half of the upward-going neutrinos should be oscillated away, while the downward-going neutrinos have very little oscillation effects, and since the number of downward-going PC events and the number of upward-going stopping muon events are expected to be approximately equal for no oscillation. The MACRO data are also consistent with neutrino oscillations.

5.5. Two-flavour neutrino oscillation analysis

Since μ-like events show the zenith-angle- and energy-dependent deficit of events, while e-like events show no evidence for inconsistency between the data and non-oscillated Monte Carlo, it can be concluded that the oscillation could be between ν_μ and ν_τ. Indeed, detailed oscillation analyses of the Super-Kamiokande data [19, 44] have concluded that the data are consistent with two-flavour $\nu_\mu \to \nu_\tau$ oscillations. In the analysis of the atmospheric neutrino data, χ^2 methods that take into account various systematic uncertainties are typically used. For example, in the analysis of the Super-Kamiokande data, the χ^2 is defined to be

$$\chi^2 = \sum_{i=1}^{180} \frac{(N_i^{\rm obs} - N_i^{\rm exp})^2}{\sigma_i^2} + \sum_{j=1}^{37} \left(\frac{\epsilon_j}{\sigma_j}\right)^2. \tag{4}$$

Events are divided into 180 bins based on the event type, momentum and zenith angle. In the first sum, $N_i^{\rm obs}$ is the number of observed events in the ith bin and $N_i^{\rm exp}$ is the expected number of events based on a Monte Carlo simulation and σ_i combines the statistical uncertainties in the data and Monte Carlo simulation. During the fit, the values of $N_i^{\rm exp}$ are recalculated to account for neutrino oscillations, and systematic variations in the predicted rates due to uncertainties in the neutrino flux model, neutrino cross-section model and detector response. The second sum in the χ^2 definition takes into account the contributions from 37 variables which parametrized the systematic uncertainties in the expected neutrino rates. σ_j represents the systematic error for the jth term. The absolute normalization is treated as a free parameter, and does not contribute to the second term in the χ^2 definition. During the fit, these parameters are varied to minimize χ^2 for each choice of the oscillation parameters $\sin^2 2\theta$ and Δm^2. (See [54] for a description of the mathematical details.)

The estimated oscillation parameters ($\sin^2 2\theta$, Δm^2) for two-flavour $\nu_\mu \to \nu_\tau$ oscillations from various experiments [44, 51, 52, 55] are shown in figure 17. All results are essentially consistent. If the most accurate result from Super-Kamiokande is referred, the oscillation parameters are determined to be $\sin^2 2\theta > 0.92$ and $1.5 \times 10^{-3} < \Delta m^2 < 3.4 \times 10^{-3}\,{\rm eV}^2$ at 90% CL. Finally, we remark that consistent results have been obtained by a recent long-baseline neutrino oscillation experiment based on a neutrino beam produced by a proton accelerator [56, 57].

5.6. L/E analysis

The deficit of ν_μ events observed by the atmospheric neutrino experiments is explained very well by neutrino oscillations. However, there are models that explain the zenith angle- and energy-dependent deficit of ν_μ events reasonably well. They are neutrino decay [58] and neutrino decoherence [59, 60] models. These models may not be particularly appealing theoretically. However, it is still important to experimentally determine which is the right explanation for the atmospheric ν_μ deficit. One of the key features of neutrino oscillations is the sinusoidal ν_μ disappearance probability as a function of L/E. On the other hand, the ν_μ survival probability for the neutrino decay and decoherence models are not sinusoidal. Therefore, in order to further confirm neutrino oscillations, it is important to measure the sinusoidal neutrino oscillation feature.

Soudan-2 [51] and MACRO [61] analysed their data in terms of L/E. Results from these analyses are shown in figure 18. Because of the limited L/E resolution, these experiments were

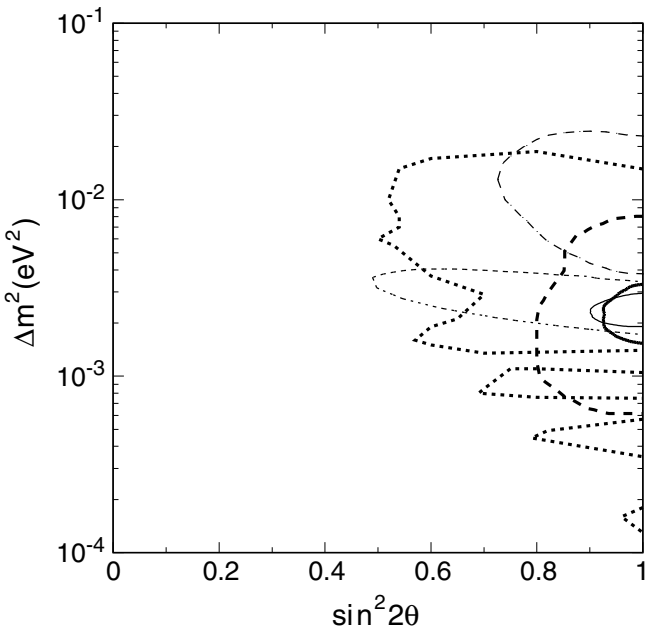

Figure 17. 90% C L allowed parameter regions of oscillation parameters from Super-Kamiokande (thick line), Kamiokande (thin broken line), Soudan-2 (thick dotted line) and MACRO (thick broken line). Two-flavour $\nu_\mu \to \nu_\tau$ oscillations are assumed. Also shown are the allowed regions from the L/E analysis in Super-Kamiokande (thin line) and the region obtained by the long-baseline experiment K2K (thin dotted line).

unable to see the first oscillation maximum (dip) that corresponds to $(1.27\Delta m^2 L)/E_\nu = \pi/2$. (Observing the second and the higher oscillation maxima is even more difficult, since an even better L/E resolution is required to observe these dips.)

Recently, Super-Kamiokande published an L/E analysis [62]. High L/E resolution events, which have an (L/E) resolution better than 70%, were used. Since L/E resolution depends on the zenith angle, energy and type of events, the events were selected using this information. Essentially, low-energy events are not used, because of the poor correlation between the neutrino and outgoing particles. Also, horizontal-going events are not used, because L changes significantly with a small change in the zenith angle near horizon. 2121 FC μ-like and 605 PC events were selected. Figure 19 (left panel) shows the number of events as a function of the reconstructed L/E, together with the MC prediction. Two clusters of events are visible below and above 150 km GeV^{-1}. They mostly correspond to downward- and upward-going events, respectively.

Figure 19 (right panel) shows the ratio of the data over non-oscillated MC as a function of L/E together with the best-fit expectation for two-flavour $\nu_\mu \leftrightarrow \nu_\tau$ oscillations with systematic errors. A dip, which should correspond to the first maximum oscillation, is observed around $L/E = 500$ km GeV^{-1}. Due to the L/E resolution of the detector, the second and higher maximum oscillation points should not be observable in the Super-Kamiokande experiment. The data points at large L/E in figure 19 (right panel) show a slight deviation from the expected flat distribution. The Super-Kamiokande experiment concluded that the energy-dependent systematic effects such as the neutrino interaction cross sections are the main sources of non-flatness.

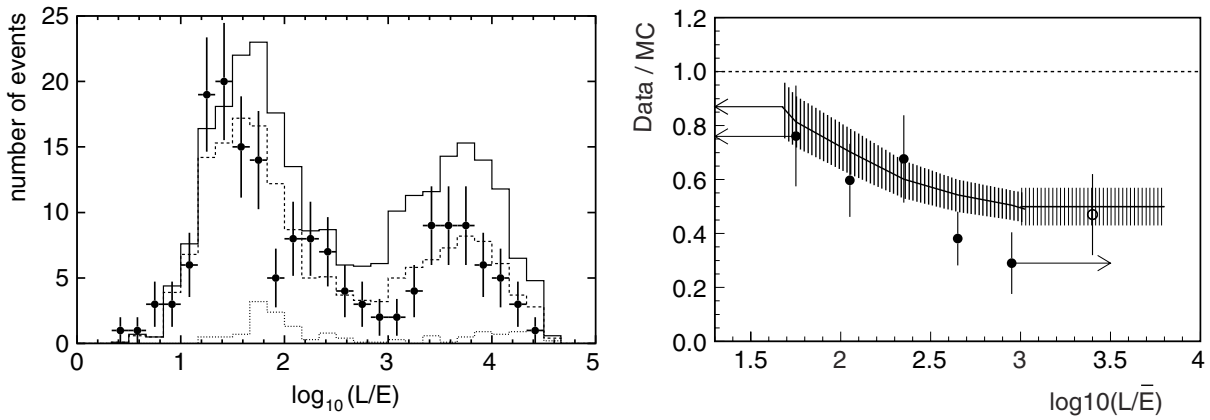

Figure 18. Left: number of μ-like events as a function of L/E for the Soudan-2 data (points) and the atmospheric neutrino MC events with and without oscillations (broken line and solid line histograms, respectively). Only high-resolution events are used. The estimated non-neutrino background events are also shown by the dotted line histogram. Right: ν_μ survival probability as a function of L/E obtained by analysis of the MACRO upward through-going muon data. The muon momentum is estimated from the multiple scattering. The expected distribution for oscillation is shown by the shaded line. The rightmost data point shows the result for upward-going PC events.

In the neutrino decay and decoherence models, it is assumed that a neutrino flavour eigenstate is a mixture of mass eigenstates. However, the mechanisms for generating ν_μ disappearance are different. In particular, these models do not predict sinusoidal ν_μ disappearance probability. Also shown in figure 19 are the L/E distributions for the best-fit expectation for the neutrino decay and decoherence models. Since these models cannot predict the dip observed in the data, the χ^2 values for these models were worse. The neutrino decay and decoherence models were disfavoured at 3.4 and 3.8 SD levels, respectively. The observed L/E distribution gives evidence that the neutrino flavour transition probability obeys a sinusoidal function as predicted by neutrino flavour oscillations.

The observed L/E distribution was used to estimate the $\nu_\mu \to \nu_\tau$ oscillation parameters. The definition for χ^2 was similar to that in equation (4). Figure 20 shows the contour plot of the allowed oscillation parameter regions. The 90% CL allowed parameter region was obtained as $1.9 \times 10^{-3}\,\mathrm{eV}^2 < \Delta m^2 < 3.0 \times 10^{-3}\,\mathrm{eV}^2$ and $\sin^2 2\theta > 0.90$. The result is consistent with that of the oscillation analysis using zenith-angle distributions (see figure 17).

5.7. Three-flavour neutrino oscillation analysis

As an extension of the two-flavour oscillation analysis, we discuss three-flavour neutrino oscillations. We assume that Δm^2_{12} is much smaller than $\Delta m^2_{23}(\Delta m^2_{13})$ as measured by solar neutrino [63, 64] and KamLAND experiments [65], and therefore assume the effect of the oscillations related to Δm^2_{12} is negligible in atmospheric neutrino experiments. The oscillation length relevant to Δm^2_{12} is shorter than the diameter of the earth for E_ν below 1 GeV. However, due to the accidental feature that the atmospheric ν_μ/ν_e ratio is ~ 2 in the absence of $\nu_\mu \to \nu_\tau$

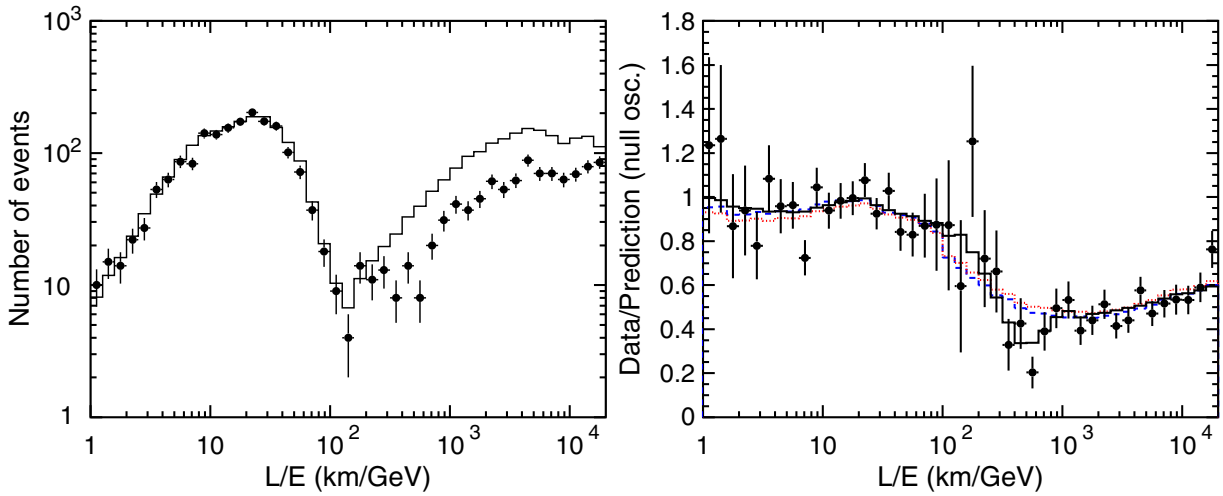

Figure 19. Left: number of events as a function of L/E for the Super-Kamiokande data (points) and the atmospheric neutrino MC events without oscillations (solid line histogram). The MC is normalized by the detector lifetime. Right: ratio of the data to the MC events without neutrino oscillation (points) as a function of the reconstructed L/E together with the best-fit expectation for 2-flavour $\nu_\mu \leftrightarrow \nu_\tau$ oscillations (solid line). Also shown are the best-fit expectation for neutrino decay (dashed line) and neutrino decoherence (dotted line).

oscillations in the relevant energy range and the (near) maximal θ_{23} mixing angle, the effect of the oscillations related to Δm^2_{12} is predicted to be small [66, 67]. Under this approximation, there are only three oscillation parameters; θ_{13}, θ_{23} and Δm^2 ($\equiv \Delta m^2_{13} = \Delta m^2_{23}$). The neutrino oscillation probability in the vacuum can be written as

$$P(\nu_e \to \nu_e) = 1 - s^2 2\theta_{13} s^2 \left(\frac{1.27 \Delta m^2_{23}(\mathrm{eV}^2) L(\mathrm{km})}{E_\nu(\mathrm{GeV})} \right), \tag{5}$$

$$P(\nu_\mu \to \nu_e) = s^2\theta_{23} s^2 2\theta_{13} s^2 \left(\frac{1.27 \Delta m^2_{23} L}{E_\nu} \right), \tag{6}$$

$$P(\nu_\mu \to \nu_\mu) = 1 - 4c^2\theta_{13} s^2\theta_{23}(1 - c^2\theta_{13} s^2\theta_{23}) s^2 \left(\frac{1.27 \Delta m^2_{23} L}{E_\nu} \right), \tag{7}$$

where s and c represent sine and cosine, respectively. For $\theta_{13} = 0$, the oscillation is identical to two-flavour $\nu_\mu \to \nu_\tau$ oscillations. Only θ_{13} is the new parameter, and it represents the first- and third-generation neutrino mixing. Since ν_e is involved in the oscillation, the matter effect [68, 69] must be taken into account. The oscillation probability in the matter is different from that in vacuum for oscillations involving ν_e. This is due to the difference in the forward scattering amplitude for ν_e and ν_μ (or ν_τ). Assuming $\Delta m^3_{23} > 0$, the instantaneous mixing parameter ($\sin^2 2\theta^m_{13}$) in matter for neutrinos with the electron number density N_e is

$$\sin^2 2\theta^m_{13} = \frac{\sin^2 2\theta_{13}}{(A/\Delta m^2_{23} - \cos 2\theta_{13})^2 + \sin^2 2\theta_{13}}, \tag{8}$$

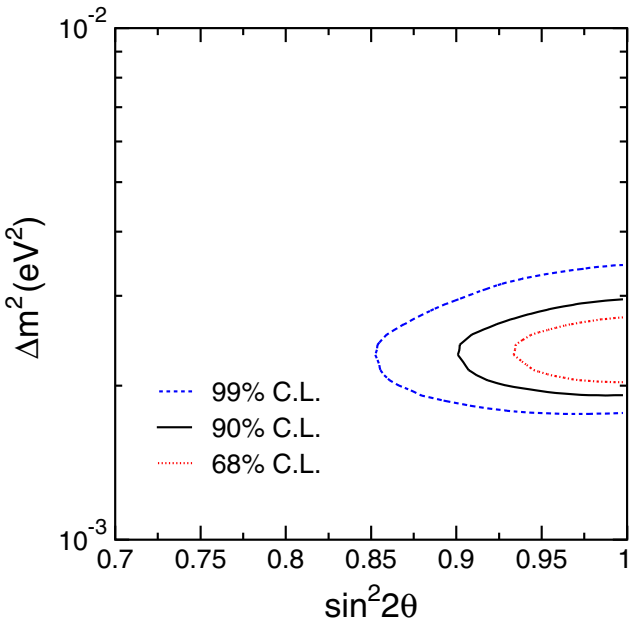

Figure 20. Oscillation parameter regions with 68, 90 and 99% allowed CL for two-flavour $\nu_\mu \leftrightarrow \nu_\tau$ oscillations obtained by the L/E analysis.

where $A = 2\sqrt{2}G_F N_e E_\nu$ (G_F is the Fermi coupling constant). For anti-neutrinos, A must be replaced by $-A$. If a condition $A = \Delta m^2 \cos 2\theta_{13}$ is satisfied, $\sin^2 2\theta_{13}^m$ is maximum (=1) even though the mixing angle θ_{13} is small. See, for example, [70, 71] for more complete discussions. For $\Delta m_{23}^2 = 2$ to 3×10^{-3} eV^2 with a small θ_{13}, the resonance could occur for neutrinos passing through the Earth with their energies between 5 and 10 GeV. Therefore, the effect of a non-zero θ_{13} could be observed as an excess of electron neutrinos in the upward-going direction. Figure 21 (left) shows the $\nu_e \leftrightarrow \nu_\mu$ oscillation probability as a function of the neutrino energy and zenith angle. A clear resonance effect is seen for upward-going neutrinos near 5 GeV. For neutrinos passing through the core of the Earth, resonances will occur in slightly lower neutrino energies. This effect can be observed as an excess of upward going e-like events. Figure 21 (right) shows the expected excess e-like events in Super-Kamiokande for a set of oscillation parameters.

The present data from Super-Kamiokande (figure 14) and Soudan-2 (figure 15) show no evidence for an excess of e-like events in the upward-going direction. The preliminary result on allowed region of the oscillation parameters on the $\sin^2\theta_{13}$ and $\sin^2\theta_{23}$ plane is shown in figure 22 (left). In this analysis, data from Super-Kamiokande were used. Since the matter resonance effect occurs only for neutrinos (anti-neutrinos) if $m_3^2 - m_2^2 \equiv \Delta m_{23}^2 > 0$ (<0), and since the sign of Δm_{23}^2 is not known, the allowed regions were estimated for both positive and negative Δm_{23}^2 cases. No evidence for non-zero $\sin^2\theta_{13}$ has been observed. The constraints on θ_{13} from reactor experiments [72, 73] are still more stringent than that from the atmospheric neutrino results, as seen in figure 22 (right).

5.8. Search for CC ν_τ events

If $\nu_\mu \to \nu_\tau$ is the dominant oscillation channel, about one CC ν_τ event per kt · year exposure can be expected to occur in an atmospheric neutrino detector. The low event rate is due to the

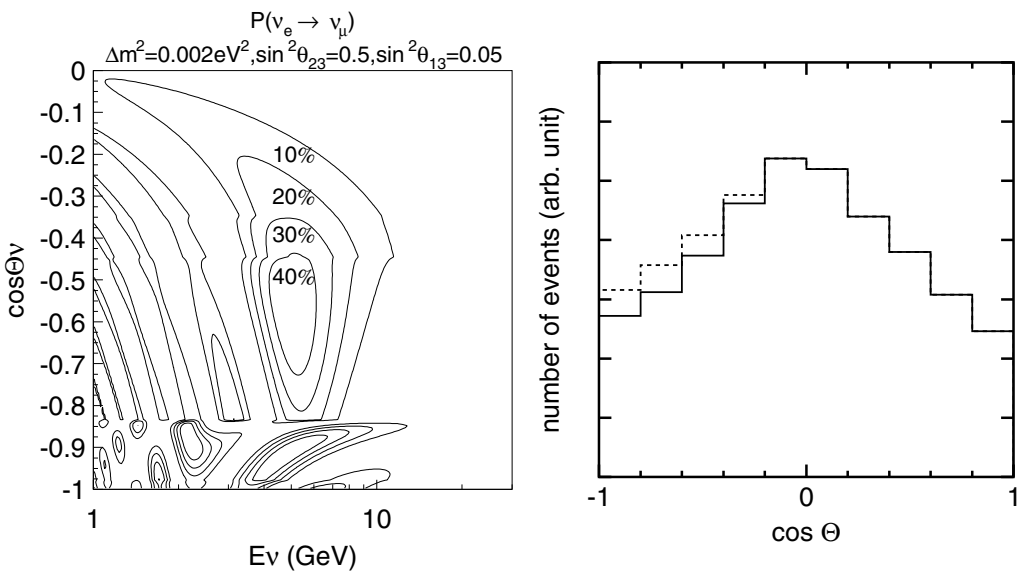

Figure 21. Left: $\nu_e \leftrightarrow \nu_\mu$ oscillation probability for neutrinos passing through the Earth as a function of the neutrino energy and zenith angle for $\Delta m^2_{23} = 2.0 \times 10^{-3}\,\mathrm{eV}^2$, $\sin^2\theta_{23} = 0.50$ and $\sin^2\theta_{13} = 0.05$. Right: expected zenith angle distribution for single + multi-ring e-like events in Super-Kamiokande with the observed energy between 2.5 and 5 GeV for oscillation with $\Delta m^2_{13} = 2.0 \times 10^{-3}\,\mathrm{eV}^2$, $\sin^2\theta_{23} = 0.50$ and $\sin^2\theta_{13} = 0.0$ (solid line histogram) and 0.05 (broken line histogram).

threshold effect of the τ production process which requires a ν_τ energy of at least 3.5 GeV to produce a τ lepton. These τ typically decay to hadrons (branching ratio is 64%) within 1 mm from the vertex point. These events should be upward-going but otherwise similar to energetic NC events, hence it is difficult to isolate ν_τ events in the on-going atmospheric neutrino experiments.

Super-Kamiokande has been searching for CC ν_τ events. The candidate ν_τ events were selected by a maximum likelihood or a neural network method. Various kinematical data were used as the inputs to the maximum likelihood or the neural network method. Even with these data, the signal-to-noise ratio was about 10%. However, the zenith-angle distribution can be used to estimate the number of ν_τ events statistically, because both the ν_τ signal and background events have accurately predicted zenith angle distributions. The best-fit numbers of ν_τ interactions that occurred in the fiducial volume of the detector during the 92 kt · year exposure were $145 \pm 44(\mathrm{stat.})^{+11}_{-16}(\mathrm{syst.})$, $99 \pm 39(\mathrm{stat.})^{+13}_{-21}(\mathrm{syst.})$ and $135^{+47}_{-44}(\mathrm{stat.} + \mathrm{syst.})$ events (preliminary) depending on the analysis [74]. The expected number was 86. The observed numbers of ν_τ interactions are consistent with the $\nu_\mu \to \nu_\tau$ expectation. The results are not statistically compelling, however they suggest that it may be possible in the near future to demonstrate the ν_τ interactions at more than 3σ level. At the time of writing, the Super-Kamiokande collaboration is finalizing the tau analysis.

5.9. Constraints on $\nu_\mu \leftrightarrow \nu_{\mathrm{sterile}}$ oscillations

An important question to ask is whether $\nu_\mu \leftrightarrow \nu_\tau$ oscillation is the only possible explanation of the atmospheric neutrino data. Since the observed effect is the energy- and zenith angle-dependent

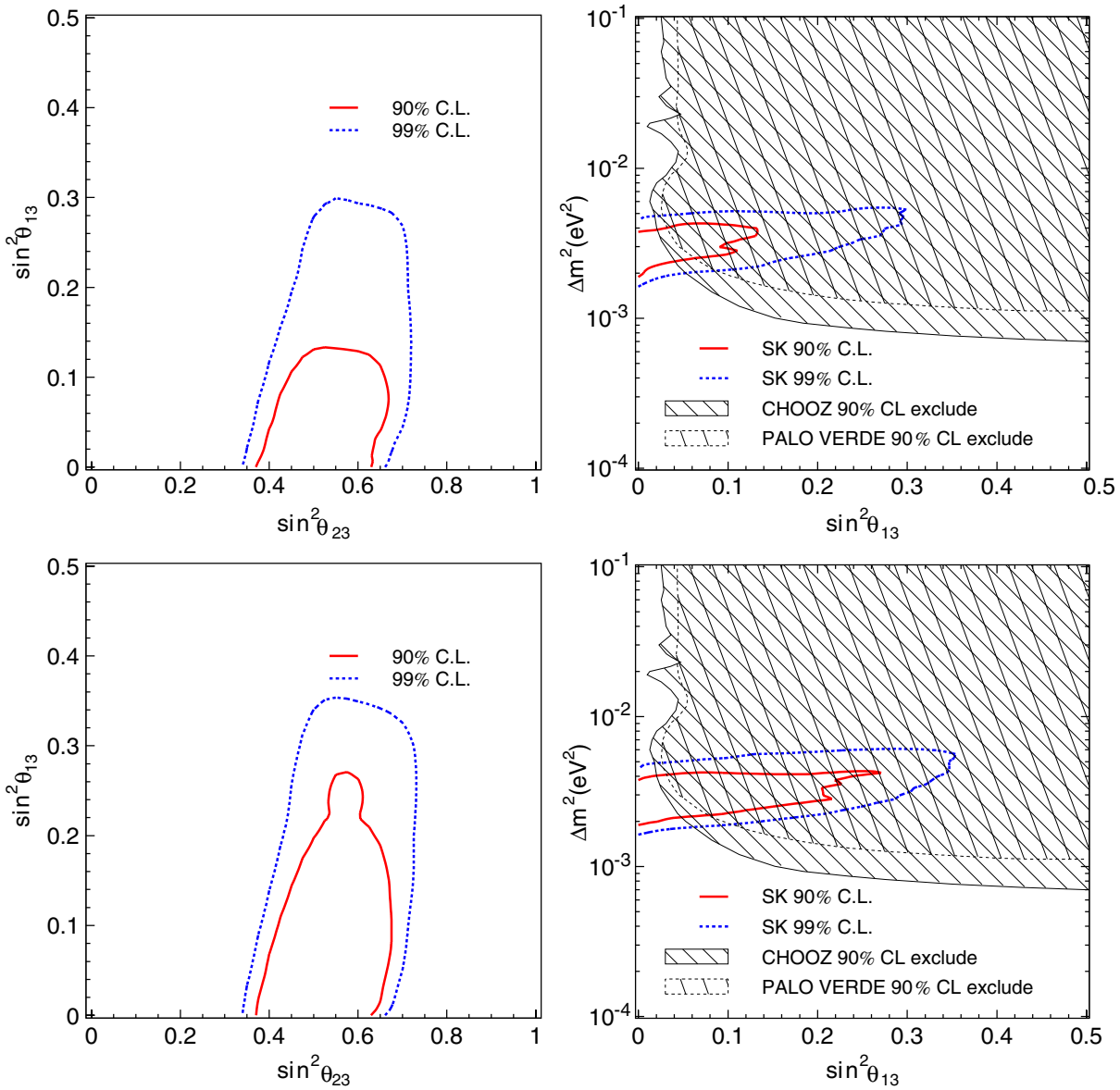

Figure 22. Allowed regions on the $\sin^2\theta_{23}$ and $\sin^2\theta_{13}$ plane (left) and the $\sin^2\theta_{13}$ and Δm^2_{23} plane (right) obtained by a three-flavour analysis of the Super-Kamiokande data (preliminary). Solid and dotted lines show the 90 and 99% CL allowed regions, respectively. Also shown in the right figures are the excluded regions by CHOOZ (shaded region) and Palo Verde (thin broken line in the shaded region) reactor experiments. The upper and lower panels are for positive and negative Δm^2_{23}, respectively.

deficit of CC ν_μ events, there have been several proposals for alternative explanations. One proposal was neutrino oscillations between ν_μ and ν_{sterile}, where ν_{sterile} is a neutrino-like particle that does not interact with matter by either CC or NC weak interactions. Since the deficit is seen for CC ν_μ events, $\nu_\mu \leftrightarrow \nu_{\text{sterile}}$ could explain the atmospheric neutrino data. Because the possible

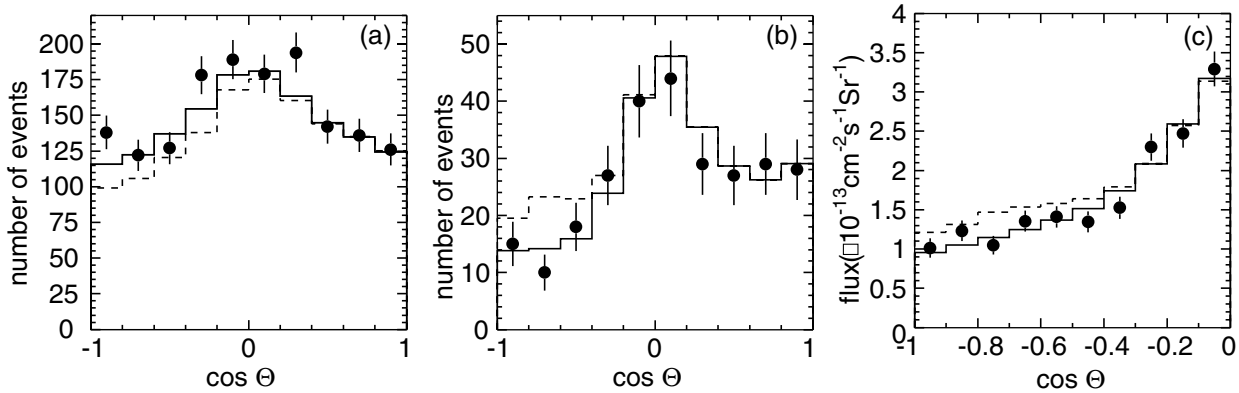

Figure 23. Zenith-angle distributions for: (a) multi-ring events with the most energetic ring being e-like and $E_{\rm vis} > 400$ MeV, (b) PC events with $E_{\rm vis} > 5$ GeV and (c) upward-through-going muon events [77]. The detector exposure was 70.5 kt · year for FC and PC events and 1138 days for upward-through-going muons. In these figures, solid (broken) histograms show predictions for $\nu_\mu \to \nu_\tau$ ($\nu_\mu \to \nu_{\rm sterile}$) oscillations with $\Delta m^2 = 3 \times 10^{-3}\,{\rm eV}^2$ and $\sin^2 2\theta = 1.0$. The predictions are normalized so that the numbers of observed and predicted events are equal at $0.4 < \cos\Theta < 1.0$ (for (a) and (b)) and $-0.4 < \cos\Theta < 0.0$ (for (c)).

existence of $\nu_{\rm sterile}$ has significant impact on particle physics and cosmology, it must be studied seriously whether $\nu_\mu \to \nu_{\rm sterile}$ oscillation is really favoured by the atmospheric neutrino data.

There are several ways to discriminate between the two possibilities. One possibility is to use a matter effect for upward going neutrino events [75, 76]. In the case of $\nu_\mu \to \nu_{\rm sterile}$ oscillations, the matter effect could change the oscillation probability significantly, while there is no change in the $\nu_\mu \to \nu_\tau$ oscillation probability. For $\Delta m^2 \sim (2\text{–}3) \times 10^{-3}\,{\rm eV}^2$, the oscillation probability is expected to be significantly different only for high-energy (>10–20 GeV) atmospheric neutrinos travelling through the Earth. In addition, the zenith-angle distribution for an NC-enriched sample is useful to discriminate between the two possibilities, because the NC events should be affected only for $\nu_\mu \to \nu_{\rm sterile}$ oscillations.

Super-Kamiokande analysed NC-enriched multi-ring, high-energy PC with $E_{\rm vis} > 5$ GeV, and upward-through-going muon events [77]. Multi-ring events with the most energetic ring being e-like and $E_{\rm vis} > 400$ MeV were used. The estimated fraction of NC events (in the absence of neutrino oscillations) was 29%. Figure 23 shows the zenith angle distributions for these samples. It is clear that all the data samples disfavour $\nu_\mu \to \nu_{\rm sterile}$ oscillations. Also, in MACRO, the zenith-angle distribution of upward-through-going muons was studied [78]. Pure $\nu_\mu \to \nu_{\rm sterile}$ oscillation has been excluded at more than 99% CL [77, 78].

Using all the atmospheric neutrino data from Super-Kamiokande, neutrino oscillations between ν_μ and ν_x have been studied, where ν_x is a mixed flavour state ($\cos\xi\nu_\tau + \sin\xi\nu_{\rm sterile}$) [79]. No evidence for a finite sterile neutrino component as a partner of the ν_μ oscillations has been observed. The upper limit on the $\nu_{\rm sterile}$ admixture is $\sin^2\xi < 0.20$ at 90% CL [50]. Very similar results based on the present data were obtained by various authors, see, for example, [80]. We, however, mention that the differences in the zenith angle distributions between $\nu_\mu \leftrightarrow \nu_\tau$ and $\nu_\mu \leftrightarrow \nu_{\rm sterile}$ are relatively small. Therefore it is important to control various systematic effects to

obtain stronger constraints on the ν_{sterile} admixture. Also, it is desirable to carry out a significantly different experiment on the ν_{sterile} admixture. One example is a long-baseline experiment to test the disappearance of NC events (such as single π^0 events) [81]. Finally, we stress that the detection of CC ν_τ interactions in future atmospheric or long-baseline experiments [82] will be further evidence against $\nu_\mu \leftrightarrow \nu_{\text{sterile}}$ oscillations.

5.10. Other interpretations

Possible non-standard neutrino interactions or properties can also generate neutrino oscillations. There have been several proposals for such mechanisms, such as neutrino oscillations generated by the violation of Lorentz invariance [83]. A list of possibilities can be found in [84]–[87]. We do not discuss the details of these models, although we mention that, in many such models, the energy dependence of the oscillation probability does not take the form $P(\nu_\mu \to \nu_\mu) = \alpha \sin(\beta L E_\nu^{-1})$, where α and β are constants. Instead, some of the models take the form, $P(\nu_\mu \to \nu_\mu) = \alpha \sin(\beta L E_\nu^n)$, where $n = 0$ or 1.

Since the atmospheric neutrino data cover the energy range from about 0.1 to 10^3 GeV, the energy dependence of the oscillation can be studied in detail. The Super-Kamiokande data (500 days of the detector exposure) were analysed in [85]. The data were fitted with n as a free parameter. It was found that $n = -0.9 \pm 0.4$ at 90% CL, thus essentially excluding non-standard oscillation models which take either $n = 0$ or 1. A similar conclusion was obtained in [84].

Some of the non-standard neutrino oscillations cannot be described by the above form. An important example of such a model is neutrino oscillations generated by flavour changing neutral currents (FCNC) [86]. In this case, the L/E_ν in the mass-generated neutrino oscillation is replaced by the column density. In this model, there is no energy dependence in the oscillations. Furthermore, since air has a density much lower than that of the Earth, down-going neutrinos are essentially unaffected. Therefore, the neutrino oscillation probability is a function of the zenith angle only. A detailed analysis of the atmospheric neutrino data in terms of FCNC was carried out in [84, 86, 87]. They observed that this model was essentially ruled out because, among other reasons, the observed upward-through-going muons had a deficit considerably smaller than the deficit of upward-going stopping muons and upward-going multi-GeV muons.

So far, we have assumed that the neutrino oscillation parameters are identical between neutrinos and anti-neutrinos. This assumption is correct under the CPT invariance. However, there are discussions that the neutrino oscillation parameters Δm^2_{ij} and θ_{ij} could be different between neutrinos and anti-neutrinos [88]. The Super-Kamiokande data have been analysed with different neutrino oscillation parameters for neutrinos and anti-neutrinos, resulting in no evidence for different neutrino and anti-neutrino oscillation parameters [50].

Finally, it should be mentioned that the recent L/E analysis from Super-Kamiokande [62] strongly disfavours these non-standard scenarios. With increasing data and improved analyses, it is getting clearer that $\nu_\mu \to \nu_\tau$ generated by neutrino mass is the dominant channel and that non-standard neutrino oscillations or flavour change does not contribute to the ν_μ deficit substantially [89].

6. Prospects of future atmospheric neutrino experiments

In addition to data described so far, unique data from several new experiments are expected to be available soon. SNO [63] is primarily a solar neutrino detector. However, because of the

great depth of the detector location (see figure 6), down-going muons near the horizon are due mostly to neutrino interactions. These neutrinos should have little oscillation effect, and should give very good calibration of the absolute neutrino flux at about 100 GeV neutrino energies. MINOS [90] is a detector designed primarily for accelerator long-baseline neutrino experiments. It has a magnetic field and can identify the charge of a long track. MINOS can make a unique contribution to atmospheric neutrino studies by measuring the μ^+/μ^- (or equivalently $\overline{\nu}_\mu/\nu_\mu$) ratio. ICARUS [91] is a 600 t liquid argon TPC. It will reconstruct events with unprecedented resolution. Although the mass of the detector is relatively small, high-resolution measurements of atmospheric neutrinos might give us unique information.

So far, there have been several considerations of future detectors that can improve our knowledge of neutrino masses and ixings through studies of atmospheric neutrinos. One type of the detectors is huge water Cherenkov detectors such as Hyper-Kamiokande [81] or UNO [92]. These detectors are assumed to have a mass of about 0.5–1 Mt. Another type of detectors is magnetized tracking detectors. Examples of such detectors are MONOLITH [93] and INO [94]. The masses for these detectors are assumed to be several tens of kt. The other possibility is a large liquid argon detector [91] with a mass similar to the other types of detectors and possibly a magnetic field inside the detector. We discuss below the physics potential of these atmospheric neutrino detectors.

6.1. Measurement of $\sin^2 2\theta_{23}$ *and* Δm^2_{23}

The mixing parameters, θ_{ij}, are one of a few fundamental parameters that could constrain theories beyond the standard model of particle physics. Therefore, it is important to measure $\sin^2 2\theta_{23}$ as accurately as possible. The atmospheric neutrino flux is accurately predicted to be up–down symmetric in the multi-GeV energy range. The numbers of downward- and upward-going ν_μ events and $\sin^2 2\theta_{23}$ are related by $(up/down)_{\rm Data}/(up/down)_{\rm MC} \simeq 1 - (\sin^2 2\theta_{23})/2$ to first approximation, assuming that there is no (full) oscillation effect for downward (upward)-going neutrinos. The systematic error in the up–down ratio measurement is about 1% in the present Super-Kamiokande experiment [44]. Hence atmospheric neutrino data are useful for an accurate measurement of $\sin^2 2\theta_{23}$. The accuracy of the $\sin^2 2\theta_{23}$ measurement will be improved with (exposure time)$^{1/2}$ and will be about $\pm 2\%$ at 1σ for 1 Mt · year exposure of a water Cherenkov detector 95.

Super-Kamiokande has shown that Δm^2_{23} can be measured accurately by measuring a dip in the L/E distribution [62]. It is difficult to predict the general sensitivity as a function of the detector exposure. Especially, in the case of water Cherenkov detectors, the sensitivity strongly depends on the true Δm^2_{23} value, because the dip moves to a lower L/E position (i.e., a higher neutrino energy for the same L) for a higher Δm^2_{23}. The number of events decreases for higher energy neutrinos. In addition, the acceptance for fully contained events decreases for higher energy neutrinos. Hence, the sensitivity in Δm^2_{23} gets worse rapidly with higher Δm^2_{23}. We, however, note that large atmospheric neutrino experiments could compete in the Δm^2_{23} measurement with future long-baseline neutrino experiments if the true Δm^2_{23} value is near the lower edge of the presently allowed Δm^2 region, where the planned long-baseline experiments have somewhat limited sensitivities. A few per cent measurement of Δm^2_{23} is possible with more than 1 Mt · year exposure of a large water Cherenkov detector, if the true Δm^2_{23} is smaller than 2.0×10^{-3} eV^2 [96].

6.2. θ_{13}

The effect of a non-zero θ_{13} could be observed as an excess of ν_e events in the upward-going direction through the matter resonance effect in the multi-GeV energy range (see figure 21). The sensitivity to θ_{13} of a large water Cherenkov detector was discussed in detail in [96]. If $\theta_{23} = 45°$, as 3 SD sensitivity is about $\sin^2 2\theta_{13} > 0.02$ for 450 kt · year exposure. The chance of observing finite θ_{13} rapidly improves for larger $\sin^2\theta_{23}$ [97]. Also, the sensitivity does not depend strongly on Δm^2_{23}. Finally, it should be mentioned that finite θ_{13} could make it possible to discriminate $\theta_{23} > 45°$ and $< 45°$.

6.3. Sign of Δm^2

The resonance effect occurs only for neutrinos for positive Δm^2 and, therefore, only appears for the e^- and μ^- spectrum. This, in turn, suggests that the sign of Δm^2_{23} could be measured by atmospheric neutrino experiments. It is generally believed that a massive magnetized detector, which can measure the charge of muons, is necessary to measure the sign of Δm^2_{23} [93]. With a 200 (400) kt · year exposure, it will be possible to determine the sign of Δm^2 at 90% CL if $\sin^2 2\theta_{13} > 0.1$ (0.05).

Super-Kamiokande and other water Cherenkov detectors are unable to distinguish ν_e and $\overline{\nu}_e$ interactions on event-by-event basis. However, the cross section and the y $(=(E_\nu - E_{\text{lepton}})/E_\nu)$ dependence of the cross section are different between ν and $\overline{\nu}$ and, therefore, it may be possible to distinguish the positive and negative Δm^2_{23}. For positive Δm^2_{23}, the resonance effect occurs only for neutrinos. Since the neutrino interactions produce more high-y events (i.e., more multi-hadron events) than the anti-neutrino interactions, a larger effect of the finite θ_{13} can be seen in multi-ring e-like events for positive Δm^2_{23} than for negative Δm^2_{23}. Detailed Monte Carlo studies showed that it is possible to measure the sign of Δm^2_{23} in water Cherenkov detectors, if the $\sin^2\theta_{13}$ and $\sin^2\theta_{23}$ values are near the present limit ($\sin^2 2\theta_{13} > (0.01\text{–}0.02)$) and $\geqslant 0.5$, respectively, provided that the detector exposure is >1 Mt · year [96].

6.4. Effects of the solar oscillation terms

The present analyses of the atmospheric neutrino data do not include the oscillation terms that are related to solar neutrinos (θ_{12} and Δm^2_{12}). It has been pointed out that these terms (and the interference terms between the terms related to θ_{13} and θ_{12}) could play a unique role in the atmospheric neutrino oscillations, such as the possible measurement of $\sin^2\theta_{23}$ (i.e., the discrimination of $\theta_{23} > 45°$ and $<45°$) [66, 67]. These effects have been studied by taking various systematic errors into account [98].

7. Summary

Atmospheric neutrinos have played essential roles in the discovery of neutrino oscillations and are still contributing significantly to the study of neutrino oscillations. The atmospheric neutrino data from various experiments are well explained by $\nu_\mu \to \nu_\tau$ oscillations. Many proposed non-standard explanations have been excluded by detailed studies of the high statistics atmospheric neutrino data. In particular, recent L/E analysis from Super-Kamiokande gives the first direct evidence that the neutrino survival probability obeys the sinusoidal function

as predicted by neutrino oscillations. The 90% CL allowed region of neutrino oscillation parameters from the Super-Kamiokande's L/E analysis is: $1.5 \times 10^{-3} < \Delta m^2_{23} < 3.4 \times 10^{-3}\,\mathrm{eV}^2$ and $\sin^2 2\theta_{23} > 0.92$. Atmospheric neutrino experiments are also sensitive to θ_{13}. However, no evidence for non-zero θ_{13} has been observed.

Although the present atmospheric neutrino data are explained by $\nu_\mu \to \nu_\tau$ oscillations, there are several open questions. These questions must be addressed in future neutrino oscillation experiments including atmospheric neutrino and long-baseline neutrino oscillation experiments. Especially, it would be possible for the future atmospheric neutrino experiments to measure the $\sin^2 2\theta_{23}$ and Δm^2_{23} values precisely, to observe a non-zero θ_{13} and to determine the sign of Δm^2_{23}, if the true θ_{13} is relatively large. The study of neutrino oscillations will continue to be an important and exciting field and atmospheric neutrino experiments are likely to contribute to this field substantially.

Acknowledgments

We gratefully acknowledge the members of the Super-Kamiokande collaboration for useful discussions and information. This work was partially supported by the Japanese Ministry of Education, Culture, Sports, Science and Technology and the Japan Society for the Promotion of Science.

References

[1] Yanagida T 1979 *Proc. Workshop Unified Theory and Baryon Number in the Universe (KEK report 79-18)* ed O Sawada and A Sugamoto, p 95
[2] Gell-Mann M, Lamond P and Slansky R 1979 *Supergravity* ed P van Nieuwenhuizen and D Z Freedman (Amsterdam: North-Holland) p 315
[3] Pati J C and Salam A 1973 *Phy. Rev. Lett.* **31** 661
[4] Georgi H and Glashow S L 1974 *Phy. Rev. Lett.* **32** 438
[5] Maki Z, Nakagawa M and Sakata S 1962 *Prog. Theor. Phys.* **28** 870
[6] Pontecorvo B 1967 *Zh. Eksp. Teor. Fiz.* **53** 1717
Pontecorvo B 1968 *Sov. Phys.—JETP* **26** 984 (Engl. transl.)
[7] Eidelman S *et al* (Particle Data Group) 2004 *Phys. Lett.* B **592** 1
[8] Achar C V *et al* 1965 *Phys. Lett.* **18** 196
Achar C V *et al* 1965 *Phys. Lett.* **19** 78
Krishnaswamy M R *et al* 1971 *Proc. R. Soc.* A **323** 489
[9] Reines F *et al* 1965 *Phys. Rev. Lett.* **15** 429
[10] Crouch M F *et al* 1978 *Phys. Rev.* D **18** 2239
[11] Haines T J *et al* 1986 *Phys. Rev. Lett.* **57** 1986
[12] Nakahata M *et al* 1986 *J. Phys. Soc. Japan* **55** 3786
[13] Hirata K S *et al* 1988 *Phys. Lett.* B **205** 416
[14] Casper D *et al* 1991 *Phys. Rev. Lett.* **66** 2561
Becker-Szendy R *et al* 1992 *Phys. Rev.* D **46** 3720
[15] Aglietta M *et al* 1989 *Europhys. Lett.* **8** 611
[16] Berger Ch *et al* 1989 *Phys. Lett.* B **227** 489
Berger Ch *et al* 1990 *Phys. Lett.* B **245** 305
[17] Daum K *et al* 1995 *Z. Phys.* C **66** 417
[18] Fukuda Y *et al* 1994 *Phys. Lett.* B **335** 237

[19] Fukuda Y *et al* 1998 *Phys. Rev. Lett.* **81** 1562
[20] Honda M, Kajita T, Kasahara K and Midorikawa S 2004 *Phys. Rev.* D **70** 043008
[21] Barr G *et al* 2004 *Phys. Rev.* D **70** 023006
[22] Battistoni G, Ferrari A, Montaruli T and Sala P R 2003 *Preprint* hep-ph/0305208
[23] Gaisser T K and Honda M 2002 *Ann. Rev. Nucl. Part. Sci.* **52** 153
[24] Honda M, Kajita T, Kasahara K and Midorikawa S 1995 *Phys. Rev.* D **52** 4985
[25] Agrawal V, Gaisser T K, Lipari P and Stanev T 1996 *Phys. Rev.* D **53** 1314
[26] Alcaraz J *et al* 2000 *Phys. Lett.* B **490** 27
[27] Sanuki T *et al* 2000 *Astrophys. J.* **545** 1135
[28] Battistoni G *et al* 2000 *Astropart. Phys.* **12** 315
[29] Lipari P 2000 *Astropart. Phys.* **14** 153
[30] Lipari P 2001 *Nucl. Phys.* B *(Proc. Suppl.)* **81** 159
[31] Llewellyn Smith C H 1972 *Phys. Rep.* **3** 261
[32] Smith R A and Moniz E J 1972 *Nucl. Phys.* B **43** 605
[33] Rein D and Sehgal L M 1981 *Ann. Phys.* **133** 79
[34] Rein D and Sehgal L M 1983 *Nucl. Phys.* B **223** 29
[35] Perkins D H 1984 *Ann. Rev. Nucl. Part. Sci.* **34** 1
[36] Becker-Szendy R *et al* 1993 *Nucl. Instrum. Methods* A **324** 363
[37] Nakamura K *et al* 1994 *Physics and Astrophysics of Neutrinos* ed M Fukugita and A Suzuki (Berlin: Springer) p 249
[38] Fukuda Y *et al* 2003 *Nucl. Instrum. Methods* A **501** 418
[39] Battistoni G *et al* 1986 *Nucl. Instrum. Methods* A **245** 277
[40] Berger Ch *et al* 1987 *Nucl. Instrum. Methods* A **262** 463
[41] Allison W W M *et al* 1996 *Nucl. Instrum. Methods* A **376** 36
Allison W W M *et al* 1996 *Nucl. Instrum. Methods* A **381** 385
[42] Alekseev E N *et al* 1998 *Phys. Part. Nucl.* **29** 254
[43] Ahlen S P *et al* 1993 *Nucl. Instrum. Methods* A **324** 337
Ambrosio M *et al* 2002 *Nucl. Instrum. Methods* A **486** 663
[44] Super-Kamiokande Collaboration 2004, in preparation
[45] Giorgini M (for the MACRO collaboration) 2002 *Proc. 3rd Int. Conf. on Particle Physics Beyond the Standard Model: Accelerator, Non-Accelerator and Space Approaches (Oulu, Finland, June 2002)*, ed H V Klapdor-Kleingrothaus p 353
[46] Hirata K S *et al* 1992 *Phys. Lett.* B **280** 146
[47] Allison W W M *et al* 1999 *Phys. Lett.* B **449** 137
[48] Clark R *et al* 1997 *Phys. Rev. Lett.* **79** 345
[49] Mann W A, Kafka T and Leeson W 1992 *Phys. Lett.* B **291** 200
[50] Kearns E, for the Super-Kamiokande Collaboration 2004 talk presented at the *XXI Int. Conf. on Neutrino Physics and Astrophysics (Neutrino 2004, Paris, June 2004)*
[51] Sanchez M *et al* 2003 *Phys. Rev.* D **68** 113004
[52] Ambrosio M *et al* 2004 *Eur. Phys. J.* C **36** 323
[53] Giacomelli G *et al* 2004 *Phys. Atom. Nucl.* **67** 1139
[54] Fogli G L *et al* 2002 *Phys. Rev.* D **66** 053010
[55] Hatakeyama S *et al* 1998 *Phys. Rev. Lett.* **81** 2016
[56] Ahn M H *et al* 2003 *Phys. Rev. Lett.* **90** 041801
[57] Nakaya T, for the K2K Collaboration 2004 talk presented at the, *XXI Int. Conf. on Neutrino Physics and Astrophysics (Neutrino 2004, Paris, June 2004)*
[58] Barger V D *et al* 1999 *Phys. Lett.* B **462** 109
[59] Grossman Y and Worah M P 1998 *Preprint* hep-ph/9807511
[60] Lisi E, Marrone A and Montanino D 2000 *Phys. Rev. Lett.* **85** 1166
[61] Ambrosio M *et al* 2003 *Phys. Lett.* B **566** 35

[62] Ashie Y *et al* 2004 *Phys. Rev. Lett.* **93** 101801
[63] Ahmed S N *et al* 2004 *Phys. Rev. Lett.* **92** 181301
[64] Smy M B *et al* 2004 *Phys. Rev.* D **69** 011104
[65] Araki T *et al* 2004 *Preprint* hep-ex/0406035
[66] Peres O L G and Smirnov Y Au 1999 *Phys. Lett.* B **456** 204
[67] Peres O L G and Smirnov Y Au 2004 *Nucl. Phys.* B **680** 479
[68] Mikheyev S P and Smirnov A Yu 1985 *Sov. J. Nucl. Phys.* **42** 1441
Mikheyev S P and Smirnov A Yu 1986 *Nuovo Cimento* C **9** 17
[69] Wolfenstein L 1978 *Phys. Rev.* D **17** 2369
[70] Fogli G L *et al* 1997 *Phys. Rev.* D **55** 4385
[71] Giunti C, Kim C W and Monteno M 1998 *Nucl. Phys.* B **521** 3
[72] Apollonio M *et al* 1999 *Phys. Lett.* B **466** 415
[73] Boehm F *et al* 2001 *Phys. Rev.* D **64** 112001
[74] Saji C, for the Super-Kamiokande Collaboration 2003 *Proc. 28th Int. Cosmic Ray Conf. (Tsukuba)* vol 3, ed T Kajita *et al* p 1267
[75] Liu Q Y, Mikheyev S P and Smirnov A Yu 1998 *Phys. Lett.* B **440** 319
[76] Lipari P and Lusignoli M 1998 *Phys. Rev.* D **58** 073005
[77] Fukuda S *et al* 2000 *Phys. Rev. Lett.* **85** 3999
[78] Ambrosio M *et al* 2001 *Phys. Lett.* B **517** 59
[79] Fogli G L, Lisi E and Marrone A 2001 *Phys. Rev.* D **63** 053008
[80] Maltoni M, Schwetz T, Tortola M and Valle J W F 2004 *Preprint* hep-ph/0405172
[81] Itow Y *et al* 2001 *Preprint* hep-ex/0106019
[82] Rubbia A 2001 *Nucl. Phys.* B *(Proc. Suppl.)* **91** 223
[83] Coleman S R and Glashow S L 1997 *Phys. Lett.* B **405** 249
[84] Lipari P and Lusignoli M 1999 *Phys. Rev.* D **60** 013003
[85] Fogli G L *et al* 1999 *Phys. Rev.* D **60** 053006
[86] Gonzalez-Garcia M C *et al* 1999 *Phys. Rev. Lett.* **82** 3202
[87] Fornengo N, Gonzalez-Garcia M C and Valle J W F 2000 *J. High Energy Phys.* JHEP07(2000)006
[88] Barenboim G, Borissov L, Lykken J and Smirnov A Yu 2002 *J. High Energy Phys.* JHEP210(2002)001
[89] Fornengo N, Maltoni M, Tomas Bayo R and Valle J W F 2002 *Phys. Rev.* D **65** 013010
[90] Michael D 2003 *Nucl. Phys. (Proc. Suppl.)* **118** 189
[91] Arneodo F *et al* 2001 *Nucl. Instrum. Methods* A **461** 324
[92] Jung C K 2000 *Preprint* hep-ex/0005046
[93] Tommaso Tabarelli de Fatis 2001 *Proc. La Thuile 2001, Results and Perspectives in Particle Physics (La Thuile, Italy)* p 677 (*Preprint* hep-ph/0106252)
[94] Rajasekaran G 2004 *Preprint* hep-ph/0402246
[95] Kajita T, for the Super-Kamiokande Collaboration 2001 *Nucl. Phys.* B *(Proc. Suppl.)* **100** 139
[96] Kajita T 2004 talk presented at the *5th Workshop on Neutrino Oscillations and their Origin (NOON 2004, Tokyo, February 2004)*
[97] Bernabeu J, Palomares-Ruiz S and Petcov S T 2003 *Nucl. Phys.* B **669** 255
[98] Gonzalez-Garcia M C, Maltoni M and Smirnov A Yu 2004 *Preprint* hep-ph/0408170

New Journal of Physics
The open-access journal for physics

Massive neutrinos and flavour violation

Antonio Masiero[1], **Sudhir K Vempati**[1] **and Oscar Vives**[2]

[1] Dipartimento di Fisica 'Galileo Galilei', Università di Padova, and INFN, Sezione di Padova, via F Marzolo 8, I-35131, Padova, Italy
[2] Theory Group, Physics Department, CERN, Geneva, Switzerland
E-mail: masiero@pd.infn.it, vempati@pd.infn.it and oscar.vives@cern.ch

New Journal of Physics **6** (2004) 202
Received 29 July 2004
Published 17 December 2004
Online at http://www.njp.org/
doi:10.1088/1367-2630/6/1/202

Abstract. In spite of the large lepton flavour violation (LFV) observed in neutrino oscillations, within the Standard Model, we do *not* expect any visible LFV in the charged lepton sector ($\mu \to e, \gamma, \tau \to \mu, \gamma$, etc). On the contrary, the presence of new physics close to the electroweak scale can enhance the amplitudes of these processes. We discuss this in general and focus on a particularly interesting case: the marriage of low-energy supersymmetry (SUSY) and seesaw mechanism for neutrino masses (SUSY seesaw). Several ideas presented in this context are reviewed both in the bottom-up and top-down approaches. We show that there exist attractive models where the rate for LFV processes can attain values to be probed in pre-LHC experiments.

1367-2630/04/010202+26$30.00
PII: S1367-2630(04)84689-5
© IOP Publishing Ltd and Deutsche Physikalische Gesellschaft

Contents

1. Introduction **2**
2. Supersymmetric models and lepton flavour violation **3**
3. Supersymmetric seesaw and leptonic flavour violation **6**
3.1. Model-independent expectations for LFV? 7
3.2. CP violation in the lepton sector 8
3.3. From LFV to seesaw parameters 9
4. What could be the neutrino Yukawa couplings? **9**
4.1. GUT models: an SO(10) example 10
4.2. What could be the neutrino Yukawa mixing matrices? 11
4.2.1. Minimal case: a model for CKM mixings 11
4.2.2. Maximal case: a method for PMNS mixings 13
4.3. Textures and other examples 16
5. Seesaw induced LFV and associated phenomenology **17**
5.1. LFV and experimental sensitivity to U_{e3} 17
5.2. Correlations with other SUSY search strategies 19
5.3. Seesaw-induced Hadronic FCNC and CPV 19
6. Alternatives to canonical seesaw and LFV **20**
7. Conclusions **21**
Acknowledgments **21**
References **21**

1. Introduction

Since the last couple of years of the previous century, tremendous progress has been made in our understanding of the nature of the most elusive Standard Model (SM) particles, the neutrinos. The main message of various experimental results has been that neutrinos have non-standard properties: they have masses and their flavour states mix and, indeed, with very large mixings. In the Standard Model, the phenomenon of flavour mixing is not surprising, as its presence has already been well established in the quark sector. Furthermore, the induced phenomenological implications such as K^0–$\bar{K}^0$ oscillations, B_d–$\bar{B}_d$ mixing and $b \to s, \gamma$ have been well understood as well as measured with high precision. Given this, and non-zero neutrino flavour mixing, one would expect that similar phenomenological and theoretical implications can now emanate from the leptonic sector.

The more obvious of the phenomenological implications of neutrino flavour mixing phenomena are processes like neutrino oscillations. On the other hand, the presence of this neutrino flavour mixing would also induce flavour mixing in its isodoublet partners, the charged leptons. This mixing, induced at the one-loop level through gauge bosons, is manifested by rare decay processes such as $\mu \to e, \gamma, \tau \to \mu, \gamma$, etc. If only the neutrinos carry this information on flavour mixing, as in the Standard Model with massive neutrinos, these processes are expected to be proportional to the ratio of masses of neutrinos over the masses of the W bosons, leading to extremely tiny branching ratios.

This situation can significantly change if there are some new additional particles carrying lepton flavour numbers, which have very large masses and simultaneously mix among themselves. The presence of such particles could lead to enhanced branching ratios for the above processes, perhaps bringing them into the realm of observability of the present and next generations of experiments. On the other hand, non-observability of these processes can lead to strong constraints on the nature of new physics, which is expected to be present just above the electroweak scale. Such constraints already exist from the hadronic sector, albeit riddled with typical uncertainties associated with them. The leptonic flavour changing processes, on the other hand, do not suffer from these uncertainties, and thus lead to stronger constraint on any new flavour violating physics. In fact, the present constraint on $\mathrm{BR}(\mu \to e, \gamma)$ has long been considered to be the most stringent constraint on any new flavour physics. To get a feeling as to where we stand, we provide here a list of present and upcoming experimental limits:

Present limits

$$\mathrm{BR}(\mu \to e\gamma) \leqslant 1.2 \times 10^{-11}\ [1],$$
$$\mathrm{BR}(\tau \to \mu\gamma) \leqslant 3.1 \times 10^{-7}\ [2],$$
$$\mathrm{BR}(\tau \to e\gamma) \leqslant 3.7 \times 10^{-7}\ [3].$$

Upcoming limits

$$\mathrm{BR}(\mu \to e\gamma) \leqslant 10^{-13}\text{–}10^{-14}\ [4],$$
$$\mathrm{BR}(\tau \to \mu\gamma) \leqslant 10^{-8}\ [3],$$
$$\mathrm{BR}(\tau \to e\gamma) \leqslant 10^{-8}\ [3].$$

The impact of these limits could be felt in a wide class of new physics models setting in at a scale close to the electroweak scale. A particularly interesting class of models are the supersymmetric (SUSY) Standard Model(s). In these models, the supersymmetric partners of the leptons, namely the sleptons, carry the same flavour quantum numbers as the SM leptons. Since they are expected to be heavy, around the TeV scale, if flavour mixing is present in the (s)leptonic sector, large branching ratios are expected for the aforementioned rare decay processes. Interestingly enough, this naturally occurs if we marry the idea of low-energy supersymmetry to the mechanism of seesaw [5] giving rise to small neutrino masses (SUSY seesaw [6]). In the present review, we will mainly concentrate on this class of models.

2. Supersymmetric models and lepton flavour violation

The study of flavour violation in supersymmetric models is certainly quite complicated. Indeed, to the usual intricacies involved in the FCNC computations in the SM, we add several new SUSY contributions. The main source of this difficulty is the soft supersymmetry breaking Lagrangian, which can in general contain a large number of flavour violating couplings, leading to significant constraints on its parameters [7, 8]. An appealing way to cope with these tight constraints is to consider only a particular classes of soft Lagrangians, which result from models that break supersymmetry in a flavour blind manner, as in mSUGRA, anomaly-mediated supersymmetry breaking (AMSB) or its several variants, gauge-mediated supersymmetry breaking (GMSB), etc [9]. However, in general, even after choosing a particular model of supersymmetry breaking,

flavour violation can still be present in the weak-scale Lagrangian. The various sources of flavour violation in such a case can be broadly classified as:[3]

(i) In models of supersymmetry breaking based on supergravity or superstring theories, although it is possible to achieve universality or even no-scale boundary conditions under some assumptions on the Kähler potential, non-universal soft terms are generically present in the high-scale effective Lagrangian [10].

(ii) In models with flavour symmetry imposed by a Froggatt–Nielsen mechanism, flavour violating corrections to the soft potential could be potentially large [11]. More so, if the flavon fields contain SUSY breaking F-VEVs [12, 13].

(iii) Finally, the existence of new particles at high scales with flavour violating couplings to the SM leptons (as right-handed neutrinos in a seesaw model [6]) or the presence of new Yukawa interactions (as in Grand Unified Theories where quark and leptonic fields sit in the same (super)multiplets [14]) can lead to flavour violation at the weak scale. In this case, the flavour violation is communicated to the low-energy fields through renormalization group equations (RGEs) [15].

Obviously, this list is not exhaustive. There can be other exotic sources which can be either additional heavy Higgs particles [16] or are related to the localization of the fermions in higher-dimensional space-time when MSSM/SUSY-GUT is embedded in a extra-dimensional model [17, 18].

In the present review, we will concentrate on the flavour violation solely due to a mechanism generating neutrino masses and mixings. To this effect, we would consider models where the *strong* universality is assumed at the high scale and thus point (i) would not be considered here. Similarly, we will not consider either effects generated by the imposition of a flavour symmetry as in (ii). Instead, the main aspect of this review will be to collect some salient features of the flavour violation induced by a neutrino mass model in a supersymmetric theory. As was mentioned in the introduction, the most natural and popular of them, the seesaw mechanism, will be our main focus. Notice that these RGE effects are always present in any SUSY seesaw model, independently of the presence of the other sources in (i) and (ii). In this sense, the effects considered here are independent of the particular mechanism of SUSY breaking and mediation. These model-dependent effects in (i) and (ii) can always be added to our results in the relevant cases.

Irrespective of the source, LFV at the weak scale can be parametrized in a model-independent manner in terms of a mass insertion (MI), Δ^l_{ij}, the flavour violating off-diagonal entry appearing in the slepton mass matrix.[4] These MI are further subdivided into LL/LR/RL/RR types, labelled by the chirality of the corresponding SM fermions.[5] Depending on the model, one or several of these types of MI can simultaneously be present at the weak scale. In the presence of any of these parameters, one-loop diagrams mediated by gauginos, higgsinos (neutral and three charged fermionic partners of gauge and Higgs bosons) and sleptons lead to lepton flavour violating processes such as $\mu \to e + \gamma$, $\mu \to 3e$, $\mu \to e$ conversion in nuclei, etc (an example diagram is shown in figure 1). The strength of these processes crucially depends on the MI factor

[3] We assume R-parity conservation throughout the present work.

[4] In the basis where the charged lepton mass matrix is diagonal.

[5] i, j, k denote generation indices throughout the work.

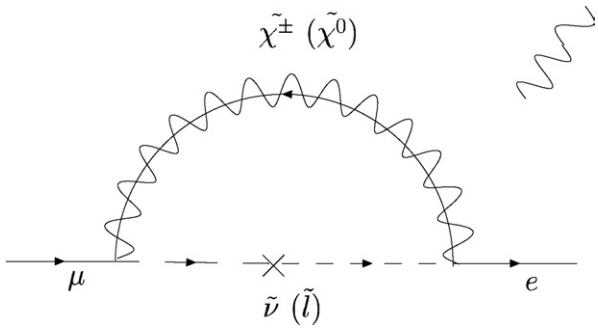

Figure 1. The diagrams contributing to $\mu \to e, \gamma$ decays.

$\delta^l_{ij} \equiv \Delta^l_{ij}/m^2_{\tilde{l}}$, where $m^2_{\tilde{l}}$ is the average slepton mass. For $|\delta| < 1$, which is expected to be the case for most models, one can always use the MI approximation [15, 19] to compute the amplitudes of the relevant processes. Such computations have been done long ago, considering the neutral gaugino diagrams [6, 7]. It has been realized later that, in addition to the flavour violating LL/RR MI, considering the Higgsinos/gaugino mixing, as well as the flavour diagonal left–right mixing in the slepton mass matrix, can significantly enhance the amplitudes of these processes at large $\tan\beta$ [20]. These computations have since then been updated by Hisano and Nomura [21] and Masina and Savoy [22], including this mixing as well as the charged gaugino/higgsino contribution.[6] Taking the $\tan\beta$ factor into account, the branching ratio of $l_j \to l_i, \gamma$ for the dominant LL MI is roughly given by

$$\mathrm{BR}(l_j \to l_i\gamma) \approx \frac{\alpha^3 |\delta^l_{ij}|^2}{G_F^2 m^4_{\mathrm{SUSY}}} \tan^2\beta, \tag{1}$$

where m_{SUSY} represents the typical supersymmetry breaking mass such as the gaugino/slepton mass. For large $|\delta| \sim 1$ or for many δ's present simultaneously, it is instructive to diagonalize the slepton mass matrix and evaluate the precise amplitudes in the mass-eigenstate basis. A complete computation in this basis has been presented in [23] for several LFV processes such as $l_j \to l_i + \gamma$, $l_j \to 3l_i$, $\mu \to e$ conversion in nuclei. The processes discussed so far are the ones mediated by neutralino and chargino sector. However, Higgs bosons (h^0, H^0, A^0) are also sensitive to flavour violation and mediate processes such as $\mu \to e$ conversion [25], $\tau \to 3\mu$ [26] and $\tau \to \mu\eta$ [27]. The amplitudes of these processes are sensitive to a higher degree in $\tan\beta$ than the chargino/neutralino ones (the BRs grow as $(\tan\beta)^6$, although they are suppressed by additional Yukawa couplings) and thus could lead to large branching fractions at large $\tan\beta$. Detailed studies on the $\mu \to \tau$ sector have been presented in the literature [28].

In the rest of the review, we will consider the decay $l_j \to l_i, \gamma$ as the prototype signature of the lepton flavour violation. We will discuss several ideas put forward in the literature on the sensitivity of this decay process in determining the seesaw parameter space as well as the supersymmetric parameter space. Before this, we will briefly review the SUSY seesaw mechanism and the generation of flavour violation in this model.

[6] Another important feature is that the interference between various contributions could lead to suppressed amplitudes in some regions of the parameter space [21]–[23]. This typically occurs for RR type MI as long as universality in the gaugino masses is maintained at the high scale. Although in a completely generic situation without any universal boundary conditions, such cancellations can also occur for LL type MI [24].

3. Supersymmetric seesaw and leptonic flavour violation

The seesaw mechanism can be incorporated in the Minimal Supersymmetric Standard Model in a manner similar to what is done in the SM, by adding right-handed neutrino superfields to the MSSM superpotential:

$$W = h^u_{ij} Q_i u^c_j H_2 + h^d_{ii} Q_i d^c_i H_1 + h^e_{ii} L_i e^c_i H_1 + h^\nu_{ij} L_i \nu^c_j H_2 + M_{R_{ii}} \nu^c_i \nu^c_i + \mu H_1 H_2, \tag{2}$$

where we are in the basis of diagonal charged lepton, down quark and right-handed Majorana mass matrices. M_R represents the (heavy) Majorana mass matrix for the right-handed neutrinos. Equation (2) leads to the standard seesaw formula for the (light) neutrino mass matrix

$$\mathcal{M}_\nu = -h^\nu M_R^{-1} h^{\nu\mathrm{T}} v_2^2, \tag{3}$$

where v_2 is the vacuum expectation value (VEV) of the up-type Higgs field, H_2. Under suitable conditions on h^ν and M_R, the correct mass splittings and mixing angles in $\mathcal{M}_\nu$ can be obtained. Detailed analyses deriving these conditions are already present in the literature [29].

Following the discussion in the previous section, we will assume that the mechanism that breaks supersymmetry and conveys it to the observable sector at the high scale $\sim M_\mathrm{P}$ is flavour blind, as in mSUGRA. However, this flavour blindness is not protected down to the weak scale [6].[7] The slepton mass matrices are no longer invariant under RG evolution from the super large scale where supersymmetry is mediated to the visible sector down to the seesaw scale, as the flavour violation present in the neutrino Dirac Yukawa couplings h^ν is now 'felt' by the slepton mass matrices in the presence of heavy right-handed neutrinos.

The weak-scale flavour violation so generated can be obtained by solving the RGEs for the slepton mass matrices from the high scale to the scale of the right-handed neutrinos. Below this scale, the running of the FV slepton mass terms is RG-invariant as the right-handed neutrinos decouple from the theory. For the purpose of illustration, a leading log estimate can easily be obtained for these equations.[8] Assuming the flavour blind mSUGRA specified by the high-scale parameters, m_0, the common scalar mass, A_0, the common trilinear coupling and $M_{1/2}$, the universal gaugino mass, the flavour violating entries in these mass matrices at the weak scale are given as

$$(\Delta^l_{ij})_\mathrm{LL} \approx -\frac{3m_0^2 + A_0^2}{8\pi^2} \sum_k (h^\nu_{ik} h^{\nu *}_{jk}) \ln \frac{M_X}{M_{R_k}}, \tag{4}$$

where h^ν are given in the basis of diagonal charged lepton masses and diagonal Majorana right-handed neutrino mass matrix M_R and M_X is the scale at which soft terms appear in the Lagrangian. Given this, the branching ratios for LFV rare decays $l_j \to l_i, \gamma$ can be roughly estimated using (1). From above it is obvious that the amount of lepton flavour violation generated by the SUSY seesaw at the weak scale crucially depends on the flavour structure of h^ν and M_R, shown in (2), the 'new' sources of flavour violation not present in the MSSM. If either the neutrino Yukawa couplings or the flavour mixings present in h^ν are very tiny, the strength of LFV

[7] This is always true in a gravity-mediated supersymmetry breaking model, but it also applies to other mechanisms under some specific conditions [30, 31].

[8] Within mSUGRA, the leading log approximation works very well for most of the parameter space, except for regions of large $M_{1/2}$ and low m_0. The discrepancy with the exact result increases with low $\tan\beta$ [32].

will be significantly reduced. Furthermore, if the right-handed neutrino masses were heavier than the supersymmetry breaking scale (as in GMSB models) they would decouple from the theory before the SUSY soft breaking matrices enter into play and hence these effects would vanish.

3.1. Model-independent expectations for LFV?

A crucial feature of the seesaw mechanism is that it has a larger number of parameters than those relevant for neutrino masses and mixings. This would inhibit us in computing model-independent expectations for, say, BR($\mu \to e, \gamma$), given that the supersymmetric seesaw mechanism works at the high scale. In fact, even after having a complete knowledge of the entire neutrino mass matrix elements, $\mathcal{M}_\nu$ as well as the heavy neutrino Majorana mass matrix eigenvalues M_{R_k}, it is still not sufficient to completely determine the rest of the seesaw parameters, namely the neutrino Dirac Yukawa coupling matrix h^ν. This is best illustrated in the parametrization given by Casas and Ibarra [33]; starting from the seesaw formula (3), one can derive h^ν in terms of low-energy parameters as

$$h^\nu = U^\star_{PMNS} \mathcal{D}_{\sqrt{\mathcal{M}_\nu}} R^{\mathrm{T}} \mathcal{D}_{\sqrt{M_R}} \frac{1}{v_2}, \tag{5}$$

where U_{PMNS} is the Pontecorvo–Maki–Nakagawa–Sakata leptonic mixing matrix, $\mathcal{D}_{\sqrt{\mathcal{M}_\nu}}$ is the square root of the diagonal matrix of light neutrino mass eigenvalues, $\mathcal{D}_{\sqrt{M_R}}$ is the square root of the diagonal matrix of heavy neutrino mass eigenvalues and R is an arbitrary complex orthogonal matrix such that $RR^{\mathrm{T}} = 1$. The matrix R parametrizes our ignorance of the neutrino Yukawas in spite of the complete knowledge of the neutrino mass matrix. Although it is difficult to give a physical definition to 'R' it is important to note that it can have physical consequences for lepton flavour violation (as well as leptogenesis), even if the neutrino masses and mixings are already accounted for. For lepton flavour violation, the relevant part of the seesaw parameter space are the entries in the matrix $h^\nu h^{\nu\dagger}$ which are now given by

$$h^\nu h^{\nu\dagger} = U^\star_{PMNS} \mathcal{D}_{\sqrt{\mathcal{M}_\nu}} R^{\mathrm{T}} \mathcal{D}_{M_R} R^\star \mathcal{D}_{\sqrt{\mathcal{M}_\nu}} U^{\mathrm{T}}_{PMNS} \frac{1}{v_2^2}. \tag{6}$$

R can be parametrized by three angles and three phases. Flavour violation is now determined in terms of the angles and phases in R, U_{PMNS}, $\mathcal{M}_\nu$ and M_R. For a given neutrino spectrum, U_{PMNS} and neutrino mass eigenvalues are (approximately) known. However, the branching ratios can now be either enhanced or suppressed depending on the parameters in R. Choosing M_R to be either completely hierarchical or degenerate leads to a reduction in the number of parameters affecting the branching ratios. It is further reduced if R is chosen to be real. For example, if M_R is completely hierarchical and R is real, basically only one angle would affect the branching ratios. Similarly, when M_R is degenerate and R is real, the branching ratios are independent of R. Lepton flavour violating rates for various cases of interest have been analysed in [33] and special cases in [34, 35].

As mentioned earlier, flavour violation at the weak scale can be treated independently of the source in terms of the mass insertion parameters Δ^l_{ij}. In the seesaw model, these Δ parameters are generated by RGE evolution and are thus proportional to the neutrino Yukawa couplings. In

Table 1. Limits on δ_{LL} parameters derived in the mSUGRA model for $\tan\beta = 10$. The average slepton mass is chosen to be around 450 GeV and $M_0 \sim 500$ GeV. Our results agree with those presented in [21, 22].

$(\delta^l)_{LL}$	Present limits	Upcoming limits
12	2×10^{-4}	8.5×10^{-6}
13	0.09	0.02
23	0.09	0.02

mSUGRA, the relation between these two parameters is given as[9]

$$(\Delta^l_{ij})_{LL} \approx -\frac{3m_0^2 + A_0^2}{8\pi^2} C_{ij}, \tag{7}$$

where C_{ij} is defined to contain all the information from neutrino Yukawa couplings, specifically, the left-mixing angles and the eigenvalues [36, 37] and is given by

$$C_{ij} = [h^\nu h^{\nu\dagger}]_{ij} \log \frac{M_X}{M_R}. \tag{8}$$

C_{ij} is the part of the 'seesaw' parameter space that can be probed by LFV experiments. The various upper bounds on δ^l_{ij} from the experimental limits on $l_j \to l_i, \gamma$ decay rates and other LFV processes can now be converted to upper bounds on off-diagonal C_{ij} parameters [36] for each point in the SUSY breaking parameter space. In table 1, we present limits on $(\delta^l_{ij})_{LL}$ from the present and upcoming limits on $l_j \to l_i + \gamma$ processes [38, 39].

The implied bounds on C_{ij} can in turn be used to study constraints on neutrino Dirac Yukawa entries, for example, arising from a flavour model. The sensitivity of LFV experiments in probing the seesaw parameter space has been analysed by Ellis *et al* [37]. Choosing well-defined points in supersymmetric parameter space, such as the popular Benchmark/Snowmass points, scatter plots of C_{ij} parameter space[10] probed by several LFV processes such as $\mu \to e, \gamma$ are presented.

3.2. CP violation in the lepton sector

In addition to LFV, the SUSY seesaw can be responsible for several CP violating phenomena at both high and low energies in the leptonic sector. This can be facilitated by large amount of complex phases present in the seesaw couplings h^ν and/or M_R. We list some of these phenomena below:

(i) Leptogenesis [40].
(ii) CP violation in neutrino oscillations [41].
(iii) CP violation in $\Delta L = 2$ processes, such as neutrinoless double beta decay [42].
(iv) CP violation in $\Delta L = 1$ processes, such as CP violation in $\mu \to 3e$ etc [43, 44].

[9] Note that only LL type Δs are generated in the SUSY seesaw mechanism as long as one sticks to the superpotential given in (2).
[10] C_{ij} is denoted as H_{ij} in [37].

(v) Leptonic EDMs [45]–[47].

(vi) Slepton oscillations and CP violation in the sleptonic sector [48].

Since the source of both LFV and some of the above phenomena, say, leptogenesis, is the same set of parameters in the Lagrangian, some amount of correlation can be expected between these phenomena for some regions of the entire seesaw parameter space. However, such a correlation is in general not guaranteed, even if the two phenomena exist simultaneously. Such a study was carried out, by random scanning of the parameter space, by Ellis and collaborators in the case of hierarchical heavy neutrinos in [49] and for degenerate heavy neutrinos in [50]. Implications of low-energy observables, specifically LFV, for leptogenesis and vice versa can also be studied by using the R-parametrization introduced above for h^ν, or any of the other suitable parametrizations of a complex generic matrix, h^ν. Such studies have been carried out in [51]–[54]; other related studies are [55, 56]. A detailed analysis of correlations between all the leptonic phenomena is clearly beyond the scope of the present work.

3.3. From LFV to seesaw parameters

As we have seen so far, measuring the neutrino mass parameters $\Delta m^2_{\rm atm}$, $\Delta m^2_\odot$ and the mixing angles θ_{ij} more precisely would not lead us to any information on either the left- or the right-mixing angles present in h^ν or its eigenvalues. While it also holds true within the SM seesaw, the major advantage in the supersymmetric seesaw is the rich FCNC and CP violating phenomena associated with it. A natural question that follows is: Can we determine all the seesaw parameters by purely low-energy experiments? At this juncture, frankly, the question looks a bit ambitious given that we have still not yet completed the determination of the neutrino mixing matrix angles and phases as well as sg($\Delta m^2_{\rm atm}$). However, taking into consideration that (i) we have the possibility of low-energy supersymmetry being observable at the LHC, (ii) being probed in great detail at linear colliders, (iii) having improved sensitivity at the upcoming facilities such as MEGA and super-B/charm factories and (iv) improved determination of neutrino mass parameters at JPARC and long-base-line experiments, such an analysis may be required in the near future. As we will discuss later on, assuming a 'best case' scenario, the first hint of SUSY seesaw might in fact come from a $\mu \to e, \gamma$ decay, probably even before the advent of the LHC [57]. Later, more detailed evidence might pile up. Davidson and Ibarra [58] have presented a discussion on evaluating the seesaw parameters from low-energy observables. It has been shown that although there is a one-to-one correspondence between measurables at the weak- and the high-scale parameters, in practice, even in the simplest supersymmetric theories, such an analysis could be formidable to achieve. This is particularly true regarding the additional phases present in the sneutrino/slepton mass matrices. However, we continue to remain optimistic and let the future decide.

4. What could be the neutrino Yukawa couplings?

In the above, we have seen that due to our lack of knowledge on the neutrino Yukawa couplings, our predictions for lepton flavour violation are not effective enough in a purely bottom-up approach. This can be considered as a limitation of the model we have been working with, namely, the MSSM with right-handed neutrinos. A possible way out then could be to enlarge

the SM gauge group to a much larger group, such as a Grand Unified Theory. In these models, typically quark and leptons sit in the same multiplets, leading to relations between their Yukawa couplings. One would expect that similar correlations would occur when the seesaw mechanism is incorporated within a GUT. Under the simplest of the GUT groups, '$SU(5)$', however, the right-handed neutrinos remain singlets and the problem with LFV predictions still persists. One needs at least a group encompassing the Pati–Salam $SU(4)_c$ symmetry, like an $SO(10)$ model. Here we review one such example.

4.1. GUT models: an SO(10) example

In the $SO(10)$ gauge theory, all the known fermions and the right-handed neutrinos are unified in a single representation of the gauge group, the **16**. The product of two **16** matter representations can only couple to **10**, **120** or **126** representations, which can be formed by either a single Higgs field representation or a non-renormalizable product of representations of several Higgs fields. In either case, the Yukawa matrices resulting from the couplings to **10** and **126** are complex-symmetric, whereas they are antisymmetric when the couplings are to the **120**. Thus, the most general $SO(10)$ superpotential relevant to fermion masses can be written as

$$W_{SO(10)} = h_{ij}^{10} 16_i 16_j 10 + h_{ij}^{126} 16_i 16_j 126 + h_{ij}^{120} 16_i 16_j 120, \tag{9}$$

where i, j refer to the generation indices. In terms of the SM fields, the Yukawa couplings relevant for fermion masses are given by[11] [59]

$$\begin{aligned} &16\,16\,10 \supset 5(uu^c + \nu\nu^c) + \bar{5}(dd^c + ee^c), \\ &16\,16\,126 \supset 1\nu^c\nu^c + 15\nu\nu + 5(uu^c - 3\nu\nu^c) + \bar{45}(dd^c - 3ee^c), \\ &16\,16\,120 \supset 5\nu\nu^c + 45uu^c + \bar{5}(dd^c + ee^c) + \bar{45}(dd^c - 3ee^c), \end{aligned} \tag{10}$$

where we have specified the corresponding $SU(5)$ Higgs representations for each of the couplings and all the fermions are left-handed fields. The resulting mass matrices can be written as

$$M^u = M_{10}^5 + M_{126}^5 + M_{120}^{45}, \tag{11}$$

$$M_{LR}^\nu = M_{10}^5 - 3M_{126}^5 + M_{120}^5, \tag{12}$$

$$M^d = M_{10}^{\bar{5}} + M_{126}^{\bar{45}} + M_{120}^{\bar{5}} + M_{120}^{\bar{45}}, \tag{13}$$

$$M^e = M_{10}^{\bar{5}} - 3M_{126}^{\bar{45}} + M_{120}^{\bar{5}} - 3M_{120}^{\bar{45}}, \tag{14}$$

$$M_{LL}^\nu = M_{126}^{15}, \tag{15}$$

$$M_R^\nu = M_{126}^1. \tag{16}$$

[11] Recently, $SO(10)$ couplings have also been evaluated for various renormalizable and non-renormalizable couplings in [60].

A simple analysis of the above mass matrices leads us to the following result: *At least one of the Yukawa couplings in* $h^\nu = v_u^{-1} M_{LR}^\nu$ *has to be as large as the top Yukawa coupling* [61]. This result holds true in general, independent of the choice of the Higgses responsible for the masses in (11) and (12), provided that no accidental fine-tuned cancellations of the different contributions in equation (12) are present. If contributions from the **10**s solely dominate, h^ν and h^u would be equal. If this occurs for the **126**s, then $h^\nu = -3h^u$ [62]. In case both of them have dominant entries, barring a rather precisely fine-tuned cancellation between M_{10}^5 and M_{126}^5 in equation (12), we expect at least one large entry to be present in h^ν. A dominant antisymmetric contribution to top quark mass due to the **120** Higgs is phenomenologically excluded, since it would lead to at least a pair of heavy degenerate up-quarks.

Apart from sharing the property that at least one eigenvalue of both M^u and M_{LR}^ν has to be large, for the rest it is clear from (11) and (12) that these two matrices are not aligned, in general, and hence we may expect different mixing angles appearing from their diagonalization. This freedom is removed if one sticks to particularly simple choices of the Higgses responsible for up-quark and neutrino masses. A couple of remarks are in order here. Firstly, note that in general there can be an additional contribution, equation (15), to the light neutrino mass matrix, independent of the canonical seesaw mechanism. Taking into consideration also this contribution leads to the so-called Type-II seesaw formula [63]. Secondly, the correlation between neutrino Dirac Yukawa coupling and the top Yukawa is in general independent of the type of seesaw mechanism, and thus holds true irrespective of the light-neutrino mass structure.

4.2. What could be the neutrino Yukawa mixing matrices?

Within the $SO(10)$ example, we have seen above that the amount of mixing present in the neutrino Dirac Yukawa couplings, h^ν depends on the type and number of Higgs representations there are in the theory. Motivated by the flavour structure of SM fermions (including neutrino mixing angles), one can imagine two cases of mixings to be present in h^ν. The first one corresponds to a case where the mixing present in h^ν is small and CKM-like. We will call this case 'the minimal case'. This is typical of models in which quarks and leptons have the same mixing angles at the high scale. The required large mixing angles in the light-neutrino sector is purely resultant of the seesaw mechanism. As a second case, we consider scenarios where the mixing in h^ν is no longer small, but large like the observed PMNS mixing. In this case, the heavy neutrino mass matrix only plays the role of a large scale due to which light neutrino masses are suppressed. We will call this case the 'the maximal case'.[12] These two cases serve as 'benchmark' scenarios for seesaw-induced lepton flavour violation in SUSY $SO(10)$. Similar studies of these two extreme cases have also been considered in [23, 37].

4.2.1. Minimal case: a model for CKM mixings. The minimal Higgs spectrum to obtain phenomenologically viable mass matrices includes two **10**-plets, one coupling to the up-sector and the other to the down-sector. In this way, it is possible to obtain the required CKM mixing [64] in the quark sector. The $SO(10)$ superpotential is now given by

$$W_{SO(10)} = \tfrac{1}{2} h_{ij}^{u,\nu} 16_i 16_j 10_u + \tfrac{1}{2} h_{ij}^{d,e} 16_i 16_j 10_d + \tfrac{1}{2} h_{ij}^{R} 16_i 16_j 126. \tag{17}$$

[12] Note that these two cases are the two examples of how one can generate large mixing angles for light-neutrino mass matrices from the seesaw mechanism [29].

We further assume that the **126**-dimensional Higgs field gives Majorana mass *only* to the right-handed neutrinos. An additional feature of the above mass matrices is that all of them are *symmetric*. From here, it is clear that the following mass relations hold between the quark and leptonic mass matrices at the GUT scale:[13]

$$h^u = h^\nu, \qquad h^d = h^e. \tag{18}$$

In the basis where charged lepton masses are diagonal, we have

$$h^\nu = V_{\rm CKM}^{\rm T} h^u_{diag} V_{\rm CKM}. \tag{19}$$

The large couplings in $h^\nu \sim \mathcal{O}(h_t)$ induce significant off-diagonal entries in $m^2_{\tilde{L}}$ through the RG evolution between $M_{\rm GUT}$ and the scale of the right-handed Majorana neutrinos,[14] M_{R_i}. The induced off-diagonal entries relevant to $l_j \to l_i, \gamma$ are of the order of

$$(m^2_{\tilde{L}})_{21} \approx -\frac{3m_0^2 + A_0^2}{8\pi^2} h_t^2 V_{td} V_{ts} \ln \frac{M_{\rm GUT}}{M_{R_3}} + \mathcal{O}(h_c^2), \tag{20}$$

$$(m^2_{\tilde{L}})_{32} \approx -\frac{3m_0^2 + A_0^2}{8\pi^2} h_t^2 V_{tb} V_{ts} \ln \frac{M_{\rm GUT}}{M_{R_3}} + \mathcal{O}(h_c^2), \tag{21}$$

$$(m^2_{\tilde{L}})_{31} \approx -\frac{3m_0^2 + A_0^2}{8\pi^2} h_t^2 V_{tb} V_{td} \ln \frac{M_{\rm GUT}}{M_{R_3}} + \mathcal{O}(h_c^2). \tag{22}$$

In these expressions, the CKM angles are small but one would expect the presence of the large top Yukawa coupling to compensate such a suppression. The required right-handed neutrino Majorana mass matrix, consistent with both the observed low-energy neutrino masses and mixings as well as with CKM-like mixings in h^ν is easily determined from the seesaw formula defined at the scale of right-handed neutrinos[15]

$$M_R = V_{\rm CKM} h^u_{diag} V_{\rm CKM}^{\rm T} m_\nu^{-1} V_{\rm CKM} h^u_{diag} V_{\rm CKM}^{\rm T}, \tag{23}$$

where we have used equation (14) for h^ν. For hierarchical neutrino mass spectrum, $m_{\nu_3} \approx \sqrt{\Delta m^2_{\rm atm}}$, $m_{\nu_2} \approx \sqrt{\Delta m^2_\odot}$ and $m_{\nu_1} \ll \sqrt{\Delta m^2_\odot}$ and for a nearly bi-maximal U_{PMNS}, it is straightforward to see that the right-handed neutrino mass eigenvalues are given by

$$M_{R_3} \approx \frac{m_t^2}{4m_{\nu_1}}, \qquad M_{R_2} \approx \frac{m_c^2}{4m_{\nu_1}}, \qquad M_{R_1} \approx \frac{m_u^2}{2m_{\nu_1}}. \tag{24}$$

[13] Clearly, this relation cannot hold for the first two generations of down-quarks and charged leptons. One expects small corrections due to non-renormalizable operators or suppressed renormalizable operators [65] to be invoked.
[14] Typically, one has different mass scales associated with different right-handed neutrino masses.
[15] The neutrino masses and mixings here are defined at M_R. Radiative corrections can significantly modify the neutrino spectrum from that of the weak scale [66]. This is more true for the degenerate spectrum of neutrino masses [67] and for some specific forms of h^ν [68]. For our present discussion, with hierarchical neutrino masses and up-quark like neutrino Yukawa matrices, we expect these effects not to play a very significant role.

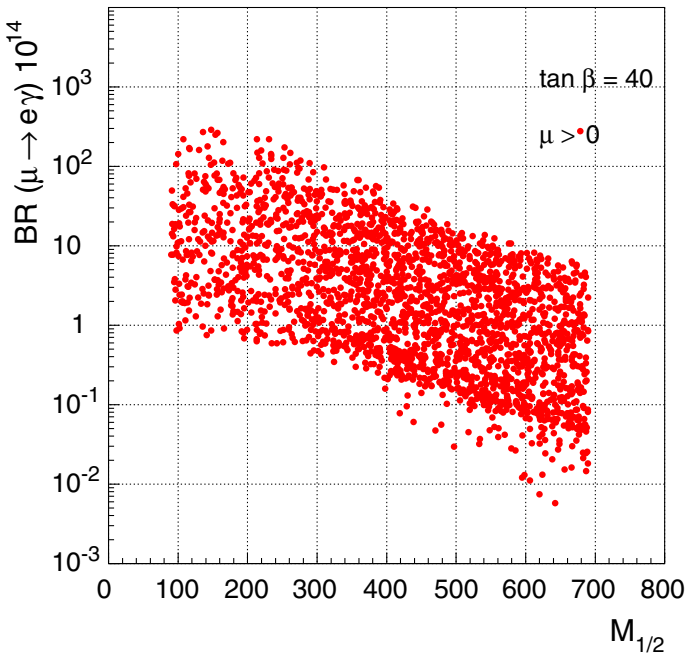

Figure 2. The scatter plots of branching ratios of $\mu \to e, \gamma$ decays as a function of $M_{1/2}$ are shown for the (minimal) CKM case for $\tan\beta = 40$. Results do not alter significantly with the change of sign(μ).

The Br($\mu \to e, \gamma$) is now predictable in this case. Considering mSUGRA boundary conditions, we compute these branching ratios numerically. In figure 2 we show the scatter plots (in mSUGRA parameter space m_0, A_0, $M_{1/2}$) for BR($\mu \to e, \gamma$) for the CKM case and $\tan\beta = 40$. We see that reaching a sensitivity of 10^{-14} for BR($\mu \to e\gamma$) would allow us to probe the SUSY spectrum completely up to $M_{1/2} = 300$ GeV (notice that this corresponds to gluino and squark masses of order 750 GeV) and would still probe large regions of the parameter space up to $M_{1/2} = 700$ GeV. Thus, in summary, although the present limits on BR($\mu \to e, \gamma$) would not induce any significant constraints on the supersymmetry-breaking parameter space, an improvement in the limit to $\sim\mathcal{O}(10^{-14})$, as foreseen, would start imposing non-trivial constraints especially for the large $\tan\beta$ region.

A further comment on the 'minimal' mixing case is in order. Strictly speaking, this is not the 'minimalest' mixing possible in the Dirac neutrino Yukawa couplings. It has been shown in models where the right-handed neutrinos attain their masses through Yukawa couplings, one can essentially set the Dirac neutrino Yukawa mixing to be zero and the entire mixing comes from the right-handed neutrino sector [69]. Such a situation can be realized within left–right symmetric models, with or without an $SO(10)$ embedding. The renormalization group flow is different in this case and the LFV is now related to Yukawa couplings of the right-handed neutrino mass matrix in an indirect manner [69, 70].

4.2.2. Maximal case: a method for PMNS mixings. The minimal $SO(10)$ model presented in the previous subsection would inevitably lead to small mixing in h^ν. In fact, with two Higgs fields in symmetric representations, giving masses to the up-sector and the down-sector separately, it would be difficult to avoid the small CKM-like mixing in h^ν. To generate mixing angles larger

than CKM angles, asymmetric mass matrices have to be considered. In general, it is sufficient to introduce asymmetric textures either in the up-sector or in the down-sector. In the present case, we assume that the down-sector couples to a combination of Higgs representations (symmetric and antisymmetric)[16] Φ, leading to an asymmetric mass matrix in the basis where the up-sector is diagonal. As we will see below, this would also require that the right-handed Majorana mass matrix be diagonal in this basis. We have

$$W_{SO(10)} = \tfrac{1}{2}h^{u,\nu}_{ii}16_i16_i10^u + \tfrac{1}{2}h^{d,e}_{ij}16_i16_j\Phi + \tfrac{1}{2}h^{R}_{ii}16_i16_i126, \tag{25}$$

where the **126**, as before, generates only the right-handed neutrino mass matrix. To study the consequences of these assumptions, we see that at the level of $SU(5)$, we have

$$W_{SU(5)} = \tfrac{1}{2}h^{u}_{ii}10_i10_i5_u + h^{\nu}_{ii}\bar{5}_i1_i5_u + h^{d}_{ij}10_i\bar{5}_j\bar{5}_d + \tfrac{1}{2}M^{R}_{ii}1_i1_i, \tag{26}$$

where we have decomposed the 16 into $10 + \bar{5} + 1$ and 5_u and $\bar{5}_d$ are components of 10_u and Φ, respectively. To have large mixing $\sim U_{PMNS}$ in h^ν we see that the asymmetric matrix h^d should now be able to generate both the CKM as well as PMNS mixing. This is possible if

$$V^{\mathrm{T}}_{\mathrm{CKM}}h^d U^{\mathrm{T}}_{PMNS} = h^d_{diag}. \tag{27}$$

This would mean that the 10 that contains the left-handed down-quarks would be rotated by the CKM matrix, whereas the $\bar{5}$ that contains the left-handed charged leptons would be rotated by the U_{PMNS} matrix to go into their respective mass bases [71, 72]. Thus we have, in analogy with the previous subsection, the following relations to hold true in the basis where charged leptons and down-quarks are diagonal:

$$h^u = V_{\mathrm{CKM}}h^u_{diag}V^{\mathrm{T}}_{\mathrm{CKM}}, \tag{28}$$

$$h^\nu = U_{PMNS}h^u_{diag}. \tag{29}$$

Using the seesaw formula of equations (3) and (29), we have

$$M_R = \mathrm{diag}\left\{\frac{m_u^2}{m_{\nu_1}}, \frac{m_c^2}{m_{\nu_2}}, \frac{m_t^2}{m_{\nu_3}}\right\}. \tag{30}$$

We now turn our attention to lepton flavour violation in this case. The branching ratio, $\mathrm{BR}(\mu \to e, \gamma)$ would now be dependent on

$$[h^\nu h^{\nu\mathrm{T}}]_{21} = h_t^2 U_{\mu 3}U_{e3} + h_c^2 U_{\mu 2}U_{e2} + \mathcal{O}(h_u^2). \tag{31}$$

It is clear from the above that in contrast to the CKM case, the dominant contribution to the off-diagonal entries depends on the unknown magnitude of the element U_{e3} [73]. If U_{e3} is very close to its present limit $\sim$0.2 [74], the first term on the rhs of the equation (31) would dominate.

[16] The couplings of Φ in the superpotential can be either renormalizable or non-renormalizable. See [71] for a non-renormalizable example.

Moreover, this would lead to large contributions to the off-diagonal entries in the slepton masses with $U_{\mu 3}$ of $\mathcal{O}(1)$. We have

$$(m_{\tilde{L}}^2)_{21} \approx -\frac{3m_0^2 + A_0^2}{8\pi^2} h_t^2 U_{e3} U_{\mu 3} \ln \frac{M_{\mathrm{GUT}}}{M_{R_3}} + \mathcal{O}(h_c^2). \tag{32}$$

The above contribution is larger than the CKM case by a factor of $(U_{\mu 3}U_{e3})/(V_{td}V_{ts}) \sim 140$ compared with the CKM case. From equation (1) we see that it would mean about a factor 10^4 times larger than the CKM case in BR($\mu \to e, \gamma$). In case U_{e3} is very small, i.e. either zero or $\lesssim (h_c^2/h_t^2)U_{e2} \sim 4 \times 10^{-5}$, the second term $\propto h_c^2$ in equation (31) would dominate. However the off-diagonal contribution in slepton masses, now being proportional to charm Yukawa, could be much smaller, in fact even smaller than the CKM contribution by a factor

$$\frac{h_c^2 U_{\mu 2} U_{e2}}{h_t^2 V_{td} V_{ts}} \sim 7 \times 10^{-2}. \tag{33}$$

If U_{e3} is close to its present limit, the current bound on BR($\mu \to e, \gamma$) would already be sufficient to produce stringent limits on the SUSY mass spectrum. Similar U_{e3} dependence can be expected in the $\tau \to e$ transitions where the off-diagonal entries are given by

$$(m_{\tilde{L}}^2)_{31} \approx -\frac{3m_0^2 + A_0^2}{8\pi^2} h_t^2 U_{e3} U_{\tau 3} \ln \frac{M_{\mathrm{GUT}}}{M_{R_3}} + \mathcal{O}(h_c^2). \tag{34}$$

The $\tau \to \mu$ transitions are instead U_{e3}-independent probes of SUSY, whose importance was first pointed out in [75]. As in the rest of the cases, the off-diagonal entry in this case is given by

$$(m_{\tilde{L}}^2)_{32} \approx -\frac{3m_0^2 + A_0^2}{8\pi^2} h_t^2 U_{\mu 3} U_{\tau 3} \ln \frac{M_{\mathrm{GUT}}}{M_{R_3}} + \mathcal{O}(h_c^2). \tag{35}$$

In the PMNS scenario, figure 3 shows the plot for BR($\mu \to e, \gamma$) for $\tan\beta = 40$. In this plot, the value of U_{e3} chosen is very close to the present experimental upper limit [74]. As long as $U_{e3} \gtrsim 4 \times 10^{-5}$, the plots scale as U_{e3}^2, while for $U_{e3} \lesssim 4 \times 10^{-5}$ the term proportional to m_c^2 in equation (32) starts dominating; the result is then insensitive to the choice of U_{e3}. For instance, a value of $U_{e3} = 0.01$ would reduce the BR by a factor of 225 and still a significant amount of the parameter space for $\tan\beta = 40$ would be excluded. We further find that with the present limit on BR($\mu \to e, \gamma$), all the parameter space would be completely excluded up to $M_{1/2} = 300$ GeV for $U_{e3} = 0.15$, for any value of $\tan\beta$ (not shown in the figure).

In the $\tau \to \mu\gamma$ decay the situation is similarly constrained. For $\tan\beta = 2$, the present bound of 3×10^{-7} starts probing the parameter space up to $M_{1/2} \leqslant 150$ GeV. The main difference is that this does not depend on the value of U_{e3}, and therefore it is already a very important constraint on the parameter space of the model. In fact, for large $\tan\beta = 40$, as shown in figure 4, reaching the expected limit of 1×10^{-8} would be able to rule out completely this scenario up to gaugino masses of 400 GeV, and only a small portion of the parameter space with heavier gauginos would survive. In the limit $U_{e3} = 0$, this decay mode would provide a constraint on the model stronger than $\mu \to e, \gamma$, which would now be suppressed as it would contain only contributions proportional to h_c^2, as shown in equation (32).

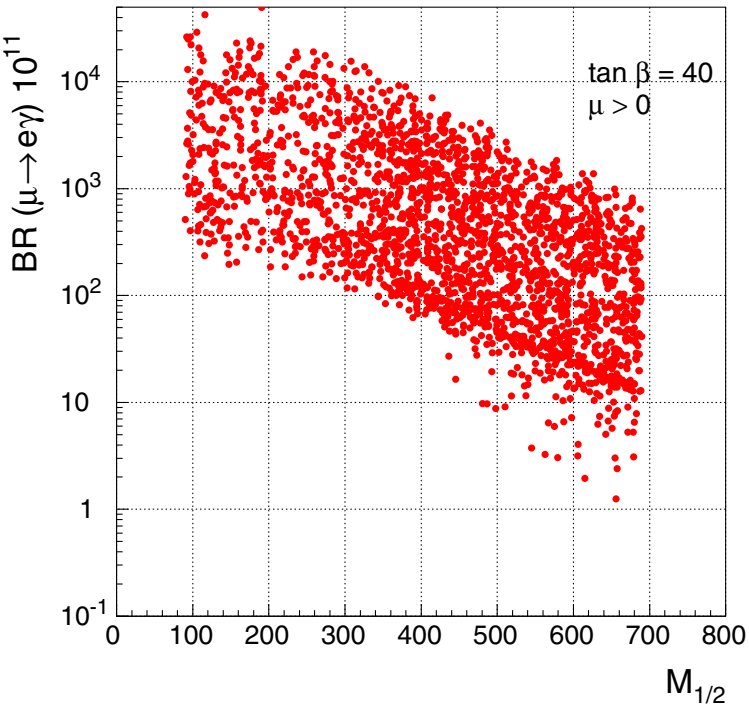

Figure 3. The scatter plots of branching ratios of $\mu \to e, \gamma$ decays as a function of $M_{1/2}$ are shown for the (maximal) PMNS case for $\tan\beta = 40$. The results do not alter significantly with the change of sign(μ).

In summary, in the PMNS/maximal mixing case, even the present limits from BR($\mu \to e, \gamma$) can rule out large portions of the supersymmetry-breaking parameter space, if U_{e3} is either close to its present limit or within an order of magnitude of it (as the planned experiments might find out soon [76]). These are more severe for the large $\tan\beta$ case. In the extreme situation of U_{e3} being zero or very small $\sim\mathcal{O}(10^{-4}$–$10^{-5})$, BR($\tau \to \mu, \gamma$) will start playing an important role, with its present constraints already disallowing large regions of the parameter space at large $\tan\beta$. While the above example concentrated on the hierarchical light neutrinos, similar 'benchmark' mixing scenarios have been explored in great detail, for degenerate spectra of light neutrinos, by Illana and Masip [77], taking also in to consideration running between the Planck scale and the GUT scale.

4.3. Textures and other examples

While the bottom-up approach studies the possibility of 'measuring' the seesaw parameters through low-energy experiments, the top-down approach gives the opportunity to study several theoretically well-motivated models encompassing the seesaw mechanism. For example, a flavour symmetry based on either abelian or non-abelian family symmetries could be at work at the scales giving rise to specific patterns in all the Yukawa coupling matrices in the Lagrangian, including that of neutrino Dirac Yukawa couplings. Low-energy flavour violation is then dependent on these patterns of the Yukawa matrices which are predictable. Several analyses of this kind have been presented in the literature mostly within a supersymmetric GUT [16, 36], [78]–[80]. A recent review of several textures presented in the literature can be found in [81].

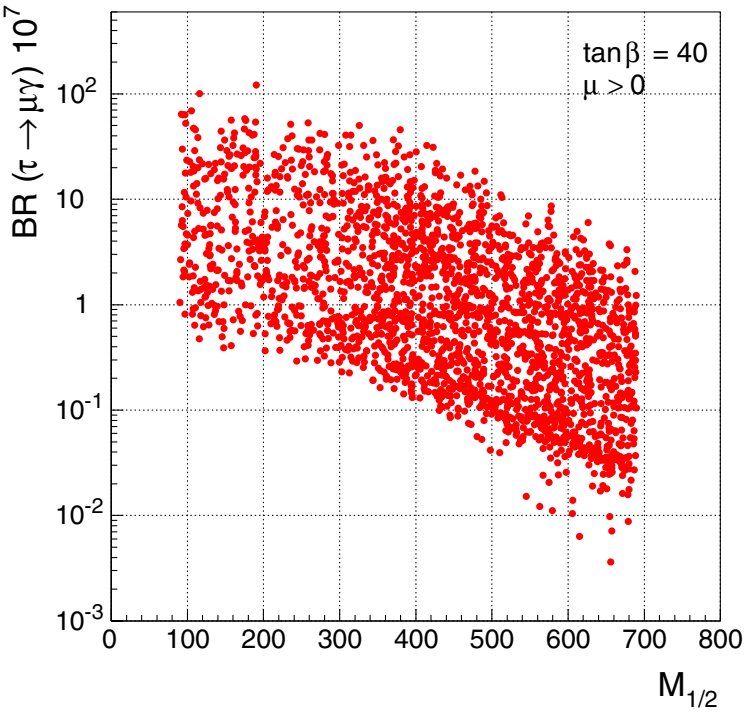

Figure 4. The scatter plots of branching ratios of $\tau \to \mu, \gamma$ decays as a function of $M_{1/2}$ are shown for the (maximal) PMNS case for $\tan\beta = 40$. The results do not alter significantly with the change of sign(μ).

Textures that tend to lead to large left-mixing in h^{ν} are typically prone to constraints from the present limits on $\mu \to e + \gamma$. A class of textures which goes by the name of 'lop-sided' generically predict large branching ratios [79] within the reach of experiments at MEGA. Finally, in addition to the $SO(10)$ example presented here, there have been several other examples both within the context of $SO(10)$ and otherwise that have been explored in the literature [82].[17]

5. Seesaw induced LFV and associated phenomenology

So far we have looked at LFV generated by a seesaw mechanism both through a bottom-up as well as top-down perspectives. In the following, we will discuss the impact the generated LFV can have on the associated phenomenology of the SUSY model. We will only concentrate on a few issues, leaving out the leptonic CP violation which we have already commented on previously. Most of these correlated effects are only valid within a class of SUSY-GUT models; as such correlations cannot be constructed from a purely bottom-up approach.

5.1. LFV and experimental sensitivity to U_{e3}

In the maximal mixing situation, which we have discussed in the previous subsection, we have seen that the BR($\mu \to e, \gamma$) would depend crucially on the neutrino mixing matrix element U_{e3}.

[17] For a study of an $SO(10)$ texture leading to interesting correlations between various flavour and CP phenomena, see [83]. We thank the author for sending us the paper before publication.

Table 2. SPS points for mSUGRA.

	m_0	$M_{1/2}$	A_0	$\tan\beta$	sg(μ)
SPS1a	100	250	−100	10	>0
SPS1b	200	400	0	30	>0
SPS2	1450	300	0	10	>0
SPS3	90	400	0	10	>0
SPS4	400	300	0	50	>0
SPS5	150	300	−1000	5	>0

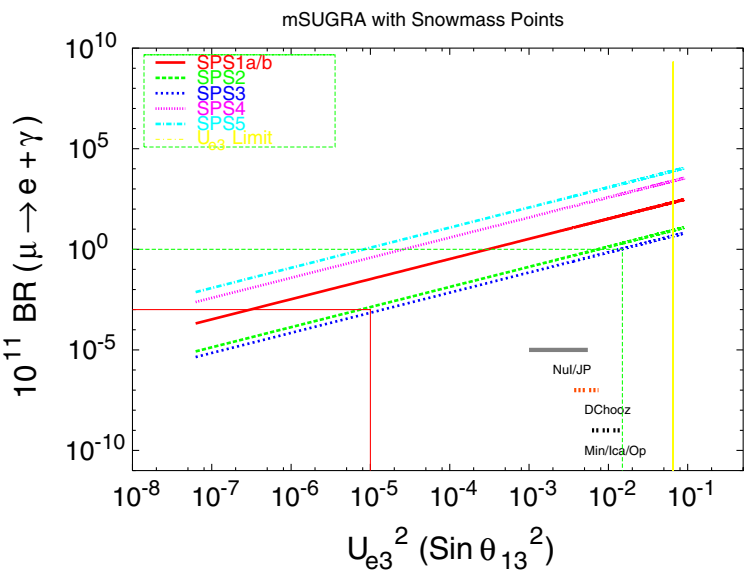

Figure 5. The variation of the BR($\mu \to e + \gamma$) with respect to U_{e3}^2 in the maximal mixing, MNS case. Each (diagonal) line corresponds to an SPS point in mSUGRA as denoted in the legend of the figure. The sensitivity of future LFV experiments $\mathcal{O}(10^{-11}$–$10^{-14})$ is projected on the U_{e3}^2 axis. The ranges probed by future long-base-line experiments are shown as horizontal lines. NuI/JP represents the projected sensitivity of Nu-MI/J-PARC, DChooz, reactor-based experiments like double CHOOZ, Min/Ica/Op represents the experiments MINOS, ICARUS and OPERA [82].

To illustrate the correlations between $\mu \to e + \gamma$ and the neutrino mixing angle U_{e3}, we chose specific points in the supersymmetric parameter space as given by the Snowmass collaboration [85], and are presented in table 2.

In figure 5, we plot BR($\mu \to e + \gamma$) with respect to U_{e3}^2 or $\sin^2\theta_{13}$. We also present the sensitivity of various future experiments probing U_{e3} and well as the expected improvements on the limits on BR($\mu \to e + \gamma$). It is seen that $\mu \to e\gamma$ can have a stronger sensitivity on U_{e3} if both SUSY seesaw and maximal mixing case are realized in nature [86]. A detailed study of the impact of U_{e3} on observability of SUSY at the LHC can be found in [57].

5.2. Correlations with other SUSY search strategies

In addition to the improvements in LFV experiments, this is also going to be the decade in which we should be able to establish whether low-energy supersymmetry exists or not through direct searches at the LHC [87]. On the other hand, improved astrophysical observations from experiments like WMAP [88] and Planck are going to determine the relic density of supersymmetric LSP at unprecedented accuracy. Within mSUGRA, correlations between these two search strategies have been studied [89]. Incorporating the seesaw mechanism in the model via $SO(10)$, would generate another discovery strategy through the lepton flavour violation channel. This is especially true when the LFV entries in the slepton mass matrices are maximized, as in the PMNS case.

We see that the following three main regions in the mSUGRA parameter space would survive after imposing all the present phenomenological and astrophysical (dark matter) constraints [57].[18] (a) The stau coannihilation regions, where the lightest stau is quasi-degenerate with the neutralino LSP and efficient stau–stau as well as stau–neutralino (co)annihilations suppress the relic density. (b) The A-pole funnel region, where the neutralino(bino)–neutralino annihilation process is greatly enhanced through a resonant s-channel exchange of the heavy neutral Higgs A and H. (c) Focus point or hyperbolic branch regions, where a non-negligible higgsino fraction in the lightest neutralino is produced. In each of these regions the LFV rates emanating from the seesaw mechanism can be computed and contrasted with the sensitivity of direct searches at the LHC. Assuming the maximal mixing PMNS case, we find [57]

- *Coannihilation regions*: In these regions, which are mostly accessible at the LHC, an improvement of two orders of magnitude in the branching ratio sensitivity from the present limit, would make $\mu \to e\gamma$ visible for most of the parameter space, as long as $U_{e3} \gtrsim 0.02$, even for the low $\tan\beta$ region. For large $\tan\beta$, independent of U_{e3}, $\tau \to \mu\gamma$ will start probing this region provided a sensitivity of $\mathcal{O}(10^{-8})$ is reached.
- *A-pole funnel regions*: In these regions the LHC reach is not complete and LFV may be competitive. If $U_{e3} \gtrsim 10^{-2}$, the future $\mu \to e\gamma$ experiments, with limit of $\mathcal{O}(10^{-14})$ will probe most of the parameter space. As before, $\tau \to \mu\gamma$ will probe this region once the BR sensitivity reaches $\mathcal{O}(10^{-8})$.
- *Focus point regions*: Since the LHC reach in this region is rather limited by the large m_0 and $M_{1/2}$ values, LFV could constitute a privileged road towards SUSY discovery. This would require improvements of at least a couple of orders of magnitude (or more, depending on the value of U_{e3}) of improvement on the present limit of $\mathrm{BR}(\mu \to e, \gamma)$. Dark matter (DM) searches will also have partial access to this region in future, leading to a new complementarity between LFV and the quest for the cold dark matter constituent of the Universe.

5.3. Seesaw-induced Hadronic FCNC and CPV

So far we have seen that the SUSY version of the seesaw mechanism can lead to potentially large leptonic flavour violations, so large that they could compete even with direct searches at the LHC. If one combines these ideas of supersymmetric seesaw with those of quark–lepton unification, as in a supersymmetric GUT, one would expect that the seesaw resultant flavour effects would now

[18] For a bottom-up analyses, see [90].

also be felt in the hadronic sector, and vice versa [14, 15]. In fact, this is what happens in a SUSY $SU(5)$ with seesaw mechanism [72], where the seesaw-induced RGE effects generate flavour violating terms in the right-handed squark multiplets. However, as is the case with the MSSM + seesaw mechanism, within the $SU(5)$ model also, information from the neutrino masses is not sufficient to fix all the seesaw parameters; a large neutrino Yukawa coupling has to be *assumed* to have the relevant phenomenological consequences in hadronic physics, such as CP violation in $B \to \Phi K_s$, etc.

As we have already seen within the $SO(10)$ model, a large neutrino Yukawa, of the order of that of the top quark, is almost inevitable. Using this, it has been pointed in [71], that the observed large atmospheric ν_μ–ν_τ transitions imply a potentially large $b \to s$ transitions in SUSY $SO(10)$. In the presence of CP violating phases, this can lead to enhanced CP asymmetries in B_s and B_d decays. In particular, the still controversial discrepancy between the SM prediction and the observed $A_{\rm CP}(B_d \to \Phi K_s)$ [91] can be attributed to these effects. Interestingly, despite the severe constraints on the $b \to s$ transitions from $B \to X_s, \gamma$ [92, 93], subsequent detailed analyses [94, 95] proved that there is still enough room for sizeable deviations from the SM expectations for CP violation in the B systems. The reader interested in various correlations in $b \to s$ transitions with all possible FV off-diagonal squark mass entries can find an exhaustive answer in [95].

Finally, let us make a short comment about possible correlations between the hadronic and leptonic FV effects in a SUSY GUT. If the FV soft breaking terms appear at a scale larger than that of the grand unification, they must be related by the GUT symmetry. This puts constraints on the boundary conditions for the running of the FV soft parameters. From this consideration, one might intuitively expect that some correlation between various leptonic and hadronic FCNC processes [38] can occur at the weak scale. If in the evolution of the sparticle masses from the grand unification scale down to the electroweak scale, one encounters seesaw physics, then the quark–lepton correlations involving the left-handed sleptons, although modified, lead to even stronger constraints on hadronic physics [38, 39]; for some other related works see [96].

6. Alternatives to canonical seesaw and LFV

In the final section before conclusions, we briefly mention lepton flavour violating studies conducted in mechanisms other than the canonical seesaw. As earlier, our list is not exhaustive or detailed.

(i) *Type II seesaw*: In the $SO(10)$ example, as we have shown, one can consider a situation where the non-seesaw contribution (15) dominates over the seesaw one. Flavour violation in this case has been studied in specific models [97].

(ii) *Triplet seesaw*: The seesaw mechanism itself can be implemented with fermionic triplets instead of singlet fermions. In the supersymmetric context, the flavour violation is then proportional to the triplet couplings and the neutrino mixing angles [98].

(iii) *3×2 seesaw*: The seesaw parameter space drastically reduces when one of the neutrinos is assumed to be too heavy and decouples from the model. The predictive power of the model is now enhanced for various low- and high-energy observables [99]–[101].

(iv) *X-dimensional models*: In models with warped X-dimensional scenarios, large LFV is expected with either Dirac- [102] or Majorana-type neutrinos [103].

Flavour violation has also been computed in various other models as R-parity violation [104], seesaw models with additional leptons (or inverse seesaw) [105], left–right symmetric models [106] and SM seesaw with a large number of Higgs bosons [107].

7. Conclusions

Since the discovery of neutrino masses in atmospheric neutrino oscillations, there has been a number of activities trying to understand the seesaw mechanism and its low-energy implications. On the one hand, we use a bottom-up approach quantifying our ignorance on the seesaw parameter space to compute the LFV, while on the other, in top-down approach, various models and textures are constrained by LFV. Associated implications to B-physics GUT models, DM abundances in SUGRA theories and implications for LHC searches have been and are being done. Although we have not discussed it here, LFV in Z-decays [108] and other collider processes [109] is also being investigated.

Undoubtedly, the seesaw mechanism represents (one of) the best proposal to generate small neutrino masses naturally. But how can we make sure that this is indeed nature's choice? Even establishing the Majorana nature of the neutrinos through a positive evidence of neutrinoless double beta decay, it will be difficult to assess that such Majorana masses come from a seesaw. Indeed, as we said at the beginning, in the SM seesaw, we expect very tiny charged LFV effects, probably without any chance of ever observing them. When moving to SUSY seesaw we add an important handle to our effort to establish the presence of a seesaw. In fact, as we tried to show in this work, SUSY extensions of the SM with a seesaw have a general 'tendency' to enhance (or even strongly enhance) rare LFV processes. Hence, the combination of the observation of neutrinoless double beta decay and of some charged LFV phenomenon would constitute an important clue for the assessment of SUSY seesaw in nature.

There is no doubt that after the discovery of the neutrino masses, among the indirect tests of SUSY through FCNC and CP violating phenomena, LFV processes have acquired a position of utmost relevance. It would be spectacular if, by the time the LHC observes the first SUSY particle, we could see also a muon decaying to an electron and a photon! After 30 years, we could have the simultaneous confirmation of two of the most challenging physics ideas: seesaw and low-energy SUSY.

Acknowledgments

We thank all our collaborators, Marco Ciuchini, Stefano Profumo, Luca Silvestrini and Carlos Yaguna, without whom the present work would not have been possible. Diagram by Jaxodraw [110].

References

[1] Brooks M L *et al* (MEGA Collaboration) 1999 *Phys. Rev. Lett.* **83** 1521 (*Preprint* hep-ex/9905013)
[2] Abe K *et al* (Belle Collaboration) 2003 *Preprint* hep-ex/0310029
[3] Inami K, for the Belle Colloboration 2003 Talk presented at the *19th Int. Workshop on Weak Interactions and Neutrinos* (WIN-03) 6–11 October, Lake Geneva, WI, USA
[4] See http://meg.psi.ch

[5] Minkowski P 1977 *Phys. Lett.* B **67** 421
Yanagida T 1979 *Proc. Workshop on Unified Theories etc.* ed O Sawada and A Sugamoto (Tsukuba)
Gell-Mann M, Ramond P and Slansky R 1980 *Supergravity* ed D Freedman *et al* (Amsterdam: North-Holland) p 315
Glashow S L 1980 *Quarks and Leptons, Cargèse 1979* ed M Lévy *et al* (New York: Plenum) p 707
Mohapatra R N and Senjanovic G 1980 *Phys. Rev. Lett.* **44** 912
[6] Borzumati F and Masiero A 1986 *Phys. Rev. Lett.* **57** 961
[7] Gabbiani F, Gabrielli E, Masiero A and Silvestrini L 1996 *Nucl. Phys.* B **477** 321 (*Preprint* hep-ph/9604387)
[8] For a recent review, see Masiero A and Vives O 2001 *Ann. Rev. Nucl. Part. Sci.* **51** 161 (*Preprint* hep-ph/0104027)
Masiero A and Vives O 2002 *New J. Phys.* **4** 4
[9] For a recent review, see Chung D J H, Everett L L, Kane G L, King S F, Lykken J and Wang L T 2003 *Preprint* hep-ph/0312378
[10] See, for example, Brignole A, Ibanez L E and Munoz C 1997 *Preprint* hep-ph/9707209 and references therein
[11] Dudas E, Pokorski S and Savoy C A 1996 *Phys. Lett.* B **369** 255 (*Preprint* hep-ph/9509410)
[12] Abel S A and Servant G 2001 *Nucl. Phys.* B **611** 43 (*Preprint* hep-ph/0105262)
Ross G G and Vives O 2003 *Phys. Rev.* D **67** 095013 (*Preprint* hep-ph/0211279)
[13] King S F, Peddie I N R, Ross G G, Velasco-Sevilla L and Vives O 2004 *Preprint* hep-ph/0407012
[14] Barbieri R and Hall L J 1994 *Phys. Lett.* B **338** 212 (*Preprint* hep-ph/9408406)
Barbieri R, Hall L J and Strumia A 1995 *Nucl. Phys.* B **445** 219 (*Preprint* hep-ph/9501334)
[15] Hall L J, Kostelecky V A and Raby S 1986 *Nucl. Phys.* B **267** 415
[16] King S F and Peddie I N R 2004 *Nucl. Phys.* B **678** 339 (*Preprint* hep-ph/0307091)
[17] See, for example, Hall L J and Nomura Y 2002 *Phys. Rev.* D **66** 075004 (*Preprint* hep-ph/0205067)
[18] Abe H, Choi K, Jeong K S and Okumura K I 2004 *Preprint* hep-ph/0407005
[19] Gabbiani F and Masiero A 1989 *Nucl. Phys.* B **322** 235
[20] Hisano J, Moroi T, Tobe K, Yamaguchi M and Yanagida T 1995 *Phys. Lett.* B **357** 579 (*Preprint* hep-ph/9501407)
[21] Hisano J and Nomura D 1999 *Phys. Rev.* D **59** 116005 (*Preprint* hep-ph/9810479)
[22] Masina I and Savoy C A 2003 *Nucl. Phys.* B **661** 365 (*Preprint* hep-ph/0211283)
[23] Hisano J, Moroi T, Tobe K and Yamaguchi M 1996 *Phys. Rev.* D **53** 2442 (*Preprint* hep-ph/9510309)
Hisano J, Moroi T, Tobe K and Yamaguchi M 1997 *Phys. Lett.* B **391** 341
Hisano J, Moroi T, Tobe K and Yamaguchi M 1997 *Phys. Lett.* B **397** 357 (erratum) (*Preprint* hep-ph/9605296)
[24] See, for example, Profumo S and Yaguna C E 2004 *Nucl. Phys.* B **681** 247 (*Preprint* hep-ph/0307225)
[25] See, for example, Kitano R, Koike M and Okada Y 2002 *Phys. Rev.* D **66** 096002 (*Preprint* hep-ph/0203110)
Kitano R, Koike M, Komine S and Okada Y 2003 *Phys. Lett.* B **575** 300 (*Preprint* hep-ph/0308021) and references therein
[26] Babu K S and Kolda C 2002 *Phys. Rev. Lett.* **89** 241802 (*Preprint* hep-ph/0206310)
Dedes A, Ellis J R and Raidal M 2002 *Phys. Lett.* B **549** 159 (*Preprint* hep-ph/0209207)
[27] Sher M 2002 *Phys. Rev.* D **66** 057301 (*Preprint* hep-ph/0207136)
[28] Brignole A and Rossi A 2003 *Phys. Lett.* B **566** 217 (*Preprint* hep-ph/0304081)
Brignole A and Rossi A 2004 *Preprint* hep-ph/0404211
[29] Some recent reviews are: Altarelli G and Feruglio F 2002 *Preprint* hep-ph/0206077
Altarelli G and Feruglio F 2003 *Preprint* hep-ph/0306265
Altarelli G and Feruglio F 2004 *New J. Phys.* **6** 106 (*Preprint* hep-ph/0405048)
Masina I 2001 *Int. J. Mod. Phys.* A **16** 5101 (*Preprint* hep-ph/0107220)
Mohapatra R N 2002 *Preprint* hep-ph/0211252
Mohapatra R N 2003 *Preprint* hep-ph/0306016
King S F 2003 *Preprint* hep-ph/0310204
Smirnov A Y 2003 *Preprint* hep-ph/0311259
[30] Tobe K, Wells J D and Yanagida T 2004 *Phys. Rev.* D **69** 035010 (*Preprint* hep-ph/0310148)

[31] Ibe M, Kitano R, Murayama H and Yanagida T 2004 *Preprint* hep-ph/0403198
[32] Petcov S T, Profumo S, Takanishi Y and Yaguna C E 2004 *Nucl. Phys.* B **676** 453 (*Preprint* hep-ph/0306195)
[33] Casas J A and Ibarra A 2001 *Nucl. Phys.* B **618** 171 (*Preprint* hep-ph/0103065)
[34] Kageyama A, Kaneko S, Shimoyama N and Tanimoto M 2002 *Phys. Lett.* B **527** 206 (*Preprint* hep-ph/0110283)
[35] Deppisch F, Paes H, Redelbach A, Ruckl R and Shimizu Y 2003 *Eur. Phys. J.* C **28** 365 (*Preprint* hep-ph/0206122)
[36] Lavignac S, Masina I and Savoy C A 2001 *Phys. Lett.* B **520** 269 (*Preprint* hep-ph/0106245)
Lavignac S, Masina I and Savoy C A 2002 *Nucl. Phys.* B **633** 139 (*Preprint* hep-ph/0202086)
[37] Ellis J R, Hisano J, Raidal M and Shimizu Y 2002 *Phys. Rev.* D **66** 115013 (*Preprint* hep-ph/0206110)
[38] Ciuchini M, Masiero A, Silvestrini L, Vempati S K and Vives O 2004 *Phys. Rev. Lett.* **92** 071801 (*Preprint* hep-ph/0307191)
[39] Ciuchini M, Masiero A, Paradisi P, Silvestrini L, Vempati S K and Vives O 2004 to appear
[40] For a recent review, see Buchmuller W, Di Bari P and Plumacher M 2004 *New J. Phys.* **6** 105
[41] See, for example, discussions in Albright C *et al* 2000 *Preprint* hep-ex/0008064
Blom M and Minakata H 2004 *New J. Phys.* **6** 130 (*Preprint* hep-ph/0404142)
[42] See, for example, discussions in de Gouvea A, Kayser B and Mohapatra R N 2003 *Phys. Rev.* D **67** 053004 (*Preprint* hep-ph/0211394)
Pascoli S and Petcov S T 2004 *Phys. Lett.* B **580** 280 (*Preprint* hep-ph/0310003)
[43] Okada Y, Okumura K I and Shimizu Y 2000 *Phys. Rev.* D **61** 094001 (*Preprint* hep-ph/9906446)
Kuno Y and Okada Y 2001 *Rev. Mod. Phys.* **73** 151 (*Preprint* hep-ph/9909265)
[44] Ellis J R, Hisano J, Lola S and Raidal M 2002 *Nucl. Phys.* B **621** 208 (*Preprint* hep-ph/0109125)
[45] Ellis J R, Hisano J, Raidal M and Shimizu Y 2002 *Phys. Lett.* B **528** 86 (*Preprint* hep-ph/0111324)
[46] Masina I 2003 *Nucl. Phys.* B **671** 432 (*Preprint* hep-ph/0304299)
[47] Farzan Y and Peskin M E 2004 *Preprint* hep-ph/0405214
[48] Arkani-Hamed N, Cheng H C, Feng J L and Hall L J 1996 *Phys. Rev. Lett.* **77** 1937 (*Preprint* hep-ph/9603431)
Arkani-Hamed N, Feng J L, Hall L J and Cheng H C 1997 *Nucl. Phys.* B **505** 3 (*Preprint* hep-ph/9704205)
[49] Ellis J R and Raidal M 2002 *Nucl. Phys.* B **643** 229 (*Preprint* hep-ph/0206174)
[50] Ellis J R, Raidal M and Yanagida T 2002 *Phys. Lett.* B **546** 228 (*Preprint* hep-ph/0206300)
[51] Davidson S and Ibarra A 2003 *Nucl. Phys.* B **648** 345 (*Preprint* hep-ph/0206304)
Davidson S 2003 *J. High Energy Phys.* JHEP03(2003)037 (*Preprint* hep-ph/0302075)
[52] Branco G C, Gonzalez F, Joaquim F R, Masina I, Rebelo M N and Savoy C A 2003 *Phys. Rev.* D **67** 073025
[53] Pascoli S, Petcov S T and Rodejohann W 2003 *Phys. Rev.* D **68** 093007 (*Preprint* hep-ph/0302054)
[54] Pascoli S, Petcov S T and Yaguna C E 2003 *Phys. Lett.* B **564** 241 (*Preprint* hep-ph/0301095)
[55] Ellis J R, Raidal M and Yanagida T 2003 *Preprint* hep-ph/0303242
[56] Siyeon K 2003 *Eur. Phys. J.* C **30** 55 (*Preprint* hep-ph/0303077)
[57] Masiero A, Profumo S, Vempati S K and Yaguna C E 2004 *J. High Energy Phys.* JHEP03(2004)046 (*Preprint* hep-ph/0401138)
[58] Davidson S and Ibarra A 2001 *J. High Energy Phys.* JHEP09(2001)013 (*Preprint* hep-ph/0104076)
[59] Barbieri R, Nanopoulos D V, Morchio G and Strocchi F 1980 *Phys. Lett.* B **90** 91
Langacker P 1981 *Phys. Rept.* **72** 185
[60] Nath P and Syed R M 2001 *Phys. Lett.* B **506** 68
Nath P and Syed R M 2001 *Phys. Lett.* B **508** 216 (erratum) (*Preprint* hep-ph/0103165)
Nath P and Syed R M 2001 *Nucl. Phys.* B **618** 138 (*Preprint* hep-th/0109116)
Nath P and Syed R M 2004 *Nucl. Phys.* B **676** 64 (*Preprint* hep-th/0310178)
Bajc B, Melfo A, Senjanovic G and Vissani F 2004 *Preprint* hep-ph/0402122
Aulakh C S and Girdhar A 2004 *Preprint* hep-ph/0405074
Fukuyama T, Ilakovac A, Kikuchi T, Meljanac S and Okada N 2004 *Preprint* hep-ph/0405300
[61] Masiero A, Vempati S K and Vives O 2003 *Nucl. Phys.* B **649** 189 (*Preprint* hep-ph/0209303)
Masiero A, Vempati S K and Vives O 2004 *Preprint* hep-ph/0405017

[62] See, for example, Mohapatra R N and Sakita B 1980 *Phys. Rev.* D **21** 1062
[63] Lazarides G, Shafi Q and Wetterich C 1981 *Nucl. Phys.* B **181** 287
Mohapatra R N and Senjanovic G 1981 *Phys. Rev.* D **23** 165
[64] Dimopoulos S and Hall L J 1995 *Phys. Lett.* B **344** 185 (*Preprint* hep-ph/9411273)
Buchmuller W and Wyler D 2001 *Phys. Lett.* B **521** 291 (*Preprint* hep-ph/0108216)
[65] Georgi H and Jarlskog C 1979 *Phys. Lett.* B **86** 297
[66] For a review, see Chankowski P H and Pokorski S 2002 *Int. J. Mod. Phys.* A **17** 575 (*Preprint* hep-ph/0110249)
[67] Ellis J R and Lola S 1999 *Phys. Lett.* B **458** 310 (*Preprint* hep-ph/9904279)
Casas J A, Espinosa J R, Ibarra A and Navarro I 1999 *Nucl. Phys.* B **556** 3 (*Preprint* hep-ph/9904395)
Haba N and Okamura N 2000 *Eur. Phys. J.* C **14** 347 (*Preprint* hep-ph/9906481)
[68] Antusch S, Kersten J, Lindner M and Ratz M 2002 *Phys. Lett.* B **544** 1 (*Preprint* hep-ph/0206078)
Antusch S and Ratz M 2002 *J. High Energy Phys.* JHEP11(2002)010 (*Preprint* hep-ph/0208136)
[69] Babu K S, Dutta B and Mohapatra R N 2003 *Phys. Rev.* D **67** 076006 (*Preprint* hep-ph/0211068)
[70] Dutta B and Mohapatra R N 2003 *Phys. Rev.* D **68** 113008 (*Preprint* hep-ph/0307163)
[71] Chang D, Masiero A and Murayama H 2003 *Phys. Rev.* D **67** 075013 (*Preprint* hep-ph/0205111)
[72] Moroi T 2000 *J. High Energy Phys.* JHEP03(2000)019 (*Preprint* hep-ph/0002208)
Moroi T 2000 *Phys. Lett.* B **493** 366 (*Preprint* hep-ph/0007328)
Akama N, Kiyo Y, Komine S and Moroi T 2001 *Phys. Rev.* D **64** 095012 (*Preprint* hep-ph/0104263)
[73] Sato J, Tobe K and Yanagida T 2001 *Phys. Lett.* B **498** 189 (*Preprint* hep-ph/0010348)
[74] Apollonio M *et al* (CHOOZ Collaboration) 1999 *Phys. Lett.* B **466** 415 (*Preprint* hep-ex/9907037)
[75] Blazek T and King S F 2001 *Phys. Lett.* B **518** 109 (*Preprint* hep-ph/0105005)
[76] Goodman M 2004 *Preprint* hep-ex/0404031
[77] Illana J I and Masip M 2004 *Eur. Phys. J.* C **35** 365 (*Preprint* hep-ph/0307393)
[78] An incomplete list of references: King S F and Oliveira M 1999 *Phys. Rev.* D **60** 035003 (*Preprint* hep-ph/9804283)
Feng J L, Nir Y and Shadmi Y 2000 *Phys. Rev.* D **61** 113005 (*Preprint* hep-ph/9911370)
Ellis J R, Gomez M E, Leontaris G K, Lola S and Nanopoulos D V 2000 *Eur. Phys. J.* C **14** 319 (*Preprint* hep-ph/9911459)
Carvalho D F, Ellis J R, Gomez M E and Lola S 2001 *Phys. Lett.* B **515** 323 (*Preprint* hep-ph/0103256)
Romanino A and Strumia A 2002 *Nucl. Phys.* B **622** 73 (*Preprint* hep-ph/0108275)
Kageyama A, Kaneko S, Shimoyama N and Tanimoto M 2002 *Phys. Rev.* D **65** 096010 (*Preprint* hep-ph/0112359)
Falcone D 2002 *Mod. Phys. Lett.* A **17** 2467 (*Preprint* hep-ph/0207308)
Hamaguchi K, Kakizaki M and Yamaguchi M 2003 *Phys. Rev.* D **68** 056007 (*Preprint* hep-ph/0212172)
Babu K S, Enkhbat T and Gogoladze I 2004 *Nucl. Phys.* B **678** 233 (*Preprint* hep-ph/0308093)
Ross G G and Velasco-Sevilla L 2003 *Nucl. Phys.* B **653** 3 (*Preprint* hep-ph/0208218)
Kaneko S, Katsumata M and Tanimoto M 2003 *J. High Energy Phys.* JHEP07(2003)025 (*Preprint* hep-ph/0305014)
Ross G G, Velasco-Sevilla L and Vives O 2004 *Nucl. Phys.* B **692** 50 (*Preprint* hep-ph/0401064)
Bando M, Kaneko S, Obara M and Tanimoto M 2004 *Preprint* hep-ph/0405071
[79] Sato J and Tobe K 2001 *Phys. Rev.* D **63** 116010 (*Preprint* hep-ph/0012333)
Bi X J 2003 *Eur. Phys. J.* C **27** 399 (*Preprint* hep-ph/0211236)
Barr S M 2004 *Phys. Lett.* B **578** 394 (*Preprint* hep-ph/0307372)
[80] Chen M C and Mahanthapa K T 2004 *Preprint* hep-ph/0409096
[81] Chen M C and Mahanthapa K T 2003 *Int. J. Mod. Phys.* **18** 5819 (*Preprint* hep-ph/0305088)
[82] Hisano J, Nomura D and Yanagida T 1998 *Phys. Lett.* B **437** 351 (*Preprint* hep-ph/9711348)
Buchmuller W, Delepine D and Vissani F 1999 *Phys. Lett.* B **459** 171 (*Preprint* hep-ph/9904219)
Baek S, Goto T, Okada Y and Okumura K I 2001 *Phys. Rev.* D **63** 051701 (*Preprint* hep-ph/0002141)
Hisano J and Tobe K 2001 *Phys. Lett.* B **510** 197 (*Preprint* hep-ph/0102315)
Baek S, Goto T, Okada Y and Okumura K I 2001 *Phys. Rev.* D **64** 095001 (*Preprint* hep-ph/0104146)

Hisano J 2002 *Preprint* hep-ph/0209005
Blazek T and King S F 2003 *Nucl. Phys.* B **662** 359 (*Preprint* hep-ph/0211368)
Huang C S, Li T j and Liao W 2003 *Nucl. Phys.* B **673** 331 (*Preprint* hep-ph/0304130)
Fukuyama T, Kikuchi T and Okada N 2003 *Phys. Rev.* D **68** 033012 (*Preprint* hep-ph/0304190)
Feng T F, Huang T, Li X Q, Zhang X M and Zhao S M 2003 *Phys. Rev.* D **68** 016004 (*Preprint* hep-ph/0305290)
Dutta B, Mimura Y and Mohapatra R N 2004 *Preprint* hep-ph/0402113
[83] Pati J C 2004 Talk presented at the *Fujihara Seminar* KEK Laboratory, Tsukuba (23–25 February) (*Preprint* hep-ph/0407220)
[84] Huber P, Lindner M, Rolinec M, Schwetz T and Winter W 2004 *Preprint* hep-ph/0403068
[85] Allanach B C *et al* 2001 *Proc. APS/DPF/DPB Summer Study on the Future of Particle Physics (Snowmass)* ed N Graf
Allanach B C *et al* 2002 *Eur. Phys. J.* C **25** 113 (eConf C010630, P125 (2001) (*Preprint* hep-ph/0202233)
[86] Masiero A, Vempati S K and Vives O, contribution to Neutrino 2004
[87] Baer H, Chen C h, Paige F and Tata X 1995 *Phys. Rev.* D **52** 2746 (*Preprint* hep-ph/9503271)
Baer H, Chen C h, Paige F and Tata X 1996 *Phys. Rev.* D **53** 6241 (*Preprint* hep-ph/9512383)
Baer H, Chen C h, Drees M, Paige F and Tata X 1998 *Phys. Rev.* D **58** 075008 (*Preprint* hep-ph/9802441)
Abdullin S *et al* (CMS Collaboration) 2002 *J. Phys. G: Nucl. Part. Phys.* **28** 469 (*Preprint* hep-ph/9806366)
[88] Spergel D N *et al* 2003 *Astrophys. J. Suppl.* **148** 175 (*Preprint* astro-ph/0302209)
[89] Baer H, Balazs C, Belyaev A, Krupovnickas T and Tata X 2003 *J. High Energy Phys.* JHEP06(2003)054 (*Preprint* hep-ph/0304303)
[90] Campbell B A, Maybury D W and Murakami B 2004 *J. High Energy Phys.* JHEP03(2004)052 (*Preprint* hep-ph/0311244)
[91] Abe K *et al* (Belle Collaboration) 2003 *Phys. Rev. Lett.* **91** 261602 (*Preprint* hep-ex/0308035)
Aubert B *et al* (BABAR Collaboration) 2004 *Preprint* hep-ex/0403026
[92] Borzumati F, Greub C, Hurth T and Wyler D 2000 *Phys. Rev.* D **62** 075005 (*Preprint* hep-ph/9911245)
Ciuchini M, Degrassi G, Gambino P and Giudice G F 1998 *Nucl. Phys.* B **534** 3 (*Preprint* hep-ph/9806308)
Degrassi G, Gambino P and Giudice G F 2000 *J. High Energy Phys.* JHEP12(2000)009 (*Preprint* hep-ph/0009337)
Carena M, Garcia D, Nierste U and Wagner C E M 2001 *Phys. Lett.* B **499** 141 (*Preprint* hep-ph/0010003)
[93] Borzumati F, Greub C and Yamada Y 2003 *Preprint* hep-ph/0305063
Borzumati F, Greub C and Yamada Y 2003 *Preprint* hep-ph/0311151
[94] Grossman Y, Isidori G and Worah M P 1998 *Phys. Rev.* D **58** 057504 (*Preprint* hep-ph/9708305)
Lunghi E and Wyler D 2001 *Phys. Lett.* B **521** 320 (*Preprint* hep-ph/0109149)
Harnik R, Larson D T, Murayama H and Pierce A 2002 *Preprint* hep-ph/0212180
Khalil S and Kou E 2003 *Phys. Rev.* D **67** 055009 (*Preprint* hep-ph/0212023)
Kane G L, Ko P, Wang H b, Kolda C, Park J h and Wang L T 2003 *Phys. Rev. Lett.* **90** 141803 (*Preprint* hep-ph/0304239)
Chakraverty D, Gabrielli E, Huitu K and Khalil S 2003 *Preprint* hep-ph/0306076
Dutta B, Kim C S, Oh S and Zhu G h 2003 *Preprint* hep-ph/0312389
[95] Ciuchini M, Franco E, Masiero A and Silvestrini L 2003 *Phys. Rev.* D **67** 075016 (*Preprint* hep-ph/0212397,v3)
[96] Hisano J and Shimizu Y 2003 *Phys. Lett.* B **565** 183 (*Preprint* hep-ph/0303071)
Hisano J and Shimizu Y 2004 *Phys. Lett.* B **581** 224 (*Preprint* hep-ph/0308255)
Hisano J, Kakizaki M, Nagai M and Shimizu Y 2004 *Preprint* hep-ph/0407169
[97] Dutta B, Mimura Y and Mohapatra R N 2004 *Preprint* hep-ph/0406262 and references therein
[98] Rossi A 2002 *Phys. Rev.* D **66** 075003 (*Preprint* hep-ph/0207006)
[99] Chankowski P H, Ellis J R, Pokorski S, Raidal M and Turzynski K 2004 *Preprint* hep-ph/0403180
[100] Dutta B and Mohapatra R N 2003 *Phys. Rev.* D **68** 056006 (*Preprint* hep-ph/0305059)

[101] Ibarra A and Ross G G 2003 *Preprint* hep-ph/0312138
[102] Kitano R 2000 *Phys. Lett.* B **481** 39 (*Preprint* hep-ph/0002279
Huber S J and Shafi Q 2004 *Phys. Lett.* B **583** 293 (*Preprint* hep-ph/0309252)
[103] Huber S J 2003 *Nucl. Phys.* B **666** 269 (*Preprint* hep-ph/0303183)
[104] Carvalho D F, Gomez M E and Romao J C 2002 *Phys. Rev.* D **65** 093013 (*Preprint* hep-ph/0202054)
[105] Deppisch F and Valle J W F 2004 *Preprint* hep-ph/0406040
[106] Cirigliano V, Kurylov A, Ramsey-Musolf M J and Vogel P 2004 *Preprint* hep-ph/0404233
Cirigliano V, Kurylov A, Ramsey-Musolf M J and Vogel P 2004 *Preprint* hep-ph/0406199
[107] Grimus W and Lavoura L 2002 *Phys. Rev.* D **66** 014016 (*Preprint* hep-ph/0204070)
[108] See, for example, Illana J I and Riemann T 2001 *Phys. Rev.* D **63** 053004 (*Preprint* hep-ph/0010193)
Illana J I and Masip M 2003 *Phys. Rev.* D **67** 035004 (*Preprint* hep-ph/0207328)
Cao J, Xiong Z and Yang J M 2004 *Eur. Phys. J.* C **32** 245 (*Preprint* hep-ph/0307126) and references therein
[109] See, for example, Hisano J, Nojiri M M, Shimizu Y and Tanaka M 1999 *Phys. Rev.* D **60** 055008 (*Preprint* hep-ph/9808410)
Deppisch F, Pas H, Redelbach A, Ruckl R and Shimizu Y 2004 *Phys. Rev.* D **69** 054014 and references therein
[110] Binosi D and Theussl L 2004 *Comput. Phys. Commun.* **161** 76 (*Preprint* hep-ph/0309015)

New Journal of Physics
The open-access journal for physics

Next generation double-beta decay experiments: metrics for their evaluation

F T Avignone III[1], G S King III[1] and Yu G Zdesenko[2,3]

[1] Department of Physics and Astronomy, University of South Carolina
Columbia, SC 29208, USA
[2] Institute for Nuclear Research, Kiev, Ukraine
E-mail: avignone@sc.edu

New Journal of Physics **7** (2005) 6
Received 03 September 2004
Published 12 January 2005
Online at http://www.njp.org/
doi:10.1088/1367-2630/7/1/006

Abstract. We discuss the six most important parameters that should be used in the computation of figures of merit of various proposed searches for neutrinoless double-beta decay ($0\nu\beta\beta$-decay). We begin by discussing the connection of this decay mode to the effective Majorana mass of the electron neutrino and the expected experimental sensitivities of favoured techniques. We then discuss the proposed next generation $0\nu\beta\beta$-decay experimental techniques in the context of an expression for the experimental figure-of-merit. Finally, we discuss the various proposed experiments in the context of their figure-of-merit parameters. We conclude that the important parameters are the nuclear structure (theoretical rate of decay), isotopic abundance of the parent nuclide and detection efficiency for $0\nu\beta\beta$-decay. These enter the equation linearly. Also important are: the mass of the source, and the background rate, although these enter to the one-half power. Energy resolution, while also entering the figure-of-merit to the one half power, is crucial for the discovery potential.

[3] Deceased.

PII: S1367-2630(05)85887-2
© IOP Publishing Ltd and Deutsche Physikalische Gesellschaft

Contents

1. Theoretical background **3**
- 1.1. Theoretical motivation of $0\nu\beta\beta$-decay . . . 3
- 1.2. The neutrino mixing matrix . . . 3
- 1.3. Neutrinoless double-beta decay . . . 4
- 1.4. Neutrino mass patterns . . . 5
- 1.5. Experimental prospects . . . 5
- 1.6. An analytic figure-of-merit for $0\nu\beta\beta$-decay experiments . . . 7

2. Next generation experimental proposals **10**
- 2.1. CUORE/CUORICINO . . . 10
- 2.2. The EXO experiment . . . 15
- 2.3. The Majorana experiment . . . 17
  - 2.3.1. Recent progress in Ge detector technology . . . 18
- 2.4. MOON . . . 20
- 2.5. Nemo and Super-NEMO . . . 24

3. Other proposals **26**
- 3.1. CARVEL: an example of a scintillator double-beta decay experiment . . . 27
  - 3.1.1. Pulse shape discrimination in scintillation detectors . . . 28
- 3.2. The ^{116}Cd CAMEO project . . . 28
- 3.3. Double-beta decay of ^{48}Ca with CANDLES . . . 31
- 3.4. The COBRA double-beta decay experiment with CdTe detectors . . . 32
- 3.5. The drift chamber beta-ray analyser (DCBA) . . . 33

4. Other proposals involving ^{76}Ge **34**
- 4.1. The GEM experiment . . . 34
- 4.2. The GENIUS project . . . 34
- 4.3. The GENIUS test facility (GENIUS—TF) . . . 36
- 4.4. The new ^{76}Ge experiment at Gran Sasso (GERDA) . . . 36
- 4.5. The GSO proposal . . . 37

5. Other proposals involving ^{136}Xe **37**
- 5.1. The ^{136}Xe experiment in BOREXINO and the BOREXINO test facility . . . 37
- 5.2. The XMASS experiment . . . 38

6. The figure-of-merit revisited **39**
- 6.1. The claim of discovery of $0\nu\beta\beta$-decay of ^{76}Ge . . . 40
- 6.2. Figure-of-merit for a sample ^{76}Ge experiment . . . 41
- 6.3. The CUORE proposal with natural abundance TeO_2 bolometers . . . 41
- 6.4. Figure-of-merit for a 10 ton ^{136}Xe TPC . . . 42

7. Conclusion **42**

Acknowledgments **43**

References **44**

1. Theoretical background

1.1. Theoretical motivation of $0\nu\beta\beta$*-decay*

Neutrinoless double-beta decay is an old subject [16, 34, 35, 41, 63, 71, 72, 82]. What is new is the fact that positive observation of neutrino oscillations in atmospheric neutrinos [37] and in solar neutrinos [6, 36] gives new motivation for more sensitive searches. In fact, recently published constraints on the mixing angles of the neutrino-mixing matrix [18, 67, 68] make a strong case that if neutrinos are Majorana particles, there are many scenarios in which next generation double-beta decay experiments should be able to observe the phenomenon and measure the effective Majorana mass of the electron neutrino, $|\langle m_\nu\rangle|$, which would provide a measure of the neutrino mass scale. One fact is clear; neutrino oscillation experiments can only provide data on the mass differences of the neutrino mass-eigenstates. The absolute scale can only be obtained from direct mass measurements, ^3H end point measurements for example [66], or in the case of Majorana neutrinos, more sensitively by neutrinoless double-beta decay. The time for large, next generation double beta-decay experiments has arrived, for if the mass scale is below ~0.2 eV, double beta-decay may be the only hope for measuring it. The most sensitive experiments carried out so far have probed the decay $^{76}\mathrm{Ge} \rightarrow {}^{76}\mathrm{Se} + 2\beta^-$ with specially built Ge detectors fabricated from germanium isotopically enriched from 7.8 to 86% in ^{76}Ge. The Heidelberg–Moscow Experiment [20, 49] and the International Germanium Experiment (IGEX) [2, 4] have placed lower bounds on the half-life for this process of 1.9×10^{25} years (90% CL) and 1.6×10^{25} years (90% CL), respectively.

1.2. The neutrino mixing matrix

The conventional form of the Kobayashi–Maskoawa matrix was suggested by Chau and Keung in 1984 [26].

$$\begin{pmatrix} |\nu_e\rangle \\ |\nu_\mu\rangle \\ |\nu_\tau\rangle \end{pmatrix} = \begin{pmatrix} c_3c_2 & s_3c_2 & s_2\mathrm{e}^{-\mathrm{i}\delta} \\ -s_3c_1 - c_3s_1s_2\mathrm{e}^{\mathrm{i}\delta} & c_3c_1 - s_3s_1s_2\mathrm{e}^{\mathrm{i}\delta} & s_1c_2 \\ s_3s_1 - c_3s_1s_2\mathrm{e}^{\mathrm{i}\delta} & -c_3s_1 - s_3c_1s_2\mathrm{e}^{\mathrm{i}\delta} & c_1c_2 \end{pmatrix} \begin{pmatrix} 1 & 0 & 0 \\ 0 & \mathrm{e}^{\mathrm{i}\varphi_2/2} & 0 \\ 0 & 0 & \mathrm{e}^{\mathrm{i}(\delta+\varphi_2/2)} \end{pmatrix} \begin{pmatrix} |\nu_1\rangle \\ |\nu_2\rangle \\ |\nu_3\rangle \end{pmatrix}, \tag{1}$$

where $c_i \equiv \cos\theta_i$ and $s_i \equiv \sin\theta_i$, and we multiply by an additional diagonal matrix that contains Majorana CP phases that do not appear in neutrino oscillations. While this looks very complicated and populated with many unknowns, neutrino oscillation data [6, 10, 36, 45] have constrained all three of the angles as shown in table 1.

In addition, these experiments have produced limits of $10^{-5}\,\mathrm{eV}^2 \leqslant \delta m_S^2 \leqslant 10^{-4}\,\mathrm{eV}^2$ (3σ) for solar neutrino oscillations and $1.1\times10^{-3}\,\mathrm{eV}^2 \leqslant \delta m_{AT}^2 \leqslant 5\times10^{-3}$ (3σ) for atmospheric neutrino oscillations. Considering the values found in table 1, one may wish to make the approximation that $\theta_2 \equiv 0$. Accordingly,

$$U = \begin{pmatrix} c_3 & s_3\mathrm{e}^{\mathrm{i}\varphi_2} & 0 \\ -s_3c_1 & c_3c_1\mathrm{e}^{\mathrm{i}\varphi_2} & s_1\mathrm{e}^{\mathrm{i}\varphi_3} \\ s_3s_1 & -c_3s_1\mathrm{e}^{\mathrm{i}\varphi_2} & c_1\mathrm{e}^{\mathrm{i}\varphi_3} \end{pmatrix} \simeq \begin{pmatrix} \frac{\sqrt{3}}{2} & \frac{1}{2}\mathrm{e}^{\mathrm{i}\varphi_2} & 0 \\ -\frac{1}{2\sqrt{2}} & \frac{\sqrt{3}}{2\sqrt{2}}\mathrm{e}^{\mathrm{i}\varphi_2} & \frac{1}{\sqrt{2}}\mathrm{e}^{\mathrm{i}\varphi_3} \\ \frac{1}{2\sqrt{2}} & -\frac{\sqrt{3}}{2\sqrt{2}}\mathrm{e}^{\mathrm{i}\varphi_2} & \frac{1}{\sqrt{2}}\mathrm{e}^{\mathrm{i}\varphi_3} \end{pmatrix}, \tag{2}$$

where $c_3 \cong \sqrt{3}/2$, $s_3 \simeq 1/2$ and $c_1 \simeq 1/\sqrt{2} = s_1$ were used in the second matrix.

Table 1. Atmospheric, reactor, and solar neutrino constraints on the mixing angles of equation (1).

Atmospheric neutrino data (Super Kamiokande detector) [37]	Solar neutrino data: Sudbury neutrino Observatory [6]	Solar neutrino data: Super Kamiokande [36]
$s_1 \geqslant 0.0557$ (3σ); $\theta_1 \geqslant 34^\circ$	$0.794 \leqslant c_3 \leqslant 0.905$	$0.769 \leqslant c_3 \leqslant 0.894$
Reactor experiments: (CHOOZ and Palo Verde)	Best fit $\theta_3 = 32^\circ$	$0.447 \leqslant s_3 \leqslant 0.639$
$s_2 \leqslant 0.16$; $0.987 \leqslant c_2 \leqslant 1.00$	$c_3 = 0.866^{+0.039}_{-0.072}$ (3σ)	$17^\circ \leqslant \theta_3 \leqslant 39^\circ$
CL = 95% [10, 24]	$s_3 = 0.50^{+0.11}_{-0.07}$ (3σ)	$\theta_3 \approx 33^\circ$
KAMLAND	Best fit $\theta_3 = 32.6^\circ$ [46]	

There have been a series of reanalyses of both solar and atmospheric neutrino oscillations. A recent global analysis of all available data was presented by M C Gonzales-Garcia on 12 February 2004 at the International Workshop on 'Neutrino Oscillations and their Origins', NOON 2004 in Tokyo. The following neutrino mixing matrix was derived from that presentation.

The error bars were obtained by using the best-fit values as central ones, and computing 1σ errors from the 3σ ranges given.

$$\begin{pmatrix} U_{e1} & U_{e2} & U_{e3} \\ U_{\mu 1} & U_{\mu 2} & U_{\mu 3} \\ U_{\tau 1} & U_{\tau 2} & U_{\tau 3} \end{pmatrix} = \begin{pmatrix} 0.83 \pm 0.02 & 0.55 \pm 0.03 & <0.23 \\ 0.37 \pm 0.06 & 0.57 \pm 0.06 & 0.70 \pm 0.04 \\ 0.36 \pm 0.06 & 0.56 \pm 0.05 & 0.69 \pm 0.05 \end{pmatrix}. \tag{3}$$

1.3. Neutrinoless double-beta decay

The decay rate for the process involving the exchange of the Majorana neutrino in the absence of right-handed currents, can be expressed as follows (for details see [35, 41]):

$$(T_{1/2})^{-1} = G^{0\nu}(E_0, Z) \left(\frac{\langle m_\nu \rangle}{m_e}\right)^2 |M_f^{0\nu} - (g_A/g_V)^2 M_{GT}^{0\nu}|^2. \tag{4}$$

In equation (4), $G^{0\nu}$ is the two-body phase-space factor including coupling constants, $M_f^{0\nu}$ and $M_{GT}^{0\nu}$ are the Fermi and Gamow–Teller nuclear matrix elements, respectively, and g_A and g_V are the axial-vector and vector relative weak coupling constants, respectively. The quantity $|\langle m_\nu \rangle|$ is the effective Majorana electron neutrino mass given by

$$|\langle m_\nu \rangle| \equiv ||U_{e1}^L|^2 m_1 + |U_{e2}^L|^2 m_2 e^{i\phi_2} + |U_{e3}^L|^2 m_3 e^{i\phi_3}|, \tag{5}$$

where $e^{i\phi_2}$ and $e^{i\phi_3}$ are the Majorana CP phases (± 1 for CP conservation) and $m_{1,2,3}$ are the neutrino mass eigenvalues. In general, prior to the approximation $\theta_2 = 0 = s_2$, we have

$$|\langle m_\nu \rangle| = |c_3^2 c_2^2 m_1 + s_3^2 c_2^2 e^{i\phi_2} m_2 + s_2^2 e^{i\phi_3} m_3|. \tag{6}$$

With the values and errors (1σ) from equation (3), this becomes:

$$|\langle m_\nu \rangle| = |(0.70 \pm 0.03) m_1 + (0.30 \pm 0.03) e^{i\phi_2} m_2 + (< 0.05) e^{i\phi_3} m_3|. \tag{7}$$

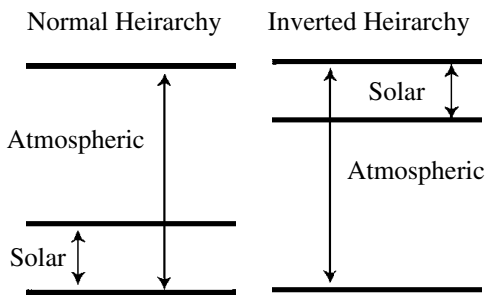

Figure 1. Normal and inverted hierarchies of the neutrino eigenstates. In the normal case, the solar neutrino oscillation occurs between the lower two states, and the atmospheric neutrino oscillation occurs between the highest and one of the lower ones. For convenience, we choose the lowest one to be m_1.

1.4. Neutrino mass patterns

The measured values of δm_S^2 (solar) and δm_{AT}^2 (atmospheric) given earlier motivate the pattern of masses in two hierarchy schemes shown in figure 1.

From the relations shown in figure 1, we can write $m_2 = \sqrt{\delta m_S^2 + m_1^2}$ and $m_3 = \sqrt{\delta m_{AT}^2 + m_1^2}$ in the case of normal hierarchy and $m_2 = \sqrt{\delta m_{AT}^2 - \delta m_S^2 + m_1^2}$ and $m_3 = \sqrt{\delta m_{AT}^2 + m_1^2}$ in the case if inverted hierarchy. From these, we can write equation (6), for normal and inverted hierarchy, respectively, in terms of mixing angles, δm_S^2, δm_{AT}^2 and CP phases as follows [17, 19, 67, 68]:

$$|\langle m_\nu \rangle| = \left| c_2^2 c_3^2 m_1 + c_2^2 s_3^2 e^{i\phi_2} \sqrt{\delta m_s^2 + m_1^2} + s_2^2 e^{i\phi_3} \sqrt{\delta m_{AT}^2 + m_1^2} \right|, \tag{8}$$

$$|\langle m_\nu \rangle| = \left| s_2^2 m_1 + c_2^2 c_3^2 e^{i\phi_2} \sqrt{\delta m_{AT}^2 - \delta m_s^2 + m_1^2} + c_2^2 s_2^2 e^{i\phi_3} \sqrt{\delta m_{AT}^2 + m_1^2} \right|. \tag{9}$$

With the approximation $\theta_2 \equiv 0$, and the further approximation of $\delta m_S^2 \ll \delta m_{AT}^2$, equations (8) and (9) are rewritten as follows in equations (10) and (11), respectively:

$$|\langle m_\nu \rangle| = m_1 \left| c_3^2 + s_3^2 e^{i\phi_2} \left(1 + \frac{\delta m_s^2}{2m_1^2} \right) \right|, \tag{10}$$

$$|\langle m_\nu \rangle| = \sqrt{m_1^2 + \delta m_{AT}^2} \left| c_3^2 e^{i\phi_2} + s_3^2 e^{i\phi_3} \right|. \tag{11}$$

When the approximate expressions (10) and (11) are used, the results for equation (10) deviate from those using equation (8) by 2.5, 0.25 and 0.03% for $m_1 = 0.01, 0.02$ and 0.03 eV, respectively. In the case of using equation (11) for equation (9), the deviations are 1.4, 1.3 and 1.2% for $m_1 = 0.00$, 0.01 and 0.02 eV, respectively. Numerical values for $|\langle m_\nu \rangle|$ using equations (10) and (11) are given in table 2.

1.5. Experimental prospects

It is interesting to compare the values given in table 2 with the projected sensitivity of a 500 kg ^{76}Ge experiment for example. A projected sensitivity, for such an experiment would

Table 2. Numerical predictions of $|\langle m_\nu\rangle|$ in meV for both hierarchies and CP phase relations. (The errors are actually limits obtained by using the 3σ bounds on the measured parameters.)

Normal hierarchy				Inverted hierarchy			
$e^{i\phi_2} = -1$		$e^{i\phi_2} = +1$		$e^{i\phi_2} = -e^{i\phi_3}$		$e^{i\phi_2} = +e^{i\phi_3}$	
m_1(eV)	$\lvert\langle m_\nu\rangle\rvert$	m_1(eV)	$\lvert\langle m_\nu\rangle\rvert$	m_1(eV)	$\lvert\langle m_\nu\rangle\rvert$	m_1(eV)	$\lvert\langle m_\nu\rangle\rvert$
0.02	10^{+3}_{-5}	0.02	20 ± 4	0.00	30^{+18}_{-20}	0.00	55 ± 29
0.04	20^{+6}_{-10}	0.04	40 ± 8	0.02	32^{+18}_{-21}	0.02	59 ± 29
0.06	32^{+7}_{-16}	0.06	61 ± 11	0.05	40^{+18}_{-25}	0.05	75 ± 29
0.08	41^{+10}_{-21}	0.08	81 ± 16	0.075	48^{+19}_{-29}	0.075	94 ± 30
0.10	51^{+13}_{-26}	0.10	101 ± 20	0.10	60^{+19}_{-33}	0.10	116 ± 31
0.20	102^{+26}_{-52}	0.20	200 ± 40	0.20	106^{+30}_{-55}		
0.40	204^{+52}_{-102}	0.40	400 ± 80				

Table 3. Nuclear factors for neutrinoless double-beta decay of ^{76}Ge from 1998–2001.

Renormalized QRPA (Simcovic *et al*)	$F_N^{-1/2} = 4.02 \times 10^6$ (year)$^{1/2}$
SQRPA large basis (Heidelberg H V K-K)	$F_N^{-1/2} = 3.93 \times 10^6$ (year)$^{1/2}$
SQRPA small basis (Heidelberg H V K-K)	$F_N^{-1/2} = 3.33 \times 10^6$ (year)$^{1/2}$
SQRPA (J Suhonen)	$F_N^{-1/2} = 3.02 \times 10^6$ (year)$^{1/2}$
$\langle F_N^{-1/2}\rangle = (3.6 \pm 0.8) \times 10^6$ (year)$^{1/2}$	

be: $T^{0\nu}_{1/2} \geqslant 4 \times 10^{27}$ years [60]. To do this, we need the nuclear structure factor in equation (4). It is convenient to define $F_N \equiv G^{0\nu}|M^{0\nu}_f - (g_A/g_V)^2 M^{0\nu}_{GT}|^2$ which leads to $|\langle m_\nu\rangle| = m_e(F_N T^{0\nu}_{1/2})^{-1/2}$ eV.

In table 3, we list a few recent values of $F_N^{-1/2}$ (year)$^{1/2}$ calculated by three different Quasi-Particle Random Phase Approximation (QRPA) models.

Using the average value of those given in table 3 and the mean-square deviation, we find that experiment predicts a sensitivity of $|\langle m_\nu\rangle|_{SENS} \cong 28^{+7}_{-6}$ meV. This value probes a significant portion of the range of values of m_1 given in the table. The Cryogenic Underground Observatory for Rare Events (CUORE) experiment [13] will probe a similar range. The equations given by Barger *et al* [19] reduce, using the approximations given above, to the following for normal and inverted hierarchies respectively:

$$|\langle m_\nu\rangle| \leqslant m_1 \leqslant \frac{|\langle m_\nu\rangle|}{c_3^2 - s_3^2}, \tag{12}$$

$$\sqrt{|\langle m_\nu\rangle|^2 + \delta m^2_{AT}} \leqslant m_1 \leqslant \frac{\sqrt{|\langle m_\nu\rangle|^2 + \delta m^2_{AT}(c_3^2 - s_3^2)}}{c_3^2 - s_3^2}. \tag{13}$$

They also derive explicit expressions for $\sum \equiv m_1 + m_2 + m_3$, the sum of the eigenstate masses, which is important in the consideration of neutrino hot dark matter [19].

$$2|\langle m_\nu\rangle|^2 + \sqrt{|\langle m_\nu\rangle|^2 \pm \delta m_{AT}^2} \leqslant \sum \leqslant \frac{2|\langle m_\nu\rangle| + \sqrt{|\langle m_\nu\rangle|^2 \pm \delta m_{AT}^2 \cos(2\theta_3)}}{\cos(2\theta_3)}, \tag{14}$$

where the plus is for normal hierarchy and the minus for inverted hierarchy. Equation (14) can be simplified significantly for values of $|\langle m_\nu\rangle|$ achievable in the next generation experiments. To invert the left-hand side of the inequality, we solve the equation $3|\langle m_\nu\rangle|^2 - 4|\langle m_\nu\rangle| \sum + (\sum^2 - \delta m_{AT}^2) = 0$. The right-hand side is solved in a similar manner. When $\delta m_{AT}^2 \ll \sum^2$, $\delta m_{AT}^2 \leqslant 0.005$ eV (99.73% CL), we have

$$|\langle m_\nu\rangle| \leqslant \frac{\sum}{3} \leqslant 2|\langle m_\nu\rangle|. \tag{15}$$

It is evident that next generation neutrinoless double-beta decay experiments are the next important step necessary for a more complete understanding of the physics of neutrinos. In this article we describe several experiments, and discuss ways to evaluate which might reach the desired sensitivity.

1.6. An analytic figure-of-merit for $0\nu\beta\beta$-decay experiments

Any $0\nu\beta\beta$-decay experiment, using presently known technology, will have background. The number of background events, B, can be written:

$$B = bMt\delta E. \tag{16}$$

In equation (16), b is the rate of background counts in keV^{-1} kg^{-1} year^{-1}, M is the source mass in kg, t is the experimental running time in years and δE is the energy window of the $0\nu\beta\beta$-decay events in keV and is proportional to the energy resolution of the detector. In this case, we have assumed as usual that the background under the $0\nu\beta\beta$-peak is approximately constant over the interval δE. In the case that δE is very large, this approximation is less valid because events from $2\nu\beta\beta$-decay can enter the interval δE.

The number of $0\nu\beta\beta$-decay events $C_{\beta\beta}$ can be expressed in terms of the decay rate $\lambda_{\beta\beta}$ as follows:

$$C_{\beta\beta} = \lambda_{\beta\beta} Nt\epsilon = \lambda_{\beta\beta}(A_0 \times 10^3/W)a\epsilon Mt, \tag{17}$$

where A_0 is Avagadro's number, W the molecular weight of the source material, a the isotopic abundance of the parent nuclide and ϵ the detection efficiency of $0\nu\beta\beta$-decay events.

A general criterion for discovery potential for a $0\nu\beta\beta$-decay experiment can be expressed as $C_{\beta\beta} = C_1\sqrt{B + C_{\beta\beta}}$, where C_1 is the confidence level expressed in units of σ of the Poisson distribution. It is convenient to require some specific signal to background ratio, for example $C_{\beta\beta}/B \simeq 1$. In this case, we require $C_{\beta\beta} = \gamma\sqrt{B}$, in which $\gamma = C_1\sqrt{2}$. Although arbitrary this, or any other choice, can be chosen the same for all experiments being compared. Accordingly,

$$\lambda_{\beta\beta}(A_0 \times 10^3)\left(\frac{a\epsilon}{W}\right) Mt = \sqrt{bMt\delta E}, \tag{18}$$

which results in the following expression for the sensitivity:

$$T_{1/2}^{0\gamma} = \alpha \left(\frac{a\epsilon}{W}\right) \sqrt{\frac{Mt}{b\delta E}}. \tag{19}$$

In equation (19), for $C_{\beta\beta} \simeq B$, $\alpha = 7.3 \times 10^{25}$ years. From this relation, a very descriptive expression for a relative figure-of-merit can be derived.

It is more correct to use the total counting rate, $B + C_{\beta\beta}$, in equation (18); however, in cases in which the background is some other multiple of the signal, the result is the same but with a different value of α. If there is no signal, then equation (19) refers to the sensitivity of a bound. If the background is zero, there is no need for equation (19). The factor of α can be chosen the same for all experiments being compared.

Next, we consider the theoretical expression given in equation (4). To account for the theoretical decay rate of the chosen parent isotope we utilize the factor $\overline{\eta} \equiv \langle F_N \rangle \times 10^{13}$, where $\overline{\eta}$ indicates the average of the factor F_N over all nuclear models, and written in shorthand as

$$F_N = G^{0\nu} |M^{0\nu}|^2. \tag{20}$$

A complete figure-of-merit would be proportional to the ratio of the predicted half-life sensitivity appearing in equation (19), and the theoretical half-life for an arbitrary neutrino mass. The latter is proportional to the inverse of the parameter $\overline{\eta}$, so we can simply multiply equation (19) by $\overline{\eta}$. We can eliminate the parameters α and t, which can be chosen the same for all experiments being compared. The resulting expression for the relative figure-of-merit f is then

$$f \equiv \overline{\eta} \left(\frac{a\epsilon}{W}\right) \sqrt{\frac{M}{b\,\delta E}}. \tag{21}$$

From this we see the importance of efficiency and isotopic abundance. They enter the figure-of-merit linearly, while the mass of the source M enters as the square root. This means that to obtain the same increase in half-life sensitivity obtained by doubling the isotopic abundance, the mass would have to be increased by a factor of four, assuming the same background. Of course it is true that the mass M can in principle be continuously expanded, while the parameters 'ϵ' and 'a' are maximum at 1.0. It is also evident that the nuclear structure factor is extremely important, although this is theoretically derived using a nuclear model and has inherent uncertainties. To estimate values of the parameters $\overline{\eta}$ all values from the published literature were used with few exceptions. Values from work that was later determined to be in error was excluded. In addition, values given earlier by the same authors, using the same model were excluded in favour of their later work. Table 4 below lists values of F_N and $\overline{\eta}$ resulting from this averaging process. All other values given in the review by Tretyak and Zdesenko were used [77].

Finally, the energy resolution of the detector is an extremely important characteristic. Foremost, with the excellent energy resolution it is possible to minimize the background produced by the $2\nu\beta\beta$ decay events in the energy window of the 0ν peak. Such a background can only be discriminated from the $0\nu\beta\beta$ decay events, in tracking detectors that have poor energy resolution, however, the better the energy resolution the smaller the contribution of the 2ν tail to the 0ν interval.

Likewise, the role of the energy resolution of the detector is even more crucial for the discovery of the $0\nu\beta\beta$ decay. Since the width of the $0\nu\beta\beta$ decay peak is determined by the energy resolution of the detector, the latter should be sufficient to discriminate this peak from background and to recognize the effect. Practically, it is very useful to determine the minimal level of the

Table 4. Average values of the nuclear structure factors $F_N \equiv G^{0\nu}|M^{0\nu}|^2$, and the corresponding normalized factors $\overline{\eta}$ and $0\nu\beta\beta$-decay energy $|Q_{\beta\beta}|$.

Parent isotope	$\langle F_N \rangle \equiv \langle G^{0\nu}\|M^{0\nu}\|^2\rangle \text{year}^{-1}$	$\overline{\eta}$	$\|Q_{\beta\beta}\|$ (keV)
^{48}Ca	$(5.4^{+3.0}_{-1.4}) \times 10^{-14}$	0.54	4271
^{76}Ge	$(7.3 \pm 0.6) \times 10^{-14}$	0.73	2039
^{82}Se	$(1.7^{+0.4}_{-0.3}) \times 10^{-13}$	1.70	2995
^{100}Mo	$(5.0 \pm 0.3) \times 10^{-13}$	5.0	3034
^{116}Cd	$(1.3^{+0.7}_{-0.3}) \times 10^{-13}$	1.30	2802
^{130}Te	$(4.2 \pm 0.5) \times 10^{-13}$	4.26	2533
^{136}Xe	$(2.8 \pm 0.4) \times 10^{-14}$	0.28	2479
^{150}Nd	$(5.7^{+1.0}_{-0.7}) \times 10^{-12}$	57.0	3367

energy resolution which is required to detect the $0\nu\beta\beta$ decay with the certain $T^{0\nu}_{1/2}$ value and at a given $2\nu\beta\beta$ decay rate. A quantitative estimate has been made in [84], thus we will follow its definition. With this aim consider figure 2 with three examples, in which the 2ν distribution of ^{116}Cd (with $T^{2\nu}_{1/2} = 3 \times 10^{19}$ years) overlaps the three 0ν peaks with half-lives corresponding to (a) 6.7×10^{23} years; (b) 1.6×10^{25} years; and (c) 3.8×10^{26} years. In figure 2(a) the 0ν peak (with the amplitude M) and $2\nu\beta\beta$ decay spectrum meet at the relative height $h/M = 0.1$, and due to this the separation of the effect is excellent. However, such a demand ($h/M = 0.1$) is very severe. At the same time figure 2(c) demonstrates the other extreme case ($h/M = 1$), which does not allow one to identify the effect at all. The example shown in figure 2(b), where the 2ν distribution and the 0ν peak meet at $h/M = 0.5$, represents the minimal requirement for the observation of the effect, which is still experimentally feasible. Therefore, if we accept the last criterion, the discovery potential of the apparatus with fixed energy resolution can be defined as the half-life of the $0\nu\beta\beta$ decay, which could be measured by satisfying this demand ($h/M = 0.5$) at a given $T^{2\nu}_{1/2}$ value. The dependence of this quantity on the energy resolution was determined for several 2β decay candidate nuclei, and they are depicted in figure 3. We stress that the 'discovery potential' in fact, is the sensitivity for observing the effect and is not the same as the sensitivity to set a limit on the effect searched for. The latter could be much longer than the half-life of the discovery potential.

At this point, we discuss the strategies of several proposed next generation $0\nu\beta\beta$-decay experiments that are designed to achieve the sensitivities to probe much of the range of effective Majorana neutrino mass compatible with neutrino oscillations. Only five are discussed in detail, and 10 others in various stages of development are briefly described.

The ideal $0\nu\beta\beta$-decay experiment has the following dream features: the lowest possible background, the best possible energy resolution, the greatest possible mass of the parent isotope, a detection efficiency near 100% for valid events, a unique signature and the lowest possible construction cost. No single experiment proposed has all of these features. In what follows we discuss in alphabetical order: CUORICINO/CUORE, Enriched Xenon Observatory (EXO), Majorana, Molybdenum Observatory of Neutrinos (MOON) and Neutrino Ettore Majorana Observatory (NEMO). While NEMO-III is by and large a $2\nu\beta\beta$-decay experiment, there is a proposal being developed to enlarge it to be a competitive $0\nu\beta\beta$-decay detector. Later, brief descriptions of the other candidates under consideration will be given.

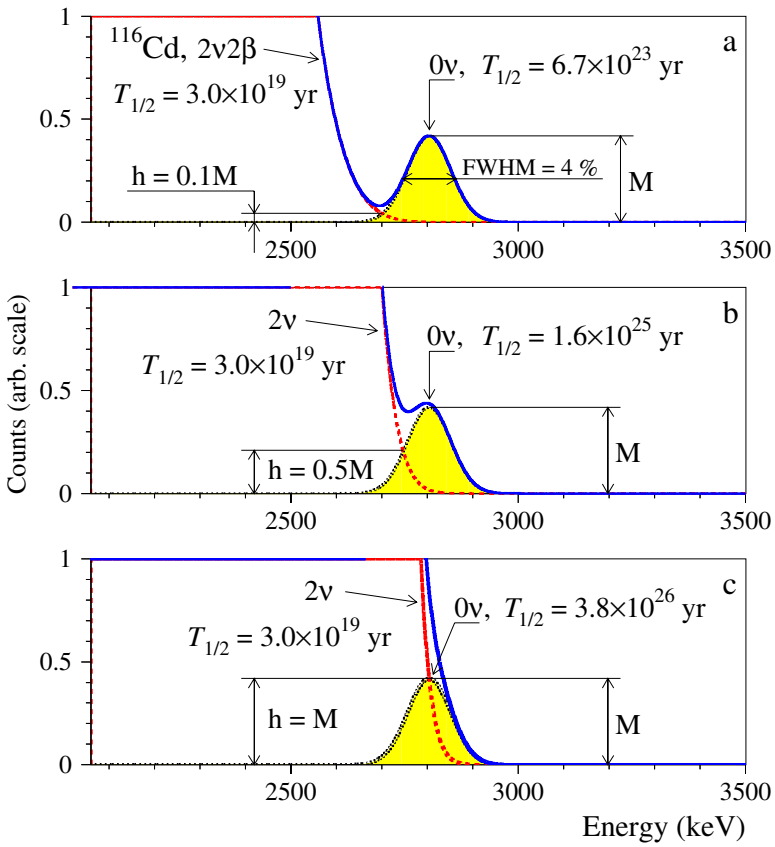

Figure 2. Example of the discovery potential of the 2β decay studies. The 2ν distribution of ^{116}Cd (with $T^{2\nu}_{1/2} = 3 \times 10^{19}$ years) overlaps the 0ν peaks with half-life corresponding to (a) 6.7×10^{23} years; (b) 1.6×10^{25} years; and (c) 3.8×10^{26} years. Correspondingly, the 0ν peak with the amplitude M (the energy resolution at 2.8 MeV is FWHM = 4%) and the 2ν spectrum meet at the relative height h/M for (a) 0.1; (b) 0.5; (c) 1.

Experiments involving Ge detectors or bolometers typically have energy resolutions between 0.2 and 0.3%, and suffer essentially no interference from the irreducible background of events from two-neutrino double-beta decay. Tracking detectors can in principle recognize the difference between neutrinoless and two-neutrino double-beta decay angular correlation; however, angular resolutions of detectors with known technologies are not good enough to eliminate all such events. It is therefore very important to design experiments with the best energy resolution possible for a given detector type. A more quantitative discussion is given at the end of section 4.

2. Next generation experimental proposals

2.1. CUORE/CUORICINO

CUORE is a proposed array of 988 TeO_2 bolometers of about 750 g each. It is best described as a cubic array formed of 19 towers, each similar to the CUORICINO tower which is already

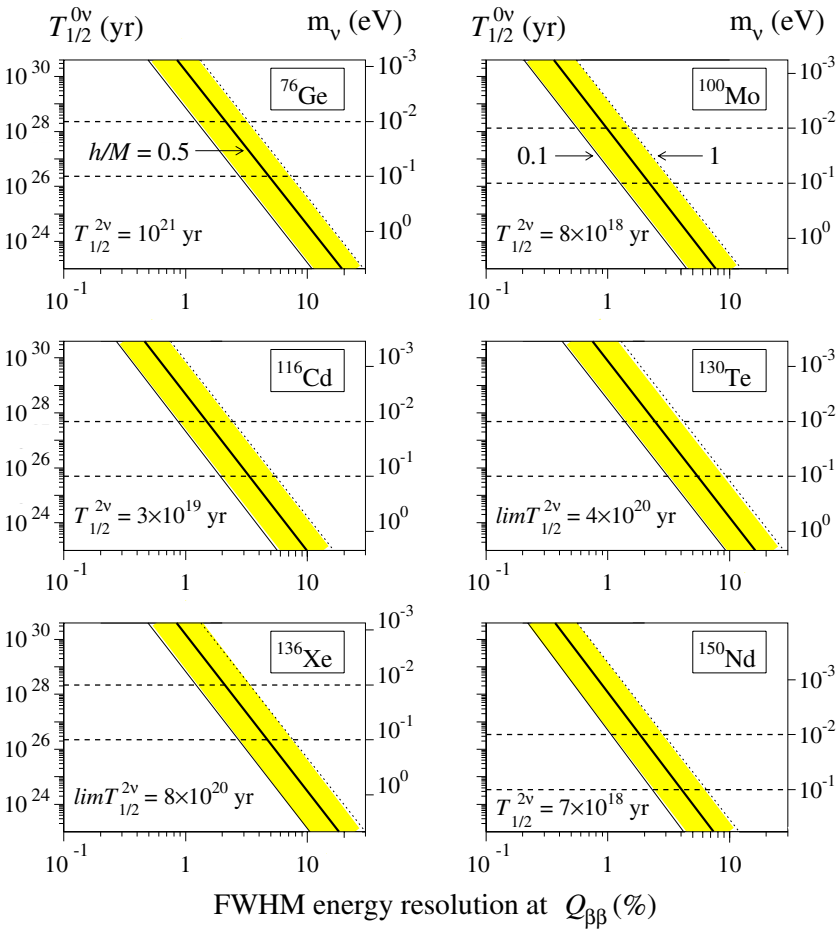

Figure 3. Dependence of the discovery potential versus the energy resolution calculated (bold line for $h/M = 0.5$, thin line for $h/M = 0.1$ and dotted line for $h/M = 1$) for 2β decay candidate nuclei ^{76}Ge, ^{100}Mo, ^{116}Cd, ^{130}Te, ^{136}Xe and ^{150}Nd. Neutrino mass scale (right) is calculated using [75].

operating and producing $0\nu\beta\beta$-decay data as discussed below. All the technical details can be found in the recent CUORE publication by Arnaboldi *et al* [13].

The present CUORICINO array differs slightly from a CUORE tower in that it consists of a tower with 13 planes containing 62 crystals of TeO_2 operating in Hall A of the Gran Sasso Underground Laboratory in the same dilution refrigerator previously used in the MIBETA experiment with 20 crystals [11]. A CUORE tower will have 13 planes of four crystals each. As shown in figure 4, the present CUORICINO structure is as follows: the upper 10 planes and the lowest one consist of four natural crystals of $5 \times 5 \times 5\,\mathrm{cm}^3$, while the 11th and 12th planes have nine, $3 \times 3 \times 6\,\mathrm{cm}^3$ crystals. In the $3 \times 3 \times 6\,\mathrm{cm}^3$ planes the central crystal is fully surrounded by the nearest neighbours.

The small crystals are also of natural tellurium except for four. Two of them are enriched in ^{128}Te and two in ^{130}Te, with isotopic abundances of 82.3 and 75%, respectively. All crystals were grown with pre-tested low radioactivity material by the Shanghai Institute of Ceramics and shipped to Italy by sea to minimize the activation due to cosmic rays. They were lapped with

Figure 4. Photographs of the CUORICINO tower (left), a single plane of four 5 cm cube TeO_2 bolometers (upper right) and one plane of $3 \times 3 \times 6\,cm^3$ bolometers. A CUORE tower will consist of 13 planes of the 5 cm cube bolometers.

specially selected low-contamination abrasives to reduce the radioactive contamination on the surface. All these operations, as well as the mounting of the tower, were carried out in a nitrogen atmosphere glove box in a clean room. The mechanical structure is made of OFHC Copper and Teflon, and both were previously tested for absence of measurable radioactive contaminations. Thermal pulses are recorded by means of neutron transmutation doped (NTD) Ge thermistors thermally coupled to each crystal. The gain of each bolometer is calibrated and stabilized by means of a resistor of 50–100 kΩ, attached to each absorber and acting as a heater. Heat pulses are periodically supplied by a calibrated pulser [7]. The tower is mechanically decoupled from the cryostat to avoid heating due to vibrations, which produce spurious pulses in the detectors. The tower is connected through a 25 mm copper bar to a steel spring fixed to the 50 mK plate of the refrigerator. The entire set-up is shielded with two layers of lead of 10 cm minimum thickness each. The outer layer is made of common low radioactivity lead, the inner layer of special lead with a contamination of 164 Bq kg^{-1} in ^{210}Pb. The electrolytic copper of the refrigerator thermal shields provides an additional shield with a minimum thickness of 2 cm. An external 10 cm layer of borated polyethylene was installed to reduce the background due to environmental neutrons.

The detector is shielded against the intrinsic radioactive contamination of the dilution unit, materials (e.g. from silver and stainless steel) by an internal layer of 10 cm of Roman lead (^{210}Pb activity <4 mBq kg^{-1} [8]), located inside of the cryostat immediately above the tower of the array. The background from the activity in the lateral thermal shields of the dilution refrigerator is reduced by a lateral internal shield of Roman lead that is 1.2 cm thick. It should

be pointed out that in order to use the MIBETA cryostat for the much larger CUORICINO array, the inner thermal shields had to be enlarged. As a consequence the lateral layer of Roman lead was substantially reduced with respect to the configuration of the MIBETA experiment with 20 crystals. The refrigerator is surrounded by a Plexiglas anti-radon box flushed with clean N_2 from a liquid nitrogen evaporator, and by a Faraday cage to eliminate electromagnetic interference.

The front-end electronics of all the $3 \times 3 \times 6\,\mathrm{cm}^3$ detectors and 20 of the 44 detectors of $5 \times 5 \times 5\,\mathrm{cm}^3$ are located at room temperature. They consist of a differential voltage sensitive pre-amplifier followed by a second stage and an anti-aliasing filter [13]. The differential configuration has been adopted to minimize signal cross-talk and microphonic noise coming from the connecting wires. Precautions have been taken to suppress any possible effect coming from room temperature drift and main power supply instability [69]. A pair of load resistors serves to bias each bolometer in a symmetric way. All the necessary settings for the front-end and the biasing system are programmed remotely via computer, to allow the optimization of the overall dynamic performance separately for each detector. The so-called cold electronics have been installed for 24 of the $5 \times 5 \times 5\,\mathrm{cm}^3$ detectors. In this case, the pre-amplifier is located near the detector in a box kept at 100 K to reduce the noise due to microphonics, which is particularly dangerous in the low energy region of the spectrum, relevant for searches for interactions of WIMPS.

The array was cooled down to approximately 8 mK with a temperature spread of 1 mK among the different detectors. A routine calibration was performed using two wires of thoriated tungsten inserted inside the external lead shield in immediate contact with the outer vacuum chamber (OVC) of the dilution refrigerator (see figure 5). This calibration, normally lasting 1–2 days, is performed at the beginning and end of each run, which lasts for approximately 2 weeks.

CUORICINO was cooled down at the beginning of 2003; however, during this operation electrical connections to 12 of the 44 detectors of $5 \times 5 \times 5\,\mathrm{cm}^3$, and to one of the crystals of $3 \times 3 \times 6\,\mathrm{cm}^3$, were lost. This was due to thermal stresses breaking the electrical connection on their thermalizer stages, which allow the transition in temperature in various steps of the electric signals from the detectors to room temperature. When the cause of the technical problem responsible for the disconnection was found, new thermalizer stages were fabricated and tested at low temperature. However, since the performance of the remaining detectors was normal, and their total mass was 30 kg, warming of the array and rewiring were postponed for several months while collecting $0\nu\beta\beta$-decay data.

The performance of the electrically connected detectors was excellent: the average FWHM resolution during the calibration runs was of 7 and 9 keV, for the $5 \times 5 \times 5\,\mathrm{cm}^3$ and the $3 \times 3 \times 6\,\mathrm{cm}^3$ detectors, respectively in the region of $0\nu\beta\beta$-decay.

Double-beta decay measurements started on April 2003 and were interrupted after 3 months due to the disconnection of the cooling water supply of the Laboratory as a consequence of environmental problems associated with the Laboratory itself. During this period CUORICINO operated with a duty factor of 72%, which is very good for a large cryogenic experiment. After the interruption, and a second short run, an independent cooling system was recently installed and CUORICINO is running again.

The first data collection period reported earlier had a total effective exposure of 2.9 and 0.26 kg year for the large and small crystals, respectively. The corresponding spectra in figure 3, show the γ-ray line due to ^{40}K, and those due to the ^{238}U and ^{232}Th chains. Also visible are the lines of ^{121}Te, ^{121M}Te, ^{123M}Te ^{125M}Te and ^{127M}Te, and those of ^{57}Co, ^{58}Co, ^{60}Co, and ^{54}Mn, most likely due to cosmogenic activation of the tellurium and the copper frame. The background counting

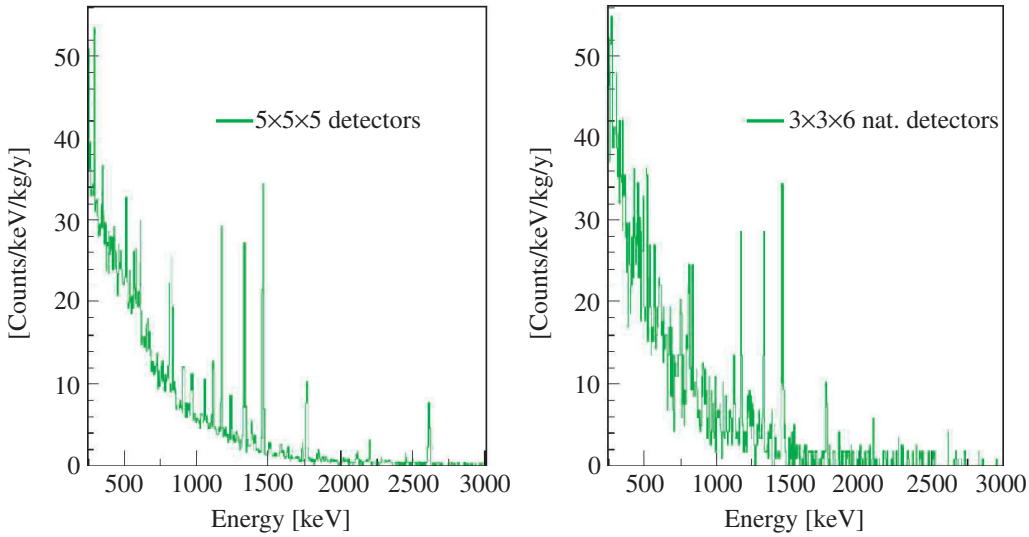

Figure 5. Two calibration spectra of CUORICINO taken with a thorium source shown for the two size detectors.

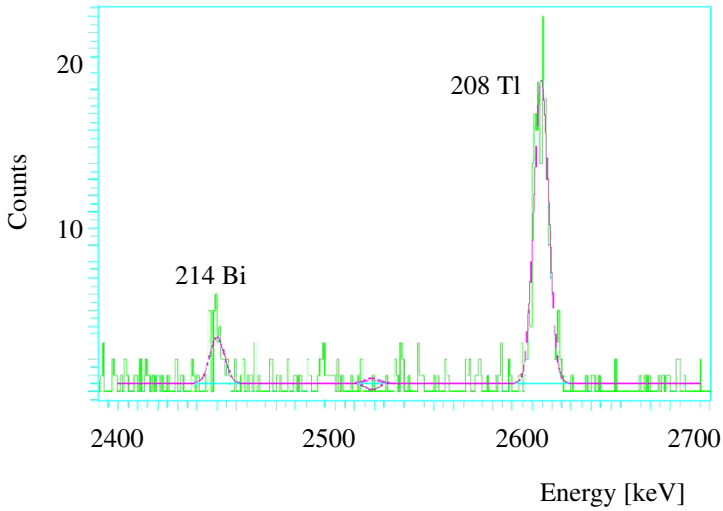

Figure 6. An experimental background spectrum summed over all 5 cm cube detectors. Clearly visible are the two well-known gamma ray lines from the thorium chain, and the energy region of the expected neutrinoless double-beta decay peak.

rates in the region of $0\nu\beta\beta$-decay are 0.20 ± 0.03 and 0.2 ± 0.1 counts keV^{-1} kg^{-1} year^{-1}, for the $5 \times 5 \times 5\,\mathrm{cm}^3$ and $3 \times 3 \times 6\,\mathrm{cm}^3$, respectively. These values are among the best ever obtained in this energy region and similar to those reached in the experiments with Ge diodes [2, 20].

The sum background spectrum of the $5 \times 5 \times 5\,\mathrm{cm}^3$ and $3 \times 3 \times 6\,\mathrm{cm}^3$ crystals is shown in figure 6. No peak appears in the region of $0\nu\beta\beta$-decay of ^{130}Te. A maximum likelihood procedure was used to establish the maximum number of $0\nu\beta\beta$ events. It is consistent with the measured background and implies an upper limit of 7×10^{23} years for $0\nu\beta\beta$-decay of ^{130}Te at a 90% CL. The limits that can be extracted from our result on the effective neutrino mass vary between 0.37

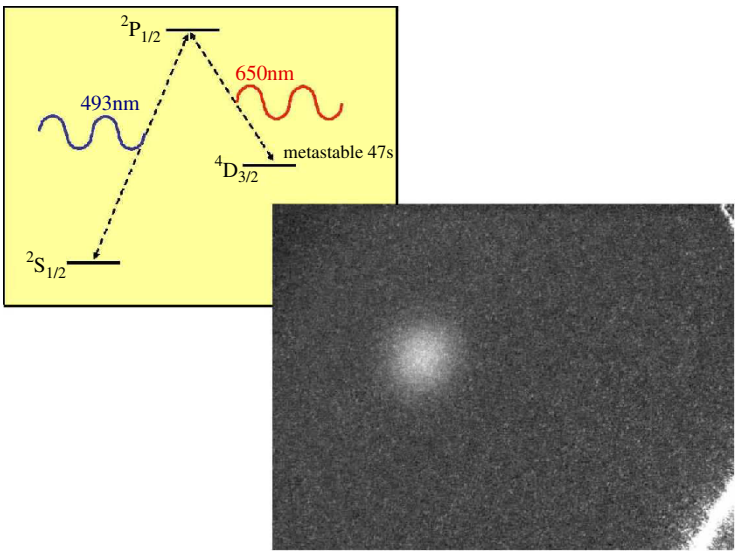

Figure 7. The atomic level scheme for the EXO laser tagging technique, and a photograph of laser light taken in a test chamber.

and 1.9 eV depending on the nuclear matrix elements used. Discussions of the application of matrix elements to arrive at this range are given in the recent paper in *Physics Letters* by the CUORICINO Collaboration [12].

2.2. The EXO experiment

The EXO experiment proposes to search for the $0\nu\beta\beta$-decay of ^{136}Xe to ^{136}Ba in a multi-ton time projection chamber (TPC) of either high-pressure gas or liquid. The decay energy of ^{136}Xe to ^{136}Ba is 2468 keV resulting in a phase-space factor that is competitive with most other candidate isotopes. It has a natural abundance of 8.9% which implies that the Xe must be isotopically enriched. As a noble gas Xe can be enriched by centrifuge with no requirement for complex chemistry, as in the case of all of the other isotopes proposed. A multi-ton detector of enriched ^{136}Xe certainly fulfils the requirement of maximum mass of the parent isotope. While TPCs do not have good energy resolution, there is a research and development program to attempt to tag the daughter $^{136}Ba^{++}$ ion after it is partially neutralized to a more stable $^{136}Ba^{+}$ ion. This was first described by the EXO collaboration in an earlier article by Danilov *et al* [28] from a concept originally introduced by Moe [62].

The scheme involves positively identifying the Ba^+ ion by isolating it and using laser induced fluorescence spectroscopy. The principle of this scheme was first demonstrated by Neuhauser *et al* [65]. The atomic physics can be easily understood from figure 7. The Ba^+ ion has a very strong allowed transition at 493 nm from the $6^2S_{1/2}$ ground state to the $6^2P_{1/2}$ excited state. Upon optical excitation to that state there is a decay branching ratio of 30% to the metastable $5^4D_{3/2}$ state. The specific identification of the Ba^+ ion is achieved by exciting it back up to the $6^2P_{1/2}$ level with photons of 650 nm and observing the 493 nm blue light from the 8 ns 70% transition back to the ground state. When in secular equilibrium, the ion will radiate $\sim 6 \times 10^7$ photons per second. Figure 7 also shows (bottom right) the image of a Ba^+ ion in

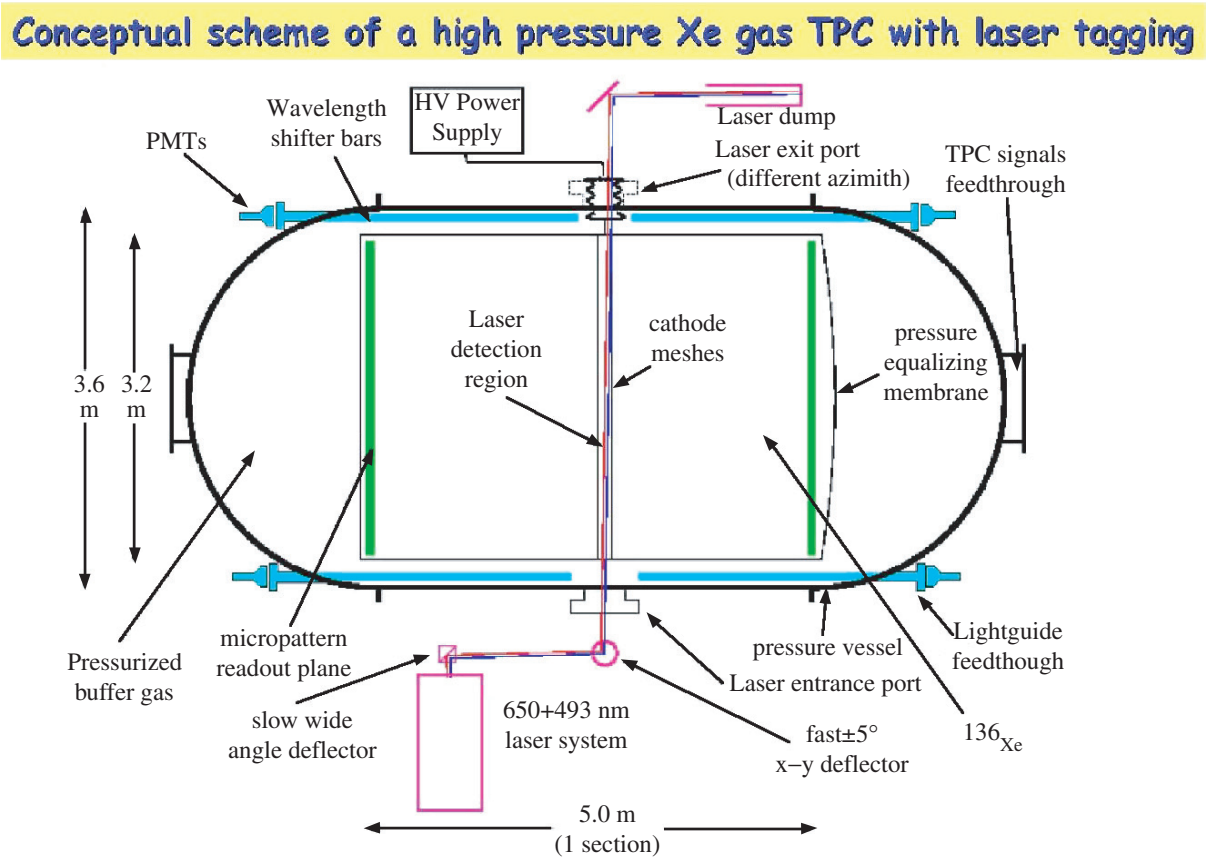

Figure 8. A conceptual drawing of the EXO high-pressure gas TPC, with laser tagging of the Ba^+ ion.

the test trap developed by the EXO group. It will be necessary to hit the ion simultaneously with two laser beams at these two frequencies. The EXO collaboration is at present investigating the spectroscopy of Ba^+ in an atmosphere of Xe at various pressures. In addition, studies are in progress to demonstrate the ability to locate the ion and subject it to the laser excitation and detect the 493 nm light by photo detectors. This principal has been established and repeated many times by the EXO collaboration; however, the main task will be to locate the ion and subject it to the laser excitation and detect the 493 nm light by photomultiplier tubes surrounding the detector.

Several interesting points beyond the principal mechanisms are made in [28]. First, in a gas TPC operated at several atmospheres, the Ba ions will be trapped for a time long enough to localize and excite them. For example, in 5 atmospheres, the Ba ion diffuses only about 0.7 mm in 1 s. In that period of time it can be optically cycled about 10^7 times with the scheme described above. If the drift of the Ba^+ ions in the electric field can be determined accurately, the direction of the laser beams can be corrected. The collaboration has determined that gas pressures of up to 10 atmospheres will also support this detection scheme.

A conceptual drawing of the gas TPC option of EXO is shown in figure 8. A volume of about 40 m^3 of Xe gas at 10 atmospheres would contain about 2 metric tons of xenon. The Xe gas and liquid Xe are also scintillators, and the energy resolution can be improved by detecting both the ionization charge and scintillator light. The collaboration has also been experimenting with a liquid chamber.

The liquid TPC option has the significant advantage of being much smaller than the gas version. The disadvantage of the liquid Xe option is that the laser light will suffer too much scattering to use the technique of locating the Ba^+ ion at the position of the $0\nu\beta\beta$-decay and guiding the lasers to it. The EXO collaboration has been successful in locating Ra ions (very similar to Ba^+ ions) in a small liquid test chamber and extracting it to a small chamber on the tip of a cold-finger electrode coated with frozen Xe. The scheme involves heating the probe and releasing the Ba^+ ion into a radio frequency quadrapole trap, where the laser identification is performed.

Xe is a good scintillator in both gas and liquid phases. This feature will be used to provide a third spatial coordinate in the TPC and improve the energy resolution. This is particularly important for the liquid version of the EXO experiment that is energetically pursued at present. By observing that the scintillation and ionization are anticorrelated, the collaboration has been able to substantially improve the energy resolution such that the resolution in the liquid phase should be able to achieve a resolution of about 2% at 2.5 MeV.

The EXO collaboration is in the process of testing the feasibility of the Ba^+ ion extraction and determining its efficiency. At the same time they have been funded to construct a 200 kg isotopically enriched xenon prototype detector without the Ba^+ ion-tagging feature, and to install and operate it in the DOE Underground Laboratory in the Waste Isolation Pilot Plant (WIPP) in Carlsbad, New Mexico. The results of this pilot experiment could likely be competitive with the most sensitive $0\nu\beta\beta$-decay experiments performed thus far for bounds on the effective Majorana mass of the electron neutrino, providing that reliable nuclear matrix elements are available.

2.3. The Majorana experiment

The proposed Majorana detector is an array of Ge detectors with a total mass of 500 kg of Ge that is isotopically enriched to 86% in ^{76}Ge. The final configuration is not fixed; however, several have been evaluated with respect to cryogenic performance and background reduction and rejection. This discussion will concentrate on a conventional modular design using ultra-low background cryostat technology developed by the International Germanium Experiment (IGEX). It will also utilize new pulse-shape discrimination hardware and software techniques developed by the Majorana collaboration and detector segmentation to reduce background.

The most sensitive $0\nu\beta\beta$-decay experiments thus far have been the Heidelberg–Moscow [20] and IGEX [2, 4] ^{76}Ge projects that set lower limits on $T^{0\nu}_{1/2}$ of 1.9×10^{25} and 1.6×10^{25} years, respectively. They both utilized Ge enriched to 86% in ^{76}Ge and operated deep underground. The projection is that the Majorana background will be reduced by a factor of 65 over the early IGEX results prior to pulse-shape analysis (from 0.2 to $\sim$0.003 $\mathrm{keV^{-1}\,kg^{-1}\,year^{-1}}$). This will occur mainly by the decay of the internal background due to cosmogenic neutron spallation reactions that produce ^{56}Co, ^{58}Co, ^{60}Co, ^{65}Zn and ^{68}Ge in the germanium by limiting the time above ground after crystal growth, careful material selection, and electroforming copper cryostats. One component of the background reduction will arise from the granularity of the detector array. In figure 9, an option for a detector configuration is shown for one module. Each of these modules would have three levels of 19 detectors in close-packed array. Each detector is 62 mm in diameter and 70 mm long with a mass of 1.1 kg. In figure 10, an alternative cooling option is shown which clusters all the detectors in a copper vacuum chamber, which can then be cooled by immersing the chamber in a vessel of liquid nitrogen or in a jacket of cooled gas.

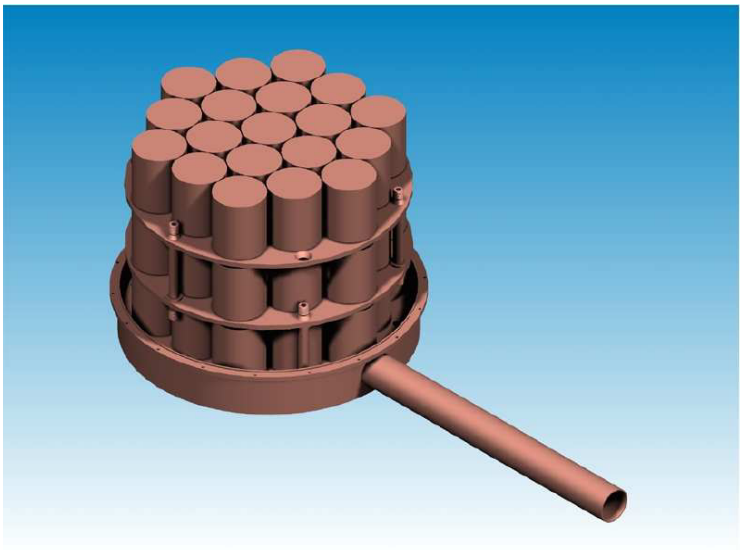

Figure 9. One proposed Majorana module of 57, 1 kg detectors in a standard ultra-low background electroformed copper cryostat.

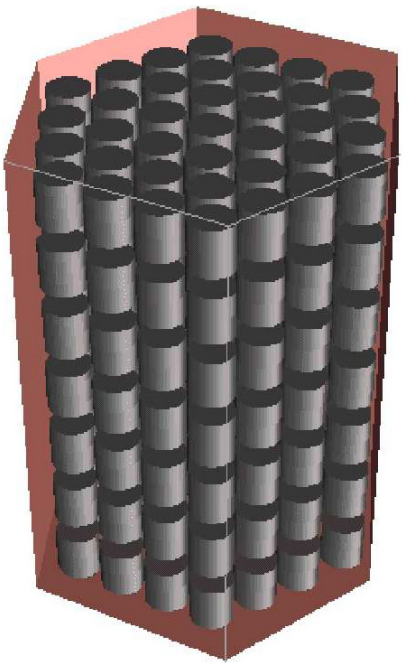

Figure 10. All 259 of the proposed 1 kg Majorana Ge detectors in an alternative cooling configuration.

2.3.1. Recent progress in Ge detector technology. New ^{76}Ge experiments must not simply be a volume expansion of IGEX or Heidelberg–Moscow. They must have superior background rejection and better electronic stability. The summing of 200–250 individual energy spectra can result in serious loss of energy resolution for the overall experiment. In IGEX, instabilities lead to a degradation of 25% in the energy resolution of the 117 mole-years of data.

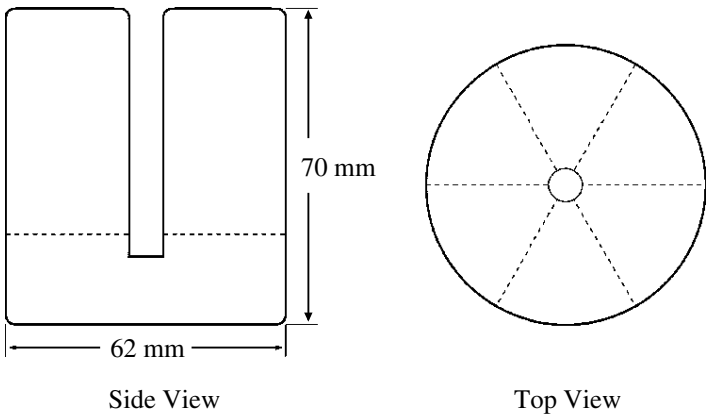

Figure 11. A standard Ge detector segmentation scheme. This is the configuration of the SEGA detector undergoing tests by the Majorana collaboration.

The IGEX collaboration has overcome these problems and the technology is now available. Firstly, detectors electronically segmented into a number of individual volumes in a single n-type intrinsic Ge detector are available from two companies: Advanced Measurement Technology (ORTEC) and Canberra Industries. Secondly, complete digital electronics from X-ray Instrumentation Associates (XIA) have been used by the group to demonstrate unprecedented stability, very low energy thresholds (<1 keV) for a 2 kg Ge detector, and a vast improvement in pulse-shape discrimination.

In the 10 years since the production of the 2 kg IGEX intrinsic Ge detectors, the new technology evolved in the two industrial companies known to us. Large semi-coaxial n-type detectors have been fitted with a series of azimuthal electrical contacts along their length, and one or more axial contacts in the central hole. A configuration with six-azimuthal-segment by two-axial-segment geometry is shown in figure 11. After Monte Carlo studies and discussions with detector manufacturers, several configurations are available that the Majorana collaboration believes will strike a good balance between cost, background reduction and production efficiency. The six-by-two configuration in figure 11 was used in the Monte Carlo simulations that produced the data shown in figure 12 for a single detector. The internal ^{60}Co modelled in the figure is produced by cosmic-ray neutrons during the preparation of the detector. Formation begins after the crystal is pulled. Its elimination by segmentation and pulse shape analysis is crucial.

The saga of pulse-shape discrimination (PSD) in the IGEX project has been slow and painful, finally culminating in success. Current techniques depend entirely on experimental calibration and do not utilize pulse shape libraries. The ability of these techniques to be easily calibrated for individual detectors makes them practical for large detector arrays.

A major contributor to this success has been the availability of commercial digital spectroscopy hardware. Digitizing a detector pre-amplifier signal, all subsequent operations on the signal are performed digitally. Programmable digital filters are capable of producing improved energy resolution, long-term stability and excellent dynamic range. The particular unit used in these studies was the 4-channel Digital Gamma Finder (DGF-4C) unit developed and manufactured by XIA.

The DGF-4C has four independent 14-bit 40 MHz ADCs. The ADCs are followed by first-in first-out (FIFO) buffers capable of storing 1024 ADC values for a single event. In parallel with each FIFO is a programmable digital filter and trigger logic. The digital filter and trigger logic

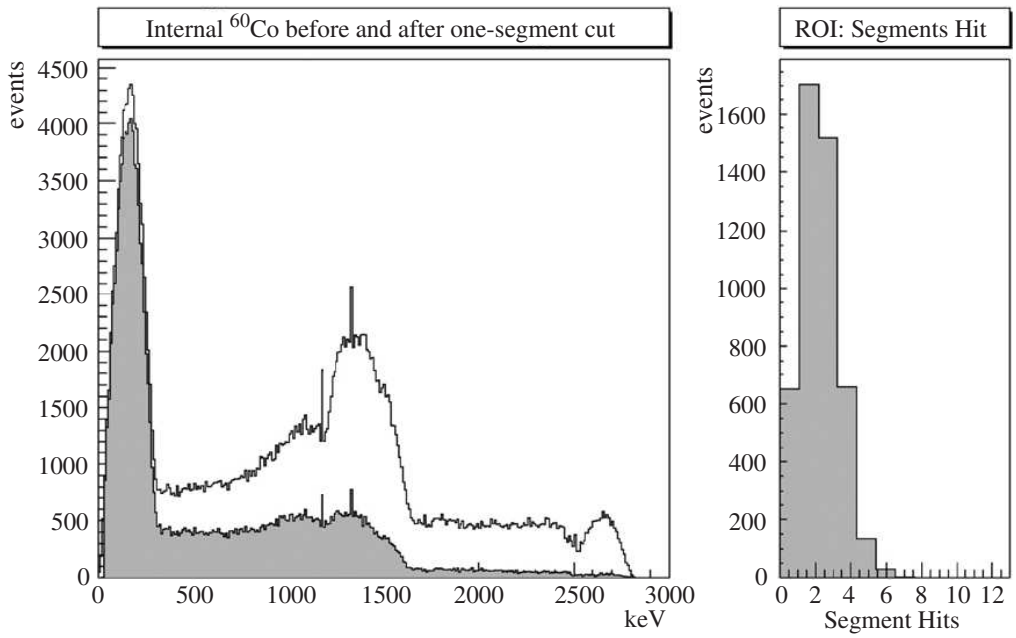

Figure 12. The results of a detailed Monte Carlo simulation of a contamination of ^{60}Co internal to a Ge detector, created by cosmogenic neutrons while the Ge was on the Earth's surface. The upper spectrum is without suppression, and the lower (dark) spectrum is the result of applying cuts that exclude events that interact in more than one segment. The plot to the right is the corresponding frequency plot of events against numbers of segments hit.

for each channel is combined into a single field programmable Gate Array (FPGA). Analog input data are continuously digitized and processed at 40 MHz.

The DGF-4C is then a smart filter of incoming pulses. If for example, a signal has a pulse-width incompatible with the usual collection time of 200–300 ns, or is oscillatory (like microphonic noise), the filters can be programmed to reject it. This feature can also be used to allow the very low energy thresholds required in dark matter searches as well as eliminating the broad spectrum of artificial pulses from high-voltage leaks and electromagnetic interference that can even add noise pulses in the region of $0\nu\beta\beta$-decay. Figure 13 contains two examples of reconstructed pulses from a DGF-4C.

The Majorana Collaboration has made an extensive analysis of the predicted backgrounds and their impact on the final sensitivity of the experiment [60]. Their conclusion is that with 500 kg of Ge, enriched to 86% in the isotope ^{76}Ge, the Majorana array operating over 10 years including construction time, can reach $T^{0\nu}_{1/2} \geqslant 4 \times 10^{27}$ years. This corresponds to an upper bound of $\langle m_\nu \rangle$ of 0.038 ± 0.007 eV [27, 74]. One advantage of ^{76}Ge is that it may well be a candidate for a future more reliable microscopic calculation of the $0\nu\beta\beta$-decay nuclear matrix element.

2.4. MOON

The MOON project involves the use of the unique nuclear structure of the isotope ^{100}Mo for both a neutrinoless double-beta decay search and a solar neutrino experiment [32]. The authors

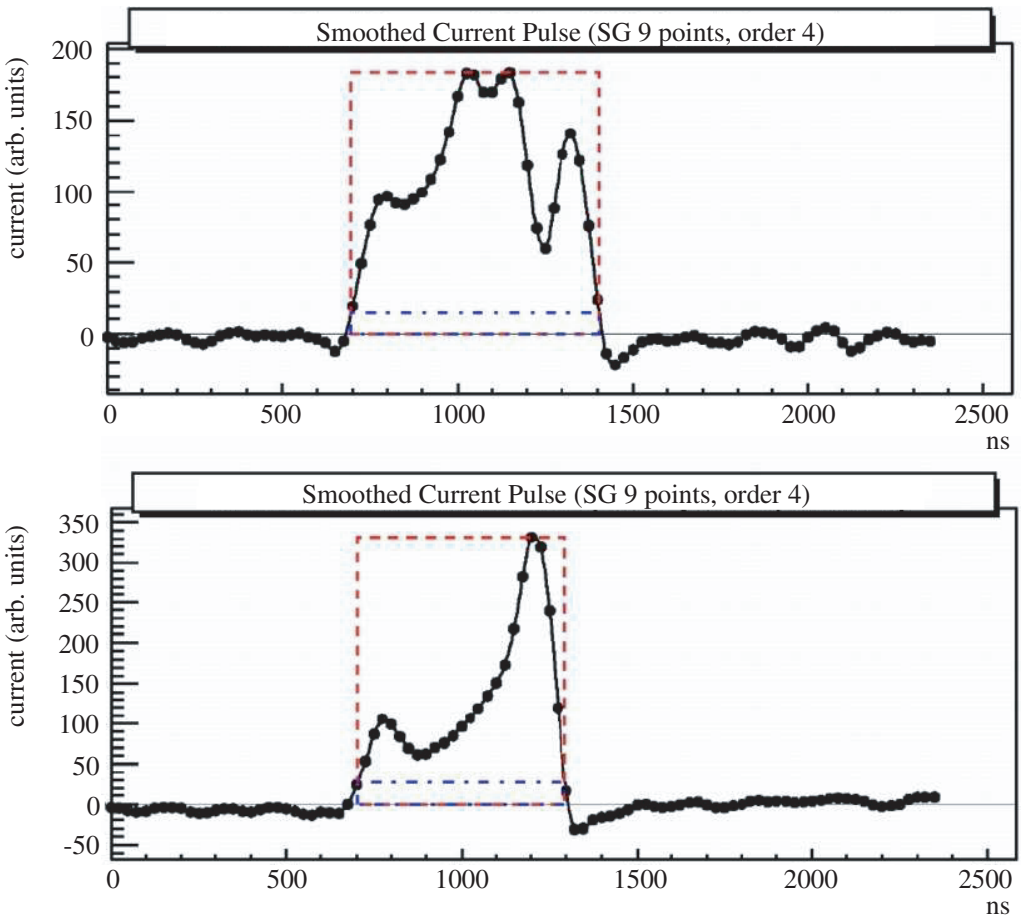

Figure 13. Two typical experimental displacement currents for a multiple-site (upper) curve, like that of a background γ-ray, and (lower) a single-site event like that expected from a neutrinoless double-beta decay event in a Ge detector.

claim that the planned apparatus could also potentially detect supernovae neutrinos [33]. The first excellent feature of ^{100}Mo is that it has a high $0\nu\beta\beta$-decay Q-value, 3034 keV, which results in a large phase space factor in the decay rate, and is above the energies of gamma rays from natural radioactivity as well. The decay of ^{100}Mo has been observed and the half-life accurately measured, most recently by the NEMO Collaboration ($T^{2\nu}_{1/2} = 7.8 \pm 0.09(\text{stat}) \pm 0.09(\text{syst}) \times 10^{18}$) years and discussed later in this article. This short half-life unfortunately has the potential effect of contributing a non-reducible background from $2\nu\beta\beta$-decay to the energy region of $0\nu\beta\beta$-decay. This implies that significant attention must be paid to achieving the best possible energy resolution near the $0\nu\beta\beta$-decay energy, 3034 keV.

The basic detector concept involves constructing a tracking chamber of series of planes of thin films of Mo sandwiched between plastic scintillating fibres. The fibres on one side would be perpendicular to those on the other side of the Mo foils. Each sandwich is followed by a 6 mm thick plastic scintillator to obtain the energy of the electrons. This configuration, shown in figures 14 and 15, is designed to track decay electrons well enough to observe the angular correlation of pairs of electrons from the source to reject background from $2\nu\beta\beta$-decay, as well as some others. Another concept under consideration is the use of plastic scintillating fibres coated

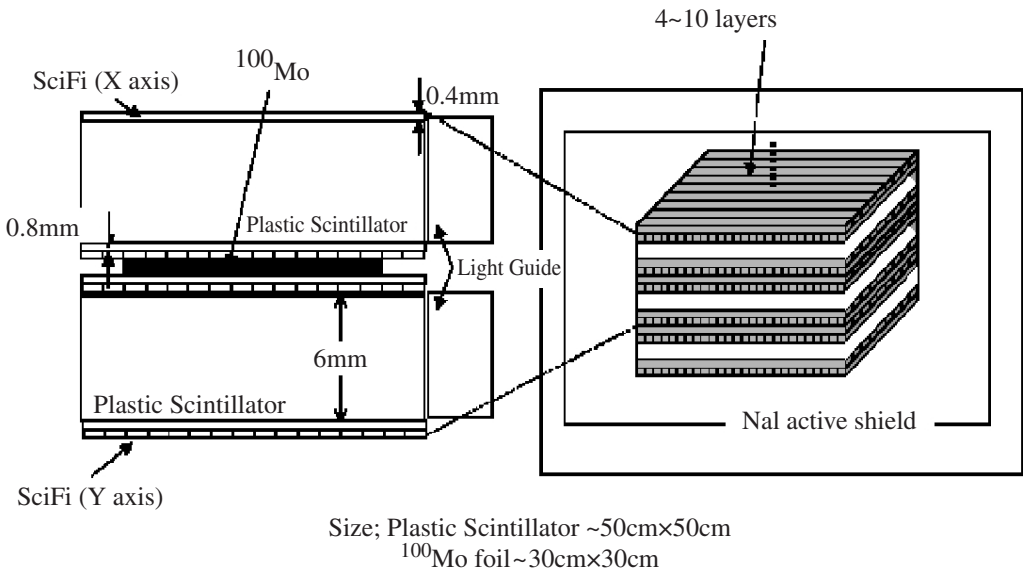

Figure 14. An artist's conception of a module of the MOON detector showing the ^{100}Mo foil, readout fibres, and the plastic scintillators.

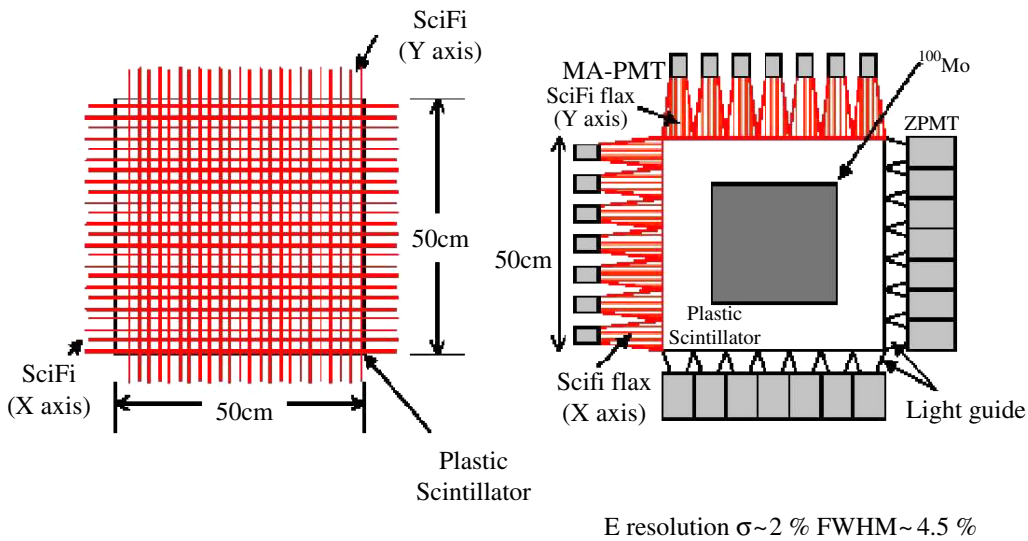

Figure 15. The configuration for testing the energy resolution of the MOON modules. The tests yielded a resolution of FWHM = 4.5% at the double-beta decay energy of ^{100}Mo.

with about 0.03 g cm^{-2} of Mo. This geometry could achieve a position resolution of the order of the fibre diameter, which is typically 1–3 mm. The signal characteristic of double beta-decay in the MOON detector is a coincidence between two beta particles in two independent parts of the detector. This will help to reduce backgrounds. This, coupled with the angular correlation, can combine to lead to significant background reduction. This is of crucial importance because in building a tracking detector it is far more difficult to control the radio-purity of all of the constituent components than in the case of Ge detectors, for example. The predicted $0\nu\beta\beta$-decay

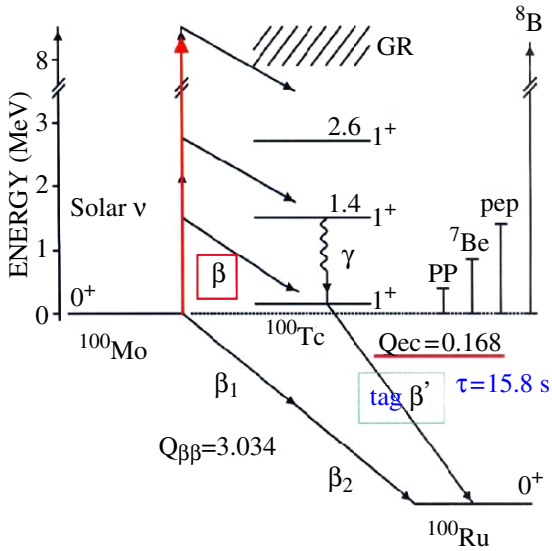

Figure 16. The nuclear decay-scheme of ^{100}Mo, demonstrating its value as a solar neutrino detector as well as a source for neutrinoless double-beta decay.

rate for the target sensitivity, $\langle m_\nu \rangle = 0.03$ eV, is ~11 counts ton^{-1} year^{-1} of enriched ^{100}Mo. The natural abundance is 9.63%.

The very special nuclear structure of the three isotopes, ^{100}Mo, ^{100}Tc and ^{100}Ru are shown in figure 16. This energy level scheme renders ^{100}Mo a good target for the study of low-energy solar neutrinos as well as an excellent candidate for the search for neutrinoless double-beta decay. There is need for a low energy, real-time spectroscopy study of solar neutrinos. The low excitation energy from the ground state of ^{100}Mo to the low-lying 1^+ state, with an electron-capture Q-value of 168 keV, decays to the ground state of ^{100}Ru with a half-life of 15.8 s. This transition would be sensitive to pp-neutrinos as well as ^{7}Be and pep neutrinos. The ^{8}B solar neutrinos would excite higher energy 1^+ states in ^{100}Tc which would decay by gamma-ray cascade to the low-lying 1^+ state that decays by β^- to the ground state of ^{100}Ru with the half-life of 15.8 s.

Energy resolution tests are underway with a $60 \times 60 \times 10\,\mathrm{mm}^3$ plate with four 2 in photomultiplier tubes at right angles. A resolution of $\sigma = 2.7\%/E^{1/2}$ has been achieved. For the full MOON modules, a resolution of FWHM = 5% is predicted at the $0\nu\beta\beta$-decay energy of 3034 keV. The two tracking measurements, together with the signal selection by the time and spatial correlation analyses, reduces most background counts from natural and cosmogenic radio isotopes and $2\nu\beta\beta$-decay. The MOON-decay experiment is planned in three phases: MOON-I, 0.003 ton year, MOON-II, 0.75 ton year and MOON-III, 5.25 ton year. The predicted half-life sensitivities are: 6×10^{25}, 8×10^{26} and 3×10^{27} years, respectively. The corresponding upper bounds on the effective Majorana mass of the electron neutrino $\langle m_\nu \rangle$ are 0.1, 0.03 and 0.02 eV, respectively.

The large area of foils could lead to significant difficulties in controlling the background from radon daughters and dust; however, this could be significantly alleviated by the use of Mo foils isotopically enriched in ^{100}Mo. This has been accomplished several times at the Electro-Chemical Plant in Zelenogorsk (Russia) by use of centrifuge separation using MoF_6 gas.

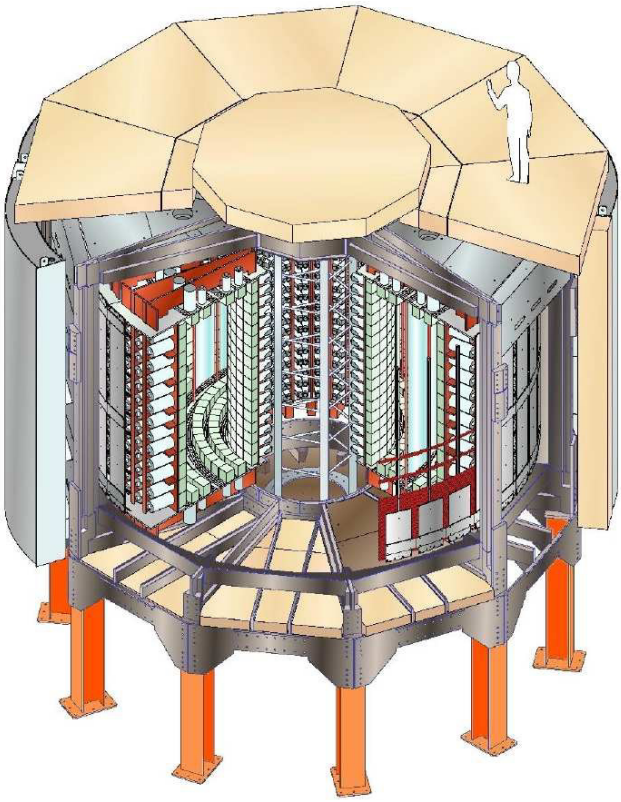

Figure 17. An artist's conception of the NEMO detector, showing a cartoon of a normal size person to demonstrate its dimensions.

2.5. Nemo and Super-NEMO

The NEMO has had several generations. Here, we describe NEMO-3, which is operating, and give projections for an expanded version that would represent a next generation $0\nu\beta\beta$-decay experiment. In this paper, we have emphasized both source = detector calorimeter experiments, CUORE, and Majorana, and two types of tracking detector experiments, a TPC in which the source is also the detector namely EXO, and finally two types of tracking chambers, MOON, and finally now NEMO [15].

The NEMO-3 detector is constructed in 20 segments of thin source planes, a three-dimensional readout drift chamber, operating in the Geiger mode for tracking, with the tracking volumes surrounded by plastic scintillating blocks as calorimeters. There are 1940 plastic scintillators that have thresholds of ~30 keV and a γ-ray detection efficiency of 50% at 1 MeV. At this energy, the energy resolution ranges between 11 and 14.5% FWHM. The planes are vertically set in a cylindrical geometry inside of a magnetic solenoid that creates a vertical induction field of ~30 G. Tracking in the field allows the differentiation between electron and positron tracks, with only a probability of ~3% of confusing the two. Figure 17 shows a schematic drawing, while figure 18 is a photograph of the open detector.

The detector is surrounded by a 20 cm shield of low background iron to reduce the external gamma ray flux. Fast neutrons from the laboratory environment are suppressed by an external shield of water, wood and polyethylene plates. The experiment is located in the Modane

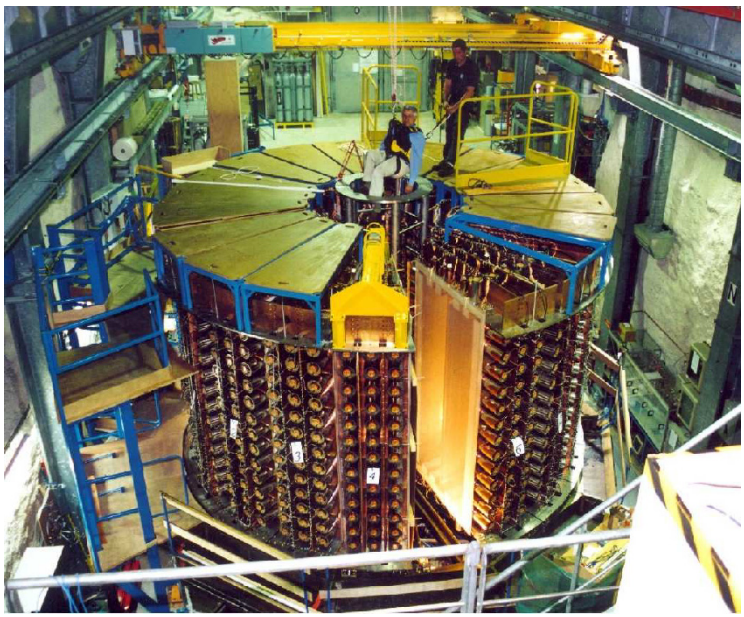

Figure 18. A photograph of the NEMO detector opened and showing one of its source foils. Note the people on top of the detector.

Underground Laboratory with an overburden of 4800 m of water equivalent (mwe). The air in the experimental hall is constantly flushed which reduces the radon levels to between 10 and 20 Bq m^{-3}. This renders the number of decays of ^{214}Bi in the detector due to radon to be below that due to the photomultiplier tubes. This level was further reduced by the installation of a tent surrounding the detector which during this year will have its atmosphere purified by a Free-Radon Purification System to reduce radon levels to ~0.2 Bq m^{-3}, with a capacity of 150 m^3 h^{-1}.

One very positive aspect of the NEMO detector is that it can make double beta-decay measurements on many different nuclei, and several simultaneously. During recent operations the following isotopes were together investigated in the detector: ^{116}Cd (0.40 kg),^{130}Te (0.45 kg), ^{150}Nd (36.5 g), ^{96}Zr (9.43 g), ^{48}Ca (6.99 g), ^{nat}Te (0.61 kg), ^{82}Se (0.93 kg) and ^{100}Mo (6.9 kg). Two neutrino double beta-decay half-lives were measured and the following three results were communicated to us at the time of the Venice conference in December 2003:

$$T^{2\nu}_{1/2}(^{150}\mathrm{Nd}) = 7.5 \pm 0.3(\mathrm{stat}) \pm 0.7(\mathrm{syst}) \times 10^{18}\mathrm{years}, \tag{22}$$

$$T^{2\nu}_{1/2}(^{82}\mathrm{Se}) = 9.52 \pm 0.25(\mathrm{stat}) \pm 0.9(\mathrm{syst}) \times 10^{19}\mathrm{years}, \tag{23}$$

and

$$T^{2\nu}_{1/2}(^{100}\mathrm{Mo}) = 7.8 \pm 0.09(\mathrm{stat}) \pm 0.09(\mathrm{syst}) \times 10^{18}\mathrm{years}. \tag{24}$$

The two-electron sum spectrum from the $2\nu\beta\beta$-decay of ^{100}Mo is shown in figure 19. This is essentially a zero background spectrum, and is the highest quality one ever published to the knowledge of the authors of this review. One of the reasons for this is that backgrounds from the usual problem sources, ^{214}Bi and ^{208}Tl for example can be recognized by their known decay chains and the life times of their daughter nuclides, and identified.

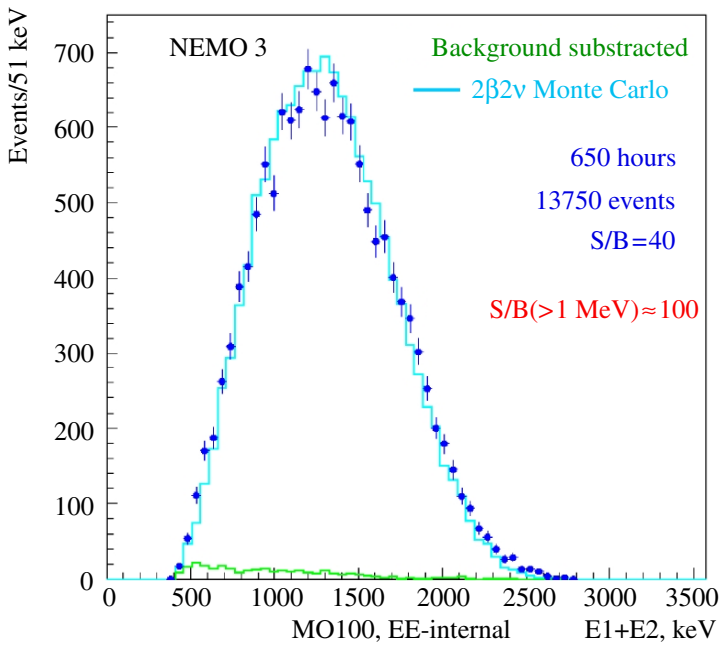

Figure 19. An energy spectrum of the sum energy of the two electrons from the two-neutrino double-beta decay of ^{100}Mo measured in the NEMO detector.

The remaining challenge concerns the energy resolution, which in NEMO-3 is about 250 keV at 3 MeV. This will require a convincing discovery experiment to have enough real counts from $0\nu\beta\beta$-decay in order to determine that a peak really exists. Nevertheless, the series of NEMO experiments have really made significant contributions to the field of double-beta decay and the technique has some promise for the future. Discussions are in progress to consider a greatly expanded version, SuperNEMO, as a next generation $0\nu\beta\beta$-decay experiment.

The basic parameters for SuperNEMO are that they be at least ten times the capacity of NEMO-3 so that it will have the capacity to contain about 100 kg of isotopically enriched isotope. Candidate isotopes are ^{82}Se, ^{100}Mo, ^{116}Cd, ^{130}Te and ^{136}Xe.

The project is conceived to have four phases: (i) (2004–2006), feasibility studies, (ii) (mid 2006–2007) engineering design and acceptance, (iii) (2008–2010) construction; and (iv) (2011–) operation.

One of the main issues in feasibility study is the attempt to improve the energy resolution. The requirement for a significant breakthrough here will quite possibly be the driving force for full proposal.

3. Other proposals

There are other proposals that merit some discussion. These proposals can be divided into two categories, those with an active source and those with a passive source. Active source experiments use detectors that are fabricated from the source material and passive source detectors use separate sources and detectors. The following are descriptions of other experiments not covered earlier in this article.

Table 5. Physical properties of $CaWO_4$ and $CdWO_4$ crystal scintillators.

Physical parameter	$CaWO_4$	$CdWO_4$
Density (g/cm^3)	6.1	8.0
Melting point (°C)	1570–1650	1325
Structural type	Sheelite	Wolframite
Cleavage plane	(1 0 1)	(0 1 0)
Hardness (Mohs)	4.5–5.0	4.0–4.5
Wavelength of emission maximum (nm)	440	480
Refractive index	1.94	2.2–2.3
Primary decay time	8 μs	13 μs
Relative light yield (for γ-rays, at indoor temperature)	≈90%	100%

3.1. CARVEL: an example of a scintillator double-beta decay experiment

The CAlcium Research for VEry Low neutrino mass (CARVEL) experiment is being developed using scintillator crystals of $^{48}CaWO_4$ [83]. A research project performed by the Institute for Nuclear Research (Kiev, Ukraine) has verified the ability of these crystals to discriminate between pulses from α-particles and electrons. There was a rather high level of radioactivity in the $CaWO_4$ crystals used in the development; nevertheless a background level of 0.07 counts kev^{-1} kg^{-1} year^{-1} was achieved in the energy region of $0\nu\beta\beta$-decay. The high decay energy, 4272 keV, of ^{48}Ca is well above the natural radioactivity level of gamma rays. In principle, 100 kg of $^{48}CaWO_4$ could reach a sensitivity of $m_\nu \simeq 40$–90 meV or $T^{0\nu}_{1/2} \sim 10^{27}$ years. One ton could reach $T^{0\nu}_{1/2} \sim 10^{28}$ years and $m_\nu \sim 20$ meV.

The difficulty of immediately proposing such an experiment at this time stems from the fact that the only known practical method for isotopically enriching Ca in ^{48}Ca in kg quantities is the atomic vapor laser ionization separation (AVLIS) technique. The cost is roughly proportional to the ratio of the final isotopic abundance to the initial one, which is only 0.187%. The atomic structure of calcium however has favourable laser wavelength requirements, and is called a 'first harmonic candidate'. The only facility to our knowledge in existence at the time of writing this paper is at the Lawrence Livermore National Laboratory, Livermore, CA, USA. This facility does not have a program for enriching large quantities of isotopes at the moment. There is a program of development at the Kurchatov Institute (Moscow), which could possibly lead to a practical solution in the future.

In table 5, the properties of $CaWO_4$ and $CdWO_4$ are given. They have very similar light output, however, earlier experiments demonstrated that the radioactive background achieved in the $CdWO_4$ crystals was much lower than that of the $CaWO_4$ scintillator. This strongly implies that the background in the $CaWO_4$ can quite probably be reduced significantly.

The scintillation properties of $CaWO_4$ crystal scintillators were studied. The energy resolution of $CaWO_4$ detectors is similar to that of NaI(TI) scintillators (e.g., FWHM ≈ 7% for the 662 keV γ line of ^{137}Cs and FWHM = 3.8% for the 2614 keV γ line of ^{208}TI). Due to the difference of $CaWO_4$ scintillation pulse shapes for α particles and γ-rays (β particles), clear discrimination between them was achieved. Radioactive contaminations of the $CaWO_4$ crystals are higher by factors from 10 to 10^3 (e.g., activity of ^{210}Po is ≈0.3 Bq kg^{-1}) than those of the $CdWO_4$ scintillators.

3.1.1. Pulse shape discrimination in scintillation detectors. The pulse shape of $CaWO_4$ scintillation signals, for example, can be described by the formula: $f(t) = \sum A_i/(\tau_i - \tau_0) \times (e^{-t/\tau_i} - e^{-t/\tau_0})$, $t > 0$, where A_i are amplitudes (in %) and τ_i are decay constants for different light-emission components, τ_0 is the integration constant of electronics ($\approx$0.2 μs). The following values were obtained by fitting the average of 4000 individual pulses: $A_1^\alpha = 0.76$ $\tau_1^\alpha = 8.8\,\mu$s, $A_2^\alpha = 0.18$, $\tau_2^\alpha = 3.2\,\mu$s, $A_3^\alpha = 0.06$, $\tau_3^\alpha = 0.3\,\mu$s, for $\approx$4.6 MeV α particles and $A_1^\gamma = 0.82$, $\tau_1^\gamma = 9.0\,\mu$s, $A_2^\gamma = 0.15$, $\tau_2^\gamma = 4.4\,\mu$s, $A_3^\gamma = 0.03$, $\tau_3^\gamma = 0.3\,\mu$s, for $\approx$1 MeV γ quanta. This difference allows one to discriminate $\gamma(\beta)$ events from those of α particles. For this purpose, the method of the optimal digital filter, previously applied successfully with $CdWO_4$ scintillators, was used. To obtain the numerical characteristic of $CaWO_4$ signals, called the shape indicator (SI), each experimental pulse $f(t)$ was processed with the following digital filter: $SI = \sum f(t_k) \times P(t_k)/\sum f(t_k)$, were the sum is over time channels k, starting from the origin of the pulse and up to 75 μs, $f(t_k)$ in the digitized amplitude (at the time t_k) of a given signal. The weight function P(t) is defined as $P(t) = \{\bar{f}_\alpha(t) - \bar{f}_\gamma(t)\}/\{\bar{f}_\alpha(t) + \bar{f}_\gamma(t)\}$, where $\bar{f}_\alpha(t)$ and $\bar{f}_\gamma(t)$ are the reference pulse shapes for α particles and γ quanta, resulting from the average of a large number of experimental pulse shapes.

The shape indicator measured by $CaWO_4$ crystals for α particles in the (1–5.3) MeV region does not depend on the direction of α irradiation relative to the crystal axes. Similarly, no dependence of the SI on γ quanta energy (from 0.1 to 2.6 MeV) was observed. The distributions of the shape indicators measured with α particles ($E_\alpha \approx 5.3$ MeV) and γ quanta ($\approx$1.2 MeV) are depicted in the inset of figure 20 (the larger value of the shape indicator corresponds to the shorter decay time of the scintillation pulse). As shown in figure 20, distinct discrimination between α particles and γ rays (β particles) was achieved. As an illustration of the PS analysis, the background data, accumulated during 171 h with $CaWO_4$ detector, is shown in figure 19 as a scatter plot for the SI values versus energy. In this plot one can see two clearly separated populations: the α events, which belong to U/Th families and $\gamma(\beta)$ events.

In figure 21, the effect of the energy resolution projected to 4272 keV on the interference from $2\nu\beta\beta$-decay is shown.

The CARVEL project has produced some interesting data associated with the properties of $CaWO_4$ and $CdWO_4$ crystal scintillators. They have the light output that results in adequate energy resolution. Pulse-shape analysis leads to clear discrimination between α-particle and γ-ray induced events allowing significant background reduction. Future availability of Ca, isotopically enriched in ^{48}Ca could render this technique competitive. These results could be interesting for the investigation of other double beta-decay scintillation detectors.

3.2. The ^{116}Cd CAMEO project

The project CAMEO [21] is a further development of the double beta-decay studies of ^{116}Cd performed by the Kiev–Florence collaboration in the Solotvina Underground Laboratory since 1989 with enriched cadmium tungstate ($^{116}CdWO_4$) crystal scintillators [29, 31]. Here, we briefly describe the main results of this experiment. $^{116}CdWO_4$ scintillators (enriched in ^{116}Cd to 83%) with a total mass of 330 g were used. They were surrounded by active and passive shields. For each event in the $^{116}CdWO_4$ detector, the amplitude of the signal, its arrival time and pulse-shape were recorded. The energy resolution of the detector was FWHM = 8.0% at 2615 keV. Due to active and passive shields, and as a result of the time-amplitude and pulse-shape analysis of the data, the background rate of the $^{116}CdWO_4$ detector in the energy interval 2.5–3.2 MeV ($Q_{\beta\beta}$

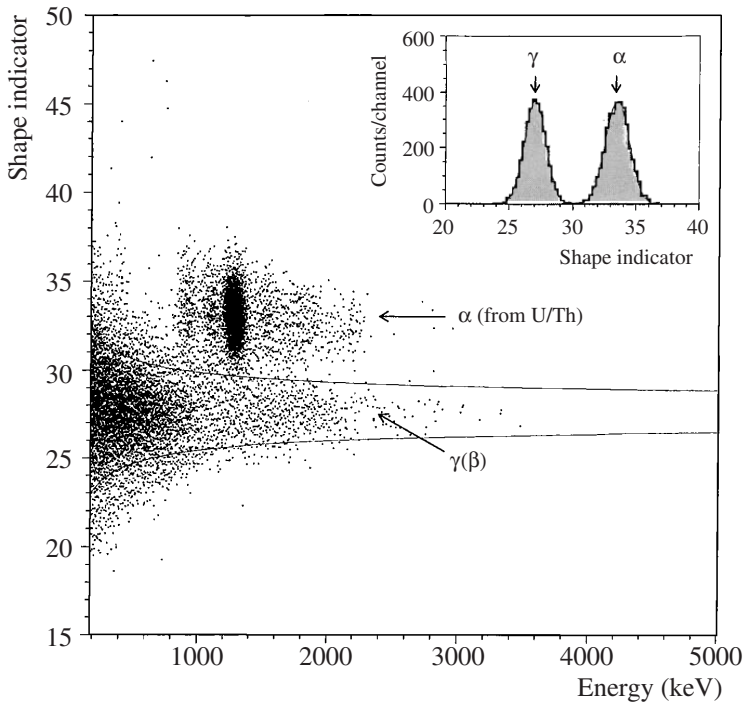

Figure 20. Scatter plot of the shape indicator SI versus energy for 171 h background data measured with the $CaWO_4$ crystal scintillator ($40 \times 34 \times 23\,mm^3$). The solid liner show $\pm 2\delta$ region of SI for $\gamma(\beta)$ events. Inset: the SI distributions measured in calibration runs with α particles ($E_\alpha = 5.3$ MeV) which corresponds to $\approx$1.2 MeV in γ scale and γ quanta ($\approx$1.2 MeV).

of ^{116}Cd is 2.8 MeV) was reduced to 0.037(10) counts year^{-1} kg^{-1} keV^{-1}. This is the lowest background rate which has ever been reached with crystal scintillators.

A fit of the data measured during 12649 h gives the half-life value of the $2\nu\beta\beta$ decay of ^{116}Cd:

$$T_{1/2}^{2\nu} = 2.9 \pm 0.06(\text{stat})^{+0.4}_{-0.3}(\text{syst}) \times 10^{19}\ \text{years}.$$

In addition, the bound on the half-life for $0\nu\beta\beta$-decay of ^{116}Cd was measured as

$$T_{1/2}^{0\nu} \geqslant 1.7(2.6) \times 10^{23}\ \text{yr at } 90\%(68\%)\text{CL}.$$

Using this limit and the calculations of [75], one can derive restrictions on the neutrino mass parameter $\langle m_\nu \rangle \leqslant 1.7(1.4)$ eV at 90% (68%) CL, or on the basis of calculations [14] $\langle m_\nu \rangle \leqslant 1.5(1.2)$ eV.

These bounds, which are among the best published to date, were obtained with very small $^{116}CdWO_4$ detectors (containing only $\approx$0.1 kg of ^{116}Cd, in contrast with those used for ^{76}Ge studies ($\approx$10 kg of enriched HP ^{76}Ge detectors). Therefore, the Solotvina experiment demonstrates that $CdWO_4$ crystals possess several unique properties required for a double beta-decay experiment: low-level intrinsic radioactivity, good scintillation characteristics and PSD ability, which allows one to reduce background. To enhance the sensitivity to $\langle m_\nu \rangle \leqslant 0.05$ eV,

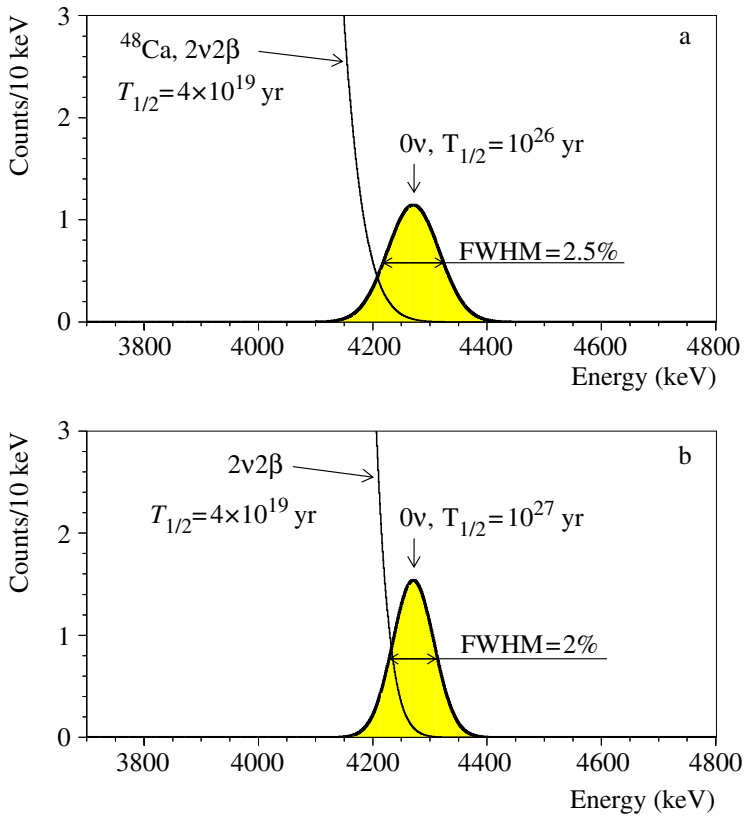

Figure 21. A demonstration of the impact of energy resolution of $|Q_{\beta\beta}|$ on the interference from $2\nu\beta\beta$-decay events.

it will be necessary to increase the mass of enriched $^{116}CdWO_4$ detector and measuring time, to improve the energy resolution and to reduce the background of the detector further.

Accordingly, the CAMEO project [21] proposes to use ≈100 kg of $^{116}CdWO_4$ crystals placed in a large volume of high purity liquid (serving as a shield and a light guide simultaneously), and calls for improvement of the energy resolution (FWHM) at 2.8 MeV to 4%, and for the background reduction by a factor ≈100. The required radioactive contamination of $^{116}CdWO_4$ crystals must be less than $\approx 10\,\mu Bq\,kg^{-1}$, both for ^{228}Th and ^{226}Ra. Actually, even existing $CdWO_4$ crystals satisfy these requirements for ^{226}Ra ($<4\,\mu Bq\,kg^{-1}$), but ^{228}Th contamination varies in different crystals from (3–39) $\mu Bq\,kg^{-1}$ [31]. At the same time, the required energy resolution FWHM = 4.3% at 2615 keV (^{232}Th) has been already achieved with the $CdWO_4$ crystal ($\varnothing 4 \times 3\,cm^3$) placed in a liquid.

In the preliminary design concept of CAMEO, 24 enriched $^{116}CdWO_4$ crystals of large volume ($\approx 350\,cm^3$) are allocated for the liquid scintillator of the BOREXINO Counting Test Facility (CTF)[2] and fixed at 0.4 m distance from the CTF centre, thus homogeneously spreading

[2] The CTF (described, e.g., in [9] is installed in the Gran Sasso Underground Laboratory (Italy). It consists of an external ≈1000 ton water tank (11 × 10 m) served as passive shield for 4.8 m^3 liquid scintillator (contained in an inner vessel of diameter 2.1 m). The radio-purity of the water is $\approx 10^{-14}\,g\,g^{-1}$ for U/Th and $\approx 10^{-10}\,g\,g^{-1}$ for K. The liquid scintillator is a solution of $1.5\,g\,l^{-1}$ of PPO in pseudocumene. The yield of emitted photons (365 nm) is $\approx 10^4\,MeV^{-1}$ and the attenuation length is ⩾5 m. The principal scintillator decay time is ≈5 ns. The ^{232}Th and

on the sphere with diameter 0.8 m. On the basis of GEANT Monte Carlo simulations, the sensitivity of the CAMEO experiment has been calculated as $T_{1/2}^{0\nu} \geqslant 10^{26}$ years, which translates to the neutrino mass parameter bound of $\langle m_\nu \rangle \leqslant 0.06$ eV. Moreover, these results can be advanced further by exploiting 1 ton of $^{116}CdWO_4$ detectors ($\approx 1.5 \times 10^{27}$ nuclei of ^{116}Cd) placed in one of existing or future large underground neutrino detectors such as BOREXINO, SNO or KamLAND. The sensitivity is estimated as $T_{1/2}^{0\nu} \geqslant 10^{27}$ years ($\langle m_\nu \rangle \leqslant 0.02$ eV). The proposed CAMEO technique with $^{116}CdWO_4$ crystals is simple and reliable, thus, such experiments can run stably for decades.

For isotopic enrichment, a new project, MCIRI, is under development at the Kurchatov Institute (Moscow), and the Joint Institute for Nuclear Research (Dubna), with the goal to enrich large quantities of ^{48}Ca (and other isotopes) by ion cyclotron resonance heating in plasma [40]. This could certainly enhance interest in $0\nu\beta\beta$-decay experiments using ^{48}Ca.

3.3. Double-beta decay of ^{48}Ca with CANDLES

The CANDLES project is a search for $0\nu\beta\beta$-decay of ^{48}Ca with scintillators of CaF_2 (pure) immersed in liquid scintillator. It will be installed in the underground Oto Cosmo Observatory. The original development work was performed using CaF_2(Eu) scintillators in the ELEGANT VI system [78].

In the developmental experiments, 25 CaF_2(Eu) crystals with dimensions $4.5 \times 4.5 \times 4.5\ cm^3$ and total mass of 7.2 kg were placed at the centre of the ELEGANT VI array. They were surrounded by CsI (Tl) scintillators and CaF_2 (pure) light pipes to reduce background. The first results from this effort had 9.6×10^{22} ^{48}Ca nuclei and placed a bound of $T_{1/2}^{0\nu} > 1.4 \times 10^{22}$ years (90% CL). This corresponds to an upper bound on the effective Majorana mass of the electron neutrino $\langle m_\nu \rangle$ between 7.2 and 44.7 eV, depending on the nuclear model used. This is far from competitive with the bound from Ge experiments [2, 4, 20]; however, one must keep in mind that the Ca used has a natural abundance of ^{48}Ca of 0.187%.

The half-life sensitivity would have been more than 250 times greater with an isotopic abundance of 50%. To explore the interesting range of neutrino mass implied by the atmospheric neutrino oscillations, the experiment would need $\sim 10^{26}$ ^{48}Ca nuclei. This will require several tons of calcium because of the low natural isotopic abundance of ^{48}Ca.

The new detector system CANDLES employs several tons of calcium in the form of $10 \times 10 \times 10\ cm^3$ CaF_2 (pure) scintillation crystals. The scintillation light from CaF_2, with no Eu doping, is in the ultraviolet (UV) region of the spectrum. It has a rise time of $\sim 1\ \mu s$. They are immersed in a liquid scintillator whose light curve rise-time is a few tens of nanoseconds. The liquid scintillator will act as a background veto, and will contain a wavelength shifting (WLS) component to convert the UV light to the sensitivity of the photomultipliers. It was shown by computational simulation that the energy resolution of such a system could be $\sim$4% at 4.3 MeV.

A complete study of PSD between α-particle and electron scintillation has been done [78]. Based on this, and the other studies, the expected performance parameters are given in table 6 below.

^{238}U contamination of the scintillator is less than $(2–5) \times 10^{-16}$ g g^{-1}. The inner vessel is made of transparent nylon film, 500 μm thick, which allows one to collect scintillation light with the help of 100 phototubes (8″ Thorn EMI 9351) fixed to a 7 m diameter support structure inside the water tank. The photomultiplier tubes are fitted with light concentrators 57 cm long and 50 cm diameter aperture. It gives a 20% optical coverage.

Table 6. The predicted performance of three future versions of the CANDLES project.

	CANDLES III	CANDLES IV	CANDLES final version
CaF_2 volume	191 kg	~3.2 ton	32 ton or 3.2 ton (2% enriched ^{48}Ca)
Energy resolution	4%	4%	4%
Measurement time	3 years	5 years	5 years
Target Purity (^{214}Bi)	30 μBq kg^{-1}	3 μBq kg^{-1}	<1 μBq kg^{-1}
(^{212}Bi)	30 μBq kg^{-1}	3 μBq kg^{-1}	<1 μBq kg^{-1}
Background rate	0.3 year	0.9 year	
Sensitivity for $\langle m_\nu \rangle$	0.5 eV	0.1 eV	0.03 eV

The values of $\langle m_\nu \rangle$ appearing in the table were computed with the matrix element published by Pantis *et al* [70].

At this point it is interesting to compute the figure-of-merit for such an experiment using the parameters of CANDLES IV. In this case: $\overline{\eta} = 0.54$, $a = 1.87 \times 10^{-3}$, $\epsilon \simeq 0.95$, $W = 78.07$, $M = 3200$ kg, $\delta E = 170.88$ keV and $b = 0.9\,\text{year}^{-1}(171\,\text{keV})^{-1}\,3200\,\text{kg}^{-1} = 1.65 \times 10^{-6}\,\text{keV}^{-1}\,\text{kg}^{-1}\,\text{year}^{-1}$. Substituting these numbers into equation (21), one deduces the figure-of-merit of: $f \simeq 0.04$. Isotopically enriching the calcium to 5% in ^{48}Ca would result in: $f \simeq 1.1$, a very respectable value, if the background rate can be controlled to this level.

Even in this case, the energy resolution, 4%, results in a full-width at half-maximum (fwhm) of ~170 keV. This makes a discovery potential very difficult if only tens of counts are spread over an energy range of ~200 keV, even with this incredible low level of background, 0.9 counts per year in the area of the $0\nu\beta\beta$-decay peak with 3200 kg of detector.

This analysis again shows how important isotopic enrichment and energy resolution are for a next generation $0\nu\beta\beta$-decay experiment with discovery potential.

3.4. The COBRA double-beta decay experiment with CdTe detectors

A $0\nu\beta\beta$-decay experiment involving CdTe ionization detectors has been developed by Zuber [85]; following earlier work [61, 79]. The main isotopes of interest in COBRA are ^{130}Te and ^{116}Cd. This approach will also allow sensitive searches for double-electron capture. A preliminary set up was constructed in the Laboratori Nazionale del Gran Sasso (LNGS) [48].

The CdTe detectors were housed in an active plastic scintillator shield, surrounding a passive lead shield, with a copper shield inside. The copper shield is a $50 \times 50 \times 50\,\text{cm}^3$ casing of copper inside and lead outside. The passive shield is placed in an airtight $60 \times 60 \times 60\,\text{cm}^3$ aluminium box flushed with dry nitrogen to minimize the content of ^{222}Rn. The CdTe detectors are inside a special copper brick.

The passive shield is surrounded by 19 plastic scintillators $130 \times 20 \times 0.5\,\text{cm}^3$ outside the aluminium box. The detection efficiency for cosmic ray muons is 95%.

The energy resolution was measured with various radioactive sources and resulted in the following equations for the named ER and CPG detectors:

$$\triangle E_{ER} = \sqrt{E/\text{keV}} \times 1.68\,\text{keV} + 3.66\,\text{keV}, \tag{25}$$

$$\triangle E_{CPG} = \sqrt{E/\text{keV}} \times 1.03\,\text{keV} - 0.72\,\text{keV}. \tag{26}$$

This implies that the energy resolution at the 2615 keV γ-ray in the decay of ^{208}Tl is ~90 keV for the ER detector and ~52 keV for the CPG detector.

The background in the region 2.7–3.4 MeV was 3.3×10^{-4} keV^{-1} kg^{-1} day^{-1}, which is ~120 keV^{-1} kg^{-1} day^{-1}, ~600 times higher than the background in the ^{76}Ge experiments.

While this technique promises the first measurement of double-electron capture, the energy resolution, and background levels published in [48] will have to be improved significantly for COBRA to be competitive in the search for $0\nu\beta\beta$-decay with $\langle m_\nu \rangle \simeq 40$ meV. Research and development to achieve this improvement continues.

3.5. The drift chamber beta-ray analyser (DCBA)

The DCBA experiment is the only current proposal and active research and development project that plans the use of ^{150}Nd as the parent isotope for a search for $0\nu\beta\beta$-decay. There are several papers that describe the project in significant detail [43, 44, 47].

The instrument is designed to measure the momentum of each beta-ray from the double beta-decay events, and the position of the vertex of the decay. This will allow a three-dimensional reconstruction of the tracks in the uniform magnetic field.

The detector concept is a drift chamber with dimensions $46.4 \times 52.4 \times 68.0$ cm^3 inside of a solenoidal coil with a 72 cm diameter bore and 110 cm in length. The detector will be surrounded by cosmic-ray veto counters.

The energy resolution for a single electron is predicted to be 140 keV for a typical energy of one electron from $0\nu\beta\beta$-decay. The spatial resolution of the vertex of the decay is less than 3 mm. This will greatly assist in the discrimination against background.

There are several phases of the DCBA program: DCBA-T is the construction of a test module for the technical development of the apparatus. The second phase DCBA-I is the construction of a chamber four times the size of DCBA-T, and its operation with a natural isotopic abundance source (5.6% ^{150}Nd). The third phase DCBA-II, will be a chamber 100 times the dimensions of DCBA-II, which they call their standard model (SM). It will operate with natural Nd, ~7.7 moles of ^{150}Nd. The fourth and final phase will be the same chamber operating with Nd isotopically enriched in ^{150}Nd containing 124 moles of ^{150}Nd, or $\sim 7.5 \times 10^{25}$ atoms of ^{150}Nd.

There is only one known practical way to isotopically enrich Nd in kg quantities, that is the AVLIS Process. The only tested facility known to the authors is at the Lawrence Livermore National Laboratory in Livermore, CA. At the time of writing, there is no program there to commercially separate large quantities of isotopes. Neodymium is however a good candidate for this process. It has a favourable atomic energy structure and is refined to be a 'first harmonic' atom for laser ionization.

There are two further concerns. One is the large uncertainly in the nuclear $0\nu\beta\beta$-decay matrix element of ^{150}Nd. This nucleus has a very large static nuclear quadrupole moment. This makes QRPA type calculations very difficult. The other is the 140 keV, single-electron energy resolution. This corresponds to ~200 keV resolution for the $0\nu\beta\beta$-decay events. This makes a discovery experiment extremely difficult, even if an extremely low background is achieved.

In the future, it will be seen if the energy resolution, efficiency and background parameters can be reached that would result in a figure-of-merit of approximately unity.

4. Other proposals involving ^{76}Ge

There are several proposals other than Majorana involving the search for $0\nu\beta\beta$-decay of ^{76}Ge. The Majorana proposal was the only one that is reported completely in this paper because a complete white paper exists and a proposal has been prepared in detail and will be submitted in the near future. The GEM and GENIUS proposals involve operating naked Ge crystals in purified liquid nitrogen [57, 81]. While a very detailed theoretical study has been made of the GENIUS concept and a detailed article written about GEM, no formal proposals for funding have been submitted, nor are expected in the near future. The leader of the GENIUS project has claimed discovery of $0\nu\beta\beta$-decay with a confidence level of 4.1 σ, with a half-life of $\sim 1.2 \times 10^{25}$ years [57]. If this is correct, a full blown GEM or GENIUS project will not be necessary. Nevertheless, these will be discussed later in this section.

There is new proposal, headed by the Max Planck Institute in Heidelberg and Munich, called GERDA. This, as well as the claim of discovery will also be discussed below [64].

4.1. The GEM experiment

The GEM project proposes to construct an array of naked Ge detectors with a mass of $\sim$ 1 ton, emersed in highly purified liquid nitrogen. The first phase, GEM-I proposes to use detectors made with natural abundance germanium, to be followed by GEM-II with 1 ton of Ge detectors made from germanium isotopically enriched to 86% in ^{76}Ge. Detailed Monte Carlo simulations of the backgrounds, and their effect on the experimental sensitivity have been performed. The results imply that with GEM-I, $T^{0\nu}_{1/2} \sim 10^{27}$ years, and $\langle m_\nu \rangle \sim 0.05$ eV, while with GEM-II a half-life of $\sim 10^{28}$ years can be reached with the corresponding sensitivity, $\langle m_\nu \rangle \sim 0.015$. The GEM apparatus could also be used to sensitively search for Cosmic Cold Dark Matter.

A sketch of the general configuration of the GEM apparatus is shown in [81]. The outer dimensions of the water shield are diameter 10 m and height 10 m. The 1 ton of Ge detectors are immersed in a double-wall copper sphere containing 40 tons of liquid nitrogen surrounded by a vacuum jacket.

The radiopurity of the liquid nitrogen is assumed to be the same as that achieved for the liquid scintillator of the BOREXINO experiment: $\sim 10^{-15}$ g g^{-1} of ^{40}K and ^{238}U, and 5×10^{-15} g g^{-1} for ^{232}Th. It has been recently demonstrated by the BOREXINO Collaboration that the liquid scintillator can be purified to $< 5 \times 10^{-16}$ g g^{-1} of ^{232}Th and ^{238}U.

All details of the simulations from which the sensitivity levels were derived for both double beta-decay and Cold Dark Matter are given in [82]. It should be pointed out that the cost of 500 HPGe detectors of about 2 kg, made from p-type, natural abundance germanium would cost roughly one third of the cost of an equal number of enriched detectors. Such an array would be more than adequate to confirm or refute the claim of [52] if the sensitivity calculations are correct.

In any case, this type of study is very useful in helping to formulate a final solution to the problem of observing or putting tight enough bounds on $\langle m_\nu \rangle$ to eliminate the inverted hierarchy or quasi-degenerate neutrino mass eigenstate spectrum.

4.2. The GENIUS project

The GENIUS concept was introduced by Klapdor-Kleingrothaus in the late 1990s and supported by a great deal of computations and experimental research [42], [55]–[57]. A very long and detailed white paper, as well as other articles on the subject, can be found in [57].

The GENIUS project preceded the GEM project, but the two share a number of similar features. The first version would involve 1 ton of HPGe detectors, made from germanium isotopically enriched to 86% in ^{76}Ge, and emersed directly in liquid nitrogen. This proposal was the original naked Ge crystal in liquid nitrogen idea, and proposes a giant tank of LN_2 as the cooling medium and shield. The computations to justify the sensitivity were based on the installation being located in the LNGS (3600 mwe), and used the environmental data on neutron and gamma-ray fluxes measured there.

The optimum size of the LN_2 tank was determined to be a cylinder 12 m in diameter and 12 m high. The naked Ge detectors would be suspended in the centre. These tank dimensions were found to be optimum for shielding the detectors sufficiently from external gamma-ray sources. The neutron flux would first be reduced by 92% by a layer of polyethylene foam outside as a thermal shield and neutron absorber. The remainder would be thermalized in the first 100 cm and captured in the reactions ^{14}N (np)^{14} C* and ^{14}N (nγ)^{15} N*. The γ-ray emissions would still have more than 4 m between the de-exicitation of the carbon and nitrogen nuclei and the germanium detectors.

The muon flux in the LNGS has been measured as 1.1 m^{-2} h^{-1}. The muon flux impact on the background was simulated by placing active veto above the tank with a 96% reduction factor. The total number of neutrons generated by cosmic rays which enter the tank was determined to be $\sim 2.5 \times 10^5$ year^{-1}. The two major cosmogenic isotopes produced in the tank would be ^{14}C (5.73×10^3 years) and ^{13}N (9.96 min). These were found to be insignificant contributions to the total background. The construction steel was assumed to be the same as that of the BOREXINO Collaboration which has a level of radiopurity of 5×10^{-9} g g^{-1} of ^{238}U and ^{232}Th. It was determined that the background from the vessel to the rate in the energy region of $0\nu\beta\beta$-decay (2000–2100 keV) would be $\sim 10^{-4}$ keV^{-1} kg^{-1} year^{-1}, where the mass is that of the detector array. The background contributions from the ^{238}U, ^{232}Th, ^{40}K and ^{222}Rd in the LN_2 were evaluated with ^{40}K contributing $\sim 4 \times 10^{-3}$ keV^{-1} kg^{-1} year^{-1}, in the region 0–100 keV, with ^{222}Rn contributing 5×10^{-3} keV^{-1} kg^{-1} year^{-1} with the other materials contributing enough to have a total of $\sim 10^{-2}$ keV^{-1} kg^{-1} year^{-1} between 10 and 100 keV which is the important energy range for Cold Dark Matter searches.

The simulations imply an expected background in the energy region of $0\nu\beta\beta$-decay of ^{76}Ge ($\sim$2039 keV) to be 5×10^{-5} keV^{-1} kg^{-1} year^{-1}. The conclusion of Klapdor-Kleingrothaus and co-workers is that a one ton version of GENIUS could reach a sensitivity of $\langle m_\nu \rangle \sim 0.01$ eV in 1 year.

The reader should be careful in accepting the background projections of any of these experiments. They are just that, projections. The projections made for GENIUS, 5×10^{-5} keV^{-1} kg^{-1} year^{-1}, result in an expectation of:

$$(10^3\,\mathrm{kg})(1\,\mathrm{year})(3.5\,\mathrm{keV})(5 \times 10^{-5}\,\mathrm{keV}^{-1}\,\mathrm{kg}^{-1}\,\mathrm{year}^{-1}) \simeq 0.18\,\mathrm{counts}. \qquad (27)$$

For a null experiment, the statistical laws say there could be 2.3 counts at (90% CL). This would result in a rate of $\sim 6.4 \times 10^{-4}$ keV^{-1} kg^{-1} year^{-1}. To a 3σ CL this is more than 10^{-3} keV^{-1} kg^{-1} year^{-1}. In this case, the maximum half-life sensitivity would be 20 times longer and the sensitivity on $\langle m_\nu \rangle$ would be reduced to 0.04 eV. On the other side of the coin, in the case of an observation, a $0\nu\beta\beta$-decay peak on a zero background does not suffer this statistical disaster.

In conclusion, while the predictions made for sensitivity of the GENIUS experiment are only predictions, and while they appear to be extremely optimistic, the concept is interesting and

merits serious consideration as a good candidate for a next generation $0\nu\beta\beta$-decay technique, also with excellent promise for Cold Dark Matter searches.

4.3. The GENIUS test facility (GENIUS—TF)

The spokesman of the GENIUS project instituted a smaller test project called GENIUS—TF [51]. It involves the immersion and operation of naked Ge detectors in liquid nitrogen. The design plan is to have 14 detectors of approximately 3 kg each in an array of about 40 kg. Thus far, four crystals are operating in the LNGS under these conditions.

They are housed in a steel vessel ~0.5 mmthick inside of a $0.9 \times 0.9 \times 0.9\,\mathrm{m}^3$ box of high purity Ge bricks. Outside the foam box there will be 10 cm of low-level copper, 30 cm of lead and 15 cm of borated polyethylene.

In the presently operating version, four naked crystals are mounted on a plate made of special Teflon, inside of a thin copper box filled with 70 litres of highly purified liquid nitrogen. The copper is thermally isolated by 20 cm of special low radioactivity styropor, enclosed in a box of 15 tons of electrolytic copper, 10 cm thick and 35 tons of lead 20 cm thick. Outside this high density shield is 10 cm of boron-loaded polyethylene to shield from neutrons. On 5th May 2003, the four crystals began operating, and all reports are that they have been operating without failure to the time of this writing (August/September 2004).

Spectra taken with calibration sources of ^{60}Co and ^{133}Ba are very normal. This technical breakthrough could very well signal a very promising cooling and shielding technique for future ^{76}Ge $0\nu\beta\beta$-decay experiments.

One of the results of interest is that the microphonics from the bubbling of the liquid nitrogen appears to be negligible in the energy region for $0\nu\beta\beta$-decay (2039 keV), however, must be eliminated at low energies of interest in Cold Dark Matter searches, by PSD.

The BOREXINO liquid nitrogen purification system was used in the tests of the facility. GENIUS TF is intended to search for the annual modulation of Cold Dark Matter claimed to have been observed by the DAMA collaboration [23]. While the background in the present set-up is still higher than anticipated, the successful demonstration that p-type naked germanium detectors can be operated for long periods of time directly immersed in liquid nitrogen is a very important technical achievement. The reduction of background and the solution of the problem of operating the field-effect transistors in close proximity to the crystals are technical problems. In principle, Ge detectors can be operated in this manner.

4.4. The new ^{76}Ge experiment at Gran Sasso (GERDA)

Recently, the MPI Heidelberg and MPI Munich-led collaboration introduced a proposal similar to a smaller GENIUS proposal. It involves the direct immersion of Ge detectors, isotopically enriched in ^{76}Ge, directly in either liquid nitrogen or liquid argon. A research pilot program is underway in the MPI laboratories, and engineering has begun on the facility which is planned for the LNGS.

The proposal involves two phases. In the first phase, the 11 kg of detectors from the Heidelberg–Moscow experiment [20, 52] and the 6 kg of detectors from the IGEX experiment [2, 5], are immersed in the well-shielded cryogenic liquid. The plan is to obtain the sensitivity to either refute the recent discovery claim of Klapdor-Kleingrothaus *et al* [52], at a 99.6% CL, or confirm it at the level of 5σ.

In the second phase, the proposal is to measure the half-life to an accuracy of 10% if the claim is correct, or to extend the lower limit on the half-life to 2×10^{26} years if it is not. In this phase, 30 kg of isotopically enriched germanium would be acquired and converted into the maximum mass of detectors.

The first phase of the project has been approved and funded. Construction will begin in early 2005 and data acquisition is scheduled to begin in 2006.

There are negotiations underway between the leadership of the Majorana collaboration and the MPI group that has already led to an agreement to cooperate on various aspects of research and development. Future negotiation will determine if both collaborations will merge to form one large international collaboration for a giant effort in the search for $0\nu\beta\beta$-decay of ^{76}Ge.

4.5. The GSO proposal

This proposal rests on an experimental investigation of $0\nu\beta\beta$-decay of ^{160}Gd with a crystal scintillator of Gd_2SiO_5(Ce), with a volume of 95 cm^3. The experiments were performed in the Solotvina Underground Laboratory (SUL) [31]. In these test experiments, the background was rather high, $\sim$1.0 keV^{-1} kg^{-1} day^{-1} in the region of the $0\nu\beta\beta$-decay energy, 1730 keV. Most of the background was attributed to ^{208}Tl, ^{212}Bi and ^{212}Po, which presumably could be vastly reduced by purification of the input materials.

The cerium-doped gadolinium silicate crystal, 4.7 cm in diameter by 5.4 cm long, was grown by the Czochralski method; it had a mass of 635 g with 3.95×10^{23} atoms of ^{160}Gd. The SUL has an overburden of $\simeq$1000 mwe. The energy resolution, measured by radioactive calibration sources was 11.2% at 1770 keV, or $\sim$198 keV. The counting efficiency $\epsilon \simeq 0.95$, while the natural abundance of ^{160}Gd is 21.86%. With two small crystals, a lower bound on the half-life is $T^{0\nu}_{1/2} > 1.3 \times 10^{21}$ years (90% CL). This effort is the first step in the development of this technique to investigate the $0\nu\beta\beta$-decay of ^{160}Gd. The isotopic abundance of ^{160}Cd is rather high, 21.86%, therefore a sensitive detector of natural abundance Gd_2SiO_5:Ce scintillators could be constructed. A 2 ton GSO multi- crystal array ($\sim$400 kg of ^{160}Gd) has been predicted to reach the sensitivity of $\langle m_\nu \rangle \sim 0.06$ eV [30].

5. Other proposals involving ^{136}Xe

5.1. The ^{136}Xe experiment in BOREXINO and the BOREXINO test facility

This proposal involves loading the liquid scintillator of the BOREXINO facilities with xenon isotopically enriched in ^{136}Xe [25]. This idea was first developed in an article by R S Raghavan [73]. The BOREXINO experimental facilities are located in Hall C of the LNGS. The BOREXINO main detector has 300 tons of ultrapure liquid scintillator viewed by 2200 photomultipliers and shielded by 3300 tons of radiopure liquids [9]. The scintillator is constantly purified and is maintained at a level of about 10^{-16} g g^{-1} of ^{238}U. It is enclosed in a transparent nylon sphere to separate the scintillator from the shielding liquid.

The BOREXINO experiment is designed to detect the low energy ^{7}Be solar neutrinos and is presently under construction after a long shut down of all activities due to a minor spill of scintillator in 2002 that contaminated water outside of the Gran Sasso Laboratory. Accordingly, if the ^{136}Xe $0\nu\beta\beta$-decay experiment is actually ever done with the BOREXINO detector it will be sometime in the distant future. The original idea of Raghavan was to do this experiment

in the Kamiokande detector, which was subsequently used for the KAMLAND experiment which has for the first time observed oscillations of reactor anti-neutrinos, and confirmed the large mixing angle solution of the solar neutrino problem. This experiment will probably run in its present configuration for some time and would not be available for a ^{136}Xe $0\nu\beta\beta$-decay experiment.

The Sudbury Neutrino Observatory (SNO) will return the deuterated water to the owning Canadian agency in the not very distant future. When that happens, a ^{136}Xe $0\nu\beta\beta$-decay experiment will be considered, along with other scientific uses of the SNO laboratory facilities. Such a possibility has been considered [59].

There is also the possibility of performing this experiment in one of the two BOREXINO test facilities with central chambers of radii 0.5 m (CTF 05) and 1 m (CTF 2). These are also in the Gran Sasso Laboratory.

Two very important parameters are energy resolution and background. A Monte Carlo computation predicts an energy resolution at $Q_{\beta\beta} = 2479$ keV of $\sigma = 79$ keV or fwhm = 186 keV for the full BOREXINO facility and 209 keV for the smaller test facilities.

The final prediction of [25] is that with 80% enriched ^{136}Xe, BOREXINO can achieve a half-life sensitivity of 1.14×10^{27} years. It is straightforward to show that using table 4, one can conclude that to reach a sensitivity of $\langle m_\nu \rangle \sim 40$ meV, this experiment needs to reach $\sim 5.8 \times 10^{27}$ years, with the full 1565 kg of Xe dissolved in the scintillator, and with no background.

From table 2 of [25] there are 81 background counts predicted for 1 year of running of the full BOREXINO experiment. This is equivalent to $b \simeq 0.0003$ keV^{-1} kg^{-1} year^{-1}. They quote an efficiency of 68%, hence this experiment has the predicted parameters: $a = 0.80$, $\overline{\eta} = 0.28$, $\epsilon = 0.68$, $W = 136$, $M = 1565$ kg, $\delta E = 186$ keV and $b = 0.0003$ keV^{-1} kg^{-1} year^{-1}. The figure-of-merit is $f = 0.19$. The second figure-of-merit f_d reflecting the signal-to-noise ratio is $f_d = 0.02$. For comparison we quote f_d for a ^{76}Ge experiment with 500 kg, and with a background reduction of only a factor of 10 below the Heidelberg–Moscow or IGEX experiments, i.e., $b = 0.01$. In this case, $f = 0.73$ and $f_d \simeq 0.18$. These parameters speak for themselves. Excellent energy resolution must be complimented by very low background, even in the case of a large mass experiment with high isotopic enrichment and good counting efficiency. The main weakness of this idea is the small mass and poor energy resolution. At the time of its conception (1994), it made sense was a clever innovation. However, at this point, much more sensitivity is required.

5.2. The XMASS experiment

The XMASS project is in the research and development phase. It is a liquid Xe experiment with the goal of observing ^{7}Be solar neutrinos from the pp-chain in real time, direct-observation of Cold Dark Matter (CDM) and the observation and measurement of the $0\nu\beta\beta$-decay of ^{136}Xe [80].

A test cryostat has been built and tested. It has 30 $\mathcal{L}$ of liquid Xe in a 30 cm cubic chamber surrounded by photomultiplier tubes which give a photocathode surface coverage of 16%. The scintillation light output of liquid Xe is $\sim 4.2 \times 10^4$ photons MeV^{-1}, approximately the same as NaI(Tl). The background in this test detector is $\sim 3 \times 10^{-2}$ keV^{-1} kg^{-1} day^{-1} at 2479 keV $\simeq Q_{\beta\beta}$, or ~ 11 keV^{-1} kg^{-1} year^{-1}. This is rather high; however, it will certainly be reduced in the 800 kg full version of XMASS, because the fiducial volume mass of 100.5 kg will be well shielded by ~ 700 kg of Xe.

Let us assume that the isotopic abundance is the canonical 80% and the efficiency is the photocathode coverage ~70%. We can estimate an improvement in the energy resolution measured in the 100 kg version (580 keV) by the ratio of the photocathode coverage of the two configurations, i.e. $0.16/0.70 = 0.229$. This yields $\delta E \sim 133$ keV. Let us assume that the background in the 100 kg test cryostat, 11 $\mathrm{keV}^{-1}\,\mathrm{kg}^{-1}\,\mathrm{year}^{-1}$ can be reduced by a factor of 1000 in the fiducial volume of the 800 kg detector. Then the estimated parameters for this configuration are: $\overline{\eta} = 0.28$, $a = 0.80$, $\epsilon = 0.70$, $W = 136$, $M = 800$ kg, $\delta E = 133$ keV and $b \simeq 0.011$. The resulting figure-of-merit, $f = 0.04$.

If on the other hand, the background is reduced by a factor of 10^{-4}, then $f = 0.09$. To achieve a figure-of-merit of unity, the background must be reduced to the very challenging level of $\sim 10^{-5}\,\mathrm{keV}^{-1}\,\mathrm{kg}^{-1}\,\mathrm{year}^{-1}$.

Certainly a 10 ton version will have a much better figure-of-merit since the fiducial volume will be far better shielded and M will be 12.5 times larger. For $0\nu\beta\beta$-decay, this is a very challenging experiment. Nevertheless, XMASS will have to experience great improvements to be competitive with those proposals with $f \simeq 1$. As for its other applications it might well be a very effective and competitive experiment. The figure-of-merit applied above only applies to $0\nu\beta\beta$-decay.

6. The figure-of-merit revisited

The computation of the figure-of-merit proposed in equation (21) has one parameter that is difficult to justify in many cases; that is the background rate b in $\mathrm{keV}^{-1}\,\mathrm{kg}^{-1}\,\mathrm{year}^{-1}$. The rest of the parameters are usually fairly well established. Another use of this equation is to make a conserverative assumption about any experiment with respect to its probable background reduction. For this we choose the Majorana experiment and choose the parameters given in tables 2–4 of the Majorana White Paper [60]. Much of the data is dependent on more than 20 years of development of the PNNL/Carolina and IGEX experiments. The results are similar for the Heidelberg–Moscow Experiment [20]. We take the projected total background rate and multiply it by a factor of 2 to make it more conservative. Direct substitution into equation (19) results in f (Majorana) $= 1$. If instead we say that the Majorana array will conservatively have only 10 times lower background than IGEX with PSD, 0.11, then $b \simeq 0.01$. In this case $f = 0.79$. So we use the similar $f = 1$ value and compare experiments to this canonical value of unity. We can then use equation (28) to determine the background level that must be achieved for an experiment to have $f \simeq 1$. In this case,

$$b = \frac{M}{\delta E}\left(\frac{\overline{\eta} a \epsilon}{W}\right). \tag{28}$$

Let us apply this to CUORE operating with 760 kg of TeO_2 bolometers with natural abundance Te (33.8% ^{130}Te). In this case $b \leqslant 0.0058\,\mathrm{keV}^{-1}\,\mathrm{kg}^{-1}\,\mathrm{year}^{-1}$. For a completely isotopically enriched CUORE (~85% ^{130}Te), this becomes $b \leqslant 0.009$, which is a factor of 22 below that already reached by CUORICINO. Research and development is underway to reduce the background which is now understood from the CUORICINO results.

This is a more realistic way to compare the competitiveness of a given proposal, rather than to accept backgrounds predicted by Monte Carlo calculations and models that are different for every proposal, and in some cases not supported by sufficient experimental data.

Finally, while equation (21) is very useful for gaining a general idea of the merits of any given proposed experiment, it has somewhat of a shortcoming in evaluating its discovery potential. For this purpose we consider a rather unconventional parameter in this application, f_d, which is directly proportional to the signal-to-background ratio. This is simply derived as follows:

$$f_d \equiv \frac{\lambda N t \epsilon}{b M \delta E t} \propto \frac{\overline{\eta}(A_0 \times 10^3) M a \epsilon t}{W b M \delta E t} \propto \frac{\overline{\eta} a \epsilon}{W b \delta E}. \tag{29}$$

This parameter emphasizes the importance in the background as well as the energy resolution in being able to make a positive statement of discovery. Equations (21) and (28) emphasize different merits of an experiment. Equation (21) emphasizes how high the counting efficiency is, and how many atoms of the parent there are, whereas equation (29) gives some indication of how easy/difficult it will be to pick the needle of discovery from the haystack of background. It is clear that f_d makes no sense when $b \to 0$, but that is a case in which no such approach is necessary. In addition, the cancellation of the source mass in equation (29) clearly implies that two experiments with vastly different masses can not be compared this way.

6.1. The claim of discovery of $0\nu\beta\beta$*-decay of* ^{76}*Ge*

In 2001, a report of evidence of the direct observation of the $0\nu\beta\beta$-decay of ^{76}Ge was published by Klapdor-Kleingrothaus *et al* [50]. Several critical papers followed pointing out 'soft spots' in the analysis [2, 38]. Since that time two new papers have been published by Klapdor-Kleingrothaus *et al* which give a new analysis, and many new experimental details as well [52, 53].

In this latest paper, [53], 71.7 kg year of data from the Heidelberg–Moscow experiment was analysed. The background rate was 0.11 keV^{-1} kg^{-1} year^{-1}. The authors of this paper are members of the collaboration and have done extensive analysis and have concluded that the most probable half-life for the $0\nu\beta\beta$-decay of ^{76}Ge is 1.19×10^{25} years, and that the signal corresponds to a positive observation at a level of confidence of 4.2σ. The 3σ range of half-life values is $(0.69–4.18) \times 10^{25}$ years and it corresponds to the range in effective Majorana mass of the electron neutrino $\langle m_\nu \rangle$ of (0.24–0.58) eV, with the best-fit value $\langle m_\nu \rangle = 0.44$ eV. In this analysis, the nuclear matrix elements of Staudt *et al* were used [75]. Using the mean value from the literature for nuclear structure factor, $F_N = 7.3 \times 10^{-14}$ year^{-1}, the parameter $\langle m_\nu \rangle$ has the range 0.29–0.72 eV, with the value corresponding to the best fit half-life of 0.55 eV, not vastly different from the value obtained by the original authors.

One notes that the authors of this paper represent only a small part of the Heidelberg–Moscow Collaboration. In fact, the Russian component of the collaboration presented a conflicting view of the interpretation [22].

Since there appears much literature supporting or refuting this issue, we shall not argue either side. Although the interpretation of the data which leads to the conclusion of a discovery is highly controversial, the high quality of the Heidelberg–Moscow experiment, and its resulting data are not being questioned by anyone. It is our conclusion that the only completely reliable way to settle this issue is to test it experimentally.

There is only one experiment running at this time that would have a sensitivity anywhere near that required to confirm this claim, and that is CUORICINO. Unfortunately, this experiment will have the capability of refuting only part of the claimed range of $\langle m_\nu \rangle$ because of the uncertaintly in the nuclear matrix elements. The new planned effort by the Max Planck Institute will test it in the next 4–5 years and so will the CUORE and Majorana experiments discussed earlier.

The IGEX experiment published a lower bound: $T_{1/2}^{0\nu} \geqslant 1.6 \times 10^{25}$ years (90% CL), which corresponds to $\langle m_\nu \rangle \leqslant 0.38$ eV, using the matrix elements of [75]. This experiment can not rule out most of the claimed range of $T_{1/2}^{0\nu}$, but has been attacked by Klapdor-Kleingrothaus *et al* as having serious flaws, mainly an arithmetical error that leads to a bound on the half-life far below their claim [54]. This has been responded to by the IGEX collaboration [4] completely answering all questions, and in particular, clearly demonstrating that there is no arithmetical error, and will appear alongside [54].

6.2. Figure-of-merit for a sample ^{76}Ge experiment

There are several proposals for ^{76}Ge $0\nu\beta\beta$-decay experiments utilizing Ge detectors isotopically enriched to 86% in ^{76}Ge. We can use the Majorana proposed experimental parameters as an example [60]. The parameters are as follows: $M = 500$ kg, $\delta E = 3.5$ keV, $\overline{\eta} = 0.73$, $\epsilon = 0.75$ (after pulse-shape analysis and segmentation cuts), $W = 76$, $a = 0.86$ and $b = 0.0028\,\mathrm{keV}^{-1}\,\mathrm{kg}^{-1}\,\mathrm{year}^{-1}$. The background rate was determined from the Majorana White Paper in which it is stated that after 2500 kg year, and after applying pulse-shape discrimination and cuts due to multiple interactions in a segmented detector, there would remain seven background events. Accordingly,

$$f = \frac{(0.73)(0.86)(0.75)}{76}\sqrt{\frac{500}{(0.0028)(3.5)}} = 1.40. \tag{30}$$

This form of figure-of-merit is good guidance for selecting a technique and an isotope; however, it does not give enough weight to the energy resolution in evaluating the discovery potential. It is straight forward to show that the signal-to-noise ratio is proportional to $f_d = \overline{\eta}/b\delta E$, which is the second type of figure-of-merit discussed earlier. In detection techniques with 10s or 100s of keV energy resolution, the background must be reduced enormously to compensate. Computing f_d in this case, we see $f_d \simeq 0.63$ which is very superior to the cases discussed above. This is an extremely important figure-of-merit when considering discovery potential.

6.3. The CUORE proposal with natural abundance TeO_2 bolometers

The CUORE proposal involves 1000, 760 g TeO_2 bolometers operated at ~10 mK. A complete description is given by Arnaboldi *et al* [13]. A pilot experiment, CUORICINO, constituting about 1/24 of CUORE has been operated successfully in the Gran Sasso Laboratory [12]. It has the following parameters: $M = 760$ kg, $\delta E = 7$ keV, $\overline{\eta} = 4.2$, $a = 0.338$, $\epsilon = 0.84$, $W = 163$ and $b = 0.01\,\mathrm{keV}^{-1}\,\mathrm{kg}^{-1}\,\mathrm{year}^{-1}$. This value of b was derived by reducing the background of CUORICINO by a conservative factor of 20, using the computed background cancellation factor employing anti-coincidence cancellation of gamma-ray background events, and the shielding effect of the outter TeO_2 crystals, as well as material quality control.

Substituting these parameters into equation (20) yields $f = 0.76$. If CUORE were to be constructed of bolometers of TeO_2 isotopically enriched to 85% in ^{130}Te, the figure-of-merit would be $f = 1.9$.

One should be cautious in evaluating these competing experimental approaches because they are very sensitive to background rates, and those used above have been calculated by the proponents of the various proposals or estimated by these authors, based on target values in the

various proposals. They may or may not ever be achieved. Nevertheless, we can clearly see that experiments involving ^{76}Ge and bolometer-type experiments yield very superior figures of merit and discovery potential. This fact is mainly due to superior energy resolutions.

6.4. Figure-of-merit for a 10 ton ^{136}Xe TPC

Let us estimate the figure-of-merit for a 10 ton TPC with some of the parameters of the EXO experiment, and some estimated from assumed improvements one might make in those from the Gotthard Tunnel experiment [58]. From that paper we estimate that in 1.465 years of operation, with 24.2 moles of ^{136}Xe, they had ~7 background counts in the 163 keV energy interval of interest. Let us further assume that the background $b = 0.043$ can be improved by a factor of 100, such that $b = 0.00043\,\mathrm{keV}^{-1}\,\mathrm{kg}^{-1}\,\mathrm{year}^{-1}$. The energy resolution in tests of EXO yield 2% at the $0\nu\beta\beta$-decay energy of 2479 keV. Let us also use the isotopic enrichment planned for EXO of 80%. We will also use the efficiency of the Gotthard experiment, 30%. The figure-of-merit is then estimated as follows:

$$f = \frac{(0.28)(0.80)(0.30)}{136}\sqrt{\frac{10000\,\mathrm{kg}}{(0.00043\,\mathrm{keV}^{-1}\,\mathrm{kg}^{-1}\,\mathrm{year}^{-1})(50\,\mathrm{keV})}} \simeq 0.34. \quad (31)$$

In order to make this figure-of-merit greater than unity, the background would have to be reduced by a factor of 1000 below that of the Gotthard experiment, or $4.3 \times 10^{-5}\,\mathrm{keV}^{-1}\,\mathrm{kg}^{-1}\,\mathrm{year}^{-1}$. This is a factor of 70 better than that projected for the Majorana ^{76}Ge experiment, $(0.003\,\mathrm{keV}^{-1}\,\mathrm{kg}^{-1}\,\mathrm{year}^{-1})$ and a factor of ~2560 lower than the lowest ever achieved with Ge detectors with pule-shape discrimination [1, 39, 53, 60]. While conceivable if the positive identification of the daughter $^{136}\mathrm{Ba}^{+}$ is successful, it will require this drastic improvement to be competitive. The background will have to be reduced to $b = 7.5 \times 10^{-5}\,\mathrm{keV}^{-1}\,\mathrm{kg}^{-1}\,\mathrm{year}^{-1}$ to match the discovery potential figure-of-merit f_d of a ^{76}Ge experiment with the parameters of Majorana.

In this section, we have tried to be as objective as possible; however, it is possible that our prejudice in favour of experimental approaches that feature excellent energy resolution has shown through. As stated in the beginning, no experimental proposal has all of the features that make an ideal neutrinoless double-beta decay experiment. All of the various proposals are clever but some have features that would only have made sense a few years ago. Recently, however, neutrino oscillation experiments give a clear indication of the required sensitivity of an experiment with discovery potential.

7. Conclusion

In this paper, we have recommended and applied two somewhat novel figure-of-merit formulae for use in comparing the relative merits of different $0\nu\beta\beta$-decay proposals. The first is similar to others used for many years but different in one important aspect. It is proportional to the ratio of the predicted experimental sensitivity to the average theoretically calculated half-life for some arbitrary value of the Majorana mass of the electron neutrino. This is achieved by multiplying the usual expression for the figure-of-merit by $\overline{\eta}$, the average of the theoretical values of $\mathrm{G}^{0\nu}|M^{0\nu}|^2 \times 10^{13}\,\mathrm{year}^{-1}$. Multiplying by the arbitrary factor 10^{13} simply yields values of order unity for convenience.

The second figure-of-merit, although unconvential, is a better measure of the experiment's ability to produce data that would lend itself to an analysis to identify a positive peak signalling the identification of $0\nu\beta\beta$-decay. This quantity is proportional to the ratio of the theoretically predicted signal, which is proportional to $\overline{\eta}$, and the expected background. It places more emphasis on the impact of energy resolution and background. It is obviously invalid for $b = 0$.

Fifteen proposals that are carefully documented in published papers and reports are discussed in some detail. Five proposals: CUORE, EXO, Majorana, MOON and NEMO/Super-NEMO are discussed in more detail because extensive research, development and documentation from previous experiments appear in the literature. Ten other experiments: CARVEL, CANDLES, DCBA, GEM, GENIUS, GENIUS-TF, GERDA, GSO, Xe (in BOREXINO) and XMASS, are discussed in enough detail to allow the reader to attempt to evaluate to some degree the figures of merit discussed in this paper.

We do evaluate a few examples in cases in which enough data are available. We do not present a table comparing the various proposals, because in most cases the background predictions are too poorly documented, and in many cases very uncertain. Tables tend to be quoted with none of the caveats of the accompanying text.

Two experimental techniques with excellent energy resolutions, cryogenic bolometers (CUORE), and Ge ionization detectors (Majorana, GEM, GENIUS and GERDA) will all have significant discovery potential if they achieve their target background levels. These experiments all have earlier versions that give some level of confidence that the steps necessary to reach the stated background goals are understood.

The canonical target experimental sensitivity for next generation experiments is chosen as the half-life that corresponds to the effective Majorana mass of the electron neutrino $\langle m_\nu \rangle \sim 0.04$ eV. This is approximately the minimum value implied by the measured atmospheric neutrino oscillation parameters in the case of the inverted neutrino mass eigenstate hierarchy.

The statements made above favouring bolometers and Ge detectors, are not intended to exclude the rest of the proposals. Tracking detectors, for example, could explore $0\nu\beta\beta$-decay of ^{150}Nd, for which at present there is no known ionization detector or bolometer. While tracking detectors do not have good energy resolution, NEMO, for example has shown that backgrounds can be identified and drastically reduced. Tracking detectors can also exploit the large value of $\overline{\eta}$ (^{100}Mo), which is almost seven times larger than that of ^{76}Ge, and slightly larger than that of ^{130}Te. In this regard, it would also be very worthwhile to attempt the development a bolometer containing a significant amount of ^{100}Mo because $|Q_{\beta\beta}| = 3034$ keV, above the natural radioactive γ-ray background. Such a project is underway in the CUORE collaboration.

The measured parameters from neutrino oscillation experiments strongly imply a large discovery area in $\langle m_\nu \rangle$—m_1 parameter space that allows values of $\langle m_\nu \rangle$ from 0.04 eV to the present bounds, and also include the range of the claim of discovery of Klapdor-Kleingrothaus *et al*.

Finally, these are very exciting times for those of us who have been working on double-beta decay for many years. There is the feeling that a confirmed discovery may be just around the corner.

Acknowledgments

The authors are grateful to S Elliott for reviewing the manuscript and for his many helpful comments. They also wish to thank Professors H Ejiri, G Gratta, and S Julian for their help

in preparing the sections and figures for the MOON, EXO and NEMO sections, respectively. Following the last corrections to this text, our colleague and co-author Y G Zdesenko passed away suddenly on 1 September 2004. We dedicate this paper to his memory. All who knew him will miss his intense interest and enthusiasm in the science of our field.

References

[1] Aalseth C E 2000 *PhD Dissertation* University of South Carolina
[2] Aalseth C E *et al* 2002 *Phys. Rev.* D **65** 092007
[3] Aalseth C E *et al* 2002 *Mod. Phys. Lett.* A **17** 1475
[4] Aalseth C E *et al* 2004 *Preprint* nucl-ex/0404036
Aalseth C E *et al* 2004 *Phys. Rev.* D **70** 078302
[5] Aalseth C E *et al* 1999 *Phys. Rev.* C **59** 2108
[6] Ahmad Q R *et al* (The SNO Collaboration) 2001 *Phys. Rev. Lett.* **87** 071301
Ahmad Q R *et al* 2004 *Phys. Rev. Lett.* **92** 181301
[7] Alessandrello A *et al* 1997 *IEEE Trans. Nucl. Sci.* **44** 416
[8] Alessandrello A *et al* 1998 *Nucl. Instrum. Methods* A **142** 454
[9] Alimonti G *et al* 1998 *Nucl. Instrum. Methods* A **406** 411
[10] Apollonio M *et al* (The CHOOZ Collaboration) 1999 *Phys. Lett.* B **466** 415
[11] Arnaboldi C *et al* 2003 *Phys. Lett.* B **557** 167
[12] Arnaboldi C *et al* 2004 *Phys. Lett.* B **584** 260
[13] Arnaboldi C *et al* 2004 *Nucl. Instrum. Methods* A **518** 775
[14] Arnold R *et al* 1996 *Z. Phys.* C **72** 239
[15] Arnold R *et al* 2003 *Nucl. Instrum. Methods* A **503** 649
[16] Avignone F T III and Brodzinski R L 1988 *Prog. Part. Nucl. Phys.* **21** 99
[17] Avignone F T III and King G S III 2003 *Proc. 4th Int. Workshop on Identification of Dark Matter* (York 2002) ed N J Spooner and V Kudryatsev (Singapore: World Scientific), p 553 (and references therein)
[18] Bahcall J N, Gonzales-Garcia M C and Pena-Garay C 2002 *Preprint* hep-ph/0204314 and 0204194
[19] Barger V, Glashow S L, Marfatia D and Whisnant K 2002 *Phys. Lett.* B **532** 15
[20] Baudis L *et al* 1999 *Phys. Rev. Lett.* **83** 41
[21] Bellini G *et al* 2000 *Phys. Lett.* B **493** 216
Bellini G *et al* 2001 *Eur. Phys. J.* C **19** 43
[22] Belyaev S T 2003 *Invited talk at the IV Int. Conf. on Non-Accelerator New Physics (NANP-03; June 23–28, Dubna) Yad. Fiz.* at press
[23] Bernabei R *et al* 2000 *Phys. Lett.* B **480** 23
[24] Boehm F *et al* 2001 *Phys. Rev.* D **64** 112001
[25] Caccianiga B and Giammarchi M G 2000 *Astropart. Phys.* **14** 15
[26] Ling-Lie Chau and Wai-Yee Keung 1984 *Phys. Rev. Lett.* **53** 1802
[27] Civaterese O and Suhonen J 2002 *Preprint* nucl-th/0208005
[28] Danilov M *et al* 2000 *Phys. Lett.* B **480** 12
[29] Danevich F A *et al* 2000 *Phys. Rev.* C **62** 045501
[30] Danevich F A *et al* 2001 *Nucl. Phys.* A **694** 375
[31] Danevich F A *et al* 2003 *Phys. Rev.* C **68** 035501
[32] Ejiri H *et al* 2000 *Phys. Rev.* C **63** 065501
[33] Ejiri H, Engle J and Kudomi N 2001 *Preprint* astro-ph/0112379
[34] Elliott S R and Vogel P 2002 *Annu. Rev. Part. Sci.* **52** 115
[35] Elliott S R and Engel J 2004 *Preprint* hep-ph/0405078
Elliott S R and Engel J 2004 *J. Phys. G: Nucl. Part. Phys.* **30** R 183
[36] Fakuda S *et al* (The SuperKamiokande Collaboration) 2002 *Phys. Lett.* B **539** 179

[37] Fakuda S *et al* (The SuperKamiokande Collaboration) 1998 *Phys. Rev. Lett.* **81** 1562
Fakuda S *et al* (The SuperKamiokande Collaboration) 1999 *Phys. Rev. Lett.* **82** 2644
[38] Feruglio F, Strumia A and Vissani F 2002 *Nucl. Phys.* B **637** 345
[39] Gonzales D *et al* (The IGEX Collaboration) 2003 *Nucl. Instrum. Methods* A **515** 634
[40] Grigoriev G and Karchevsky A 2001 *Proc. 3rd Int. Conf. on Non-Accelerator New Physics (NANP-2001; June 19–23, Dubna)* (http://nanp.dubna.ru)
[41] Haxton W C and Stephenson G J Jr 1984 *Prog. Part. Nucl. Phys.* **12** 409
[42] Hellmig J and Klapdor-Kleingrothaus H V 1997 *Z. Phys.* A **359** 372
[43] Ishihara N *et al* 2001 *Nucl. Instrum. Methods* A **433** 101
[44] Ishihara N *et al* 2002 *Nucl. Phys.* B (Proc. Suppl.) **111** 309
[45] Kajita T (The SuperKamiokande Collaboration) 1999 *Nucl. Phys.* (Proc. Suppl.) **77** 123
[46] Eguchi K *et al* (The KAMLAND Collaboration) 2004 *Phys. Rev. Lett.* **92** 071301 (*Preprint* hep-ex/0406035)
[47] Kato Y *et al* 2003 *Nucl. Instrum. Methods* A **498** 430
[48] Kiel H, Munstermann D and Zuber K 2003 *Nucl. Phys.* A **723** 499
[49] Klapdor-Kleingrothaus H V *et al* 2001 *Eur. Phys. J.* A **12** 147
[50] Klapdor-Kleingrothaus H V, Deitz A, Harney H L and Krivosheina I V 2001 *Mod. Phys. Lett.* **16** 2409
[51] Klapdor-Kleingrothaus H V 2003 Naked crystals go underground *Preprint* hep-ph/0307329
[52] Klapdor-Kleingrothaus H V, Krivosheina I V, Dietz A and Chkvorets O 2004 *Phys. Lett.* B **586** 198
[53] Klapdor-Kleingrothaus H V, Krivosheina I V, Dietz A and Chkvorets O 2004 *Nucl. Instrum. Methods* **522** 367 (see many Klapdor-Kleingrothaus references therein)
[54] Klapdor-Kleingrothaus H V, Dietz A and Krivosheina I V 2004 *Phys. Rev.* D, at press (*Preprint* hep-ph/0403056)
[55] Klapdor-Kleingrothaus H V and Hirsch M 1997 *Z. Phys.* A **359** 361
[56] Klapdor-Kleingrothaus H V 1997 *CERN Courier* (Dec.) 19
[57] Klapdor-Kleingrothaus H V, Hellmig J and Hirsch M 1998 *J. Phys. G: Nucl. Part. Phys.* **24** 483
For a complete white paper see Klapdor-Kleingrothaus H V *et al* 2000 *Preprint* hep-ph/991 0205 V4
[58] Luescher R *et al* 1998 *Phys. Lett.* B **434** 407
[59] McDonald A 2000 private communication
[60] The Majorana White Paper 2003 *Preprint* Nucl.ex//0311013
[61] Mitchel L V and Fisher P H 1988 *Phys. Rev.* C **38** 895
[62] Moe M K 1991 *Phys. Rev.* C **44** R 931
[63] Moe M and Vogel P 1994 *Ann. Rev. Nucl. Part. Sci.* **44** 247
[64] Abt I *et al* 2004 A new ^{76}Ge double-beta decay experiment at LNGS' Max Planck Institute letter of intent *Preprint* hep-ex/040 4039 V1
[65] Neuhauser W *et al* 1978 *Phys. Rev. Lett.* **41** 233
[66] Osipowicz A *et al* 2001 (The KATRIN collaboration) *Preprint* hep-ex/0109033
Drexlin G 2004 Helmholtz-Gemeinschaft (HGF) Pre-Meeting, Forschungszentrum Karlsruhe
[67] Pascoli S and Petcov S T 2002 *Phys. Rev.* D *Preprint* hep-ph/0205022
[68] Pascoli S and Petcov S T 2003 *Preprint* hep-ph/031 0003 Vi
[69] Pessina G 1999 *Rev. Sci. Instrum.* **70** 3473
[70] Pantis G *et al* 1992 *J. Phys. G: Nucl. Part. Phys.* **18** 605
[71] Primakoff H and Rosen S P 1969 *Phys. Rev.* **184** 1925
[72] Primakoff H and Rosen S P 1981 *Ann. Rev. Nucl. Part. Sci.* **31** 145
[73] Raghavan R S 1994 *Phys. Rev. Lett.* **72** 1411
[74] Rodin V A, Faessler A, Simkovic F and Petr Vogel 2003 *Phys. Rev.* C **68** 044302
[75] Staudt A, Muto K and Klapdor-Kleingrothaus H V 1990 *Europhys. Lett.* **13** 31
[76] Tomei C, Dietz A, Krivosheina I and Klapdor-Kleingrothaus H V 2003 *Preprint* hep-ph/0306257
[77] Tretyak V I and Zdesenko Yu G 2002 *At. Data Nucl. Data Tables* **80** 83
[78] Umehara S *et al* 2003 *Proc. 1st Yamada Symp. on Neutrinos and Dark Matter in Nucl. Phys.* (http://ndm03.phys.sci.osaka-u.ac.jp/proc/index.htm) XII-23

[79] Watanabe T *et al* 1990 *Nucl. Instrum Methods* A **436** 155
[80] Moriyama S 2001 (For the XMASS collaboration) *Proc. Int. Workshop on Techniques and Applications of Xenon Detectors (Tokyo, Japan, 3–4 December)* (Singapore: World Scientific) p 123; see also http://www-sk.icrr.u-tokyo.ac.jp/∼minamino/doc/KEKPH_Mar_2004.pdf
[81] Zdesenko Yu G, Ponkratenko O A and Tretyak V I 2001 *J. Phys. G: Nucl. Part. Phys.* **27** 2129
[82] Zdesenko Yu G 2002 *Rev. Mod. Phys.* **74** 663
[83] Zdesenko Yu G *et al* 2004 *Nucl. Instrum. Methods* at press (*INR Kiev Preprint*)
[84] Zdesenko Yu G *et al* 2004 *J. Phys. G: Nucl. Part. Phys.* **30** 971
[85] Zuber K 2001 *Phys. Lett.* B **519** 1

New Journal of Physics
The open-access journal for physics

Neutrino mixing and nucleosynthesis in core-collapse supernovae

A B Balantekin[1,2] **and H Yüksel**[1]

[1] Department of Physics, University of Wisconsin, 1150 University Avenue, Madison, WI 53706, USA
[2] Physics Department, Tohoku University, Sendai 980, Japan
E-mail: baha@physics.wisc.edu and yuksel@physics.wisc.edu

New Journal of Physics **7** (2005) 51
Received 5 November 2004
Published 11 February 2005
Online at http://www.njp.org/
doi:10.1088/1367-2630/7/1/051

Abstract. A simple description of core-collapse supernovae is given. Properties of the neutrino-driven wind, neutrino fluxes and luminosities, reaction rates and the equilibrium electron fraction in supernova environments are discussed. Neutrino mixing and neutrino interactions that are relevant to core-collapse supernovae are briefly reviewed. The values of electron fraction under several evolution scenarios that may impact rapid neutron-capture process (r-process) nucleosynthesis are calculated.

Contents

1. Introduction **2**
2. A simple description of core-collapse supernovae **3**
2.1. Neutrino-driven wind . . . 3
2.2. Neutrino fluxes and luminosities . . . 5
2.3. Reaction rates . . . 6
2.4. Electron fraction . . . 7
2.5. Alpha effect . . . 9
3. Neutrino mixing **11**
4. Results and discussion **13**
5. Conclusions **16**
Acknowledgments **17**
References **17**

PII: S1367-2630(05)89041-X
© IOP Publishing Ltd and Deutsche Physikalische Gesellschaft

1. Introduction

Massive stars, losing energy to radiation and photons, evolve until an iron core is formed (for a recent review see [1]). This core, which has a very low entropy per baryon, is supported by the electron degeneracy pressure. As a consequence, such a core is dynamically unstable and collapses until the matter is mostly neutronized and supernuclear densities are reached. Only when the density significantly exceeds the nuclear density, does the pressure become sufficiently repulsive to stop the collapse. In the current paradigm, the innermost shell of matter reaches to these densities first, rebounds and sends a pressure wave through the rest of the core. Such waves, produced by the subsequent shells and travelling faster than the infalling matter, collect near the sonic point. As that point reaches nuclear density, a shock wave breaks out. The subsequent evolution of this bounce shock is not yet well understood and is subject to much study [2, 3]. Current models fail to explode.

Even though it has not yet been demonstrated that explosion is an outcome of the core-collapse, it is well established that the newly formed hot proto-neutron star cools by neutrino emission. (It was those neutrinos that were observed in Supernova 1987A.) Almost all (99%) of the gravitational binding energy of the neutron star

$$\frac{3}{5}\frac{GM_{NS}^2}{R_{NS}} \approx 3 \times 10^{53}\text{ergs}\frac{(M_{NS}/1.4M_\odot)^2}{R_{NS}/10\,\text{km}} \tag{1}$$

is radiated away in neutrinos of all flavours. Altogether a star with mass $\sim 8M_\odot$ will emit $\sim 10^{59}$ neutrinos. Thus, after the explosion ejects the material from the outer layers, a 'neutrino-driven' wind may blow the medium above the neutron star, heating it to an entropy per baryon of several hundreds in units of Boltzmann's constant. For such high entropies, nuclear statistical equilibrium is not established for nuclei heavier than alpha particles.

The rapid neutron-capture process (r-process) is responsible for the formation of a number of nuclei heavier than iron. (For a recent review see [4].) The astrophysical site of the r-process nucleosynthesis is not yet identified. For r-process nucleosynthesis to successfully take place, a large number of neutrons are required to interact in a relatively short time, indicating that r-process sites are associated with explosive phenomena. Indeed, the seminal Burbidge *et al* paper suggested the neutron-rich ejecta outside the core in a type II supernova as a possible site of the r-process [5]. More recent work pointed to the neutrino-driven wind in the supernovae as a possible site [6]–[8]. Meteoric data and observations of metal-poor stars indicate that r-process nuclei may be coming from diverse sources [9]. Binary neutron star systems were also proposed as a site of the r-process (see e.g. [10]). In outflow models, r-process nucleosynthesis results from the freeze-out from nuclear statistical equilibrium. The outcome of the freeze-out process is determined by the neutron-to-seed ratio. This ratio in the post-core-bounce supernova environment is controlled by the intense neutrino flux radiating from the neutron star.

Neutrino interactions play a crucial role in core-collapse supernovae (for a brief summary, see [11]). Neutrino heating is one of the possible mechanisms for reheating the stalled shock [12]. The neutrino fluxes control the proton-to-neutron ratio in the high-entropy hot bubble. As we describe in the next section, there is a hierarchy of energies for different neutrino flavours. Hence swapping active neutrinos via neutrino oscillations changes the n/p ratio and may alter the r-process nucleosynthesis conditions [13]. Neutrino oscillations in a core-collapse supernova differ from the matter-enhanced neutrino oscillations in the Sun as in the former there are

additional effects coming from both neutrino–neutrino scattering [14, 15] and antineutrino flavour transformations [16].

We present a simple description of the core-collapse supernovae in the next section. In this section after summarizing properties of the neutrino-driven wind, we discuss neutrino fluxes, luminosities, reaction rates and the equilibrium electron fraction. A brief description of neutrino mixing and neutrino interactions, relevant to core-collapse supernovae, is given in section 3. In section 4 we calculate values of the electron fraction under several evolution scenarios that may impact r-process nucleosynthesis.

2. A simple description of core-collapse supernovae

2.1. Neutrino-driven wind

A careful treatment of the neutrino-driven wind in post-core bounce supernova environment was given in [17]. Here we present a heuristic description following [18]. One can assume that at sufficiently large radius, above the heating regime, there is hydrostatic equilibrium [19]:

$$\frac{\mathrm{d}P}{\mathrm{d}r} = -\frac{GM_{\mathrm{NS}}\rho}{r^2}, \tag{2}$$

where P is the hydrostatic pressure, G is Newton's constant, M_{NS} is the mass of the hot proto-neutron star and ρ is the matter density. Using the thermodynamic relation for the entropy at constant chemical potential, μ,

$$S_{\mathrm{total}} = \left(\frac{\delta P}{\delta T}\right)_{\mu}, \tag{3}$$

and on integrating equation (2), we can write the entropy per baryon, S, as

$$TS = \frac{GM_{\mathrm{NS}}m_B}{r}, \tag{4}$$

where m_B is the average mass of one baryon, which we take to be the nucleon mass. In the region above the neutron star, the material is radiation dominated and the entropy per baryon can be written in the relativistic limit as

$$\frac{S}{k} = \frac{2\pi^2}{45}\frac{g_s}{\rho_B}\left(\frac{kT}{\hbar c}\right)^3, \tag{5}$$

where the statistical weight factor is given by

$$g_s = \sum_{\mathrm{bosons}} g_b + \frac{7}{8}\sum_{\mathrm{fermions}} g_f. \tag{6}$$

Assuming a constant entropy per baryon, equations (4) and (6) give the baryon density, ρ_3, in units of $10^3\,\mathrm{g\,cm^{-3}}$ as

$$\rho_3 \sim 38\left(\frac{g_s}{11/2}\right)\frac{1}{S_{100}^4 r_7^3}, \tag{7}$$

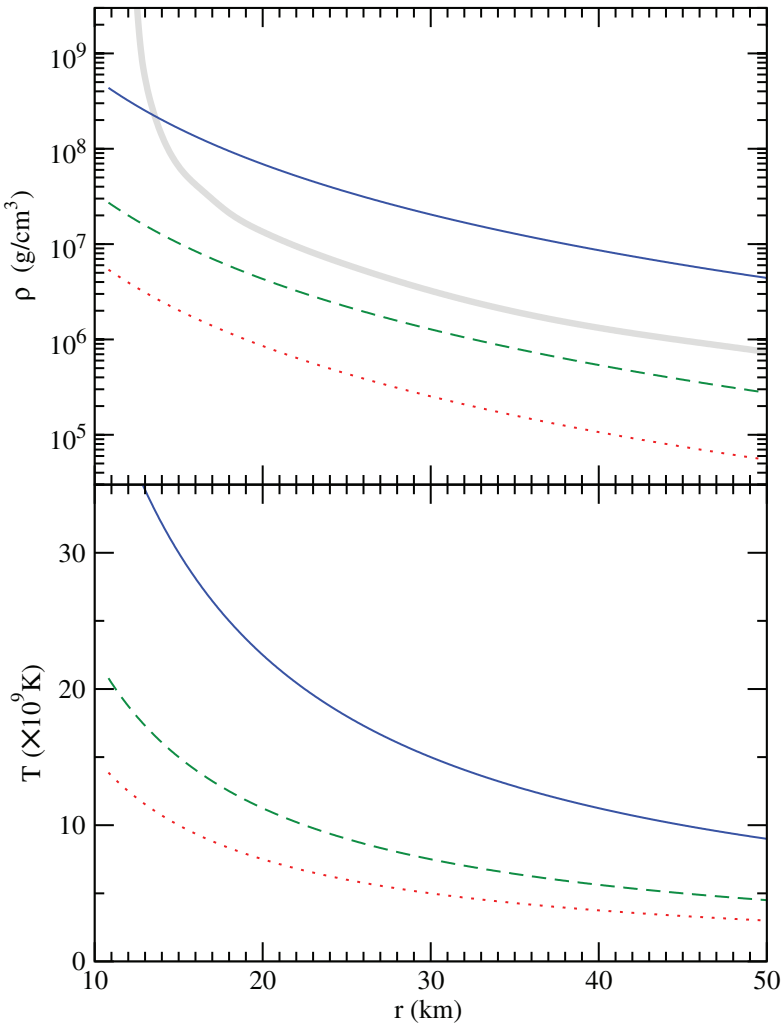

Figure 1. Solid ($S_{100} = 0.5$), dashed ($S_{100} = 1$), and dotted ($S_{100} = 1.5$) lines correspond to matter density profiles (upper panel), and temperature profiles (lower panel) based on heuristic description. The thick band in the upper panel is the matter density profile from numerical supernova models for $t_{PB} \approx 4$ s (taken from [13]).

where S_{100} is the entropy per baryon in units of 100 times Boltzmann's constant, r_7 is the distance from the centre in units of 10^7 cm, and we assumed that $M_{\rm NS} = 1.4 M_\odot$. Defining T_9 to be the temperature in units of 10^9 K, equation (4) takes the form

$$T_9 S_{100} \sim \frac{2.25}{r_7}. \tag{8}$$

In figure 1, we present matter density and temperature profiles based on a heuristic description given in this section. Several values of S_{100} can be used to describe stages in the evolution of supernovae. Smaller entropies per baryon, $S_{100} \lesssim 0.5$, provide a better description of the shock reheating epoch, while larger values, $S_{100} \gtrsim 1$, describe late times in supernova evolution, namely the neutrino-driven wind epoch. Higher entropy corresponds to less-ordered

configurations with smaller baryon densities. In figure 1, the statistical weight factor, g_s, is taken to be 11/2 in the calculation of matter density, since temperature and entropy per baryon are $T_9 \gtrsim 4$ and $S_{100} \lesssim 1.5$, respectively. Under these conditions both photons and electron–positron pairs are present in the plasma. When temperature drops, $T_9 \lesssim 4$, only photons are present in the medium and statistical weight factor has to be taken as $g_s \approx 2$.

2.2. Neutrino fluxes and luminosities

We adopt the prescription in [14] for the neutrino fluxes. If we take the density of particles to be ρ, the number of particles that go through an expanding surface of radius r per unit time is

$$\frac{\mathrm{d}N}{\mathrm{d}t} = \rho\frac{\mathrm{d}V}{\mathrm{d}t} = 4\pi r^2\rho\frac{\mathrm{d}r}{\mathrm{d}t}, \tag{9}$$

where N is the total number of particles and $V = 4\pi r^3$. Assuming a Fermi–Dirac distribution function for the neutrino number densities, ignoring neutrino mass in comparison to its energy and taking the particle velocity to be c, equation (9) gives for the flux of neutrinos emitted from the neutrinosphere as

$$\begin{aligned}\mathrm{d}\phi_\nu &= \frac{\mathrm{d}^2\phi_\nu}{\mathrm{d}E_\nu \mathrm{d}\Omega_\nu}\mathrm{d}E_\nu \mathrm{d}\Omega_\nu \\ &= \frac{1}{8\pi^3}\frac{c}{(\hbar c)^3}\frac{E_\nu^2 \mathrm{d}E_\nu}{1+\exp\left[(E_\nu-\mu_\nu)/kT_\nu\right]}\mathrm{d}\Omega_\nu,\end{aligned} \tag{10}$$

where μ_ν is the neutrino chemical potential. Choosing the z-direction as the vector that connects the point where the flux is to be calculated (with radial position r) to the centre of the neutron star, one sees that the azimuthal symmetry still holds, but the polar angle is bounded by the finite size of the neutrinosphere. Thus

$$\int \mathrm{d}\Omega_\nu = 2\pi(1-\cos\theta_0), \tag{11}$$

where

$$\cos\theta_0 = \sqrt{1-\frac{R_\nu^2}{r^2}} \approx 1-\frac{R_\nu^2}{2r^2} \tag{12}$$

with R_ν being the radius of the neutrinosphere. Within this approximation one then obtains the differential neutrino flux as

$$\frac{\mathrm{d}\phi_\nu}{\mathrm{d}E_\nu} = \frac{1}{8\pi^2}\frac{c}{(\hbar c)^3}\frac{R_\nu^2}{r^2}\frac{E_\nu^2}{1+\exp[(E_\nu-\mu_\nu)/kT_\nu]}. \tag{13}$$

Using similar reasoning one can write an expression for the neutrino luminosity. Replacing N in equation (9) by the total energy and the matter density ρ by the energy density one can write down

$$L_\nu = 4\pi r^2 c\frac{1}{2\pi\hbar^2}\int\frac{E_\nu \mathrm{d}^3\mathbf{p}_\nu}{1+\exp[(E_\nu-\mu_\nu)/kT_\nu]}. \tag{14}$$

Again ignoring the neutrino mass in comparison to its energy and using equations (11) and (12) to do the angular integration we obtain

$$L_\nu = \frac{cR_\nu^2}{2\pi(\hbar c)^3}(kT_\nu)^4 F_3(\eta), \tag{15}$$

where $\eta = \mu_\nu/kT_\nu$ and $F_3(\eta)$ is the relativistic Fermi integral

$$F_3(\eta) = \int_0^\infty \frac{x^3}{1+\exp(x-\eta)}\,\mathrm{d}x. \tag{16}$$

In our calculations, we take $\eta = 0$ and use the value $F_3(0) = 7\pi^4/120$. Often it is convenient to express the neutrinosphere radius in terms of the neutrino luminosity. Rewriting R_ν in terms of L_ν and inserting it into equation (13), we get

$$\frac{\mathrm{d}\phi_\nu}{\mathrm{d}E_\nu} = \frac{1}{4\pi r^2}\frac{L_\nu}{(kT_\nu)^4 F_3(\eta)}\left(\frac{E_\nu^2}{1+\exp[(E_\nu-\mu_\nu)/kT_\nu]}\right). \tag{17}$$

2.3. Reaction rates

The dominant reactions that control the n/p ratio are the capture reactions on free nucleons

$$\nu_e + \mathrm{n} \rightleftharpoons \mathrm{p} + \mathrm{e}^-, \tag{18}$$

and

$$\bar{\nu}_e + \mathrm{p} \rightleftharpoons \mathrm{n} + \mathrm{e}^+. \tag{19}$$

We take the cross sections for the forward reactions to be [16]

$$\sigma_{\nu_e}(E_{\nu_e}) \approx 9.6\times 10^{-44}\left(\frac{E_{\nu_e}+\Delta_{np}}{\mathrm{MeV}}\right)^2 \mathrm{cm}^2, \tag{20}$$

and

$$\sigma_{\bar{\nu}_e}(E_{\bar{\nu}_e}) \approx 9.6\times 10^{-44}\left(\frac{E_{\bar{\nu}_e}-\Delta_{np}}{\mathrm{MeV}}\right)^2 \mathrm{cm}^2, \tag{21}$$

where $\Delta_{np} \approx 1.293$ MeV is the mass difference between neutron and proton. For simplicity we ignore weak magnetism and recoil corrections which may be important [20]. These corrections cancel for the former cross section, but add for the latter one. The rates of these reactions can be written as [21]

$$\lambda = \int \sigma(E)_\nu \frac{\mathrm{d}\phi_\nu}{\mathrm{d}E_\nu}\,\mathrm{d}E_\nu. \tag{22}$$

To calculate the neutrino capture rates of nuclei, one needs to include all possible transitions from the parent to the daughter nucleus, including not only the allowed transitions, but also

transitions to the isobaric analogue states, Gamow–Teller resonance states, transitions into the continuum as well as forbidden transitions. Aspects of such calculations are discussed in [22, 23] (see also [24]). Careful input of such reaction rates in supernova simulations is especially crucial to assess the possibility of core-collapse supernovae as a site of r-process nucleosynthesis [11, 25].

Because of their charged-current interactions, electron neutrinos may play a role in reheating the stalled shock as well as regulating the neutron-to-proton ratio. In contrast, since the energies of the muon and tau neutrinos and antineutrinos produced are too low to produce charged leptons, these neutrinos interact only with the neutral-current interactions. Recently, significant attention was directed towards understanding the ν_μ and ν_τ spectra formation. Neutrinos remain in local thermal equilibrium as long as they can participate in reactions that allow exchange of energy and neutrino pair creation or annihilation. It turns out that the neutrino bremsstrahlung process

$$N + N \leftrightarrow N + N + \nu + \bar{\nu} \tag{23}$$

is more effective than the annihilation process, $\nu + \bar{\nu} \leftrightarrow e^+ + e^-$, at equilibrating neutrino number density [26]. (However, the neutrino–neutrino annihilation process $\nu_e + \bar{\nu}_e \leftrightarrow \nu_\mu + \bar{\nu}_\mu$ is one of the primary sources of muon and tau neutrinos [28]). The impact of the neutrino bremsstrahlung process on equilibrating the energy spectra seems to be comparable to that of

$$\nu_{\mu,\tau} + e^- \rightarrow \nu_{\mu,\tau} + e^-. \tag{24}$$

The most effective process to exchange energy is [27]

$$\nu + N + N \rightarrow N + N + \nu, \tag{25}$$

which dominates the neutrino spectra formation. Finally, recoil corrections to the νN interactions are very important in the formation of the ν_μ and ν_τ spectra as they permit energy exchange [29].

2.4. Electron fraction

The electron fraction, Y_e, is the net number of electrons (number of electrons minus the number of positrons) per baryon:

$$Y_e = (n_{e^-} - n_{e^+})/n_B, \tag{26}$$

where n_{e^-}, n_{e^+} and n_B are number densities of electrons, positrons and baryons, respectively. Introducing N_j, the number of species of the kind j per unit volume, and A_j, the atomic weight of the jth species, one can write down expressions for the mass fraction, X_j as

$$X_j = \frac{N_j A_j}{\sum_i N_i A_i}, \tag{27}$$

and the number abundance relative to baryons, Y_j, as

$$Y_j = \frac{X_j}{A_j} = \frac{N_j}{\sum_i N_i A_i}. \tag{28}$$

The electron fraction defined in equation (26) can then be rewritten as

$$Y_e = \sum_i Z_i Y_i = \sum_i \left(\frac{Z_i}{A_i}\right) X_i$$
$$= X_p + \tfrac{1}{2} X_\alpha + \sum_h \left(\frac{Z_h}{A_h}\right) X_h, \tag{29}$$

where Z_i is the charge of the species of kind i, and the mass fractions of protons, X_p, alpha particles, X_α and heavier nuclei ('metals'), X_h, are explicitly indicated.

The rate of change of the number of protons can be expressed as

$$\frac{\mathrm{d}N_p}{\mathrm{d}t} = -(\lambda_{\bar{\nu}_e} + \lambda_{e^-})N_p + (\lambda_{\nu_e} + \lambda_{e^+})N_n, \tag{30}$$

where λ_{ν_e} and λ_{e^-} are the rates of the forward and backward reactions in equation (18) and $\lambda_{\bar{\nu}_e}$ and λ_{e^+} are the rates of the forward and backward reactions in equation (19). Since the quantity $\sum_i N_i A_i$ does not change with neutrino interactions, one can rewrite equation (30) in terms of mass fractions

$$\frac{\mathrm{d}X_p}{\mathrm{d}t} = -(\lambda_{\bar{\nu}_e} + \lambda_{e^-})X_p + (\lambda_{\nu_e} + \lambda_{e^+})X_n. \tag{31}$$

In the hot bubble, the rates are usually expressed in terms of the radial velocity field, $v(r)$, above the neutron star, i.e. $\mathrm{d}Y/\mathrm{d}t = v(r)[\mathrm{d}Y/\mathrm{d}r]$. A careful study of the influence of nuclear composition on Y_e in the post-core bounce supernova environment is given in [30] to which we refer the reader for further details.

If no heavy nuclei are present, we can write

$$Y_e = X_p + \tfrac{1}{2} X_\alpha. \tag{32}$$

Because of the very large binding energy, the rate of alpha particle interactions with neutrinos is nearly zero and we can write $\mathrm{d}Y_e/\mathrm{d}t = \mathrm{d}X_p/\mathrm{d}t$. Using the constraint $X_p + X_n + X_\alpha = 1$ and equation (32), equation (31) can be rewritten as

$$\frac{\mathrm{d}Y_e}{\mathrm{d}t} = \lambda_n - (\lambda_p + \lambda_n)Y_e + \frac{1}{2}(\lambda_p - \lambda_n)X_\alpha, \tag{33}$$

where we introduced the total proton loss rate $\lambda_p = \lambda_{\bar{\nu}_e} + \lambda_{e^-}$ and the total neutron loss rate $\lambda_n = \lambda_{\nu_e} + \lambda_{e^+}$. It has been shown that when the rates of these processes are rapid as compared to the outflow rate, a 'weak chemical equilibrium' is established [13]. The weak freeze-out radius is defined to be where the neutron-to-proton conversion rate is less than the outflow rate of the material. If the plasma reaches a weak equilibrium stage then Y_e is no longer changing, i.e. $\mathrm{d}Y_e/\mathrm{d}t = 0$. From equation (33) one can write the equilibrium value of the electron fraction as

$$Y_e = \frac{\lambda_n}{\lambda_p + \lambda_n} + \frac{1}{2}\frac{\lambda_p - \lambda_n}{\lambda_p + \lambda_n} X_\alpha. \tag{34}$$

Different flavours of neutrinos decouple at different radii. Since ν_μ and ν_τ (and their antiparticles) interact with ordinary matter only through the neutral current interactions, they

decouple deeper in the core and have a large average energy. Electron neutrinos and antineutrinos have additional charged-current interactions with neutrons and protons, respectively. Since in the supernova environment there are more neutrons, electron antineutrinos decouple after ν_μ's and ν_τ's, but before electron neutrinos. Consequently, one has a hierarchy of average neutrino energies:

$$\langle E_{\nu_e}\rangle \leqslant \langle E_{\bar{\nu}_e}\rangle \leqslant \langle E_{\nu_x,\bar{\nu}_x}\rangle, \tag{35}$$

where ν_x stands for any combination of ν_μ's and ν_τ's. However, a more complete description of the microphysics suggests that this hierarchy of average energies may not be very pronounced [28, 29, 31]. This microphysics is dominated by the inelastic neutrino–nucleon interactions discussed in section 2.3.

In figure 2, we present initial differential neutrino fluxes. In figure 2(a) the typical post-bounce neutrino energies are taken as the representative values of $\langle E_{\nu_e}\rangle = 10\,\mathrm{MeV}$, $\langle E_{\bar{\nu}_e}\rangle = 15\,\mathrm{MeV}$ and $\langle E_{\nu_x,\bar{\nu}_x}\rangle = 24\,\mathrm{MeV}$. (Average neutrino temperature for each flavour can be calculated using the relation, $T_\nu = \langle E_\nu\rangle/3.151$.) Here neutrino and antineutrino luminosities are taken to be equal for all flavours. We express the neutrino luminosities in more convenient units of $10^{51}\,\mathrm{ergs\,s^{-1}}$. Equal luminosities of $L_\nu^{51} = 1$ is typically a good approximation for the neutrino-driven wind epoch. However, at earlier epochs, ν_e and $\bar{\nu}_e$ luminosities can be as large as $L_\nu^{51} = 10$. Except, through the neutronization burst, for few milliseconds ν_e luminosity can reach values of $L_\nu^{51} = 100$, an order of magnitude larger than $\bar{\nu}_e$ during the same period. In figure 2(b), we examine a less-pronounced hierarchy of neutrino energies. Here we adopt the representative values of $\langle E_{\nu_e}\rangle = 13\,\mathrm{MeV}$, $\langle E_{\bar{\nu}_e}\rangle = 15\,\mathrm{MeV}$ and $\langle E_{\nu_x,\bar{\nu}_x}\rangle = 16\,\mathrm{MeV}$. Here the luminosities of ν_x and $\bar{\nu}_x$ are taken to be half of the value of the equal luminosities of ν_e and $\bar{\nu}_e$.

In our calculations in section 4, we adapt these initial distributions of ν_e, $\bar{\nu}_e$, ν_x and $\bar{\nu}_x$ at neutrinosphere, $R_\nu = 10\,\mathrm{km}$, with the indicated luminosities and follow the evolution of differential neutrino fluxes (number of neutrinos per unit energy per unit volume).

2.5. Alpha effect

At high temperatures, alpha particles are absent and the second term in equation (34) can be dropped. In the region just below where the alpha particles are formed, ~1 s after the bounce, the temperature is less than ~1 MeV. Here both the electron and positron capture rates are very small and Y_e can be approximated as

$$Y_e^{(0)} = \frac{1}{1 + \lambda_{\bar{\nu}_e}/\lambda_{\nu_e}}. \tag{36}$$

As the alpha particle mass fraction increases (when T_9 drops below 8) free nucleons get bound in alphas and, because of the large binding energy of the alpha particle, cease to interact with neutrinos. This phenomenon is called the 'alpha effect' [22]. Using equation (36) one can rewrite equation (34) as

$$Y_e = Y_e^{(0)} + \left(\tfrac{1}{2} - Y_e^{(0)}\right) X_\alpha. \tag{37}$$

Hence if the initial electron fraction is small ($Y_e^{(0)} < 1/2$), the alpha effect increases the value of Y_e. Since higher Y_e implies fewer free neutrons, the alpha effect negatively impacts r-process nucleosynthesis [25].

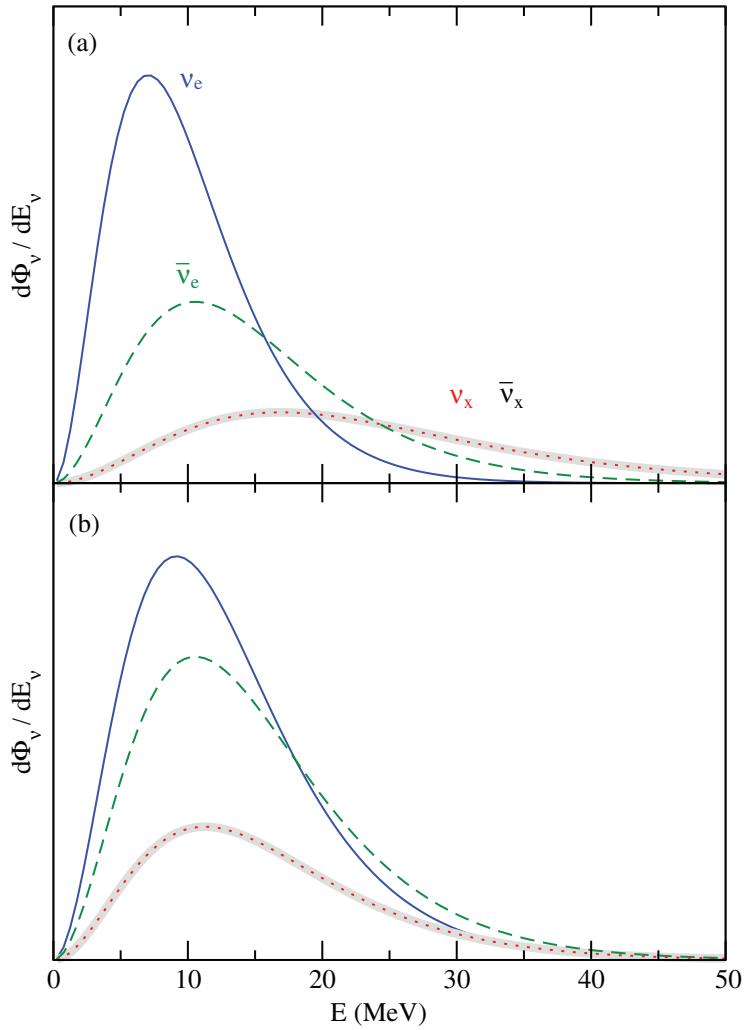

Figure 2. Initial differential neutrino fluxes in arbitrary units. Solid, dashed, dotted, and thick lines correspond to the distributions of ν_e, $\bar{\nu}_e$, ν_x and $\bar{\nu}_x$. (a) Fluxes with $\langle E_{\nu_e}\rangle = 10\,\mathrm{MeV}$, $\langle E_{\bar{\nu}_e}\rangle = 15\,\mathrm{MeV}$ and $\langle E_{\nu_x,\bar{\nu}_x}\rangle = 24\,\mathrm{MeV}$. Neutrino and antineutrino luminosities are taken to be equal for all flavours. Distributions of ν_x,$\bar{\nu}_x$ have much longer tails up to 100 MeV not shown in the figure. (b) Fluxes with $\langle E_{\nu_e}\rangle = 13\,\mathrm{MeV}$, $\langle E_{\bar{\nu}_e}\rangle = 15\,\mathrm{MeV}$ and $\langle E_{\nu_x,\bar{\nu}_x}\rangle = 16\,\mathrm{MeV}$. ν_e and $\bar{\nu}_e$ luminosities are taken to be equal. Luminosities of other flavours are taken to be half of the ν_e and $\bar{\nu}_e$ luminosities.

Neutrino oscillations, since they can swap energies of different flavours, may affect the energy-dependent rates in equations (36) and (37), changing the electron fraction. Indeed, transformations between active flavours heat up ν_e's and increase λ_{ν_e}, driving the electron fraction to rather large values. Consequently, a very large mixing between active neutrino flavours would have prohibited the r-process nucleosynthesis in a core-collapse supernova [13, 14].

Actually electron neutrinos radiated from the proto-neutron stars are just too energetic to prevent the alpha effect in most cases. One possibility to reduce λ_{ν_e} is to convert active electron neutrinos into sterile ones which do not contribute to this rate. This possibility is explored in [18, 32, 33].

3. Neutrino mixing

Neutrino interactions in matter is a rich subject (for a brief review see [34]). While neutrinos are produced through weak interactions in flavour eigenstates, they propagate in mass eigenstates. Mixing angles correspond to rotations describing unitary connection between two bases:

$$\begin{pmatrix} \nu_e \\ \nu_\mu \\ \nu_\tau \end{pmatrix} = U_{\alpha i} \begin{pmatrix} \nu_1 \\ e^{i\phi_1}\nu_2 \\ e^{i\phi_2}\nu_3 \end{pmatrix}. \tag{38}$$

In our discussion, we follow the notation in [35] and denote the neutrino mixing matrix by $U_{\alpha i}$, where α denotes the flavour index and i denotes the mass index:

$$U_{\alpha i} = \begin{pmatrix} 1 & 0 & 0 \\ 0 & C_{23} & S_{23} \\ 0 & -S_{23} & C_{23} \end{pmatrix} \begin{pmatrix} C_{13} & 0 & S_{13}^* \\ 0 & 1 & 0 \\ -S_{13} & 0 & C_{13} \end{pmatrix} \begin{pmatrix} C_{12} & S_{12} & 0 \\ -S_{12} & C_{12} & 0 \\ 0 & 0 & 1 \end{pmatrix}. \tag{39}$$

In equation (39) C_{13}, etc is the shorthand notation for cos θ_{13}, etc. The notation S_{13}^* was used to indicate $(\sin\theta_{13})e^{i\phi}$, where ϕ is a CP-violating phase. We will ignore this phase in our discussion.

We have compelling evidence supporting non-zero neutrino masses and mixings. Two-flavour solar neutrino solution corresponding to $\theta_{12} \sim \pi/6$ and $\delta m_{12}^2 \sim 8 \times 10^{-5}\,\mathrm{eV}^2$ was identified using the recent Sudbury Neutrino Observatory (SNO) results (cf [36, 37]). Measurement of antineutrinos from nuclear power reactors in Japan by the KamLAND experiment confirmed this solution and improved the limits on the solar mass-squared difference, δm_{12}^2, significantly [38]. While it is known that the solar neutrino mixing angle is large, but not maximal, the atmospheric mixing angle is large and could be maximal, $\theta_{23} \sim \pi/4$, as shown by the Super-Kamiokande experiment [39]. The latter angle is consistent with the KEK-to-Kamioka oscillation experiment, K2K [40]. The corresponding atmospheric mass-squared difference is $\delta m_{23}^2 \sim 3 \times 10^{-3}\,\mathrm{eV}^2$.

The size of the last mixing angle, θ_{13} is currently best limited by the combined CHOOZ [41] and Palo Verde [42] reactor experiments and SK atmospheric data. This is due to the null results from the reactor $\bar{\nu}_e$ disappearance over the δm_{23}^2 distance scale. The upper bound on this angle from KamLAND and the solar neutrino data gets stronger (especially in the region with small atmospheric mass-squared difference where the CHOOZ reactor bound is relatively weak), and even dominates, as these data get refined [43]. Both measurements of the width of the Z boson and oscillation interpretation of the neutrino data, with the notable exception of the LSND signal [44], favour three generations of light active neutrino species. If LSND is confirmed, the most likely explanation could be the existence of a fourth neutrino (a relatively heavier sterile neutrino), since agreement between KamLAND and the combined solar experiments already disfavours the interpretation of the LSND anomaly with CP violation.

In the region above the supernova, core density is still high but steeply decreases. Matter-enhanced oscillations mediated by the solar mass-squared difference are impossible in the region close to the core, which is suitable for the r-process. However, at the late neutrino-driven epoch, baryon density could be low enough to allow resonances through δm_{13}^2, which is comparable to the atmospheric mass-squared difference. At such late times, neutrino flux is expected to be low. We examine prospects of r-process at such environments in the next section.

We describe neutrino mixing within the density matrix formalism [14], [45]–[47]. We assume that the electron neutrino mixes with a linear combination of μ and τ neutrinos. The neutrino oscillations are mediated by the matter mixing angle for transformation between the first and third mass eigenstates, θ_{13}, and the corresponding atmospheric mass-squared difference, δm^2_{13}. The mixing between μ and τ neutrino flavours does not have any significant effect on our results as long as total luminosities and corresponding average energies are equal and their mixing is maximal. In this limit, mixing between the second and third mass eigenstates can be rotated away and effectively electron neutrinos oscillate into some linear combination of μ and τ neutrinos [48].

In the rest of the paper, θ and δm^2 refer to θ_{13} and δm^2_{13}. This assumption simplifies the discussion and allows us to write the two-flavour density matrices as

$$\rho = \begin{pmatrix} \rho_{ee} & \rho_{ex} \\ \rho_{xe} & \rho_{xx} \end{pmatrix} = \tfrac{1}{2}(P_0 + \mathbf{P}\cdot\sigma) \tag{40}$$

and

$$\bar{\rho} = \begin{pmatrix} \bar{\rho}_{ee} & \bar{\rho}_{ex} \\ \bar{\rho}_{xe} & \bar{\rho}_{xx} \end{pmatrix} = \tfrac{1}{2}(\bar{P}_0 + \bar{\mathbf{P}}\cdot\sigma), \tag{41}$$

where we introduced the polarization vectors for neutrinos and antineutrinos, $\mathbf{P}_p$ and $\bar{\mathbf{P}}_p$. The diagonal elements in these expressions are initially given by the expression in equation (17). Non-diagonal elements are initially zero but may become non-zero during the neutrino evolution.

Equations governing the evolution of neutrinos and antineutrinos can be cast into the following forms [49]

$$\partial_r \mathbf{P}_p = \left\{ +\mathbf{\Delta}_p + \sqrt{2}\, G_{\mathrm{F}} \left[N_e \hat{\mathbf{z}} + \int \mathrm{d}\mathbf{q} \left(1 - \frac{\mathbf{p}\cdot\mathbf{q}}{p\,q} \right) (\mathbf{P}_{\mathbf{p}} - \bar{\mathbf{P}}_{\mathbf{q}}) \right] \right\} \times \mathbf{P}_p \tag{42}$$

and

$$\partial_r \bar{\mathbf{P}}_p = \left\{ -\mathbf{\Delta}_p + \sqrt{2}\, G_{\mathrm{F}} \left[N_e \hat{\mathbf{z}} + \int \mathrm{d}\mathbf{q} \left(1 - \frac{\mathbf{p}\cdot\mathbf{q}}{p\,q} \right) (\mathbf{P}_{\mathbf{p}} - \bar{\mathbf{P}}_{\mathbf{q}}) \right] \right\} \times \bar{\mathbf{P}}_p, \tag{43}$$

where

$$\mathbf{\Delta}_p = \frac{\delta m^2}{2p} (\sin 2\theta \hat{\mathbf{x}} - \cos 2\theta \hat{\mathbf{z}}). \tag{44}$$

Integrating equations (42) and (43) exactly in the supernova environment is, at the moment, an unsolved problem. Indeed, the exact solutions of these coupled, nonlinear differential equations are expected to be very complicated. Instead, we adopt the approximation proposed in [14] and also adopted in [49]. In this approximation, one uses flux-averaged values to obtain

$$\partial_r \mathbf{P}_p = (+\mathbf{\Delta}_p + \sqrt{2}\, G_{\mathrm{F}} N_e \hat{\mathbf{z}} + \sqrt{2} G_{\mathrm{F}} F(r)(\mathbf{J} - \bar{\mathbf{J}})) \times \mathbf{P}_p \tag{45}$$

and

$$\partial_r \bar{\mathbf{P}}_p = (-\mathbf{\Delta}_p + \sqrt{2}\, G_{\mathrm{F}} N_e \hat{\mathbf{z}} + \sqrt{2} G_{\mathrm{F}} F(r)(\mathbf{J} - \bar{\mathbf{J}})) \times \bar{\mathbf{P}}_p. \tag{46}$$

In these equations $\mathbf{J}$ is the polarization integrated over all momentum modes and $F(r) = \frac{1}{2}[1 - (1 - R_\nu^2/r^2)^{1/2}]$ is the geometrical factor introduced earlier (cf equations (11) and (12)).

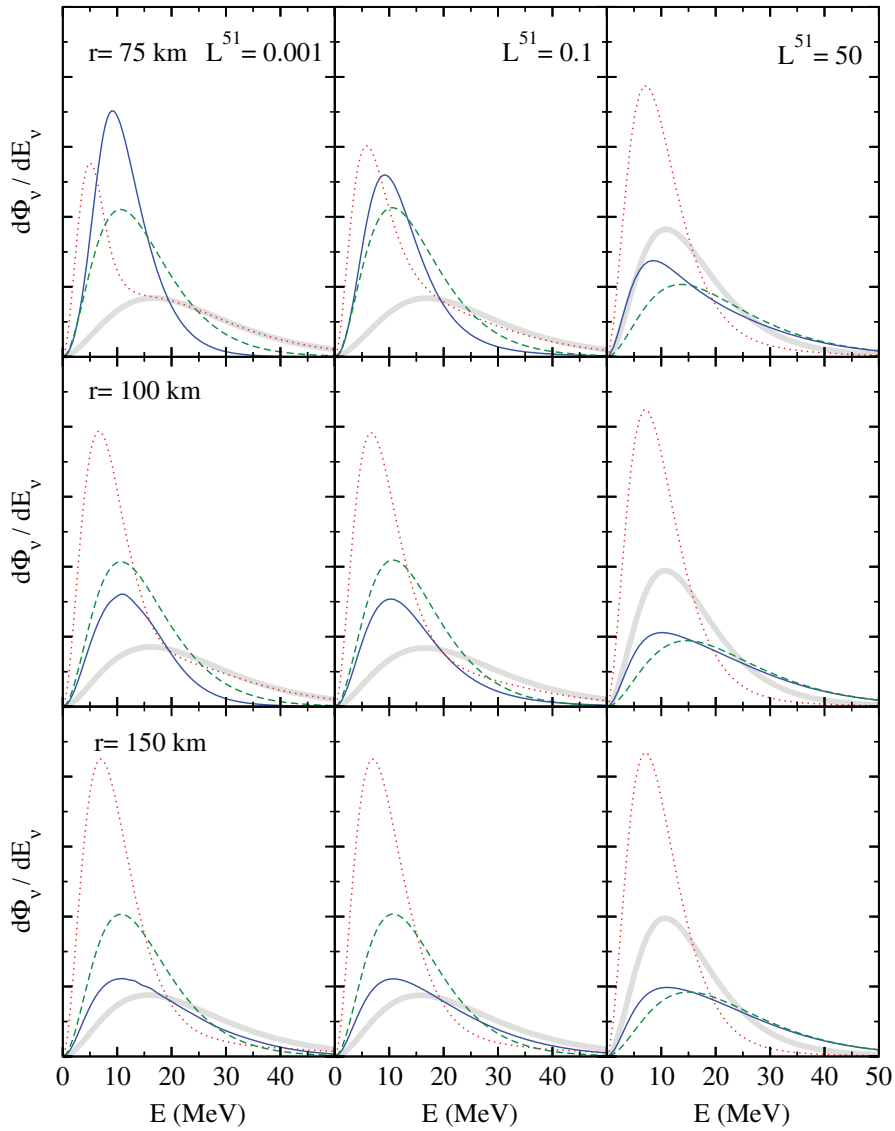

Figure 3. Evolution of differential neutrino fluxes in arbitrary units. Solid, dashed, dotted, and thick lines correspond to the distributions of ν_e, $\bar{\nu}_e$ ν_μ, and $\bar{\nu}_\mu$. In each panel, $1/r^2$ dependence is removed. Columns are for $L^{51} = 0.001$, 0.1 and 50 from the left to the right corresponding to very weak, moderate and very strong neutrino self-interaction contributions to the evolution. Rows are calculated at $r = 75$, 100 and 150 km showing the evolution of distributions along a neutrino path (see the text for details).

4. Results and discussion

In our calculations, we concentrate on the late neutrino-driven wind epoch which is expected to have a larger entropy. We adopt $S_{100} = 1.5$ and the $g_S = 2$, since in this epoch the temperature is too low at later times to have electron–positron pairs to be adequately represented.

In figure 3, we present differential neutrino fluxes at several stages of the evolution in order to provide a better understanding of this mechanism. The mixing parameters are chosen as $\theta \sim \pi/10$

and $\delta m^2 \sim 3 \times 10^{-3}\,\mathrm{eV}^2$. Solid, dashed, dotted, and thick lines correspond to the distributions of ν_e, $\bar{\nu}_e$, ν_x and $\bar{\nu}_x$. In each panel, $1/r^2$ dependence is removed. For this figure, the initial distributions are taken as the values given in figure 2(a). Columns are for $L^{51} = 0.001$, 0.1 and 50 from the left to the right corresponding to very weak, moderate and very strong neutrino self-interaction contributions to the evolution. Rows show neutrino flux at $r = 75$, 100 and 150 km, exhibiting the evolution of neutrino distributions along the neutrino path. These should be compared to the initial (at ~10 km) neutrino distributions given in figure 2(a). Electron fractions corresponding to these luminosities are given in the left column of figure 4.

First column of figure 3, $L^{51} = 0.001$: Initially differential neutrino fluxes for ν_e and ν_x are the same at ~20 MeV as seen in figure 2(a). At energies lower than 20 MeV, differential flux of ν_e is higher than that of ν_x, whereas at energies higher than 20 MeV the numbers reverse. The transformation starts at the low energy tail of the distributions. As we gradually move to lower densities, resonance moves up to higher energies. Until we reach the resonance at 20 MeV, the luminosity of ν_e's decreases. At r = 100 km electron neutrinos below 20 MeV are mostly swapped with ν_x's, while above 20 MeV there is yet no significant transformation. This point corresponds to the minimum of λ in equation (22) for neutrinos (after the $1/r^2$-dependence is taken out). Since antineutrinos are not transformed, λ is a constant for them. As a result, $r \sim 100$ km corresponds to a dip in Y_e (solid line in figure 4(a)). Since above 20 MeV the initial differential flux of ν_e's is smaller than that of ν_x's, transformations after $r \sim 100$ km would increase the number of high energy ν_e's. As neutrinos travel to regions further away (r = 150 km, where baryon density is much lower), swapping of the high energy tail of the ν_e and ν_x distributions is completed, and Y_e approaches to the asymptotic fixed value.

Second column of figure 3, $L^{51} = 0.1$: This column describes the same evolution of neutrinos except that neutrino self-interaction effects play a more pronounced role. The chosen value of the luminosity could be representative of such late times in neutrino-driven wind epoch. Because of the small contributions of the self-interactions, the resonance region is relatively wider. No dip is observed in Y_e (dashed line in figure 4(a)) at r = 100 km because the transformation of low and high energy ends of the distributions happen almost simultaneously. There is also a small transformation between $\bar{\nu}_e$'s and $\bar{\nu}_x$'s.

Third column of figure 3, $L^{51} = 50$: This is an extreme case to illustrate the limit at which neutrino self-interactions dominate. Exchanges of both neutrinos and antineutrinos occur and Y_e reaches its equilibrium value rapidly. After the transformation, electron neutrinos and antineutrinos assume similar luminosities and distributions since they are swapped with ν_x's and $\bar{\nu}_x$'s. Note that this equilibrium value is again different from 0.5 because of the threshold effects (due to the neutron–proton mass difference) in the reaction cross sections (cf equations (20) and (21)).

In the left column of figure 4, initial neutrino fluxes and luminosities are taken to be those in figure 2(a) and in the right column initial neutrino fluxes and luminosities are taken to be those in figure 2(b). In figure 4(a), we present the equilibrium electron fraction, Y_e, as a function of the distance from the core for the three different cases of neutrino flux, $L^{51} = 0.001$, 0.1 and 50, each corresponding to one of the columns in figure 3. In figure 4(a), we use the same neutrino parameters as in figure 3. One could argue that the relatively large mixing angle of $\pi/10$ is already disfavoured by CHOOZ. To explore the implications of a smaller mixing angle in figure 4(b), we show electron fractions calculated with the more realistic mixing parameters $\theta \sim \pi/20$ and $\delta m^2 \sim 3 \times 10^{-3}\,\mathrm{eV}^2$. The dip in the Y_e plot is sharper since the resonance region will be much narrower with a smaller mixing angle.

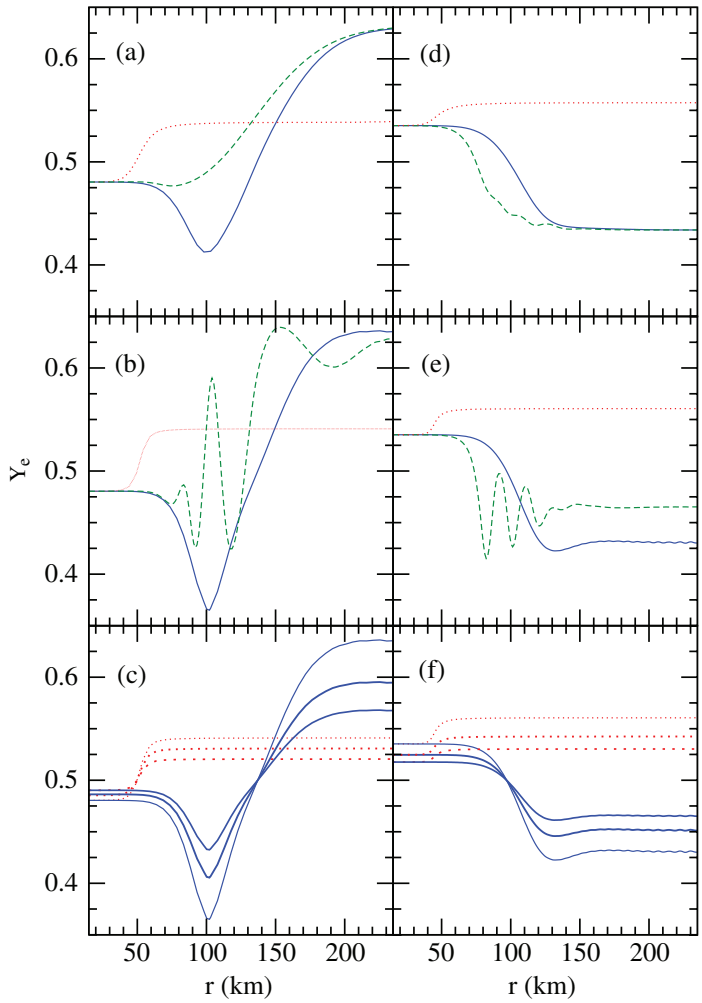

Figure 4. Initial neutrino fluxes and luminosities are taken to be those in figure 2(a) in the left column and those in figure 2(b) in the right column. S_{100} is taken to be 1.5. In panels (a) and (b), solid, dashed and dotted, lines correspond to the equal luminosities of $L^{51} = 0.001$, 0.1 and 50 for all flavours, indicating very weak, moderate and very-strong neutrino self-interaction contributions to the evolution. In panels (d) and (e), ν_e and $\bar{\nu}_e$ luminosities are taken to be $L^{51} = 0.002$, 0.2 and 200 (solid, dashed, and dotted lines, respectively). In (d) and (e), the luminosities of other flavours are taken to be $L^{51} = 0.001$, 0.1 and 100 (solid, dashed, and dotted lines, respectively). (a, d) Equilibrium electron fraction as a function of the distance from the core with mixing parameters $\theta_{13} \sim \pi/10$ and $\delta m^2_{13} \sim 3 \times 10^{-3}\,\mathrm{eV}^2$. (b, e) Equilibrium Y_e as a function of the distance from the core with mixing parameters $\theta_{13} \sim \pi/20$ and $\delta m^2_{13} \sim 3 \times 10^{-3}\,\mathrm{eV}^2$. (c) Same as (b) but the impact of alpha particle formation is included according to the equation (34). Y_e is shown when $X_\alpha = 0$, 0.3 and 0.5 (thin, medium and thick lines) for $L^{51} = 0.001$ and 50 (solid and dotted sets of lines). (f) Same as (e) but the impact of alpha particle formation is included as in (c). Y_e is shown when $X_\alpha = 0$, 0.3 and 0.5 (thin, medium and thick lines) for $L^{51}_{\nu_e} = 0.002$ and 200 (solid and dotted sets of lines).

In figures 4(a) and (b), to calculate the equilibrium electron fraction, we ignored possible effects of the alpha particles and used equation (36) to evaluate Y_e. In figure 4(c), we explore possible effects of alpha particles by using equation (34) to calculate Y_e for three different values of X_α. The 'alpha effect' is manifest: as X_α gets larger, it pulls the value of the electron fraction closer to 0.5.

In the right column of figure 4, initial neutrino fluxes and luminosities are taken as the generic 'almost equal' energies and different luminosities case shown in figure 2(b). It is immediately obvious that the situation is markedly different in this case. Even though the initial ν_e and $\bar{\nu}_e$ spectra are almost the same (cf figure 2(b)), Y_e is, initially greater than 0.5 because of the effect of the neutron–proton mass difference in equations (20) and (21). When the effects of the neutrino self-interaction terms are minimal (the low-luminosity case indicated by the solid lines in (d) and (e)) after ν_e's and ν_x's swap, ν_e luminosity decreases significantly causing a big drop in the value of Y_e. When the effects of the self-interaction terms are dominant (the high-luminosity cases indicated by the dotted lines in (d) and (e)), all flavours swap and the electron fraction eventually reaches the asymptotic values. The impact of alpha formation, when the hierarchy of average neutrino energies is less pronounced, is presented in figure 4(f).

5. Conclusions

In this paper we investigated conditions for the r-process nucleosynthesis at late neutrino-driven wind epoch in a core-collapse supernova. We considered the region where the matter-enhanced neutrino transformation is driven by δm^2_{13}, which we took to be comparable to the mass difference observed in the atmospheric neutrino oscillations.

We found that, when initial luminosities are taken to be equal with a pronounced hierarchy of neutrino energies, the asymptotic value (at large distances from the core) of the electron fraction always exceeds 0.5, hindering r-process nucleosynthesis. In this case, we found that neutrino self-interactions decrease the electron fraction. In general, these self-interaction terms, unlike the MSW effect, tend to transform both neutrinos and antineutrinos. Hence, one expects that when the self-interaction terms are dominant (e.g. when the neutrino luminosities are very large) the electron fraction would reach the value of 0.5. However, we showed that, because of the threshold effects in the neutrino interactions, electron fraction exceeds 0.5 even when the background neutrinos are in abundance. Clearly, these conditions are not favourable for r-process nucleosynthesis. We also found that, when background effects are small, with the parameters we adopted for baryon density and neutrino mixing, there exists a region around 100 km in which the electron fraction is smaller than 0.5. Even in this region, the alpha effect pulls the value of the electron fraction closer to 0.5. Although the conditions are favourable, the r-process in this region could not contribute reasonable quantities of elements since the baryon density is rather low.

In contrast, when the initial luminosities of the ν_e's and $\bar{\nu}_e$'s are taken to be twice the other flavours with a much less-pronounced neutrino hierarchy, we found that the asymptotic electron fraction is less than 0.5 when neutrino self-interactions are negligible. However, once again the baryon density is low and the r-process in this asymptotic region is likely to produce insignificant quantities. When neutrino self-interactions are dominant, the asymptotic electron fraction shows the same behaviour as the first generic case (with a pronounced hierarchy of neutrino energies and equal luminosities) we considered.

It is not surprising that the two cases are markedly different for low neutrino luminosities (late times). If all the initial average neutrino energies and luminosities were the same, neutrino oscillations would clearly have no impact. Our analysis highlights the significance of having a precise knowledge of the muon and tau neutrino spectra and luminosities in assessing core-collapse supernovae as a site of r-process nucleosynthesis. In both of the two generic, but markedly different, cases we studied and found that neutrino self-interactions are crucial in setting the value of the electron-fraction to be rather large. We should emphasize that our treatment of the neutrino self-interactions in equations (45) and (46) is an approximation using flux-averaged values. Hence an exact treatment of the neutrino self-interactions remains the key issue in the proper description of the neutrino transport in core-collapse supernovae.

Acknowledgments

We thank G Fuller and G McLaughlin for useful conversations. ABB also thanks the Nuclear Theory Group at Tohoku University for their hospitality during the latter part of this work. This work was supported in part by the US National Science Foundation grant No PHY-0244384 and in part by the University of Wisconsin Research Committee with funds granted by the Wisconsin Alumni Research Foundation.

References

[1] Woosley S E, Heger A and Weaver T A 2002 *Rev. Mod. Phys.* **74** 1015
[2] Buras R, Rampp M, Janka H T and Kifonidis K 2003 *Phys. Rev. Lett.* **90** 241101 (*Preprint* astro-ph/0303171)
[3] Mezzacappa A 2004 *Preprint* astro-ph/0410085
[4] Qian Y Z 2003 *Prog. Part. Nucl. Phys.* **50** 153 (*Preprint* astro-ph/0301422)
[5] Burbidge E M, Burbidge G R, Fowler W A and Hoyle F 1957 *Rev. Mod. Phys.* **29** 29
[6] Woosley S E, Wilson J R, Mathews G J, Hoffman R D and Meyer B S 1994 *Astrophys. J.* **433** 229
[7] Takahashi K, Witti J and Janka H-T 1994 *Astron. Astrophys.* **286** 857
[8] Wanajo S, Kajino T, Mathews G J and Otsuki K 2001 *Astrophys. J.* **554** 578 (*Preprint* astro-ph/0102261)
[9] Qian Y Z, Vogel P and Wasserburg G J 1998 *Astrophys. J.* **494** 285 (*Preprint* astro-ph/9706120)
[10] Rosswog S, Liebendoerfer M, Thielemann F K, Davies M B, Benz W and Piran T 1999 *Astron. Astrophys.* **341** 499 (*Preprint* astro-ph/9811367)
[11] Balantekin A B and Fuller G M 2003 *J. Phys. G: Nucl. Part. Phys.* **29** 2513 (*Preprint* astro-ph/0309519)
[12] Bethe H A and Wilson J R 1985 *Astrophys. J.* **295** 14
[13] Qian Y Z, Fuller G M, Mathews G J, Mayle R, Wilson J R and Woosley S E 1993 *Phys. Rev. Lett.* **71** 1965
[14] Qian Y Z and Fuller G M 1995 *Phys. Rev.* D **51** 1479 (*Preprint* astro-ph/9406073)
[15] Pantaleone J 1995 *Phys. Lett.* B **342** 250 (*Preprint* astro-ph/9405008)
[16] Qian Y Z and Fuller G M 1995 *Phys. Rev.* D **52** 656 (*Preprint* astro-ph/9502080)
[17] Qian Y Z and Woosley S E 1996 *Astrophys. J.* **471** 331 (*Preprint* astro-ph/9611094)
[18] McLaughlin G C, Fetter J M, Balantekin A B and Fuller G M 1999 *Phys. Rev.* C **59** 2873 (*Preprint* astro-ph/9902106)
[19] Bethe H A 1993 *Astrophys. J.* **412** 192
[20] Horowitz C J and Li G 1999 *Phys. Rev. Lett.* **82** 5198 (*Preprint* astro-ph/9904171)
Horowitz C J 2002 *Phys. Rev.* D **65** 043001 (*Preprint* astro-ph/0109209)
Horowitz C J and Perez-Garcia M A 2003 *Phys. Rev.* C **68** 025803 (*Preprint* astro-ph/0305138)
[21] Fuller G M, Fowler W A and Newman M J 1982 *Astrophys. J.* **252** 715
[22] Fuller G M and Meyer B S 1995 *Astrophys. J.* **453** 792

[23] McLaughlin G C and Fuller G M 1995 *Astrophys. J.* **455** 202
[24] Volpe C 2004 *Preprint* hep-ph/0409249
[25] Meyer B S, McLaughlin G C and Fuller G M 1998 *Phys. Rev.* C **58** 3696 (*Preprint* astro-ph/9809242)
[26] Suzuki H1993 *Proc. Int. Symp. on Neutrino Astrophysics* ed Y Suzuki and K Nakamura (Tokyo: Universal Academy Press)
[27] Hannestad S and Raffelt G 1998 *Astrophys. J.* **507** 339 (*Preprint* astro-ph/9711132)
[28] Buras R, Janka H T, Keil M T, Raffelt G G and Rampp M 2003 *Astrophys. J.* **587** 320 (*Preprint* astro-ph/0205006)
[29] Raffelt G G 2001 *Astrophys. J.* **561** 890 (*Preprint* astro-ph/0105250)
[30] McLaughlin G C, Fuller G M and Wilson J R 1996 *Astrophys. J.* **472** 440 (*Preprint* astro-ph/9701114)
[31] Keil M T, Raffelt G G and Janka H T 2003 *Astrophys. J.* **590** 971 (*Preprint* astro-ph/0208035)
[32] Caldwell D O, Fuller G M and Qian Y Z 2000 *Phys. Rev.* D **61** 123005 (*Preprint* astro-ph/9910175)
[33] Fetter J, McLaughlin G C, Balantekin A B and Fuller G M 2003 *Astropart. Phys.* **18** 433 (*Preprint* hep-ph/0205029)
[34] Balantekin A B 1999 *Phys. Rep.* **315** 123 (*Preprint* hep-ph/9808281)
[35] Balantekin A B and Yuksel H 2003 *J. Phys. G: Nucl. Part. Phys.* **29** 665 (*Preprint* hep-ph/0301072)
[36] Ahmed S N *et al* (SNO Collaboration) 2004 *Phys. Rev. Lett.* **92** 181301 (*Preprint* nucl-ex/0309004)
[37] Balantekin A B and Yuksel H 2003 *Phys. Rev.* D **68** 113002 (*Preprint* hep-ph/0309079)
[38] Araki T *et al* (KamLAND Collaboration) 2004 *Preprint* hep-ex/0406035
[39] Ashie Y *et al* (Super-Kamiokande Collaboration) 2004 *Phys. Rev. Lett.* **93** 101801 (*Preprint* hep-ex/0404034)
[40] Ahn M H *et al* (K2K Collaboration) 2003 *Phys. Rev. Lett.* **90** 041801 (*Preprint* hep-ex/0212007)
[41] Apollonio M *et al* 2003 *Eur. Phys. J.* C **27** 331 (*Preprint* hep-ex/0301017)
[42] Boehm F *et al* 2001 *Phys. Rev.* D **64** 112001 (*Preprint* hep-ex/0107009)
[43] Balantekin A B, Barger V, Marfatia D, Pakvasa S and Yuksel H 2004 *Preprint* hep-ph/0405019
[44] Aguilar A *et al* (LSND Collaboration) 2001 *Phys. Rev.* D **64** 112007 (*Preprint* hep-ex/0104049)
[45] Sigl G and Raffelt G 1993 *Nucl. Phys.* B **406** 423
[46] Raffelt G, Sigl G and Stodolsky L 1993 *Phys. Rev. Lett.* **70** 2363 (*Preprint* hep-ph/9209276)
[47] Loreti F N and Balantekin A B 1994 *Phys. Rev.* D **50** 4762 (*Preprint* nucl-th/9406003)
[48] Balantekin A B and Fuller G M 1999 *Phys. Lett.* B **471** 195 (*Preprint* hep-ph/9908465)
[49] Pastor S and Raffelt G 2002 *Phys. Rev. Lett.* **89** 191101 (*Preprint* astro-ph/0207281)
Pastor S, Raffelt G G and Semikoz D V 2002 *Phys. Rev.* D **65** 053011 (*Preprint* hep-ph/0109035)

New Journal of Physics
The open-access journal for physics

Neutrino masses from cosmological probes

Øystein Elgarøy[1] **and Ofer Lahav**[2]

[1] Institute of Theoretical Astrophysics, University of Oslo, PO Box 1029, N-0315 Oslo, Norway
[2] Department of Physics and Astronomy, University College London, Gower Street, London WC1E 6BT, UK
E-mail: oelgaroy@astro.uio.no and lahav@star.ucl.ac.uk

New Journal of Physics **7** (2005) 61
Received 1 December 2004
Published 17 February 2005
Online at http://www.njp.org/
doi:10.1088/1367-2630/7/1/061

Abstract. There is a renewed interest in constraining the sum of the masses of the three neutrino flavours by using cosmological measurements. Solar, atmospheric, reactor and accelerator neutrino experiments have confirmed neutrino oscillations, implying that neutrinos have non-zero mass, but without pinning down their absolute masses. While it has been established that the effect of light neutrinos on the evolution of cosmic structure is small, the upper limits derived from a large-scale structure could help significantly to constrain the absolute scale of the neutrino masses. It is also important to know the sum of neutrino masses as it is degenerate with the values of other cosmological parameters, e.g. the amplitude of fluctuations and the primordial spectral index. A summary of the cosmological neutrino mass limits is given. Current results from cosmology set an upper limit on the sum of the neutrino masses at $\sim$1 eV, somewhat dependent on the datasets used in the analyses and assumed priors on cosmological parameters. It is important to emphasize that the total neutrino mass ('hot dark matter') is derived by assuming that the other components in the universe are baryons, cold dark matter and dark energy. We assessed the impact of neutrino masses on the matter power spectrum, the cosmic microwave background, peculiar velocities and gravitational lensing. We also discuss possible methods to improve the mass upper limits by an order of magnitude.

1367-2630/05/010061+19$30.00
PII: S1367-2630(05)90618-6
© IOP Publishing Ltd and Deutsche Physikalische Gesellschaft

Contents

1. Introduction **2**
2. Massive neutrinos and structure formation **3**
3. Constraints from the CMB alone **8**
4. Recent cosmological neutrino mass limits **10**
5. Other cosmological probes of neutrino masses **11**
5.1. The clustering amplitude 11
5.2. The Lyman-α forest 12
5.3. Peculiar velocities 13
5.4. Gravitational lensing 15
6. Discussion **15**
Acknowledgments **16**
References **16**

1. Introduction

The connection between neutrino masses and cosmic structure formation was realized in the 1970s by Zeldovich and others, but for a long time cosmologists were mostly interested in neutrino masses in the ~10 eV range, i.e. massive enough to make up all of the dark matter. The downfall of the top-down 'hot dark matter' scenario of structure formation and the fact that no evidence for neutrino masses existed before Super-Kamiokande detected oscillations of atmospheric neutrinos in 1998 explain why there was very little continuous interest in this sub-field. However, the detection of neutrino oscillations showed that neutrinos indeed have a mass, i.e. 'hot dark matter' does exist, even though only in a very small amount.

The wealth of new data from the cosmic microwave background (CMB) and large-scale structure (LSS) in the last few years indicate that we live in a flat Universe where ~70% of the mass-energy density is in the form of dark energy, with matter making up the remaining 30%. The WMAP data combined with other large-scale structure data [1, 2] give impressive support to this picture. Furthermore, the baryons contribute only a fraction $f_b = \Omega_b/\Omega_m \sim 0.15$ (Ω_b and Ω_m are, respectively, the contributions of baryons and of all matter to the total density expressed in terms of the critical density $\rho_c = 3H_0^2/8\pi G = 1.879 \times 10^{-29} h^2\,\mathrm{g\,cm^{-3}}$, where $H_0 = 100h\,\mathrm{km\,s^{-1}\,Mpc^{-1}}$ is the present value of the Hubble parameter) of this, so that most of the matter is dark. The exact nature of the dark matter in the Universe is still unknown. Relic neutrinos are abundant in the Universe and, from the observations of oscillations of solar and atmospheric neutrinos, as well as in the reactor-based KamLAND experiment and in the accelerator-based long-baseline K2K experiment, we know that neutrinos have a mass [3]–[12] and will make up a fraction of the dark matter. The KamLAND collaboration has also reported evidence for spectral distortion in the $\overline{\nu}_e$ spectrum [13], further strengthening the case for neutrino oscillations and allowing rather strict bounds on the neutrino oscillation parameters to be found. However, the oscillation experiments can only measure differences in the squared masses of the neutrinos and not the absolute mass scale, so they cannot, at least not without extra assumptions, tell us how much of the dark matter is in neutrinos. From the general arguments on structure formation in the Universe, we know that most of the dark matter has to be cold, i.e. non-relativistic when it is decoupled from the

thermal background. Neutrinos with masses on the eV scale or below will be a hot component of the dark matter. If they were the dominant dark-matter component, structure in the Universe would have formed first at large scales, and smaller structures would form by fragmentation (the 'top-down' scenario). However, the combined observational and theoretical knowledge about a large-scale structure gives strong evidence for the 'bottom-up' picture of structure formation, i.e. that the structure is formed first at small scales. Hence, neutrinos cannot make up all of the dark matter (see, e.g., [14] for a review). Neutrino experiments give some constraints on how much of the dark matter can be in the form of neutrinos. Studies of the energy spectrum in tritium decay [15] provide an upper limit on the effective electron neutrino mass involved in this process of 2.2 eV (95% confidence limit). For the effective neutrino mass scale involved in neutrino-less double β decay, a range 0.1–0.9 eV has been inferred from the claimed detection of this process [16, 17]. If confirmed, this result would not only show that neutrinos are Majorana particles (i.e. their own antiparticles), but also that the neutrino masses are in a range where they are potentially detectable with cosmological probes.

The structure of this review is as follows. Sections 2 and 3 describe the role of massive neutrinos in structure formation and for the CMB anisotropies, respectively. In section 4, we give an overview of recent cosmological neutrino mass limits. Section 5 discusses other methods for constraining neutrino masses. We discuss challenges for the future in section 6.

2. Massive neutrinos and structure formation

The relic abundance of neutrinos in the Universe today is straightforwardly found from the fact that they continue to follow the Fermi–Dirac distribution after freeze-out, and their temperature is related to the CMB temperature $T_{\rm CMB}$ today by $T_\nu = (4/11)^{1/3} T_{\rm CMB}$, giving

$$n_\nu = \frac{6\zeta(3)}{11\pi^2} T_{\rm CMB}^3, \tag{1}$$

where $\zeta(3) \approx 1.202$, which gives $n_\nu \approx 112\,{\rm cm}^{-3}$ at present. By now, massive neutrinos have probably become non-relativistic, so that their present contribution to the mass density can be found by multiplying n_ν with the total mass of the neutrinos $m_{\nu,{\rm tot}} \equiv \sum m_\nu$, giving

$$\Omega_\nu h^2 = \frac{m_{\nu,{\rm tot}}}{94\,{\rm eV}}, \tag{2}$$

for $T_{\rm CMB} = 2.726\,{\rm K}$. Several effects could modify this simple relation. If any of the neutrino chemical potentials were initially non-zero or there were a sizable neutrino–antineutrino asymmetry, this would increase the energy density in neutrinos and give an additional contribution to the relativistic energy density. However, from Big Bang Nucleosynthesis (BBN), one gets a very tight limit on the electron neutrino chemical potential, since the electron neutrino is directly involved in the processes that set the neutron-to-proton ratio. Also, within the standard three-neutrino framework, one can extend this limit to the other flavours as well. The results of the KamLAND experiment [18] confirmed the large mixing angle (LAM) solution for the solar neutrino oscillations and, combined with the atmospheric data indicating maximal mixing in this sector, it has been shown that flavour equilibrium is established between all three neutrino species before the epoch of BBN [19]–[22], so that the BBN constraint on the electron neutrino

asymmetry applies to all flavours, which in turn implies that the lepton asymmetry cannot be large enough to give a significant contribution to the relativistic energy density. One should note, however, that these bounds can be evaded if there is an additional source of energy density to compensate the ν_e asymmetry [23]. Analyses of WMAP and 2dFGRS data give independent, although not quite as strong, evidence for small lepton asymmetries [24, 25]. Within the standard picture, equation (1) should be accurate, and therefore any constraint on the cosmic mass density of neutrinos should translate straightforwardly into a constraint on the total neutrino mass, according to equation (2). If a fourth, light 'sterile' neutrino exists, sterile-active oscillations would modify this conclusion and could also have implications to, e.g., BBN [26]; see [27] for a review. No sterile neutrinos are required to explain the solar and atmospheric neutrino oscillation data [28], and the only hint so far comes from the possible detection of $\overline{\nu}_\mu \to \overline{\nu}_e$ oscillations with a small mixing angle and a mass-squared difference $\sim 1\,\mathrm{eV}^2$ at the liquid scintillating neutrino detector (LSND) [29]. Since there are only two independent mass-squared differences in the standard three-neutrino scenario, and they are orders of magnitude smaller, this hints at the existence of a fourth, light sterile neutrino. However, this was found to be highly disfavoured by the solar and atmospheric neutrino oscillation data [30, 31]. The status of the LSND results will, in the near future, be clarified by the MiniBooNE experiment [32].

In a recent paper, Beacom *et al* [33] pointed out that if neutrinos couple to a light scalar field, they might annihilate as they become non-relativistic. If this were the case, massive neutrinos would have a negligible effect on the matter power spectrum. However, Hannestad [34] has pointed out that such a scenario would have a marked effect on the CMB power spectrum and is strongly disfavoured by the current data. We will therefore assume in the following that no such non-standard couplings of neutrinos exist.

Finally, we assume that the neutrinos are nearly degenerate in mass. Current cosmological observations are sensitive to neutrino masses $\sim 1\,\mathrm{eV}$ or greater. Since the mass-squared differences are small, the assumption of a degenerate mass hierarchy is therefore justified. This is illustrated in figure 1, where we have plotted the mass eigenvalues m_1, m_2, m_3 as functions of $m_{\nu,\mathrm{tot}} = m_1 + m_2 + m_3$ for $\Delta m_{21}^2 = 7 \times 10^{-5}\,\mathrm{eV}^2$ (solar) and $\Delta m_{32}^2 = 3 \times 10^{-3}\,\mathrm{eV}^2$ (atmospheric) for the cases of a normal hierarchy ($m_1 < m_2 < m_3$) and an inverted hierarchy ($m_3 < m_1 < m_2$). As seen in the figure, for $m_{\nu,\mathrm{tot}} > 0.4\,\mathrm{eV}$ the mass eigenvalues are essentially degenerate.

Here, we look at cosmological models with four components: baryons, cold dark matter, massive neutrinos and a cosmological constant. Furthermore, we restrict ourselves to adiabatic, linear perturbations. The basic physics is then fairly simple. A perturbation mode of a given wavelength λ can grow if it is greater than the Jeans wavelength λ_J determined by the balance of gravitation and pressure, or rms velocity in the case of massless particles. Above the Jeans scale, perturbations grow at the same rate independent of the scale. Long after matter–radiation equality, all interesting scales are above λ_J and grow at the same rate and, in models where all the dark matter is cold, the time and scale dependence of the power spectrum can therefore be separated at low redshifts. Light, massive neutrinos can, however, move unhindered out of regions below a certain limiting length scale and will therefore tend to damp a density perturbation at a rate which depends on their rms velocity. The presence of massive neutrinos therefore introduces a new length scale, given by the size of the co-moving Jeans length when the neutrinos became non-relativistic. In terms of the co-moving wavenumber, this is given by

$$k_\mathrm{nr} = 0.026 \left(\frac{m_\nu}{1\,\mathrm{eV}}\right)^{1/2} \Omega_\mathrm{m}^{1/2}\, h\mathrm{Mpc}^{-1}, \tag{3}$$

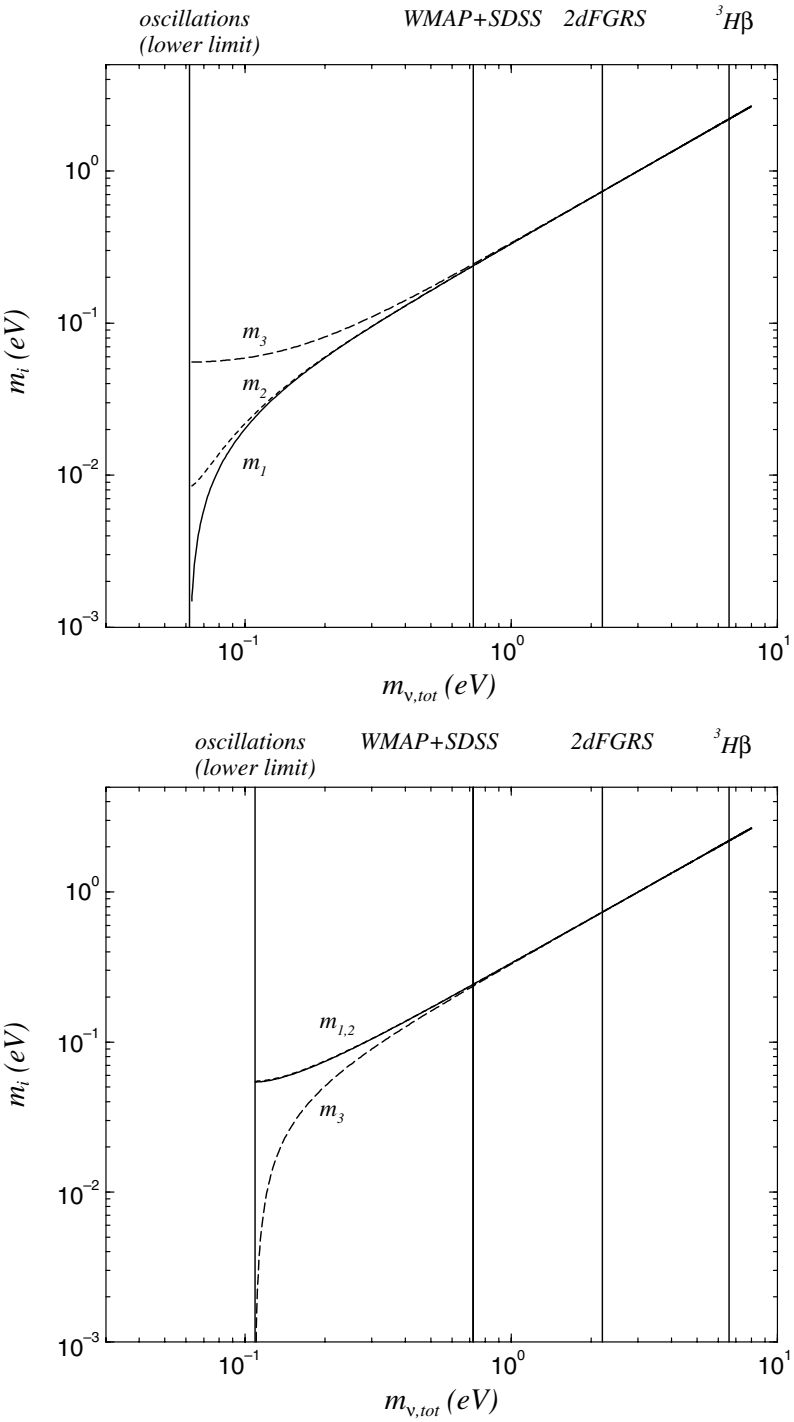

Figure 1. Neutrino mass eigenvalues as functions of $m_{\nu,\mathrm{tot}}$ for the cases of normal (upper panel) and inverted (lower panel) hierarchies. The vertical line marked 'oscillations' is the lower limit derived from the measured mass-squared differences. The vertical line marked 'WMAP + SDSS' is the recent limit derived in [55] from WMAP + SDSS, the vertical line marked '2dFGRS' is the limit from the 2dFGRS derived in [51] and the line marked '^{3}Hβ' is the upper limit from tritium β decay.

for three equal-mass neutrinos, each with mass m_ν. The growth of Fourier modes with $k > k_{\rm nr}$ will be suppressed because of neutrino free-streaming. The free-streaming scale varies with the cosmological epoch, and the scale and time dependence of the power spectrum cannot be separated, in contrast to the situation for models with cold dark matter only.

The transfer functions of the perturbations in the various components provide a convenient way of describing their evolution on different scales. Using the redshift z to measure time, the transfer function is formally defined as

$$T(k, z) = \frac{\delta(k, z)}{\delta(k, z = z_*)D(z_*)}, \tag{4}$$

where $\delta(k, z)$ is the density perturbation with wavenumber k at redshift z and D is the linear growth factor. The normalization redshift z_* corresponds to a time long before the scales of interest have entered the horizon. The transfer function thus gives the amplitude of a given mode k at redshift z relative to its initial value and is normalized so that $T(k = 0, z) = 1$. The power spectrum of the matter fluctuations can be written as

$$P_{\rm m}(k, z) = P_*(k)T^2(k, z), \tag{5}$$

where $P_*(k)$ is the primordial spectrum of matter fluctuations, commonly assumed to be a simple power law $P_*(k) = Ak^n$, where A is the amplitude and the spectral index n is close to 1. It is also common to define power spectra for each component, see [35] for a discussion. Note that the transfer functions and power spectra are insensitive to the value of the cosmological constant as long as it does not shift the epoch of matter–radiation equality significantly.

The transfer function is found by solving the coupled fluid and Boltzmann equations for the various components. This can be done using one of the publicly available codes, e.g. CMBFAST [36] or CAMB [37]. In figure 2, we show the transfer functions for models with $\Omega_{\rm m} = 0.3$, $\Omega_{\rm b} = 0.04$, $h = 0.7$ held constant, but with varying neutrino masses per flavour $m_\nu \equiv m_{\nu,{\rm tot}}/3$. One can clearly see that the small-scale suppression of power becomes more pronounced as the neutrino fraction $f_\nu \equiv \Omega_\nu/\Omega_{\rm m}$ increases.

The effect is also seen in the power spectrum, as shown in figure 3. Note that the power spectra shown in the figure have been convolved with the 2dFGRS window function, as described in [38]. Furthermore, we have taken the possible bias of the distribution of galaxies with respect to that of the dark matter into account by leaving the overall amplitude of each power spectrum as a free parameter to be fitted to the 2dFGRS power spectrum data (the vertical bars in the figure). For a discussion of bias in the context of neutrino mass limits, see [39]. Because the errors on the data points are smaller at small scales, these points are given most weight in the fitting, and hence the power spectra in the figure actually deviate more and more from each other on *large* scales as m_ν increases. One can see from the figure that a neutrino mass of $m_\nu = 0.5$ eV or larger is in conflict with the data. The suppression of the power spectrum on small scales is roughly proportional to f_ν:

$$\frac{\Delta P_{\rm m}(k)}{P_{\rm m}(k)} \approx -8 f_\nu. \tag{6}$$

This result can be understood qualitatively from the equation of linear growth of density perturbations and the fact that only a fraction $(1 - f_\nu)$ of the matter can cluster when massive neutrinos are present [40].

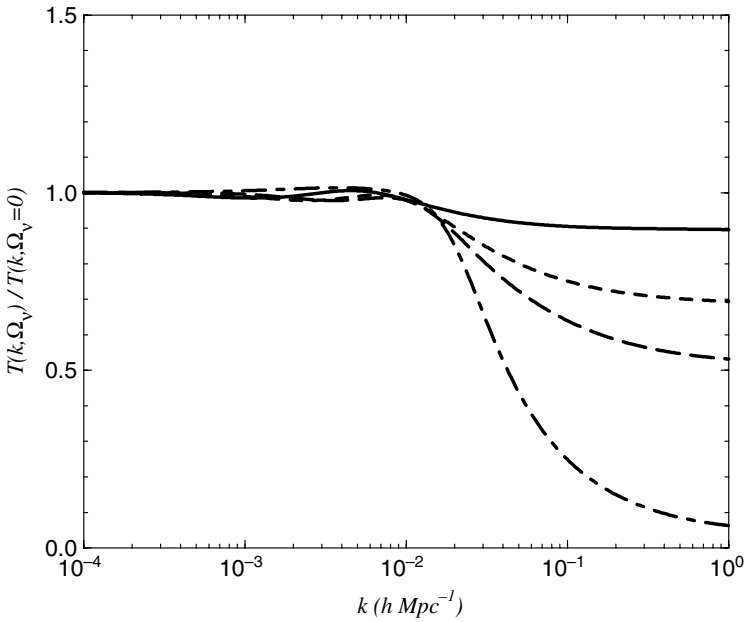

Figure 2. Ratio of the transfer functions (at $z = 0$) for various values of Ω_ν to the one for $\Omega_\nu = 0$. The other parameters are fixed at $\Omega_m = 0.3$, $\Omega_b = 0.04$, $h = 0.7$. The solid line is for neutrino mass per flavour $m_\nu = 0.1$ eV, the dashed line is for $m_\nu = 0.3$ eV, the long-dashed line is for $m_\nu = 0.5$ eV and the dot–dashed line corresponds to $m_\nu = 2$ eV.

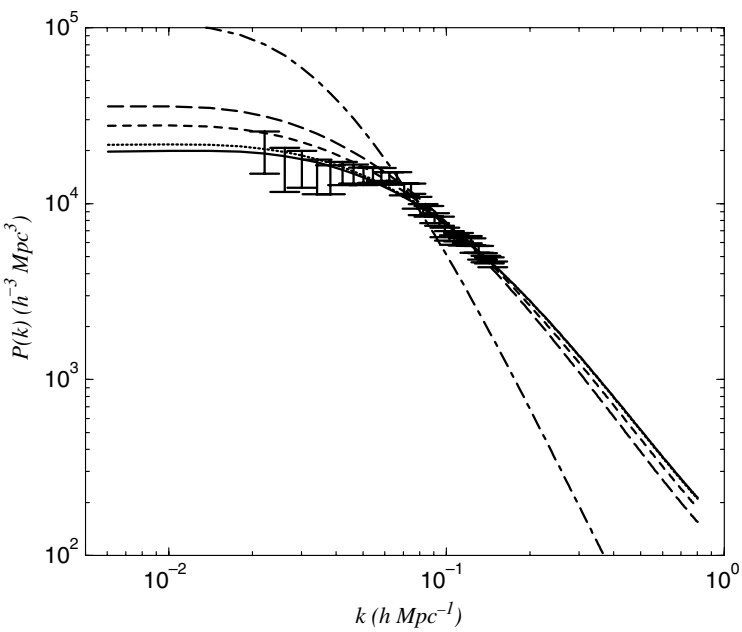

Figure 3. Power spectra for neutrino mass per flavour $m_\nu = 0$ (———), $m_\nu = 0.1$ (.....), $m_\nu = 0.3$ (- - - - -), $m_\nu = 0.5$ (– – – –), and $m_\nu = 3$ eV (– · – · –·). The other parameters are fixed at $\Omega_m = 0.3$, $\Omega_b = 0.04$ and $h = 0.7$. The vertical bars are the 2dFGRS power spectrum data points.

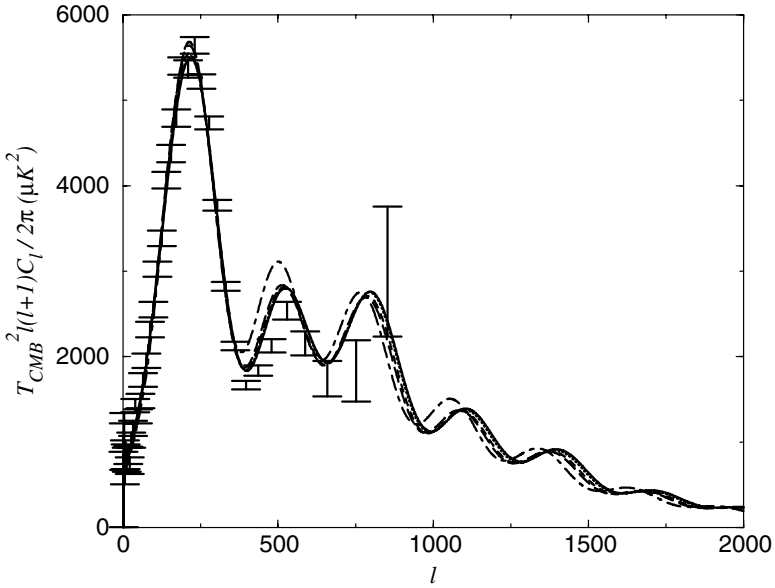

Figure 4. CMB power spectra for neutrino mass per flavour $m_\nu = 0$ (———), $m_\nu = 0.1$ (.....), $m_\nu = 0.3$ (- - - - -), $m_\nu = 0.5$ (– – – – –), and $m_\nu = 3$ eV (·–·–·–·–·). The other parameters are fixed at $\Omega_m = 0.3$, $\Omega_b = 0.04$ and $h = 0.7$. The vertical bars are the WMAP power spectrum data points.

3. Constraints from the CMB alone

Neutrino masses also give rise to effects in the CMB power spectrum. If their masses are smaller than the temperature at recombination, their effect is very similar to that of massless neutrinos [41]. For slightly larger masses, there is an enhancement of the acoustic peaks with respect to the massless case, as shown in figures 4 and 5. In figure 5, we show two cases, one (upper panel) where we fix $\Omega_m = \Omega_b + \Omega_c + \Omega_\nu = 0.3$, $\Omega_b = 0.04$, $\Omega_\Lambda = 0.7$ and $h = 0.7$. At the second (lower panel), we fix $\Omega_c = 0.26$, $\Omega_b = 0.04$ and $h = 0.7$, while keeping a flat universe $\Omega_b + \Omega_c + \Omega_\nu + \Omega_\Lambda = 1.0$. The purpose of this comparison is to check if the change caused by adding massive neutrinos is not just due to the decrease in the amount of cold dark matter. Indeed, we see that, qualitatively, the effect is the same in both cases and even somewhat larger when the amount of cold dark matter is held fixed. Note that, in this case, the position of the peaks will change slightly with Ω_ν since varying it now also implies changing Ω_Λ and hence the angular diameter distance to the last scattering surface. This effect is not obvious in the figure, since we plot the ratios of the angular power spectra.

From figure 4, it appears that the WMAP data alone should be sufficient to provide an upper limit on the neutrino masses. For example, in the case of fixed total $\Omega_m = 0.3$, we find that $\Delta\chi^2$, for the model with $m_\nu = 0.3$ compared with the reference model with $m_\nu = 0$, is larger than 40. However, note that all other parameters have been fixed in figures 4 and 5, and that there are severe degeneracies between m_ν and other parameters such as n and $\Omega_b h^2$. There are severe degeneracies between m_ν and other parameters like n and $\Omega_b h^2$. The full analysis of the WMAP data alone in [44] gave no upper limit on m_ν. On the other hand, Ichikawa *et al* [42] have claimed an upper limit of 2.0 eV from CMB alone, but emphasizing that one cannot improve the

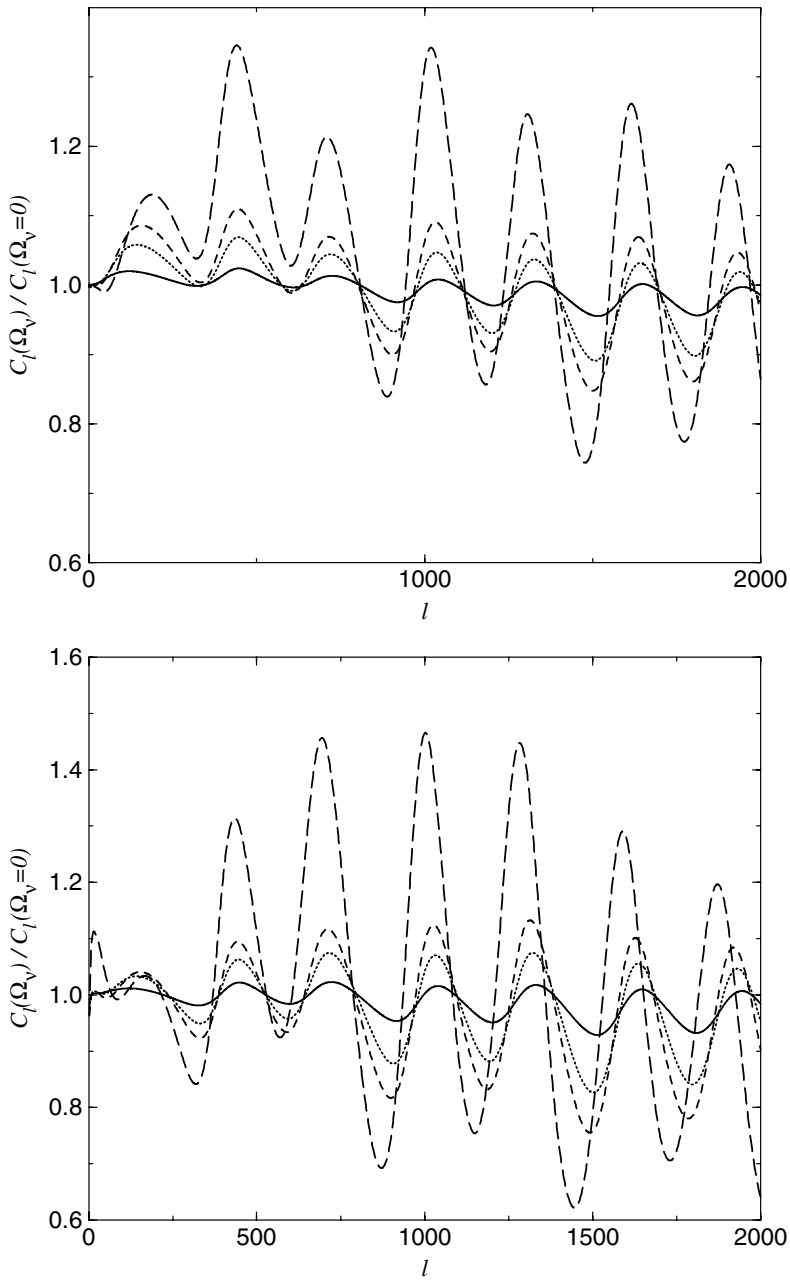

Figure 5. Top: the ratio of CMB angular power spectra for various values of Ω_ν to that for $\Omega_\nu = 0$. The other parameters are fixed at $\Omega_m = \Omega_b + \Omega_c + \Omega_\nu = 0.3$, $\Omega_b = 0.04$, $\Omega_\Lambda = 0.7$ and $h = 0.7$. The solid line is for neutrino mass per flavour $m_\nu = 0.1$ eV, the dotted line is for $m_\nu = 0.3$ eV, the dashed line is for $m_\nu = 0.5$ eV, and the long-dashed line corresponds to $m_\nu = 2$ eV. Bottom: the ratio of CMB angular power spectra for various values of Ω_ν to that for $\Omega_\nu = 0$. The other parameters are fixed at $\Omega_c = 0.26$, $\Omega_b = 0.04$, $h = 0.7$, while keeping a flat universe $\Omega_b + \Omega_c + \Omega_\nu + \Omega_\Lambda = 1.0$. The lines have the same meaning as in figure 4.

limit below 1.5 eV. The differences in the conclusions from various studies in the literature on neutrino masses from CMB alone might be due to the assumed priors over other cosmological parameters.

Analytic considerations in [42] provide insight into the effect of neutrinos on the CMB. A key point is to consider the redshift when neutrino mass becomes non-relativistic, $1 + z_{nr} = 6.24 \times 10^4 \Omega_\nu h^2$. For a recombination redshift $z_{rec} = 1088$, this means that neutrinos became non-relativistic before recombination $z_{nr} > z_{rec}$ if $\Omega_\nu h^2 > 0.017$ (i.e. a total neutrino mass $m_{\nu,\mathrm{tot}} > 1.6$ eV). In other words, if they are heavier than the above value, they act as matter and, if neutrinos are very light, they nearly behave like radiation. Indeed, as shown in [42], the dependence of the position of the first peak and the normalized height of the first peak on $\Omega_\nu h^2$ has a turning point at $\Omega_\nu h^2 \approx 0.017$. This value also affects CMB anisotropy via the modification of the integrated Sachs–Wolfe effect due to the massive neutrinos.

Future CMB missions like Planck (http://www.esa.int/science/planck) will provide high-resolution maps of the CMB temperature and polarization anisotropies. Gravitational lensing of these maps causes distortions, and Kaplinghat *et al* [43] have shown that this effect can be used to obtain very stringent limits on neutrino masses from the CMB alone. For Planck, they predict a sensitivity down to 0.15 eV, whereas a future experiment with higher resolution and sensitivity can possibly reach the lower bound ~0.06 eV set by the neutrino oscillation experiments.

4. Recent cosmological neutrino mass limits

In an important paper, Hu *et al* [45] showed that one could obtain useful upper limits on neutrino masses from a galaxy redshift survey of the size and quality of the Sloan Digital Sky Survey (SDSS). Based on a Fisher matrix analysis, their prediction was that the SDSS should be able to obtain a 2σ detection of N nearly degenerate massive neutrino species with mass

$$m_\nu \geqslant 0.65 \left(\frac{\Omega_\mathrm{m} h^2}{0.1N}\right)^{0.8} \mathrm{eV}, \tag{7}$$

which for $N = 3$, $\Omega_\mathrm{m} h^2 = 0.135$ predicts that a 95% confidence upper limit $m_{\nu,\mathrm{tot}} \leqslant 1.03$ eV should be obtainable.

As far as we know, the first cosmological neutrino mass limit after the detection of neutrino oscillations was derived by Croft *et al* [46]. Their main piece of data on large-scale structure was the matter power spectrum derived from the Lyman-α forest. Combining with two other measurements of the amplitude of matter fluctuations, the COBE normalization and σ_8, they obtained a 95% confidence upper limit of $m_{\nu,\mathrm{tot}} < 16.5$ eV, see table 1. Shortly thereafter, Fukugita *et al* [47] derived a stronger upper limit of 2.7 eV by combining the COBE normalization of the matter power spectrum with constraints on σ_8 from cluster abundances, using strong priors $\Omega_\mathrm{m} < 0.4$, $h < 0.8$ and $n = 1.0$. The first limit derived from a combined analysis of CMB and large-scale structure data was that of Wang *et al* [49]. They included the power spectrum of galaxies derived from the PSCz survey [50] and obtained an upper limit of 4.2 eV. Going down table 1, one notes a marked improvement in the constraints after the 2dFGRS power spectrum became available. After WMAP, there is a further tendency towards stronger upper limits, reflecting the dual role of the CMB and large-scale structure in constraining neutrino masses: the matter power spectrum is most sensitive to the ratio $\Omega_\nu/\Omega_\mathrm{m}$, but one needs good

Table 1. Upper limits on the total neutrino mass from recent CMB and large-scale structure studies.

Reference	CMB	LSS	Other data	$m_{\nu,\mathrm{tot}}$ upper limit (eV)
[46]	–	Lyα	COBE norm., $h = 0.72 \pm 0.08$, $\sigma_8 = 0.56\Omega_{\mathrm{m}}^{0.47}$	16.5
[47]	–	σ_8	$\Omega_{\mathrm{m}} < 0.4$, $\Omega_{\mathrm{b}}h^2 = 0.015$, $h < 0.8, n = 1.0$	2.7
[49]	Pre-WMAP	PSCz, Lyα	–	4.2
[51]	None	2dFGRS	BBN, SNIa, HST, $n = 1.0 \pm 0.1$	2.2
[52]	Pre-WMAP	2dFGRS	–	2.5
[53]	Pre-WMAP	2dFGRS	SNIa, BBN	0.9
[1]	WMAP + CBI + ACBAR	2dFGRS	Lyα	0.71
[24]	WMAP + Wang comp.	2dFGRS	HST, SNIa	1.01
[48]	WMAP + CBI + ACBAR	2dFGRS	X-ray	$0.56^{+0.30}_{-0.26}$
[44]	WMAP	SDSS	–	1.7
[54]	WMAP	2dFGRS + SDSS	–	0.75
[41]	WMAP + ACBAR	2dFGRS + SDSS	–	1.0
[55]	WMAP	SDSS	Bias	0.54
[47]	WMAP alone	–	–	2.0
[56]	WMAP	SDSS + Lyα	–	0.42

constraints on the other relevant cosmological parameters to break degeneracies in order to obtain low upper-mass limits. The limit will depend on the datasets and priors used in the analysis, but it seems like we are now converging to the precision envisaged in [45]. In [55], galaxy–galaxy lensing was utilized to extract information about the linear bias parameter in the SDSS, making a direct association between the galaxy and matter power spectra, and hence resulting in a stronger constraint on the neutrino mass than would have been possible using just the shape of the galaxy power spectrum. Finally, in [56], Lyman-α forest constraints were added to the datasets in [55], resulting in the very strong limit $m_{\nu,\mathrm{tot}} < 0.42$ eV at 95% confidence.

5. Other cosmological probes of neutrino masses

5.1. The clustering amplitude

Direct probes of the total matter distribution avoid the issue of bias and are therefore ideally suited for providing limits on the neutrino masses. Several ideas of how this can be done exist. In [47], the normalization of the matter power spectrum on large scales derived from COBE was combined with constraints on σ_8 from cluster abundances and a constraint $m_{\nu,\mathrm{tot}} < 2.7$ eV obtained, although with a fairly restricted parameter space. However, σ_8 is probably one of the most debated numbers in cosmology at the moment [57], and a better understanding of systematic uncertainties connected with the various methods for extracting it from observations is needed before this method can provide useful constraints. The potential of this method to push the value

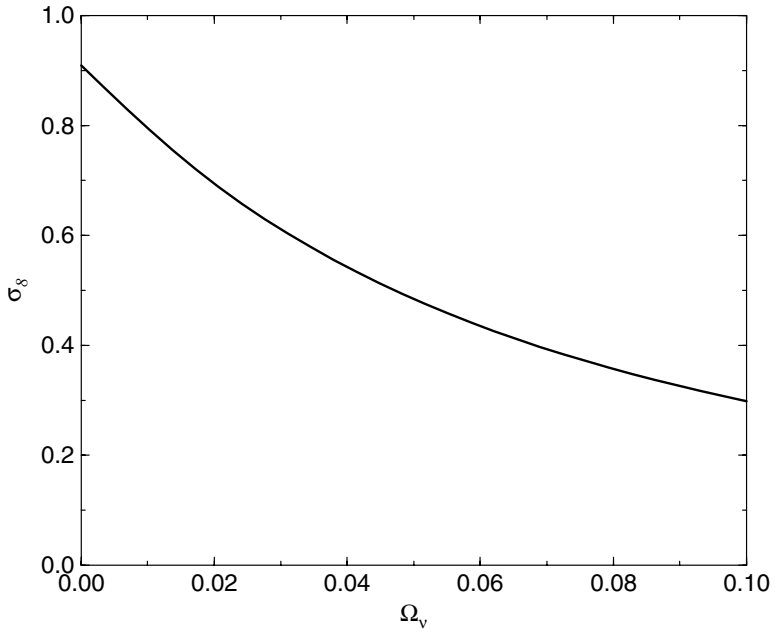

Figure 6. The clustering amplitude σ_8 as a function of Ω_ν for models with amplitude fitted to the WMAP data. Other parameters are fixed at 'concordance' values.

of the mass limit down also depends on the actual value of σ_8: the higher σ_8 turns out to be, the less room there will be for massive neutrinos. As an illustration, we show in figure 6 the value of σ_8 as a function of varying Ω_ν, with the remaining cosmological parameters fixed at their 'concordance' values. For a given value of m_ν, one fits the corresponding CMB power spectrum to the data. This in turn leads to a best-fit amplitude and a prediction for σ_8 for the given value of m_ν. If one then has an independent measurement of σ_8, one can infer the value of m_ν. In figure 6, the amplitude of the power spectrum has been fixed by fitting to the WMAP data. The claimed detection of a non-zero neutrino mass in [48] can be seen to be due to the use of the cluster x-ray luminosity function to constrain σ_8, giving $\sigma_8 = 0.69 \pm 0.04$ for $\Omega_\mathrm{m} = 0.3$ [58]. If a value of σ_8 at the higher end of the results reported in the literature is used instead, e.g. $\sigma_8 = 0.9$ for $\Omega_\mathrm{m} = 0.3$ from [59], one gets a very tight upper limit on m_ν, but no detection of $m_\nu > 0$. It is clearly important that systematic issues related to the various methods of obtaining σ_8 are settled. The evolution of cluster abundance with redshift may provide further constraints on neutrino masses [60].

5.2. The Lyman-α forest

Simulations support the picture that the matter density field is locally related to the optical depth for absorption of light emitted by quasars by the Lyman-α clouds. Hence the Lyman-α forest provides constraints on the matter power spectrum on scales of $k \sim 1h\,\mathrm{Mpc}^{-1}$, where the effect of massive neutrinos is most visible. It was used in [46] to derive a limit $m_{\nu,\mathrm{tot}} < 16.5\,\mathrm{eV}$. However, it is non-trivial to use the information contained in the Lyman-α forest data in cosmological parameter estimation [61]–[63]. Intriguingly, the upper limit on $m_{\nu,\mathrm{tot}}$ quoted in [1] with the

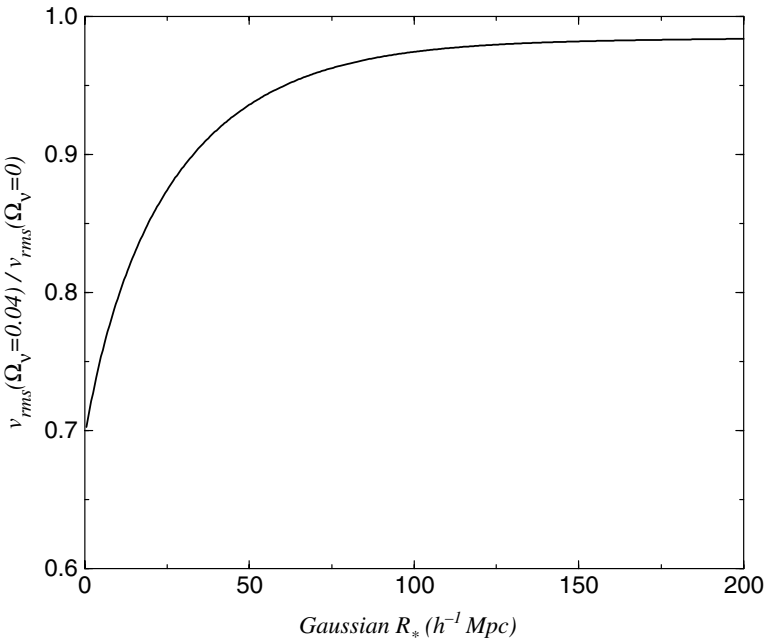

Figure 7. The ratio of the bulk flows in Gaussian spheres for two universes with the same primordial power spectra, same $\Omega_m = 0.3$; $\Omega_b = 0.04$; $h = 0.7$; $n = 1$ but different $\Omega_\nu = 0$ and 0.04.

Lyman-α forest data included is actually *weaker* than the one without. The strongest limit to date is, as mentioned in the section 5.1, the one derived by Seljak *et al* [56] by combining the power spectrum from the Lyman-α forest with SDSS data on galaxy clustering and galaxy–galaxy lensing and the WMAP CMB power spectrum. Such an upper limit $m_{\nu,\mathrm{tot}} < 0.42$ already gives a non-degenerate mass hierarchy.

5.3. Peculiar velocities

The rms bulk flow is predicted in linear theory as

$$\langle v^2(R_*)\rangle = (2\pi^2)^{-1} H_0^2 f^2(\Omega_m, \Omega_\Lambda) \int \mathrm{d}k P(k) W_G^2(kR_*), \tag{8}$$

where $W_G(kR_*)$ is a window function, e.g. $W(kR_*) = \exp(-k^2R_*^2/2)$ for a Gaussian sphere of radius R_*. The perturbations growth factor is $f(\Omega_m, \Omega_\Lambda) \approx \Omega_m^{0.6}$, and hence the peculiar velocity field is insensitive to the cosmological constant or dark energy (e.g. [64, 65]). If we parametrize the power spectrum as $P(k) \equiv Ak^nT^2(k)$, we can then consider two model universes with the same early universe primordial power spectrum Ak^n but different transfer functions $T(k)$ according to the contribution of the neutrinos. We define the total mass density parameter as $\Omega_m = \Omega_c + \Omega_b + \Omega_\nu$ due to the contributions of cold dark matter and neutrinos.

Figure 7 shows the ratio of the bulk flows in two universes with the same primordial power spectra, the same $\Omega_m = 0.3$; $\Omega_b = 0.04$; $h = 0.7$; $n = 1$ but different $\Omega_\nu = 0$ and 0.04. we can see the suppression of ~20% of the velocities on radii $R_* < 50h^{-1}$ Mpc due to the massive neutrinos.

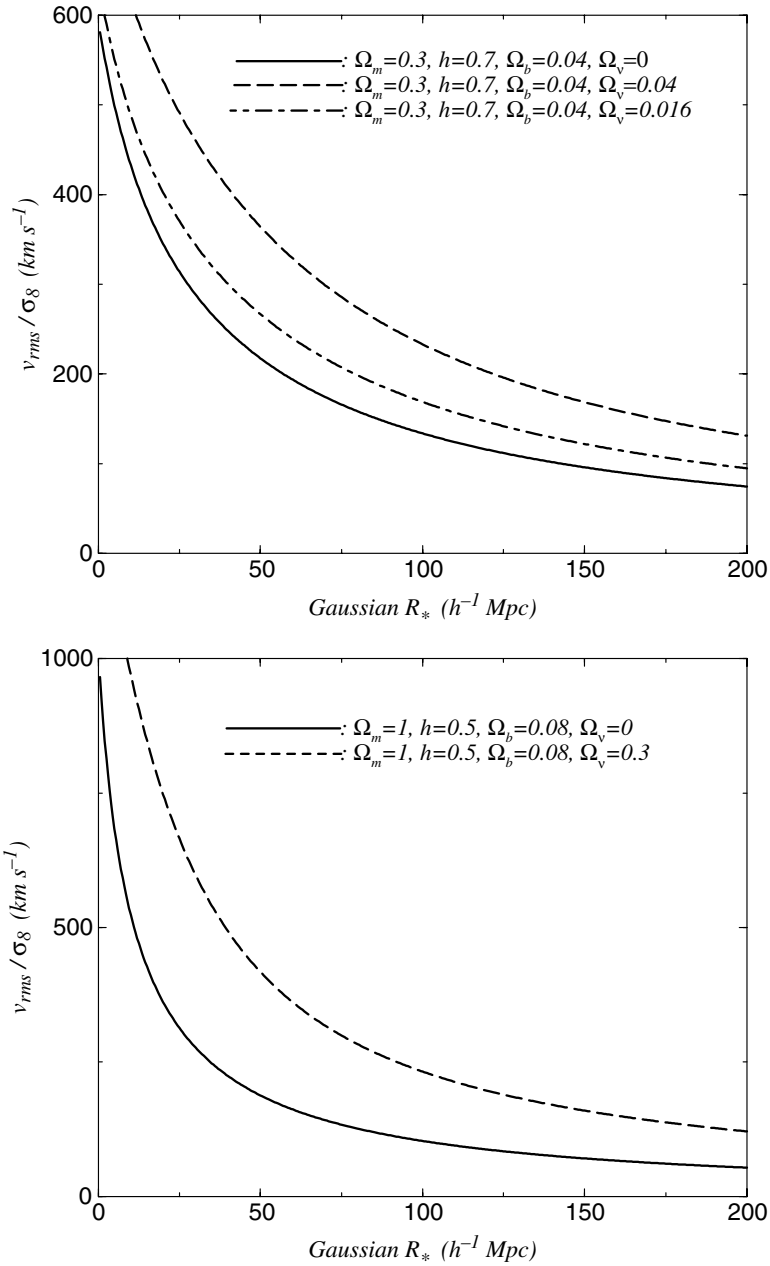

Figure 8. The effect of massive neutrinos on peculiar velocities in ΛCDM models (upper panel) and MDM models (lower panel).

If the power spectrum normalization σ_8 is known from another independent measurement, then the amplitude A itself is inversely proportional to an integral over the power spectrum as

$$\sigma_8^2 = (2\pi^2)^{-1} A \int \mathrm{d}k k^2 k^n T^2(k) W_{TH}^2(8k), \tag{9}$$

where W_{TH} is an $8h^{-1}$ Mpc radius spherical top-hat window function. One can then make predictions for the bulk flows v_{rms}/σ_8 in different models, as shown in figure 8. In part,

the significant differences for models with and without massive neutrinos are due to the σ_8 normalization procedure. While it is encouraging that the effect of massive neutrinos is significant for small scales, where peculiar velocities can be measured more accurately to nearby galaxies, we should be aware of complications due to non-linear effects and systematic errors.

5.4. Gravitational lensing

Deep and wide weak lensing surveys will in the future make it possible to perform a weak lensing tomography of the matter density field [66, 67]. By binning the galaxies in a deep and wide survey in redshift, one can probe the evolution of the gravitational potential. However, because massive neutrinos and dark energy have similar effects on this evolution, complementary information is required in order to break this degeneracy. Several studies of the potential of lensing tomography to constrain cosmological parameters, in particular dark energy and neutrino masses, have been carried out, see, e.g., [68] for an overview. Even when taking the uncertainties in the properties of dark energy into account, the combination of weak lensing tomography and high-precision CMB experiments may reach sensitivities down to the lower bound of 0.06 eV on the sum of the neutrino masses set by the current oscillation data [68].

6. Discussion

The significant increase in the amount and quality of CMB and large-scale structure data we have seen in cosmology in the last few years have made it possible to derive fairly stringent limits on the neutrino mass scale. Even though the CMB is less sensitive to neutrino masses compared with large-scale structure data, it plays a crucial role in breaking parameter degeneracies. With the WMAP and SDSS data, the upper limit has been pushed down to $\sim$1 eV for the total mass, assuming three massive neutrino species. Results from Lyman-α clouds combined with the WMAP and SDSS galaxy clustering data provide a tighter upper limit of $\sim$0.4 eV.

One point to bear in mind is that all these limits assume the 'concordance' ΛCDM model with adiabatic, scale-free primordial fluctuations. While the wealth of cosmological data strongly indicate that this is the consistent basic picture, one should keep in mind that cosmological neutrino mass limits are model-dependent and that there might still be surprises. For example, as the suppression of the power spectrum depends on the ratio $\Omega_\nu/\Omega_{\rm m}$, we found in [51] that the out-of-fashion mixed dark matter (MDM) model, with $\Omega_\nu = 0.2$, $\Omega_{\rm m} = 1$ and no cosmological constants, fits the 2dFGRS power spectrum well, but only for a Hubble constant $H_0 < 50\,{\rm km\,s^{-1}\,Mpc^{-1}}$. A similar conclusion was reached in [69], and they also found that the CMB power spectrum could be fitted well by the same MDM model if one allows features in the primordial power spectrum. Another consequence of this is that excluding low values of the Hubble constant, e.g. with the HST Key Project, is important in order to get a strong upper limit on the neutrino masses.

If the future observations live up to their promise, the prospects for pushing the cosmological neutrino mass limit down towards 0.1 eV are good. Then, as pointed out in [70], one may even start to see effects of the different mass hierarchies (normal or inverted), and thus one should take this into account when calculating CMB and matter power spectra. For example, with a non-degenerate mass hierarchy, one will get more than one free-streaming scale, and this will leave an imprint on the matter power spectrum. The coming years will see further comparison

between the effective neutrino mass in tritium β decay, the effective Majorana neutrino mass in neutrinoless double β decay and the sum of the neutrino masses from cosmology [71, 72]. It would be a great triumph for cosmology if the neutrino mass hierarchy were finally revealed by the distribution of large-scale structures in the Universe.

Acknowledgments

We thank S Bridle and M Fukugita for valuable discussions. ØE acknowledges support from the Research Council of Norway (grant no 159637/V30) and OL thanks PPARC for a Senior Research Fellowship.

References

[1] Spergel D N *et al* 2003 First Year Wilkinson Microwave Anisotropy Probe (WMAP) Observations: determination of cosmological parameters *Astrophys. J. Suppl. Ser.* **148** 175 (*Preprint* astro-ph/0302209)

[2] Tegmark M *et al* (the SDSS collaboration) 2004 Cosmological parameters from SDSS and WMAP *Phys. Rev.* D **69** 103501 (*Preprint* astro-ph/0310723)

[3] Abdurashitov J N *et al* 1999 Measurement of the solar neutrino capture rate with gallium metal *Phys. Rev.* C **60** 055801 (*Preprint* astro-ph/9907113)

[4] Ahmad Q R *et al* 2001 Measurement of the rate of $\nu_e + d \rightarrow p + p + e^-$ interactions produced by ^{8}B solar neutrinos at the Sudbury Neutrino Observatory *Phys. Rev. Lett.* **87** 071301 (*Preprint* nucl-ex/0106015)

[5] Ahmed S N *et al* (the SNO collaboration) 2004 Measurement of the total active ^{8}B solar neutrino flux at the Sudbury Neutrino Observatory with enhanced neutral current sensitivity *Phys. Rev. Lett.* **92** 181301 (*Preprint* nucl-ex/0309004)

[6] Ambrosia M *et al* 2001 Matter effects in upward-going muons and sterile neutrino oscillations *Phys. Lett.* B **517** 59 (*Preprint* hep-ex/0106049)

[7] Altmann M *et al* 2000 GNO solar neutrino observations: results for GNO I *Phys. Lett.* B **490** 16 (*Preprint* hep-ex/0006034)

[8] Cleveland B T *et al* 1998 Measurement of the solar electron neutrino flux with the homestake chlorine detector *Astrophys. J.* **496** 505

[9] Fukuda S *et al* 2000 Tau neutrinos favored over sterile neutrinos in atmospheric muon neutrino oscillations *Phys. Rev. Lett.* **85** 3999

[10] The Gallex Collaboration 1999 GALLEX solar neutrino observations: results for GALLEX IV *Phys. Lett.* B **447** 127

[11] The KamLAND Collaboration 2003 First results from KamLAND: evidence for reactor anti-neutrino disappearance *Phys. Rev. Lett.* **90** 021802 (*Preprint* hep-ex/0212021)

[12] The K2K Collaboration 2004 Evidence for muon neutrino oscillation in an accelerator-based experiment *Preprint* hep-ex/0411038

[13] The KamLAND Collaboration 2004 Measurement of neutrino oscillation with KamLAND: evidence of spectral distortion *Preprint* hep-ex/0406035

[14] Primack J R and Gross M A K 2000 Hot dark matter in cosmology *Current Aspects of Neutrino Physics* (Berlin: Springer) p 287 (*Preprint* astro-ph/0007165)

[15] Bonn J *et al* 2001 The Mainz neutrino mass experiment *Nucl. Phys. Proc. Suppl.* **91** 273

[16] Klapdor-Kleingrothaus H V *et al* 2001 Latest results from the HEIDELBERG-MOSCOW double beta decay experiment *Eur. Phys. J.* A **12** 147 (*Preprint* hep-ph/0103062)

[17] Klapdor-Kleingrothaus H V, Krivosheina I V, Dietz A and Chkvorets O 2004 Search for neutrinoless double beta decay with enriched ^{76}Ge in Gran Sasso 1990-2003 *Phys. Lett.* B **586** 198 (*Preprint* hep-ph/0404088)

[18] Eguchi K *et al* (the KamLAND Collaboration) 2003 First results from KamLAND: evidence for antineutrino disappearance *Phys. Rev. Lett.* **90** 021802 (*Preprint* hep-ex/0212021)
[19] Lunardini C and Smirnov A Y 2001 High-energy neutrino conversion and the lepton asymmetry in the universe *Phys. Rev.* D **64** 073006 (*Preprint* hep-ph/0012056)
[20] Dolgov A D, Hansen S H, Pastor S, Petcov S T, Raffelt G G and Semikoz D V 2002 Cosmological bounds on neutrino degeneracy improved by flavor oscillations *Nucl. Phys.* B **632** 363 (*Preprint* hep-ph/0201287)
[21] Wong Y Y Y 2002 Analytical treatment of neutrino asymmetry equilibration from flavor oscillations in the early universe *Phys. Rev.* D **66** 025015 (*Preprint* hep-ph/0203180)
[22] Abazajian K N, Beacom J F and Bell N F 2002 Stringent constraints on cosmological neutrino-antineutrino asymmetries from synchronized flavor transformation *Phys. Rev.* D **66** 013008 (*Preprint* astro-ph/0203442)
[23] Barger V, Kneller J P, Langacker P, Marfiata D and Steigman G 2003 Hiding relativistic degrees of freedom in the early universe *Phys. Lett.* B **569** 123 (*Preprint* hep-ph/0306061)
[24] Hannestad S 2003 Neutrino masses and the number of neutrino species from WMAP and 2dFGRS *J. Cosmol. Astropart. Phys.* JCAP05(2003)004 (*Preprint* astro-ph/0303076)
[25] Pierpaoli E 2003 Constraints on the cosmic neutrino background *Mon. Not. R. Astron. Soc.* **342** L63 (*Preprint* astro-ph/0302465)
[26] Abazajian K, Bell N F, Fuller G M and Wong Y Y Y 2004 Cosmological lepton asymmetry, primordial nucleosynthesis, and sterile neutrinos *Preprint* astro-ph/0410175
[27] Cirelli M, Marandella G, Strumia A and Vissani F 2004 Probing oscillations into sterile neutrinos with cosmology, astrophysics and experiments *Preprint* hep-ph/0403158
[28] Pakvasa S and Valle J W F 2004 Neutrino properties before and after KamLAND *Proc. Indian Natl Sci. Acad.* **70A** 189 (*Preprint* hep-ph/0301061)
[29] Aguilar A *et al* (the LSND Collaboration) 2001 Evidence for neutrino oscillations from the observation of $\overline{\nu}_e$ appearance in a $\overline{\nu}_\mu$ beam *Phys. Rev.* D **64** 112007 (*Preprint* hep-ex/0104049)
[30] Maltoni M, Schwetz T, Tórtola M A and Valle J W F 2002 Ruling out four-neutrino oscillation interpretations of the LSND anomaly? *Nucl. Phys.* B **643** 321 (*Preprint* hep-ph/0207157)
[31] Maltoni M, Schwetz T, Tórtola M A and Valle J W F 2003 Constraining neutrino oscillation parameters with current solar and atmospheric data *Phys. Rev.* D **67** 013011 (*Preprint* hep-ph/02072276)
[32] Bazarko A *et al* (the MiniBooNE collaboration) 2000 MiniBooNE: status of the booster neutrino experiment *Nucl. Phys. B. Proc. Suppl.* **91** 210 (*Preprint* hep-ex/0009056)
[33] Beacom J F, Bell N F and Dodelson S 2004 Neutrinoless universe *Phys. Rev. Lett.* **93** 121302 (*Preprint* astro-ph/0404585)
[34] Hannestad S 2004 Structure formation with strongly interacting neutrinos—implications for the cosmological neutrino mass bound *Preprint* astro-ph/0411475
[35] Eisenstein D J and Hu W 1999 Power spectra for cold dark matter and its variants *Astrophys. J.* **511** 5 (*Preprint* astro-ph/9710252)
[36] Seljak U and Zaldarriaga M 1996 A line-of-sight integration approach to cosmic microwave background anisotropies *Astrophys. J.* **469** 437 (*Preprint* astro-ph/9603033)
[37] Lewis A, Challinor A and Lasenby A 2000 Efficient computation of cosmic microwave background anisotropies in closed Friedmann–Robertson–Walker models *Astrophys. J.* **538** 473 (*Preprint* astro-ph/9911177)
[38] Percival W J *et al* (the 2dFGRS Team) 2001 The 2dF Galaxy Redshift Survey: the power spectrum and the matter content of the universe *Mon. Not. R. Astron. Soc.* **327** 1297 (*Preprint* astro-ph/0105252)
[39] Elgarøy Ø and Lahav O 2003 Upper limits on neutrino masses from the 2dFGRS and WMAP: the role of priors *J. Cosmol. Astropart. Phys.* JCAP04(2003)004 (*Preprint* astro-ph/0303089)
[40] Bond J R, Efstathiou G and Silk J 1980 Massive neutrinos and the large-scale structure of the universe *Phys. Rev. Lett.* **45** 1980
[41] Crotty P, Lesgourgues J and Pastor S 2004 Current cosmological bounds on neutrino masses and relativistic relics *Phys. Rev.* D **69** 123007 (*Preprint* hep-ph/0402049)
[42] Ichikawa K, Fukugita M and Kawasaki M 2004 *Preprint* astro-ph/0410166

[43] Kaplinghat M, Knox L and Song Y-S 2003 Determining neutrino mass from the cosmic microwave background alone *Phys. Rev. Lett.* **91** 241301 (*Preprint* astro-ph/0303344)

[44] Tegmark M *et al* 2003 Cosmological parameters from SDSS and WMAP *Phys. Rev.* D **69** 103501 (*Preprint* astro-ph/0310723)

[45] Hu W, Eisenstein D and Tegmark M 1998 Weighing neutrinos with galaxy surveys *Phys. Rev. Lett.* **80** 5255 (*Preprint* astro-ph/9712057)

[46] Croft R A C, Hu W and Davé R 1999 Cosmological limits on the neutrino mass from the LyAlpha forest *Phys. Rev. Lett.* **83** 1092 (*Preprint* astro-ph/9903335)

[47] Fukugita M, Liu G-C and Sugiyama N 2000 Limits on neutrino mass from cosmic structure formation *Phys. Rev. Lett.* **84** 1082 (*Preprint* astro-ph/9908450)

[48] Allen S W, Schmidt R W and Bridle S L 2003 A preference for a non-zero neutrino mass from cosmological data *Mon. Not. R. Acad. Soc.* **346** 593 (*Preprint* astro-ph/0306386)

[49] Wang X, Tegmark M and Zaldarriaga M 2002 Is cosmology consistent? *Phys. Rev.* D **65** 123001 *Preprint* astro-ph/0105091)

[50] Hamilton A J S, Tegmark M and Padmanabhan N 2000 Linear redshift distortions and power in the PSCz survey *Mon. Not. R. Astron. Soc.* **317** L23 (*Preprint* astro-ph/0004334)

[51] Elgarøy Ø *et al* (the 2dFGRS Team) 2002 New upper limit on the total neutrino mass from the 2 degree Field Galaxy Redshift Survey *Phys. Rev. Lett.* **89** 061301 (*Preprint* astro-ph/0204152)

[52] Hannestad S 2002 Cosmological limit on the neutrino mass *Phys. Rev.* D **66** 125011 (*Preprint* astro-ph/0205223)

[53] Lewis A and Bridle S L 2002 Cosmological parameters from CMB and other data: a Monte Carlo approach *Phys. Rev.* D **66** 103511 (*Preprint* astro-ph/0205436)

[54] Barger V, Marfiata D and Tregre A 2003 Neutrino mass limits from SDSS, 2dFGRS and WMAP *Preprint* hep-ph/0312065

[55] Seljak U *et al* 2004 SDSS galaxy bias from halo mass-bias relation and its cosmological implications *Preprint* astro-ph/0406594

[56] Seljak U *et al* 2004 Cosmological parameter analysis including SDSS Lyα forest and galaxy bias: constraints on the primordial spectrum of fluctuations, neutrino mass, and dark energy *Preprint* astro-ph/0407372

[57] Wang X, Tegmark M, Jain B and Zaldarriaga M 2003 The last stand before MAP: cosmological parameters from lensing, CMB and galaxy clustering *Phys. Rev.* D **68** 123001 (*Preprint* astro-ph/0212417)

[58] Allen S W, Schmidt R W, Fabian A C and Ebeling H 2003 Cosmological constraints from the local X-ray luminosity function of the most X-ray luminous galaxy clusters *Mon. Not. R. Astron. Soc.* **342** 287 (*Preprint* astro-ph/0208394)

[59] Bahcall N A and Bode P 2003 The amplitude of mass fluctuations *Astrophys. J.* **588** L1 (*Preprint* astro-ph/0212363)

[60] Arhipova N A, Kahniashvili T and Lukash V N 2002 Abundance and evolution of galaxy clusters in cosmological models with massive neutrino *Astron. Astrophys.* **386** 775 (*Preprint* astro-ph/0110426)

[61] Seljak U, McDonald P and Makarov A 2003 Cosmological constraints from the CMB and Ly-alpha forest revisited *Mon. Not. R. Astron. Soc.* **342** L79 (*Preprint* astro-ph/0302571)

[62] Viel M, Haehnelt M G and Springel V 2004 Inferring the dark matter power spectrum from the Lyman-α forest in high-resolution QSO absorption spectra *Mon. Not. R. Astron. Soc.* **354** 654 (*Preprint* astro-ph/0404600)

[63] Viel M, Weller J and Haehnelt M G 2004 Constraints on the primordial power spectrum from high resolution Lyman-α forest spectra and WMAP *Preprint* astro-ph/0407294

[64] Lahav O, Lilje P B, Primack J R and Rees M J 1991 Dynamical effects of the cosmological constant *Mon. Not. R. Astron. Soc.* **251** 128

[65] Wang L and Steinhardt P J 1998 Cluster abundance constraints for cosmological models with a time-varying, spatially inhomogeneous energy component with negative pressure *Astrophys. J.* **508** 483 (*Preprint* astro-ph/9804015)

[66] Hu W 1999 Power spectrum tomography with weak lensing *Astrophys. J.* **522** 21 (*Preprint* astro-ph/9904152)

[67] Hu W 2002 Dark energy and matter evolution from lensing tomography *Phys. Rev.* D **66** 083515 (*Preprint* astro-ph/0208093)

[68] Song Y-S and Knox L 2004 Determination of cosmological parameters from cosmic shear data *Phys. Rev.* D **70** 063510 (*Preprint* astro-ph/0312175)

[69] Blanchard A, Douspis M, Rowan-Robinson M and Sarkar S 2003 An alternative to the cosmological 'concordance model' *Astron. Astrophys.* **412** 35 (*Preprint* astro-ph/0304237)

[70] Lesgourgues J, Pastor S and Perotto L 2004 Probing neutrino masses with future galaxy redshift surveys *Phys. Rev.* D **70** 045016 (*Preprint* astro-ph/0403296)

[71] Fogli G L *et al* 2004 *Preprint* hep-ph/0408045

[72] Zuber K 2004 *Neutrino Physics* (Bristol: Institute of Physics Publishing)

New Journal of Physics
The open-access journal for physics

Leptonic CP violation and neutrino mass models

Gustavo C Branco and M N Rebelo

Departamento de Física and Centro de Física Teórica de Partículas (CFTP), Instituto Superior Técnico, Av. Rovisco Pais, 1049-001 Lisboa, Portugal
E-mail: gbranco@cftp.ist.utl.pt and rebelo@ist.utl.pt

New Journal of Physics **7** (2005) 86
Received 25 October 2004
Published 1 April 2005
Online at http://www.njp.org/
doi:10.1088/1367-2630/7/1/086

Abstract. We discuss leptonic mixing and CP violation at low and high energies, emphasizing possible connections between leptogenesis and CP violation at low energies, in the context of lepton flavour models. Furthermore, we analyse weak-basis invariants relevant for leptogenesis and for CP violation at low energies. These invariants have the advantage of providing a simple test of the CP properties of any lepton flavour model.

Contents

1. Introduction **2**
2. Neutrino mass terms **3**
2.1. The general case 4
2.2. The case of minimal see-saw 6
3. WB invariants and CP violation **9**
3.1. WB invariants relevant for CP violation at low energies 9
3.2. WB invariants relevant for leptogenesis 11
4. The case of degenerate neutrinos **13**
5. On the relation between low-energy CP violation and CP violation required for leptogenesis **15**
5.1. A brief summary of low-energy data 15
5.2. On the need for a lepton flavour symmetry 16
5.3. Towards a minimal scenario 17
6. Summary and conclusions **18**
Acknowledgments **19**
References **19**

PII: S1367-2630(05)88446-0
© IOP Publishing Ltd and Deutsche Physikalische Gesellschaft

1. Introduction

The experimental data on atmospheric and solar neutrinos have provided evidence for non-vanishing neutrino masses and for non-trivial leptonic mixing [1]. These important discoveries rendered even more pressing the fundamental question of understanding the spectrum of fermion masses and the pattern of their mixing. In the Standard Model (SM) neutrinos are strictly massless. No Dirac mass terms can arise in the SM due to the absence of right-handed (rh) neutrinos and no left-handed (lh) Majorana masses can be generated at tree level due to the simple Higgs structure of the SM. Furthermore, no Majorana masses can be generated in higher orders due to the exact B–L conservation. Therefore, the discovery of neutrino masses and leptonic mixing provides clear evidence for physics beyond the SM.

It is remarkable that a simple extension of the SM, through the introduction of rh neutrinos, leads to non-vanishing but naturally small neutrino masses. With the addition of rh neutrinos to the SM, the most general Lagrangian consistent with renormalizability and gauge invariance leads to both Dirac and rh Majorana neutrino mass terms. The natural scale for the Dirac neutrino masses is v, the scale of electroweak symmetry breaking. On the other hand, since the rh neutrinos transform trivially under $\mathrm{SU}(2) \times \mathrm{U}(1)$, the rh Majorana mass term is gauge invariant and as a result its scale V can be much larger, being identified with the scale of lepton number violation. In the context of grand unified theories (GUT) this scale can be naturally taken as the GUT scale. The presence of both Majorana and Dirac masses of the above indicated order of magnitude, automatically leads to light neutrinos with masses of order v^2/V, through the see-saw mechanism [2]. Strictly speaking, in order to have naturally small neutrino masses it is not necessary to introduce rh neutrinos, one may have only lh neutrinos, provided lepton number violation occurs at a high-energy scale. The introduction of rh neutrinos is well motivated in the framework of some GUT theories like S0(10) and it has the special appeal of establishing a possible connection between neutrinos and the generation of the baryon asymmetry of the universe (BAU). In fact, one of the most attractive mechanisms to generate BAU is baryogenesis through leptogenesis [3], a scenario where the out-of-equilibrium decays of heavy rh neutrinos create a lepton asymmetry which is later converted into a baryon asymmetry by B + L violating (but B–L conserving) sphaleron interactions [4].

It is well known [5] that pure gauge theories do not violate CP. In fact, the fermionic sector (kinetic energy terms and fermion interactions with vector bosons) as well as the vector boson sector of gauge theories are always CP symmetric. The same is true for the couplings of scalars with gauge fields. In the SM, CP violation in the quark sector arises from the simultaneous presence of charged current gauge interactions and complex Yukawa couplings [6]. In general, for three or more generations there is no CP transformation which leaves invariant both the Yukawa couplings and the charged current gauge interactions. This leads to the well-known Kobayashi–Maskawa mechanism [7] of CP violation operating in the quark sector. In the leptonic sector and in the context of the SM, there is no CP violation since for massless neutrinos leptonic mixing in the charged currents can always be rotated away through a redefinition of neutrino fields. In any extension of the SM with non-vanishing neutrino masses and mixing, there is in general leptonic CP violation. In the case of an extension of the SM consisting of the addition of three rh neutrinos, one has in general both leptonic CP violation at low energies, visible for example through neutrino oscillations and CP violation at high energies relevant for the generation of baryogenesis through leptogenesis.

In this paper, we review leptonic mixing and CP violation at low and high energies, with emphasis on the possible connection between leptogenesis and low-energy data as well as on the analysis of weak-basis (WB) invariants relevant for CP violation. In fact, by writing the most general CP transformation for the fermion fields in a WB one can derive simple conditions for CP conservation which can be applied without going to the physical basis. This strategy was followed for the first time in the context of the SM in [8]. These invariants provide a simple way of testing whether a specific lepton flavour model [9] leads to CP violation either at low or high energies. The crucial advantage of these invariants stems from the fact that for any lepton flavour model, they can be calculated in any WB, without requiring cumbersome changes of basis. The paper is organized as follows. In section 2, we establish our notation introducing the various leptonic mass terms, derive necessary conditions for CP invariance and identify the independent CP violating phases, both in a WB and in the mass eigenstate basis. In section 3, we derive WB invariants which are relevant for CP violation at low energies, as well as WB invariants sensitive to CP violation at high energies relevant for leptogenesis. In section 4, we analyse the special limit of exactly degenerate neutrino masses. The relationship between low-energy CP violation and CP violation at high energies is discussed in section 5. Finally, in section 6, we present our summary and conclusions.

2. Neutrino mass terms

We consider a simple extension of the SM where three rh neutrinos (one per generation) are introduced. In this case, the most general form for the leptonic mass terms after spontaneous symmetry breaking is

$$\begin{aligned}\mathcal{L}_m &= -[\tfrac{1}{2}\nu_L^{0T} C m_L \nu_L^0 + \overline{\nu_L^0} m_D \nu_R^0 + \tfrac{1}{2}\nu_R^{0T} C M_R \nu_R^0 + \overline{l_L^0} m_l l_R^0] + \text{h.c.} \\ &= -[\tfrac{1}{2} n_L^T C \mathcal{M}^* n_L + \overline{l_L^0} m_l l_R^0] + \text{h.c.},\end{aligned} \tag{1}$$

where m_L, M_R, denote the lh and rh neutrino Majorana mass matrices, while m_D, m_l stand for the neutrino Dirac mass matrix and the charged lepton mass matrix, respectively. The generation at tree level of a mass term of the form $\nu_L^{0T} C m_L \nu_L^0$ also requires the extension of the Higgs sector (e.g., a Higgs triplet). The introduction of the column vector $n_L = (\nu_L^0, (\nu_R^0)^c)$ allows one to write $\mathcal{L}_m$ in a more compact form, with the 6×6 matrix $\mathcal{M}$ given by

$$\mathcal{M} = \begin{pmatrix} m_L^* & m_D \\ m_D^T & M_R \end{pmatrix}. \tag{2}$$

The mass terms in $\mathcal{L}_m$ contain all the information on CP violation arising from the charged gauge interactions, irrespective of the mechanism which generates the lepton mass terms and will be analysed in the next subsection. An enlarged Higgs sector will in general provide new sources of CP violation which we do not discuss in this work. In fact most of our analysis will be done in the framework of the minimal Higgs structure (no Higgs triplets), thus implying that the term m_L in equation (1) is absent. The corresponding matrix $\mathcal{M}$ has then a zero block entry in its upper left block.

For simplicity, in most of our discussions in this paper, we will consider that the number of rh neutrinos equals the number of lh neutrinos. It should be pointed out that this is not required for the generation of appropriate neutrino masses.

2.1. The general case

In this subsection, we study leptonic CP violation in the case corresponding to the most general mass terms given by equation (1). There are two aspects in which leptonic CP non-conservation differs from CP violation in the quark sector. One aspect has to do with the fact that being neutral, neutrinos can have both Majorana and Dirac mass terms. The other one results from the fact that the full leptonic mixing matrix appearing in the charged currents is a 3×6 matrix, consisting of the first three lines of a 6×6 unitary matrix. Of course, in the low-energy limit, where only the light neutrinos are active, the leptonic mixing is described by a 3×3 unitary matrix. For the analysis of leptonic mixing and CP violation mediated through the charged gauge bosons the relevant part of the Lagrangian is $\mathcal{L}_m$ given by equation (1) together with the charged gauge interaction

$$\mathcal{L}_W = -\frac{g}{\sqrt{2}} W_\mu^+ \overline{l_L^0} \gamma^\mu \nu_L^0 + \text{h.c.} \tag{3}$$

The simplest way of determining the number of independent CP violating phases [10] is by working in a conveniently chosen WB and analysing the restrictions on the Lagrangian implied by CP invariance. We follow this approach, but also identify the CP violating phases appearing in the charged weak interactions, written in the mass eigenstate basis.

The most general CP transformation which leaves the gauge interaction invariant is

$$\begin{aligned} &\mathrm{CP} l_L^0 (\mathrm{CP})^\dagger = U' \gamma^0 C \overline{l_L^0}^T, \qquad \mathrm{CP} l_R^0 (\mathrm{CP})^\dagger = V' \gamma^0 C \overline{l_R^0}^T, \qquad \mathrm{CP} \nu_L^0 (\mathrm{CP})^\dagger = U' \gamma^0 C \overline{\nu_L^0}^T, \\ &\mathrm{CP} \nu_R^0 (\mathrm{CP})^\dagger = W' \gamma^0 C \overline{\nu_R^0}^T, \qquad \mathrm{CP} W_\mu^+ (\mathrm{CP})^\dagger = -(-1)^{\delta_{0\mu}} W_\mu^-, \end{aligned} \tag{4}$$

where U', V' and W' are unitary matrices acting in the flavour space. This transformation combines the CP transformation of a single fermion field with a WB transformation [11]. Invariance of the mass terms under the above CP transformation, requires that the following relations have to be satisfied:

$$U'^{\mathrm{T}} m_L U' = -m_L^*, \tag{5}$$

$$W'^{\mathrm{T}} M_R W' = -M_R^*, \tag{6}$$

$$U'^\dagger m_D W' = m_D{}^*, \tag{7}$$

$$U'^\dagger m_l V' = m_l{}^*. \tag{8}$$

It can be easily seen that if there are unitary matrices U', V', W' satisfying equations (5)–(8) in one particular WB, then a solution exists for any other WB. In order to analyse the implications of the above conditions, it is convenient to choose the WB, where both m_L and M_R are real diagonal. In this WB and assuming the eigenvalues of m_L and M_R to be all non-zero and non-degenerate, equations (5) and (6) constrain U' and W' to be of the form

$$U' = \mathrm{diag}\,(\exp(\mathrm{i}\alpha_1), \exp(\mathrm{i}\alpha_2), \ldots \exp(\mathrm{i}\alpha_n)), \tag{9}$$

$$W' = \mathrm{diag}\,(\exp(\mathrm{i}\beta_1), \exp(\mathrm{i}\beta_2), \ldots \exp(\mathrm{i}\beta_n)), \tag{10}$$

where n denotes the number of generations. Here, we are assuming, for simplicity that there is an equal number of fields ν_L^0 and ν_R^0. The phases α_i and β_i have to satisfy

$$\alpha_i = (2p_i + 1)\frac{\pi}{2}, \qquad \beta_i = (2q_i + 1)\frac{\pi}{2} \tag{11}$$

with p_i, q_i integer numbers. Then equations (7) and (8) constrain m_D and $m_l m_l^\dagger \equiv h_l$ in the following way:

$$\text{phase}(m_D)_{ij} = (p_i - q_j)\frac{\pi}{2}, \tag{12}$$

$$\text{phase}(h_l)_{ij} = (p_i - q_j)\frac{\pi}{2}. \tag{13}$$

As a result, CP invariance restricts all the phases of m_D and h_l to be either zero or $\pm\pi/2$. Since in general m_D is an arbitrary $n \times n$ complex matrix whilst h_l is an arbitrary $n \times n$ Hermitian matrix the number of independent CP restrictions is

$$N_g = n^2 + \frac{n(n-1)}{2}. \tag{14}$$

For three generations $N_g = 12$. It is clear that if the number of rh fields were n' rather than n, the matrix m_D would have dimension $n \times n'$ and N_g would be given by

$$N_g' = nn' + \frac{n(n-1)}{2}. \tag{15}$$

It can be checked that this number of CP restrictions coincides with the number of CP violating phases which arise in the leptonic mixing matrix of the charged weak current after all leptonic masses have been diagonalized. Let us now choose the WB such that m_l is already diagonal, real and positive. The diagonalization of the $2n \times 2n$ matrix $\mathcal{M}$, which in general is given by equation (2), is performed via the unitary transformation

$$V^{\mathrm{T}}\mathcal{M}^* V = \mathcal{D}, \tag{16}$$

for $\mathcal{D} = \text{diag}\,(m_{\nu_1}, m_{\nu_2}, m_{\nu_3}, M_{\nu_1}, M_{\nu_2}, M_{\nu_3})$, with m_{ν_i} and M_{ν_i} denoting the physical masses of the light and heavy Majorana neutrinos, respectively. It is convenient to write V and $\mathcal{D}$ in the following block form:

$$V = \begin{pmatrix} K & R \\ S & T \end{pmatrix}, \tag{17}$$

$$\mathcal{D} = \begin{pmatrix} d & 0 \\ 0 & D \end{pmatrix}. \tag{18}$$

The neutrino weak-eigenstates are related to the mass eigenstates by

$$\nu_{i\,L}^0 = V_{i\alpha}\nu_{\alpha L} = (K, R)\begin{pmatrix} \nu_{iL} \\ N_{iL} \end{pmatrix} \quad \begin{pmatrix} i = 1, 2, 3 \\ \alpha = 1, 2, \ldots 6 \end{pmatrix} \tag{19}$$

and thus the leptonic charged current interactions are given by

$$\mathcal{L}_W = -\frac{g}{\sqrt{2}}(\overline{l_{iL}}\gamma_\mu K_{ij}\nu_{jL} + \overline{l_{iL}}\gamma_\mu R_{ij}N_{jL})W^\mu + \text{h.c.} \tag{20}$$

with K and R being the charged current couplings of charged leptons to the light neutrinos ν_j and to the heavy neutrinos N_j, respectively. From equation (17), we see that K and R correspond to the first n rows of the $2n \times 2n$ unitary matrix V which diagonalizes the full neutrino mass matrix $\mathcal{M}^*$. The most general $n \times 2n$ leptonic mixing matrix can then be exactly parametrized by the first n rows of a $2n \times 2n$ unitary matrix provided that it is chosen in such a way that a minimal number of phases appears in these first n rows. This is the case of the parametrization proposed in [12]. Its particularization for a 6×6 matrix is given by

$$V = \hat{V}P, \tag{21}$$

where $P = \text{diag}\,(1, \exp(\mathrm{i}\sigma_1), \exp(\mathrm{i}\sigma_2), \ldots, \exp(\mathrm{i}\sigma_5))$ and $\hat{V}$ is given by

$$\hat{V} = O_{56}I_6(\delta_{10})O_{45}O_{46}I_5(\delta_9)I_6(\delta_8)\left(\prod_{j=4}^{6} O_{3j}\right)I_4(\delta_7)I_5(\delta_6)I_6(\delta_5)$$
$$\times\left(\prod_{j=3}^{6} O_{2j}\right)I_3(\delta_4)I_4(\delta_3)I_5(\delta_2)I_6(\delta_1)\left(\prod_{j=2}^{6} O_{1j}\right), \tag{22}$$

where O_{ij} are orthogonal matrices mixing the ith and jth generation and $I_j(\delta_k)$ are unitary diagonal matrices of the form

$$I_j(\delta_k) = \begin{pmatrix} 1 & & & & & \\ & \cdot & & & & \\ & & 1 & & & \\ & & & e^{i\delta_k} & & \\ & & & & 1 & \\ & & & & & \cdot \\ & & & & & & 1 \end{pmatrix} \leftarrow j. \tag{23}$$

This parametrization is particularly useful, for instance, in models with vectorial quarks [13]. It can be readily verified that the first three rows of $\hat{V}$, contain seven phases. The Majorana character of the physical neutrinos does not allow for the five phases in P to be rotated away and we are finally left with 12 phases in the mixing matrix (K, R). The generalization to $n + n'$ dimensional unitary matrices leads to $\frac{1}{2}(n-1)(n-2+2n')$ phases in the first n rows of $\hat{V}$ [13] which, together with the $(n + n' - 1)$ phases that cannot be rotated away, adds up to $nn' + \frac{n(n-1)}{2}$ thus coinciding with the general result obtained in equation (15).

2.2. The case of minimal see-saw

The minimal see-saw case corresponds to $\mathcal{L}_m$ with no lh Majorana mass terms included, together with the assumption that the bare rh Majorana mass terms are much larger than the weak scale.

From equations (2), (16), (17) and (18), with $m_L = 0$, one obtains

$$S^\dagger m_D^T K^* + K^\dagger m_D S^* + S^\dagger M_R S^* = d, \tag{24}$$

$$S^\dagger m_D^T R^* + K^\dagger m_D T^* + S^\dagger M_R T^* = 0, \tag{25}$$

$$T^\dagger m_D^T R^* + R^\dagger m_D T^* + T^\dagger M_R T^* = D. \tag{26}$$

We assume, as before, that we are already in a WB where m_l is real and diagonal. These equations allow us to derive the following relations which hold to an excellent approximation:

$$S^\dagger = -K^\dagger m_D M_R^{-1}, \tag{27}$$

$$-K^\dagger m_D \frac{1}{M_R} m_D^T K^* = d. \tag{28}$$

It is clear from equation (27) that S is of order m_D/M_R and therefore is very suppressed. Equation (28) is the usual see-saw formula with the matrix K frequently denoted by V_{PMNS}, the Pontecorvo, Maki, Nakagawa and Sakata matrix [14]. Although the block K in equation (17) is not a unitary matrix its deviations from unitarity are of the order m_D^2/M_R^2. It is from equation (28) that the low-energy physics of the leptonic sector is derived. The decoupling limit corresponds to an effective theory with only lh neutrinos and a Majorana mass matrix, m_{eff} defined as

$$m_{eff} = -m_D \frac{1}{M_R} m_D^T, \tag{29}$$

showing that for m_D of the order of the electroweak scale and M_R of the scale of grand unification, the smallness of light neutrino masses is a natural consequence of the see-saw mechanism [2]. From the relation $\mathcal{M}^* V = V^* \mathcal{D}$ and taking into account the zero entry in $\mathcal{M}$, one derives the following exact relation:

$$R = m_D T^* D^{-1}. \tag{30}$$

This equation plays an important role in the connection between low- and high-energy physics in the leptonic sector. If we choose to work in a WB where both m_l and M_R are diagonal, equation (26) shows that $T = 1$ up to corrections of order m_D^2/M_R^2, leading to an excellent approximation to

$$R = m_D D^{-1}. \tag{31}$$

The matrices K and R are again the charged current couplings. The counting of the number of physical CP violating phases can be done in various ways [15]–[17]. The simplest approach [17] is by choosing a WB where M_R and m_l are simultaneously real and diagonal. From the CP transformations given by equation (4), we now obtain conditions of equations (6), (7) and (8). Once again, equation (6) constrains the matrix W' to be of the form of equation (10) with β_i given by equation (11). Multiplying equation (8) by its Hermitian conjugate, with m_l real and diagonal, one concludes that U' has to be of the form of equation (9), where in this case the α_i are

arbitrary phases. From equations (7), (10) and (9) it follows then that CP invariance constrains the matrix m_D to satisfy

$$\arg(m_D)_{ij} = \tfrac{1}{2}(\alpha_i - \beta_j). \tag{32}$$

Note that the β_i are fixed up to discrete ambiguities whilst the α_i are free. Therefore, CP invariance constrains the matrix m_D to have only n free phases α_i. Since m_D is an arbitrary matrix, with n^2 independent phases, it is clear that the number of independent CP restrictions is given by:

$$N_m = n^2 - n. \tag{33}$$

In the minimal see-saw model, for three generations, there are six CP violating phases instead of the 12 of the general case. The decrease in the number of independent phases is to be expected since in this case m_L, which in general is a complex symmetric matrix and would have six phases for three generations, is not present in the theory. We may still use the explicit parametrization given before by equations (21) and (22). Yet, now the angles and phases introduced are no longer independent parameters, there will be special constraints among them. The number of mixing angles [16] is also $(n^2 - n)$, i.e., six mixing angles for three generations. The exact form of these constraints can be derived from $\mathcal{M}^* = V^*\mathcal{D}V^\dagger$ taking into account that $\mathcal{M}$ has a zero entry in the upper left block, which implies

$$K^* dK^\dagger + R^* D R^\dagger = 0. \tag{34}$$

An important physical question is how to distinguish experimentally minimal see-saw from the general case. This is obviously a very difficult (if not impossible) task, since it would require the knowledge of the heavy neutrino masses as well as a detailed knowledge of the matrix R. So far, we have not made any assumption on the type of hierarchy in the light neutrino masses (i.e. normal hierarchy, inverted hierarchy or almost degeneracy). Recently it was argued that in grand unified models with minimal see-saw inverted hierarchy for light neutino masses is theoretically disfavoured [18].

At this stage, it is useful to compare the number of physical parameters—three light and three heavy neutrino masses, three charged lepton masses, six mixing angles and six CP violating phases, giving a total of 21 parameters—to the number of parameters present in the WB where M_R and m_l are simultaneously real and diagonal. In this case these two matrices contain six real parameters. Since m_D is a 3×3 general matrix, it contains nine real parameters and six phases due to the possibility of rotating away three phases on its left-hand side. Thus, there are also 21 parameters in this WB. Obviously, not all WB have the property of containing the minimum number of parameters. It is useful to parametrize m_D as a product of a unitary matrix U times a Hermitian matrix H, which can be done without loss of generality

$$m_D = UH = P_\xi \hat{U}_\rho P_\alpha \hat{H}_\sigma P_\beta. \tag{35}$$

In the second equality, a maximum number of phases were factored out of U and H leaving them with one phase each—ρ and σ respectively, and $P_\xi = \mathrm{diag}\,(\exp(\mathrm{i}\xi_1), \exp(\mathrm{i}\xi_2), \exp(\mathrm{i}\xi_3))$, $P_\alpha = \mathrm{diag}\ (1, \exp(\mathrm{i}\alpha_1), \exp(\mathrm{i}\alpha_2))$ and $P_\beta = \mathrm{diag}\,(1, \exp(\mathrm{i}\beta_1), \exp(\mathrm{i}\beta_2))$. The phases in P_ξ can be eliminated by rotating simultaneously ν_L^0 and l_L^0. Alternatively, one may write m_D, without loss of generality, as the product of a unitary times a lower triangular matrix [19]. This choice may be particularly useful in specific scenarios and it is easy to show how the six independent phases may be chosen [17].

3. WB invariants and CP violation

In this section, we derive simple conditions for CP conservation in the form of WB invariants which have to vanish in order for CP invariance to hold. These conditions are very useful, since they allow us to determine whether or not a given Lagrangian violates CP without the need to go to any special WB or to the physical basis. This is specially relevant in the analysis of lepton flavour models, where the various matrices of Yukawa couplings may have special textures in flavour space reflecting, for example, the existence of a lepton flavour symmetry. In the presence of texture zeros, WB invariants provide the simplest method to investigate whether a specific lepton flavour model leads to leptonic CP violation at low energies or whether the model allows for CP violation at high energies, necessary to generate BAU through leptogenesis.

The method to build WB invariants relevant for CP violation was first proposed in [8] to the quark sector and was soon afterwards extended to the low-energy physics of the leptonic sector [10]; the WB invariant relevant for CP violation with three degenerate light neutrinos was obtained later in [20]. In [17], similar conditions relevant for leptogenesis in the minimal see-saw model with three generations were derived. This approach has been widely applied in the literature [21] to the study of CP violation in many different scenarios.

It was shown in the previous section that CP invariance of the charged gauge currents requires the existence of unitary matrices U', V', W' satisfying equations (5)–(8) or just (6)–(8) depending on whether m_L is introduced. These matrices have different forms in different WB. On the other hand, physically meaningful quantities must be invariant under WB transformations. In order to derive conditions for CP invariance expressed in terms of WB invariants, we combine these equations in a non-trivial way and eliminate the dependence on the above unitary matrices by using the fact that traces and determinants are invariant under similarity transformations. In the next subsections, we present and discuss conditions relevant for different physical situations.

3.1. WB invariants relevant for CP violation at low energies

The different terms of $\mathcal{L}_m$ lead to conditions (5)–(8) for CP invariance. The strategy outlined above can be applied directly to this Lagrangian [10] leading among other interesting possibilities, to the following WB invariant CP conserving condition:

$$\mathrm{tr}[(m_L^* m_L)^a, h_l{}^b]^q = 0, \tag{36}$$

with $h_l = m_l m_l^\dagger$, a, b and q are integers and q is odd. An analogous condition with m_L and h_l replaced by M_R and $h_D = m_D^\dagger m_D$ also holds. In the framework of minimal see-saw, m_L is not present at tree level. However, the low-energy limit of the minimal see-saw corresponds to an effective theory with only lh neutrinos, with an effective Majorana mass matrix m_{eff} given by equation (29) in terms of m_D and M_R. Invariance under CP of the effective Lagrangian implies the following condition for m_{eff}:

$$U'^\dagger m_{eff} U'^* = -m_{eff}^*, \tag{37}$$

which is analogous to equation (5) with m_L replaced by m_{eff}^*. This implies that the conditions relevant to discuss the CP properties of the leptonic sector at low-energies are similar to those involving m_L and h_l in [10] and can be translated into, for instance,

$$\mathrm{tr}[(m_{eff}\ m_{eff}^*)^a,\ h_l{}^b]^q = 0, \tag{38}$$

$$\mathrm{Im\,tr}[(h_l)^c(m_{eff}\ m_{eff}^*)^d(m_{eff}\ h_l^*\ m_{eff}^*)^e(m_{eff}\ m_{eff}^*)^f] = 0, \tag{39}$$

$$\mathrm{Im\,det}[(m_{eff}^*\ h_l\ m_{eff}) + r(h_l^*\ m_{eff}^*\ m_{eff})] = 0, \tag{40}$$

where $a, b, \ldots, f$ are integers, q is odd and r is an arbitrary real number. These relations are necessary conditions for CP invariance. The non-vanishing of any of these WB invariants implies CP violation. However, these relations may not be sufficient to guarantee CP invariance. In fact, there are cases where some of them vanish automatically and yet CP may be violated.

It is well known that the minimal structure that can lead to CP violation in the leptonic sector is two generations of lh Majorana neutrinos requiring that their masses be non degenerate and that none of them vanishes. In this case, it was proved [10] that the condition

$$\mathrm{Im\,tr}\ Q = 0 \tag{41}$$

with $Q = h_l m_{eff} m_{eff}^* m_{eff} h_l^* m_{eff}^*$ is a necessary and sufficient condition for CP invariance.

In the realistic case of three generations of light neutrinos there are three independent CP violating phases relevant at low-energies. In the physical basis they appear in the V_{PMNS} matrix—one of them is a Dirac-type phase analogous to the one appearing in the Cabibbo, Kobayashi and Maskawa matrix, V_{CKM}, of the quark sector and the two additional ones can be factored out of V_{PMNS} but cannot be rephased away due to the Majorana character of the neutrinos. Selecting from the necessary conditions a subset of restrictions which are also sufficient for CP invariance is in general not trivial. For three generations it was shown that the following four conditions are sufficient [10] to guarantee CP invariance

$$\mathrm{Im\,tr}[h_l\ (m_{eff}\ m_{eff}^*)(m_{eff}\ h_l^*\ m_{eff}^*)] = 0, \tag{42}$$

$$\mathrm{Im\,tr}[h_l\ (m_{eff}\ m_{eff}^*)^2(m_{eff}\ h_l^*\ m_{eff}^*)] = 0, \tag{43}$$

$$\mathrm{Imtr}[h_l(m_{eff}\ m_{eff}^*)^2(m_{eff}\ h_l^*\ m_{eff}^*)\ (m_{eff}\ m_{eff}^*)] = 0, \tag{44}$$

$$\mathrm{Im\,det}[(m_{eff}^*\ h_l\ m_{eff}) + (h_l^*\ m_{eff}^*\ m_{eff})] = 0 \tag{45}$$

provided that neutrino masses are non-zero and non-degenerate. It can be easily seen that these conditions are trivially satisfied in the case of complete degeneracy ($m_1 = m_2 = m_3$). Yet there may still be CP violation in this case, as will be discussed in section 4.

Leptonic CP violation at low-energies can be detected through neutrino oscillations which are sensitive to the Dirac-type phase, but insensitive to the Majorana-type phases in V_{PMNS}. In any given model, the strength of Dirac-type CP violation can be obtained from the following low-energy WB invariant:

$$Tr[h_{eff}, h_l]^3 = 6\mathrm{i}\Delta_{21}\Delta_{32}\Delta_{31}\mathrm{Im}\{(h_{eff})_{12}(h_{eff})_{23}(h_{eff})_{31}\}, \tag{46}$$

where $h_{eff} = m_{eff} m_{eff}{}^\dagger$ and $\Delta_{21} = (m_\mu{}^2 - m_e{}^2)$ with analogous expressions for Δ_{31} and Δ_{32}. This invariant is, of course a special case of equation (38). For three lh neutrinos there is a Dirac-type CP violation if and only if this invariant does not vanish. This quantity can be computed

in any WB and can also be fully expressed in terms of physical observables since

$$\mathrm{Im}\{(h_{eff})_{12}(h_{eff})_{23}(h_{eff})_{31}\} = -\Delta m^2_{21}\Delta m^2_{31}\Delta m^2_{32}\mathcal{J}_{CP}, \tag{47}$$

where the Δm^2_{ij}'s are the usual light neutrino mass squared differences and $\mathcal{J}_{CP}$ is the imaginary part of an invariant quartet of the leptonic mixing matrix U_ν, appearing in the difference of the CP-conjugated neutrino oscillation probabilities, such as $P(\nu_e \to \nu_\mu) - P(\bar{\nu}_e \to \bar{\nu}_\mu)$. It is given by

$$\mathcal{J}_{CP} \equiv \mathrm{Im}[(U_\nu)_{11}(U_\nu)_{22}(U_\nu)^*_{12}(U_\nu)^*_{21}] = \tfrac{1}{8}\sin(2\theta_{12})\sin(2\theta_{13})\sin(2\theta_{23})\cos(\theta_{13})\sin\delta, \tag{48}$$

where θ_{ij} and δ are the mixing angles and the Dirac-type phase appearing in the standard parametrization adopted in [22]. The most salient feature of leptonic mixing is the fact that two of the mixing angles (θ_{12}, θ_{23}) are large, with only θ_{13} being small. This opens the possibility of detecting leptonic CP violation through neutrino oscillations, which requires $\mathcal{J}_{CP}$ to be of order 10^{-2}, a value that can be achieved, provided θ_{13} is not extremely small (at present one only has an experimental bound $\theta_{13} < 0.26$). A similar invariant condition is useful in the quark sector [8], where the corresponding $\mathcal{J}_{CP}$ is of the order 10^{-5}. The search for CP violation in the leptonic sector at low-energies is at present one of the major experimental challenges in neutrino physics. Experiments with superbeams and neutrino beams from muon storage rings (neutrino factories) have the potential [23] to measure directly the Dirac phase δ through CP and T asymmetries or indirectly through oscillation probabilities which are themselves CP conserving but also depend on δ. An alternative method [24] is to measure the area of unitarity triangles defined for the leptonic sector [25].

3.2. WB invariants relevant for leptogenesis

One of the most plausible scenarios for the generation of the BAU is the leptogenesis mechanism [3] where a CP asymmetry generated through the out-of-equilibrium L-violating decays of the heavy Majorana neutrinos leads to a lepton asymmetry which is subsequently transformed into a baryon asymmetry by (B + L)-violating sphaleron processes [4].

In this section, we consider thermal leptogenesis in the minimal see-saw scenario. In what follows the notation will be simplified into m and M for m_D and M_R. The lepton number asymmetry, ε_{N_j}, arising from the decay of the jth heavy Majorana neutrino is defined in terms of the family number asymmetry $\Delta A^j{}_i = N^j{}_i - \overline{N}^j{}_i$ by

$$\varepsilon_{N_j} = \frac{\sum_i \Delta A^j{}_i}{\sum_i (N^j{}_i + \overline{N^j}_i)}, \tag{49}$$

the sum in i runs over the three flavours $i = \mathrm{e}\mu\tau$. The evaluation of ε_{N_j}, involves the computation of the interference between the tree-level diagram and one-loop diagrams for the decay of the heavy Majorana neutrino N^j into charged leptons $l_i^\pm (i = \mathrm{e}, \mu, \tau)$ which leads to [26]

$$\begin{aligned}\varepsilon_{N_j} &= \frac{g^2}{M_W{}^2}\sum_{k\neq j}\left[\mathrm{Im}((m^\dagger m)_{jk}(m^\dagger m)_{jk})\frac{1}{16\pi}\left(I(x_k) + \frac{\sqrt{x_k}}{1-x_k}\right)\right]\frac{1}{(m^\dagger m)_{jj}} \\ &= \frac{g^2}{M_W{}^2}\sum_{k\neq j}\left[(M_k)^2\mathrm{Im}((R^\dagger R)_{jk}(R^\dagger R)_{jk})\frac{1}{16\pi}\left(I(x_k) + \frac{\sqrt{x_k}}{1-x_k}\right)\right]\frac{1}{(R^\dagger R)_{jj}},\end{aligned} \tag{50}$$

where M_k denote the heavy neutrino masses, the variable x_k is defined as $x_k = \frac{M_k{}^2}{M_j{}^2}$ and $I(x_k) = \sqrt{x_k}(1 + (1 + x_k)\log(\frac{x_k}{1+x_k}))$. From equation (50) it can be seen that the lepton-number asymmetry is only sensitive to the CP-violating phases appearing in $m^\dagger m$ in the WB, where $M_R \equiv M$ is diagonal (notice that this combination is insensitive to rotations of the lh neutrinos). Making use of the parametrization given by equation (35) for $m_D \equiv m$ it becomes clear that leptogenesis is only sensitive to the phases β_1, β_2 and σ. The second equality of equation (50) is established with the help of equation (31).

WB invariant conditions relevant for leptogenesis must be sensitive to these three phases, clearly meaning that they must be expressed in terms of $h = m^\dagger m$. From condition equation (7), we obtain

$$W'^\dagger h W' = h^*. \tag{51}$$

Only the matrix M is also sensitive to the W' rotation. From condition equation (6), we derive

$$W'^\dagger H W' = H^*, \tag{52}$$

where $H = M^\dagger M$. From these two new conditions, together with equation (6) it can be readily derived that CP invariance requires [17]:

$$I_1 \equiv \mathrm{Im\,Tr}[hHM^*h^*M] = 0, \tag{53}$$

$$I_2 \equiv \mathrm{Im\,Tr}[hH^2M^*h^*M] = 0, \tag{54}$$

$$I_3 \equiv \mathrm{Im\,Tr}[hH^2M^*h^*MH] = 0 \tag{55}$$

as well as many other expressions of the same type. These conditions can be computed in any WB and are necessary and sufficient to guarantee that CP is conserved at high energies. This was shown by going to the WB where M is real and diagonal. In this basis the I_i's are then of the form:

$$\begin{aligned} I_1 = {} & M_1M_2(M_2{}^2 - M_1{}^2)\mathrm{Im}(h_{12}{}^2) + M_1M_3(M_3{}^2 - M_1{}^2)\mathrm{Im}(h_{13}{}^2) \\ & + M_2M_3(M_3{}^2 - M_2{}^2)\mathrm{Im}(h_{23}{}^2), \end{aligned} \tag{56}$$

$$\begin{aligned} I_2 = {} & M_1M_2(M_2{}^4 - M_1{}^4)\mathrm{Im}(h_{12}{}^2) + M_1M_3(M_3{}^4 - M_1{}^4)\mathrm{Im}(h_{13}{}^2) \\ & + M_2M_3(M_3{}^4 - M_2{}^4)\mathrm{Im}(h_{23}{}^2), \end{aligned} \tag{57}$$

$$\begin{aligned} I_3 = {} & M_1{}^3M_2{}^3(M_2{}^2 - M_1{}^2)\mathrm{Im}(h_{12}{}^2) + M_1{}^3M_3{}^3(M_3{}^2 - M_1{}^2)\mathrm{Im}(h_{13}{}^2) \\ & + M_2{}^3M_3{}^3(M_3{}^2 - M_2{}^2)\mathrm{Im}(h_{23}{}^2) = 0. \end{aligned} \tag{58}$$

These are a set of linear equations in terms of the variables $\mathrm{Im}(h_{ij}{}^2) = \mathrm{Im}((m^\dagger m)_{ij}(m^\dagger m)_{ij})$ appearing in equation (50). The determinant of the coefficients of this set of equations is

$$\mathrm{Det} = M_1{}^2M_2{}^2M_3{}^2\Delta^2{}_{21}\Delta^2{}_{31}\Delta^2{}_{32}, \tag{59}$$

where $\Delta_{ij} = (M_i{}^2 - M_j{}^2)$. Non-vanishing of the determinant implies that all imaginary parts of $(h_{ij})^2$ should vanish, in order for equations (53)–(55) to hold. Conversely, the non-vanishing of any of the I_i implies CP violation at high energies, relevant for leptogenesis.

4. The case of degenerate neutrinos

The present experimental data on light neutrino masses rule out the exact degeneracy. However, since neutrino oscillations measure neutrino mass differences and not the absolute mass scale, both hierarchical neutrino masses and quasi-degenerate neutrino masses are allowed, by present experimental data. If neutrinos turn out to be almost degenerate the limit of exact degeneracy may be relevant in explaining some of the features of the leptonic mixing matrix, for instance, the observed smallness of one of the mixing angles. An open question is whether there is a model in which this limit corresponds to a symmetry of the Lagrangian. In this case, the quasi-degeneracy of neutrino masses would be natural, since it would correspond to small deviations of an exact symmetry. In the case of Dirac neutrinos, the limit of exact mass degeneracy is trivial, since there is no mixing or CP violation in that limit. The situation is entirely different for Majorana neutrinos, since in that case one can have both mixing and CP violation even in the limit of exact degeneracy. The proof is simple [10] and follows from equation (37) together with

$$U'^{\dagger} h_l U' = h_l^*, \tag{60}$$

which is readily obtained from equation (8). Let us consider the low-energy limit, where only lh neutrinos are relevant and assume that there are three lh Majorana neutrinos with exact degenerate masses. Without loss of generality, one can choose to work in a WB where the effective lh neutrino mass matrix is diagonal, real. Since, we are assuming the exact degeneracy limit, the mass matrix is just proportional to the unit matrix. We have seen that invariance under CP requires equation (37) to be satisfied by some unitary matrix U'. In the case of degeneracy and in the WB we have chosen, equation (37) is satisfied provided that $U' = iO$ (with O an orthogonal matrix). In addition, we still have the freedom to make a change of WB such that m_{eff} is unchanged and $\mathrm{Re}h_l$ becomes diagonal. In this basis equation (60) can be split into

$$O^T(\mathrm{Re}h_l)O = \mathrm{Re}h_l, \tag{61}$$

$$O^T(\mathrm{Im}h_l)O = -\mathrm{Im}h_l. \tag{62}$$

From equation (61) and assuming $\mathrm{Re}h_l$ to be non-degenerate the matrix O is constrained to be of the form $O = \mathrm{diag}(\epsilon_1, \ldots, \epsilon_n)$ with $\epsilon_i = \pm 1$. This in turn implies from equation (62) that, in the general case of non vanishing $(\mathrm{Im}h_l)_{ij}$, the ϵ_i have to obey the conditions

$$\epsilon_i \cdot \epsilon_j = -1, \quad i \neq j. \tag{63}$$

Clearly these conditions cannot be simultaneously satisfied for more than two generations.

In the general case of three light neutrinos V_{PMNS} can be parametrized by three angles and three phases. In the limit of exact degeneracy, in general mixing cannot be rotated away and V_{PMNS} is parametrized by two angles and one CP violating phase. We shall denote the corresponding leptonic mixing matrix by U_0. It has been shown [20] that in general this matrix cannot be rotated away. Only in the case where the theory is CP invariant and the three degenerate neutrinos have the same CP parity can U_0 be rotated away.

In the WB, where the charged lepton mass matrix is diagonal, real and positive the neutrino mass matrix is diagonalized by the transformation

$$U_0^{\dagger} \cdot m_{eff} \cdot U_0^* = \mu \cdot \mathbb{1}, \tag{64}$$

where μ is the common neutrino mass. Let us define the dimensionless matrix $Z_0 = m_{eff}/\mu$. From equation (64), we obtain

$$Z_0 = U_0 \cdot U_0^T, \tag{65}$$

which is unitary and symmetric. The matrix Z_0 can be written without loss of generality as

$$Z_0 = \begin{pmatrix} 1 & 0 & 0 \\ 0 & c_\phi & s_\phi \\ 0 & s_\phi & -c_\phi \end{pmatrix} \cdot \begin{pmatrix} c_\theta & s_\theta & 0 \\ s_\theta & z_{22} & z_{23} \\ 0 & z_{23} & z_{33} \end{pmatrix} \cdot \begin{pmatrix} 1 & 0 & 0 \\ 0 & c_\phi & s_\phi \\ 0 & s_\phi & -c_\phi \end{pmatrix}. \tag{66}$$

Unitarity of Z_0 implies that either s_θ or z_{23} must vanish. The case $s_\theta = 0$ automatically leads to CP invariance. Assuming $s_\theta \neq 0$, the most general form for the symmetric unitary matrix Z_0 is then given by

$$Z_0 = \begin{pmatrix} 1 & 0 & 0 \\ 0 & c_\phi & s_\phi \\ 0 & s_\phi & -c_\phi \end{pmatrix} \cdot \begin{pmatrix} c_\theta & s_\theta & 0 \\ s_\theta & -c_\theta & 0 \\ 0 & 0 & e^{i\alpha} \end{pmatrix} \cdot \begin{pmatrix} 1 & 0 & 0 \\ 0 & c_\phi & s_\phi \\ 0 & s_\phi & -c_\phi \end{pmatrix}. \tag{67}$$

This choice of Z_0 does not include the trivial case where CP is a good symmetry and all neutrinos have the same CP parity. In fact, in the CP conserving case where $\mathrm{e}^{\mathrm{i}\alpha} = \pm 1$ one has $\mathrm{Tr}(Z_0) = -\det(Z_0) = \pm 1$ corresponding to the eigenvalues $(1, -1, 1)$ and $(1, -1, -1)$ and permutations. It is well known [27] that different relative signs correspond to different CP parities. From equations (65) and (67), we conclude that the mixing matrix U_0 must be of the form

$$U_0 = \begin{pmatrix} 1 & 0 & 0 \\ 0 & c_\phi & s_\phi \\ 0 & s_\phi & -c_\phi \end{pmatrix} \cdot \begin{pmatrix} \cos(\frac{\theta}{2}) & \sin(\frac{\theta}{2}) & 0 \\ \sin(\dfrac{\theta}{2}) & -\cos(\frac{\theta}{2}) & 0 \\ 0 & 0 & \mathrm{e}^{\mathrm{i}\alpha/2} \end{pmatrix} \cdot \begin{pmatrix} 1 & 0 & 0 \\ 0 & \mathrm{i} & 0 \\ 0 & 0 & 1 \end{pmatrix}. \tag{68}$$

up to an arbitrary orthogonal transformation $U_0 \to U_0 \cdot O$. Notice that U_0 cannot be rotated away due to the fact that it is not an orthogonal matrix, even in the CP conserving case. The matrix U_0 is parametrized by two angles θ, ϕ and one-phase α. In the limit of exact degeneracy a necessary and sufficient condition [20] for CP invariance is

$$G \equiv \mathrm{Tr}[(m_{eff}^* \cdot h_l \cdot m_{eff}), h_l^*]^3 = 0. \tag{69}$$

In the WB where h_l is diagonal, i.e., $h_l = \mathrm{diag}\,(m_e^2,\ m_\mu^2,\ m_\tau^2)$, it can be written as

$$G = 6\mathrm{i}\ \Delta_m \mathrm{Im}[(Z_0)_{11}^*(Z_0)_{22}^*(Z_0)_{12}(Z_0)_{21}] = -\frac{3\mathrm{i}}{2}\Delta_m \cos(\theta)\sin^2(\theta)\sin^2(2\phi)\sin(\alpha), \tag{70}$$

where $\Delta_m = \mu^6(m_\tau^2 - m_\mu^2)^2(m_\tau^2 - m_e^2)^2(m_\mu^2 - m_e^2)^2$ is a multiplicative factor which contains the different masses of the charged leptons and the common neutrino mass μ. One may wonder whether equation (68) would be a realistic mixing matrix for the case of three non-degenerate neutrinos. It has been shown [20] that this is indeed the case. In fact this matrix corresponds to $\sin\theta_{13} = 0$ (of the standard parametrization), solar neutrino data only constrain the angle θ, whilst atmospheric neutrino data only constrain ϕ. Neutrinoless double beta decay depends

on θ and light neutrino masses. The angle α can be factored out in U_0 and is thus a Majorana-type phase.

Heavy Majorana neutrinos may play a crucial role in the generation of the BAU. If these particles are indeed responsible for BAU they must obey certain constraints (such as a lower limit in their mass). It is common to assume heavy neutrino masses to be hierarchical in the study of thermal leptogenesis since this corresponds to the simplest scenario, which is sometimes called minimal leptogenesis. Currently, there are no direct experimental constraints on heavy neutrino masses and the possibility of quasi-degenerate heavy Majorana neutrinos remains open.

5. On the relation between low-energy CP violation and CP violation required for leptogenesis

5.1. A brief summary of low-energy data

There has been great experimental progress in the determination of leptonic masses and mixing in the last few years. The evidence for solar and atmospheric neutrino oscillations is now solid. The pattern of leptonic mixing (V_{PMNS}) is very different from that of the quark sector (V_{CKM}), since only one of the leptonic mixing angles, θ_{13}, is small. The latest great progress reported is in the measurement of the square mass difference relevant for solar oscillations, Δm^2_{21}, and is due to recent KamLAND results [28]. KamLAND is a terrestial long baseline experiment which has great sensitivity to Δm^2_{21}, but it does not constrain θ_{12} much better than the current set of solar experiments. The combined result including those of SNO [29] and previous solar experiments [30] is for the 1σ range [1]

$$\Delta m^2_{21} = 8.2^{+0.3}_{-0.3} \times 10^{-5}\mathrm{eV}^2, \tag{71}$$

$$\tan^2\theta_{12} = 0.39^{+0.05}_{-0.04} \tag{72}$$

and corresponds to the large mixing angle solution (LMA) of the Mikheev, Smirnov and Wolfenstein effect [31] with the upper island excluded. On the other hand, atmospheric neutrino results from Super-Kamiokande [32] and recent important progress by K2K [33], which is also a terrestrial long baseline experiment, are consistent with, for the 1σ range [1]:

$$\Delta m^2_{32} = 2.2^{+0.6}_{-0.4} \times 10^{-3}\mathrm{eV}^2, \tag{73}$$

$$\tan^2\theta_{23} = 1.0^{+0.35}_{-0.26}. \tag{74}$$

The present bounds for $\sin^2\theta_{13}$ from the CHOOZ experiment [34] have been somewhat relaxed since they depend on Δm^2_{31} and this value went down. Assuming the range for Δm^2_{32} from Super-Kamiokande and K2K, the 3σ bound [1] lies in $\sin^2\theta_{13} < 0.05$–0.07. A higher value for the angle θ_{13} is good news for the prospectives of detection of low-energy leptonic CP violation, mediated through a Dirac-type phase, whose strength is given by $\mathcal{J}_{CP}$ defined in section 3. Direct kinematic limits on neutrino masses [35] from Mainz and Troitsk and neutrinoless double beta decay experiments [36] when combined with the given square mass differences exclude light neutrino masses higher than order 1 eV. Non-vanishing light neutrino masses also have an important impact in cosmology. Recent data from the Wilkinson microwave anisotropy probe,

WMAP [37, 38], together with other data, put an upper bound on the sum of light neutrino masses of 0.7 eV.

In the context of the see-saw mechanism, the smallness of light neutrino masses is related to the existence of heavy neutrinos. These heavy neutrinos may in turn play an important cosmological role via the generation of BAU through leptogenesis. Since leptogenesis requires CP violation at high energies, one may ask whether there is a connection between CP violation at low energies and CP violation at high energies. This question will be addressed in the next subsection.

5.2. *On the need for a lepton flavour symmetry*

The expression for the lepton-number asymmetry resulting from the decay of heavy Majorana neutrinos is given by equation (50). Yet leptogenesis is a complicated thermodynamical non-equilibrium process and depends on additional parameters. The simplest scenario corresponds to heavy hierarchical neutrinos, where M_1 is much smaller than M_2 and M_3. The case of almost degeneracy of heavy neutrinos has been considered by several authors [39] and corresponds to a resonant enhancement of ε_{N_j}. In the hierarchical case, the baryon asymmetry depends only on four parameters [40]: the mass M_1 of the lightest heavy neutrino, together with the corresponding CP asymmetry ε_{N_1} in their decays, as well as the effective neutrino mass $\tilde{m}_1$ defined as [41]

$$\tilde{m}_1 = (m^\dagger m)_{11}/M_1, \tag{75}$$

in the WB where M is diagonal, real and positive and, finally, the sum of all light neutrino masses squared, $\bar{m}^2 = m_1^2 + m_2^2 + m_3^2$. It has been shown that this sum controls an important class of washout processes. Successful leptogenesis would require ε_{N_1} of order 10^{-8}, if washout processes could be neglected, in order to reproduce the observed ratio of baryons to photons [37]

$$\frac{n_B}{n_\gamma} = (6.1^{+0.3}_{-0.2}) \times 10^{-10}. \tag{76}$$

Leptogenesis is a non-equilibrium process that takes place at temperatures $T \sim M_1$. This imposes an upper bound on the effective neutrino mass $\tilde{m}_1$ given by the 'equilibrium neutrino mass' [42]

$$m_* = \frac{16\pi^{5/2}}{3\sqrt{5}} g_*^{1/2} \frac{v^2}{M_{Pl}} \simeq 10^{-3}\text{eV}, \tag{77}$$

where M_{Pl} is the Planck mass ($M_{Pl} = 1.2 \times 10^{19}$ GeV), $v = \langle\phi^0\rangle/\sqrt{2} \simeq 174$ GeV is the weak scale and g_* is the effective number of relativistic degrees of freedom in the plasma and equals 106.75 in the SM case. Yet, it has been shown [43] that successful leptogenesis is also possible for $\tilde{m}_1 > m_*$, in the range from $\sqrt{\Delta m_{12}^2}$ to $\sqrt{\Delta m_{23}^2}$. In this case the full out-of-equilibrium condition is not verified and the temperature where the inverse decays freeze out is smaller than M_1. This range is particularly interesting since it corresponds to the strong washout regime where theoretical uncertainties are small. Furthermore, the value of the baryonic asymmetry of the universe can still be large enough and is entirely determined by neutrino properties. The square root of the sum of all neutrino masses squared $\bar{m}$ is constrained, in the case of normal hierarchy, to be below 0.20 eV [43], which corresponds to an upper bound on light neutrino masses very close to 0.10 eV. This result is sensitive to radiative corrections which depend on top

and Higgs masses as well as on the treatment of thermal corrections. In [44], a slightly higher value of 0.15 eV is found. This bound can be relaxed for instance in various scenarios including models with quasi-degenerate heavy neutrinos [39], non-thermal leptogenesis scenarios [45] or also theories with Higgs triplets [46] leading to non-minimal see-saw mechanism. In the limit $M_1 \ll M_2, M_3$, ε_{N_1} can be simplified into

$$\varepsilon_{N_1} \simeq -\frac{3}{16\pi v^2}\left(I_{12}\frac{M_1}{M_2} + I_{13}\frac{M_1}{M_3}\right), \tag{78}$$

where

$$I_{1i} \equiv \frac{\mathrm{Im}[(m^\dagger m)^2_{1i}]}{(m^\dagger m)_{11}} \tag{79}$$

and a lower bound on the lightest heavy neutrino mass M_1 is derived. Depending on the cosmological scenario, the range for minimal M_1 varies from order 10^7 to 10^9 Gev [40, 44].

Viability of leptogenesis is thus closely related to low-energy parameters, in particular the light neutrino masses. This raises the question of whether the same is true for CP violation at both low and high energies. Part of the answer to this question [47] is given here in section 3.2 where it was shown that leptogenesis depends only on three of the phases of the parametrization introduced by equation (35), to β_1, β_2 and σ, whilst the phases in V_{PMNS} depend on all six phases [17]. The question remains whether a CP conserving low-energy theory (no Dirac-type and no Majorana-type phases) would still allow for high-energy CP violation. The answer is yes [48], since the matrix m can be parametrized in such a way that V_{PMNS} cancels out in the product $m^\dagger m$ and all the additional phases remaining in this product cancel out in m_{eff}. As a result, any connection between CP violation at low and at high energies is model dependent. More specifically, in order to establish the above connection, one has to restrict the number of free parameters in the lepton flavour sector. An elegant way of obtaining such restrictions is through the introduction of a lepton-flavour symmetry. There is another motivation for restricting the number of free parameters in the lepton flavour sector. This has to do with the fact that, contrary to what happens in the quark sector, without lepton flavour restrictions, it is not possible to fully reconstruct the low energy neutrino mass matrix from low-energy data obtainable through feasible experiments [49].

Several authors have studied the connection between CP violation at low and at high energies in various interesting scenarios [50]. An important motivation for such studies is the attempt to show whether or not the BAU was generated through leptogenesis.

5.3. Towards a minimal scenario

A particular minimal scenario allowing to establish a link between BAU generated through leptogenesis and CP violation at low energies was considered in [51]. The starting point was to write m, the Dirac-type neutrino mass matrix, as the product of a unitary times a lower triangular matrix in the WB where M and m_l are diagonal and real. As pointed out before there is no lack of generality in choosing this parametrization. The strategy was then to simplify this matrix m in order to obtain physical constraints. Starting from

$$m_D = UY_\triangle, \tag{80}$$

with $Y_\triangle$ of the form

$$Y_\triangle = \begin{pmatrix} y_{11} & 0 & 0 \\ y_{21}e^{i\phi_{21}} & y_{22} & 0 \\ y_{31}e^{i\phi_{31}} & y_{32}e^{i\phi_{32}} & y_{33} \end{pmatrix}, \tag{81}$$

where y_{ij} are real positive numbers, it follows that U does not play any role for leptogenesis since it cancels out in the product $m^\dagger m$. It is clear that a necessary condition for a direct link between leptogenesis and low-energy CP violation to exist is the requirement that the matrix U contains no CP violating phases. The simplest possible choice, corresponding to $U = \mathbb{1}$, was made. Next, further simplifying restrictions were imposed on $Y_\triangle$ in order to obtain minimal scenarios based on the triangular decomposition. These correspond to special zero textures together with assumptions on the hierarchy of the different entries. Only two patterns with one additional zero in $Y_\triangle$ were found to be consistent with low-energy physics (either with hierarchical heavy neutrinos or two-fold quasi degeneracy)

$$\begin{pmatrix} y_{11} & 0 & 0 \\ y_{21}e^{i\phi_{21}} & y_{22} & 0 \\ 0 & y_{32}e^{i\phi_{32}} & y_{33} \end{pmatrix}, \qquad \begin{pmatrix} y_{11} & 0 & 0 \\ 0 & y_{22} & 0 \\ y_{31}e^{i\phi_{31}} & y_{32}e^{i\phi_{32}} & y_{33} \end{pmatrix}. \tag{82}$$

In both cases, there are two independent phases. A further simplification is to assume one of these phases to vanish. Special examples were built and it was shown that it is possible to obtain viable leptogenesis in this class of models and at the same time obtain specific predictions for low-energy physics once the known experimental constraints are imposed. In particular all the textures considered predicted the existence of low-energy CP violating effects in the range of sensitivity of future long baseline experiments. It should be noted that strong hierarchies in the entries of masses matrices could in principle be generated by the Froggatt–Nielsen mechanism [52].

The question of whether the sign of the BAU can be related to CP violation in neutrino oscillation experiments was addressed by considering models with only two heavy neutrinos [53]. In this case, the Dirac mass matrix has dimension 3×2. The interesting examples correspond to textures of the form given above in equation (82) with the third column eliminated and corresponds to the most economical extension of the SM leading to leptogenesis. With the elimination of the third column one more phase in the third row can be rotated away, hence only one physical phase remains. In fact, there are fewer parameters in this case and these are strongly constrained by low-energy physics thus leading to a definite relative sign between $\mathrm{Im}\,(m^\dagger m)^2_{12}$ and $\sin 2\delta$ (with δ the Dirac-type phase of V_{PMNS}).

6. Summary and conclusions

We have reviewed leptonic CP violation and neutrino mass models, with emphasis on the use of WB invariants to study CP violation at low and high energies, as well as on the possible connection between leptonic CP violation at low energies and CP violation required for the generation of the BAU through leptogenesis. We have identified the WB invariant which measures the strength of Dirac-type CP violation at low energies for three generations of light neutrinos and have presented

the simplest WB invariants which are sensitive to CP violation required by leptogenesis. These WB invariants are specially relevant for the study of any given lepton-flavour model, where Yukawa couplings are constrained by lepton-flavour symmetries leading, for example, to texture zeros in the leptonic mass matrices. The usefulness of the invariants stems from the fact that they can be applied in any WB, without having to perform any cumbersome change of basis.

Most of our analysis was done in the framework of the minimal see-saw mechanism, where there is a closer connection between low-energy data and leptogenesis. We have also considered some special cases such as the limit of exact degeneracy, illustrating the fact that for three Majorana neutrinos, both leptonic mixing and CP violation can exist even in the limit where neutrinos are exactly degenerate.

In conclusion, neutrino physics provides an invaluable tool to the study of the question of leptonic flavour and CP violation at low energies, while at the same time having profound implications to the physics of the early universe, in particular to the generation of the BAU.

Acknowledgments

The authors thank P Di Bari for discussing some details of his work. This work was partially supported by Fundação para a Ciência e a Tecnologia (FCT) (Portugal) through the Projects POCTI/FNU/44409/2002, PDCT/FP/FNU/ 50250/2003, PDCT/FP/FAT/50167/2003 and CFTP-FCT UNIT 777, which are partially funded through POCTI (FEDER).

References

[1] Gonzalez-Garcia M C 2004 *Preprint* hep-ph/0410030
Altarelli G 2004 *Preprint* hep-ph/0410101
Goswami S, Bandyopadhyay A and Choubey S 2004 *Preprint* hep-ph/0409224
Gonzalez-Garcia M C, Maltoni M and Smirnov A Y 2004 *Phys. Rev.* D **70** 093005 (*Preprint* hep-ph/0408170)
Bandyopadhyay A, Choubey S, Goswami S, Petcov S T and Roy D P 2004 *Preprint* hep-ph/0406328
Bahcall J N, Gonzalez-Garcia M C and Pena-Garay C 2004 *J. High Energy Phys.* JHEP08(2004)016 (*Preprint* hep-ph/0406294)
Maltoni M, Schwetz T, Tortola M A and Valle J W F 2004 *New J. Phys.* **6** 122 (*Preprint* hep-ph/0405172)
Fogli G L, Lisi E, Marrone A and Palazzo A 2004 *Phys. Lett.* B **583** 149 (*Preprint* hep-ph/0309100)
[2] Minkowski P 1977 *Phys. Lett.* B **67** 421
Yanagida T 1979 *Proc. of the Workshop on Unified Theory and Baryon Number in the Universe*, KEK, March 1979
Glashow S L 1980 *Quarks and Leptons, Cargèse Lectures* ed M Lévy *et al* (New York: Plenum) p 707
Gell-Mann M, Ramond P and Slansky R 1979 *Supergravity* (Proc. of the Workshop, Stony Brook, NY, September 1979) ed P Van Nieuwenhuizen and D Z Freeman (Amsterdam: North-Holland)
Mohapatra R N and Senjanovic G 1980 *Phys. Rev. Lett.* **44** 912
[3] Fukugita M and Yanagida T 1986 *Phys. Lett.* B **174** 45
[4] Kuzmin V A, Rubakov V A and Shaposhnikov M E 1985 *Phys. Lett.* B **155** 36
[5] Grimus W and Rebelo M N 1997 *Phys. Rep.* **281** 239 (*Preprint* hep-ph/9506272)
[6] For a review see: Branco G C, Lavoura L and Silva J P 1999 'CP Violation' (*International Series of Monographs on Physics* No. 103) (Oxford, UK: Oxford University Press) p 511
[7] Kobayashi M and Maskawa T 1973 *Prog. Theor. Phys.* **49** 652
[8] Bernabéu J, Branco G C and Gronau M 1986 *Phys. Lett.* B **169** 243
[9] For reviews on lepton flavour models and an extended list of references see: Altarelli G and Feruglio F 2002 *Preprint* hep-ph/0206077

[10] Branco G C, Lavoura L and Rebelo M N 1986 *Phys. Lett.* B **180** 264
[11] Ecker G, Grimus W and Konetschny W 1981 *Nucl. Phys.* B **191** 465
[12] Anselm A A, Chkareuli J L, Uraltsev N G and Zhukovskaya T A 1985 *Phys. Lett.* B **156** 102
[13] Branco G C and Lavoura L 1986 *Nucl. Phys.* B **278** 738
[14] Pontecorvo B 1958 *Sov. Phys.—JETP* **7** 172
Pontecorvo B 1957 *Zh. Eksp. Teor. Fiz.* **34** 247
Maki Z, Nakagawa M and Sakata S 1962 *Prog. Theor. Phys.* **28** 870
Pontecorvo B 1968 *Sov. Phys.—JETP* **26** 984
Pontecorvo B 1967 *Zh. Eksp. Teor. Fiz.* **53** 1717
[15] Korner J G, Pilaftsis A and Schilcher K 1993 *Phys. Rev.* D **47** 1080 (*Preprint* hep-ph/9301289)
[16] Endoh T, Morozumi T, Onogi T and Purwanto A 2001 *Phys. Rev.* D **64** 013006
Endoh T, Morozumi T, Onogi T and Purwanto A 2001 *Phys. Rev.* D **64** 059904 (erratum) (*Preprint* hep-ph/0012345)
[17] Branco G C, Morozumi T, Nobre B M and Rebelo M N 2001 *Nucl. Phys.* B **617** 475 (*Preprint* hep-ph/0107164)
[18] Albright C H 2004 *Phys. Lett.* B **599** 285 (*Preprint* hep-ph/0407155)
[19] Hashida J, Morozumi T and Purwanto A 2000 *Prog. Theor. Phys.* **101** 379
Hashida J, Morozumi T and Purwanto A 2000 *Prog. Theor. Phys.* **103** 865 (erratum) (*Preprint* hep-ph/9909208)
[20] Branco G C, Rebelo M N and Silva-Marcos J I 1999 *Phys. Rev. Lett.* **82** 683 (*Preprint* hep-ph/9810328)
[21] Branco G C and Rebelo M N 1986 *Phys. Lett.* B **173** 313
Gronau M, Kfir A and Loewy R 1986 *Phys. Rev. Lett.* **56** 1538
Branco G C and Kostelecky V A 1989 *Phys. Rev.* D **39** 2075
Branco G C, Rebelo M N and Valle J W F 1989 *Phys. Lett.* B **225** 385
Lavoura L and Silva J P 1994 *Phys. Rev.* D **50** 4619 (*Preprint* hep-ph/9404276)
Botella F J and Silva J P 1995 *Phys. Rev.* D **51** 3870 (*Preprint* hep-ph/9411288)
del Aguila F and Aguilar-Saavedra J A 1996 *Phys. Lett.* B **386** 241 (*Preprint* hep-ph/9605418)
del Aguila F, Aguilar-Saavedra J A and Zralek M 1997 *Comput. Phys. Commun.* **100** 231 (*Preprint* hep-ph/9607311)
Aguilar-Saavedra J A 1998 *J. Phys. G: Nucl. Part. Phys.* **24** L31 (*Preprint* hep-ph/9703461)
Pilaftsis A 1997 *Phys. Rev.* D **56** 5431 (*Preprint* hep-ph/9707235)
Lebedev O 2003 *Phys. Rev.* D **67** 015013 (*Preprint* hep-ph/0209023)
Davidson S and Kitano R 2004 *J. High Energy Phys.* JHEP03(2004)020 (*Preprint* hep-ph/0312007)
Botella F J, Nebot M and Vives O 2004 *Preprint* hep-ph/0407349
[22] Eidelman S *et al* [Particle Data Group Collaboration] 2004 *Phys. Lett.* B **592** 1
[23] De Rujula A, Gavela M B and Hernandez P 1999 *Nucl. Phys.* B **547** 21 (*Preprint* hep-ph/9811390)
Romanino A 2000 *Nucl. Phys.* B **574** 675 (*Preprint* hep-ph/9909425)
Koike M and Sato J 2000 *Phys. Rev.* D **62** 073006 (*Preprint* hep-ph/9911258)
Freund M, Lindner M, Petcov S T and Romanino A 2000 *Nucl. Phys.* B **578** 27 (*Preprint* hep-ph/9912457)
Barger V D, Geer S, Raja R and Whisnant K 2001 *Phys. Rev.* D **63** 113011 (*Preprint* hep-ph/0012017)
Lipari P 2001 *Phys. Rev.* D **64** 033002 (*Preprint* hep-ph/0102046)
Akhmedov E K, Huber P, Lindner M and Ohlsson T 2001 *Nucl. Phys.* B **608** 394 (*Preprint* hep-ph/0105029)
Freund M, Huber P and Lindner M 2001 *Nucl. Phys.* B **615** 331 (*Preprint* hep-ph/0105071)
Gonzalez-Garcia M C, Grossman Y, Gusso A and Nir Y 2001 *Phys. Rev.* D **64** 096006 (*Preprint* hep-ph/0105159)
Itow Y *et al* 2001 *Preprint* hep-ex/0106019
Fukugita M and Tanimoto M 2001 *Phys. Lett.* B **515** 30 (*Preprint* hep-ph/0107082)
Burguet-Castell J, Gavela M B, Gomez-Cadenas J J, Hernandez P and Mena O 2002 *Nucl. Phys.* B **646** 301 (*Preprint* hep-ph/0207080)
Huber P 2003 *J. Phys. G: Nucl. Part. Phys.* **29** 1853 (*Preprint* hep-ph/0210140)
Campanelli M, Bueno A and Rubbia A 2003 *Nucl. Instrum. Methods* A **503** 133
Lindner M 2003 *Int. J. Mod. Phys.* A **18** 3921

Diwan M V *et al* 2003 *Phys. Rev.* D **68** 012002 (*Preprint* hep-ph/0303081)
Winter W 2004 *Phys. Rev.* D **70** 033006 (*Preprint* hep-ph/0310307)
Minakata H, Nunokawa H and Parke S J 2003 *Preprint* hep-ph/0310023
Mena O 2003 *J. Phys. G: Nucl. Part. Phys.* **29** 1847
Harris D A 2004 *Int. J. Mod. Phys.* A **19** 1201
Yasuda O 2004 *New J. Phys.* **6** 83 (*Preprint* hep-ph/0405005)
[24] Farzan Y and Smirnov A Y 2002 *Phys. Rev.* D **65** 113001 (*Preprint* hep-ph/0201105)
[25] Aguilar-Saavedra J A and Branco G C 2000 *Phys. Rev.* D **62** 096009 (*Preprint* hep-ph/0007025)
Sato J 2000 *Nucl. Instrum. Methods* A **472** 434 (*Preprint* hep-ph/0008056)
[26] Liu J and Segre G 1993 *Phys. Rev.* D **48** 4609 (*Preprint* hep-ph/9304241)
Flanz M, Paschos E A and Sarkar U 1995 *Phys. Lett.* B **345** 248
Flanz M, Paschos E A and Sarkar U 1995 *Phys. Lett.* B **382** 447 (erratum)
Covi L, Roulet E and Vissani F 1996 *Phys. Lett.* B **384** 169
Pilaftsis A 1997 *Phys. Rev.* D **56** 5431 (*Preprint* hep-ph/9707235)
Buchmüller W and Plümacher M 1998 *Phys. Lett.* B **431** 354 (*Preprint* hep-ph/9710460)
[27] Wolfenstein L 1981 *Phys. Lett.* B **107** 77
[28] Eguchi K *et al* [KamLAND Collaboration] 2003 *Phys. Rev. Lett.* **90** 021802 (*Preprint* hep-ex/0212021)
Araki T *et al* [KamLAND Collaboration] 2004 *Preprint* hep-ex/0406035
[29] Ahmed S N *et al* [SNO Collaboration] 2004 *Phys. Rev. Lett.* **92** 102004 (*Preprint* hep-ex/0310030)
Aharmim B *et al* [SNO Collaboration] 2004 *Preprint* hep-ex/0407029
[30] Fukuda Y *et al* [Kamiokande Collaboration] 1996 *Phys. Rev. Lett.* **77** 1683
Cleveland B T *et al* [Homestake] 1998 *Astrophys. J.* **496** 505
Hampel W *et al* [GALLEX Collaboration] 1999 *Phys. Lett.* B **447** 127
Abdurashitov J N *et al* [SAGE Collaboration] 1999 *Phys. Rev.* C **60** 055801 (*Preprint* astro-ph/9907113)
Altmann M *et al* [GNO Collaboration] 2000 *Phys. Lett.* B **490** 16 (*Preprint* hep-ex/0006034)
Fukuda S *et al* [Super-Kamiokande Collaboration] 2001 *Phys. Rev. Lett.* **86** 5656 (*Preprint* hep-ex/0103033)
Fukuda S *et al* [Super-Kamiokande Collaboration] 2002 *Phys. Lett.* B **539** 179 (*Preprint* hep-ex/0205075)
[31] Wolfenstein L 1978 *Phys. Rev.* D **17** 2369
Mikheev S P and Smirnov A Y 1985 *Sov. J. Nucl. Phys.* **42** 913
Mikheev S P and Smirnov A Y 1985 *Yad. Fiz.* **42** 1441
Mikheev S P and Smirnov A Y 1986 *Nuovo Cimento* C **9** 17
[32] Ashie Y *et al* [Super-Kamiokande Collaboration] 2004 *Phys. Rev. Lett.* **93** 101801 (*Preprint* hep-ex/0404034)
[33] Ishii T [K2K Collaboration] 2004 *Preprint* hep-ex/0406055
Ahn M H *et al* [K2K Collaboration] 2004 *Phys. Rev. Lett.* **93** 051801 (*Preprint* hep-ex/0402017)
[34] Apollonio M *et al* [CHOOZ Collaboration] 1999 *Phys. Lett.* B **466** 415 (*Preprint* hep-ex/9907037)
[35] Weinheimer C *et al* 1999 *Phys. Lett.* B **460** 219
Lobashev V M *et al* 1999 *Phys. Lett.* B **460** 227
[36] Klapdor-Kleingrothaus H V, Dietz A, Harney H L and Krivosheina I V 2001 *Mod. Phys. Lett.* A **16** 2409 (*Preprint* hep-ph/0201231)
Aalseth C E *et al* [16EX Collaboration] 2002 *Phys. Rev.* D **65** 092007 (*Preprint* hep-ex/0202026)
[37] Bennett C L *et al* 2003 *Astrophys. J. Suppl.* **148** 1 *Preprint* astro-ph/0302207)
[38] Spergel D N *et al* [WMAP Collaboration] 2003 *Astrophys. J. Suppl.* **148** 175 (*Preprint* astro-ph/0302209)
[39] Pilaftsis A 1997 *Nucl. Phys.* B **504** 61 (*Preprint* hep-ph/9702393)
Ellis J R, Raidal M and Yanagida T 2002 *Phys. Lett.* B **546** 228 (*Preprint* hep-ph/0206300)
Pilaftsis A and Underwood T E J 2004 *Nucl. Phys.* B **692** 303 (*Preprint* hep-ph/0309342)
González Felipe R, Joaquim F R and Nobre B M 2004 *Phys. Rev.* D **70** 085009 (*Preprint* hep-ph/0311029)
Hambye T, Lin Y, Notari A, Papucci M and Strumia A 2004 *Nucl. Phys.* B **695** 169 (*Preprint* hep-ph/0312203)
Turzynski K 2004 *Phys. Lett.* B **589** 135 (*Preprint* hep-ph/0401219)
Hambye T, March-Russell J and West S M 2004 *J. High Energy Phys.* JHEP07(2004)070 (*Preprint* hep-ph/0403183)

[40] Buchmüller W, Di Bari P and Plümacher M 2002 *Nucl. Phys.* B **643** 367 (*Preprint* hep-ph/0205349)
Buchmüller W, Di Bari P and Plümacher M 2002 *Phys. Lett.* B **547** 128 (*Preprint* hep-ph/0209301)
For other recent detailed studies on thermal leptogenesis see: Davidson S 2003 *Preprint* hep-ph/0304120
Davidson S and Ibarra A 2002 *Phys. Lett.* B **535** 25 (*Preprint* hep-ph/0202239)
as well as references in [43, 44]

[41] Plümacher M 1997 *Z. Phys.* C **74** 549 (*Preprint* hep-ph/9604229)

[42] Kolb E W and Turner M S 1990 *The Early Universe* (*Frontiers in Physics* vol 69) (Reading, MA: Addison-Wesley) p 547
Fischler W, Giudice G F, Leigh R G and Paban S 1991 *Phys. Lett.* B **258** 45
Buchmüller W and Yanagida T 1993 *Phys. Lett.* B **302** 240
Hambye T, Lin Y, Notari A, Papucci M and Strumia A in [39]

[43] Buchmüller W, Di Bari P and Plümacher M 2003 *Nucl. Phys.* B **665** 445 (*Preprint* hep-ph/0302092)
Buchmüller W, Di Bari P and Plümacher M 2005 *Ann. Phys.* **315** 305 (*Preprint* hep-ph/0401240)
Buchmüller W, Di Bari P and Plümacher M 2004 *New J. Phys.* **6** 105 (*Preprint* hep-ph/0406014)
Di Bari P 2005 *Preprint* hep-ph/0502082
Buchmuller W, Peccei R D and Yanagida T 2005 *Preprint* hep-ph/0502169

[44] Giudice G F, Notari A, Raidal M, Riotto A and Strumia A 2004 *Nucl. Phys.* B **685** 89 (*Preprint* hep-ph/0310123)

[45] Lazarides G and Shafi Q 1991 *Phys. Lett.* B **258** 305
Murayama H and Yanagida T 1994 *Phys. Lett.* B **322** 349 (*Preprint* hep-ph/9310297)
Giudice G F, Peloso M, Riotto A and Tkachev I 1999 *J. High Energy Phys.* JHEP08(1999)014 (*Preprint* hep-ph/9905242)

[46] Hambye T and Senjanovic G 2004 *Phys. Lett.* B **582** 73 (*Preprint* hep-ph/0307237)
Rodejohann W 2004 *Preprint* hep-ph/0403236
Antusch S and King S F 2004 *Phys. Lett.* B **597** 199 (*Preprint* hep-ph/0405093)
Sahu N and Uma Sankar S 2004 *Preprint* hep-ph/0406065

[47] Buchmüller W and Plümacher M 1996 *Phys. Lett.* B **389** 73 (*Preprint* hep-ph/9608308)

[48] Rebelo M N 2003 *Phys. Rev.* D **67** 013008 (*Preprint* hep-ph/0207236)
See also Rebelo M N 2003 *Preprint* hep-ph/0311226, Invited talk at BEYOND 03 (Castle Ringberg, Tegernsee, Germany, 9–14 Jun 2003)

[49] Frampton P H, Glashow S L and Marfatia D 2002 *Phys. Lett.* B **536** 79 (*Preprint* hep-ph/0201008)
Frigerio M and Smirnov A Y 2002 *Nucl. Phys.* B **640** 233 (*Preprint* hep-ph/0202247)
Frigerio M and Smirnov A Y 2003 *Phys. Rev.* D **67** 013007 (*Preprint* hep-ph/0207366)
Branco G C, Gonzalez Felipe R, Joaquim F R and Yanagida T 2003 *Phys. Lett.* B **562** 265 (*Preprint* hep-ph/0212341)
Rodejohann W 2004 *Phys. Lett.* B **579** 127 (*Preprint* hep-ph/0308119)

[50] A partial list, together with some works already cited above, is: Mohapatra R N and Zhang X 1992 *Phys. Rev.* D **46** 5331
Nielsen H B and Takanishi Y 2001 *Phys. Lett.* B **507** 241 (*Preprint* hep-ph/0101307)
Nezri E and Orloff J 2003 *J. High Energy Phys.* JHEP04(2003)020 (*Preprint* hep-ph/0004227)
Joshipura A S, Paschos E A and Rodejohann W 2001 *J. High Energy Phys.* JHEP08(2001)029 (*Preprint* hep-ph/0105175)
Buccella F, Falcone D and Tramontano F 2002 *Phys. Lett.* B **524** 241 (*Preprint* hep-ph/0108172)
Rodejohann W and Balaji K R S 2002 *Phys. Rev.* D **65** 093009 (*Preprint* hep-ph/0201052)
Branco G C, Gonzalez Felipe R, Joaquim F R and Rebelo M N 2002 *Nucl. Phys.* B **640** 202 (*Preprint* hep-ph/0202030)
Ellis J R and Raidal M 2002 *Nucl. Phys.* B **643** 229 (*Preprint* hep-ph/0206174)
Xing Z z 2002 *Phys. Lett.* B **545** 352 (*Preprint* hep-ph/0206245)
Davidson S and Ibarra A 2003 *Nucl. Phys.* B **648** 345 (*Preprint* hep-ph/0206304)
Endoh T, Kaneko S, Kang S K, Morozumi T and Tanimoto M 2002 *Phys. Rev. Lett.* **89** 231601 (*Preprint* hep-ph/0209020)

Hambye T 2002 *Preprint* hep-ph/0210048
King S F 2003 *Phys. Rev.* D **67** 113010 (*Preprint* hep-ph/0211228)
Pascoli S, Petcov S T and Rodejohann W 2003 *Phys. Rev.* D **68** 093007 (*Preprint* hep-ph/0302054)
Akhmedov E K, Frigerio M and Smirnov A Y 2003 *J. High Energy Phys.* JHEP09(2003)021 (*Preprint* hep-ph/0305322)
Broncano A, Gavela M B and Jenkins E 2003 *Nucl. Phys.* B **672** 163 (*Preprint* hep-ph/0307058)
Velasco-Sevilla L 2003 *J. High Energy Phys.* JHEP10(2003)035 (*Preprint* hep-ph/0307071)
Dutta B and Mohapatra R N 2003 *Phys. Rev.* D **68** 113008 (*Preprint* hep-ph/0307163)
Barger V, Dicus D A, He H J and Li T j 2004 *Phys. Lett.* B **583** 173 (*Preprint* hep-ph/0310278)
Guo W l and Xing Z z 2004 *Phys. Lett.* B **583** 163 (*Preprint* hep-ph/0310326)
Rodejohann W 2004 *Eur. Phys. J.* C **32** 235 (*Preprint* hep-ph/0311142)
Grimus W and Lavoura L 2004 *J. Phys. G: Nucl. Part Phys.* **30** 1073 (*Preprint* hep-ph/0311362)
Chen M C and Mahanthappa K T 2004 *Preprint* hep-ph/0411158 as well as [51] and [53].

[51] Branco G C, Gonzalez Felipe R, Joaquim F R, Masina I, Rebelo M N and Savoy C A 2003 *Phys. Rev.* D **67** 073025 (*Preprint* hep-ph/0211001)

[52] Froggatt C D and Nielsen H B 1979 *Nucl. Phys.* B **147** 277

[53] Frampton P H, Glashow S L and Yanagida T 2002 *Phys. Lett.* B **548** 119 (*Preprint* hep-ph/0208157)

New Journal of Physics
The open-access journal for physics

Neutrino detection with inclined air showers

Enrique Zas

Departamento de Física de Partículas, Facultad de Física, Campus Sur, Universidad de Santiago, 15706 Santiago de Compostela, Spain
Kavli Institute for Cosmological Physics, University of Chicago, 5640 South Ellis Av., Chicago, IL 60637, USA
E-mail: zas@fpaxp1.usc.es

New Journal of Physics **7** (2005) 130
Received 14 March 2005
Published 23 May 2005
Online at http://www.njp.org/
doi:10.1088/1367-2630/7/1/130

Abstract. The possibilities of detecting high-energy neutrinos through inclined showers produced in the atmosphere are addressed with an emphasis on the detection of air showers by arrays of particle detectors. Rates of inclined showers produced by both down-going neutrino interactions and by up-coming τ decays from Earth-skimming neutrinos as a function of shower energy are calculated with analytical methods using two sample neutrino fluxes with different spectral indices. The relative contributions from different flavours and charged, neutral current and resonant interactions are compared for down-going neutrinos interacting in the atmosphere. No detailed description of detectors is attempted but rough energy thresholds are implemented to establish the ranges of energies which are more suitable for neutrino detection through inclined showers. Down-going and up-coming rates are compared.

PII: S1367-2630(05)96282-4
© IOP Publishing Ltd and Deutsche Physikalische Gesellschaft

Contents

1. Introduction **2**
2. EeV neutrino detection: generalities **4**
2.1. Inclined showers from cosmic rays 5
2.2. Inclined showers produced by hard muons 6
2.3. The neutrino cross-sections 7
3. Down-going neutrino-induced air showers **9**
3.1. Relative contributions of different channels 12
4. Earth-skimming neutrinos **14**
4.1. Propagation in the Earth 15
4.2. Lepton propagation: energy loss and decay 15
4.3. The emerging τ flux 18
4.4. The τ decay in the atmosphere 19
4.5. The resulting shower rate for an air-shower array 21
5. Discussion **22**
Acknowledgments **24**
References **24**

1. Introduction

The observation of ultra high-energy cosmic rays (UHE CR) of energy $\sim 10^{20}$ eV [1]–[4] has stimulated much theoretical and experimental activity in the field of astroparticle physics. These cosmic rays are expected to be suppressed by interactions with the cosmic microwave background (CMB) radiation, what is known as the Greisen–Zatsepin–Kuzmin (GZK) cut-off [5, 6]. Although many mysteries remain to be solved [7], we know it is virtually impossible to produce these energetic particles without associated fluxes of gamma rays and neutrinos from pion decays. The gamma rays pair produce in the background photon fields and the electrons loose energy through synchrotron emission in a 'cosmic cascading' process which degrades their energy down to the 100 MeV region. Neutrinos travel undisturbed carrying a 'footprint' of the production model. It is remarkable that the diffuse gamma rays in the 100 MeV region, UHE neutrinos and UHE CR are deeply related. Their precise measurements, crucial for unravelling the mysterious origin of the highest energy particles in the Universe, must be considered part of the same priority.

High-energy cosmic ray production mechanisms are basically of two types, namely acceleration models and 'top-down' scenarios [8]. Neutrino fluxes in the EeV range are difficult to avoid but their fluxes are uncertain [9]. In models that accelerate protons and nuclei, pions are believed to be produced by cosmic ray interactions with matter or radiation at the source. In 'top-down' scenarios, protons and neutrons are produced from quark and gluon fragmentation, a mechanism which is known to produce about 30 times more pions than nucleons. Furthermore, protons and nuclei also produce pions in their unavoidable interactions responsible for the GZK cut-off which decay to produce the cosmological neutrinos [10]. Cosmological neutrinos could dominate in some acceleration models but in top-down scenarios they should be well below the neutrinos from the decays of the fragmented pions. The UHE proton-to-neutrino flux ratio is thought to carry important information concerning the origin of UHE CR.

High-energy neutrinos produce extensive air showers and can be detected by the very same detectors that measure the cosmic ray spectrum. The main challenge lies in separating showers initiated by neutrinos by those induced by regular cosmic rays. It was already suggested in the 1960s that this could be done at high zenith angles [11] because the atmosphere slant depth is quite large. Neutrinos, having very small cross-sections, can interact at any point along their trajectories while most of the air showers induced by protons, nuclei or photons are absorbed before reaching ground level. The signature for neutrino events is thus inclined showers that interact deep in the atmosphere.

Inclined showers were first observed in the 1960s by several groups [12, 13]. The observed rate for shower sizes between 10^3 and 10^5 particles detected in the Tokyo (INS) array [12] is however consistent with hard processes induced by energetic muons that interact deep into the atmosphere [14]–[17]. For shower sizes above 10^5 particles, AKENO has published an upper bound on muon-poor air showers at zenith angles greater than 60° [18]. These observations have been very useful for establishing bounds on models for high-energy diffuse neutrino fluxes at the Earth [19, 20]. Inclined showers were also detected in Haverah Park (HP), a 12 km^2 air-shower array in the UK [20A]. The largest events detected by HP were actually coming at very large zenith angles [13]. The inclined dataset was recently studied and shown to be consistent with baryonic origin [21]. When the Auger project was conceived as the largest and most accurate air-shower detector [22], it became clear that it would have a competitive acceptance for inclined showers induced by neutrinos compared to devoted neutrino experiments in planning or construction [23, 24]. Other experiments have been proposed to search for deep-inclined showers in the atmosphere from satellites at orbital altitudes that allow large volumes of atmosphere to be monitored to increase the chances of detecting neutrinos [25, 26] or from behind mountains [27]–[29].

Although neutrinos of τ flavour are heavily suppressed at production, neutrino flavour oscillations [30], a maximal θ_{23} mixing and a $2:1$ ratio of $\nu_\mu : \nu_e$ at production, lead to approximately equal fluxes of all three flavours after propagation over cosmological distances [31]. When the ν_τ undergoes a charged-current interaction it produces a τ which, having a short lifetime, typically decays in flight. The process can induce two showers separated by a distance gap that is on average proportional to the τ energy. These events were soon discussed in the context of deep underground neutrino telescopes and referred to as 'double bang events' [32]. More recently double bang events have been explored for higher energy neutrinos in the atmosphere [33]. As a ν_τ propagates through the Earth, charged-current interactions followed by τ decays (which always include a lower energy ν_τ) effectively shift the neutrino energy 'regenerating' the ν_τ flux [34]. For the higher energy neutrinos these processes can occur several times. For neutrinos traversing most of the Earth the emerging flux has a characteristic 'pile-up' at an energy region around the PeV scale, except for those entering with high zenith angles.

It was remarked in 1999 [35, 36] that the perspectives of detecting ν_τ fluxes can increase dramatically for neutrinos that enter the Earth surface just below the horizon, traversing a relatively small Earth matter depth. These neutrinos can undergo a charged-current interaction to produce a τ that actually exits the Earth and decays in the atmosphere producing an up-coming air shower. These 'Earth-skimming' neutrinos can be very effective in producing τ's because of the long τ range at high energies ($\sim$10 km) which sets the scale of the effective volume. This has turned into a promising field that has been studied by a number of authors [29], [35]–[43]. Monte Carlo calculations have been performed for the surface array of the Auger detector [37], for mountain ranges [29] and in general for atmospheric τ production rates in general [39], and there

are analytical calculations for the fluorescence part of the Auger experiment [43] and for HiRes and the Telescope array [38, 40]. In this paper, we calculate both down-going and up-coming rates of neutrino-induced air showers relevant for arrays of particle detectors using analytical methods. Comparative studies made by simulation have also been discussed in the context of shower detection from satellites [39]. Although the detailed rates in an air-shower array are expected to be very dependent on detector technicalities, we examine the energy spectra of the induced showers to compare the down-going neutrino event rate to the up-coming rate induced by Earth-skimming neutrinos.

2. EeV neutrino detection: generalities

Above 1 PeV the Earth becomes opaque to neutrinos and only down-going or Earth-skimming EeV neutrinos can be detected. The challenge lies in the identification of these showers in the background of down-going cosmic rays and atmospheric muons. Inclined showers in the atmosphere are expected to play a crucial role for the detection of EeV neutrinos.

The main background for the detection of inclined showers produced by neutrinos is due to showers induced by protons and nuclei. These are expected to develop high in the atmosphere so that when the shower front reaches ground level it has very different properties from 'ordinary' showers that are observed in the vertical direction. Deep-inclined showers induced by neutrinos can develop close to ground level so that their shower front resembles that of a typical vertical proton cosmic ray shower. There is a second type of background to inclined showers induced by neutrinos which is due to deep showers induced otherwise, mostly through hard muon bremsstrahlung. Unlike those produced by cosmic rays, these cannot be distinguished from down-going neutrino-induced showers on the basis of the muon interaction point because they can also be deep. It is difficult to believe this background could be separately identified, alternatively it is thought that it sets the detectability limits for neutrino interactions.

The success in the search for inclined showers induced by neutrinos depends crucially on obtaining reliable information on shower properties related to the depth of the first interaction. Fluorescence detectors actually register the depth development of the air shower and the depth of shower maximum, which is closely related to it, can be directly obtained. Up-coming showers, such as typical neutrino Earth-skimming events, can be in principle easily identified with these detectors. In these respects the fluorescence technique is most reliable and only good reconstruction accuracy is required for neutrino identification. Unfortunately, background light introduces a duty cycle which limits its acceptance both for cosmic ray and neutrino detection. Air-shower arrays measure the particle densities as the shower front reaches ground level and thus the inference of the depth of the first interaction is a far more indirect measurement. For close-to-horizontal events, it is actually not possible to distinguish up-coming from down-going events from the arrival times of the signals, so that other shower characteristics must be used to identify potential neutrino-induced events. The study of the difference between deep and shallow inclined showers has been the subject of much activity in the recent past. It is now believed that there are a number of properties of the shower front that can be easily used to distinguish neutrino-induced showers, mostly stemming from the time distribution of the shower particles. We discuss briefly the basis of these differences. However, the detailed calculation of the efficiency of a given detector to separate deep showers from those induced by protons and nuclei is quite a technical issue which lies beyond the scope of this paper.

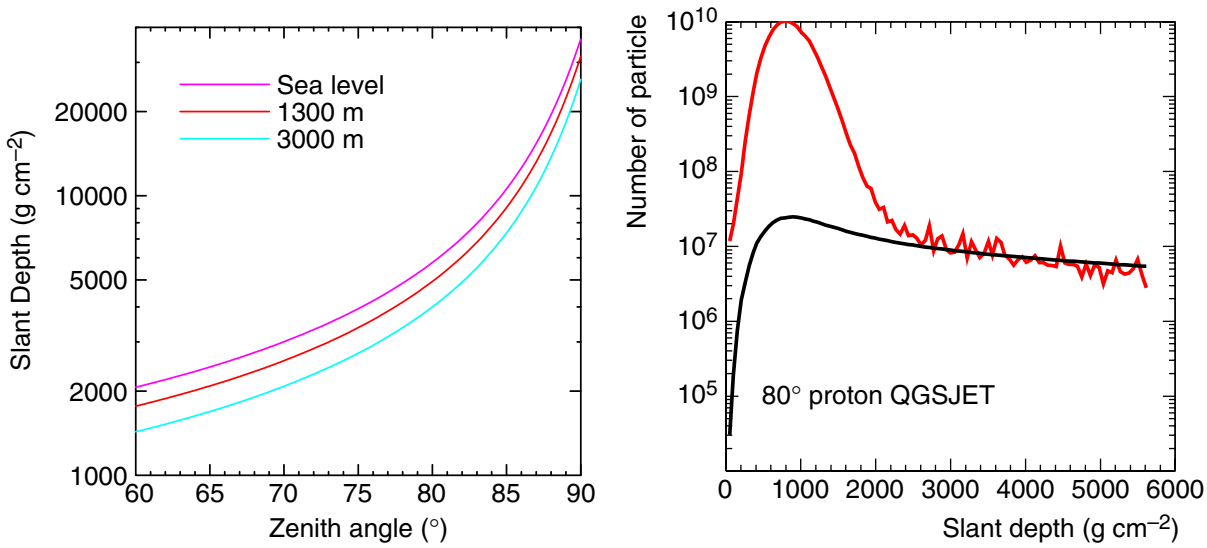

Figure 1. Left: slant depth as a function of zenith angle for three different altitudes: from top to bottom sea level, 1300 and 3000 m. Right: depth development of electromagnetic (red) and muonic (black) components of a typical shower induced by a proton (qualitatively identical to that induced by a nucleus).

The neutrino cross-sections have a direct impact on the expected shower rates. Unfortunately, the cross-section has to be calculated using quite significant extrapolations of data obtained in accelerators and there is uncertainty involved. At the end of this section, we briefly review the basics of the standard model neutrino interactions and give the details of the cross-sections used for completeness. The effects of non-standard model behaviours of the cross-section can be quite dramatic in the shower rates. These have been discussed several times in the literature [44] and will not be further addressed here.

2.1. Inclined showers from cosmic rays

Atmospheric air showers are produced by high-energy cosmic rays that interact soon after entering the upper part of the atmosphere and they are regularly registered by air shower detectors [45]–[47]. The atmosphere has just the adequate matter depth ($\sim$1000 g cm^{-2}) so that vertical showers fully develop not too far above ground level, where the shower front contains large numbers of gamma rays, electrons and positrons (the electromagnetic component) as well as muons in rough proportions 100 : 6 : 4 : 1. As the arrival direction of the cosmic ray particles increases in zenith angle, θ, the slant depth to ground level rises, in proportion to $\sec\theta$ for low-zenith angles and with a modified behaviour for $\theta > 60^\circ$ because of the Earth's curvature. The maximum slant depth for a completely horizontal (60°) shower at sea level is $\sim$36000 (2000) g cm^{-2}, see figure 1, about 36 (2) times larger than for vertical showers. As a result, most of the electromagnetic component of showers with $\theta > 60^\circ$ is much absorbed before reaching ground level.

The analysis of the HP inclined dataset established the cosmic ray EeV background for neutrino detection [49]. A fairly general model to describe the inclined showers induced by protons, nuclei and photons [48] was developed which allowed the first analysis of EeV data at

zenith angles between 60° and 85° on an event-by-event basis. The observed rate was shown to be consistent with a baryonic origin of the cosmic rays and a limit on photon abundance above 10^{19} eV was set [21, 49, 50]. The electromagnetic part of cosmic ray showers at high zenith develops and gets practically absorbed in the first 2000 g cm^{-2} and to a very good approximation only muons reach the ground. The lower energy muons actually decay in flight and can contribute a small electromagnetic component that follows closely that of the muons. As a result, the average energy of the muons reaching ground increases rapidly as the zenith angle rises. The magnetic field of the Earth acts as a spectrometer for the surviving muons separating the negative from the positive in inverse proportion to their energy and producing complex density patterns on the ground [48]. The shower front that reaches ground level for inclined showers is very different from vertical showers. Inclined shower fronts practically only contain energetic muons and their density patterns have lost the cylindrical symmetry because of the Earth's magnetic field. The degree to which this symmetry is broken depends on the relative strength and orientation of the magnetic field with respect to shower axis as well as the characteristic distance travelled by the muons which is governed by the zenith angle [48].

Studies have been made of the time structure of the shower front induced by inclined cosmic rays and deep showers [51]. While the former are very close to a plane front, deep showers display a front with significant curvature, in similar fashion to ordinary vertical showers. This can be characterized by an effective radius of curvature that is directly related to the distance at which shower maximum is achieved. The time structure of the arriving particles has been shown to be very different because it is due to muons that are produced very far away. The muons do not have much multiple elastic scattering and, as a result, their arrival time distribution can be related to a very good approximation only to their geometrical path and the kinematic delays associated with the muon sub-luminal velocity [52]. At large zenith, ordinary cosmic rays produce the shower muons very far from ground level and both the front curvature and its width are very small. In contrast, vertical and deep-inclined showers, with large numbers of electrons, positrons and photons, display both a small radius of curvature because shower maximum is relatively close, as well as a large signal dispersion in time which increases as the distance to shower axis increases. The time structure of the showers detected with the Auger observatory have clearly shown these effects [53, 54].

The inclined shower technique must exploit these differences to search for neutrino induced inclined air showers. A simple signature can be used: inclined showers that look like ordinary vertical showers with a significant electromagnetic component. More sophisticated analysis methods can enhance the performance of the detectors to search for deep showers for instance relating the time structure of the muons to the depth development of the shower [55]. It has been recently shown that it is possible to establish the depth of production of the muons in a shower from the time distributions of the muons which are far from the shower axis [56]. If this technique can be effectively exploited, it could allow the selection of deep showers also for showers that have had their electromagnetic component absorbed.

2.2. Inclined showers produced by hard muons

High-energy muons can produce deep air showers by bremsstrahlung, pair production and nuclear interactions. Although these processes typically contribute similar amounts to muon energy loss, bremsstrahlung is the hardest process and when folded with a steeply falling atmospheric muon spectrum, is the most important for producing high-energy showers. This is, in fact, the

dominant mechanism for explaining the observed inclined shower rates in the energy range between 100 TeV and 10 PeV [16]. The high-energy muons that are mostly travelling along the shower axis must undergo the bremsstrahlung interaction in which a large fraction of the muon energy is transferred to the photon. This must be produced at about 400 g cm^{-2} of slant depth before the muon reaches ground level, in a relatively narrow range of depth so that the shower reaches its maximum close to ground level. Both bremsstrahlung and pair production will give rise to pure electromagnetic showers that would hardly contain any muons, but the hadronic interactions of the muons will produce showers that are of hadronic type.

Since atmospheric muons are produced in air showers, these energetic muons must come from extensive air showers which exceed the muon energy by some factor, which is, incidentally, dependent on the nature of the primary particle. The hard process itself generates a sub-shower of a fraction of the muon energy which develops along shower axis. It is even possible that several of these hard-muon processes combine in a single larger shower. The softer muons, spread laterally in patterns which are governed by the geomagnetic field, could in principle also be detected if the primary shower energy is sufficiently high.

The deep showers induced by these hard processes are thus 'embedded' in a larger shower which may or may not be detectable. If they are detected it could in principle be possible to distinguish the deep sub-shower within the cosmic ray shower which would clearly signal this kind of processes but this seems a rather difficult task. If not, it would be impossible to distinguish from a charged-current electron–neutrino shower for instance. Fortunately, the atmospheric muon flux is very soft and (at sufficiently high energy) the expected rate of showers from hard-muon processes is expected to be very small. However, the muon bremsstrahlung rate is subject to uncertainties, mainly due to the production of prompt muons through charmed mesons, a subject that has not been resolved [57]. Inclined showers of shower size between 10^5 and 10^7 are expected to give valuable information concerning prompt charm production [58]. Backgrounds of hard-muon processes for neutrino detection in the context of the Auger detector have been discussed in [59].

2.3. The neutrino cross-sections

The dominant interaction for neutrinos in matter is deep inelastic scattering (DIS) on nucleons ($\nu + N \to l + X$, where N stands for a nucleon and l for a lepton). The cross-sections are given in terms of the standard structure functions. Within the standard model propagator effects associated with the mass of the weak exchange bosons, M_B, become important at high energies:

$$\frac{\mathrm{d}\sigma}{\mathrm{d}y} = \frac{G_F^2 m_p E_\nu}{\pi} \int_0^1 \mathrm{d}x \left[\frac{M_B^2}{M_B^2 + 2m_p E_\nu xy}\right]^2 \times \left[\left(1 - y - \frac{m_p xy}{2E_\nu}\right) F_2(x, Q^2) + y^2 x F_1(x, Q^2) \pm y\left(1 - \frac{y}{2}\right) x F_3(x, Q^2)\right]. \quad (1)$$

Here, y is the fraction of energy transferred to the nucleon in the laboratory frame, Q^2 is the negative of the square of the four-momentum transfer, G_F is the Fermi constant, m_p is the proton mass and x is defined by the relation $Q^2 = 2m_p Exy$. For charged (neutral) current interactions the boson mass is taken to be $M_B = M_W(M_Z)$, the $W^\pm(Z^0)$ boson mass. The $\pm$ sign in equation (1) implies a + sign for ν and a − sign for $\bar{\nu}$.

$F_{1,2,3}$ are the structure functions which can be expressed in terms of universal parton distributions of the nucleons, obtained from fits to accelerator data and QCD evolution equations.

For charged-current interactions on isoscalar targets at leading order (LO), they are given by

$$F_2^{\nu cc}(x, Q^2) = x(u + d + 2s + 2b + \bar{u} + \bar{d} + 2\bar{c} + 2\bar{t}), \tag{2}$$

$$xF_3^{\nu cc}(x, Q^2) = x(u + d + 2s + 2b - \bar{u} - \bar{d} - 2\bar{c} - 2\bar{t}), \tag{3}$$

$$F_2^{\bar{\nu} cc}(x, Q^2) = x(u + d + 2c + 2t + \bar{u} + \bar{d} + 2\bar{s} + 2\bar{b}), \tag{4}$$

$$xF_3^{\bar{\nu} cc}(x, Q^2) = x(u + d + 2c + 2t - \bar{u} - \bar{d} - 2\bar{s} - 2\bar{b}), \tag{5}$$

$$F_2(x, Q^2) = 2xF_1(x, Q^2). \tag{6}$$

where x is to be interpreted as the momentum fraction carried by the quark distributions (u, d, s, c, b, t, their dependence on x and Q^2 has been omitted for clarity). For neutral currents, the structure functions involve different combinations of the parton distributions with neutral coupling factors that depend on $z = \sin^2\theta_W$, where θ_W is the electroweak mixing angle

$$F_2^{nc}(x, Q^2) = \left[\frac{8z^2}{9} - \frac{2z}{3} + \frac{1}{4}\right] x(u + c + t + \bar{u} + \bar{c} + \bar{t}) + \left[\frac{z^2}{9} - \frac{z}{3} + \frac{1}{4}\right] \times x(d + s + b + \bar{d} + \bar{s} + \bar{b}), \tag{7}$$

$$xF_3^{nc}(x, Q^2) = \left[\frac{1}{4} - \frac{2z}{3}\right] x(u + c + t - \bar{u} - \bar{c} - \bar{t}) + \left[\frac{1}{4} - \frac{z}{3}\right] x(d + s + b - \bar{d} - \bar{s} - \bar{b}), \tag{8}$$

which together with the Callan–Gross relation (equation (6)) apply to both ν and $\bar{\nu}$.

Unfortunately, the neutrino cross-section at the energies of interest must be deduced from extrapolations of the parton distributions to high-Q^2 and low-x values, where there is no accelerator data. As accelerator experiments provide more accurate data on parton distributions, new sets of parametrizations are developed which lead to somewhat different cross-section calculations [60]–[63]. For energies above 10^6 GeV, charged-current interactions are about 2.5 times more likely than neutral current interactions. Uncertainties can represent up to a factor of two for the total cross-section at energies around 10^{20} eV as recently estimated in [64]. Next to LO [63] and the atomic number of the target [65] have been shown to imply changes in the cross-sections which are smaller than the uncertainties due to the extrapolations of the structure functions. In the work that follows here, we will use one of the most recently updated sets, CTEQ6 [66] for reference.

This adds an additional interest to neutrino detection because neutrino experiments may provide new insights into particle physics. Besides the obvious role of the neutrino cross-section in the actual interaction that leads to the possible neutrino detection there are other more subtle effects. The y distribution of the cross-section also has an impact on the detection rate. The average value obtained with standard parametrizations is $\langle y \rangle \simeq 0.2$ for energies above 10^6 GeV. Since the average energy transfer to the nucleon is very dependent on the low x behaviour of the parton distributions in a region which is not yet accessible to accelerator experiments [67], it has been pointed out that simultaneous measurements of different neutrino channels could provide insight

Table 1. Contributing channels to down-going shower rates indicating the neutrino reactions, the corresponding neutrino flavours, the normalization factors, the shower type, its fraction of the neutrino energy and the relevant expression applied.

Reaction	Type	Flavour ν	Norm fact	Shower type	Energy frac	Equation
$\nu + \mathrm{N} \to \mathrm{l}^{\pm}\mathrm{X}$	Charged	$\bar{\nu}_e\,\nu_e$	1.	Mixed	1	(13)
$\nu + \mathrm{N} \to \mathrm{l}^{\pm}\mathrm{X}$	Charged	$\bar{\nu}_\mu\nu_\mu\,\bar{\nu}_\tau\nu_\tau$	1	Hadronic	~ 0.2	(15)
$\nu + \mathrm{N} \to \mathrm{l}^{\pm}\mathrm{X}$	Charged	$\bar{\nu}_\tau\nu_\tau$	1.	Hadronic	~ 0.2	(16)
$\nu + \mathrm{N} \to \nu\mathrm{X}$	Neutral	All $\nu\bar{\nu}$'s	3.	Hadronic	~ 0.2	(15)
$\nu + \mathrm{e} \to \mathrm{q}\bar{\mathrm{q}}$	Resonant	$\bar{\nu}_e$	$0.5 \times 6 = 3$	Hadronic	1	(13)
$\mathrm{W}^- \to \mathrm{e}\bar{\nu}_e$	Resonant	$\bar{\nu}_e$	0.5	Electromg	0.25	(15)
$\mathrm{W}^- \to \tau\bar{\nu}_\tau$	Resonant	$\bar{\nu}_e$	0.5	elmg/had	0.25	(16)

on the low-x behaviour of the parton distributions [68]. For down-going neutrino-induced air showers the interaction rate is proportional to the cross-section, for Earth-skimming up-coming showers the cross-section acts in the opposite way increasing the neutrino absorption in the Earth. A very interesting idea has been discussed that a simultaneous measurement of the two rates could lead to an indirect measurement of the neutrino cross-section at energies well beyond the accelerator range [69]. The relative rates of down-going and up-coming showers are thus of great relevance from this perspective too.

Finally, we also give an approximate cross-section for the Glashow resonance, $\mathrm{e}\bar{\nu}_e \to \mathrm{W}^- \to \bar{\mathrm{l}}\mathrm{l}'$ considering only the first-order s-channel diagram and neglecting mass corrections

$$\frac{\mathrm{d}\sigma}{\mathrm{d}y} = \frac{2G_F^2 m_e E_\nu}{\pi}\left[\frac{M_W^4}{(2m_e E_\nu - M_W^2)^2 + M_W^2\Gamma_W^2}\right](1-y)^2, \tag{9}$$

where y is to be taken as the fraction of energy carried by the most negative charged lepton, and Γ_W is the W boson width. The average fraction of energy transferred to the most negative lepton is $\langle y\rangle = 0.25$. In practice, electron cross-sections are suppressed by the ratio of the electron to proton mass and this interaction is only relevant for $\bar{\nu}_e$ energy of around 6.4×10^6 GeV, where it dominates over DIS interactions. This expression is only adequate for the resonance region. The reactions are explicitly shown in table 1.

3. Down-going neutrino-induced air showers

There are multiple channels for producing down-going neutrino-induced showers. In order of importance, first are charged-current interactions with atmospheric nuclei and then neutral current interactions followed by $\bar{\nu}_e$ resonant interactions with atmospheric electrons. Both charged and neutral current neutrino DIS interactions break up atmospheric nuclei. The collision debris initiates a hadronic air shower of energy yE_ν regardless of the flavour of the original neutrino. For charged current ν_e ($\bar{\nu}_e$) interactions the emitted electron (positron) generates, in addition, an electromagnetic cascade, carrying the remaining energy $(1-y)E_\nu$. For charged current ν_τ interaction, the τ decay can add to the hadronic shower or not depending on where it decays. Because of the smaller electron mass the interaction of neutrinos with atomic electrons is in

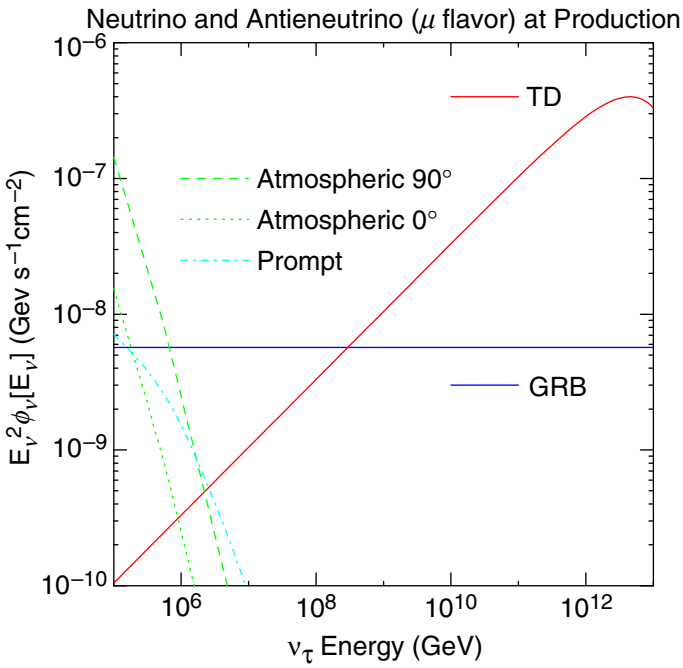

Figure 2. Flux of ν and $\bar{\nu}$ of each flavour arriving to the Earth according to the two parametrizations used for GRB and Topological Defect (TD) models, compared to the vertical and horizontal atmospheric neutrino fluxes and prompt atmospheric neutrinos from charm decays.

general suppressed except for the Glashow resonance, $\bar{\nu}_e + e^- \rightarrow W^-$, which dominates over all other processes at the resonance energy $E_{\bar{\nu}_e} \sim 6.4 \times 10^6$ GeV [60]. The decay of the W^- boson into $q\bar{q}$ pairs dominates because of the six possible final states. If it decays into an $e\bar{\nu}_e$ pair, the electron generates a purely electromagnetic shower with energy $E \sim 3 \times 10^6$ GeV and if it decays into a $\tau\bar{\nu}_\tau$ the shower is produced by τ decay (64% of the times into hadrons and 18% into $e\bar{\nu}_e$).

The calculations of the shower rates induced by a differential neutrino flux (per unit energy E_ν, area A, solid angle Ω and time t) are based on [16] and give

$$\phi_\nu[E_\nu] = \frac{d^6 N_\nu}{dE_\nu dA d\Omega\, dt} \tag{10}$$

We will use a simple neutrino flux with a constant spectral index of 2 and compatible in the 10^6–10^8 GeV region with the gamma ray burst (GRB) flux which is given in [70] as well as a spectrum from a characteristic top-down scenario (TD).[1] This last model has been chosen because it is similar to that used in [37] and it is consistent with experimental data [71, 72]. They are illustrated in figure 2. The choices are driven by their different energy dependences in the most interesting region between 10^{16} and 10^{18} eV and for comparison with other calculations. The total flux ν is obtained multiplying the (ν_μ and $\bar{\nu}_\mu$)-flux at production by a factor 1.5 to approximately account for ν_e production according to naive counting.

[1] Mass of particle X is $M_X = 3 \times 10^{14}$ GeV, evolution parameter $p = 2$ and injection normalization $Q_0 = 10^{-34}$ erg cm^{-3} s^{-1}.

The basic expression for the calculation of the number of showers, $\mathrm{d}N_{sh}$, induced by this flux interacting in the interval of atmospheric matter depth $\mathrm{d}x$, is simply given by

$$\mathrm{d}N_{sh} = \phi_\nu[E_\nu]\,[\mathrm{d}A\mathrm{d}\Omega\,\mathrm{d}t]\,\mathrm{d}E_\nu N_A \mathrm{d}x \frac{\mathrm{d}\sigma}{\mathrm{d}y}\mathrm{d}y, \tag{11}$$

where N_A is Avogadro's number. Depending on the interaction, the differential rates in shower energy have slightly different expressions involving the cross-sections discussed in section 2.3. In charged current ν_e interactions, all the interaction energy is transferred to the shower: $E_\nu = E_{sh}$ and the differential shower rate produced is

$$\phi_{sh}[E_{sh}] = \frac{\mathrm{d}N_{sh}}{\mathrm{d}E_{sh}\mathrm{d}A\mathrm{d}t\mathrm{d}\Omega} = \phi_\nu[E_{sh}]N_A\sigma^{cc}\int_0^{x_{max}}\mathrm{d}x, \tag{12}$$

where $x_{max}(\theta)$ is the slant depth available in the atmosphere for the neutrino to interact.

Unfortunately, not all the showers induced by neutrinos can be detected and distinguished from showers produced by cosmic rays. The shower rate that can be identified to be produced by a neutrino depends crucially on detector performance and capabilities. We can establish a probability for detection $\mathcal{P}_{det}$, a function that necessarily depends on shower energy, arrival direction, $\mathrm{d}\Omega$, depth at which the shower is produced, x, fraction of energy transfer, y, and impact parameter, $\vec{l}_\perp$. When this probability is included the shower rate becomes

$$\phi_{sh}[E_{sh}] = \phi_\nu[E_{sh}]N_A\int_0^1 \mathrm{d}y\frac{\mathrm{d}\sigma^{cc}}{dy}\int_0^{x_{max}}\mathrm{d}x\,\mathcal{P}_{det}[y, E_{sh}, \Omega, x, \vec{l}_\perp]. \tag{13}$$

The above expression can be integrated both in solid angle and in impact parameter over the surface detector of area A_d to give

$$\iint \mathrm{d}\Omega\,\mathrm{d}A\phi_{sh}[E_{sh}] = \phi_\nu[E_{sh}]N_A\int_0^1\mathrm{d}y\frac{\mathrm{d}\sigma^{cc}}{\mathrm{d}y}\left[\int\mathrm{d}\Omega\int_{A_d}\mathrm{d}^2\vec{l}_\perp\int_0^{x_{max}}\mathrm{d}x\,\mathcal{P}^{mix}_{det}[y, E_{sh}, \Omega, x, \vec{l}_\perp]\right]. \tag{14}$$

Here, $\mathcal{P}^{mix}_{det}$ refers to the subsequent shower of mixed electromagnetic and hadronic components, respectively carrying fractions $(1-y)$ and y of the incident neutrino energy. If edge effects are ignored, the $\mathrm{d}^2\vec{l}_\perp$ integral simply factorizes as A_d and introduces a '$\cos\theta$' factor in the remaining integral. The acceptance (as expressed between the large brackets) for the surface detector of the Pierre Auger Observatory was calculated in [24]. Expressions for both purely hadronic and purely electromagnetic showers were obtained integrating in solid angle for $\theta \geqslant 75^\circ$ and demanding that the shower intercepts ground level with a significant electromagnetic component.

An important contribution to the inclined shower rate induced by neutrinos is due to neutral current interactions. In these processes, the shower energy is simply $E_{sh} = yE_\nu$. The result above is modified in the argument of the neutrino flux which takes a dependence on y, in the y integral that must include a y^{-1} factor from the change of variables and on $\mathcal{P}^{had}_{det}$ which is now only for hadronic type showers

$$\phi_{sh}[E_{sh}] = N_A\int_0^1\frac{\mathrm{d}y}{y}\phi_\nu[E_{sh}/y]\frac{\mathrm{d}\sigma^{nc}}{\mathrm{d}y}\int_0^{x_{max}}\mathrm{d}x\,\mathcal{P}^{had}_{det}[E_{sh}, \Omega, x, \vec{l}_\perp]. \tag{15}$$

The same expression accounts for charged current ν_μ interactions (replacing σ^{nc} by σ^{cc}) because the produced μ is unlikely to decay in the whole atmospheric depth unless its energy is below 1 TeV. In the case of ν_τ charged-current interactions, the emerging τ is likely to decay provided that its energy is below $\sim 10^9$ GeV [33]. Since a radiation length in the atmosphere is of order 300 m, for τ energies below about 10^7 GeV the decay will merge with that from the hadronic debris and a result similar to equation (14) can be expected. For the τ decay shower the fraction of τ energy that goes into the shower after its decay (f) must also be accounted for. Assuming a constant fraction, $E_{sh} = yfE_\nu$, the expression becomes

$$\phi_{sh}[E_{sh}] = N_A \int_0^1 \frac{\mathrm{d}y}{fy} \frac{\mathrm{d}\sigma^{cc}}{\mathrm{d}y} \phi_\nu \left[\frac{E_{sh}}{fy}\right] \int_0^{x_{max}} \mathrm{d}x\, \mathcal{P}^\tau_{det}[E_{sh}, \Omega, x, \vec{l}_\perp] \tag{16}$$

with $\mathcal{P}^\tau_{det}$ modified according to the shower details. For larger energies, the double bang nature of the process will be manifested and each of the two showers could be separately detected.

The calculation proceeds in analogous ways for resonant W^- production with σ^{cc} replaced by σ^{res} in the corresponding expressions. When the W boson decays into $q\bar{q}$ pairs it can be assumed that all the energy is channelled after fragmentation into a hadronic shower and equation (14) applies with a hadronic detection probability function $\mathcal{P}^{had}_{det}$ that does not depend in y. As a result, the integral in y can be trivially performed, which amounts to substituting the y-integral for the corresponding total cross-section, σ^{res}. When a $e\bar{\nu}_e$ pair is produced equation (15) must be used provided that y (for the resonant differential cross-section) is taken to be the fraction of the neutrino energy carried by the charged lepton in the laboratory frame. When the W decays into $\tau\bar{\nu}_\tau$ pair and the shower is produced by τ decay equation (16) applies.

3.1. Relative contributions of different channels

The precise form of the detection probability $\mathcal{P}_{det}$ is crucial in the calculation of the shower rates. This calculation is complex and dependent on technical details of the detector response that must include the capabilities to identify showers produced by deep interactions. To establish some level of comparison with up-coming showering events from Earth-skimming neutrinos, we make a very simple assumption to evaluate it: provided the zenith angle is greater than 60° all showers that start developing in the second half of the slant depth of the atmosphere can in principle be distinguished from those produced by cosmic rays. This is not necessarily a conservative assumption. For air-shower arrays, the particle detectors must be capable of resolving the arrival time and time spread of the signals and this is necessarily challenging near a detector threshold. However, by demanding that the neutrino travels through at least the first $\sim$1000 g cm^{-2} without interacting, because of geometrical considerations it can be assumed that the subsequent shower must have different properties (such as radius of curvature) from a cosmic shower of the same zenith.[2]

We then require that showers at ground level have more than a fixed number of electrons and positrons (N_e) to be detected. This requirement will determine the depths at which the neutrino can interact to give a significant signal. We make several choices of $N_e = 10^5$, 10^6 and

[2] We remark here that the atmosphere is split into halves in depth. This implies that for a detector 1.3 km above sea level and a zenith angle of 60°, the midpoint is 10.5 km away while the typical first interaction point for a proton or nucleus is $\sim$40 km away. A ν shower that develops in the second half is closer to the detector by more than a factor of two.

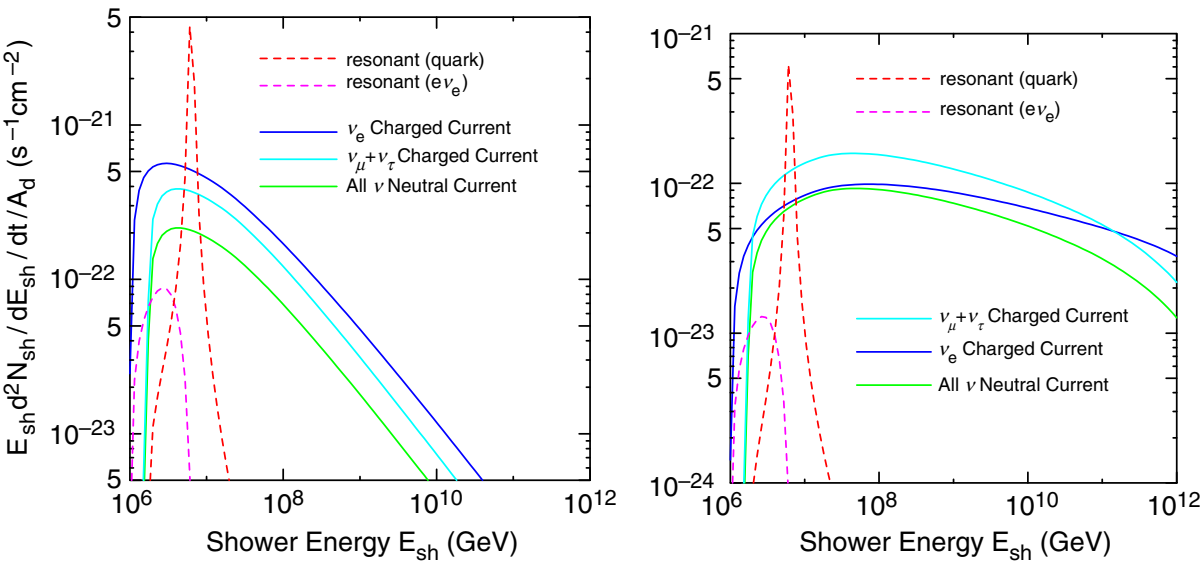

Figure 3. Shower rates produced by the main DIS processes (full) and resonant $\bar{\nu}_e$e interactions (dashed) for the GRB model (left) and the TD model (right). DIS interactions are separated in charged currents $\nu_e + \bar{\nu}_e$, $\nu_\mu + \bar{\nu}_\mu + \nu_\tau + \bar{\nu}_\tau$ (neglecting τ decay) and neutral current interactions for all neutrino flavours. The q$\bar{\text{q}}$ and e$\bar{\nu}_e$ channels for the Glashow resonance are shown.

10^7 to simulate different detector responses naively. These are arbitrary (a shower of 10^{15} eV has about 10^6 particles at shower maximum) and set a fairly abrupt low-energy cut-off for the calculations that follow. By choosing deliberately low values, the limits of the technique are explored by examining its potential low-energy behaviour. In a realistic calculation, this is very much dependent on the detector, on the geometry, on the lateral distribution of the different particles in the shower front and on many other aspects which have been ignored. However, as the energy of the shower rises, the range of depths in which the neutrino can interact to be detected increases, to eventually reach half the atmospheric depth. For high energies, when any detector is most likely to detect deep showers, we do not expect this simple calculation to be very far off.

The calculations have been made using the above-described methods together with parametrizations for the depth development of hadronic [73] and of electromagnetic showers [74] to calculate x_{max}. All neutrino flavours are assumed to have the same flux when reaching the Earth after mixing. In table 1 different channels are summarized, together with the resulting normalization factors (relative to each neutrino flavour), the type of shower generated, the energy fraction transferred to the shower and the appropriate expression in which $\mathcal{P}$ has to be chosen according to the shower type. The grouping results from the combinations of the neutrino flavour(s) involved, the shower type, the fraction of energy transferred to the shower and the cross-section. The normalization factors are associated to the number of neutrino flavours, and in the case of q$\bar{\text{q}}$ production a factor of six is included to account for the sum over all final-state possibilities (two weak doublets and three colours).

The results of the main contributions are compared in figure 3. We have included all the neutral interactions, the $\nu_e, \bar{\nu}_e$ charged-current interaction and the $\nu_\mu, \bar{\nu}_\mu$, the $\nu_\tau, \bar{\nu}_\tau$

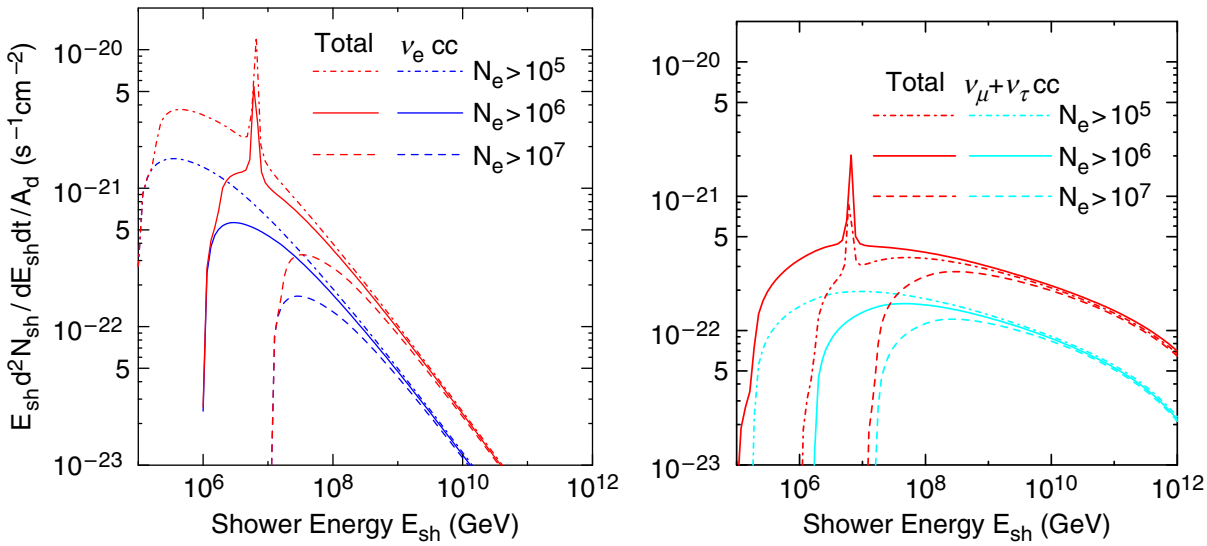

Figure 4. Down-going shower rates produced by all channels and flavours added up, compared to charged current $\nu_e + \bar{\nu}_e$ for the GRB model (left) and to charged current $\nu_\mu + \bar{\nu}_\mu + \nu_\tau + \bar{\nu}_\tau$ for the TD model (right). Detector efficiency is roughly estimated by requiring shower size (N_e) at ground level to be above nominal threshold values.

charged-current interactions neglecting τ decay (a detailed calculation of this effect will be presented elsewhere [75]) as well as the resonant $q\bar{q}$ and $e\bar{\nu}_e$ channels. Basically, for DIS interactions the calculated shower rate follows closely that of the incident neutrino flux. The relative contributions of each channel depend on its spectral index. This is not surprising since the main difference between channels is the fraction of energy that goes to the shower. If the ν spectrum is steep, the charged-current electron–neutrino interactions dominate because all the neutrino energy goes to the shower, but for hard fluxes, like the topological defect models discussed here, the shift in shower energy for neutral current channels is compensated by the increase in flavours and hence this channel dominates.

The total shower rates produced by the discussed DIS and resonant channels are plotted for the two fluxes chosen in figure 4, together with the dominant DIS channel for each case. In this figure, we also compare the effects of different thresholds as discussed above. The figure illustrates that the overall shower rate flux is close to a factor of three times above that calculated using the dominant neutrino channel only (the precise factor depends on the spectral shape of the flux in question). The figure illustrates the dramatic effect that the low-energy behaviour of an air-shower array can have in the total event rate calculation. Naturally, this is particularly significant for the GRB model which is much steeper.

4. Earth-skimming neutrinos

As neutrinos go through the Earth they can undergo charged-current interactions close to their exit point below the surface of the Earth. Under certain circumstances these interactions can produce extensive air showers that develop upwards in the atmosphere. Only those produced by

ν_τ's are of significance from the quantitative point of view, because they lead to large detectable shower rates in the high-energy range of interest. This is due to the combined effect of the lepton lifetime, its energy loss and the neutrino cross-section. For ν_τ the mechanism can be described in three stages, namely the ν_τ enters the Earth and propagates through it, it then has a charged-current interaction just below the surface producing a τ that continues the propagation in matter with considerable energy loss and finally the τ exits the surface and decays in the atmosphere inducing an air shower.

4.1. Propagation in the Earth

Neutrinos have a cross-section which increases as the neutrino energy rises. As a flux of neutrinos goes through a given amount of matter a characteristic energy scale is selected, the energy at which the neutrinos are likely to interact. Above this energy the flux is attenuated while below it is practically undisturbed. Both charged and neutral current interactions contribute to neutrino attenuation. For a neutrino crossing the Earth the amount of matter depth is a rapidly varying function depending on the impact parameter. If they travel through the centre, that is they enter with a relatively low-zenith angle, the matter depth is not much below $6.6 \times 10^9\,\mathrm{g\,cm^{-2}}$ (the depth of a diameter). Using the cross-section discussed in section 2.3, this corresponds to the attenuation length of a 100 TeV neutrino. As the impact point gets farther away from the Earth's centre, and both the incidence (zenith) angle and exit (nadir) angle (which are the same) approach 90°, the matter depth decreases to zero. At an incidence zenith of 89° the depth has reduced by over a factor 100 to a value (which depends on local density) typically $\sim$2–5 $\times 10^7\,\mathrm{g\,cm^{-2}}$. Since the cross-section rises with energy approximately as $E^{\frac{1}{3}}$ in this range, the characteristic energy scale at which the neutrinos become attenuated changes from 1 PeV to about 10^{19}–10^{20} eV at 89°. The Earth thus filters the neutrino spectrum in a complex way suppressing the high-energy part in a rapidly changing way as the zenith angle approaches the horizontal.

Besides attenuation there is a regeneration effect. Neutral current interactions shift the neutrino energy, transferring part of the absorbed flux into lower energies. In addition, the τ (μ) lepton produced in charged-current interactions can in turn decay producing ν_τ (ν_μ). This double sequence also regenerates the neutrino flux [34]. Typically, the absorbed high-energy ν_τ flux gives a τ which only decays when it is below a characteristic energy scale $\sim 10^8$ GeV (this is described in section 4.2). Regeneration is important below the smaller of this scale and the energy scale fixed by the absorption. For low zenith, the regeneration is important in the 1 PeV region [34] but for Earth-skimming neutrinos regeneration is most important at about 2×10^7 GeV as shown by simulations [76]. These neutrinos have to interact, produce a τ, exit the Earth and decay in the atmosphere so that the shower energy is further reduced. Since the electron is stable, there is no such effect for ν_e while for ν_μ the long μ lifetime results in regeneration at a low energy which is not relevant for this work. We will here consider neutral current regeneration but will not further discuss the ν_τ regeneration. The Earth-skimming rates obtained, particularly for the topological defect flux, will be somewhat underestimated at around 10^7 GeV.

4.2. Lepton propagation: energy loss and decay

Once a ν_μ or a ν_τ undergoes a charged-current interaction, the produced lepton has a probability to decay which increases as it loses energy while propagating in matter. The propagation of the lepton in the Earth determines the effective volume that is available for detection in this channel.

Following procedures similar to those described in [43, 52], we calculate the survival probabilities for leptons with continuous energy losses. The survival probability has the following differential equation:

$$\mathrm{d}P_{\mathrm{Surv}} = P_{\mathrm{Surv}} \frac{\mathrm{d}l}{c\beta\tau} \frac{mc^2}{E(l)}, \tag{17}$$

where l is the distance travelled, βc the lepton velocity, m its mass, τ its decay lifetime and $E(l)$ its energy, which decreases as l increases.

The energy loss can be expressed by an approximate expression

$$\frac{\mathrm{d}E}{\mathrm{d}x} = a + bE = \frac{\epsilon + E}{\xi} \tag{18}$$

in which the energy loss per unit depth (x) has a constant energy loss term associated with ionization (a) and a linear term in energy which is due to hard processes, bremsstrahlung, pair production and hadronic interactions. This is usually expressed in terms of a characteristic grammage, $\xi = 1/b$, and a critical energy, $\epsilon = a\xi$ above which radiative processes dominate. These values are slightly varying with energy and somewhat uncertain but they have implications for the τ production rate [37]. We here use the values $\xi = 1.25 \times 10^6\,\mathrm{g\,cm^{-2}}$ and $\epsilon = 3000\,\mathrm{GeV}$ consistent with results for the $10^8\,\mathrm{GeV}$ region in [77]. This equation can be integrated to give [78]

$$\frac{E + \epsilon}{E' + \epsilon} = \mathrm{e}^{-x/\xi}, \tag{19}$$

which relates E', the initial lepton energy, to E, the lepton energy after propagation over depth x. This expression can be used to express E in equation (17) in terms of l, assuming the lepton propagates at the speed of light in a constant density medium. With this substitution equation (17) can be integrated in x to obtain

$$P_{\mathrm{Surv}} = \left[\frac{E}{E'}\frac{E' + \epsilon}{E + \epsilon}\right]^{\eta} \simeq \left[1 - \epsilon\left(\frac{1}{E} - \frac{1}{E'}\right)\right]^{\eta}, \tag{20}$$

where the second approximate expression holds for $E \gg \epsilon$ and the exponent, η, is a constant that depends on the medium density ρ, on the lepton mass, m_l, its decay constant, τ_l, and the loss parameters ξ and ϵ:

$$\eta = \frac{m_l c^2 \xi}{\epsilon \rho c \tau_l}. \tag{21}$$

The value of η for muons in rock of density $2.65\,\mathrm{g\,cm^{-3}}$ is $\sim 3.5 \times 10^{-4}$ which implies that decay can be ignored for all cases of interest here (the muon lifetime is very long compared to energy loss time). In the atmosphere, $\eta \sim 0.66$ and the muon can decay in flight. However, for the energies of interest here, the muon exits the atmosphere well before decaying.

For the τ lepton propagating in standard rock, $\eta \simeq 3.2 \times 10^4$ is very large. This implies that unless the ratio of energies in equation (20) is very close to unity, the τ does not survive. We can

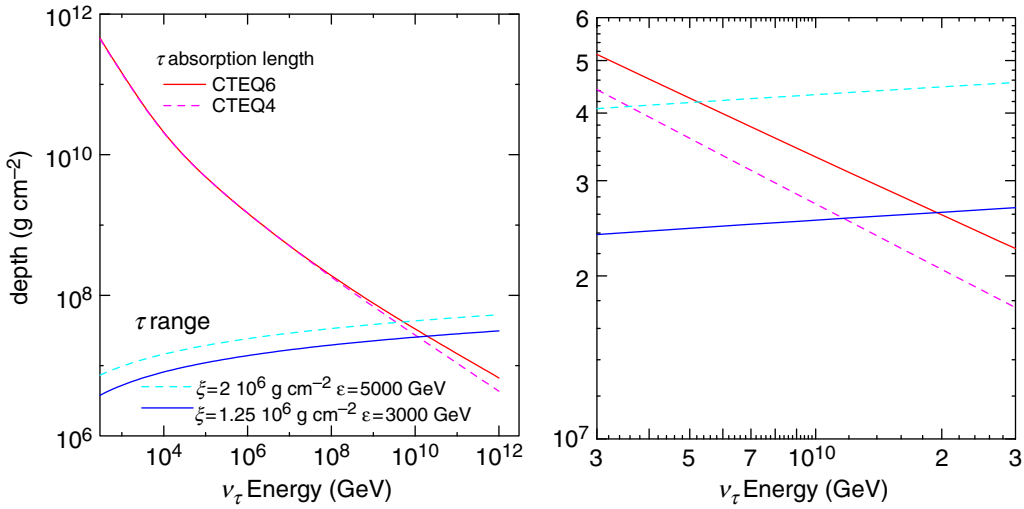

Figure 5. Comparison of the τ range and the ν_τ absorption length, using two different neutrino cross-sections (CTEQ4 and CTEQ6) and two different sets of parameters for τ energy loss. The right-hand side panel is a blow up of the intersection region.

then approximate equation (20) as

$$P_{\mathrm{Surv}} \simeq \exp\left[-\eta\frac{1-E/E'}{1+E/\epsilon}\right] = \exp\left[-\eta\frac{\epsilon}{E+\epsilon}\frac{E'-E}{E'}\right]. \tag{22}$$

For the τ not to decay the absolute value of the exponent must be small and the fraction of energy lost by τ is limited:

$$\frac{E'-E}{E'} < \frac{E+\epsilon}{\eta\epsilon} \simeq 3.1\times 10^{-5}\left[1+\frac{E}{\epsilon}\right]. \tag{23}$$

For E is below ϵ ionization losses dominate and the fraction of energy loss must be below a very small value. When $E \gg \epsilon$ this bound increases linearly with E, the energy of the τ after propagation, until it becomes 1 when $E \simeq \epsilon\eta$. This introduces a new energy scale for the emerging τ: $\epsilon\eta \simeq 9\times 10^7$ GeV.

The fraction of energy loss can be related to the τ range in rock through equation (19). Expanding the range for $x \ll \xi$ we obtain

$$E' - E \simeq \frac{x}{\xi}[E'+\epsilon]. \tag{24}$$

For $E < \epsilon\eta \simeq 9\times 10^7$ GeV the fraction of energy loss is below 1 and the above approximation holds. The range increases approximately linearly with E and so does the effective volume for neutrino detection through Earth-skimming neutrinos. This is an important energy scale because above it, the effective volume for neutrinos ceases to grow linearly with E. A second energy scale arises because of absorption. In figure 5, the range at which the survival probability is 0.5 is shown, plotted as a function of E'. It is compared to the matter depth at which the flux has been

reduced by a factor of 2 because of absorption. Two different cross-sections and two different values of the energy loss parameters have been used to illustrate the uncertainties involved. The crossover energy sets the limiting scale to a value between 10^9 and 10^{10} GeV above which neutrino absorption suppresses the τ rate.

4.3. The emerging τ flux

The calculation of the emerging τ flux proceeds in a relatively simple manner. Neutrinos arriving at a given zenith angle propagate through the Earth to a point along the corresponding Earth chord at which they interact. The total matter depth along the chord is $x_T(\theta)$ and the depth of the interaction point, x, is measured along the chord from the exit point. We assume that the neutrino flux at x can be expressed as $\phi_\nu[E_\nu]\mathrm{e}^{-g(x_T-x,E_\nu)}$. The τ rate produced in an interval of distance $\mathrm{d}x$ is simply obtained convoluting the differential neutrino flux at the interaction point with the differential cross-section $\mathrm{d}\sigma^{cc}/\mathrm{d}y$ multiplied by the τ survival probability

$$\frac{\mathrm{d}^5 N_\tau}{\mathrm{d}A\mathrm{d}\Omega\,\mathrm{d}t} = \phi[E_\nu]\mathrm{e}^{-g(x_T-x,E_\nu)}\mathrm{d}E_\nu\, N_A \mathrm{d}x \frac{\mathrm{d}\sigma^{cc}}{\mathrm{d}y}\mathrm{d}y \left[\frac{E_\tau}{E'_\tau}\frac{E'_\tau+\epsilon}{E_\tau+\epsilon}\right]^\eta, \tag{25}$$

where E'_τ and E_τ are respectively the τ energies at the interaction and exit points and ρ is the matter density at the interaction point.

Using equation (18), we can express $\mathrm{d}x$ in terms of $\mathrm{d}E_\tau$ to get the differential τ rate as the following integral:

$$\phi_\tau[E_\tau,\theta] = \frac{\xi}{E_\tau+\epsilon} N_A \int_{E_\tau}^{\infty} \mathrm{d}E_\nu\, \phi[E_\nu]\mathrm{e}^{-g(x_T-x,E_\nu)} \int_{y_{min}}^{y_{max}} \mathrm{d}y \frac{\mathrm{d}\sigma^{cc}}{\mathrm{d}y}\left[\frac{E_\tau}{E'_\tau}\frac{E'_\tau+\epsilon}{E_\tau+\epsilon}\right]^\eta. \tag{26}$$

The interaction point enters the expression through the function $g(x_T - x, E_\nu)$. Once E_ν and y are established, the τ lepton is produced with fixed energy $E'_\tau = E_\nu(1-y)$. If E_τ is also fixed, the interaction point x can be expressed in terms of the three variables $x(E_\nu, E_\tau, y)$ as

$$x = \xi \ln\left[\frac{E_\nu(1-y)+\epsilon}{E_\tau+\epsilon}\right]. \tag{27}$$

The limits of the y integral in (26) are

$$y_{\min} = \frac{1}{E_\nu}\max\left[E_\nu+\epsilon-(E_\tau+\epsilon)e^{x_T/\xi}, 0\right]; \tag{28a}$$

$$y_{\max} = 1 - \frac{E_\tau}{E_\nu}. \tag{28b}$$

The corresponding fluxes at different zeniths close to the horizontal are illustrated in figure 6 for the GRB flux used. A strong zenith-angle dependence is observed which arises in equation (26) from x_T, both in the function $g(\bar{x}, E_\nu)$ (with $\bar{x} = x_T - x$) and in the limit $y_{\min}$. To a good approximation, the function $g(\bar{x}, E_\nu)$ can be thought of as an attenuation due to the total cross-section σ_{tot} which is effectively reduced by regeneration. If we ignore regeneration due to the τ decays in matter, we can simply express it as $g(\bar{x}, E_\nu) = (x_T - x)\sigma_{eff}$, where the

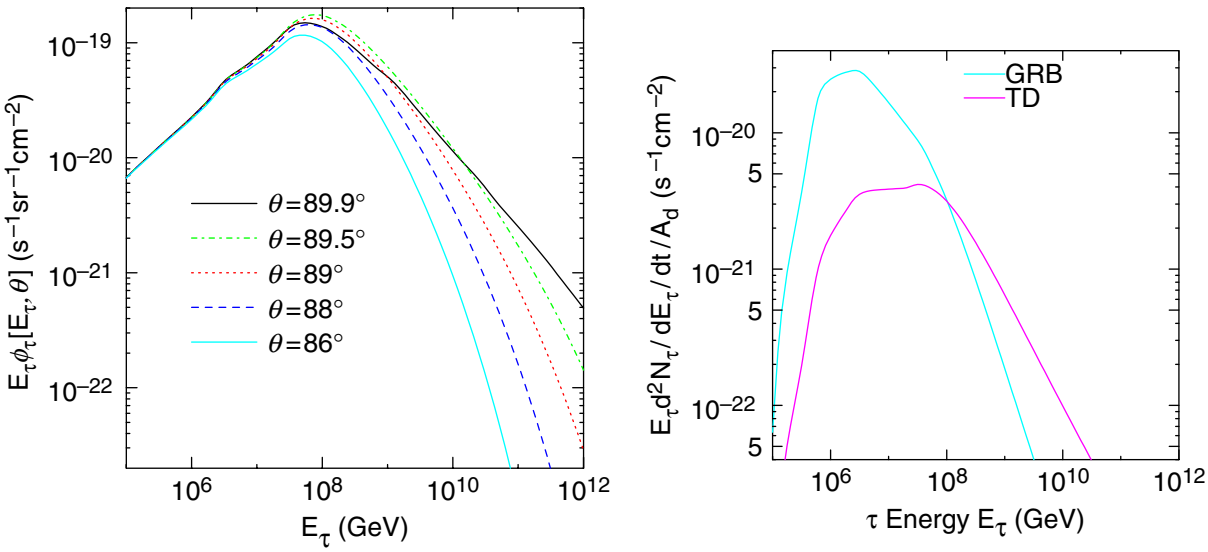

Figure 6. Differential τ spectra produced by Earth-skimming neutrinos. All τ's are included and the spectra are differential in τ energy, E_τ. Left panel: τ spectra for the GRB flux at different zenith angles. Right panel: τ spectra after solid angle integration for both the TD and GRB fluxes.

effective absorption cross-section is given by

$$\sigma_{eff} = \sigma_{tot} - \sigma_{reg} = \sigma_{tot} - \frac{1}{\phi_\nu(E_\nu)} \int_0^1 \mathrm{d}y \phi_\nu \left(\frac{E_\nu}{1-y}\right) \frac{\mathrm{d}\sigma^{nc}}{\mathrm{d}y} \left(\frac{E_\nu}{1-y}, y\right) \tag{29}$$

and $\mathrm{d}\sigma^{nc}/\mathrm{d}y$ is the differential neutral current interaction cross-section. It thus depends strongly on the zenith angle. We can finally integrate equation (26) over the solid angle to obtain the energy spectrum of the total emerging τ rate. The results for both fluxes are also shown in figure 6. We note that the bulk of the τ lepton spectrum is contained within about 3×10^5–10^7 GeV for the prediction from GRBs, while for topological defects, which is a harder flux, the range is $\sim 10^6$–3×10^8 GeV.

The Earth-skimming τ flux as a function of E_τ is a complex result from the competition of an increasing effective volume and cross-section for the neutrinos and a decreasing solid angle because of neutrino absorption. This is convoluted with a neutrino flux spectrum which often falls with energy like $\sim E_\nu^{-\gamma}$. The effective volume increases linearly with E_τ until the scale of 9×10^7 GeV is reached above which the rise is slow. The cross-section increases with energy as $E^{\sim 1/3}$ for $E_\tau > 100$ TeV while the solid angle decreases with approximately the inverse energy dependence. If $\gamma > 2$, the dominant part of the τ flux will be for energies at the 100 TeV scale which include all directions. But if $\gamma < 2$, the rate will be dominated by the turnover scale of 9×10^7 GeV. For hard spectral indices of order one, the dominant part of the flux shifts to the absorption scale $\sim 10^{10}$ eV and is strongly beamed in the horizontal direction.

4.4. The τ decay in the atmosphere

Finally, the emerging τ must decay to produce a detectable shower. The decay process is mediated by a W boson and always involves a ν_τ which is irrelevant from the point of view of the developed

shower. The charged boson couples to both electron and muon lepton pairs with probabilities close to 18%. When a $\mu\nu_\mu$ pair is produced there is no shower, while if a $e\nu_e$ pair is produced about one-third of the τ energy is expected to go into an electromagnetic shower. The remaining 64% of the times it couples to a quark–antiquark pair that fragments into hadrons, mostly between one and three hadrons. These showers can be considered hadronic. Assuming that the shower carries all the quark energy, we can expect about two-thirds of the total τ energy to go into the air shower. When all the probabilities are weighted together, the average fraction of energy carried by the shower is just below 50%.

The τ travels a distance l in the atmosphere to decay and produce a secondary shower that develops to reach the shower maximum at a further distance l_{sh}, which is a slowly varying function of shower energy (of order 10 radiation lengths or ~3 km in air for both electromagnetic and hadronic showers). The altitude at which the shower reaches the shower maximum is crucial for its detection and affects different types of detectors in different ways. This altitude is a combination of both the decay length and the distance to the shower maximum ($l + l_{sh}$), the nadir angle with which the τ exits and the curvature of the Earth. The differential decay probability is again given by equation (20), where we can now neglect the τ energy loss which is very small. The survival probability after travelling a distance l is simply

$$P_{\mathrm{Surv}} = \exp\{-l/(c\tau)mc^2/E_\tau\}. \tag{30}$$

For a given flux τ exiting the Earth, we can estimate the detection rate, integrating in length the flux multiplied by both the differential decay probability and the probability of detecting the shower

$$\frac{\mathrm{d}N_{sh}}{\mathrm{d}E_\tau} = \frac{\mathrm{d}l}{c\tau}\frac{mc^2}{E_\tau}\exp\{-l/(c\tau)mc^2/E_\tau\}\mathcal{P}^\tau_{det}[l, E_{sh}, \theta]\phi[E_\tau, \theta]. \tag{31}$$

We note that provided that $\mathcal{P}^\tau_{det}$ is known, the l integral can be in principle performed independently of the τ flux and expressed as an overall probability factor for detection, to multiply the rate obtained in equation (26). Unfortunately, this requires detailed knowledge of the detector response and it is extremely dependent on the threshold behaviour of the detector, which depends critically on shower development, geometry and the trigger conditions. The calculation of this is quite technical and difficult to estimate analytically. Precise calculations of $\mathcal{P}^\tau_{det}$ must be performed for each experiment. These functions are now being studied for detectors such as the surface array and fluorescence detector of the Pierre Auger Observatory, EUSO and others.

To understand the effect of this factor for an air-shower array, we consider that the shower will be detected provided that the particle density exceeds a given threshold at the point when the plane of shower maximum intercepts the ground level. The centre of the shower in this plane lies at a distance $r_g = h\sin\theta$ to the ground level where h is the altitude at which it lies above ground. The expression of h is simple in terms of l and l_{sh}

$$h = \sqrt{R_\oplus^2\cos^2\theta + (l + l_{sh})^2 + 2(l + l_{sh})R_\oplus\cos\theta} - R_\oplus, \tag{32}$$

where $R_\oplus$ is the Earth's radius. For a given shower energy we calculate r_{max}, the lateral distance below which the electron density of the shower is above threshold ρ_e. We make $h = r_{\max}\sin\theta$ and invert equation (32) to obtain the corresponding l. This value of l which we will denote $l_{\max}$

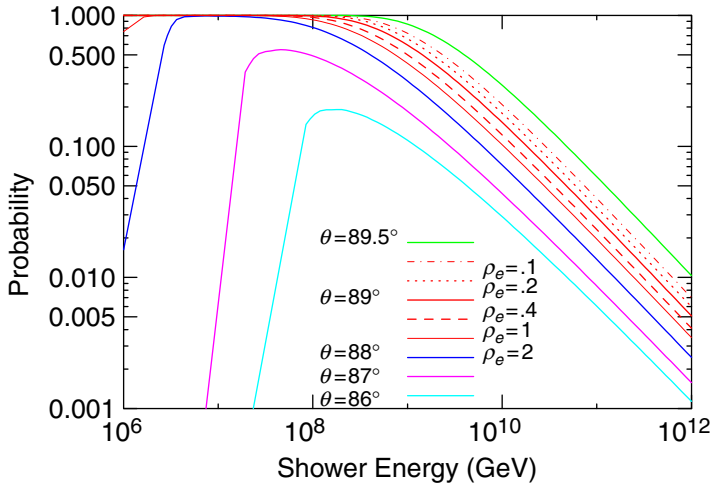

Figure 7. Integrated probability for the τ to decay in the atmosphere producing a shower that reaches ground level with electron number density (ρ_e) above different threshold values (in m^{-2}).

is the maximum distance the τ can travel before decaying to be successfully detected according to our simplifying assumptions.

The function chosen for $\mathcal{P}^{\tau}_{det}$ allows analytic integration of the probability factor, thus simplifying the calculation

$$\frac{\mathrm{d}N_{sh}}{\mathrm{d}E_\tau} = \mathcal{P}_{det}[E_\tau, \theta]\phi[E_\tau, \theta] = \{1 - \exp[-l_{\max}(c\tau)^{-1}mc^2E_\tau^{-1}]\}\phi[E_\tau, \theta]. \qquad (33)$$

We have expressed the detection probability integrated over decay length as an overall factor to multiply the τ flux rate. The corresponding suppression factor has been plotted in figure 7 for different zenith angles and different conditions to fix the minimum particle density to be detected at ground level. The probability is reduced for both low and high-energy showers. Low-energy showers do not meet the threshold requirement while high-energy showers have a maximum too high above the ground. At energies around 10^8 GeV, the detection restriction becomes important even for showers with 87° nadir angle.

4.5. The resulting shower rate for an air-shower array

The final shower rate recorded with an air-shower array is severely constrained by the probability that the shower has sufficient particle density at ground level to be detected and identified as deep shower. This rate can be estimated by taking the τ flux rate obtained in equation (26) and multiplying it by the integrated probability (as in equation (33)). We have calculated the resulting rates approximately as a function of the τ energy, taking into account that on average the τ decay showers carry about half the energy of τ. Different detection sensitivities are crudely implemented using $\rho_e = 0.1, 0.4$ and $1\ \mathrm{m}^{-2}$.

The total shower rates for the two models chosen are compared in figure 8 to the actual rate when the shower is required to be detected by an air-shower array. The total shower rates are just those shown in the right-hand panel of figure 6 rescaled to be differential in shower energy. When

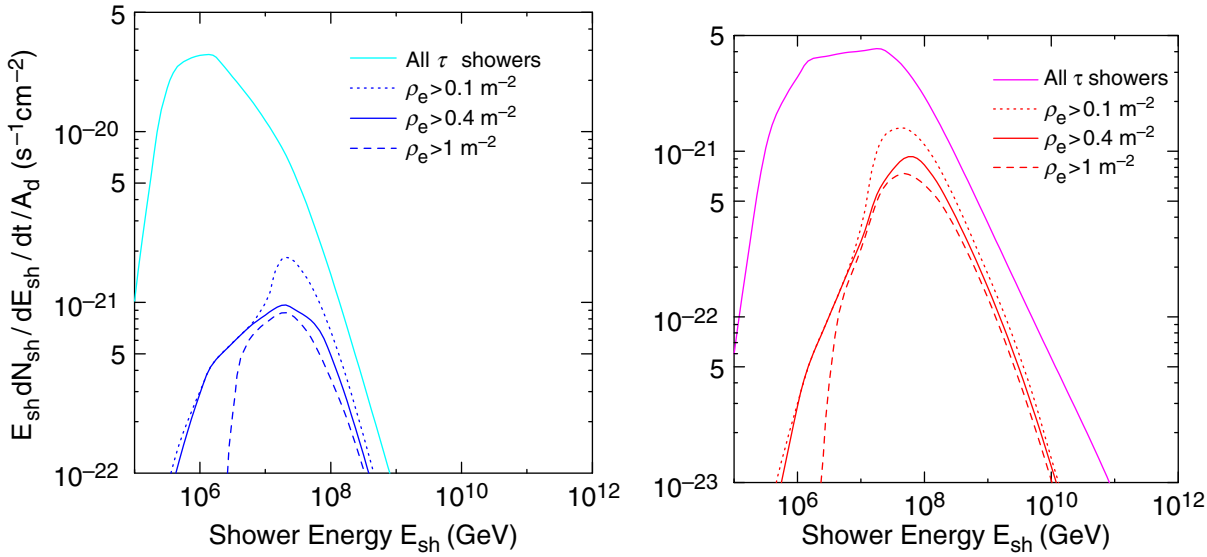

Figure 8. Comparison of the total τ shower rate produced by Earth-skimming $\nu_\tau + \bar{\nu}_\tau$ flux assuming that all τ's make showers and the detected shower rate in an air-shower array accounting for τ decay in the atmosphere and requiring electron number density at ground to be above different thresholds ($\rho_e > 0.1, 0.4, 1\ \mathrm{m}^{-2}$ from top to bottom). The left panel is for the GRB flux and the right panel for the TD model.

the decay probability and curvature of the Earth are accounted for as described in the previous subsection, the shower rate decreases quite dramatically at low energies when compared to the production rate, as illustrated by the figure. At high energies, the detection is suppressed simply because the showers decay too far away from the surface and this is not too dependent on ρ_e. At low energies, detection details become crucial and constrain the detection in an intricate way.

5. Discussion

We have finally plotted the rates of down-going showers induced by neutrinos compared to the up-coming shower rate induced by Earth-skimming neutrinos in figure 9 for the two fluxes discussed in this paper. The figure compares the results of figures 4 and 8. In this figure the maximum Earth-skimming τ shower rate (assuming all τ's induce a shower) is clearly shown to be larger than the down-going neutrino-induced shower rate in the energy region between 10^5 and 10^9 GeV. A fully efficient 1000 km^2 active area operating for a year corresponds to 3×10^{20} s cm^2 of aperture. This is the order of magnitude required for detection of the τ produced by Earth-skimming τ neutrinos for the lowest of the two discussed models (TD) assuming all τ's decay and are detected.

Unfortunately, it is not possible to detect all these τ decays with most existing detectors. Fluorescence detectors would be limited by duty cycle while detection of these showers by arrays of particle detectors on Earth surface is made complicated by an awkward geometry as indicated by the curves corresponding to the different thresholds. Moreover, the energy region

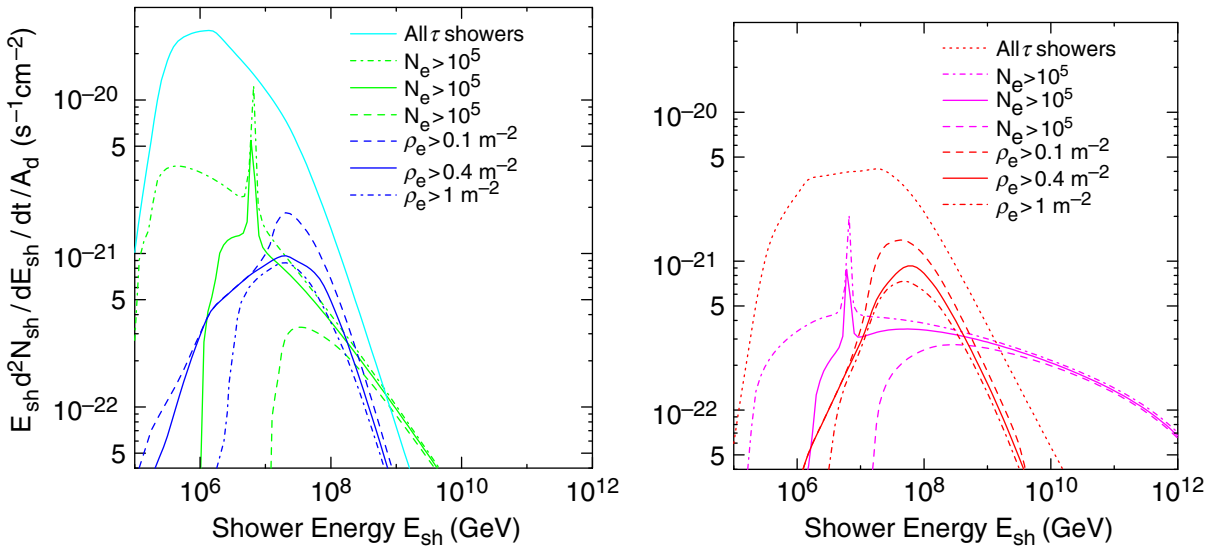

Figure 9. Down-going inclined shower rates compared to Earth-skimming up-coming shower rates from τ decays. The plot is the same as figure 8 but it also includes the shower rates obtained for down-going neutrinos as shown in figure 4.

where the Earth-skimming rates dominate is somewhat below the typical energies for detectors in construction such as the Auger detector. For a 1000 km^2 area, the expected peak rate is of order 4 (14) events per year for the TD (GRB) model between 10^6 and 4×10^7 GeV (3×10^5 and 3×10^6 GeV). This implies that if neutrinos are to be detected they would induce showers of energy very close to the detector threshold. As a result, the rate calculations are quite uncertain unless very detailed simulations are performed. Some of these have been made and results are in agreement with our calculations [37, 43].

The restriction introduced by air-shower arrays somewhat compensates the duty factor for fluorescence detection and this explains why roughly similar rates can be obtained for the fluorescence and surface detector calculations of the Earth-skimming event rates.

When decay probability, Earth curvature and detector sensitivity are included, the obtained rates for down-going and Earth-skimming events are not very different for an air-shower array. The differential shower rate from τ decay (induced by Earth-skimming neutrinos) dominates mostly in the energy region around 10^8 GeV and is limited to an interval of about one-and-a-half decades around this value. The relative rates will be very much dependent on the detector sensitivity in this energy range. The potential for neutrino detection relies on the detector capability to identify very inclined showers which are almost horizontal in the case of ν_τ Earth-skimming events. Once the zenith angle has been established, the detector must also identify them as late development or deep showers. Although τ decay showers induced by Earth-skimming neutrinos have higher potential for neutrino detection than down-going neutrino events, the actual relative rates in the air-shower arrays is very much dependent on detector details and should be quite comparable for detectors having energy thresholds in the 10^8 GeV range.

Acknowledgments

I thank the Kavli Institute for Cosmological Physics at the University of Chicago for its hospitality, where part of this work was developed and most of it written up. Much of the work and many ideas discussed here have been developed together with J Alvarez Muñiz, M Ave, J J Blanco Pillado, J W Cronin, F Halzen, J Hinton, A Husain, G Parente, T Stanev, R A Vázquez and A A Watson, over many years. I also thank P Privitera for several discussions, A A Watson for careful reading of the manuscript and Centro de Supercomputación de Galicia (CESGA) for computer resources. This work was supported in part by Ministerio de Educación y Ciencia (FPA 2001-3237, FPA 2002-01161, FPA 2004-01198), by Secretaría de Estado de Educación y Univesidades (Plan de Movilidad 2004), by Xunta de Galicia (PGIDIT02 PXIC 20611PN), by ESF neutrino network N-86, by Feder Funds and by the KICP under NSF grant PHY-0114422.

References

[1] Bird D J *et al* 1993 *Phys. Rev. Lett.* **71** 3401
[2] Hayashida N *et al* 1994 *Phys. Rev. Lett.* **73** 3491
[3] Takeda M *et al* 2003 *Astropart. Phys.* **19** 447 (*Preprint* astro-ph/0209422)
[4] Abbasi R U *et al* 2004 [High Resolution Fly's Eye Collaboration] *Phys. Rev. Lett.* **92** 151101 (*Preprint* astro-ph/0208243)
[5] Greisen K 1966 *Phys. Rev. Lett.* **16** 748
[6] Zatsepin G T and Kuzmin V A 1966 *Pis. Zh. Eksp. Teor. Fiz.* **4** 114
Zatsepin G T and Kuzmin V A 1966 *JETP Lett.* **4** 78 (Engl. Transl.)
[7] See for instance, Nagano M and Watson A A 2000 *Rev. Mod. Phys.* **72** 689 and references therein
[8] For a review see for instance, Olinto A V 2000 *Phys. Rep.* **333** 329
Bhattacharjee P and Sigl G 2000 *Phys. Rep.* **327** 109–247
[9] For a review see for instance, Gaisser T K, Halzen F and Stanev T 1995 *Phys. Rep.* **258** 173
Gaisser T K, Halzen F and Stanev T 1996 *Phys. Rep.* **271** 355 (erratum)
Learned J G and Mannheim K 2000 *Ann. Rev. Nucl. Part. Sci.* **50** 679
Halzen F and Hooper D 2002 *Rep. Prog. Phys.* **65** 1025
Waxman E 2004 *New J. Phys.* **6** 140
[10] Stecker F W, Done C, Salomon M H and Sommers P 1991 *Phys. Rev. Lett.* **66** 2697
[11] Berezinsky V S and Zatsepin G T 1969 *Phys. Lett.* B **28** 423
Berezinsky V S and Smirnov A Yu 1975 *Astrophys. Space Sci.* **32** 461
[12] Hara T *et al* 1970 *Proc. 11th Int. Cosmic Ray Conf. (Budapest) Acta Phys. Acad. Sci. Hung.* **29** (Suppl 3) 361
Nagano M *et al* 1971 *J. Phys. Soc. Japan* **30** 33
[13] Hillas A M *et al* 1969 *Proc. 11th Int. Cosmic Ray Conf. (Budapest) Acta Phys. Acad. Sci. Hung.* **29** (Suppl 3) 533–80
Andrews D *et al* 1970 *Acta Phys. Acad. Sci. Hung.* **29** 337–42
[14] Kiraly P *et al* 1971 *J. Phys. A: Gen. Phys.* **4** 367
[15] Mikamo S *et al* 1982 *Lett. Nuovo Cimento* **34** 273
[16] Zas E, Halzen F and Vázquez R A 1993 *Astropart. Phys.* **1** 297
[17] Parente G, Shoup A and Yodh G B 1995 *Astropart. Phys.* **3** 17
[18] Nagano M *et al* 1986 *J. Phys. G: Nucl. Part. Phys.* **12** 69
[19] Halzen F and Zas E 1992 *Phys. Lett.* B **289** 184
[20] Blanco-Pillado J J, Vázquez R A and Zas E 1997 *Phys. Rev. Lett.* **78** 3614
Tennent R M 1967 *Proc. Phys. Soc.* **92** 622
Lawrence M A, Reid R J O and Watson A A 1991 *J. Phys. G. Nucl. Part. Phys.* **17** 733

[21] Ave M, Hinton J A, Vazquez R A, Watson A A and Zas E 2003 *Phys. Rev.* D **67** 043005
[22] Design Report of the Pierre Auger Collaboration, October 1995
[23] Parente G and Zas E 1996 *Proc. 7th Int. Symp. on Neutrino Telescopes, Venice* ed M Baldo Ceolin, p 345
[24] Capelle K S, Cronin J W, Parente G and Zas E 1998 *Astropart. Phys.* **8** 321
[25] Agnetta G *et al* [EUSO Collaboration] 2003 *28th Int. Cosmic Ray Conf. (ICRC 2003) Tsukuba, 31 July–7 August 2003*
[26] Stecker F W 2003 *J. Phys. G: Nucl. Part. Phys.* **29** R47 (*Preprint* astro-ph/0309027)
[27] Fargion D, Aiello A and Conversano R 1999 *Preprint* astro-ph/9906450
[28] Yeh P *et al* [NuTel Collaboration] 2004 *Mod. Phys. Lett.* A **19** 1117
[29] Cao Z, Huang M A, Sokolsky P and Hu Y 2004 *Preprint* astro-ph/0411677
[30] Fukuda S *et al* [Super-Kamiokande Collaboration] 2001 *Phys. Rev. Lett.* **86** 5656 (*Preprint* hep-ex/0103033)
[31] Athar H, Jezabek M and Yasuda O 2000 *Phys. Rev.* D **62** 103007
[32] Learned J G and Pakvasa S 1995 *Astropart. Phys.* **3** 267 (*Preprint* hep-ph/9405296)
[33] Athar H, Parente G and Zas E 2000 *Phys. Rev.* D **62** 093010
[34] Halzen F and Saltzberg D 1998 *Phys. Rev. Lett.* **81** 4305
[35] Letessier-Selvon A 2001 *AIP Conf. Proc.* **566** 157 (*Preprint* astro-ph/0009444)
[36] Fargion D 2002 *Astrophys. J.* **570** 909 (*Preprint* astro-ph/0002453)
Fargion D 2003 *Proc. Int. Conf on Neutrino Telescopes, Venice* vol 2, pp 433–55 (*Preprint* hep-ph/0306238)
[37] Bertou X, Billoir P, Deligny O, Lachaud C and Letessier-Selvon A 2002 *Astropart. Phys.* **17** 183 (*Preprint* astro-ph/0104452)
[38] Feng J L, Fisher P, Wilczek F and Yu T M 2002 *Phys. Rev. Lett.* **88** 161102 (*Preprint* hep-ph/0105067)
[39] Bottai S and Giurgola S 2003 *Astropart. Phys.* **18** 539 (*Preprint* astro-ph/0205325)
[40] Gupta N 2002 *Phys. Lett.* B **541** 16 (*Preprint* astro-ph/0205451)
Gupta N 2003 *Phys. Rev.* D **68** 063006
[41] Tseng J J, Yeh T W, Athar H, Huang M A, Lee F F and Lin G L 2003 *Phys. Rev.* D **68** 063003 (*Preprint* astro-ph/0305507)
[42] Athar H, Cheung K, Lin G L and Tseng J J 2004 *Eur. Phys. J.* C **33** S959 (*Preprint* astro-ph/0311586)
[43] Aramo C, Insolia A, Leonardi A, Miele G, Perrone L, Pisanti O and Semikoz D V 2005 *Astropart. Phys.* **23** 65 (*Preprint* astro-ph/0407638)
[44] Han T and Hooper D 2004 *New J. Phys.* **6** 150 (*Preprint* hep-ph/0408348)
[45] Abbasi R U *et al* [High Resolution Fly's Eye Collaboration] 2004 *Phys. Rev. Lett.* **92** 151101
Abbasi R U 2004 *Astropart. Phys.* **22** 139
[46] Takeda M *et al* 2003 *Astropart. Phys.* **19** 135
[47] Abraham J *et al* 2004 *Nucl. Instrum. Methods* A **523** 50
[48] Ave M, Vázquez R A and Zas E 2000 *Astropart. Phys.* **14** 91
[49] Ave M, Vazquez R A, Zas E, Hinton J A and Watson A A 2000 *Astropart. Phys.* **14** 109
[50] Ave M, Hinton J A, Vazquez R A, Watson A A and Zas E 2000 *Phys. Rev. Lett.* **85** 2244
[51] Billoir P 1999 *8th Int. Workshop on Neutrino Telescopes, Venice, 23–26 February 1999* vol 2, ed M Baldo Ceolin, p 111
[52] Cazon L, Vazquez R A, Watson A A and Zas E 2004 *Astropart. Phys.* **21** 71
[53] Cronin J W 2005 *Nucl. Phys.* (Proc. Suppl.) B **138** 465
[54] Ave M (Auger Collaboration) 2003 *28th Int. Cosmic Ray Conf. (ICRC), Tsukuba*, vol 1, p 365
[55] Mccomb T J L and Turver K E 1982 *J. Phys. Soc. Japan* **51** 3087
[56] Cazon L, Vazquez R A and Zas E 2005 *Astropart. Phys.* **23** 393
[57] Gelmini G, Gondolo P and Varieschi G 2003 *Phys. Rev.* D **67** 017301
[58] González-García M C, Halzen F, Vázquez R A and Zas E 1994 *Phys. Rev.* D **49** 2310
[59] Parente G and Zas E 1997 *Proc. XXV Int. Cosmic Ray Conf.* (*Durban*) vol 7, p 201
[60] Gandhi R *et al* 1996 *Astropart. Phys.* **5** 81
[61] Parente G and Zas E 1995 *Proc. Int. Europhys. Conf. on High Energy Physics (HEP 95), Brussels*
Parente G and Zas E 1997 *Proc. XXV Int. Cosmic Ray Conf.* (*Durban*) vol 7, p 109

[62] Gandhi R, Quigg C, Reno M H and Sarcevic I 1998 *Phys. Rev.* D **58** 093009 (*Preprint* hep-ph/9807264)
[63] Kretzer S and Reno M H 2002 *Phys. Rev.* D **66** 113007 (*Preprint* hep-ph/0208187)
[64] Reno M H 2004 *Preprint* hep-ph/0410109
[65] Castro Pena J A, Parente G and Zas E 2001 *Phys. Lett.* B **507** 231
[66] Pumplin J, Stump D R, Huston J, Lai H L, Nadolsky P and Tung W K 2002 *J. High Energy Phys.* JHEP207(2002)012 (*Preprint* hep-ph/0201195)
[67] Castro Pena J A, Parente G and Zas E 2001 *Phys. Lett.* B **500** 125 (*Preprint* hep-ph/0011043)
[68] Alvarez-Muñiz J, Vázquez R A and Zas E 2000 *Phys. Rev.* D **61** 023001
[69] Weiler T J 2003 *Int. J. Mod. Phys.* A **18** 4065
[70] Waxman E and Bahcall J N 1997 *Phys. Rev. Lett.* **78** 2292
Razzaque S, Meszaros P and Waxman E 2004 *Phys. Rev. Lett.* **93** 181101
[71] Protheroe R J and Stanev T 1996 *Phys. Rev. Lett.* **77** 3708
Protheroe R J and Stanev T 1997 *Phys. Rev. Lett.* **78** 3420 (erratum) (*Preprint* astro-ph/9605036)
[72] Semikoz D V and Sigl G 2004 *J. Cosmol. Astropart. Phys.* JCAP404(2004)003 (*Preprint* hep-ph/0309328)
[73] Gaisser T K 1990 *Cosmic Rays and Particle Physics* (Cambridge: Cambridge University Press)
[74] Greisen K 1956 *Progress in Cosmic Ray Physics* vol III, ed J G Wilson (Amsterdam: North-Holland) p 1
[75] Parente G and Zas E 2005 in preparation
[76] Dutta S I, Reno M H and Sarcevic I 2002 *AIP Conf. Proc.* **624** 271
Jones J, Mocioiu I, Sarcevic I and Reno M H 2004 *Preprint* hep-ph/0408060
[77] Dutta S I, Reno M H, Sarcevic I and Seckel D 2001 *Phys. Rev.* D **63** 094020 (*Preprint* hep-ph/0012350)
[78] Lipari P and Stanev T 1991 *Phys. Rev.* D **44** 3543